National Library
of Canada

Acquisitions and
Bibliographic Services Branch

395 Wellington Street
Ottawa, Ontario
K1A 0N4

Bibliothèque nationale
du Canada

Direction des acquisitions et
des services bibliographiques

395, rue Wellington
Ottawa (Ontario)
K1A 0N4

Your file Votre référence

Our file Notre référence

NOTICE

The quality of this microform is heavily dependent upon the quality of the original thesis submitted for microfilming. Every effort has been made to ensure the highest quality of reproduction possible.

If pages are missing, contact the university which granted the degree.

Some pages may have indistinct print especially if the original pages were typed with a poor typewriter ribbon or if the university sent us an inferior photocopy.

Reproduction in full or in part of this microform is governed by the Canadian Copyright Act, R.S.C. 1970, c. C-30, and subsequent amendments.

AVIS

La qualité de cette microforme dépend grandement de la qualité de la thèse soumise au microfilmage. Nous avons tout fait pour assurer une qualité supérieure de reproduction.

S'il manque des pages, veuillez communiquer avec l'université qui a conféré le grade.

La qualité d'impression de certaines pages peut laisser à désirer, surtout si les pages originales ont été dactylographiées à l'aide d'un ruban usé ou si l'université nous a fait parvenir une photocopie de qualité inférieure.

La reproduction, même partielle, de cette microforme est soumise à la Loi canadienne sur le droit d'auteur, SRC 1970, c. C-30, et ses amendements subséquents.

Canada

UNIVERSITY OF ALBERTA

Geomechanics of the Steam Assisted Gravity Drainage Process in Heavy Oil Reservoirs

by

Richard John Chalaturnyk

©

A thesis submitted to the Faculty of Graduate Studies and Research in partial fulfillment of the requirements of the degree of **Doctor of Philosophy**.

in

Geotechnical Engineering

Department of Civil Engineering

Edmonton, Alberta

Spring 1996

National Library
of Canada

Acquisitions and
Bibliographic Services Branch

395 Wellington Street
Ottawa, Ontario
K1A 0N4

Bibliothèque nationale
du Canada

Direction des acquisitions et
des services bibliographiques

395, rue Wellington
Ottawa (Ontario)
K1A 0N4

Your file Votre référence

Our file Notre référence

The author has granted an irrevocable non-exclusive licence allowing the National Library of Canada to reproduce, loan, distribute or sell copies of his/her thesis by any means and in any form or format, making this thesis available to interested persons.

L'auteur a accordé une licence irrévocable et non exclusive permettant à la Bibliothèque nationale du Canada de reproduire, prêter, distribuer ou vendre des copies de sa thèse de quelque manière et sous quelque forme que ce soit pour mettre des exemplaires de cette thèse à la disposition des personnes intéressées.

The author retains ownership of the copyright in his/her thesis. Neither the thesis nor substantial extracts from it may be printed or otherwise reproduced without his/her permission.

L'auteur conserve la propriété du droit d'auteur qui protège sa thèse. Ni la thèse ni des extraits substantiels de celle-ci ne doivent être imprimés ou autrement reproduits sans son autorisation.

ISBN 0-612-10577-6

Canada

University of Alberta

LIBRARY RELEASE FORM

NAME OF AUTHOR:	Richard John Chalaturnyk
TITLE OF THESIS:	Geomechanics of the Steam Assisted Gravity Drainage Process in Heavy Oil Reservoirs
DEGREE	Doctor of Philosophy
YEAR THIS DEGREE GRANTED:	1996

Permission is hereby granted to the University of Alberta Library to reproduce single copies of this thesis and to lend or sell such copies for private, scholarly or scientific research purposes only.

The author reserves all other publication and other rights in association with the copyright in the thesis, and except as hereinbefore provided neither the thesis nor any substantial portion thereof may be printed or otherwise reproduced in any material form whatever without the author's prior written permission.

Permanent Address:

#18 Oakmont Drive
St. Albert, Alberta
T8N 6K6

DATE: April 17, 1996

UNIVERSITY OF ALBERTA

FACULTY OF GRADUATE STUDIES AND RESEARCH

The undersigned certify that they have read, and recommend to the Faculty of Graduate Studies and Research for acceptance, a thesis entitled ***Geomechanics of the Steam Assisted Gravity Drainage Process in Heavy Oil Reservoirs*** submitted by Richard John Chalaturnyk in partial fulfillment of the requirements for the degree of Doctor of Philosophy in Geotechnical Engineering.

Dr. P.K. Robertson, Professor
Committee Chair & Examiner
Department of Civil Engineering
University of Alberta

J. D. Scott
Dr. J.D. Scott, Professor Emeritus
Supervisor
Department of Civil Engineering
University of Alberta

D C Sego
Dr. D.C. Sego, Professor
Co-Supervisor
Department of Civil Engineering
University of Alberta

Dr. N.R. Morgenstern, University Professor
Department of Civil Engineering
University of Alberta

D W Murray
Dr. D.W. Murray, Professor Emeritus
Department of Civil Engineering
University of Alberta

Dr. S.M. Farouq Ali, Professor
Department of Petroleum Engineering
University of Alberta

Dr. P.M Byrne, Professor
Department of Civil Engineering
University of British Columbia

Date: December 5, 1995

ABSTRACT

Over the past two decades, the decline in reserves of conventional crude oil has led to the development of several methods of enhanced oil recovery for heavy oil deposits. A special form of steam flooding, known as steam assisted gravity drainage (SAGD), was developed to provide a process which could recover more oil than is possible by conventional steam flooding processes. The SAGD process results in a complex interaction of geomechanics and multiphase thermal flow in cohesionless porous media. Mean stress and/or shear induced volume changes within the reservoir from fluid pressure and temperature changes will result in changes in absolute permeability. Absolute permeability of the reservoir affects the drainage of fluids from the steam front and therefore the frontal advance rate and the production rate; it is one the most important parameters in the effectiveness of the SAGD process.

This research encompassed the analysis of laboratory, field instrumentation and numerical modeling results to identify geomechanical phenomena which influence the steam assisted gravity drainage recovery process. A laboratory testing program characterized thermal volume change, thermal conductivity, compressibility, stress-strain-strength and gas evolution and composition of oil sands, shale and limestone materials. Field instrumentation results from steam assisted gravity drainage process trials provided field evidence of geomechanical phenomena in the SAGD process. Numerical modeling studies served to elucidate fundamental geomechanical principles affecting the SAGD process. It was shown that formation displacements within the reservoir are capable of significantly influencing reservoir properties. Vertical extensional strains of 2.5%, horizontal extensional strains of 0.3%, volumetric strains of 2.5% and a 30% to 40% increase in absolute permeability were measured within the reservoir as a result of the SAGD process.

ACKNOWLEDGEMENTS

"Ability is of little account without opportunity"

The author wishes to express his appreciation and gratitude for the support and "'opportunity" provided by his supervisor Dr. J.D. (Don) Scott. The guidance given by Dr. Scott, both personally and professionally, is warmly acknowledged. The assistance of the author's co-supervisor, Dr. D.C. Sego, is appreciated; especially in the late stages of thesis completion where the words of encouragement " is it finished yet" served to provide ample motivation.

The time and sacrifice required to complete a thesis are not endured entirely by the author. The love and support provided by my wife Tracy and our children; Lauren and Jonathan during my academic tenure are lovingly acknowledged.

To my father, John, who while unable to share in the joy of his son completing a Ph.D. thesis, provided the words of encouragement "you **will** get a University education" - Thanks Dad.

A special thank you to the project team involved in the Underground Test Facility Phase A program: Neil Edmunds, Jack Suggett, Simon Gittins, Pat Collins and many others. The many discussions with Jim Laing and John Graham of Thurber Engineering helped with understanding the intracacies of geotechnical instrumentation.

A large component of this research was a thermomechanical laboratory program. Successfully completing this testing program was due in part to the diligent and supportive assistance of Jan Radziszewski, Linda Bobey and Hal Soderberg; thank you for the help. As well, the unseemingly endless support provided by Gerry Cyre, Steve Gamble and Christine Hereygers is gratefully acknowledged.

A special thank you for the support and sacrifices made by colleagues at PRO•MORE Engineering, in particular Terry Moffatt, who gave me an "opportunity" to complete my thesis.

TABLE OF CONTENTS

Chapter Page

1. INTRODUCTION

1.1 Problem Statement 1
1.2 Reservoir Geomechanics 2
1.2.1 Constitutive Behavior of Oil Sands and Related Strata 2
1.2.2 Reservoir Processes 4
1.2.3 Numerical Modeling 5
1.2.4 Geomechanics Monitoring of Reservoir Processes 5
1.3 Objective of Research Program 5
1.4 Organization of Thesis 10

2. UNDERGROUND TEST FACILITY

2.1 Project Description 12
2.2 Principles of the Steam Assisted Gravity Drainage Process 13
2.2.1 Process Facilities 13
2.2.2 Mechanics of SAGD 14
2.3 Geology 15
2.3.1 Local Phase A Geology 18
2.4 Geotechnical Cross Section 20

3. RESERVOIR INSTRUMENTATION PROGRAM

3.1 Introduction 35
3.2 Types of Instrumentation 35
3.2.1 Temperature 35
3.2.1.1 Thermocouples 35
3.2.1.2 Vibrating Wire Piezometers 36
3.2.1.3 Extensometer Thermistor 36
3.2.2 Pore Pressure 36
3.2.2.1 Vibrating Wire Piezometer 36
3.2.2.2 Pneumatic Piezometer 36
3.2.3 Vertical Strains 37
3.2.4 Horizontal Displacements 38
3.2.4.1 Gyrodata Wellbore Surveyor 39
3.3 Instrumentation Layout 41
3.3.1 Thermocouples 41
3.3.2 Inclinometers 41

3.3.3 Extensometers 42
3.3.4 Piezometers 42
3.4 Summary 42

4. THERMOMECHANICAL PROPERTIES

4.1 Introduction 57
4.2 Specimen Description and Location 58
4.3 Thermal Volume Change 59
4.3.1 Implications for SAGD Processes 59
4.3.2 McMurray Formation Oil Sands 62
4.3.3 McMurray Formation Shale 64
4.3.4 Waterways Formation Limestone 65
4.4 Thermal Conductivity 66
4.4.1 Implications for SAGD Processes 66
4.4.2 McMurray Formation Oil Sands 68
4.4.3 McMurray Formation Shale 69
4.4.4 Waterways Formation Limestone 70
4.5 Bulk Compressibility 71
4.5.1 Implications for SAGD Processes 71
4.5.2 Compressibility in Reservoir Geomechanics 71
4.5.3 McMurray Formation Oil Sands 75
4.5.4 McMurray Formation Shale 76
4.5.5 Waterways Formation Limestone 78
4.6 Strength and Stress-Strain Behavior 78
4.6.1 Implications for SAGD Processes 78
4.6.2 McMurray Formation Oil Sands 80
4.6.2.1 Stress-Deformation Behavior 81
4.6.2.2 Stress-Induced Permeability Changes 83
4.6.3 Upper McMurray Formation Shale 86
4.6.4 Lower McMurray Formation Shale 87
4.6.5 Waterways Formation Limestone 89
4.6.5.1 Unconfined Compression 90
4.6.5.2 Triaxial Compression 91
4.7 Gas Evolution and Composition 94
4.7.1 Implications for SAGD Processes 94
4.7.2 Oil Sands 95

4.8 Summary 97

5. PARAMETRIC ANALYSES OF IDEALIZED SAGD PROCESS

5.1 Introduction 153
5.2 Numerical Models 153
  5.2.1 ISCOM 154
  5.2.2 FLAC 154
5.3 Idealized Reservoir 154
  5.3.1 Geometry 154
  5.3.2 Material Properties 155
5.4 Analysis Procedure 156
  5.4.1 Temperature and Pore Pressures 157
  5.4.2 Base Analysis 157
  5.4.2 Parametric Analyses 158
5.5 Base Analysis Results 158
  5.5.1 Mobilized Strength 158
  5.5.2 Deformation 161
  5.5.3 Strain 161
    5.5.3.1 Vertical Strain 161
    5.5.3.2 Maximum Shear Strain 162
5.6 Parametric Analyses 163
  5.6.1 Stiffness 163
  5.6.2 Initial Stress Ratio, K_o 165
  5.6.3 Shear Induced Volume Change 165
  5.6.4 Thermal Expansion 166
  5.6.5 Bulk Modulus from Lab Measurements 167
5.7 Summary 168

6. FORMATION RESPONSE TO SAGD PROCESS

6.1 Introduction 236
6.2 Process History 236
  6.2.1 Injection/Production Pressures 236
  6.2.2 Steam Chamber Development 237
    6.2.2.1 Prior to Time 0.0 239
    6.2.2.2 Time 0.0 to 2.9 240
    6.2.2.3 Time 2.9 to 4.3 242

6.2.2.4 Time 4.3 to 5.7 243
6.2.2.5 Time 5.7 to 7.1 243
6.2.2.6 Time 7.1 to 8.6 243
6.2.2.7 Time 8.6 to 10.0 244
6.3 Theory for Full Strain Field Determination 244
6.4 Vertical Strains 248
6.4.1 Extensometer Histories 248
6.4.1.1 Well AGE2 248
6.4.1.2 Well AGE3 250
6.4.1.3 Well AGE4 253
6.4.1.4 Summary 255
6.4.2 Operation of Extensometers 255
6.4.2.1 Introduction 256
6.4.2.2 Calibration 256
6.4.3 Vertical Strains within Geotechnical Cross Section 258
6.5 Horizontal Displacements 258
6.5.1 Horizontal Displacements within Geotechnical Cross Section . 259
6.6 Full Strain Field in Geotechnical Cross Section 260
6.6.1 Bounday Conditions 260
6.6.2 Strain Field 261
6.6.2.1 Vertical Strain 261
6.6.2.2 Horizontal Strain 263
6.6.2.3 Maximum Shear Strain 263
6.6.2.4 Volumetric Strain 264
6.6.2.5 Absolute Permeability 264
6.7 Summary 265

7. GEOTECHNICAL CROSS SECTION ANALYSIS

7.1 Introduction 331
7.2 Problem Statement 331
7.2.1 Modeling Procedure 331
7.2.1.1 Field Pore Pressures 331
7.2.1.2 Field Temperatures 332
7.2.2 Geotechnical Cross-Section Geometry 332
7.2.3 Material Properties 332
7.3 Geotechnical Cross Section Analysis 333

7.3.1 Mobilized Strength 333
7.3.2 Maximum Shear Strain 334
7.4 Comparison of Field Instrumentation and Numerical Results 334
7.4.1 Inclinometer 334
7.4.2 Extensometer 335
7.5 Summary 335

8. CONCLUSIONS

8.1 General 357
8.2 Geomechanical Properties for SAGD Process 358
8.3 Geomechanical Modeling for SAGD Processes 360
8.3.1 Parametric Analysis 360
8.3.2 Geotechnical Cross Section Analysis 361
8.4 Geomechanical Response of Resrvoir to SAGD Processes 362
8.5 Recommendations for Further Research 363
REFERENCES 365
APPENDIX A Field Thermocouple Results 372
APPENDIX B Field Piezometer Results 392
APPENDIX C Field Extensometer Results 431
APPENDIX D Field Inclinometer Results 462
APPENDIX E Temperature Distribution within Geotechnical Cross Section 506
APPENDIX F Pore Pressure Distribution within Geotechnical Cross Section 526
APPENDIX G Specimen Data 546

LIST OF TABLES

Table 2.1 Facies Description 21

Table 4.1 Nomenclature for Thermomechanical Testing Codes 103

Table 4.2 Summary of Initial Specimen Data (continued) 104

Table 4.3 Comparison of Index Properties for Oil Sands Thermal Expansion Tests 106

Table 4.4 Summary for Consolidated Drained Triaxial Compression Tests - Oil Sands 107

Table 4.5 Specimen Properties from Experimetal Program of Oldakowski (1994) 108

Table 4.6 Summary of Consolidated Drained Triaxial Compressions Tests - Upper Shale 109

Table 4.7 Summary of Consolidated Drained Triaxial Compressions Tests - Lower Shale 110

Table 4.8 Summary of Unconfined Compression Tests - Limestone 111

Table 4.9 Summary of Consolidated Drained Triaxial Compression Tests - Limestone 111

Table 5.1 Material Properties for Reservoir and Geomechanical Analyses 170

Table 5.2 Range of Material Properties Chosen for Parametric Analyses 171

Table 6.1 Summary of Significant Events - Phase A Steaming Trials: Time 8.2 to 10.0 267

Table 6.2 Pore Pressure Values within Geotechnical Cross Section 270

Table 6.3 Relative Displacement/Vertical Strain History for Well AGE2 271

Table 6.4 Relative Displacement/Vertical Strain History for Well AGE3 272

Table 6.5 Relative Displacement/Vertical Strain History for Well AGE4 273

Table 7.1 Material Properties for Geotechnical Cross Section Analyses 337

Table D1 Well AGI1 Borehole Uncertainty Analysis 464

Table D2 Well AGI2 Borehole Uncertainty Analysis 471

Table D3 Well AGI3 Borehole Uncertainty Analysis 479

Table D4 Well AGI4 Borehole Uncertainty Analysis 486

Table D5 Well AT1 Borehole Uncertainty Analysis 493

Table D6 Well AT7 Borehole Uncertainty Analysis 500

LIST OF FIGURES

Figure 2.1 Location of the Underground Test Facility 23
Figure 2.2 Overall Layout of the Underground Test Facility 23
Figure 2.3 Schematic Representation of the UTF Phase A SAGD Process 24
Figure 2.4 Schematic of SAGD Process 24
Figure 2.5 Ceiling vs. Slope Drainage Processes 25
Figure 2.6 Steam Chamber Growth in Homogeneous, Isotropic Sand 26
Figure 2.7 Steam Chamber Growth in Homogeneous, Anisotropic Sand 26
Figure 2.8 Geology of the UTF Site 27
Figure 2.9 Location Map for Regional Structural Cross Sections 27
Figure 2.10 Structural Cross-Sections A-A' and B-B' 28
Figure 2.11 Stratigraphic Column for McMurray Formation 29
Figure 2.12 Isopach's of Geological Units Within the McMurray Formation 30
Figure 2.13 Location of Phase A Stuctural Cross Sections 31
Figure 2.14 West-East Structural Cross Section A-A' 31
Figure 2.15 West-East Structural Cross Section B-B' 32
Figure 2.16 West-East Structural Cross Section C-C' 32
Figure 2.17 West-East Structural Cross Section D-D' 33
Figure 2.18 Isometric View of Shale Barriers - Looking from North to the South 33
Figure 2.19 Isometric View of Shale Barriers - From the South and the Southeast 34
Figure 3.1 Schematic Illustration of Vibrating Wire Piezometer 43
Figure 3.2 Schematic Illustration of Pneumatic Piezometer 43
Figure 3.3 Schematic of Piezometer Actuator Device 44
Figure 3.4 Configuration of Typical Piezometer Instrumentation Well 45
Figure 3.5 Configuration of Typical Extensometer Instrumentation Well 46
Figure 3.6 Photograph of Extensometer Module Anchor 47
Figure 3.7 Technical Information on Gryodata Wellbore Surveyor 48
Figure 3.8 Wellbore Geometry Assumed for Minimum Curvature Method 49
Figure 3.9 Pre-Steaming Multiple GWS Surveys in Well AGI2 50
Figure 3.10 Level of Repeatibility for Multiple Surveys in Well AGI2 51
Figure 3.11 Magnitude of Error for Repeat Surveys in Well AGI2 52
Figure 3.12 Plan View of Instrument Well Locations 53
Figure 3.13 Location of Temperature Measurement Points within Geotechnical Cross Section 54

Figure 3.14 Location of Inclinometer Wells within Geotechnical Cross Section 55
Figure 3.15 Location of Extensometer Modules within Geotechnical Cross Section 56
Figure 3.16 Location of Piezometers within Geotechnical Cross Section 56
Figure 4.1 Schematic of High Temperature Triaxial Cell 112
Figure 4.2 Schematic of High Temperature Oedometer Cell 113
Figure 4.3 Schematic of Transient State Thermal Conductivity Test Cell 114
Figure 4.4 Schematic of Gas Evolution Mercury Triaxial Cell 115
Figure 4.5 Plan View of Wells Used for Geotechnical Sampling 116
Figure 4.6 Relative Position of Test Specimens within Phase A Reservoir 116
Figure 4.7 Role of Thermal Expansion Processes during SAGD 117
Figure 4.8 Constrained Bulk Thermal Expansion of McMurray Formation Oil Sands 118
Figure 4.9 Comparison of OSDTE1 and OSDTE2 Thermal Expansion to Kosar (1989) Results 118
Figure 4.10 Structural Response of McMurray Formation Oil Sands during Constrained Thermal Expansion 119
Figure 4.11 Coefficient of Constrained Bulk Thermal Expansion for McMurray Formation Oil Sands 119
Figure 4.12 Constrained Bulk Thermal Expansion of Upper McMurray Formation Shale 120
Figure 4.13 Coefficient of Constrained Bulk Thermal Expansion for Upper McMurray Formation Shale 120
Figure 4.14 Comparison of Upper McMurray Formation Shale and Clearwater Formation Shale Thermal Expansion Behavior 121
Figure 4.15 Constrained Bulk Thermal Expansion of Limestone 121
Figure 4.16 Process of Heat Conduction for Two Primary Flow Mechanisms of SAGD 122
Figure 4.17 Impact of Heat Conduction on Temperature of Produced Fluids 123
Figure 4.18 Thermal Conductivity of McMurray Formation Oil Sands 124
Figure 4.19 Comparison of Thermal Conductivities for Oil Sands 124
Figure 4.20 Thermal Conductivity of Lower and Upper McMurray Formation Shale 125
Figure 4.21 Thermal Conductivity of Waterways Formation Limestone 125
Figure 4.22 Constrained Bulk Volume Change of McMurray Formation Oil Sands 126
Figure 4.23 Coefficient of Constrained Bulk Compressibility fo McMurray Formation Oil Sands 126
Figure 4.24 Isotropic Bulk Compressibility of McMurray Formation Oil Sands 127

Figure 4.25 Coefficients of Isotropic Bulk (C_b), Rock (C_R), and Pore (C_ϕ), Compressibility 128
Figure 4.26 Coefficients of Constrained Bulk (C_{cb}), Rock (C_{cR}), and Pore ($C_{c\phi}$), Compressibility 129
Figure 4.27 Constrained Bulk Compressibility of Upper McMurray Formation Shale (USUTE2) 130
Figure 4.28 Coefficient of Constrained Bulk Compressibility for Upper McMurray Formation Shale (USUTE2) 130
Figure 4.29 Influence of Shale Interbedding on Bulk Compressibility of McMurray Formation Oil Sands 131
Figure 4.30 Constrained Bulk Compressibility of Waterways Formation Limestone 132
Figure 4.31 Coefficient of Constrained Bulk Compressibility for Waterways Formation Limestone 132
Figure 4.32 Major Stress Path Followed within Reservoir during SAGD Process 133
Figure 4.33 Isotropically Consolidated Drained Triaxial Compression Tests on McMurray Formation Oil Sands - 20 °C 134
Figure 4.34 Peak Failure Envelope for McMurray Formation Oil Sands 135
Figure 4.35 Variation of Young's Modulus with Effective Confining Stress - McMurray Formation Oil Sands 136
Figure 4.36 Comparison E vs. σ'_3 Relationships for Dense Sands 137
Figure 4.37 Absolute Permeability Change versus Porosity Change for Reconstituted, Oil-Free McMurray Formation Oil Sands 137
Figure 4.38 Relative Permeability and Bitumen Viscosity Relationships for UTF Phase A Reservoir 138
Figure 4.39 Equivalent Hydraulic Conductivity of Oil Sands as a Function of Water Saturation and Temperature 139
Figure 4.40 Effect of Water Saturation on Effective Permeability to Water 140
Figure 4.41 Isotropically Consolidated Drained Triaxial Compression Tests on Upper McMurray Formation Shale - 20 °C 141
Figure 4.42 Isotropically Consolidated Drained Triaxial Compression Tests on Upper McMurray Formation Shale - 225 °C 142
Figure 4.43 Peak Failure Envelope for Upper McMurray Formation Shale: 20°C & 225 °C 143
Figure 4.44 Variation of Young's Modulus with Effective Confining Stress for Upper McMurray Formation Shale: 20°C & 225 °C 143
Figure 4.45 Isotropically Consolidated Drained Triaxial Compression Tests on Lower McMurray Formation Shale - 20 °C 144
Figure 4.46 Isotropically Consolidated Drained Triaxial Compression Tests on Upper McMurray Formation Shale - 225 °C 145
Figure 4.47 Peak Failure Envelope for Lower McMurray Formation Shale: 20°C & 225 °C 146

Figure 4.48 Variation of Young's Modulus with Effective Confining Stress for Lower McMurray Formation Shale: 20°C & 225 °C 146
Figure 4.49 Unconfined Compression Tests on Waterways Formation Limestone 147
Figure 4.50 Isotropically Consolidated Drained Triaxial Compression Tests on Waterways Formation Limestone - 20 °C 148
Figure 4.51 Isotropically Consolidated Drained Triaxial Compression Tests on Waterways Formation Limestone - 225 °C 149
Figure 4.52 Peak Failure Envelope for Waterways Formation Limestone: 20°C & 225 °C 150
Figure 4.53 Variation of Young's Modulus with Effective Confining Stress Waterways Formation Limestone: 20°C & 225 °C 150
Figure 4.54 Gas Evolution Test on McMurray Formation Oil Sands 151
Figure 4.55 Composition of Evolved Gas from McMurray Formation Oil Sands 152
Figure 5.1 Idealized Geology and Cross Section of UTF Phase A Reservoir 172
Figure 5.2 Zone of Symmetry for Ideal Analyses 172
Figure 5.3 Finite Difference Grids used in Numerical Analyses: a)ISCOM and b) FLAC 173
Figure 5.4 Idealized Relation for Dilation Angle, ψ, from Triaxial Test Results 174
Figure 5.5 Temperature Distribution at 10 Days 175
Figure 5.6 Temperature Distribution at 85 Days 176
Figure 5.7 Temperature Distribution at 100 Days 177
Figure 5.8 Temperature Distribution at 101 Days 178
Figure 5.9 Temperature Distribution at 180 Days 179
Figure 5.10 Temperature Distribution at 250 Days 180
Figure 5.11 Temperature Distribution at 365 Days 181
Figure 5.12 Temperature Distribution at 458 Days 182
Figure 5.13 Temperature Distribution at 591 Days 183
Figure 5.14 Temperature Distribution at 730 Days 184
Figure 5.15 Pore Pressure Distribution at 10 Days 185
Figure 5.16 Pore Pressure Distribution at 85 Days 186
Figure 5.17 Pore Pressure Distribution at 100 Days 187
Figure 5.18 Pore Pressure Distribution at 101 Days 188
Figure 5.19 Pore Pressure Distribution at 180 Days 189
Figure 5.20 Pore Pressure Distribution at 250 Days 190
Figure 5.21 Pore Pressure Distribution at 365 Days 191
Figure 5.22 Pore Pressure Distribution at 458 Days 192

Figure 5.23 Definition of Failure Index for Describing Mobilized Strength 193

Figure 5.24 Failure Index Distribution at 85 Days - Base Case 194

Figure 5.25 Failure Index Distribution at 180 Days - Base Case 195

Figure 5.26 Failure Index Distribution at 250 Days - Base Case 196

Figure 5.27 Schematic Diagram Showing Process of Shear Yield in Reservoir 197

Figure 5.28 Failure Index Distribution at 365 Days - Base Case 198

Figure 5.29 Failure Index Distribution at 458 Days - Base Case 199

Figure 5.30 Failure Index Distribution at 730 Days - Base Case 200

Figure 5.31 Stress Path for Element along Left Boundary of Grid 201

Figure 5.32 Volumetric Strain Behavior for Active Compression Stress Path Triaxial Test 202

Figure 5.33 Variation in k_a/k_a^o with Mobilized Strength Derived from Active Compression Triaxial Test Results 203

Figure 5.34 Shear Induced Permeability Changes at 180 and 365 Days 204

Figure 5.35 Variation of Absolute Permeability within Reservoir at Time 365 Days 205

Figure 5.36 Displacement Field at 101 Days - Base Case 206

Figure 5.37 Displacement Field at 365 Days - Base Case 207

Figure 5.38 Vertical Strains above Wellpairs and Along Left Boundary 208

Figure 5.39 Maximum Shear Strain Distribution at 85 Days - Base Case 209

Figure 5.40 Maximum Shear Strain Distribution at 180 Days - Base Case 210

Figure 5.41 Maximum Shear Strain Distribution at 250 Days - Base Case 211

Figure 5.42 Vertical Effective Stress, Stress Tensors and Plasticity Indicator at 250 Days - Base Case 212

Figure 5.43 Maximum Shear Strain Distribution at 365 Days - Base Case 213

Figure 5.44 Maximum Shear Strain Distribution at 458 Days - Base Case 214

Figure 5.45 Maximum Shear Strain Distribution at 730 Days - Base Case 215

Figure 5.46 Failure Index Distribution at 365 Days - Low Stiffness Parametric Analysis 216

Figure 5.47 Failure Index Distribution at 365 Days - High Stiffness Parametric Analysis 217

Figure 5.48 Maximum Shear Strain Distribution at 365 Days - Low Stiffness Parametric Analysis 218

Figure 5.49 Maximum Shear Strain Distribution at 365 Days - High Stiffness Parametric Analysis 219

Figure 5.50 Variation in Young's Modulus at 365 Days - High Stiffness Parametric Analysis 220

Figure 5.51 Failure Index Distribution at 365 Days - E = 200 MPa Parametric Analysis 221

Figure 5.52 Failure Index Distribution at 365 Days - E = 1200 MPa Parametric Analysis 222

Figure 5.53 Failure Index Distribution at 365 Days - $K_o = 1.0$ Parametric Analysis 223

Figure 5.54 Failure Index Distribution at 365 Days - $K_o = 2.0$ Parametric Analysis 224

Figure 5.55 Stress Path for Elements Within Reservoir - K_o Parametric Analyses 225

Figure 5.56 Stress Strain Relationship for Base Case Mohr-Coulomb Parameters 226

Figure 5.57 Stress Strain Relationship for Enhanced Dilation/Constant Stiffness Mohr-Coulomb Parameters 227

Figure 5.58 Maximum Shear Strain Distribution at 365 Days - Enhanced Dilation/Constant Stiffness Parametric Analysis 228

Figure 5.59 Comparison of Elastic-Plastic Stress Strain Relationships to Active Compression Triaxial Test Results 229

Figure 5.60 Failure Index Distribution at 365 Days - $\beta_b = 0.0$ Parametric Analysis 230

Figure 5.61 Failure Index Distribution at 365 Days - Low Thermal Expansion Parametric Analysis 231

Figure 5.62 Failure Index Distribution at 365 Days - High Thermal Expansion Parametric Analysis 232

Figure 5.63 Stress Paths Followed for Thermal Expansion Parametric Analyses 233

Figure 5.64 Maximum Shear Strain Distribution at 365 Days - High Thermal Expansion Parametric Analysis 234

Figure 5.65 Maximum Shear Strain Distribution at 365 Days - Laboratory Bulk Modulus/Effecitve Confining Stress Relationship 235

Figure 6.1 Simplified Pressure History for Wellpair A1 274

Figure 6.2 Simplified Pressure History for Wellpair A2 275

Figure 6.3 Simplified Pressure History for Wellpair A3 276

Figure 6.4 Initial Pore Pressure Distribution within McMurray Formation 277

Figure 6.5 Temperature and Pore Pressure Distribution within Geotechnical Cross Section for Time 1.4 278

Figure 6.6 Temperature and Pore Pressure Distribution within Geotechnical Cross Section for Time 2.9 279

Figure 6.7 Three Dimensional Representation of Steam Chamber at Time 2.9 280

Figure 6.8 Temperature Distribution within Geotechnical Cross Section: Time 3.9 and 4.3 281

Figure 6.9 Pore Pressure Distribution within Geotechnical Cross Section: Time 3.9 and 4.3 282

Figure 6.10 Three Dimensional Representation of Steam Chamber at Time 4.3 283

Figure 6.11 Pore Pressure Distribution within Geotechnical Cross Section: Time 5.0 and 5.4 284

Figure 6.12 Temperature Distribution within Geotechnical Cross Section: Time 5.0 and 5.4 285

Figure 6.13 Temperature and Pore Pressure Distribution within Geotechnical Cross Section for Time 5.7 286

Figure 6.14 Three Dimensional Representation of Steam Chamber at Time 5.7 287

Figure 6.15 Temperature Distribution within Geotechnical Cross Section: Time 6.1 and 7.4 288

Figure 6.16 Pore Pressure Distribution within Geotechnical Cross Section: Time 6.1 and 7.4 289

Figure 6.17 Three Dimensional Representation of Steam Chamber at Time 7.1 290

Figure 6.18 Temperature Distribution within Geotechnical Cross Section: Time 7.9 and 8.6 291

Figure 6.19 Pore Pressure Distribution within Geotechnical Cross Section: Time 7.9 and 8.6 292

Figure 6.20 Three Dimensional Representation of Steam Chamber at Time 8.6 293

Figure 6.21 Temperature and Pore Pressure Distribution within Geotechnical Cross Section for Time 10.0 294

Figure 6.22 Three Dimensional Representation of Steam Chamber at Time 10.0 295

Figure 6.23 Mesh Used for Full Strain Field Analysis 296

Figure 6.24 Detailed Position of AGE2 Modules and AGE2 Bulk Volume Analysis 297

Figure 6.25 Displacement History for Well AGE2 298

Figure 6.26 Detailed Position of AGE3 Modules and AGE3 Bulk Volume Analysis 299

Figure 6.27 Displacement History for Well AGE3 300

Figure 6.28 Detailed Position of AGE4 Modules and AGE4 Bulk Volume Analysis 301

Figure 6.29 Displacement History for Well AGE4 302

Figure 6.30 Displacement Degrees of Freedom for Bof-Ex Extensometer Modules 303

Figure 6.31 Full Displacement Calibration Curve for Bof-Ex LVDT 304

Figure 6.32 Corrected Displacement History for Module 240 (AGE3) Based on Full Displacement Calibration Curve 305

Figure 6.33 Vertical Strain History for AGE2 306

Figure 6.34 Vertical Strain History for AGE3 307

Figure 6.35 Vertical Strain History for AGE4 308

Figure 6.36 Plan View of Horizontal Displacement Vectors at Elevation 280 m - Time 4.3 309

Figure 6.37 Plan View of Horizontal Displacement Vectors at Elevation 280 m - Time 5.5 310

Figure 6.38 Plan View of Horizontal Displacement Vectors at Elevation 280 m - Time 7.9 311

Figure 6.39 Plan View of Horizontal Displacement Vectors at Elevation 280 m - Time 9.7 312

Figure 6.40 West-East Horizontal Displacements Within Geotechnical Cross Section: Time 4.3 313

Figure 6.41 West-East Horizontal Displacements Within Geotechnical Cross Section: Time 5.5 314

Figure 6.42 West-East Horizontal Displacements Within Geotechnical Cross Section: Time 7.9 315

Figure 6.43 West-East Horizontal Displacements Within Geotechnical Cross Section: Time 9.7 316

Figure 6.44 Geometry for Roof Extensometer and Convergence Arrays at Station E12-2 317

Figure 6.45 Interpolated Displacement History of Oil Sands-Limestone Interface 318

Figure 6.46 Vertical Strain Distribution within Geotechnical Cross Section: Time 4.3 and 5.5 319

Figure 6.47 Vertical Strain Distribution within Geotechnical Cross Section: Time 7.9 and 9.7 320

Figure 6.48 Estimated Vertical Displacement of Top of Reservoir (Elevation 293 m) 321

Figure 6.49 Horizontal Strain Distribution within Geotechnical Cross Section: Time 4.3 and 5.5 322

Figure 6.50 Horizontal Strain Distribution within Geotechnical Cross Section: Time 7.9 and 9.7 323

Figure 6.51 Maximum Shear Strain Distribution within Geotechnical Cross Section: Time 4.3 and 5.5 324

Figure 6.52 Maximum Shear Strain Distribution within Geotechnical Cross Section: Time 7.9 and 9.7 325

Figure 6.53 Maximum Shear Strain Distribution at Time 9.7 for Region Within Reservoir Comparable to Boundary Conditions Used in Ideal Analyses 326

Figure 6.54 Volumetric Strain Distribution within Geotechnical Cross Section: Time 4.3 and 5.5 327

Figure 6.55 Volumetric Strain Distribution within Geotechnical Cross Section: Time 7.9 and 9.7 328

Figure 6.56 Absolute Permeability Distribution within Geotechnical Cross Section: Time 4.3 and 5.5 329

Figure 6.57 Absolute Permeability Distribution within Geotechnical Cross Section: Time 7.9 and 9.7 330

Figure 7.1 Complete Finite Difference Grid used for Geotechnical Cross Section Analysis 338

Figure 7.2 Schematic Illustration of Finite Difference Grid Showing Dimensions and Assumed Geology 339

Figure 7.3 Failure Index at Time 3.9 340
Figure 7.4 Failure Index at Time 5.4 341
Figure 7.5 Failure Index at Time 7.9 342
Figure 7.6 Failure Index at Time 9.3 343
Figure 7.7 Minor Principal Effective Stress at Time 7.9 344
Figure 7.8 Schematic Illustration of Mechanism for Shear Strain in Advance of Growing Steam Chamber 345
Figure 7.9 Maximum Shear Strain at Time 3.9 346
Figure 7.10 Maximum Shear Strain at Time 5.4 347
Figure 7.11 Maximum Shear Strain at Time 7.9 348
Figure 7.12 Maximum Shear Strain at Time 9.3 349
Figure 7.13 Comparison of Predicted versus Observed Horizontal Displacements at AGI1 350
Figure 7.14 Comparison of Predicted versus Observed Horizontal Displacements at AGI2 351
Figure 7.15 Comparison of Predicted versus Observed Horizontal Displacements at AGI3 352
Figure 7.16 Comparison of Predicted versus Observed Horizontal Displacements at AT1 353
Figure 7.17 Comparison of Predicted versus Observed Horizontal Displacements at AT7 354
Figure 7.18 Predicted Horizontal Displacement at AGI1, AGI2 and AGI3: Constant Stiffness Analyses - E=200 MPa, E=400 MPa and E=800 MPa 355
Figure 7.19 Predicted Vertical Strain Response at AGE2, AGE3 and AGE4 356
Figure A1 Temperature Profile in Well AT1 373
Figure A2 Temperature Profile in Well AT2 374
Figure A3 Temperature Profile in Well AT3 375
Figure A4 Temperature Profile in Well AT4 376
Figure A5 Temperature Profile in Well AT5 377
Figure A6 Temperature Profile in Well AT6 378
Figure A7 Temperature Profile in Well AT7 379
Figure A8 Temperature Profile in Well AT8 380
Figure A9 Temperature Profile in Well AT9 381
Figure A10 Temperature Profile in Well AT10 382
Figure A11 Temperature Profile in Well AT11 383
Figure A12 Temperature Profile in Well AT12 384
Figure A13 Temperature Profile in Well AT13 385
Figure A14 Temperature Profile in Well AT14 386
Figure A15 Temperature Profile in Well AGP4 387

Figure A16 Temperature Profile in Well AGI1 388

Figure A17 Temperature Profile in Well AGI2 389

Figure A18 Temperature Profile in Well AGI3 390

Figure A19 Temperature Profile in Well AGI4 391

Figure B1 Change in Pressure for Piezometer at Elevation 280.4 m in Well AGP1 393

Figure B2 Relationship Between Injection and Production Pressures Changes and Change in Pressure for Piezometer at Elevation 280.4 m in Well AGP1 394

Figure B3 Change in Pressure for Piezometer at Elevation 275.4 m in Well AGP1 395

Figure B4 Relationship Between Injection and Production Pressures Changes and Change in Pressure for Piezometer at Elevation 275.4 m in Well AGP1 396

Figure B5 Change in Pressure for Piezometer at Elevation 281.2 m in Well AT14 397

Figure B6 Relationship Between Injection and Production Pressures Changes and Change in Pressure for Piezometer at Elevation 281.2 m in Well AT14 398

Figure B7 Change in Pressure for Piezometer at Elevation 282.1 m in Well AGP2 399

Figure B8 Relationship Between Injection and Production Pressures Changes and Change in Pressure for Piezometer at Elevation 282.1 m in Well AGP2 400

Figure B9 Change in Pressure for Piezometer at Elevation 275.1 m in Well AGP2 401

Figure B10 Relationship Between Injection and Production Pressures Changes and Change in Pressure for Piezometer at Elevation 275.1 m in Well AGP2 402

Figure B11 Change in Pressure for Piezometer at Elevation 295.9 m in Well AT4 403

Figure B12 Relationship Between Injection and Production Pressures Changes and Change in Pressure for Piezometer at Elevation 295.9 m in Well AT4 404

Figure B13 Change in Pressure for Piezometer at Elevation 289.9 m in Well AT4 405

Figure B14 Relationship Between Injection and Production Pressures Changes and Change in Pressure for Piezometer at Elevation 289.9 m in Well AT4 406

Figure B15 Change in Pressure for Piezometer at Elevation 282,9 m in Well AT4 407

Figure B16 Relationship Between Injection and Production Pressures Changes and Change in Pressure for Piezometer at Elevation 282.9 m in Well AT4 408

Figure B17 Change in Pressure for Piezometer at Elevation 284.8 m in Well AGP4 409

Figure B18 Relationship Between Injection and Production Pressures Changes and Change in Pressure for Piezometer at Elevation 284.8 m in Well AGP4 410

Figure B19 Change in Pressure for Piezometer at Elevation 272.8 m in Well AGP4 411

Figure B20 Relationship Between Injection and Production Pressures Changes and Change in Pressure for Piezometer at Elevation 272.8 m in Well AGP4 412

Figure B21 Change in Pressure for Piezometer at Elevation 306.9 m in Well AGP5 413

Figure B22 Relationship Between Injection and Production Pressures Changes and Change in Pressure for Piezometer at Elevation 306.9 m in Well AGP5 414

Figure B23 Change in Pressure for Piezometer at Elevation 290.9 m in Well AGP5 415

Figure B24 Relationship Between Injection and Production Pressures Changes and Change in Pressure for Piezometer at Elevation 290.9 m in Well AGP5 416

Figure B25 Change in Pressure for Piezometer at Elevation 281.9 m in Well AGP5 417

Figure B26 Relationship Between Injection and Production Pressures Changes and Change in Pressure for Piezometer at Elevation 281.9 m in Well AGP5 418

Figure B27 Change in Pressure for Piezometer at Elevation 289.8 in Well AT9 419

Figure B28 Relationship Between Injection and Production Pressures Changes and Change in Pressure for Piezometer at Elevation 289.8 in Well AT9 420

Figure B29 Change in Pressure for Piezometer at Elevation 281.8 m in Well AT9 421

Figure B30 Relationship Between Injection and Production Pressures Changes and Change in Pressure for Piezometer at Elevation 281.8 m in Well AT9 422

Figure B31 Change in Pressure for Piezometer at Elevation 295.3 m in Well AT12 423

Figure B32 Relationship Between Injection and Production Pressures Changes and Change in Pressure for Piezometer at Elevation 295.3 m in Well AT12 424

Figure B33 Change in Pressure for Piezometer at Elevation 288.3 m in Well AT12 425

Figure B34 Relationship Between Injection and Production Pressures Changes and Change in Pressure for Piezometer at Elevation 288.3 m in Well AT12 426

Figure B35 Change in Pressure for Piezometer at Elevation 285.7 m in Well AGP6 427

Figure B36 Relationship Between Injection and Production Pressures Changes and Change in Pressure for Piezometer at Elevation 285.7 m in Well AGP6 428

Figure B37 Change in Pressure for Piezometer at Elevation 277.7 m in Well AGP6 429

Figure B38 Relationship Between Injection and Production Pressures Changes and Change in Pressure for Piezometer at Elevation 277.7 m in Well AGP6 430

Figure C1 Extensometer History for Module 250 in Well AGE2: Elevation 291.0 to 288.0 432

Figure C2 Well AGE2 - Module 250 History during Extensometer Installation 433

Figure C3 Extensometer History for Module 249 in Well AGE2: Elevation 288.0 to 285.0 434

Figure C4 Well AGE2 - Module 249 History during Extensometer Installation 435

Figure C5 Extensometer History for Module 244 in Well AGE2: Elevation 285.0 to 282.0 436

Figure C6 Well AGE2 - Module 244 History during Extensometer Installation 437

Figure C7 Extensometer History for Module 245 in Well AGE2: Elevation 282.0 to 279.0 438

Figure C8 Well AGE2 - Module 245 History during Extensometer Installation 439

Figure C9 Extensometer History for Module 243 in Well AGE3: Elevation 298.1 to 293.1 440

Figure C10 Well AGE3 - Module 243 History during Extensometer Installation 441

Figure C11 Extensometer History for Module 242 in Well AGE3: Elevation 293.1 to 288.1 442

Figure C12 Well AGE3 - Module 242 History during Extensometer Installation 443

Figure C13 Extensometer History for Module 236 in Well AGE3: Elevation 288.1 to 283.1 444

Figure C14 Well AGE3 - Module 236 History during Extensometer Installation 445

Figure C15 Extensometer History for Module 238 in Well AGE3: Elevation 283.1 to 278.1 446

Figure C16 Well AGE3 - Module 238 History during Extensometer Installation 447

Figure C17 Extensometer History for Module 240 in Well AGE3: Elevation 278.1 to 273.1 448

Figure C18 Well AGE3 - Module 240 History during Extensometer Installation 449

Figure C19 Extensometer History for Module 248 in Well AGE3: Elevation 273.1.0 to 268.1 450

Figure C20 Well AGE3 - Module 248 History during Extensometer Installation 451

Figure C21 Extensometer History for Module 239 in Well AGE3: Elevation 293.5 to 288.5 452
Figure C22 Well AGE3 - Module 239 History during Extensometer Installation 453
Figure C23 Extensometer History for Module 241 in Well AGE3: Elevation 288.5 to 283.5 454
Figure C24 Well AGE3 - Module 241 History during Extensometer Installation 455
Figure C25 Extensometer History for Module 247 in Well AGE3: Elevation 283.5 to 278.5 456
Figure C26 Well AGE3 - Module 247 History during Extensometer Installation 457
Figure C27 Extensometer History for Module 246 in Well AGE3: Elevation 278.5 to 273.5 458
Figure C28 Well AGE3 - Module 246 History during Extensometer Installation 459
Figure C29 Extensometer History for Module 235 in Well AGE3: Elevation 273.5 to 268.5 460
Figure C30 Well AGE3 - Module 235 History during Extensometer Installation 461
Figure D1 Horizontal Displacement Profile at Well AGI1 463
Figure D2 Horizontal Displacement Profile at Well AGI2 470
Figure D3 Horizontal Displacement Profile at Well AGI3 478
Figure D4 Horizontal Displacement Profile at Well AGI4 485
Figure D5 Horizontal Displacement Profile at Well AT1 492
Figure D6 Horizontal Displacement Profile at Well AT7 499
Figure E1 Temperature Distribution within Geotechnical Cross Section at Time 1.4 507
Figure E2 Temperature Distribution within Geotechnical Cross Section at Time 2.1 508
Figure E3 Temperature Distribution within Geotechnical Cross Section at Time 2.5 509
Figure E4 Temperature Distribution within Geotechnical Cross Section at Time 2.9 510
Figure E5 Temperature Distribution within Geotechnical Cross Section at Time 3.2 511
Figure E6 Temperature Distribution within Geotechnical Cross Section at Time 3.6 512
Figure E7 Temperature Distribution within Geotechnical Cross Section at Time 3.9 513
Figure E8 Temperature Distribution within Geotechnical Cross Section at Time 4.3 514
Figure E9 Temperature Distribution within Geotechnical Cross Section at Time 4.6 515

Figure E10 Temperature Distribution within Geotechnical Cross Section at Time 5.0 516
Figure E11 Temperature Distribution within Geotechnical Cross Section at Time 5.4 517
Figure E12 Temperature Distribution within Geotechnical Cross Section at Time 5.7 518
Figure E13 Temperature Distribution within Geotechnical Cross Section at Time 6.1 519
Figure E14 Temperature Distribution within Geotechnical Cross Section at Time 6.4 520
Figure E15 Temperature Distribution within Geotechnical Cross Section at Time 7.1 521
Figure E16 Temperature Distribution within Geotechnical Cross Section at Time 7.9 522
Figure E17 Temperature Distribution within Geotechnical Cross Section at Time 8.6 523
Figure E18 Temperature Distribution within Geotechnical Cross Section at Time 9.3 524
Figure E19 Temperature Distribution within Geotechnical Cross Section at Time 10.0 525
Figure F1 Pore Pressure Distribution within Geotechnical Cross Section at Time 1.4 527
Figure F2 Pore Pressure Distribution within Geotechnical Cross Section at Time 2.1 528
Figure F3 Pore Pressure Distribution within Geotechnical Cross Section at Time 2.5 529
Figure F4 Pore Pressure Distribution within Geotechnical Cross Section at Time 2.9 530
Figure F5 Pore Pressure Distribution within Geotechnical Cross Section at Time 3.2 531
Figure F6 Pore Pressure Distribution within Geotechnical Cross Section at Time 3.6 532
Figure F7 Pore Pressure Distribution within Geotechnical Cross Section at Time 3.9 533
Figure F8 Pore Pressure Distribution within Geotechnical Cross Section at Time 4.3 534
Figure F9 Pore Pressure Distribution within Geotechnical Cross Section at Time 4.6 535
Figure F10 Pore Pressure Distribution within Geotechnical Cross Section at Time 5.0 536
Figure F11 Pore Pressure Distribution within Geotechnical Cross Section at Time 5.4 537
Figure F12 Pore Pressure Distribution within Geotechnical Cross Section at Time 5.7 538
Figure F13 Pore Pressure Distribution within Geotechnical Cross Section at Time 6.1 539

Figure F14 Pore Pressure Distribution within Geotechnical Cross Section at Time 6.4 540
Figure F15 Pore Pressure Distribution within Geotechnical Cross Section at Time 7.1 541
Figure F16 Pore Pressure Distribution within Geotechnical Cross Section at Time 7.9 542
Figure F17 Pore Pressure Distribution within Geotechnical Cross Section at Time 8.6 543
Figure F18 Pore Pressure Distribution within Geotechnical Cross Section at Time 9.3 544
Figure F19 Pore Pressure Distribution within Geotechnical Cross Section at Time 10.0 545

Discovery consists of seeing what everybody has seen and thinking what nobody has thought.

Albert Szent-Gyorgyi (1893-1986)

CHAPTER 1 INTRODUCTION

"Another damned, thick, square book! Always scribble, scribble, scribble, eh, Mr. Gibbon?"
William Henry, Duke of Gloucester (1743-1805)

1.1 Problem Statement

Over the past two decades, the decline in reserves of conventional crude oil has led to the development of several methods of enhanced oil recovery (EOR) for heavy oil deposits. The most common form of EOR is thermal recovery which includes processes such as steam stimulation, steamflooding, hot water flooding and in situ combustion. Competing forms of nonthermal EOR include surfactant flooding, polymer flooding, and miscible and immiscible flooding processes such as carbon dioxide flooding.

Thermal processes depend largely upon the reduction in oil viscosity which accompanies heating. Steam flooding, for instance, is a continuous process in which steam is injected into the reservoir at certain wells and oil is driven to remote production wells. The zones around the injection wells become heated to the saturation temperature of the steam and these zones expand towards the production wells. Oil and considerable condensed steam are removed from the producers. With viscous oil there is a considerable tendency for the steam to override the reservoir and this tends to limit the downwards penetration of the heat and hence the recovery (Butler, 1992).

A special form of steam flooding, known as steam assisted gravity drainage (SAGD), was developed to provide a process which could recover more oil than is possible by conventional steam flooding processes. In the steam assisted gravity drainage process, the movement of oil to the production well is caused by gravity forces and the geometry is such that the oil moves approximately parallel to the interface which forms the boundary of a growing, steam-saturated zone known as the steam chamber.

Phenomenologically, SAGD is more accurately described as a physical phenomenon than a recovery process (Edmunds et al., 1992). SAGD is a combined conduction-convection mechanism more similar to *ablation* (i.e., the propagation of a melt front into a solid material), than *displacement*, the usual petroleum engineering paradigm for thermal recovery. Cold bitumen can not be displaced at any practical rate, and fills the pore space so completely that it also prevents entry of steam or other hot fluids into the sand matrix. If a steam zone can be established, however, SAGD will cause it to rise and spread through the sand. Conduction heats a thin layer of oil sand adjacent to the steam chamber, mobilizing the bitumen. The difference in density between steam and bitumen causes the latter to drain to the bottom of the chamber, along with the steam condensate. The steam gains access to new faces in the formation as the bitumen drains, and so the front advances upward and outward. This will continue as long as more steam and oil sand are available, and as long as the draining bitumen and condensate are removed from the bottom of the chamber (Edmunds et al., 1992).

The SAGD process described above results in a complex interaction of geomechanics and multiphase thermal flow in cohesionless porous media. The geomechanical response of an oil sands reservoir to fluid pressure changes or to temperature changes results in stress and deformations that affect formation shearing, hydraulic properties such as absolute permeability and the stability of underground openings (uncased wells, tunnels and shafts). Temperature increase causes thermal expansion of the sand grains and sand structure. A pore pressure increase during steam injection decreases the effective confining stress. For an anisotropic in situ stress state in the reservoir, pore pressure injection will also generate shear stresses and shear strains in the sand structure. These processes combine to result in a net change in reservoir pore volume and permeability.

Most reservoir models used in simulating the steam assisted gravity drainage process do not account for the geomechanical responses described above. Several important parameters which affect process performance are howeve, directly impacted by the geomechanical response of the reservoir. Porosity is directly proportional to the bitumen production yet porosity can be altered due to shear induced volume changes or changes in effective confining stress. Absolute permeability of the reservoir affects the drainage of fluids from the steam front and therefore the frontal advance rate and the production rate; it is one the most important parameters in the simulation of the SAGD process. Stress change induced volume changes within the reservoir, especially within non-heated zones, will result in changes in absolute permeability. A complete understanding of an in situ recovery process requires knowledge of the interaction between the geomechanical behavior and changes in stress state in a reservoir (Kry et al., 1989).

1.2 Reservoir Geomechanics

The body of literature encompassing oil sands related research; from geology to geotechnical and the associated petroleum engineering processes is vast and beyond the scope of this thesis to review in detail. The following sections provide brief summaries of research relevant to the geomechanics of the steam assisted gravity drainage process.

1.2.1 Constitutive Response of Oil Sands and Related Strata

Early work conducted by Dusseault (Dusseault, 1977; Dusseault and Morgenstern, 1977, 1978a, 1978b) identified the Athabasca oil sands as a *locked sand*. The locked nature of the sands is a result of diagenetic processes creating an interpenetrative fabric. Locked sands have the following characteristics: absence of cohesion, highly quartzose mineralogy, high strength, steeply curved failure envelopes, low porosities, lack of interstitial cement, brittle behavior, and exceptionally large dilation rates at failure. Shear testing of locked sands demonstrates very small strains to failure.

Several researchers have followed on the original research conducted by Dusseault (1977) to further investigate the geotechnical characteristics of oil sands. Sterne (1982) conducted hollow cylinder testing of oil sands and Barnes (1980) continued the strength studies initiated by Dusseault (1977). It is interesting to note that the shear and consolidation characteristics of oil sands was investigated as early as 1949 by T.G. Tustin. Au (1983) summarized the strength-deformation properties of oil sands and related clay shales. Au (1983) notes in his conclusion that the basal clay shales and intraformational clays in the McMurray Formation follow the Mohr-Coulomb strength relationship with peak friction angles up to 29° and residual friction angles as low as 7°.

With an increase in interest for thermal recovery projects in the early 1980's, the influence of elevated temperatures on the geotechnical properties of oil sands and related strata was investigated by Agar (1984). Experimental procedures were developed and laboratory experiments were performed over a range of temperatures to measure: 1) drained and undrained thermal expansion; 2) drained and undrained compressibility; 3) pore pressure generation during undrained heating; 4) shear strength and stress-strain parameters; and 5) permeability properties. With an understanding of the thermal-stress-strain constitutive behavior of oil sands and numerical analyses of heat consolidation problems, Agar (1984) offered the following conclusions on the implications of ground heating:

- heating to temperatures of 300°C has little influence on properties of quartzose sand;
- the shearing resistance of cohesionless oil sands is entirely frictional - an increase in pore pressure due to ground heating causes a proportional decrease in the available shear resistance;
- oil sands containing 10 to 20% fine grained particles by mass (or more) are more highly susceptible to thermal pore pressure generation and shear strength reduction. There is considerable potential for shear failure by undrained heating in low permeability materials such as clay shales;
- thermally generated pore pressures are relatively small in oil rich oil sands;
- rapid diffusion of injection pressures can be expected in oil rich oil sands; and
- correct modeling of incremental stress changes and deformations due to transient heating and consolidation of oil sand requires the ability to predict non-recoverable plastic deformations.

Plewes (1987) investigated the undrained behavior of Athabasca oil sands using triaxial laboratory tests. The influence of initial pore pressure, effective confining stress, stress path and deformation behavior were examined. He determined a critical confining pressure, the pressure above which the volume change behavior becomes contractant, of 7.3 MPa. The undrained deformation modulus was less than one-third that mobilized under drained conditions. A conclusion of Plewes(1987) with direct relevance to SAGD processes was that strains induced by fluid injection or thermal heating of reservoirs will be larger if sufficient pore fluid drainage and pore pressure dissipation are not permitted.

Kosar (1989) conducted an extensive experimental program to further elucidate the strength-deformation properties of oil sands, both Athabasca (McMurray Formation) and Cold Lake (Clearwater Formation) oil sands. With Agar (1984) identifying that stress path testing of oil sands was required and an increased understanding of the recovery processes being attempted in the oil sands, Kosar (1989) specifically examined the influence of stress path on the constitutive response of oil sands. It is difficult in a short synopsis of this nature to summarize the substantial volume of experimental observations obtained by Kosar (1989). The following highlights several conclusions related to McMurray Formation oil sands which are applicable to the examination of the SAGD process:

- thermal stresses during drained heating of rich McMurray Formation oil sands always increase because the coefficient of thermal expansion is positive;
- drained heating of interbedded oil sands and shale may cause an increase or decrease in stresses and strains depending on the in situ effective stress field and the rate of heating due to the time and pressure dependent thermal consolidation characteristics of the shale material;
- the presence of shale interbedding has a major influence on the compressibility of McMurray Formation causing it to be larger than rich oil sands;
- the compressibility of oil sands and shale is dependent on the temperature, pressure and stress path followed during the test;
- as concluded by Agar(1984), the shear strength and deformation behavior of rich, low fines oil sands is not significantly influenced at elevated temperature; and
- the presence of shale interbedding in oil sands results in a significant decrease in the maximum shear strength of McMurray Formation oil sands in comparison to rich, low fines oil sands.

Mori and Tamura (1986) provide fascinating evidence of the relationship between permeability and dilatancy of dense sands. These authors conducted triaxial compression tests on dense sands stabilized by silicate and acrylamide grout. This research demonstrated that the permeability of grouted sand may increase remarkably due to flow channels caused by the shear stress increment and depends upon density, grain size and type of chemical grout. As an analogy to oil sands, silicate grout would be similar to the highly viscous, "stiff" bitumen found at the UTF. Acrylamide grout would be analogous to a less viscous heavy oil. Acrylamide gel shows elastic behavior similar to that of soft rubber and is more easily restored to its original shape than silicate grout. For silicate grouted sand tested at σ'_3 = 100 kPa, a two order of magnitude increase in permeability was measured at peak strength. No permeability changes were measured for acrylamide grouted sand.

1.2.2 Reservoir Processes

The mechanics of gravity drainage in thermal stimulation projects has been known for some time, being first suggested by Doscher (1966). Towson and Boberg (1967) present a formulation for gravity drainage mechanisms in vertical steam stimulated wells and through comparisons with a case history conclude that:

- gravity drainage can be an important producing mechanism in thermally stimulated reservoirs where the bulk of the oil production must come from the heated zone; and
- the effect of gravity drainage, when compared to radial steady-state flow, is to increase the production rate at early times. The degree of increase is greater in reservoirs with high permeability, thick pay zones and low reservoir pressure.

The problem with gravity drainage in this application is that the vertical wells have limited contact with the reservoir and the requirement of radial flow provides a substantial resistance to flow. The rapid advance of horizontal drilling in the early 1980's provided a substantial "boost" to steam assisted gravity drainage as an economical EOR process. With horizontal wells, a much greater contact with the reservoir is achieved than with conventional wells and adequate flows can be achieved with heads equivalent to that obtained from gravity; this is not possible with vertical wells (Butler, 1992). It is the use of horizontal wells which allows oil to be produced at economic rates with the main driving force being gravity.

In his review of SAGD, Butler (1992) discusses one significant problem with the application of SAGD; the establishment of initial communication between the injection and production wells. Initial communication is required so that condensate from the steam can be removed and allow further steam to flow into the reservoir and continue heating. At the UTF, initial communication was achieved by close vertical spacing of the injector and producer which allowed conduction heating to mobilize the intervening bitumen. Butler (1992) also provides an interesting note concerning initial communication involving hydraulic fracturing. This would involve the initial injection of steam at fracturing pressure so as to develop a heated vertical plane above the production well. If the wells were located with their axes in the direction of the fracture trend, this could allow a rapid heating of a plane vertically above the horizontal well and along its length. Economically, the startup phase would be reduced dramatically in comparison to conduction heating and would provide immediate oil production.

1.2.3 Numerical Modeling

The volume of literature under the category of "numerical modeling" is vast, for both geotechnical and petroleum engineering fields. With particular reference to literature pertinent to the modeling of coupled thermal-stress-fluid flow problems (the essence of reservoir geomechanics modeling), Tortike (1991) offers a clear, concise summary of numerical modeling efforts aimed at including geomechanical behavior in reservoir models. A more detailed and exhaustive review on the modeling of coupled thermal-stress-fluid flow processes can be found in Morgenstern and Scott (1985). The majority of the references cited in the above reviews as well as other reported modeling efforts in reservoir geomechanics, have focussed on the phenomena of formation fracturing. While this remains a challenging problem and an area of ongoing research, many of the complexities involved in modeling fracturing are not applicable to the analysis of SAGD. By design, the steam injection pressures for SAGD processes are maintained below the formation fracture pressure. The following, then, summarizes previous work related to the issue of geomechanical phenomenon in SAGD processes as well as reservoir engineering references related to SAGD.

The concept or theory of steam assisted gravity drainage as applied at the Underground Test Facility (UTF) was described in Butler et al., (1981), Butler and Stephens (1981), Butler (1981). The following equation for the flow of oil was obtained from this theoretical work:

$$q = 2L\sqrt{\frac{2kg\alpha\phi\Delta S_o h}{mv_s}} \qquad [1.1]$$

where q = oil flow rate to production well [m^3/s];
L = length of horizontal well [m];
k = effective permeability for oil flow [m^2];
g = acceleration due to gravity [m/s^2];
α = thermal diffusivity of reservoir [m^2/s];
ϕ = fractional porosity of reservoir;
ΔS_o = initial fraction of oil saturation less residual oil saturation in steam chamber;
h = steam chamber height [m];
m = dimensionless parameter (typically 3-4) determined by viscosity-temperature characteristics of oil; and
v_s = dynamic viscosity of oil.

Equation 1.1 indicates that each of the variables under the square root sign are equally important; changing any of them by a factor of 2 will change the rate by a factor equal to the square root of 2. The equation also provides insight into the coupling between heat transfer and oil drainage mechanisms. For example, increasing permeability increases the rate but tends to decrease the thickness of the heated oil layer. Thus any change that improves the transport of bitumen is partially counteracted by a reduction in the quantity of mobile bitumen. Similarly, increasing the thermal diffusivity increases the thickness of the heated oil layer and also increases the rate. Equation 1.1 also shows that the production rate is only a function of the height of the slope not the angle of its recline. The reason for this is that shallow angle slopes have lower gravity components parallel to the slope "driving bitumen" to the production well, but have longer slopes exposed to steam which provides a greater volume of bitumen - the two factors cancel out.

Edmunds et al., (1988) describe the analysis and implementation of the steam assisted gravity drainage process at the AOSTRA UTF (Underground Test Facility). Specific attention is paid to the two basic types of SAGD mechanisms occurring within a reservoir: 1) ceiling ; and 2) slope drainage. Issues of permeability anisotropy, geological heterogeneities, solution gas and capillary pressure effects are discussed relative to the SAGD process.

With the benefit of the Phase A field trial results, Edmunds and Gittins (1991) provide a more quantitative and rigorous development of the SAGD process as well as presenting results from numerical analyses with a coupled wellbore/reservoir simulator. Issues of wellbore pressure gradients, wellbore sinuosity and wellbore length are addressed. It is interesting to note the authors conclude their paper with a disclaimer stating that "because of the highly nonlinear nature of some of the phenomena involved, it is very risky to extrapolate these results, even qualitatively, to situations where key parameters such as permeability, bitumen viscosity, steam pressure, tubular diameters, etc. fall outside the studied range".

Simulations of the SAGD process at the UTF were also undertaken by Siu et al., (1991). They perform a history match analysis for early injection and production data. In order to match field performance, the initial bitumen saturations were increased slightly and the vertical permeability in the reservoir was increased to enhance bitumen movement. As well, heat capacity of the rock was reduced slightly to improve the spreading of the steam front. While the adjustments are reported to be within physical bounds, the need to make adjustments for history matching highlights the need for high quality laboratory experiments to provide accurate input data.

Settari (1988 and 1989), and Settari et al., (1988) describe a new formulation for non-linear soil mechanics and multiphase, thermal flow for particular application to modeling the conditions present during isothermal leak-off from fractures faces. The "soil mechanics" features added include nonlinear compressibility of oil sands at low effective confining stresses and shear (dilatant) failure which combine to increase porosity and permeability. The phenomenon of dilation at shear failure was handled as an abrupt volume and permeability change; it was not handled consistently through an appropriate constitutive model.

Fung (1990) describes the development of a control-volume finite element (CVFE) model for analysing coupled geomechanic-multiphase flow in cohesionless oil sands. Byrne and Elderidge's (1982) shear-dilatant hyperbolic stress-strain model is utilized to describe the geomechanical response of oil sands. To provide the link between permeability changes due to shear induced volume changes, permeability multipliers specified as a function of mobilized strength were used.

The incorporation of geomechanics has been necessary for the successful modeling of cyclic steam stimulation in the Cold Lake oil sands. Beattie et al., (1991) and subsequently, Denbina et al., (1991) utilize an empirical approach to model dilation. A deformation model based on two pore compressibility values for increasing pressure and two pore compressibility values for decreasing pressure was implemented in a numerical thermal reservoir simulator. The authors note in their abstract as the foundation for this empirical approach that "rigorous geomechanical modeling is not economical". No economic figures were provided but it is assumed this is based on the cost of appropriate modifications to the reservoir simulator. Formation compaction was identified as the most significant production mechanism (>60%) with solution gas drive as the second most important.

The most ambitious effort to date concerning fully coupled geomechanic-multiphase flow analysis is the work of Tortike (1991). He developed a wholly finite element model and a coupled finite element deformation model and finite difference flow model. While the finite element model was unable to solve satisfactorily the complex nature of thermal multiphase flow in a porous medium, the couple finite element/difference model provided useful results. On the basis of several parametric analyses run to observe different material responses, Tortike (1991) concluded that the deformation response should be included in reservoir simulations to model oil recover processes in unconsolidated oil sands.

1.2.4 Geomechanics Monitoring of Reservoir Processes

For thermal recovery projects undertaken in Alberta oil sands deposits, the most intense geomechanical instrumentation operation, with the exception of the Underground Test Facility (UTF), was a geomechanics monitoring program of the cyclic steam stimulation operations in the Clearwater Formation (Gronseth, 1989). The program was aimed at characterizing the role that the geomechanical behavior of the reservoir had on bitumen production and casing impairments. The program consisted of: 1) a systematic program on in situ stress determinations by hydraulic fracturing; 2) the installation and monitoring of vertical control benchmark arrays to quantify near surface vertical displacements; and 3) the installation of dedicated observation wells to monitor vertical and horizontal formation movements and reservoir temperatures. Gronseth (1989) reported that measured surface uplifts near the steam injection wells exceeded 100 mm. Within the reservoir, extensional (i.e. vertical) displacements exceeding 160 mm had been observed. Inclinometers within the reservoir revealed lateral displacements of approximately 60 mm. Gronseth (1989) concluded that shear displacements during the thermal recovery operation were the result of dilation of the in situ sand structure.

Several publications can be found describing the Underground Test Facility; from early papers describing the overall project (Haston et al., 1989; Haston at al., 1988; Suggett, 1987) to papers describing the geotechnical instrumentation program (Laing et al., 1988; Rottenfusser and Stokes, 1987).

1.3 Objectives of Research Program

The accuracy of performance predictions and history matching analysis of the SAGD process will depend on how well a reservoir simulator matches the physics and fluid flow in the reservoir. The simulators used for history matching the UTF Phase A SAGD test did not include "geomechanical" physics. If the process of shear yield and effective confining stress changes leading to pore volume changes and concomitant permeability enhancements was an integral component of the UTF Phase A SAGD process , then not including it in numerical simulations for process design in different reservoirs may have negative consequences on SAGD predictions.

The overall objective of this research then, is the analysis of laboratory, field instrumentation and numerical modeling results to identify geomechanical phenomena which influence the steam assisted gravity drainage recovery process. Results from steam assisted gravity drainage process trials conducted at the Underground Test Facility are utilized to examine the geomechanical response of the reservoir.

The objective of the laboratory testing program is the determination of thermomechanical properties of the reservoir materials, namely McMurray Formation oil sands, intraformational McMurray Formation shales and Waterways limestone. Material property characterization focussed on thermal volume change, thermal conductivity, compressibility, stress-strain-strength and gas evolution and composition. In terms of constitutive modeling, complex stress path testing was considered beyond the scope of this thesis. As well, minimal testing was completed on oil sands, as extensive testing programs have previously been conducted and was available from Dusseault (1977), Agar (1984); and Kosar (1989).

The objective in analyzing the field instrumentation response is to provide field evidence of geomechanical phenomena in the SAGD process. Use of field instrumentation results in this research are restricted to their response during the SAGD process trials. While development and implementation of geotechnical instrumentation for thermal reservoir environments is worthy of independent research, these topics will not be considered in this thesis. A review of instrument installation procedures and raw data collection was conducted however, in order to ensure postulates concerning geomechanical phenomena were based on reliable instrumentation results. Except for use in determining the deformational history of the limestone-oil sands interface, consideration of the tunnel instrumentation is outside the scope of this thesis.

The objective of the numerical modeling studies is to aid in elucidating fundamental geomechanical principles affecting the SAGD process and to gain insight in the reservoir response to thermal and pore pressure changes. Fully coupled thermal-stress-fluid flow analyses are extremely complex (Tortike, 1991) and few models exist which incorporate the necessary physics to permit a fully coupled analysis of the SAGD process. Existing models capable of conducting an effective stress analysis incorporating temperature, in an uncoupled manner, were chosen for the numerical analyses performed in this research. The development or implementation of a fully coupled thermal-stress-fluid flow model was considered outside the scope of this thesis.

1.4 Organization of Thesis

Due to the confidential nature of the process data during the initial stages of this thesis, the time frame for the Phase A SAGD test was scaled to a normalized time scale from time 0 to time 10. Consequently, all figures within this thesis have been plotted against this time scale. With the passage of time however, the need for confidentiality has lessened so for reference, the following table provides a cross reference between actual time scales and the normalized time scale. The complete date for time 0.0 was November 11, 1987.

Normalized Time	Elapsed Time (days)
0.0	0.0
1.4	100
2.1	150
2.5	175
2.9	200
3.2	225
3.6	250
3.9	275
4.3	300
4.6	325
5.0	350
5.4	375
5.7	400
6.1	425
6.4	450
7.1	500
7.9	550
8.6	600
9.3	650
10.0	700

The overall Phase A project at the Underground Test Facility is discussed in Chapter 2. The basic mechanics of the steam assisted gravity drainage process and the regional and local geological setting of the Underground Test Facility are presented.

Chapter 3 summarizes the instrumentation program undertaken at the UTF. As many of the instruments installed within the reservoir for the Phase A SAGD tests were specially designed high temperature versions of conventional geotechnical instrumentation, this chapter is included to discuss the various types of instrumentation and their distribution within the reservoir.

The results of a thermomechanical properties testing program conducted on McMurray Formation oil sands, intraformational McMurray Formation shales and Waterways limestone is presented in Chapter 4. The role of thermomechanical properties within the SAGD process is reviewed and discussed. The determination of reservoir parameters from geomechanical tests, specifically thermal expansion and compressibility tests, is reviewed. Previous experimental work

(Dusseault, 1977; Au, 1983; Agar, 1984; Plewes, 1987; Kosar, 1989) is synthesized in order to develop the most suitable properties database applicable to the case study of the Underground Test Facility.

Chapter 5 presents numerical analyses results of the SAGD process in an ideal reservoir. These analyses were conducted to explore, parametrically, the geomechanical issues which may influence the SAGD process. As well, it highlighted the sensitivity of formation material property selection on analysis results. These analyses provide the basis for material property selection for the geomechanical analyses presented in Chapter 7.

Chapter 6 presents a detailed review and analysis of the reservoir instrumentation response to SAGD. The evolution of temperature and pore pressure within the main instrumented section of the reservoir and the three dimensional development of the steam chamber are reviewed. The extensometer and inclinometer performance are discussed in detail and their results are used to generate a full strain field distribution within the reservoir. Reconstruction of the strain field allows inferences to be made concerning the deformation response of the reservoir without the presupposition of a stress-strain law or model.

Chapter 7 describes an uncoupled thermal-effective stress analysis of the geotechnical cross section using field measured temperatures and pore pressures. The results of this numerical analysis are compared with field instrumentation responses to help elucidate relevant geomechanical phenomena to the process of SAGD.

Chapter 8 summarizes and provides conclusions on the salient geomechanical issues of the steam assisted gravity drainage process. Topics for further research are identified and discussed.

CHAPTER 2 THE UNDERGROUND TEST FACILITY

"Would there be this eternal seeking if the found existed?"
Antonio Porchia

2.1 Project Description

Since 1968, Suncor has successfully proven the surface mining concept and by 1978, Syncrude would also be employing surface mining techniques in the recovery of bitumen from oil sands. Unfortunately, a significant quantity of oil sands are too deeply buried to be economically recovered by surface mining techniques.

In the mid-1970's, AOSTRA began to receive several proposals for bitumen recovery using underground mining techniques. The most interesting proposals suggested underground tunnels be constructed within or adjacent to the oil sands reservoir. This would permit people and equipment to be placed in or near the pay zone for the application of an in situ recovery process. Other concepts involved mining the oil sands with hydraulic jets or mechanized longwall mining techniques. While many of the proposals had merit, no underground field experience existed which could be used to evaluate the proposals.

To provide fundamental data for assessing these proposals, a mine assisted in situ processing (MAISP) study was initiated in late 1976 to examine the feasibility of applying the thermal mining concept to the Athabasca oil sands. The study included a visit to the Yarega operation in Northern Russia in December, 1976. At Yarega, tunnels are utilized to place people and equipment near a heavy oil reservoir. At that time, the Soviets estimated thermal stimulation from underground tunnels had increased the percentage recovery of oil from 10% to 57%. In 1979, as part of the MAISP study, a horizontal drilling, steam injection and production test was carried out from an oil sands outcrop. At the same time, AOSTRA and Gulf Canada began specific reviews of two concepts: (1) the Surface Access Concept (SAC), where wells are drilled from the surface and diverted horizontally through the reservoir, and (2) the Shaft and Tunnel Access Concept (SATAC), where the horizontal wells for injection and production are drilled from underground tunnels. It was concluded from these reviews that a greater amount of oil could be recovered with SATAC compared to the use of surface drilled holes. Esso Resources Canada Ltd. had reached the same conclusion from in-house studies on the use of horizontal wells drilled from tunnels.

The results from these reviews led AOSTRA to initiate a feasibility study in 1982 on the construction of an Underground Test Facility (UTF), which would permit the assessment of two discrete but complementary technologies: (1) the SATAC technology and (2) the process technology of horizontal well in situ recovery. A detailed design of the UTF was completed in

January, 1984 and construction began in June, 1984. The selection of a process for initial piloting at the UTF was made in 1985 with the selection of the Steam Assisted Gravity Drainage (SAGD) concept. In 1986, six oil companies: Chevron Canada Resources Limited; Texaco Canada Resources Ltd.; Mobil Oil Canada Ltd.; Petro-Canada Inc.; Shell Canada Limited; Amoco Canada Petroleum Company Ltd. and CANMET joined AOSTRA as participants in a Phase A program. The Phase A program was a pre-pilot program established for preliminary investigation of the SAGD process at approximately one-tenth pilot scale, to provide added assurance of project feasibility and to confirm a full pilot design basis. The UTF was also used for testing Chevron Canada's proprietary HASDrive (Heated Annulus Steam Drive) process.

The UTF project is located north of Fort McMurray, Alberta about 20 km due west of the Syncrude Canada surface mining operation, as shown in Figure 2.1. Tunnel access consists of two 3 m diameter vertical shafts sunk to a depth of 213 m. Shaft drilling was done using a blind boring technique with a modified, conventional, deep hole drilling rig.

The underground tunnel system was constructed in two stages: (1) an initial 350 m pit bottom development from the shafts and (2) a later extension of 580 m of tunnel to access and support the Phase A horizontal well drilling chambers. Tunneling was achieved using drill-and-blast methods. Where required, roof support was provided by 2.3 m and 3 m long Swellex bolts. Tunnel walls were shotcreted along main access routes and in the drilling chambers. Figure 2.2 illustrates overall configuration of the UTF for the Phase A program.

In conjunction with the Phase A trial of the SAGD process, an extensive geotechnical instrumentation program was undertaken to monitor safety and to evaluate the impact of geotechnical factors on the SAGD process. The geotechnical program was comprised of four elements: (1) tunnel instrumentation; (2) reservoir instrumentation; (3) laboratory testing and (4) numerical modeling.

2.2 Principles of the SAGD Process

A detailed discussion of the process physics of SAGD are beyond the scope of this thesis. A fundamental understanding of SAGD mechanics, however is required in order to study the interaction of reservoir and geomechanical processes. Prior to discussing the mechanics of SAGD, a brief description of the overall Phase A process is provided. While not critical to the examination of geomechanics of the SAGD process, an overall understanding of the Phase A operation is necessary to discuss the instrumentation results relative to steam chamber growth within the reservoir.

2.2.1. Process Facilities

The process facilities required for the Phase A operation are shown in Figure 2.3. Water was pumped from surface acquifers, treated, and passed through a propane fuel steam generator to produce 80% quality steam. The water fraction (or blowdown) was separated prior to injection, both to facilitate metering, and avoid injection of high pH steam. Steam was supplied to each injector via pressure controllers. While steam consumption rates varied according to demand in the reservoir, the pressure controllers maintained the steam chamber at a constant pressure. Produced fluids from the production wells was piped to surface.

Under normal circumstances, production pressures were high enough to flow up the shaft riser without the aid of artificial lift. Steam injection pressure was at approximately 2500 kPa whereas hydrostatic pressure at the bottom of the shaft was 1800 kPa. The produced fluids were cooled at surface, passed through a gas separator and stored in one of two product storage tanks. The fluids from the two product tanks and the waste water tank were trucked off site (Haston, et al, 1988).

The process or control scheme adopted for Phase A, termed steam trap control, controlled the temperature of the production, rather than its pressure or rate (Edmunds et al., 1992). The temperature setpoint was chosen based on flowing pressures, so that fluids were produced to maintain the wellhead temperature a specified value below the boiling point of water. Correct drawdown was automatically maintained, since no steam can be produced but neither can the production accumulate and cool at the bottom of the chamber.

2.2.2 Mechanics of SAGD

The recovery process chosen for testing in the Phase A program was the steam assisted gravity drainage (SAGD) process. The process of steam assisted gravity drainage involves the movement of oil to a production well under the force of gravity. The geometry of the process, schematically illustrated in Figure 2.4, is such that oil moves approximately parallel to the interface which forms the boundary of a growing steam saturated zone known as a steam chamber. In some respects, the process is analogous to that of water draining from a bathtub. In SAGD, steam does not "push" the oil out any more than air pushes water from the tub as it empties. Yet eventually steam fills the volume originally occupied by oil just as air eventually fills the tub (Butler, 1992). Start-up of the SAGD process requires that communication exist between the injector and producer. Unlike conventional or heavy oil, bitumen has negligible mobility. Typically, hydraulic fracturing or the availability of water sands would permit initial well communication to be achieved. For the Phase A trials, conductive heating between the well pairs was used as a means of effecting communication. Hot water steam was circulated under pressure, in both wells, with a small pressure differential of approximately 350 kPa applied between wells by circulating at different pressure. Details of the actual process history are reviewed in detail in Chapter 4. When the bitumen becomes warm enough to move, convective heating starts to become significant. This leads to steam breakthrough and the development of an initial steam chamber around the injector. At this point, the process of SAGD begins and involves ceiling and slope drainage; each characterized by their orientation to the steam front. Figure 2.5 illustrates the flow geometry associated with each drainage mode. In slope drainage, bitumen is continuously pulled away from the front by gravity. Ceiling drainage is controlled by countercurrent flow; steam is flowing upwards while bitumen and condensate are draining downwards. Conduction heating does not significantly influence the rise rate because only the next pore space must be heated for the front to advance; at the pore scale conduction heating is a rapid process (Edmunds et al., 1988). In terms of flow however, the requirement that all three phases (water, bitumen, steam) must exist within the same pore system, all at mobile saturation, results in low permeabilities for all three phases.

Countercurrent flow does not play a leading role in slope drainage. Bitumen is heated by conduction in a thin layer ahead of the advancing front. This layer of mobilized bitumen moves down the slope, as shown in Figure 2.5, according to the component of gravity parallel to the front. Vectorily, the direction of bitumen flow is different than the direction of steam flow.

The actual growth of a steam chamber within the reservoir will be a combination of both drainage processes. The initial growth of the steam chamber is controlled by ceiling drainage. The upward flow of steam creates a significant pressure gradient which tends to reduce the gravity potential of the bitumen, causing it to "hold up" on the sides of the growing steam chamber. When the top of the rising steam chamber reaches the top of the pay, ceiling drainage of bitumen ceases and steam consumption at the top begins to decline. Pressure gradients in the steam chamber are reduced and the full gravity head is available to move bitumen down the sides of the steam chamber. Slope drainage then begins to dominate and the edges begin to recline, rapidly widening the steam chamber. Edmunds et al., (1988) provide a simulation of steam chamber growth in a homogeneous, isotropic oil sands reservoir. The vertical growth of the steam chamber followed by rapid widening is clearly evident from the simulation results presented in Figure 2.6. Note that the assumption of isotropic permeability was made for the simulations. The influence of anisotropic permeabilities are shown in Figure 2.7. A reduction in kv significantly retards the ceiling drainage and the rise rate of the steam chamber.

2.3 Geology

The general stratigraphy at the UTF is shown in Figure 2.8. The upper 30 m of the Devonian Waterways Formation consists of alternating layers of argillaceous, nodular and massive limestone units. The top surface of the limestone occasionally exhibits a pyritized or weathered zone approximately 2 to 3 cm thick. While the McMurray Formation within the Phase A site rests unconformably on the Devonian limestone, the oil sands-limestone contact is generally very well defined. The main pay or reservoir is about 23 m thick interrupted by several shaley zones within the bottom few metres of the pay zone. Overlying the rich oil sands, 17 m of interbedded oil sand and shale grade up to sandy shale at the top of the formation. The McMurray is overlain by 2 m of water saturated Wabiskaw sand, a member of the Clearwater Formation. The remainder of the overburden at the Phase A site consists of 75 m of Clearwater Formation shales overlain by 30 m of sandy shales of the Grand Rapids Formation, which in turn is capped by 15 to 20 m of till and sand and gravel.

In order to understand the impact geology may have on the Phase A trials, detailed knowledge of the McMurray Formation is required. Rottenfusser et al., (1990) conducted a regional depositional study to identify environments and deposits at the UTF. Core taken from several drilling programs were extensively studied and a series of facies identified. Figure 2.9 shows the location of wells, relative to the Phase A site, which were used in constructing structural cross sections. Figures 2.10 and 2.11 provide the local geology surrounding the Phase A site. Structural cross-sections were developed to show the main depositional regions within the AOSTRA UTF lease.

The McMurray Formation within the UTF lease contains a sand body deposited in a tidal channel which was part of an estuarine complex developed during a transgression of the Clearwater Sea into Northeastern Alberta from the North. During deposition of the McMurray Formation, conditions gradually changed from fluvial to estuarine and finally to nearshore marine. Facies changes along the western or erosional edge of the channel are very abrupt, but along the eastern edge, facies changes are gradational. Muddy off-channel deposits along either side of the north-south trending channel were laid down in channel margin and tidal flat settings (Rottenfusser et. al., 1990).

Carrigy (1959) identified three formal divisions within the Lower Cretaceous McMurray Formation; lower, middle and upper. Typically, the lower member is composed of water saturated point bar sands. At the UTF site, the lower member is absent and the middle member rests unconformably on the Devonian limestone. Historically, the origin or deposition of the middle member has received a great deal of attention as this zone usually contains the highest oil saturations (Carrigy, 1959, 1971; Stewart and MacCallum, 1978; Stewart, 1981; James and Oliver, 1978; Mossop and Flack, 1983; Cuddy and Muwais, 1987; Rennie, 1987)

Both cross sections show a unit of oil sand with a variable percentage of interbedded shale overlying the Devonian limestone. This unit is interpreted to have been deposited in a fluvial/estuarine environment. Where tidal channel sands overly this unit, and wells AO24 and AO36 in Figure 2.10 and wells AGB1, AO13 and AO25 in Figure 2.11, distinction between the two facies is difficult.

The shale content and degree of bioturbation in the channel sediments reflects the depth of water and energy in the depositional environment (Rottenfuser et al., 1990). Tidal channel facies along the eastern edge are gradational and blend into each other. The western edge of the tidal channel is abrupt and erosional with clean, bitumen bearing sands in sharp contact against the interbedded sands and shales of the rhythmic bedded units. The rhythmic bedded sand/mud tidal flat sediments are interbedded with breccias and clean sands which were deposited by shallow tidal creeks which meandered across the tidal flats.

The rhythmic bedded sand/mud tidal flat sediments and the tidal channel sediments are overlain by sand and mixed tidal flat deposits. Point bar sediments also overly these deposits and thicken towards the east. At Well AO28 in Figure 2.11, sand tidal flat sediments overly the point bar deposits. Evidence of a thin coarse grained transgressive lag is also found in Well AO28.

Mattison (1987) reports that MacCallum and Stewart (1983) feel the upper and middle McMurray were disconformable with another and the transgressive lag mentioned above developed through transgressive incision into the middle McMurray. MacCallum and Stewart (1983) place the thin facies within the Upper McMurray. Mattison (1987), however, provides evidence that most geological data does not support an hiatus within the McMurray Formation. Rather, the transgression lag is an areally restricted facies which comprises a transitional zone between the estuarine regime of the middle McMurray and the marginal marine region of the Upper McMurray. Figure 2.12 illustrates the stratigraphic column of the McMurray Formation as given by Mattison (1987). These "bay-sound" deposits, as labelled by Mattison (1987), are characterized by dark grey, calcareous muds which are usually interbedded with medium-to-coarse grained sands. Rottenfusser, et al(1990) describe the transgressive lag facies as a medium grey mudstone interbedded with lenses and beds of fine to coarse grained sand. Although these competing interpretations are of geological interest in defining the regional depositional history of the UTF lease, the characteristics of the transgressive lag will not impact the Phase A site since there is no evidence of its presence there.

Overlying the tidal flat sediments and transgressive lag are widespread marine shoreface sediments, which form the Upper McMurray Formation. The entire sequence is capped by the offshore marine bar sands of the Wabiskaw Member at the base of the Clearwater Formation. Table 2.1 summarizes the facies descriptions for these environments of deposition.

The above discussion on the regional geology of the UTF lease is important, and serves to illustrate the complex despositional history of the McMurray Formation. However, an understanding of the detailed geology at the Phase A site is of greater importance in order to assess the role of geology during the Phase A steam trials. Figure 2.13 shows an expanded plan view of the Phase A site shown in Figure 2.9. Twenty six vertical wells were drilled within the

7500 m^2 limits of the Phase A pad. An extensive coring and logging program was completed as part of the drilling program. A total of 514 m of core were recovered from 14 wells and a minimum suite of open hole geophysical logs were run for each well. A complete log suite, including a dipmeter tool, was completed on 13 wells. Figure 2.14 shows the extent of the coring and geophysical logging program.

This information was utilized by Rottenfusser et al., (1989) to provide a detailed geological characterization of the Phase A reservoir including stratigraphy, description of the stratigraphic units, depositional interpretation and reservoir parameters. The stratigraphic section at Phase A was informally divided into like units, A to H, each of which can be correlated throughout the Phase A site. Figure 2.15 illustrates the general configuraton of these units. Given the continuity of these units across the Phase A site all reference to geological horizons at Phase A will be made to these units. In the following discussion describing these units, however, the facies identified by Rottenfusser et al (1990) will be identified with the appropriate stratigraphic well.

2.3.1 Local Phase A Geology

Unit A - Figure 2.16

Unit A consists of a medium to coarse grained, light grey, friable, salt and pepper sand and forms the Wabiskaw Member of the Clearwater Formation. Glauconite is visible at the top of the unit where it is gradational into the overlying marine shale of the Clearwater Formation and is interbedded with shales at the base of the unit. This unit represents the offshore marine bar deposits mentioned previously.

Unit B - Figure 2.17

Unit B is composed of light to dark grey soft shales mixed with sand. The shales are generally bioturbated with sand filled horizontal burrows and sand lenses. This unit comprises Facies 1; the uppermost unit in the McMurray Formation. Unit B was deposited in a marine lower shoreface environment. The unit is laterally continuous throughout the Phase A site and throughout the UTF lease, as shown in Figure 2.10 and Figure 2.11

Unit C - Figure 2.18

Unit C consists of fine to medium grained dark brown, oil sand interbedded with light brown shale. The upper part of this unit is bioturbated with vertical and horizontal burrows. A shale zone with no bioturbation forms the base of Unit C. The upper contact with Unit B is gradational and the lower contact with Unit D is abrupt. The environment of deposition has been defined as tidal flat zones by Rottenfusser, et al (1990). Based on the regional depositional environment, Unit C is comprised of Facies 4 and 5. Facies 4, which consists of bioturbated muddy sand with some preservation of primary stratification, forms the upper portion of Unit C. This facies corresponds to a sand tidal flat depositional environment. This facies grades into Facies 5, which forms the lower portion of Unit C. Facies 5 is comprised of interbedded, very fine to fine grained sand and mudstone. Mudstone interbeds are strongly bioturbated and dominantly composed of thin, wavy, continuous to discontinuous laminate mixed with sand lenses and sand filled burrows. Sand-mudstone interbed contacts are sharp and irregular. This facies was deposited on lateral acretion bars or point bars along the depositional side of the tidal channel. The thin mud beds were deposited during periods of slack water.

Unit D - Figure 2.19

Unit D consists of dark brown, bitumen saturated oil sands with cross bedding dips of approximately 20°, interbedded with shale laminae. The shale is moderately bioturbated with horizontal and vertical burrows. The amount of shale present decreases towards the base of the unit where the sands show low angle cross beds with shale stringers with low bioturbation. This unit forms the upper portion of the tidal channel sediments and contains Facies 10, 11 and possibly 12 at the very bottom of the unit. Facies 10 is characterized by very thin to thin bedded, medium to high angle, trough and planar cross stratified sand. This facies is associated with sand deposited under moderate to high energy conditions on bars and sand waves in tidal channels. Facies 11 is comprised of low-angle very thin to thin bedded, cross-stratifed sand. Medium, light grey, wavy mudstone laminations with variable bioturbation and scattered mudstone clasts do occur within this facies. Bedding contacts between sandbeds and mud laminations are sharp and undulatory. The depositional environment is the same as Facies 10 except that mud laminations were deposited during low water flow. Facies 12 is a massive, structurelss, fine to medium grained sand with occasional medium light grey mudstone clasts. Facies 12 is associated with the depostional regime as Facies 10 and 11.

Unit E - Figure 2.20

This unit is the main pay within the Phase A site. It consists of interbedded oil sands and shale breccia. The breccia consist of grey to light brown shale fragments showing some bioturbation in the oil sands. This unit is dominantly associated with Facies 12, as described for Unit D.

Unit F - Figure 2.21

Unit F is dominantly shale, grey to light brown in color and thinly bedded with an abrupt contact with the overlying oil sands (Unit E). Unit F is Facies 13, a massive, structureless mudstone which is distributed sporadically throughout the McMurray Formation. Facies 13 is difficult to correlate from well to well. It exhibits rare occurrences of bioturbation and contains occasional sand lenses. Basal contacts with related facies are sharp, smooth and low angle. This unit was formed by suspension deposits laid down under conditions of very low water flow at the top of the basal fluvial/estuarine sequence.

Unit G - Figure 2.22

At the Phase A site, Unit G is extremely variable but generally consists of bitumen saturated, medium to coarse grained sand. The unit is strongly bioturbated and contains occasional light grey, bioturbated shale clasts. This unit forms the fluvial/estuarine regional depositional regime and is comprised of Facies 12 and 13, as described in Units E and F, respectively.

In the same fashion as the regional geological cross sections provided in Figures 2.10 and 2.11, Figures 2.24, 2.25, 2.26, and 2.27 provide structural cross sections defining the position of the stratigraphic units within the Phase A site. Figure 2.23 provides the well to well orientations of the structural cross sections.

Of prime importance within the Phase A site is the dilineation of shale barriers. As pointed out in the discussion of the process of SAGD, shale barriers of limited extent will not havea large impact. For the purposes of this study, a shale barrier constitutes a zone of > 50% shale of at least 0.5 m thickness. Continuous barriers within the reservoirs, however, will play a large role in the development of the steam chambers. F igures 3.28 and 3.39 offer two perspective views of the Phase A McMurray Formation and the interpreted location of significant shale seams. The locations of these shale seams have been selected based on Rottenfusser et al.(1989), Thurber Consultants (1990) and personal observations of geological data. At this point, Figures 2.28 and 2.29 are offered without discussion. These diagrams will be used further in presenting data on the development of the steam chamber within the Phase A reservoir.

2.4 Geotechnical Cross-Section

While dealing in three dimensions to visualize the geologic configuration of the reservoir is ideal, it becomes impractical and time consuming to present all the results in a three dimensional format. Consequently, most data in this thesis will be presented on a west-east plane cutting through the reservoir. This plane, which will be referred to as the geotechnical cross-section, will pass through wells AGI1 on the west and AGI3 on the east. Figure 2.30 shows the location of the shale barriers within the geotechnical cross section.

Facies	Lithology	Geometry	Facies Sequence & Dominant Assoc.	Depositional Environment
1	Medium to medium-dark gray, lenticular, very thin bedded, sandy mudstone.	Laterally continuous throughout the area ranging in thickness from 3.4 to 14 m. Thickens to the SW.	Sequence A: Overlie Facies 2	Marine Lower Shoreface
2	Medium to dark gray mudstones interbedded with fine to coarse grained sand.	Thin and discontinuous across the area. Ranges in thickness from 0 1.5 m.	Sequence A: Underlie Facies 1	Transgressive Lag
3	Completely bioturbated, very fine grained, muddy sand. Muds are pale yellowish-brown to light tan.	Confined to the NE corner of the study area. Ranges in thickness from 0 to 12.8 m.	Sequence B: Overlies Facies 4,7	Mixed Tidal Flat
4	Intensely bioturbated, very fine grained, muddy sand containing occasional zones of preserved primary stratification.	Exists as three isolated bodies w/in the central and eastern regions. Thickness ranges from 0 to 6.4 m.	Sequence B: Underlies Facies 3,7	Sand Tidal Flat
5	Moderately bioturbated, interbedded, very fine to fine grained sand and mudstone.	Distributed throughout eastern half of study area. Ranges in thickness from 0 to 10.2 m.	Sequence C: Overlies Facies 10, 11, 12, 15	Channel Point Bar
6	Interbedded to interlaminated, very fine to fine grained sand & mudstone. Bioturbation is absent except for rare Planolites.	Confined to the NW quadrant of study area. Ranges in thickness from 0 - 9.6 m.	Sequence B Interbedded with Facies 8,9	Mid Tidal Flat
7	Planar, very thinly laminated, low-angle, very fine grained sand.	Occurs as very thin, discontinuous beds located primarily in the E portion of study area.	Sequence B: Interbedded with Facies 3,4	Flood Deposits
8	Matrix supported, mudstone clast breccia consisting of poorly sorted, angular clasts (< 3 cm) w/in fine grained sand.	Confined to the west central region. When combined with Facies 9 appears as a north-south trending body.	Sequence B: Interbedded with Facies 6,9	Tidal Creek Channel Lag
9	Matrix to clast supported mudstone breccia comprised of poorly sorted, angular to sub-rounded clasts (< 3 cm) w/in fine grained sand.	Confined to the west central region. Facies 9 and 8 together attain a max. thickness of 15.5 m.	Sequence B: Interbedded with Facies 6,8	Tidal Creek Channel Lag
10	Very thin to thin bedded, medium to high-angle, cross-stratified sand.	Occurs throughout the UTF lease, but is thickest w/in the central region.	Sequence C: Interbedded with Facies 11,12,15	Channel Sand
11	Very thin to thin bedded low-angle, fine grained sand. Mudstone laminations and clasts are occasionally present.	Occurs throughout the UTF lease, but is thickest w/in the central region.	Sequence C: Interbedded with Facies 10,12,15	Channel Sand

Table 2.1 Facies Description

Facies	Lithology	Geometry	Facies Sequence & Dominant Assoc.	Depositional Environment
12	Massive, fine to medium grained sand.	Occurs throughout the UTF lease, but is thickest w/in the central region.	Sequence C: Interbedded with Facies 10,11,15	Channel Sand
13	Light to medium gray, massive, mudstone with occasional horizontal burrows and sand lenses.	Occurs as a thin, discontinuous unit which is generally less than 1m thick. Commonly present in the lower McMurray.	Sequence C: Interbedded with Facies 10,11,12	Channel Abandonment
14	Light to medium gray, thinly laminated, silty mudstone. Bioturbation is slight to strong.	Occurs w/in the eastern and western portions of study area and is generally < 2m thick.	Sequence B: Overlies/Interbedded with Facies 18,19,21	Mud Tidal Flat
15	Very fine grained, ripple cross-laminated sand with occasional mud laminations and carbonaceous remains.	Common throughout the study area but occurs most frequently w/in the central region.	Sequence C: Overlies/Interbedded with Facies 10,11,12	Channel Sand
16	Buff to gray, fossiliferous, nodular textured, argillaceous limestone.	Waterways limestone unconformably underlies the McMurray Fm. throughout the study area.	n/a	Open Marine
17	Dense, chaotically orientated, accumulation of shell debris.	Confined to an isolated bed w/in AO-30, in the western quadrant of the study area.	Sequence B: interbedded with Facies 6	Storm Lag Deposit
18	Light to medium brown, very thinly laminated to intensely bioturbated silt.	Found w/in the western and eastern portions of the study area, rarely exceeding 30 cm thick.	Sequence B & C: Interbedded with Facies 13,14,19	Mud Tidal Flat
19	Medium-light gray to light brown, bioturbated, interbedded, sandy mudstone.	Confined to the eastern and western margins of the study area, attaining thicknesses of up to 7 m.	Sequence B: Interbedded with Facies 3,14,18	Mud Tidal Flat
20	Very fine grained sand containing silt filled burrows and thin, discontinuous silt laminae.	Primarily occurs w/in the east central region. The deposits are commonly thin, but can be up to 4m thick.	Sequence C: Interbedded with Facies 5, 11	Sand Shoal
21	Medium yellowish-brown, microlaminated, muddy, silt and sand.	Restricted to the west central area and ≤ 3 m thick.	Sequence B: Interbedded with Facies 14,18,19	Mud Tidal Flat

Table 2.1 (cont'd) Facies Description

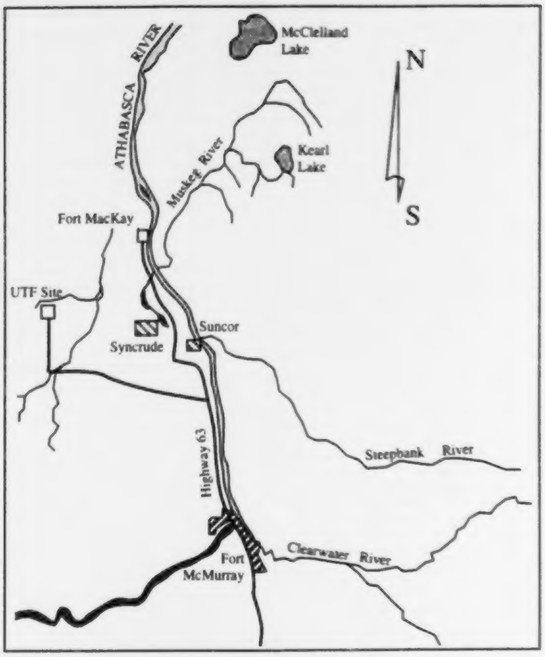
McClelland Lake
N
S
ATHABASCA RIVER
Muskeg River
Kearl Lake
Fort MacKay
UTF Site
Syncrude
Suncor
Highway 63
Steepbank River
Clearwater River
Fort McMurray

Figure 2.1 Location of the Underground Test Facility

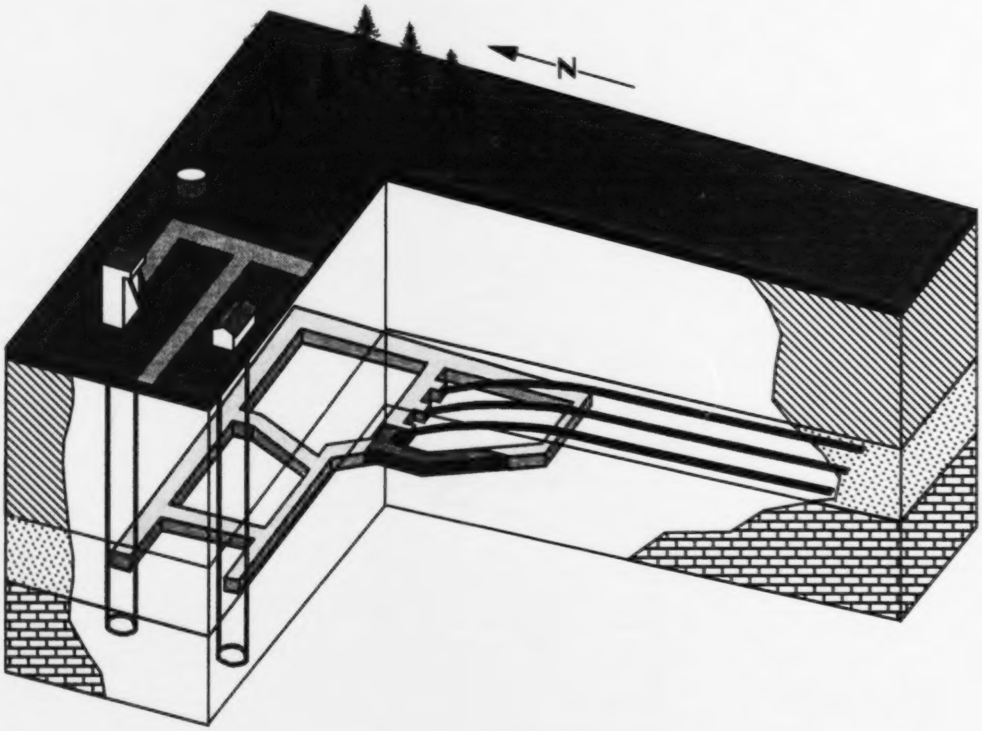

Figure 2.2 Overall Layout of the Underground Test Facility

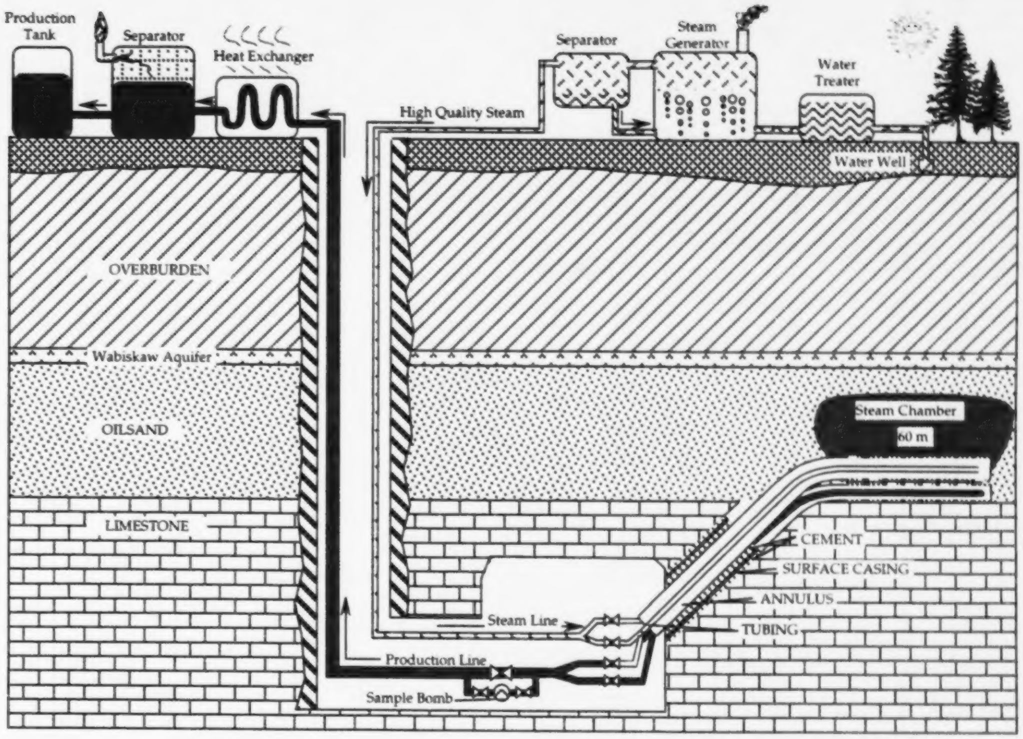
Production Tank
Separator
Heat Exchanger
Separator
Steam Generator
Water Treater
High Quality Steam
Water Well
OVERBURDEN
Wabiskaw Aquifer
OILSAND
Steam Chamber
60 m
LIMESTONE
CEMENT
SURFACE CASING
ANNULUS
TUBING
Steam Line
Production Line
Sample Bomb

Figure 2.3 Schematic Representation of the UTF Phase A SAGD Process

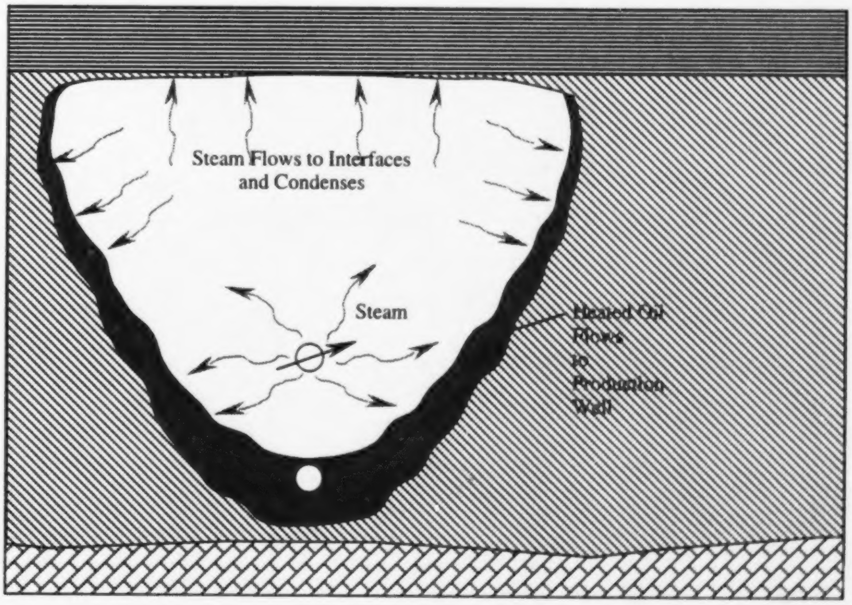
Steam Flows to Interfaces and Condenses
Steam
Heated Oil Flows to Production Well

Figure 2.4 Schematic of SAGD Process

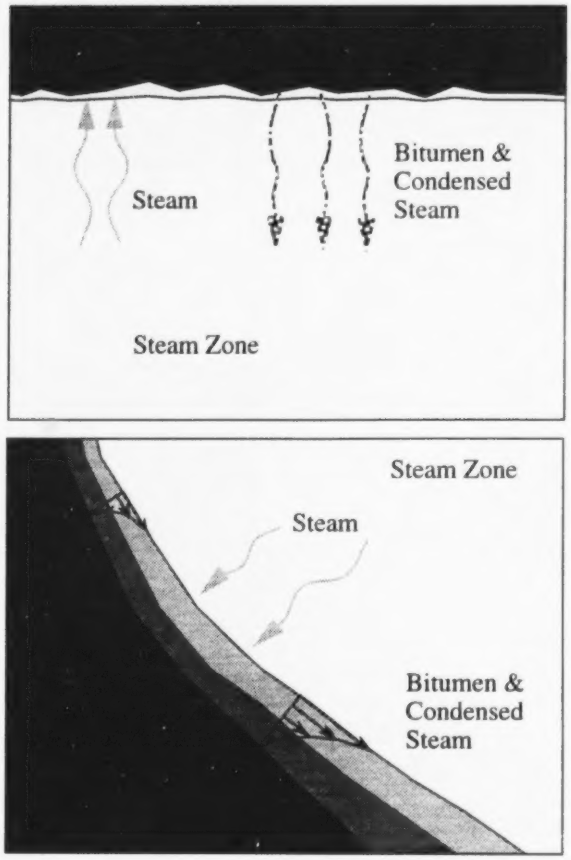
Steam
Bitumen &
Condensed
Steam
Steam Zone
Steam Zone
Steam
Bitumen &
Condensed
Steam

Ceiling Drainage:

Bitumen is pulled away from the front immediately after mobilization; steam rise usually impedes liquid drainage.

Slope Drainage:

Gravity holds mobilized bitumen against the slope; bitumen accumulates in a progressively thicker layer. Steam and liquids usually do not interfere with each other.

Figure 2.5 Ceiling vs. Slope Drainage Processes (modified from Edmunds and Collins, 1988)

Isotropic Permeabilities

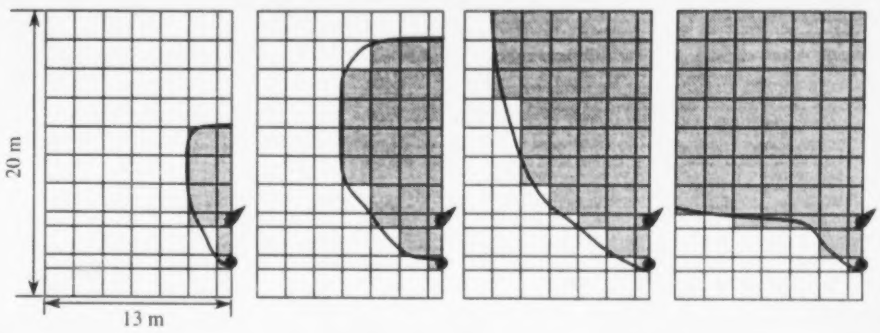

Parameters: $k_v/k_h = 1.0$, $k_h = 5.0$ Darcys
$\phi = 30\%$
$S_{oi} = 85\%$
$S_{or} = 20\%$
Injection Pressure = 2500 kPa
Production Constraint = 0.005 m ^{3}/day steam (CWE)/m of wellbore

Figure 2.6 Steam Chamber Growth in Homogeneous, Isotropic Sand (modified from Edmunds et al., 1988)

Anisotropic Permeabilities

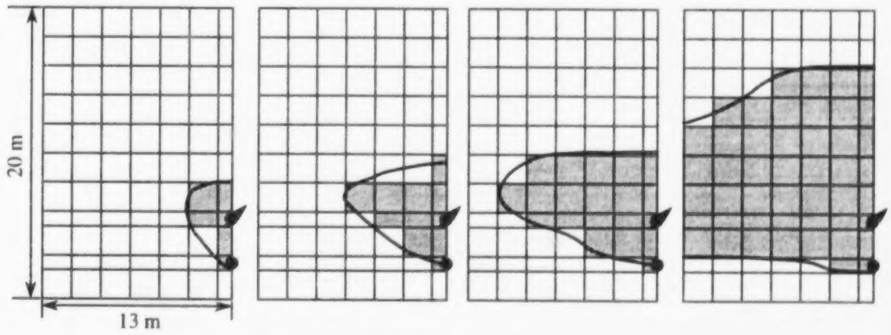

Parameters: $k_v/k_h = 0.1$, $k_h = 5.0$ Darcys
$\phi = 30\%$
$S_{oi} = 85\%$
$S_{or} = 20\%$
Injection Pressure = 2500 kPa
Production Constraint = 0.005 m ^{3}/day steam (CWE)/m of wellbore

Figure 2.7 Steam Chamber Growth in Homogeneous, Anisotropic Sand (modified from Edmunds et al., 1988)

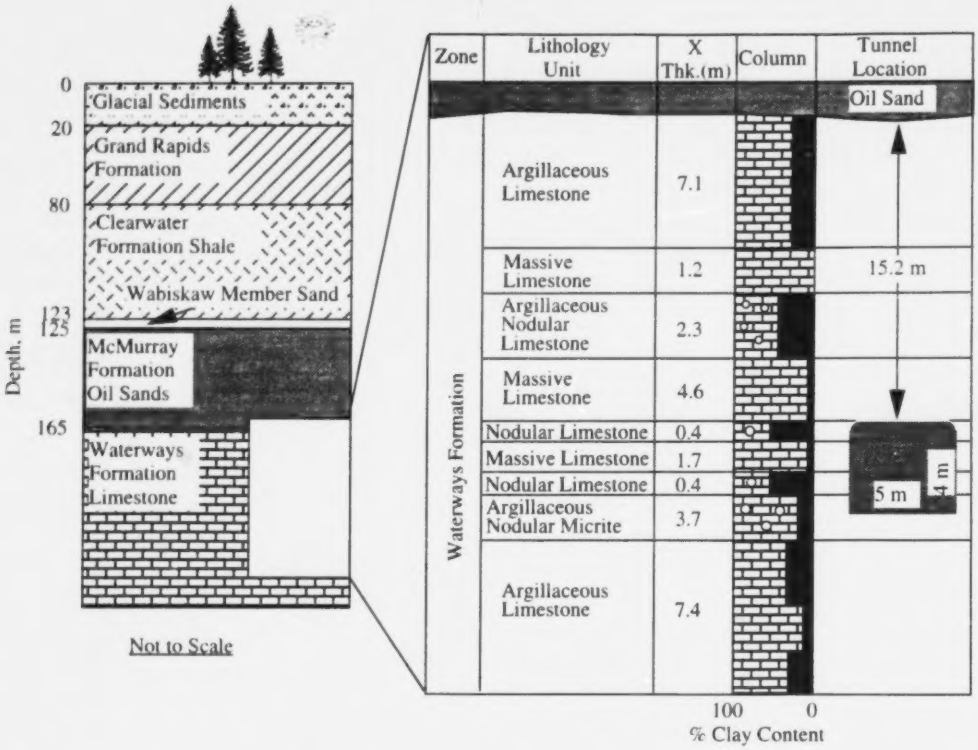
0
Glacial Sediments
20
Grand Rapids Formation
80
Clearwater Formation Shale
Wabiskaw Member Sand
123
125
Depth, m
McMurray Formation Oil Sands
165
Waterways Formation Limestone
Not to Scale
Zone
Lithology Unit
X Thk.(m)
Column
Tunnel Location
Oil Sand
Waterways Formation
Argillaceous Limestone
7.1
Massive Limestone
1.2
15.2 m
Argillaceous Nodular Limestone
2.3
Massive Limestone
4.6
Nodular Limestone
0.4
Massive Limestone
1.7
Nodular Limestone
0.4
Argillaceous Nodular Micrite
3.7
Argillaceous Limestone
7.4
5 m
4 m
100
0
% Clay Content

Figure 2.8 Geology of the UTF Site

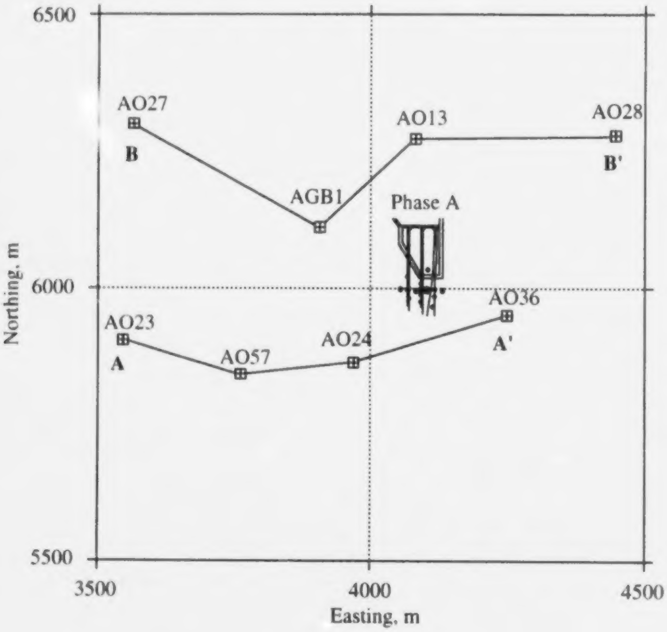
6500
6000
5500
Northing, m
3500
4000
4500
Easting, m
AO27
B
AGB1
AO13
AO28
B'
Phase A
AO23
A
AO57
AO24
AO36
A'

Figure 2.9 Location Map for Regional Structural Cross Sections

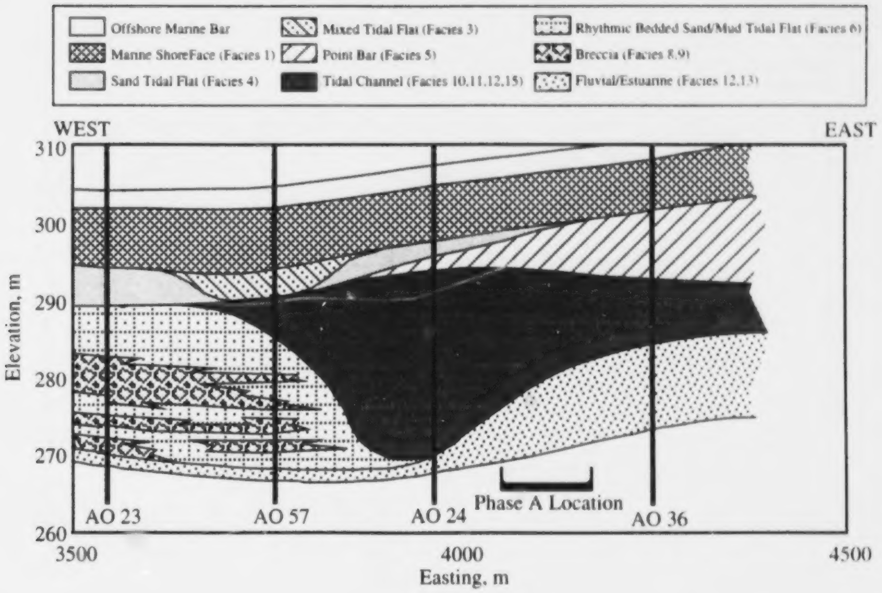
Offshore Marine Bar
Marine ShoreFace (Facies 1)
Sand Tidal Flat (Facies 4)
Mixed Tidal Flat (Facies 3)
Point Bar (Facies 5)
Tidal Channel (Facies 10,11,12,15)
Rhythmic Bedded Sand/Mud Tidal Flat (Facies 6)
Breccia (Facies 8,9)
Fluvial/Estuarine (Facies 12,13)
WEST
EAST
310
300
290
280
270
260
Elevation, m
AO 23
AO 57
AO 24
Phase A Location
AO 36
3500
4000
4500
Easting, m

Section A-A'

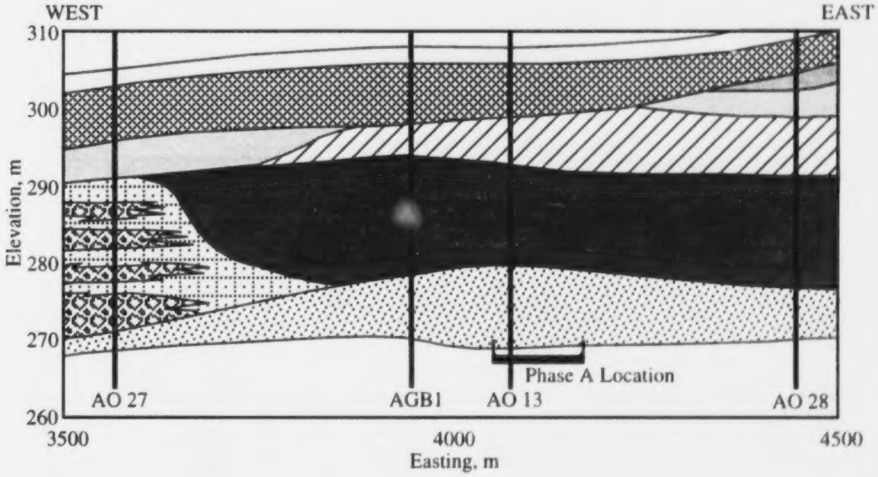
WEST
EAST
310
300
290
280
270
260
Elevation, m
Phase A Location
AO 27
AGB1
AO 13
AO 28
3500
4000
4500
Easting, m

Section B-B'

Figure 2.10 Regional Structural Cross-Sections A-A' and B-B'

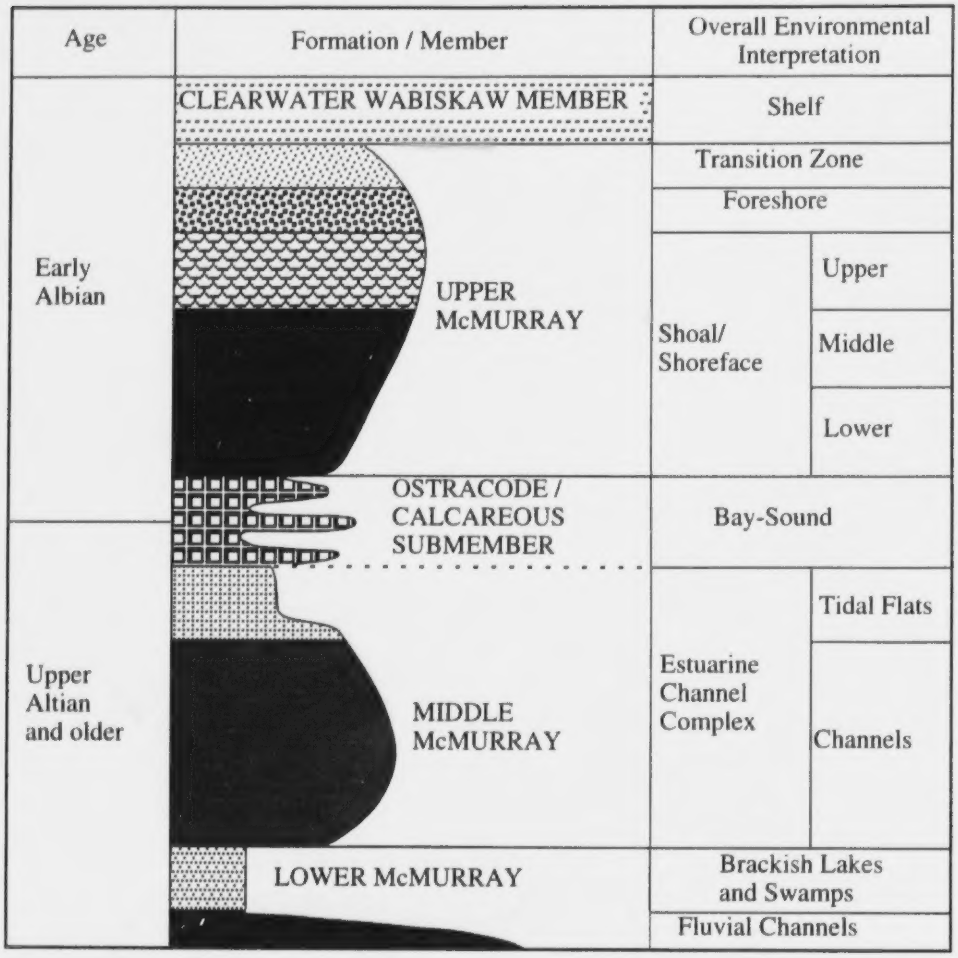
Age
Formation / Member
Overall Environmental Interpretation
CLEARWATER WABISKAW MEMBER
Shelf
Transition Zone
Foreshore
Early Albian
UPPER McMURRAY
Shoal/ Shoreface
Upper
Middle
Lower
OSTRACODE / CALCAREOUS SUBMEMBER
Bay-Sound
Tidal Flats
Upper Altian and older
MIDDLE McMURRAY
Estuarine Channel Complex
Channels
LOWER McMURRAY
Brackish Lakes and Swamps
Fluvial Channels

Figure 2.11 Stratigraphic Column for McMurray Formation (modified from Mattison, 1987)

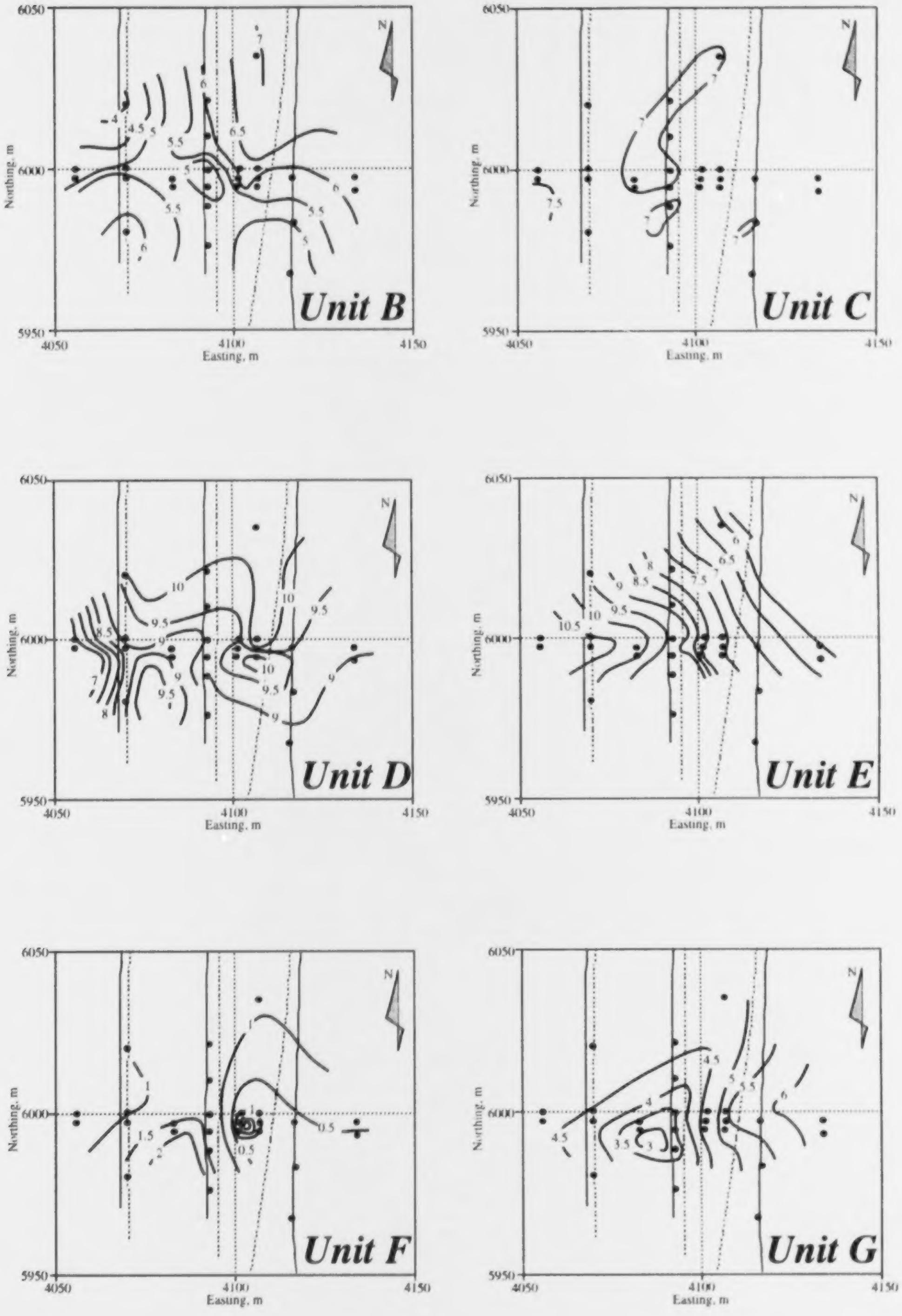
Unit B
Unit C
Unit D
Unit E
Unit F
Unit G
N
6050
6000
5950
4050
4100
4150
Northing, m
Easting, m

Figure 2.12 Isopach's of Geological Units Within the McMurray Formation (modified from Rottenfusser, 1989)

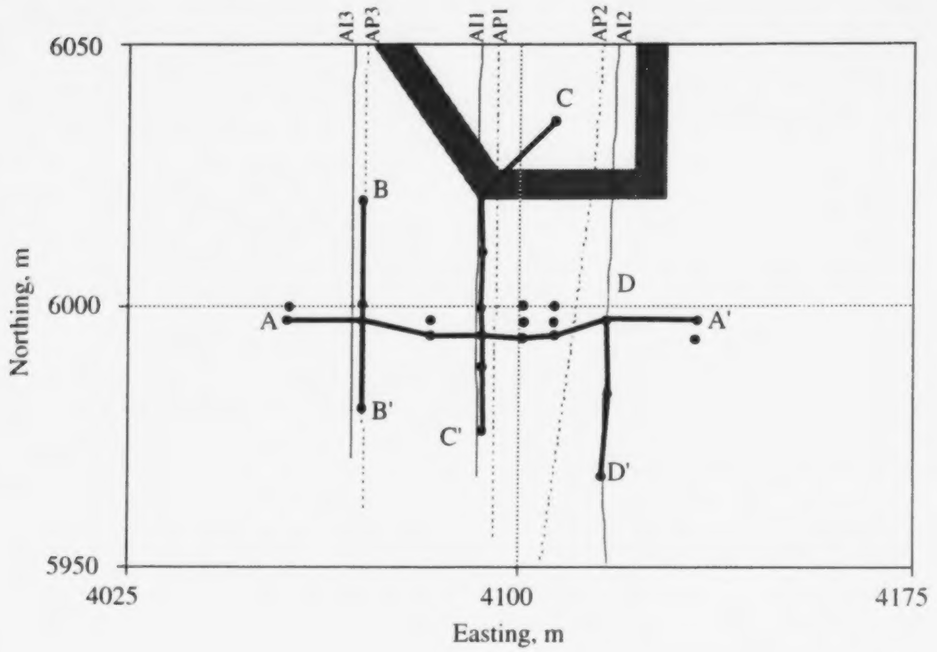
AI3
AP3
AI1
AP1
AP2
AI2
6050
6000
5950
Northing, m
4025
4100
4175
Easting, m
A
A'
B
B'
C
C'
D
D'

Figure 2.13 Location of Phase A Stuctural Cross Sections

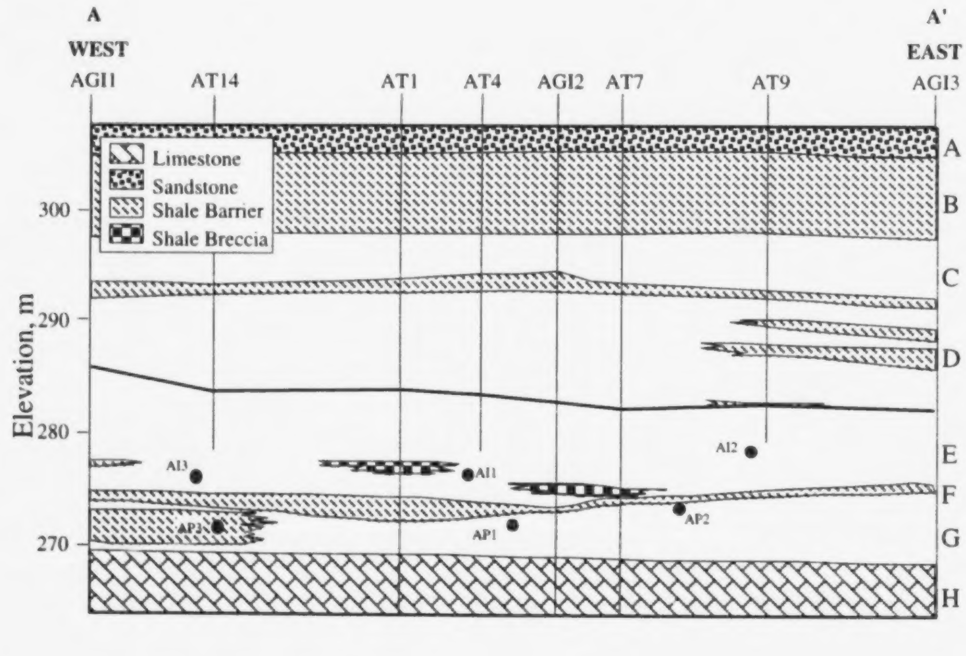
A
WEST
A'
EAST
AGI1
AT14
AT1
AT4
AGI2
AT7
AT9
AGI3
Limestone
Sandstone
Shale Barrier
Shale Breccia
300
290
280
270
Elevation, m
A
B
C
D
E
F
G
H
AI3
AI1
AI2
AP3
AP1
AP2

Figure 2.14 West-East Structural Cross Section A-A'

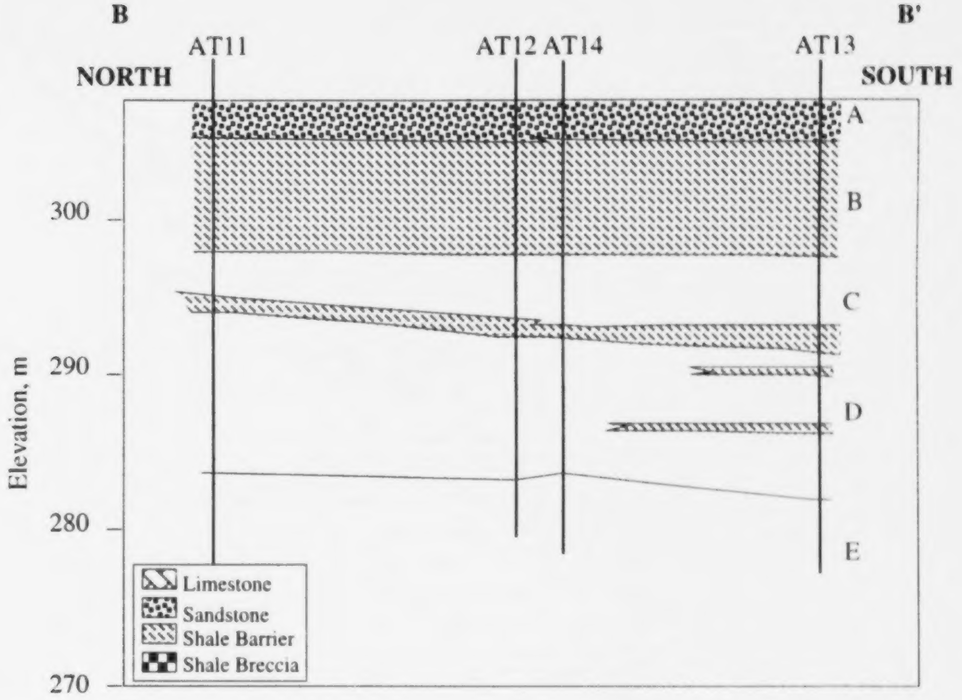
B
B'
AT11
AT12 AT14
AT13
NORTH
SOUTH
A
B
C
D
E
Elevation, m
300
290
280
270
Limestone
Sandstone
Shale Barrier
Shale Breccia

Figure 2.15 West-East Structural Cross Section B-B'

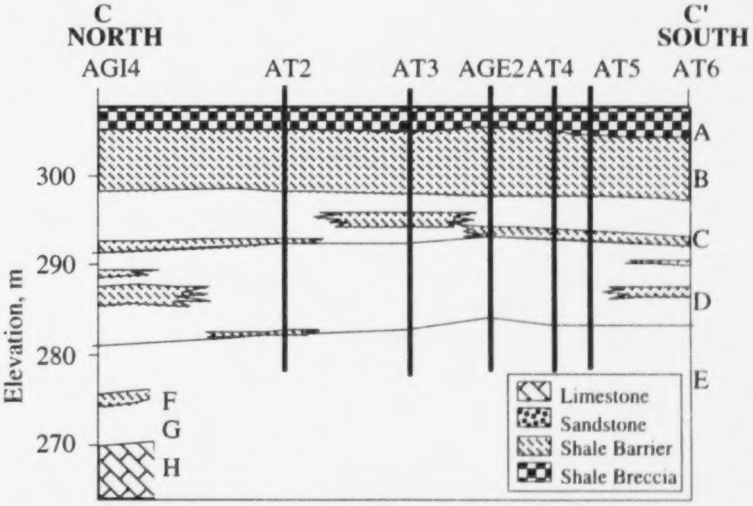
C
NORTH
C'
SOUTH
AGI4
AT2
AT3
AGE2
AT4
AT5
AT6
A
B
C
D
E
F
G
H
Elevation, m
300
290
280
270
Limestone
Sandstone
Shale Barrier
Shale Breccia

Figure 2.16 West-East Structural Cross Section C-C'

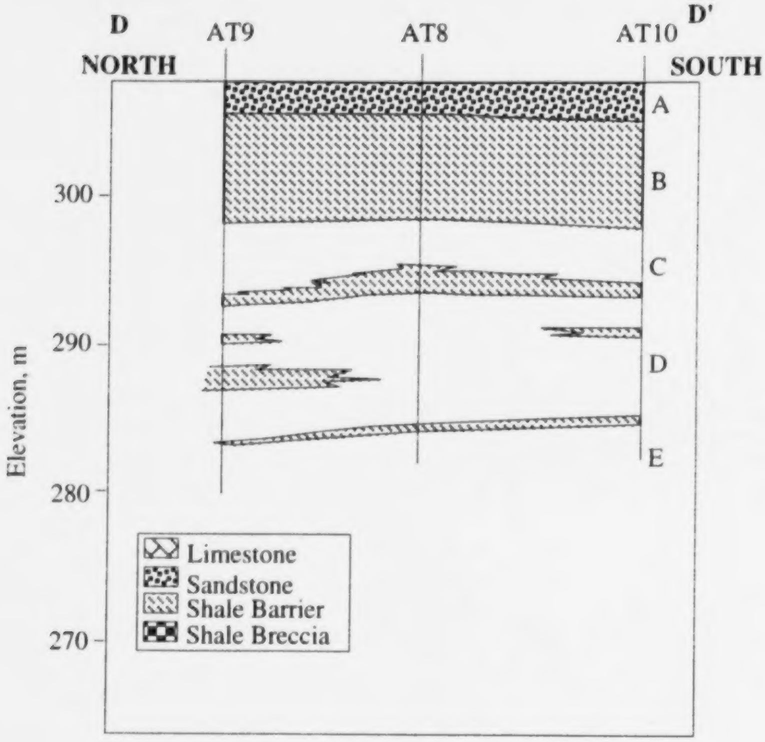
D
NORTH
AT9
AT8
AT10
D'
SOUTH
A
B
C
D
E
300
290
280
270
Elevation, m
Limestone
Sandstone
Shale Barrier
Shale Breccia

Figure 2.17 West-East Structural Cross Section D-D'

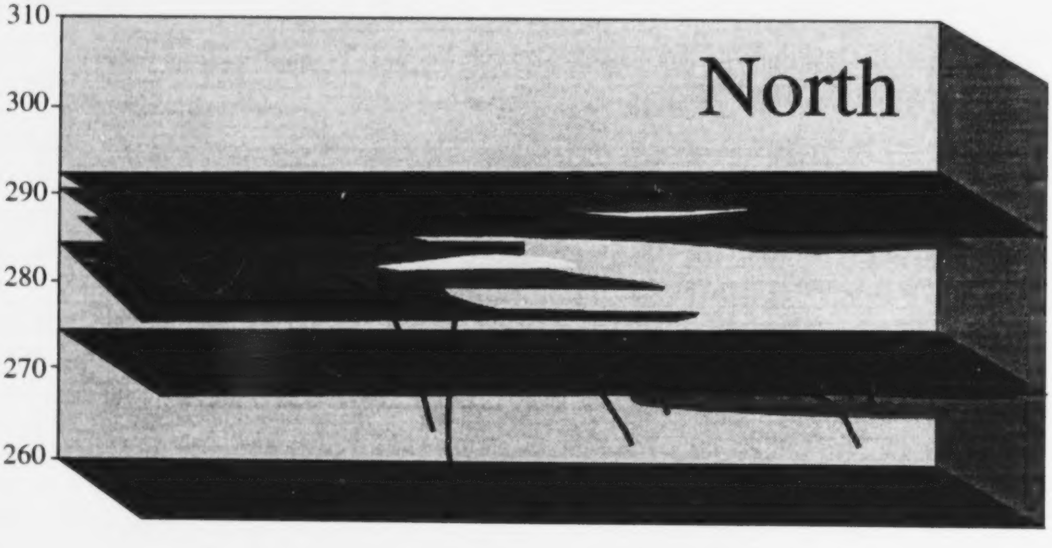
310
300
290
280
270
260
North

Figure 2.18 Isometric View of Shale Barriers - Looking from North to the South

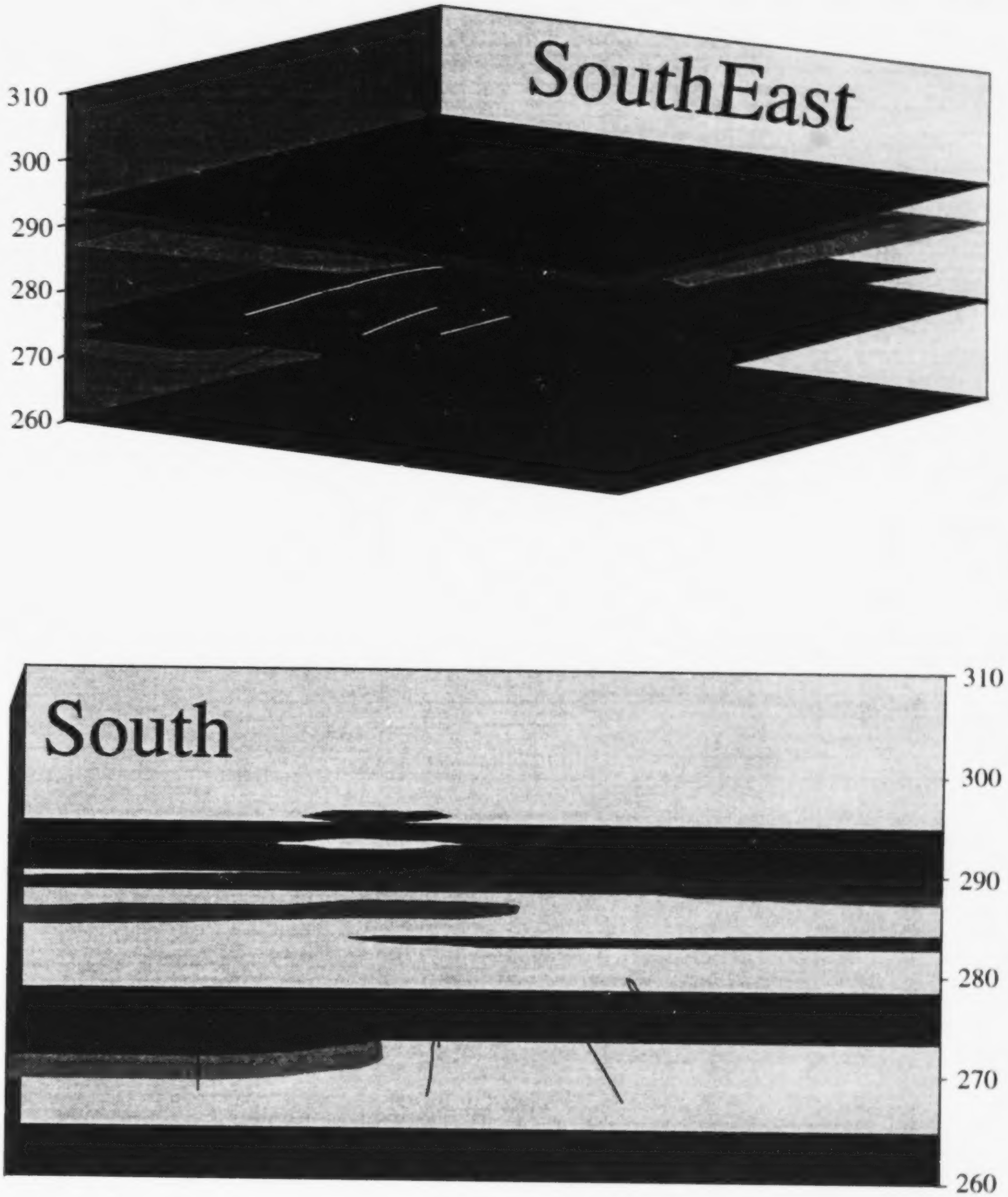
SouthEast
310
300
290
280
270
260
South
310
300
290
280
270
260

Figure 2.19 Isometric View of Shale Barriers - From the South and the Southeast

CHAPTER 3 RESERVOIR INSTRUMENTATION PROGRAM

"Get your facts first, and then you can distort them as much as you please"
Mark Twain

3.1 Introduction

Field instrumentation is vital to the practice of geomechanics. Field observations, including quantitative measurements obtained by field instrumentation, provide the means by which the geotechnical engineer, in spite of the inherent unknowns of dealing with natural materials, can design a project to be safe and efficient (Peck, 1988). Reservoir performance assessment during SAGD, the major objective of instrumentation installed for the Phase A steaming trials, was achieved with a wide array of instruments and installation techniques.

This section describes the instrumentation installed for the Phase A pilot. With each type of instrumentation, the reasons for its installation are briefly reviewed. As stated by Ralph Peck in the foreword to John Dunnicliff's(1988) landmark book on geotechnical instrumentation, "every instrument installed on a project should be selected and placed to assist in answering a specific question ... if there is no question, there should be no instrumentation."

3.2 Types of Instrumentation

3.2.1 Temperature

3.2.1.1 Thermocouples

Thermocouples were the most extensively used instrumentation in Phase A. Historically, thermocouples have provided the basis for instrumentation in most steam related recovery projects. Assuming steam saturated conditions, it is convenient to convert bottomhole temperature to pressure based on steam tables.

One hundred and twenty seven thermocouple measurement points, divided into 14 strings of up to 12 sensors each, were installed in 14 wells. Each thermocouple string was sealed inside 1/8" diameter inconel-sheathed magnesium oxide-insulated cable up to an elevation where negligible temperature increases would occur. The type J thermocouples were created by joining the tips of a copper wire and a constantan wire. All thermocouple strings were suspended inside open casings except for wells AT9, AT4, AT12 and AT14, where the thermocouples were cemented in the hole along with piezometers. Occasional problems were encountered with fluid in the open casing flashing to steam and masking any temperature profile within the well. These problems were generally overcome by blowing the well dry. A traversing thermocouple string was also available for monitoring temperatures in any open cased wells. The general accuracy of thermocouples can be considered as ± 2°C.

3.2.1.2 Vibrating Wire Piezometers

Each vibrating wire piezometer (discussed subsequently) was equipped with an integral vibrating wire temperature sensor. Consequently, an additional 18 temperature measurement points were available with the Phase A reservoir. These temperature sensors were rated to 200°C, the upper limit for materials used in the construction of the vibrating wire temperature sensors.

3.2.1.3 Extensometer Thermistor

A thermistor bead, rated to 300 °C was incorporated within each extensometer module (described subsequently). A thermistor is composed of semiconductor material that changes its resistance very markedly with temperature and is capable of highly accurate temperature measurements; typically ±0.1°C. The installation of 15 extensometer modules provided 15 additional temperature measurement locations.

3.2.2 Pore Pressure

3.2.2.1 Vibrating Wire Piezometers

A total of 18 high temperature vibrating wire piezometers were installed within the Phase A reservoir. One ambient temperature piezometer was installed within the Wabiskaw Member, a zone not expected to experience any significant temperature increase. These piezometers were constructed from stainless steel due to the extremely aggressive environment within the reservoir. Each vibrating wire piezometer had a pressure rating of 2800 kPa and a temperature rating of 200 °C. A schematic of the construction for these piezometers is shown in Figure 3.1. Also shown in Figure 3.1 is the integral vibrating wire temperature sensor.

Each piezometer was attached to teflon insulated cable, rated to 200 °C, up to the Wabiskaw Member, and spliced to ambient temperature cable above this level. The manufacturers stated accuracy of these piezometers is ±0.1% of full scale (2800 kPa) or approximately ±3.0 kPa. Vibrating wire piezometers were also installed in two baseline piezometer wells offset from the Phase A area. These piezometers were intended to provide baseline data concerning zero drift or creep within the sensors.

3.2.2.2 Pneumatic Piezometer

A total of 18 pneumatic piezometers, installed adjacent to each vibrating wire piezometer, were utilized within the Phase A reservoir. A pneumatic piezometer consists of a twin-tube assembly connected across a flexible diaphragm attached to the piezometer transducer body, schematically illustrated in Figure 3.2. As gas pressure is increased on the inlet tube under a constant but very low flow, the surface inlet pressure reading will rise. When the gas pressure exceeds the pore pressure P, the diaphragm moves outward, allowing gas to circulate through the outlet tube, such that the maximum indicated pressure gage reading is P.

Dual installations, vibrating wire and pneumatic piezometers, provided the redundancy in pressure measurement required at each location. The high temperature rating of 230°C for the pneumatic piezometers was achieved through stainless steel construction and attachment to stainless steel tubing up to a level where negligible temperature increases were expected to occur. The pneumatic piezometers were rated to 3000 kPa with an estimated accuracy of ±10 kPa.

As with all field instrumentation projects, a degree of redundancy in the number of instruments is a necessity. For this reason, a pneumatic and vibrating wire piezometer were installed at each pore pressure measurement location. The depth of the reservoir and the aggressive environment imposed during steaming precluded traditional techniques for piezometer installation, such as bentonite seals. Consequently, a piezometer actuator device was developed to simplify the installation procedure (Laing et al., 1988). The actuator consisted of two opposing spring-loaded steel trays which jam tightly against the borehole walls when actuated. Figure 3.3 illustrates the configuration of the actuator device as well as the location of the piezometers within the steel trays; one steel tray contains the pneumatic and vibrating wire piezometers embedded in a pervious sand epoxy pack, and the other tray provides space for the tubing and cables. A preassembled string containing a number of actuators are lowered into the well, the wires restraining the actuators are severed, the actuators seal the piezometers against the borehole wall and the well was cemented. Figure 3.4 shows the typical configuration for a completed piezometer instrument hole. All piezometers were installed with this device. The following advantages (AOSTRA, 1990a) for this installation method are:

- installations are simple and rapid;
- risk of damaged installations are reduced;
- multiple installations are completed with ease; and
- requirements for steel well casing are reduced.

3.2.3 Vertical Strains

Vertical strains within the Phase A reservoir were measured using LVDT-based extensometer modules grouted in three vertical boreholes. These modules were based on a high temperature LVDT, rated to 225 °C, mounted inside an invar tube which connected the extensometer modules. The LVDT was accurate to ±0.2 mm and had a linear range of ±25 mm. The core of the LVDT straddled a telescoping joint in the invar rod adjacent to the lower anchor. A schematic of the module configuration is provided in Figure 3.5. Figure 3.6 provides a photograph of an anchor module.

The telescoping joint was fixed during installation by rivets. The rivets were designed to shear under a small load, approximately 200 kg, allowing relative movement of the anchors. The telescoping joint was fixed with rivets such that the LVDT showed an initial compression of approximately 6.0 mm. This effectively left a linear range of 30 mm for extension and 20 mm for compression. The extensometer modules were separated by grouted anchors at 3 m spacing in well AGE2 and 5 m spacing in wells AGE3 and AGE4. With this spacing, the extensometers were accurate to 0.007% strain in AGE2 and 0.004% strain in AGE3 and AGE4. The modules were connected to high temperature resistant cable within the reservoir and spliced to ambient temperature cable above that level.

During installation, each anchor was retracted using a cable. The entire extensometer string, along with a grout pipe, were lowered into the borehole. When in place, the retracting cables were released, setting the anchors into the borehole wall. The well was cemented while removing the grout pipe. Figure 3.5 illustrates a typical configuration for the extensometers holes. While the installations were successful, it was difficult and time consuming (AOSTRA, 1990a).

3.2.4 Horizontal Displacements

Within the field of geotechnical engineering, inclinometers are typically used to monitor landslide movements, movements within earth dams or tunnels and deflections of piles or retaining walls. They provide a measure of deformation normal to the axis of a pipe by measuring inclination with respect to the vertical using a gravity sensing transducer. Tracking grooves are usually placed within the pipe for controlling orientation of the probe. The most common inclinometer contains a biaxial force balance accelerometer which provides probe inclination in two mutually perpendicular planes. Dunnicliff (1988) reports that this instrument can determine the horizontal position of one end of a near vertical casing with respect to the other to within ± 1 to 13 mm in 30 m. Factors which can affect this precision include systematic errors related to the transducer, the wheel assembly on the probe, casing misalignment, casing diameter, casing backfilling procedures, depth of measurement locations, depth interval between readings and spiralling of the casing (Dunnicliff, 1988). In most cases, corrections for these errors are possible.

Horizontal deformations within the reservoir were measured using a Gyrodata Wellbore Surveyor (GWS), an advanced directional surveying system used in the oil industry for wellbore positioning. A conventional Slope Indicator type inclinometer was not employed due to the elevated temperatures anticipated within the reservoir and limited experience with conventional inclinometers at 150 m depth.

The GWS operates in open cased wells without the need for special grooved casing as required with conventional slope indicator equipment. The GWS contains a biaxial inclinometer as well as a rate gyro which provides azimuth information. Figure 3.7 provides a schematic diagram illustrating the components of the GWS. Manufacturer stated accuracy for the GWS was 0.1° in azimuth and 0.05° in inclination. The following advantages over conventional slope indicator equipment have been noted (AOSTRA, 1990):

- it can operate continuously in a 100 °C environment and with attachments, at much higher temperatures for a limited period of time;
- it does not require grooved casing;
- the maximum depth of 185 m is well within the range of this probe; and
- if the tool was found unsatisfactory, a switch to slope indicator equipment was still possible through the use of aluminum inclinometer casing.

3.2.4.1 Gyrodata Wellbore Surveyor

The Gyrodata Wellbore Surveyor employs an inertial grade rate gyro which in combination with its other electronics, can sense the orientation of the earth's spin vector at each survey station. A rate gyro is an angular-rate-of-motion measuring device. It measures the earth's rate of rotation and senses the horizontal component of the earth's spin vector with respect to the hole axis. Details on the operation of the rate gyro can be found in Uttecht and deWardt (1983). The calculation of incremental horizontal displacements remains the same for both conventional inclinometer systems and the GWS; successive surveys are subtracted from an original base survey.

Since the GWS had not been used previously for these types of measurements, an examination of the accuracy or more precisely, repeatibility of the instrument was undertaken. The statistical approach used in examing instrument accuracy follows the model presented by Wolff and deWardt(1981), herein referred to as the WdW model. The GWS measures azimuth and inclination and through wireline measurements, measured depth at each survey station. Uncertainty in borehole position is associated with errors in each measurement. Azimuth error is composed of two physical errors: (1) compass error; and (2) tool misalignment error. Compass error, as defined in the WdW model, was based on early versions of gyro instruments where the orientation of the tool to a reference of known direction was required prior to surveying. Typical azimuth accuracies for this procedure were 0.5° to 2.5°. The GWS used at the UTF was a second generation instrument which did not require pysically aligning the tool to a geographical reference thus elimnating this component of compass error. Compass error then is attributed only to the quality of the sensors, system electronics and software and the procedure for taking and processing measurements. For these elements, Uttecht and de Wardt (1983) found azimuth errors of 0.015° to 0.03° during early testing of the GWS: product literature states azimuth accuracy of 0.1°.

Tool misalignment errors result from poor centralization of the tool within the casing. This can lead to inaccuracies in azimuth, inclination and measured depth. For GSW surveys conducted during Phase A, tool misalignment errors were minimized by surveying during the tool "inrun" and "outrun". This allowed all surveys to be corrected for misalignment using a correction program supplied by Gryrodata Inc.. Non-axial wireline pull and sensitivity of the inclinometer within the GWS can also lead to inclination errors. Warren (1981) and Wolff and de Wardt (1983) report inclination errors of 0.2° while the manufacturer's literature reports an inclination accuracy to 0.05°.

The minimum curvature method was used in interpreting the GWS survey data. This method assumes the well path is a smooth curve between survey stations, a valid assumption for the cased UTF observation wells. Figure 3.8 illustrates the geometry and nomenclature assumed in the minimum curvature method. The uncertainty for each survey can been computed using a statistical model first presented by Wolff and de Wardt (1983). Dubrule and Nelson (1986) in their evaluation of directional survey errors at Prudhoe Bay concluded that the WdW model adequately described survey errors, although they did incorporate one modification to the WdW model. Wolff and de Wardt(1983) assumed that the tool misalignment error was entirely systematic. Examination of an extensive dataset of surveys lead Dubrule and Nelson (1986) to conclude that the misalignment error was random and incoporated this modification in the WdW model. The mathematics of this uncertainty model, including the detailed minimum curvature calculations, are provided in Appendix D.

To assess GWS accuracy, multiple surveys were run on well AGI2 prior to the start of steaming. The results from these surveys are shown in Figure 3.9. The error bars or uncertainty associated with each survey were computed using the WdW model assuming the following error limits:

relative depth error	5 mm
inclination error	.05°
azimuth error	.10°
tool misalignment error	.01°.

Figure 3.10 shows the difference between the successive surveys conducted on well AGI2. Based on these figures it could be concluded that accuracies of ±1 mm would be possible.

Unfortunately, due to azimuth, inclination, misalignment and depth errors, each survey has its own inherent uncertainty which is compounded when computing the difference between the surveys; the errors are additive. Figure 3.11 shows a replot of Figure 3.10 with the addition of uncertainty limits. These error bars represent the level of accuracy for the incremental displacements between successive surveys. The shape of the Northing and Easting difference curves also reveal the systematic nature of the survey errors; random errors would tend towards a mean difference of zero. Figure 3.10 however reveals a systematic departure from a zero mean as the survey progresses upward. Analyses of the initial survey of AGI2 show that horizontal displacements measured during Phase A are, on average, only accurate to ±5 mm. While this may seem sufficently accurate, it will be seen subsequently that this error amounts to approximately 20% of the maximum horizontal displacement measured during the Phase A steaming trials.

3.3 Instrumentation Layout

In total, 14 dedicated thermocouple (AT series), 4 inclinometer (AGI series), 3 extensometer (AGE series) and 5 piezometer (AGP series) wells were installed. Figure 3.12 shows a plan view of the instrumentation well locations. Several wells, AT1 and AT7, were also used as inclinometer wells. Piezometers were installed in wells AT4, AT9, AT12 and AT14 and a traversing thermocouple string was used to measure temperature in wells AGI1, AGI2, AGI3 and AGI4.

Because it was anticipated the steam chambers would begin development reasonably uniformly along a horizontal well pair, most instrumentation was placed within a west-east plane at the midpoint along the horizontal wellpairs. This instrumented section was called the geotechnical cross-section. For uniform development of the steam chamber, the reservoir behaviour within the geotechnical cross-section would be close to plane strain conditions and would provide the most representative data on formation response to the SAGD process.

3.3.1 Thermocouples

Figure 3.13 provides the thermocouple locations within the geotechnical cross-section. Thermocouple wells were also located longitudinally along each wellpair, as shown in Figure 3.12.

3.3.2 Inclinometers

Figure 3.14 shows the position of wells AGI1, AT1, AGI2, AT7 and AGI3, relative to the well pair locations within the geotechnical cross-section. The position of well AGI4 relative to the position of the well pairs in a west-east section is shown in the plan view included in

Figure 3.14. Note the substantial difference in "geology" for well AGI1 and AGI3. As will be shown subsequently, this is manifested in the horizontal displacements measured in these wells.

3.3.3 Extensometers

All three extensometer wells were installed within the geotechnical cross-section. Figure 3.15 provides the locations of each module in wells AGE2, AGE3, and AGE4. For the curious, the numbering begins at AGE2 because AGE1 was dropped from the instrumentation program due to economic considerations. Similarly, the position of the extensometers modules "geologically" has an impact on their response to steaming.

3.3.4 Piezometers

Except for baseline piezometers installed outside the Phase A area, all pore pressure measurement points were located along the geotechnical cross-section. The location of each pore pressure measurement point, which generally contain both a pneumatic and vibrating wire piezometer, is shown in Figure 3.16. For the pressures presented in this thesis, the vibrating wire and pneumatic piezometer pressures were combined to provide a single pore pressure measurement at each instrument location.

3.4 Summary

One of the main objectives of the geotechnical instrumentation program undertaken at the UTF site was monitoring the geomechanical response of the reservoir to steaming. The instrumentation to achieve this desired result were subjected to a temperature and pressure (and possibly a chemical) environment that was uniquely aggressive for geotechnical instrumentation. A major design challenge existed in achieving a safe, reliable and economical instrumentation installation within a steam zone (Laing et al., 1988). This chapter has reviewed the types and geometry of the instrumentation selected for installation within the Phase A reservoir. The surface installed instrumentation included 127 thermocouples for temperature measurement, 43 piezometers for pore pressure measurement, 15 extensometer modules for strain measurement and 5 open cased wells for horizontal deflection measurement. In addition, 25 of the piezometers and the 15 extensometer modules were equipped with temperature sensors. A traversing thermocouple string is also used to monitor temperatures in the 5 open cased wells. The foregoing instruments are installed in 28 wells; all but 2 are located within or very close to the expected steam zone. The latter two are offset from the test area to measure baseline pressures and temperatures.

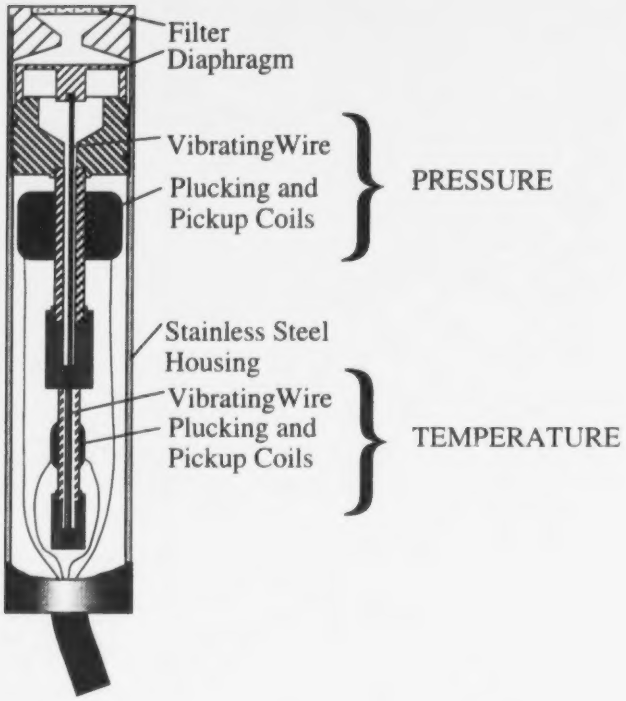
Filter
Diaphragm
VibratingWire
Plucking and
Pickup Coils
PRESSURE
Stainless Steel
Housing
VibratingWire
Plucking and
Pickup Coils
TEMPERATURE

Figure 3.1 Schematic Illustration of Vibrating Wire Piezometer (modified from Solinst, 1989)

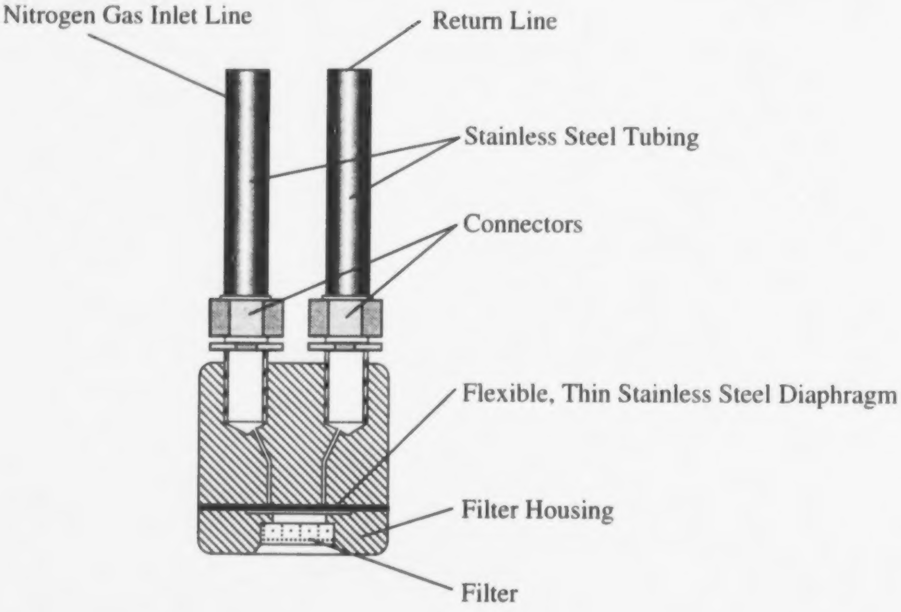
Nitrogen Gas Inlet Line
Return Line
Stainless Steel Tubing
Connectors
Flexible, Thin Stainless Steel Diaphragm
Filter Housing
Filter

Figure 3.2 Schematic Illustration of Pneumatic Piezometer (modified from Roctest, 1989)

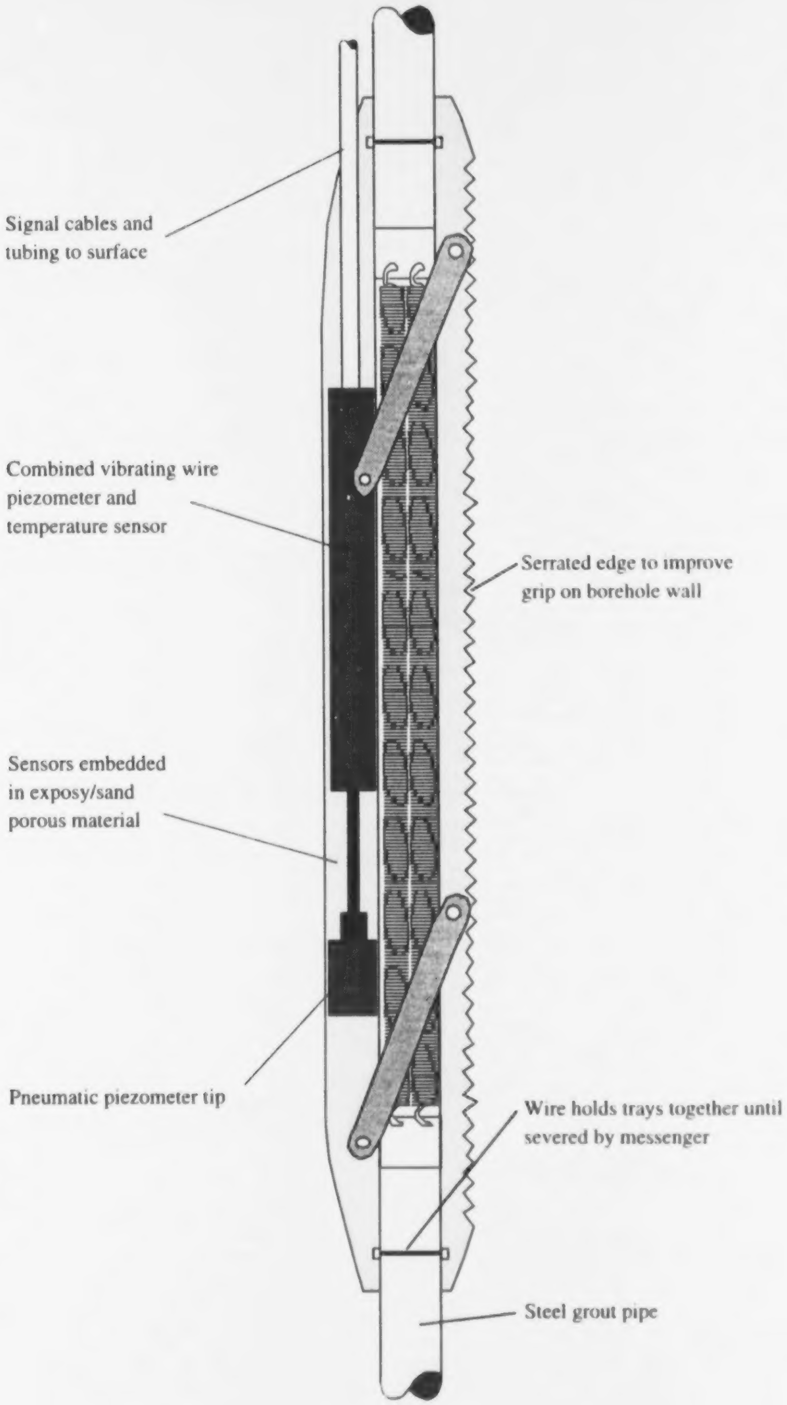
Signal cables and
tubing to surface
Combined vibrating wire
piezometer and
temperature sensor
Serrated edge to improve
grip on borehole wall
Sensors embedded
in exposy/sand
porous material
Pneumatic piezometer tip
Wire holds trays together until
severed by messenger
Steel grout pipe

Figure 3.3 Schematic of Piezometer Actuator Device (modified from Laing et al., 1988)

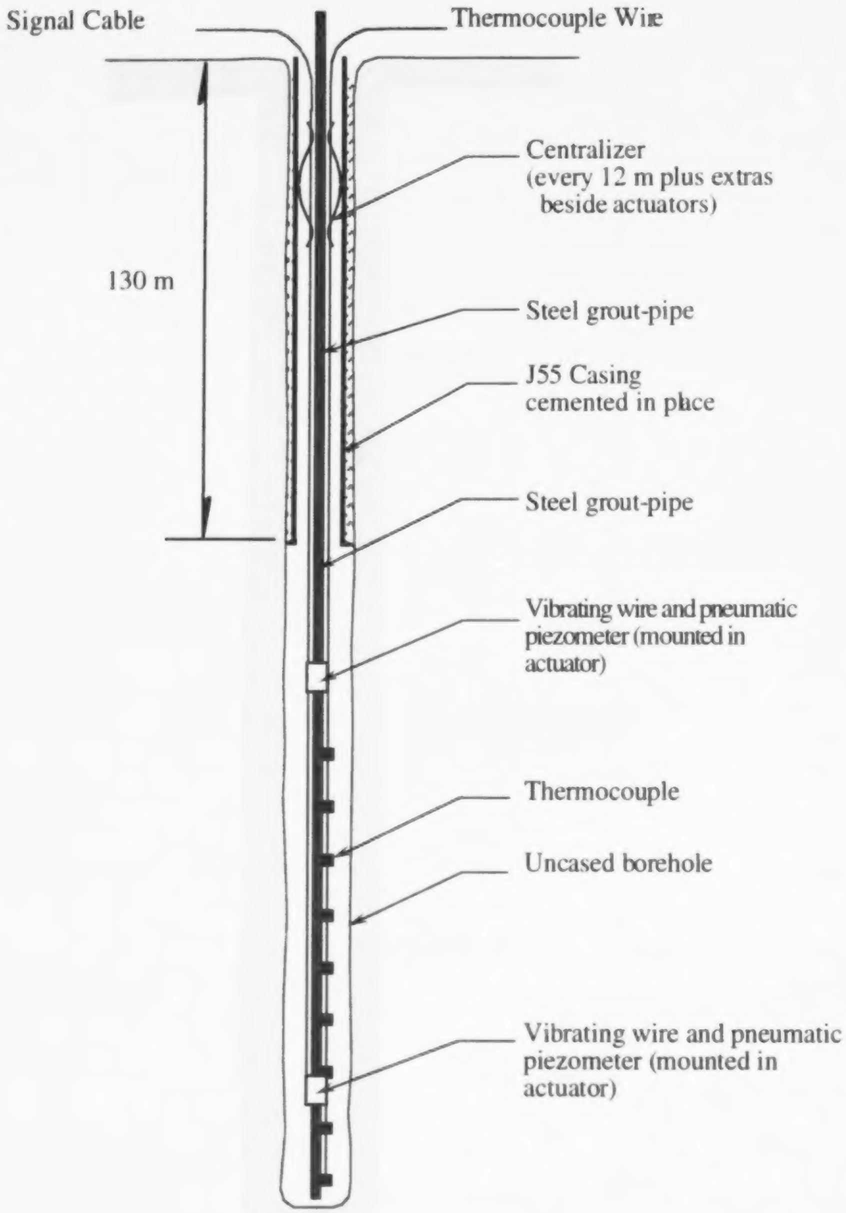
Signal Cable
Thermocouple Wire
130 m
Centralizer
(every 12 m plus extras
beside actuators)
Steel grout-pipe
J55 Casing
cemented in place
Steel grout-pipe
Vibrating wire and pneumatic
piezometer (mounted in
actuator)
Thermocouple
Uncased borehole
Vibrating wire and pneumatic
piezometer (mounted in
actuator)

Figure 3.4 Configuration of Typical Piezometer Instrumentation Well (modified from AOSTRA, 1990a)

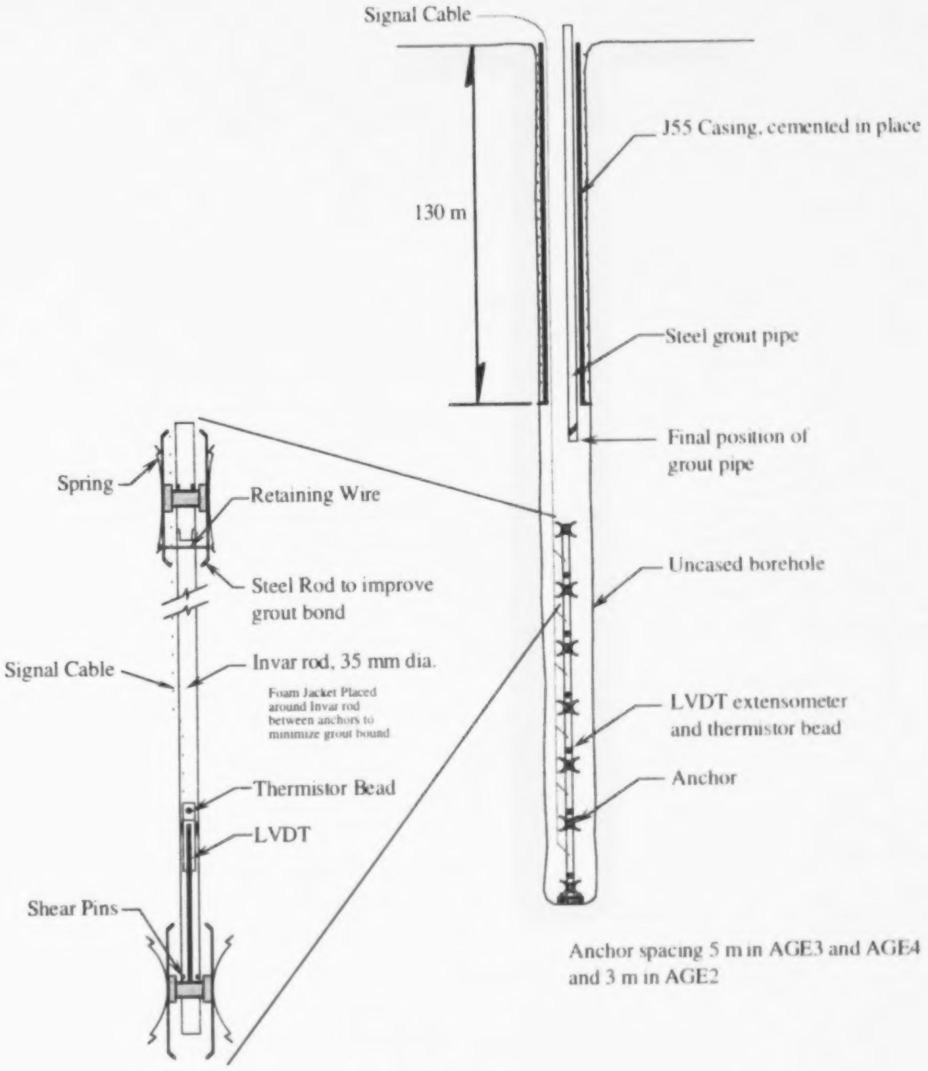
Signal Cable
130 m
J55 Casing, cemented in place
Steel grout pipe
Final position of grout pipe
Uncased borehole
LVDT extensometer and thermistor bead
Anchor
Spring
Retaining Wire
Steel Rod to improve grout bond
Signal Cable
Invar rod, 35 mm dia.
Foam Jacket Placed around Invar rod between anchors to minimize grout bound
Thermistor Bead
LVDT
Shear Pins

Anchor spacing 5 m in AGE3 and AGE4 and 3 m in AGE2

Figure 3.5 Configuration of Typical Extensometer Instrumentation Well (modified from AOSTRA, 1990a)

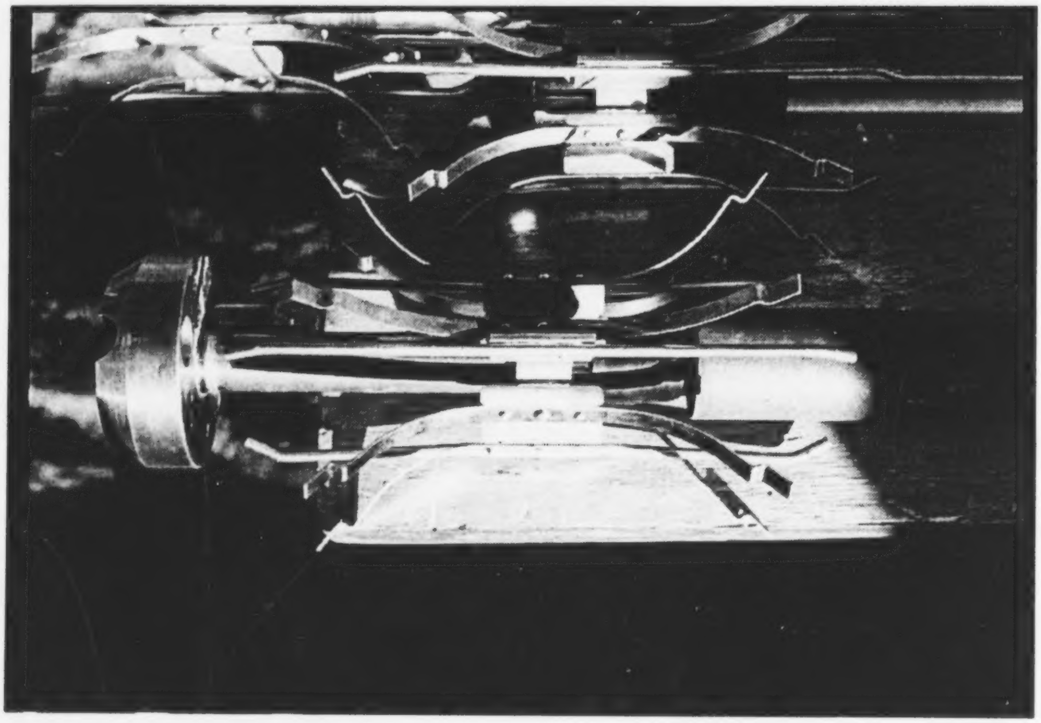

Figure 3.6 Photograph of Extensometer Module Anchor

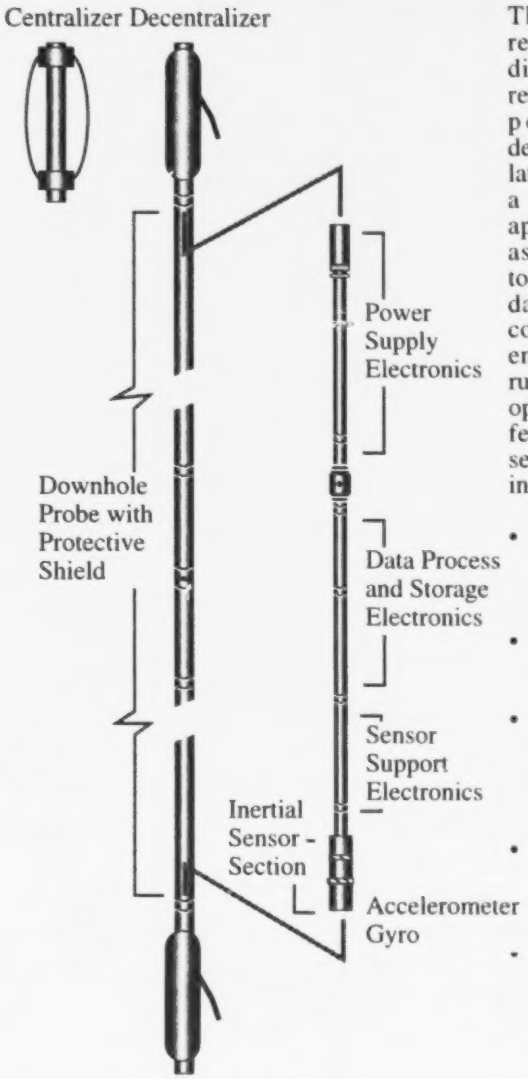
Centralizer
Decentralizer
Downhole Probe with Protective Shield
Power Supply Electronics
Data Process and Storage Electronics
Sensor Support Electronics
Inertial Sensor - Section
Accelerometer
Gyro

The Gyrodata Wellbore Surveyor represents a major advancement in directional surveying -meeting today's requirement for more precise wellbore positioning and reservoir delineation.Gyrodata has incorporated the latest aerospace guidance technology into a gyroscopic survey device offering approximately ten times the accuracy assurance of conventional surveying tools. The system consists of a downhole data-acquisition probe and a surface computing terminal designed for harsh-environment service. A wide array of running gear is also available for versatile operation. Several important performance features make Gyrodata the optimum selection for reliable wellbore trajectory information:

- Inertial-grade guidance sensors assure measurements to 0.1° azimuth and 0.05°inclination.
- Real-time surface readout optimises system performance and data quality.
- Faster surveying speed and elimination of conventional gyro alignments and drift checks save rig-time.
- Small diameter downhole probe provides versatile operation in various pipe sizes.
- High shock resistance and elimination of time-dependent errors allow decentralised out-run operation for improved wellbore tracking and log-data correlation.

Figure 3.7 Technical Information on Gryodata Wellbore Surveyor (modified from SDI, 1989)

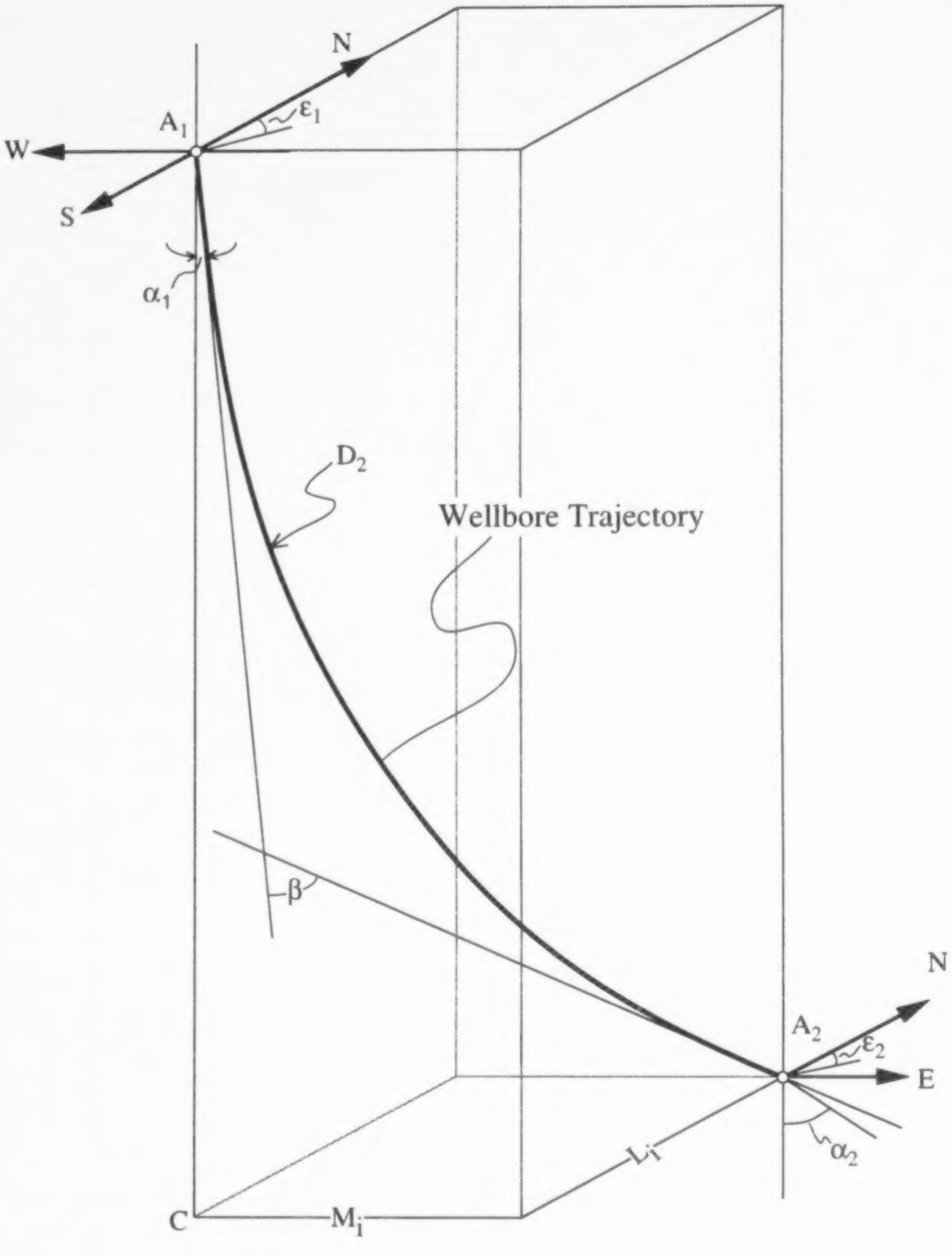
N
A$_1$
ε_1
W
S
α_1
D$_2$
Wellbore Trajectory
β
N
A$_2$
ε_2
E
α_2
L$_i$
C
M$_i$

Figure 3.8 Wellbore Geometry Assumed for Minimum Curvature Method

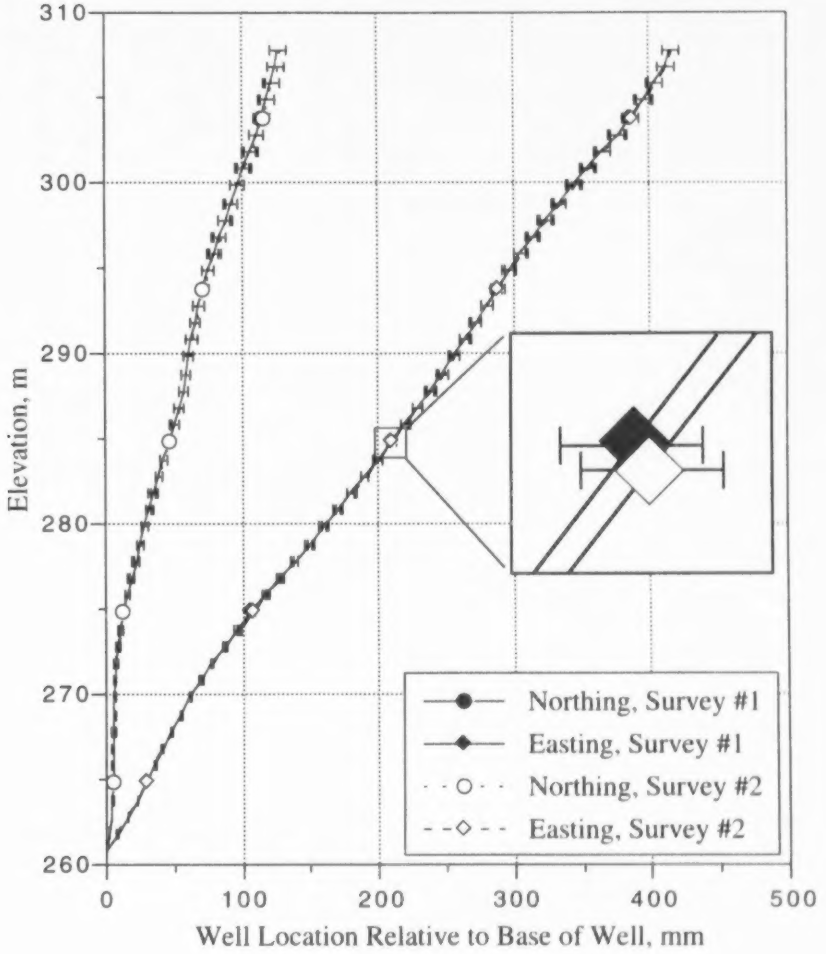

Figure 3.9 Pre-Steaming Multiple GWS Surveys in Well AGI2

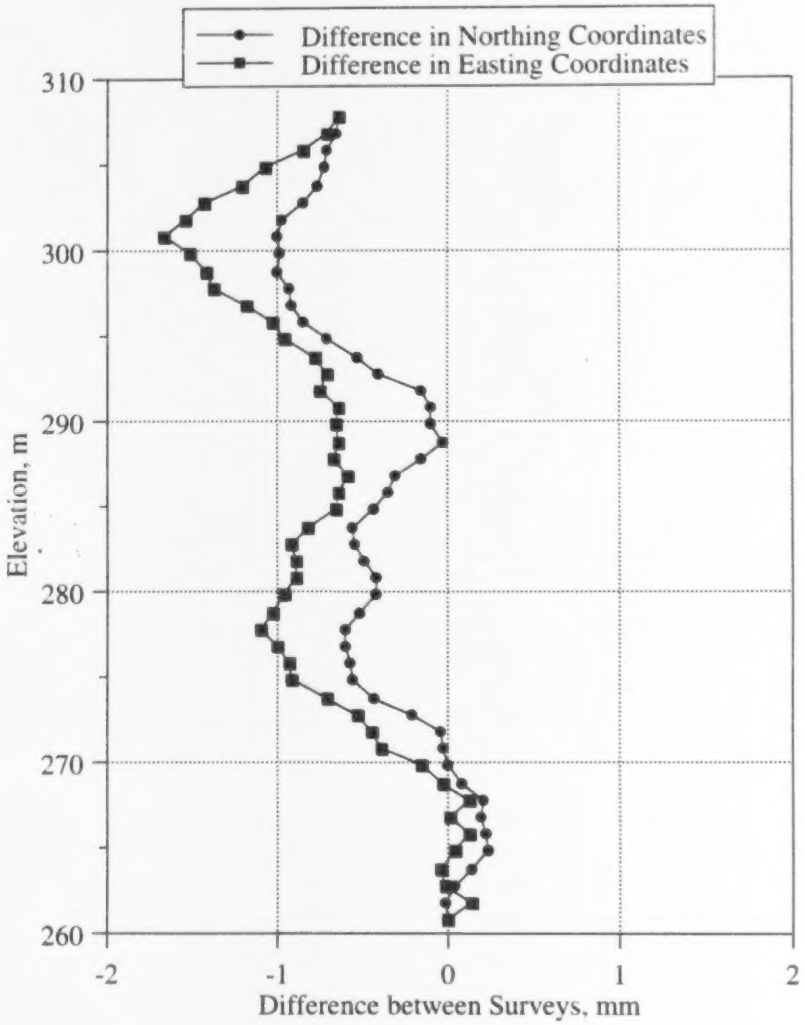

Figure 3.10 Level of Repeatibility for Multiple Surveys in Well AGI2

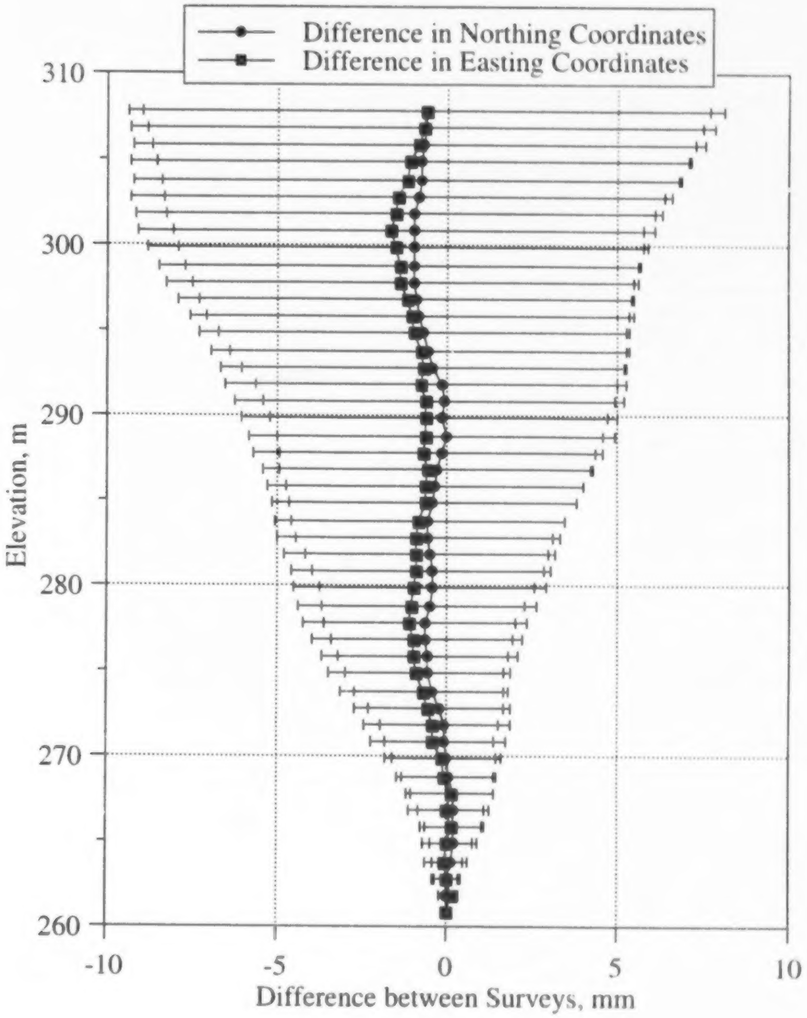

Figure 3.11 Magnitude of Error for Repeat Surveys in Well AGI2

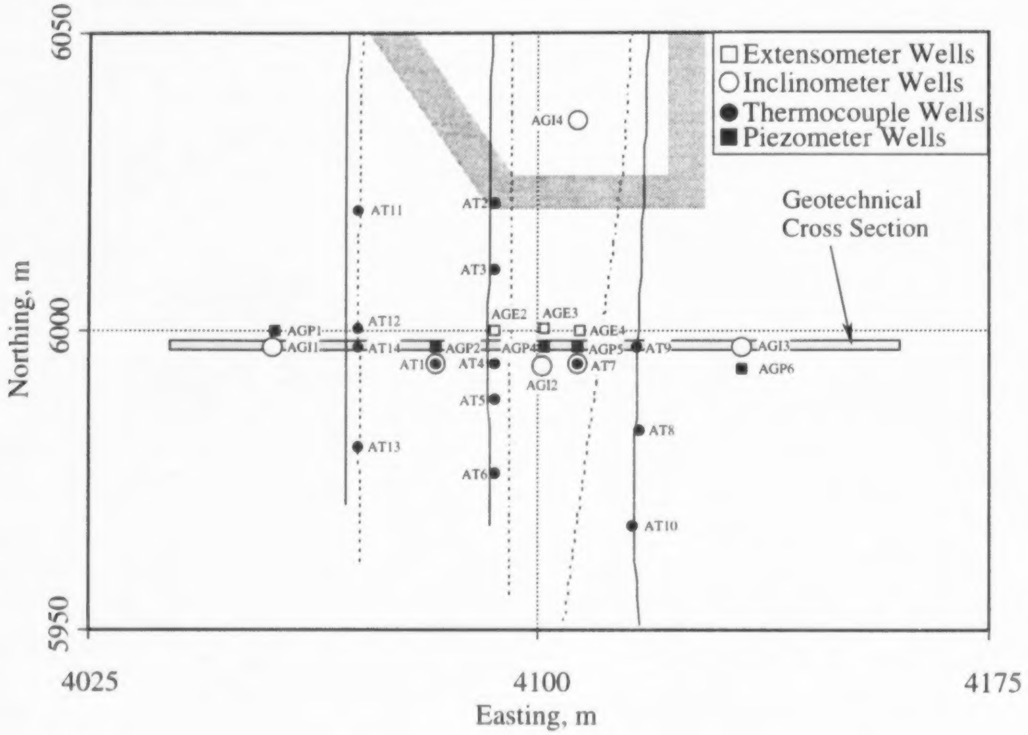

□ Extensometer Wells
○ Inclinometer Wells
● Thermocouple Wells
■ Piezometer Wells
Geotechnical Cross Section
AGI4
AT2
AT11
AT3
AT12
AGE2
AGE3
AGE4
AGP1
AGI1
AT14
AGP2
AGP4
AGP5
AT9
AGI3
AT1
AT4
AGI2
AT7
AGP6
AT5
AT8
AT13
AT6
AT10
6050
6000
5950
Northing, m
4025
4100
4175
Easting, m

Figure 3.12 Plan View of Instrument Well Locations

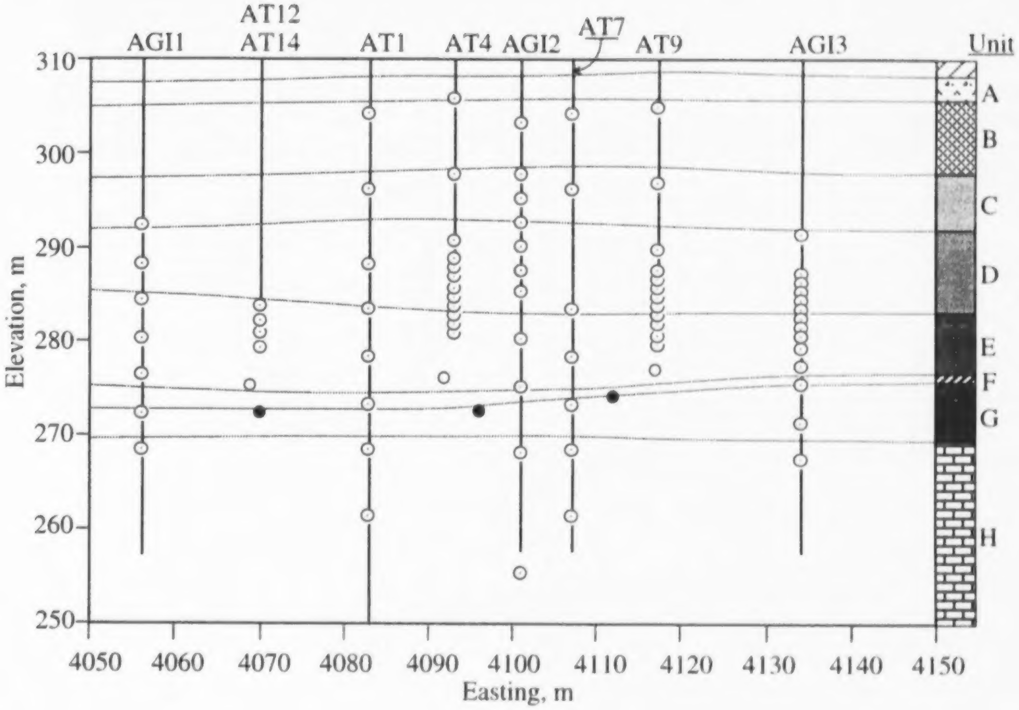

Figure 3.13 Location of Temperature Measurement Points within Geotechnical Cross Section

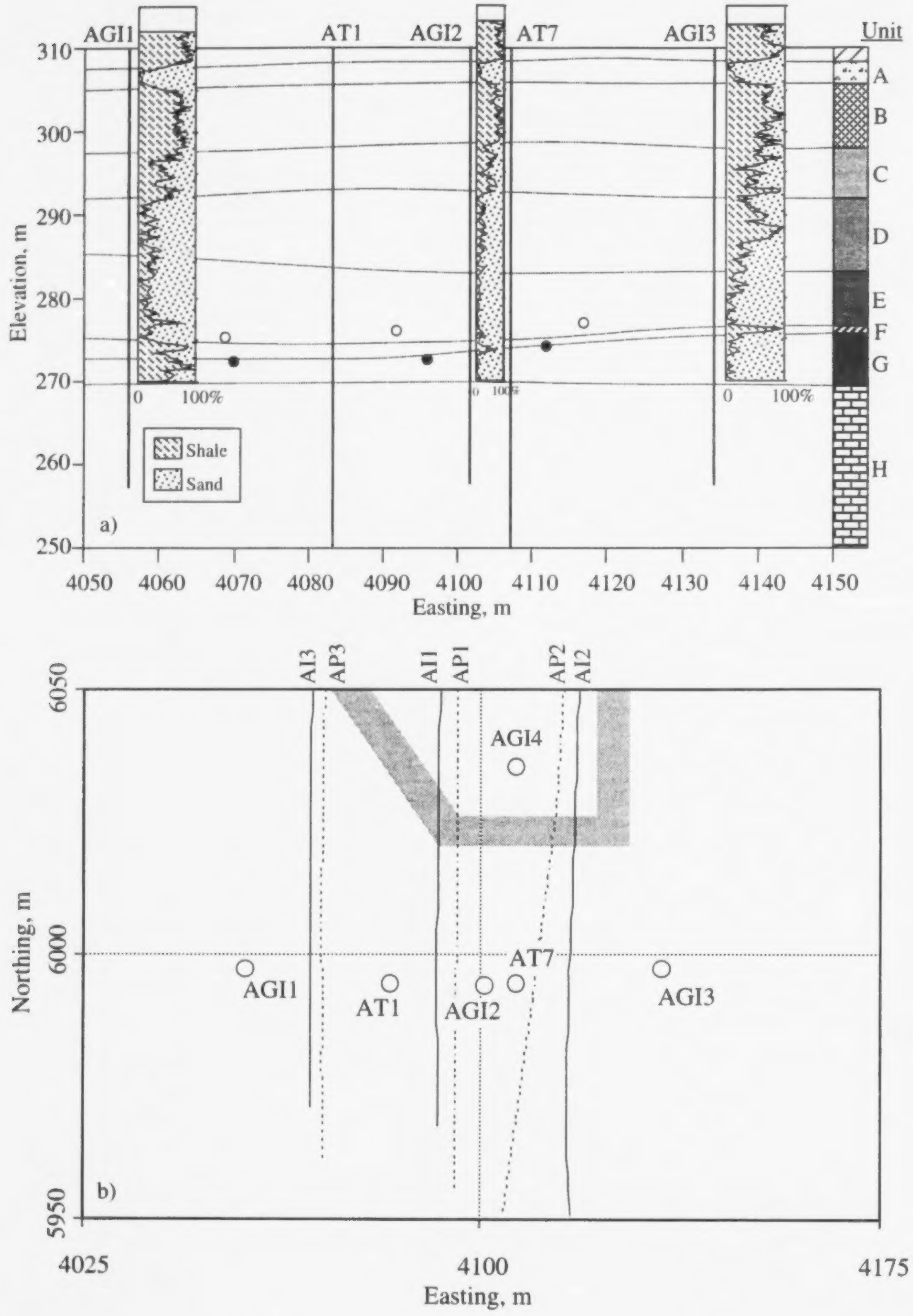
AGI1
AT1
AGI2
AT7
AGI3
Unit
A
B
C
D
E
F
G
H
310
300
290
280
270
260
250
Elevation, m
0
100%
Shale
Sand
a)
4050
4060
4070
4080
4090
4100
4110
4120
4130
4140
4150
Easting, m
AI3
AP3
AI1
AP1
AP2
AI2
AGI4
AT7
AGI1
AT1
AGI2
AGI3
6050
6000
5950
Northing, m
b)
4025
4100
4175
Easting, m

Figure 3.14 Location of Inclinometer Wells within Geotechnical Cross Section

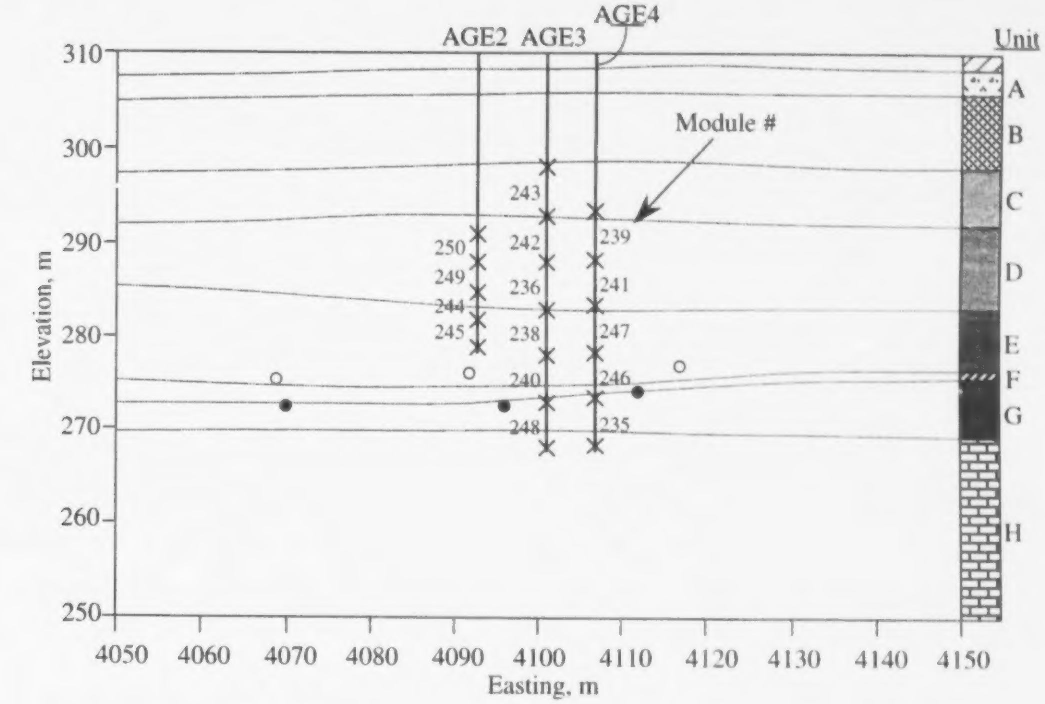

Figure 3.15 Location of Extensometer Modules within Geotechnical Cross Section

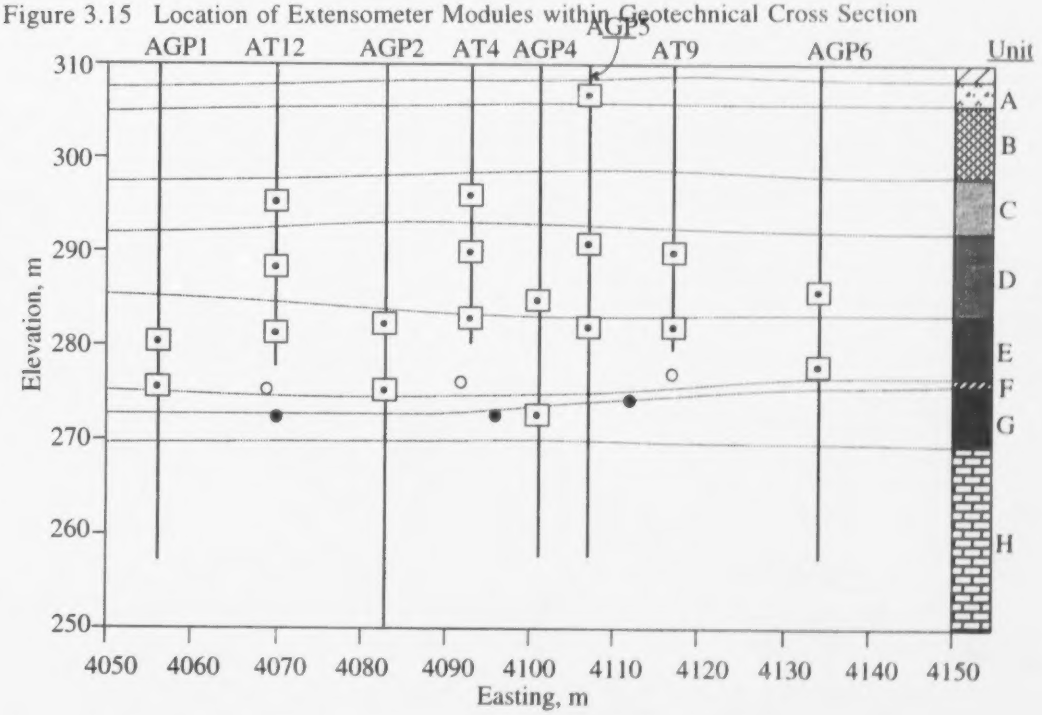

Figure 3.16 Location of Piezometers within Geotechnical Cross Section

CHAPTER 4 THERMOMECHANICAL PROPERTIES

"Results! Why, man, I have gotten a lot of results. I know of several thousand things that won't work."
Thomas Edison

4.1 Introduction

The objective of the laboratory testing program was the development of a material properties database for geologic horizons within the Phase A pilot area. These geologic horizons included the McMurray Formation oil sands; shale units within the McMurray Formation, and the underlying Waterways Formation limestone. The properties database was intended for use in understanding the reservoir response during steaming and for input into present and future numerically modeling studies of the SAGD process.

The laboratory program comprised thermal expansion, thermal conductivity, compressibility, stress-strain, strength and gas evolution tests. A total of 78 experiments were conducted on core specimens from the Phase A reservoir. The testing program was conducted in the University of Alberta's Oil Sands Geotechnical Research Facility. This facility was originally constructed in 1980 through the work of Agar (1984). Subsequent to Agar's work, Kosar (1989), provided upgrading to the facility with emphasis on:

- providing greater control of pressure, temperature and load during testing to improve the quality of measured results;
- developing the capability to conduct stress path testing;
- eliminating or modifying components, such as seals and membranes, which are susceptible to degradation or failure at elevated temperatures and pressures; and
- isolating the triaxial and oedometer systems such that tests could be performed simultaneously.

With additional, related research conducted by Seto (1985) and Branco (1988), the facility now includes two separate and independent high temperature triaxial compression systems, two high temperature oedometer systems, one transient state thermal test cell and two ambient temperature triaxial cells modified to allow mercury as a confining fluid. The latter triaxial cells were utilized for gas evolution testing.

Short of a brief description of each testing system and any modifications required for the current testing program, details regarding test procedures will not be repeated in this thesis. This is not to denigrate the value of understanding the intricacies of testing systems, especially the requirements for high temperature testing systems. But rather, the reader is referred to respective references of the individual researchers responsible for the original development of the equipment. It is in these references that the specific technical details on the testing systems and procedures will be found.

The high temperature/pressure triaxial cell can measure the compressibility and shear strength properties of oil sands and related strata under confining stresses up to 27 MPa and temperatures up to 300 °C. Axial loads up to 400 kN can be applied during shear testing. Pore fluid pressure, vertical strains and volume change of the test specimen can be measured. A schematic of the triaxial cell is provided in Figure 4.1. The high temperature/pressure oedometer systems can measure compressibility and thermal expansion properties of oil sands and related strata under vertical stresses up to 30 MPa and temperatures to 300 °C. Vertical displacement, pore fluid pressure and volume change of the specimens can be measured. Figure 4.2 illustrates the construction of the oedometer cell. Sample preparation and test procedures for triaxial and oedometer testing were conducted in accordance with the directions provided in Appendix B of Kosar (1989).

The transient state thermal test cell can measure the thermal conductivity and diffusivity of oil sands and related strata under vertical confining loads of 400 kN, temperatures up to 200 °C and pore fluid pressures up to 10 MPa. A cross-sectional diagram illustrating the major components of the cell is shown in Figure 4.3. Thermal conductivity experiments were conducted in accordance with procedures developed by Seto (1985).

The mercury triaxial cells were used to measure the gas evolution behavior of oil sands (Branco, 1988). These triaxial cells allow the specimen to be surrounded by mercury to inhibit gas diffusion from the specimen, through the membrane and into the triaxial cell confining fluid. The cells can withstand internal pressures up to 14 MPa and pore pressures up to 3 MPa. These cells also permit the evolved gas to be sampled for gas chromatography analysis. Configuration of the mercury triaxial cell is shown in Figure 4.4. The gas evolution and composition testing were conducted in accordance with the test procedures outlined by Branco (1988).

4.2 Specimen Description and Location

For a pilot project of the UTF's magnitude, the density of wells drilled through the Phase A reservoir, for both observation wells and for coring, was unparalleled. The well density thus permitted specimen selection from within the same geologic environment. Figure 4.5 illustrates on a plan view of the Phase A project the coring and geophysical logging wells. Wells AGI1, AT7, AT2, AT3 and AGI4 were all cored using the core barrel design of

McKay (1989). McKay modified two sizes of triple tube wireline core barrels in an attempt to reduce sampling disturbance when coring gas saturated oil sands. These modifications included reduced liner clearances, end restraints within the liner and a built-in liner core catcher.

As will be presented in §4.7 the low dissolved gas content in the oil sands samples led to high quality sample recovery, but prevented a conclusive evaluation on the success of the core barrel modifications. Details on the coring program for these wells can be found in McKay (1989). Samples from the Clearwater Formation Shales, the Wabiskaw Member of the Clearwater Formation, the upper and lower shales (Unit B, C, and F) of the McMurray Formation and the Waterways Limestone were obtained during coring operations. They were immediately wrapped in plastic, cheesecloth and coated with protopet, a paraffin wax. Oil sands core from wells AGI1, AGI2, AGI3, AT7 and AT3 were immediately frozen at surface using dry ice and were stored in portable freezers. Complete details on the coring program can be found in Rottenfusser (1989).

Table 4.1 provides the coding used in identifying the test material and nature of the test. This terminology will be adopted for the remainder of the thesis. A summary of initial specimen data is provided in Table 4.2. The results from a shale seam sampling program aimed at evaluating the index properties of the muddy interbeds within the McMurray Formation has also been included in Table 4.2. No geomechanical tests other than index tests were conducted on these specimens. Figure 4.6 shows the relative geologic positions of the test specimens.

4.3 Thermal Volume Change

4.3.1 Implications for SAGD Processes

Volumetric deformations within the reservoir resulting from temperature changes influence both stress and strain fields in situ. The extent of these deformations is a function of the "restraint" boundary conditions existing within the reservoir. For the UTF, the relatively shallow depth of the reservoir creates limited restraint for vertical deformations. Owing to the horizontal continuity of the reservoir, horizontal deformations in response to in situ heating are highly restrained in comparison to vertical deformations. Consequently, horizontal stresses increase more than vertical stresses and thermally induced vertical deformations are larger than horizontal deformations. This is particularly true for the well pair geometry of Phase A where the formation between opposing wellpairs may be subjected to large increases in horizontal stress. This is conceptually illustrated in Figure 4.7. In order to predict the magnitude of these thermally induced stresses and deformations, the thermal volume change behavior of the reservoir materials must be understood.

According to the theory of thermoelasticity, volumetric thermal strain and the compressive stress required to suppress this thermal strain are provided by:

$$\varepsilon_v = \beta_b \Delta T \text{ and } \sigma_m = -\beta_b E \Delta T \qquad [4.1]$$

where ε_v = volumetric thermal strain;
β_b = volumetric coefficient of bulk thermal expansion;
ΔT = temperature increment;
σ_m = mean stress; and
E = Young's modulus.

In the reservoir simulation of the SAGD process, the coefficient of pore thermal expansion is used to determine the pore volume change with an increment in temperature and is generally defined as:

$$\phi = \phi_o\left[1 + C_\phi \Delta p - \beta_\phi \Delta T\right] \qquad [4.2]$$

where ϕ = porosity;
ϕ_o = original porosity;
β_ϕ = formation (pore) thermal expansion coefficient;
C_ϕ = formation (pore) compressibility
ΔT = temperature increment;
σ = mean stress; and
E = Young's modulus.

A negative sign occurs in front of β_ϕ since it is generally assumed porosity will decrease with increasing temperature. The calculation of a new porosity value based on Equation 4.2 is used in evaluating accumulation terms in reservoir simulations to account for fluid volume.

It is clear then that the coefficient of thermal expansion is an important variable for both reservoir and geomechanical analyses of the SAGD process. It is evident from above that the definition of "thermal expansion coefficient" suffers from the same inherent problem as compressibility; geomechanical tests generally provide "bulk" values while reservoir simulators (not modified to incorporate geomechanics) generally require "pore" values. This issue related to compressibility will be addressed in §4.5.2. The following clarifies the relationships for thermal expansion. Note that thermal expansion under fully drained conditions are assumed. Agar at al., (1986) provide an excellent review of geomechanical thermal expansion parameters for both drained and undrained conditions.

Simplifying Equation 4.2 for temperature change only gives:

$$\phi = \phi_o + \Delta\phi_T \qquad [4.3]$$

where $\Delta\phi_T$ = $-\beta_\phi \Delta T \phi_o$.

Knowing that $\phi = V_v/V$, Equation 4.3 can be expanded as:

$$\frac{\phi - \phi_o}{\phi_o} = \frac{\left(\dfrac{V_v}{V_b}\right) - \left(\dfrac{V_v^o}{V_b^o}\right)}{\left(\dfrac{V_v^o}{V_b^o}\right)} = -\beta_\phi \Delta T \qquad [4.4]$$

where V_v = void volume;
V_b = bulk total volume;
V_v^o = original void volume; and
V_b^o = original bulk total volume.

Equation 4.4 can be simplified to:

$$\beta_\phi = \frac{1}{\Delta T}\left[1 - \left(\frac{V_v}{V_b^o\left(1 + \beta_b \Delta T\right)}\right)\right] \qquad [4.5]$$

Equation 4.5 now provides a means of relating the pore volume thermal expansion coefficient, β_ϕ, and the bulk thermal expansion coefficient, β_b. Assuming the thermal expansion for quartz grains, β_{quartz}, is constant, the term V_v in Equation 4.5 can be expressed as:

$$V_v = V_b^o\left(1 + \beta_b \Delta T\right) - V_s^o\left(1 + \beta_{quartz} \Delta T\right) \qquad [4.6]$$

Substituting Equation 4.6 into Equation 4.5 and simplifying provides the following expression relating β_ϕ, and β_b:

$$\beta_\phi = \frac{1}{\Delta T}\left[\frac{\left(1 - B^*\right)\phi_o + B^* - 1}{\phi_o}\right] \qquad [4.7]$$

where $B^* = \dfrac{\left(1 + \beta_{quartz} \Delta T\right)}{\left(1 + \beta_b \Delta T\right)}$

The value of β_b would be the bulk thermal expansion coefficient determined in a triaxial cell under isotropic mean stress or the constrained bulk thermal coefficient, β_{cb}, determined in an oedometer cell. Equation 4.7 will be discussed relative to the constrained thermal expansion tests conducted on oil sands. It will be seen subsequently that the stress path followed during a test and more importantly, the stress path followed in a reservoir will dramatically affect that value of β_e which should be chosen for reservoir simulations; geomechanical analyses would utilize β_{cb}.

The following sections present and discuss the thermal volume change behavior for oil sands, lower and upper shale and limestone.

4.3.2 McMurray Formation Oil Sands

Two drained thermal volume change tests were conducted; OSDTE1 and OSDTE2. Both specimens were selected from within Unit D in Well AGI4. The specimens are part of Facies 12 a fine-grained sand with a high bitumen saturation. Initial specimen data are provided in Table 4.2. OSDTE1 had a lower bulk fines content (4.2%) than OSDTE2 (13.3%) due to occasional mud laminations within OSDTE2. For both thermal volume change tests, a vertical effective confining stress of 2.0 MPa and a back pore pressure of 4.0 MPa were maintained during heating. Prior to heating, both specimens were cycled over the σ'_v range 1 MPa to 9 MPa. Specimen compressibility was measured during this stage of the test and is discussed in more detail in §4.5.

Figure 4.8 illustrates the constrained thermal volume change behavior for OSDTE1 and OSDTE2. Both specimens exhibit essentially linear thermal expansion behavior up to 225 °C. Kosar (1989) conducted four drained thermal volume change tests on oil sands specimen obtained from core taken near the UTF. As described in §2.3, these specimens were located in an estuarine channel margin depositional environment. Using the same specimen nomenclature as Kosar (1989), specimens UFCOS1, UFCOS3, UFCOS4 and UFCOS5 are representative of Facies 8 or 9; a matrix-supported mudstone clast breccia within fine grained sand of medium to low bitumen saturation. Specimens OSDTE1 and OSDTE2 however, are representative of Facies 12, a massive, structureless, fine to medium grained sand with high bitumen saturations. The index properties for these specimens, as listed in Table 4.3 clearly indicate their differences. The oil sands specimens tested by Kosar (1989) contain, on average 48% fines (< 74 µm) and 5% bitumen; OSDTE1 and OSDTE2 contain, on average, 13% fines (< 74 µm) and 13.5% bitumen. These differences are manifest in the volume change behavior over the temperature range 20 °C to 225 °C, as illustrated in Figure 4.9. The most notable difference in thermal response between the specimen is in comparison to the volume change of a quartz sand grain; estimated by Clark (1966) to be $3.4 \cdot 10^{-5}$ °C^{-1} at 20 °C to $5.0 \cdot 10^{-5}$ °C^{-1} at 225 °C. The higher fines, low bitumen saturation specimens experience less cumulative volume change while the low fines, high bitumen saturation specimens experience greater cumulative volume change. The major reason for the difference in behavior lies in the soil structure response during heating. Figure 4.10 shows the structural response during heating for each specimen. As noted by Kosar (1989), that while the increase in total volume during heating is controlled by the thermal expansion of the mineral grains, thermal consolidation or structural collapse occurs simultaneously for highly interbedded oil sands. For low fines, dense oil sands, the structural response during constrained thermal expansion is shear induced volume increases or dilation. During a thermal expansion test in the high temperature oedometer, shear stresses and strains develop primarily from different thermal expansion of test specimen and the oedometer ring. If the thermally induced shear stresses overcome the overall shearing resistance of the soil matrix, a dense sand will dilate, a loose sand will contract.

Owing to the original dense structure for OSDTE1 and OSDTE2, achieved through stress cycling from 1.0 to 9.0 MPa the structural response during heating was predominantly dilatant, as shown in Figure 4.10. A small volume decrease occurred at the onset of heating; 20 °C to 50 °C. This same early response was found by Agar (1984) and Kosar (1983) for rich Saline Creek oil sands specimens. From 50 °C to approximately 175 °C, an increase in volume occurs due to shear dilation. Beyond 175 °C, no structural changes are occurring. This can also be seen in Figure 4.9 where beyond 175 °C, the rate of volume change for OSDTE1 and OSDTE2 becomes asymptotic with that of a quartz grain. For each temperature increment, the constrained bulk thermal expansion coefficient, β_{cb}, was computed for OSDTE1 and OSDTE2 and for specimens tested by Kosar (1989). Figure 4.11 illustrates the variability of β_{cb} over the temperature range 20 °C to 225 °C. For low fines, oil sands, an average value for β_{cb} of $6.0 \cdot 10^{-5}$ °C^{-1} appears reasonable and for the highly interbedded oil sands, a value for β_{cb} of $3.0 \cdot 10^{-5}$ °C^{-1} appears reasonable.

As discussed above, thermal expansion of the oil sands formation at the shallow depth of the Phase A reservoir can be approximately classed as confined thermal expansion. The proximity of the ground surface in relation to the horizontal extent of the reservoir creates boundary conditions similar to a constrained thermal expansion test in oedometer. Consequently, it could be argued that the pore thermal expansion coefficient for SAGD reservoir simulations should be chosen from constrained thermal expansion tests. Using Equation 4.7, β_{cb} obtained from the tests conducted on OSDTE1 and OSDTE2 can be converted to an equivalent β_ϕ. Selecting $\beta_{quartz} = 3.5 \times 10^{-5}$ °C^{-1}, $\Delta T = 200$ °C, $\phi_o = 0.32$ and from above, $\beta_{cb} = 6.0 \times 10^{-5}$ °C^{-1} Equation 4.7 yields $\beta_\phi = -5.3 \times 10^{-5}$ °C^{-1}. Since Equation 4.7 was developed consistent with Equation 4.2, a negative value of β_ϕ indicates that the porosity of the oil sands, as measured during a constrained thermal expansion test, ***increased*** with increasing temperature. This is contrary to the assumption embodied in Equation 4.2 which assumes porosity decreases with increasing temperature. For reference, most SAGD simulations were conducted with $\beta_\phi = +3.5\text{x}10^{-5}$ °C^{-1}. The following summarizes the impact on porosity change dependent on the assumptions in choosing β_ϕ:

$\phi_o = 0.320$ and $\Delta T = 200$ °C
Conventional Equation: $\phi = \phi_o(1 - \beta_\phi \Delta T)$
$\beta_\phi = +3.5\text{x}10^{-5}$ °C^{-1} leads to $\phi = .318$
Constrained Thermal Expansion: β_ϕ chosen from β_{cb} as per Equation 4.7
$\beta_\phi = -5.3\text{x}10^{-5}$ °C^{-1} leads to $\phi = .323$.

4.3.3 McMurray Formation Shale

Due to a limited number of lower McMurray Formation shale specimens (Unit F), no drained thermal expansion tests were conducted on this material. One drained test was conducted on an upper McMurray Formation shale specimen. Specimen USDTE1 was obtained from Unit C in well AGI1. This specimen is representative of Facies 5, a zone of interbedded, very fine to fine grained sand and mudstone. Volumetrically, USDTE1 was approximately 30% oil sands (distributed in specimen as lenses) and 70% shale (fraction < 74 μm = 69%). The constrained bulk thermal expansion of USDTE1 was measured at a vertical effective confining stress of 2.0 MPa with no stress cycling prior to heating. The specimen was heated at a rate of 25 °C per hour while maintaining a back pore pressure of 40 MPa. Based on thermal volume change tests on Clearwater Formation Shale, Kosar (1989) classified a rate of 25 °C per hour as a short term test. This classification came from consideration of the time required for complete drainage of pore fluids during each increment. A long term test determined that the time required to attain steady state conditions ranged from 40 to 20 hours. For the thermal test conducted on USDTE1, a rate of 25 °C per hour was determined to be a mid-term test. The presence of sand lenses permitted more rapid drainage than experienced by Kosar (1989). An extended thermal consolidation period at 225 °C did reveal a time dependent component related to structural collapse of the shale.

Figure 4.12 illustrates the bulk thermal volume change behavior for USDTE1. A rapid volume decrease of 0.1% occurs over the first heating increment of 25 °C. This initial response is indicative of an initial structural collapse as the matrix attempts to maintain $\sigma'_V = 2.0$ MPa.

From 50 °C to 175 °C, the specimen undergoes incremental volume increases with each increment of temperature. Between 100 °C and 125 °C, the rate of thermal volume expansion approaches the theoretical rate for an illite clay particle. It is postulated that thermal expansion during this phase of heating is dominated by mineral grain expansion, especially the quartz mineral component, and non-recoverable structural changes. Following 175 °C, significant structural collapse occurs; resulting in a final bulk volume decrease of 0.10% at 225 °C. To examine the effects of long term heating, the specimen was held at 225 °C for 10 hours. An additional thermal consolidation of 0.05% occurred over this period. Figure 4.13 illustrates the variation in β_{cb} over the temperature range 20 °C to 225 °C. Over 20 °C to 50 °C, $\beta_{cb} = {}^{-}3.0 \cdot 10^{-5}\ {}^{\circ}C^{-1}$ increasing to ${}^{+}2.4 \cdot 10^{-5}\ {}^{\circ}C^{-1}$ at 100 °C. At the final temperature of 225 °C, $\beta_{cb} = {}^{-}5.0 \cdot 10^{-5}\ {}^{\circ}C^{-1}$. For long term conditions, it may be suitable to select $\beta_{cb} = {}^{-}4.0 \cdot 10^{-5}\ {}^{\circ}C^{-1}$ to compute constrained (one-dimensional) thermal volume change of the shale zones within the McMurray Formation.

For comparison purposes, Figure 4.14 provides the thermal response of two Clearwater Formation Shale specimens tested under the same vertical effective confining stress as USDTE1 (Kosar 1989). Note that these two specimens (UFCSS3 and UFCCS4) consisted of medium high to high plastic shale with no oil sands. USDTE1 contains approximately 30% oil sands and the shale is non-plastic. As shown in Figure 4.14, the constitutive response of these materials is extremely complex; a function of stress history, rate of heating, mineralogy of the specimen and magnitude of the temperature increase.

4.3.4 Waterways Formation Limestone

The limestone testing component of the laboratory program was aimed at determining material properties for tunnel behavior analyses. While this thesis does not address the topic of tunnel response, the behavior of the Waterways Limestone is important for understanding the reservoir response during SAGD. Consequently, the testing results for limestone are included in the thesis. In a regional Devonian core study conducted by Norwest Resources Consultants Ltd. (1986), three main rock types were identified:

1) argillaceous limestone;
2) intraclast breccia limestone; and
3) organic limestone

Two drained thermal volume change tests were conducted, LTDTE1 and LTDTE2. Both specimens were cut from sample GT6 obtained from well AT1. The sample was a nodular, argillaceous limestone having poorly sorted light gray, hard micrite nodules within an olive green calcite mud matrix. Table 4.2 provides the initial specimen data for LTDTE1 and LTDTE2. Each test was conducted over a temperature range of 20 °C to 250 °C at an effective vertical confining stress of 2.0 MPa.

Figure 4.15 shows the thermal volume change response for LTDTE1 and LTDTE2. Early volumetric response over the temperature range 20 °C to 100 °C indicates structural collapse in response to increasing thermal induced shear stresses within the calcite mud matrix as the specimen attempts to remain at equilibrium with $\sigma'_v = 2.0$ MPa.

Beyond 100 °C, both specimens exhibit essentially linear volumetric expansion up to 250 °C. The coefficient of constrained bulk thermal expansion over this range was computed as $6.7 \cdot 10^{-5}\ {}^{\circ}\mathrm{C}^{-1}$ and $8.5 \cdot 10^{-5}\ {}^{\circ}\mathrm{C}^{-1}$ for LTDTE1 and LTDTE2, respectively. This value is larger than the value of $3.9 \cdot 10^{-5}\ {}^{\circ}\mathrm{C}^{-1}$ quoted by Kosar (1989) for a crystalline limestone specimen. The thermal expansion curve for this specimen is included in Figure 4.15. The reason for the discrepancy between these volumetric expansion values is unclear. Post-analysis of specimens LTDTE1 and LTDTE2 revealed the presence of cracking, which were not present or not visible prior to testing. The larger expansion exhibited by LTDTE1 and LTDTE2 in comparison to a crystalline limestone specimen may be the result of thermal cracking. Due to the confinement within the oedometer, thermal cracking would lead to "dilation" of the micritic nodules within the calcite mud matrix leading to the higher volumetric expansion at elevated temperature.

4.4 Thermal Conductivity

4.4.1 Implications for SAGD Process

Heat conduction is important to thermal recovery processes, but it is very slow. It is ineffective for large scale heat transfer, but over short distances it is quite effective. It plays a particularly important (and undesirable) role in allowing the unwanted loss of heat to the overburden, and underburden during reservoir heating (Butler, 1985). Initially, startup processes for the SAGD process depend on conduction and of course, gravity. Hot water circulation through the injector and producer provides the energy for conductive heating which leads to bitumen mobilization and initial communications of the wells. Once SAGD begins, thermal conductivity plays a role in the slope and ceiling drainage components of SAGD. Heat capacity and thermal conductivity of the reservoir rock directly affect the steam front advance rate. Figure 4.16a illustrates the process of steam front advance for slope drainage. As bitumen drains along the slope, the rate of heating of the "exposed" reservoir is controlled by its thermal properties. Conduction, however, is not a controlling factor in ceiling drainage, Figure 4.16b, because mobilization and removal of bitumen can occur over a distance of a few sand grains (Edmunds et al., 1992). At this range, conduction heating is very rapid, so the speed of rise becomes limited only by how fast the steam arriving at the front can trade places with the bitumen and condensate that are falling away.

Thermal conductivity also affects the producing temperature of the bitumen and condensate; an important diagnostic measure of process performance. Figure 4.17 illustrates how conduction impacts the temperature of the produced fluids. From a process design basis, all these "heat loss" components combine to impact the heat input required for the SAGD process and its concomitant influence on the steam-oil ratio (SOR); a measure of economic efficiency for the process.

To provide material properties for both reservoir and geomechanical analyses of SAGD, thermal conductivity experiments were conducted on McMurray Formation oil sands and shale, and on Waterways Formation limestone. All thermal conductivity testing was carried out in the transient state thermal test cell developed by Seto (1985). Seto originally constructed the cell to enable thermal diffusivity testing to be conducted which required the test cell to be placed within the high temperature/pressure triaxial cell. As no thermal diffusivity testing was conducted in the current test program, modifications were made to a Wykeham-Farrance load frame within the Oil Sands Geotechnical Research Facility to eliminate the need to place the cell inside the high temperature triaxial cell. For a description of the general features and design criteria for the transient state thermal test cell, the reader is referred to Section 4.2 of Seto (1985). In particular, Section 4.3.2. describes the test procedure for conducting a thermal conductivity test; this procedure was adopted for all tests. The thermal conductivity of a test specimen is determined from the slope of the straight-line portion of a temperature versus natural logarithm of time of the plot. This procedure follows from the transient state line source technique of thermal conductivity determination; assuming the following set boundary conditions:

1. zero initial temperature throughout the medium; and
2. continuous heat source of strength, q, supplied instantaneously at the center line at time, t, greater than zero.

Solution of the partial differential equation governing one dimensional radial heat flow:

$$\frac{\partial^2 T}{\partial r^2}+\frac{1}{r}\frac{\partial T}{\partial r}=\frac{1}{\alpha}\frac{\partial T}{\partial t} \qquad [4.8]$$

for these boundary conditions (Carslaw and Jaeger, 1959) yields:

$$T = -\frac{q_l}{4\pi k} E_i\left(\frac{-r^2}{4\alpha t}\right) \qquad [4.9]$$

where T = temperature, [°C];
q_l = power input per unit length of line source, [W/m];
k = thermal conductivity, [W/m°C];
α = thermal diffusivity, [m^2/s];
r radial distance from the line source, [m]; and
t time from start of power input, [s]

As presented by Seto (1985), if the difference in temperature at two separate times of measurement are taken, the following equation indicating a linear relationship between temperature and the natural logarithm of time is obtained:

$$T_2 - T_1 = \frac{q_l}{4\pi k} \ln\left(\frac{t_2}{t_1}\right) \qquad [4.10]$$

For each thermal conductivity test, temperature, time and power input, q_l, were measured. Consequently, k was computed using Equation 4.10. The following sections present the results from the thermal conductivity testing program.

4.4.2 McMurray Formation Oil Sands

Two thermal conductivity tests were conducted, OSTHC1 and OSTHC2. Both specimens were selected from Unit E in well AGE1. These specimens are associated with Facies 10, 11 and 12; tidal channel deposits of fine to medium grained sand with high bitumen saturations. These sands were deposited under moderate to high energy conditions on bars and sand waves in tidal channels.

Initial specimen data are provided in Table 4.2. For both thermal conductivity tests, specimens were thawed and saturated under an effective confining stress of σ'_V = 500 kPa and subsequently consolidated to σ'_V = 2.0 MPa. Thermal conductivity tests were conducted at the nominal temperatures of 25 °C, 50 °C, 75 °C, 100 °C, 125 °C, 150 °C, 175 °C, 200 °C and 225 °C.

Figure 4.18 provides the variation in k over the temperature range 25 °C to 225 °C. Since the initial specimen properties were very similar, all data points were utilized for the linear regression curve fit represented by the dashed line. For the high bitumen saturated zones of Unit E, k decreases from 1.7 W/m °C at 25 °C to 1.5 W/m °C at 225 °C. The decrease in thermal conductivity with increasing temperature is consistent with other investigators (Karim and Hanafi, 1981; Somerton, 1973; Seki, Cheng and Fukusako, 1981). Figure 4.19 presents the results from OSTHC1 and OSTHC2 along with the thermal conductivity test results of Seto (1985). The results from OSTHC1 and OSTHC2 compare remarkably well with Seto's results for differing bitumen saturations. Figure 4.19 provides an effective tool for estimating the distribution of k within the oil sands units of the Phase A reservoir. The following sections provide data on the shale units within the McMurray Formation.

4.4.3 McMurray Formation Shale

Two thermal conductivity tests were conducted on McMurray Formation Shale units: (1) specimen LSTHC1, lower McMurray shale; and (2) specimen USTHC1, upper McMurray shale. Specimen LSTHC1 was selected from Unit F in well AGI3, and is associated with Facies 13, a light to medium gray, massive mudstone with thin silty sand laminations. This facies is associated with channel abandonment where suspension deposits were laid down under conditions of very low water flow. Specimen USTHC1 was selected from Unit C in well AT7 and is associated with Facies 2; a medium to dark gray mudstone containing small discontinuous sand lenses and sand filled burrows. Facies 2 was deposited as a transgressive lag during the southern advance of the sea from the north. The initial specimen data for LSTHC1 and USTHC1 are provided in Table 4.2. Note that USTHC1 contains 5.4% bitumen. Both specimens were saturated under an effective vertical confining stress of $\sigma'_v = 500$ kPa and consolidated to a pre-test condition of $\sigma'_v = 2.0$ MPa. Thermal conductivity tests were conducted at 25 °C, 50 °C, 100 °C, 125 °C, 150 °C, 175 °C, 200 °C, and 225 °C.

Specimen LSTHC1 experienced significant heat consolidation during the thermal conductivity test. This same phenomena was observed during the thermal volume change tests for highly interbedded oil sands specimens and the upper shale specimen. Figure 4.20 illustrates the variation in k over the temperature range 25 °C to 225 °C for LSTHC1 and USTHC1. For the lower shale material, LSTHC1, k at 25 °C was measured at 3.0 W/m °C (based on linear regression) and decreased to 1.75 W/m °C at 225 °C.

For the upper shale material, USTHC1, a lower ambient temperature thermal conductivity of 2.25 W/m °C was measured which decreased to the same k of 1.75 W/m °C as the lower shale material at 225 °C. For comparison, the thermal conductivity of a shale material tested by Martinez-Baez (1980) are included; also showing a reduction in k with increasing temperature.

Several competing factors contribute to the variations in k shown in Figure 4.20. These factors include:

- heat consolidation as the temperature rises, leading to a denser soil structure which should lead to an increase in k;
- at a constant porosity, an increase in bitumen and/or water saturation will lead to a decrease in k;
- the thermal conductivity of bitumen decreases as temperature increases; and
- the thermal conductivity of water initially increases from 0.55 W/m °C to 0.80 W/m °C over 25 °C to approximately 130 °C and then decreases from 0.70 W/m °C to 0.61 W/m °C over 130 °C to 250 °C.

As an initial thermal conductivity value for the lower and upper shale materials, 3.0 W/m °C and 2.25 W/m °C, respectively, correspond well to previous testing conducted on fine-grained sediments. Martinez-Baez (1980) suggests a value of 2.77 for kaolinite, while De Vries (1966) provides a value of 2.93 W/m °C for the broad class of "clay" minerals. Roy et al., (1981) obtained a thermal conductivity value for feldspar of 2.5 W/m °C. A bitumen content of 5.4% within specimen USTHC1 led to a lower k at 25 °C than for the lower shale specimen, LSTHC1, which contained only 2% bitumen and a higher water content.

4.4.4 Waterways Formation Limestone

Three thermal conductivity tests were conducted on Waterways Formation limestone. Specimen LTTHC1 was selected from an elevation of 263.25 m within well AGI1 and specimens LTTHC2 and LTTHC3 were selected from elevations 265.7 and 260.9 m, respectively, within well AT1. Specimen LTTHC1 comprised a nodular, argillaceous limestone having poorly sorted light gray, hard micrite nodules within an olive green calcite mud matrix. Specimen LTTHC2 and LTTHC3, however, are comprised of massive, argillaceous limestone. The initial specimen data for these three specimens are provided in Table 4.2. Each specimen was saturated under an effective vertical confining stress of σ'_v = 500 kPa and consolidated to σ'_v = 2.0 MPa prior to the thermal conductivity testing. Thermal conductivity was measured at 25 °C, 50 °C, 75 °C, 100 °C, 125 °C, 150 °C, 175 °C, 200 °C and 225 °C.

The variation of thermal conductivity for LTTHC1, LTTHC2 and LTTHC3 over the temperature range 25 °C to 225 °C is illustrated in Figure 4.21. The linear regression curve fit shown in Figure 4.21 displays only a weak correlation to temperature. Based on the scatter of the data points, a constant value of 2.1 W/m°C would seem appropriate for the argillaceous limestone horizon immediately underlying the McMurray Formation.

It is speculated that the data scatter arises from the incompatibility between an essentially incompressible rock (at $\sigma'_v = 2.0$ MPa) and the physical boundary conditions of the transient state thermal test cell. As part of the test procedure, a small diameter hole is drilled into each specimen to allow insertion of the probe heater and thermocouple. In order to achieve effective contact between the probe and specimen after insertion, pulverized limestone is compacted in the small annular space. This same technique was used with the oil sands and shale specimens. The premise for this procedure is that after back saturation and initial consolidation to test conditions, sample compression will have caused the "filler" material to come in intimate contact with the probe and specimen, thus minimizing all thermal contact resistance. While this was effective for oil sands and shale, the limestone specimens were sufficiently stiff preventing initial compression. Combined with the difficulty in maintaining quality control in the back fill procedure, the additional thermal resistance or temperature drop across the filler material resulted in scatter in the thermal conductivity measurements.

4.5 Bulk Compressibility

4.5.1 Implications for SAGD Process

The reservoir mechanics of SAGD are not dominated by the "displacement" mechanisms typically associated with steam injection processes such as cyclic steam stimulation. Reservoirs undergoing cyclic steam stimulation typically have extremely high oil viscosity and low native water mobility resulting in negligible initial injectivity (Beattie et. al, 1989). Steam injection at commercial rates requires injection pressures high enough to cause both localized fracturing and widespread pore volume increases in the formation. In these cases, pore volume compressibility is a critical reservoir parameter for understanding reservoir production.

In the SAGD process, the only "drive" mechanism at work is gravity. Consequently, compressibility of the formation will only have a minor effect on long term production. Compressibility may have an effect on the startup or initial communication phase of the SAGD process (see §2.2.2). In start-up, hot water or steam is circulated under pressure in both wells, with a small pressure differential applied between the wells. Variations in pore volume as a function of effective confining stress during this stage of SAGD will influence the rate of initial bitumen production.

4.5.2 Compressibility in Reservoir Geomechanics

In the dual jargon world of reservoir engineering (e.g. porosity) and geotechnical engineering (e.g. void ratio) , compressibility is perhaps the most difficult material property to assimilate in both worlds. Fundamentally, compressibility is based on the same concept in both sciences; a pore volume change results from a change in stress. The nature of the pore volume change and the definition of "a change in stress" constitute the divergence in the concept of compressibility for both sciences. To illustrate the relationship between "geotechnical" compressibility and "reservoir" compressibility, the relationships presented by Settari (1989) and Tortike (1991) are discussed. Their original formulations are modified to cast the equations in terms of effective stress.

As stated by Settari (1989), the various measures of compressibility can be derived by examining the mass accumulation term in a set of fluid flow equations. The numerical treatment of the mass accumulation terms will influence the form of the compressibility equations. For example, the general accumulation equation provided by Tortike (1991):

$$\frac{\partial}{\partial t}(\phi\rho_\alpha S_\alpha) = \phi\frac{\partial}{\partial t}(\rho_\alpha S_\alpha) + \rho_\alpha S_\alpha \frac{\partial\phi}{\partial t} \qquad [4.11]$$

will be assumed for the subsequent derivations. The second term on the right side of Equation 4.11 relates to the physical change in porosity and is conventionally handled through a pore compressibility term. As described by Settari (1989), pore compressibility is sometimes confused with rock compressibility; the differences are discussed below.

The typical reservoir engineering formulation for rock compressibility assumes it is measured at constant total stress. Therefore, rock compressibility is explicitly defined as

$$C_R = \frac{1}{\phi}\frac{\partial\phi}{\partial p} \qquad [4.12]$$

Equation 4.12 is typically simplified and restated as:

$$\phi = \phi_o[1 + C_R \Delta p] \qquad [4.13]$$

In geotechnical engineering however, it is the drained bulk compressibility of a specimen that is measured and defined as a function of effective stress. Classically, the drained bulk compressibility is represented by a parameter m_v, the coefficient of volume compressibility. The parameter, m_v, is defined in terms of void ratio, e, but knowing:

$$e = \frac{\phi}{1-\phi} \qquad [4.14]$$

the equation can be recast in the following form:

$$m_v = \frac{1}{1-\phi_o}\left(\frac{\Delta\phi}{\Delta\sigma'}\right) \qquad [4.15]$$

Equation 4.15 inherently assumes the solid grains are incompressible. Replacing m_v with the symbol C_b (to represent coefficient of bulk compressibility) and recasting Equation 4.13 to include C_s, the solid compressibility, the following relationship is obtained:

$$\phi = \phi_o + \left[(1-\phi_o)C_b - C_s\right]\Delta\sigma \qquad [4.16]$$

For the conventional reservoir engineering assumption of no change in total stress, $\Delta\sigma' = \Delta p$, (since $\sigma' = \sigma_t - p$) therefore equating Equation 4.13 and 4.16 provides the following relationship between C_R and C_b and C_s:

$$\phi_o C_R = (1-\phi_o)C_b - C_s = C_\phi \qquad [4.17]$$

It is important to note that the correct definition of pore volume compressibility, expressed as a function of effective stress, is by Equation 4.16. Compressibility tests based on changes in effective stress can be conducted in two ways in order to obtain equal increments of effective stress:

1) holding σ_t constant and decreasing p; or
2) holding p constant and increasing σ_t.

In general, drained compressibility of a specimen is measured by maintaining a constant fluid pressure, p, (drained conditions) and varying the total stress σ_t, applied to the specimen (method 2 above). Geomechanical testing typically employs method 2 since the interpretation of bulk compressibility from this type of test does not require knowledge of fluid compressibility. By varying total stress and holding pore pressure constant by allowing any excess pore pressures to dissipate, fluid compressibility does not influence the bulk compressibility measurement.

As Equation 4.17 reveals, several definitions of compressibility exist and their corresponding values depend on the type of test used to derive these parameters. For example, if the bulk compressibility is obtained from a geomechanical test (oedometer or triaxial) and a rock compressibility is required, then C_R will be given by:

$$C_R = \frac{C_b(1-\phi_o) - C_s}{\phi_o} \qquad [4.18]$$

As well, compressibility can be measured either by isotropic compression in the triaxial cell or constrained compression in the oedometer. The following concise explanation of the differences between isotropic and constrained compression was taken from Kosar (1989):

> "in a constrained compression test a specimen experiences both shear strain and volume change, whereas during isotropic compression, a specimen does not undergo shear straining. As a result, the stress path followed by a specimen in each test is different and a distinction must be made between constrained modulus, D, measured in the oedometer and the bulk modulus, K, measured during isotropic compression in the triaxial cell."

When isotropic compressibility results are plotted in terms of volumetric strain ($\Delta V/V_o$), the inverse slope of the compression curve is the bulk modulus, K, or

$$K = \frac{\Delta\sigma'_m}{\left(\Delta V_b / V_b\right)} = \frac{1}{C_b} \qquad [4.19]$$

The constrained modulus, D, is the ratio of axial stress to volumetric strain during confined compression, or

$$D = \frac{\Delta\sigma'_v}{\left(\Delta V_b / V_b\right)} = \frac{1}{C_{cb}} \qquad [4.20]$$

where C_{cb} = coefficient of constrained bulk compressibility. The isotropic and constrained volume compressibility parameters are related through elastic theory as follows:

$$K = \frac{D(1+\nu)}{3(1-\nu)} \quad \text{or} \quad C_b = \frac{C_{cb}3(1-\nu)}{(1+\nu)} \qquad [4.21]$$

and similarly, the effective stress change between two types of compressibility tests are:

$$\sigma'_m = \frac{\sigma'_v(1+\nu)}{3(1-\nu)} \qquad [4.22]$$

Within the confines of elastic theory then, and selecting $\nu = 0.3$ for oil sands, the following equations can be used to convert between respective compressibility values:

$$C_b = 1.62 \times C_{cb} \qquad [4.23]$$

$$\sigma'_m = 0.62 \times \sigma'_v \qquad [4.24]$$

Using the results from oedometer and triaxial tests on oil sands, shale and limestone, the computation and interpretation of C_R, C_ϕ and C_b will be presented. As noted above the oedometer provides only a measure of the constrained bulk volume change. Consequently, compressibility derived from oedometer tests will be referred to as C_{cR}, $C_{c\theta}$ and C_{cb} to signify that they are constrained compressibility values.

4.5.3 McMurray Formation Oil Sands

Constrained bulk compressibility tests were conducted as part of all thermal expansion tests: OSDTE1, OSDTE2, OSUTE1 and OSUTE2. The main purpose of the cyclic compression of the specimens was to re-compact the specimens prior to thermal expansion tests in attempt to reduce sampling disturbance and to measure the coefficient of constrained bulk compressibility. All test specimens were selected from within Unit D in well AGI4. The specimens are part of Facies I2, a fine-grained sand with high bitumen saturation. The fines content (< 74 μm) ranged from 3.3% for USUTE2 to 13.3% for OSDTE2. The increased fines content was due to occasional mud laminations within the specimen. The initial specimen conditions are provided in Table 4.2.

Each specimen was saturated under an effective vertical confining stress of 0.5 to 1.0 MPa, with a pore pressure of 4.0 MPa. The effective vertical confining stress was cycled two times between approximately 1.0 MPa and 9.0 MPa. Figure 4.22 illustrates the bulk volume change for each specimen. The relatively large initial volume decrease experienced by specimen OSUTE1 is due to recompaction of specimen expansion which occurred prior to the application of an effective confining stress. Test set-up difficulties provided sufficient time for expansion to occur as a result of specimen thaw and gas evolution.

Figure 4.23 illustrates the variation in the coefficient of constrained bulk compressibility, C_{cb}, for each test. The tests results from Kosar (1989) on interbedded oil sands compare well with the results for the massive oil sands specimens. While the results presented in Figure 4.23 provide data for the selection of C_{cb} over the effective stress range 2.0 MPa to 9 MPa, the zone of interest for SAGD processes encompasses the effective stress range below 2 MPa. At the lower effective stress range, special attention must be given to test setup and procedure. To the author's knowledge, the definitive work in this stress range for oil sands was conducted by Plewes (1987). Plewes (1987) conducted isotropic compressibility tests as part of a triaxial testing program aimed at evaluating the undrained shear strength of oil sand. A number of high quality (indices of disturbance <10%), low bitumen content oil sand specimens from the Syncrude site were isotropically compressed over the stress range 81 kPa to 791 kPa. More moderately disturbed specimens from the oil sand outcrop in the Saline Creek valley wall near Fort McMurray, Alberta were tested over the range 100 kPa to 5,000 kPa. Summaries of specimen properties can be found in Plewes (1987). Figure 4.24 illustrates the variation of the isotropic bulk compressibility from Plewes (1987) testing combined with the results from the current test program and previous researchers (Agar, 1984; Kosar, 1989). Equations 4.23 and 4.24 have been used to convert coefficients of constrained bulk compressibility to equivalent isotropic bulk compressibility.

As shown in Figure 2.24, isotropic bulk compressibility is a strong function of effective confining stress; especially below 1.0 MPa. The following relationship, based on a curve fit through the data ($r^2 = 0.72$), provides a means of estimating C_b based on estimated effective stress levels;

$$C_b = 0.6 \times 10^{-6} + 2.5\,(\sigma'_m)^{-2} \qquad [4.25]$$

This equation is applicable only in the range of σ'_m from 100 kPa to 7,000 kPa.

Using Equation 4.17 and the relationship developed for C_b (Equation 4.25), C_R, C_ϕ and C_b can be computed. Figure 4.25 illustrates the variation of C_R, C_ϕ and C_b as a function of effective isotropic confining stress. These curves are based on the assumption of an initial porosity of 32%, and a solid or grain compressibility of $5.0 \cdot 10^{-9}$ kPa^{-1}. For the case of one-dimensional or constrained compression, the isotropic compressibility curves presented in Figure 4.25 were converted to equivalent constrained compressibility's using Equations 4.23 and 4.24. The variation of C_{cR}, $C_{c\phi}$ and C_{cb} as a function of effective vertical confining stress is show in Figure 4.26.

4.5.4 McMurray Formation Shale

The paucity of McMurray Formation Shale specimens permitted only one compressibility test to be performed. A constrained bulk compressibility test was conducted on specimen USUTE2, selected from Unit B in well AGI1. The specimen is part of Facies I, a medium dark gray, lenticular very thin-bedded, sandy mudstone. These facies are marine lower shoreface deposits. The initial specimen characteristics are provided in Table 4.2. Note that the bitumen content for this specimen is much lower than most upper shale specimens.

Specimen USUTE2 was saturated under an effective vertical confining stress of 500 kPa with a back pore pressure of 2.6 MPa. The effective vertical confining stress was cycled twice between approximately, 2.0 MPa and 11.0 MPa. The results of a constrained compressibility test on specimen USUTE1 are shown on Figure 4.27. The constrained bulk compressibility varies between approximately $2.0 \cdot 10^{-6}$ kPa^{-1} at $\sigma'_v = 2.0$ MPa and $0.2 \cdot 10^{-6}$ kPa^{-1} at

$\sigma'_v = 20.0$ MPa. The variation of C_{cb} with σ'_v is described reasonably well by:

$$C_{cb} = 2.995e^{(-0.267 \times \sigma'_v)} \qquad [4.26]$$
$$\text{for } 2.0\,\text{MPa} \le \sigma'_v \le 10\,\text{MPa}$$

Within the Phase A reservoir, the shale content, by volume, of the McMurray Formation oil sands decreases with depth, with the exception of Unit F. At the risk of providing a very simplistic summary of an extremely complex geological environment, the following is the approximate sand/shale proportions within each major unit of the Phase A reservoir:

Unit B	35% sand / 65% shale
Unit C	70% sand / 30% shale
Unit D	80% sand / 20% shale
Unit E	90% sand / 10% shale
Unit F	30% sand / 70% shale
Unit G	80% sand / 20% shale

Kosar (1989) concluded that geological complexity of oil sands in the form of inclusions of more compressible argillaceous material may have a controlling effect on the compressibility characteristics of otherwise high quality oil sands. In the search for material parameter selection based on limited test results, it would be worthwhile to explore whether compressibility characteristics could be estimated based on sand/shale proportions, *within the boundaries of the Phase A reservoir*. Using compressibility data from the highly interbedded oil sands testing conducted by Kosar (1989), the low fines, high quality oil sand compressibility data presented in Figure 4.24 and the compressibility results from USUTE2, the possibility of using the volumetric proportions as a reference base for estimating bulk compressibility will be explored.

The constrained compressibility obtained for Unit B shale (test USUTE2) was converted to equivalent isotropic values using Equation 4.23 and 4.24. Figure 4.29 provides the range of isotropic compressibility values for specimens of varying sand/shale proportions. While stating the obvious, the presence of any distinct relationship between sand/shale proportions and bulk compressibility is vague and obscure given the limited data. It is reasonable to expect that a lower bound would exist - good quality samples tested under rigorous conditions should provide a reasonable estimate of in situ compressibility for low fines, rich oil sands. The establishment of an upper bound is more tenuous. The list of factors affecting the compressible behavior of shale and interbedded oil sands, such as mineralogy, depositional environment, geological history is long. With that caveat however, the compressibility data generated for the upper McMurray Formation shale should provide a reasonable upper limit. So within the boundaries of the Phase A reservoir, the trend in isotropic bulk compressibility illustrated in Figure 4.29 is offered for estimating the compressibility of different units or facies.

4.5.5 Waterways Formation Limestone

One constrained bulk compressibility test was conducted on Waterways Formation limestone. Specimen LTUTE1 was selected from Unit H in well AGE2. Specimen LTUTE1 comprised a nodular, argillaceous limestone having poorly sorted, light gray, hard micrite nodules within an olive green calcite mud matrix. The initial specimen data is provided in Table 4.2. LTUTE1 was saturated under an effective vertical confining stress of $\sigma'_v = 750$ kPa. Two loading cycles over the range 2.0 MPa to 10.5 MPa were conducted. Figure 4.30 shows the constrained volume change behavior for specimen LTUTE1. The volume change response of specimen LTUTE1 reflects the compressibility of the mud matrix with little contribution from the hard micrite nodules. Figure 4.31 provides a comparison of the computed C_{ch} values for the argillaceous limestone (LTUTE1) with the C_{ch} value obtained by Kosar (1989) on a massive, crystalline limestone specimen. The constrained compressibility for the argillaceous limestone is consistent with the compressibility of the oil sands specimens (OSDTE1, OSDTE2, OSUTE1 and OSUTE2). The massive limestone displays approximately one-half the compressibility of argillaceous limestone.

4.6 Strength and Stress-Strain Behavior

4.6.1 Implications for SAGD Process

In geotechnical practice, it is accepted that the stress-strain response of sands are stress path dependent and the testing by Dusseault (1981), Agar (1984), Plewes (1987), Kosar (1989) and Oldakowski (1994) have confirmed this to be true for McMurray Formation oil sands. For the SAGD process trials at the UTF, two predominant stress paths are followed within the reservoir:

1) first, under initially anisotropic stress conditions ($K_0 \approx 1.5$), pore pressure increases result in equal reductions in σ'_1 and σ'_3. In p'-q space, the stress path is horizontal because ($\sigma'_1 - \sigma'_3$) is unchanged along this path. The stress ratio σ'_1 / σ'_3, however, increases due to a reduction in σ'_3;

2) Following the pore pressure injection stage, increasing horizontal stresses due to thermal expansion of the reservoir within the developing steam chamber initiate an extension (relative to triaxial test configuration) a stress path where the deviatoric stress and mean

effective stress increase together. These stress increases are due primarily to an increase in σ_H; σ_V remains relatively constant due to the shallow depth of the reservoir.

This stress path is schematically illustrated in Figure 4.32. For SAGD processes, it is the ***deformation*** response along this stress path that is of primary importance. If, under the actions of shear stress or changes in mean effective stress, reservoir deformations result in volumetric dilation or contraction, the porosity and hence k_a will be altered. Absolute permeability, k_a, which is inherently linked to porosity, imparts a substantial influence on the drainage of fluids from the reservoir. Related to absolute permeability is the effective permeability to water, k_{ew}. At the reservoir temperature of 8 °C, bitumen is essentially immobile (μ=1,000,000 cp) and in the rich portions of the oil sands (Unit E and G), water saturation is very near the connate water saturation of 15%. If SAGD processes create shear-induced volume changes within the ambient temperature zones of the reservoir, the effective permeability to water in this zone will increase dramatically. An increase in k_{ew} will increase the hydraulic conductivity and will permit injection pore pressures to migrate further into the reservoir. This leads to a reduction in effective confining stress, a reduction in strength and an increased propensity for volumetric deformations. These concurrent phenomena act to alter the reservoir conditions in advance of the steam chamber. Correctly identifying the magnitude of the strength-deformation behavior and its resulting impact on reservoir processes is important for understanding the effectiveness of the SAGD process. To this end, laboratory experiments examining the stress-induced permeability changes of oil sands (Adhikary, 1991; Oldakowski, 1994) will be summarized. The work conducted by Oldakowski (1994) provides the first high quality experimental evidence on the impact of shear induced changes on the absolute permeability and the effective permeability to water in Athabasca oil sands; an important aspect of the pore pressure development within the Phase A reservoir.

An issue unrelated to the mechanics of SAGD but extremely important with regard to success of SATAC (Shaft and Tunnel Access Concept) was the integrity of the shafts as a result of creating steam chambers within the oil sands. Scott and Kosar (1986) identified five modes of stress changes and deformations at the shaft locations which must be considered:

- horizontal deformations and horizontal stresses caused by thermal expansion of the oil sand matrix in and adjacent to the steam chambers;
- shear stresses and shear strains from changes in the ratio of the horizontal effective stress to the vertical effective stress in the oil sands formation;
- shear stresses and shear strains from changes in the ratio of the maximum horizontal effective stress to the minimum horizontal effective stress in the oil sands formation;
- shear stresses and shear strains from effective stress changes caused by increases in pore fluid pressures from heating of pore fluids or from steam injection pressures; and

- horizontal or vertical fracturing from thermal expansion of pore fluids and/or from steam injection pressures.

To examine these issues, then would require a clear understanding of the stress-strain-strength behavior of McMurray Formation oil sands and intraformational shale.

With respect to the underlying tunnels, an extensive instrumentation program was undertaken to monitor the safety of the underground excavations. A secondary role for the instrumentation was to provide data during Phase A steaming that could either be appropriately scaled or used to derive fundamental properties, so that the impact of future larger scale steaming activities could be predicted (AOSTRA, 1990a). To achieve this aim, a clear understanding of the stress-strain-strength behavior of the limestone would be required for conducting thermal-stress analyses.

The stress-strain behavior of oil sands, both Athabasca McMurray Formation oil sands (Dusseault, 1977; Agar, 1984; Plewes, 1987; Kosar, 1989; Oldakowski, 1994) and Cold Lake Clearwater Formation oil sands (Kosar, 1989; Wong et al., 1993; Zhang, 1994) have been studied extensively. Comprehensive laboratory testing programs encompassing the following:

- constrained thermal expansion;
- constrained compressibility;
- isotropic drained compressibility;
- isotropic undrained compressibility;
- consolidated drained triaxial compression;
- consolidated undrained triaxial compression;
- J_1 constant consolidated drained triaxial compression;
- pore pressure injection;
- consolidated drained axial extension;
- consolidated undrained axial extension;
- unconfined axial extension;
- J_1 constant drained extension;
- active drained compression; and
- direct shear,

have been conducted with the goal of determining the constitutive behavior of oil sands. As confirmed by the above list, the majority of the testing has focused on stress-strain-strength properties of oil sands and related strata.

4.6.2 McMurray Formation Oil Sands

This section presents the results of a limited triaxial test program in combination with the stress-deformation behavior determined by previous researchers. The intent is to summarize as consistently as possible the stress-deformation behavior which may influence the geomechanical response of the Phase A reservoir during the SAGD process. The intent of the current laboratory testing program was not to conduct all the necessary testing required to formulate the parameters of a constitutive model. In fact, for the design of the current testing program, little emphasis was placed on oil sands testing given the extensive testing previously conducted by several researchers. The following sections will summarize the current state of knowledge concerning the stress-deformation and strength of Athabasca oil sands and the phenomena of stress-induced permeability changes.

4.6.2.1 Stress-Deformation Behavior

Conventional consolidated drained compression (CID) tests were conducted in the high temperature-pressure triaxial cell. The CID tests were conducted to serve as a basis for comparison to previous researchers. Based on the conclusion that strength-deformation behavior of low fines, rich oil sands was not significantly influenced at high temperatures (Kosar, 1989), no high temperature tests were conducted on oil sands. The strength-deformation properties at 20 °C were assumed to be valid at 225 °C.

Three isotropically consolidated, drained compression tests were conducted; OSRTR1, OSRTR2 and OSRTR3. Specimens OSRTR1 and OSRTR2 were selected from Unit E in well AGI1. Specimen OSRTR3 was selected from Unit E in well AGI4. These specimens are part of Facies 12, a fine-grained sand with a high bitumen saturation. As shown in the summary data provided in Table 4.2, the specimens were moderately disturbed with OSRTR3 being highly disturbed exhibiting an I_d of 21.9%. Each specimen was isotropically consolidated to the appropriate effective confining stress; no isotropic cyclic compression was conducted prior to shearing. As will be seen subsequently, eliminating the cyclic compression phase of the testing was an oversight. One of the primary reasons for cyclically compressing the specimen prior to shearing is to reduce the impact of sample disturbance on the stress-strain response of the specimen. Confining stresses of 1.0, 3.0 and 4.0 MPa were chosen for specimens OSRTR2, OSRTR1, and OSRTR3, respectively. Table 4.4 provides specimen data during each phase of the compression tests. Figure 4.33 illustrates the stress-strain and volume change relationships obtained for OSRTR1, OSRTR2, and OSRTR3. Due to large sample disturbance, (I_d's > 10%) all three specimens behaved as disturbed oil sands (Kosar, 1989; Agar, 1984).

Oldakowski (1994) tested 13 specimens from the UTF reservoir, with substantially improved indices of disturbance; $4.8 \leq I_d \leq 18.3$. Specimen characteristics are summarized in Table 4.5.

While the major focus of Oldakowski's (1994) testing was stress-induced permeability changes (discussed in §4.6.2.2), data was obtained on the stress-strain response of low fines, rich oil sands at low effective stresses.

Combining the results of OSRTR2, OSRTR2 and OSRTR3, Oldakowski (1994), Kosar (1989), Plewes (1987), Agar (1984) and Dusseault (1983), the most suitable peak failure envelope over the effective stress ranges anticipated during SAGD process trials at the UTF was developed. The peak failure envelope is shown in Figure 4.34.

Over the stress range of interest; $0\ \text{MPa} \leq p' \leq 10\ \text{MPa}$, the Mohr Coulomb failure criterion is used to define the failure envelope. The Mohr Coulomb yield function is defined as:

$$f^s = \sigma_1' - \sigma_3' N_\phi + 2c\sqrt{N_\phi} \quad \Big\| \quad N_\phi = \frac{(1+\sin\phi')}{(1-\sin\phi')} \qquad [4.27]$$

As noted in Figure 4.34, a linear failure envelope of $\phi' = 60°$ and $c = 0\ \text{kPa}$ defines reasonably well the envelope over the range $p' = 0$ MPa to 10 MPa. Consequently for high grade, low fines oil sands at the UTF; Units E & G, the failure criterion is defined as:

$$\frac{\sigma_1'}{\sigma_3'} = \frac{(1+\sin\phi')}{(1-\sin\phi')} = 13.9 \qquad [4.28]$$

For low grade, high fines oil sands at the UTF, Units D & C, the failure criterion is defined as:

$$\frac{\sigma_1'}{\sigma_3'} = \frac{(1+\sin\phi')}{(1-\sin\phi')} = 8.8 \qquad [4.29]$$

which corresponds to a friction angle, ϕ' of 53° and cohesion of 0 kPa.

In terms of stiffness parameters, namely Young's Modulus, substantial variation in reported values have been obtained. Figure 4.35 illustrates a dataset of Young's Modulus for compression tests conducted on high quality, high grade, low fines oil sands. Note that the data of Dusseault (1983) are absent from this dataset. Excessive cyclic compressive stresses were used to re-compress the specimens prior to shear testing. This created a structure of substantial initial stiffness which is likely unrepresentative of the in situ stiffness. For the data show in Figure 4.35, the following relationship defines reasonably well the dependence of E on effective confining stress;

$$E = 343\ \sigma_3'^{\,0.875} \qquad [\text{MPa}] \qquad [4.30]$$

A direct functional relationship between E and σ'_3 has been provided by Equation 4.30 which differs from the standard "hyperbolic" form typically chosen for defining this relationship:

$$E_i = k_E P_a \left(\frac{\sigma'_3}{P_a} \right)^n \qquad [4.31]$$

where E_i = initial Young's modulus at low strain level;
k_E = Young's modulus number;
P_a = atmospheric pressure; and
n Young's modulus exponent.

Byrne et al., (1987) provide excellent guidelines for the selection of k_E and n for sand. Based on laboratory test results, both static and dynamic, and even more critical, the back analysis of field measurements of foundation movements, the authors develop a database of parameters for Equation 4.31 and the other relationships associated with an incremental linear elastic hyperbolic model. Byrne et al., (1987) suggest for sands with relative densities, D_R, of 100 that k_E ranges from 1500 to 3000 and n=0.5. The diagenetic fabric of McMurray Formation oil sands results in relative densities greater than 100% (Dusseault and Morgenstern, 1979); they are found in situ at porosities less than can be attained by ASTM tests for achieving minimum porosity. Selecting $k_E = 2000$, the results obtained from Equation 4.31 can be compared to Equation 4.30. This comparison is illustrated in Figure 4.36. The comparison at low effective stresses is poor, a difference of approximately two at $\sigma'_3 = 1.0$ MPa. It is important to realize that E_i calculated from Equation 4.31 is a low strain level Young's modulus, typically $\varepsilon_a < 0.1\%$. The Young's moduli computed from a curve fit through experimental data, Equation 4.30, were calculated from stress-strain curves at a substantially higher axial strain, typically $\varepsilon_a < 0.25\%$.

4.6.2.2 Stress-Induced Permeability Changes

The geomechanical phenomena of volumetric straining under the combined effect of pore pressure changes (i.e. effective confining stress changes) and shear stress constitutes the primary factor influencing SAGD processes. Scott et al., (1991) outline the effects of steam stimulation on oil sands pore volume changes. A temperature increase causes thermal expansion of sand grains and matrix and in an anisotropic medium results in shear stresses. Pore pressure increase during steam injection decreases the effective confining stress and causes an unloading of the reservoir. For an anisotropic in situ stress state, pore pressure injection will also generate shear stresses and shear strains in the reservoir. These processes combine to result in a net change in the reservoir pore volume and permeability. To examine these porosity/permeability variations, Oldakowski (1994) conducted a laboratory testing program to investigate changes in absolute permeability and effective permeability to water in response to deformations induced by different stress paths. The tests were performed on Athabasca McMurray Formation oil sands from the UTF Phase A site at the in situ temperature of 8 °C. While the evolution of geomechanical testing on oil sands is mature (Dusseault (1977), Dusseault and Morgenstern (1978), Barnes (1980), Sterne (1981) Agar (1984), Plewes (1987), Kosar (1989), Wong (1991), all these laboratory programs were conducted at 20 °C or ambient laboratory temperatures. At 20 °C, bitumen viscosity is approximately 400,000 cp. Decreasing the temperature to 8 °C, the initial in situ temperature at the UTF, increases the viscosity to approximately 7,000,000 cp; an increase of 1,650%. At 8 °C, bitumen acts like a solid phase in the pore spaces and would likely contribute to the mechanical behavior of oil sands. While several field cases of oil sands exhibiting "tensile" properties have been reported, Plewes (1987) concluded that these tensile properties do not originate from the interlocking structure of the sand grains and postulates that bitumen viscosity at lower temperatures (his testing was also conducted at 20°C) may be the source of the apparent tensile strength.

Consequently, the testing program of Oldakowski (1994) represents the first data set available of hydraulic and geomechanical properties of oil sands obtained for an in situ temperature of 8 °C, the ambient temperature of the Phase A reservoir.

Absolute Permeability

For reconstituted, oil-free Athabasca McMurray Formation oil sands, it was concluded that the change in absolute permeability was a function of change in porosity, and was independent of the stress path followed. Based on the relationship shown in Figure 4.37, Oldakowski (1994) proposed the following relationship to describe the change in k_a with a change in ϕ;

$$\Delta k_a = 31 \times \Delta\phi \qquad [4.32]$$

Rewriting Equation 4.32 in terms of initial porosity and volumetric strains provides the following:

$$\Delta k_a = 31 \times \left[\frac{\varepsilon_v(1-\phi_o)}{1+\varepsilon_v}\right] \qquad [4.33]$$

Equation 4.33 then lends itself to incorporation into geomechanical analyses of Phase A and the concomitant changes in k_a with volumetric straining.

Of more significance however, to the SAGD process within the Phase A reservoir is the variation in effective permeability to water resulting from stress-induced deformations. At initial conditions, S_{wi} = 15%, the injectivity to water is considered to be negligible. For multiphase flow; the mobility of each fluid phase is considered separately. The overall or total phase mobility is calculated as:

$$\text{Total Mobility} = \left[\frac{k_{rw}}{\mu_w} + \frac{k_{ro}}{\mu_o} + \frac{k_{rg}}{\mu_g}\right] \times k_a \qquad [4.34]$$

The total phase velocity is expressed as:

$$\Sigma\left(V_\phi\right) = \left[\Sigma\left(\frac{k_{r\phi}}{\mu_\phi}\right)\right] \times k_a \times \Delta p \qquad [4.35]$$

The total phase velocity is a function of the water, oil and gas saturation, temperature and fluid pressure. Owing to the low levels of dissolved gas within the bitumen of the Phase A reservoir, Equation 4.28 can be simplified by not including the effects of gas:

$$\Sigma\left(\frac{k_{r\phi}}{\mu_\phi}\right) \times k_a = \left(\frac{k_{rw}}{\mu_w} + \frac{k_{ro}}{\mu_o}\right) \times k_a \qquad [4.36]$$

To illustrate the sensitivity of this system to the effective permeability of water, a single phase equivalent fluid system approach is adopted for hydraulic conductivity and is defined as:

$$k_{eq} = \left(\frac{\gamma_w k_{rw}}{\mu_w} + \frac{\gamma_o k_{ro}}{\mu_o}\right) \times k_a \qquad [4.37]$$

It is noted that at an in situ temperature of 8 °C, the viscosity of the bitumen phase is 7,000,000 cp; the value of k_{ro}/μ_o becomes very small. Consequently, minor variations in k_{rw}/μ_w will significantly influence k_{eq}. Using curve fit equations to define the relationship between k_{rw} and k_{ro} and S_w and the variation in bitumen viscosity with increasing temperature, as illustrated in Figure 4.38; a three dimensional relationship is obtained defining how keq varies as a function of S_w and T. Figure 4.39 illustrates the 3^D surface defining $k_{eq} = f(S_w, T)$; note the rapid increase in k_{eq} for small increases in S_w or T. As noted by Scott et al., (1991), porosity increases due to stress-induced deformations affect water saturation. Under initial conditions of S_{wi} = 15%, the ability to conduct water is very low ($k_{eq} \approx 10^{-11}$ m/s, Figure 4.39), which can lead to shear deformations under partly undrained conditions.

With these processes as a basis for motivation, Oldakowski (1994) conducted isotropic unloading, triaxial shear and "pure" triaxial shear tests to investigate relationship between oil sands volumetric deformations and changes in effective permeability to water. The initial effective permeability to water of UTF oil sands specimens, recompacted under 6 to 7 MPa effective confining stresses and unloaded to between 3,000 and 240 kPa effective confining stresses, varied from $5.3 \cdot 10^{-6}$ to $2.3 \cdot 10^{-3}\ \mu m^2$ (Oldakowski, 1994). The measured permeability values were affected by such factors as specimen water porosity ($\phi_w = V_w/V_t$), fines content, mode of fines distribution and grain size distribution of sand. For low fines oil sands, the following relationship was obtained for initial k_{ew};

$$\log k_{ew} = -5.868 + 36.2(S_w \phi) \qquad [4.31]$$

For stress-induced volume increases, the increase in k_{ew} was found to be only a function of change in water porosity; stress path had little effect. Whether volume increases occur by isotropic unloading or by shear dilation, the resulting effective permeabilities are the same. Figure 4.40 illustrates the variation in k_{ew} as a function S_w, clearly showing a linear semi-logarithmic relationship between k_{ew} and S_w. The position of the linear trends shown in Figure 4.40 is a result of the different fines contents in the oil sands specimens.

4.6.3 Upper McMurray Formation Shale

Consolidated-drained triaxial tests conducted at 20 °C and 220 °C on specimens selected from Unit B, (USRTR1, USRTR3, USRTR4, USHTR1, USHTR3, USHTR4) typically consisted of shale with clasts of oil sands within a shale matrix. Proportionally, the specimens ranged from 30-40% lean oil sands to 60-70% shale. Specimens selected from Unit D (USRTR2 and USHTR2) contain a higher proportion of oil sands with the shale component existing as lenticular clasts within the oil sands matrix. Initial specimen properties are provided in Table 4.2.

Each specimen was saturated under an effective confining stress of 0.3 to 0.5 MPa, with a back pore pressure of 3.0 MPa. The specimens were then allowed to saturate overnight and a B test was carried out prior to the isotropic consolidation pressure being applied. The confining stress was then increased to the effective confining stress required for the shear test. The volume change, density and porosity after isotropic consolidation at 20 °C is summarized in Table 4.6. All specimens sheared at 220 °C were heated under fully drained conditions after the completion of isotropic consolidation at 20 °C.

Results from four triaxial tests at 20 °C and four tests at 220 °C are summarized in Table 4.6. The stress-strain relationship obtained at 20 °C and 220 °C are shown in Figures 4.41 and 4.42, respectively. The behavior of these specimens, both 20 °C and 220 °C is similar to medium overconsolidated clay:

- moderate post-peak softening behavior; and
- an initial volume decrease followed by volumetric increase upon reaching its maximum deviator stress.

At 220 °C, the sharp strain softening response beyond peak strength displayed by USHTR2 is a reflection of the large volume of dense, medium rich oil sands in the specimen (approximately 70% sand-30% shale).

The drained shear strength data from both the 20 °C and 225 °C tests are plotted in p' - q space in Figure 4.43. The failure envelope is defined by the Mohr Coulomb parameters c'= 556 MPa and $\phi' = 35°$. For comparison, the results from drained passive compression tests on Clearwater Formation k_{cc} shale (Kosar, 1989) are also plotted on Figure 4.43. Kosar determined that the k_{cc} shale behaved as heavily overconsolidated shale, with a post peak strength reduction of approximately 35%. The upper McMurray Formation shales display only moderate to light overconsolidated response under shear condition yet the peak drained strength for these materials correspond very well, as shown in Figure 4.43. The correspondence in strengths is likely coincidental and not related to the constitutive behavior of each material. This follows from a conclusion of Kosar (1989) that the drained strength of these shale materials is dominated by the density or soil fabric which exists just before shear; pre-shear porosity for upper McMurray shale specimens was 0.29, pre-shear porosity's for k_{cc} shale specimens was 0.27.

The variation in Young's moduli with effective confining pressure for upper McMurray Formation Shale is shown in Figure 4.44. Again, for comparison, the results obtained by Kosar (1989) for Athabasca Clearwater for k_{cc} shale are also included in this figure. At 20 °C, E for upper k_m shale varies between 75 MPa at $\sigma'_3 = 0.5$ MPa and 680 MPa at 4.0 MPa. At 220 °C, E ranges from 75 MPa at $\sigma'_3 = 0.5$ MPa to 650 MPa at 4.0 MPa. While strength properties of upper k_m shale show minimal dependence on temperature, Figure 4.44 clearly shows that heat consolidation within the shale results in a substantial increase in stiffness in comparison to 20 °C; an increase of 100% at $\sigma'_3 = 2.0$ MPa.

4.6.4 Lower McMurray Shale

Specimens obtained from Unit F were subjected to consolidated drained triaxial shear tests at 20 °C and 220 °C. These specimens are part of Facies 13; a massive, structureless mudstone. It is distributed sporadically throughout the McMurray Formation in relatively thin, isolated, discontinuous units; except within the Phase A reservoir where it had a dramatic influence on the evolution of the SAGD process. Facies 13 are suspension deposits of low plasticity laid down under conditions of very low water flow (Rottenfusser et al., 1990). Initial specimen properties are provided in Table 4.2 as well as Appendix G. The composition of the lower McMurray shale specimens varied greatly (e.g. $S_h = 6.0\%$ for LSRTR1 and $S_h = 0.1\%$ for LSRTR2). Proportionally, the following summary provides an indication of the variability between specimens:

LSRTR1:	50% oil sands / 50% shale
LSRTR2:	0% oil sands / 100% shale
LSRTR3:	10% oil sands / 90% shale
LSHTR1:	50% oil sands / 50% shale
LSHTR2:	40% oil sands / 60% shale
LSHTR3:	5% oil sands / 95% shale

The distribution of these materials within each specimen was primarily laminations of oil sands within a shale matrix.

Each specimen was saturated under an effective confining stress of 0.3 to 0.5 MPa; with a back pore pressure of 3.0 MPa. The specimens were then allowed to saturate overnight and a B test was carried out prior to application of the isotropic consolidation pressure. The confining stress was then increased to required effective confining stress for the shear test. The volume change, density and porosity after isotropic consolidation at 20 °C are summarized in Table 4.7.

All specimens sheared at 220 °C were heated under fully drained conditions after the completion of isotropic consolidation at 20 °C. Specimens LSHTR3 was sheared at 206 °C due to an inability to raise the cell temperature to 220 °C. Figure 4.45 and 4.46 illustrate the stress-strain relationships obtained for lk_m (lower McMurray Formation Shale) at 20 °C and 220 °C, respectively. Results for these triaxial tests are summarized in Table 4.7. Similar to uk_m (upper McMurray Formation Shale), lk_m exhibits a strain softening behavior indicative of overconsolidated clay. The magnitude of post peak strength reduction in lk_m is larger than uk_m and occurs more suddenly (i.e. brittle) indicating a higher degree of overconsolidation. Volumetrically, lk_m displays contractant behavior until peak strength followed by a volume increase. Unlike uk_m, the strain-softening behavior of lk_m at 20 °C does not disappear at 220 °C.

The drained shear strength data, both peak and residual, are plotted in terms of a p'-q diagram in Figure 4.47. The limited number of tests and variability among specimens makes the determination of peak and residual strength envelope tenuous at best. In spite of these experimental vagaries, which are common to all testing programs, the following peak and residual strength parameters were chosen based on the data presented in Figure 4.47:

$c'_{peak(20°C)} \approx 0$ MPa $\phi_{peak(20°C)} = 48°$ / $c'_{peak(225°C)} \approx 0$ MPa $\phi_{peak(225°C)} = 46°$

$c'_{res(20°C)} \approx 0$ MPa $\phi_{res(20°C)} = 52°$ / $c'_{res(225°C)} \approx 0$ MPa $\phi_{res(225°C)} = 46°$

Effective cohesion values of appriximately 0 MPa have been selected since the data does not allow a more precise estimate. Other high temperature testing on clays has found similar results (Green, 1984; Williams, 1982; Kosar, 1989). Soil specimens that were consolidated to test temperatures under drained conditions display an increase in peak shear strength and stiffness with increasing temperature.

For the stress-strain curves shown in Figure 4.45 and 4.46, the pre-peak stress-strain response is nearly linear. Figure 4.48 illustrates the variation in Young's modulus for Ik_m as a function of initial effective confining stress. Clearly, heat consolidation leads to a denser pre-shear structure resulting in higher Young's modulus at 220 °C than 20 °C at a given effective confining stress. It is interesting to note that the magnitude of E for Ik_m is larger than for oil sands above $\sigma'_3 = 1.0$ MPa. At $\sigma'_3 = 2.0$ MPa, E for Ik_m is approximately twice the value of E for oil sands.

The implication of this high stiffness for SAGD processes relates more to wellbore integrity issues than to reservoir dynamics. While sporadically distributed throughout the McMurray Formation, if sufficient thickness is encountered through which the horizontal wells must be drilled, the stiffness contrast between the oil sands and the lower McMurray shale may produce zones of preferential shear upon the application of thermally-induced deformations. If large enough, these shear stresses may cause casing/liner deformations which may impair steam injection and/or bitumen production. This is entirely supposition however, since no distress within A1 wellpair, drilled through Unit F, was found during the Phase A pilot.

4.6.5 Waterways Formation Limestone

Three main rock types were identified within the Waterways Formation (Norwest Resources, 1986) underlying the Phase A reservoir:

- argillaceous limestone;
- intraclast breccia limestone; and
- organic limestone.

All specimens were selected from within the Moberly Member of the Waterways Formation. The majority of the Moberly Member is argillaceous limestone, more specifically, nodular argillaceous limestone. Nodular limestone is the product of complex processes. The fine-grained ovaloid carbonate nodules are thought to form soon after deposition as a product of concretionary action and differential compaction. The nodules often appear to grade into the surrounding argillaceous clay matrix. The nodular lithologies are generally poorly indurated and contain random fractures which tend to propagate around the nodules. The argillaceous content is dark gray to dark brown calcareous mud (Norwest Resources, 1986).

The process of deposition is visualized as occurring in deeper, quiet water where settling of fine calcite was continuous while deposition of clay that had been eroded and transported from land was periodic; resulting in clay-rich and calcite-rich layers. Compaction and squeezing could have caused lensing of these layers. Subsequent processes of gentle to turbulent slumping would result in fragmentation of partially cemented calcite lenses and the transport, partial rounding and redeposition of the still plastic fragments. The uncemented clay-rich mud would have behaved as loose sediment and been redeposited as laminae or partially squeezed or resettled between the fragments. As will be seen subsequently, this depositional history results in bimodal stress-strain behavior where the initial behavior is controlled by the clay matrix and the ultimate strength is controlled by the micritic nodules.

4.6.5.1 Unconfined Compression

Three unconfined compressive tests were conducted (LTRUC1, LTRUC2 and LTRUC3) to determine the unconfined compressive strength of the limestone units. Specimen LTRUC1, selected from well AGI3, consisted of a nodular argillaceous limestone with micritic nodules set in a calcareous claystone matrix. Specimens LTRUC2 and LTRUC3, however, consisted of a intraclastic biogenic limestone with micro crystalline clasts, identified as being generally well indurated and very strong. Table 4.2 summarizes the initial properties for these specimens.

Figure 4.49 illustrates the stress-strain relationship obtained for unconfined compression tests on argillaceous and massive limestone specimens. Test results are summarized in Table 4.8. For the argillaceous specimen, LTRUC1, a uniaxial compressive strength of 24.8 MPa was obtained at an axial strain of 1.2%. Previously quoted values of σ_c for these materials ranged from 19.3 to 34.0 MPa (AOSTRA, 1984). Williams et al.(1980) report uniaxial compressive strengths of approximately 40 MPa for dry argillaceous limestone specimens . The Young's modulus of elasticity at 50% of ultimate strength was 3.4 GPa. An average Young's modulus of 13.3 GPa was reported by AOSTRA (1984) for argillaceous limestone. For the massive, biogenic limestone materials, specimen LTRUC2 and LTRUC3, uniaxial compressive strengths of 34.5 MPa and 75.0 MPa, respectively, were obtained. A value of σ_c = 75.0 MPa was chosen for LTRUC3 based on the axial stress response immediately prior to unloading due to load cell limitations as noted in Figure 4.49. Previous reported values of σ_c for massive limestone range from 44.0 to 84.0 MPa (AOSTRA, 1984). Young's modulus of elasticity was 6.7 MPa and 15.2 MPa for LTRUC2 and LTRUC3, respectively. Previous testing (AOSTRA, 1984) found E ranging from 9.8 GPa to 28.2 GPa, with an average of 18.3 GPa and a Poisson's ratio of 0.08.

4.6.5.2 Triaxial Compression

Consolidated drained triaxial tests were conducted at 20 °C and 220 °C on specimens selected from the Moberly Member of the Waterways Formation. Generally, specimens can be defined as nodular argillaceous limestone with mainly sub-horizontal, elongated micrite nodules set in an olive to light gray soft calcareous claystone matrix. The exceptions are specimen LTRTR2, which is composed of alternating layers of intraclastic and biogenic limestone and specimen LTHTR5, a massive, textureless biohermal limestone. Initial specimen properties are provided in Table 4.2.

Each specimen was saturated overnight under an effective confining stress of 1.0 MPa, with a back pore pressure of 5.0 MPa. The confining stress was then increased to give the effective confining stress required for the shear test. All specimens sheared at 220 °C were heated under fully drained conditions after completion of isotropic consolidation at 20 °C.

Table 4.9 summarizes the result from five triaxial compression tests at 20 °C and five tests at 220 °C. The stress-strain relationships obtained at 20 °C and 220 °C over an effective confining stress range of 1.0 MPa to 8.0 MPa are illustrated in Figures 4.50 and 4.51, respectively. The argillaceous, nodular limestone displays a bi-modal stress-strain response at 20 °C. Except at a σ'_3 = 1.0 MPa, an initial "pre-yield" is reached followed by a period of plastic deformation. At some degree of plastic yield, the material begins to follow a secondary stress-strain path to ultimate yield.

The initial constitutive response of the nodular argillaceous limestone is controlled by the claystone matrix; no interaction is occurring between the harder, micritic nodules. With increased deformation and plastic yield, the nodules begin to interact, forming a "new" structure with increased stiffness and a subsequent increase in load carrying capability. The shear resistance in the secondary portion of deformation appears however, to be still controlled by the claystone matrix.

Caution is urged in interpreting the volumetric response of these specimens, as shown in Figure 4.50 and 4.51. The volume changes were calculated using standard triaxial equations based on volume of fluid expelled or imbibed during shear. The failure modes for these specimens did not however satisfy the homogeneous strain conditions such that the volume changes are indicative of its true constitutive behavior. The mode of failure was primarily axial splitting combined with some development of shear planes.

The failure modes likely will influence to a greater degree the hydraulic conductivity of the rock mass than its ultimate failure behavior. Brittle deformation at 20 °C in the form of axial splitting may enhance the hydraulic conductivity of the rock mass sufficiently to enable reservoir fluids to penetrate significant distances into the underburden. If the pore pressure migrates to the tunnel horizon, water ingress or tunnel wall stability issues may occur.

The influence of temperature is apparent in the different stress-strain responses at 20 °C and 220 °C. At 20 °C, a "pre-yield" threshold and a post-peak softening are components of the shear behavior. At 220 °C, the stress-strain response is more ductile, does not show a "pre-yield" threshold and except for LTHTR2, a massive, biohermal limestone specimen, exhibits minimal post peak softening. In contrast, however, the more ductile response at 220 °C does not influence Young's modulus of elasticity. Owing to heat consolidation of the claystone matrix, the modulus of elasticity increases slightly at 220 °C, as shown in Figure 4.52. The scatter in the data is a result of the variability in the specimens. This is in contrast to Lo and Wai (1982) who report that as a result of thermal cracking, the strength and stiffness of Darlington limestone (massive) decreases at elevated temperatures.

As part of a testing program for Gulf Canada's Surmont Project, Golder Associates (1981) conducted triaxial compression tests on Devonian limestone samples. The results from these tests suggested Hoek and Brown's general failure criterion might be applicable to the Devonian limestone. The Hoek-Brown failure criterion is based on a non-linear relation between major and minor principal stresses σ'_1 and σ'_3:

$$\sigma'_1 = \sigma'_3 + \sqrt{\sigma'_3 \sigma_c m + \sigma_c^2 s} \qquad [4.32]$$

The material constants m and s can be obtained by plotting $(\sigma_1 - \sigma_3)^2/\sigma_c^2$ versus σ'_3/σ_c for each test and fitting a linear curve through the data. The slope of this line provides the constant m and the y-intercept provides s. For tests conducted at 20 °C and 220 °C, the following material constants were calculated:

$m_{20°C} = 26.1$ $s_{20°C} = 1.47$ $r = 0.945$ (5 tests)
$m_{220°C} = 15.7$ $s_{220°C} = 0.32$ $r = 0.835$ (4 tests)

An unconfined compressive strength, σ_c of 25.0 MPa was chosen for Hoek-Brown failure criteria calculations. The resulting non-linear failure surfaces at 20 °C and 220 °C are illustrated in Figure 4.53. The triaxial compression test results are also plotted in Figure 4.53. While based on limited test results, over the effective confining stress range existing within the Waterways Formation immediately below the Phase A reservoir, the argillaceous, nodular limestone horizons will exhibit a reduction in strength; at $\sigma'_3 = 4.0$ MPa; a reduction of approximately 25% occurs between 20 °C and 220 °C.

For purposes of comparison to the previous materials tested whose strength results were presented as c' and ϕ', the Hoek-Brown failure criterion can be utilized to provide equivalent c' and ϕ' values *for a given value of* σ'_3. For a given value of σ'_3 the tangent to Equation 4.32 will represent an equivalent Mohr-Coulomb yield criterion in the form:

$$\sigma_1' = N_\phi \sigma_3' + \sigma_c^M \qquad [4.33]$$

By substitution, σ_c^M is :

$$\sigma_c^M = \sigma_3'(1 - N_\phi) + \sqrt{\sigma_3'\sigma_c m + s\sigma_c^2} \qquad [4.34]$$

The tangent to Equation 4.32 is then defined by:

$$N_\phi(\sigma_3') = \frac{\partial\sigma_1'}{\partial\sigma_3'} = 1 + \frac{\sigma_c m}{2\sqrt{\sigma_3'\sigma_c m + s\sigma_c^2}} \qquad [4.35]$$

The cohesion, c', and friction, ϕ', can then be obtained from N_ϕ and σ_c^M:

$$\phi' = 2\tan^{-1}\left(\sqrt{N_\phi}\right) - 90° \qquad [4.36]$$

$$c' = \frac{\sigma_c^M}{2\sqrt{N_\phi}} \qquad [4.37]$$

For the test results presented in Figure 4.53, at a $\sigma'_3 = 4.0$ MPa, the following equivalent Mohr-Coulomb parameters are obtained:

for $\sigma'_3 = 4.0$ MPa; $c'_{20°C} = 7.3$ MPa $\phi'_{20°C} = 47°$
$c'_{220°C} = 4.9$ MPa $\phi'_{220°C} = 44°$

Assuming then, that the Hoek-Brown failure criteria is valid, the modest reduction in ϕ' but large reduction in c' also provide evidence that the claystone matrix undergoes the majority of strength loss during heating. Other investigators have shown minimal influence of temperature on the behavior of saturated (wet) crystalline limestone up to 200°C (Kosar, 1989; Rutter, 1974).

4.7 Gas Evolution and Composition

The presence of a gaseous phase within Athabasca oil sands has been known for many years. Upon reduction of confining stress and/or pore pressure, dissolved gas tends to come out of solution in large quantities. With regard to the geotechnical implications of gas evolution, ground breaking work by Sobkowicz(1982) on the mechanics of gassy sediments, followed by specific research on oil sands by Peacock(1988) and Branco(1988), have provided an excellent understanding of the process of gas evolution.

The treatment of gas evolution (commonly referred to as solution gas drive) in reservoir engineering is concerned primarily with its impact on fluid flow. In conventional reservoirs, gas evolution can represent a significant drive force in displacing oil to production wells. In heavy oil reservoirs, gas evolution leads to the creation of "foamy oil" which is postulated to be a major production support mechanism in the primary production of heavy oil (Metwally and Solanki, 1995). In thermal EOR projects, the role of gas evolution becomes more complex by not only effecting fluid flow characteristics but heat and mass transfer within the reservoir. The following section describes the impact of gas evolution (solution gas) on the steam assisted gravity drainage process.

4.7.1 Implications for SAGD Process

Non-condensable gas accumulation is an important factor in the SAGD process (AOSTRA, 1990d). With a thermal process, such as SAGD, gas accumulation within the reservoir can arise from both GOR (solution gas) and gas production from aquathermolysis, a myriad of chemical reactions which generate additional methane, carbon dioxide and hydrogen sulfide. (Hyne et al. 1982). A high GOR would likely lead to significant gas accumulation during SAGD which would lead to reduced steam temperature. A lower steam temperature would lower the steam front advance and reduce the oil production rates. The addition of gaseous components to water vapor will dilute the vapor and shift the pressure/temperature equilibrium point. For instance, for an absolute pressure of 2000 kPa and no non-condensable gases (NCG), the equilibrium or saturated temperature would be 212 °C. The addition of 50% methane (CH_4) would reduced the equilibrium temperature to approximately

180 °C. This dilution effect on temperature insulates and impairs the mass transfer of steam within the reservoir.

Based on a detailed study of the mechanics of the SAGD process, Edmunds and Collins, (1989) offer the following conclusions regarding non-condensable gas effects:

- solution and other non-condensable gases can be expected to accumulate at the ceiling of a rising steam chamber due to the "trapping" effect of countercurrent flow;
- the impact of non-condensable gases is greatest on the ceiling drainage rate and was found to be a complex function of the amount and composition of the gas, the permeability of the formation and time;
- in a high permeability sand (k_v> 1 d) , small amounts of gas greatly impede the rise rate of the steam chamber by preventing transport of steam to the advancing front;
- in a low permeability sand (k_v< 1 d), the presence of gas can actually improve drainage rates. Because steam transport is already restricted by the low permeability, a relatively thick zone of reservoir ahead of the front is heated by conduction to intermediate temperatures. This allows for the drainage of reasonably mobile oil (with respect to gas) before steam temperatures are achieved;
- carbon dioxide has much less of an impairment effect in high permeability sands, as compared to methane in similar quantities, because much more of it can dissolve in the oil phase - its high solubility will promote viscosity reduction of the bitumen in the conduction heated zone.

Clearly, the need to determine both the volume of dissolved gas within the oil sands and the composition of the gas is important to the understanding of the Phase A SAGD process. The following describes gas evolution and composition testing conducted for this purpose.

4.7.2 Oil Sands

Two gas evolution tests were conducted; OSGAS1 and OSGAS2, with a primary aim of determining the combined solubility coefficient, H_{comb}. It defines the amount of gas present in the pore liquid at any given pressure under equilibrium conditions. Specimen OSGAS1 was selected from within Unit E in Well AGI1. Specimen OSGAS2 was selected from within Unit G in Well AGI4. The specimens are part of Facies 12 a fine-grained sand with a high bitumen saturation. Initial specimen data is provided in Table 4.2. For both gas evolution tests, the specimen was initially placed under a confining pressure of 825 kPa and left for three days to achieve saturation; a B test was conducted to confirm saturation. The confining pressure was increased to 2000 kPa with a back pore pressure of 1900 kPa prior to beginning the undrained unloading test. The confining pressure was reduced in increments of 200 kPa in each unloading step. This gas evolution testing technique followed the test procedures outlined in Branco (1988).

Figure 4.54 illustrates the results from the two unloading undrained tests (i.e., gas evolution tests). Each data point in Figure 4.54 represents the equilibrium volume of evolved gas converted to equivalent volumes at atmospheric pressure at each stabilized pore pressure increment. Testing difficulties with OSGAS2 permitted only one large step in pore pressure reduction to be completed.

An average combined solubility coefficient of 0.16 cm^3/cm^3 was obtained for McMurray Formation oil sands. Branco(1988) obtained H_{comb} values ranging from 0.116 to 0.205 for specimens obtained from the mining benches at Syncrude Canada Ltd.. The bubble point pressure obtained for OSGAS1 was 413 kPa and for OSGAS2 was 445 kPa. It is generally accepted that the bubble point pressure for oil sands equals the in situ pore pressure (Peacock, 1988; Branco, 1988). For specimens OSGAS1 and OSGAS2, this would correspond to approximately 475 kPa and 560 kPa, respectively, which are substantially higher than the test results. Observations in the laboratory of bubble point pressures lower that the in situ original pore pressure can be attributed to the fact that during saturation, the samples absorb relatively large amounts of water that are air saturated at atmospheric pressure (Branco, 1988). The extraneous water lowers the average gas concentration within the specimen which results in a decrease in the original gas bubble point pressure.

Solution gas estimates made for reservoir simulations (Edmund et al., 1991) for UTF conditions was 0.85 m^3 of methane / m^3 of bitumen. Using an H_{comb}=0.16 cm^3/cm^3 and adjusting the bubble point pressure to an average 520 kPa yields a solution gas estimate of 0.83 m^3 of "gas"/m^3 of pore fluid. The type of "gas" will be discussed subsequently. For initial saturation conditions of S_{oil} = 85 % and S_w = 15 %, a GOR of 0.83 m^3 of "gas" / m^3 of pore fluid would equate to 0.71 m^3 of methane / m^3 of bitumen. This is lower than the UTF estimate from reservoir simulations and may be a contributing factor in the relatively low influence of non-condensable gases on the Phase A SAGD performance (Gittins et al., 1992).

The types and quantities of gas present in an oil sand specimen, as well as the ratio of pore liquids, will determine its solubility coefficient. Consequently, three gas sampling tests, OSGSS1, OSGSS2 and OSGSS3, were performed to measure gas types and proportions for UTF McMurray Formation oil sands. Gas content is measured through gas chromatography. Specimens OSGSS1 and OSGSS2 were obtained from Unit E in well AGI1 and OSGSS3 was obtained from Unit G in well AGI4; all three specimens are part of Facies 12, a fine-grained sand with a high bitumen saturation. Initial specimen properties are provided in Table 4.1.

Figure 4.55 illustrates the results of the gas compositions testing. On average, UTF McMurray Formation oil sands were found to contain 18% carbon dioxide, 79% methane, 2% nitrogen and 1% ethane. Robinson (1985) determined the types and amounts of gases that were released from Athabasca oil sand cores taken from the Syncrude mine site; 9% carbon dioxide, 37% methane, 37% nitrogen and 17% oxygen. In general, the dissolved gas type has been assumed to be entirely methane. Analysis of produced gas samples during the early stages of the Phase A SAGD test showed methane/carbon dioxide ratios of 55%/37%.

4.8 Summary

The thermomechanical properties of the UTF McMurray Formation oil sands, lower and upper McMurray Formation shale and the Waterways limestone have been characterized in an extensive laboratory testing program involving thermal expansion, thermal conductivity, compressibility, strength-deformation and gas evolution tests. The significance of each material property within the context of the SAGD process was discussed. The following summarizes the influence of these properties:

Thermal Volume Change:

- a relationship between the coefficient of pore volume thermal expansion, a value typically employed in reservoir simulators, and the coefficient of bulk thermal expansion, β_b , a value typically measured in geomechanical tests, was developed. Significant differences in the coefficient of pore volume thermal expansion can occur if careful attention is not given to the type of geomechanical test used in determining β_ϕ and the stress path followed within the reservoir;

- higher fines, low bitumen saturated oil sands will experience less cumulative volume change than low fines, high bitumen saturated oil sands. An average value of β_{cb}, the coefficient of constrained bulk thermal expansion, for low fines, rich oil sands was determined to be 6.0×10^{-5} °C^{-1}. For high fines oil sands, β_{cb} reduces to 3.0×10^{-5} °C^{-1}.

- the constitutive response of upper McMurray shale to temperature increases was complex showing sensitivity to stress history, rate of heating, mineralogy and magnitude of temperature increase. The coefficients of constrained bulk thermal expansion can be summarized as follows:

20°C to 50°C	$\beta_{cb} = -3.0 \times 10^{-5}$ °C^{-1};
50°C to 100°C	$\beta_{cb} = +2.4 \times 10^{-5}$ °C^{-1}; and
100°C to 225°C	$\beta_{cb} = -5.0 \times 10^{-5}$ °C^{-1};

- under conditions of constrained thermal expansion, nodular, argillaceous Waterways limestone exhibited minor structural collapse from 20°C to 100°C and essentially linear volumetric thermal expansion up to 250°C. From 100°C to 250°C, the coefficient of constrained bulk thermal expansion was approximately $7.5 \times 10^{-5}\ °C^{-1}$.

Thermal Conductivity:

- thermal conductivity of oil sands directly affects the steam front advance rate. It also affects the producing temperature of bitumen and condensate which is used as a process control variable (steam-trap control).
- for UTF McMurray Formation low fines, rich oil sands, k (thermal conductivity) decreases from 1.7 W/m°C at 25°C to 1.5 W/m°C at 225°C.
- for UTF lower McMurray Formation shale, k decreases from 3.0 W/m°C at 25°C to 1.75 W/m°C at 225°C.
- for UTF upper McMurray Formation shale, k decreases from 2.25 W/m°C at 25°C to 1.75 W/m°C at 225°C.
- a constant k of 2.1 W/m°C was determined for UTF Waterways argillaceous limestone.

Compressibility:

- formation compressibility has a greater influence during the initial startup phase of the SAGD process than on long term production.
- the importance of recognizing the type of test from which compressibility was determined was discussed. In a constrained compression test a specimen experiences both shear strain and volume change, whereas during isotropic compression, a specimen does not undergo shear straining. As a result, the stress path followed by a specimen in each test is different and a distinction must be made between constrained compressibility and isotropic compressibility.
- a relationship between reservoir engineering "compressibility" and geotechnical engineering "compressibility was defined. Three coefficients of compressibility, namely rock (C_R), pore (C_ϕ) and bulk (C_b), were identified and the following equation developed which describes their interrelationship:

$$\phi_o C_R = (1-\phi_o)C_b - C_s = C_\phi$$

- isotropic bulk compressibility is a strong function of effective confining stress. As defined above, this creates a strong dependence of C_ϕ and C_R on effective confining stress.

Consequently, reservoir simulations of SAGD must include the influence of effective confining stress in order to correctly simulate the compressibility behavior of oil sands.

- combining the results of previous testing with tests results from the current test program, the following equation, applicable over the range 100 kPa $\leq \sigma'_m \leq$ 7,000 kPa, was found to provide a reasonable estimate of C_b for McMurray Formation oil sands:

$$C_b = 0.6 \times 10^{-6} + 2.5\ (\sigma'_m)^{-2}$$

- the variation of C_{cb}, the constrained coefficient of bulk compressibility, with vertical effective stress for upper McMurray Formation shale was found to be reasonably defined by:

$$C_{cb} = 2.995\text{x}10^{-6}\ e^{-.267*\sigma'_v}\ (2.0\text{ MPa} \leq \sigma'_v \leq 10\text{ MPa})$$

- for Waterways argillaceous limestone, C_{cb} was found to vary between $2.0\text{x}10^{-6}$ kPa^{-1} at σ'_v = 2.5 MPa and $0.2\text{x}10^{-6}$ kPa^{-1} at σ'_v = 10.0 MPa. Waterways massive limestone was shown to have approximately one-half the compressibility of the argillaceous limestone.

Strength and Stress-Strain Behavior:

- For SAGD processes, it is the ***deformation*** response along a particular stress path that is of primary importance. If, under the actions of shear stress or changes in mean effective stress, reservoir deformations result in volumetric dilation or contraction, the porosity and hence k_a will be altered. Absolute permeability, k_a, which is inherently linked to porosity, imparts a substantial influence on the drainage of fluids from the reservoir. If SAGD processes create shear-induced volume changes within the ambient temperature zones of the reservoir, the effective permeability to water in this zone will increase dramatically. An increase in k_{ew} will increase the hydraulic conductivity and will permit injection pore pressures to migrate further into the reservoir. This leads to a reduction in effective confining stress, a reduction in strength and an increased propensity for volumetric deformations. These concurrent phenomena act to alter the reservoir conditions in advance of the steam chamber. Correctly identifying the magnitude of the strength-deformation behavior and its resulting impact on reservoir processes is important for understanding the effectiveness of the SAGD process.

- over the past 18 years, extensive laboratory testing of Athabasca oil sands has been conducted to determine the geotechnical properties of oil sands; from the early pioneering work of Dusseault (1977) who identified Athabasca oil sands as a "locked" sand to the most recent testing of Kosar (1989) who examined stress path effects on stress-deformation behavior and of Oldakowski (1994) who experimentally examined the phenomena of shear induced changes on absolute permeability and effective permeability to water.

- based in the current testing program and a review of previous experimental results, the following were found for McMurray Formation oil sands:

  1) the presence of shale interbedding results in a decrease in the maximum shear strength as compared to low fines oil sands. Over the effective mean confining stress range 0 MPa to 10 MPa, low fines UTF oil sands had strength properties of c'=0 kPa and ϕ'=60°. For the same stress range, high fines UTF oil sands had strength properties of c'=0 kPa and ϕ'=53°;

  2) strains to failure varied with the stress path followed in a test. This indicates that the strain at which mobilization of shear strength occurs can be significantly different from the conventional drained triaxial compression test;

  3) Young's modulus for low fines McMurray Formation oil sands is heavily dependent on the level of effective confining stress. The variation of E with σ'_3 was reasonably defined by:

$$E = 343\ \sigma_3'^{\,.875}\ [\mathrm{MPa}]$$

  4) the change in absolute permeability can be defined in terms of volumetric strain and initial porosity by:

$$\Delta k_a = 31\left[\frac{\varepsilon_v(1-\phi_o)}{1+\varepsilon_v}\right]$$

  5) for stress-induced volume increases, stress path had little effect with k_{ew}, the effective permeability to water, found to be only a function of a change in water porosity. Water porosity is defined as the ratio of water volume to total volume.

- the stress-strain behavior for upper McMurray shale showed moderate post-peak softening and an initial volume decrease followed by volumetric increase upon reaching its maximum deviator stress. For the limited number of tests conducted at 20°C and 225°C, the shear strength behavior of upper McMurray shale was not significantly influenced by temperature. Shear strength parameters determined for upper McMurray shale were c'=556 kPa and ϕ'=35°.

- while strength properties showed minimal dependence on temperature, Young's modulus for upper McMurray shale increased with increasing temperature; due mostly to heat consolidation phenomena creating a denser pre-shear structure at 225°C than at 20°C.

- lower McMurray shale exhibits strain softening behavior with a post-peak strength reduction of approximately 4% at 20°C and 12% at 225°C. The strength parameters were influenced by temperature. The process of heat consolidation caused an increase in the friction angle from 48° at 20°C to 52° at 225°C.
  $c'_{peak(20°C)} \approx 0.0$ MPa $\phi_{peak(20°C)} = 48°$ / $c'_{peak(225°C)} \approx 0.0$ MPa $\phi_{peak(225°C)} = 52°$
  $c'_{res(20°C)} \approx 0.0$ MPa $\phi_{res(20°C)} = 46°$ / $c'_{res(225°C)} \approx 0.0$ MPa $\phi_{res(225°C)} = 46°$

- argillaceous, nodular Waterways limestone displays a bi-modal stress strain response. The initial stress strain behavior is controlled by the claystone matrix and the secondary stress strain behavior is controlled by the interaction of the stiff, micritic nodules within the claystone matrix.

- Young's modulus for argillaceous Waterways limestone increases with increasing temperature and is dependent on the level of effective confining stress. For σ'_3 = 4.0 MPa, E at 20°C was approximately 4 GPa while at 220°C it was approximately 6 GPa.

- the non-linear Hoek-Brown failure criterion adequately describes the shear strength of argillaceous Waterways limestone for both 20°C and 220°C. A strength reduction of approximately 25% occurs over this temperature range.

Gas Evolution and Composition:

- the impact of non-condensable gases is greatest on the ceiling drainage rate and was found to be a complex function of the amount and composition of the gas, the permeability of the formation and time. In a high permeability sand (k_v> 1 d) , small amounts of gas greatly impede the rise rate of the steam chamber by preventing transport of steam to the advancing front. In a low permeability sand (k_v< 1 d), the presence of gas can actually improve drainage rates. Because steam transport is already restricted by the low permeability, a relatively thick zone of reservoir ahead of the front is heated by conduction to intermediate temperatures. This allows for the drainage of reasonably mobile oil (with respect to gas) before steam temperatures are achieved;

- two gas evolution tests and three gas composition tests were conducted on low fines, rich UTF McMurray Formation oil sands. An average combined solubility coefficient of 0.16 cm^3/cm^3 @ 101 kPa was determined from the gas evolution tests. The low in situ pore pressure within the Phase A reservoir has resulted in low dissolved volume of gas within the UTF McMurray Formation oil sands. An initial gas-oil ratio (GOR) of approximately 0.83 m^3/m^3 of pore liquid was also computed from the gas evolution tests.

- gas composition for the dissolved gases present at the UTF Phase A site were on average, 18% carbon dioxide, 79% methane, 1% ethane and 2% nitrogen.

Test Codes:

Material

OS	Oil Sand
US	Upper McMurray Shale
LS	Lower McMurray Shale
LT	Limestone

Test Type

DTE	Drained Thermal Expansion
UTE	Undrained Thermal Expansion
MTE	Mineral Thermal Expansion
THC	Thermal Conductivity
RPI	Room Temp. Pore Pressure Injection
RTR	Room Temp. Drained Triaxial
HTR	High Temp. Drained Triaxial
GSE	Gas Evolution
GSS	Gas Sampling
RUC	Room Temp. Unconfined Compression

EXAMPLE:

OS_DTE_1

Material Code Test Type Test Number

NOTE: All Room Temperature tests were conducted at 20 °C

All High Temperature tests were conducted at 220 °C

The following fluid density and specific gravity values were used in the calculation of specimen properties:

Gs for sand = 2.65
Gs for shale = 2.70
Gs for limestone = 2.75
Density of bitumen = 1.03 g/cm3
Density of water = 1.00 g/cm3

Table 4.1 Nomenclature for Thermomechanical Testing Codes

Specimen Initial Properties

Test Code	Hole Number	Geologic Unit (Elev. Interval)	%water (mass)	%bitumen (mass)	%solids (mass)	%fines (< .074 mm)	S_r (%)	Bulk Density (g/cm^3)	ϕ_c (%)	ϕ_i (%)	I_d (%)
OSDTE1	AGI4	D (284.3-284.1)	4.2	14.1	81.7	7.8	77.7	1.86	42.7	36.7	16.4
OSDTE2	AGI4	D (284.6-284.3)	3.0	13.1	83.9	17.3	85.6	2.00	36.7	33.2	10.5
OSUTE1	AGI4	D (284.6-284.3)	1.4	15.1	83.5	17.3	87.0	2.00	36.9	33.8	9.2
OSUTE2	AGI4	D (284.6-284.3)	1.4	15.1	83.5	17.3	87.4	2.00	36.8	33.8	8.9
OSTHC1	AGI1	E (280.4-280.2)	1.9	14.3	83.8	5.5	76.6	1.91	39.5	33.3	18.5
OSTHC2	AGI1	E (280.2-279.9)	1.9	14.6	83.5	4.6	79.2	1.93	39.3	33.8	16.0
OSRPI1	AGI1	E (278.3-278.1)	2.5	14.5	83.0	**	83.3	1.96	38.8	34.5	12.2
OSRPI2	AGI1	E (278.8-278.6)	2.8	13.9	83.3	**	86.8	1.99	37.4	34.1	9.5
OSRPI3	AGI1	E (278.4-278.3)	2.5	14.5	83.0	**	82.1	1.94	39.2	34.5	13.6
OSRPI4	AGI1	E (274.6-274.4)	1.6	16.4	82.0	**	83.4	1.92	40.5	36.2	11.9
OSRTR1	AGI1	E (274.9-274.7)	2.1	15.7	82.2	**	77.3	1.87	42.0	35.9	17.0
OSRTR2	AGI1	E (275.5-275.9)	1.8	16.7	81.5	**	84.3	1.92	41.0	36.9	11.0
OSRTR3	AGI4	E (280.5-280.3)	1.8	15.5	82.7	**	72.3	1.84	42.7	35.1	21.9
OSGAS1	AGI1	E (279.9-279.8)	1.3	14.6	84.1	2.0	80.9	1.96	37.6	32.9	14.7
OSGAS2	AGI4	G (272.2-271.9)	2.8	15.9	81.3	1.9	84.6	1.92	41.3	37.4	10.7
OSGSS1	AGI1	E (279.9-279.8)	1.5	15.1	83.4	1.9	82.4	1.92	38.3	34.3	13.2
OSGSS2	AGI1	E (279.8-279.6)	1.1	15.4	83.5	**	**	**	**	**	**
OSGSS3	AGI4	G (272.2-272.1)	1.1	15.8	83.1	1.9	78.4	1.92	40.0	34.4	16.6

Supplementary Index Tests on Oil Sands Specimens

Specimen Number											
OS1	AGI4	E (280.3-280.2)	2.0	15.4	82.6	**	87.8	1.98	38.2	35.2	8.6
OS2	AGI1	E (279.5-279.3)	3.3	13.8	82.9	**	83.9	1.96	38.8	34.8	11.8
OS3	AGI1	E (278.6-278.4)	2.3	14.1	83.6	**	82.3	1.96	38.1	33.6	13.3
OS4	AGI1	E (275.9-275.7)	2.5	14.2	83.3	**	81.4	1.94	39.0	34.2	13.9
OS5	AGI4	G (271.9-271.7)	2.6	16.5	80.9	**	77.9	1.84	43.9	37.8	15.9

Test Code	Specimen Number	Geologic Unit (Elev. Interval)	%water (mass)	%bitumen (mass)	%solids (mass)	Bulk Density (g/cm^3)	W (%)	ϕ_c (%)	ϕ_i (%)	W_P (%)	W_L (%)	I_P (%)
LSUTE1	GT-92	F (275.9-275.8)	6.7	2.0	91.3	2.29	5.5	22.6	20.1	15.4	24.5	9.1
LSTHC1	GT-93	F (275.8-275.6)	**	**	**	2.34	5.1	20.8	*	**	**	**
LSRTR1	GT-98	F (275.1-274.9)	4.8	6.0	89.2	2.07	5.8	31.6	24.0	**	**	**
LSRTR2	GT-22	F (271.5-271.4)	5.8	0.1	94.2	2.32	5.0	19.3	14.0	**	**	**
LSRTR3	GT-23	F (270.7-270.5)	6.4	0.7	92.9	2.27	10.0	21.9	16.8	**	**	**
LSHTR1	GT-100	F (273.7-273.6)	7.2	2.1	90.7	2.21	7.1	24.8	21.2	**	**	**
LSHTR2	GT-99	F (273.8-273.7)	7.4	3.8	88.8	2.21	2.7	26.8	24.9	**	**	**
LSHTR3	GT-91	F (276.1-275.9)	9.2	0.8	91.0	2.25	7.8	25.1	22.4	**	**	**

Table 4.2 Summary of Initial Specimen Data

Test Code	Specimen Number	Geologic Unit (Elev. Interval)	%water (mass)	%bitumen (mass)	%solids (mass)	Bulk Density (g/cm³)	W (%)	ϕ_r (%)	ϕ (%)	W_p (%)	W_l (%)	I_p (%)
USDTE1	GT-54	C (291.8-291.7)	8.3	2.0	89.7	2.24	3.8	25.6	23.4	20.3	30.8	10.5
USUTE1	GT-81	C (293.8-293.8)	4.6	5.4	90.0	2.28	6.8	23.9	22.6	19.8	33.0	13.2
USUTE2	GT-41	B (304.8-304.7)	11.0	0.6	88.4	2.10	9.0	31.1	25.9	* *	* *	* *
USTHC1	GT-80	C (295.1-294.9)	4.6	5.4	90.0	2.22	8.0	26.0	22.4	* *	* *	* *
USRTR1	GT-44	B (302.4-302.2)	7.5	1.2	91.3	2.15	6.3	26.5	20.1	* *	* *	* *
USRTR2	GT-89	D (287.5-287.4)	5.7	7.1	87.2	2.08	6.9	32.1	27.7	* *	* *	* *
USRTR3	GT-137	B (304.5-304.3)	11.2	0.3	88.5	2.09	12.7	31.1	25.6	15.3	38.0	22.7
USRTR4	GT-45	B (301.5-301.4)	7.1	2.9	90.0	2.05	9.1	31.0	22.6	* *	* *	* *
USHTR1	GT-47	B (300.0-299.9)	6.3	4.6	89.1	2.10	* *	30.3	24.3	* *	* *	* *
USHTR2	GT-97	D (284.0-283.9)	6.4	3.0	90.6	2.16	* *	26.9	21.4	* *	* *	* *
USHTR3	GT-43	B (302.7-302.6)	5.5	0.9	93.6	2.03	* *	28.9	15.3	* *	* *	* *
USHTR4	GT-49	B (298.4-298.2)	2.6	4.7	92.7	2.03	* *	29.7	17.0	* *	* *	* *
Shale Seam Sampling Program												
SS1	AGI3	B (304.8)	13.7	0.1	86.2		15.9		* *	16.8	40.2	23.4
SS2	AGI3	B (300.4-300.3)	8.8	2.0	89.2		9.9		* *	17.6	35.7	18.1
SS3	AGI3	B (299.7)	9.6	1.4	89.0		10.8		* *	18.3	34.5	16.2
SS4	AGI3	B (302.6-302.5)	10.5	1.5	88.0		11.9		* *	17.6	35.7	18.1
SS5	AGI3	B (301.4)	10.0	1.0	89.0		11.2		* *	17.3	38.6	21.3
SS6	AGI2	C (293.0-292.9)	8.6	1.4	90.0		9.5		* *	19.6	34.0	14.4
SS7	AGI2	C (292.9-292.8)	8.1	3.5	88.4		9.2		* *	20.3	30.8	10.5
SS8	AGI2	C (293.1-293.0)	8.1	1.1	90.8		8.9		* *	19.6	34.3	14.7
SS9	AGI2	F (273.1)	5.8	1.7	92.5		6.2		* *	15.4	24.5	9.1

Test Code	Specimen Number	Geologic Unit (Elev. Interval)	w (%)	Bulk Density (g/cm³)	ϕ (%)
LTDTE1	GT-6	H (265.2-265.1)	2.0	2.66	5.1
LTDTE2	GT-6	H (265.1-265.0)	2.0	2.62	6.7
LTUTE1	GT-101	H (269.2-269.1)	2.0	2.39	13.2
LTTHC1	GT-29	H (263.4-263.1)	0.7	2.57	7.4
LTTHC2	GT-5	H (265.8-265.6)	1.9	2.67	4.6
LTTHC3	GT-11	H (261.0-260.8)	0.5	2.64	2.7
LTRUC1	GT-94	H (268.6-268.2)	5.4	2.67	6.2
LTRUC2	GT-32	H (260.1-259.9)	0.7	2.63	3.3
LTRUC3	GT-31	H (261.0-260.7)	0.7	2.65	2.6
LTRTR1	GT-8	H (262.8-262.6)	1.6	2.56	6.7
LTRTR2	GT-13	H (258.1-258.0)	1.9	2.63	4.4
LTRTR3	GT-15	H (256.0-255.8)	2.4	2.66	3.8
LTRTR4	GT-25	H (268.5-268.3)	1.3	2.63	3.9
LTRTR5	GT-68	H (256.8-256.5)	0.3	2.69	0.8
LTHTR1	GT-9	H (262.1-261.9)	1.3	2.59	5.2
LTHTR2	GT-1	H (269.1-268.7)	2.0	2.62	4.8
LTHTR3	GT-25	H (268.5-268.6)	1.3	2.62	4.3
LTHTR5	GT-19	H (251.4-251.2)	0.3	2.60	4.0
LTHTR6	GT-65	H (261.9-261.7)	0.4	2.61	3.7

Table 4.2 Summary of Initial Specimen Data (continued)

Test Code	% Water	% Bitumen	% solids	% fines (<74 µm)	γ_b	I_d
OSDTE1	4.2	14.1	81.7	7.8	1.86	16.4
OSDTE2	3.0	13.1	83.9	17.3	2.00	10.5
UFCOS1 (Kosar, 1989)	9.4	4.3	86.3	47.5	2.00	18.0
UFCOS3 (Kosar, 1989)	9.4	4.3	86.3	47.5	1.91	27.9
UFCOS4 (Kosar, 1989)	6.9	4.9	88.2	44.8	2.00	27.8
UFCOS5 (Kosar, 1989)	5.3	8.3	86.4	51.8	2.03	15.4

Table 4.3 Comparison of Index Properties for Oil Sands Thermal Expansion Tests

Initial Conditions

Test Code	ρ_t (g/cm^3)	ρ_d (g/cm^3)	% water (mass)	% bitumen (mass)	% solids (mass)	Porosity (%)	S_f (%)	I_d (%)
OSRTR1	1.87	1.54	2.1	15.7	82.2	42.0	77	17.0
OSRTR2	1.92	1.56	1.8	16.7	81.5	41.0	84	11.0
OSRTR3	1.84	1.52	1.8	15.5	82.7	42.7	72	21.9

Isotropic Consolidation

Test Code	Volume Change (%) from σ' = 0.5 MPa to (*) MPa	ρ_t (g/cm^3)	ρ_t (g/cm^3)	Porosity (%)	I_d (%)
OSRTR1	-1.5 (3.0)	1.98	1.56	41.1	14.4
OSRTR2	-3.7 (1.0)	2.02	1.62	38.7	5.0
OSRTR3	-	-	-	-	-

Drained Shear Test

Test Code	σ'_3 (MPa)	Back Pressure (MPa)	B	$(\sigma_1 - \sigma_3)$ at failure (MPa)	ε_a at failure (%)	ε_v at failure (%)	Modulus of Elasticity (MPa)	
							ε_a= .1%	ε_a= .25%
OSRTR1	3.0	3.0	-	10.8	2.2	.13	1400	1012
OSRTR2	1.0	3.0	.96	6.2	3.1	2.8	131	97
OSRTR3	4.0	3.0	.90	15.0	5.9	-2.3	1114	857

Table 4.4 Summary for Consolidated Drained Triaxial Compression Tests - Oil Sands

Table 4.1 Specimen Initial Conditions

Specimen Number	Well Number	Geologic Unit (Depth, m)	Water (%)**	Bitumen (%)**	Solids (%)**	Saturation Ratio (%)	Dry Density (g/cm^3)	Bulk Density (g/cm^3)	Porosity (%)	In-situ Porosity (%)	Disturb. Index (%)	In-situ Water Porosity (%)
S1	AGI4	E (153.4-153.7)	1.1	15.1	83.8	78.8	1.62	1.94	38.8	33.3	16.4	2.3
S2	AGI4	E (153.2-153.4)	1.0	15.2	83.8	76.9	1.61	1.92	39.3	33.0	18.3	2.1
S3	AGI4	E (152.1-153.0)	1.4	14.7	83.9	93.1	1.73	2.06	34.7	33.1	4.8	2.9
S4	AGI4	E (152.1-153.0)	1.4	14.7	83.9	82.1	1.65	1.97	37.6	33.1	13.6	2.9
S5	AGI4	E (152.1-153.0)	1.4	14.7	83.9	83.5	1.67	1.98	37.2	33.1	12.4	2.9
S6	AGI1*	E (152.4-152.8)	1.3	15.2	83.5	87.3	1.67	2.00	36.8	33.7	9.2	2.7
S7	AT3	D (149.4-149.6)	2.3	14.6	83.1	86.0	1.64	1.98	38.0	34.5	10.1	4.9
S8	AT3	D (149.4-149.6)	2.3	14.6	83.1	85.5	1.64	1.98	38.1	34.5	10.5	4.9
S9	AGI4	E (155.2-155.3)	2.3	15.0	82.7	90.0	1.66	2.00	37.5	35.0	6.9	4.8
S10	AGI4	D (149.0-149.2)	1.7	14.9	83.4	89.2	1.68	2.02	36.5	33.9	7.7	3.6
S11	AT3	D (149.0-149.2)	1.9	14.6	83.5	82.1	1.63	1.96	38.3	33.4	13.5	4.0
S12	AT3	D (148.6-148.8)	2.7	14.6	82.8	84.7	1.62	1.96	38.8	35.0	11.0	5.5
S13	AT3	D (148.4-149.6)	3.5	11.7	84.9	81.2	1.69	1.99	36.3	31.4	15.6	7.4
S14	AT3	D (147.5-147.7)	2.0	13.8	84.2	83.9	1.68	1.99	36.7	32.7	12.2	4.2
S15	AT3	D (147.5-147.7)	2.0	13.8	84.2	87.3	1.70	2.02	35.7	32.7	9.3	4.2
S16	AT3	D (147.2-147.4)	1.4	14.5	84.1	83.1	1.67	1.99	37.0	32.8	12.8	2.9
S17	AT3	D (147.2-147.4)	1.4	14.5	84.1	85.1	1.67	2.00	36.4	32.8	11.1	2.9
S18	AT3	D (147.2-147.4)	1.4	14.5	84.1	85.8	1.69	2.01	36.2	32.8	10.5	3.0
S19	AT3	D (147.0-147.1)	2.9	13.9	83.3	86.4	1.66	1.99	37.5	34.2	9.8	6.0
S20	AT3	D (147.1-147.3)	2.3	13.4	84.3	83.1	1.68	1.99	36.7	32.5	12.9	4.9
S21	AT3	D (146.6-151.1)	1.7	14.5	83.8	87.7	1.69	2.02	36.2	33.3	8.9	3.6
S22	AT3	D (150.9-151.1)	2.0	14.5	83.5	84.7	1.65	1.98	37.6	33.8	11.2	4.1
S23	AT3	D (150.8-150.9)	1.5	14.4	84.1	82.6	1.67	1.98	37.1	32.8	13.3	3.3

* core ø 10.2 cm, in thin plastic liner

** content by mass

Table 4.5 Specimen Properties from Experimental Program of Oldakowski (1994)

Initial Conditions

Test Code	ρ_t (g/cm^3)	ρ_d (g/cm^3)	% water (mass)	% bitumen (mass)	% solids (mass)	Porosity (%)	S_f (%)
USRTR1	2.15	1.96	7.5	1.2	91.3	26.5	70
USRTR2	2.08	1.81	5.7	7.1	87.2	32.1	82
USRTR3	2.09	1.85	11.2	0.3	88.5	31.1	77
USRTR4	2.05	1.84	7.1	2.9	90.0	31.0	66
USHTR1	2.10	1.87	6.3	4.6	89.1	30.3	74
USHTR2	2.16	1.96	6.4	3.0	90.6	26.9	75
USHTR3	2.03	1.90	5.5	0.9	93.6	28.9	45
USHTR4	2.03	1.89	2.6	4.7	92.7	29.7	49

Isotropic Consolidation

Test Code	Volume Change (%) from σ' = 0.5 MPa to (*) MPa	ρ_t (g/cm^3)	ρ_t (g/cm^3)	Porosity (%)
USRTR1	0.0 (0.5)	2.23	1.96	26.5
USRTR2	-0.8 (1.0)	2.15	1.83	31.5
USRTR3	-0.1 (2.0)	2.16	1.85	31.0
USRTR4	-2.6 (4.0)	2.18	1.89	29.1
USHTR1	0.0 (0.5)	2.17	1.87	30.3
USHTR2	-	-	-	-
USHTR3	-1.2 (2.0)	2.20	1.92	28.1
USHTR4	-2.5 (4.0)	2.22	1.93	27.9

Drained Shear Test

Test Code	σ'_3 (MPa)	Back Pressure (MPa)	B	$(\sigma_1 - \sigma_3)$ at failure (MPa)	ε_a at failure (%)	ε_v at failure (%)	Modulus of Elasticity (MPa)	ν
USRTR1	0.5	3.0	1.0	2.5	3.6	-1.3	70	0.25
USRTR2	1.0	3.0	0.92	3.9	2.8	-.62	148	0.18
USRTR3	2.0	3.0	0.97	5.9	2.9	-.91	71	0.27
USRTR4	4.0	3.0	1.0	9.5	2.8	-1.0	89	0.23
USHTR1	0.5	3.0	1.0	1.8	3.9	-1.4	67	0.0
USHTR2	1.0	3.0	0.98	6.5	2.6	-1.6	328	0.11
USHTR3	2.0	3.0	1.0	5.7	2.3	-0.5	491	.44
USHTR4	4.0	3.0	1.0	6.6	2.2	-0.7	470	.37

Table 4.6 Summary of Consolidated Drained Triaxial Compressions Tests - Upper Shale

Initial Conditions

Test Code	ρ_t (g/cm^3)	ρ_d (g/cm^3)	% water (mass)	% bitumen (mass)	% solids (mass)	Porosity (%)	S_f (%)
LSRTR1	2.07	1.85	4.8	6.0	89.2	31.6	70
LSRTR2	2.32	2.18	5.8	0.1	94.2	19.3	70
LSRTR3	2.27	2.11	6.4	0.7	92.9	21.9	73
LSHTR1	2.21	2.01	7.2	2.1	90.7	24.8	83
LSHTR2	2.21	1.96	7.4	3.8	88.8	26.8	92
LSHTR3	2.25	2.02	9.2	0.8	90.0	25.1	89

Isotropic Consolidation

Test Code	Volume Change (%) from σ' = 0.5 MPa to (*) MPa	ρ_t (g/cm^3)	ρ_t (g/cm^3)	Porosity (%)
LSRTR1	1.6 (0.5)	2.16	1.85	31.6
LSRTR2	-0.8 (1.0)	2.39	2.20	18.6
LSRTR3	-	-	-	-
LSHTR1	0.0 (0.5)	2.21	2.01	24.8
LSHTR2	-1.0 (1.0)	2.25	1.98	26.0
LSHTR3	-1.4 (2.0)	2.29	2.05	24.0

Drained Shear Test

Test Code	σ'_3 (MPa)	Back Pressure (MPa)	B	$(\sigma_1 - \sigma_3)$ at failure (MPa)	ε_a at failure (%)	ε_v at failure (%)	Modulus of Elasticity (MPa)	ν
LSRTR1	0.5	3.0	.90	1.5	3.2	0.29	180	0.43
LSRTR2	1.0	3.0	.90	5.3	2.5	-1.1	280	0.16
LSRTR3	2.0	3.0	.85	13.0	1.6	-.47	972	-
LSHTR1	0.5	3.0	.94	4.6	3.0	-1.5	189	0.20
LSHTR2	1.0	3.0	1.0	9.4	1.9	-.03	629	0.42
LSHTR3	2.0	3.0	1.0	7.7	0.9	.08	1364	0.24

Table 4.7 Summary of Consolidated Drained Triaxial Compressions Tests - Lower Shale

Initial Conditions

Test Code	ρ_t (g/cm^3)	ρ_d (g/cm^3)	w (%)	Porosity (%)
LTRUC1	2.67	2.58	5.4	6.2
LTRUC2	2.63	2.62	0.7	3.3
LTRUC3	2.65	2.64	0.7	2.6

Unconfined Compression Test

Test Code	Axial stress σ_a at failure (MPa)	ε_a at failure (%)	Modulus of Elasticity at σ_a = 50% of ultimate strength (MPa)
LTRUC1	24.8	1.2	3350
LTRUC2	34.5	0.7	6670
LTRUC3	≈ 74.0*	≈ 2.8*	

* calculated from 1st loading increment

Table 4.8 Summary of Unconfined Compression Tests - Limestone

Initial Conditions

Test Code	ρ_t (g/cm^3)	ρ_d (g/cm^3)	w (%)	Porosity (%)
LTRTR1	2.56	2.56	1.3	5.2
LTRTR2	2.63	2.57	2.0	4.8
LTRTR3	2.66	2.59	1.3	4.3
LTRTR4	2.63	2.59	0.3	4.0
LTRTR5	2.69	2.60	0.4	3.7
LTHTR1	2.59	2.52	1.6	6.7
LTHTR2	2.62	2.58	1.9	4.4
LTHTR3	2.62	2.60	2.4	3.8
LTHTR4	2.60	2.60	1.3	3.9
LTHTR5	2.61	2.68	0.3	0.8

Drained Shear Test

Test Code	σ'_3 (MPa)	Back Pressure (MPa)	$(\sigma_1 - \sigma_3)$ at failure (MPa)	ε_a at failure (%)	ε_v at failure (%)	Modulus of Elasticity (MPa)	ν
LTRTR1	1.0	5.0	33	2.2	-.20	1750	.35
LTRTR2	2.0	5.0	79	1.6	-.20	5000	-.14
LTRTR3	4.0	5.0	69	1.8	-.10	4800	.28
LTRTR4	8.0	5.0	73	1.2	-.55	4860	.26
LTRTR5	8.0	5.0	80	1.4	-.13	6100	.40
LTHTR1	1.0	5.0	27	1.2	5.0	2703	-
LTHTR2	2.0	5.0	45	1.8	.85	5087	-
LTHTR3	4.0	5.0	48	1.5	.41	8538	-
LTHTR4	8.0	5.0	no peak reached	-	-	8578	-
LTHTR5	4.0	5.0	35	1.7	.12	4678	-

Table 4.9 Summary of Consolidated Drained Triaxial Compression Tests - Limestone

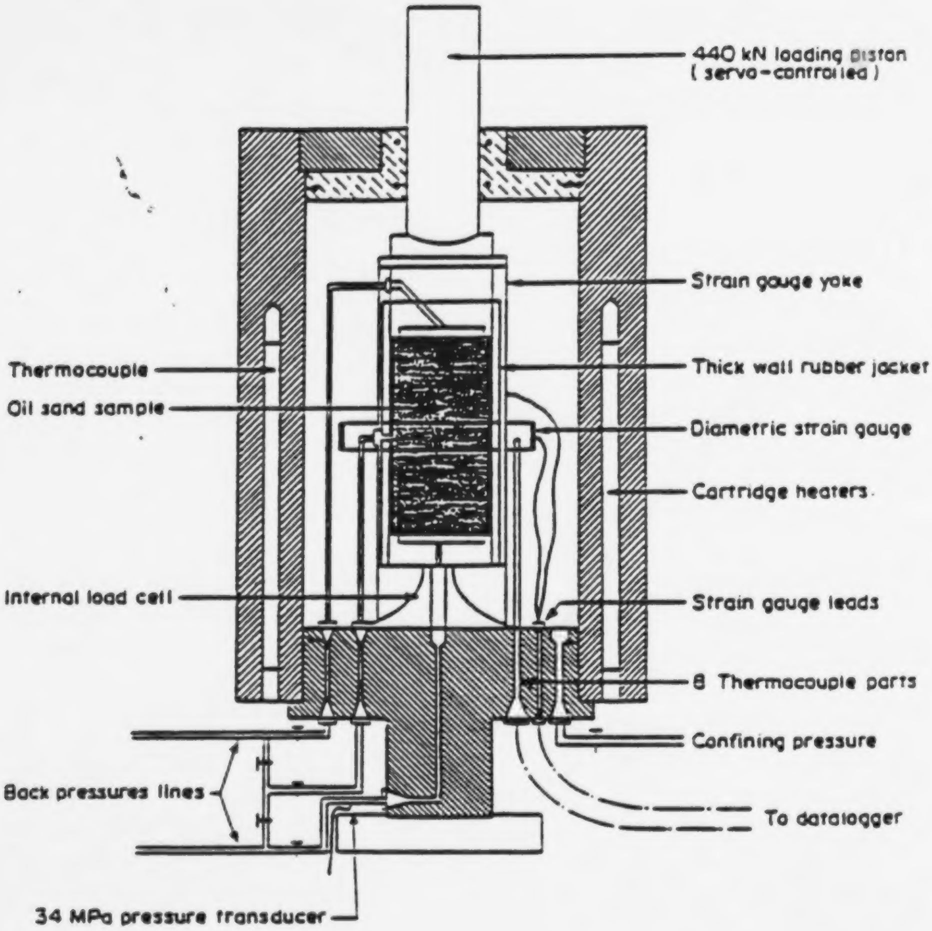
440 kN loading piston
(servo-controlled)
Strain gauge yoke
Thermocouple
Thick wall rubber jacket
Oil sand sample
Diametric strain gauge
Cartridge heaters.
Internal load cell
Strain gauge leads
8 Thermocouple parts
Confining pressure
Back pressures lines
To datalogger
34 MPa pressure transducer

Figure 4.1 Schematic of High Temperature Triaxial Cell

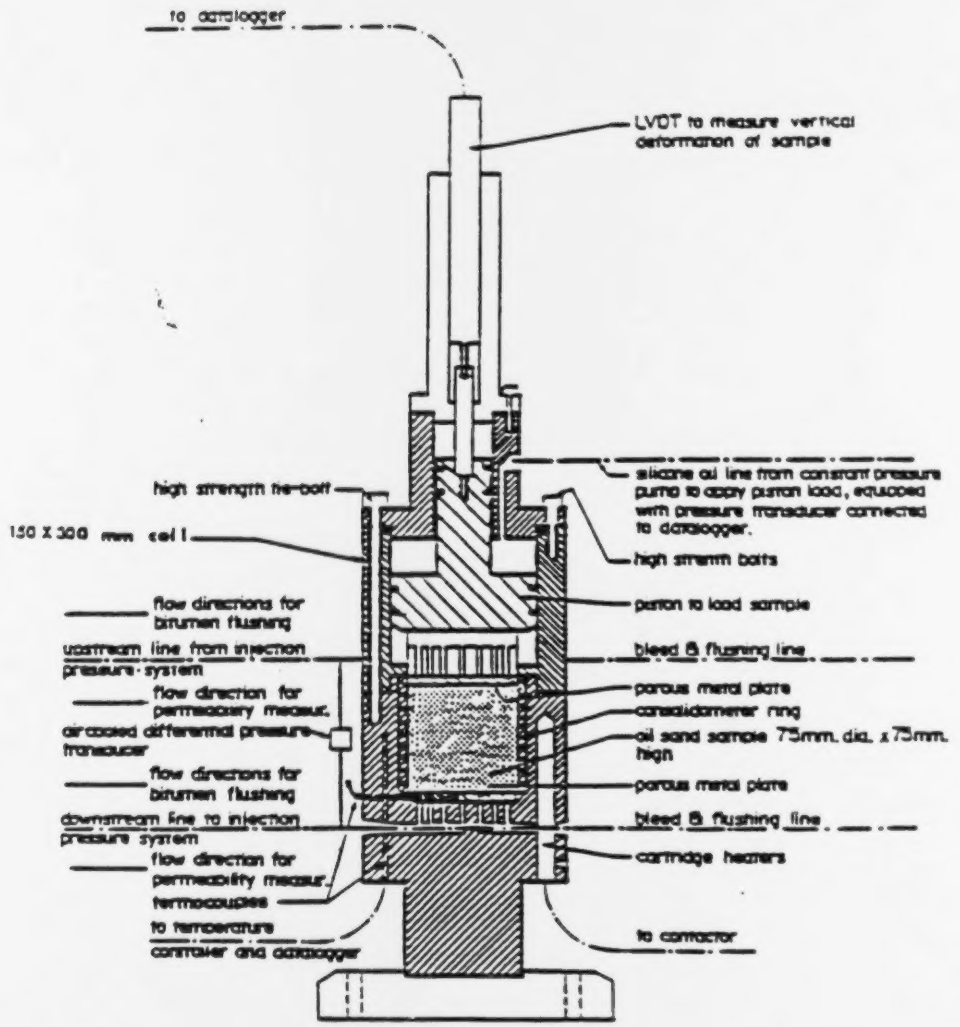
to datalogger
LVDT to measure vertical deformation of sample
silicone oil line from constant pressure pump to apply piston load, equipped with pressure transducer connected to datalogger.
high strength tie-bolt
150 X 300 mm cell
high strength bolts
flow directions for bitumen flushing
piston to load sample
upstream line from injection pressure system
bleed & flushing line
flow direction for permeability measur.
porous metal plate
consolidometer ring
air cooled differential pressure transducer
oil sand sample 75mm. dia. x 75mm. high
flow directions for bitumen flushing
porous metal plate
downstream line to injection pressure system
bleed & flushing line
flow direction for permeability measur.
cartridge heaters
termocouples
to temperature controller and datalogger
to contactor

Figure 4.2 Schematic of High Temperature Oedometer Cell

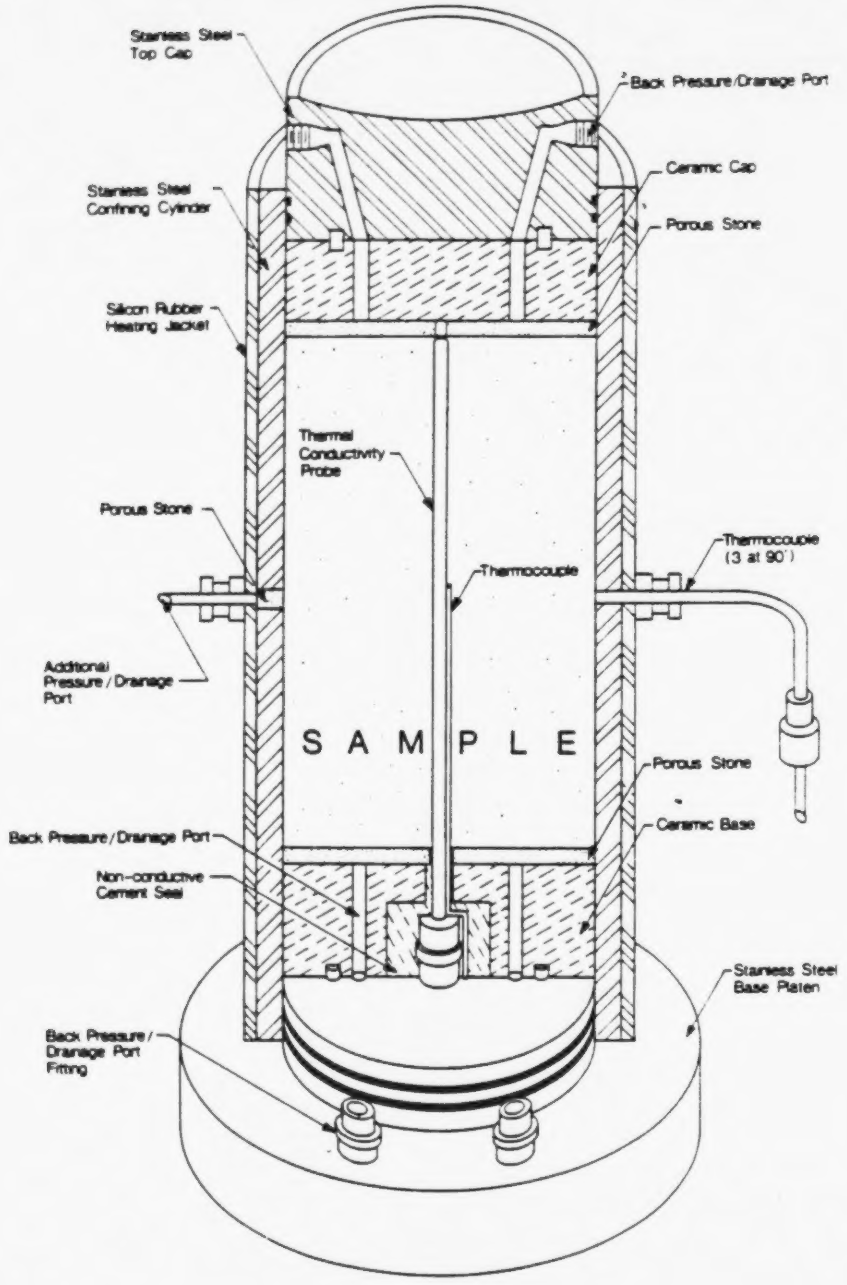
Stainless Steel Top Cap
Back Pressure/Drainage Port
Stainless Steel Confining Cylinder
Ceramic Cap
Porous Stone
Silicon Rubber Heating Jacket
Thermal Conductivity Probe
Porous Stone
Thermocouple (3 at 90°)
Thermocouple
Additional Pressure / Drainage Port
SAMPLE
Porous Stone
Ceramic Base
Back Pressure/Drainage Port
Non-conductive Cement Seal
Stainless Steel Base Platen
Back Pressure / Drainage Port Fitting

Figure 4.3 Schematic of Transient State Thermal Conductivity Test Cell

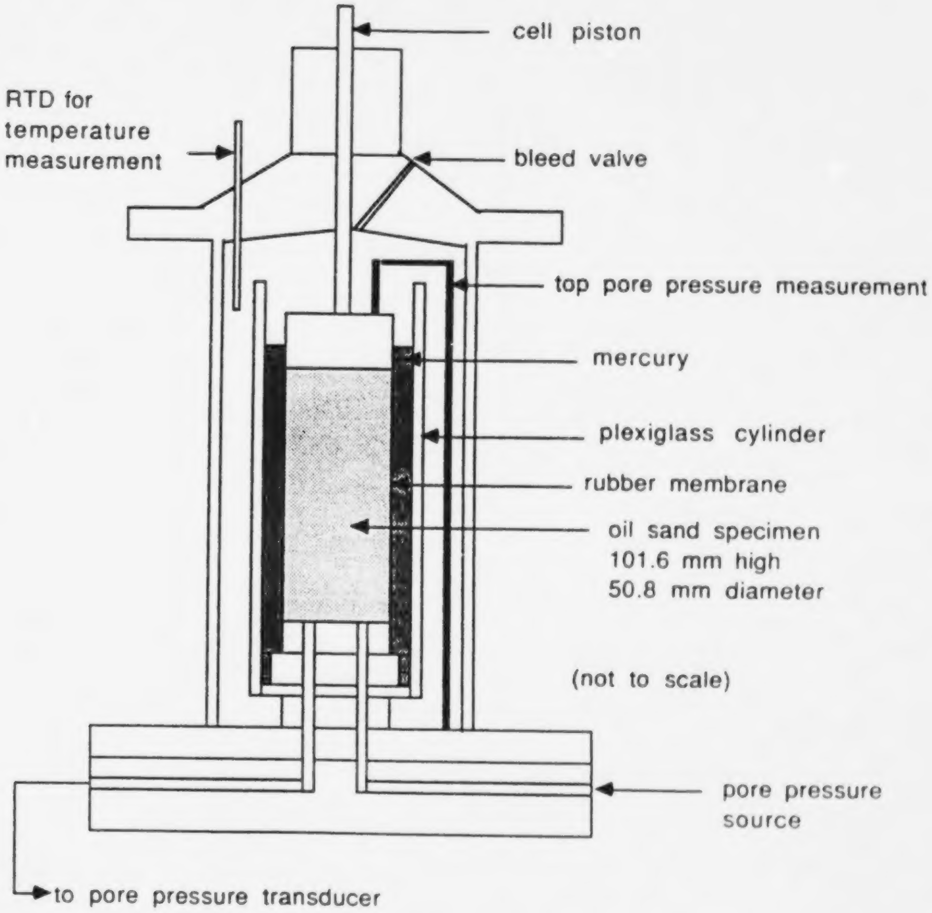
cell piston
RTD for temperature measurement
bleed valve
top pore pressure measurement
mercury
plexiglass cylinder
rubber membrane
oil sand specimen 101.6 mm high 50.8 mm diameter
(not to scale)
pore pressure source
to pore pressure transducer

Figure 4.4 Schematic of Gas Evolution Mercury Triaxial Cell

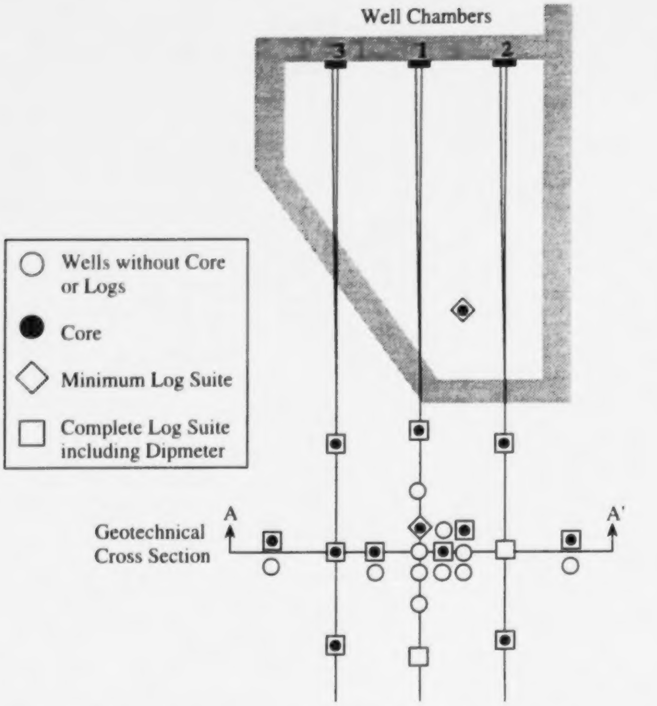
Well Chambers
3
1
2
○ Wells without Core or Logs
● Core
◇ Minimum Log Suite
□ Complete Log Suite including Dipmeter
A
A'
Geotechnical Cross Section

Figure 4.5 Plan View of Wells Used for Geotechnical Sampling

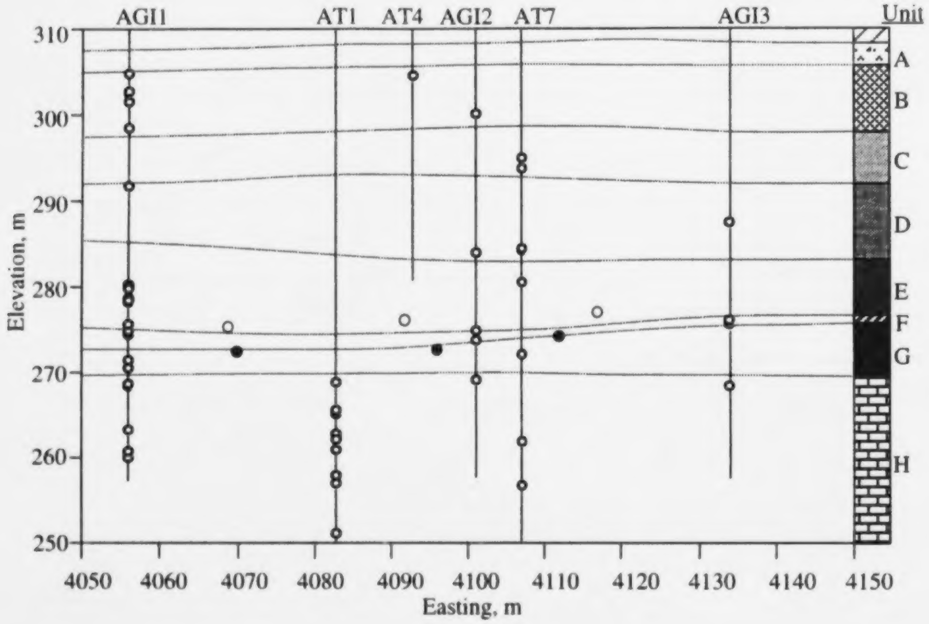

Figure 4.6 Relative Position of Test Specimens within Phase A Reservoir

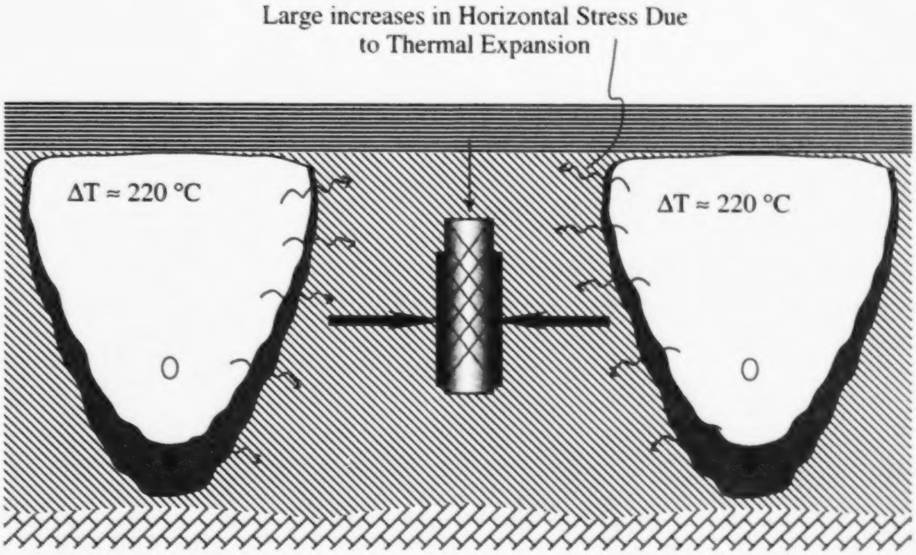
Large increases in Horizontal Stress Due
to Thermal Expansion
ΔT ≈ 220 °C
ΔT ≈ 220 °C
O
O

Figure 4.7 Role of Thermal Expansion Processes during SAGD

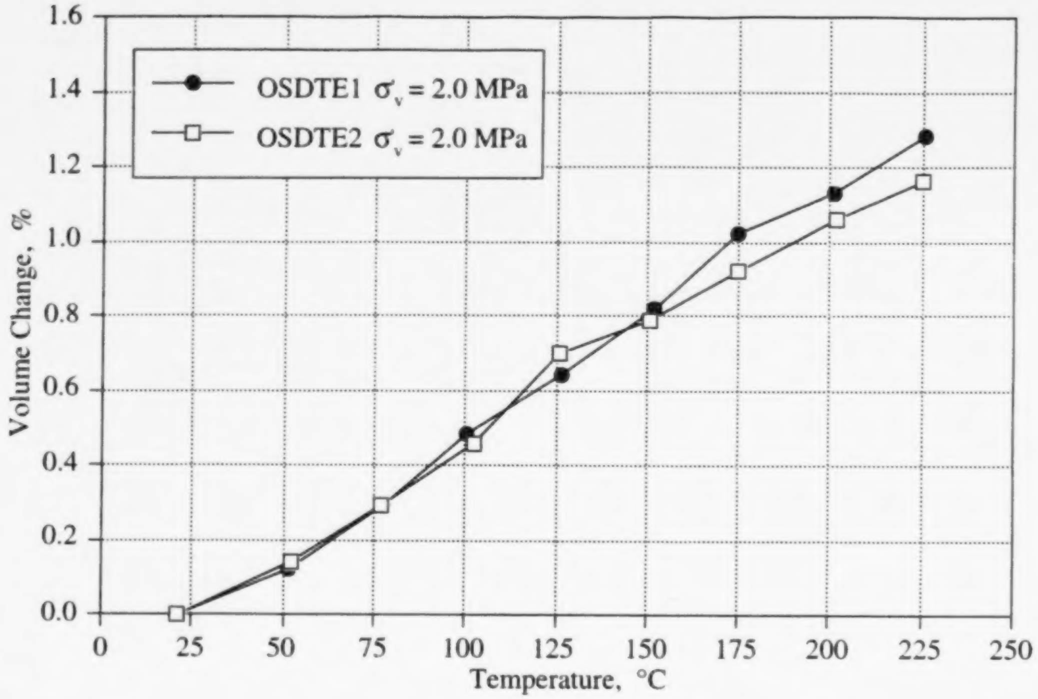

Figure 4.8 Constrained Bulk Thermal Expansion of McMurray Formation Oil Sands

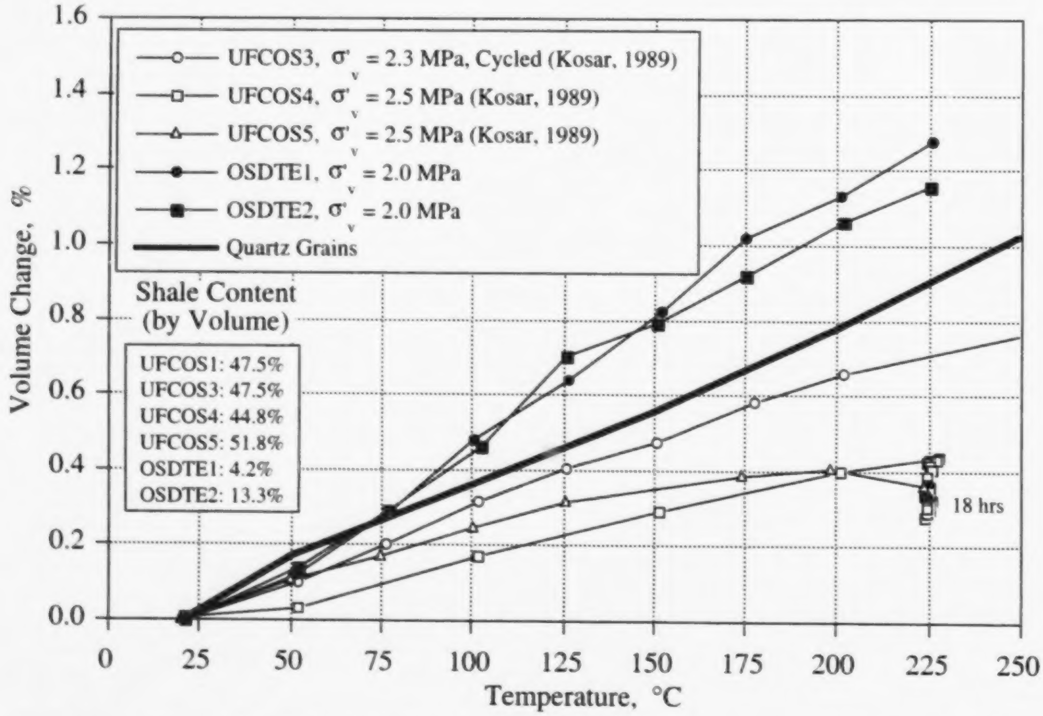

Figure 4.9 Comparison of OSDTE1 and OSDTE2 Thermal Expansion to Kosar (1989) Results

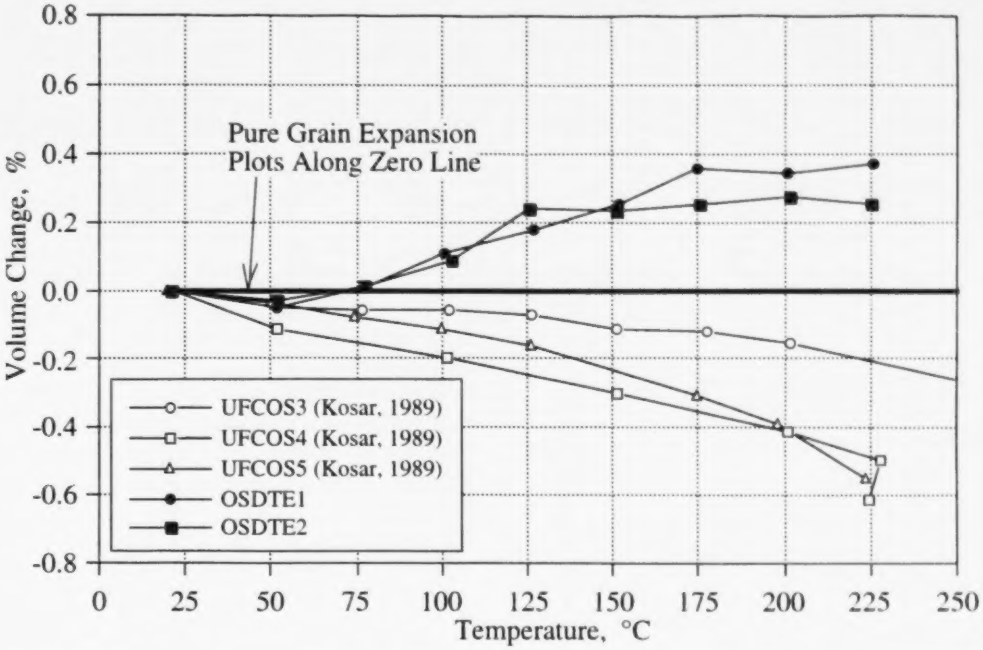

Figure 4.10 Structural Response of McMurray Formation Oil Sands during Constrained Thermal Expansion

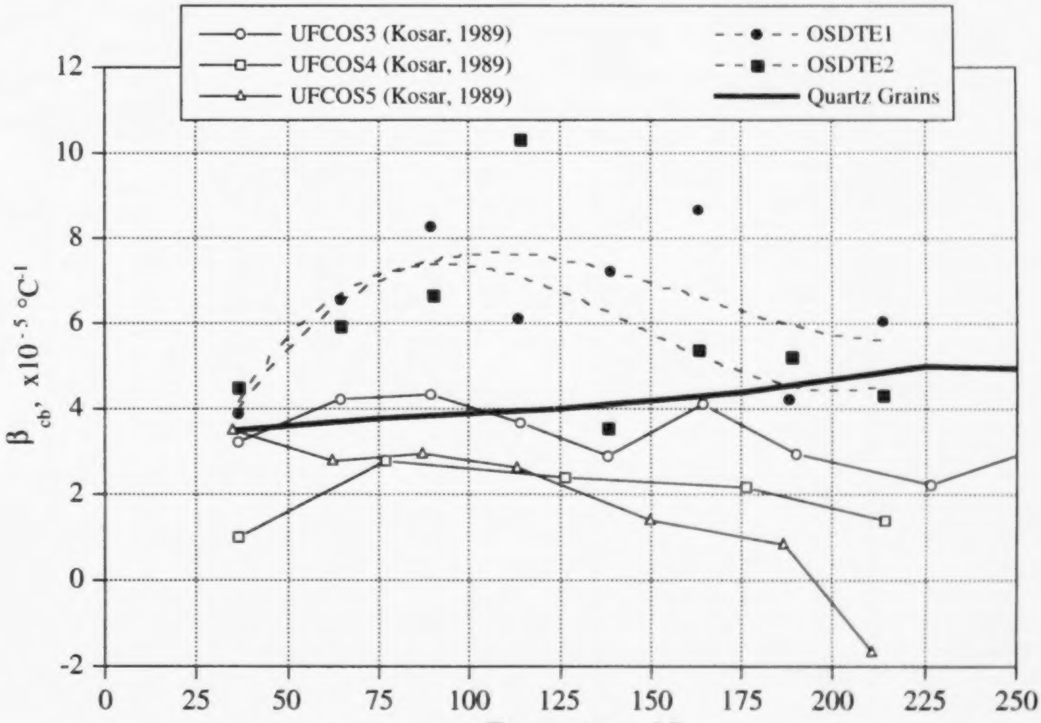

Figure 4.11 Coefficient of Constrained Bulk Thermal Expansion for McMurray Formation Oil Sands

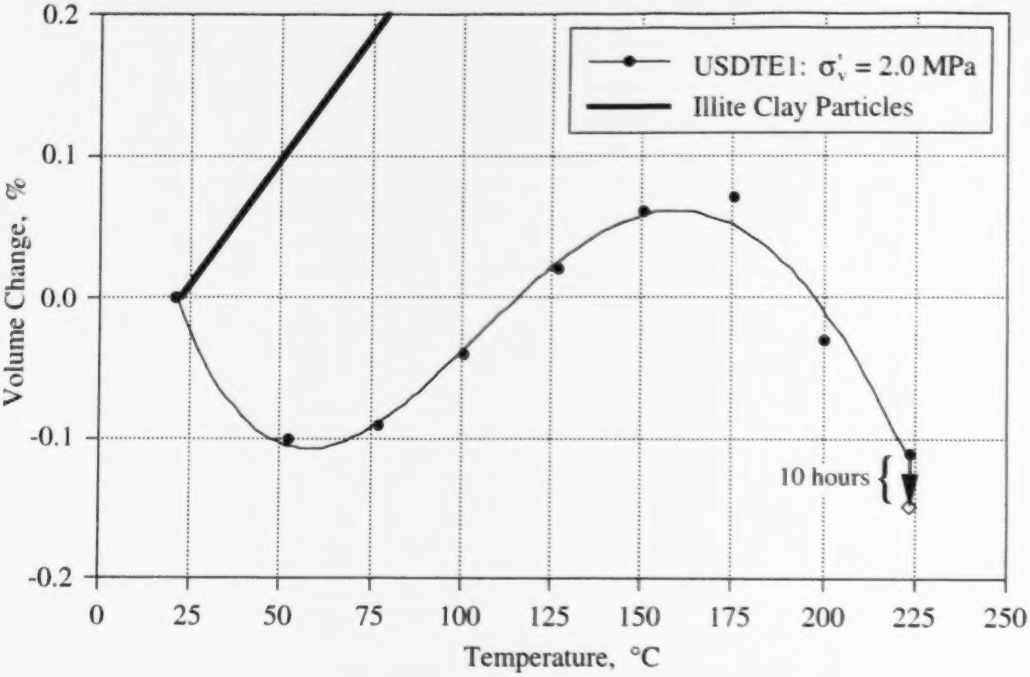

Figure 4.12 Constrained Bulk Thermal Expansion of Upper McMurray Formation Shale

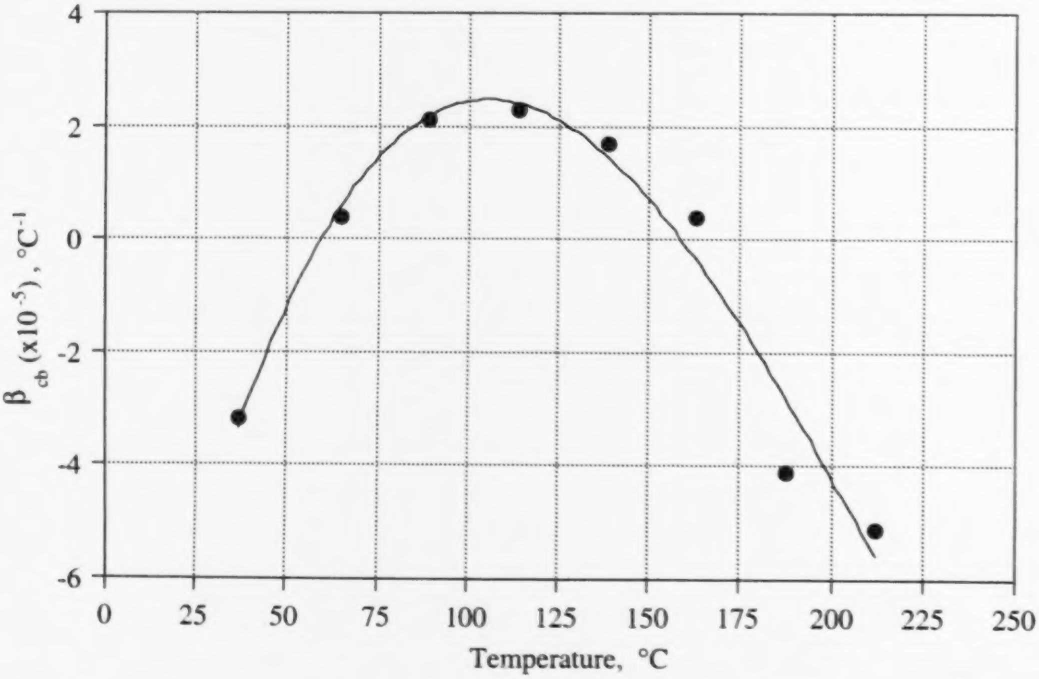

Figure 4.13 Coefficient of Constrained Bulk Thermal Expansion for Upper McMurray Formation Shale

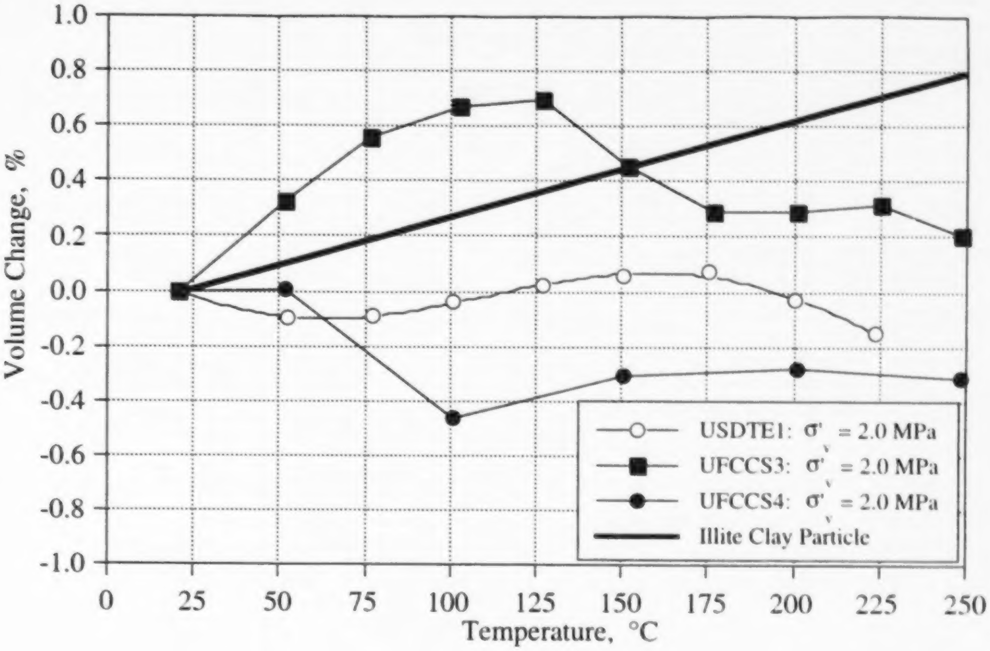

Figure 4.14 Comparison of Upper McMurray Formation Shale and Clearwater Formation Shale Thermal Expansion Behavior

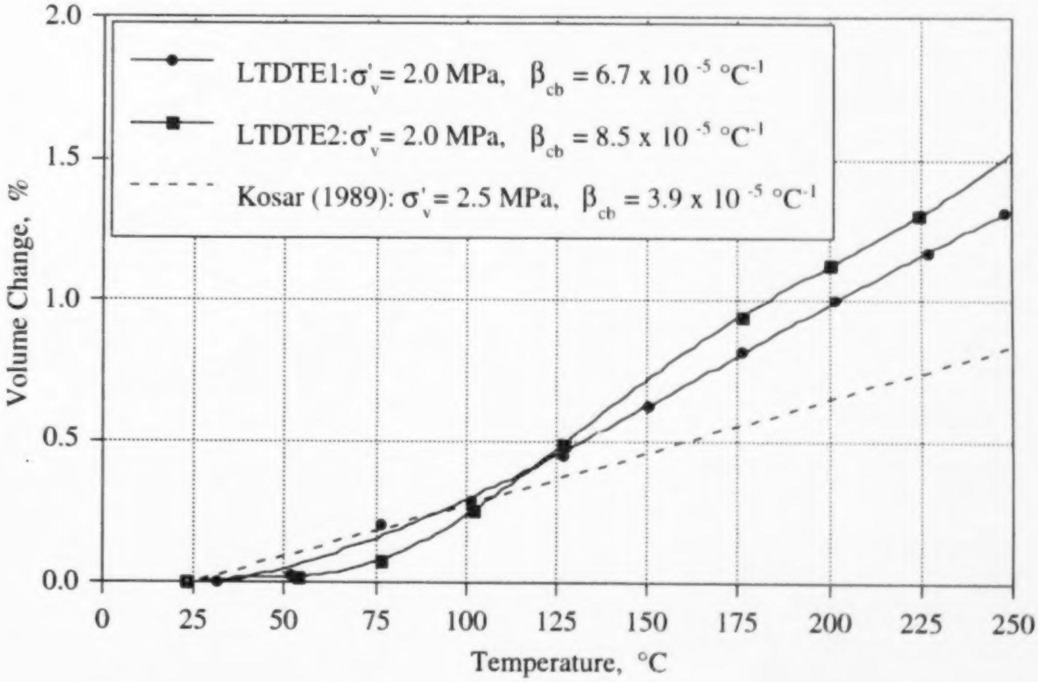

Figure 4.15 Constrained Bulk Thermal Expansion of Limestone

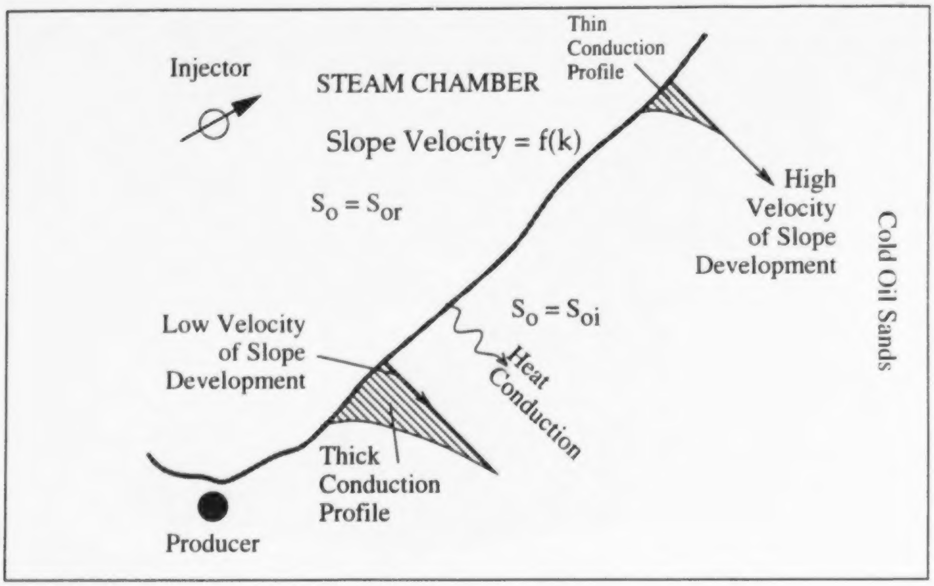
Injector
STEAM CHAMBER
Thin Conduction Profile
Slope Velocity = f(k)
High Velocity of Slope Development
$S_o = S_{or}$
Cold Oil Sands
$S_o = S_{oi}$
Low Velocity of Slope Development
Heat Conduction
Thick Conduction Profile
Producer

a) Slope Drainage Component of SAGD

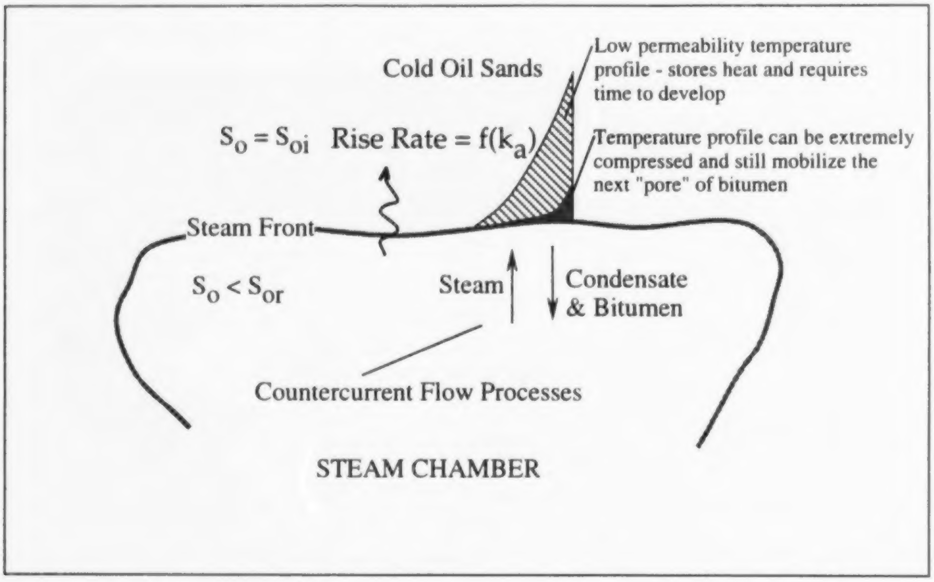
Cold Oil Sands
Low permeability temperature profile - stores heat and requires time to develop
$S_o = S_{oi}$
Rise Rate = $f(k_a)$
Temperature profile can be extremely compressed and still mobilize the next "pore" of bitumen
Steam Front
$S_o < S_{or}$
Steam
Condensate & Bitumen
Countercurrent Flow Processes
STEAM CHAMBER

b) Ceiling Drainage Component of SAGD

Figure 4.16 Process of Heat Conduction for Two Primary Flow Mechanisms of SAGD (modified from Edmunds, 1992)

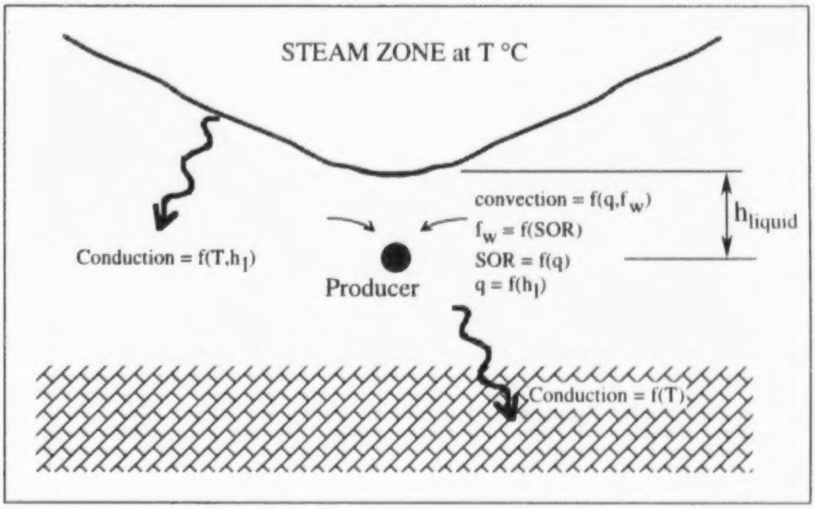
STEAM ZONE at T °C
Conduction = f(T,h_l)
Producer
convection = f(q,f_w)
f_w = f(SOR)
SOR = f(q)
q = f(h_l)
h_liquid
Conduction = f(T)

Figure 4.17 Impact of Heat Conduction on Temperature of Produced Fluids (modified from Edmunds, 1992)

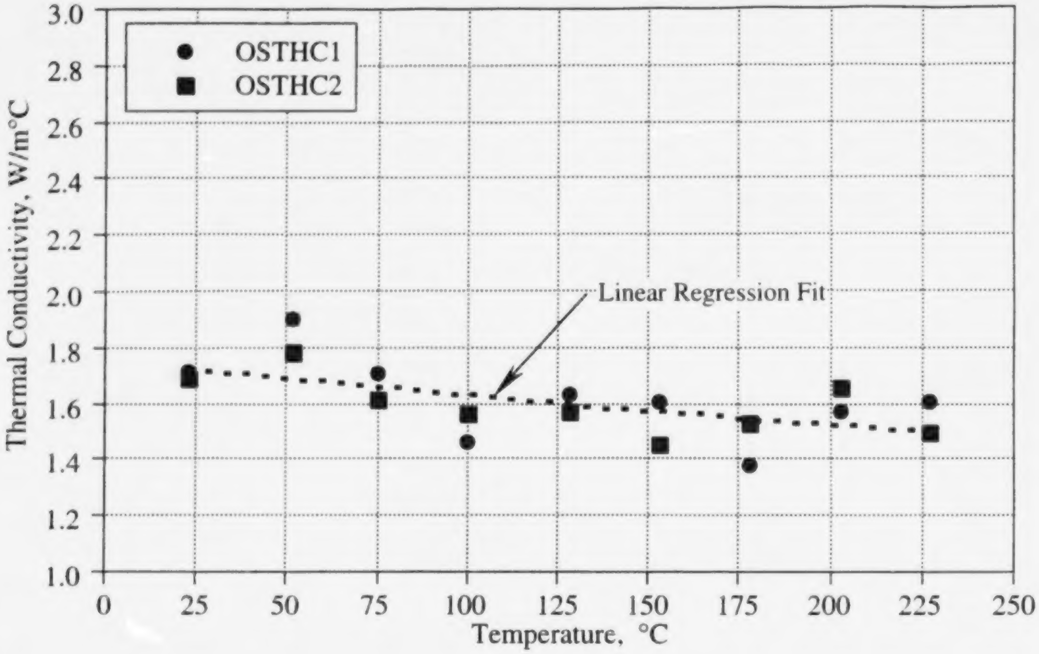

Figure 4.18 Thermal Conductivity of McMurray Formation Oil Sands

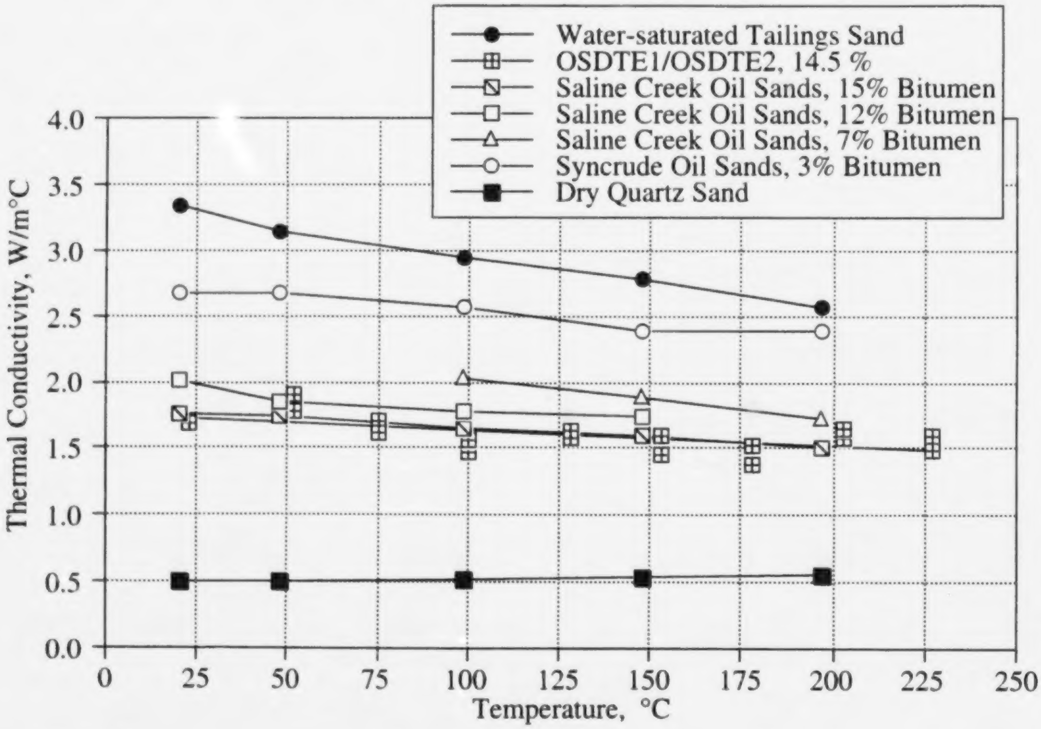

Figure 4.19 Comparison of Thermal Conductivities for Oil Sands

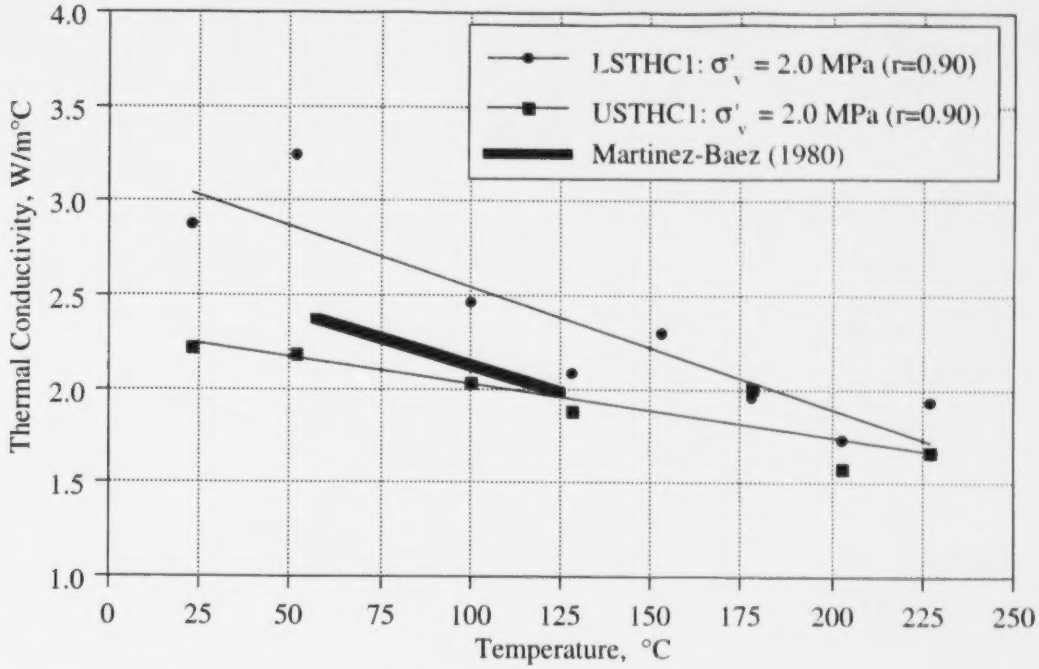

Figure 4.20 Thermal Conductivity of Lower and Upper McMurray Formation Shale

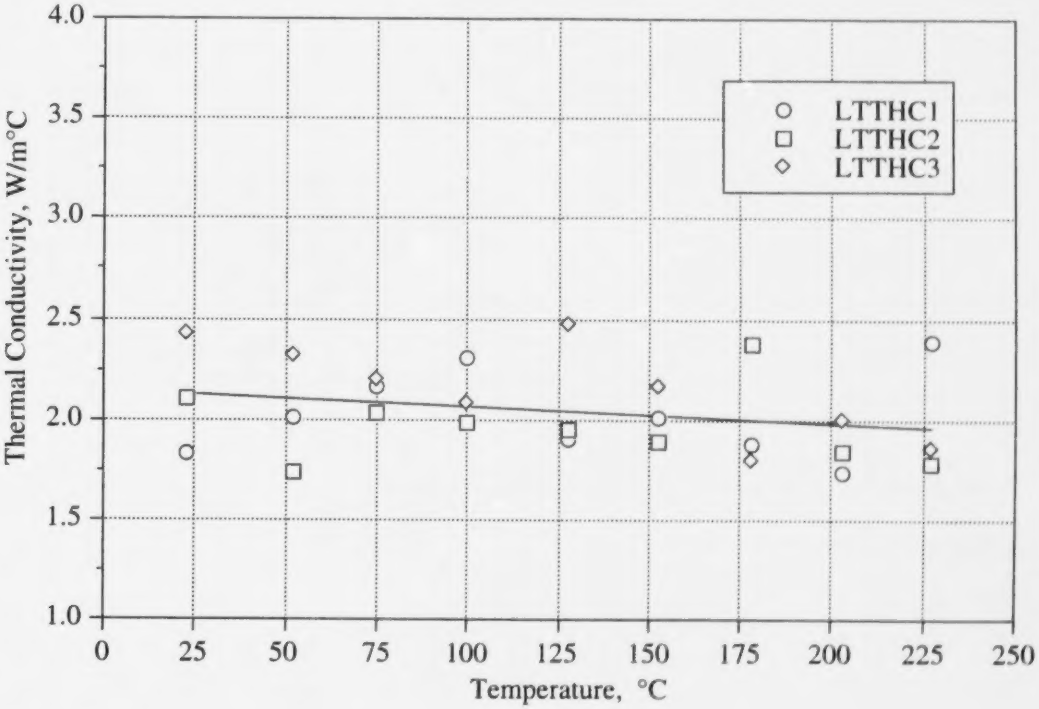

Figure 4.21 Thermal Conductivity of Waterways Formation Limestone

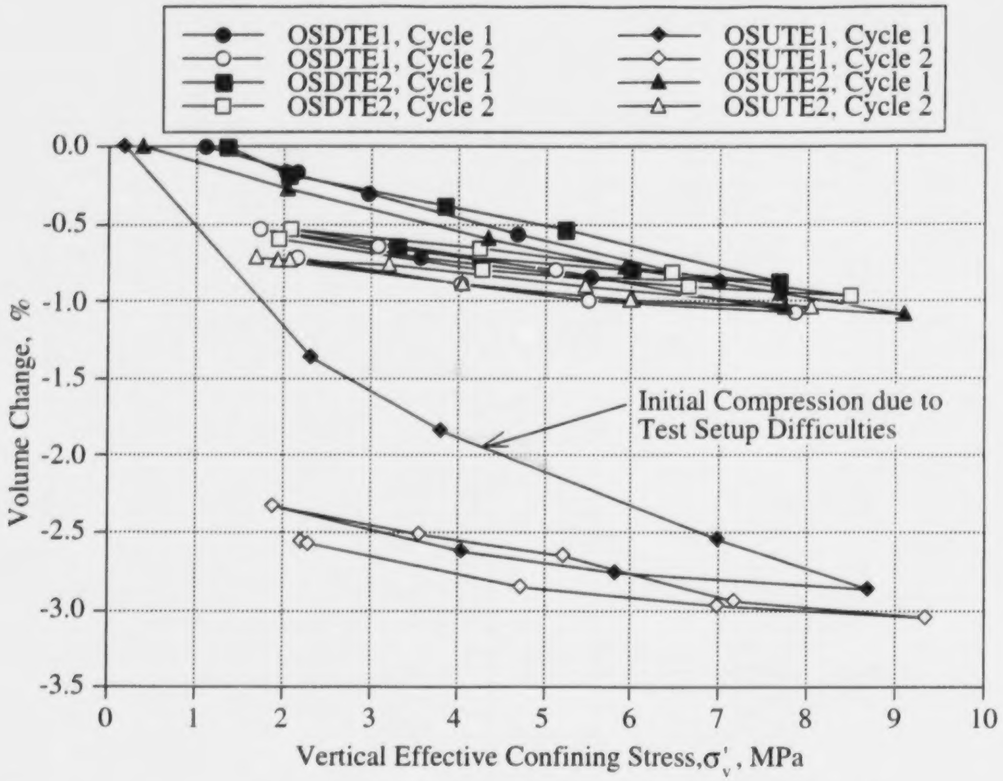

Figure 4.22 Constrained Bulk Volume Change of McMurray Formation Oil Sands

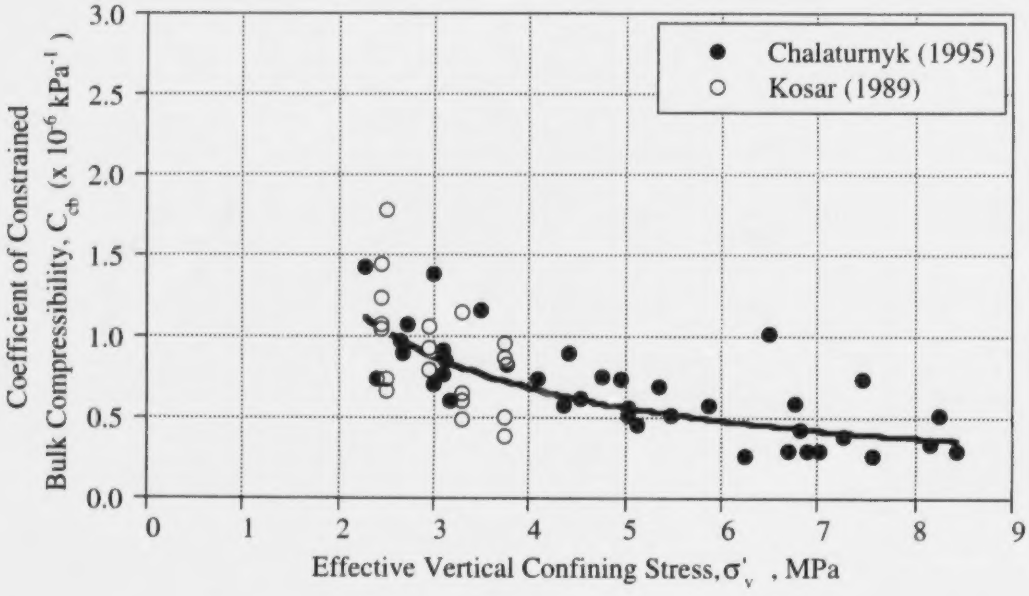

Figure 4.23 Coefficient of Constrained Bulk Compressibility of McMurray Formation Oil Sands

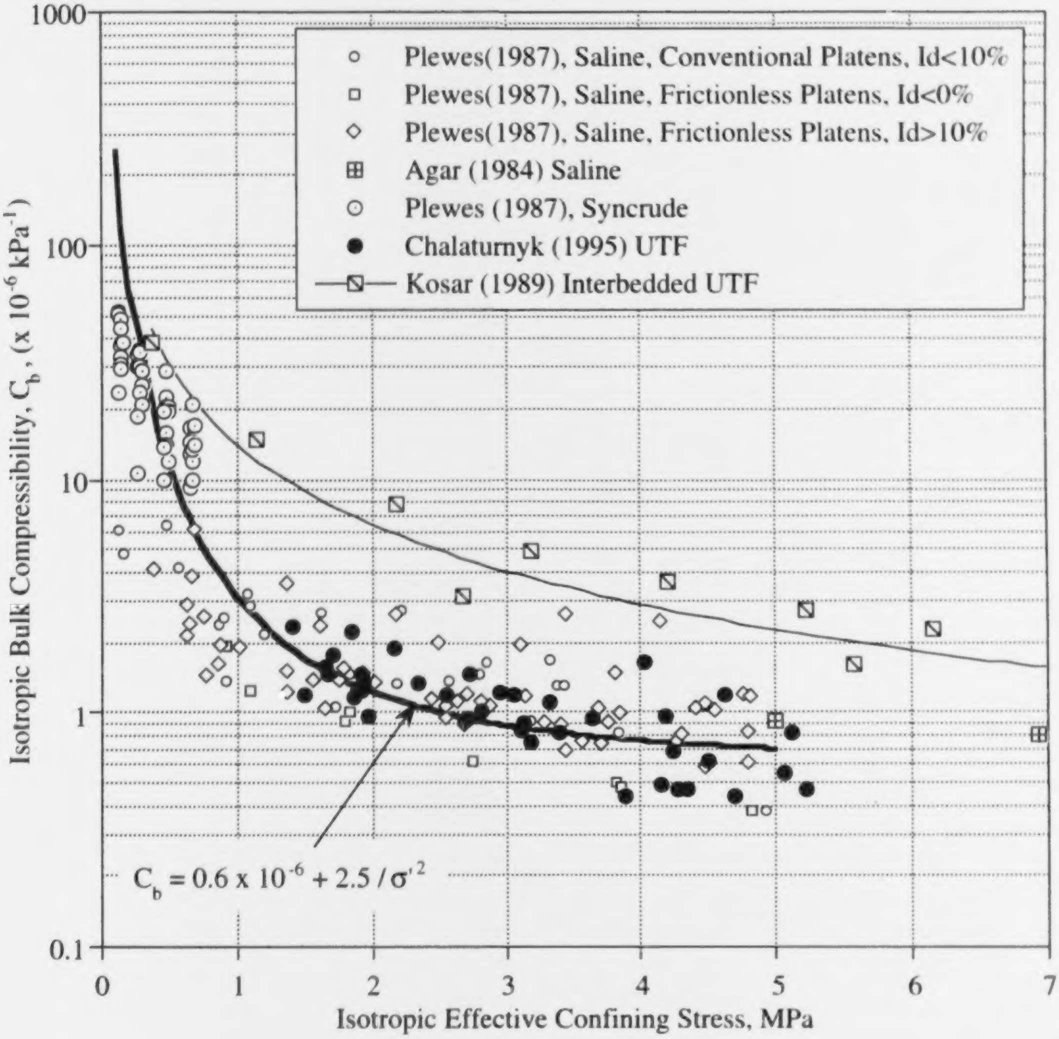

Figure 4.24 Isotropic Bulk Compressibility of McMurray Formation Oil Sands

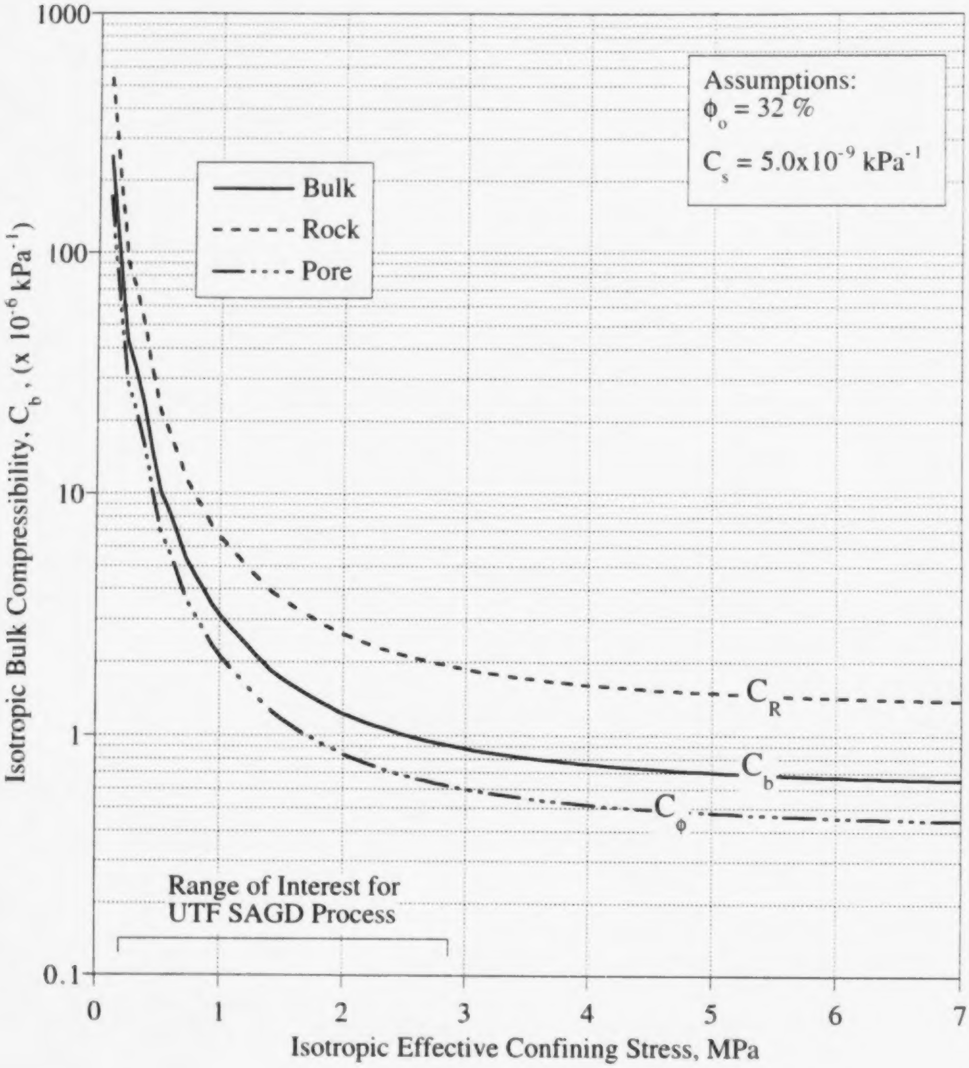

Figure 4.25 Coefficients of Isotropic Bulk (C_b), Rock (C_R), and Pore (C_ϕ), Compressibility

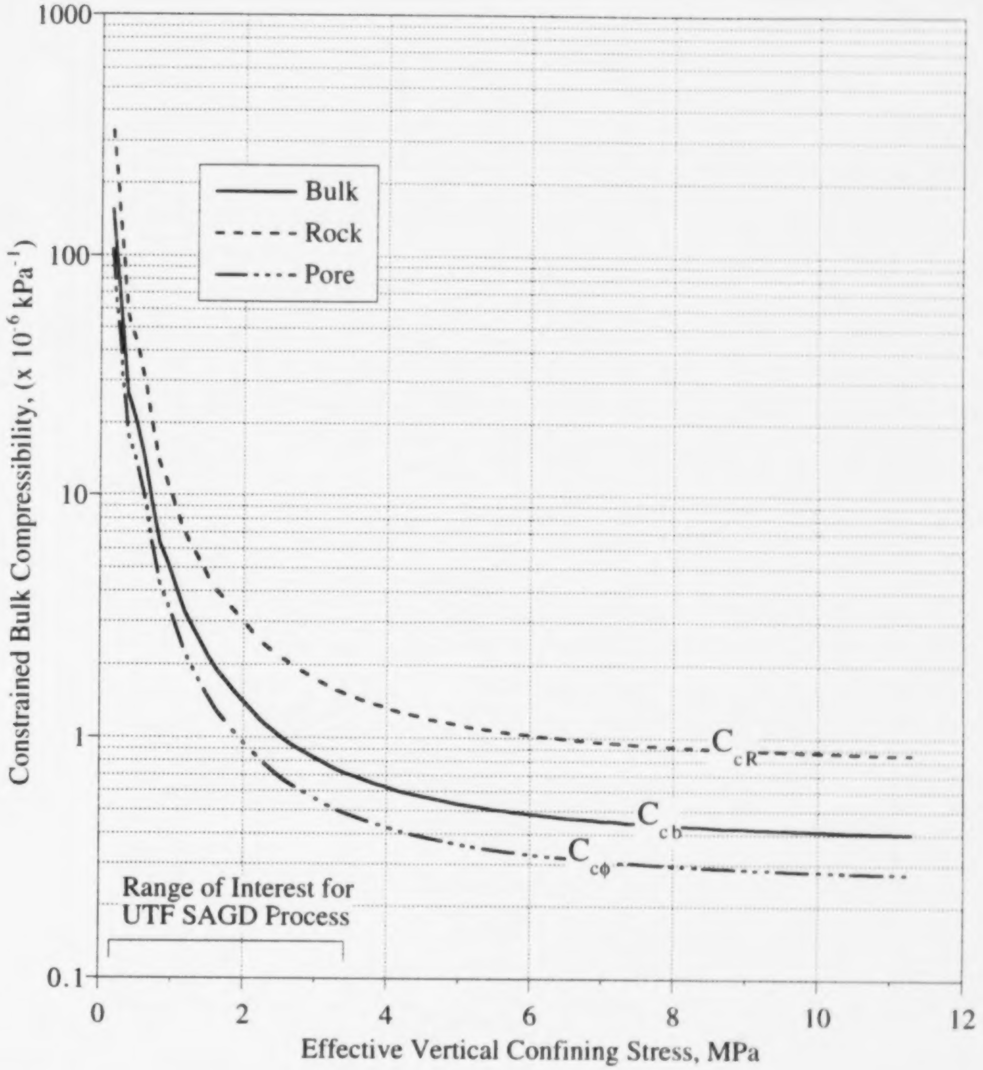

Figure 4.26 Coefficients of Constrained Bulk (C_{cb}), Rock (C_{cR}), and Pore ($C_{c\phi}$), Compressibility

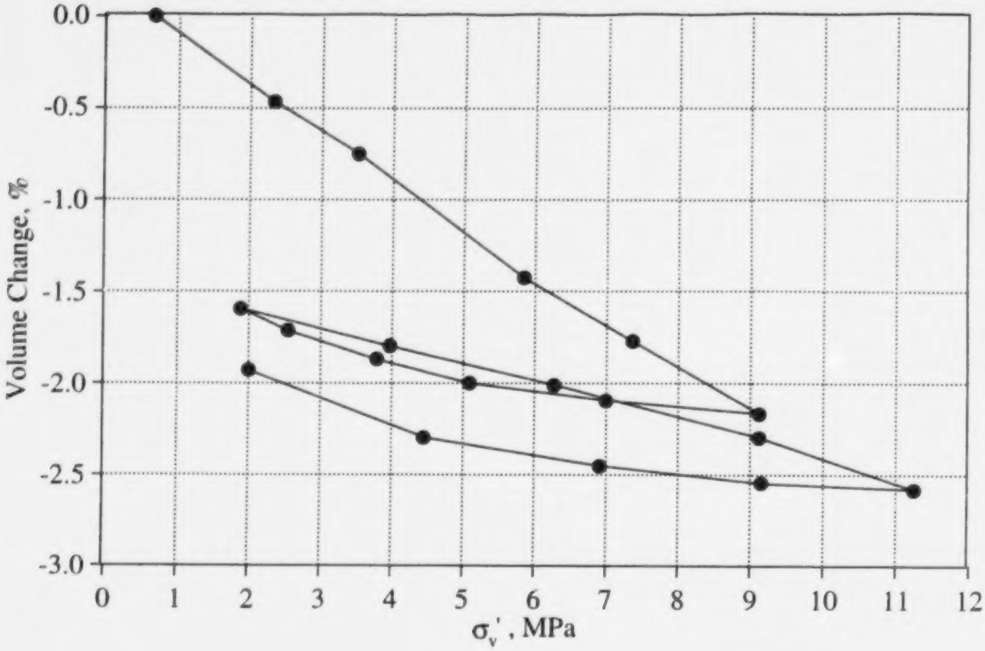

Figure 4.27 Constrained Bulk Compressibility of Upper McMurray Formation Shale (USUTE2)

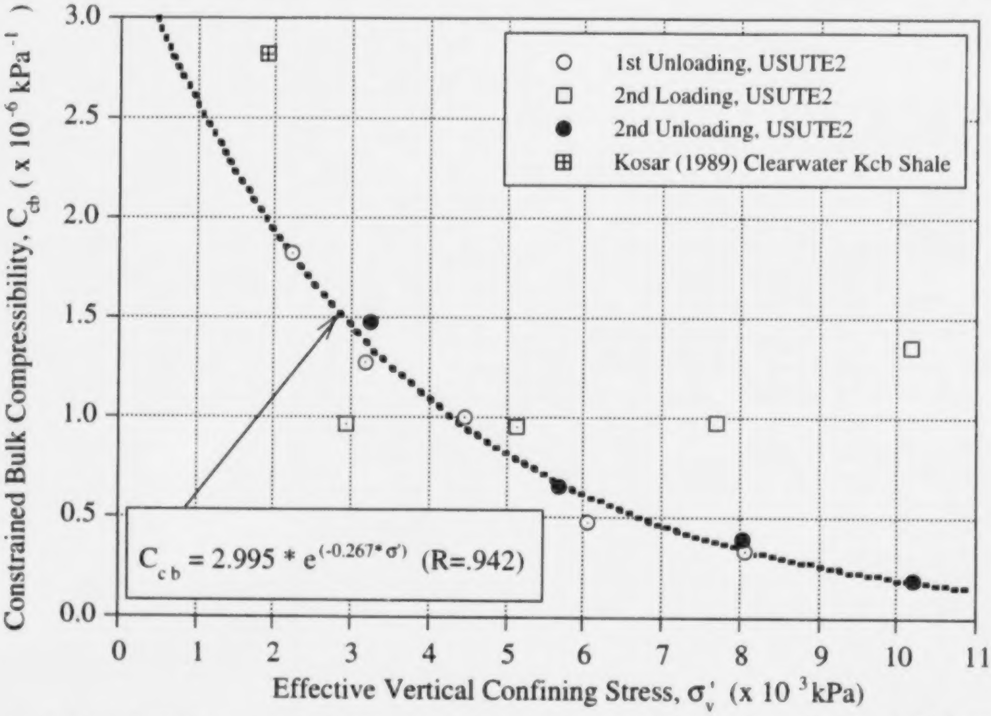

Figure 4.28 Coefficient of Constrained Bulk Compressibility for Upper McMurray Formation Shale (USUTE2)

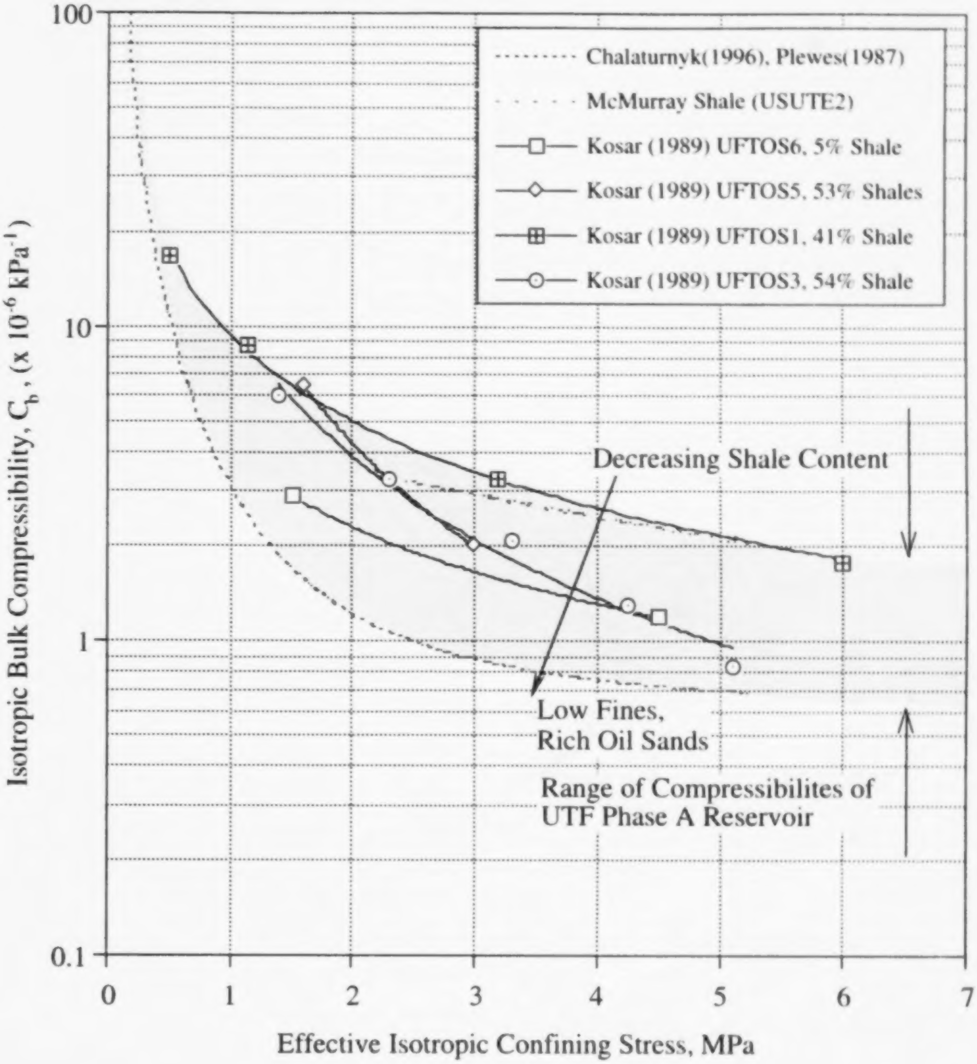

Figure 4.29 Influence of Shale Interbedding on Bulk Compressibility of McMurray Formation Oil Sands

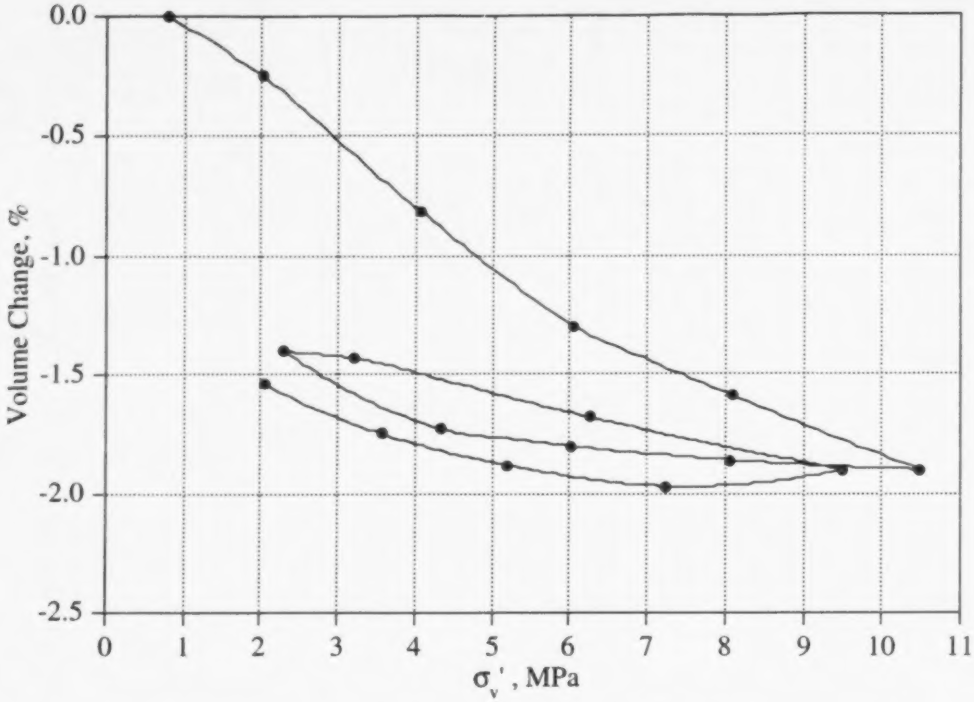

Figure 4.30 Constrained Bulk Compressibility of Waterways Formation Limestone

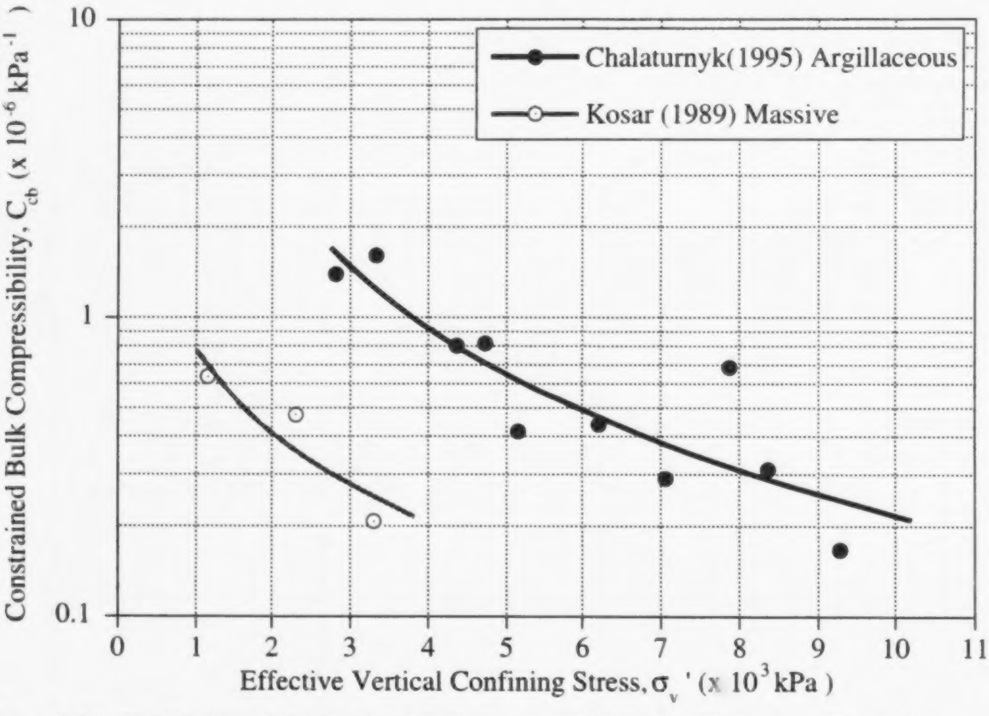

Figure 4.31 Coefficient of Constrained Bulk Compressibility for Waterways Formation Limestone

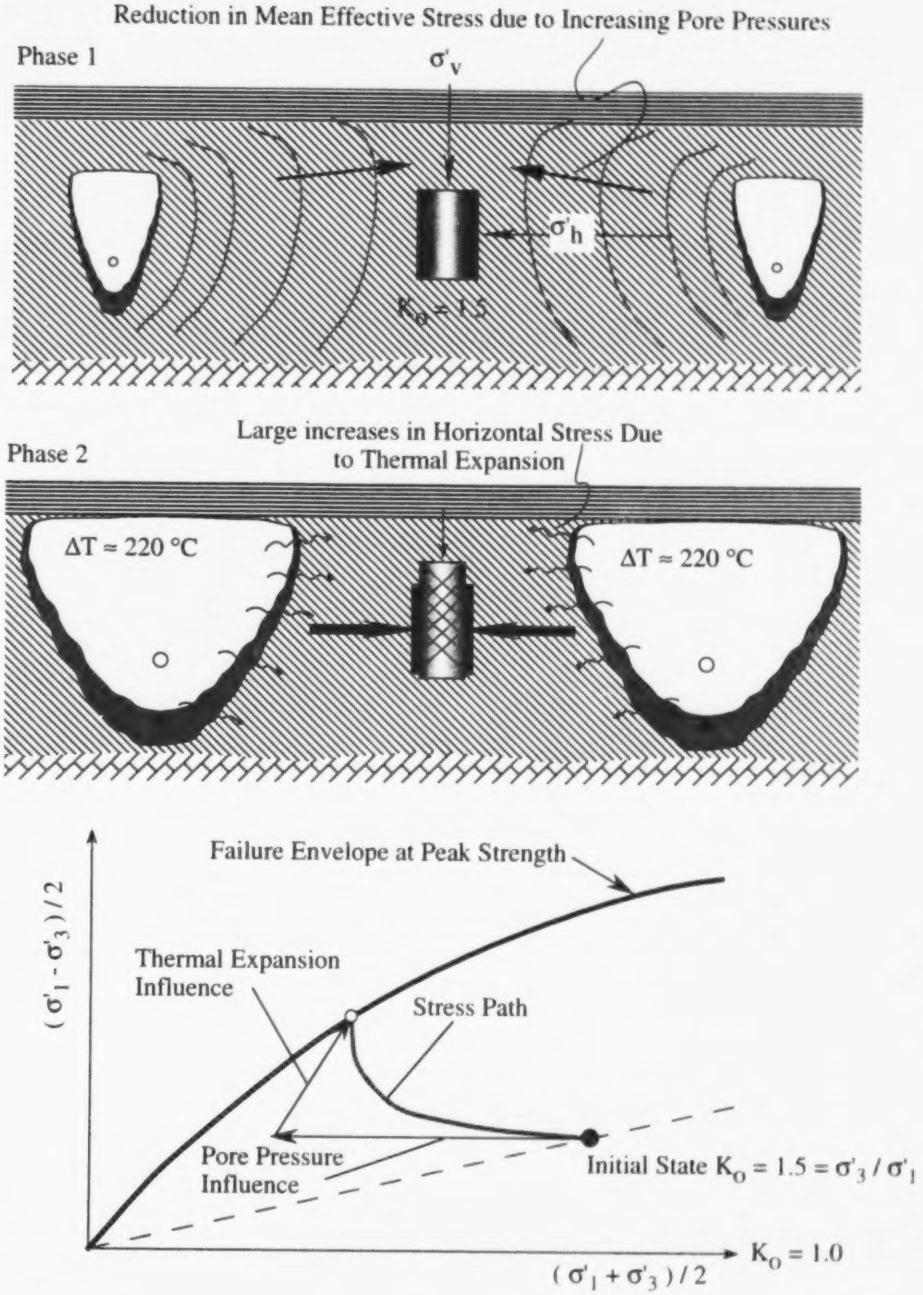
Reduction in Mean Effective Stress due to Increasing Pore Pressures
Phase 1
σ'v
σ'h
Ko ≈ 1.5
Large increases in Horizontal Stress Due to Thermal Expansion
Phase 2
ΔT ≈ 220 °C
ΔT ≈ 220 °C
Failure Envelope at Peak Strength
(σ'1 - σ'3) / 2
Thermal Expansion Influence
Stress Path
Pore Pressure Influence
Initial State Ko = 1.5 = σ'3 / σ'1
Ko = 1.0
(σ'1 + σ'3) / 2

Figure 4.32 Major Stress Path Followed within Reservoir during SAGD Process

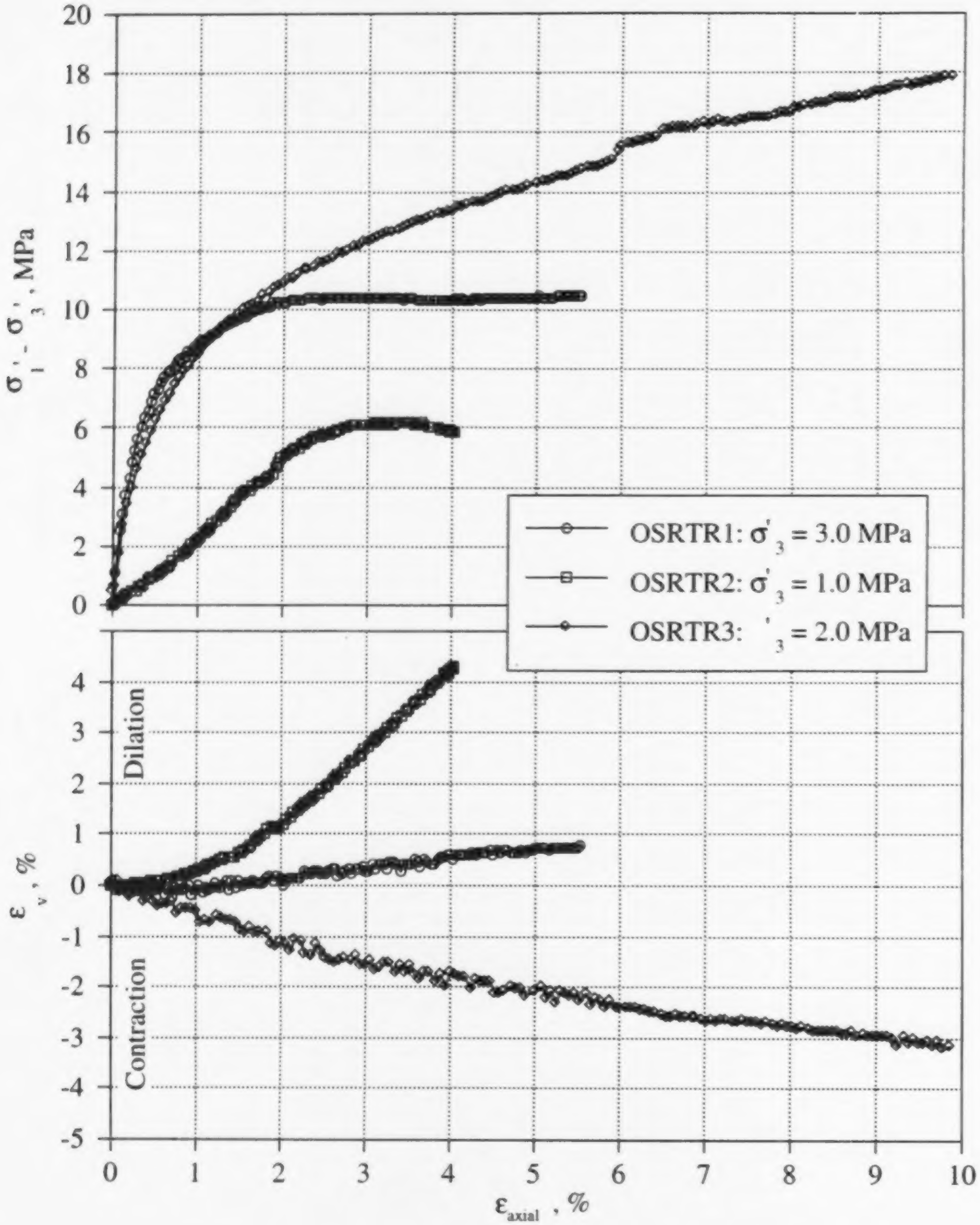

Figure 4.33 Isotropically Consolidated Drained Triaxial Compression Tests on McMurray Formation Oil Sands - 20 °C

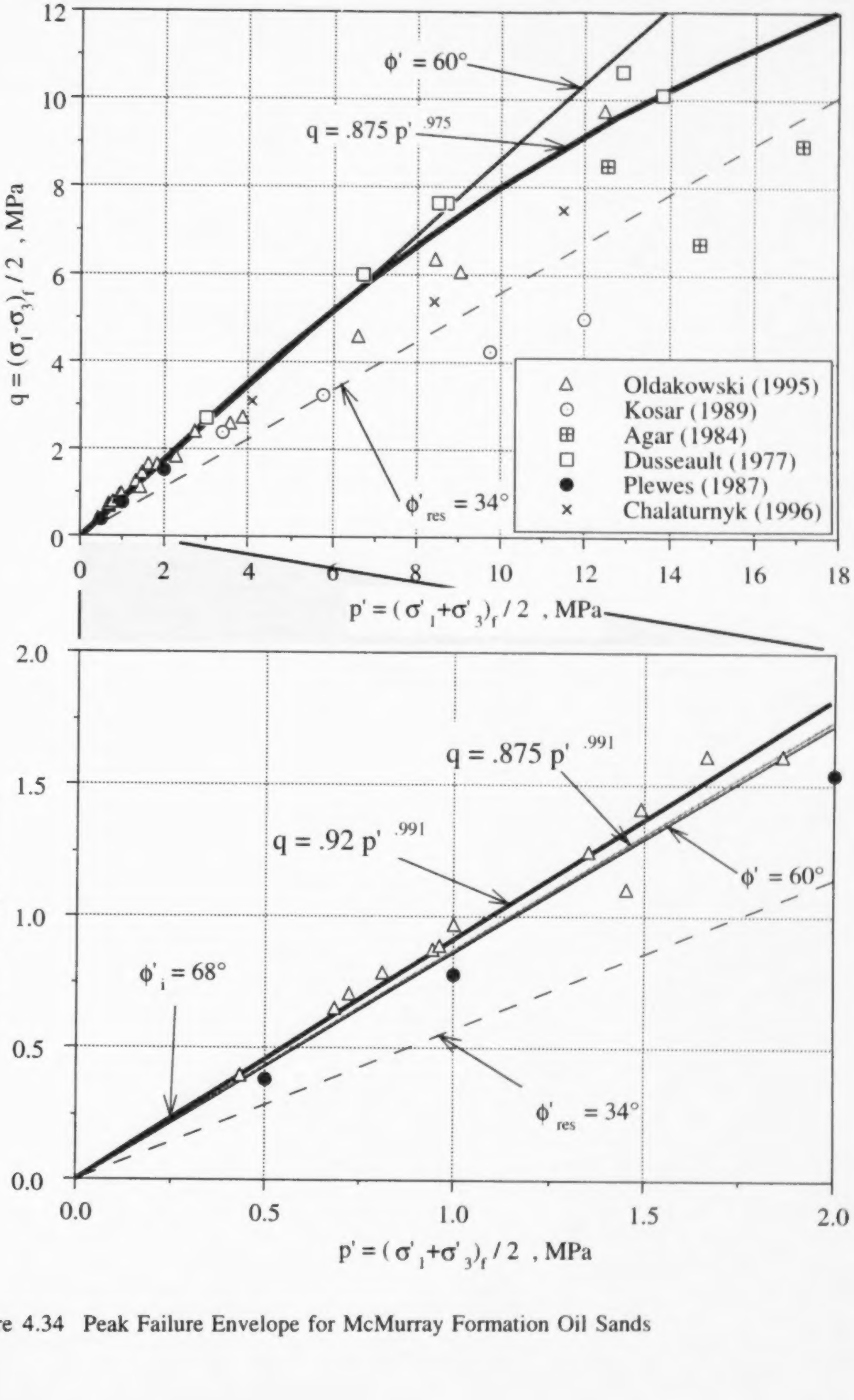

Figure 4.34 Peak Failure Envelope for McMurray Formation Oil Sands

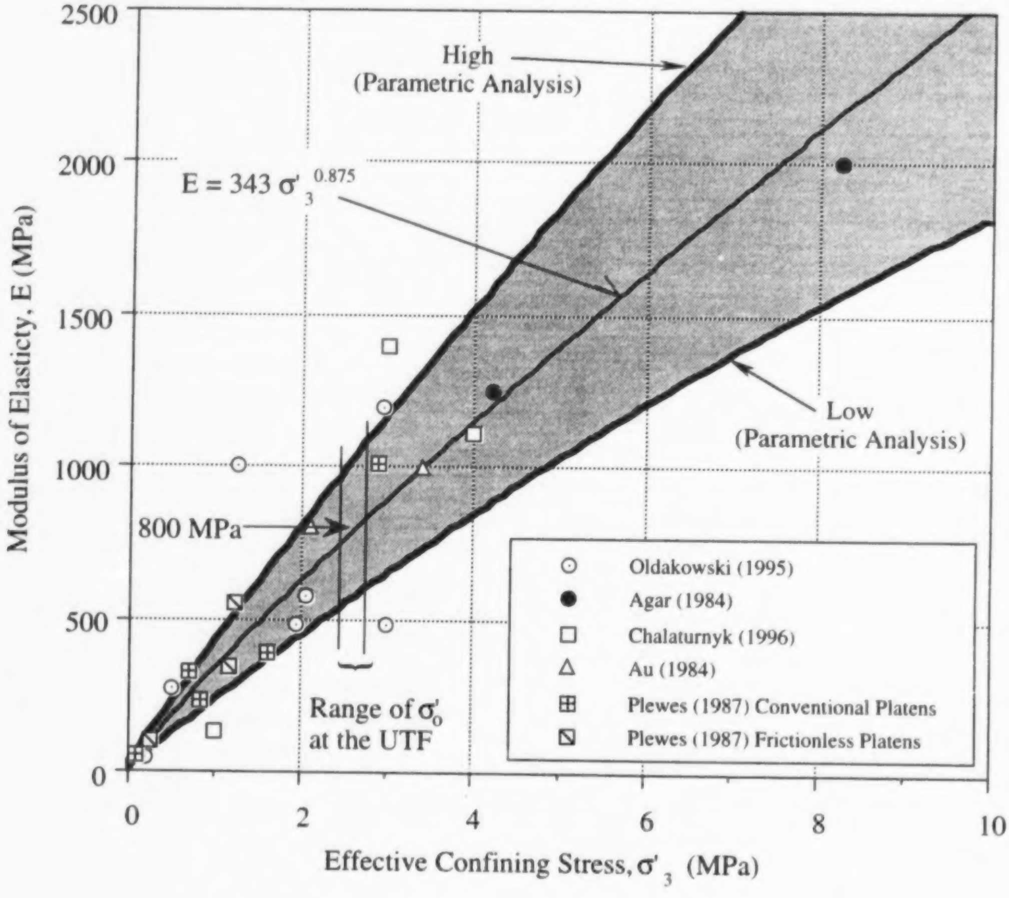

Figure 4.35 Variation of Young's Modulus with Effective Confining Stress - McMurray Formation Oil Sands

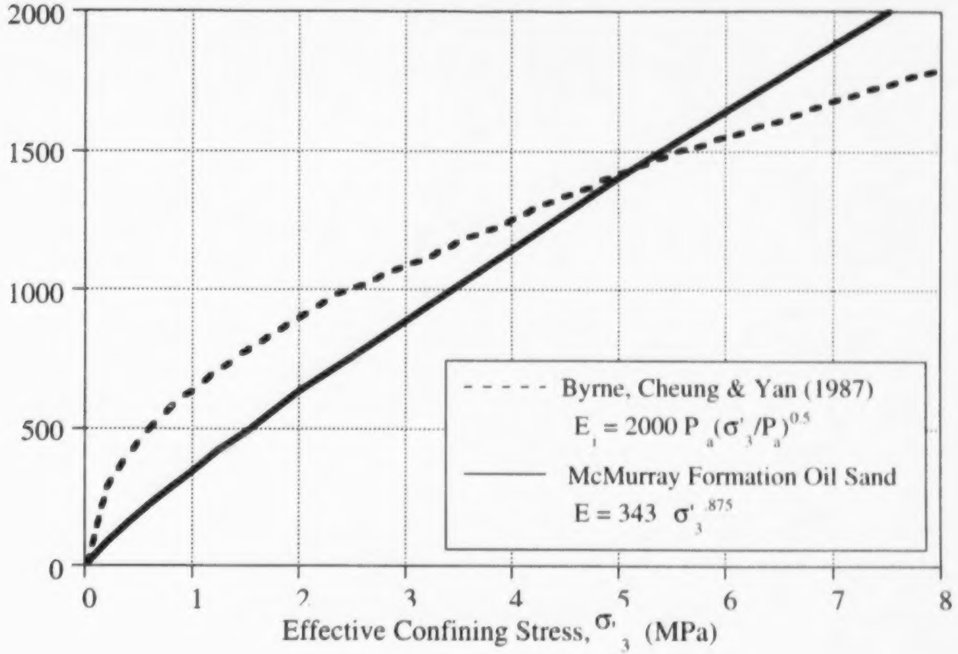

Figure 4.36 Comparison E vs. σ'_3 Relationships for Dense Sands

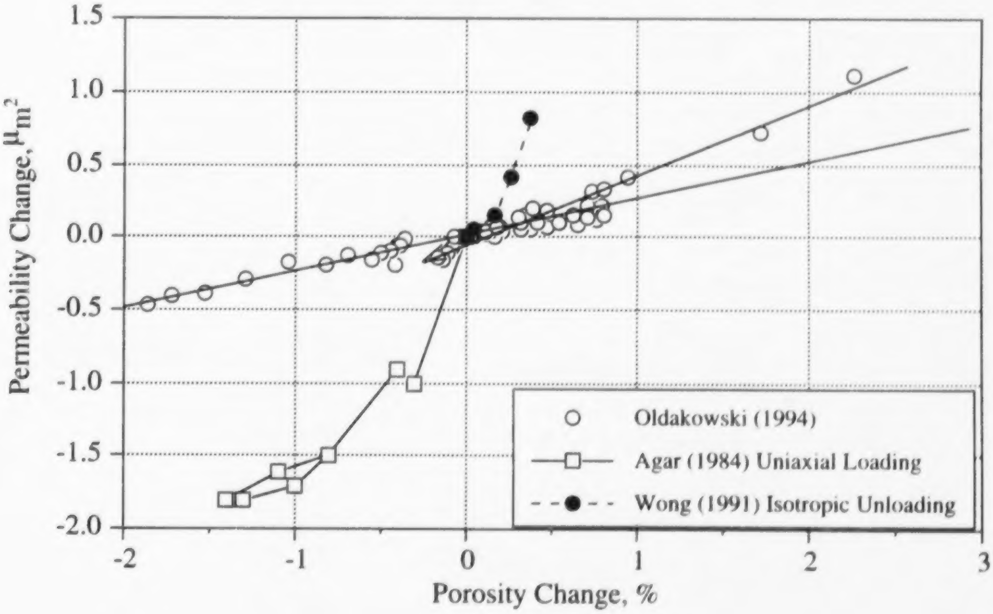

Figure 4.37 Absolute Permeability Change versus Porosity Change for Reconstituted, Oil-Free McMurray Formation Oil Sands

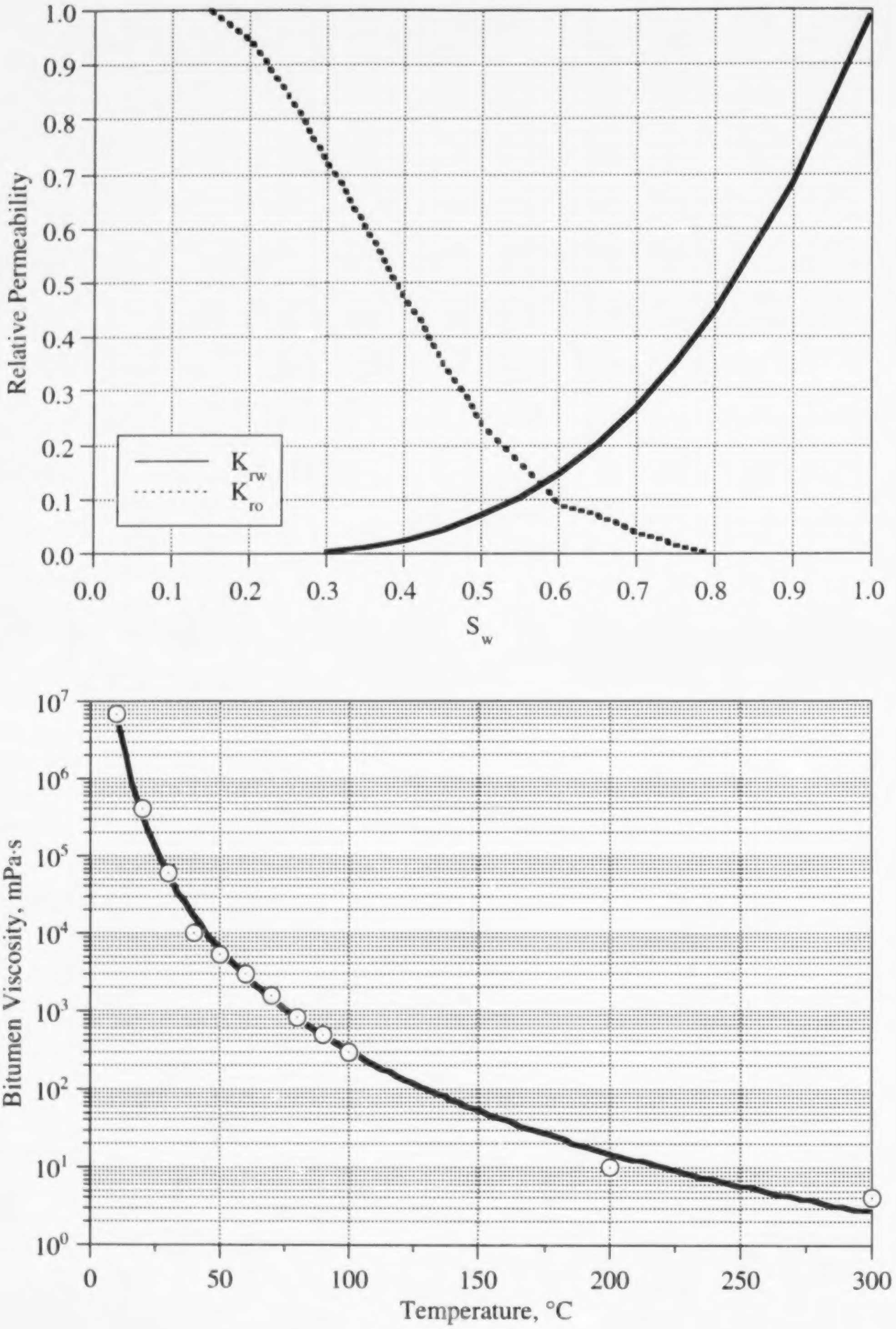

Figure 4.38 Relative Permeability and Bitumen Viscosity Relationships for UTF Phase A Reservoir

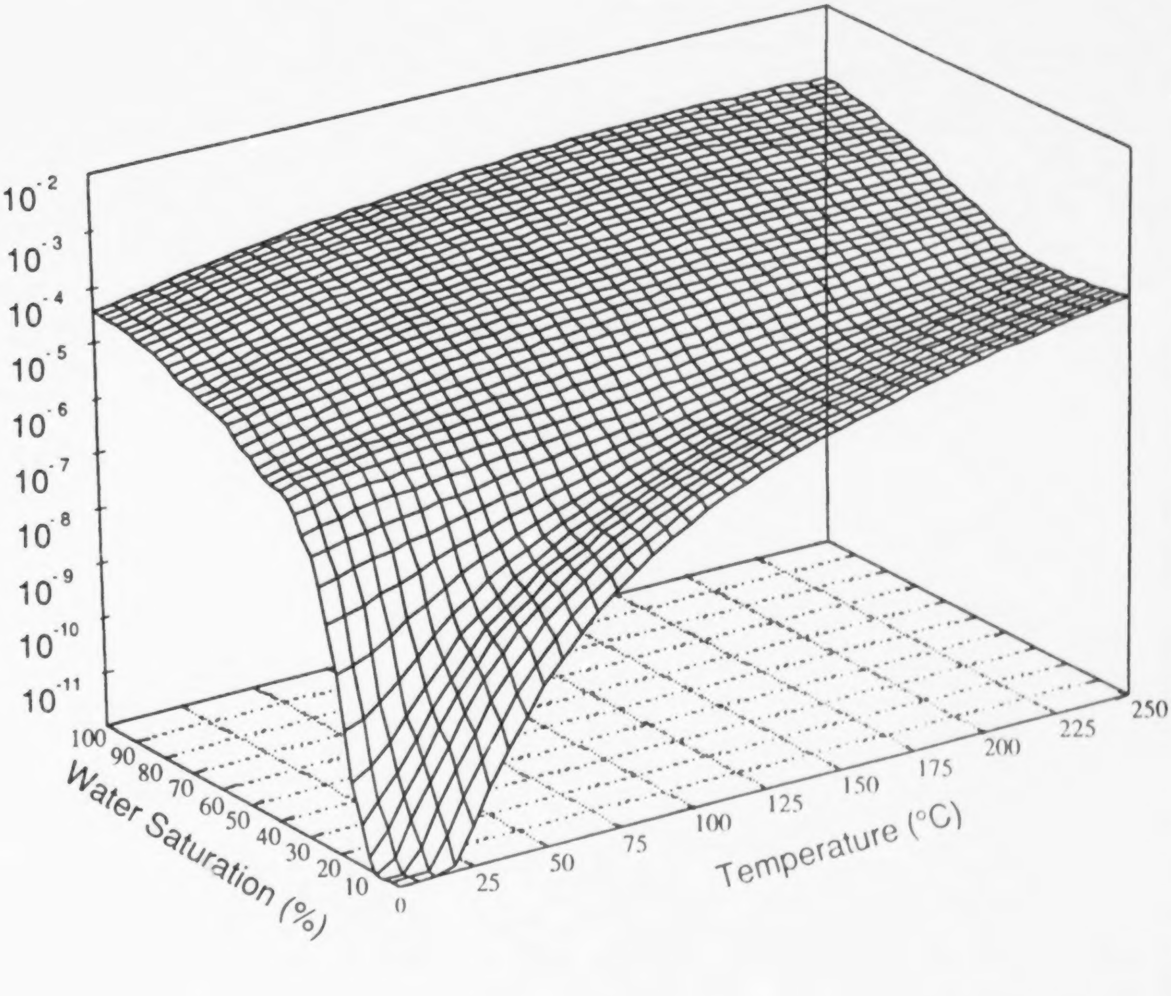

Figure 4.39 Equivalent Hydraulic Conductivity of Oil Sands as a Function of Water Saturation and Temperature

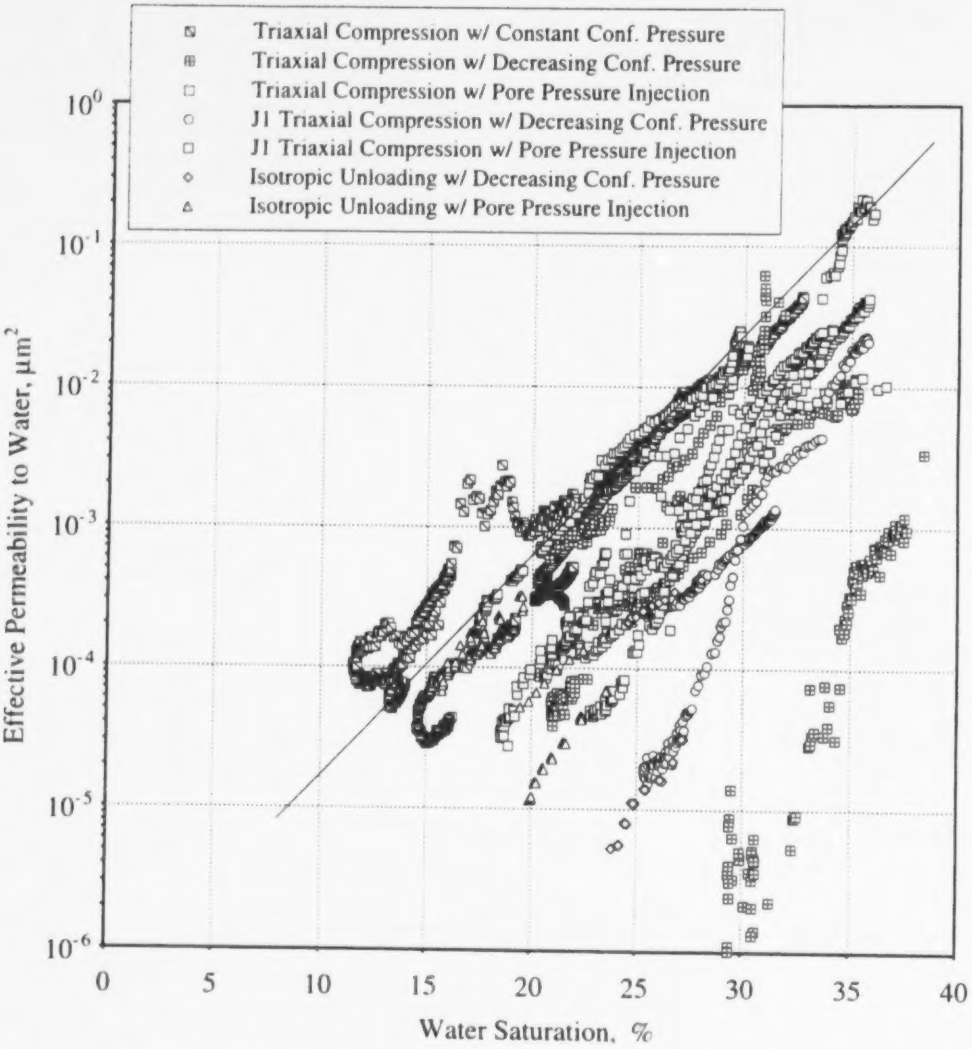

Figure 4.40 Effect of Water Saturation on Effective Permeability to Water (modified from Oldakowski, 1994)

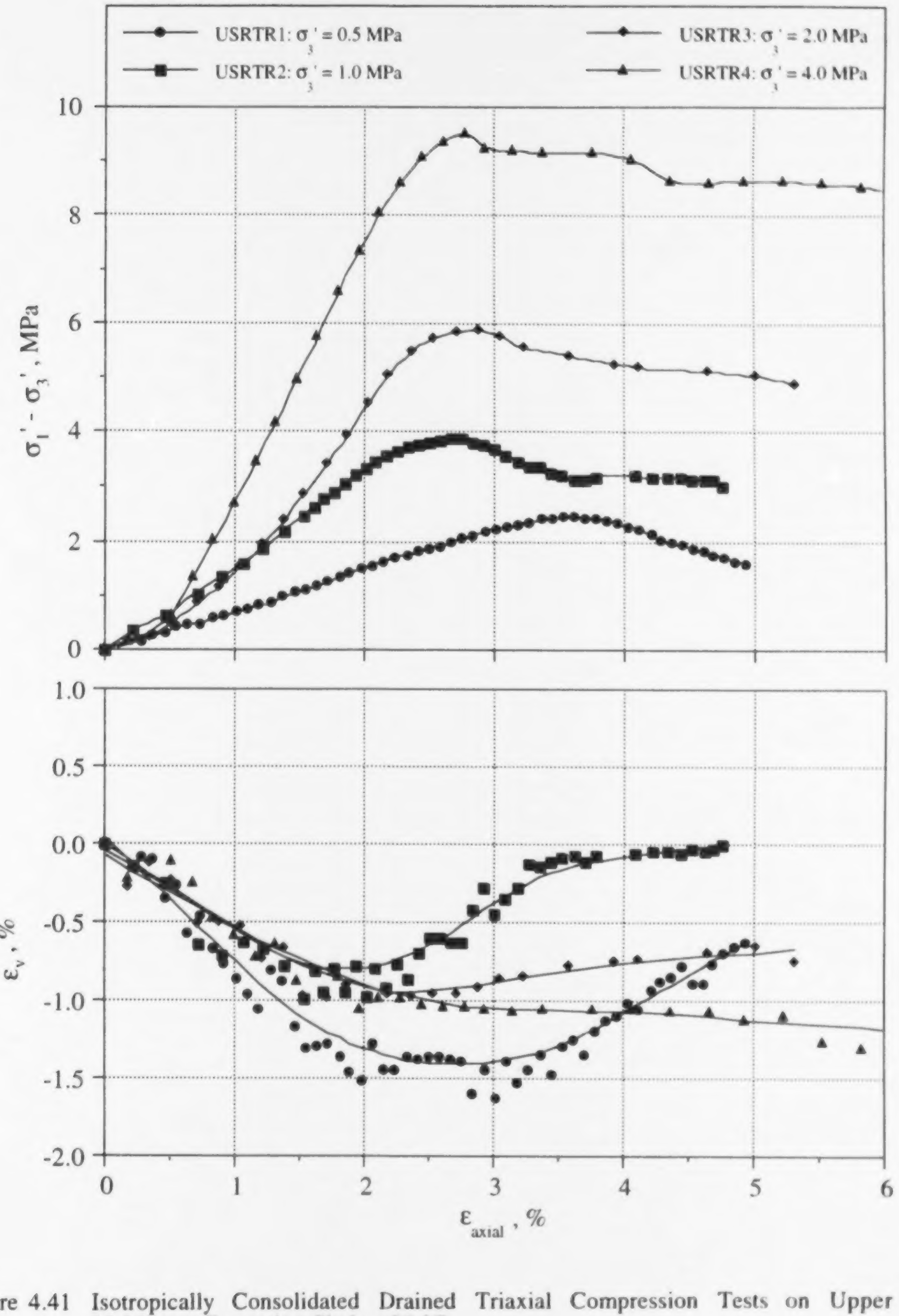

Figure 4.41 Isotropically Consolidated Drained Triaxial Compression Tests on Upper McMurray Formation Shale - 20 °C

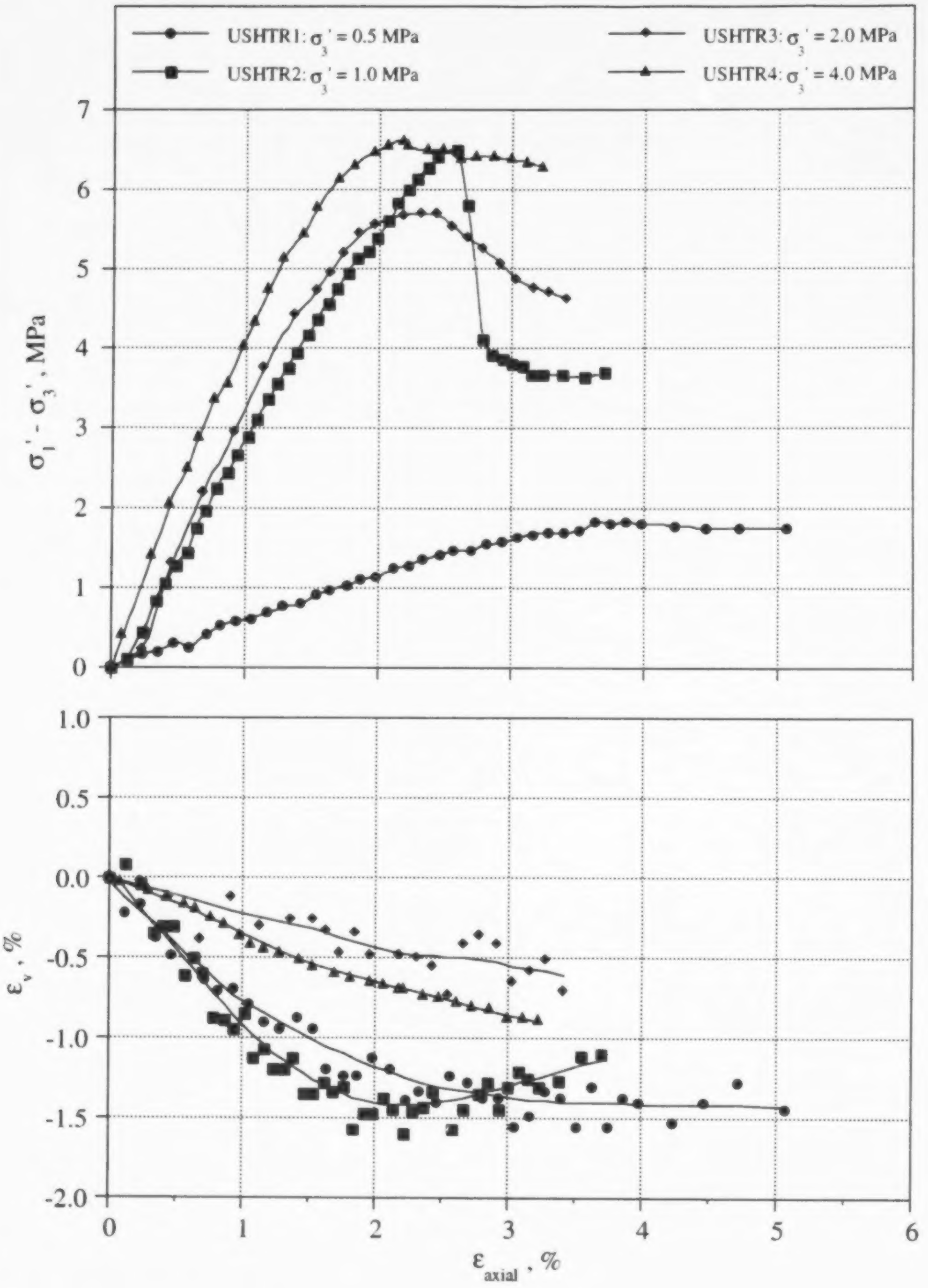

Figure 4.42 Isotropically Consolidated Drained Triaxial Compression Tests on Upper McMurray Formation Shale - 225 °C

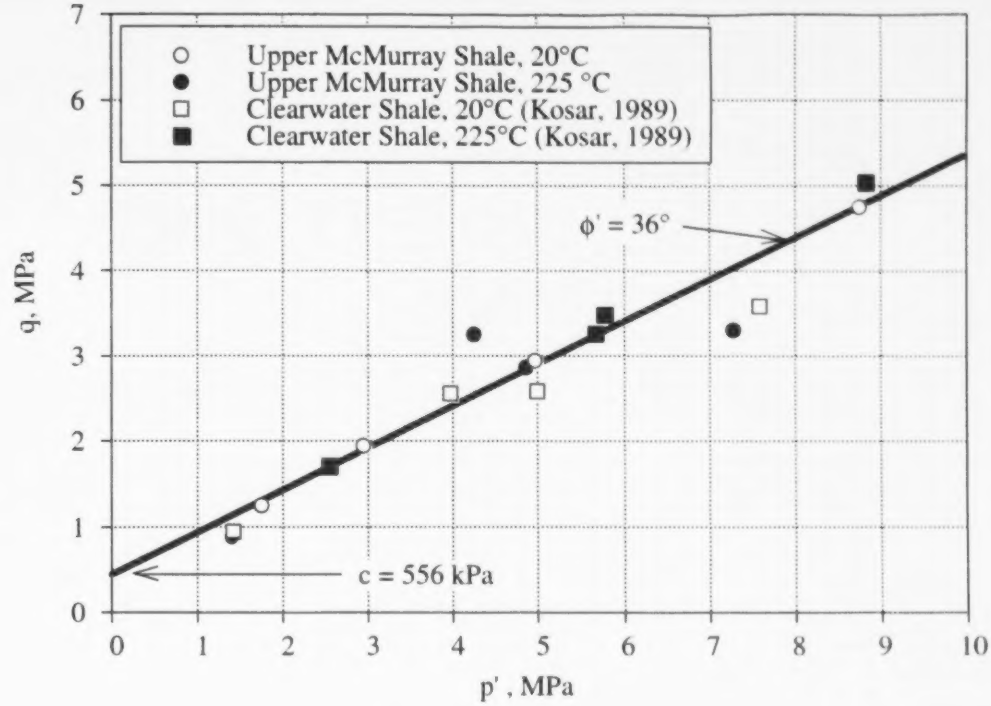

Figure 4.43 Peak Failure Envelope for Upper McMurray Formation Shale: 20°C & 225 °C

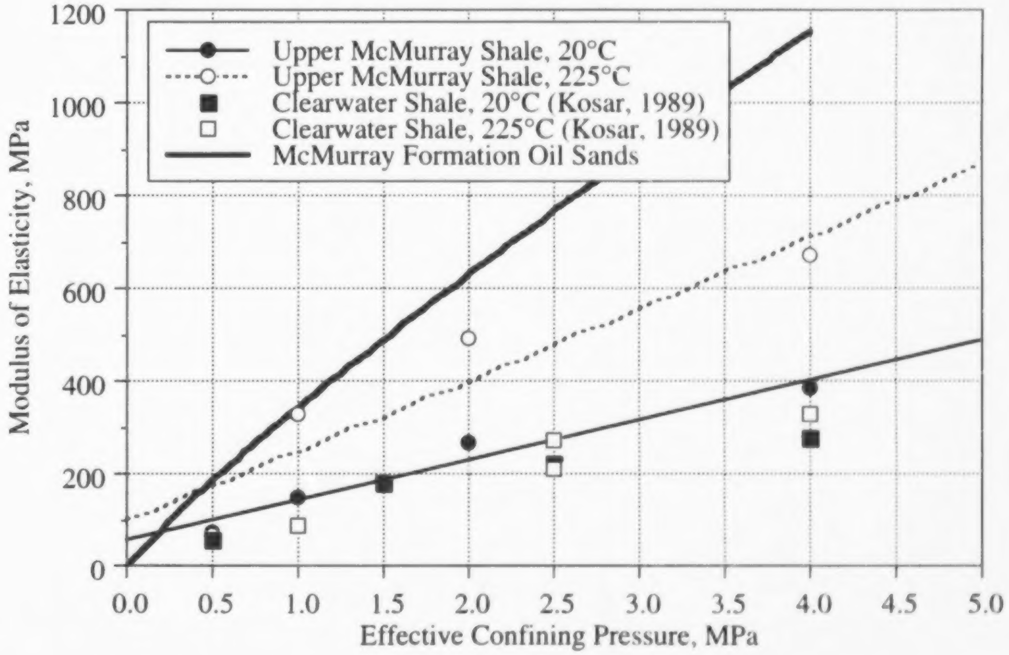

Figure 4.44 Variation of Young's Modulus with Effective Confining Stress for Upper McMurray Formation Shale: 20°C & 225 °C

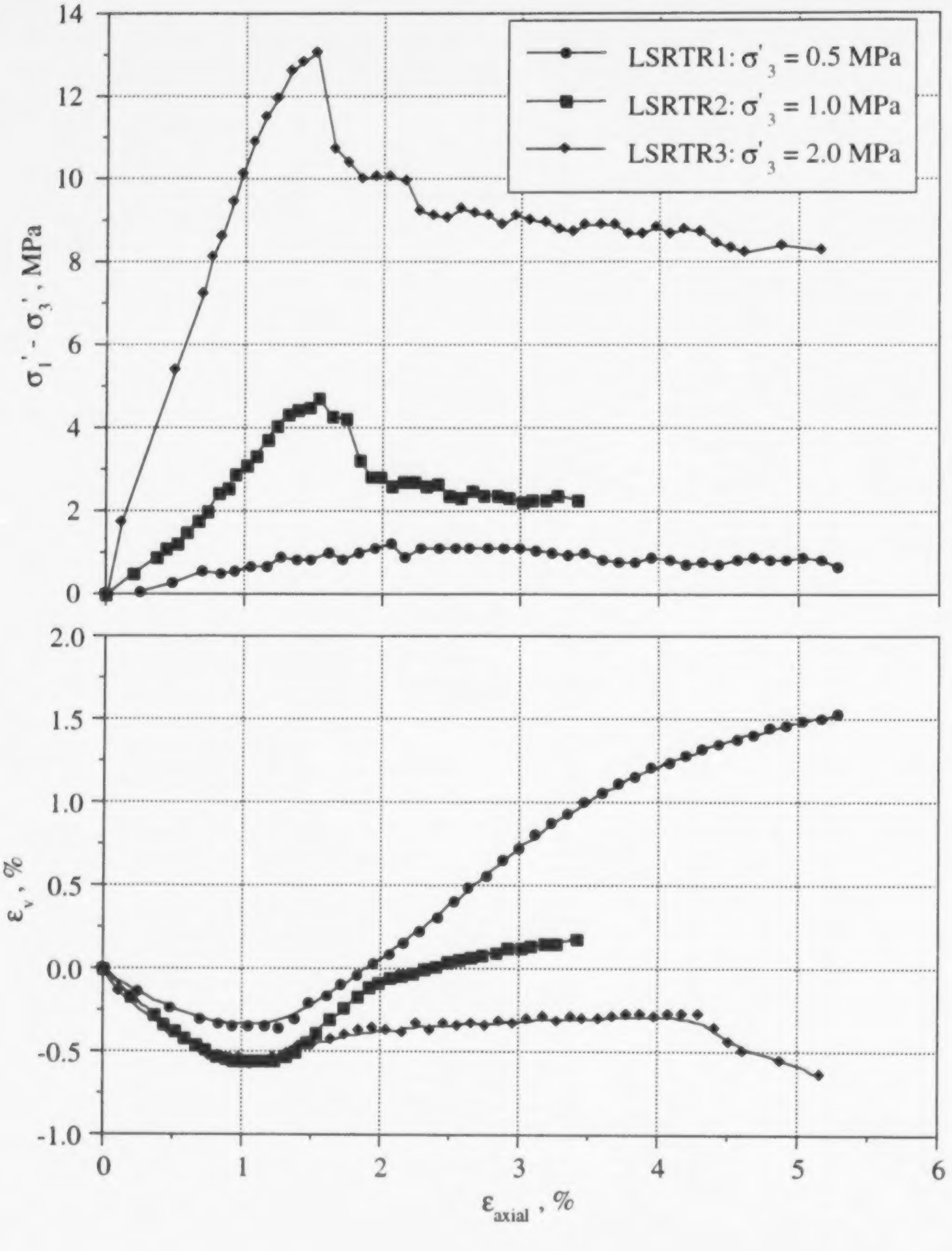

Figure 4.45 Isotropically Consolidated Drained Triaxial Compression Tests on Lower McMurray Formation Shale - 20 °C

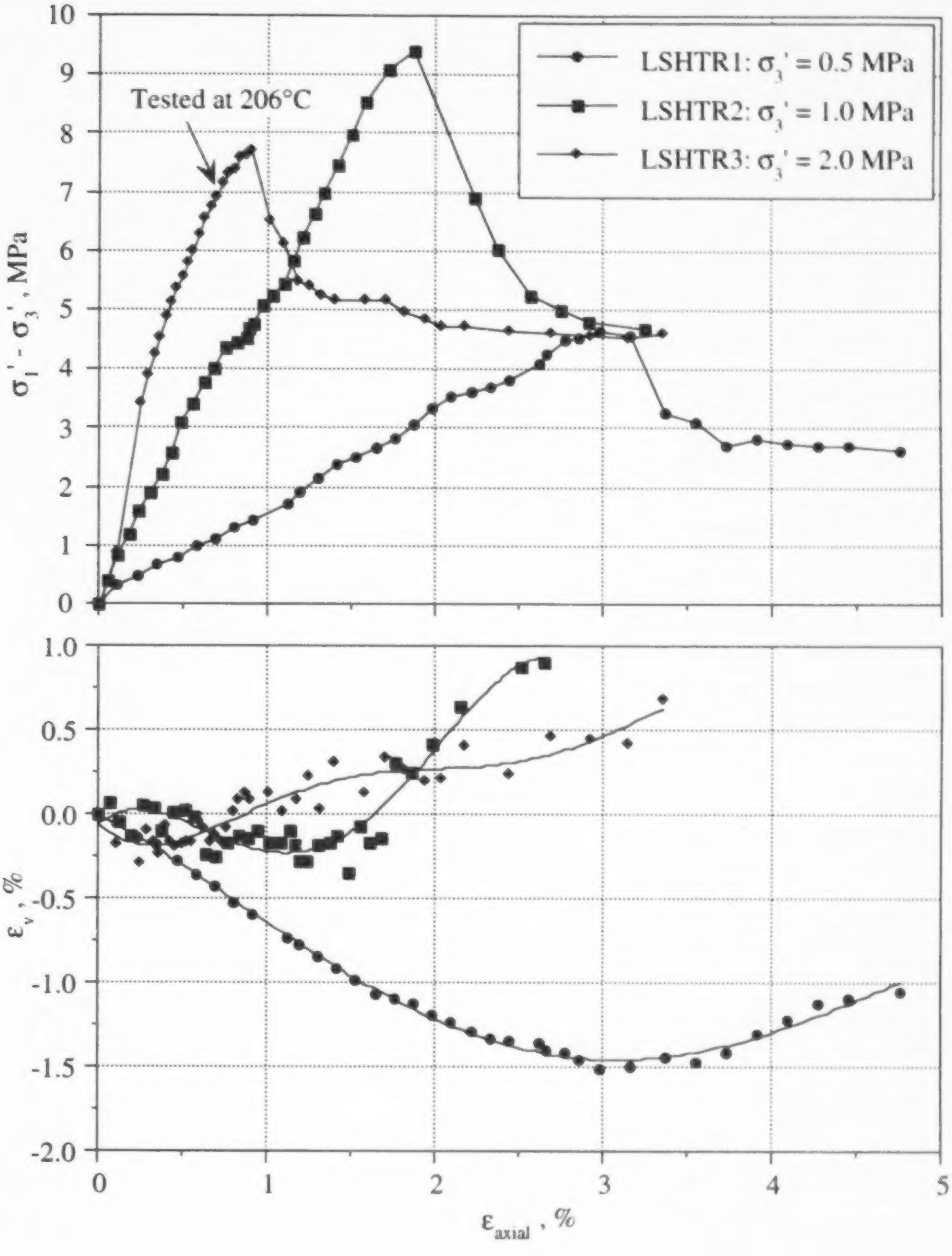

Figure 4.46 Isotropically Consolidated Drained Triaxial Compression Tests on Upper McMurray Formation Shale - 225 °C

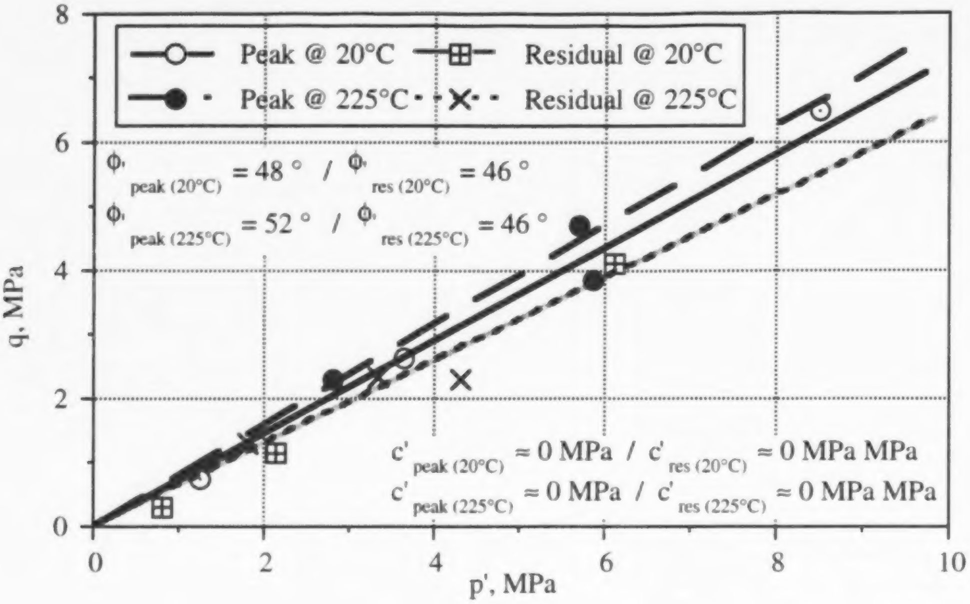

Figure 4.47 Peak Failure Envelope for Lower McMurray Formation Shale: 20°C & 225 °C

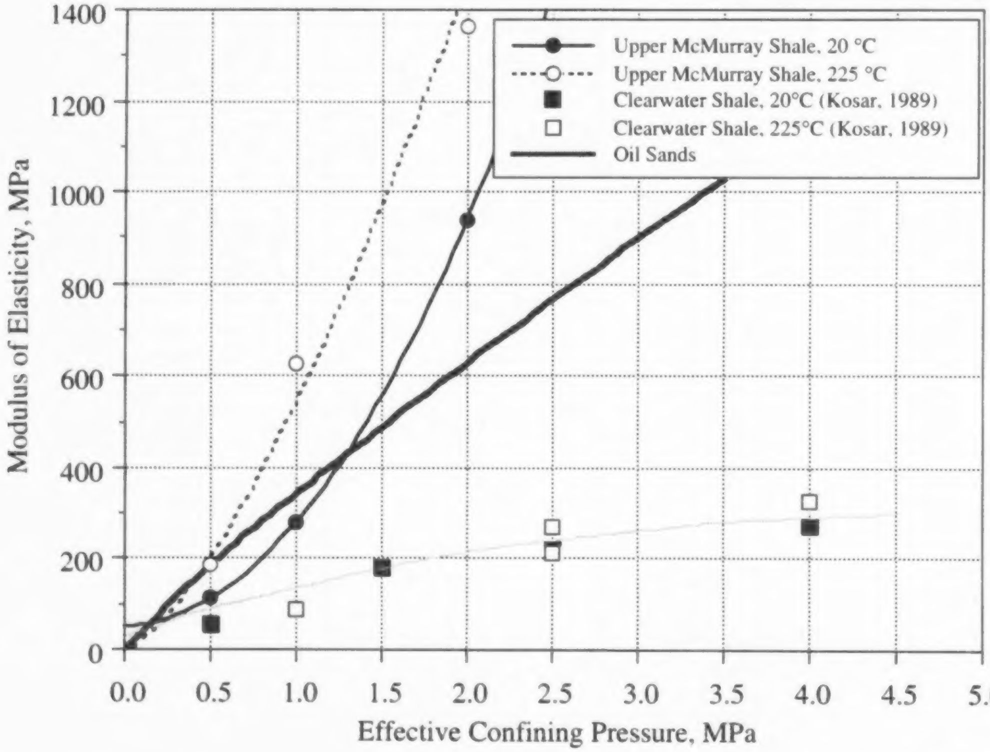

Figure 4.48 Variation of Young's Modulus with Effective Confining Stress for Lower McMurray Formation Shale: 20°C & 225 °C

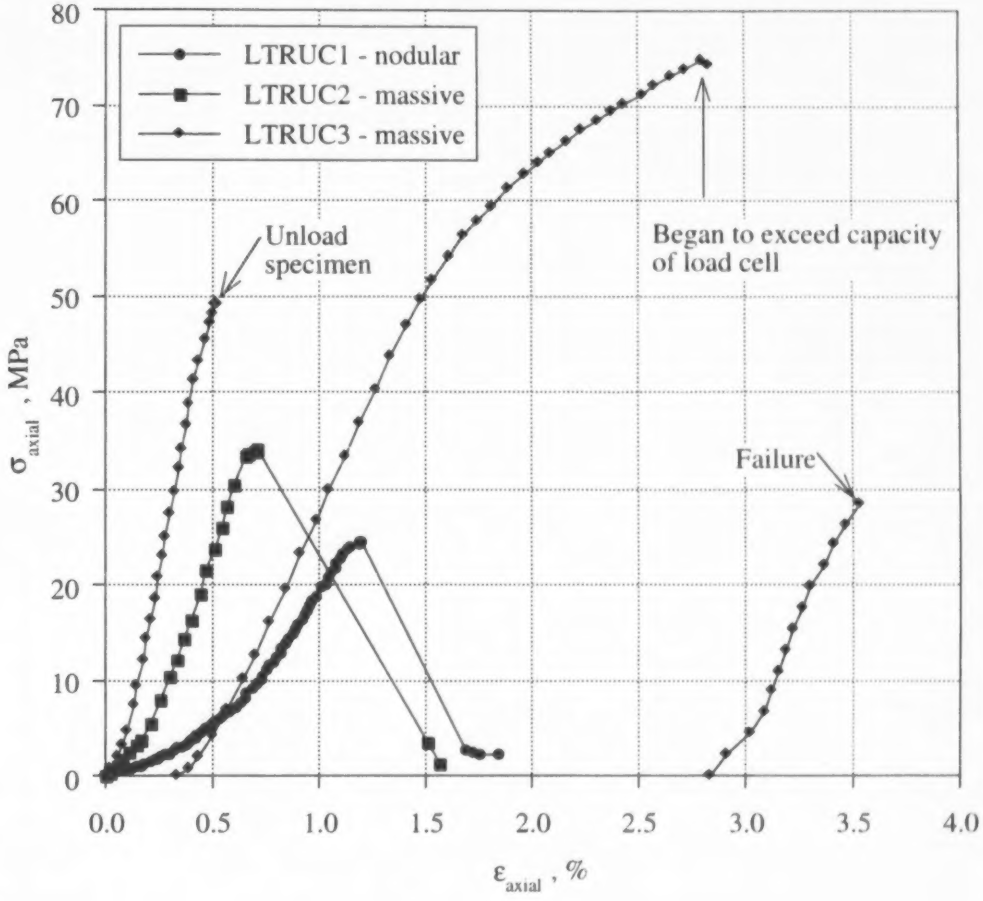

Figure 4.49 Unconfined Compression Tests on Waterways Formation Limestone

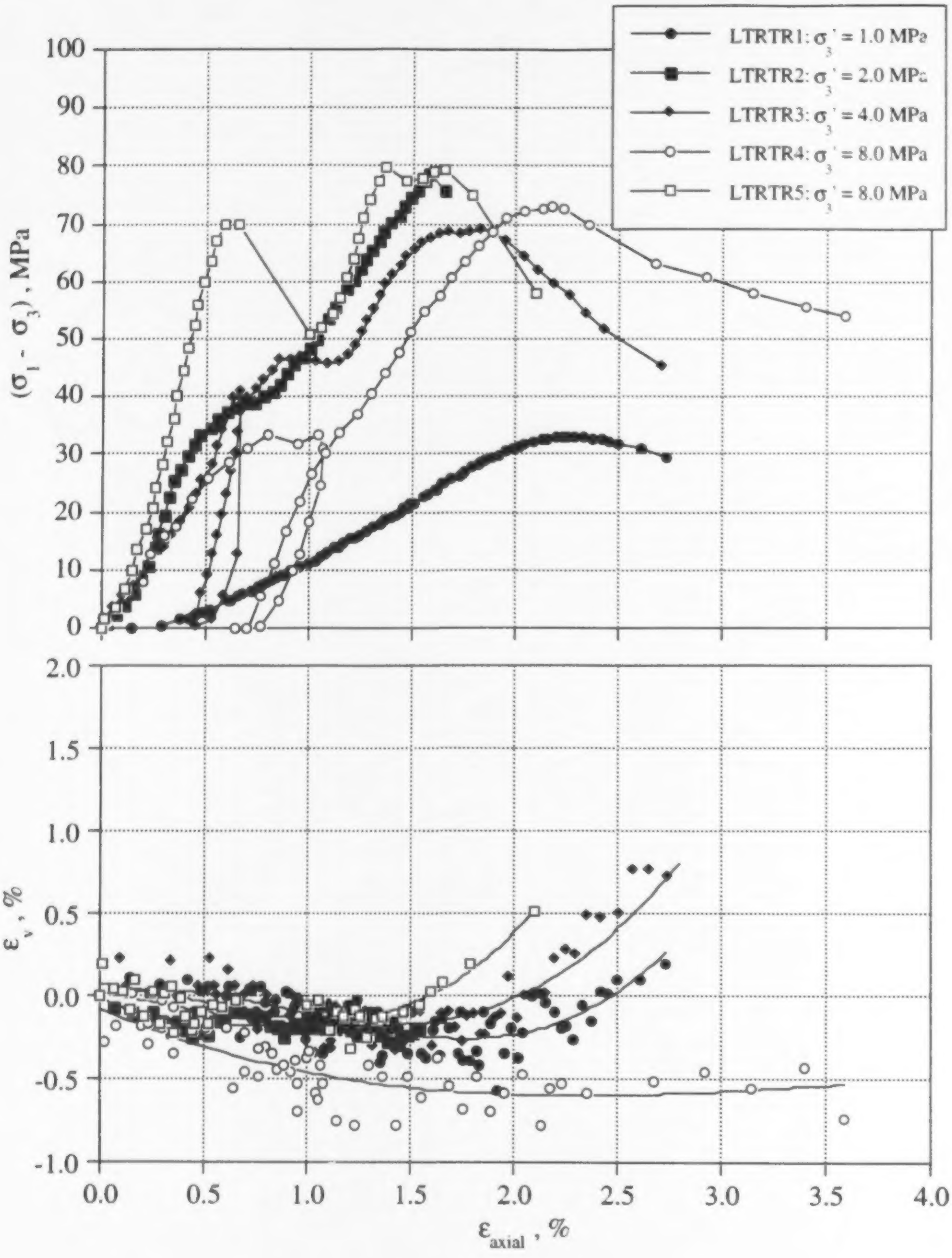

Figure 4.50 Isotropically Consolidated Drained Triaxial Compression Tests on Waterways Formation Limestone - 20 °C

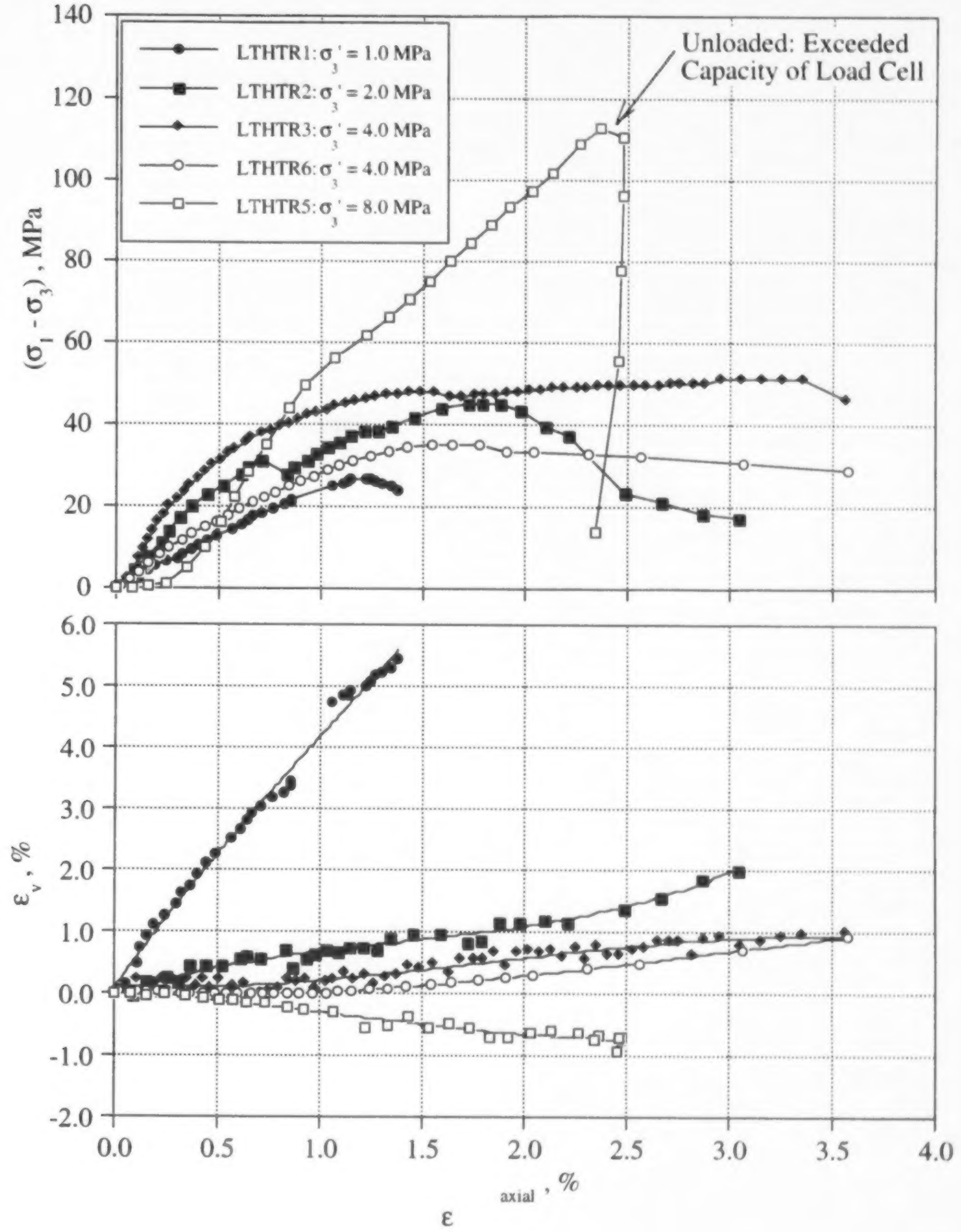

Figure 4.51 Isotropically Consolidated Drained Triaxial Compression Tests on Waterways Formation Limestone - 225 °C

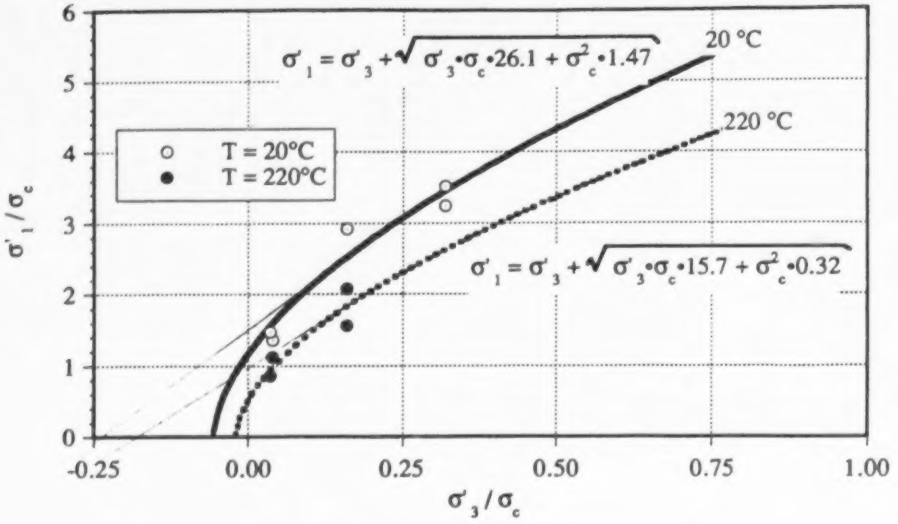

Figure 4.52 Peak Failure Envelope for Waterways Formation Limestone: 20°C & 225 °C

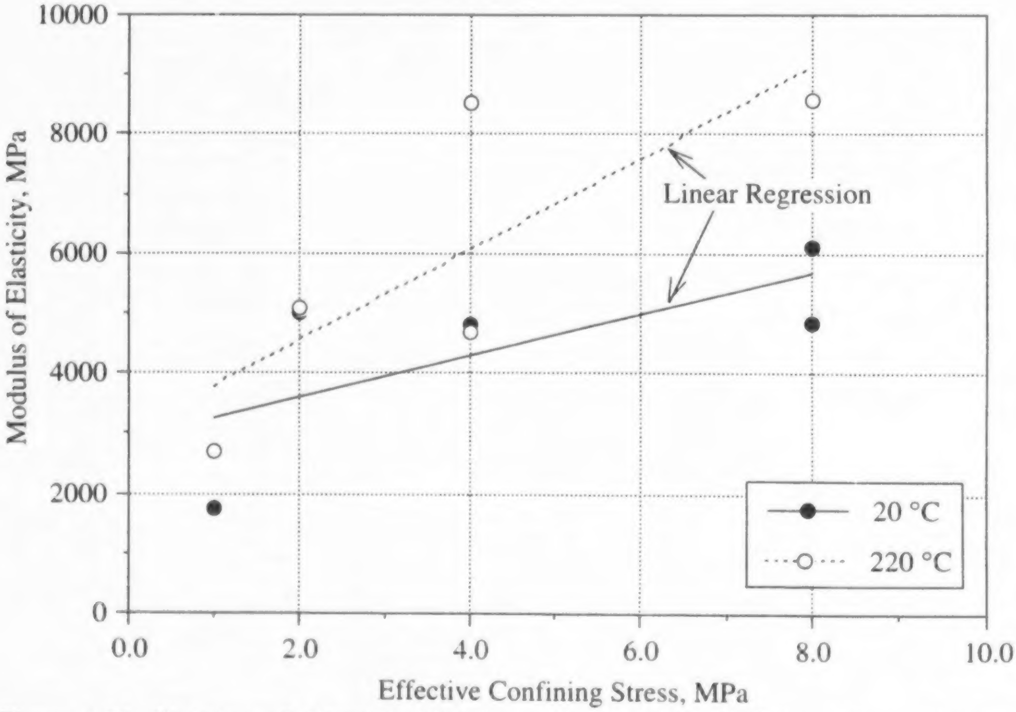

Figure 4.53 Variation of Young's Modulus with Effective Confining Stress Waterways Formation Limestone: 20°C & 225 °C

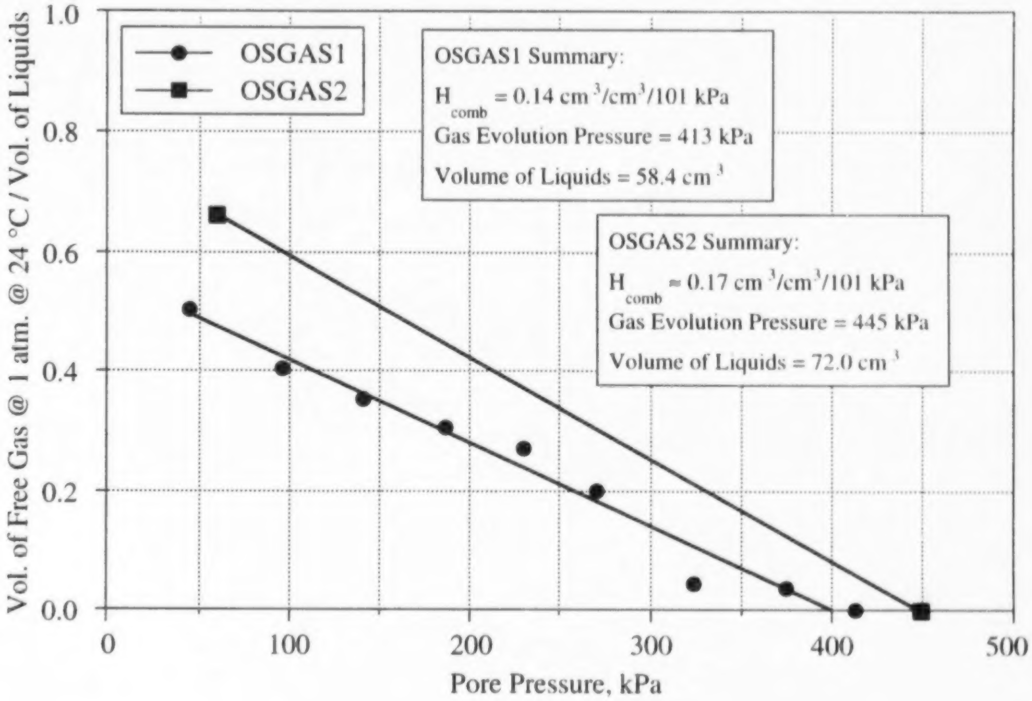

Figure 4.54 Gas Evolution Test on McMurray Formation Oil Sands

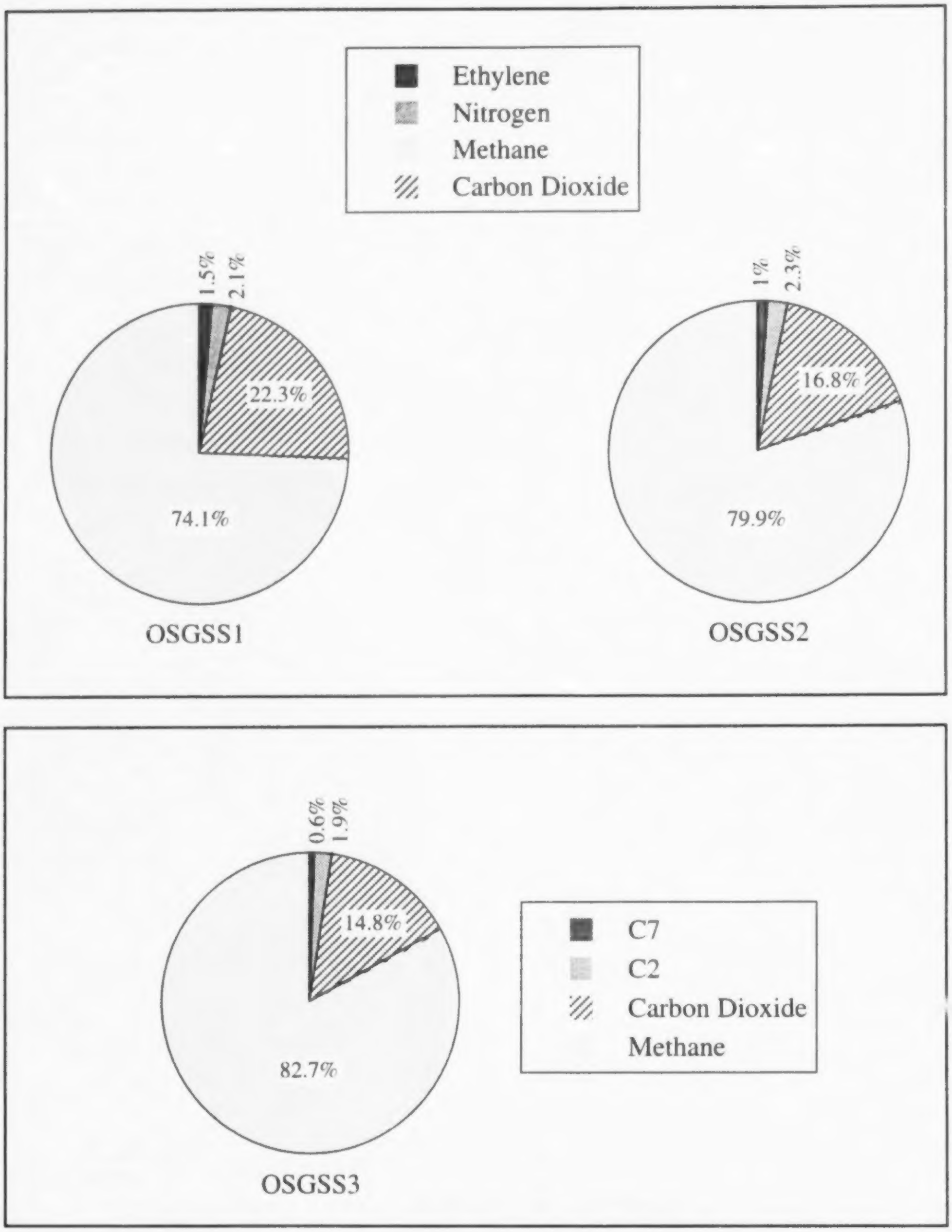

Figure 4.55 Composition of Evolved Gas from McMurray Formation Oil Sands

CHAPTER 5 PARAMETRIC ANALYSIS OF SAGD PROCESS

"What is research but a blind date with knowledge?"
Will Henry

5.1 Introduction

As will be seen subsequently in Chapter 6, the geomechanical response of the Phase A reservoir was complex; reacting to both near and far-field temperatures and pore pressures. The instrumentation response to the SAGD process was equally complex, especially the extensometers which measured abrupt changes in behavior. To aid in elucidating fundamental geomechanical principles affecting the SAGD process and to gain insight into the reservoir response to thermal and pore pressure loading, a parametric analysis of the SAGD process was conducted. Recognition of the aforementioned complexities resulted in selecting an "ideal" Phase A geological cross-section for the parametric analyses. An ideal (meaning simplified not the most correct) cross-section, with geologic simplicity and reasonable boundary conditions provided a problem of tractable size for analyses to identify the important or relevant geomechanical processes which may be occurring during SAGD. The parametric analyses also provided a framework for the rational selection of formation properties for the full geotechnical cross-section analysis presented in Chapter 7.

Fully coupled thermal-stress-fluid flow analyses are extremely difficult to conduct. While fully coupled mathematical formulations exist (Hart, 1983; Aboustit et al., 1982; Tortike, 1991), the computational effort in their solution would at best be described as staggering and continues to be an area of active research, one thankfully outside the scope of this thesis. Consequently, a decoupled approach was adopted for conducting the parametric analyses. The decoupled approach consisted of conducting a reservoir simulation of SAGD for the ideal cross-section conditions and utilizing the temperature and pore pressures as input to an effective stress geomechanical simulation of the formation response to SAGD. In agreement with Tortike (1991), that while the removal of "feedback" to the fluid flow model would not allow conclusions to be drawn regarding the fluid solution, this decoupled approach would permit conclusions to be drawn and inferences to be made concerning the likely response of the formation to the SAGD process.

5.2 Numerical Models

Two numerical programs were utilized for the parametric analyses: 1) ISCOM, a fully implicit, four phase numerical reservoir model for simulating hot water injection, steam injection and dry or wet combustion and 2) FLAC, a two dimensional explicit finite difference code which simulates the behavior of structures built of soil, rock or other materials which undergo plastic flow when their yield limit is reached. The following sections briefly describe the two numerical models.

5.2.1 ISCOM

ISCOM is a reservoir simulation program developed by the Computer Modelling Group. It is a multi-component, four phase finite difference model capable of one, two, or three dimensional simulations in radial Cartesian or curvilinear coordinates. Reservoir properties such as porosity, permeability, pressure, temperature, and fluid saturations can vary spatially. Heat transport includes both convection and conduction. The heat transfer and fluid flow equations are solved fully implicitly. Fluid and rock properties are functions of both fluid pressure and temperature. Details on the models theoretical development and solution techniques can be found in Rubin and Buchanan (1985). ISCOM was used extensively for reservoir modeling studies of the Phase A steam trials.

5.2.2 FLAC

FLAC is a two-dimensional explicit finite difference program for engineering mechanics computation. This program simulates the behavior of structures built of soil, rock or other materials that may undergo plastic flow when their yield limits are reached. Materials are represented by elements, or zones, which form a grid that is adjusted by the user to fit the shape of the object to be modeled. Each element behaves according to a prescribed linear or non-linear stress/strain law in response to the applied forces or boundary restraints. The material can yield and flow, and the grid can deform (in large strain mode) and move with the material that is represented. The explicit, Lagrangian, calculation scheme and the mixed discretization zoning technique used in FLAC ensures that plastic collapse and flow are modeled very accurately. Several built-in constitutive models are available that permit the simulation of highly non-linear, irreversible response representative of geologic, or similar, materials. FLAC also contains a built-in programming language FISH (short for FLACish). Details of FLAC, its capabilities and application examples can be found in Cundall and Board (1988), Itasca (1995), and Larsson, et al.,(1989).

5.3 Idealized Reservoir

5.3.1 Geometry

An ideal cross-section with simplistic geology and boundary conditions provides a problem of manageable size for conducting a parametric study. Figure 5.1 illustrates the idealized cross-section and geology of the UTF Phase A reservoir. A 20 m oil sands reservoir, underlain by limestone, is exploited using a series of horizontal wellpairs spaced 26 m apart. The injection and production wells are 4 m apart, vertically, with the production well 3 m above the limestone. Assuming ideal start-up conditions, each wellpair begins steaming operations simultaneously, consequently, the problem can be reduced to a 13 m wide symmetrical zone; as illustrated in Figure 5.2.

The finite difference grid developed for reservoir simulations is shown in Figure 5.3 (a). All four sides of the reservoir were no flow boundaries; the left and right sides are lines of symmetry and the upper and lower boundaries are assumed to be effectively sealed by the shale overburden and limestone underburden. The left and right boundaries were also treated as no heat loss boundaries. Conduction heat losses were assumed to occur at the overburden and underburden boundaries. Figure 5.3 b) illustrates the finite difference grid developed for the geomechanical analyses. The bottom boundary was assumed fixed and the left and right boundaries allow only vertical displacement.

5.3.3 Material Properties

Table 5.1 provides the reservoir and fluid properties used for the ISCOM reservoir simulation. The reservoir simulations were completed prior to the completion of the thermomechanical properties testing program so several variables do not correspond with the laboratory results. One example is "rock" thermal conductivity, which was chosen as 1.74 W/m°C. As described in §4.4.2, oil sands has a bulk thermal conductivity closer to 1.6 W/m°C over the temperature range 20 °C to 225 °C

The selection of material properties for geomechanical analyses is controlled to some extent by the "constitutive" model chosen to represent formation materials. Suitable models available within FLAC include: 1) transversely isotropic elastic; 2) modified Cam-clay plasticity; 3) Drucker-Prager plasticity; 4) double-yield (cap) plasticity; 5) isotropic elastic; 6) Mohr-Coulomb plasticity; and 7) strain-softening/hardening plasticity. The strain-softening/hardening and double yield models are variants of the Mohr-Coulomb plasticity model. In the selection of an appropriate model for engineering analysis, a compromise between matching the "real" behavior as closely as possible and keeping it as simple as possible, especially in the case of parametric analyses was sought; for the present numerical study, a Mohr-Coulomb plasticity model was chosen.. The following properties are required with the Mohr Coulomb plasticity model:

1) Young's modulus;
2) Poisson's ratio;
3) cohesion;
4) friction angle;

5) dilation; and

6) tension.

Using the FISH capabilities of FLAC, the variation of Young's modulus with effective confining stress, as illustrated in Figure 4.37 and described by Equation 4.24, was also implemented within the material model. The FISH capabilities were also utilized for examining the influence of inputting the laboratory determined relationship between bulk modulus and effective confining stress. This is discussed in §5.6.6.

For the Mohr-Coulomb plasticity model, the failure envelope is defined by the yield function, f^s:

$$f^s = \sigma'_1 - \sigma'_3 N_\phi + 2c\sqrt{N_\phi} \qquad [5.1]$$

and a shear potential function, g^s, which follows a non-associated flow rule and has the form:

$$g^s = \sigma'_1 - \sigma'_3 N_\psi \qquad [5.2]$$

where $N_\psi = \dfrac{1+\sin\psi}{1-\sin\psi}$; and

ψ = dilation angle

Detailed theoretical of this model can be found in Vermeer and de Borst (1984). Figure 5.5 illustrates the idealized form of the stress-strain curve represented by the Mohr-Coulomb plasticity model. A comparison with oil sands triaxial test results will be presented in §5.6.4.

5.4 Analysis Procedure

As stated previously, an uncoupled analysis was conducted to examine the geomechanical response of an ideal reservoir undergoing SAGD processes. The reservoir simulation results utilized in this thesis were obtained from the results of reservoir simulations conducted by AOSTRA on the SAGD process. The process history assumed for the reservoir simulations was as follows:

1) For the first 100 days of steaming, steam is injected in the producer and the injection well serves as the production well. This arrangement helps promote the growth of a steam chamber;

2) At 100 days, communication is achieved between the two wells;

3) At 101 days, the top well is switched to injection and the bottom to production. The process is placed on steam trap control, as discussed in Section 3.2; and

4) A steam injection pressure of 2600 kPa and a production pressure of 2400 kPa are maintained throughout the simulation. The complete simulation period was 730 days.

5.4.1 Temperature and Pore Pressure

The temperature and pore pressure results from the reservoir simulations were treated as known variables for input into FLAC. Temperature and pore pressure were selected at 10 days, 85 days, 100 days, 101 days, 180 days, 250 days, 365 days, 458 days, 591 days and 730 days. The total time of 730 days corresponds closely to the period of instrumentation observation during the Phase A SAGD trials. Figures 5.5 through 5.14 illustrate the temperature distribution for these time intervals while Figures 5.15 through 5.22 show the pore pressure distribution. Pore pressure distributions for time 591 and 730 days have not been shown as no change occurred beyond time 458 days.

In reviewing Figures 5.5 to 5.24, it is important to note the significant time lag between temperature and pore pressure development within the reservoir. At a simulation time of 365 days, essentially the entire reservoir has reached injection pore pressures while the 200°C isotherm bounding the steam chamber encompasses only about 40% of the reservoir. As will be shown subsequently, this "time lag" aspect of steam chamber development is a significant factor controlling formation response to the SAGD process.

5.4.2 Base Analysis

A "base" analysis was conducted utilizing a selection of material properties estimated to be "average" values for the UTF Phase A oil sands formation. Table 5.1 lists the material properties assumed for both the ISCOM (reservoir) and FLAC (geomechanics) base case analyses. Results from the base analysis provides:

- insight into possible geomechanical mechanisms occurring within the reservoir; and
- a reference point for comparison with the results from the parametric analysis.

The selection of $K_o = 1.5$ as a base case value was based on mini-frac tests conducted prior to the Phase A project. Chinna and Bassi (1987) report on two sets of mini-frac tests conducted at various injection rates in both the oil sands and underlying limestone. The authors conclude the minimum stress gradient in the oil sands to be 21.6 kPa/m. This value was used as a bulk density value in the geomechanical analyses. Chinna and Bassi (1987) do not provide estimates of K_o. In subsequent mini-frac testing (Thurber, 1989), a range of K_o of 1.3 to 1.7 was estimated based on fracture extension pressure analyses. Consequently, K_o=1.5 was chosen for the base analysis.

Uncoupled geomechanical analyses were conducted using the following steps:

1) in situ stresses equilibrated within grid;
2) pore pressures obtained at 10 days were applied to grid and stress equilibrium solved;

3) temperatures obtained at 10 days were applied to grid and stress equilibrium solved; and
4) steps 2) and 3) repeated sequentially for all time steps up to 730 days.

5.4.3 Parametric Analyses

Table 5.2 provides the material properties which were varied for the parametric analyses. Analyses were completed for five parameters whose values were chosen both lower and higher than the base case value. Through comparison of the base analysis results and each parametric analysis, the magnitude of influence of a particular parameter can be assessed. These comparisons provide a framework for evaluation of laboratory geomechanical test results and the selection of material parameters for the geotechnical cross-section analyses presented in Chapter 7. Kovari (1977) in a review of elasto-plastic analysis in the design practice of underground openings succinctly states that "the real purpose of numerical computations is mostly a parameter analysis" - the author could not agree more.

5.5 Base Analysis Results

The following discussion provides pertinent results from the base analysis to describe the formation response to the steam assisted gravity drainage process.

5.5.1 Mobilized Strength

For presentation of the analysis results, mobilized strength will be defined as a strength/stress ratio or failure index. The state of stress within any zone in the model can be expressed in terms of principal stresses, σ'_1 and σ'_3. This stress state, in general, will plot as a Mohr circle "a", with a radius r_a, as illustrated in Figure 5.23. The strength for this stress state is determined by holding σ'_3 constant while increasing or decreasing σ'_1 until the circle "b", with radius r_b, touches the failure envelope. The ratio of the radii for these two circles, r_b / r_a, is defined as the failure index. The ratio is expressed as:

$$ {}^{r_b}\!/_{r_a} = \frac{\sigma'_{1f} - \sigma'_3}{\sigma'_1 - \sigma'_3} \qquad [5.3]$$

where $\sigma'_{1f} = \left(\frac{1+\sin\phi'}{1-\sin\phi'}\right)\sigma'_3$

Figures 5.24, 5.25, 5.26, 5.27, 5.28, 5.29, and 5.30 illustrate the failure index distribution within the reservoir for the simulation times 85, 180, 250, 365, 458 and 730 days, respectively.

For early times, 85 and 180 days, the failure index is relatively low reaching a value of approximately 3.0 at 180 days. Even though the steam chamber has begun to develop at 180 days, the thermal expansion induced stress increases are sufficiently low so that for the level of effective confining stress at 180 days, the failure index remains high. At 250 days however, the mechanism changes dramatically. The injection pore pressures encompass a majority of the lower region of the reservoir and under the influence of an expanding steam chamber and its concomitant thermal expansion induced stresses, a large zone along the left boundary exhibits shear failure. Note that since an elastic-perfectly plastic model was chosen for the oil sands, by definition, the failure index will not fall below a value of unity.

As postulated in §4.6.1, Figure 5.27 illustrates schematically the mechanism leading to the development of yield zones within the reservoir, as shown in Figure 5.26. The primary geomechanical processes leading to yield conditions are:

1) shallow depth of the reservoir results in small increases in vertical total stress;
2) opposing zones of thermal expansion from adjacent steam chambers cause large increases in the horizontal total stress; and
3) rapid advance of pore pressure ahead of the thermal front reduces the effective confining stress.

At 365 days (Figure 5.28), the extent of the yield zone increases as a result of continued horizontal stress increases from a growing steam chamber. The entire reservoir has essentially reached a pore pressure equal to the injection pressure. At 458 days (Figure 5.29), the shear yield zone has grown to the full height of the reservoir in response to the vertical growth of the steam chamber. With the steam chamber completely enveloping the reservoir at 730 days (Figure 5.30), the lack of opposing zones of thermal expansion which cause a reduction in induced shear stress, the distribution of failure indices has changed dramatically, increasing to approximately 4.0 along the left boundary. The magnitude of the failure index is instructive only in that it reveals an unloading response after the coalescence of the opposing steam chambers. The model chosen for oil sands does not incorporate its actual strain-softening behavior so post-peak response is based solely on perfect plastic behavior.

Figure 5.31 illustrates the stress path followed by an element along the left boundary at the same elevation as the wellpairs. The impact of reduced effective confining stress is clearly shown in this figure. From time 101 days to 350 days, q increases by only 0.6 MPa, due mainly to thermal induced horizontal stresses, while p' decreases by 1.9 MPa. This clearly highlights the impact of a rapid advance in pore pressure within the reservoir ahead of the heating front.

In analyzing mobilized strength, the failure index was determined only by stress levels and the strength parameters ϕ' and c'. It is interesting then to address issues linking strength to deformation and stress path effects in light of the previous discussion. The stress path shown in Figure 5.31, which is representative of the critical geomechanically influenced zones within the reservoir, is generally termed an "active compression" stress path. While no oil sands triaxial tests were conducted along this stress path in the current research, Oldakowski (1994) conducted four active compression stress path tests on McMurray Formation oil sands. The results of these four tests are illustrated in Figure 5.32. Following an extremely small volumetric contraction, typically less than 0.01%, dense oil sands dilates very quickly along the active compression stress path. This is not unique to oil sands. Khatrush (1987) conducted a detailed study of the yielding of a fine sand in triaxial stress space and found that along an active compression stress path, expansive volume change took place almost right from the beginning of shearing. As one would expect for dense sand, the change in volume is largely dependent on the change in the mean normal stress, p', which decreases during active compression.

Tortike and Farouq Ali (1991) provide a relationship linking absolute permeability change to volumetric strain. The relationship was based on the Kozeny-Carmen equation (Amyx, Bass and Whiting, 1960) and is expressed as:

$$\frac{k_a}{k_a^o} = \frac{\left(1+\frac{\varepsilon_v}{\phi_o}\right)^3}{\left(1+\varepsilon_v\right)} \qquad [5.4]$$

where k_a = new absolute permeability;
k_a^o = original absolute permeability;
ε_v = volumetric strain; and
ϕ_0 = original porosity.

Recognizing that the Mohr-Coulomb model chosen for the ideal analyses does not adequately model volumetric strains, an approximation to the possible shear induced changes in absolute permeability which may occur within the reservoir can be obtained by applying Equation 5.4 to the active compression test results of Oldakowski (1994). This will permit the development of a relationship between the failure index (mobilized strength) and absolute permeability ratio, k_a/k_a^o.

The deviatoric stress-strain curves shown in Figure 5.32 can be converted to equivalent mobilized strength versus volumetric strain curves. Based on Equation 5.4 then, Figure 5.33 illustrates the relationship between mobilized strength and k_a/k_a^o. Since shear induced volume changes are highly dependent on the minor effective principal stress, σ'_3, it is not surprising the change in k_a/k_a^o is also dependent on the σ'_3. No attempt was made to normalize these curves to σ'_3. For the purposes of examining the possible variation of k_a within the reservoir, the analytical expression given in Figure 5.33 was used for generating contours of k_a/k_a^o.

Figure 5.34 illustrates the distribution of k_a/k_a^o for time 180 days and 365 days. At 180 days, the magnitude of shear induced permeability changes are small, increases of approximately 3.5%. At 365 days however, the relationships developed above indicate increases of approximately 45%.

To provide a "better feel" for the magnitude of change in absolute permeability, Figure 5.35 illustrates the distribution of k_a assuming k_a^o = 7.5 d. A value of 7.5 d was chosen based on the average of k_h=10 d and k_v= 5 d, typical formation properties assumed for the UTF Phase A reservoir (Gittins et al., 1992). A large volume of the reservoir has exhibited shear induced volume changes ***in advance*** of the approaching steam chamber. The reservoir properties in this zone will have changed and as such, reservoir simulations which do not account for the increase in absolute permeability may be in error.

5.5.2 Deformation

As previously discussed, the ideal analysis was limited in its representation of expected deformations since a linear elastic perfectly plastic model was chosen for the analyses. Most researchers (Agar, 1984; Kosar, 1989) have concluded that oil sands are generally non-linear and exhibit strain softening behavior. Consequently, the deformation response predicted in the ideal analysis would tend to underestimate the deformations under field conditions. Regardless of this limitation however, examining the pattern of displacements and their variation with time is instructive for interpreting field instrumentation response.

Figures 5.36 and 5.37 present the displacement vectors for times 101 days and 365 days, respectively. At 101 days, the major component of deformation is laterally outward from the wellpairs with the maximum displacements occurring near the wellpairs. The maximum displacement at 101 days was 9 mm. This displacement response changes dramatically at time 365 days where vertical displacements along the left boundary represent the major component of deformation. The maximum displacement at 365 days was a vertical displacement at the top of the reservoir of 63 mm.

5.5.3 Strain

5.5.3.1 Vertical Strain

Within the UTF Phase A reservoir, an extensometer (AGE2) was placed above wellpair A1 and at the midpoint between A1 and A3 (AGE3 and AGE4). The position of these extensometers was illustrated in Figure 3.15. Deformations computed from the base analysis were utilized to calculate the vertical strain response with time for these two extensometer locations. Figure 5.38 illustrates the variation in vertical strain along the left boundary of the model, representing the response of extensometer AGE3 and AGE4 and along the wellpair boundary, representing the response of extensometer AGE2. The following are the main observations:

1) the development of extensional strains at "AGE2" is related directly to the vertical growth of the steam chamber. Recalling the location of the steam chamber ceiling, represented by the

200°C isotherms in Figures 5.5 to 5.14, the top of the steam chamber directly correlates with the elevation where the vertical strain changes from extension to compression;

2) above the steam chamber, "AGE2" exhibits compressional vertical strains. Even though the reservoir is at shallow depth, sufficient confinement exists to create a zone of compression above the thermally expanding steam chamber; and

3) development of extensional strains at "AGE3" occur very rapidly and exhibit high gradients of vertical strain.

5.5.3.2 Maximum Shear Strain

Figures 5.39 to 5.45 present the maximum shear strain history within the reservoir from 85 to 730 days. A plasticity indicator has also been included in each figure to correlate zones of largest maximum shear strain with zones undergoing shear yield. As anticipated from the previous examination of mobilized strength, the peak shear strain contours correspond directly with zones at a condition of shear yield.

At 85 days (Figure 5.39), the magnitude of maximum shear strain is small, approximately 0.12%, and is situated at the boundaries of the thermal front. At 180 days (Figure 5.40), shear straining is still controlled by the geometry of thermal front but shear strains are beginning to increase along the left boundary. No plastic yield has been detected at this time step.

At 250 days (Figure 5.41) however, the shear strain behavior reflects the impact of reduced effective stresses from pore pressure increases and increasing horizontal total stresses from thermal expansion of the growing steam chamber. The magnitude of maximum shear strain reaches 0.6% at this time step and corresponds well with the location of plastic yield. The primary cause of shear distortion along the left or midpoint boundary is the reduction in the vertical effective stress and the increase in horizontal total stress. Figure 5.42 illustrates the distribution of σ'_y along with the principal stress tensor and plasticity indicator clearly showing the correlation of yield with the reduction in σ'_y.

The areal extent of shear distortion enlarges in response to a growing steam chamber at time 365 days (Figure 5.43) reaching a magnitude of 0.7%. Injection pressures essentially encompass the entire reservoir while the thermal zone is only beginning to grow rapidly; the steam chamber occupies approximately 40% of the reservoir. At 458 days (Figure 5.44), the pore pressure within the reservoir has reached steam injection pressure or 2600 kPa. The development of the thermal front is beginning to be dominated by slope drainage mechanisms as the steam chamber progresses laterally through the reservoir. Vertical unloading is continuing with a large region along the midpoint boundary existing at an $\sigma'_y < 500$ kPa. Shear straining within this region where $1 \leq F_i \leq 2$ (see Figure 5.30) is controlled largely by the reduction in σ'_3.

While there is a slight change in the distribution of shear strain at 730 days (Figure 5.45), it is important to note that the maximum shear strains have decreased slightly along the left boundary and points previously at yield have unloaded into elastic stress space. This stress path was discussed in §5.5.1 and illustrated in Figure 5.32.

A small increase in shear strain above the wellpairs is indicative of the deformation response of the reservoir as the steam chamber "coalesces" with its symmetric counterpart along the left boundary. The minor principal effective stress has increased from a minimum of 500 kPa seen at earlier time steps to approximately 1000 kPa at 730 days leading to an increase in mean normal effective stress and shear strength.

The observations from shear strain development can be summarized as follows:

1) shear strains corresponding to shear yield conditions occur at the midpoint between the wellpairs in a cooler region of the reservoir; T≈20°C; and

2) the maximum shear strain occurs at the same elevation as the wellpairs.

5.6 Parametric Analysis Results

5.6.1 Stiffness

The variation of Young's modulus with effective confining stress for the low, base and high cases was illustrated in Figure 4.35. At the outset, it is expected that lower modulus material should, for equivalent conditions, exhibit less shear straining and show a lower failure index than the base case. The primary reason for this expectation is that the base case clearly showed that once pore pressures were equal to the steam injection pressure, shear stress and strain within the reservoir were controlled by thermal expansion induced stress changes. Temperature changes cause stress changes according to:

$$\Delta\sigma_{ij} = -\delta_{ij}\ \frac{E}{(1-2\nu)}\ \alpha\ \Delta T \qquad [5.5]$$

where $\Delta\sigma_{ij}$ = change in stress ij (plane strain);
δ_{ij} = Kronecker delta;
E = Young's modulus;
ν = Poisson's ratio
α = linear thermal expansion coefficient; and
ΔT = temperature change.

As seen be Equation 5.5 , a reduction in E will result in a decrease in $\Delta\sigma$ and subsequently less thermal induced stress. Of course, the corollary to this is that a higher Young's modulus will result in greater shear strain and a larger zone undergoing shear yield in comparison to the base case.

Figures 5.46 and 5.47 illustrate the failure index distribution at 365 days for the low and high stiffness cases, respectively. The base case failure index at 365 days was provided in Figure 5.28. As expected, the low stiffness case shows a smaller zone of yield and the high stiffness case, a larger yield zone than the base case. The magnitude of the difference between all three cases is small. This is due to the convergence of the E versus σ'_3 curves selected for the low, base and high cases. As shown in Figure 4.35, all three curves converge in the range of low effective confining stress. As discussed in §5.5.1, prior to the arrival of any significant thermal induced stresses, the pore pressures within the reservoir become equal to the steam injection pressure thus reducing the effective confining stress. The corresponding distributions of maximum shear strain for the low and high stiffness parametric analysis are shown in Figure 5.48 and 5.49, respectively. The results to note from these two figures is that while the difference in failure index distribution was small, the magnitude of maximum shear strain more than doubles from the low stiffness to the high stiffness case. This serves again to illustrate the interrelationship between pore pressure (effective stress) and temperature (thermal induced stresses) throughout the SAGD process history. The magnitude of thermal induced stress is a direct function of Young's modulus, as described in Equation 5.5. For a time of 365 days, Figure 5.50 provides the distribution of Young's modulus for the high stiffness analysis. The stiffness within and around the steam chamber is higher than the stiffness along the left boundary. This creates a condition where an increment of thermal induced stress is computed using a stiffness substantially higher than the stiffness of the region resisting the thermal induced stress increment. Consequently, the magnitude of distortional strain increases substantially for the higher stiffness case.

As discussed in §4.6.2.1, Byrne et al., (1987) provide evidence to suggest the stiffness at lower effective stress may be larger than Young's modulus values computed in accordance with Equation 4.30. Consequently, several constant stiffness analyses were conducted. Figure 5.51 illustrates the failure index distribution for an E=200 MPa analysis and Figure 5.52 shows the failure index distribution for an E=1200 MPa analysis, each at time 365 days. For the E=200 MPa analysis, the zone of smallest failure index (highest mobilized strength) continues to occur along the left boundary but does not indicate shear yield as the failure index has only reached a value of approximately 2.5. This follows from the previous discussion regarding the relationship between E and thermal induced stresses. For the E=1200 MPa analysis however, large zones within the reservoir are undergoing shear yield with a substantial portion of the remaining reservoir approaching yield conditions.

This series of parametric analyses have shown that the Young's modulus value chosen for oil sands has a dramatic effect on the stress-deformation response of the reservoir.

5.6.2 Initial Stress Ratio, K_o

As discussed in §5.4.2, $K_o = 1.5$ was chosen for the base analysis based on the results of mini-frac tests conducted prior to the steaming trials. To examine the sensitivity of the formation response to the initial stress state, two analyses, one for K_o=1.0 and one for K_o=2.0 were conducted. Figure 5.53 shows the failure index distribution at 365 days for the K_o=1.0 analysis. Figure 5.54 illustrates the failure index distribution at 365 days for the K_o=2.0 analysis. Immediately apparent from these two figures in comparison with the base case result (see Figure 5.28) is the relatively small effect the initial stress ratio has had on the final extent of shear yield. For each initial stress state, the stress path followed by an element along the left boundary is illustrated in Figure 5.55a. From time 180 days to 250 days, the rapid evolution of pore pressure results in substantial reduction in the mean normal effective stress. For K_o=1.0, the magnitude of the pore pressure increase is just sufficient to cause yield in the element. For the K_o=2.0 analysis, the element yields sooner, that is, a smaller increment of p' is required to cause yield for an initial K_o=2 stress state. The relative impact of initial stress ratio on the stress path and incipient yield is more clearly shown in Figure 5.55b, a stress path plot for an interior element..

This is an interesting result in that for most geotechnical problems, K_o is an influential parameter for stress analysis. The relative insensitivity of the analysis results to the selection of K_o suggests that the assumption of K_o = 1.5 would be reasonable for any geomechanical analyses of the SAGD process within the limits of the UTF reservoir.

5.6.3 Shear Induced Volume Change

The selection of an elastic-perfectly plastic model for the ideal analyses results in an underestimation of the shear induced volume changes occurring during SAGD processes. A closer examination of the stress-strain relationships will clarify this issue for the present analyses. Utilizing the base analysis material properties listed in the Table 5.2, Figure 5.56 illustrates the idealized stress-strain relationship for the oil sands formation. While the deviatoric stress and stiffness of oil sands are represented reasonably well by the model, the modeled volumetric strain does not represent the strong dilatant potential of locked sands (Dusseault and Morgenstern, 1979). Modifications to the strength parameters can be made to force the model to yield much quicker and hence, initiate shear induced volume changes. The following changes were made to the strength properties assumed for the base analysis:

E = 1200 MPa (constant);
$\phi' = 60°$ (remains unchanged); and
$\psi = 40°$ (increased from 15°).

To permit comparison to analysis results, the stress-strain relationship based on the above parameters has been plotted against shear strain and is illustrated in Figure 5.57. With the earlier onset of yield and a substantially higher dilation angle, improved dilatancy characteristics are evident in the model. A ψ=40° is not unrealistic for the unique, very dense, locked nature of McMurray Formation oil sands. A constant Young's modulus however does not correlate well with material behavior shown in Figure 4.35 but for the purposes of examining the potential for shear induced volume changes is considered adequate. It is interesting to recall that the maximum shear strain developed at 730 days for the base case analysis was approximately 0.8%. For a shear strain of this magnitude, the volumetric versus shear strain relationship shown in Figure 5.57 shows that negligible shear induced volumetric strains would occur. Figure 5.58 illustrates the maximum shear strain distribution for an additional analysis conducted for the above set of parameters. The maximum shear strain only reaches a magnitude of 0.9% indicating that even for the modified material parameters, the model is incapable of capturing the dilatant volume changes which would occur along the left boundary. The distribution of mobilized strength (i.e. failure index) for this dilation analysis was identical to the base analysis case.

The primary reason for the model's inability to represent adequately the dilatant volume changes is related to the method used in computing volumetric strains. Plastic volume change is only computed when an element is at a state of yield. Below yield, the model only calculates elastic volume change. The stress paths illustrated in Figure 5.55 show that elements along the left boundary reach the peak failure envelope only briefly. They then undergo an increase in the mean normal effective stress causing a return to an elastic state and no further calculation of plastic volume changes. In reality, oil sands is a strain softening material and would continue to deform and soften once the peak failure envelope was reached. The substantial difference in stress-strain response, especially volumetrically, between the numerical model and laboratory test results can be seen in Figure 5.59. The triaxial results of Oldakowski (1994) for an active compression stress path, which were utilized in §5.5.1, show the potential for shear induced volume change; approximately 6.0% for an effective confining stress of 0.56 MPa.

5.6.4 Thermal Expansion

The discussion to this point has clearly shown that thermal induced stress changes in zones of reduced effective stress are a controlling factor in the reservoir's geomechanical response to SAGD. To examine the sensitivity of formation response to the magnitude of the coefficient of bulk thermal expansion, three analyses were conducted for the following conditions:

1) $\beta_b = 0.0$ (zero case)

2) β_b = 3.0 x 10^{-5} °C^{-1} (low case)
3) β_b = 6.0 x 10^{-5} °C^{-1} (base case)
4) β_b = 12.0 x 10^{-5} °C^{-1} (high case)

The impact of setting $\beta_b = 0$ is illustrated in Figure 5.60 for time 365 days. Along the left boundary where for all previous analyses yielding had occurred, the level of mobilized strength is low as evidenced by a failure index of approximately 9.5. The higher failure index region in the upper portion of the reservoir is a function of the overburden properties and does not reflect a formation response to SAGD processes. The development of mobilized strength for increasing values of β_b are illustrated in Figure 5.61 and 5.62 for the low and high β analyses, respectively. Note the large yield zone developed in the high case. The impact of the selection of β_b on formation response is directionally the same as for Young's modulus; the larger β_b (E), the larger the zone of shear yield. The degree of sensitivity is difficult to assess. Figure 5.63 illustrates the stress path followed by the "now famous" formation element for each of the thermal expansion parametric analyses, including the base analysis. Note the curve highlighting the stress state at time 180 days. The proximity of the stress state within this element to yield at time 180 days shows the sensitivity of the formation response to the selected value of bulk thermal expansion. The dramatic change in behavior between the β_{base}=6.0x10^{-5} °C^{1} and β_{high}=12.0x10^{-5} °C^{1} suggests that even a moderate increase in β_b will significantly affect the predicted formation response to SAGD processes.

Examination of the shear strain distribution for the high thermal expansion coefficient analysis permits one final comment regarding shear induced volume changes discussed in the previous section. As illustrated in Figure 5.63, the element along the left boundary continues to yield from time 180 days to 250 days under the influence of increasing thermal induced stresses. The impact of this continued loading under yield conditions on the development of shear strains is evident in Figure 5.64; this shear strain distribution was obtained for ψ=15°. The maximum shear strain reaches a value of 2.7%, three times the maximum shear strain attained in the base analysis. The selection of the coefficient of bulk thermal expansion then, will significantly influence the predicted deformation response of the reservoir.

5.6.5 Bulk Modulus from Lab Measurements

The material models within FLAC are formulated based on the shear modulus, G and bulk modulus, K. Using the FISH capabilities of FLAC, the experimentally determined relationship between K and σ', as shown in Figure 4.24, was input directly into the elastic-perfectly plastic Mohr-Coulomb model. The shear modulus was assumed to vary in accordance with the variation of E with effective confining stress. The objective of this parametric analysis was to examine the influence of the rapid decline in stiffness at low effective confining stress.

Figure 5.65 illustrates the impact of a decrease in bulk modulus (increasing compressibility) at low effective confining stress; the magnitude of volume change within the reservoir increases dramatically over the base case conditions. Figure 5.43, which showed the failure index distribution at 365 days for the base case, indicated a maximum volume change of 0.6% within a small region along the left boundary. The failure index distribution shown in Figure 5.65 indicates that volume changes increase substantially, to approximately 1.2%, along the left boundary. As well, the predicted volume change within the steam zone is effected. The base case predicts very low volume changes while the experimental bulk modulus relationship predicts a volume change in excess of 1.0% within the steam chamber. This effect highlights the role that changes in effective confining stress can play on volumetric changes within the reservoir.

5.7 Summary

To aid in determing the fundamental geomechanical principles affecting the SAGD process and to evaluate the reservoir response to thermal and pore pressure loading, a parametric analysis of the SAGD process was conducted. An ideal cross-section, with geologic simplicity and reasonable boundary conditions provided a problem of tractable size for analyses to identify the important and relevant geomechanical processes occurring during SAGD.

The parametric analyses revealed that for a series of horizontal wellpairs, zones of yield within the reservoir occur between wellpairs, *in front of a growing of the steam chamber*. The primary geomechanical phenomena contributing to yielding conditions are:

- the shallow depth of the reservoir results in small increases in vertical total stress;
- the opposing zones of thermal expansion from adjacent steam chambers cause large increases in the horizontal total stress; and
- rapid advance of pore pressure ahead of the thermal front reduces the effective confining stress. For the UTF reservoir conditions, steam injection pressures were chosen very close to the total overburden stress creating low effective stress conditions within the reservoir.

Detailed examination of the results of a base case analysis and of a series of parametric analyses conducted to examine formation response to material property selection resulted in the following observations:

- zones within the reservoir which undergo shear yield follow an active compression stress path to failure. Following an extremely small volumetric contraction, dense oil sands dilate very quickly along the active compression stress path. The resulting shear induced volume changes lead to a 45% increase in the reservoir absolute permeability, in a zone in front of the steam chamber;
- pore pressure increases within the reservoir resulting in very low effective confining stresses will also result in substantial volume change;
- early in the SAGD process, formation displacements are primarily horizontal or laterally outward from the wellpairs. At later times, in response to shear yield and an expanding steam chamber, the formation displacements are primarily vertical;

- at the wellpairs, the top of the steam chamber directly correlates with the elevation where vertical strains change from extension to compression; extension within the steam chamber, compression above the steam chamber;
- the development of extensional vertical strains midway between wellpairs occurs rapidly and exhibits high gradients of vertical strain;
- the zones of largest maximum shear strain correspond directly with zones undergoing shear yield;
- the selection of Young's modulus for oil sands has a significant effect on the stress-deformation response of the formation to SAGD;
- a high friction angle for oil sands combined with an active compression stress path results in relative insensitivity to the selection of K_o. The final extent of shear yield within the reservoir is not greatly affected for $1.0 \le K_o \le 2.0$; and
- the selection of the coefficient of bulk thermal expansion significantly influences the predicted deformation response of the reservoir, the larger the coefficient, the larger the thermal induced stress increment and consequently, the larger the zone of shear yield.

Parameter	**Model**	**Oil Sands**	**Overburden**
Bulk Density, γ_t	FLAC	2.153 kPa/m	2.153 kPa/m
Initial Temperature, T_o	ISCOM	8 °C	
Original Reservoir Pore Pressure, p_o	Both	550 kPa	varies to 0 kPa at surface
Porosity, n_o	Both	32 %	
Horizontal Permeability, k_h	ISCOM	4 darcies	
Permeability Ratio, k_h/k_v	ISCOM	4	
Friction Angle, ϕ'	FLAC	60°	60°
Cohesion,c'	FLAC	0 kPa	0 kPa
Dilation Angle, ψ	FLAC	15°	0°
Initial Vertical Effective Stress (@160 m)	FLAC	2780 kPa	varies to 0 kPa at surface
Initial Stress Ratio, K_o	FLAC	1.5	1.5
Young's' Modulus Number, E_o	FLAC	343	
Young's Modulus Exponent, α	FLAC	0.875	
Bulk Modulus, K	FLAC		667 MPa
Shear Modulus, G	FLAC		308 MPa
Poisson's ratio, ν	FLAC	0.3	0.3
Rock Thermal Conductivity, k	ISCOM	1.736 W/m°C	
Rock Heat Capacity, C	ISCOM	2056 + 1.22*T	
Rock Compressibility, C_R	ISCOM	$5.0\text{x}10^{6}$	
Rock Thermal Expansion, β_R	ISCOM	$3.84\text{x}10^{5}$	
Volumetric Coefficient of Bulk Thermal Expansion	FLAC	$6.0\text{x}10^{5}$	$6.0\text{x}10^{5}$
Bitumen Density	ISCOM	1008.0 kg/m^3	
Bitumen Heat Capacity	ISCOM	1692.6	
Bitumen Compressibility	ISCOM	$4.5\text{x}10^{7}$	
Bitumen Thermal Expansion	ISCOM	$6.41\text{x}10^{4}$	
Bitumen Thermal Conductivity	ISCOM	1.736 W/m°C	
Water Density	ISCOM	999.9 kg/m^3	
Water Heat Capacity	ISCOM	4185.0	
Water Compressibility	ISCOM	$5.8 \text{ x } 10^{7}$	
Water Thermal Expansion	ISCOM	$1.93 \text{ x } 10^{4}$	
Initial Fluid Saturation:			
S_{oil}	ISCOM	85%	
S_{water}	ISCOM	15%	
S_{gas}	ISCOM	0%	
Steam Thermal Conductivity	ISCOM	.0246 W/m°C	
Overburden (& Underburden) Heat Capacity	ISCOM		2175 kg/m^3
Overburden (& Underburden) Thermal Conductivity	ISCOM		1.73 W/m°C

Table 5.1 Material Properties for Reservoir and Geomechanical Analyses

Parameter	Low	Base	High
Stiffness[‡]		$E = E_o \sigma'_3{}^{\alpha}$	
	$E_o = 250$ $\alpha = 0.875$	$E_o = 343$ $\alpha = 0.875$	$E_o = 450$ $\alpha = 0.875$
Initial Stress Ratio, K_o	1.0	1.5	2.0
Dilatancy[†], ψ	5°	15°	25°
Thermal Expansion*, β_b	3.0×10^{-5}	6.0×10^{-5}	12.0×10^{-5}

[‡] four additional constant stiffness analyses were conducted for E equal to 200, 400, 800 and 1200 MPa

[†] in order to exaggerate the dilatancy response of the formation , ϕ' was reduced to 34°. This caused "premature" shear failure resulting in the initiation of dilatant shear induced volume changes. An additional analysis for $\psi=40°$ was also conducted.

* volumetric coefficient of bulk thermal expansion. This was divided by 3 to obtain the linear coefficient of thermal expansion required by FLAC. An additional analysis was conducted for $\beta_b = 0$.

Table 5.2 Range of Material Properties Chosen for Parametric Analyses

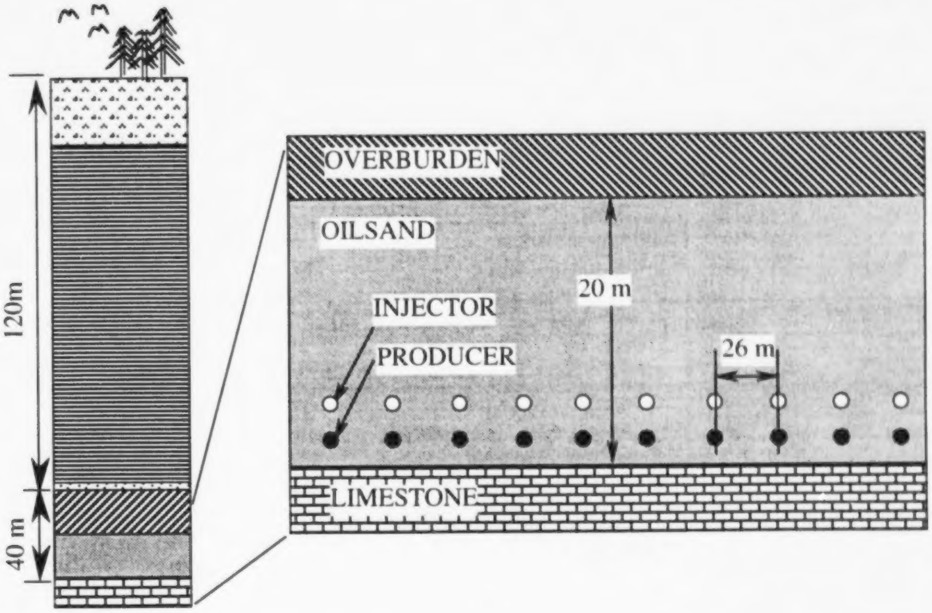
120m
40 m
OVERBURDEN
OILSAND
20 m
INJECTOR
PRODUCER
26 m
LIMESTONE

Figure 5.1 Idealized Geology and Cross Section of UTF Phase A Reservoir

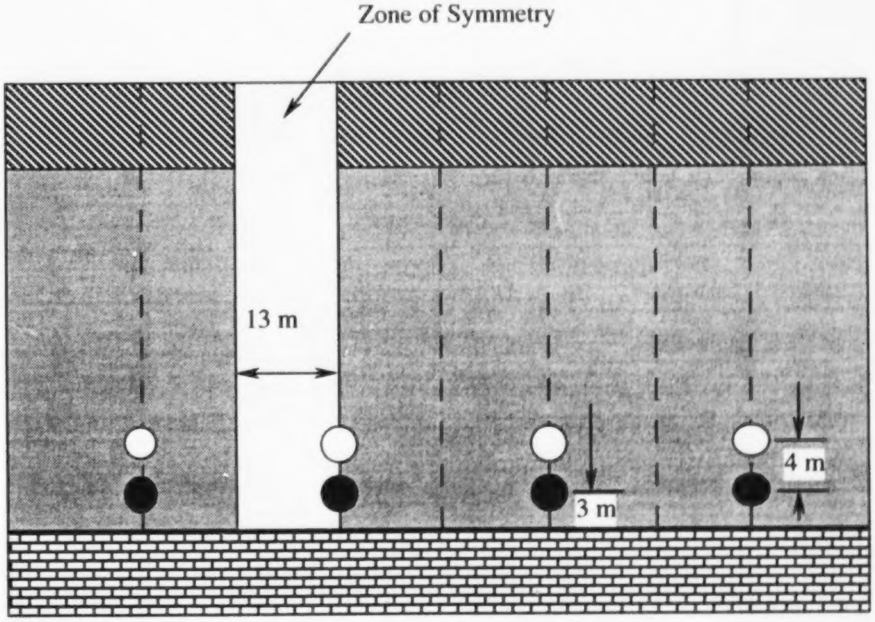
Zone of Symmetry
13 m
3 m
4 m

Figure 5.2 Zone of Symmetry for Ideal Analyses

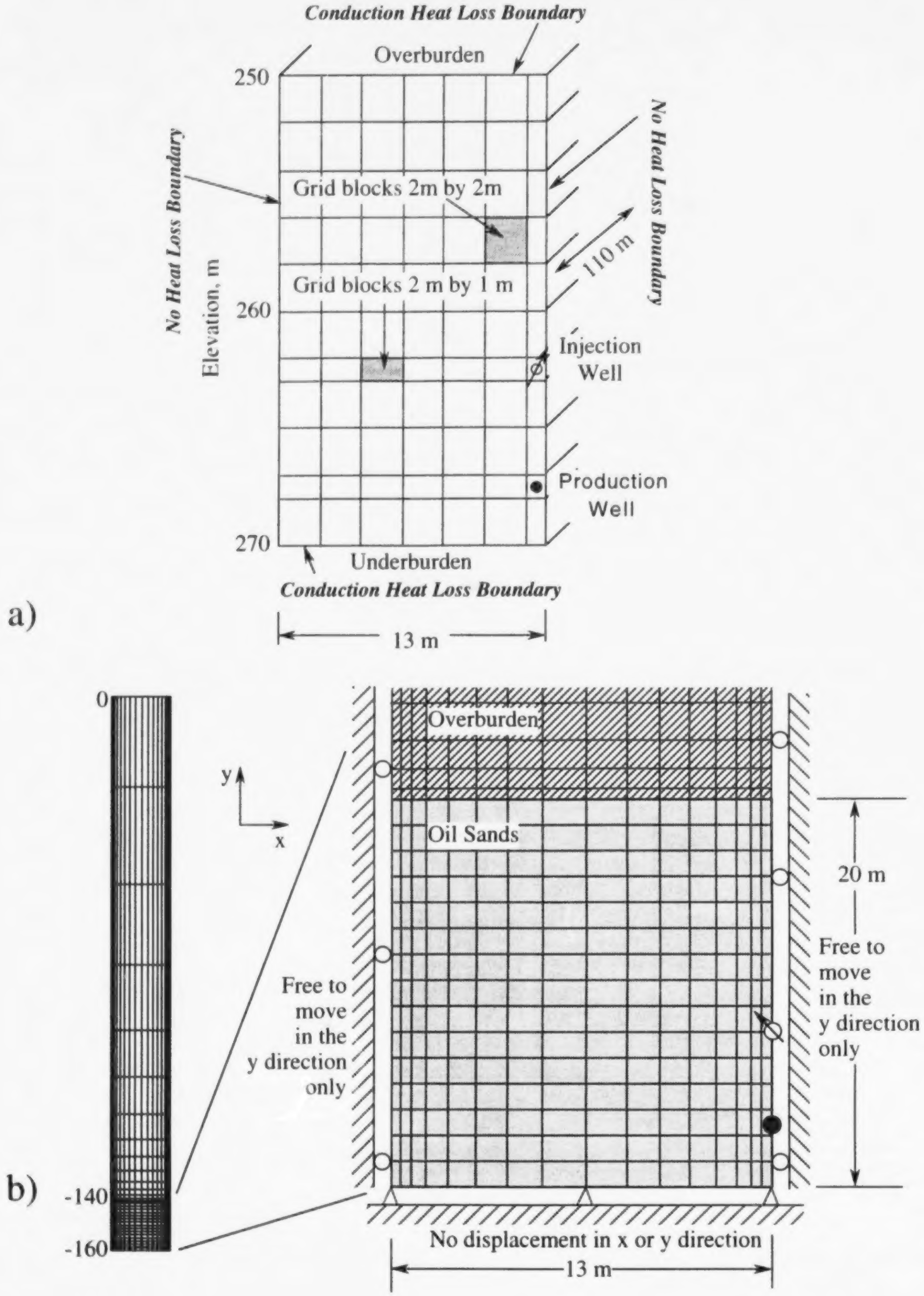
Conduction Heat Loss Boundary
Overburden
250
No Heat Loss Boundary
Grid blocks 2m by 2m
No Heat Loss Boundary
110 m
Grid blocks 2 m by 1 m
Elevation, m
260
Injection Well
Production Well
270
Underburden
Conduction Heat Loss Boundary
a)
13 m
0
Overburden
y
x
Oil Sands
20 m
Free to move in the y direction only
Free to move in the y direction only
b)
-140
-160
No displacement in x or y direction
13 m

Figure 5.3 Finite Difference Grids used in Numerical Analyses: a)ISCOM and b) FLAC

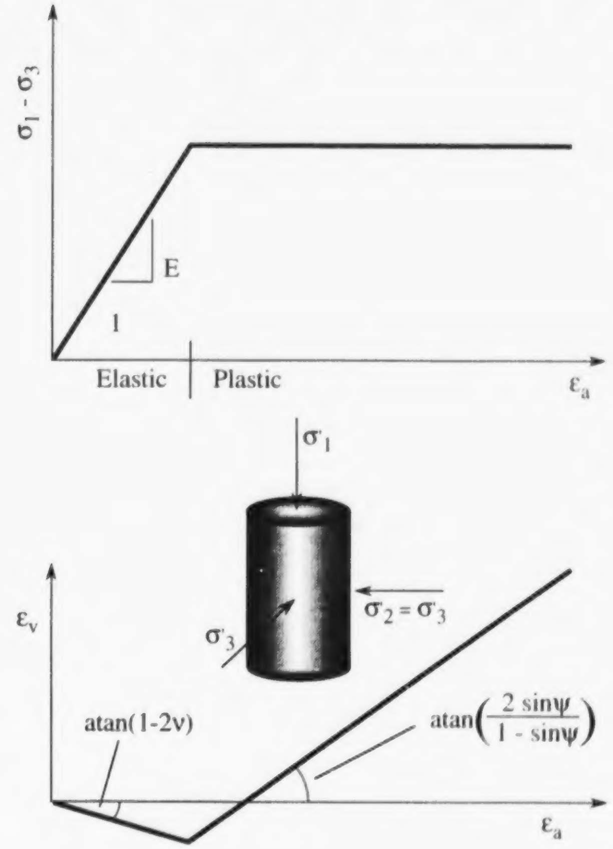
$\sigma_1 - \sigma_3$
E
1
Elastic
Plastic
ε_a
σ'_1
ε_v
σ'_3
$\sigma'_2 = \sigma'_3$
atan(1-2ν)
$\mathrm{atan}\left(\frac{2\sin\psi}{1-\sin\psi}\right)$
ε_a

Figure 5.4 Idealized Relation for Dilation Angle, ψ, from Triaxial Test Results (modified from Vermeer and de Borst, 1984)

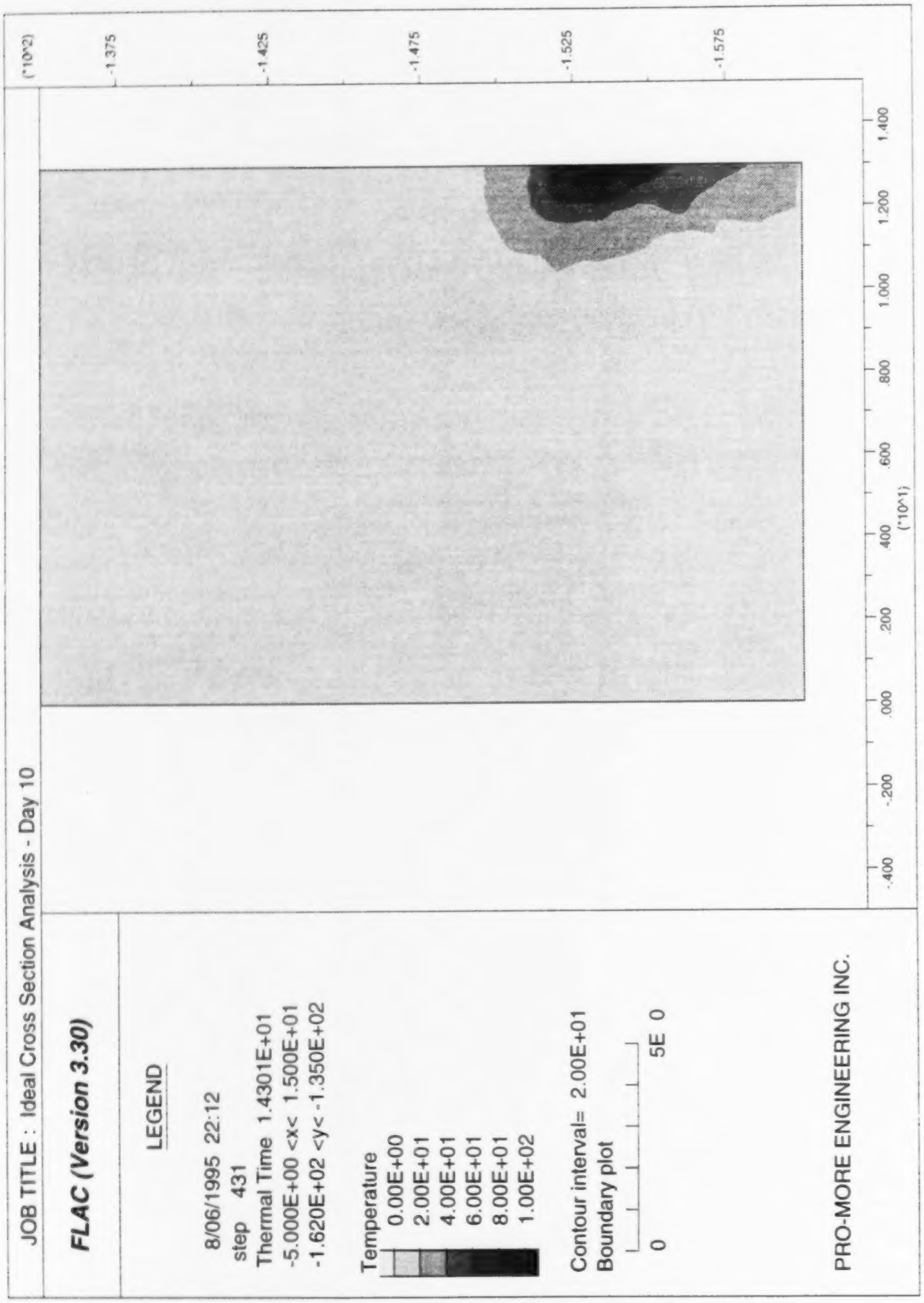

Figure 5.5 Temperature Distribution at 10 Days

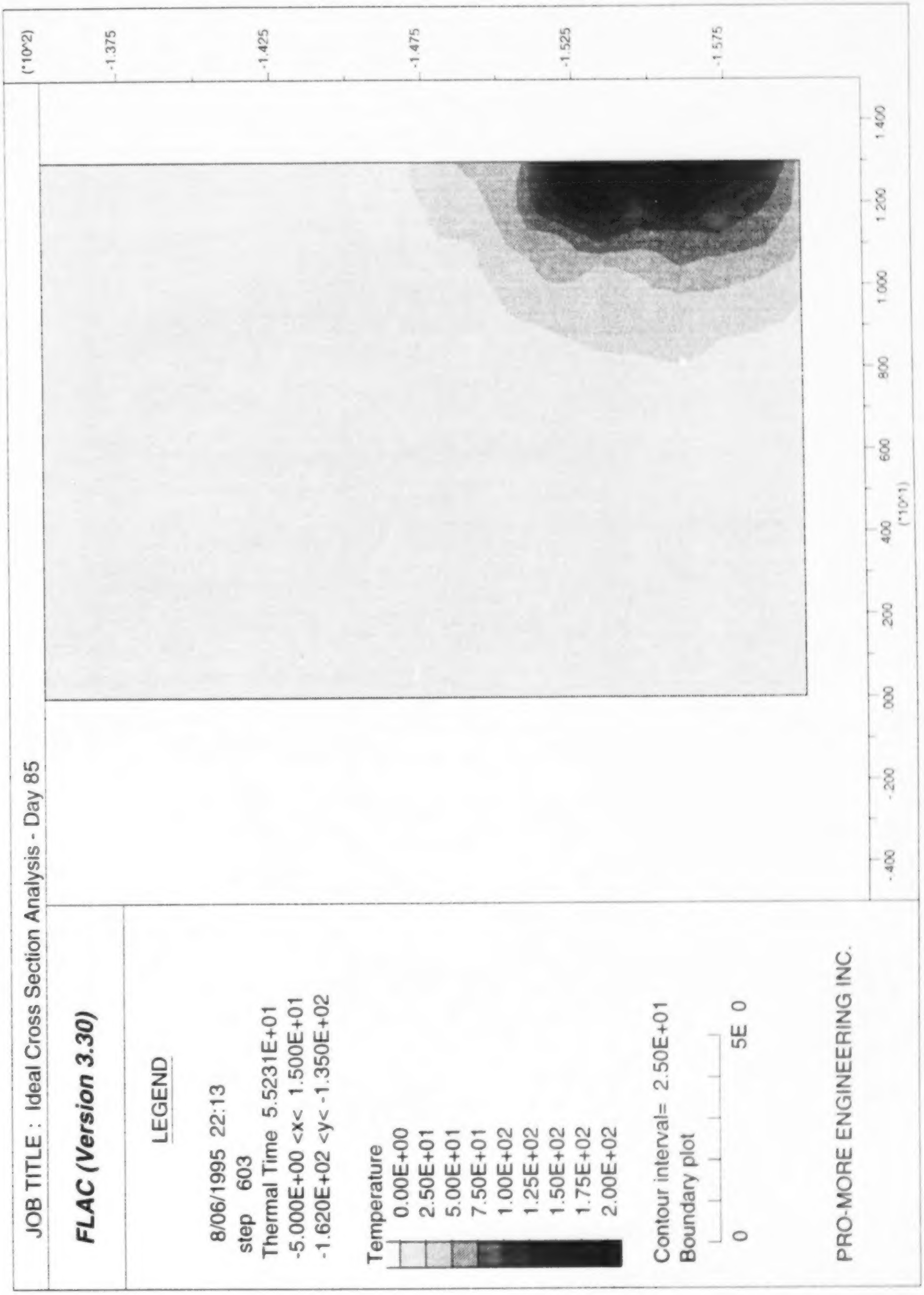

Figure 5.6 Temperature Distribution at 85 Days

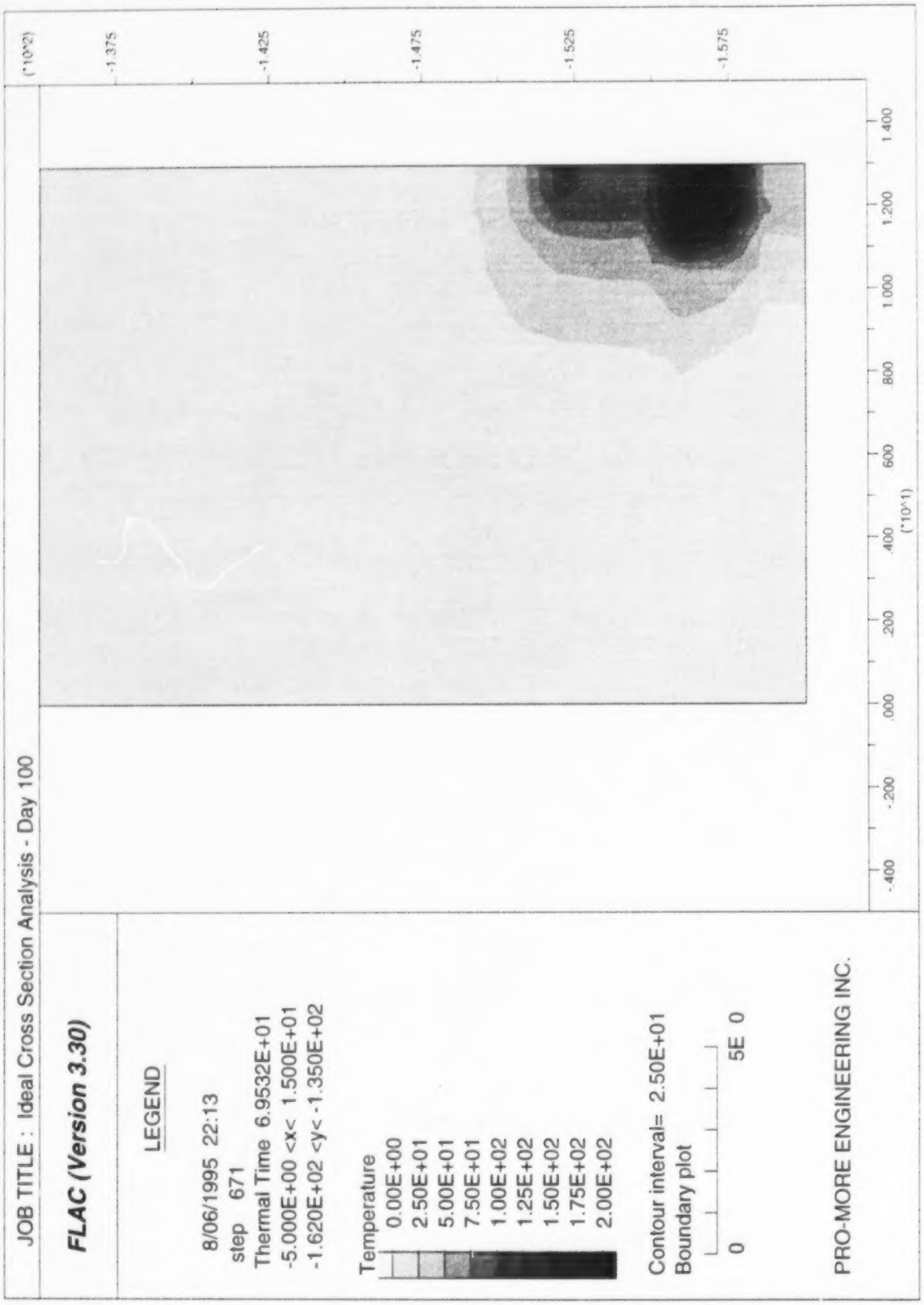

Figure 5.7 Temperature Distribution at 100 Days

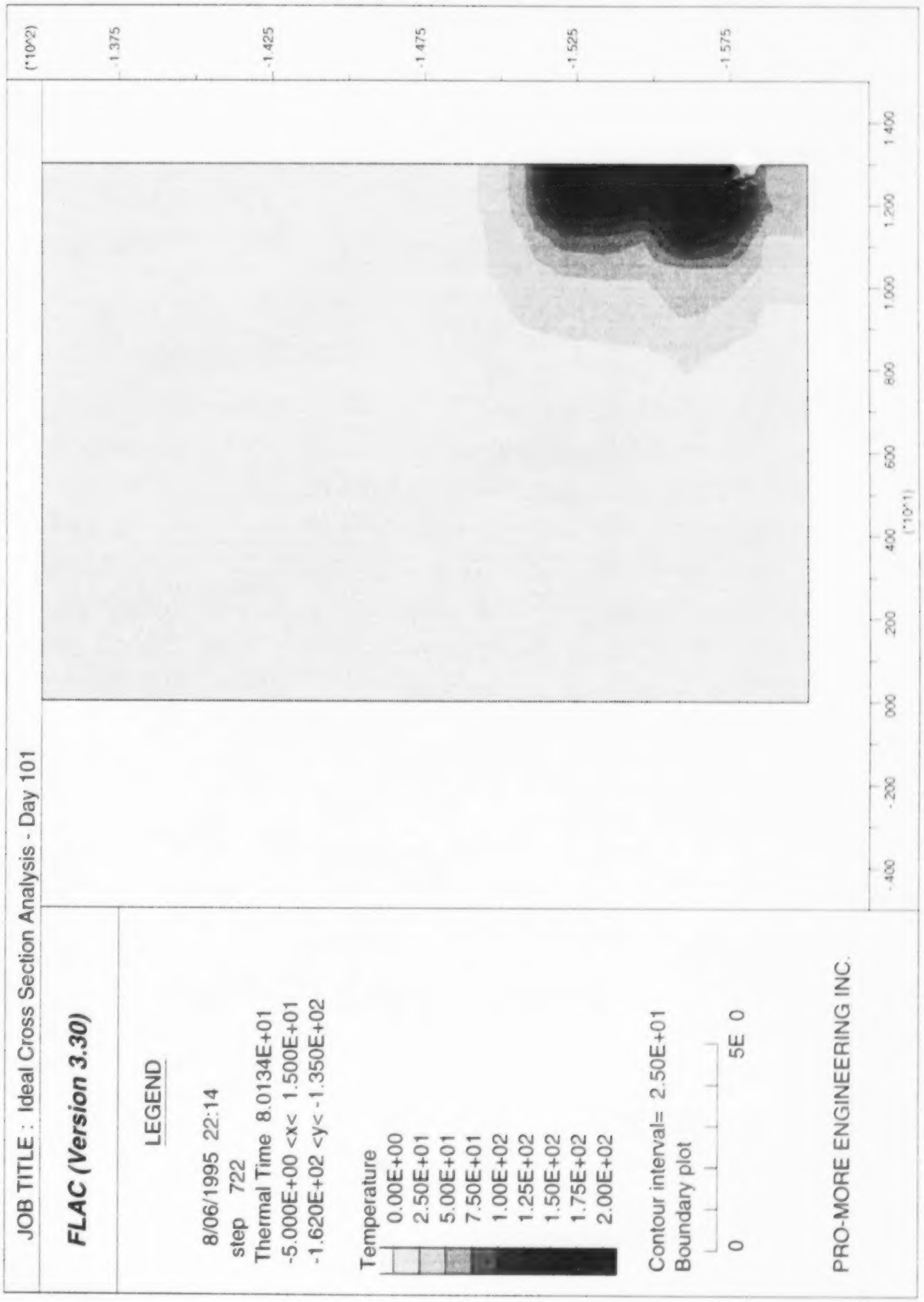

Figure 5.8 Temperature Distribution at 101 Days

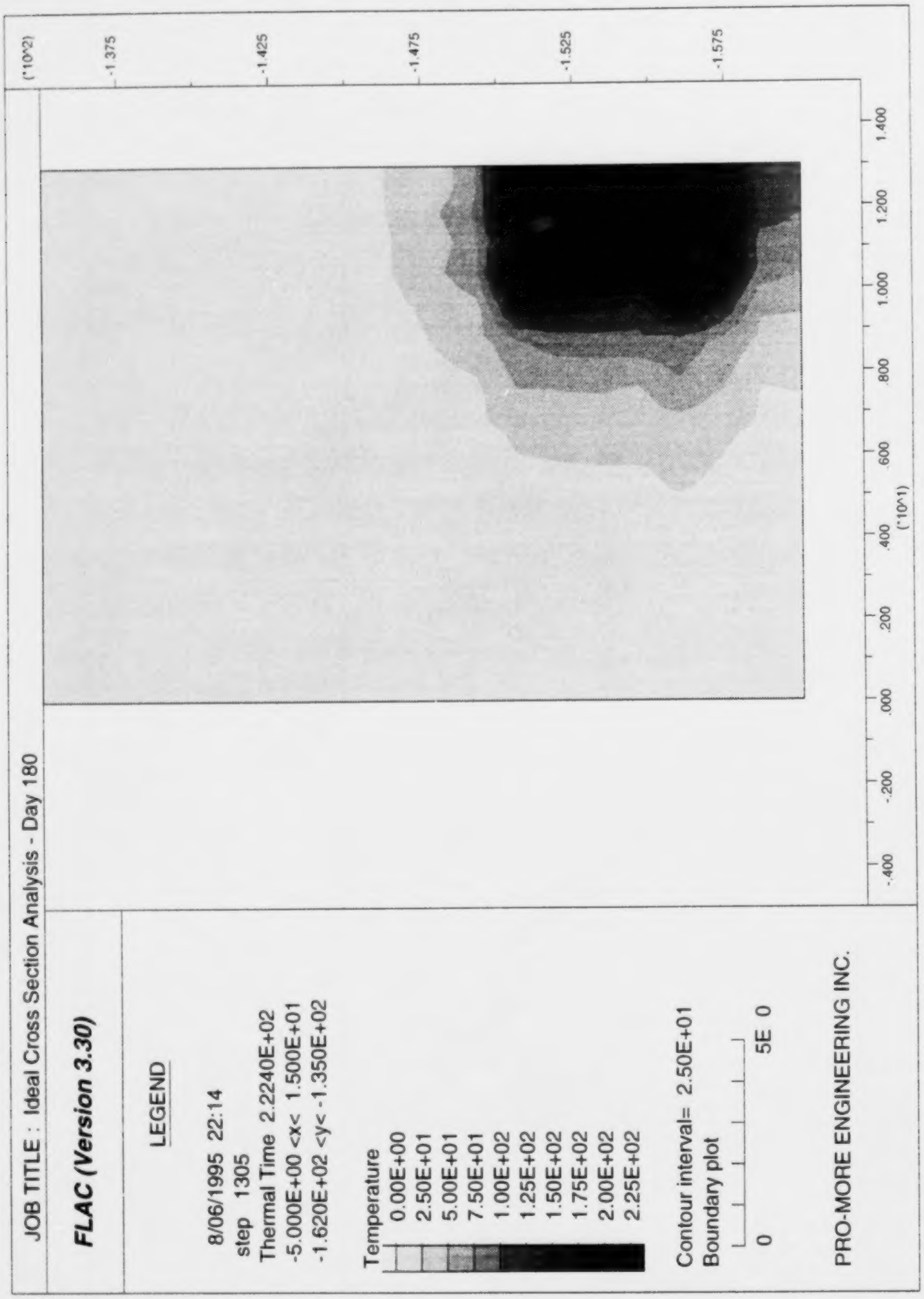

Figure 5.9 Temperature Distribution at 180 Days

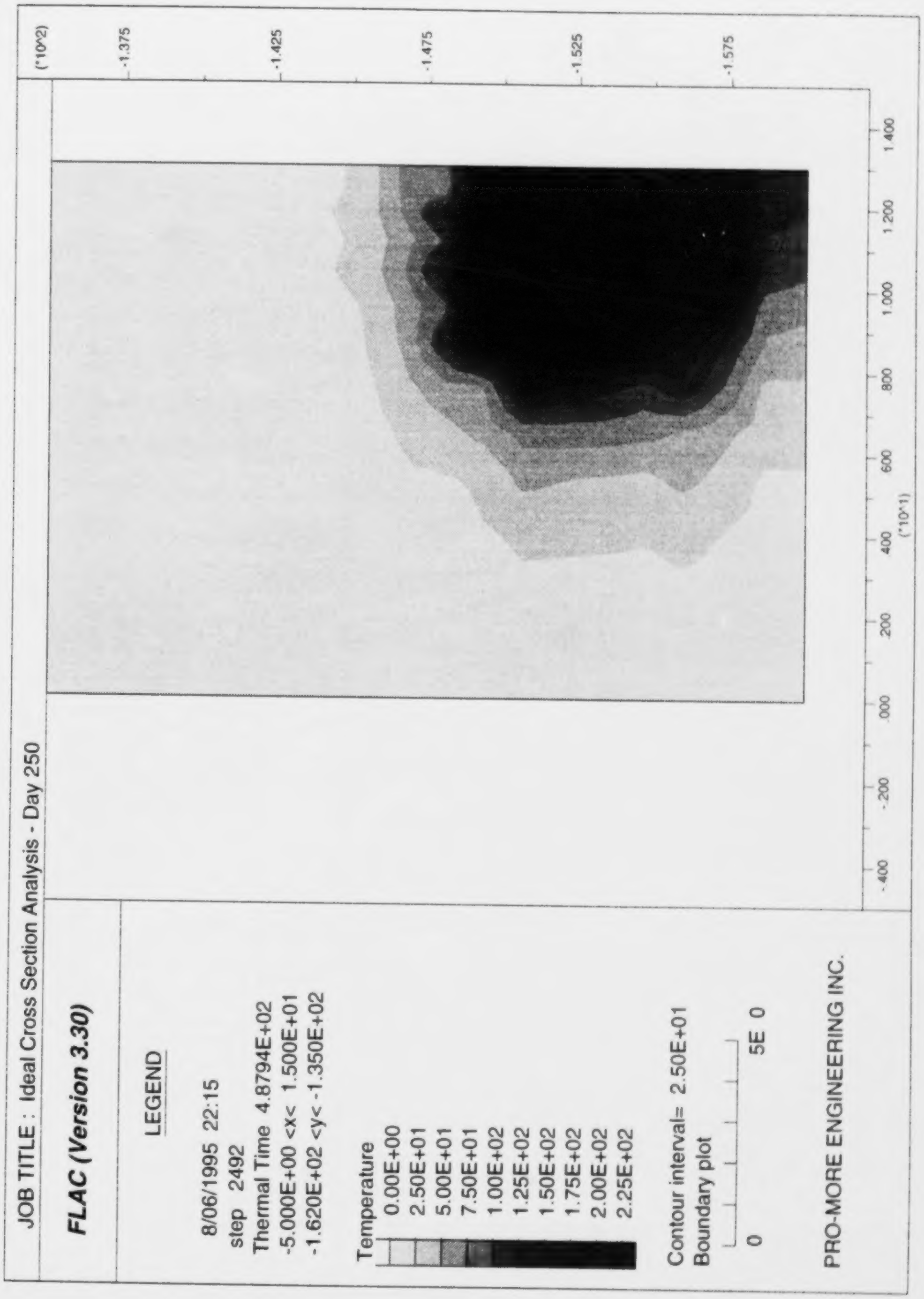

Figure 5.10 Temperature Distribution at 250 Days

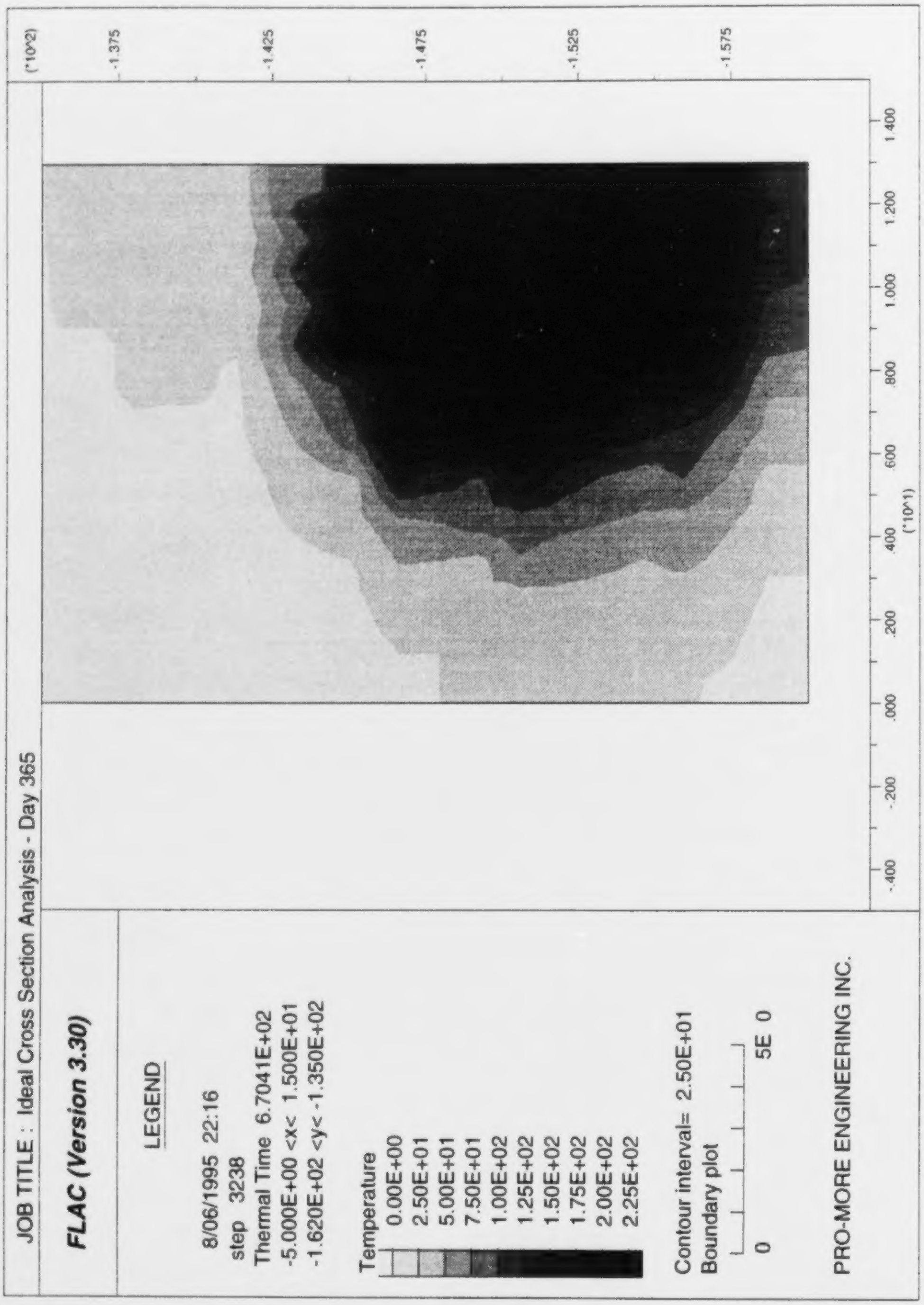

Figure 5.11 Temperature Distribution at 365 Days

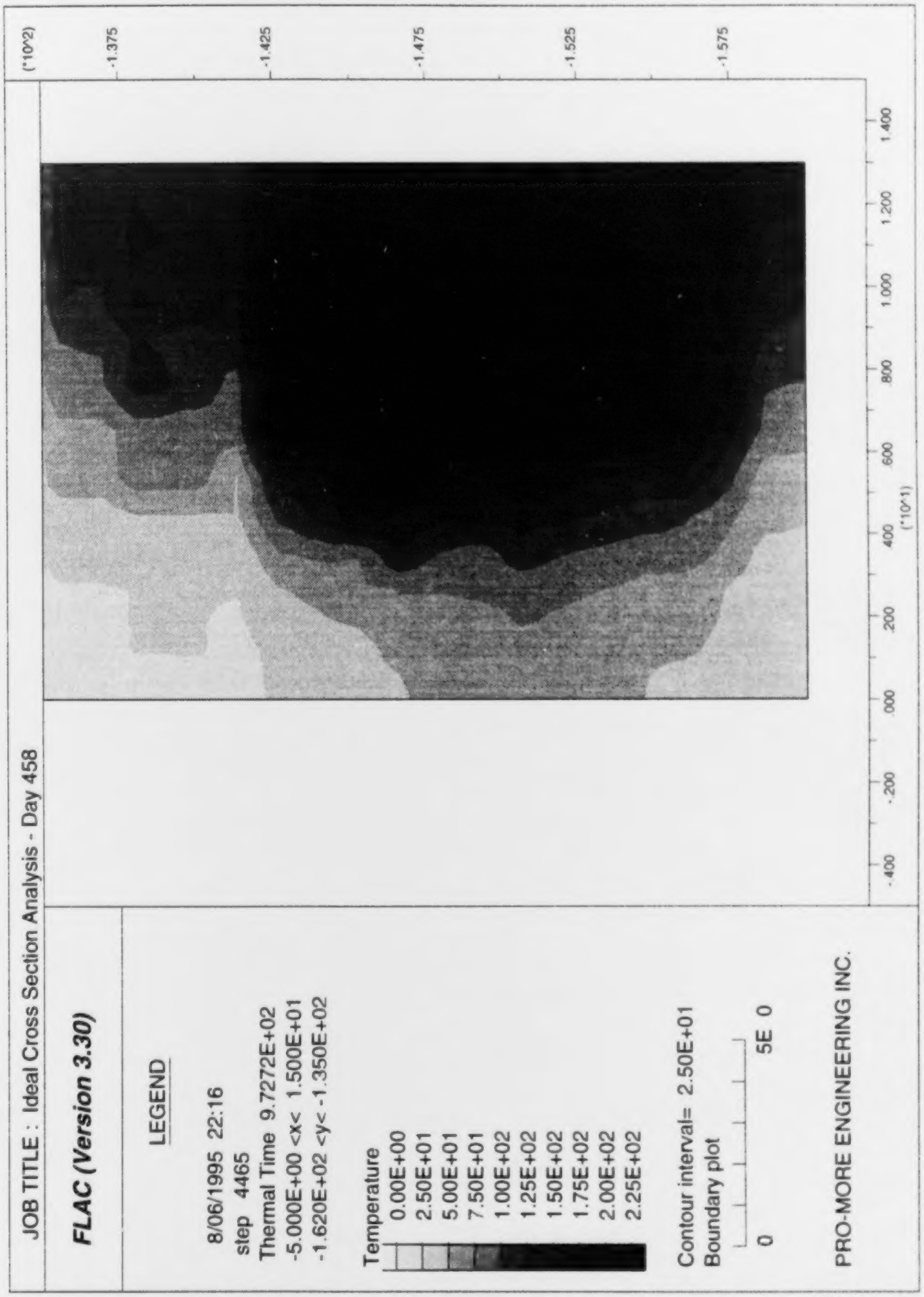

Figure 5.12 Temperature Distribution at 458 Days

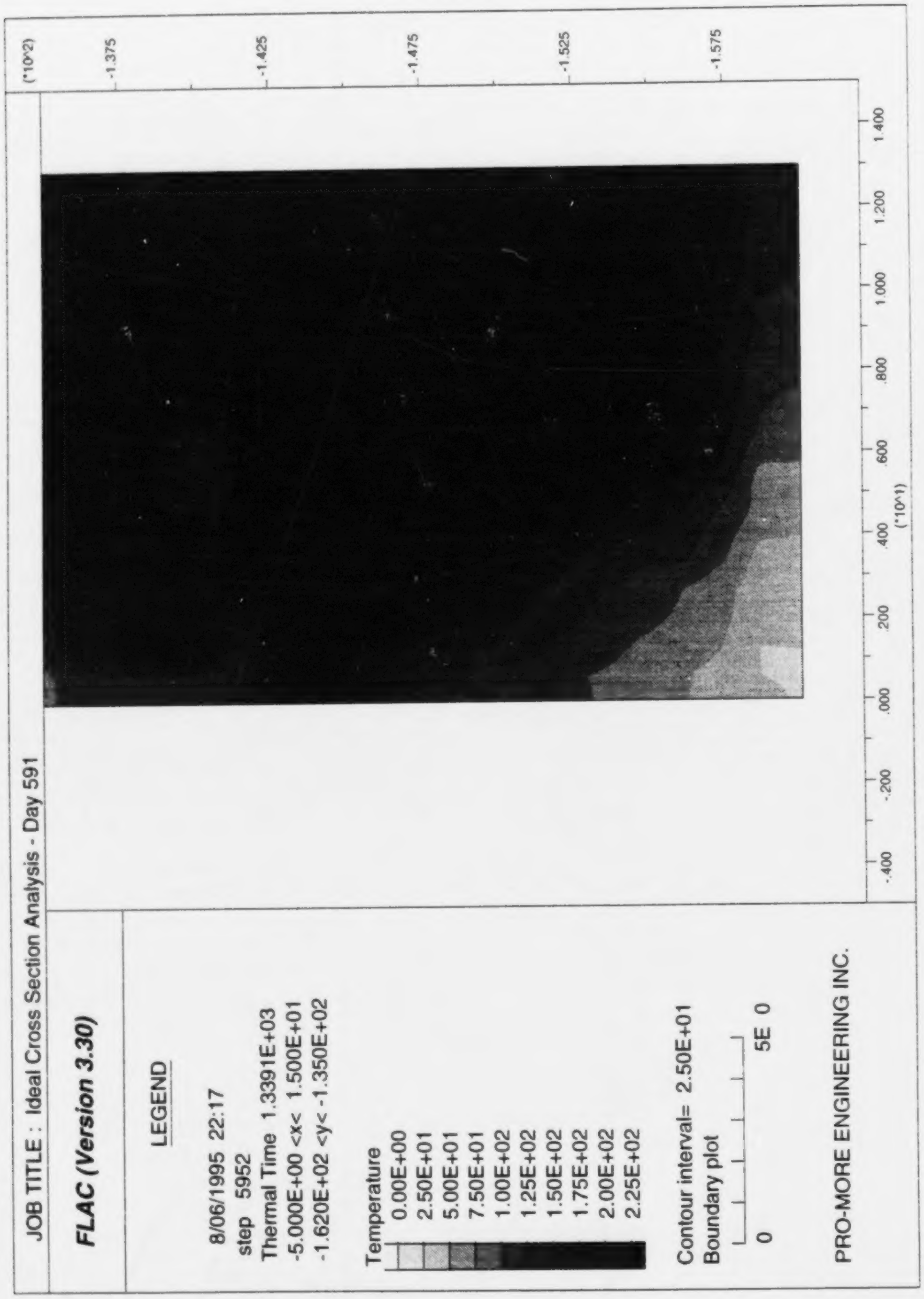

Figure 5.13 Temperature Distribution at 591 Days

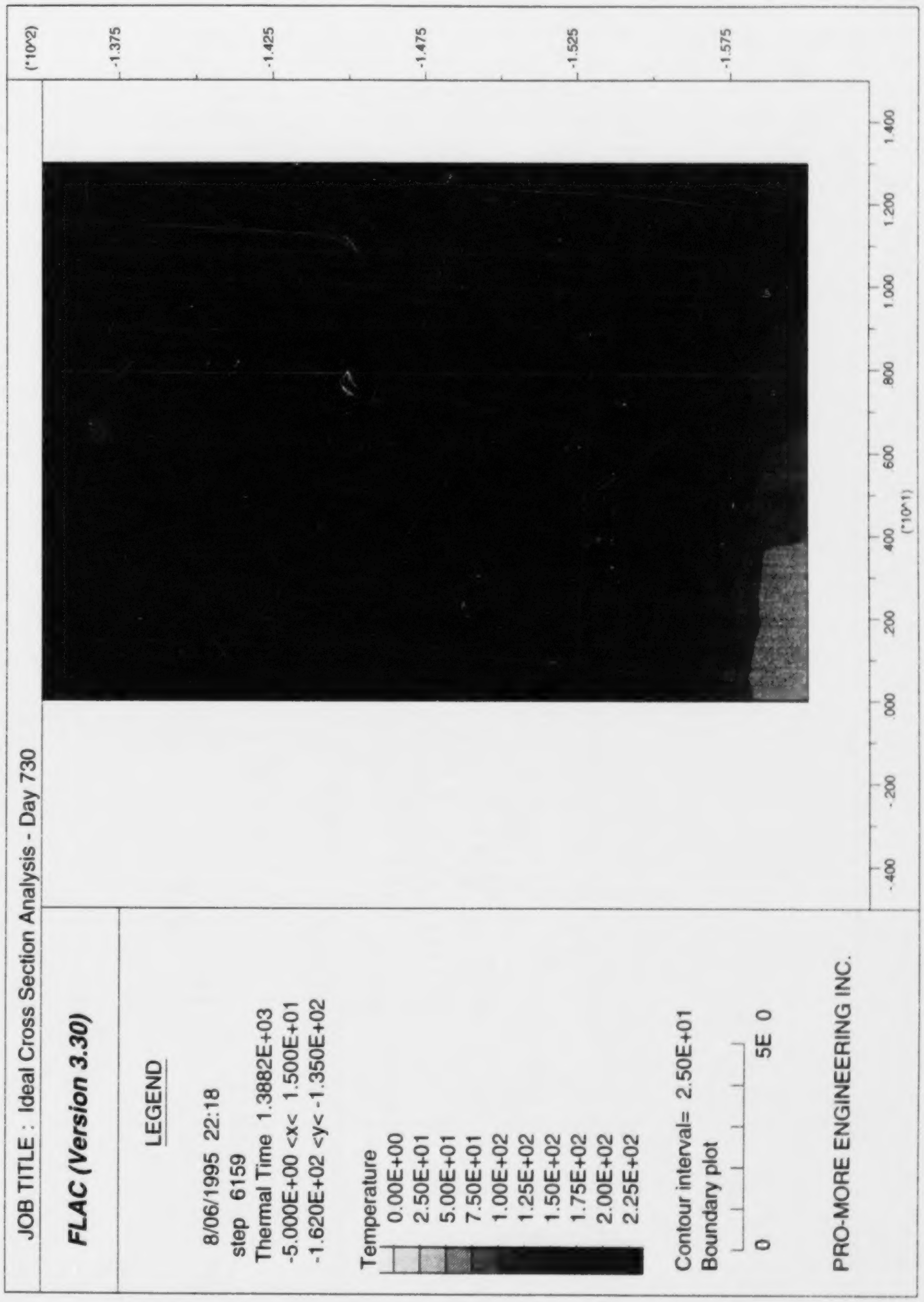

Figure 5.14 Temperature Distribution at 730 Days

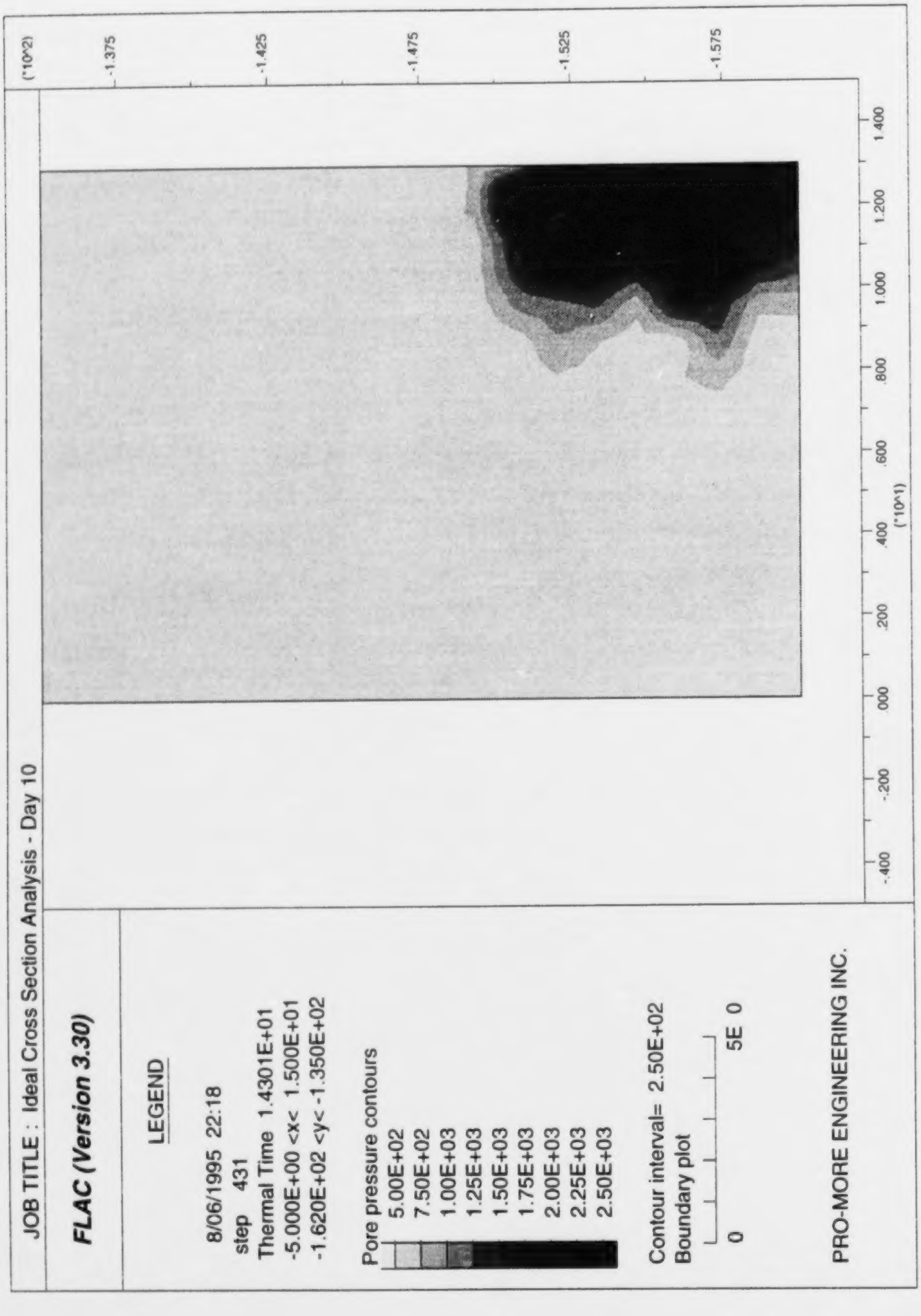

Figure 5.15 Pore Pressure Distribution at 10 Days

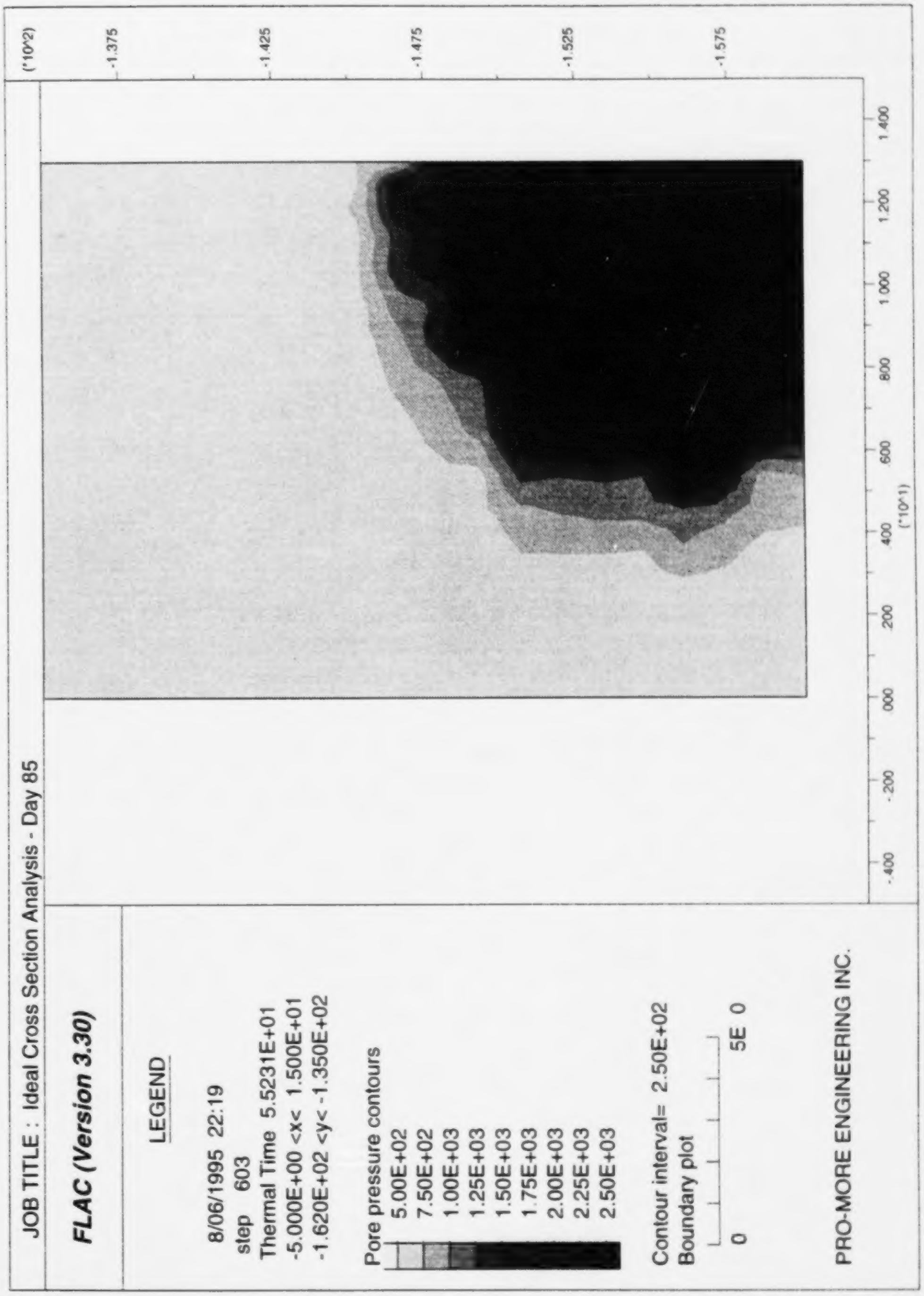

Figure 5.16 Pore Pressure Distribution at 85 Days

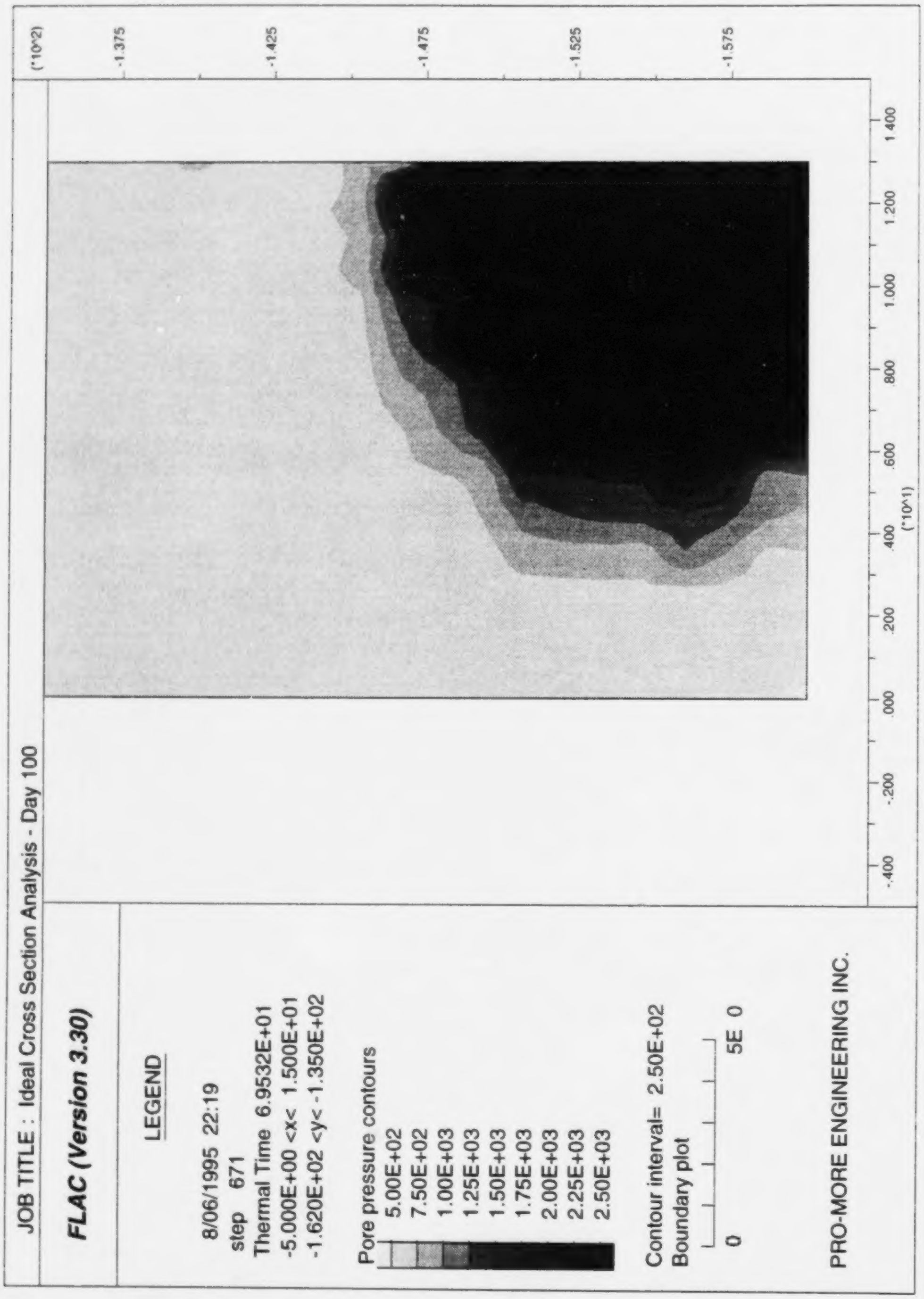

Figure 5.17 Pore Pressure Distribution at 100 Days

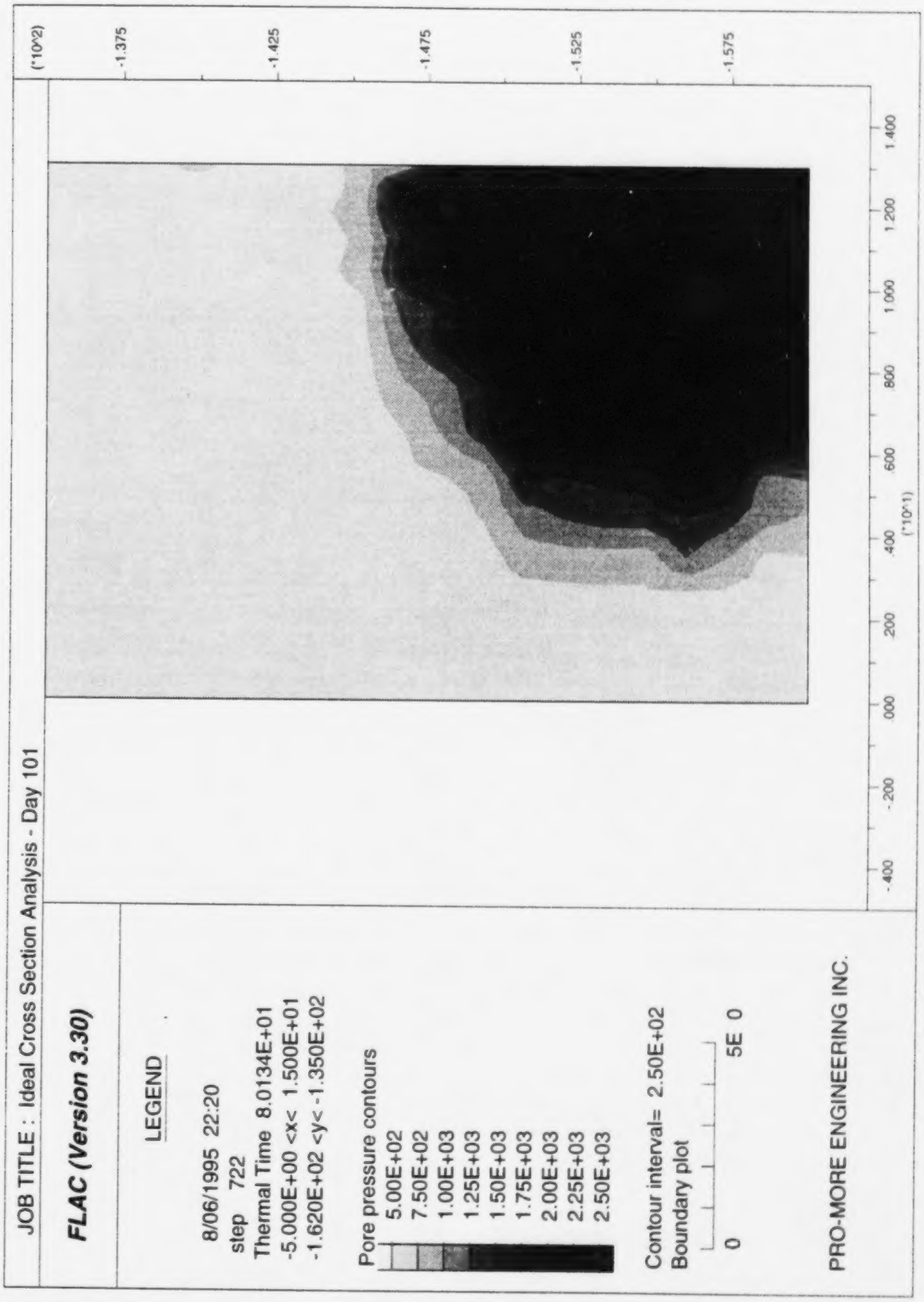

Figure 5.18 Pore Pressure Distribution at 101 Days

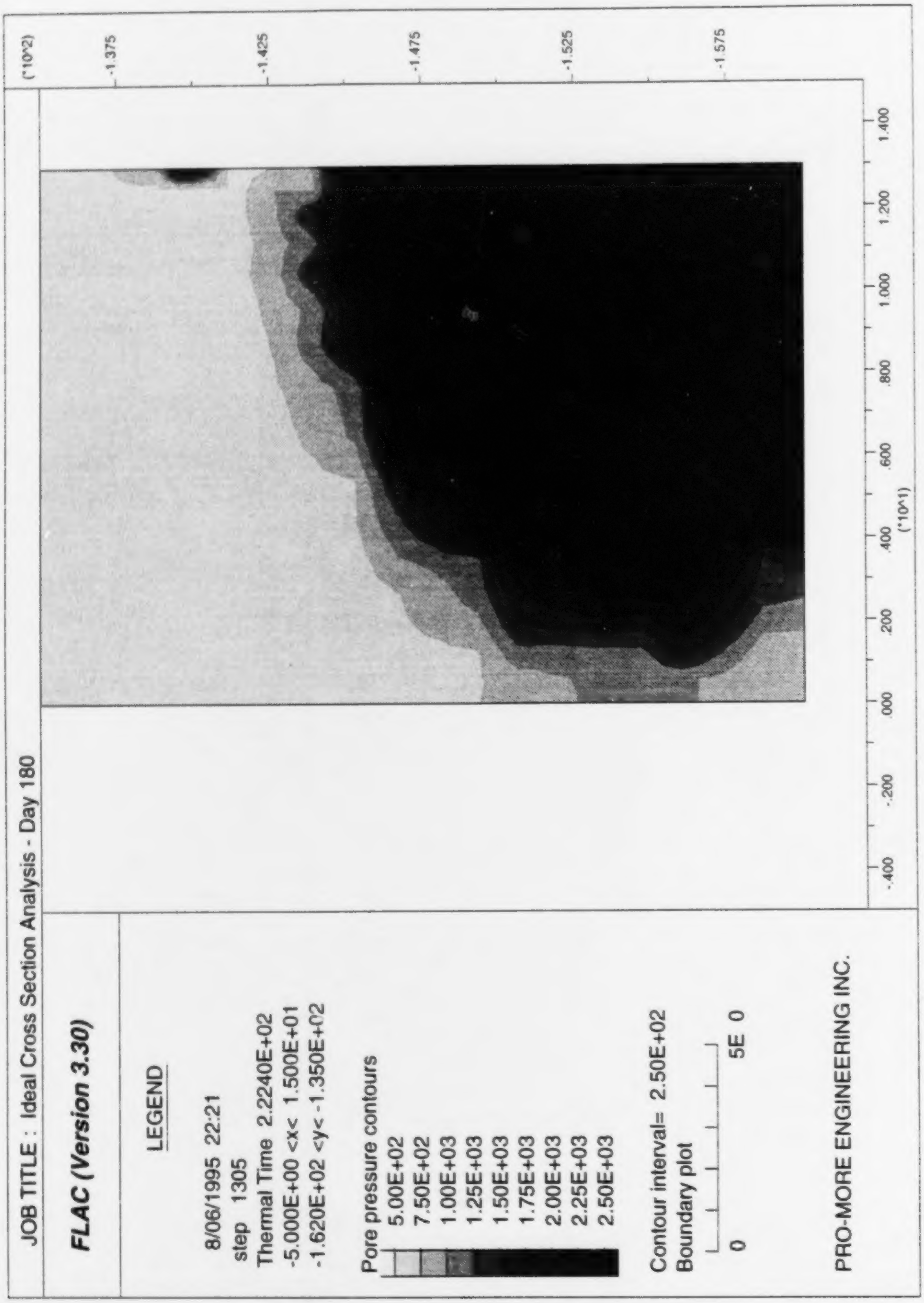

Figure 5.19 Pore Pressure Distribution at 180 Days

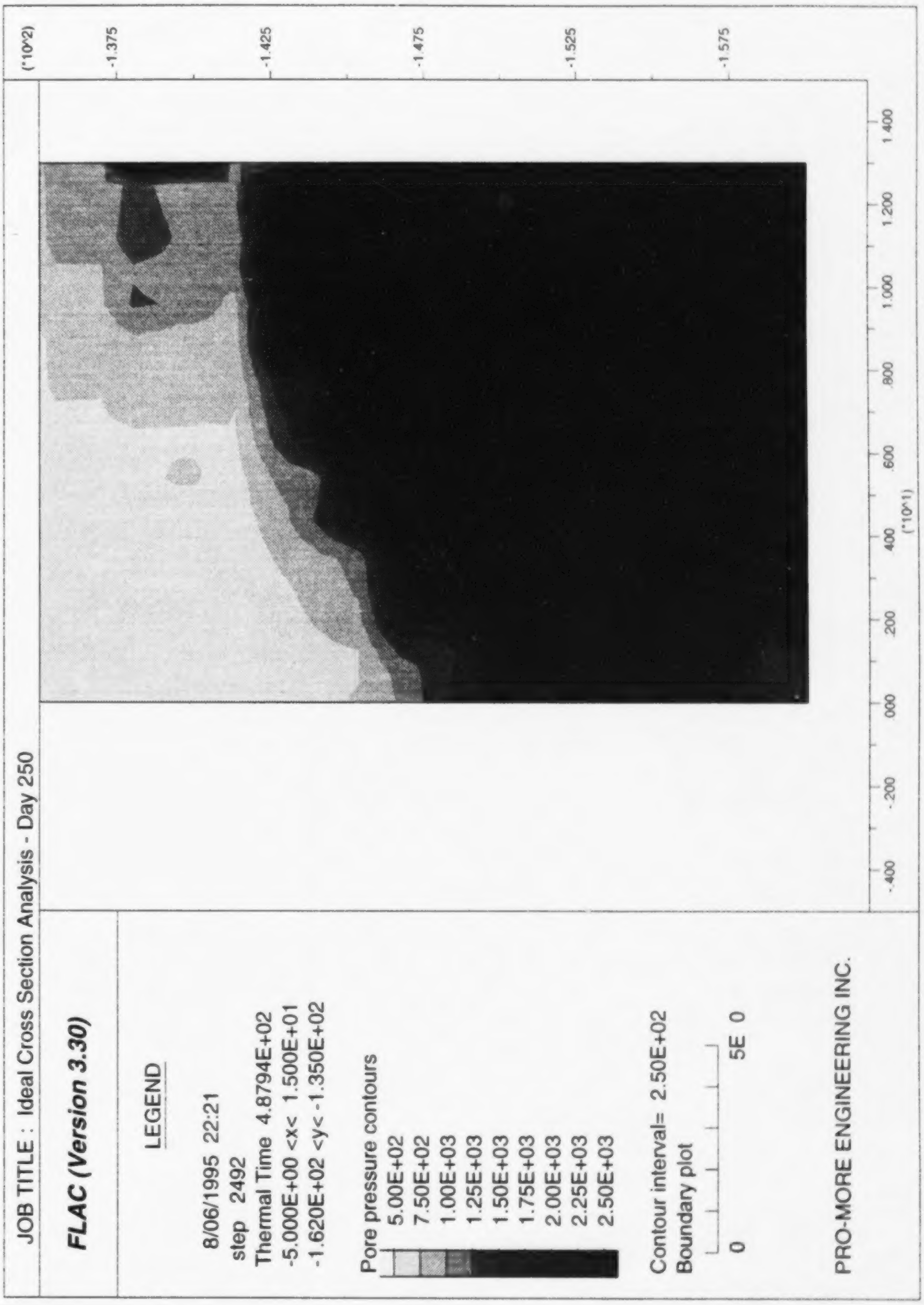

Figure 5.20 Pore Pressure Distribution at 250 Days

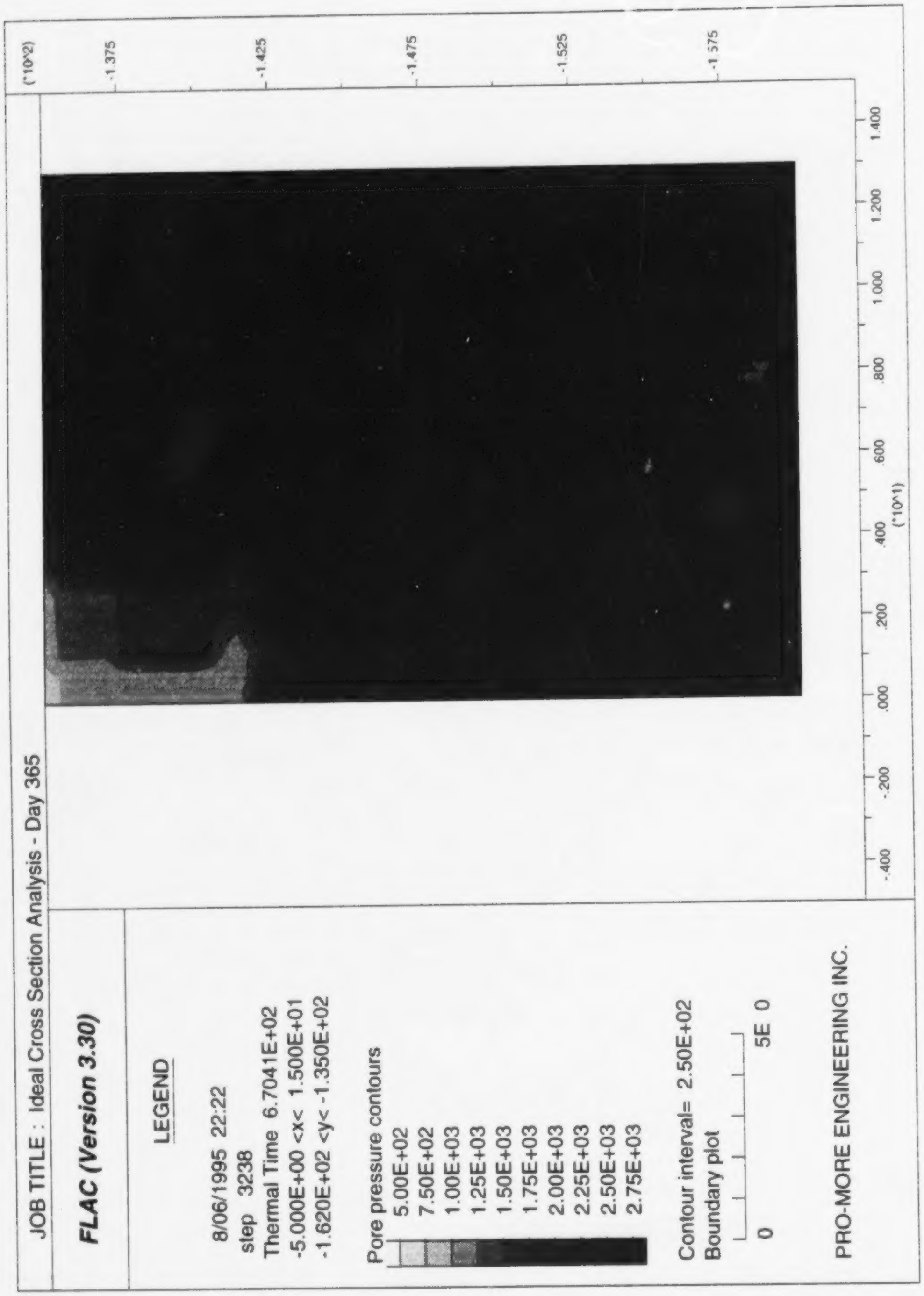

Figure 5.21 Pore Pressure Distribution at 365 Days

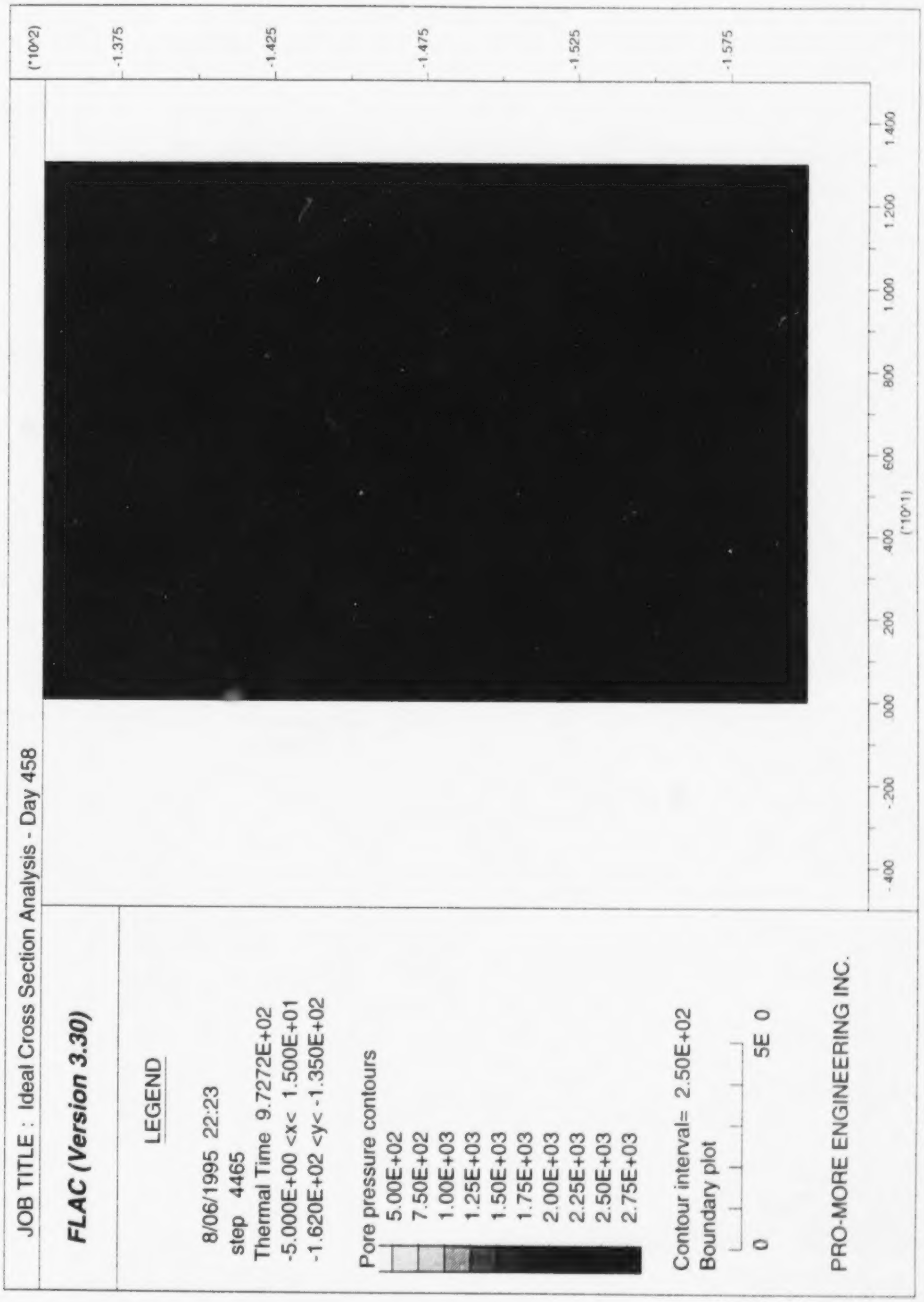

Figure 5.22 Pore Pressure Distribution at 458 Days

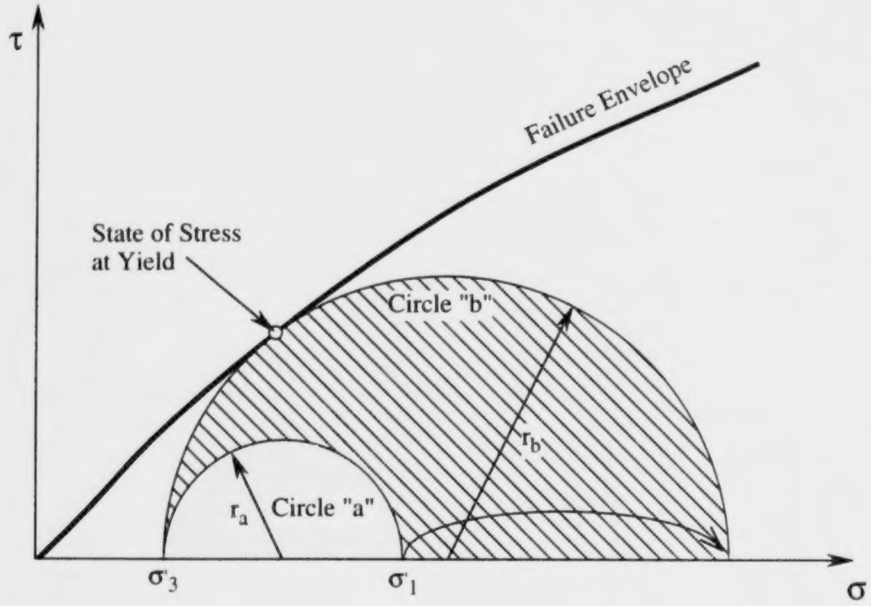
τ
Failure Envelope
State of Stress at Yield
Circle "b"
r_b
r_a
Circle "a"
σ'$_3$
σ'$_1$
σ

Figure 5.23 Definition of Failure Index for Describing Mobilized Strength

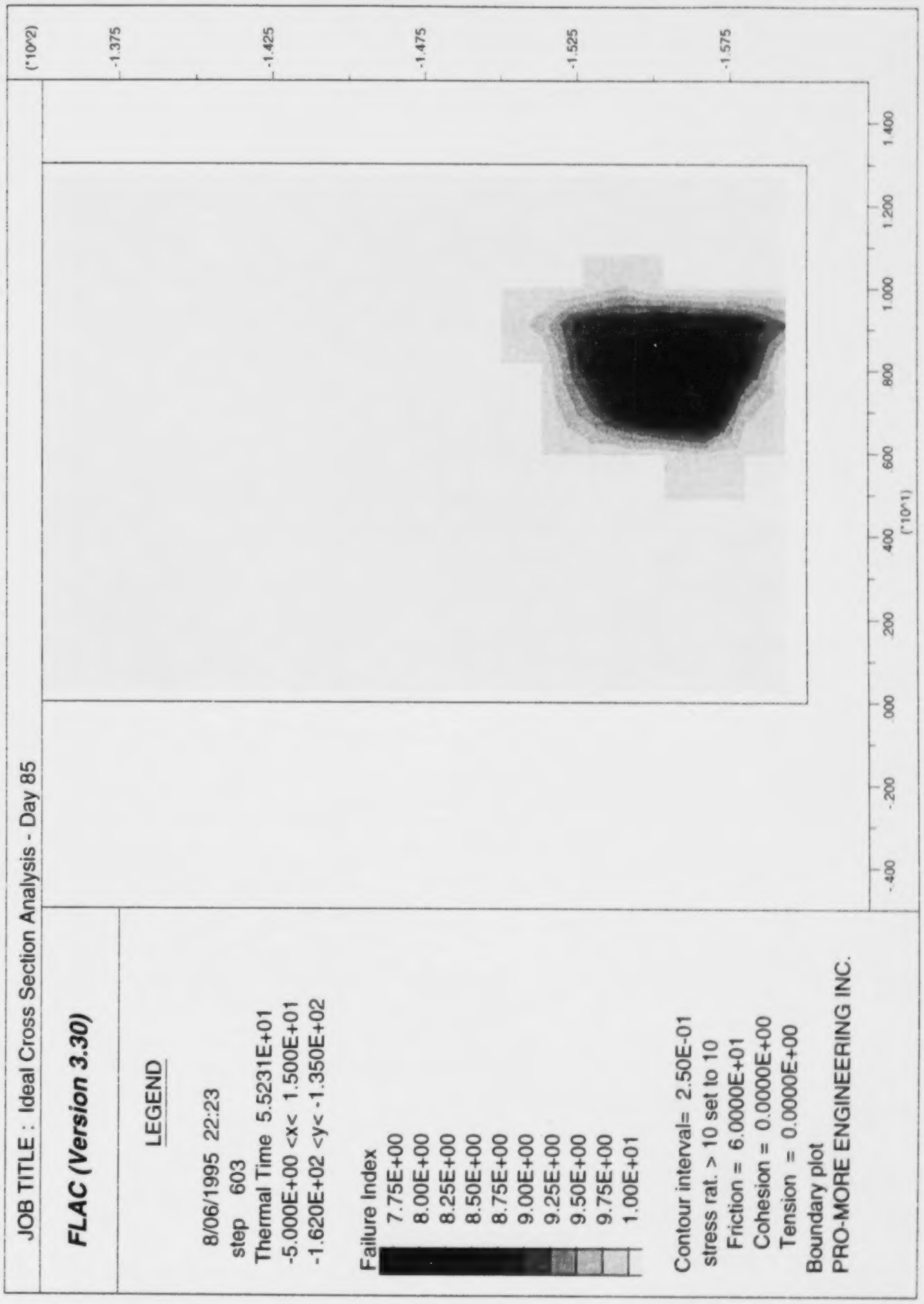

Figure 5.24 Failure Index Distribution at 85 Days - Base Case

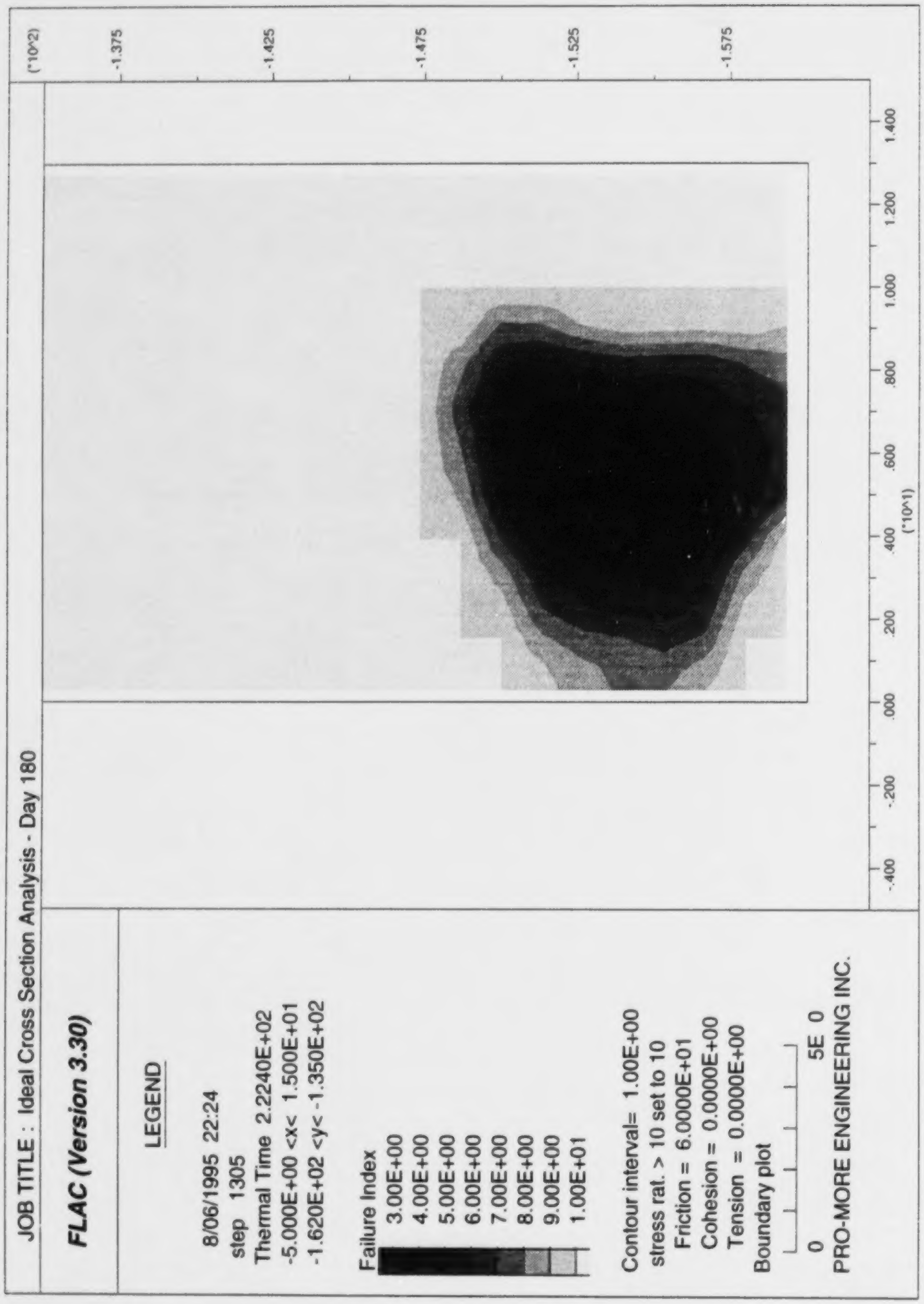

Figure 5.25 Failure Index Distribution at 180 Days - Base Case

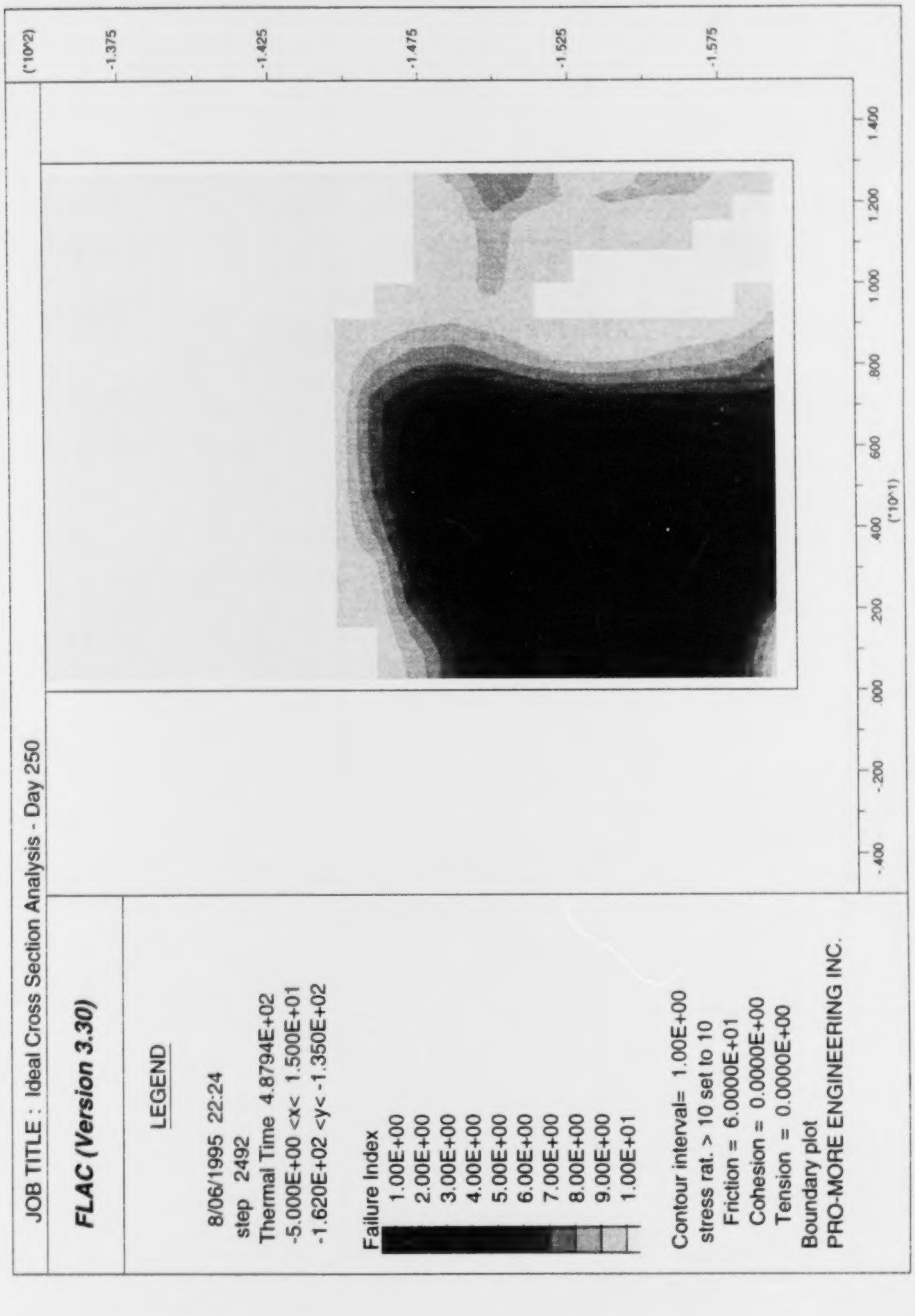

Figure 5.26 Failure Index Distribution at 250 Days - Base Case

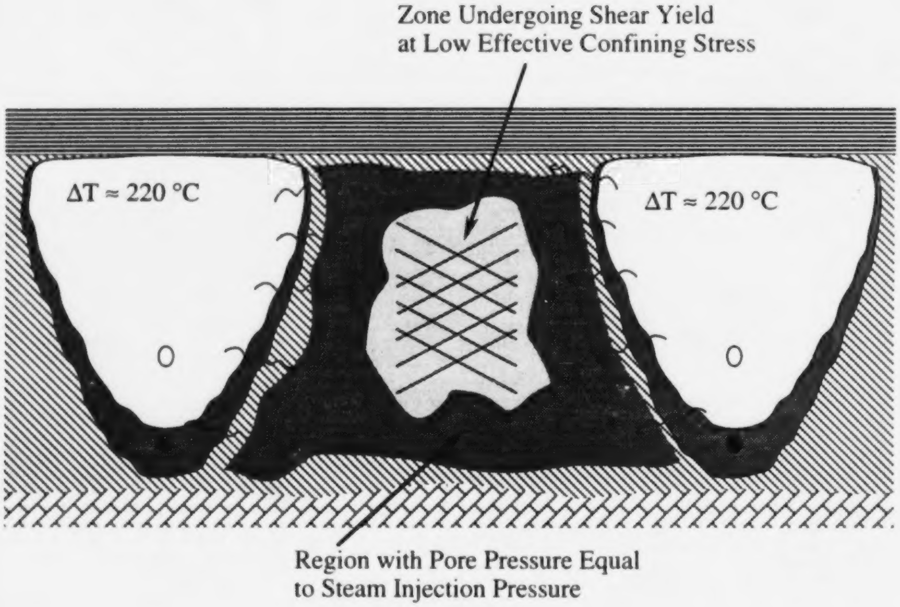
Zone Undergoing Shear Yield
at Low Effective Confining Stress
ΔT ≈ 220 °C
ΔT ≈ 220 °C
O
O
Region with Pore Pressure Equal
to Steam Injection Pressure

Figure 5.27 Schematic Diagram Showing Process of Shear Yield in Reservoir

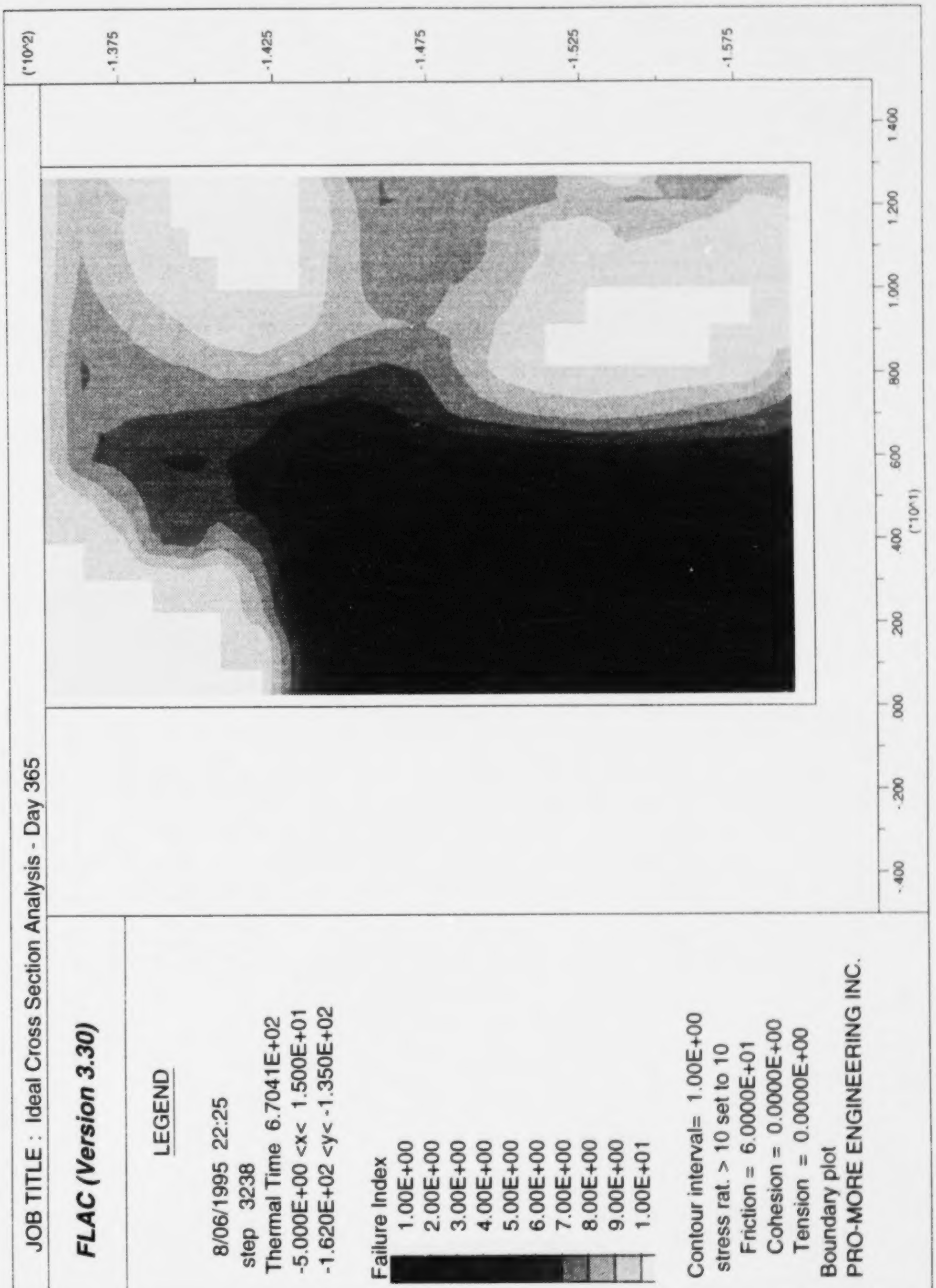

Figure 5.28 Failure Index Distribution at 365 Days - Base Case

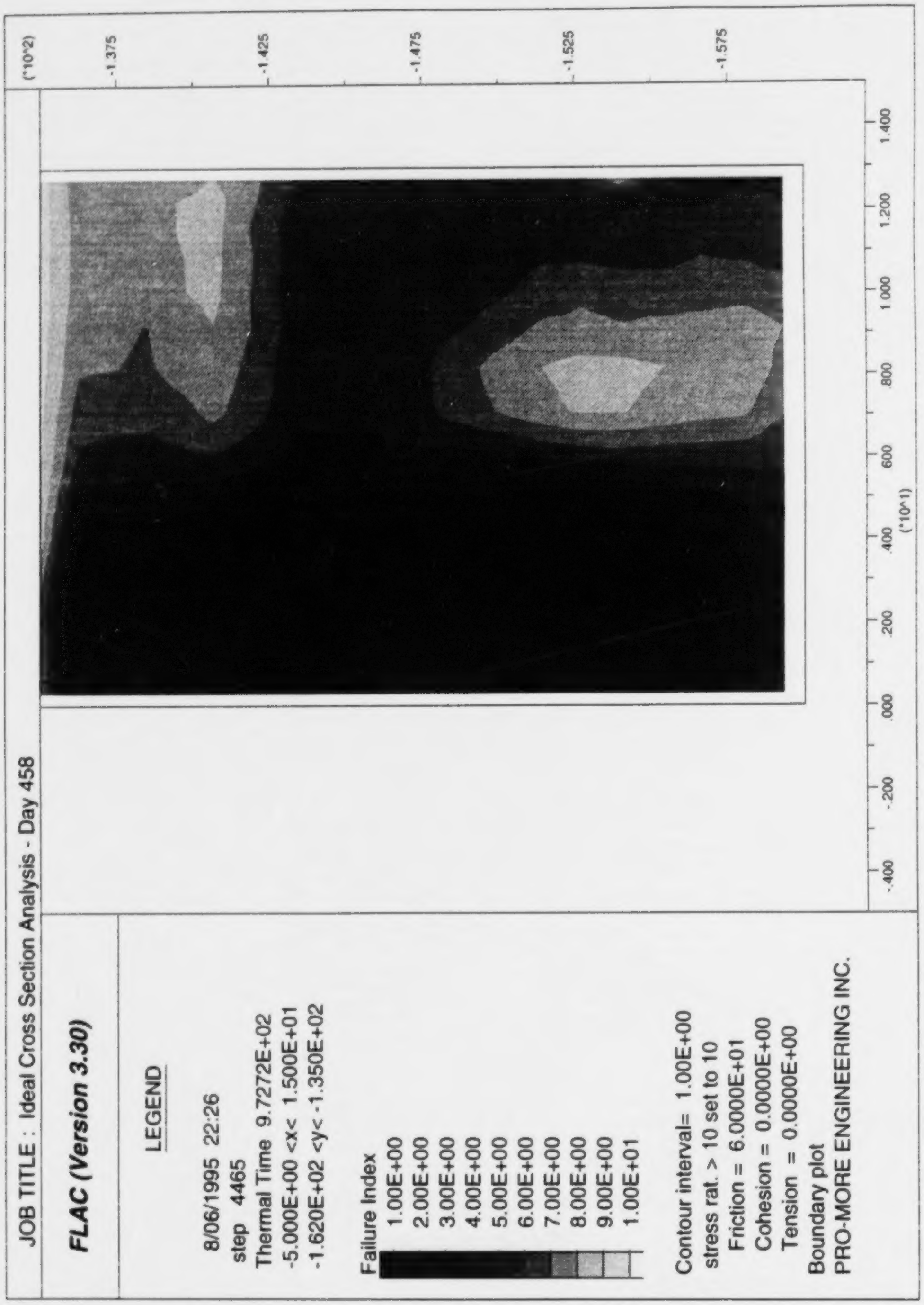

Figure 5.29 Failure Index Distribution at 458 Days - Base Case

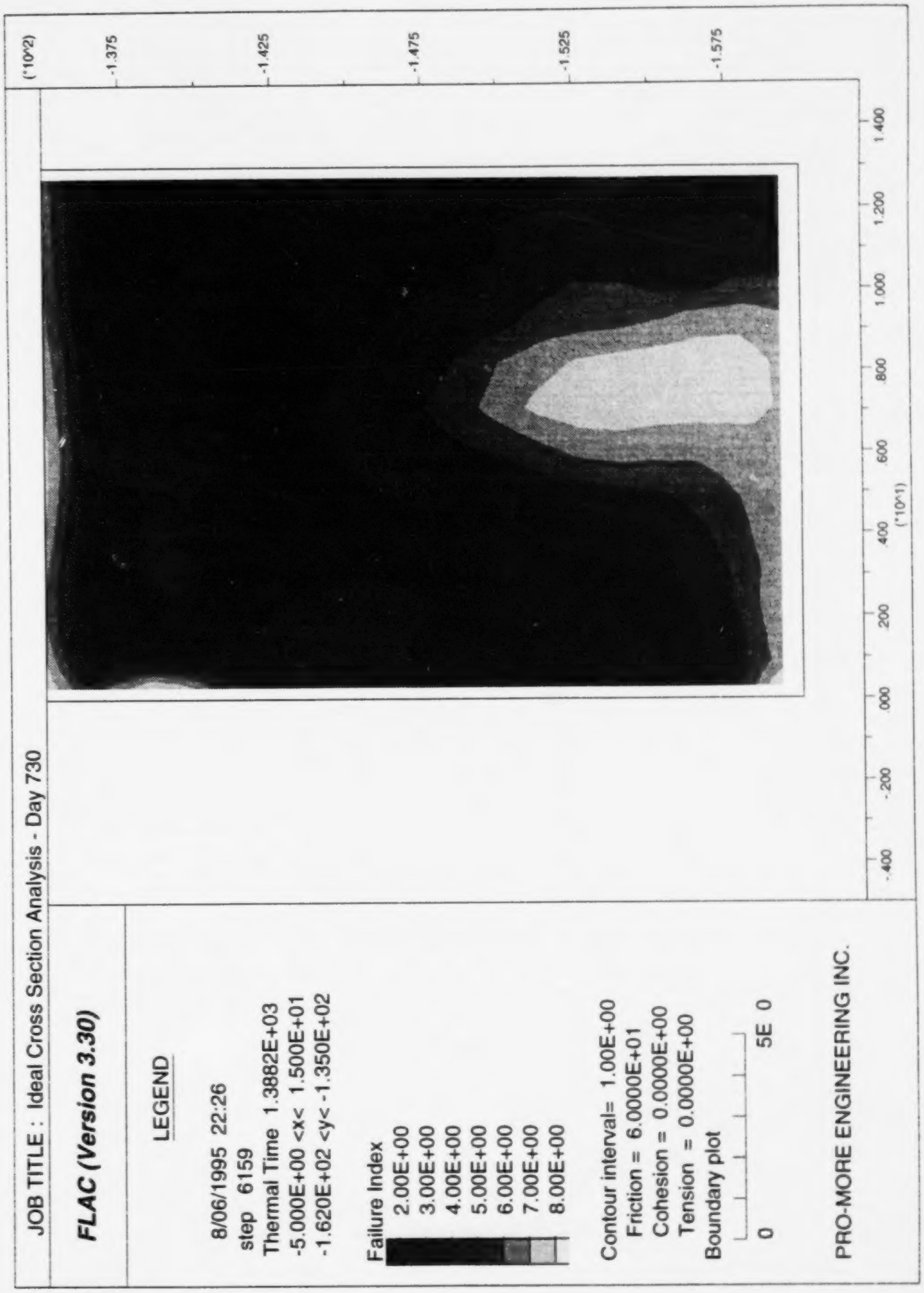

Figure 5.30 Failure Index Distribution at 730 Days - Base Case

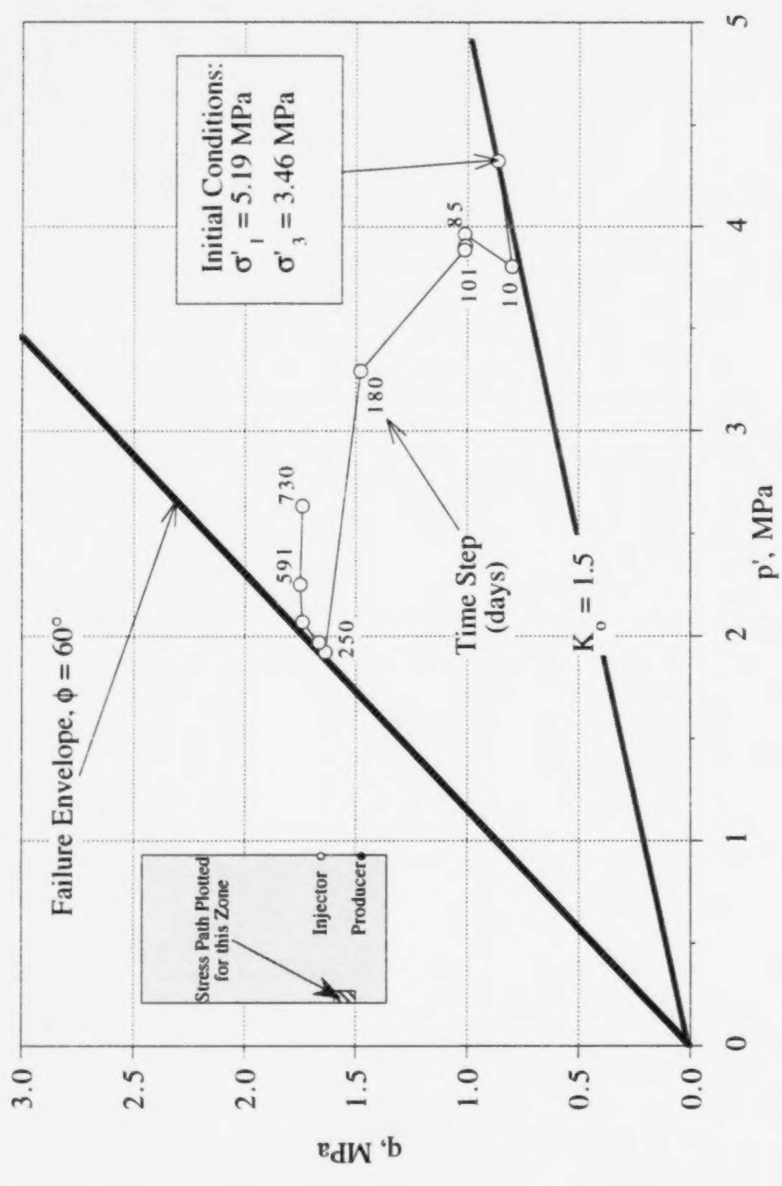

Figure 5.31 Stress Path for Element along Left Boundary of Grid

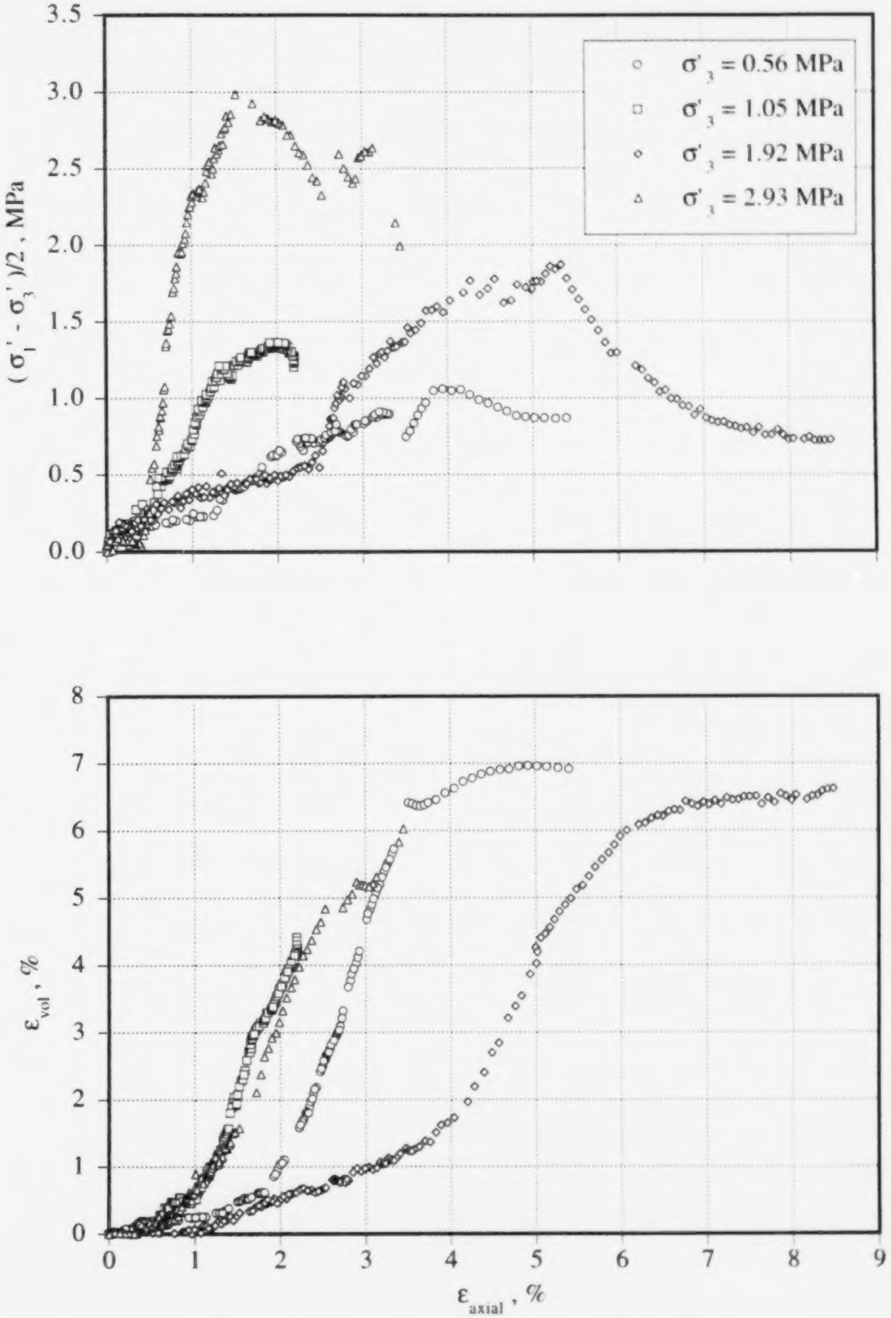

Figure 5.32 Volumetric Strain Behavior for Active Compression Stress Path Triaxial Test

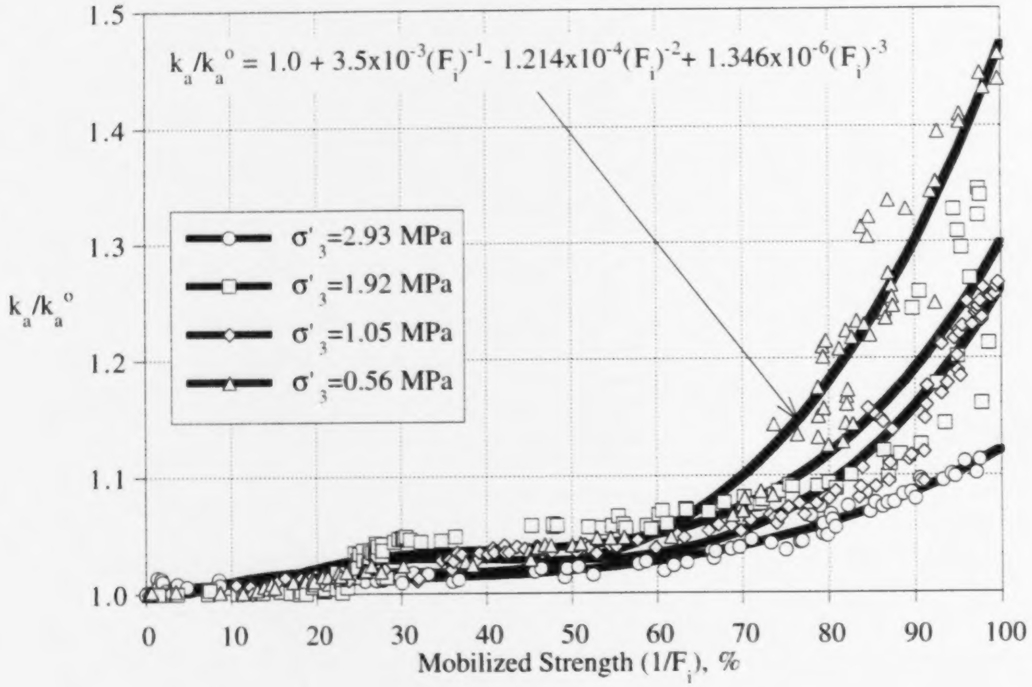

Figure 5.33 Variation in k_a/k_a^o with Mobilized Strength Derived from Active Compression Triaxial Test Results

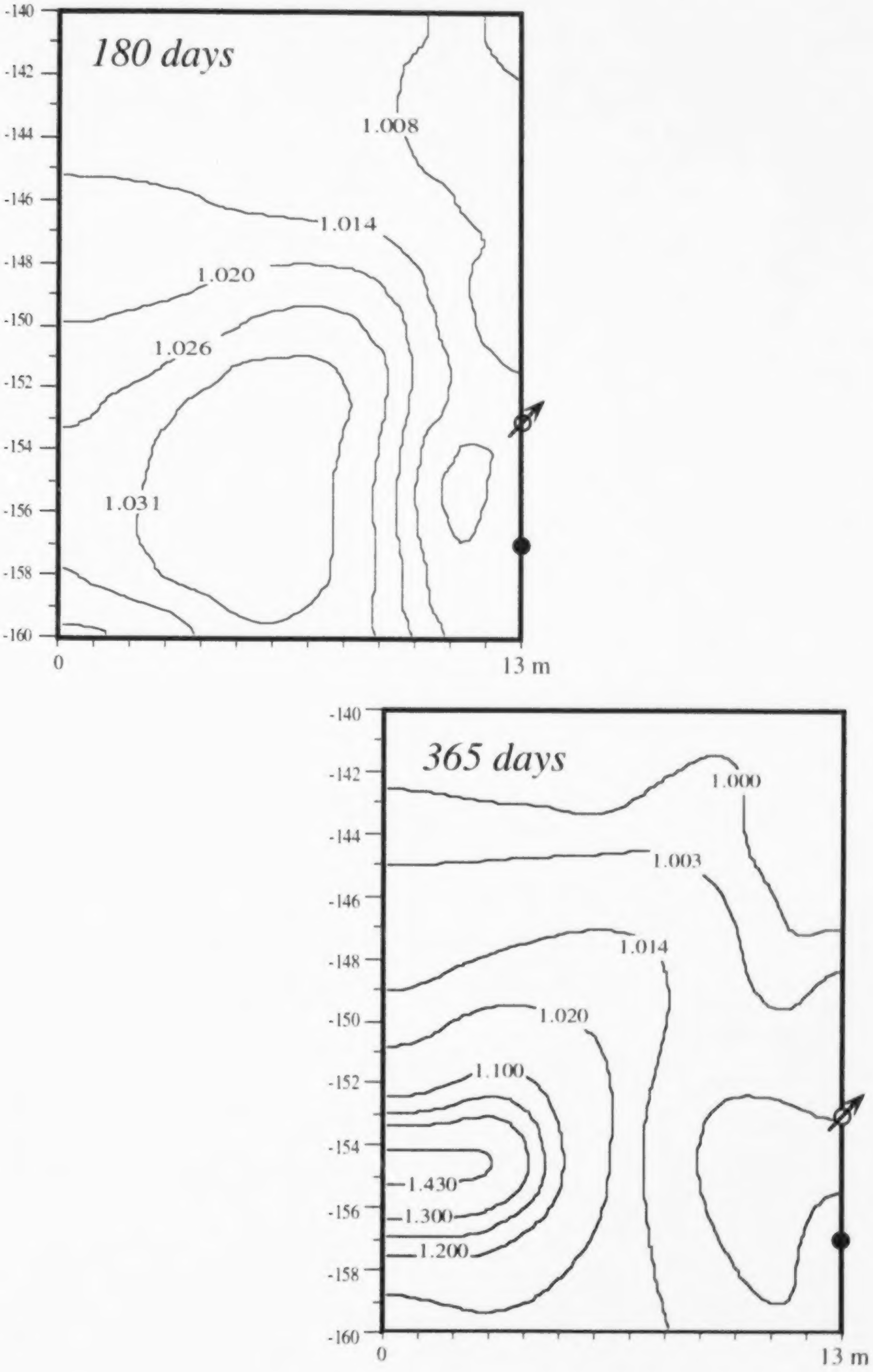

Figure 5.34 Shear Induced Permeability Changes at 180 and 365 Days

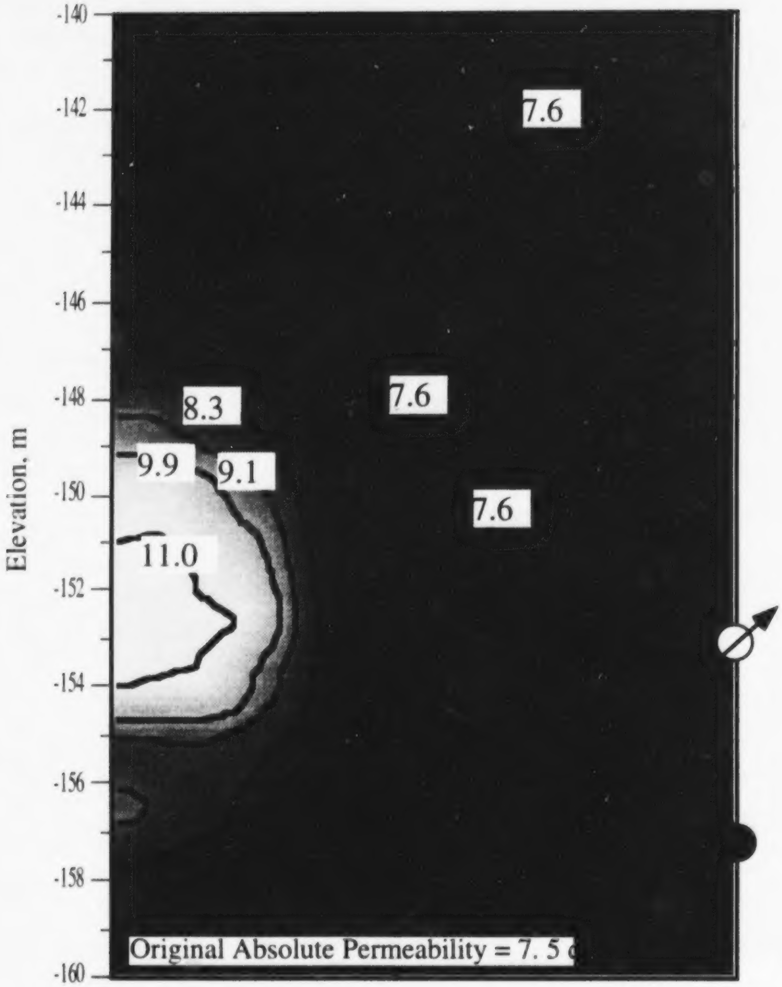

Figure 5.35 Variation of Absolute Permeability within Reservoir at Time 365 Days

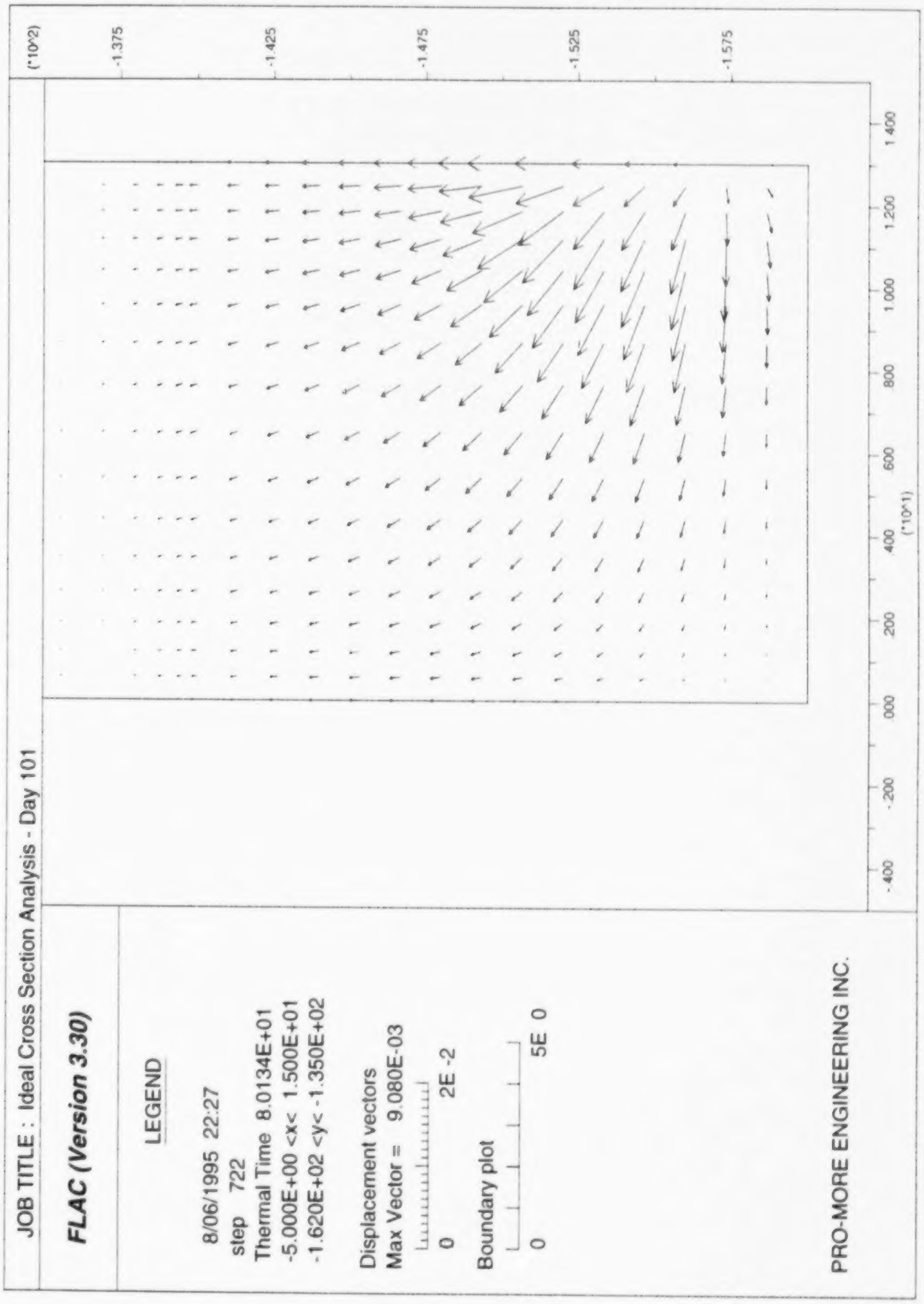

Figure 5.36 Displacement Field at 101 Days - Base Case

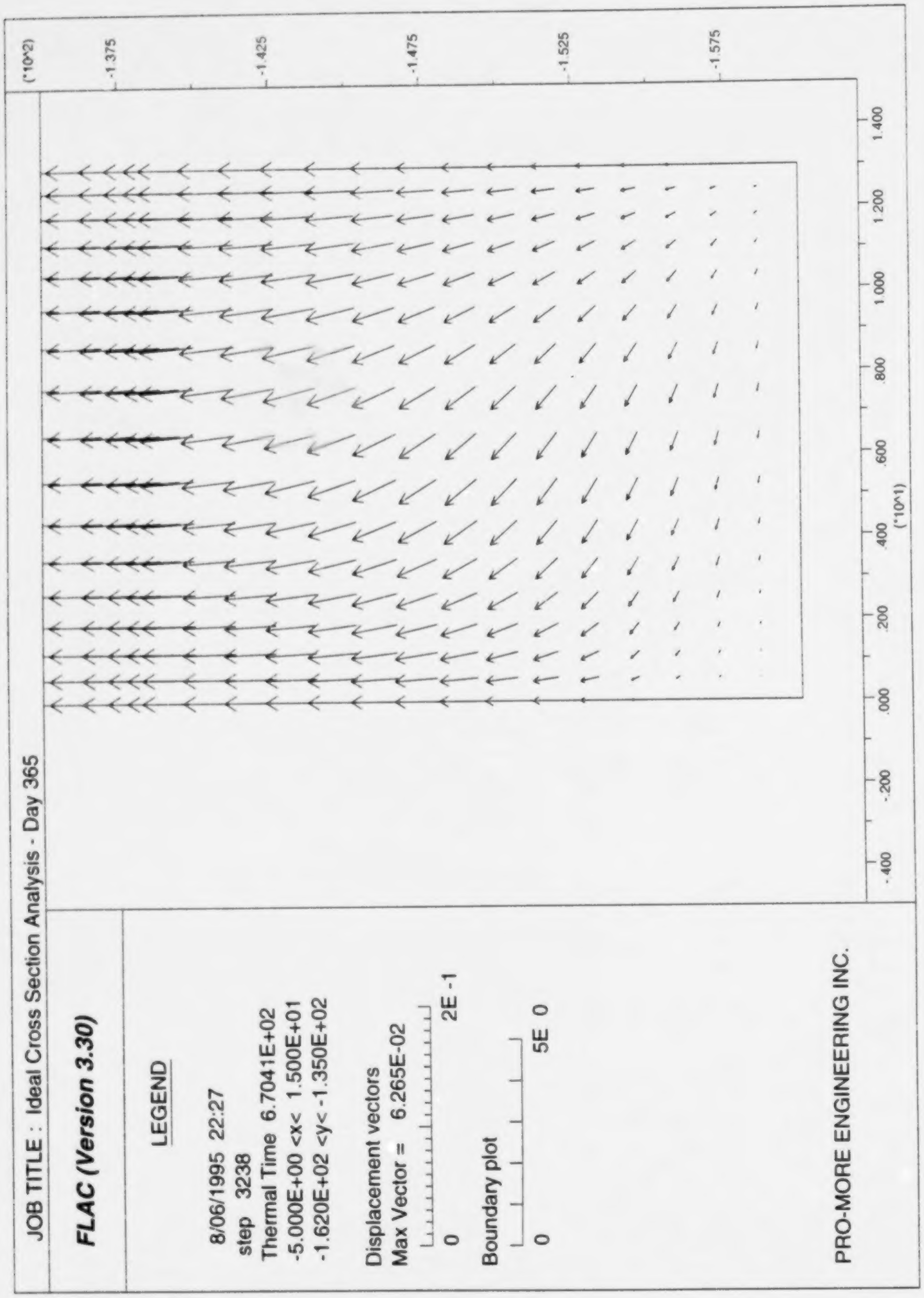

Figure 5.37 Displacement Field at 365 Days - Base Case

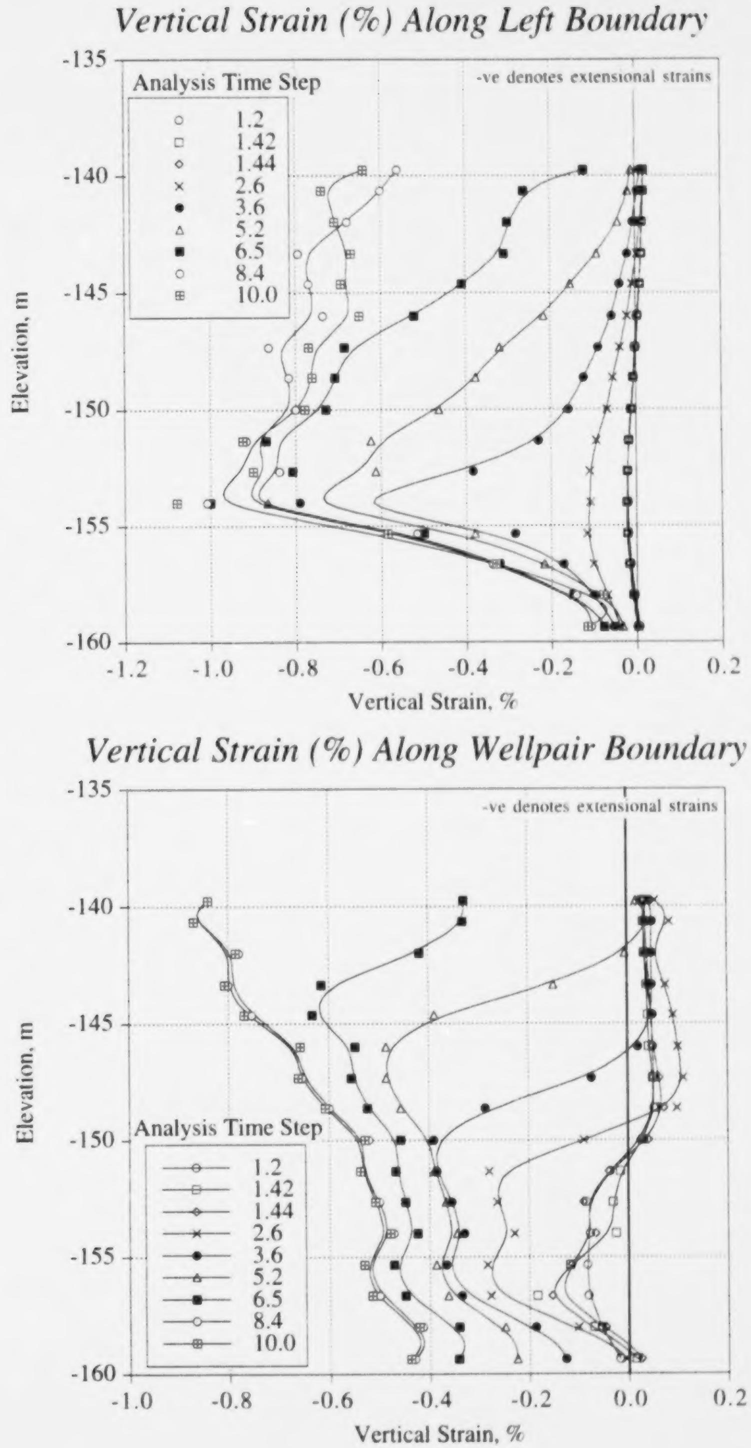

Figure 5.38 Vertical Strains above Wellpairs and Along Left Boundary

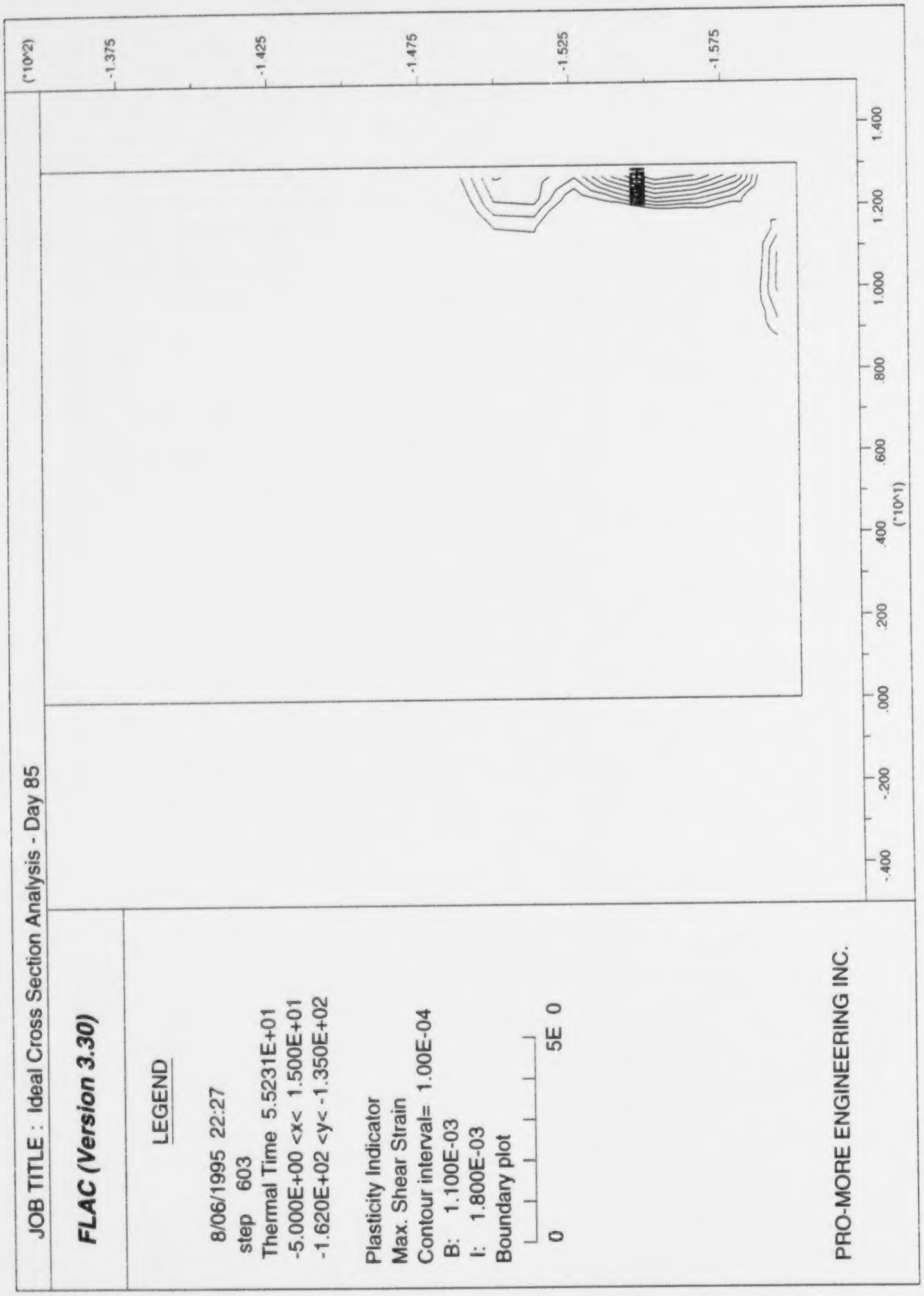

Figure 5.39 Maximum Shear Strain Distribution at 85 Days - Base Case

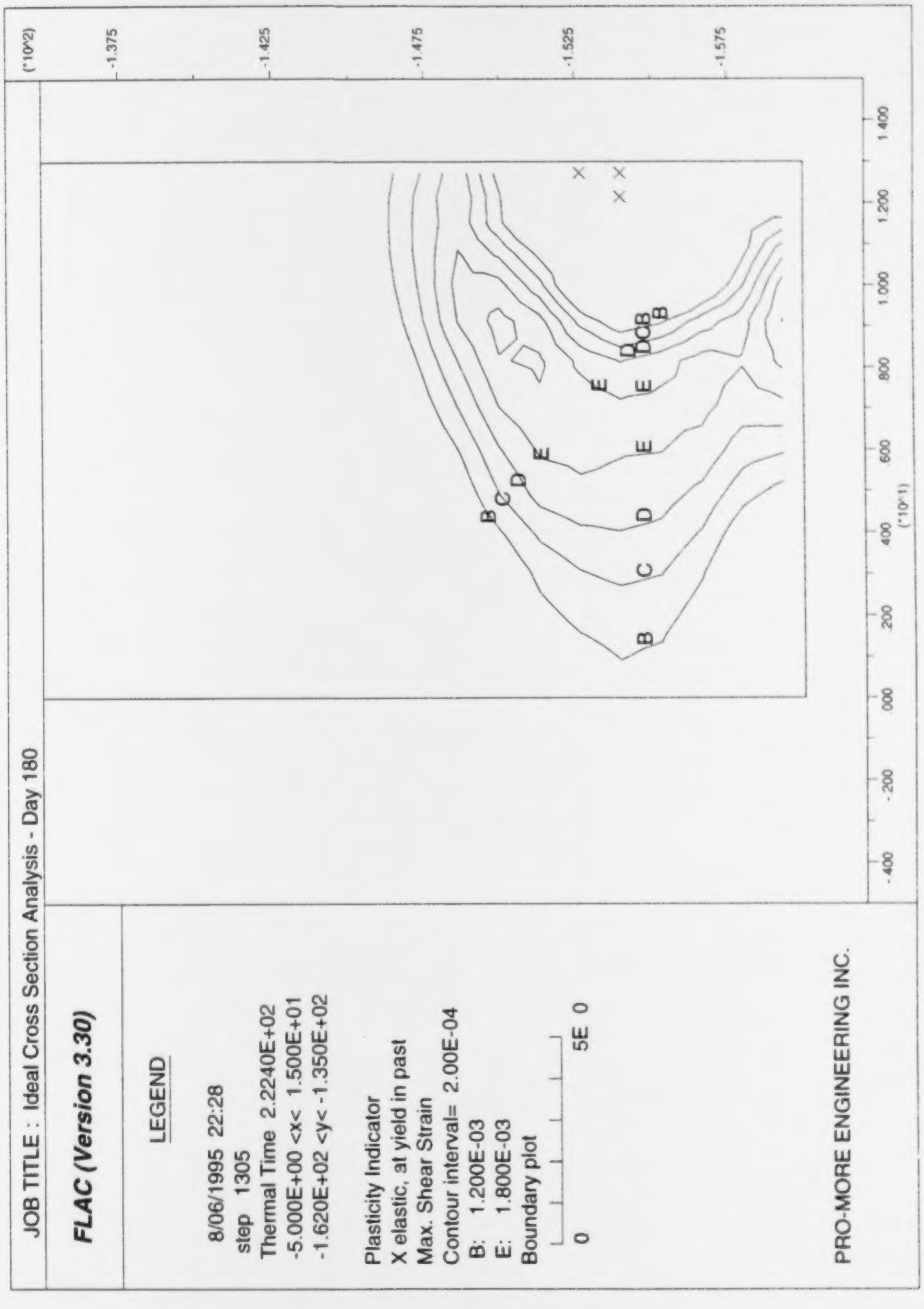

Figure 5.40 Maximum Shear Strain Distribution at 180 Days - Base Case

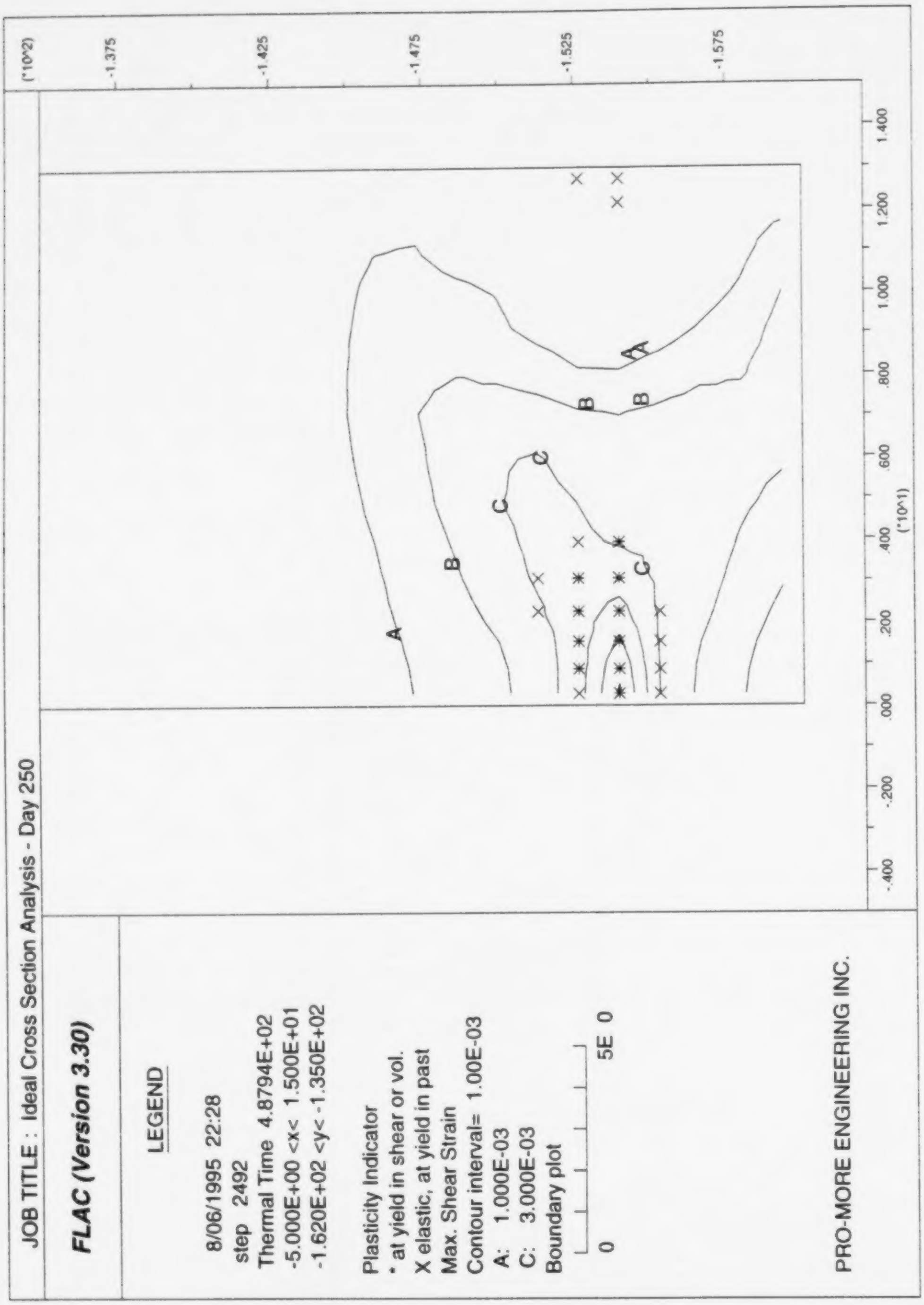

Figure 5.41 Maximum Shear Strain Distribution at 250 Days - Base Case

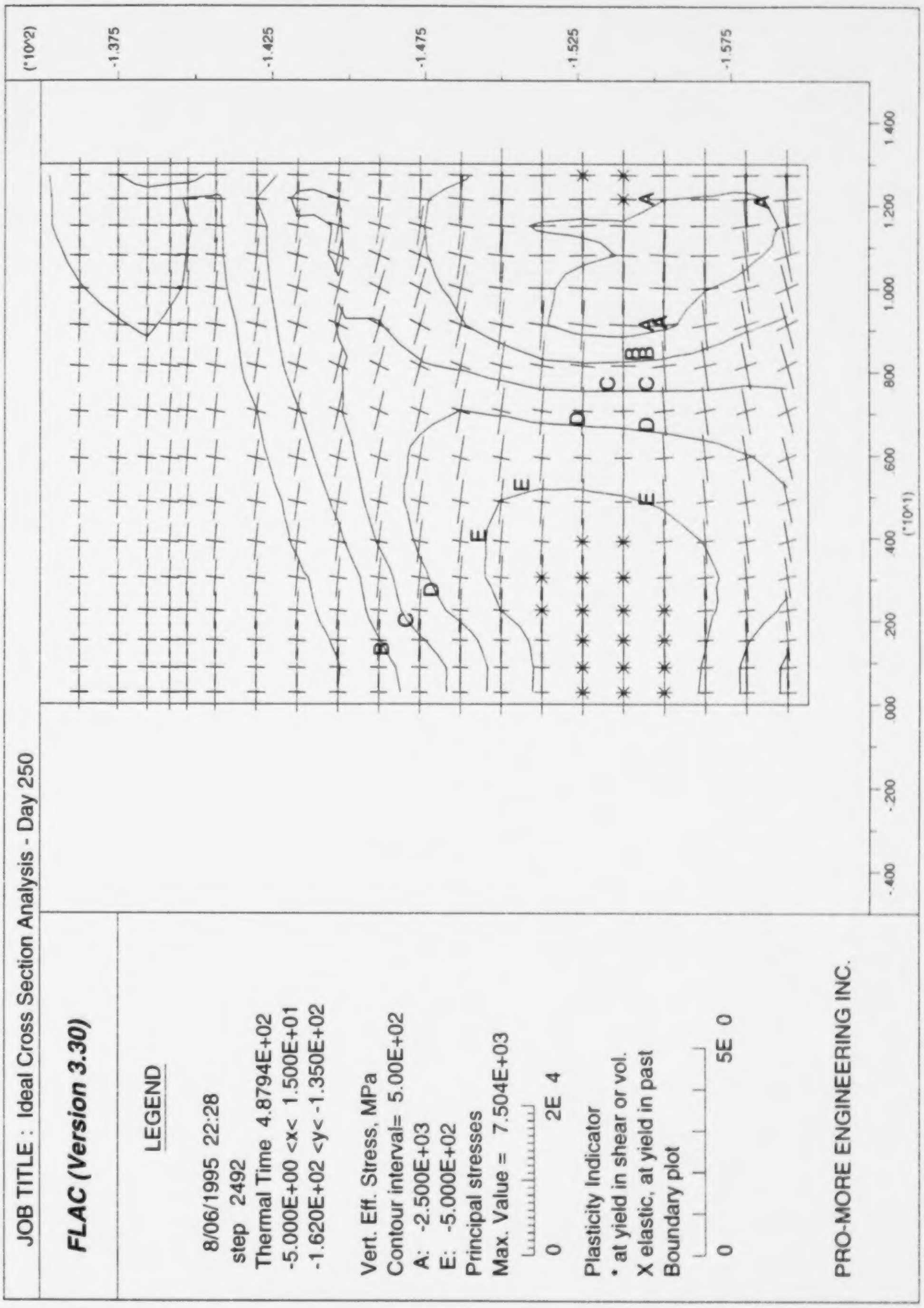

Figure 5.42 Vertical Effective Stress, Stress Tensors and Plasticity Indicator at 250 Days - Base Case

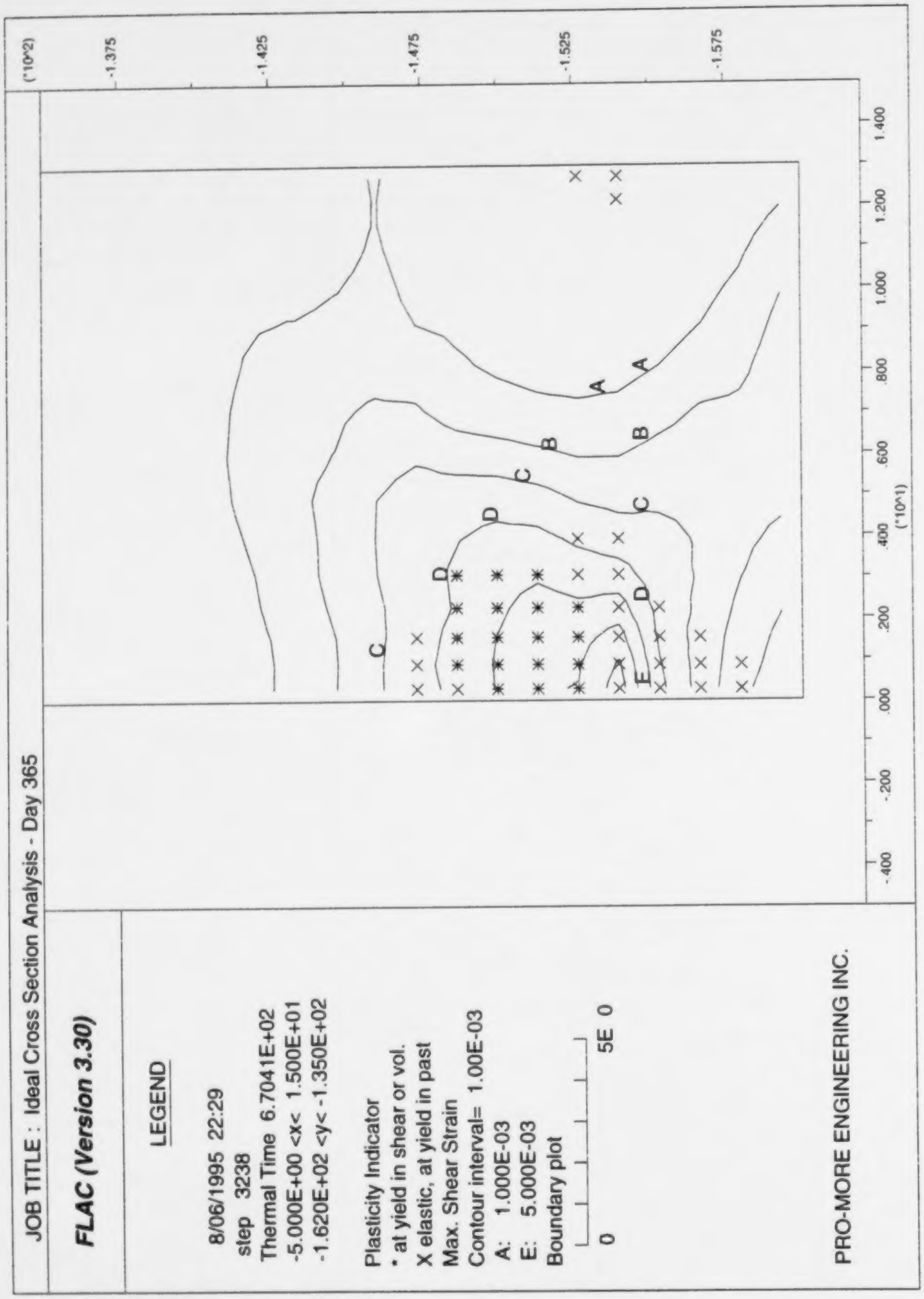

Figure 5.43 Maximum Shear Strain Distribution at 365 Days - Base Case

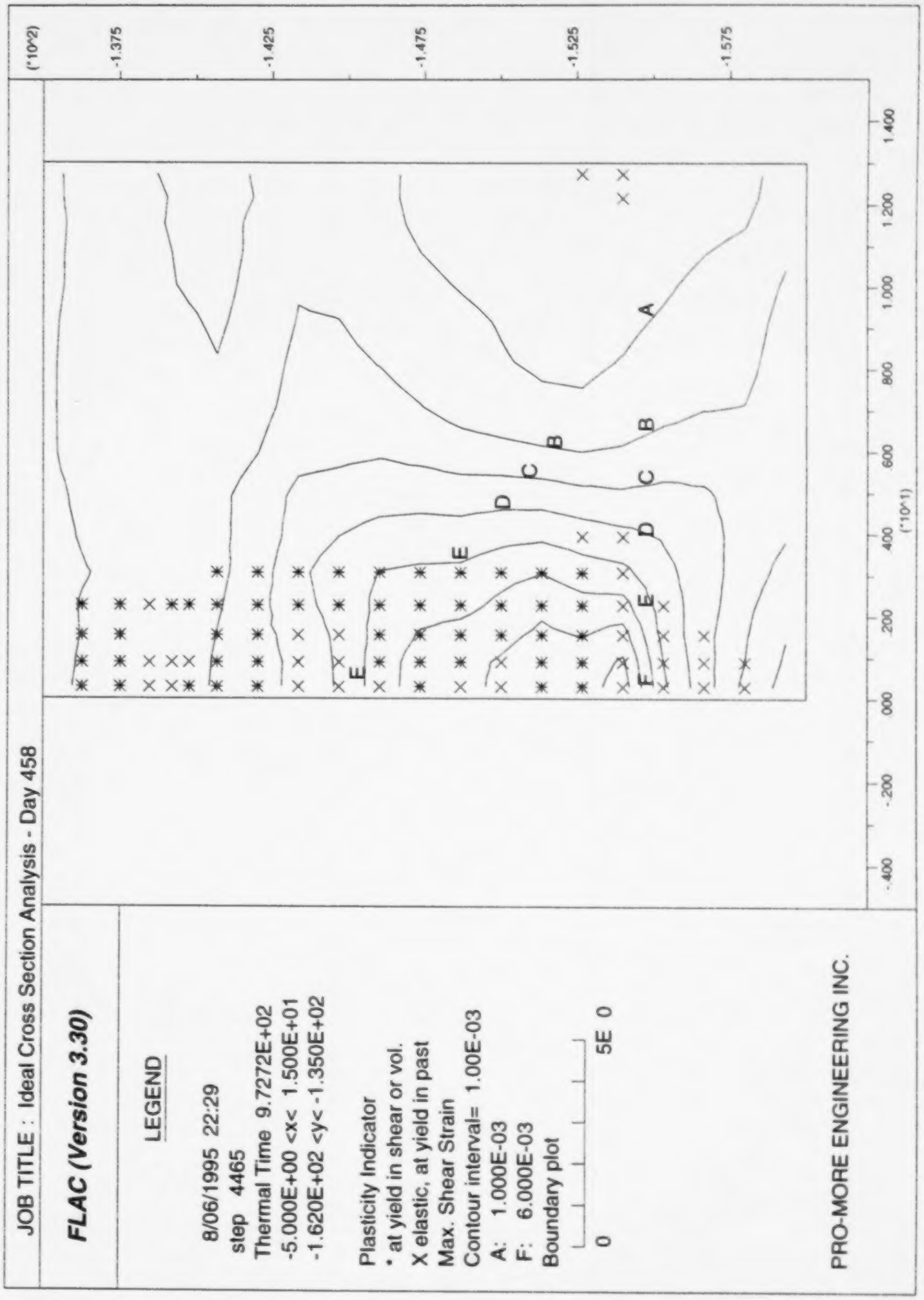

Figure 5.44 Maximum Shear Strain Distribution at 458 Days - Base Case

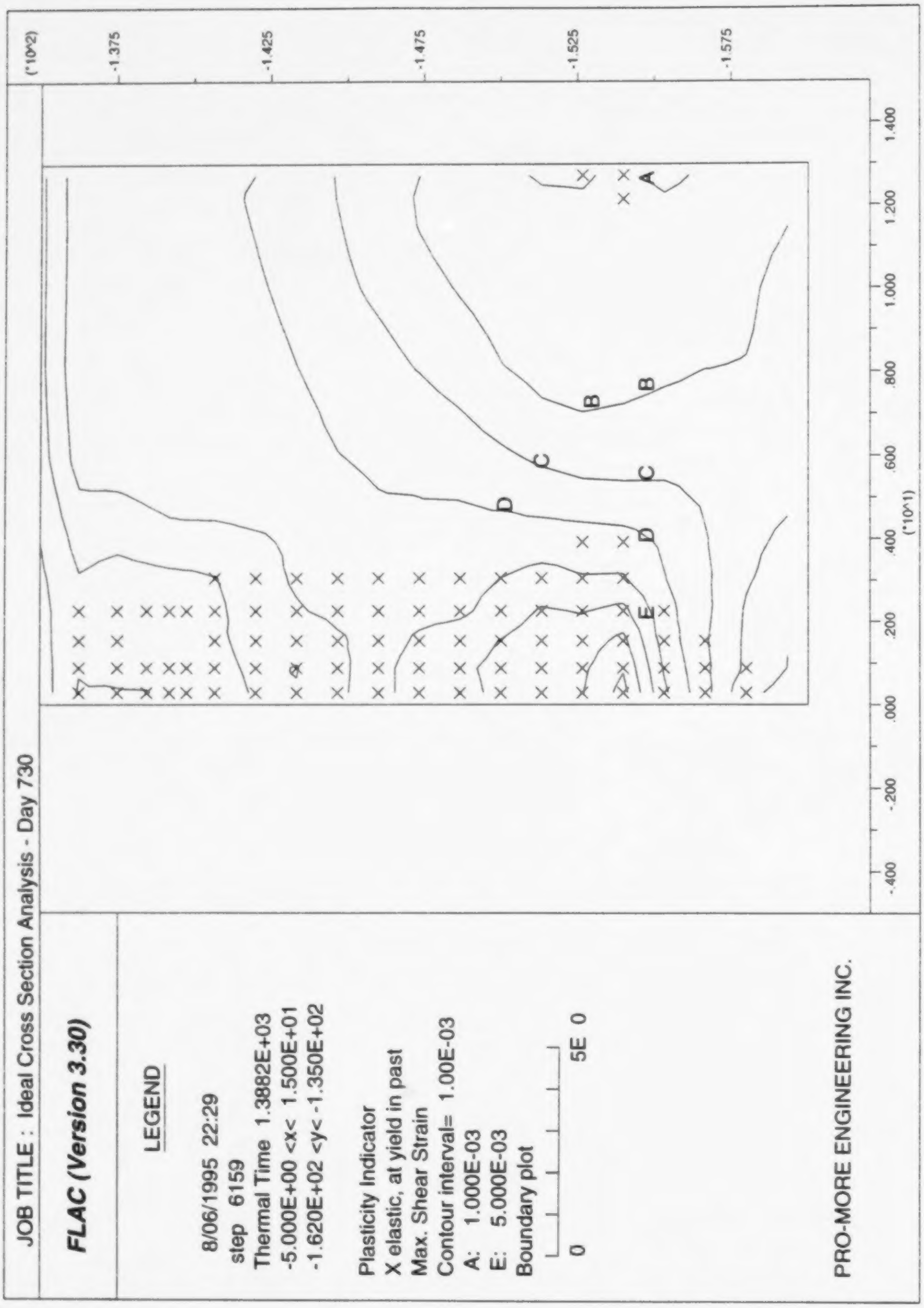

Figure 5.45 Maximum Shear Strain Distribution at 730 Days - Base Case

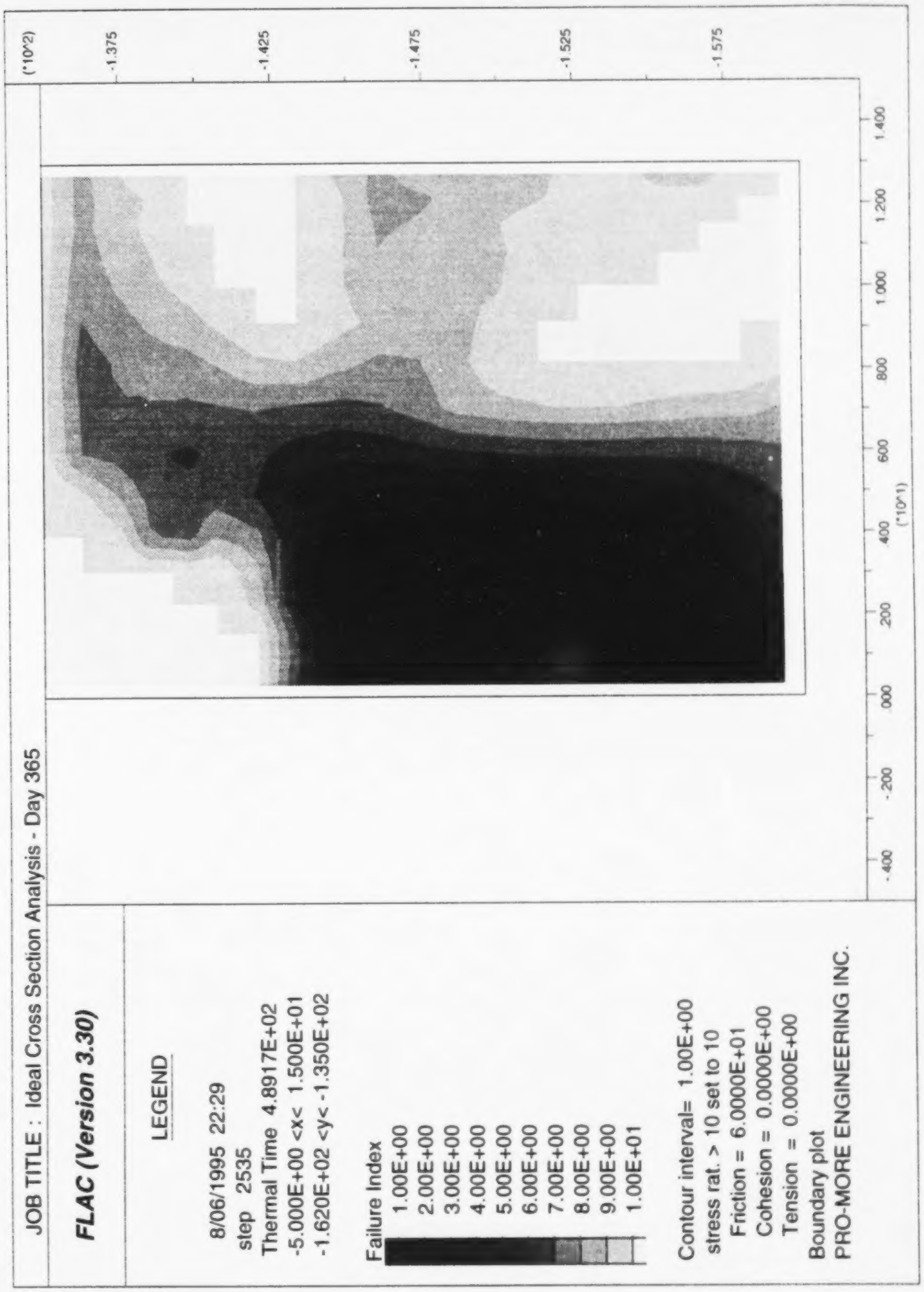

Figure 5.46 Failure Index Distribution at 365 Days - Low Stiffness Parametric Analysis

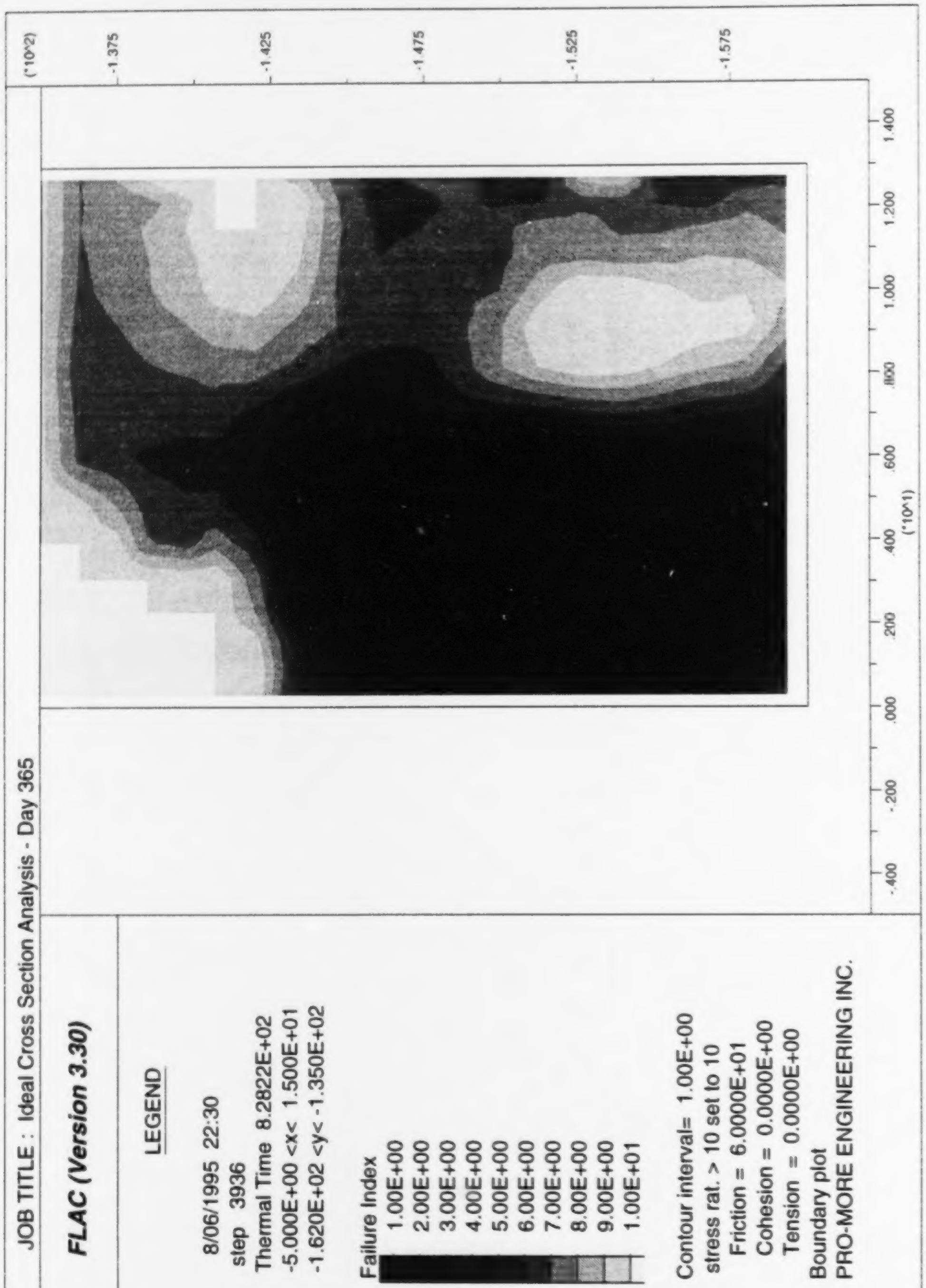

Figure 5.47 Failure Index Distribution at 365 Days - High Stiffness Parametric Analysis

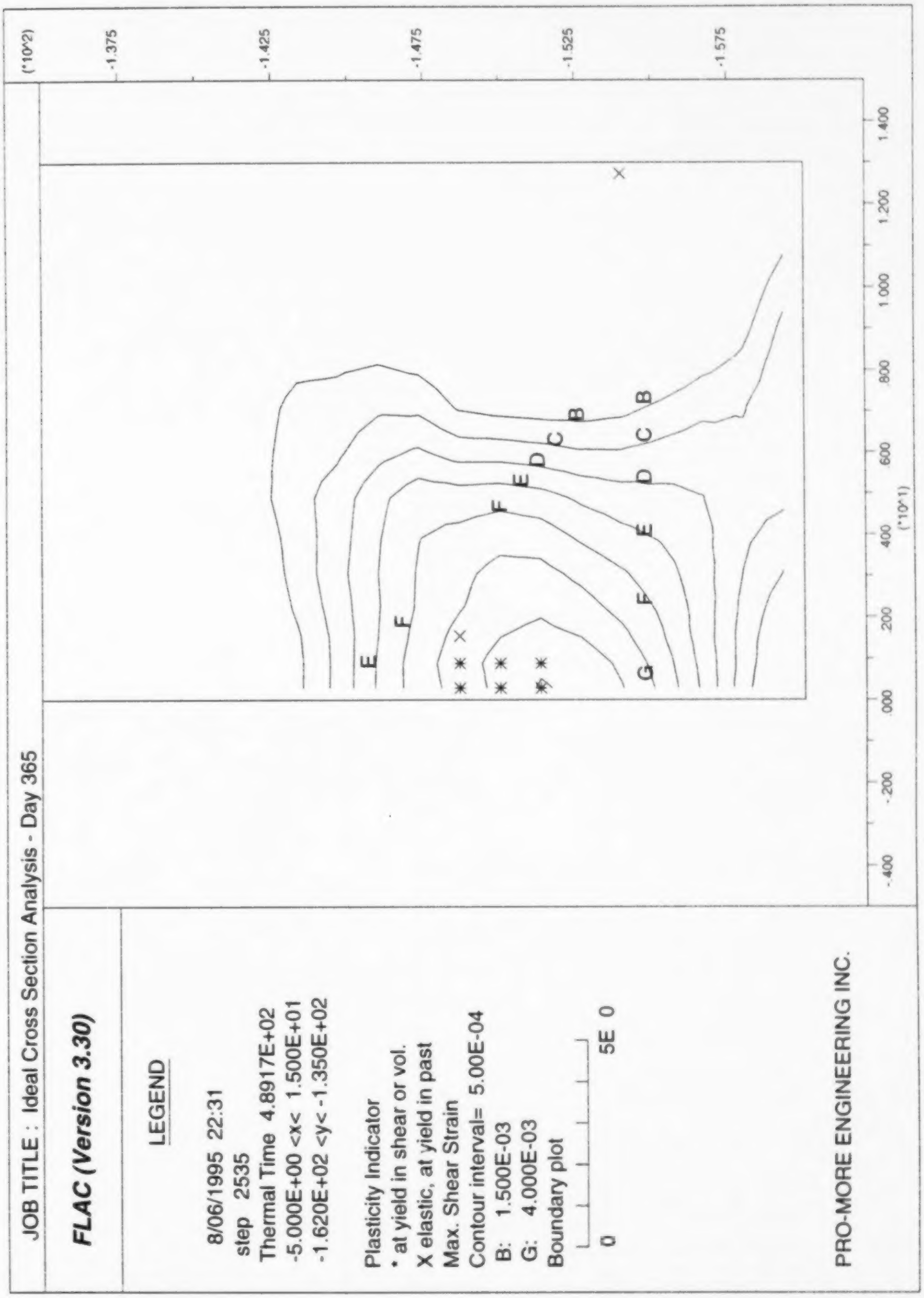

Figure 5.48 Maximum Shear Strain Distribution at 365 Days - Low Stiffness Parametric Analysis

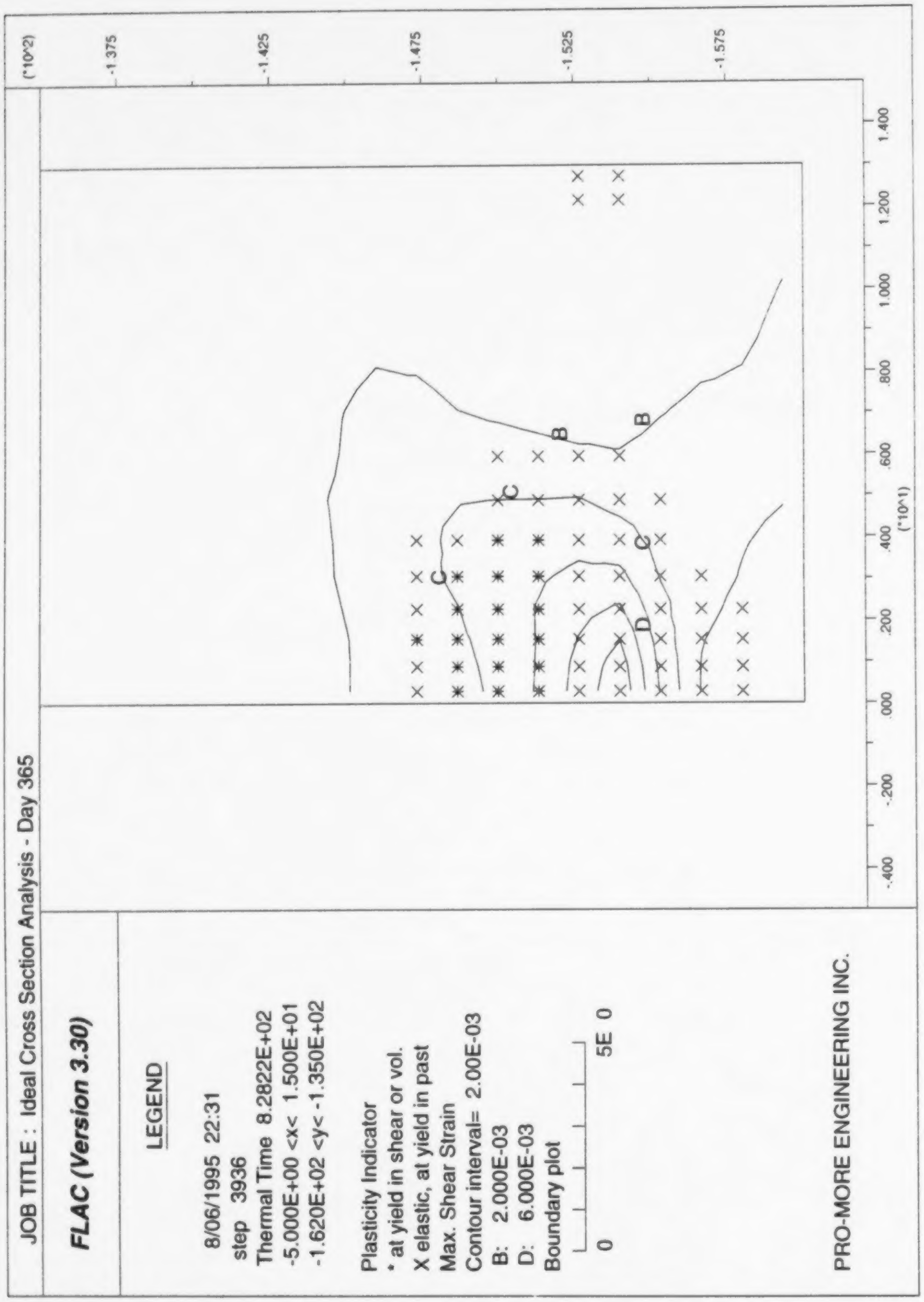

Figure 5.49 Maximum Shear Strain Distribution at 365 Days - High Stiffness Parametric Analysis

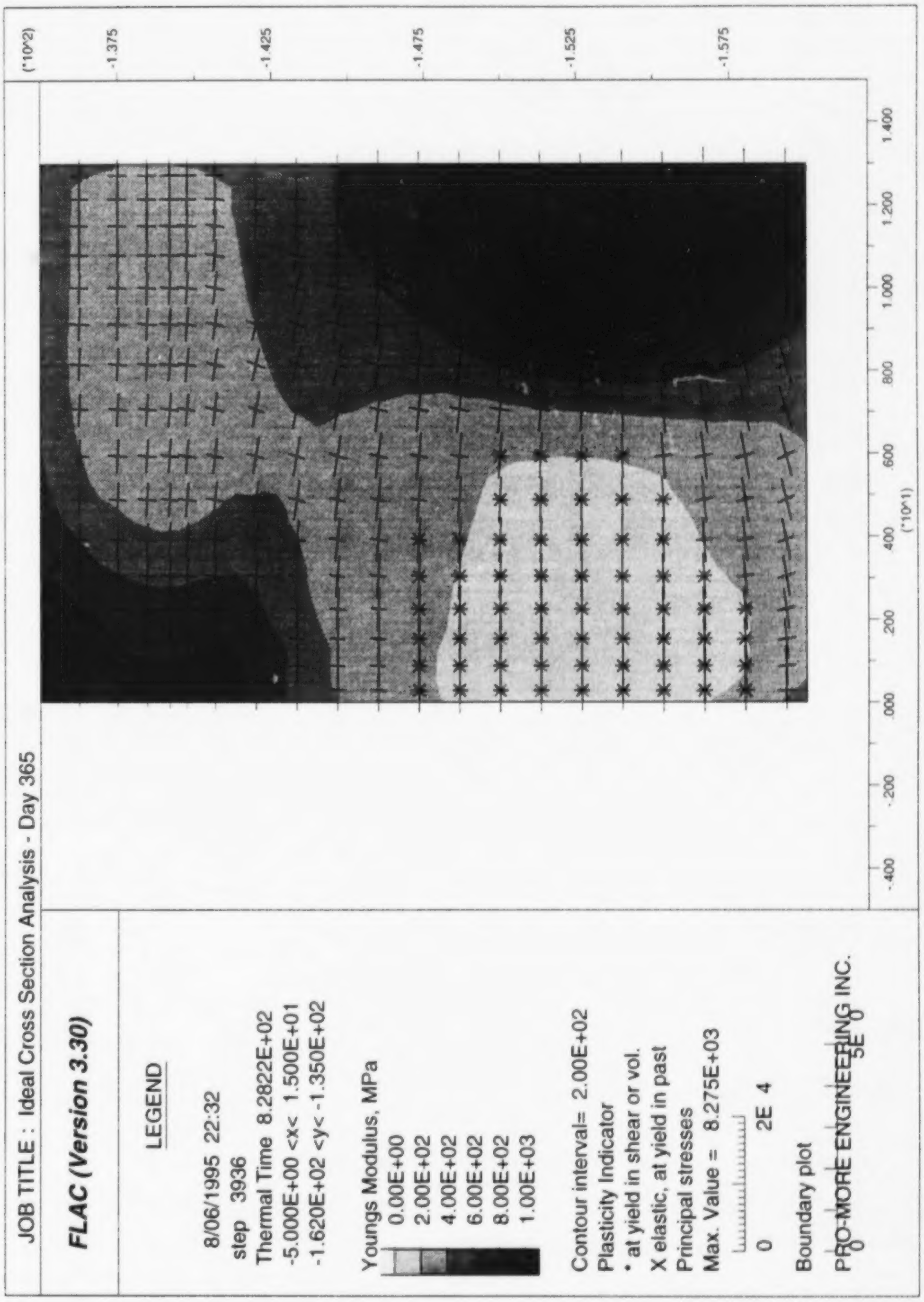

Figure 5.50 Variation in Young's Modulus at 365 Days - High Stiffness Parametric Analysis

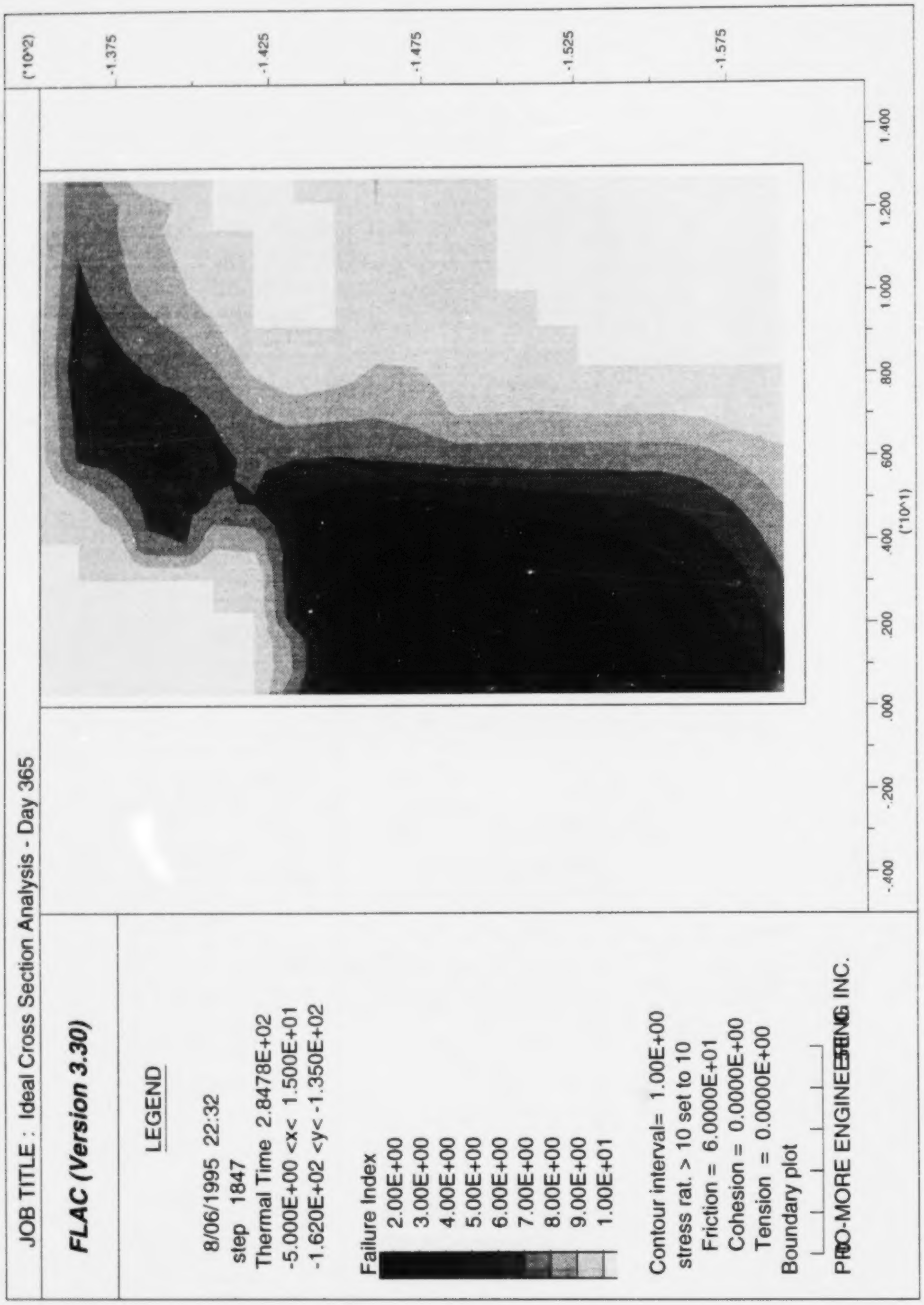

Figure 5.51 Failure Index Distribution at 365 Days - E = 200 MPa Parametric Analysis

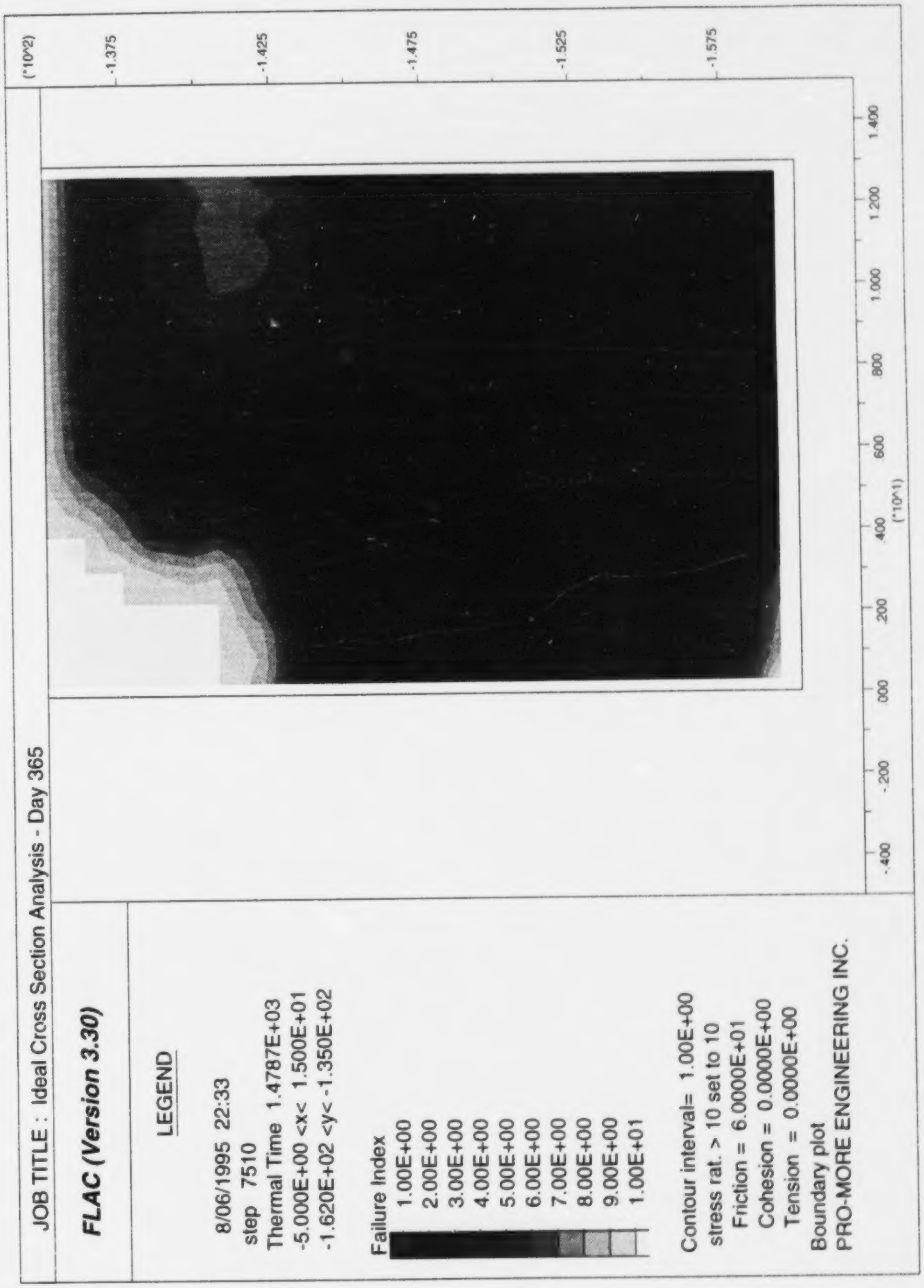

Figure 5.52 Failure Index Distribution at 365 Days - E = 1200 MPa Parametric Analysis

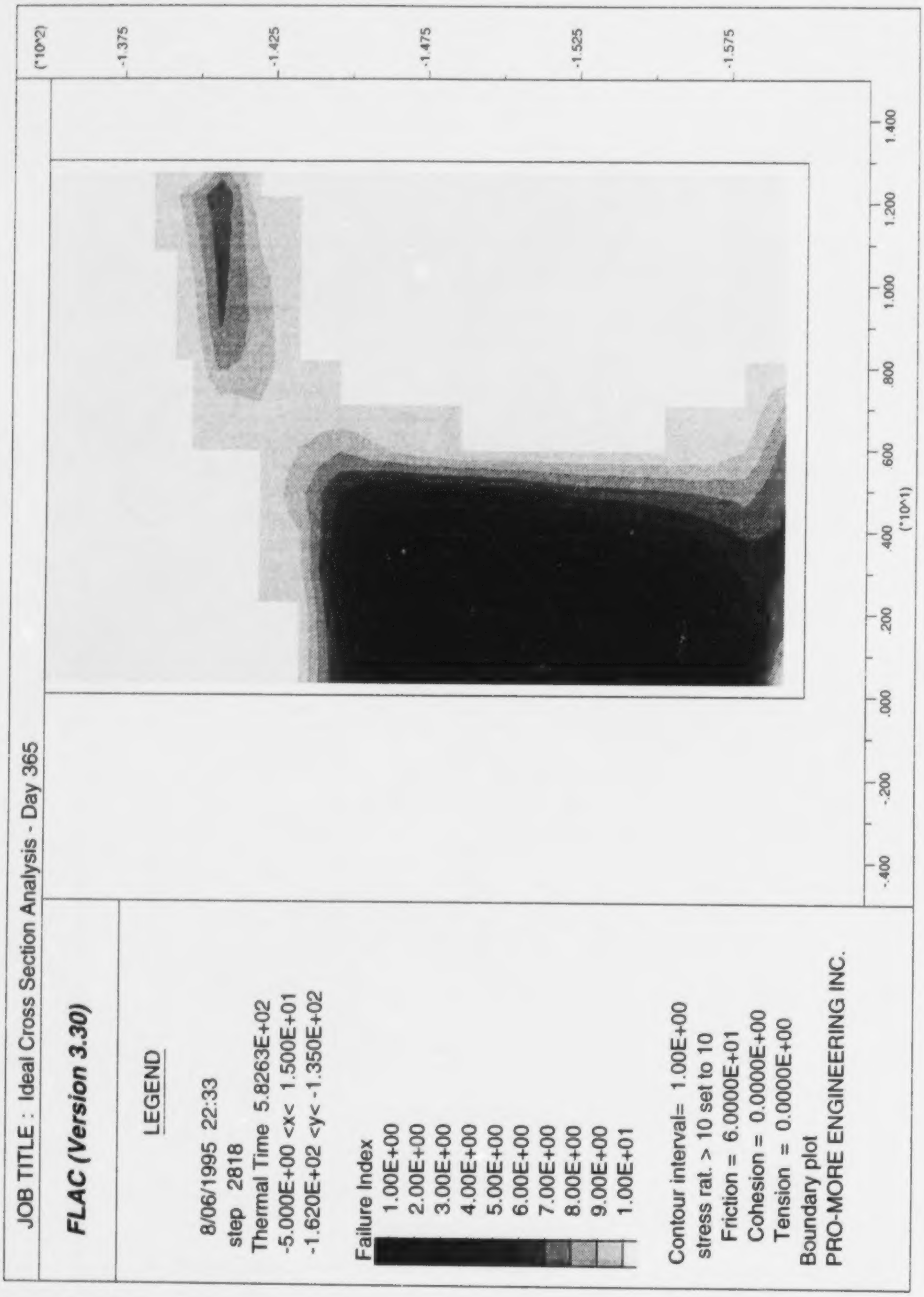

Figure 5.53 Failure Index Distribution at 365 Days - K_o = 1.0 Parametric Analysis

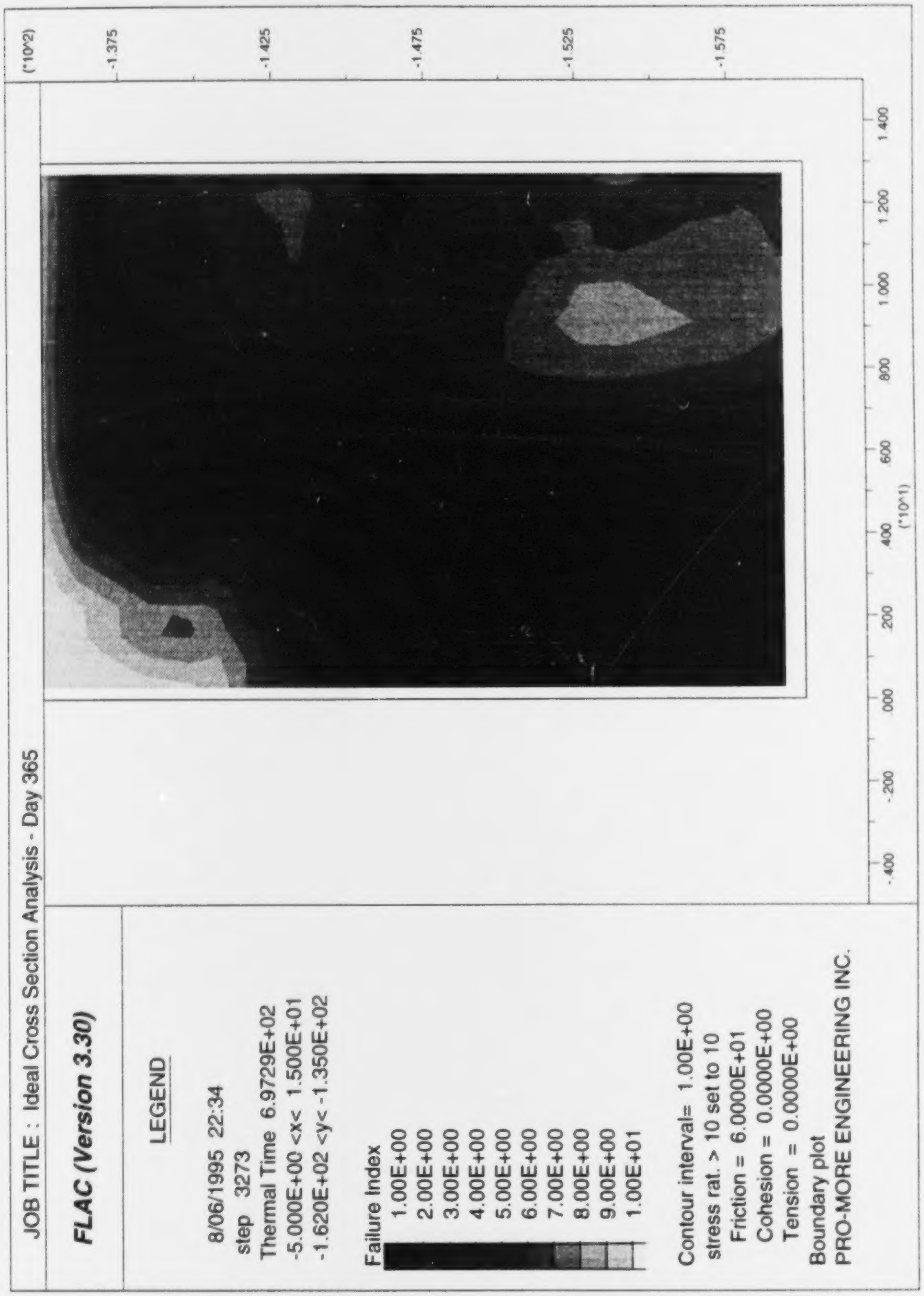

Figure 5.54 Failure Index Distribution at 365 Days - K_o = 2.0 Parametric Analysis

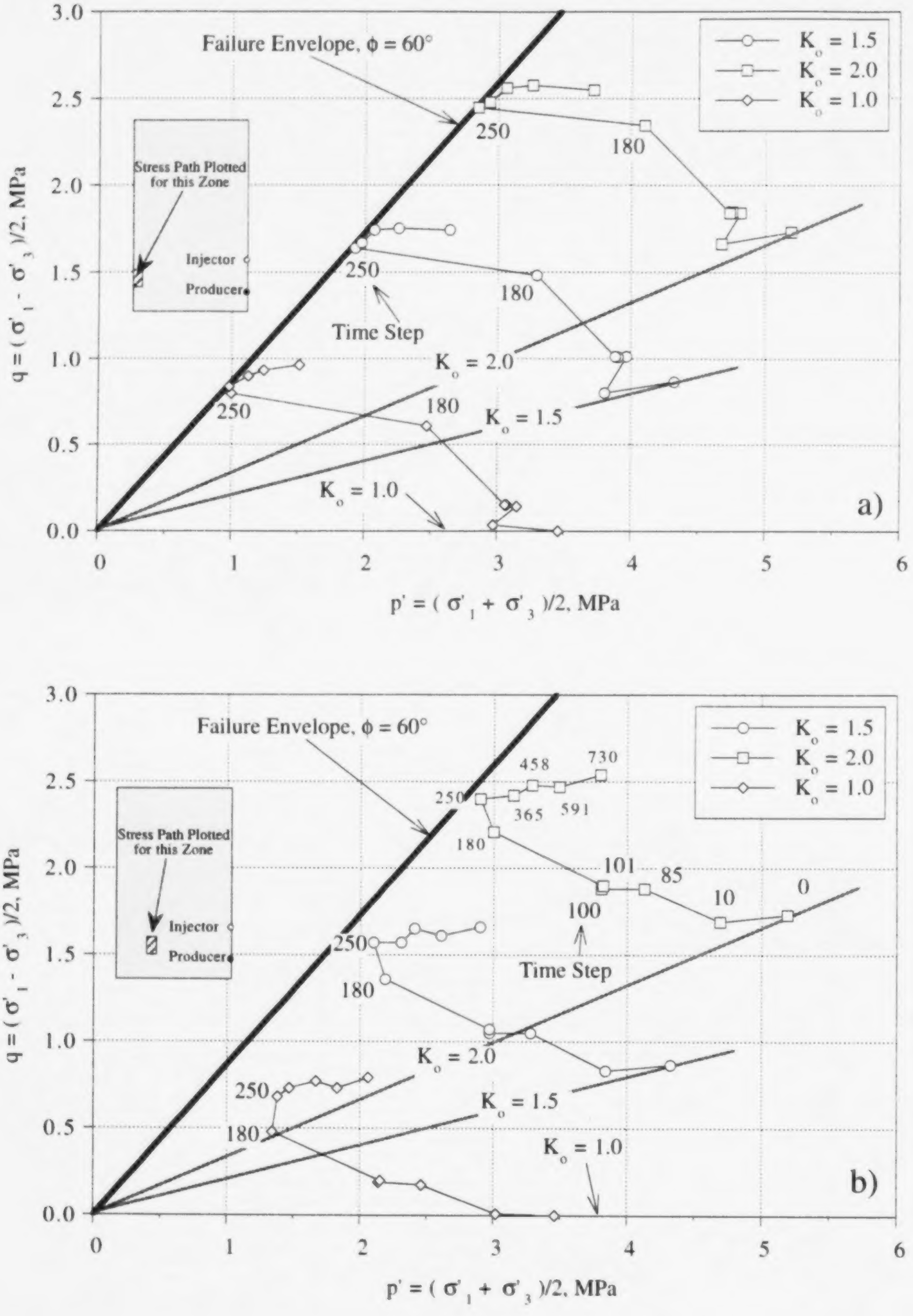

Figure 5.55 Stress Path for Elements Within Reservoir - K_o Parametric Analyses

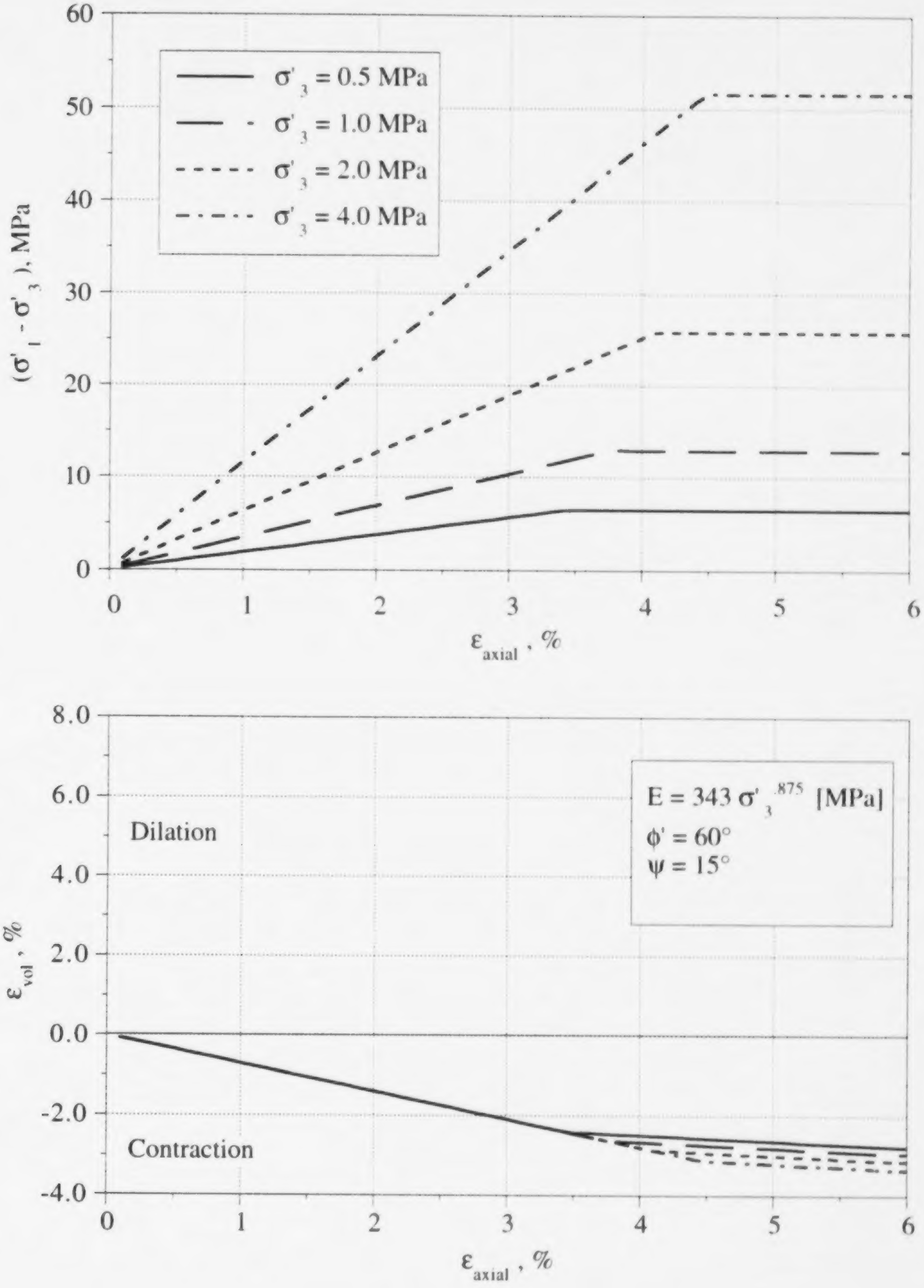

Figure 5.56 Stress Strain Relationship for Base Case Mohr-Coulomb Parameters

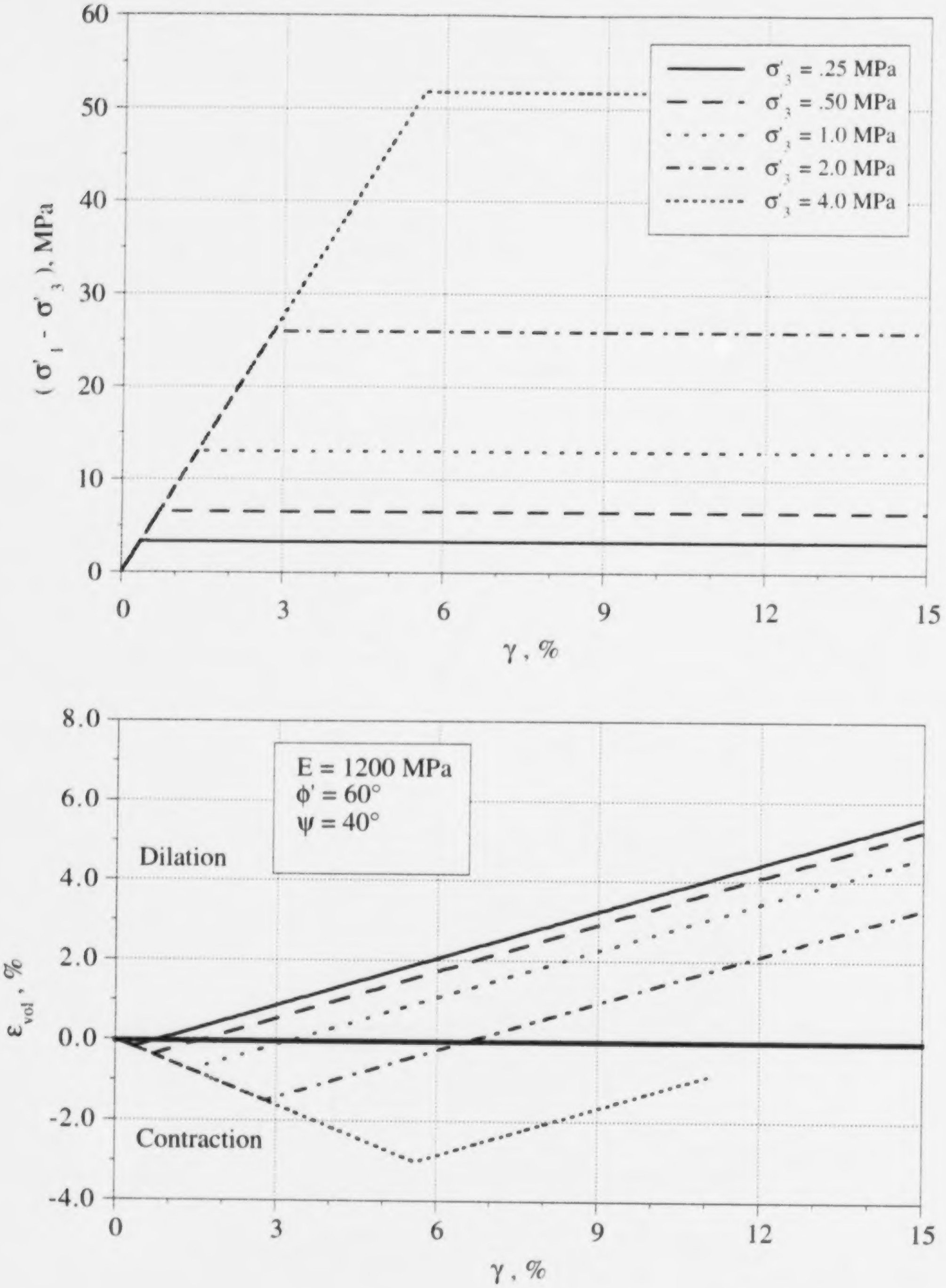

Figure 5.57 Stress Strain Relationship for Enhanced Dilation/Constant Stiffness Mohr-Coulomb Parameters

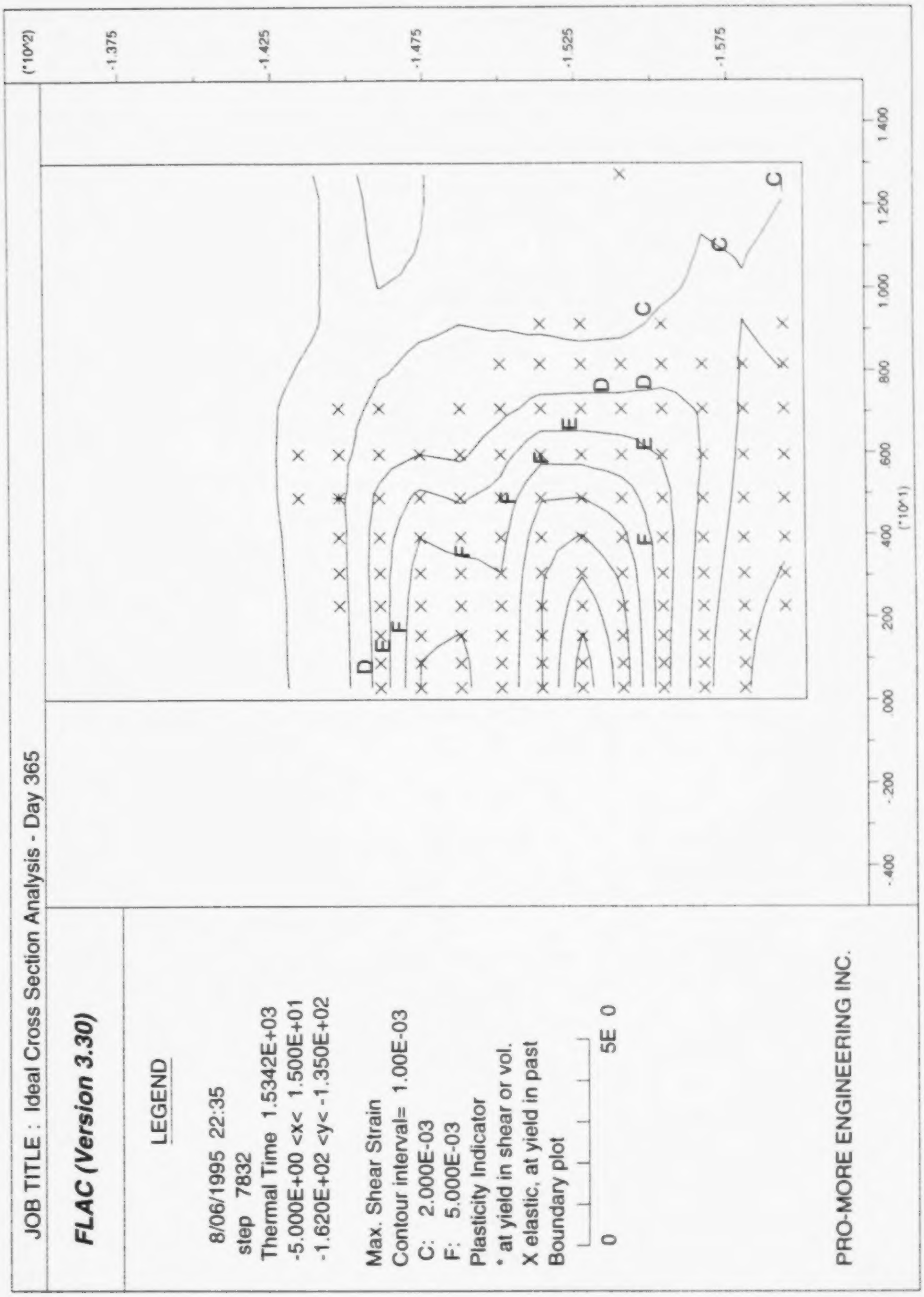

Figure 5.58 Maximum Shear Strain Distribution at 365 Days - Enhanced Dilation/Constant Stiffness Parametric Analysis

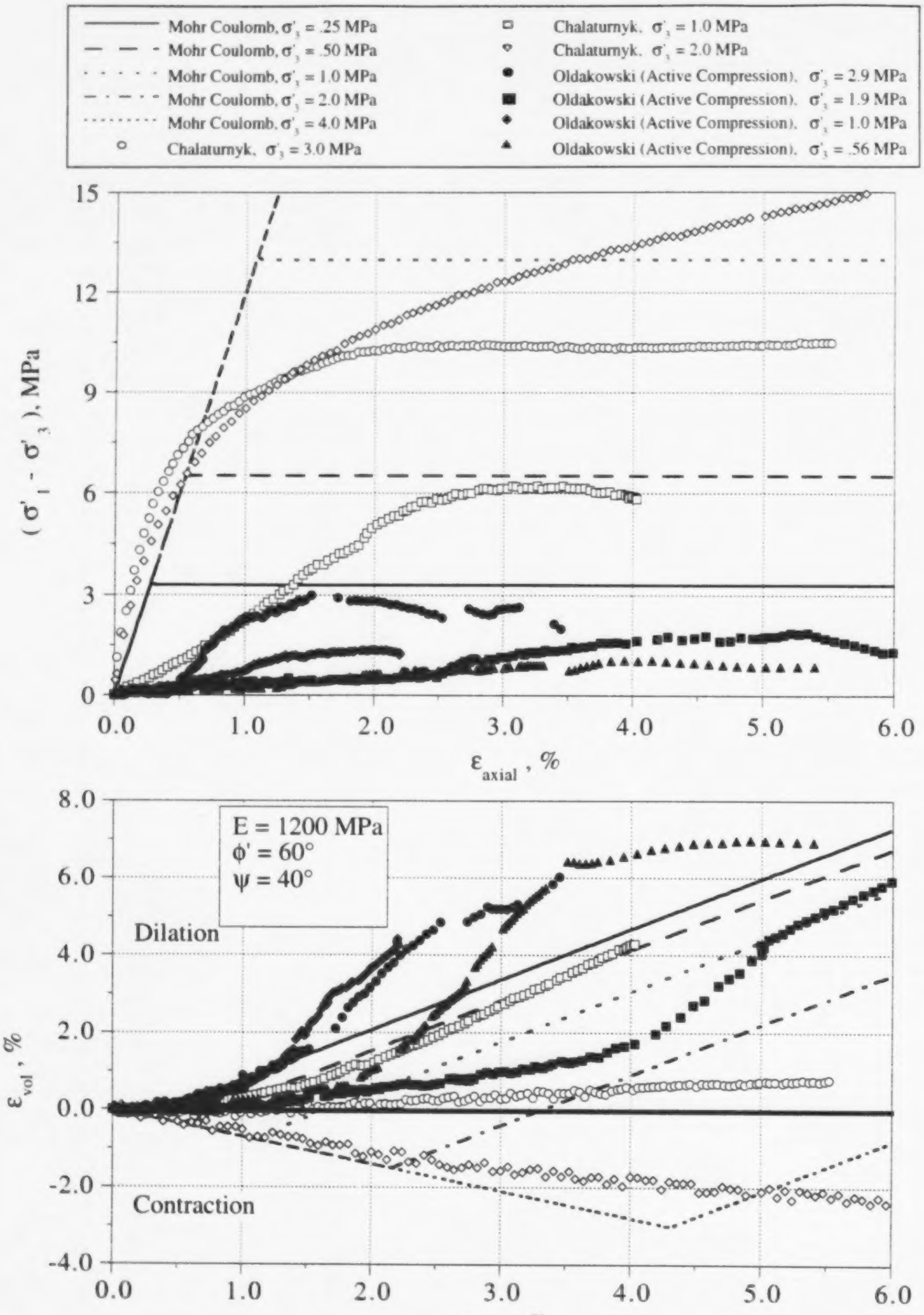

Figure 5.59 Comparison of Elastic-Plastic Stress Strain Relationships to Active Compression Triaxial Test Results

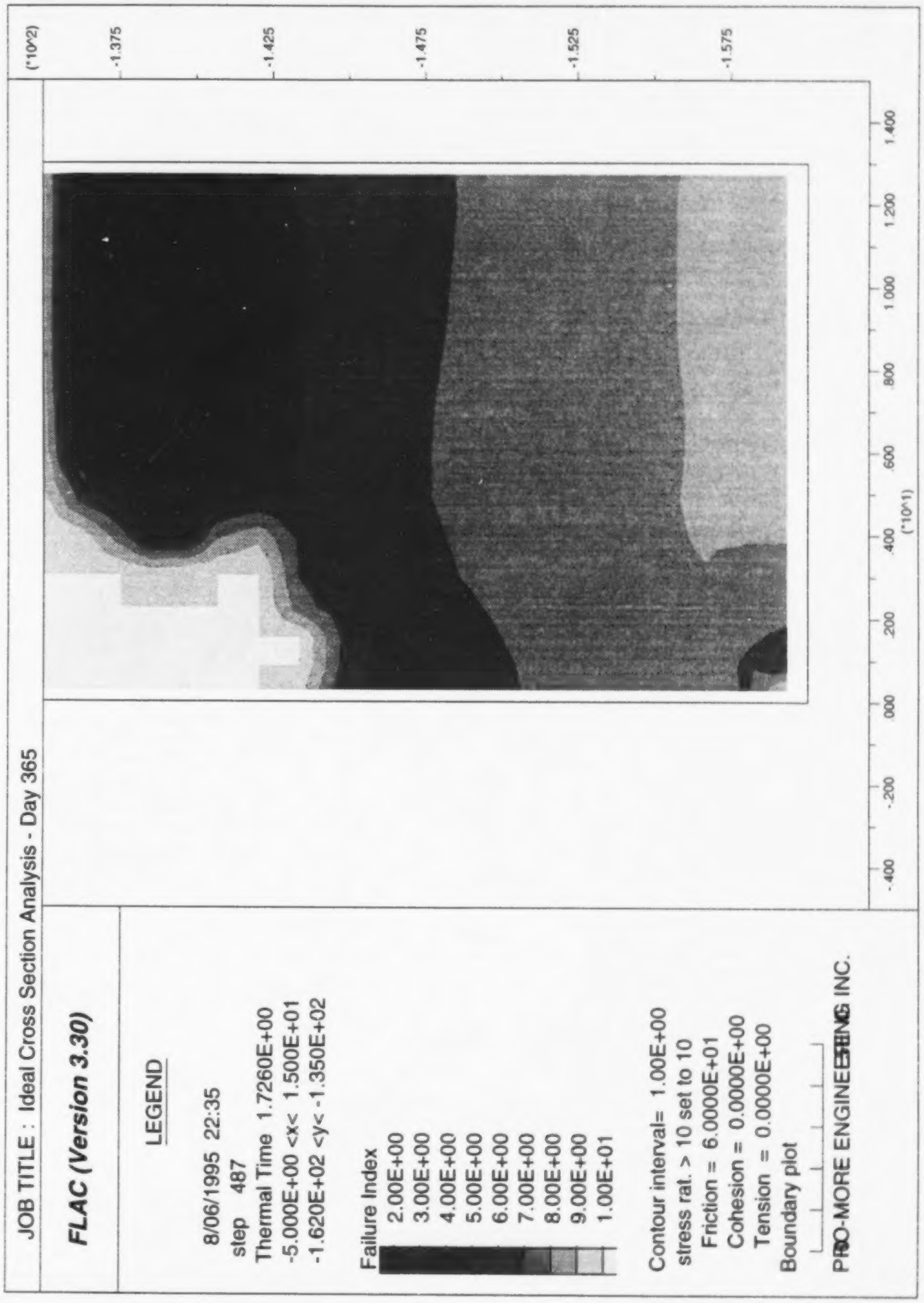

Figure 5.60 Failure Index Distribution at 365 Days - $\beta_b = 0.0$ Parametric Analysis

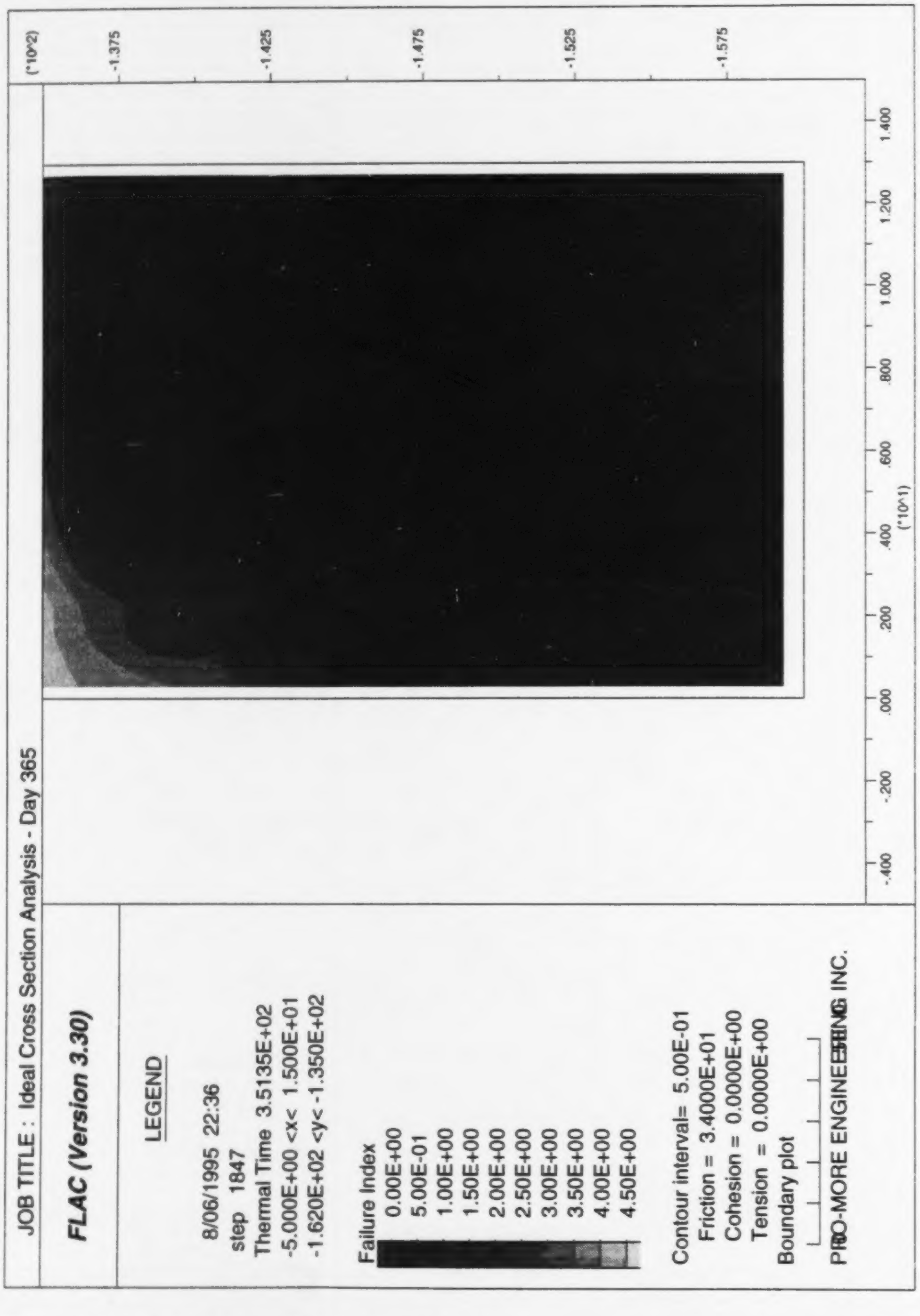

Figure 5.61 Failure Index Distribution at 365 Days - Low Thermal Expansion Parametric Analysis

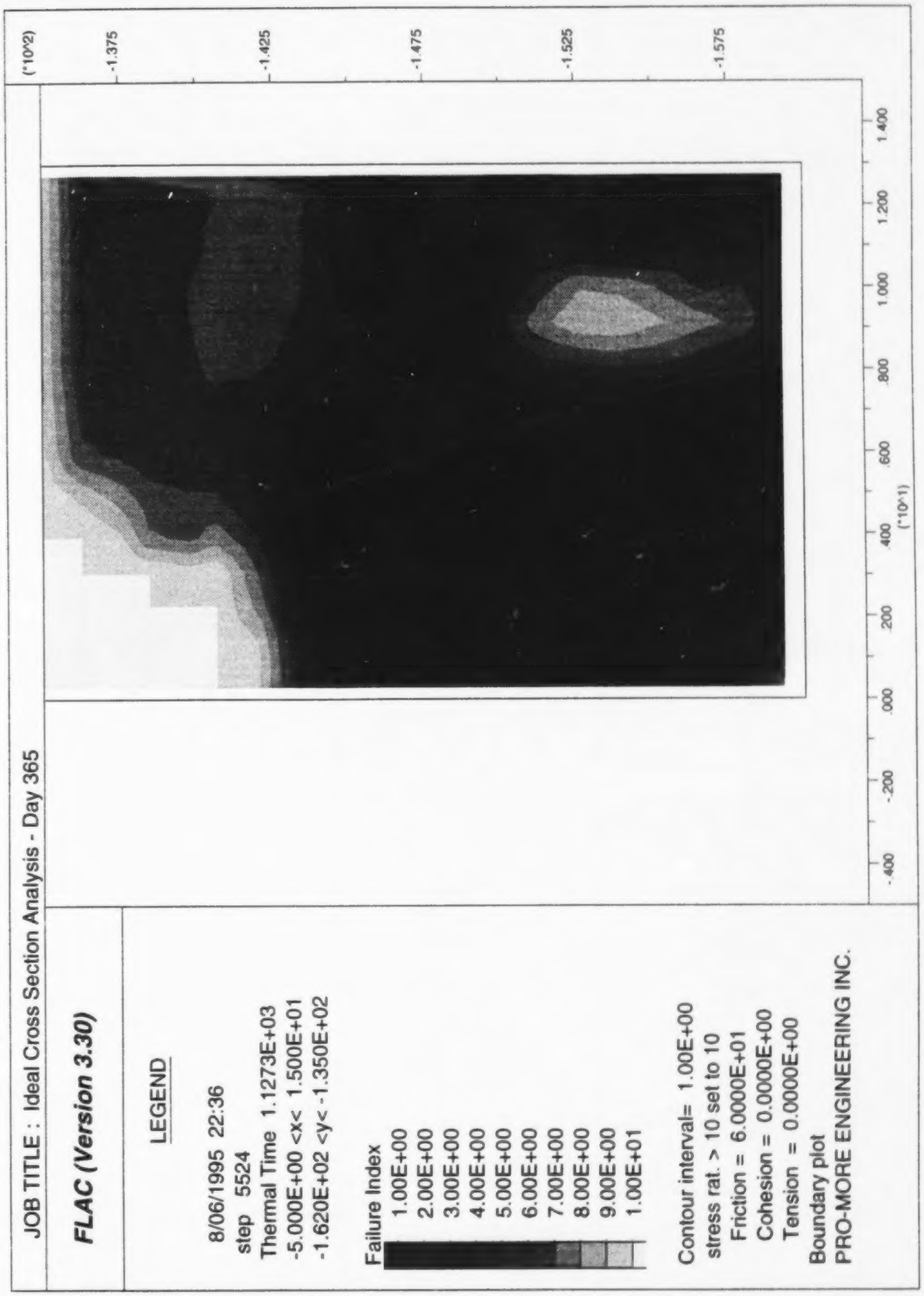

Figure 5.62 Failure Index Distribution at 365 Days - High Thermal Expansion Parametric Analysis

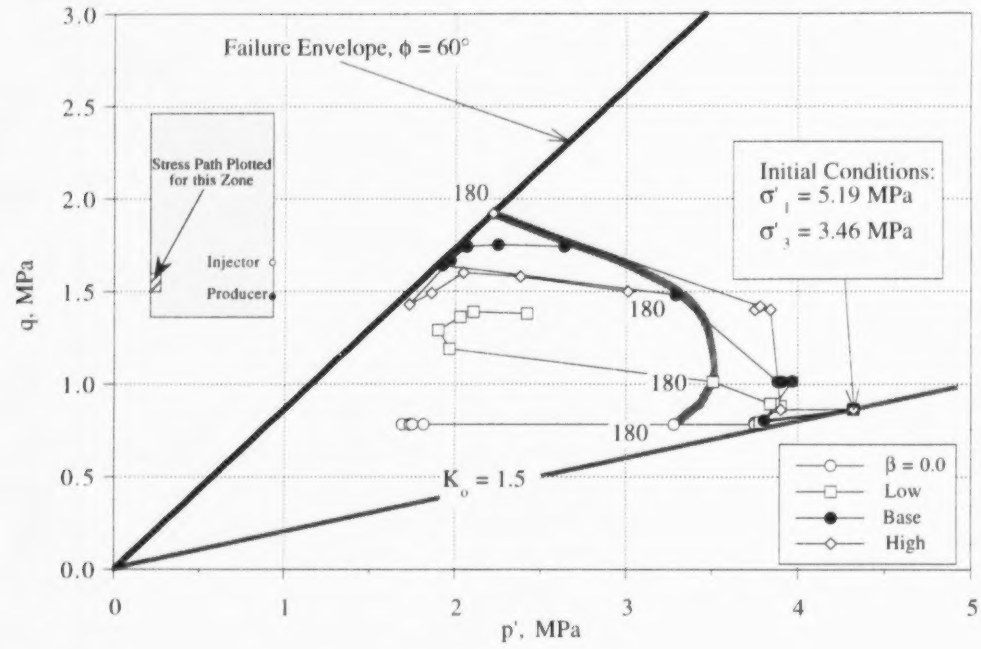

Figure 5.63 Stress Paths Followed for Thermal Expansion Parametric Analyses

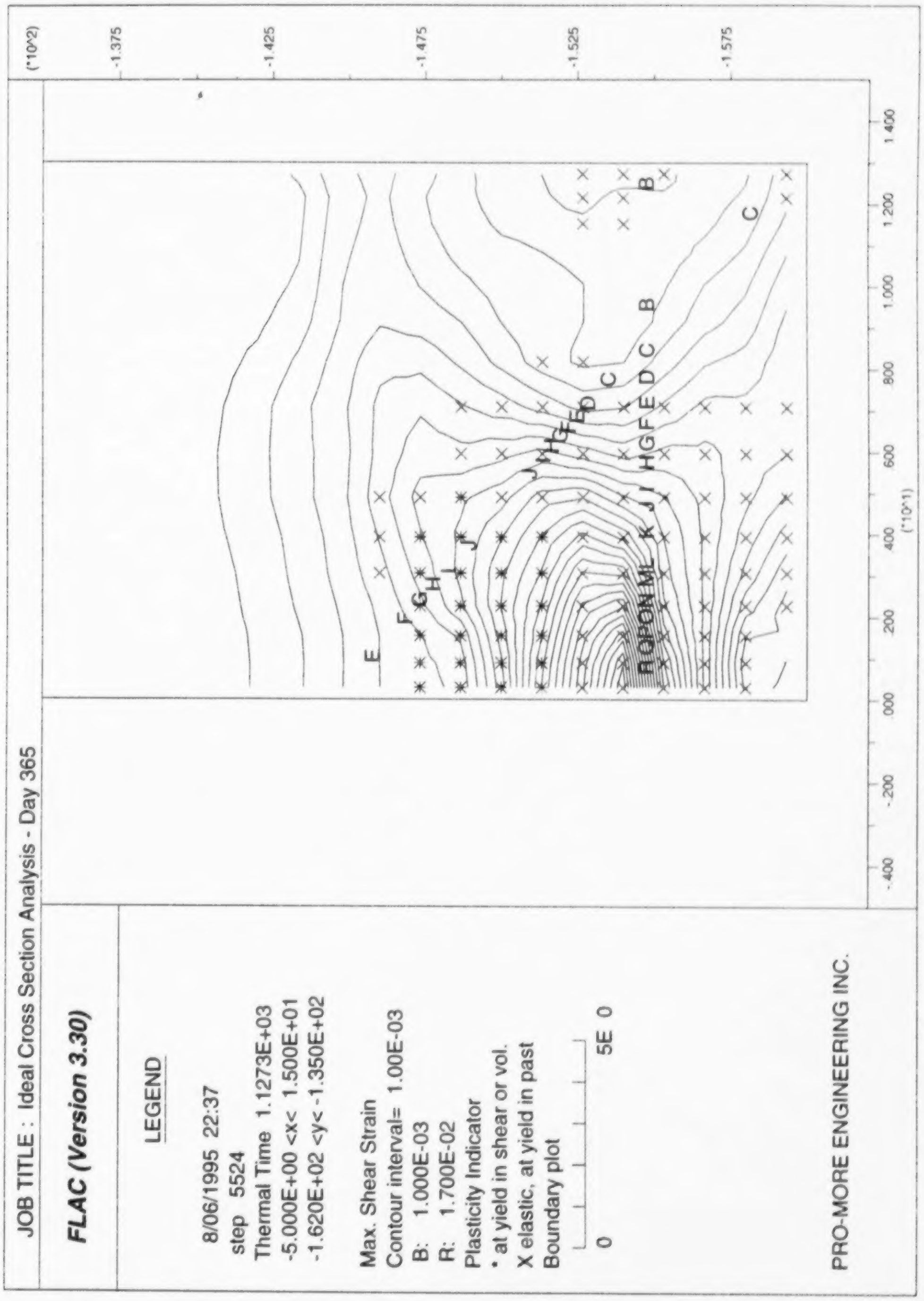

Figure 5.64 Maximum Shear Strain Distribution at 365 Days - High Thermal Expansion Parametric Analysis

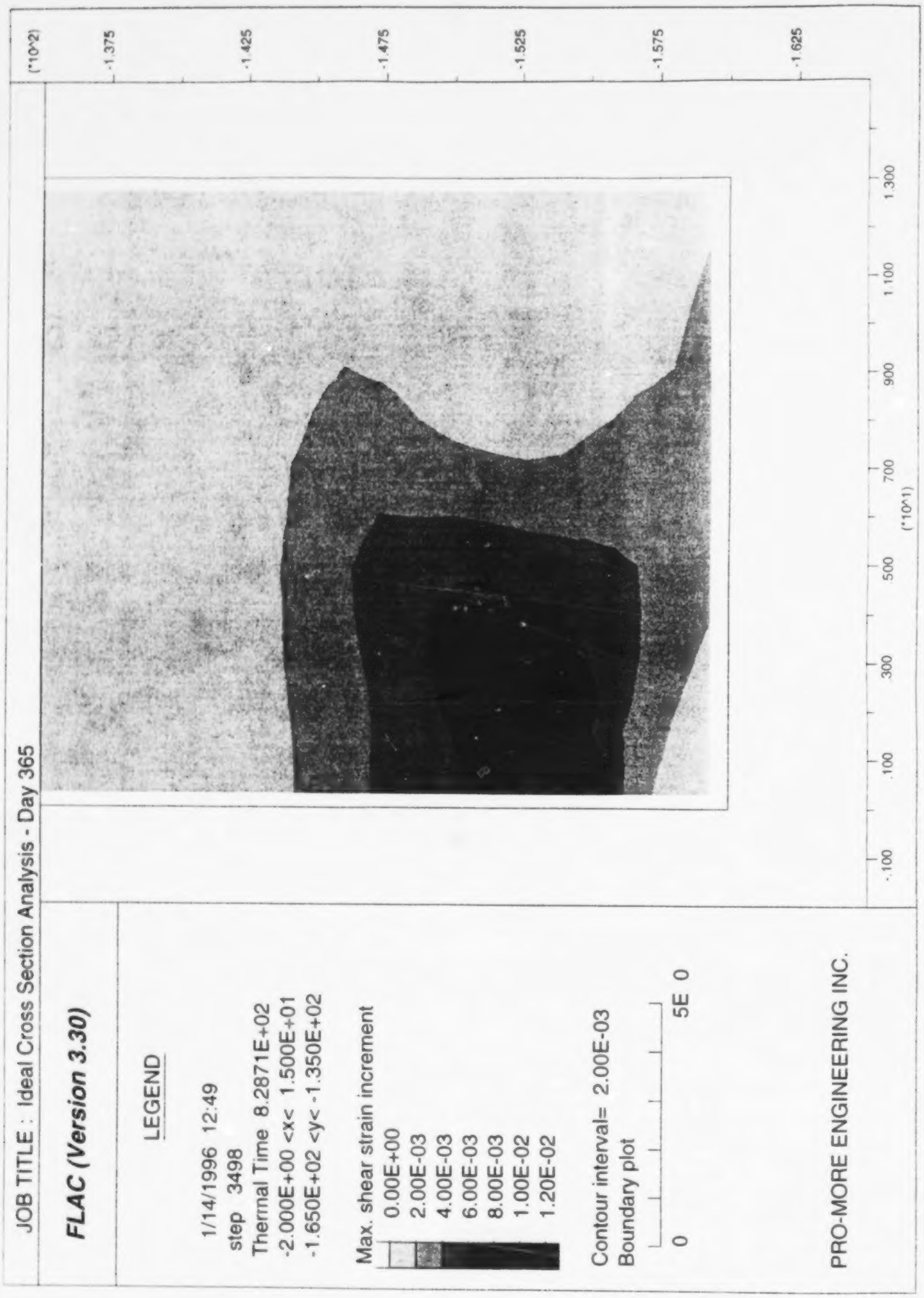

Figure 5.65 Maximum Shear Strain Distribution at 365 Days - Laboratory Bulk Modulus/Effective Confining Stress Relationship

CHAPTER 6 FORMATION RESPONSE TO SAGD PROCESS

"Some circumstantial evidence is very strong, as when you find a trout in the milk"
Henry David Thoreau, 1854

6.1 Introduction

No new theory in soil mechanics should be accepted for practical use without ample demonstration by field observations that it is at least reasonably accurate under a variety of conditions (Terzaghi and Peck, 1967). While the role of geomechanics in the steam assisted gravity drainage process is not strictly a new theory in soil mechanics, one of the primary objectives of the geotechnical instrumentation program at the UTF was to evaluate the influence of geomechanical phenomena on the SAGD recovery process. The objective of this chapter is to review the process history and to determine the detailed response of the reservoir instrumentation to the SAGD recovery process. The field instrumentation response is then synthesized to provide field evidence of geomechanical phenomena in the SAGD process.

The analyses presented in this chapter are framed within a west-east plane dissecting the wellpairs; the geotechnical cross section. In anticipation of uniformly developing steam chambers along the length of each wellpair, the geotechnical instrumentation was installed along this west-east plane. For uniform development of the steam chambers, the reservoir behavior within the geotechnical cross section would be close to plane strain conditions and would provide representative data on formation response to the SAGD process. The location of the instrumentation wells relative to the geotechnical cross section was reviewed in Chapter 3 and is illustrated in Figure 3.12. As will be seen subsequently, the steam chambers unfortunately did not develop uniformly and the field instrumentation response within the geotechnical cross section was the result of more three dimensional rather than plane strain deformation conditions within the reservoir.

6.2 Process History

6.2.1 Injection / Production Pressures

As part of the "steam trap" process control procedures, all injection and production pressures were monitored at the wellhead locations. For the purposes of analysis within the reservoir then, the wellhead pressures were adjusted to equivalent reservoir injection and production pressures. Friction and head losses of approximately 200 kPa have been assumed between the wellheads and the reservoir (Edmunds et al., 1992). Friction losses during steam injection serve to reduce the well screen injection pressures by 200 kPa in comparison to the wellhead pressures. A reduction of 200 kPa between the well screen and the wellhead pressures for the production well are mainly due to the head difference between the two locations.

In assessing the geomechanical response of the reservoir to SAGD, change in fluid pressure rather than its absolute value was considered. Consequently, pressure histories of the wells were modified to account for original hydrostatic pore pressure within the formation. The initial reservoir pore pressures at the wellpair elevations within the geotechnical cross-section were chosen as reference pore pressures.

Figures 6.1, 6.2 and 6.3 illustrate the resulting injection and production pressure histories for wellpairs A1, A2 and A3, respectively. For reasons of ease and increased clarity when comparing injection and production pressures to instrumentation behavior, the injection and production pressure histories were simplified. These figures also show the detailed pressure history response for each wellpair. As shown by the shaded lines in Figures 6.1, 6.2 and 6.3, which depict the detailed pressure histories, care has been taken to retain significant pressure fluctuations for the simplified pressure histories.

6.2.2 Steam Chamber Development

A tabulated history of the Phase A process events for each wellpair is provided in Table 6.1 This table describes the major operational conditions for each wellpair throughout the Phase A trials. The following discussion links the growth of the steam chamber within the reservoir and operational history of the wellpairs to the temperature and pore pressure evolution within the geotechnical cross section. An understanding of these interrelationships is important when assessing the response of instrumentation to SAGD processes. As well, the anticipated plane strain development of the SAGD process within the geotechnical cross section did not occur primarily due to the unexpected occurrence of Unit F between the injector and producer of wellpair A1; the world is truly ruled by geology. As discussed subsequently, this increases the need to understand the three dimensional development of the steam chambers.

A detailed assessment of the temperature field within the geotechnical cross-section was completed in order to provide adequate data for comparison with piezometer, extensometer, and inclinometer results and for use in numerical modeling. Contours of temperature were generated from instrument results within or near the geotechnical cross section. Specifically, temperature measurements from the following wells were used in generating the isotherms:

1) Thermocouple Wells: AT1, AT4, AT7, AT9, AT12, AT14;
2) Piezometer Wells: AGP1, AGP2, AGP4, AGP5, AGP6; and

3) Inclinometer Wells: AGI1, AGI3.

A complete record of all thermocouple well measurements is provided in Appendix A. Due to the detailed nature of the contouring, the paucity of data and the requirement for applying engineering judgment to the contouring process, no acceptable numerical interpolation technique could be found which would adequately provide "infill" temperature values for detailed contouring. Consequently, a regularly spaced grid of temperatures was created manually.

For each time step, measured temperatures were plotted in their correct position within a scaled diagram of the geotechnical cross-section. Contours were drawn, by hand, based on these values. Once drawn, a detailed overlay grid was used to extract the temperatures for each isotherm. An in situ temperature of 8 °C was subtracted from each value in order to obtain the change in temperature at each point. Note that these temperatures will continue to be referred to as temperature contours. The change in temperature along with the coordinates of each overlay grid point were used to generate contour plots from a commercially available software package (SYSTAT©, 1990). A smoothing function based on distributed weighted least squares regression was used for contouring. Use of the smoothing function generally resulted in the loss of some detail in the contours. For this reason, the temperature contour plots do not provide an absolute representation of detailed temperatures within the geotechnical cross section but can be used to study the "evolution" of temperatures. For numerical modeling or detailed data analysis, the temperatures recorded on the detailed overlay grid were used.

As with temperature, a detailed assessment of pore pressure development within the geotechnical cross section was necessary for field data analysis and numerical modeling. Since most piezometers were located within the geotechnical cross-section, they were of extreme importance in understanding the formation response to SAGD.

To correspond with wellpair injection and production pressures, which have been adjusted for initial reservoir pressures, the change in pore pressure at each piezometer location was also utilized for contouring. Table 6.2 provides a complete record of the pore pressure history for each measurement point along with the estimated initial reservoir pressures. The pore pressures provided in Table 6.2 were obtained from consideration of both the vibrating wire and pneumatic piezometers installed at each measurement point. Appendix B provides the detailed records for each pore pressure measurement as well as its comparison to the injection/production pressures for each wellpair. Figure 6.4 illustrates the initial pore pressure gradient within the reservoir. This agrees with a regional hydrogeologic study of the UTF area (Hardy Associates(1978) Ltd., 1984). The slope of the pressure head line is steeper than hydrostatic pressure indicating an upward component of groundwater flow. The low absolute value of pore pressure combined with the upward flow gradient towards the Wabiskaw Sand (Unit A), are the major reasons postulated for the low amount of dissolved gas in the McMurray Formation bitumen at the UTF site.

Using the initial pore pressure distribution shown in Figure 6.4, the original pore pressure at each piezometer location was subtracted from the pore pressure readings to provide the change in pore pressure; noted by the italicized values in Table 6.2. The contours for pore pressure were generated in the same fashion as temperature with one major exception; the hand drawn contours were scanned and retraced on a computer in order to maintain as much detail as possible;

The temperature and pore pressure contours have been generated for 19 time steps from 1.9 to 10.0; these detailed contours can be found in Appendix E and F, respectively. The discussion of steam chamber development, wellpair operations and pressure/temperature evolution in the geotechnical cross section has been subdivided into seven time steps; pre-time 0, times 0 to 2.9, 2.9 to 4.3, 4.3 to 5.7, 5.7 to 7.1, 7.1 to 8.6 and 8.6 to 10.0.

6.2.2.1 Prior to Time 0.0

Prior to initial steaming of the A1 wellpair, a cold water injection test was performed on both wells (Edmunds et al., 1988). This test was designed to confirm laboratory measurements of the initial relative permeability to water in the oil sands, which typically gave values of about 10^{-4}. In addition, it was hoped to characterize the apparent bulk permeability anisotropy of the reservoir by monitoring the pressure change at the piezometers. The test was implemented by supplying cold water to each well in turn for about 10 days at a constant sand face pressure of about 1600 kPa. Both wells accepted significant quantities of water during the 20 day test with virtually no piezometer response; even piezometers within metres of the A1 wellpair. The following conclusions were reached based on the test (Edmunds et al., 1988):

- the water did not enter the rich pay but likely entered the top few meters of the limestone, traveling back down the outside of the liner from the well screens. The limestone was found in other tests to have sufficient permeability to account for the injection flow rates of the test; and

- there is virtually no water permeability within the rich oil sands. With bitumen as the only mobile phase, the reservoir pressure diffusivity is low enough to explain the lack of measurable response during the test period.

6.2.2.2 Time 0.0 to 2.9

From time 0.0 to 0.6, steam was circulated into the annulus and out of the tubing in both AI1 and AP1. A pressure differential of approximately 350 kPa was maintained between AI1 and AP1 over this period. As shown in Figure 6.1, the injection and production well pressure change was 1750 kPa and 1600 kPa, respectively. At time 0.6 and for the remainder of the Phase A trials, the direction of circulation was reversed to circulation into the tubing and out of the annulus.

Up to time 2.0, steam circulation continued at these conditions in AI1 and AP1. Figure 6.5 illustrates the temperature and pore pressure distribution within the geotechnical cross section at time 1.4. During this startup phase, conduction was controlling the heat distribution as evidenced by a modest temperature increase of 30 °C very near the A1 wellpair. This modest temperature increase, however, is sufficient to reduce the bitumen viscosity such that the fluid mobility is increased and pore pressures can develop within this zone. As shown in Figure 4.38, a 30 °C temperature rise from 8 °C to 38°C will reduce the bitumen viscosity two orders of magnitude from 7,000,000 centipoise to approximately 70,000 centipoise.

Around wellpair A1, the change in pressure reflects the injection pressure. The pressure gradient becomes large as you progress from the 30 °C temperature zone around the wells outward towards cooler regions within the reservoir. Again, this gradient reflects the large influence temperature has on bitumen viscosity. In terms of pore pressure development within the reservoir, this highlights a specific phenomena which occurs during thermal pilots. As warm bitumen flows or moves into cooler regions of the reservoir, it will increase in viscosity, the fluid phase mobility will decrease and the evolution of fluid pressures in the cooler region will be retarded.

Of particular interest during this time period is the region beyond the zone of pore pressure increase which is exhibiting a modest decrease in pore pressure. Close examination of the pore pressure data presented in Table 6.2 confirms that statistically, these pore pressure reductions were true measurements. The one exception may be the piezometer located at elevation 281.8 m in well AT9 which tended to have a large standard deviation about its initial mean pressure.

Over this period, wells AI1 and AP1 were subject to fluid injection only, no production or drawdown was occurring. Consequently, a pore pressure reduction occurring under injection only conditions is indicative of a stress change under undrained conditions. For an isotropic stress change, a pore pressure reduction would require a corresponding reduction in σ_m. Pore pressure reduction is also possible with shear stress under undrained conditions. The magnitude of the pressure reduction is small however; a maximum pore pressure decrease of 60 kPa was measured at elevation 277.7 in Well AGP6. For all undrained tests conducted on oil sands (Agar, 1984; Plewes, 1987; Kosar, 1989), the initial application of shear stress results in an increase in pore pressure. It is postulated then that the pore pressure reduction measured within the geotechnical cross section is the result of a reduction in σ_m caused by the expanding heated zone at the north end of wellpair A1. As vertical total stress is increased slightly near the newly growing steam chamber, minor reductions in vertical total stress will occur beyond the steam chambers which under undrained conditions, will lead to minor reductions in pore pressure. While this does not provide any marvelous insight into the influence of geomechanics on the SAGD process, it is instructive in that it is the first evidence of the three dimensional evolution of the steam chamber relative to the geotechnical cross section and its influence on instrumentation response.

At time 2.0, hot water was injected into AI1 at just below fracture pressure while AP1 was pumped down. Breakthrough, or pressure communication between AI1 and AP1 occurred almost immediately. At time 2.04, the well pair was converted to normal operating mode with steam injected into AI1 at a constant pressure and producing from the tubing in AP1 at constant temperature, or steam trap control. Substantial production rates at excellent oil steam ratios (OSR) were obtained immediately. Thermocouple well data showed that the steam chamber began to grow near Well AT2; rising rapidly to the base of Unit D and then spreading out laterally due to slope drainage. The position of well AT2 is illustrated in Figure 3.12. Produced fluid cuts soon reached approximately 35% bitumen (Edmunds et al., 1991).

At time 2.4, wellpair A1 was shut-in to prepare piping for wellpair A3. Cool water was injected at time 2.43. The data listed in Table 6.2 and the pressure contours between time 2.1 and 2.5, which are shown in Figures F.2 and F.3, reflect the pressure changes resulting from shutting-in wellpair A1; the piezometer at elevation 275.1 in Well AGP2 drops from 2236 kPa at time 2.1 to 1000 kPa at time 2.5. Steam injection was resumed into wellpairs A1 and A3 at time 2.8. The temperature and pore pressure distributions within the geotechnical cross section at time 2.9 are shown in Figures 6.6. As conduction is a slow process for heat transfer, the temperature distribution at time 2.9 is not substantially different than at time 1.4. The pore pressure distribution, however, has changed primarily in response to the initiation of steaming in A3. The maximum pressure change remains near wellpair A1 and the zone of pressure reduction has expanded slightly in response to the growing steam chambers at the north end of A1.

Spatially, the development of the steam chamber was complex. It did not, as originally hoped, begin uniformly along the length of the wellpair and its development was sensitive to the location of significant flow barriers. To provide an improved description of steam chamber growth within the reservoir, three-dimensional diagrams were generated assuming the 200 °C isotherm adequately defined the boundary of the steam chamber. Figure 6.7 illustrates the steam chamber position at time 2.9. The dots on each west-east plane define the point of intersection with each injection or production well. The position of the newly formed steam chamber is approximately 25 m north of the geotechnical cross-section. Clearly the response of the instrumentation within the geotechnical cross section will not be that for plane strain conditions within the reservoir. This issue is discussed further in the presentation of the extensometer and inclinometer results.

6.2.2.3 Time 2.9 to 4.3

Except for minor shut-in periods due to environmental conditions (see Table 6.1), steam was continually injected until time 3.5. It should be noted that wellpair A3 was operated differently than wellpairs A1 and A2. Because AP3 was inadvertently drilled within a zone of massive mudstone, Unit F (Facies 12), over a majority of its length, a single well cyclic process was tested with AI3. Steam was injected into the tubing until a wellhead pressure of 2500 kPa (equivalent to a pressure change in the geotechnical cross section of 1800 kPa) was achieved. Steam injection was ceased until the wellhead pressure fell to 2000 kPa when it was resumed again. Production from the annulus was more or less continuous during this time. At time 3.5, steam circulation was initiated in wellpair A2. Steam injection was into the tubing on both AI2 and AP2. Well AI3 was shut-in at time 3.5, and remained shut-in until time 4.6. Wellpairs A1 and A2 were also shut-in at approximately time 4.0. Over the shut-in period of time 4.0 to 4.3, a blow-down test was conducted. This test consisted of placing the injection and production well on production to lower the steam chamber pressure rapidly in an attempt to remove non-condensable gases such as methane from the upper zones of the steam chamber; these gases significantly impair ceiling drainage mechanisms. The dramatic drop in pressure during the blowdown test was captured by the piezometers, as evidenced by the drop in pressure from time 3.9 to time 4.3. Figures 6.8 and 6.9 illustrate the distribution of temperature and pore pressure, respectively over this time interval. The deformation response of the formation during this blowdown phase is captured by the inclinometer and extensometer instrumentation, discussed in §6.5 and §6.4, respectively.

The estimated three dimensional configuration of the steam chamber at time 4.3 is illustrated in Figure 6.10. While it has increased in size, it remains anchored around its initiation point at the base of A1. As will be seen subsequently, the introduction of steam from A2, which did not have a significant shale barrier between the injector and producer, causes the steam chambers to grow rapidly; propagating axially along the wellpairs.

6.2.2.4 Time 4.3 to 5.7

At approximately time 4.5, steaming was reinitiated into A1 and A2 and steaming recommenced in AI3 with AP3 remaining shut-in. Note that at time 4.5, breakthrough had not yet been detected at A2. Breakthrough or pressure communication was confirmed in A2 at time 4.93. While a stable pore pressure distribution exists within the geotechnical cross section (Figure 6.11), the temperature distribution illustrated in Figure 6.12 shows a dramatic change as a result of A2 breakthrough. The localized temperature increase around A2 in the absence of steam chamber pressures is indicative of the rapid heating which occurs between wells following breakthrough.

Following time 5.4, the temperature and pore pressure distribution within the geotechnical cross section began to reflect the axial propagation of the steam chambers along A1 and A2, and their eventual coalescence. As discussed previously, the steam chamber pressure, represented by a pore pressure change of 2000 kPa, evolves in advance of the steam chamber. This phenomena is clearly illustrated in Figure 6.13 where the temperature within the geotechnical cross section at time 5.7 remains below steam chamber temperature, represented by a temperature change of 200 °C, yet two distinct "bulbs" of pressure delineating steam chamber pressure are measured within the geotechnical cross section. Figure 6.14 illustrates the approximate location of the steam chambers giving rise to the temperature and pore pressure distribution shown in Figure 6.13. Note the close proximity of the steam chambers to the geotechnical cross section.

6.2.2.5 Time 5.7 to 7.1

Over the subsequent time period 5.7 to 7.1, all three wellpairs, A1, A2 and A3, remained on normal production. At approximately time 6.0, the A1 and A2 steam chambers coalesced just north of the geotechnical cross section to form a single common steam chamber.

For times 6.1 and 7.1, Figures 6.15 and 6.16 illustrate the temperature and pore pressure growth within the geotechnical cross section as the steam chambers continue to grow axially along the A1 and A2 wellpairs. The local "rises" in pore pressure distribution at Easting 4101 m are the result of a localized "hole" in shalely Units C and D. The isometric views of shale barriers provided in Figures 2.28 and 2.29 illustrate the position of this localized increase in vertical permeability. The three dimensional "seal-like" geometry of the steam chamber at time 7.1 is shown in Figure 6.17.

6.2.2.6 Time 7.1 to 8.6

From time 7.1 to approximately time 7.7, normal production continued in the three wellpairs, as described in Table 6.1. At time 7.7, however, the localized steam chamber forming around AI3 had coalesced with the A1/A2 steam chamber. Consequently, AI3 was placed on steam trap production control for the remainder of the Phase A trials. The common steam chamber was supplied with steam from AI1 and AI2. From time 7.7 to 8.6, several small shut-in periods were encountered. Figure 6.18 provides the temperature distribution within the geotechnical cross section at time 7.9 and 8.6. Note that at this point in the process history, steam chamber pressures are proceeding approximately 20m in advance of the steam chamber temperature, as shown in Figure 6.19. A pore pressure change of 2000 kPa occurs in a zone to the west of A3 whose temperature is only approximately 40 °C. The reservoir steam zone at time 8.6 is schematically illustrated in Figure 6.20.

6.2.2.7 Time 8.6 to 10.0

At time 8.2, cyclic steam circulation began in AP3. The intent was either to achieve communication through Unit F with the growing chamber above AI3 and/or develop an independent chamber that would grow under the shale towards AP1 (Edmunds, et al, 1991). The detection of communication with the steam chamber developing around AI3 at time 9.8 lead to AP3 being placed on production. This was manifested by a rapid decrease in wellhead pressure as shown in Figure 6.3. Up to time 10.0, A1 and A2 were operated normally except for some injection process modifications as described in Table 6.1. The temperature and pore pressure change distributions at time 10.0 are illustrated in Figure 6.21. The estimated configuration of the steam chamber at time 10.0 is shown in Figure 6.22.

6.3 Theory for Full Strain Field Determination

The basis for interpreting the full strain field from the instrumentation results within the geotechnical cross section derives from finite element analysis procedures. Finite element analysis requires the adoption of a distribution of field variables within each element. The field variable in a stress/deformation analysis is displacement. Within the Phase A reservoir, inclinometers provided horizontal displacements and extensometers provided vertical strains. The calculation of vertical displacements from vertical strains will be discussed in §6.4.3. Generally, the displacement distribution model follows the interpolating functions provided by Bathe(1982). The displacements can be described by:

$$\begin{aligned} u &= \langle N \rangle \{U\} \\ v &= \langle N \rangle \{V\} \end{aligned} \qquad [6.1]$$

where u = x displacement anywhere in element;
v = y displacement anywhere in element;
$\{U\}$ = x displacement at the nodes;
$\{V\}$ = y displacement at the nodes; and

<N> = vector of interpolation functions.

The interpolation functions <N>, described in terms of local coordinates r and s, are defined as:

$$\begin{aligned} N_1 &= 1/4\,(1+r)\,(1+s) \\ N_2 &= 1/4\,(1-r)\,(1+s) \\ N_3 &= 1/4\,(1-r)\,(1-s) \\ N_4 &= 1/4\,(1+r)\,(1-s) \end{aligned} \qquad [6.2]$$

These interpolation functions are applicable to quadrilateral elements with four nodes.

For the geometry along the geotechnical cross section, plane strain boundary conditions are assumed. In plane strain, $\varepsilon_z=0$ so the full strain vector becomes:

$$\{\varepsilon\} = \begin{Bmatrix} \varepsilon_x \\ \varepsilon_y \\ \gamma_{xy} \end{Bmatrix} \qquad [6.3]$$

where ε_x = x direction or horizontal strain;
ε_y = y direction or vertical strain; and
γ_{xy} = shear strain in x-y plane.

The three basic strain components, ε_x, ε_y, and γ_{xy} are related to displacement as follows:

$$\begin{aligned} \varepsilon_x &= \frac{\partial u}{\partial x} \\ \varepsilon_y &= \frac{\partial v}{\partial x} \\ \gamma_{xy} &= \frac{\partial u}{\partial y} + \frac{\partial v}{\partial x} \end{aligned} \qquad [6.4]$$

Knowing the displacements at any point within an element are related to the nodal displacements by Equation 6.1, the strain in terms of nodal displacements can be defined as:

$$\{\varepsilon\} = [B]\begin{Bmatrix} U \\ V \end{Bmatrix} \qquad [6.5]$$

where [B] is known as the strain transformation matrix. For two dimensional plane strain conditions, [B] is defined as:

$$[B] = \begin{bmatrix} \frac{\partial\langle N\rangle}{\partial x} & 0 \\ 0 & \frac{\partial\langle N\rangle}{\partial y} \\ \frac{\partial\langle N\rangle}{\partial y} & \frac{\partial\langle N\rangle}{\partial x} \end{bmatrix} \qquad [6.6]$$

Separation of these matrices permits each strain variable to be examined relative to its field measurement. Each component of strain is then described as:

$$\{\varepsilon_x\} = \langle B_x\rangle\{U\} \qquad [6.7]$$

$$\{\varepsilon_y\} = \langle B_y\rangle\{V\} \qquad [6.8]$$

$$\{\gamma_{xy}\} = \langle B_{xy}\rangle\begin{Bmatrix} U \\ V \end{Bmatrix} \qquad [6.9]$$

To develop the complete strain field for the geotechnical cross section, it is first necessary to reconstruct the full displacement field. Figure 6.23 illustrates the "finite element" mesh selected for reconstruction of the displacement field. The correspondence between inclinometer and extensometer wells and the grid is also shown in Figure 6.23. Using the horizontal displacement results from the inclinometer surveys, {U} can be developed using interpolation techniques. The interpolation procedure is discussed in §6.5. The horizontal strain, ε_x, can then be computed using Equation 6.7.

The extensometers, however, do not provide vertical displacements explicitly; they provide vertical strain. The vector of vertical displacements can be deduced from the following:

$$\{V\} = \langle B_y\rangle^{-1}\{\varepsilon_y\} \qquad [6.10]$$

Equation 6.10 will not provide a unique solution for {V}. An infinite combination of {V}'s will satisfy Equation 6.10. In the construction of soil and/or rock structures such as dam foundations, tunnels, embankments, the back analysis approach is increasingly being used in analyzing and interpreting field measurement results. It is termed "back analysis" because the mechanical constants such as Young's modulus, cohesion, and friction angle, are determined by analyzing the measured values of displacement, strain and/or pore pressure. While a full back analysis will not be attempted in this thesis, it is referred to because it suffers from the same theoretical limitation of uniqueness. To overcome this limitation in this research, a boundary condition of imposed vertical nodal displacements are provided along the base of the mesh. The determination of these nodal displacements from extensometer measurements in the roof of an observation tunnel below the Phase A reservoir will be discussed in §6.6.1. These specified nodal displacements provide a reference from which a unique set of vertical nodal displacements can be computed from the vertical strain distribution obtained from the extensometer measurements.

The solution scheme for the vertical displacement distribution proceeded as follows:

1) utilizing the vertical displacement data for the oil sands - limestone interface obtained from observation tunnel measurements, a prescribed {V} is adopted for the nodes within Row 1 (see Figure 6.23);

2) utilizing the $\{\varepsilon_y\}$'s at the integration points within the first row of elements (Elements 1 to 8), the nodal displacements for nodes along Row 2 are computed. All the equations for one row of elements were assembled and solved simultaneously for the nodal displacements - this ensured strain compatibility between adjacent elements;

3) the nodal displacements determined for Row 2 now serve as the base boundary condition for elements 9 to 16. Step #2 is repeated using the $\{\varepsilon_y\}$'s in elements 9 to 16 to compute the vertical nodal displacements along Row 3; and

4) this process is continued incrementally, row by row, until all nodal displacements are computed. These displacements represent the actual vertical displacements within the reservoir and are compatible with the measured vertical strain distribution.

With the back analysis of {V} and the measurement of {U}, the shear strain distribution within the geotechnical cross section can be computed using Equation 6.9. Determination of all elements of the strain field; $\{\varepsilon_x\}$, $\{\varepsilon_y\}$, and $\{\gamma_{xy}\}$, permit the computation of the maximum shear strain and volumetric strain distribution using the following plane strain equations:

$$\gamma_{max} = \sqrt{\left(\varepsilon_x - \varepsilon_y\right)^2 + 4\gamma_{xy}^{\ 2}} \qquad [6.11]$$

$$\varepsilon_v = \left(\varepsilon_x + \varepsilon_y\right) \qquad [6.12]$$

which can be recast in terms of principal strains:

$$\gamma_{max} = \left(\varepsilon_1 - \varepsilon_3\right) \qquad [6.13]$$

$$\varepsilon_v = \left(\varepsilon_1 + \varepsilon_3\right) \qquad [6.14]$$

6.4 Vertical Strain

The behavior of the extensometers was complex, reacting to both temperature and pore pressure. Understanding the actions of each module is important for understanding the behavior throughout the reservoir especially within the geotechnical cross section. The temperatures and pore pressures provided with the extensometer results presented herein have been computed from detailed data generated during the temperature and pore pressure contouring process. The change in pore pressure is provided at each anchor location while temperature is provided at the LVDT location within each extensometer. The general configuration of an extensometer completion was provided in Figure 3.7. A positive displacement implies compressive strains; a negative displacement implies extensional strains.

6.4.1 Extensometer Histories

6.4.1.1 Well AGE2

Well AGE2 was located directly above wellpair A1 in order to measure vertical strains resulting from vertical growth of the steam chamber. Five anchors comprising four measurement modules were installed in AGE2. Figure 6.24 provides a detailed completion diagram for AGE2 along with the bulk volume analysis results for the well. The bulk volume analysis provides a rough guide concerning the geological horizons spanned by each module. A complete relative displacement history for all AGE2 modules is provided in Figure 6.25. Detailed plots of AGE2 response to steaming can be found in Figures C.1 to C.8. The following section serves to briefly describe the history for each extensometer module, highlighting any specific process events pertinent to the module history.

Module 250

Module 250 measures the relative displacement between anchors at elevations 291.0 and 288.0 m. No discernible displacements are recorded until time 3.9. At time 3.9 a small amount of expansion is registered in response to rising pore pressures within the module. During the blowdown test, over time 3.9 to 4.6, extensometer response was not captured as most electrical instrument readouts, including the extensometer readout, were sent away for repair and recalibration. This is true for all remaining modules in this well and AGE3 and AGE4. From time 4.6 to 7.2, the module 250 records formation compression. Over this period, 1.8 mm of compression or a compressive vertical strain of 0.06% has occurred. As will be seen with other modules, the transition from expansive to compressive behavior generally begins in advance of the approaching thermal front.

At time 7.2, module 250 records a change from compressive to expansive behavior. The maximum expansion following time 7.5 was not obtained due to repairs to the readout instrument from time 7.5 to 7.7. Between time 7.7 and 8.3, very steep gradients of compression followed by expansion are noted. Following time 8.4, module 250 records extensional vertical strains until time 10.0. At time 10.0, the relative separation between anchors reaches 11.1 mm or an extensional strain of -0.37%.

Module 249

Module 249 measures the relative displacement between anchors at elevations 288.0 and 285.0 m. Extremely small compressional displacements were recorded up to time 2.4. At time 3.1, very small extensional strains begin to be recorded; on the order of -0.01% which is approaching the accuracy of the LVDT. The transition from extensional to compressional behavior occurred sometime between time 4.1 to 4.4. The rate of compression increased at time 4.9, leveled off at time 5.5 and increased sharply at time 5.9. These dramatic changes in the rate of compression correspond very well with the timing of the approaching thermal front. As the steam chamber enveloped the module, a rapid extension of 23 mm was recorded over a time interval of 0.1, approximately 7 days. This corresponds to a vertical extensional strain of -0.77%. As mentioned previously, the geometry of the module only permits approximately 20 mm of compression to be recorded, which immediately places the readings between time 6.9 and 7.5 out of range. The readings following time 8.4, while showing some fluctuation or instability, are recording the maximum compression of the module or 0.75%.

Module 244

Module 244 measures the relative displacement between anchors at elevations 285.0 and 282.0 m. Note the earlier rise in pore pressure, especially within the lower half, for module 244 due to its proximity to AI1. Up to time 3.1, module 244 recorded small extensional and compressional strains in concert with the fluctuating pore pressures. From time 3.1 to 3.9, the module recorded an extensional strain of -0.03% in response to the rise in pore pressure throughout the module. The beginning of a compressional trend was recorded just prior to time 4.0 which corresponds well with the rapid drop in pore pressure during the shut-in period and blowdown test from time 3.9 to 4.3. These compression/extension measurements continue to respond to fluctuating pore pressures up to time 5.2. The reason for the abrupt change in the behavior of module 244 at time 5.2 is unknown. As the thermal front advanced, extensional strains were measured between time 4.2 and 6.65, with a sharp change to compressional behavior up to time 6.84. Between time 6.85 and 7.05, the formation within module 244 undergoes rapid extension, recording an extensional strain of -0.93%. The time period for this abrupt response corresponds directly with the abrupt change in behavior in module 249. Readings following time 8.4 indicate an extensional trend for module 244 through to time 10.0.

Module 245

Module 245 measures the relative displacement between anchors at elevations 282.0 and 279.0 m. As with the previous modules in AGE2, module 245 recorded extensional behavior as the pore pressure rose within the formation. In the period up to time 4.1 or the first repair period, an extensional strain of -0.09% for a pore pressure increase of approximately 2000 kPa was measured. From time 4.3 to approximately 6.1, progressive compressional behavior of the formation was measured as the temperature rose within the module. Up to time 6.1, when the temperature rose to steam temperature, compressional strains reached a value of 0.08%. Between time 6.1 and 7.0, the extensometer readings indicate a compressional trend. As with module 244, the readings beyond time 8.4 show some instability but tend to confirm that module 245 remained in compression until time 10.0

6.4.1.2 Well AGE3

Well AGE3 was located at Easting 4101 m, approximately 6 m east of wellpair A1. Well AGE3 measured vertical strains resulting from horizontal and at later times, vertical growth of the steam chamber. Seven anchors comprising six measurement modules were installed in AGE3. Figure 6.26 provides a detailed completion diagram for AGE3 along with the bulk volume analysis results for the well. The bulk volume analysis provides a rough guide concerning the geological horizons spanned by each module. A complete history for all AGE3 modules is provided in Figure 6.27. Detailed plots of AGE3 response to steaming can be found in Figures C.9 to C.20. The following section serves to briefly describe the history for each extensometer module, highlighting any specific process events pertinent to the module history.

Module 243

Module 243 measures the relative displacement between anchors at elevations 298.1 and 293.1 m. This is the uppermost extensometer module within the geotechnical cross-section. The extensional strain response of this module at time 3.5 occurs at the same time steam circulation is initiated in wellpair A2, reaching a maximum of -.12% at time 4.0. As the blowdown test begins at time 4.0, the response begins to dramatically change from extension to compression and by the conclusion of the blowdown test at time 4.3, vertical strain is very near zero. As the pore pressure began to rise slightly around time 4.5, the formation undergoes extensional straining. At time 6.5, an extensional strain of -0.04% was measured just prior to an abrupt change to compression of the extensometer module. This period of compression returned the module anchors to their original relative position at time 6.74. From time 6.75 to 7.5, an increase in the relative separation between anchors was measured. The rate of extension accelerated up to time 7.4, recording an extensional strain of -0.09%. The formation response at this module location displayed compressional behavior from time 8.4 to 10.0.

Module 242

Module 242 measures the relative displacement between anchors at elevations 293.1 and 288.1 m. No discernible movements were measured prior to time 3.24. Extremely small extensional displacements were measured between time 3.25 and 3.71 in response to the rise in pore pressure. These displacements, however, remained within the accuracy of the LVDT. From time 3.71 to 4.1, a slightly different formation response was measured by module 242 than was measured by the other modules. All previous modules did not exhibit compressional behavior until the temperature front was encroaching on the module. From time 3.71 to 4.1, module 242 recorded a compressional trend without any significant rise in formation temperature. As for module 243, this displacement response does correspond with the initiation of steaming into wellpair A2. It is postulated that the compression is a reflection of the three dimensional growth of the steam chamber as it approaches the geotechnical cross section from the north and the rapid growth of the A2 steam chamber.

At approximately time 3.9, the compressional strain was 0.02%. From time 4.5 to 5.5, a gradual compression of the anchors was recorded. From time 5.5 to 6.25, an increase in the rate of compression corresponds to increasing temperature within the module. At time 6.25, the vertical compressive strain was 0.08%. Following time 6.25, the readings became unstable but since the magnitude of instability was not recorded, it is difficult to judge whether these readings are representative of the formation response. The module failed to provide any readings after time 8.5.

Module 236

Module 236 measures the relative displacement between anchors at elevations 288.1 and 283.1 m. No discernible measurements were recorded prior to time 3.4. Between time 3.5 and 4.0, relative extension of module 236 occurred in response to rising pore pressure. Just prior to time 3.9, a small vertical extensional strain of -0.007% was measured, which is roughly the accuracy of the instrument. Very small extensional measurements were recorded following time 4.3 until time 4.9 when the formation began to undergo compression in response to the rise in temperature. Between time 5.5 and 5.8, a very sharp increase in compression occurred due to the aggressive temperature rise within the module. The extensometer measurements from time 5.8 through to time 9.3 indicate the compressional limit for the extensometer was reached. Following time 9.3, some small extension of the anchors is occurring.

Module 238

Module 238 measures the relative displacement between anchors at elevations 283.1 and 278.1 m. As with previous modules, modules 238 recorded relative extension of the anchors in conjunction with rising pore pressures. The magnitude of the extensional strains however were much larger, reaching a value -0.22% at time 5.3. At time 5.3, the formation responded to the increasing temperature by compressing under the thermal strains. This compression reduced the total extensional strains to -0.14% at time 5.4. The response of module 238 after time 5.5 differs substantially from the behavior recorded in the previous modules for both AGE2 and AGE3. The previous modules generally showed increasing compression with increasing temperature. The maximum extensional strain measured at module 238 at time 5.8 is -0.38%. Following time 5.8, the formation response within module 238 returned to compressional behavior, eventually reducing the extensional strain within the module to -0.085% at time 6.3. Between time 6.3 and time 7.5, the readings were less erratic showing extension in the earlier part of the time period and compression in the latter part with a final extensional strain of -0.07% reached at time 7.5. A period of unreliable readings from time 8.3 to 9.4 is followed by several readings indicating compressive strains within module 238 at time 10.0.

Module 240

Module 240 measures the relative displacement between anchors at elevations 278.1 and 273.1 m. In response to rising pore pressure at time 2.0, module 240 recorded extensional strains through until time 7.2 when it reaches a magnitude of -0.25%. It is important to note the delayed temperature rise within this module relative to the previous AGE3 modules. Relative to the steam chambers, module 240 is low within the formation but is at the same elevation as the wellpairs. Consequently, the temperature rise within the module was delayed in comparison to modules at higher elevations. The lowest module, module 248, shows an even greater delay in terms of temperature rise.

From time 7.2 to 7.5, compressional strains within module 240 reduce the total vertical extensional strain to -0.20%. At time 8.4, the module had recorded an extensional strain of -0.58% or a relative extension between anchors of 29 mm. Unlike compression, the extensometer design does not limit the amount of extension that can occur; even to the point where the core exits from the LVDT, as discussed in detail in §6.4.2. Following time 8.4, the rate of extension was very rapid and reached a maximum at time 8.9 where the relative extension had reached 83 mm or an extensional strain of -1.66%. Abruptly, the behavior changed to that of compression and reduced the vertical extensional strain to -1.03% at time 9.3. Between time 9.3 and 9.7, very rapid periods of extension and compression left the module recording a vertical compressive strain of 0.14%, which stays constant until time 10.0.

The relative displacement history for this module is reviewed and reanalyzed in §6.4.2.

Module 248

Module 248 measures the relative displacement between anchors at elevations 273.1 and 268.1 m. The shear pins holding the relative displacement between anchors at approximately 6 mm were sheared during installation (see Figure C.10). Consequently, module 248 was grouted in place at its compressional limit leaving no room for measurement of compressional strains at the beginning of steaming. From the onset of steaming, however, module 248 recorded extensional movements between anchors. At time 1.25, the relative displacement reaches a magnitude of 1.35 mm. From time 1.25 to 3.0, the module slowly "compressed" to its original position. In response to the rising pore pressure, particularly near the top of the module, vertical extensional straining occurred until time 5.0 where slight compressive straining reduced the total vertical extensional strain to -0.01%. From time 6.0 to 10.0, module 248 showed a steady increase in the relative distance between the anchors. At time 10.0, a relative extension of approximately 12 mm or an extensional strain of -0.24% was recorded.

6.4.1.3 Well AGE4

Well AGE4 was located at Easting 4107 m, approximately 12 m east of wellpair A1, approximately the midpoint between A1 and A2. Well AGE4 measured vertical strains resulting from horizontal and at later times, vertical growth of the steam chamber. Six anchors comprising five measurement modules were installed in AGE4. Figure 6.28 provides a detailed completion diagram for AGE3 along with the bulk volume analysis results for the well. The bulk volume analysis provides a rough guide concerning the geological horizons spanned by each module. Note the absence of Unit F across module 246. A complete history for all AGE4 modules is provided in Figure 6.29. Detailed plots of AGE4 response to steaming can be found in Figures C.21 to C.29. The following section serves to briefly describe the history for each extensometer module, highlighting any specific process events pertinent to the module history.

Module 239

Module 239 measures the relative displacement between anchors at elevations 293.5 and 288.5 m. From time 2.1 to 3.0, relative extension of the anchors was recorded in response to pore pressure increases. No relative displacements were recorded until time 5.0 when in conjunction with an accelerating rise in pore pressure, module 239 recorded an increasing rate of relative expansion. A maximum relative expansion of 6.75 mm was reached at time 6.75, after which it remained relatively constant until time 7.5. Most previous modules exhibited some degree of compression as the temperature rose within the formation between module anchors. Note that this module recorded no distinct compressive straining period in response to heating. All readings after time 7.5 were recorded in the field as unstable but do show a tendency towards compression of the module in a similar fashion as module 243 in AGE3.

Module 241

Module 241 measures the relative displacement between anchors at elevations 288.5 and 283.5 m. As with the other modules, the first reaction of module 241 was to measure relative expansion in response to rising pore pressures. At time 5.0, just prior to a rapid rise in temperature, the relative extension was 1.78 mm or a vertical extensional strain of -0.04%. This module also did not record a period of distinct compressive straining due to the rapid temperature rise from time 5.3 to 6.0. Extensional straining continued until time 6.6 , where at a relative displacement of 7 mm, the module began to record compressive straining. At time 7.25, the relative extension between anchors was 1.7 mm. After time 7.25, the readings were noted as unstable in field records. The readings at time 10.0 would tend to suggest that the final position of module 241 was a relative compressive displacement of approximately 2.0 mm.

Module 247

Module 247 measures the relative displacement between anchors at elevations 283.5 and 278.5 m. As the pore pressure began to rise at time 2.0, module 247 began to record relative extension of the anchors. Unfortunately, there is a paucity of data from time 3.7 to 4.8. The trend, however, continued to indicate relative extension of the anchors and at about time 5.2, the relative extension had reached approximately 15 mm or an extensional strain of approximately -0.30%. Again, limited readings between time 5.2 and 6.2 do not allow any assessment of the compression behavior over this time period. It is clear that compressive straining has occurred up to time 6.5, followed by relative expansion up to time 7.5. Following time 8.4, module 247 indicated compressive straining of the formation with a final compressive strain of approximately 0.04% at time 10.0.

Module 246

Module 246 measures the relative displacement between anchors at elevations 278.5 and 273.5 m. Relative expansion of the anchors was clearly measured by module 246 as the pore pressures rose. Just prior to the decrease in pore pressure at time 3.7, the relative expansion between anchors was 5.6 mm. As all the wellpairs were put back on injection/production following time 4.3, module 246 continued to record extensional relative displacements, which up to time 5.4, amounted to an extensional strain of -0.33%. From time 5.4 to 7.7, field readings were noted as erratic and were not available for analysis. Following time 7.7, readings appear to indicate compression within the module and a relatively constant compression of 2.5 mm beyond time 8.6.

Module 235

Module 235 measured the relative displacement between anchors at elevations 273.5 and 268.5 m. In the same manner as module 248 at the base of AGE3, module 235 indicated a period of small relative extension between anchors prior to any significant increase in pore pressure. There was some recovery of these extensional strains before the module began to respond to rising pore pressures. Extensional behavior continued until time 3.6 when the relative extension had reached 2.4 mm. Coincident with a fall in pore pressure, the module recorded compressional straining up to time 3.9. At time 5.0, a significant increase in the rate of compression occurred, reaching a maximum compression of 3 mm at time 6.0. From this time through to time 10.0, a constant compression of approximately 2.5 mm was measured.

6.4.1.4 Summary

Although installation was difficult, complex and time consuming (AOSTRA, 1990a), the extensometers have provided an excellent record of the vertical strains occurring within the reservoir. They show clear and defined responses to both pore pressure and temperature developments at the module location. Also shown are relative displacements in response to the three dimensional steam chamber growth.

6.4.2 Operation of Extensometer

As part of the detailed review of the extensometer results, the design and construction of the extensometer modules were also reviewed. This assessment discovered that elements within the extensometer design permitted displacement degrees of freedom of a module which had not been characterized. The following section describes the operation of the extensometer modules and a recalibration conducted to better understand the module response and its impact on reservoir deformations measured during the Phase A SAGD test.

6.4.2.1 Introduction

As discussed in §3.3.2, the operation of the Bof-Ex extensometer is based on a high temperature LVDT. The extensometer consists of telescoping invar rods which move relative to one another to measure strain (i.e., relative displacement) between two anchors. The configuration of the extensometers, however, provided for unique degrees of freedom relative to both compressive and expansive movements. First, regardless of the propensity to compress, the anchor points will shoulder with the invar rods after approximately 30 to 60 mm, depending on the setpoint of the shear pins after initial setup. Figure 6.30 schematically illustrates the limiting displacement possible for the compressive mode. Second, formation extension displacements larger than 40 mm will result in extensometer readings going beyond the linear range of its calibrations. For larger extension displacements, the calibration curve will reach a peak value and then decrease afterwards as relative extension movements increase. As shown in Figure 6.30, the rod of the LVDT can displace completely out of the body - there is no structural limitation to this displacement. These displacement degrees of freedom result in nonlinear calibration curves for the Bof-Ex extensometer. To aid in the evaluation of the field data pertaining to the vertical strains, specifically module 240 in well AGE3, a calibration test was conducted to ascertain the "true" calibration curve for the Bof-Ex extensometer. This calibration test is described in the following section.

6.4.2.2 Bof-Ex Calibration

Utilizing a spare Bof-Ex extensometer module which was not installed, a full calibration curve over the complete displacement range of the LVDT was obtained. Displacement of the LVDT rod was achieved by connecting it to a large displacement micrometer typically used for calibrating LVDT's. Readings from the Bof-Ex were taken with the same RDP Readout device used for field readings. Figure 6.31 shows the complete shape of the calibration curve. Over the manufacturer's stated linear range of +25 to -25 mm, a linear curve is obtained, even for the relatively coarse displacements used for this calibration test. Two important deviations from linearity, however, are clearly represented in Figure 6.31. First, just beyond the +25 to -25 mm linear range, a small slope change occurs in the calibration curve. The most dramatic result however is the peak RDP reading reached for a displacement of approximately 65 mm and the subsequent decrease in RDP readings for increasing displacements. The consequence of this calibration curve on the interpretation of the field data is two fold: 1) since only a linear slope was utilized in the conversion of the field readings, extension displacements beyond the peak will have been interpreted not as increasing extensions, but relative compression of the module, and 2) back analysis of the field readings will be difficult because of uniqueness at any particular RDP reading. (i.e. is the true extension corresponding to an RDP reading of -53, 57 mm or 128 mm?).

A second phenomena occurring within the Bof-Ex is a shift in the readings as a function of temperature. Due to the short lead time prior to installing the Bof-Ex extensometers, calibration data over the temperature range 20 °C to 220 °C were provided only for the LVDT in module 248 (AOSTRA, 1990b). For this LVDT, the calibration factor decreased by 7% and the zero reading shifted the equivalent of approximately 0.5 mm. To provide additional information related to temperature effects on the Bof-Ex or more specifically the LVDT, a heating cycle was applied to the LVDT housed in the invar tube of the model chosen the present calibration studies. No inner core was present. The heating cycle was conducted by placing the LVDT portion of the Bof-Ex in a temperature controlled oven set at 220 °C.

The following table summarizes the shift in readings during heating:

	Elapsed Time (min.)	RDP Reading
initial	0 (20 °C)	+0227 (2.27 mm)
	5	+0212 (2.12 mm)
	25	+0050 (0.50 mm)
	35	+0027 (0.27 mm)
stable	60 (220 °C)	+0020 (0.20 mm)

Two observations are possible from this heating cycle; 1) a shift in the RDP reading occurs very quickly, and 2) a change in temperature of 200 °C causes a shift of approximately 2 mm, which corresponds to an extensional displacement.

Based on the previous review of extensometer responses, the nonlinear calibration curve for the LVDT's in the Bof-Ex impact only one module, module 240 in Well AGE3. The magnitude of relative displacement within the remaining modules do not exceed the peak RDP reading or extension of 65 to 70 mm. Using the calibration curve from Figure 6.31, Figure 6.32 illustrates the "as recorded" and the "corrected" displacement history of module 240. The peak displacement increases from approximately 80 mm (as recorded) to approximately 175 mm (re-calibrated).

The mechanical restraint on compression, as illustrated in Figure 6.30, manifests itself in the response of several modules. For example, the response of module 236 given in Figure 6.27 shows a limiting compression response beyond time 5.7.

6.4.3 Vertical Strains within Geotechnical Cross Section

As discussed previously, interpretation of the vertical strain distribution within the geotechnical cross section was difficult due to the complex behavior of the extensometers and the localized position of the measurements; AGE2, AGE3 and AGE4 are relatively closely spaced. With prudent application of engineering judgment following the detailed review of the extensometer responses described above, Tables 6.3, 6.4 and 6.5 summarize the strain history for wells AGE2, AGE3 and AGE4, respectively. The extensometer readings where assumptions, re-calibration or engineering judgment have been applied are noted as shaded boxes in the tables. Brief explanations for the respective values chosen are provided as footnotes in each table.

Figures 6.33, 6.34 and 6.35 each provide a detailed plot of the vertical strain development within AGE2, AGE3 and AGE4, receptively, throughout the Phase A trials. In general, extensional vertical strains occurred at the elevation of the steam chambers while above the steam chamber, compressive vertical strains of 0.25% to 0.5% were measured. The evolution of ε_y is discussed further in §6.6.2.

6.5 Horizontal Displacements

Inclinometer surveys were conducted at times 4.1, 5.5, 7.9 and 9.7. As discussed in §6.2, the steam chamber development was complex and three dimensional. The three dimensional growth is represented in the pattern of horizontal displacements measured in the inclinometer wells. Figure 6.36, 6.37, 6.38 and 6.39 illustrate the displacement vectors at an elevation of 280 m in the inclinometer wells at times 4.1, 5.5, 7.9 and 9.7, respectively. Also shown is a plan view of the approximate steam chamber location (200°C isotherm) for each time interval.

At time 4.1, the west-east displacement patterns reflect the developing thermal and pore pressure induced expansion occurring around wellpair A1. The north-south displacements do not correspond with expected behavior which suggests the displacements should be predominantly south indicative of outward radial thermal expansion. The displacement at AGI4 is indicative of outward radial expansion. The reason for this displacement pattern highlights the interplay between pore pressure and temperature in determining the evolution of displacements within reservoir.

Recalling the process history of the wellpairs between time 4.09 and 4.23, it is noted that all three wellpairs were shut-in to perform a blowdown test on wellpair A1 (see §6.2). This results in a dramatic reduction in pore pressure within the steam chamber, as evidenced by the change in pore pressure within the geotechnical cross section between time 3.9 and 4.3 and illustrated in Figure 6.9. The impact of this pore pressure change is reflected in the bulk modulus equation:

$$\Delta\varepsilon_v = \frac{\Delta\sigma'_m}{K} \qquad [6.15]$$

where $\Delta\varepsilon_v$ = increment of volume strain, $\Delta V/V$; (+ve = compression)
$\Delta\sigma'_m$ = increment of mean effective stress; and
K = bulk modulus.

Equation 6.15 shows that for a positive increment or increase in mean effective stress, a corresponding compression increment of volumetric strain will occur. The pore pressure reduction during blowdown results in an increase in mean effective confining stress within the steam chamber and subsequent compressive volumetric strain. The compressive volumetric strains create the northerly component of displacement measured at the geotechnical cross section inclinometers at time 4.1. The northerly component of displacement is small relative to the west-east displacement which reflects the low compressibility of oil sands and the dominance of thermal expansion in controlling the horizontal displacement pattern.

As the SAGD process is re-initiated at approximately time 4.5, the injection pressure is re-established within the reservoir and by the time of the next inclinometer survey at time 5.5 (Figure 6.37), the A1 and A2 steam chambers have coalesced. At this point, horizontal displacements are controlled by thermal expansion effects; the displacement vectors are generally normal to the advancing steam chambers. At time 7.9 (Figure 6.38) however, inclinometer well AGI2, AT7 and AGI4 exhibit a northerly displacement component which is not normal to steam chamber growth. The displacement vectors suggest compressive strains within the steam chamber but unlike at time 4.3, no dramatic change in pore pressure occurs as a results of process conditions. It is interesting to note that it is over the time interval 7.0 to 8.0 that the extensometers adjacent to AT7 also begin to indicate relatively large extensional displacements occurring between the A1 and A2 wellpairs. At time 9.7 (Figure 6.39), the horizontal displacements are primarily directed normally outward from the steam chamber.

6.5.1 Horizontal Displacements within Geotechnical Cross Section

In order to calculate the full strain field within the geotechnical cross section, the west-east displacement component from inclinometers AGI1, AT1, AGI2, AT7 and AGI3 were interpolated to provide the horizontal displacements at each of the nodes in the mesh illustrated in Figure 6.23. Figures 6.40, 6.41, 6.42 and 6.43 illustrate the resulting horizontal displacement distribution within the geotechnical cross section for times 4.1, 5.5, 7.9 and 9.7, respectively. To aid in the interpretation of horizontal displacement patterns, each figure contains both the temperature and pore pressure distribution at the relevant time intervals.

At time 4.1, the direction of displacements is westerly to the left of and easterly to the right of wellpair A1. This is also shown on the plan view of displacements illustrated in Figure 6.35. No specific relationship to the temperature distribution is evident but as discussed previously, the pore pressure changes within the steam chamber are controlling the displacement field over this time period.

The horizontal displacements at time 5.5 (Figure 6.41) show the same general trend of displacement direction as at time 4.1 but have decreased in magnitude. The notable exception is well AT7 where horizontal displacements have continued to increase. The pore pressures have continued to evolve but perhaps more significantly, the temperature distribution within the geotechnical cross section is beginning to develop more quickly.

At time 7.9 (Figure 6.42), the horizontal displacement patterns show a direct correlation to the geometry of the steam chamber which is evolving through the geotechnical cross section. Relatively large horizontal displacements were measured in well AT7 at time 7.9. It is postulated that this displacement is a response to the rapid upward growth of the steam chamber through a localized "break" in Unit C. The geologic position of this localized increase in vertical permeability was discussed in Chapter 2 and illustrated in Figures 2.29 and 2.30. The rapid upward growth is evident from the response of the thermocouple measurement points surrounding AT7. Figure A.7 illustrates the temperature profile within AT7 and clearly shows the rapid rise in temperature at approximately time 7.0. At time 7.9, at elevation 292.0 m, the temperature measured in AT7 was 150 °C. In surrounding wells; AT9, AGP4, AGI2, AT8, AT4, the temperature at elevation 292.0 m was approximately 50 °C. The horizontal displacement at AT7 is the result of the horizontal displacements associated with the localized thermal expansion occurring around well AT7.

The horizontal displacements all decrease in magnitude at time 9.7 but they reflect to a greater degree than previous measurements, the temperature and pore pressure distribution within the geotechnical cross section. Of interest is the reduction in horizontal displacements, especially in the upper zones of the reservoir, that have occurred. As the steam chamber within the geotechnical cross section increases in lateral extent, the displacement pattern above the reservoir becomes more vertical with less of an horizontal component to displacement. This is clearly reflected in the inclinometer response at time 9.7.

6.6 Full Strain Field in Geotechnical Cross Section

6.6.1 Boundary Conditions

As discussed in §6.3, uniqueness in the solution for vertical displacements from vertical strain can be obtained by using the extensometer response in the tunnel roof below the Phase A reservoir. The geometry and location of the instrumented tunnel section (Station E12-2) is provided in Figure 6.44. The extensometer measurements for E12-2 are made assuming the deepest anchor, E12-2/4, is fixed. Using the convergence readings taken between points 2 and 4 and 2 and 5, and assuming the floor of the tunnel does not deform during the Phase A trials , the absolute movement of the tunnel roof can be computed. Tunnel roof displacement then allows the relative displacement measured in E12-2 to be converted to absolute movements within the limestone. For times 4.3, 5.5, 7.9 and 9.7, Figure 6.45 shows the measured temperature distribution within the limestone above the tunnel as well as the converted extensometer displacements. These displacements were extrapolated to the oil sands-limestone interface to provide the initial displacement boundary condition required to compute the vertical displacements from the vertical strain measurements within the reservoir. As shown in Figure 6.45, these displacements are 0 mm, 1 mm, 3 mm and 7 mm for times 4.3, 5.5, 7.9 and 9.7, respectively.

6.6.2 Strain Field

Reconstruction of the strain field within the geotechnical cross section will allow inferences to be made concerning the deformation response of the reservoir without the presupposition of a stress-strain law or model. Since strain is kinematically related to displacement, strain distributions in the formation can be obtained directly from the measured displacements without performing any stress analyses. This procedure of back analysis of measured displacements has been used in analyzing tunnel and slope stability (Sakurai and Takeuchi, 1983) with the primary objective being the back calculation of the initial stresses and material properties. This step will not be undertaken in the current research. The current focus is on the calculation of the shear strain and volumetric strain distribution and the estimated variation of absolute permeability within the geotechnical cross section.

6.6.2.1 Vertical Strain

Utilizing the interpolation procedure described in §6.3 and the vertical displacement measurements obtained from the extensometers, the vertical strain distribution within the geotechnical cross section was constructed for times 4.3, 5.5, 7.9 and 9.7; these are illustrated in Figures 6.46 and 6.47. Regions outside the dotted outline have been estimated based on the behavior measured at AGE2, AGE3 and AGE4.

The relatively few vertical strain measurement points offered by AGE2, AGE3 and AGE4 made the computation of the vertical strain distribution difficult. Several assumptions were required and they can be summarized as follows:

- vertical strain was assumed equal to zero at the upper (Elevation 300 m) and lower

(Elevation 270 m) boundaries;

- the vertical strain distribution at AGI1 (Easting 4056 m) and AGI3 (Easting 4134 m), the left and right boundaries, respectively, and the vertical strain distribution between wellpair A3 and A1 were chosen equal to one-half the average of AGE3 and AGE4, at the same elevation; and
- vertical strain behavior above wellpairs A3 and A2 was assumed identical to that above wellpair A1.

As stated above, the region within the dotted outline in each figure represents the variable distribution with the highest degree of reliability. Outside this region, the data becomes less representative due to the above assumptions.

Over the time period 0.0 to 5.5, minimal vertical straining occurred within the geotechnical cross section. At time 5.5 (Figure 6.46), a maximum extensional vertical strain of approximately 0.25% occurs between wellpair A1 and A2. This is similar to the deformation results predicted from the ideal analyses presented in Chapter 5. At time 7.9 (Figure 6.47), extensional vertical strains have increased dramatically to approximately 2.0% within the same region between wellpairs A1 and A2. At time 9.7 (Figure 6.47), a final vertical extensional strain of 2.5% centered at Elevation 277 m and Easting 4098 m has occurred.

The vertical displacement at the top of the reservoir (Elevation 293 m) for the previous vertical strain distributions is illustrated in Figure 6.48. The inherent variability in the displacement data illustrates the difficulty in reconstructing the vertical strain history as well as the assumptions incorporated into the computations. For the sake of comparison to vertical displacements measured in other thermal pilots (Gronseth, 1989), linear regression is utilized to obtain the vertical displacement at the center of the reservoir at times 4.3, 5.5, 7.9 and 9.7. A maximum vertical displacement of 191 mm is estimated for time 9.7. This corresponds closely to Gronseth(1989) who reports extensional displacements within the Clearwater Formation reservoir in excess of 160 mm. For the production process reported by Gronseth(1989), the reservoir is hydraulically fractured during steam injection but this alone did not explain the observed displacements. In his analysis of the monitoring program, Gronseth(1989) concludes that shear induced dilation does occur within the Clearwater Formation during cyclic steam stimulation and is partly responsible for the large extensional displacements.

With the understanding of the geomechanical processes involved in SAGD culled from the ideal analysis results presented in Chapter 5 and the process review presented in §6.2, it is postulated that the extensional vertical strains are the result of a combination of effective confining stress and shear induced volume changes occurring between the wellpairs A1 and A2. These extensional strains however, are not entirely the result of process changes within the geotechnical cross section. The three dimensional steam chamber growth and its associated displacement patterns will have exhibited a large influence on the development of vertical strain within the geotechnical cross section.

6.6.2.2 Horizontal Strain

The evolution of horizontal strain within the geotechnical cross section for time 4.3, 5.5, 7.9 and 9.7 is illustrated in Figure 6.49 and 6.50. The distribution of horizontal strain is more reliable than vertical strain as an indicator of formation response to SAGD processes due to the increased number of measurement points. As discussed in §3.2.4, however, the horizontal displacement measurements may in error by up to 20% due to systematic errors with the Gyrodata Wellbore Surveyor tool.

Extensional horizontal strains are measured throughout the central region of the geotechnical cross section. At time 4.3 (Figure 6.49), ε_x reaches a magnitude of -.18% in the upper region of the reservoir at approximately Easting 4090 m. The position of this extensional strain region is directly correlated with the location of wellpair A1, which was the only wellpair in operation through to time 4.3. At time 5.5 (Figure 6.49), ε_x remains at -0.18% in the upper region of the reservoir but its position has moved eastward to reflect the operation of wellpair A2. Increased compressional horizontal strains are also occurring to the right of wellpair A2. As the steam chambers coalesce along A1 and A2 and continue to expand within the geotechnical cross section, the magnitude of horizontal extensional strains increases. At time 7.9 (Figure 6.50), ε_x has increased to -0.30%. At time 9.7, the horizontal strains within the reservoir have decreased dramatically. The reduction is the result of a widening steam chamber creating a condition of primarily vertical displacements.

6.6.2.3 Maximum Shear Strain

The reason for examining the maximum shear strain distribution was to examine the magnitude and distribution of distortional straining within the geotechnical cross section and its relationship to stress induced volume changes. Utilizing $\{\varepsilon_x\}$, $\{\varepsilon_y\}$, and $\{\gamma_{xy}\}$ at the integration points within the geotechnical cross section mesh, the corresponding maximum shear strains were computed using Equation 6.11.

At early times, time 4.3 and 5.5, the distribution and magnitude of γ_{max} is dominated by the horizontal strain within the formation. Figure 6.51 clearly shows that the position of γ_{max} occurs in the same location the maximum value of ε_x. The value of γ_{max} increases from 0.15% at time 4.3 to 0.25% at time 5.5. At time 5.5 there is no indication of the development of distortional strain between wellpairs. At time 7.9 (Figure 6.52) the first evidence of shear strain between wellpairs occurs with γ_{max} equal to 2.0% very near where wellpair A2 passes through the geotechnical cross section. The maximum shear strain reaches a magnitude of 3.0% at time 9.7 (Figure 6.52). The zone affected has also shifted to the west and is situated more centrally between wellpair A1 and A2.

The occurrence of distortional straining between wellpair A1 and A2 follows the predicted formation response discussed in Chapter 5. To further illustrate the comparison, Figure 6.53 shows an extracted region of the geotechnical cross section which closely matches the boundary conditions assumed for the ideal analyses presented in Chapter 5. The location of wellpair A2 is approximate only. While the results for γ_{max} from the full strain field analysis and the ideal analysis results are similar in location, they differ in time and distribution. The ideal analysis suggested specific, defined zones of shear strain occurring early in the process history. The distribution shown in Figure 6.53 is for time 9.7, the end of the Phase A SAGD trials and indicates a more gradual distribution of distortional strain. This reflects the three dimensional development of the steam chambers and the non-plane strain reaction of the geotechnical cross section instrumentation.

6.6.2.4 Volumetric Strain

Utilizing Equation 6.12, the distribution of volumetric strain within the reservoir for the times 4.3, 5.5, 7.9 and 9.7 was computed. Small expansive volumetric strains are measured for time 4.3; a maximum of 0.17% is recorded near wellpair A1. This volumetric expansion is primarily due to the rising pore pressures around A1 (Figure 6.9). The volumetric expansion indicated at the top of the reservoir is related to the extensional horizontal strains measured in the same region. At time 5.5 (Figure 6.54), a distinct region of volumetric expansion developed between the A1 and A2 wellpairs. For the same time period, the maximum shear strain distribution did not indicate an equivalent distinct region of shear strain. Consequently, the volumetric strain of 0.40% measured at time 5.5 is likely due to bulk volume expansion in response to rising pore pressures and is not influenced greatly by shear induced volume changes. At time 7.9 (Figure 6.55) however, the volumetric strain distribution correlates well with γ_{max}; an indication that shear induced volume changes are beginning to dominate the volumetric formation response, within this region of the reservoir. A localized volumetric strain of 2.0% was measured at time 7.9. At time 9.7 (Figure 6.55), a maximum volumetric strain of 2.6% was measured within a region of the reservoir lying between wellpairs A1 an A2.

6.6.2.5 Absolute Permeability

The volumetric strain distributions computed in §6.6.2.4 combined with Equation 5.4 provide an opportunity to examine the change in absolute permeability within the geotechnical cross section. An initial absolute permeability of 7.5 darcies will be assumed for these calculations. Figure 6.56 illustrates the relatively small increases in k_a that result from pore pressure increases alone. Based on bulk compressibility of oil sands ($C_b=3.0\mathrm{x}10^{-6}$ kPa^{-1}), a pore pressure increase of 1500 kPa and an initial porosity of 32%, Equation 5.4 would predict an increase in k_a from the original value of 7.5 to 7.8; an increase of 4%. This matches exactly the computed value of k_a at time 5.5 of 7.8, as illustrated in Figure 6.56. As demonstrated for volumetric strain, the formation response between wellpairs A1 and A2 becomes increasingly influenced by the combination of shear induced volume changes and effective confining stress reductions. The impact on absolute permeability is shown in Figure 6.57 at time 7.9. Absolute permeability increases approximately 19% from 7.5 to 9.5 darcies. For time 9.7, the absolute permeability shows an increase of 30%, increasing from 7.5 to 9.8 darcies.

6.7 Summary

The density of instrumentation wells within the UTF Phase A reservoir has permitted a detailed study of the evolution of pore pressure and temperature within the geotechnical cross section. The three dimensional growth of the steam chamber and the operational history of the wellpairs have been linked to the pore pressure and temperature within the geotechnical cross section to assist in the interpretation of geotechnical instrumentation results. The pore pressures increased in advance of the steam chamber boundaries and the resulting thermal front. In general, the distance between the pore pressure isobar equivalent to steam injection pressure and the temperature isotherm equivalent to steam temperature was approximately 20 m.

Pore pressure development during the startup phase for wellpair A1 clearly illustrated the large influence temperature has on bitumen viscosity and its concomitant impact on hydraulic conductivity. A temperature increase of 30°C is sufficient to reduce the bitumen viscosity such that the fluid mobility is increased and pore pressures can develop rapidly. A 30 °C temperature rise from 8 °C to 38°C will reduce the bitumen viscosity two orders of magnitude from 7,000,000 centipoise to approximately 70,000 centipoise.

Pore pressure reductions were measured within the geotechnical cross section as a result of a reduction in total mean stress caused by the expanding heated zone at the north end of wellpair A1. As vertical total stress is increased slightly near the newly growing steam chamber, minor reductions in vertical total stress occur beyond the steam chambers, which under undrained conditions, lead to small reductions in pore pressure.

A method was developed for interpreting the full strain field within the geotechnical cross section based on inclinometer and extensometer measurements. Uniqueness in the solution of vertical displacements from vertical strains was achieved by utilizing the results from a roof extensometer in an observation tunnel below the Phase A reservoir.

The behavior of the extensometers was complex, reacting to both temperature and pore pressure. A detailed review of the displacement history of each extensometer module revealed the complexity of their response to SAGD processes and highlighted their importance in understanding formation behavior, especially within the geotechnical cross section. A maximum vertical extensional strain of 2.5% was measured in the reservoir between wellpair A1 and A2.

A review of the design and construction of the extensometer modules discovered that elements within the extensometer design permitted displacement degrees of freedom which impacted the operation of the extensometer modules. For extension displacements, the rod of the LVDT can displace completely out of the LVDT body - there are no structural limitations to extension displacements. Beyond approximately 40 mm of extension, the calibration curve for the extensometer LVDT is nonlinear. A full displacement calibration curve was developed for the extensometers. For compression, the Invar rod separating module anchors will "shoulder" against the anchor after approximately 45 mm of compression effectively eliminating the possibility of monitoring compression behavior beyond this level.

Horizontal displacements within the geotechnical cross section were sensitive to both pore pressure and temperature changes. Early horizontal formation displacements were controlled primarily by pore pressure development within the reservoir. At later stages, the three dimensional steam chamber growth and the resulting thermal strains created a more complex horizontal displacement pattern. In general, thermal expansion controlled the direction of horizontal displacements in the latter stages of the Phase A test. Full strain field analyses showed a maximum horizontal extensional strain of -.30% occurred within the reservoir.

Based on the full strain field analyses, a maximum shear strain of 3.0% and a volumetric strain of 2.6% occurred between wellpair A1 and A2. Based on empirical correlation's linking absolute permeability change to volumetric strains, the absolute permeability within this region of the reservoir increased approximately 30%; increasing from 7.5 darcies to 9.8 darcies.

Time	Wellpair A1	Wellpair A2	Wellpair A3
0.0 - 0.4	Start Up. Pressure maintained at 2400 kPa. Pressure differential between wells kept at 350 kPa.	n/a	n/a
0.4 - 0.9	Operated all period. Brief shut-in at 0.6. Circulation was reversed from annulus to tubing.	n/a	n/a
0.9 - 1.3	Operated all period. Maintained ≈350 kPa differential pressure.	n/a	n/a
1.3 - 1.7	Operated all period. Maintained ≈350 kPa differential pressure.	n/a	n/a
1.7 - 2.2	Operated all period. Breakthrough achieved at time 2.0. Normal mode resumed at time 2.04.	n/a	n/a
2.2 - 2.6	Operated 1/2 of period. Shut in at time 2.4 for piping construction. Cool water injected at time 2.43. Shut in for remainder of period.	n/a	n/a Pre-Commissioning.
2.6 - 3.0	Shut in/cool water injected for 1/2 of period. Steam injection resumed at time 2.8.	n/a	Start up at time 2.8. Pressure cycling from time 2.99.
3.0 - 3.5	Operated all period. Injection pressure reduced slightly at time 3.13. Shut in from time 3.13 to 3.19 (road wash-out).	Pre-Commissioning.	Operated all period. Cycling of AI, AP shut in. Shut in from time 3.13 to 3.19 (road wash-out).
3.5 - 3.9	Operated all period.	Start up at time 3.54.	Shut in at time 3.53 to allow for A2 startup.
3.9 - 4.3	Shut in from time 4.09 to 4.23 for blow down test.	Shut in at time 3.99.	Shut in all period.

Table 6.1 Summary of Significant Events - Phase A Steaming Trials: Time 0 to 4.3 (modified from AOSTRA, 1990)

Time	Wellpair A1	Wellpair A2	Wellpair A3
4.3 - 4.8	AI1 shut in until time 4.47 & AP1 shut in until time 4.59.	Shut in until time 4.50. Start circulation at time 4.53.	AI3: Shut in until time 4.61 after which inject steam into tubing & produce through annulus. AP3: Shut in all period.
4.8 - 5.2	Normal production.	Circulation until time 4.93 at which breakthrough was confirmed. Normal production for remainder of period.	AI3: Circulation all period except for shut in from time 4.93 to 5.10. AP3: Shut in all period.
5.2 - 5.7	Normal production.	Normal production.	AI3: Producing through annulus while injecting into tubing. Pressure cycling into tubing began at time 5.34. (Normal production) AP3: Shut in all period.
5.7 - 6.1	Normal Production.	Normal Production.	Normal Production.
6.1 - 6.5	Normal Production.	Normal Production.	Normal Production except for AI3 shut in from time 6.44 to 6.45.
6.5 - 6.9	Normal Production.	Normal Production.	Normal Production.
6.9 - 7.4	Normal Production.	Normal Production.	Normal Production.
7.4 - 7.8	Normal Production until time 7.71 after which AI1 steam throttled into annulus to increase injection.	Normal Production except AI2 & AP2 shut in from time 7.66 to 7.71.	Normal Production until time 7.63 after which: AI3: shut in to test for communication between A1 & AI3. AI3: annulus shut in while producing through tubing on time 7.76. AP3: shut in all period.
7.8 - 8.2	AI1: Steam throttled into annulus all period. AP1: Shut in from time 7.91 to 7.99 due to bad roads.	Normal Production except: AI2: Shut in during times 7.91 to 8.00 and 8.07 to 8.14. AI2: Throttled injection into annulus during times 8.03 to 8.06 and 8.16 to 8.24. AP2: Shut in during times 7.91 to 8.00 and 8.07 to 8.19.	AI3: Annulus shut in while producing through tubing all period. AP3: Shut in until time 8.03. Time 8.04 to 8.05 start up with throttled injection into tubing while producing through annulus. Shut in from time 8.07 to 8.16 for repairs.

Table 6.1 Summary of Significant Events - Phase A Steaming Trials: Time 4.3 to 8.2

Time	Wellpair A1	Wellpair A2	Wellpair A3
8.2 - 8.7	AI1: Steam throttled into annulus all period. AP1: Shut in for time 8.60 to 8.61.	AI2: Shut for time 8.29 to 8.30. AP2: Shut in during times 8.30 to 8.33 and 8.61 to 8.62.	AI3: Shut in for time 8.64 to 8.69. Production through tubing while annulus shut in. AP3: From time 8.26 to 8.51, production through tubing while injection in annulus. From 8.53 to 8.63, production through annulus while injecting in tubing. Shut in from time 8.63 to 8.70.
8.7 - 9.1	AI1: Steam injection into tubing and annulus. AP1: Produced through tubing while annulus shut in.	AI2: Shut in from time 8.70 to 8.76. Injection into tubing w/ annulus shut in from time 8.77 to 8.89. Injection into tubing w/ throttled injection into annulus for rest of period. AP2: Shut in from time 8.87 to 8.90.	AI3: Shut in from time 8.70 to 8.86. AP3: Shut in from time 8.70 to 8.83. At time 8.84, injection into tubing & annulus. From time 8.86 to 8.90, injection into annulus while producing through tubing. From time 8.88 to 9.10, injection into tubing while producing through annulus.
9.1 - 9.6	AI1: Shut in from time 9.31 to 9.34. AP1: Shut in from time 9.31 to 9.34.	AI2: Injection into tubing and throttled injection into annulus.	AI3: Shut in from time 9.41 to 9.44, production through tuning while annulus shut in. AP3: Shut in from time 9.31 to 9.34, injection through tubing while producing through annulus.
9.6 - 10.0	AI1: Injection into tubing with throttled injection into annulus.	AI2: Injection into tubing and throttled injection into annulus.	AI3: Production through tubing while annulus shut in. AP3: Pressured cycled tubing from time 9.60 to 9.61. Pressured cycled annulus while producing through tubing from time 9.63 to 9.81. Shut in from time 9.83 to 9.84. Produced through annulus while tubing shut in from time 9.85 to 10.0

Table 6.1 Summary of Significant Events - Phase A Steaming Trials: Time 8.2 to 10.0

Well Name	Easting (m)	Elev. (m)	Init. PP (kPa)	Elapsed Time																		
				1.4	2.1	2.5	2.9	3.2	3.6	3.9	4.3	4.6	5.0	5.4	5.7	6.1	6.4	7.1	7.9	8.6	9.3	10.0
AGP1	4056	280.4	459 ±4	475	489	467	502	680	622	592	602	609	606	652	683	729	1008	1330	1582	2113	2463	2584
AGP1	*4056*	*280.4*	*0*	*16*	*30*	*8*	*43*	*221*	*163*	*133*	*143*	*150*	*147*	*193*	*224*	*270*	*549*	*871*	*1123*	*1654*	*2004*	*2125*
AGP1	4056	275.4	544 ± 18	572	621	634	962	1186	855	779	925	838	976	1262	1462	1517	1613	1917	1903	2351	2441	2455
AGP1	*4056*	*275.4*	*0*	*28*	*77*	*90*	*418*	*642*	*311*	*235*	*381*	*294*	*432*	*718*	*918*	*973*	*1069*	*1373*	*1359*	*1807*	*1897*	*1911*
AGP2	4083	282.1	454 ± 1	539	672	673	822	1480	1930	2124	1472	2250	2230	2335	2477	2449	2409	2262	2317	2600	2600	2600
AGP2	*4083*	*282.1*	*0*	*85*	*218*	*219*	*368*	*1026*	*1476*	*1670*	*1018*	*1796*	*1776*	*1881*	*2023*	*1995*	*1955*	*1808*	*1863*	*2146*	*2146*	*2146*
AGP2	4083	275.1	517 ± 5	2281	2236	1000	2600	2600	2600	2600	2600	2600	2600	2600	2600	2600	2600	2600	2600	2600	2600	2600
AGP2	*4083*	*275.1*	*0*	*1764*	*1719*	*483*	*2083*	*2083*	*2083*	*2083*	*2083*	*2083*	*2083*	*2083*	*2083*	*2083*	*2083*	*2083*	*2083*	*2083*	*2083*	*2083*
AGP4	4101	284.8	447 ± 2	439	448	455	460	487	1006	1735	1015	1862	2071	2248	2349	2322	2234	2530	2600	2600	2600	2600
AGP4	*4101*	*284.8*	*0*	*-8*	*1*	*8*	*13*	*40*	*559*	*1288*	*568*	*1415*	*1624*	*1801*	*1902*	*1875*	*1787*	*2083*	*2153*	*2153*	*2153*	*2153*
AGP4	4101	272.8	606 ± 11	1075	871	1012	1361	1718	1962	2016	1225	1982	2019	2120	2317	2352	2319	2318	2247	2506	2593	2558
AGP4	*4101*	*272.8*	*0*	*469*	*265*	*406*	*755*	*1112*	*1356*	*1410*	*619*	*1376*	*1413*	*1514*	*1711*	*1746*	*1713*	*1712*	*1641*	*1900*	*1987*	*1952*
AGP5	4107	306.9	133 ± 1	125	124	122	121	122	119	117	116	115	114	112	112	111	109	108	102	98	95	87
AGP5	*4107*	*306.9*	*0*	*-8*	*-9*	*-11*	*-12*	*-11*	*-14*	*-16*	*-17*	*-18*	*-19*	*-21*	*-21*	*-22*	*-24*	*-25*	*-31*	*-35*	*-38*	*-46*
AGP5	4107	290.9	366 ± 2	371	351	355	355	361	537	515	427	463	464	494	657	1132	1522	2320	2179	2524	2510	2455
AGP5	*4107*	*290.9*	*0*	*5*	*-15*	*-11*	*-11*	*-5*	*171*	*149*	*61*	*97*	*98*	*128*	*291*	*766*	*1156*	*1954*	*1813*	*2158*	*2144*	*2089*
AGP5	4107	281.9	460 ± 10	425	410	408	405	418	1310	2536	959	2389	2173	2146	2300	2600	2600	2600	2600	2600	2600	2600
AGP5	*4107*	*281.9*	*0*	*-35*	*-50*	*-52*	*-55*	*-42*	*850*	*2076*	*499*	*1929*	*1713*	*1686*	*1840*	*2140*	*2140*	*2140*	*2140*	*2140*	*2140*	*2140*
AGP6	4134	285.7	406 ± 1	403	402	396	396	396	398	398	414	414	421	427	434	469	662	1503	2300	2600	2600	2600
AGP6	*4134*	*285.7*	*0*	*-3*	*-4*	*-10*	*-10*	*-10*	*-8*	*-8*	*8*	*8*	*15*	*21*	*28*	*63*	*256*	*1097*	*1894*	*2194*	*2194*	*2194*
AGP6	4134	277.7	495 ± 1	462	435	432	433	432	431	457	473	485	507	507	518	490	449	637	2187	2556	2404	2600
AGP6	*4134*	*277.7*	*0*	*-33*	*-60*	*-63*	*-62*	*-63*	*-64*	*-38*	*-22*	*-10*	*12*	*12*	*23*	*-5*	*-46*	*142*	*1692*	*2061*	*1909*	*2105*
AT4	4093	295.9	308 ± 2	306	305	304	304	305	307	307	319	313	318	322	326	332	336	342	402	409	483	675
AT4	*4093*	*295.9*	*0*	*-2*	*-3*	*-4*	*-4*	*-3*	*-1*	*-1*	*11*	*5*	*10*	*14*	*18*	*24*	*28*	*34*	*94*	*101*	*175*	*367*
AT4	4093	289.9	399 ± 2	380	380	377	379	385	397	1434	655	1071	1016	1215	1481	1864	2241	2290	2303	2596	2600	2600
AT4	*4093*	*289.9*	*0*	*-19*	*-19*	*-22*	*-20*	*-14*	*-2*	*1035*	*256*	*672*	*617*	*816*	*1082*	*1465*	*1842*	*1891*	*1904*	*2197*	*2201*	*2201*
AT4	4093	282.9	459 ± 5	480	1272	812	1529	1929	2223	2282	1454	2284	2086	2214	2290	2315	2234	2200	2300	2400	2600	2600
AT4	*4093*	*282.9*	*0*	*21*	*813*	*353*	*1070*	*1470*	*1764*	*1823*	*995*	*1825*	*1627*	*1755*	*1831*	*1856*	*1775*	*1741*	*1841*	*1941*	*2141*	*2141*
AT9	4117	289.8	361 ± 2	354	355	352	321	371	380	384	398	406	429	394	367	600	1062	2257	2151	2551	2524	2475
AT9	*4117*	*289.8*	*0*	*-7*	*-6*	*-9*	*-40*	*10*	*19*	*23*	*37*	*45*	*68*	*33*	*6*	*239*	*701*	*1896*	*1790*	*2190*	*2163*	*2114*
AT9	4117	281.8	464 ± 13	456	454	439	442	445	677	1395	776	2166	2137	2500	2500	2500	2500	2500	2500	2500	2500	2500
AT9	*4117*	*281.8*	*0*	*-8*	*-10*	*-25*	*-22*	*-19*	*213*	*931*	*312*	*1702*	*1673*	*2036*	*2036*	*2036*	*2036*	*2036*	*2036*	*2036*	*2036*	*2036*
AT12	4070	295.3	292 ± 2	265	268	273	278	282	291	298	316	325	333	350	368	384	393	418	461	453	472	489
AT12	*4070*	*295.3*	*0*	*-27*	*-24*	*-19*	*-14*	*-10*	*-1*	*6*	*24*	*33*	*41*	*58*	*76*	*92*	*101*	*126*	*169*	*161*	*180*	*197*
AT12	4070	288.3	410 ± 3	392	381	379	377	373	381	375	385	399	416	417	491	548	859	1063	1339	2488	2506	2565
AT12	*4070*	*288.3*	*0*	*-18*	*-29*	*-31*	*-33*	*-37*	*-29*	*-35*	*-25*	*-11*	*6*	*7*	*81*	*138*	*449*	*653*	*929*	*2078*	*2096*	*2155*
AT14	4070	281.2	452 ± 4	466	515	543	572	700	820	831	799	888	1119	1500	1712	1850	1900	2015	2055	2635	2552	2550
AT14	*4070*	*281.2*	*0*	*14*	*63*	*91*	*120*	*248*	*368*	*379*	*347*	*436*	*667*	*1048*	*1260*	*1398*	*1448*	*1563*	*1603*	*2183*	*2100*	*2098*

Table 6.2 Pore Pressure Values within Geotechnical Cross Section

Time	Relative Displacement (mm)				Vertical Strain(%)			
	Module							
	245	244	249	250	245	244	249	250
0	0.00	0.00	0.00	0.00	0.000	0.000	0.000	0.000
1.4	0.29	0.70	0.43	-0.09	0.010	0.023	0.014	-0.003
2.1	-0.06	0.95	0.57	-0.02	-0.002	0.032	0.019	-0.001
2.5	-0.24	0.79	0.62	0.02	-0.008	0.026	0.021	0.001
2.9	-0.66	1.05	0.61	0.04	-0.022	0.035	0.020	0.001
3.2	-1.07	0.82	0.38	0.06	-0.036	0.027	0.013	0.002
3.6	-2.14	0.33	0.14	0.09	-0.071	0.011	0.005	0.003
3.9	-2.33	0.02	-0.08	0.06	-0.078	0.001	-0.003	0.002
4.3	-1.92	0.58	-0.06	-0.08	-0.064	0.019	-0.002	-0.003
4.6	-1.50	1.00	0.02	-0.11	-0.050	0.033	0.001	-0.004
5.0	-0.65	1.98	0.43	-0.23	-0.022	0.066	0.014	-0.008
5.4	0.90	-1.55	1.83	0.34	0.030	-0.052	0.061	0.011
5.7	1.58	-3.25	1.85	0.37	0.053	-0.108	0.062	0.012
6.1	2.43	-4.71	5.53	0.43	0.081	-0.157	0.184	0.014
6.4	26.50	-5.07	10.77	0.58	0.883	-0.169	0.359	0.019
7.1	15.00	-25.81	25.70	1.34	0.500	-0.860	0.857	0.045
7.9	12.30	-11.80	25.70	-1.80	0.410	-0.393	0.857	-0.060
8.6	10.15	-7.68	22.65	-6.37	0.338	-0.256	0.755	-0.212
9.3	30.23	-30.40	24.10	-9.18	1.008	-1.013	0.803	-0.306
10	22.68	-28.40	25.60	-11.11	0.756	-0.947	0.853	-0.370

Note: -ve denotes expansion

Table 6.3 Relative Displacement/Vertical Strain History for Well AGE2

Time	Relative Displacement (mm)						Vertical Strain (%)					
	Module											
	248	240	238	236	242	243	248	240	238	236	242	243
0.0	0.00	0.00	0.00	0.00	0.00	0.00	0.000	0.000	0.000	0.000	0.000	0.000
1.4	-1.13	0.31	0.12	0.11	-0.04	0.02	-0.023	0.006	0.002	0.002	-0.001	0.000
2.1	-0.50	-0.20	0.05	0.22	-0.02	0.01	-0.010	-0.004	0.001	0.004	0.000	0.000
2.5	0.08	-0.68	-0.06	0.19	0.01	0.07	0.002	-0.014	-0.001	0.004	0.000	0.001
2.9	-0.05	-0.85	-0.10	0.35	0.02	0.06	-0.001	-0.017	-0.002	0.007	0.000	0.001
3.2	-0.32	-1.35	-0.59	0.43	-0.07	0.06	-0.006	-0.027	-0.012	0.009	-0.001	0.001
3.6	-0.69	-3.45	-1.27	0.10	-0.08	0.52	-0.014	-0.069	-0.025	0.002	-0.002	0.010
3.9	-0.84	-3.79	-2.66	-0.16	0.15	-5.28	-0.017	-0.076	-0.053	-0.003	0.003	-0.106
4.3	-0.90	-3.51	-3.32	0.03	0.93	-2.20	-0.018	-0.070	-0.066	0.001	0.019	-0.044
4.6	-1.05	-3.52	-3.77	0.10	0.81	0.05	-0.021	-0.070	-0.075	0.002	0.016	0.001
5.0	-1.06	-5.00	-7.21	0.52	0.78	-0.71	-0.021	-0.100	-0.144	0.010	0.016	-0.014
5.4	-0.57	-7.55	-8.39	2.66	1.23	-0.94	-0.011	-0.151	-0.168	0.053	0.025	-0.019
5.7	-0.60	-7.75	-18.22	14.86	2.25	-0.70	-0.012	-0.155	-0.364	0.297	0.045	-0.014
6.1	-0.83	-10.65	-13.61	17.06	3.92	-0.46	-0.017	-0.213	-0.272	0.341	0.078	-0.009
6.4	-1.90	-11.23	-4.55	16.56	3.32	-1.16	-0.038	-0.225	-0.091	0.331	0.066	-0.023
7.1	-4.90	-12.25	-4.30	14.56	3.52	-1.06	-0.098	-0.245	-0.086	0.291	0.070	-0.021
7.9	-11.47	-16.90	-11.26	14.56	3.37	-6.30	-0.229	-0.338	-0.225	0.291	0.067	-0.126
8.6	-12.32	-42.68	-42.68	17.06	3.23	-7.25	-0.246	-0.854	-0.854	0.341	0.065	-0.145
9.3	-11.40	-150.0	-150.0	13.76	3.23	1.60	-0.228	-3.000	-3.000	0.275	0.065	0.032
10.0	-11.52	-200.0	-200.0	13.76	3.23	8.25	-0.230	-4.000	-4.000	0.275	0.065	0.165

Note: -ve denotes expansion

this data was assumed identical to Module 240. Module 238 response over this time period was extremely unstable. Data following time 10.0 for Module 238 exhibits the same response as Module 240 concerning the core of the LVDT displacing out of the body of the LVDT.

▨ this data was assumed constant over remaining time periods. Valid readings ended at ≈ time 8.54.

Table 6.4 Relative Displacement/Vertical Strain History for Well AGE3

Time	Relative Displacement (mm)					Vertical Strain (%)				
	Module									
	235	246	247	241	239	235	246	247	241	239
0	0.00	0.00	0.00	0.00	0.00	0.000	0.000	0.000	0.000	0.000
1.4	-0.39	-0.07	0.01	0.18	0.00	-0.008	-0.001	0.000	0.004	0.000
2.1	-0.69	-0.43	-0.35	0.11	-0.04	-0.014	-0.009	-0.007	0.002	-0.001
2.5	-0.77	-0.57	-0.64	0.16	-0.44	-0.015	-0.011	-0.013	0.003	-0.009
2.9	-0.90	-0.82	-0.47	0.09	-0.74	-0.018	-0.016	-0.009	0.002	-0.015
3.2	-1.36	-1.74	-0.72	-0.04	-0.91	-0.027	-0.035	-0.014	-0.001	-0.018
3.6	-2.44	-4.33	-2.28	-0.16	-0.93	-0.049	-0.087	-0.046	-0.003	-0.019
3.9	-1.39	-5.55	-2.50	-0.56	-1.02	-0.028	-0.111	-0.050	-0.011	-0.020
4.3	-0.90	-5.95	-1.50	-0.72	-1.00	-0.018	-0.119	-0.030	-0.014	-0.020
4.6	-1.75	-6.30	-6.50	-0.90	-1.04	-0.035	-0.126	-0.130	-0.018	-0.021
5.0	-2.20	-10.43	-14.00	-1.78	-1.15	-0.044	-0.209	-0.280	-0.036	-0.023
5.4	2.00	-16.38	-13.01	-2.81	-1.40	0.040	-0.328	-0.260	-0.056	-0.028
5.7	3.00	-23.20	-10.00	-4.61	-1.89	0.060	-0.464	-0.200	-0.092	-0.038
6.1	3.41	-33.30	-6.50	-5.31	-3.13	0.068	-0.666	-0.130	-0.106	-0.063
6.4	3.27	-40.80	-5.91	-5.50	-4.01	0.065	-0.816	-0.118	-0.110	-0.080
7.1	2.80	-59.56	-8.73	-1.44	-5.86	0.056	-1.191	-0.175	-0.029	-0.117
7.9	1.96	-150.0	-7.50	0.08	-3.12	0.039	-3.000	-0.150	0.002	-0.062
8.6	2.69	1.91	-5.78	1.49	1.91	0.054	0.038	-0.116	0.030	0.038
9.3	2.40	3.11	-3.91	2.19	1.86	0.048	0.062	-0.078	0.044	0.037
10	-1.15	2.96	2.39	1.19	3.91	-0.023	0.059	0.048	0.024	0.078

Note: -ve denotes expansion

▒ obtained from linear interpolation

▨ assumed response based on behavior of neighboring AGE3 response and module response beyond time 8.6.

Table 6.5 Relative Displacement/Vertical Strain History for Well AGE4

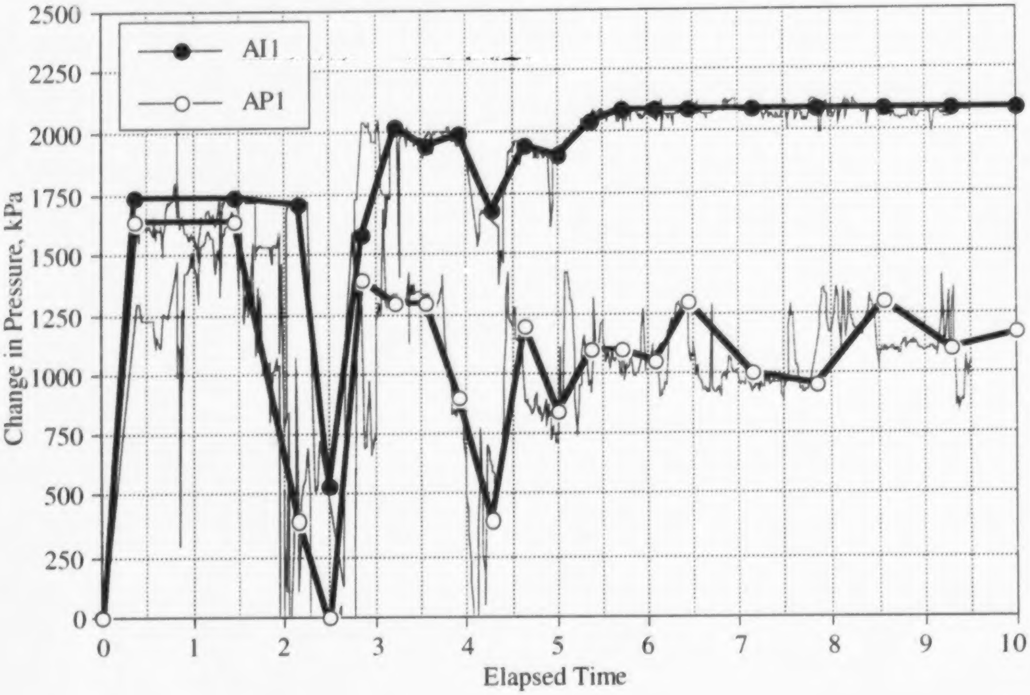

Figure 6.1 Simplified Pressure History for Wellpair A1

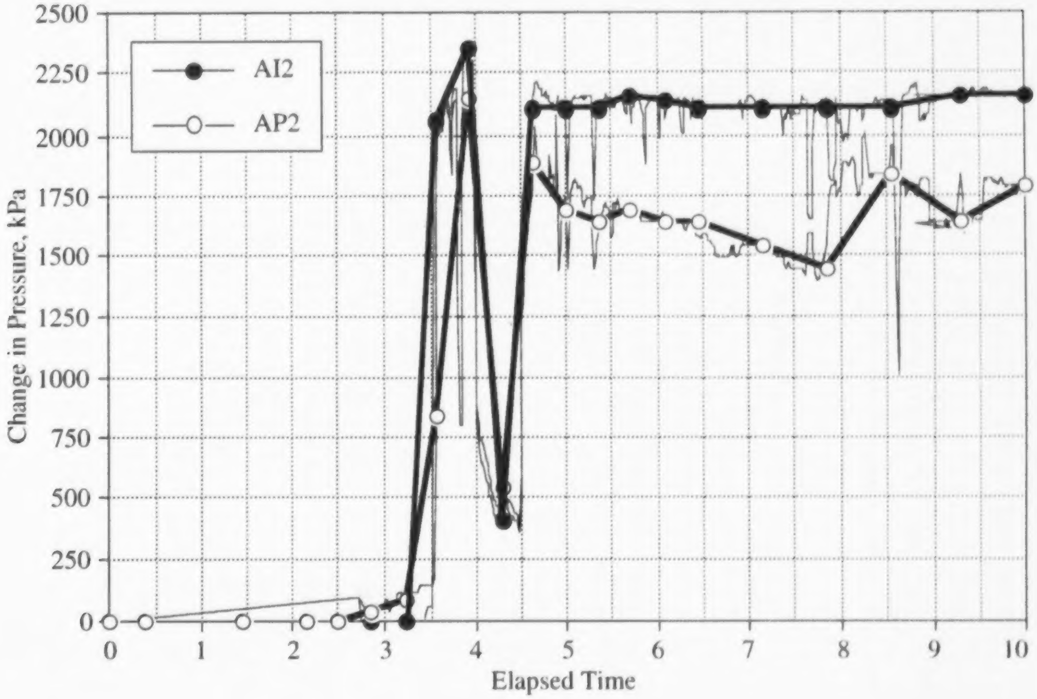

Figure 6.2 Simplified Pressure History for Wellpair A2

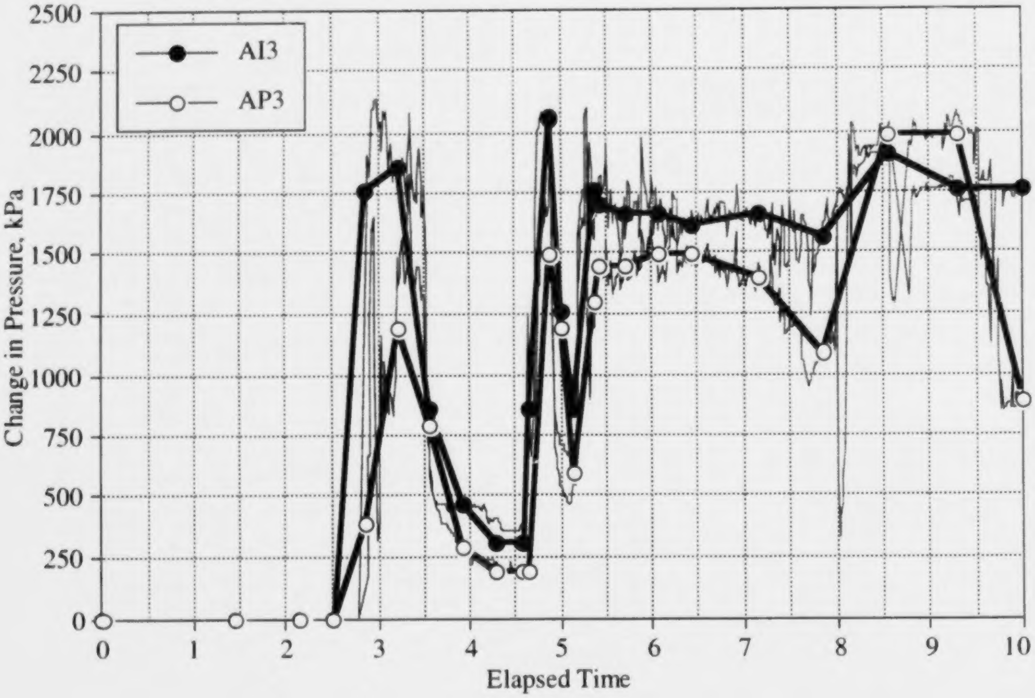

Figure 6.3 Simplified Pressure History for Wellpair A3

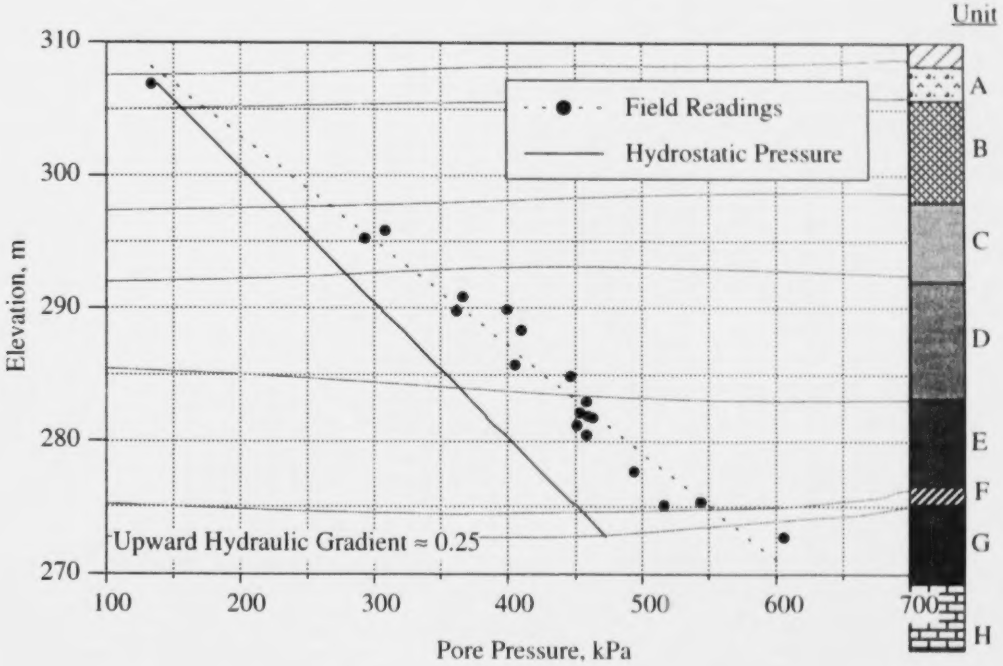

Figure 6.4 Initial Pore Pressure Distribution within McMurray Formation (modified from AOSTRA, 1990)

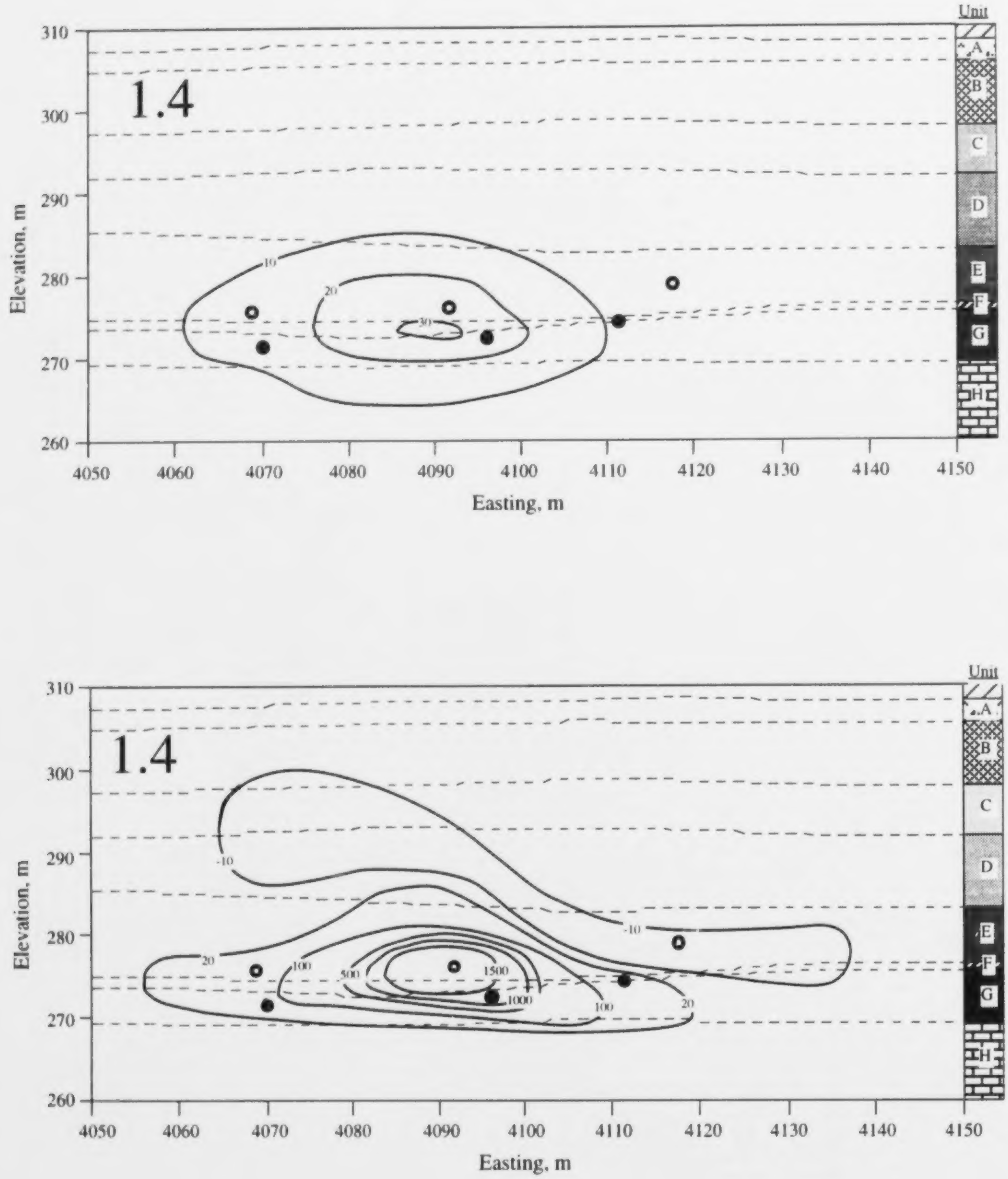

Figure 6.5 Temperature and Pore Pressure Distribution within Geotechnical Cross Section for Time 1.4

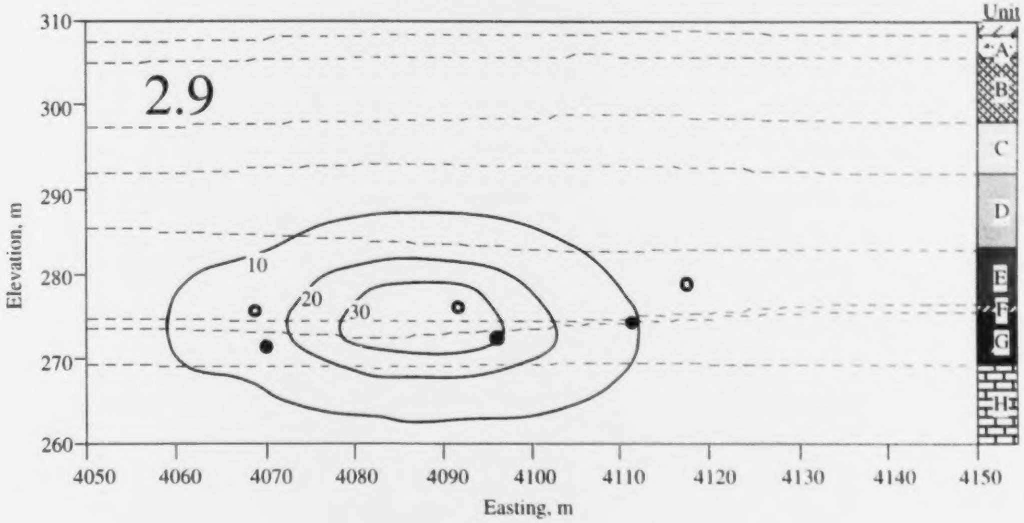

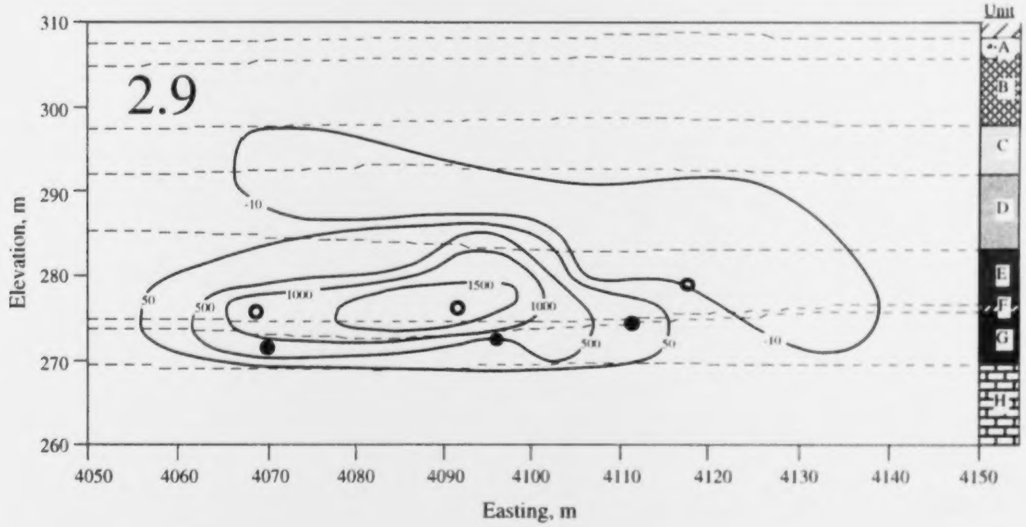

Figure 6.6 Temperature and Pore Pressure Distribution within Geotechnical Cross Section for Time 2.9

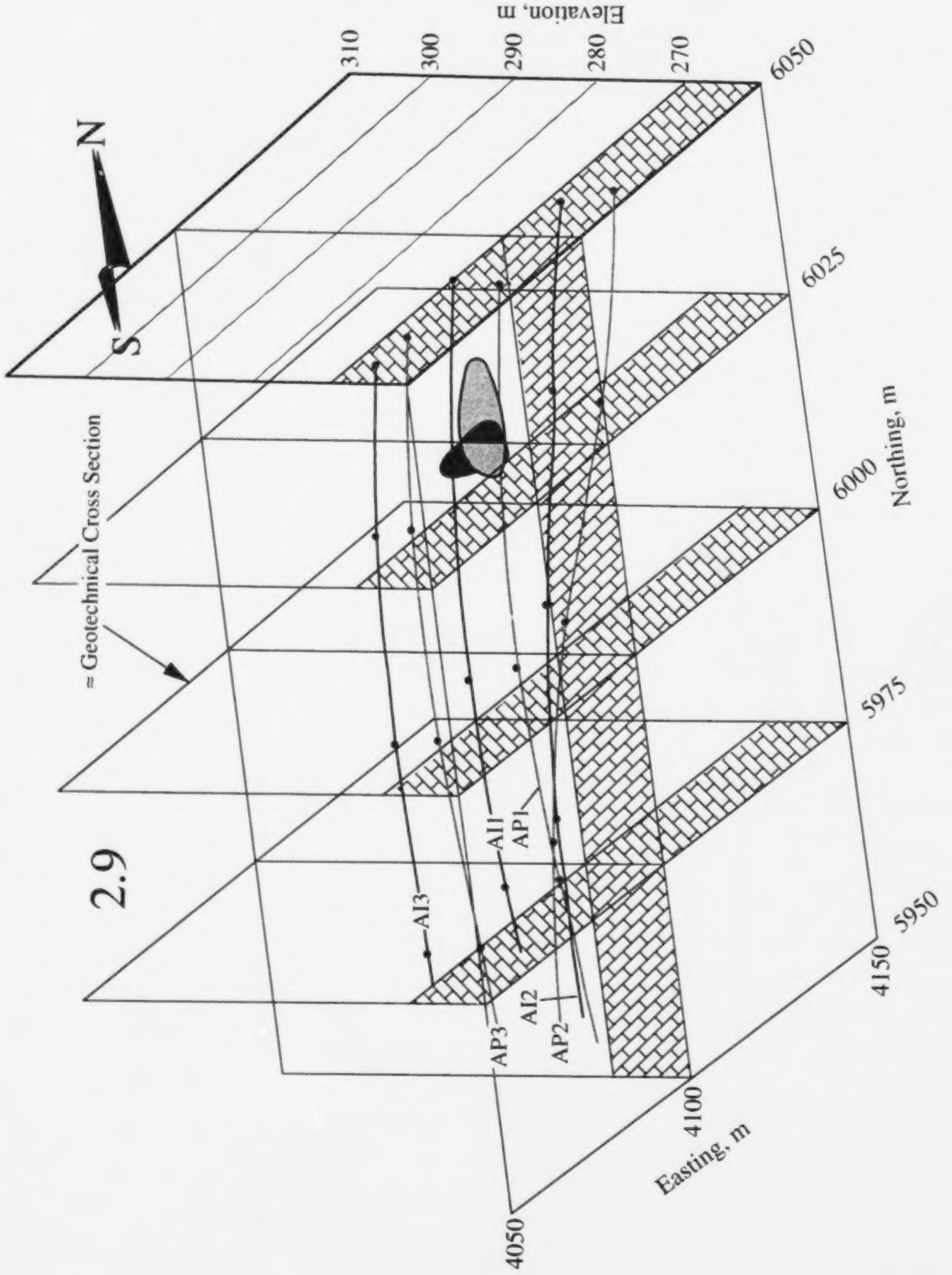
2.9
≈ Geotechnical Cross Section
N
S
Elevation, m
310
300
290
280
270
6050
6025
6000
5975
5950
Northing, m
4150
4100
4050
Easting, m
AI3
AI1
AP1
AI2
AP2
AP3

Figure 6.7 Three Dimensional Representation of Steam Chamber at Time 2.9

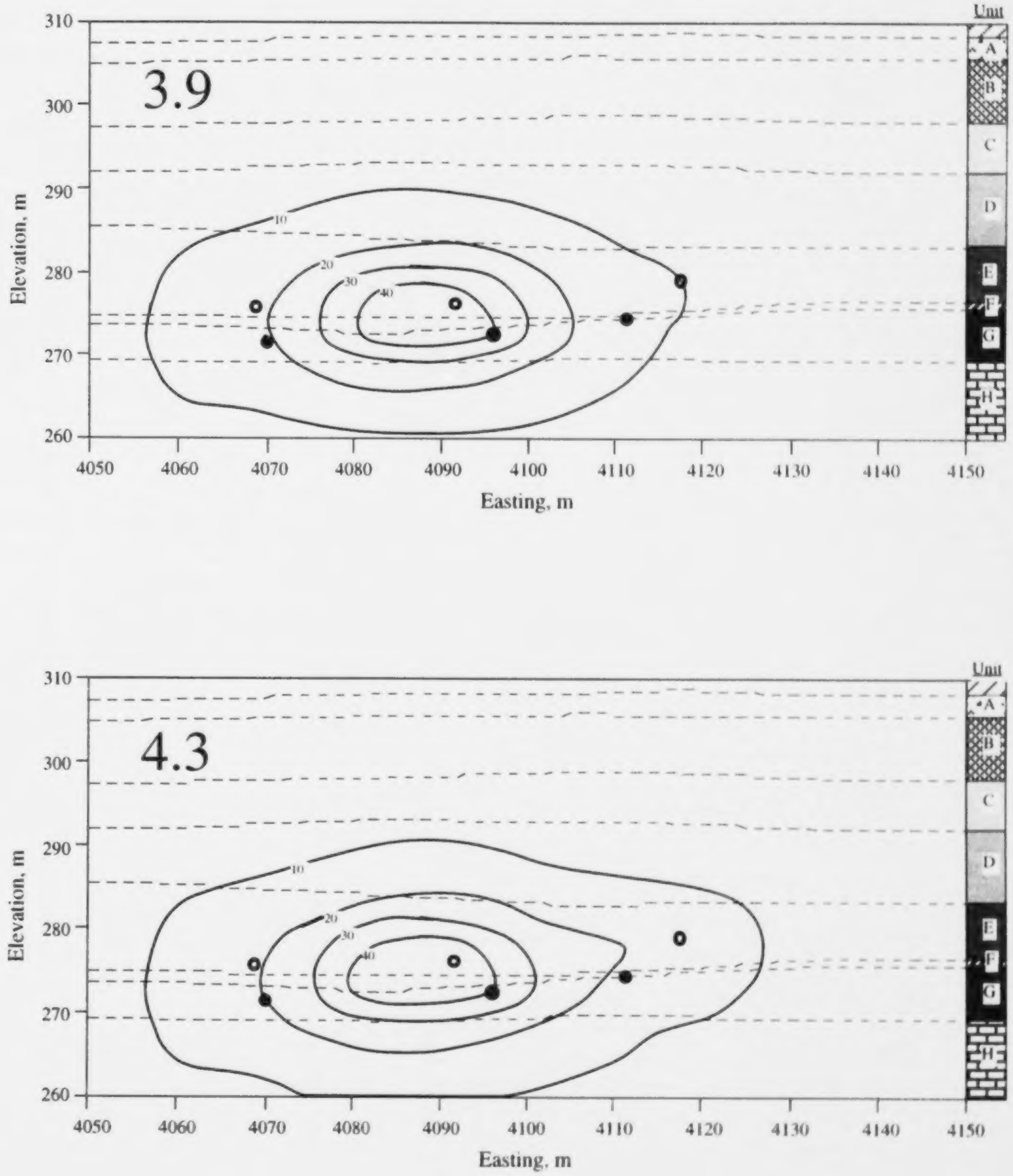

Figure 6.8 Temperature Distribution within Geotechnical Cross Section: Time 3.9 and 4.3

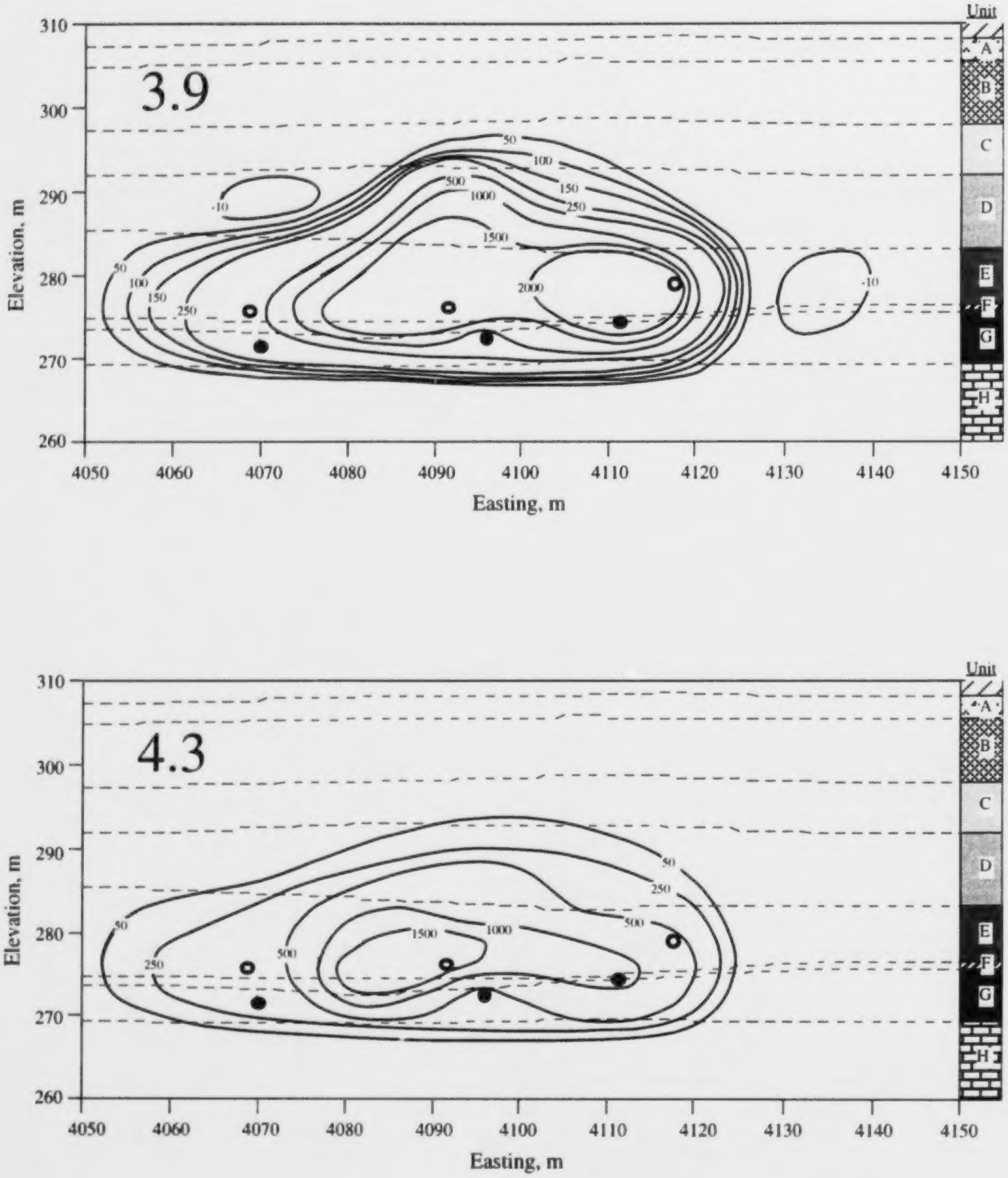

Figure 6.9	Pore Pressure Distribution within Geotechnical Cross Section: Time 3.9 and 4.3

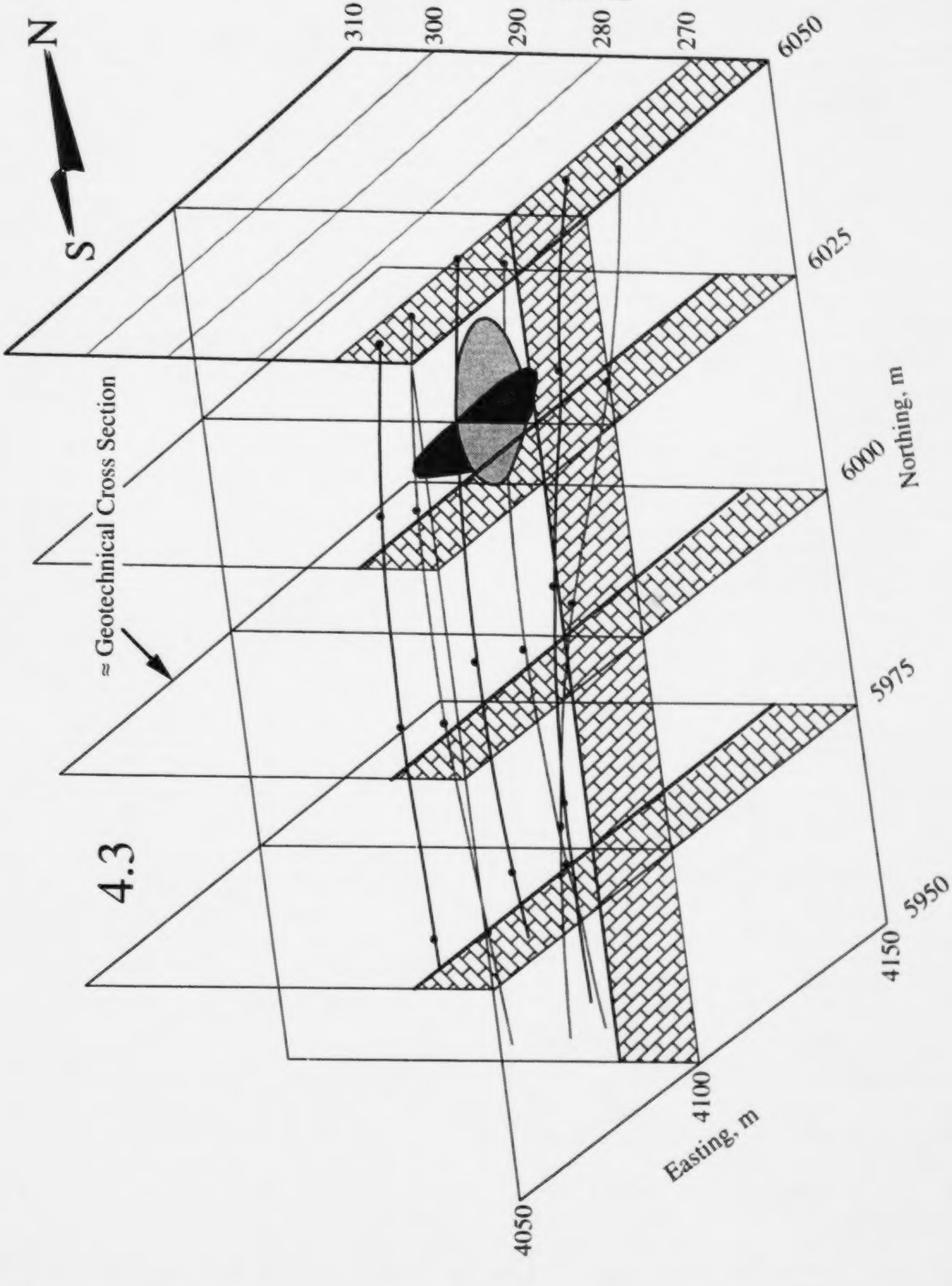
4.3
≈ Geotechnical Cross Section
S
N
Elevation, m
310
300
290
280
270
6050
6025
6000
5975
5950
Northing, m
4050
4100
4150
Easting, m

Figure 6.10 Three Dimensional Representation of Steam Chamber at Time 4.3

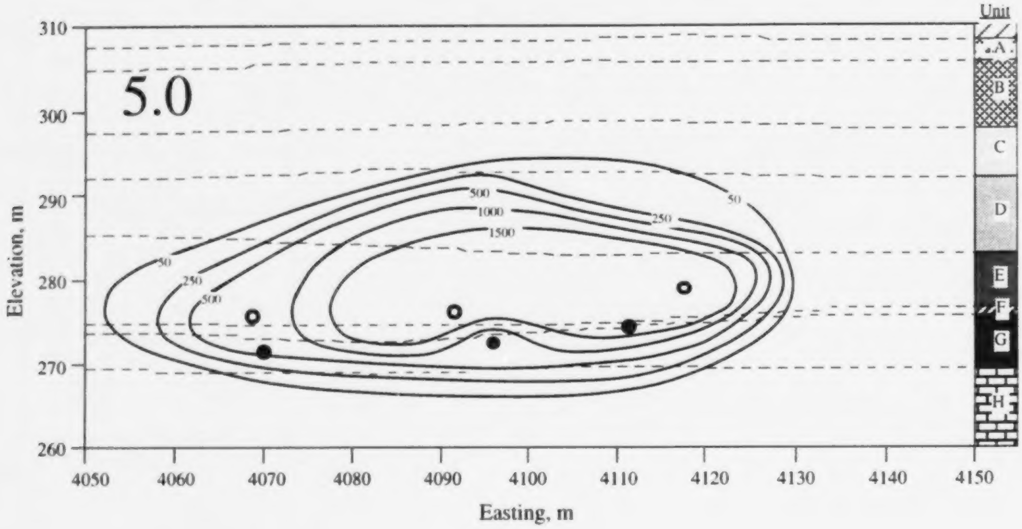

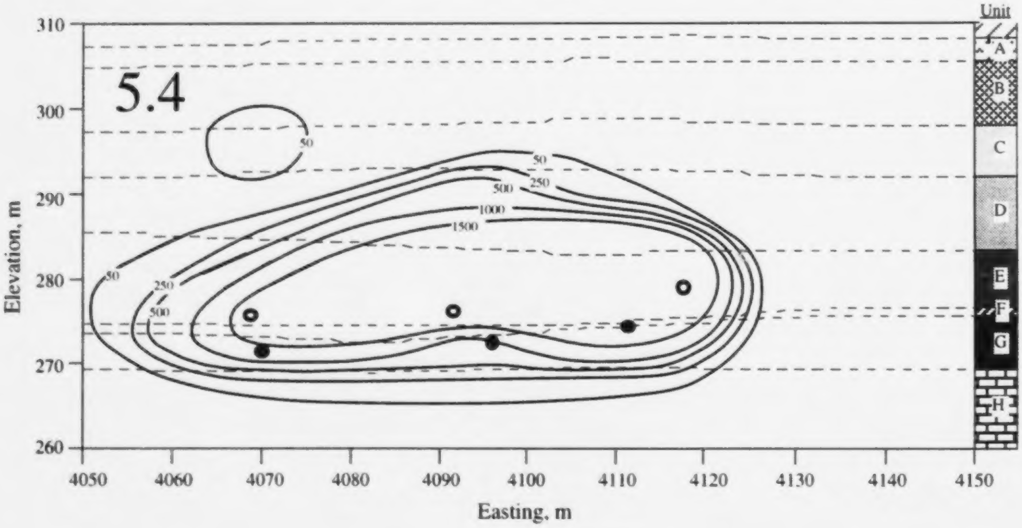

Figure 6.11 Pore Pressure Distribution within Geotechnical Cross Section: Time 5.0 and 5.4

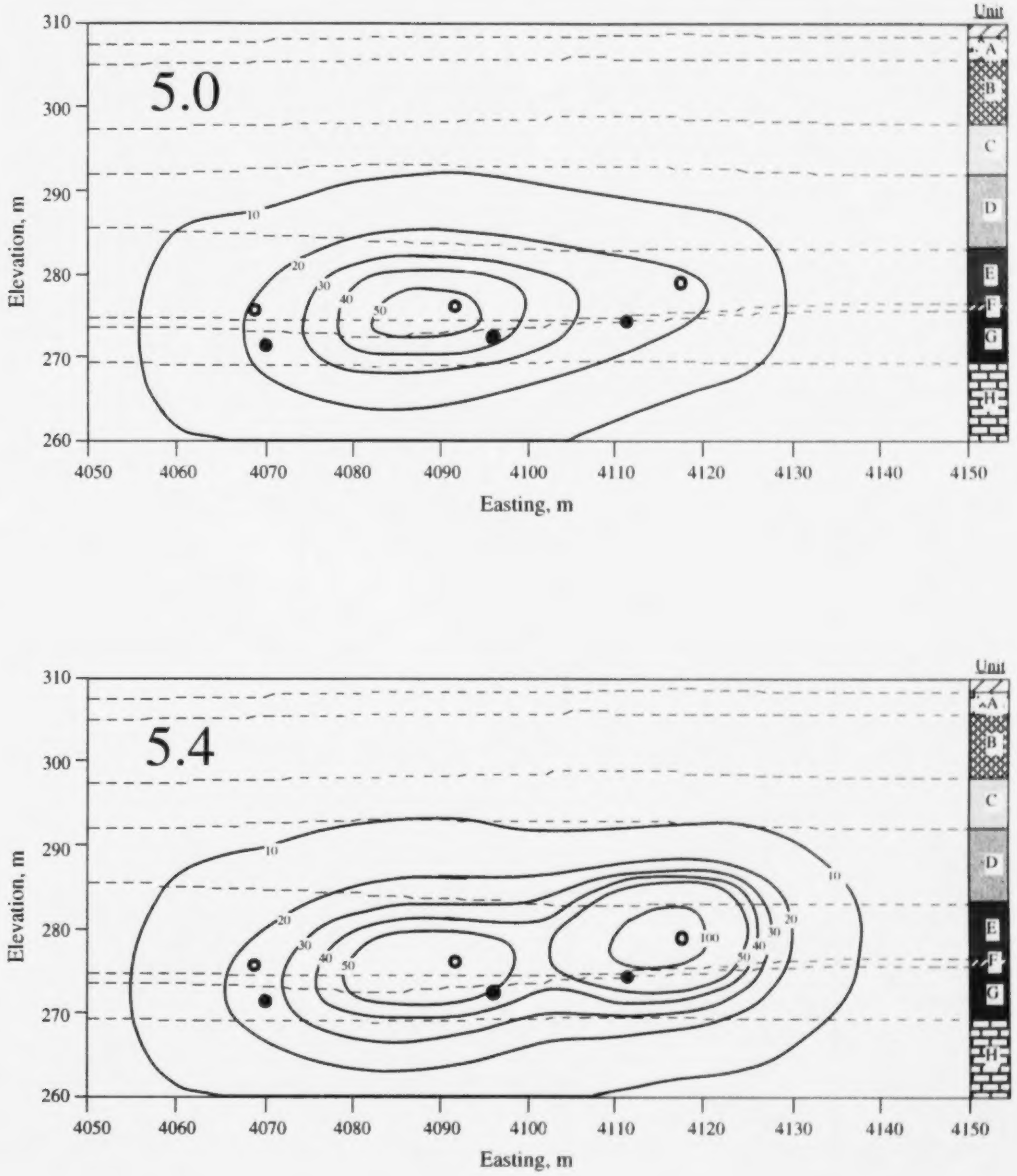

Figure 6.12 Temperature Distribution within Geotechnical Cross Section: Time 5.0 and 5.4

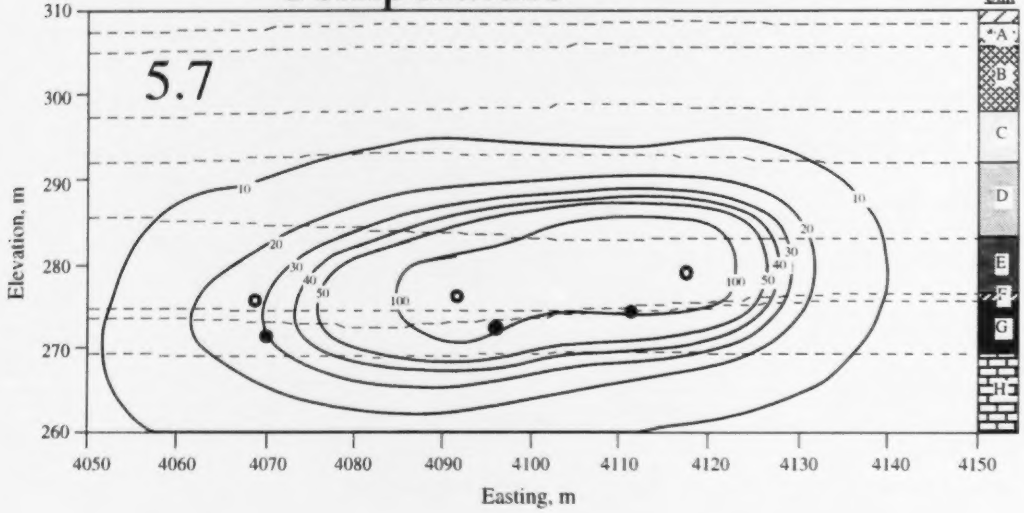

Temperature

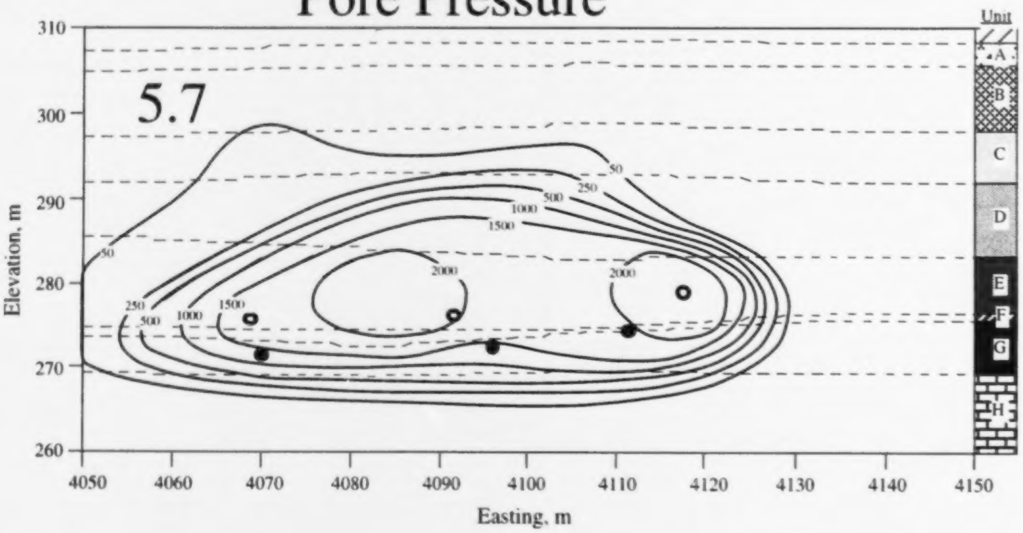

Pore Pressure

Figure 6.13 Temperature and Pore Pressure Distribution within Geotechnical Cross Section for Time 5.7

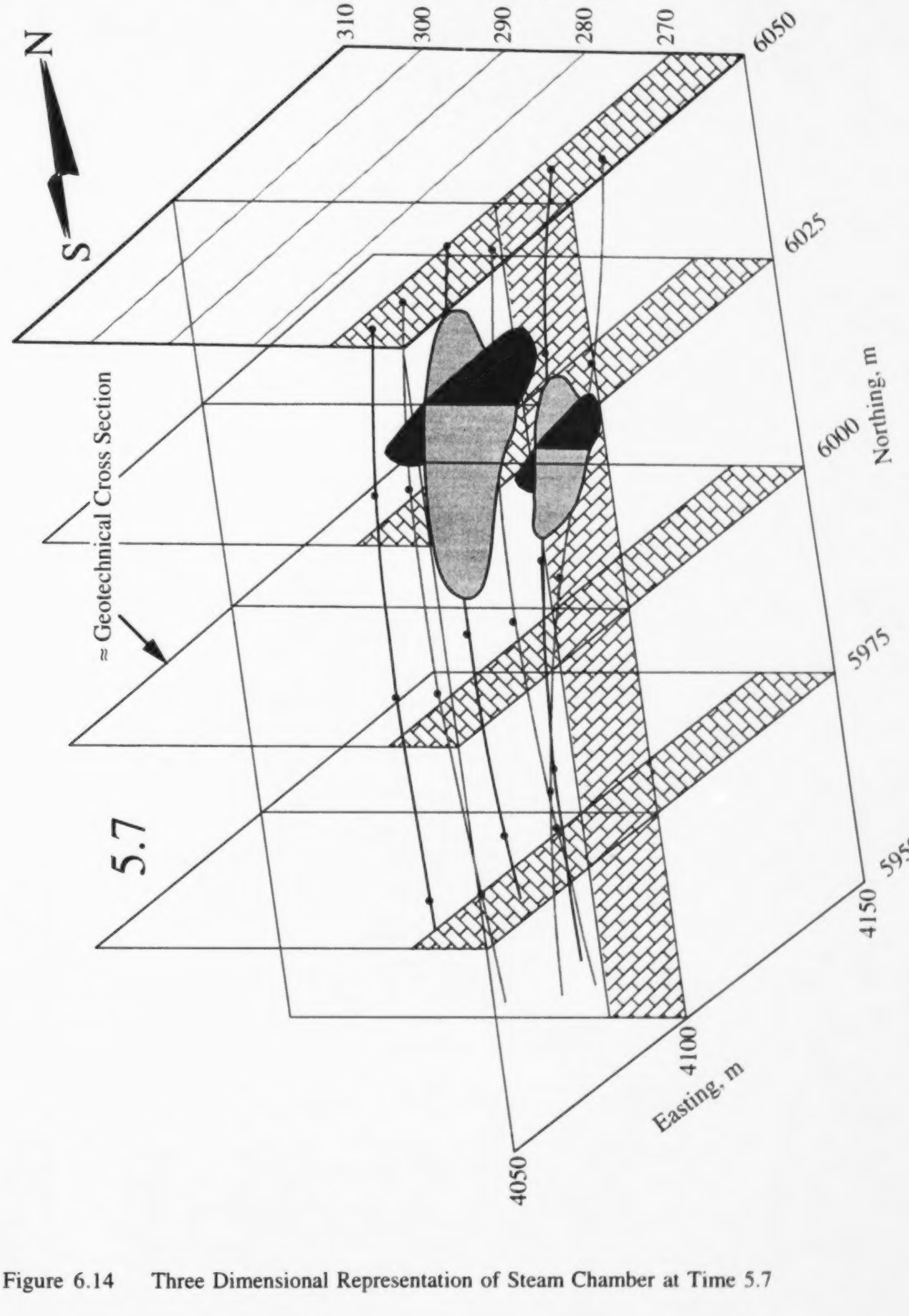
5.7
≈ Geotechnical Cross Section
S
N
Elevation, m
310
300
290
280
270
6050
6025
6000
5975
5950
Northing, m
4150
4100
4050
Easting, m

Figure 6.14 Three Dimensional Representation of Steam Chamber at Time 5.7

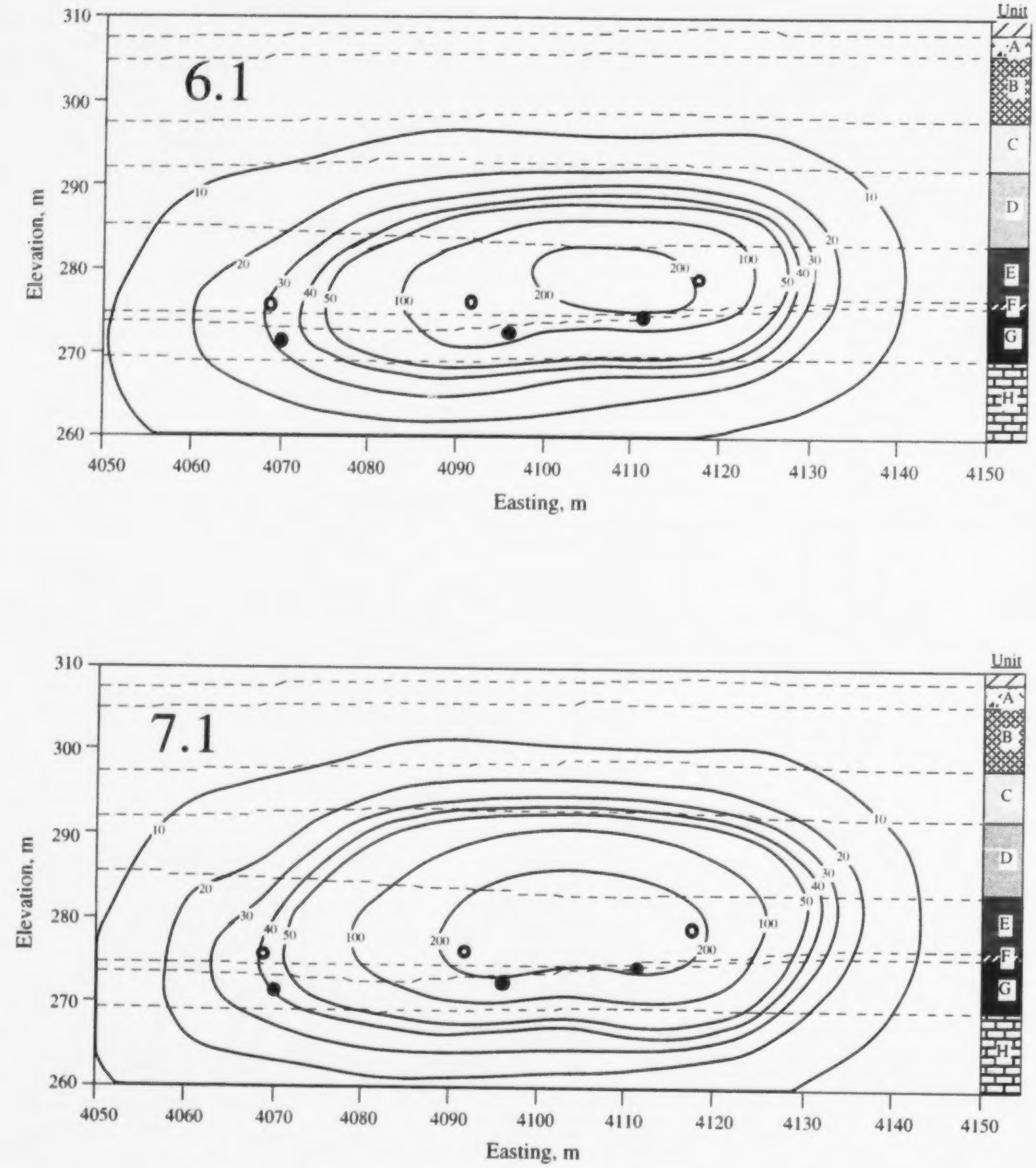

Figure 6.15 Temperature Distribution within Geotechnical Cross Section: Time 6.1 and 7.4

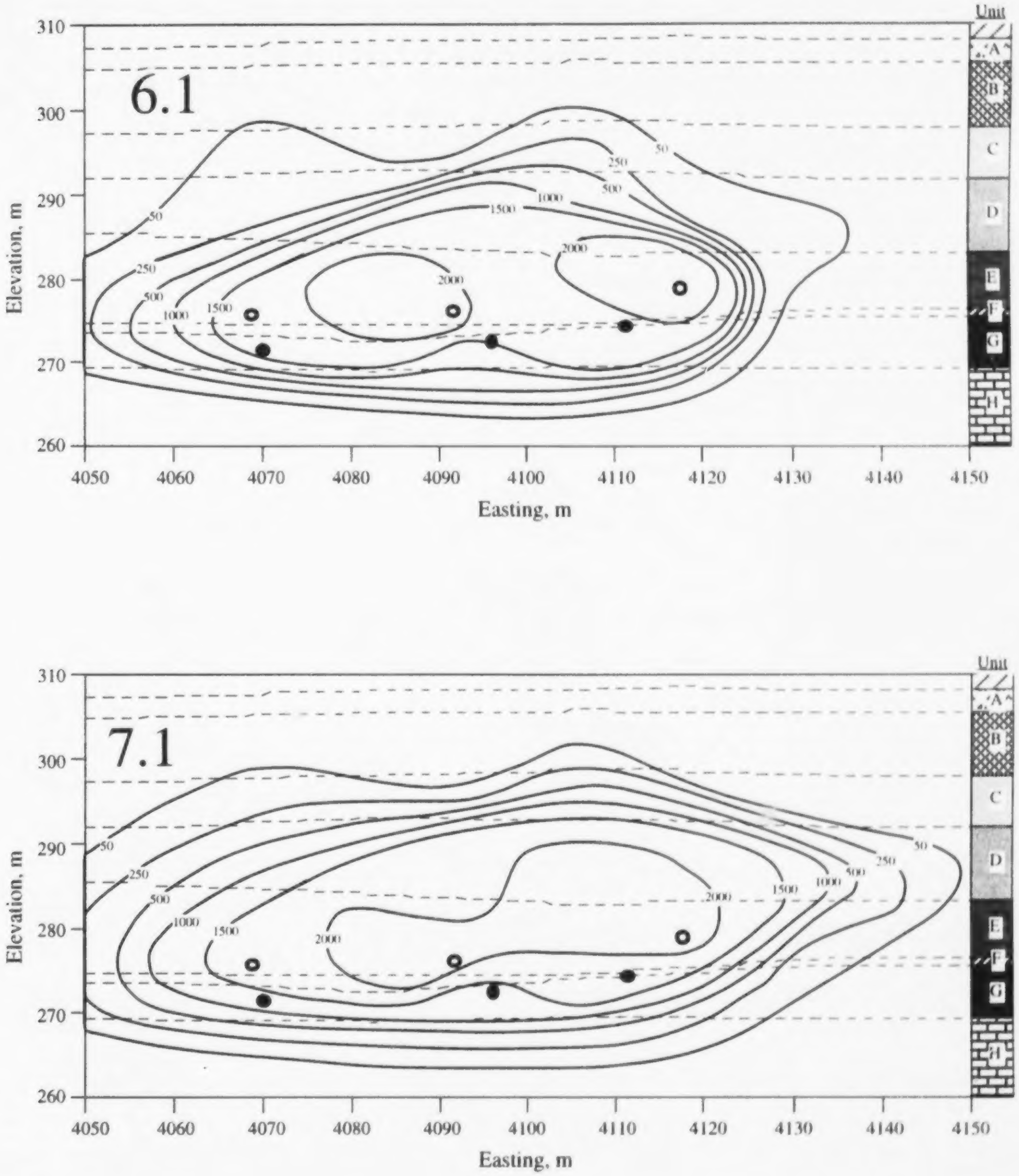

Figure 6.16 Pore Pressure Distribution within Geotechnical Cross Section: Time 6.1 and 7.4

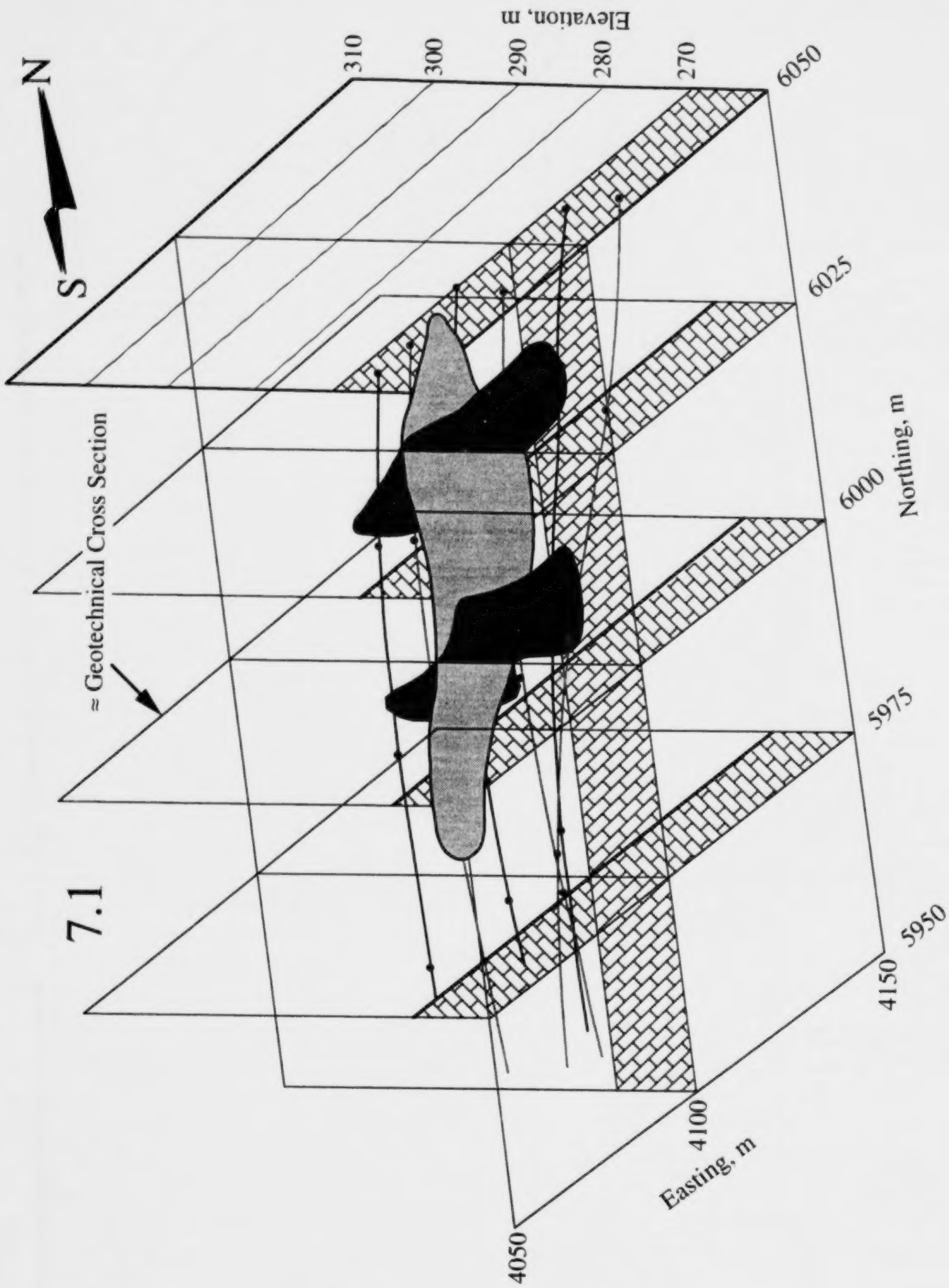
7.1
S
N
≈ Geotechnical Cross Section
Elevation, m
310
300
290
280
270
6050
6025
6000
5975
5950
Northing, m
4150
4100
4050
Easting, m

Figure 6.17 Three Dimensional Representation of Steam Chamber at Time 7.1

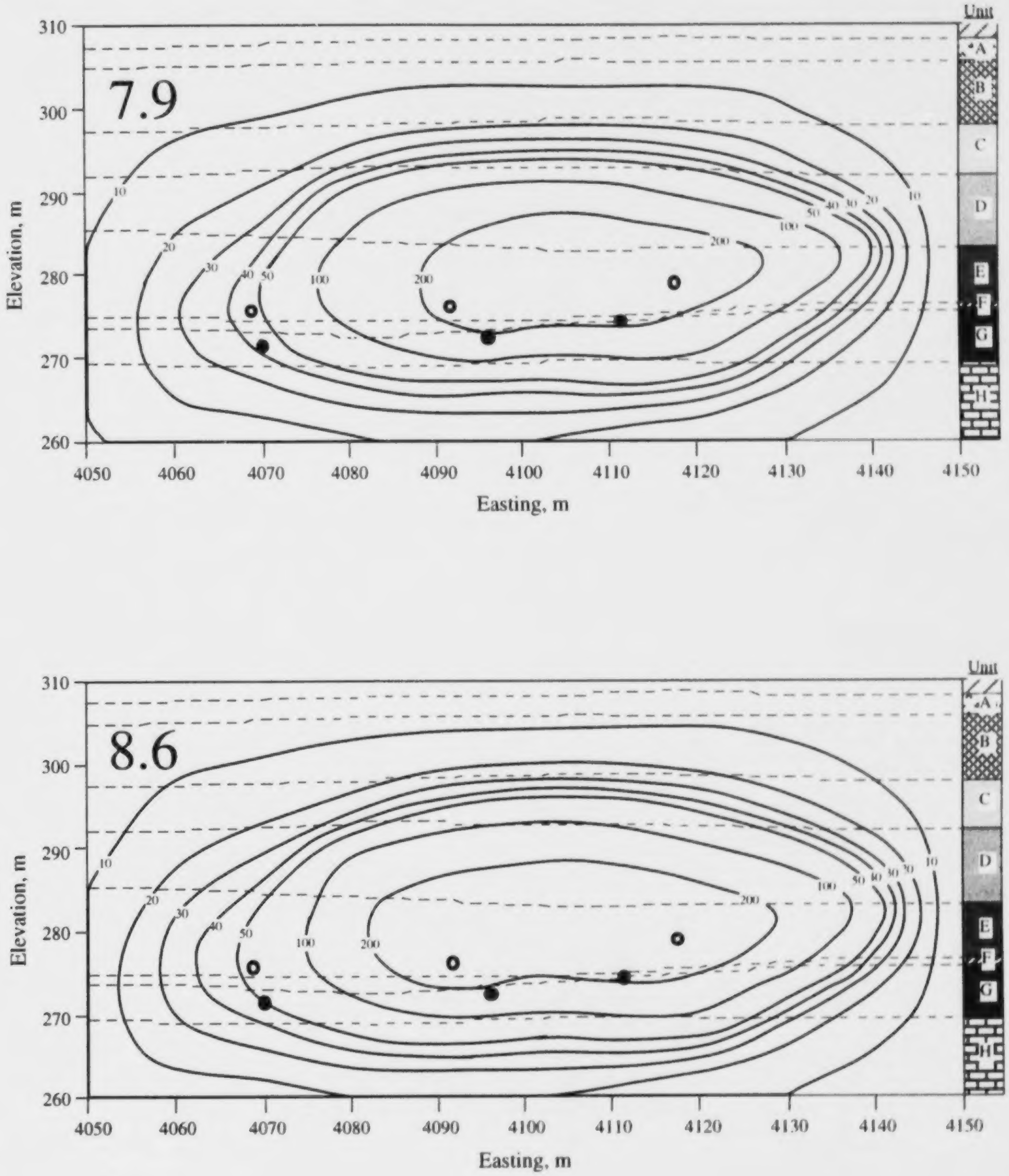

Figure 6.18 Temperature Distribution within Geotechnical Cross Section: Time 7.9 and 8.6

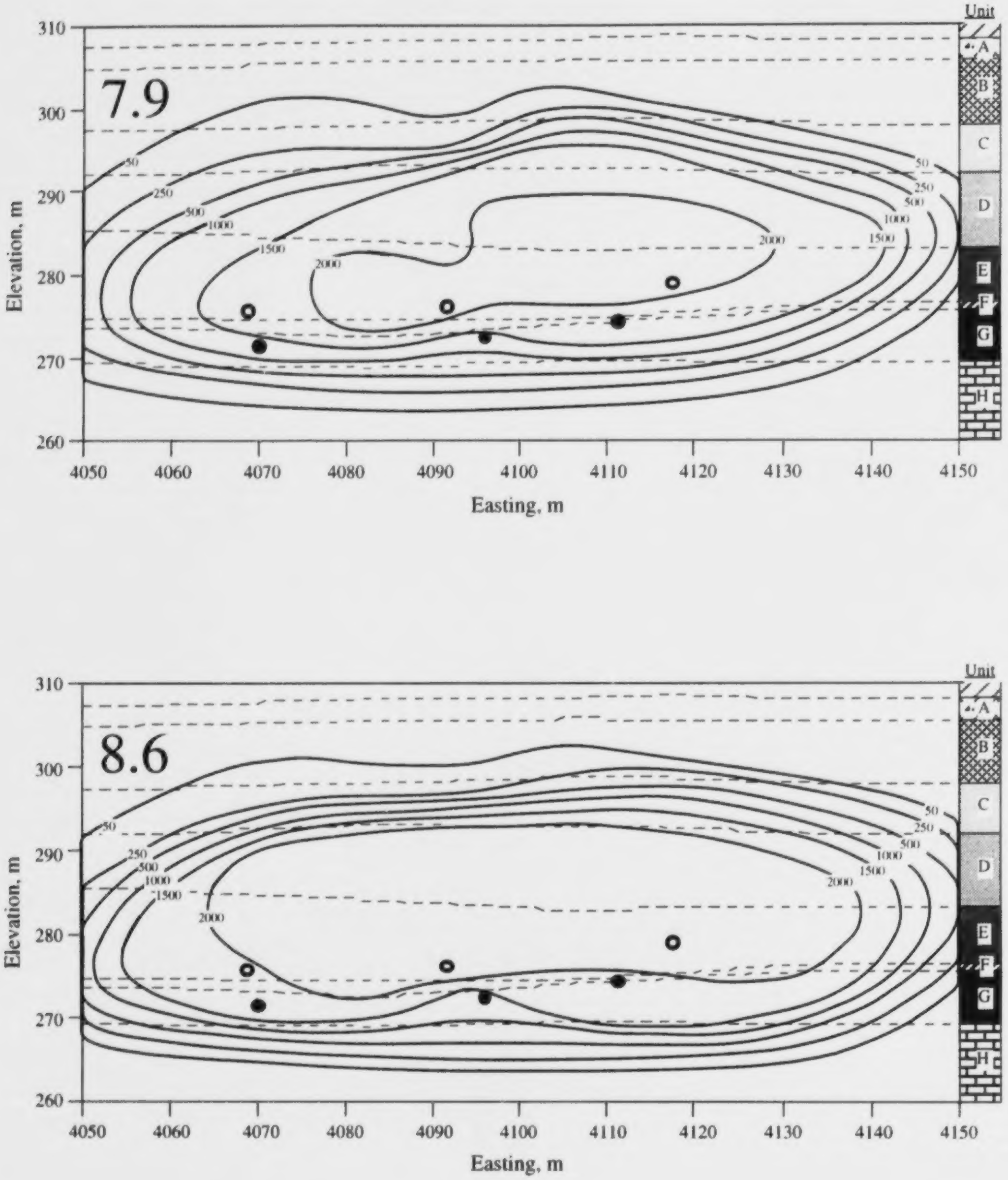

Figure 6.19 Pore Pressure Distribution within Geotechnical Cross Section: Time 7.9 and 8.6

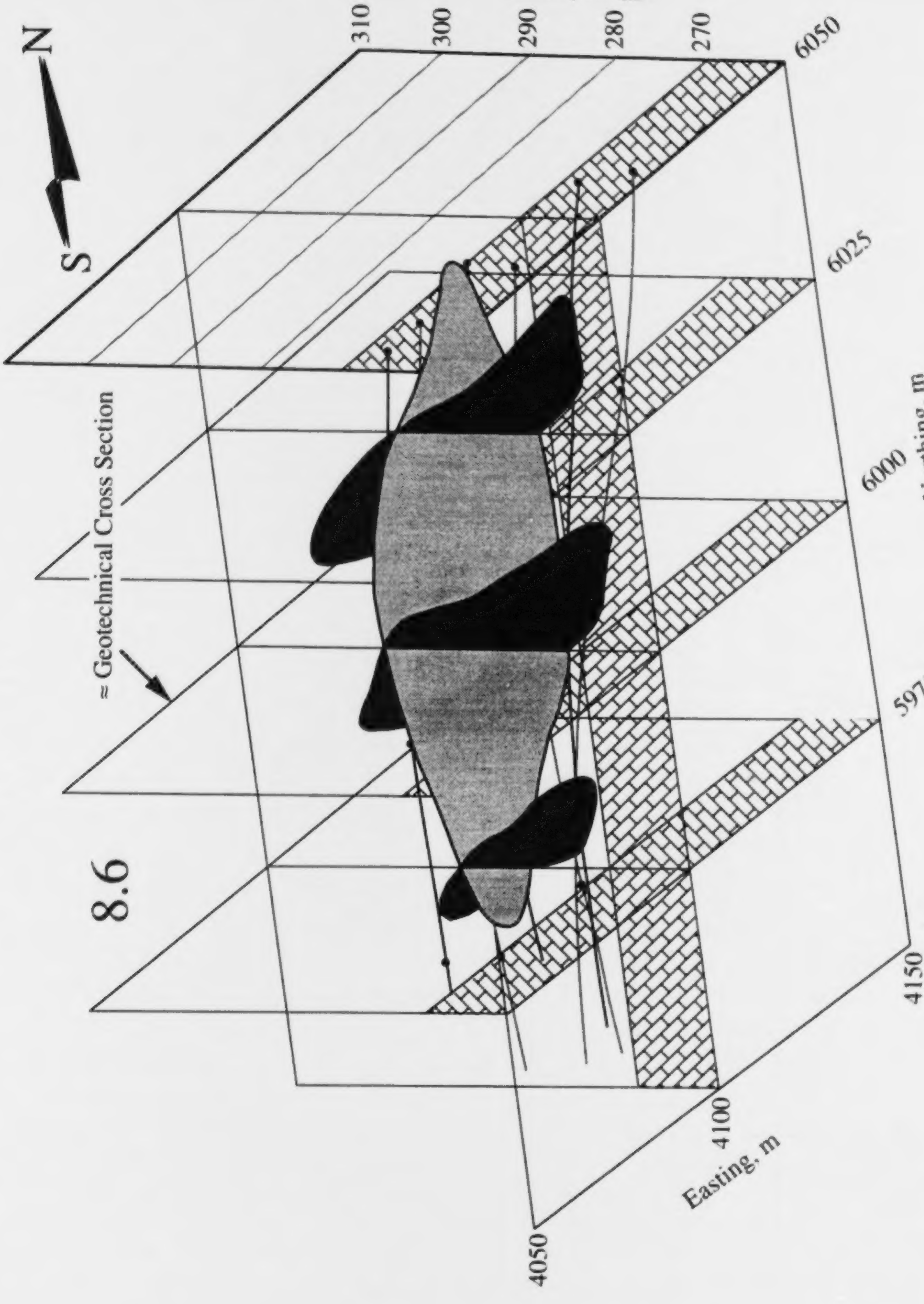
8.6
Geotechnical Cross Section
S
N
Elevation, m
310
300
290
280
270
6050
6025
6000
5975
5950
Northing, m
4150
4100
4050
Easting, m

Figure 6.20 Three Dimensional Representation of Steam Chamber at Time 8.6

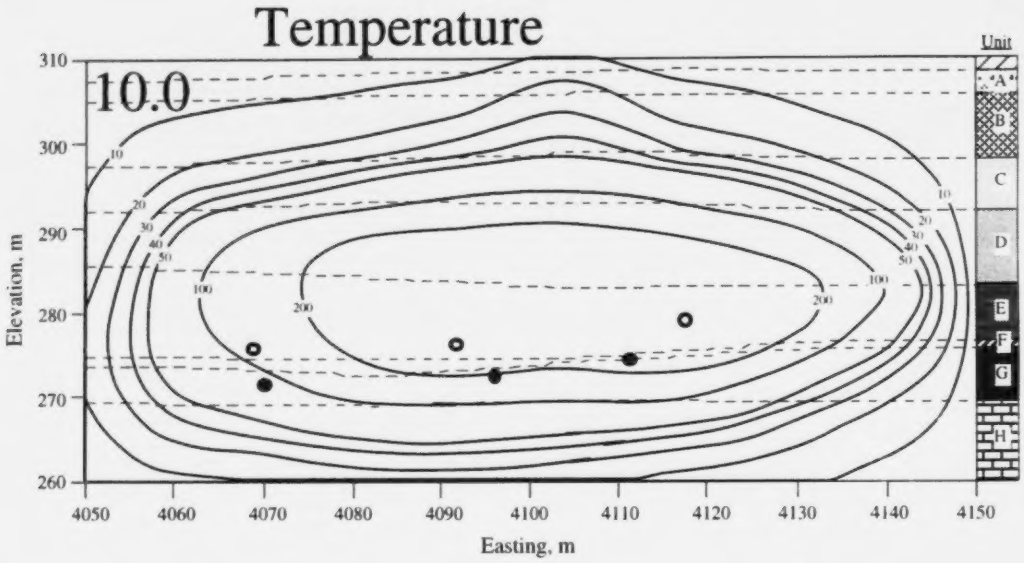

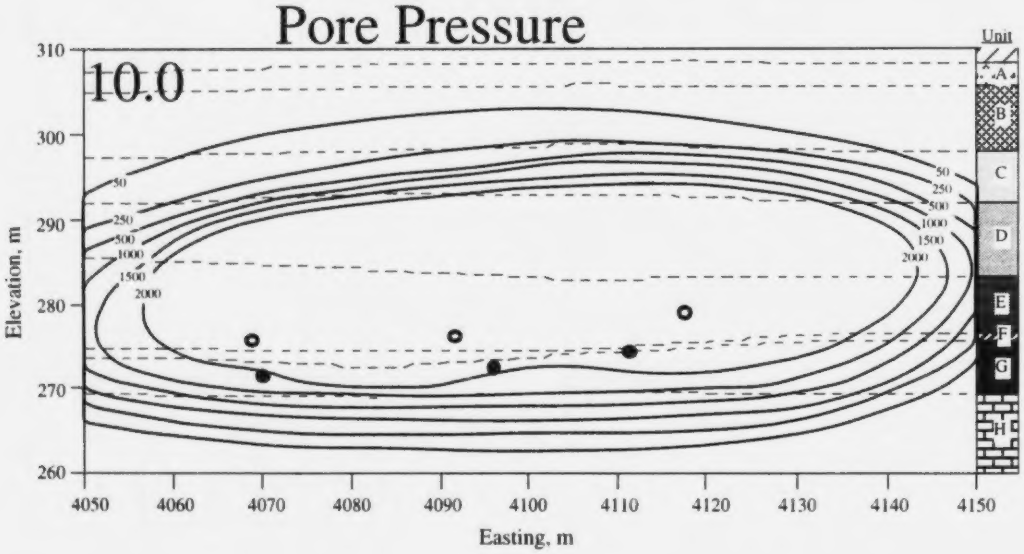

Figure 6.21 Temperature and Pore Pressure Distribution within Geotechnical Cross Section for Time 10.0

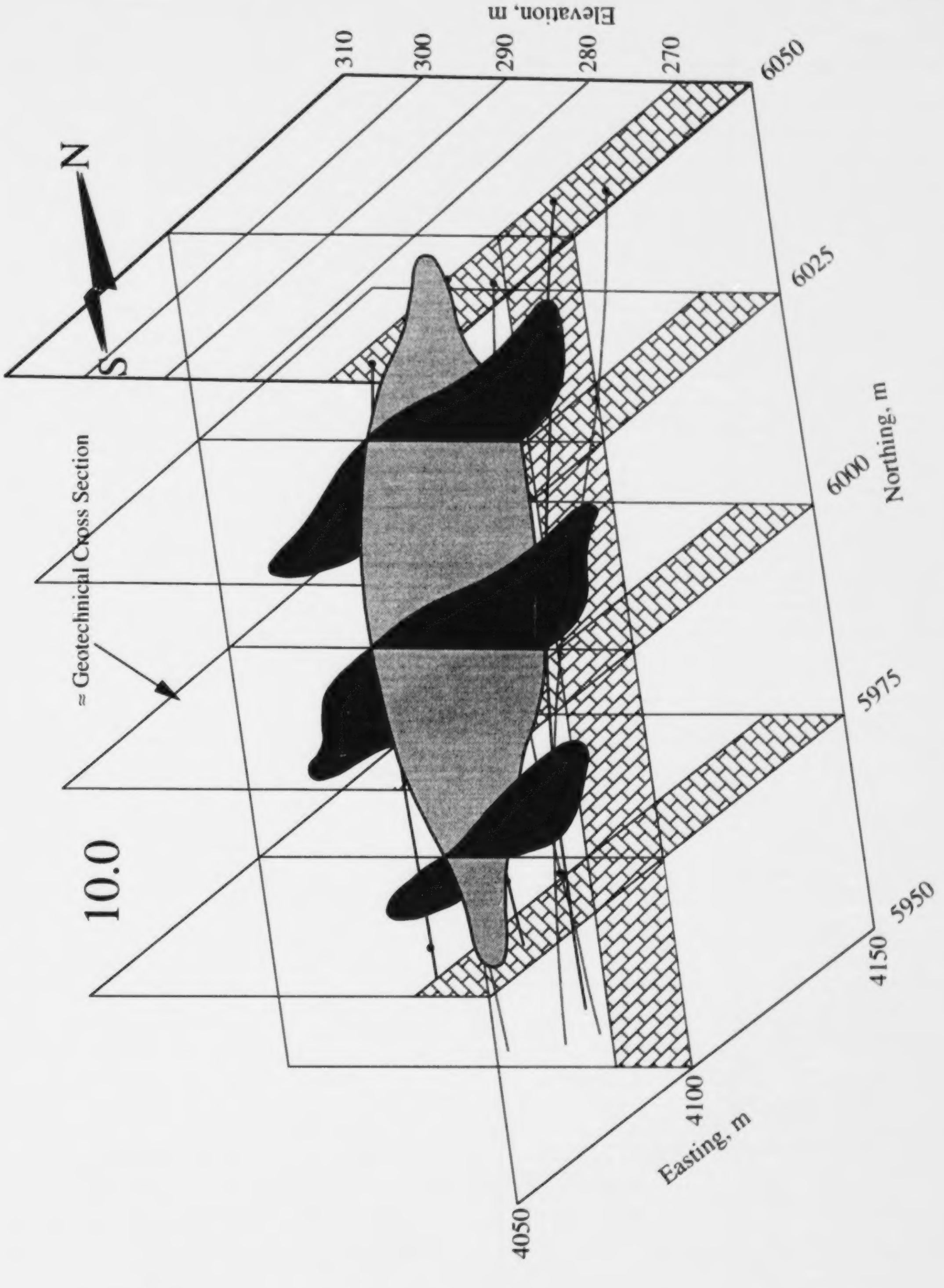
10.0
= Geotechnical Cross Section
N
S
Elevation, m
310
300
290
280
270
6050
6025
6000
5975
5950
Northing, m
4150
4100
4050
Easting, m

Figure 6.22 Three Dimensional Representation of Steam Chamber at Time 10.0

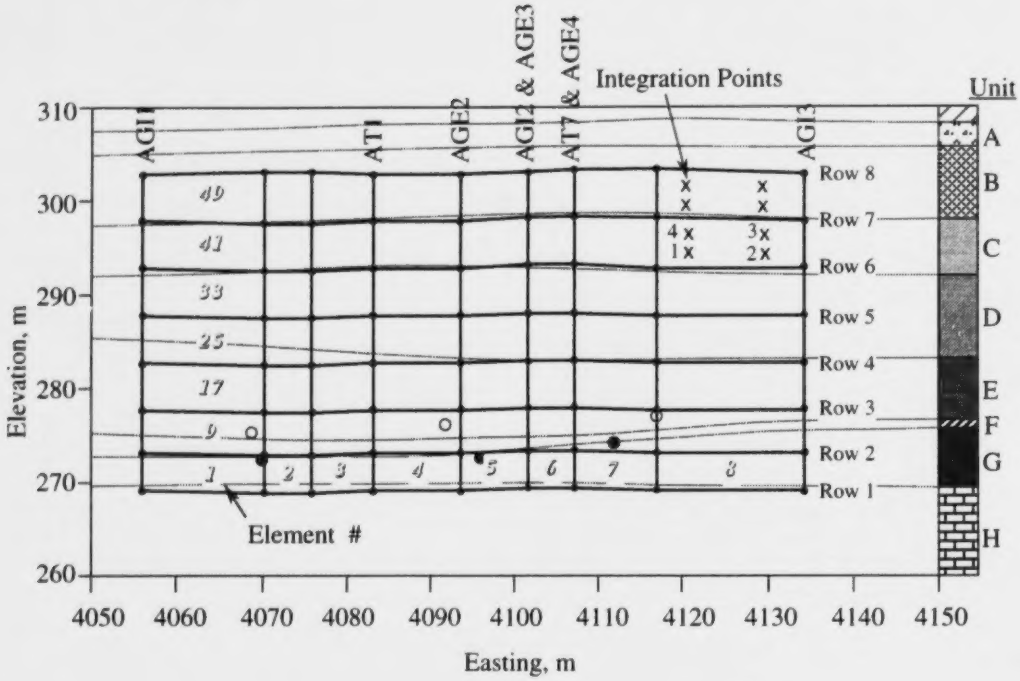
AGI1
AT1
AGE2
AGI2 & AGE3
AT7 & AGE4
AGI3
Integration Points
Unit
A
B
C
D
E
F
G
H
Row 8
Row 7
Row 6
Row 5
Row 4
Row 3
Row 2
Row 1
49
41
33
25
17
9
1
2
3
4
5
6
7
8
4 x
1 x
3 x
2 x
Element #
Elevation, m
310
300
290
280
270
260
4050
4060
4070
4080
4090
4100
4110
4120
4130
4140
4150
Easting, m

Figure 6.23 Mesh Used for Full Strain Field Analysis

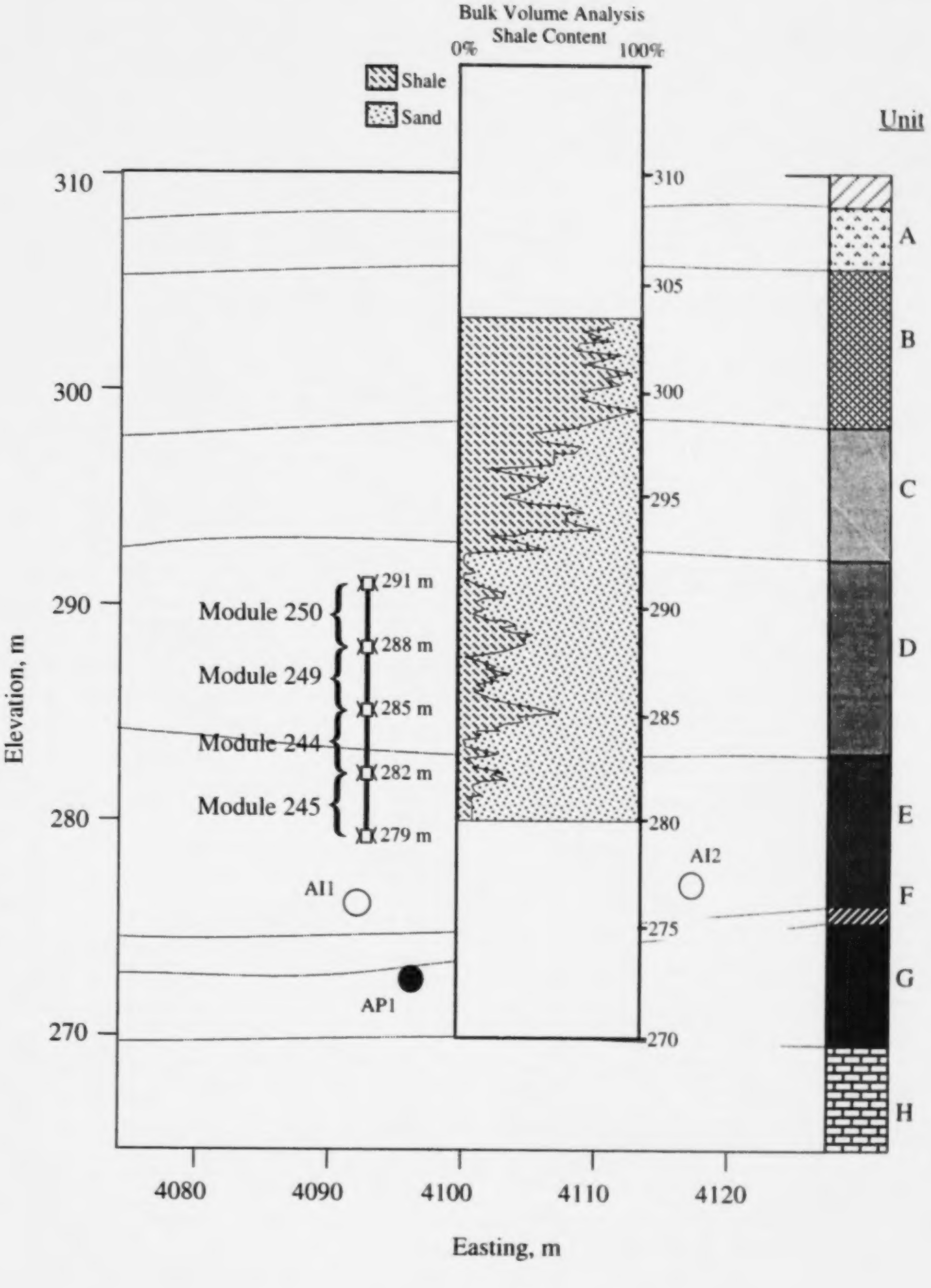
Bulk Volume Analysis
Shale Content
0%
100%
Shale
Sand
Unit
310
300
290
280
270
Elevation, m
310
305
300
295
290
285
280
275
270
291 m
288 m
285 m
282 m
279 m
Module 250
Module 249
Module 244
Module 245
AI1
AI2
AP1
A
B
C
D
E
F
G
H
4080
4090
4100
4110
4120
Easting, m

Figure 6.24 Detailed Position of AGE2 Modules and AGE2 Bulk Volume Analysis

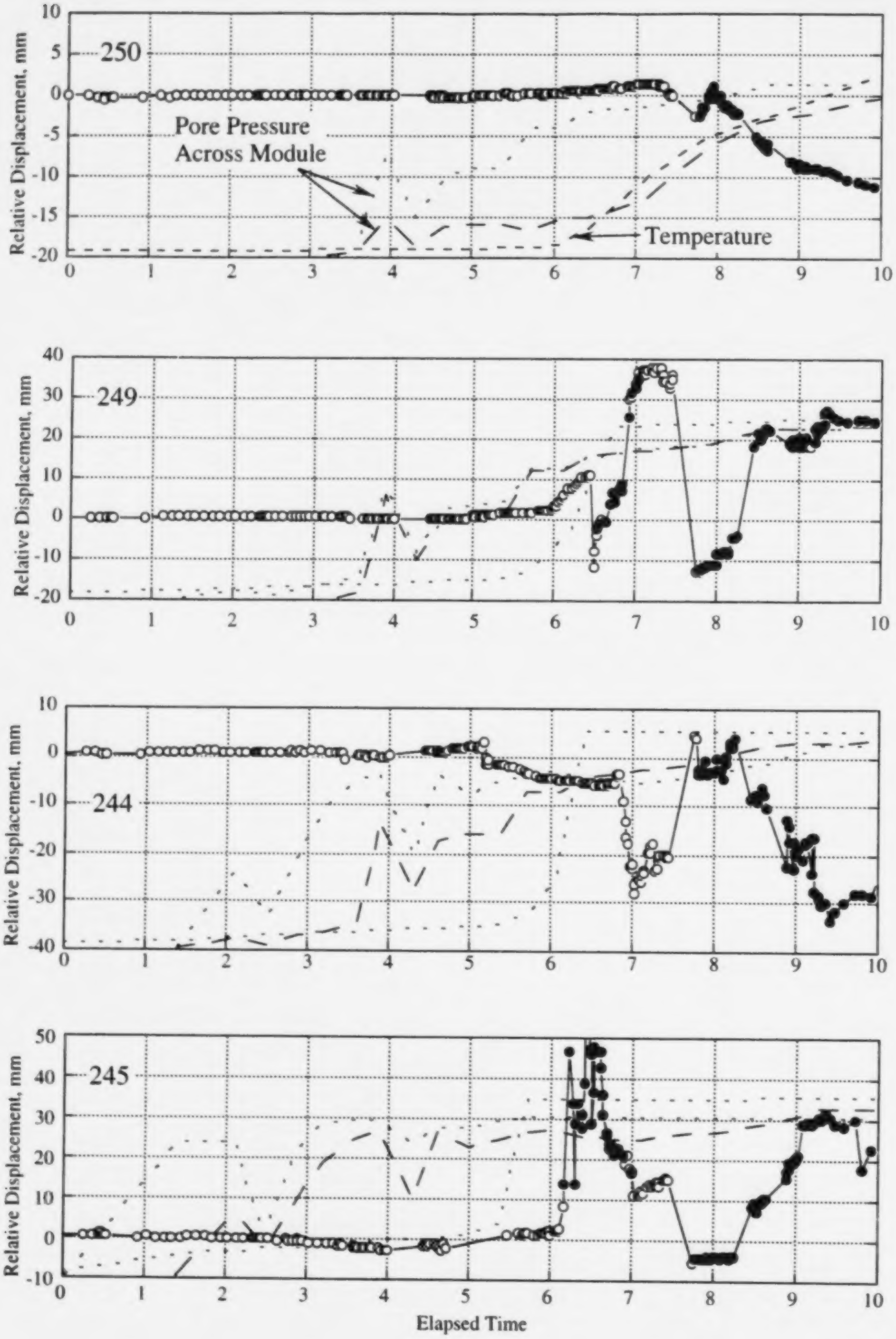

Figure 6.25 Displacement History for Well AGE2

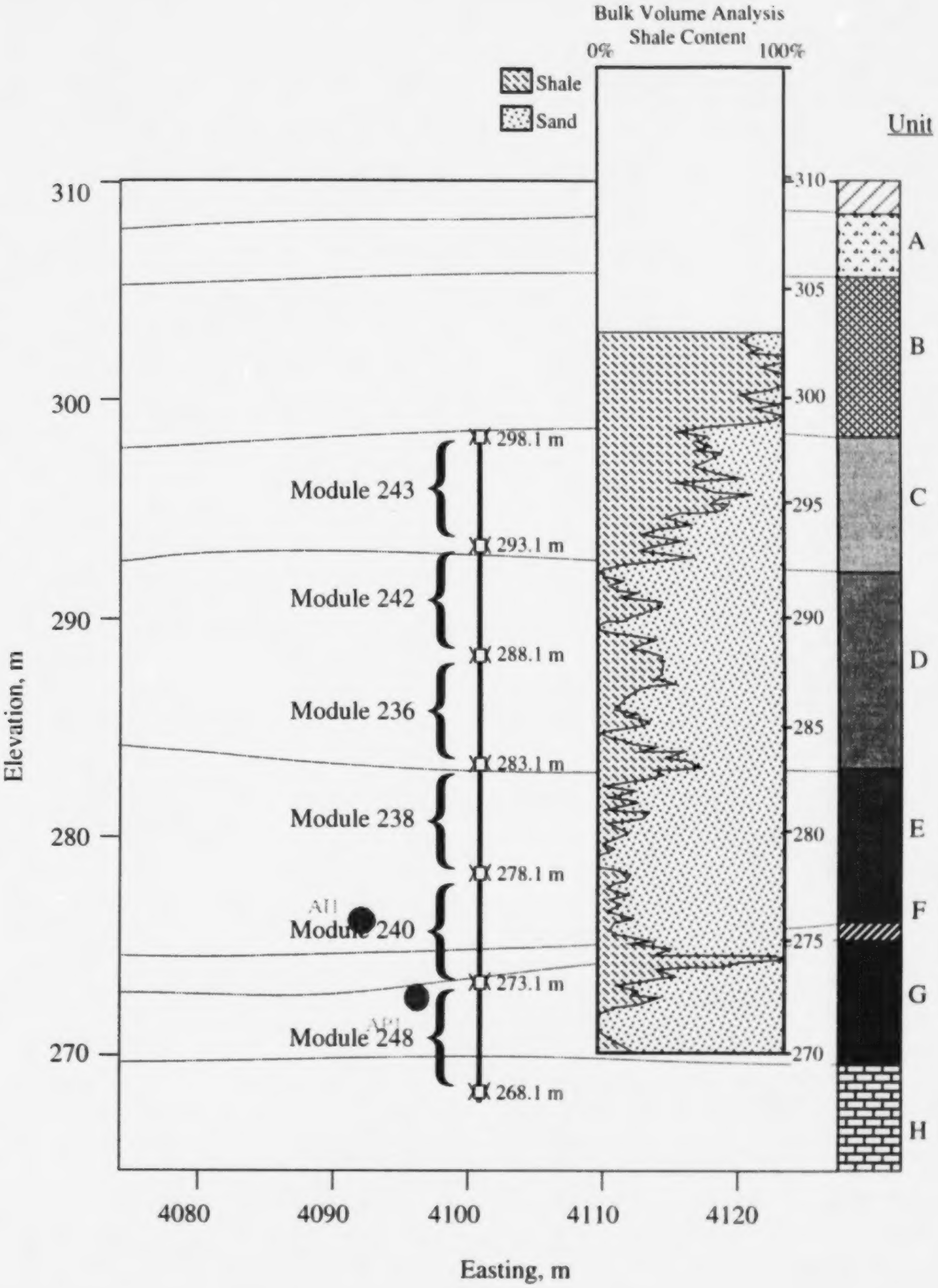

Figure 6.26 Detailed Position of AGE3 Modules and AGE3 Bulk Volume Analysis

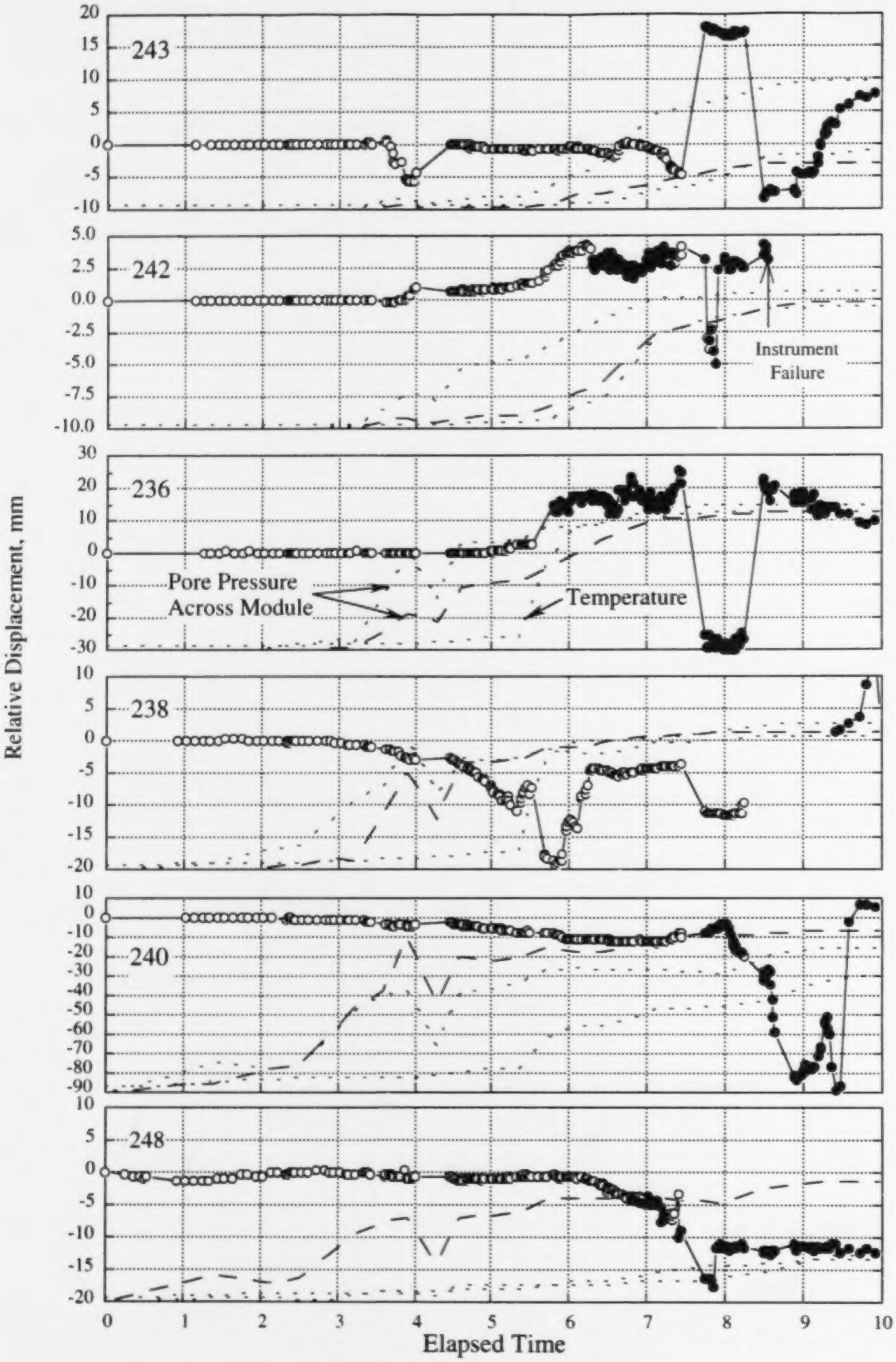

Figure 6.27 Displacement History for Well AGE3

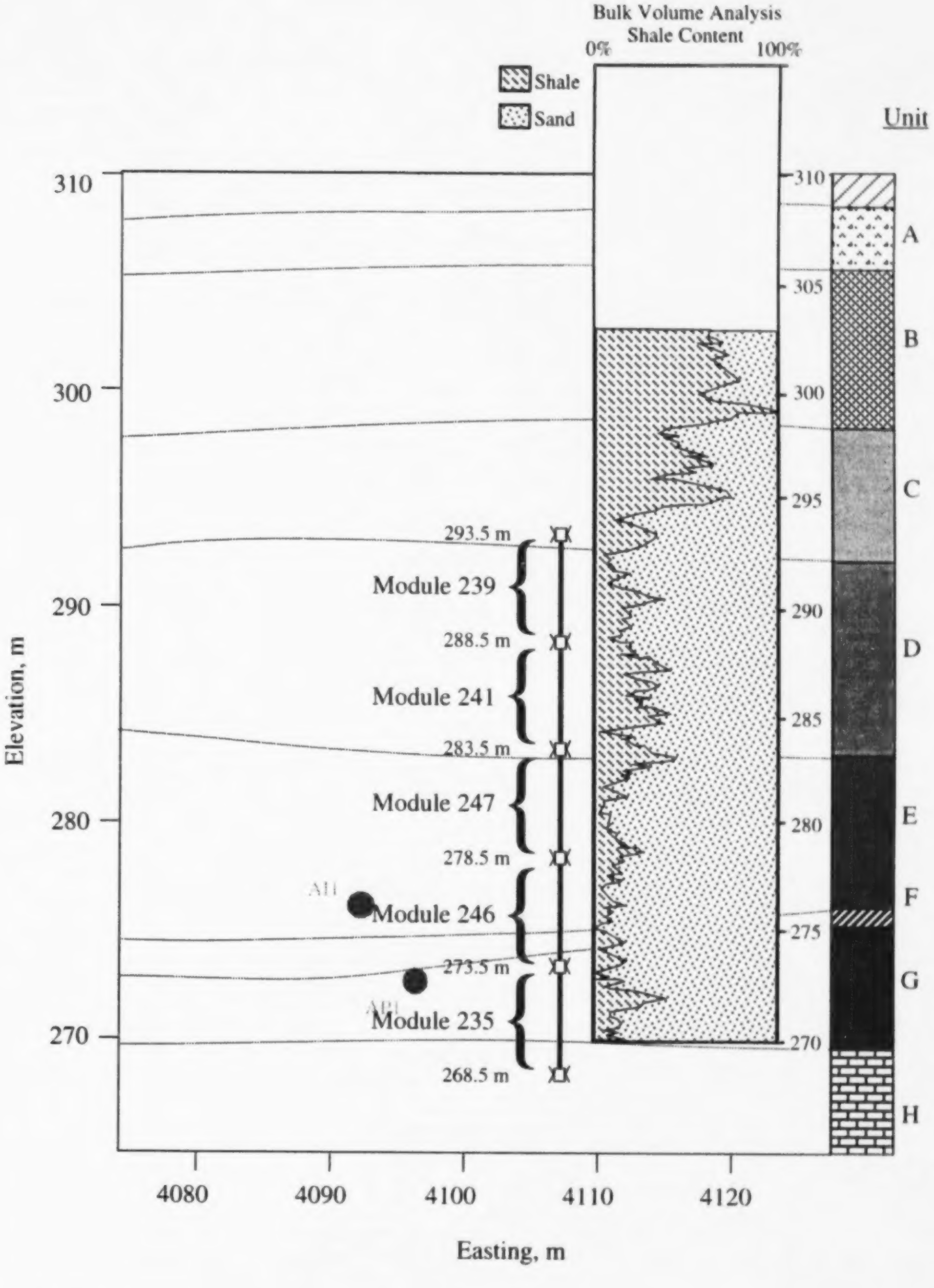

Figure 6.28 Detailed Position of AGE4 Modules and AGE4 Bulk Volume Analysis

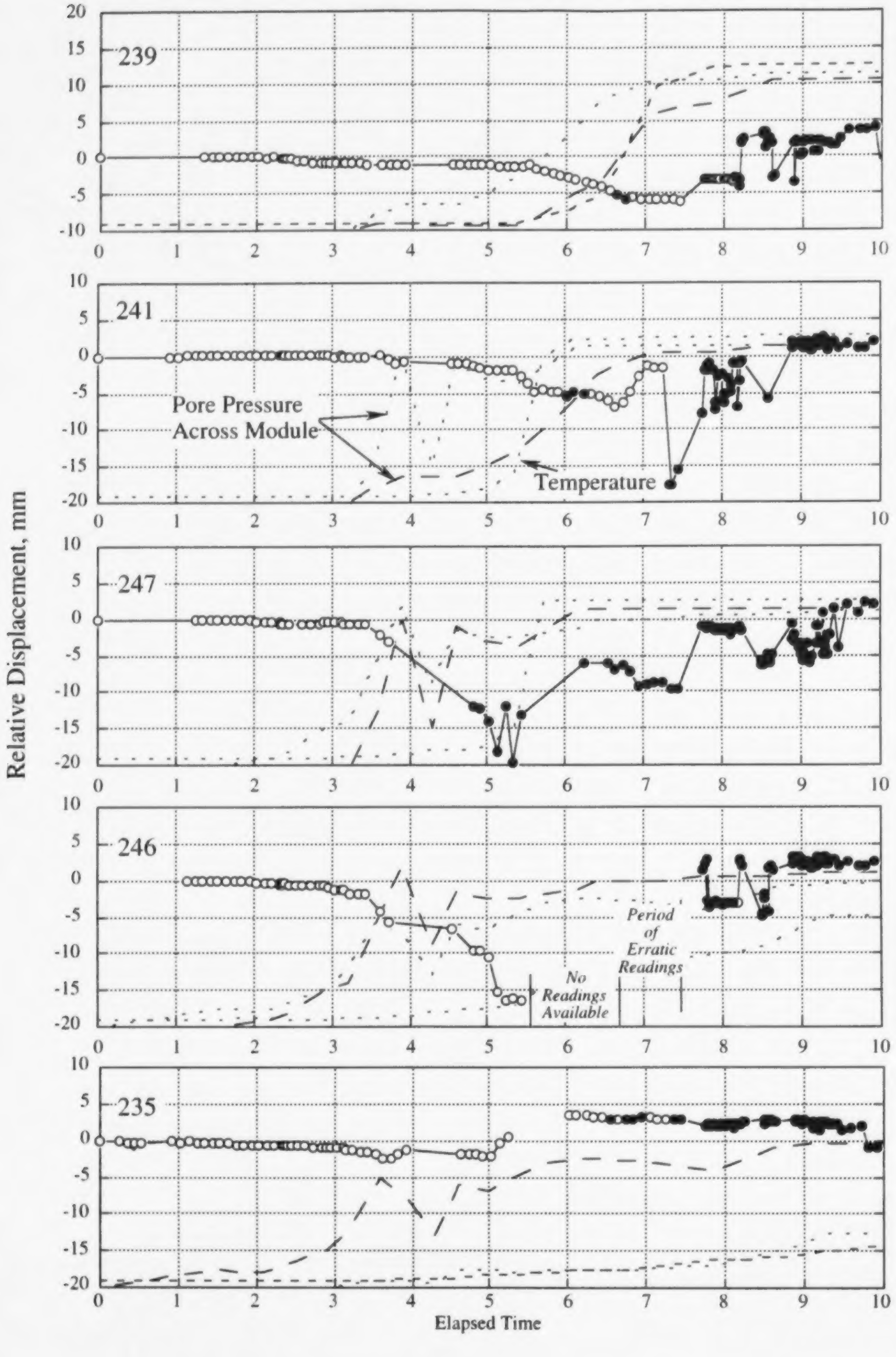

Figure 6.29 Displacement History for Well AGE4

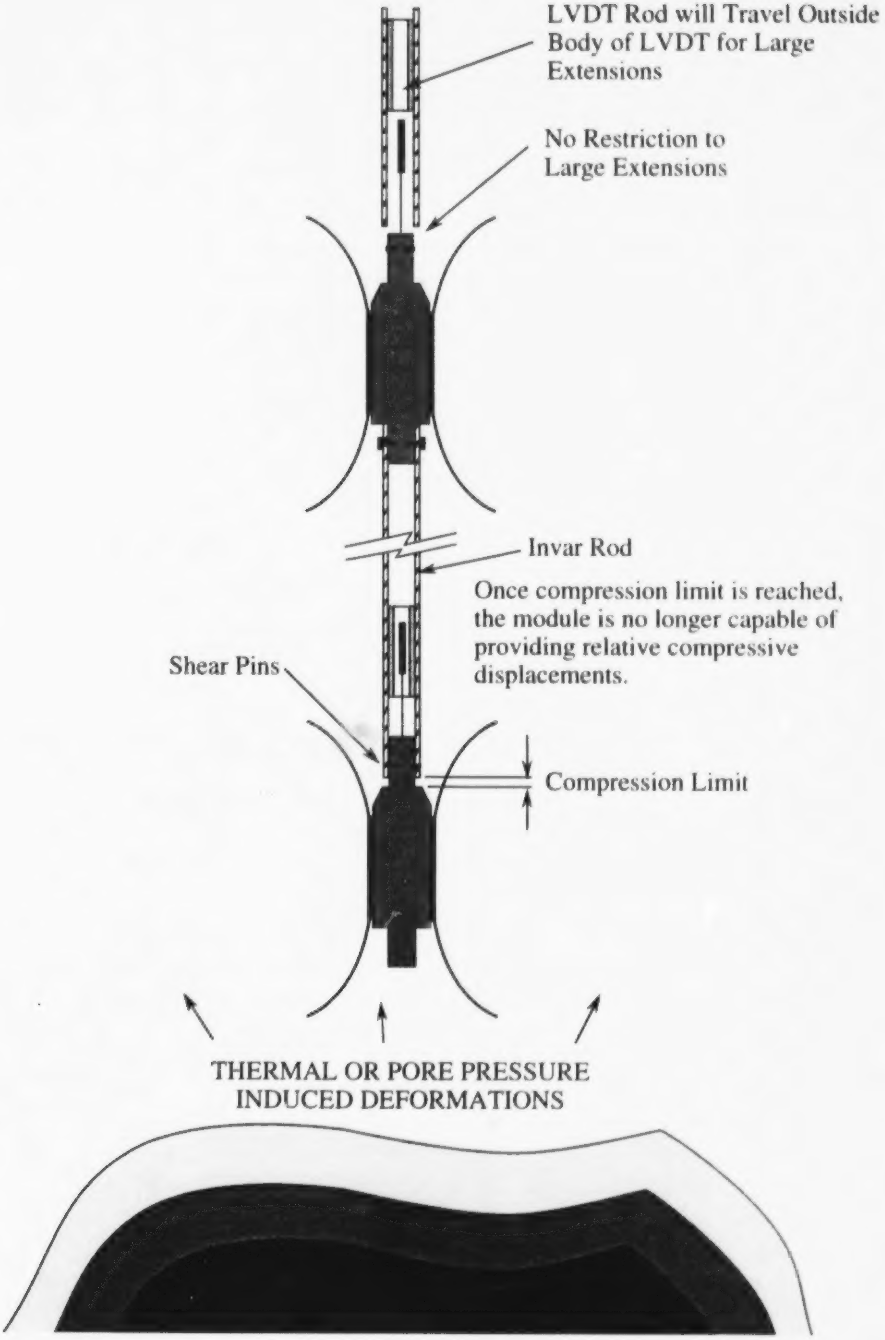
LVDT Rod will Travel Outside Body of LVDT for Large Extensions
No Restriction to Large Extensions
Invar Rod
Once compression limit is reached, the module is no longer capable of providing relative compressive displacements.
Shear Pins
Compression Limit
THERMAL OR PORE PRESSURE INDUCED DEFORMATIONS

Figure 6.30 Displacement Degrees of Freedom for Bof-Ex Extensometer Modules

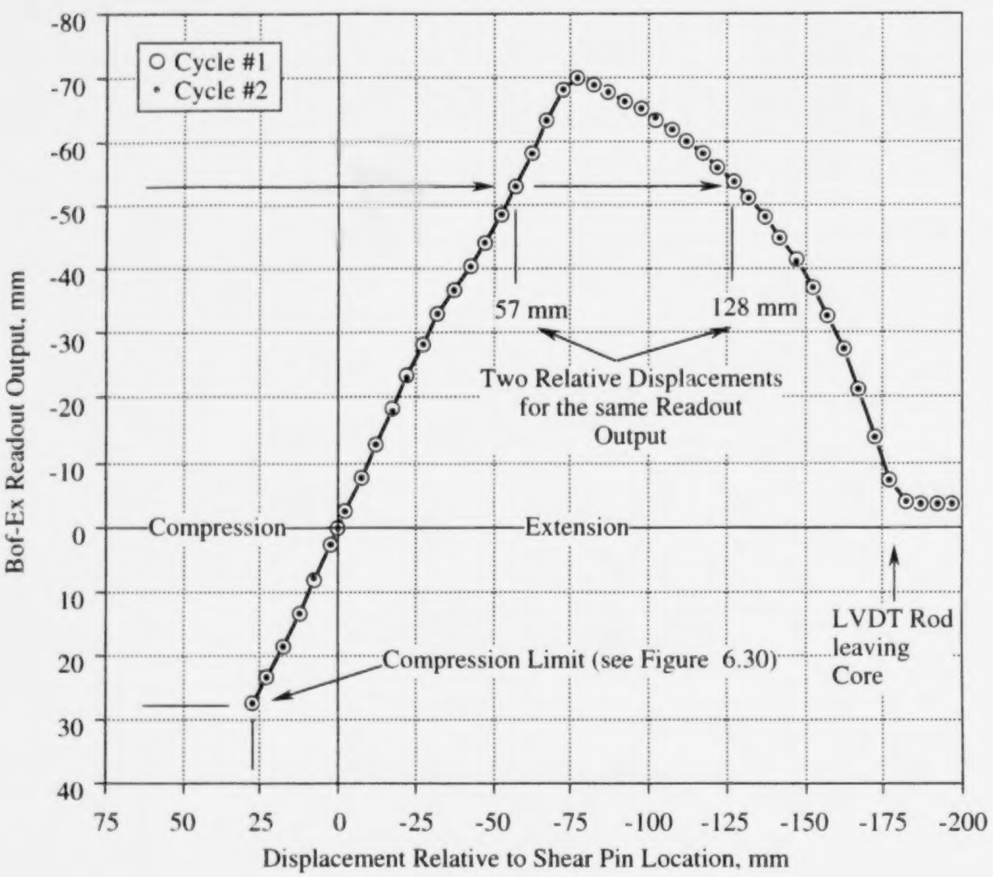

Figure 6.31 Full Displacement Calibration Curve for Bof-Ex LVDT

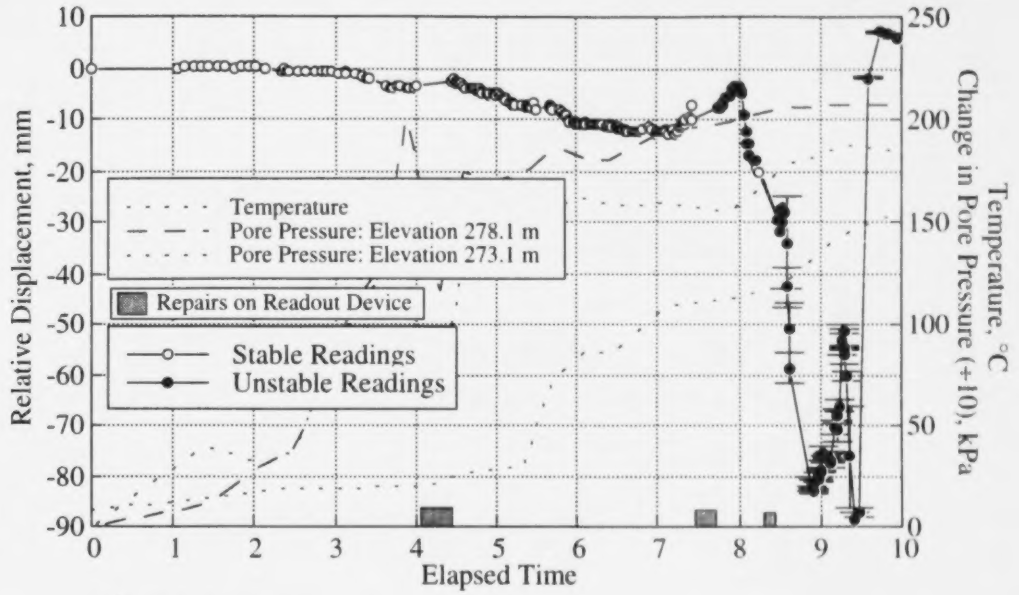

a) ***Original***

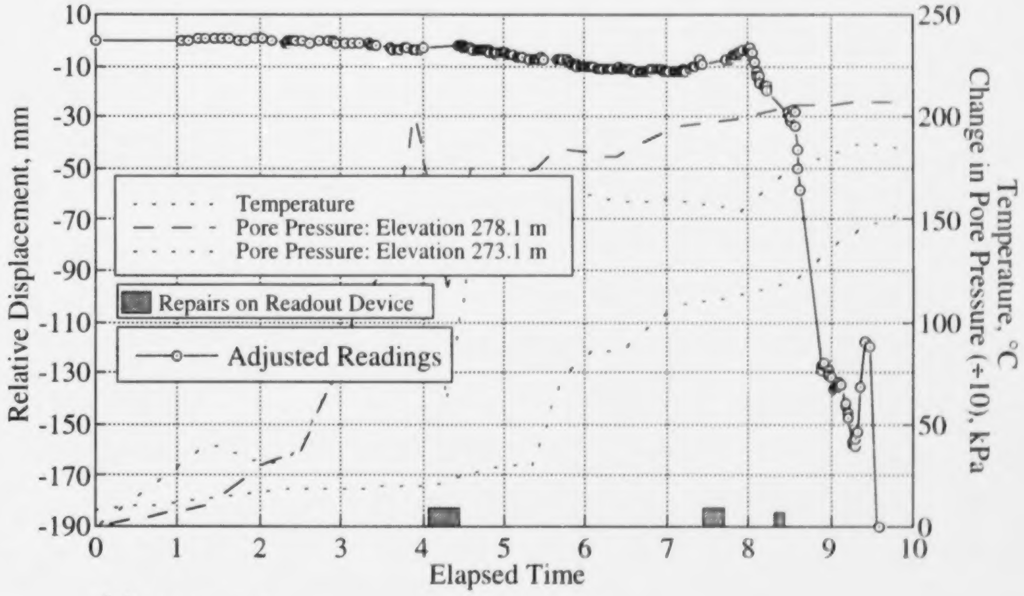

b) ***Adjusted***

Figure 6.32 Corrected Displacement History for Module 240 (AGE3) Based on Full Displacement Calibration Curve

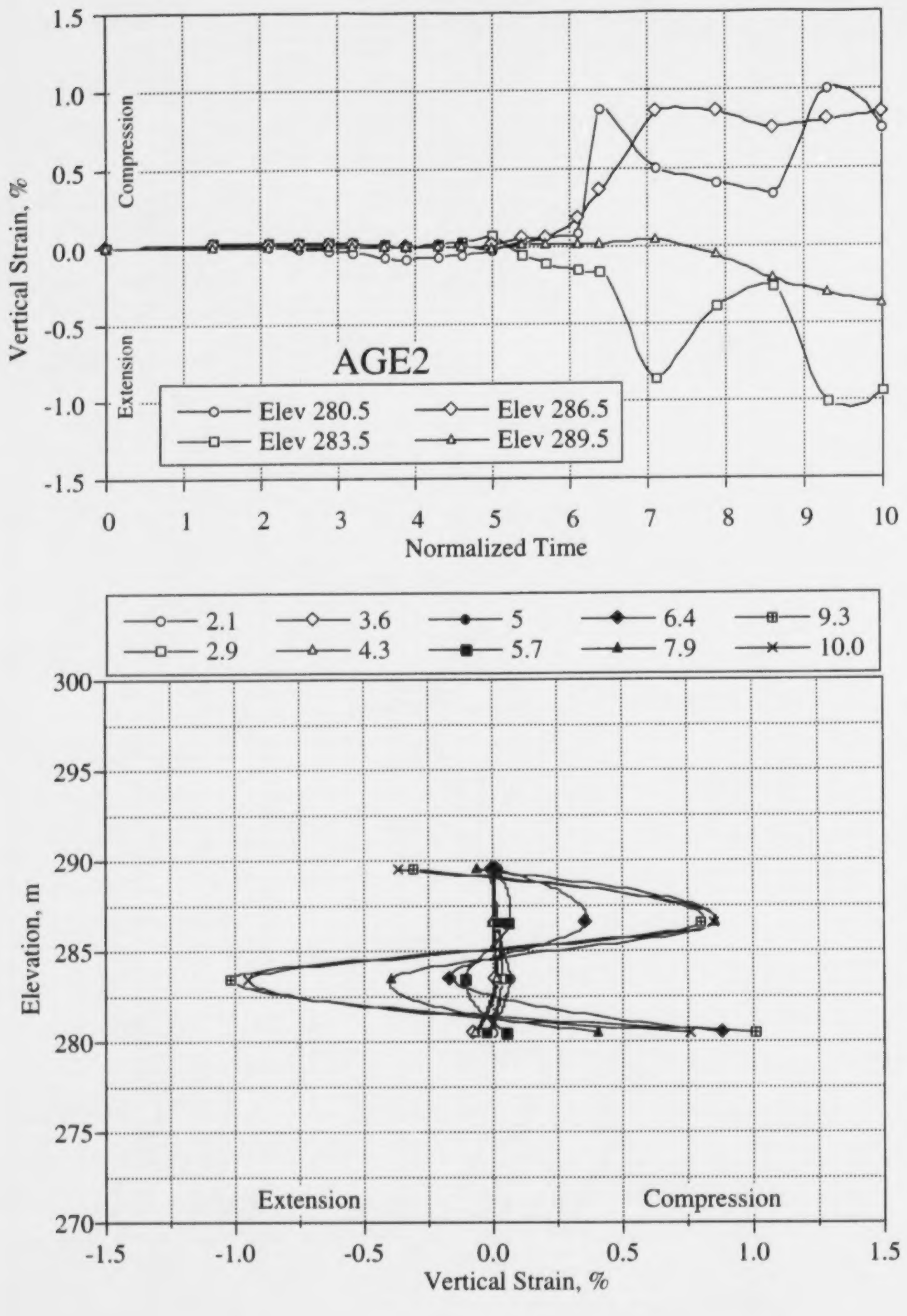

Figure 6.33 Vertical Strain History for AGE2

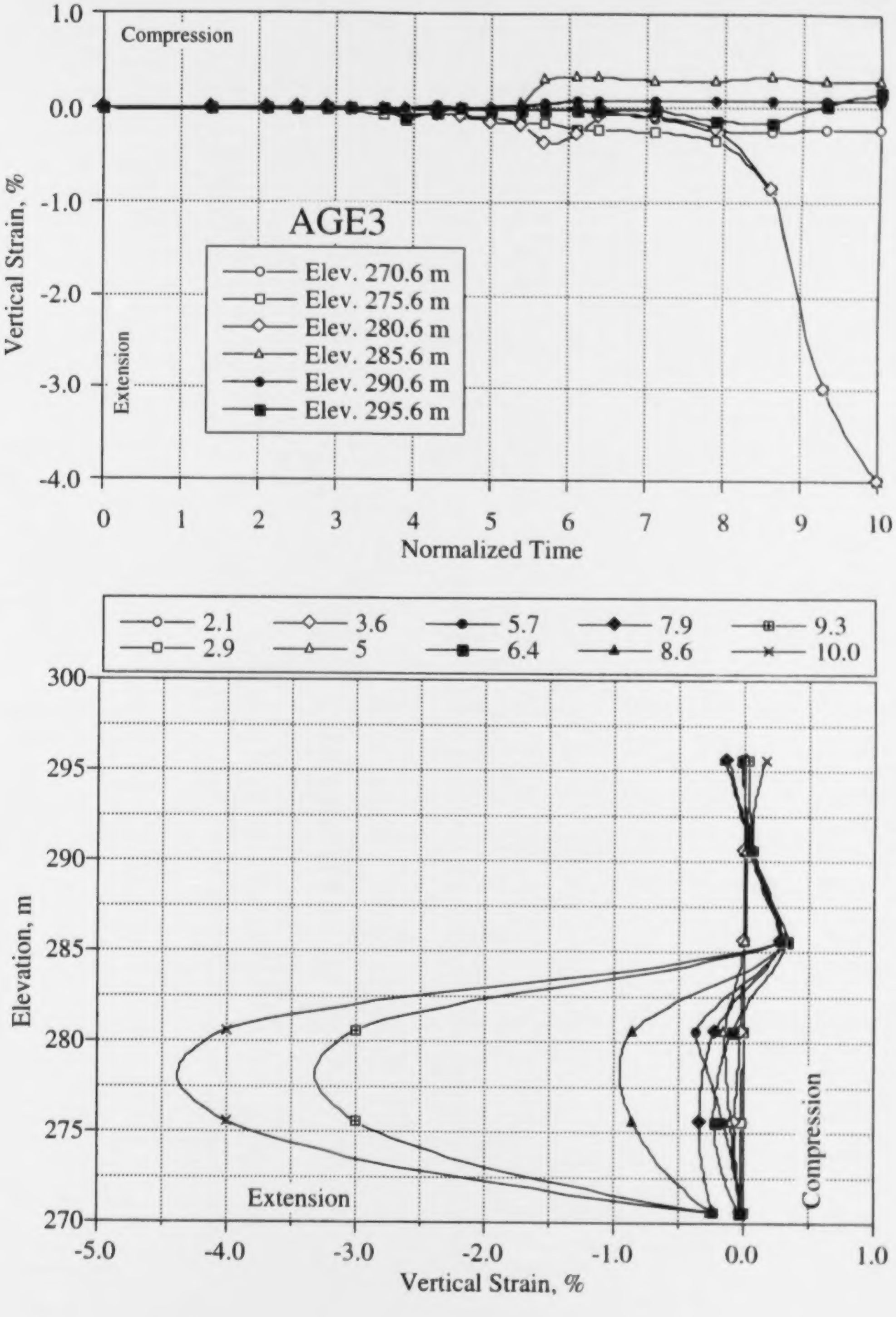

Figure 6.34 Vertical Strain History for AGE3

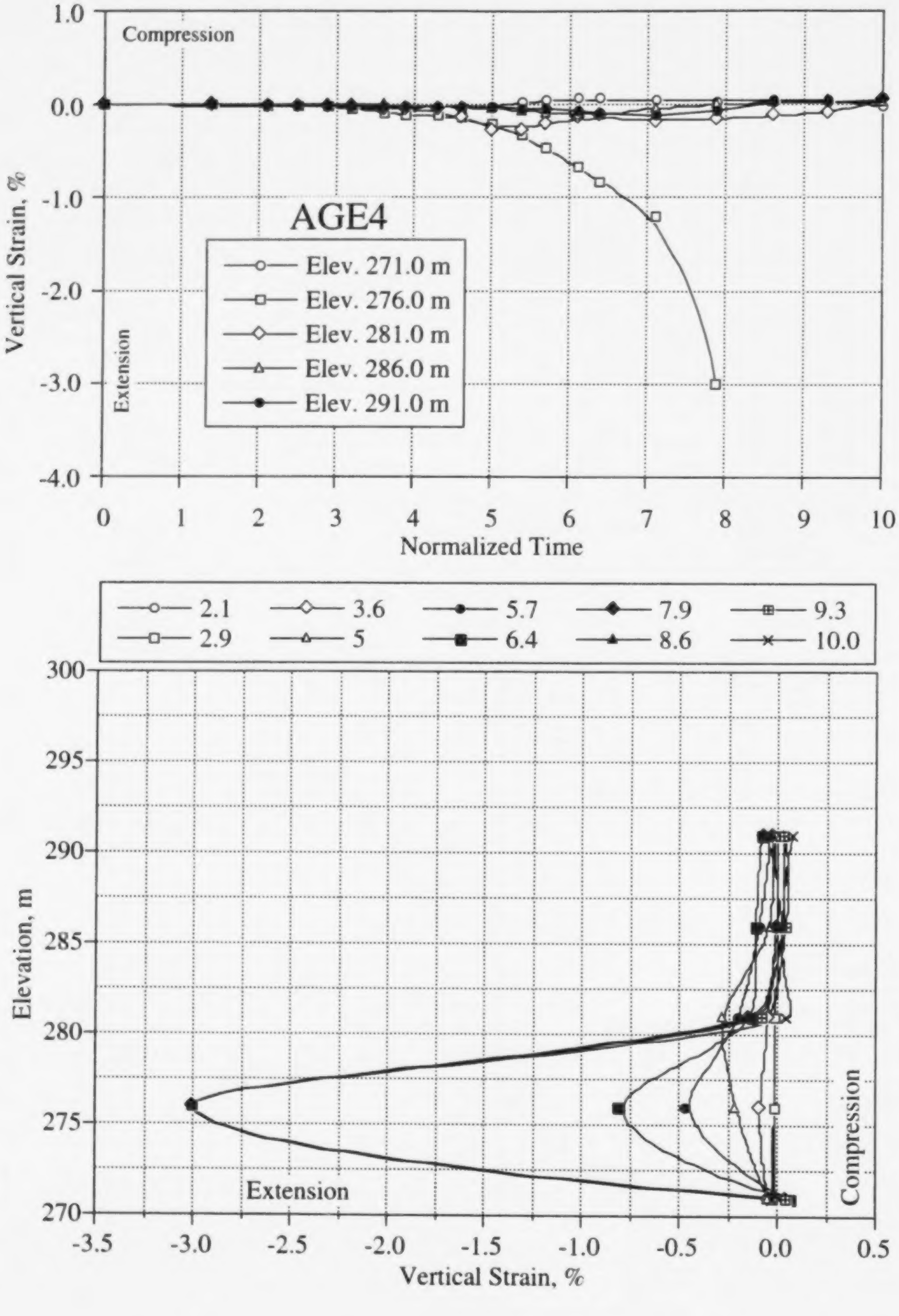

Figure 6.35 Vertical Strain History for AGE4

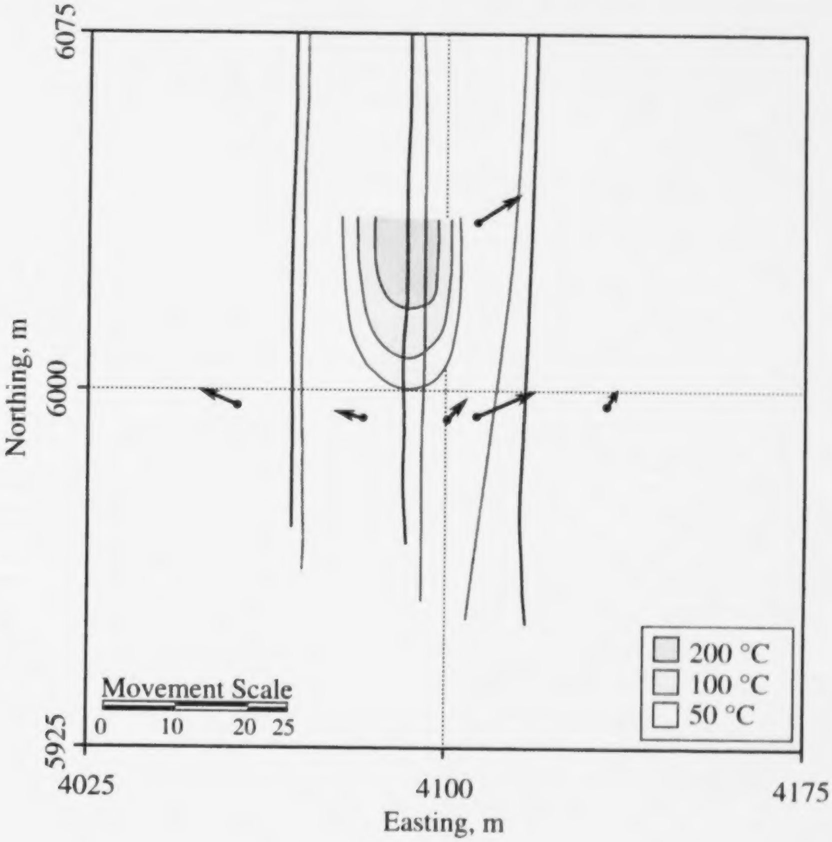

Figure 6.36 Plan View of Horizontal Displacement Vectors at Elevation 280 m - Time 4.3

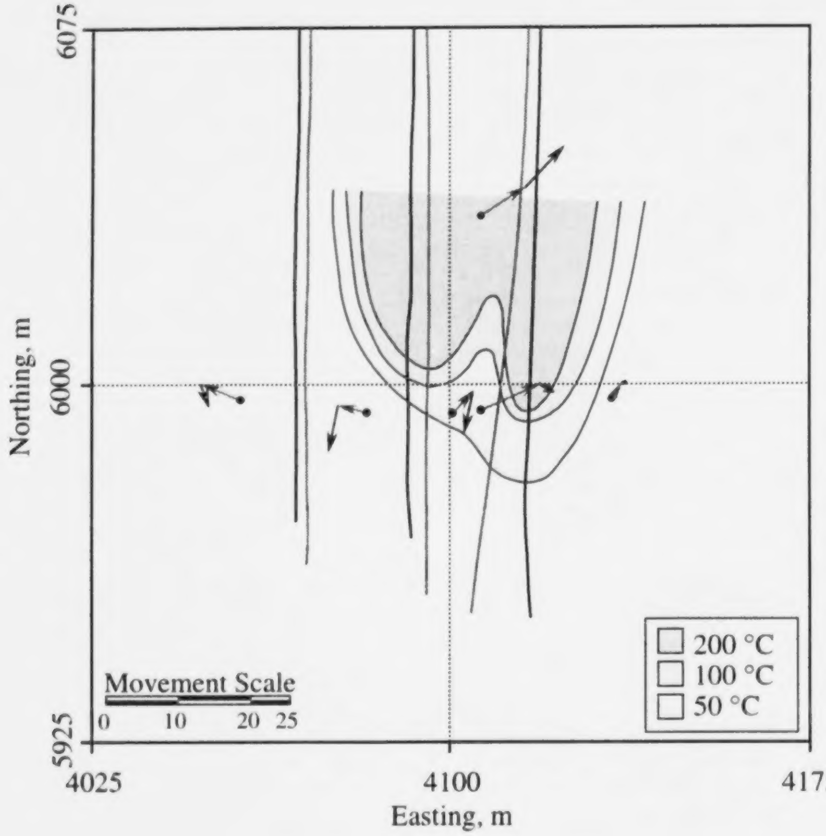

Figure 6.37 Plan View of Horizontal Displacement Vectors at Elevation 280 m - Time 5.5

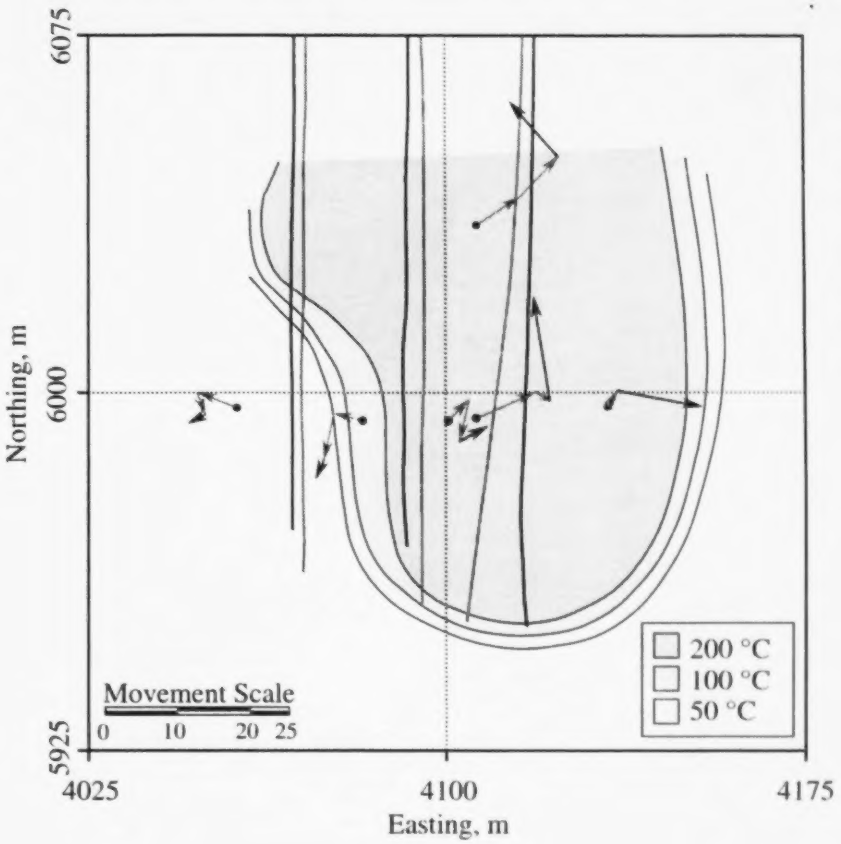

Figure 6.38 Plan View of Horizontal Displacement Vectors at Elevation 280 m - Time 7.9

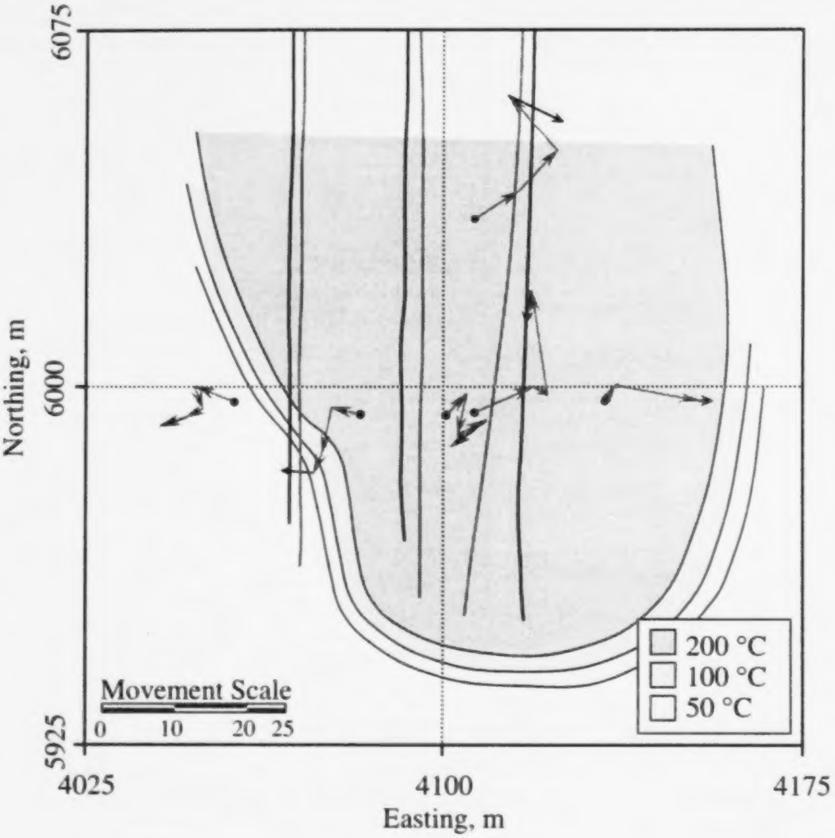

Figure 6.39 Plan View of Horizontal Displacement Vectors at Elevation 280 m - Time 9.7

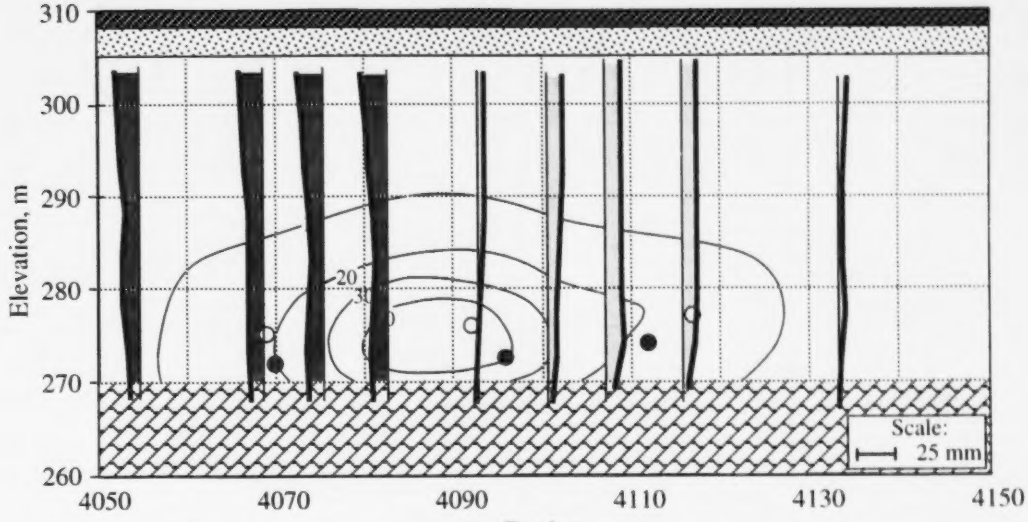

a) with Temperature (contours in °C)

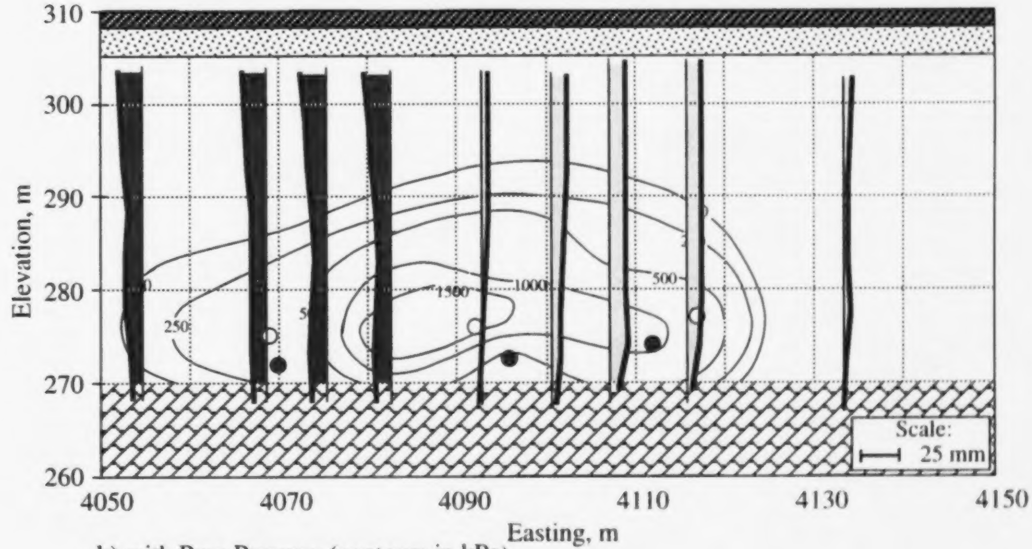

b) with Pore Pressure (contours in kPa)

Figure 6.40 West-East Horizontal Displacements Within Geotechnical Cross Section: Time 4.3

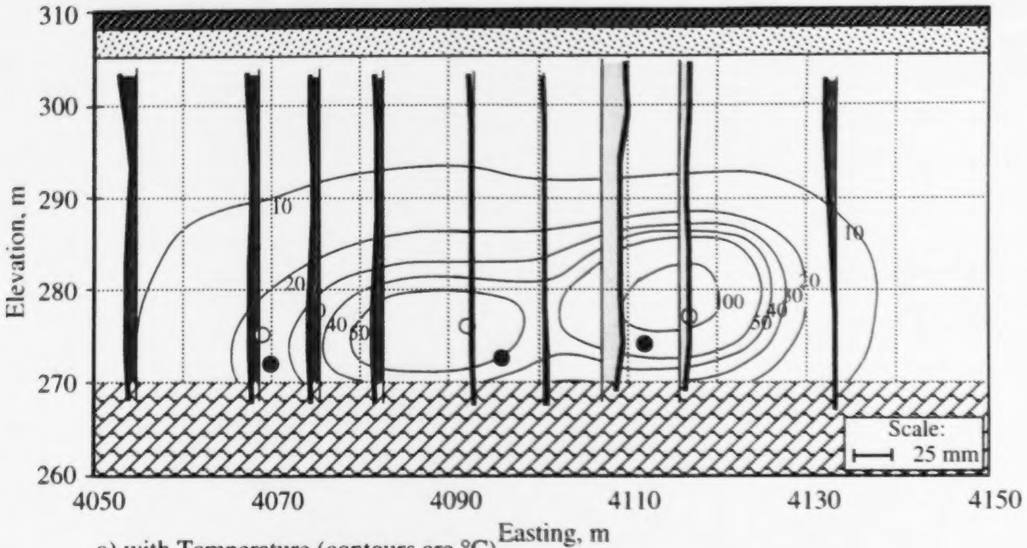

a) with Temperature (contours are °C)

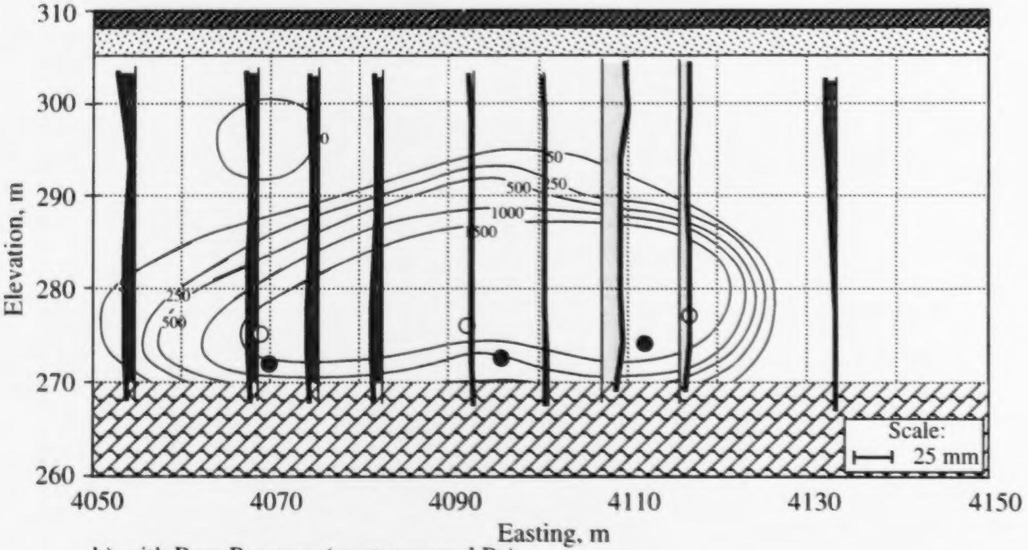

b) with Pore Pressure (contours are kPa)

Figure 6.41 West-East Horizontal Displacements Within Geotechnical Cross Section: Time 5.5

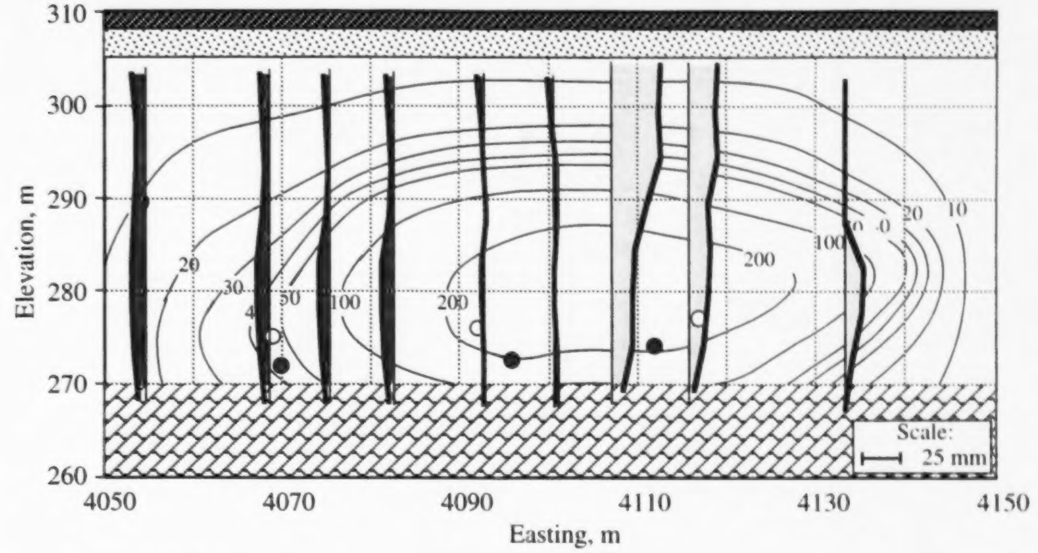

a) with Temperature (contours are °C)

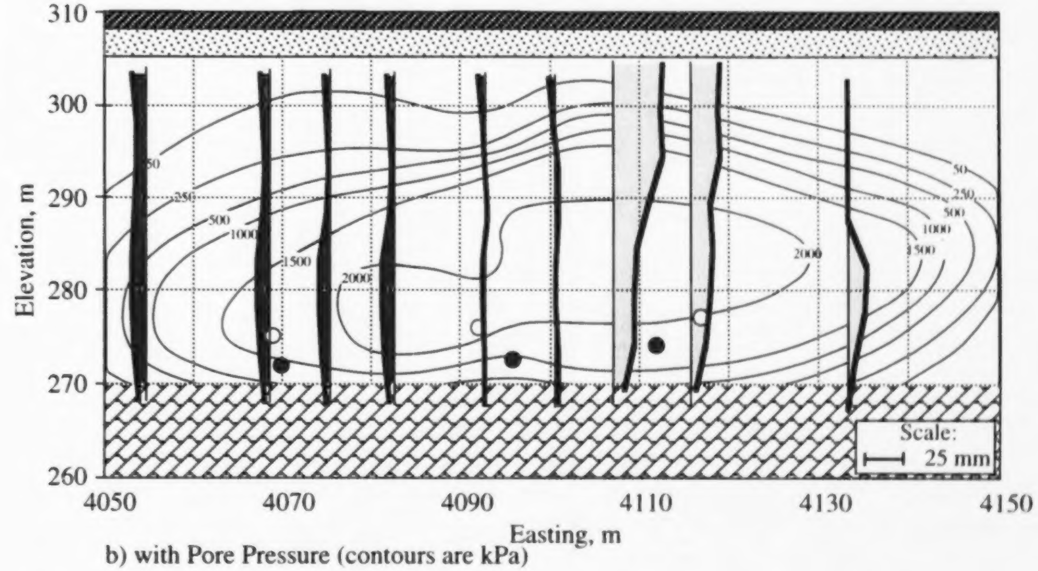

b) with Pore Pressure (contours are kPa)

Figure 6.42 West-East Horizontal Displacements Within Geotechnical Cross Section: Time 7.9

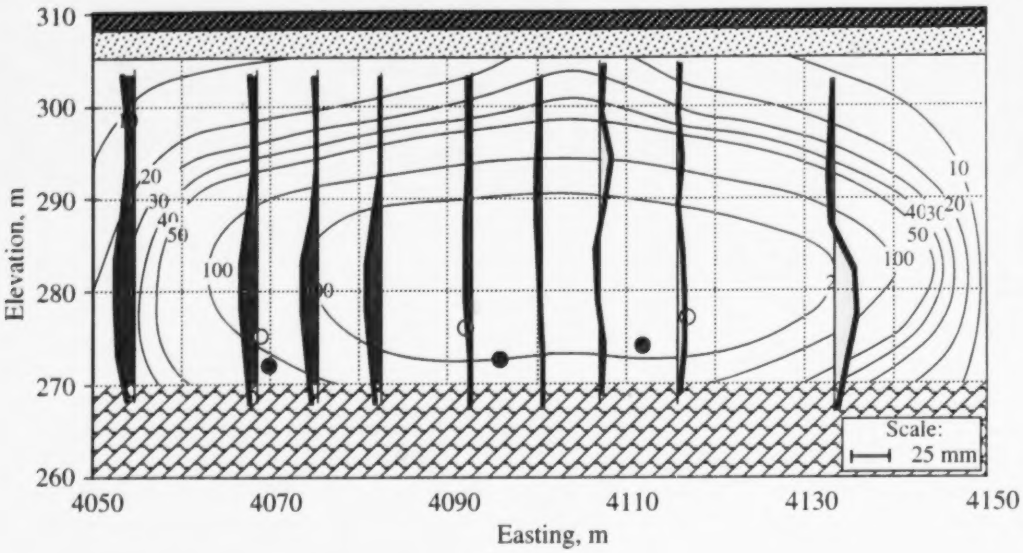

a) with Temperature (contours are °C)

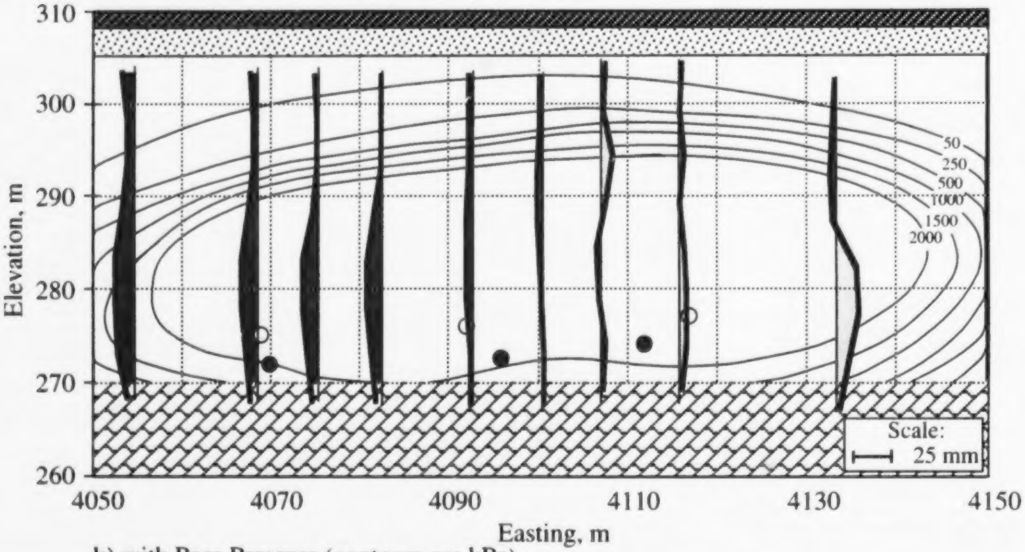

b) with Pore Pressure (contours are kPa)

Figure 6.43 West-East Horizontal Displacements Within Geotechnical Cross Section: Time 9.7

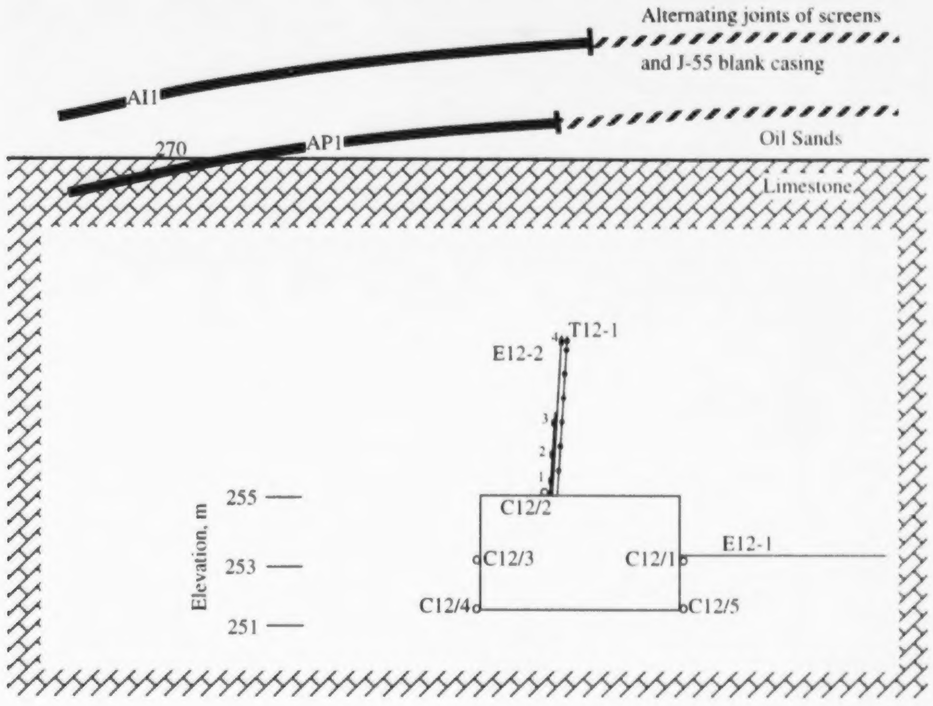
Alternating joints of screens
and J-55 blank casing
AI1
270
AP1
Oil Sands
Limestone
T12-1
E12-2
4
3
2
1
255
253
251
Elevation, m
C12/2
C12/3
C12/1
E12-1
C12/4
C12/5

Extensometer		RTD	
Depth from Collar	Point #	Depth from Collar	Point #
1.026	1	1.6	1
3.026	2	3.1	2
5.026	3	4.67	3
10.026	4	6.15	4
		7.65	5
		9.15	6
		9.62	7

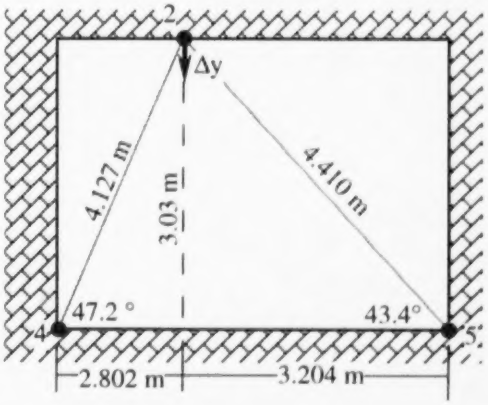
2
Δy
4.127 m
3.03 m
4.410 m
47.2 °
43.4°
4
5
2.802 m
3.204 m

Convergence

Pt. 2 to Pt. 5 $\Delta y = 0.687 * (\text{Convergence from 2 to 5})$

Pt. 2 to Pt. 4 $\Delta y = 0.734 * (\text{Convergence from 2 to 4})$

} Use the Average To Obtain Vertical Displacement of Tunnel Roof

Figure 6.44 Geometry for Roof Extensometer and Convergence Arrays at Station E12-2

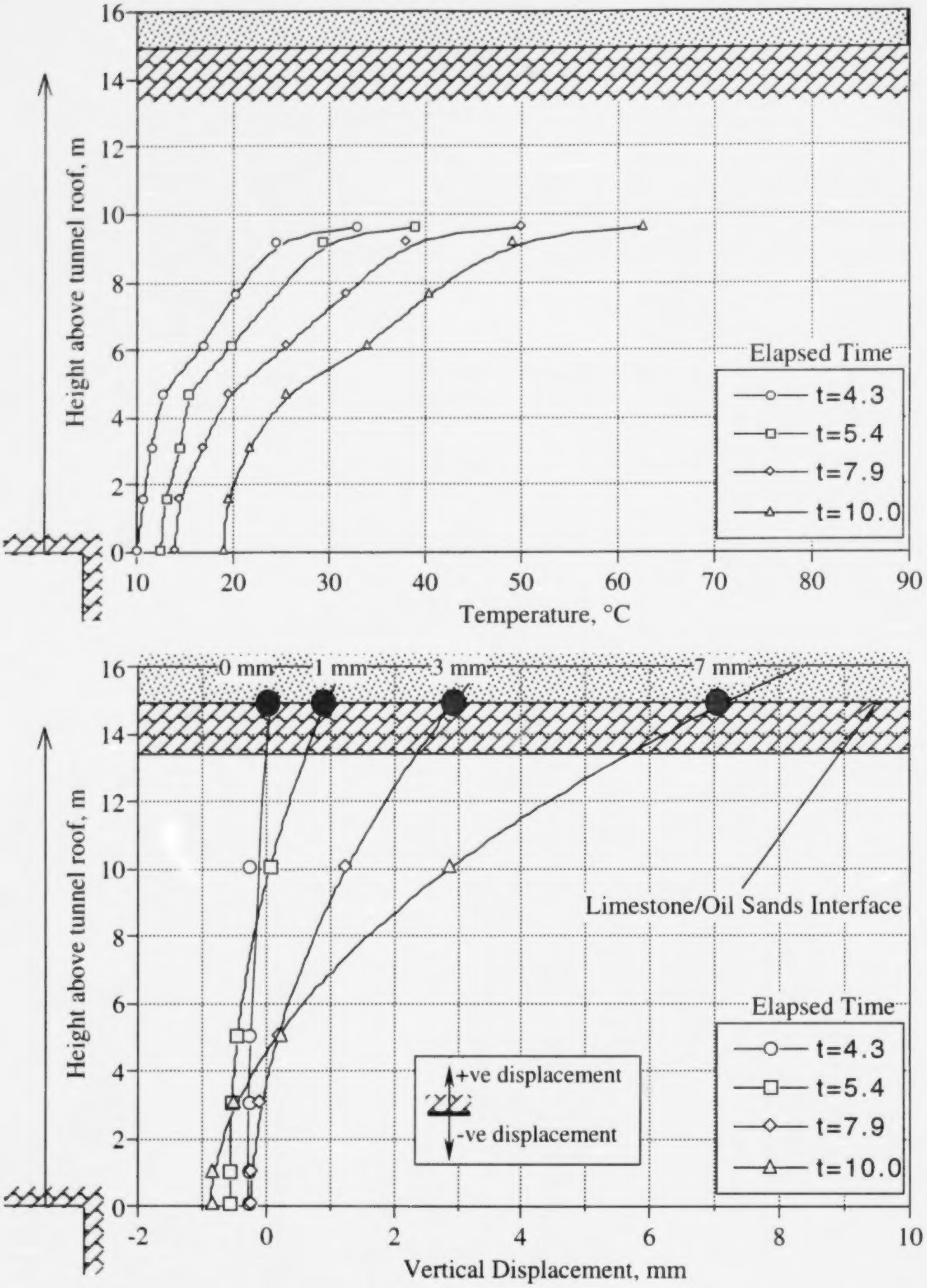

Figure 6.45 Interpolated Displacement History of Oil Sands-Limestone Interface

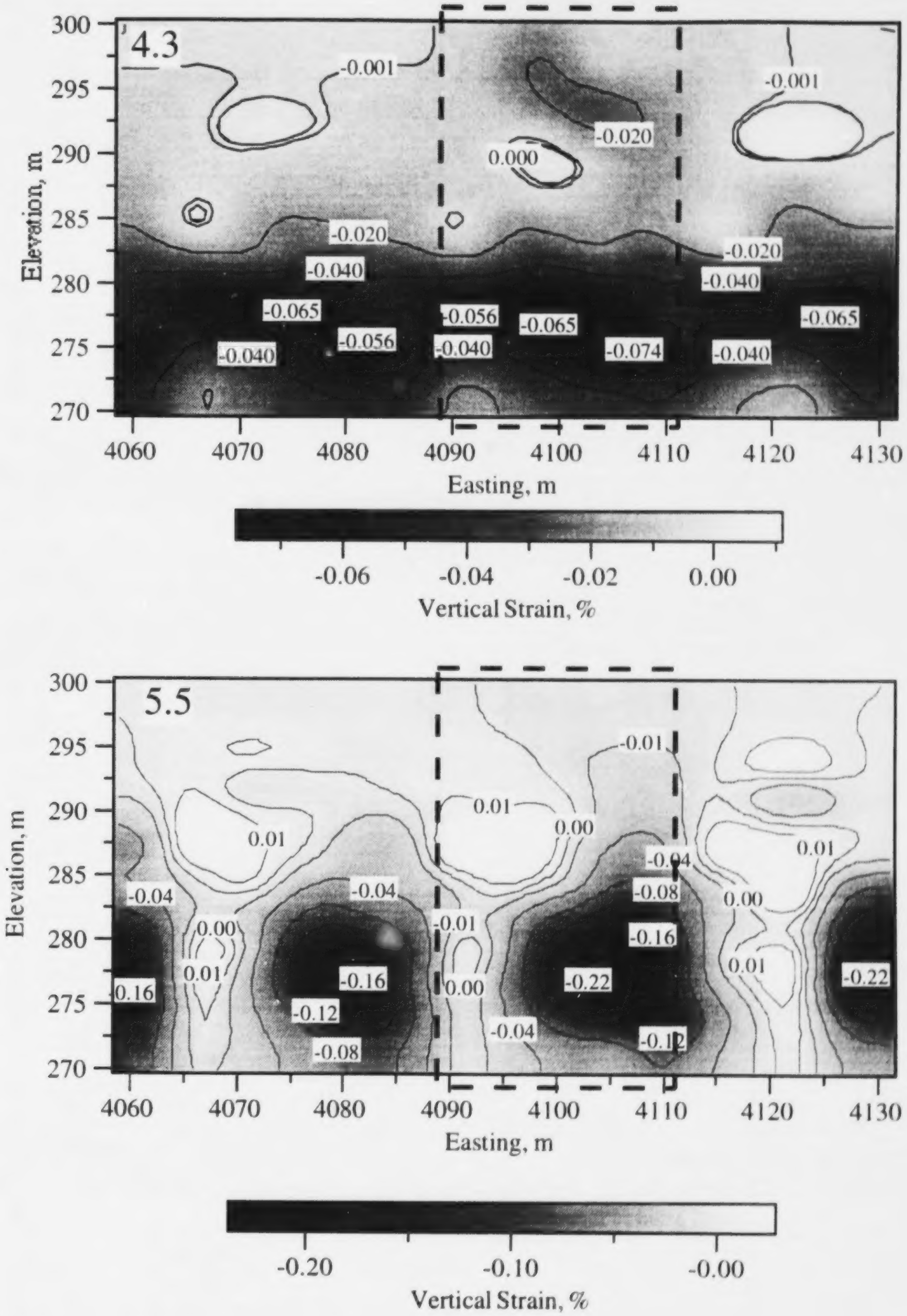

Figure 6.46 Vertical Strain Distribution within Geotechnical Cross Section: Time 4.3 and 5.5

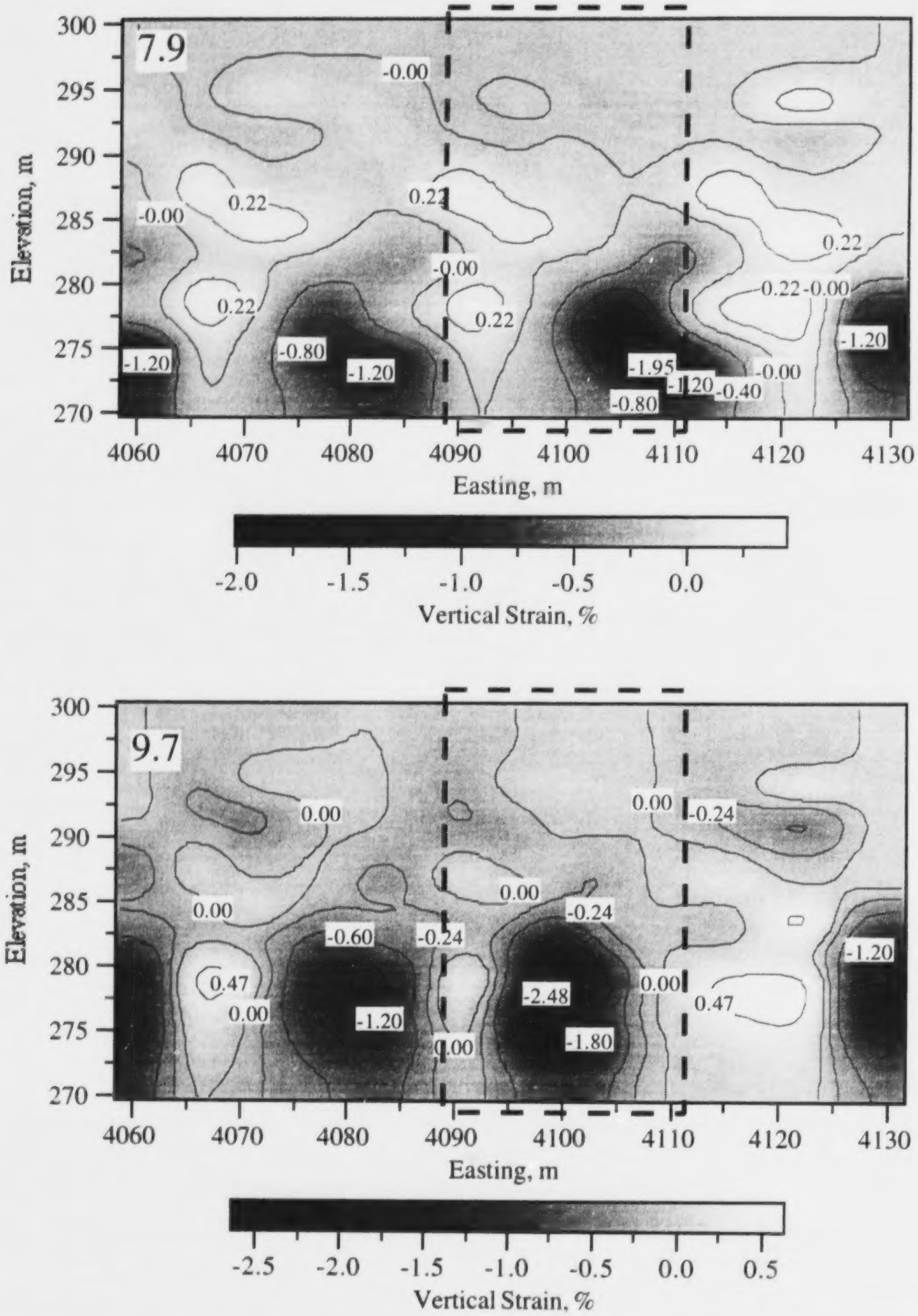

Figure 6.47 Vertical Strain Distribution within Geotechnical Cross Section: Time 7.9 and 9.7

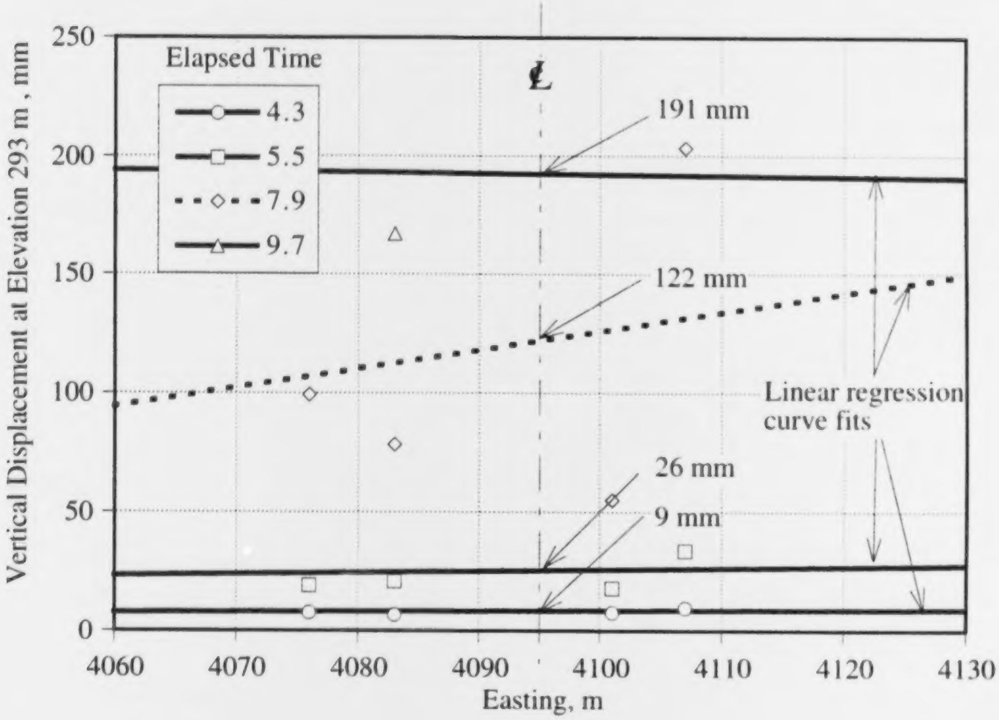

Figure 6.48 Estimated Vertical Displacement of Top of Reservoir (Elevation 293 m)

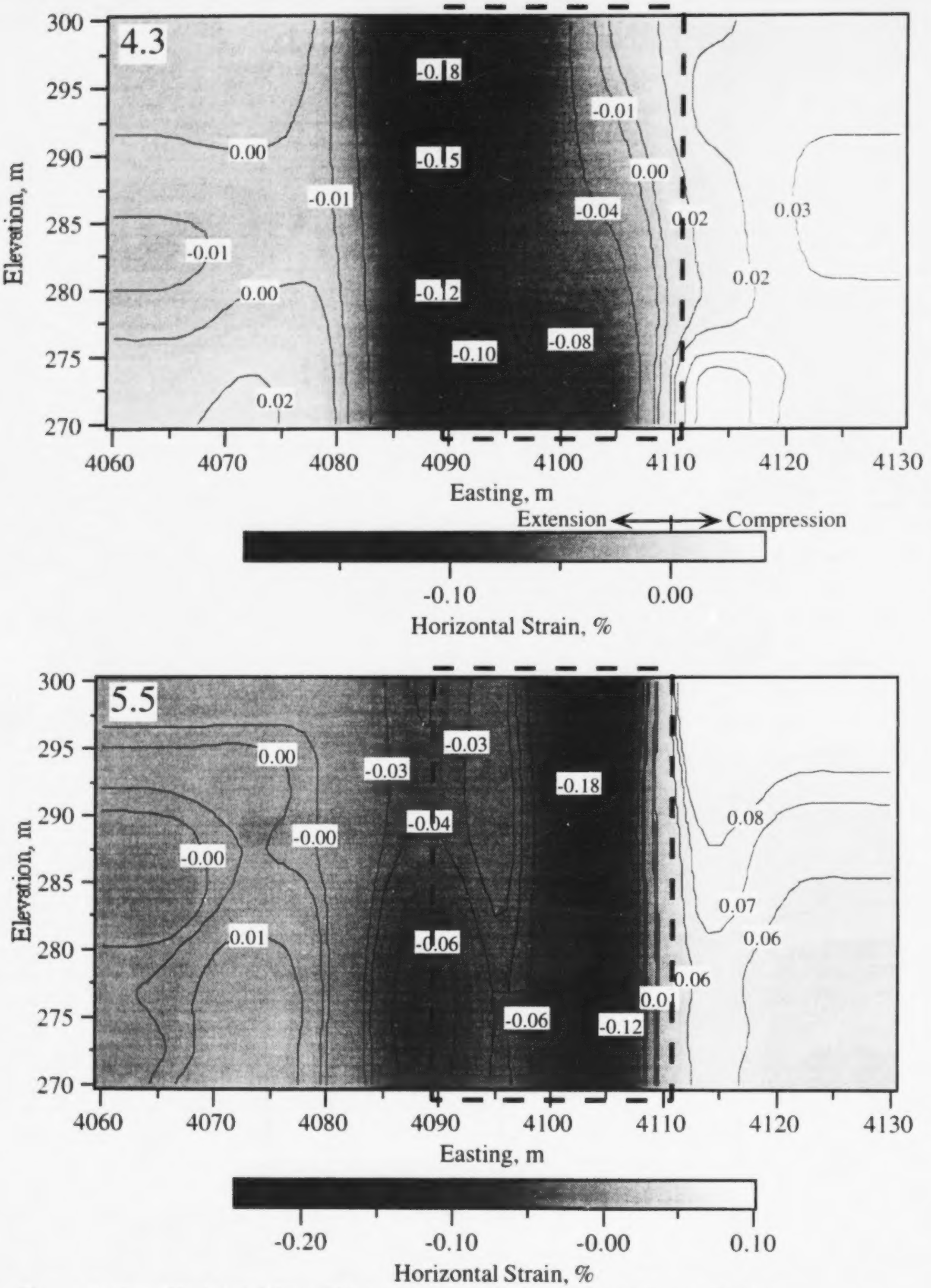

Figure 6.49 Horizontal Strain Distribution within Geotechnical Cross Section: Time 4.3 and 5.5

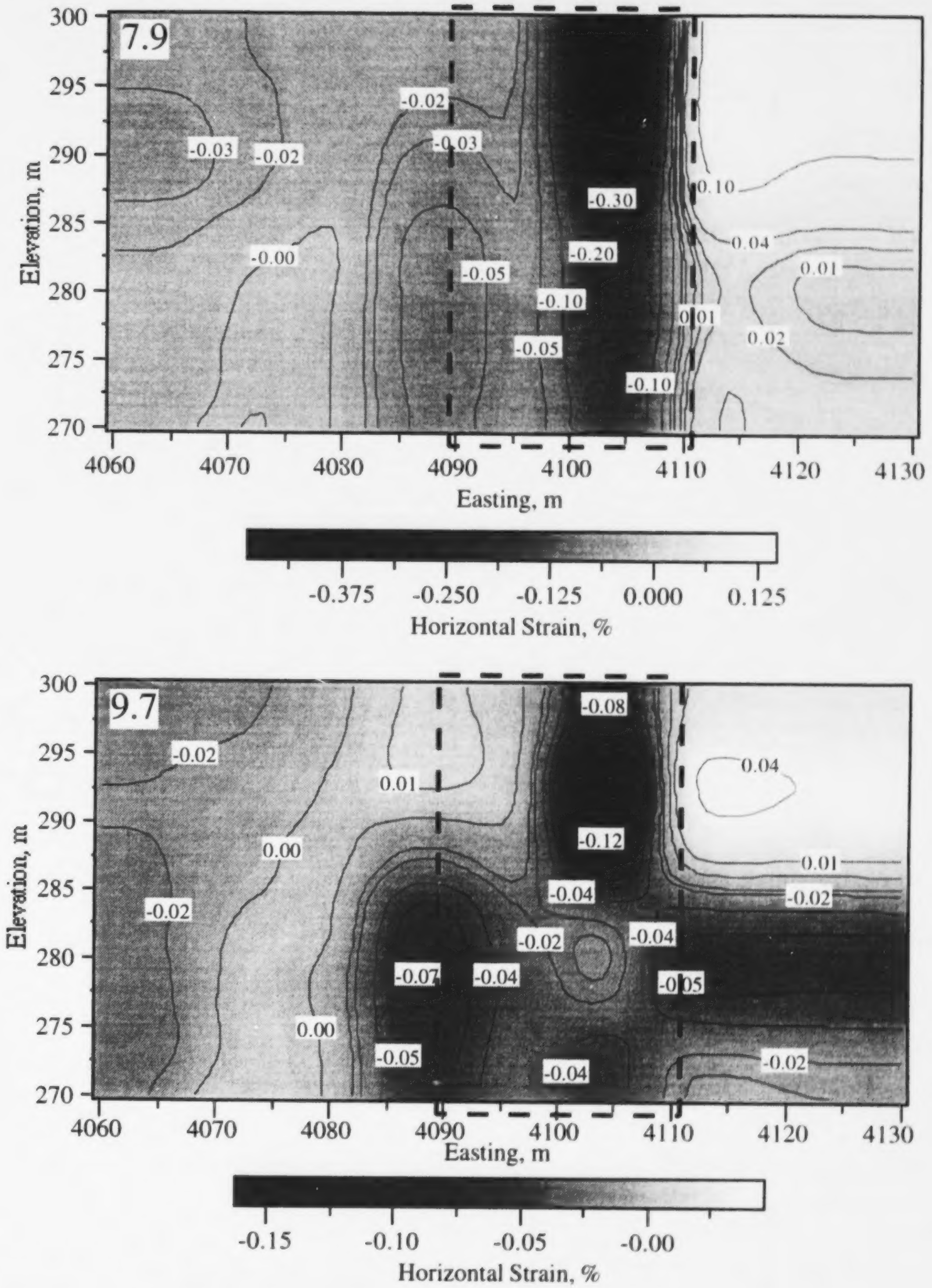

Figure 6.50 Horizontal Strain Distribution within Geotechnical Cross Section: Time 7.9 and 9.7

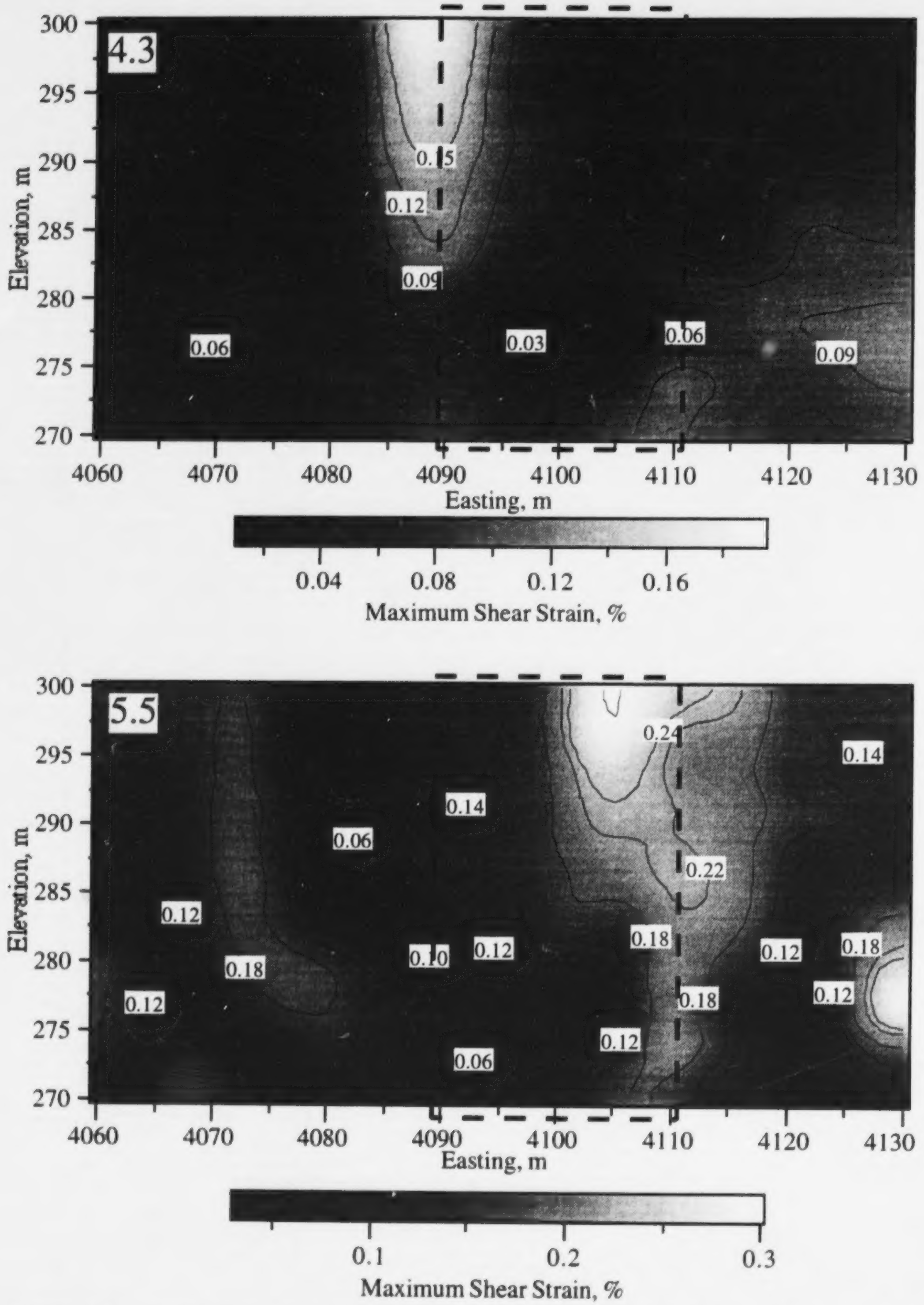

Figure 6.51 Maximum Shear Strain Distribution within Geotechnical Cross Section: Time 4.3 and 5.5

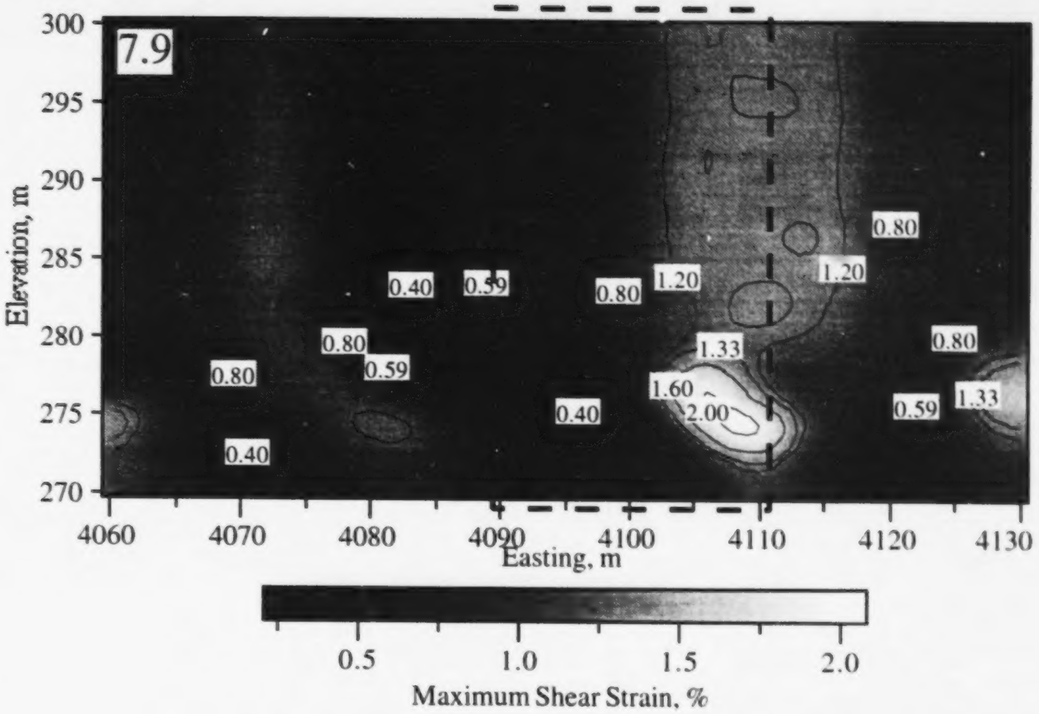

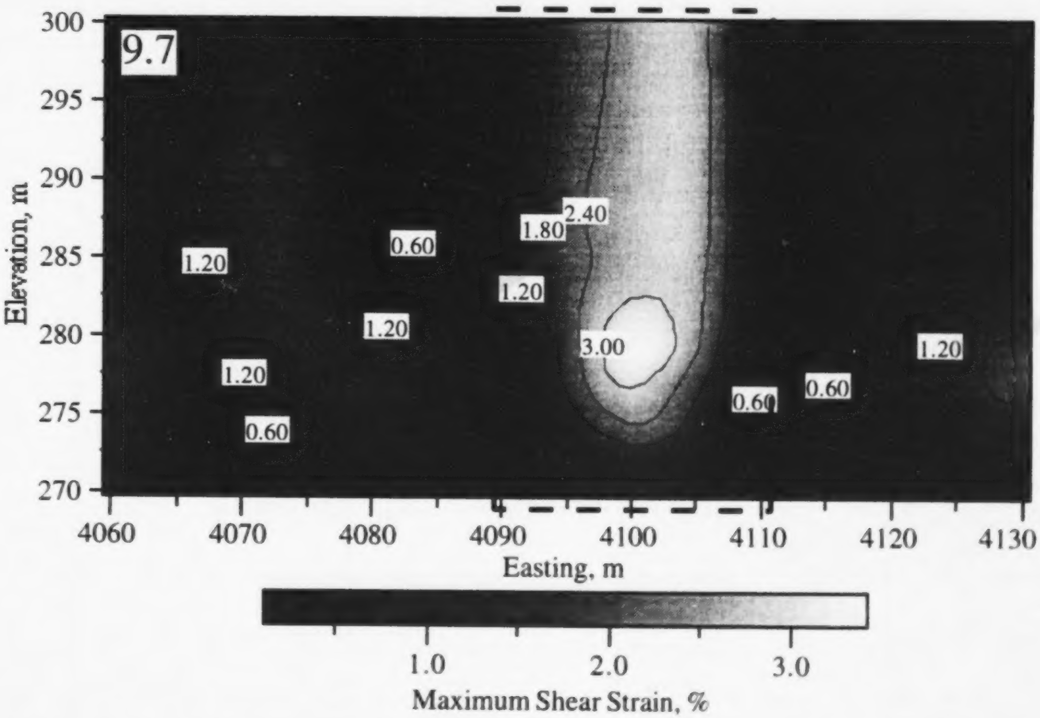

Figure 6.52 Maximum Shear Strain Distribution within Geotechnical Cross Section: Time 7.9 and 9.7

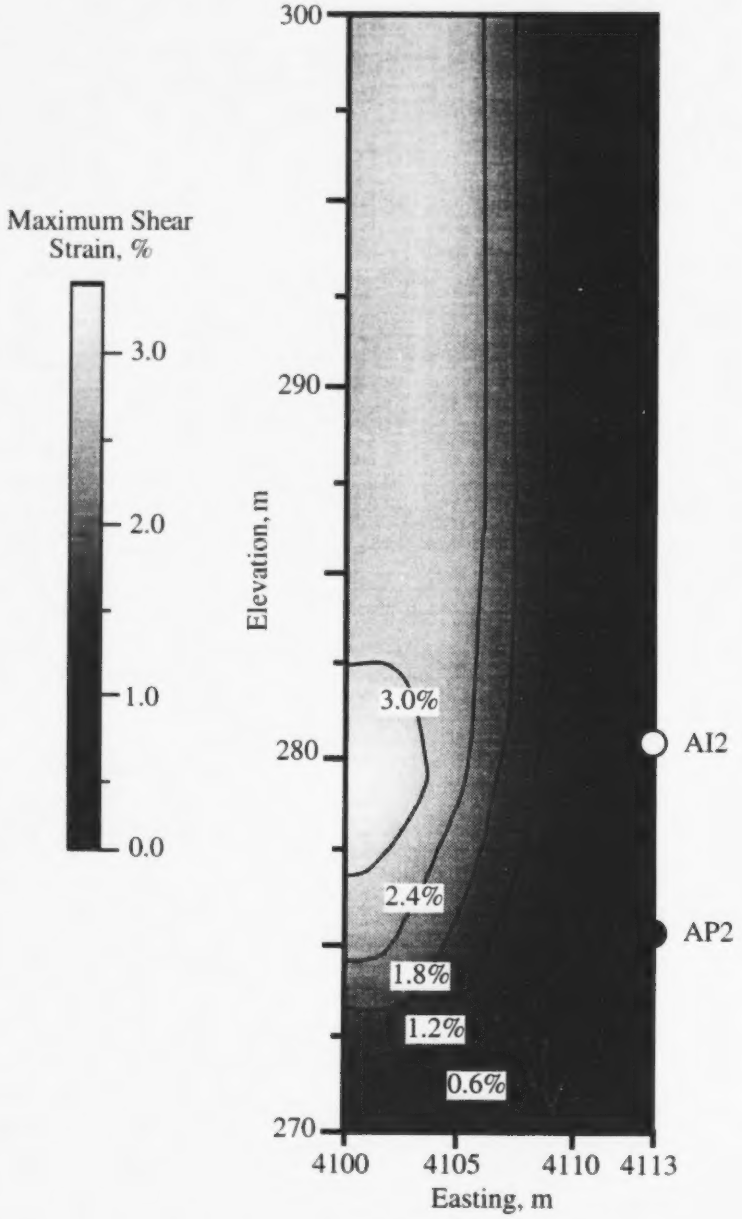

Figure 6.53 Maximum Shear Strain Distribution at Time 9.7 for Region Within Reservoir Comparable to Boundary Conditions Used in Ideal Analyses

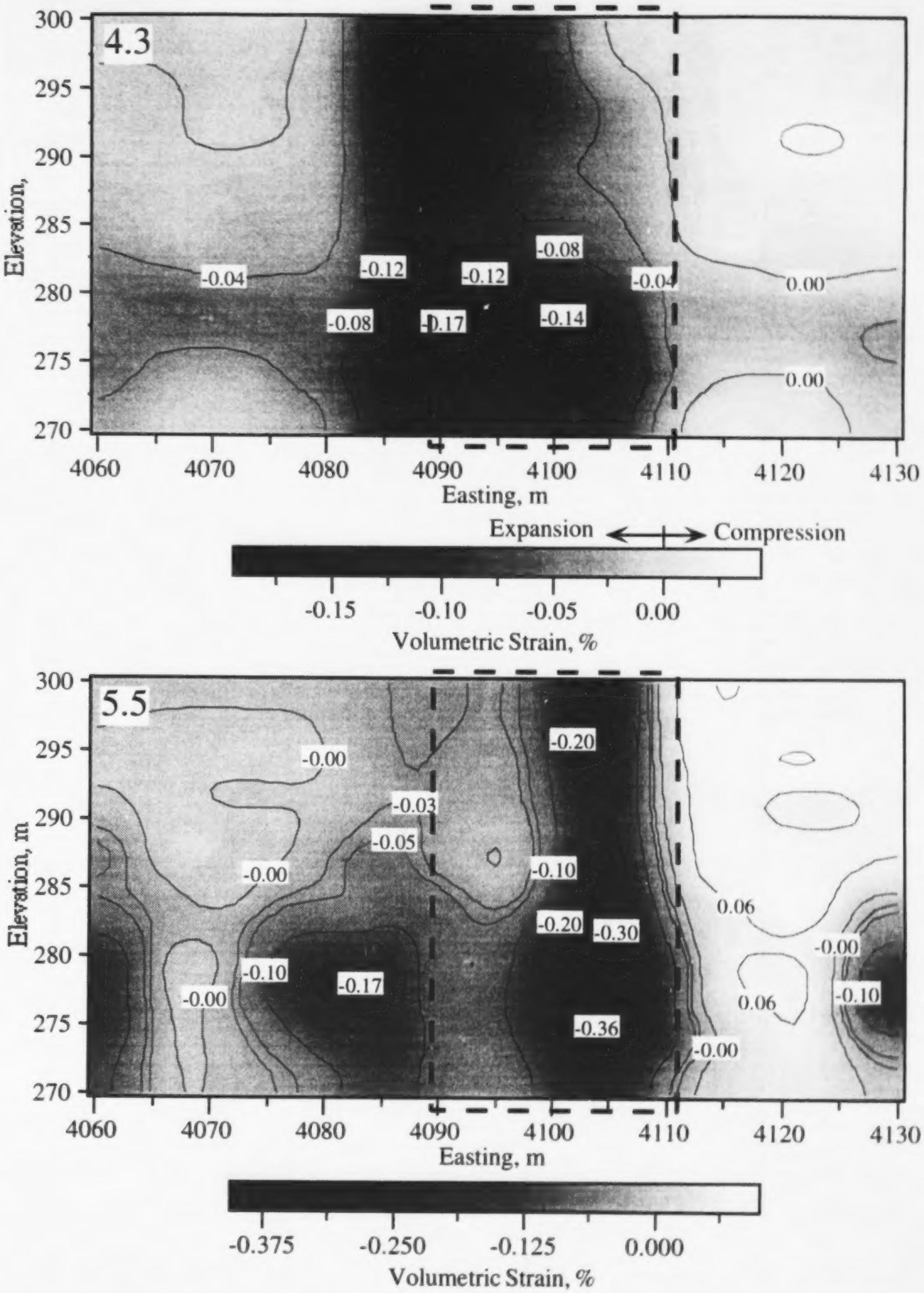

Figure 6.54 Volumetric Strain Distribution within Geotechnical Cross Section: Time 4.3 and 5.5

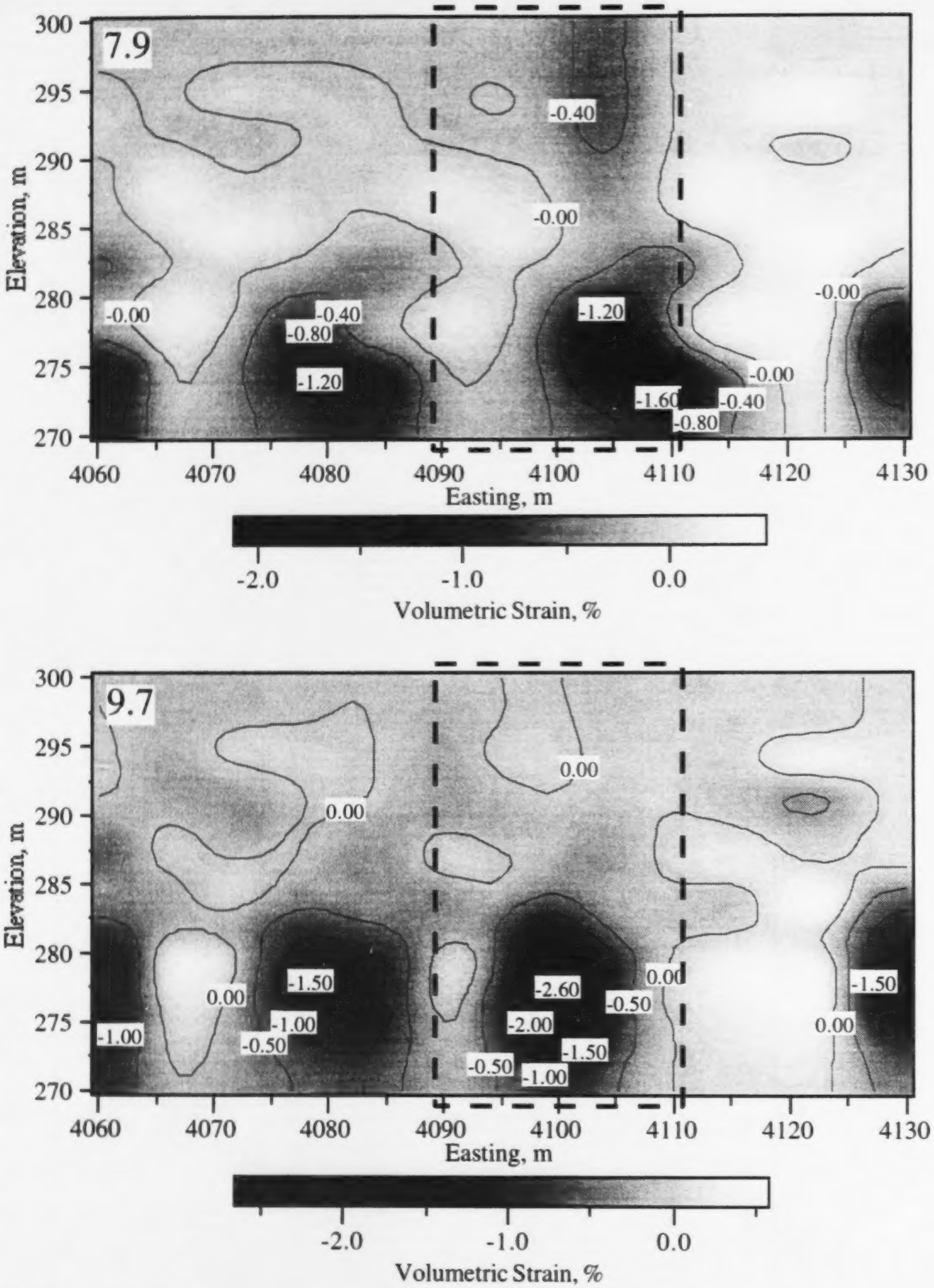

Figure 6.55 Volumetric Strain Distribution within Geotechnical Cross Section: Time 7.9 and 9.7

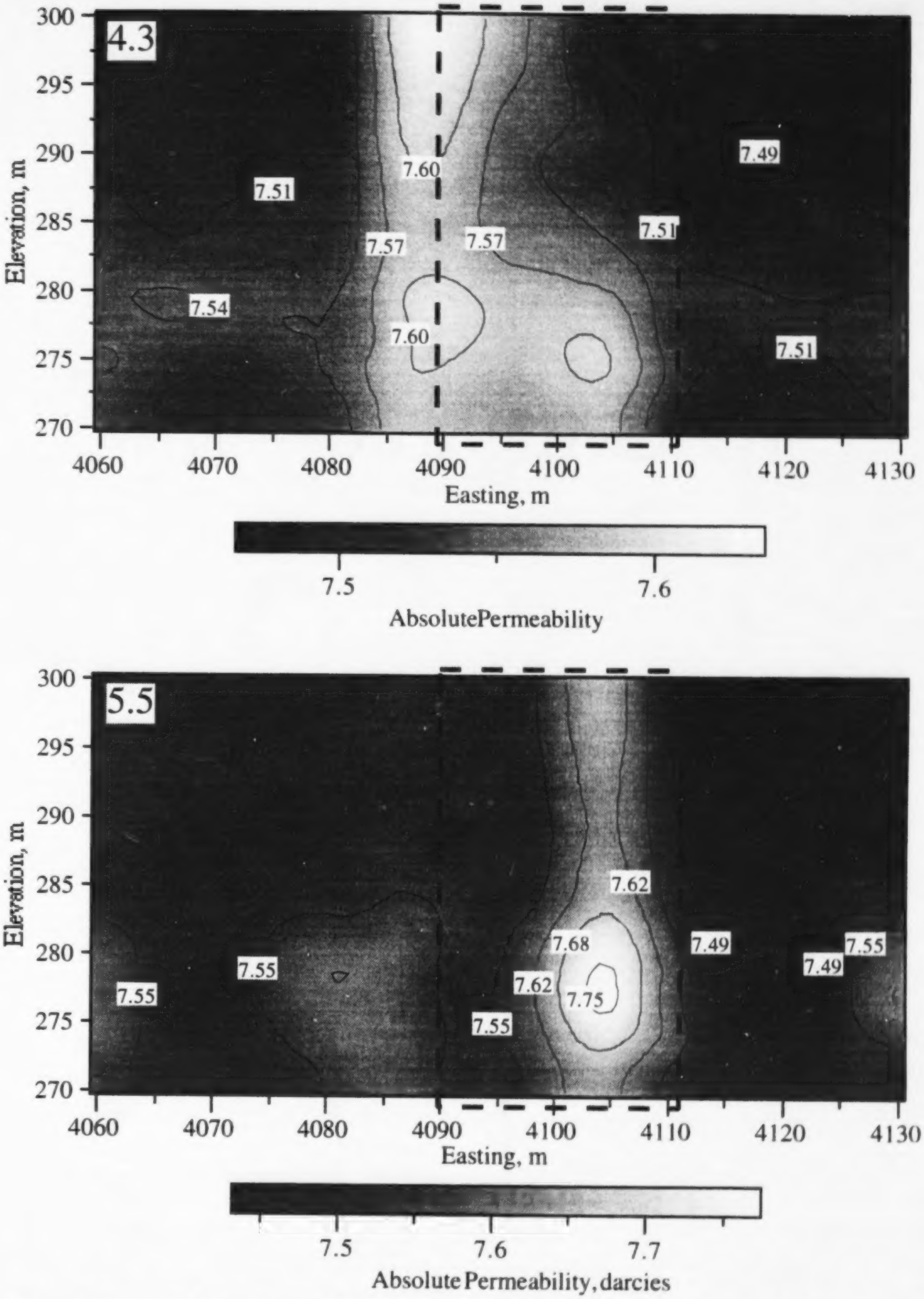

Figure 6.56 Absolute Permeability Distribution within Geotechnical Cross Section: Time 4.3 and 5.5

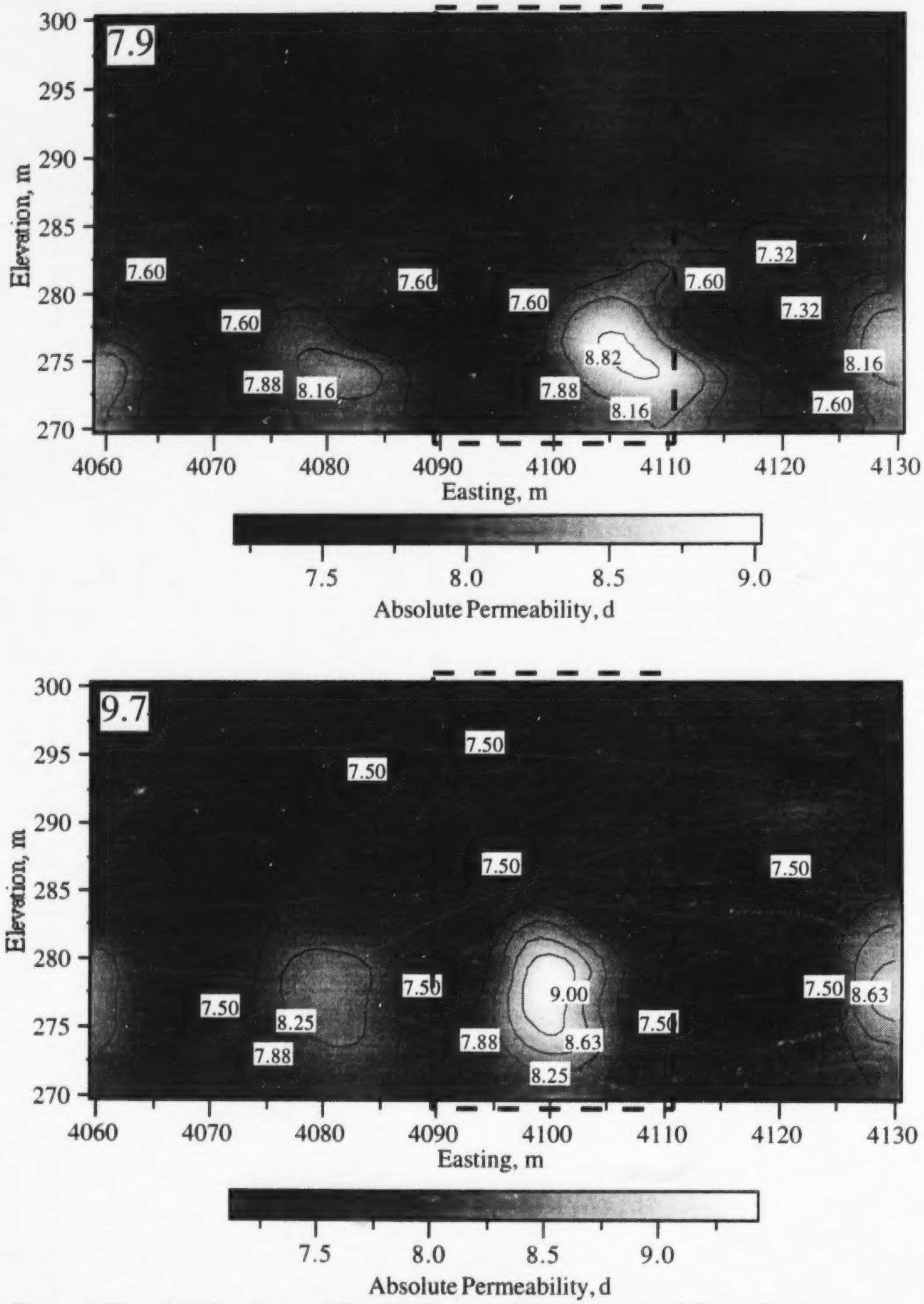

Figure 6.57 Absolute Permeability Distribution within Geotechnical Cross Section: Time 7.9 and 9.7

CHAPTER 7 GEOTECHNICAL CROSS SECTION ANALYSIS

" Comparisons are odorous"
Shakespeare, *Much Ado about Nothing*

7.1 Introduction

The objective of this chapter was to incorporate field measurements of temperature and pore pressure into a thermal-effective stress analysis of the geotechnical cross section. While this allows several factors concerning the geomechanical response of the formation to be examined, the primary interest was the corroboration between predicted deformations and instrumentation response within the geotechnical cross section and the full strain field results presented in §6.6.2.

The successful incorporation of measured pore pressures into effective stress finite element analyses has been reported by Alencar (1988). He concluded that the finite element method (stress-deformation analysis) combined with relatively simple material models can be a very efficient and powerful instrument of analysis. Based on the success of Alencar (1988), the same procedure is adopted for an analyis of the geotechnical cross section.

7.2 Problem Statement

7.2.1 Modeling Procedure

The modeling procedure adopted for the present analyses consisted of implementing the field measured pore pressures into a thermal-effective stress analysis. The field temperatures are also treated as a known values. The model FLAC has a built-in capability for inputting known values of pore pressure for use in computing the effective stress and temperature for the calculation of thermal induced stress at all points in the model. In general, the analysis procedure was conducted in the same fashion as the ideal analyses presented in Chapter 5 and can be summarized as follows:

1) in situ stresses equilibrated within grid;
2) pore pressures measured at time 1.4 were applied to grid and stress equilibrium solved;
3) temperatures obtained at time 1.4 were applied to grid and stress equilibrium solved; and
4) steps 2) and 3) repeated sequentially for all time steps up to time 10.0.

Analysis results were obtained for time steps 1.4, 2.1, 2.5, 2.9, 3.2, 3.6, 3.9, 4.3, 4.6, 5.0, 5.4, 5.7, 6.1, 6.4, 7.1, 7.9, 8.6, 9.3 and 10.0.

7.2.1.1 Field Pore Pressures

The history of pore pressure development within the geotechnical cross section has been provided in §6.2.2. These pore pressures were interpolated onto the geotechnical cross section finite difference grid for each time step. The same Easting and elevation coordinate system as the figures presented in §6.22 has been utilized in defining the finite difference grid for the present analyses. Consequently, the pore pressure distribution is not repeated here and the reader is referred to Figures 6.5 to 6.21 for the appropriate pore pressure plot.

7.2.1.2 Field Temperatures

The history of temperature evolution within the geotechnical cross section has been provided in §6.2.2. In the same fashion as pore pressure, temperatures were interpolated onto the geotechnical cross section finite difference grid for each time step. The temperature distribution for each time step is illustrated in Figures 6.5 to 6.21.

7.2.2 Geotechnical Cross Section Geometry

Figure 7.1 illustrates the finite difference grid for the geotechnical cross section analysis. Because the pore pressure and temperature development were not symmetric, a full cross section was required. The base of the grid is fixed and the left and right boundaries allow only vertical displacements. The upper boundary represents the ground surface and as such, is a free displacement boundary. The specific dimensions of the grid are provided in Figure 7.2. The location of the formation region for which pore pressure and temperature data was provided in §6.2.2 is highlighted in Figure 7.2.

7.2.2 Material Properties

Utilizing the results from the thermomechanical testing program, the geologic units within the reservoir were treated independently, that is, separate material properties were provided. Table 7.1 lists the material properties chosen for each region within the reservoir. The initial stress distribution is also provided in Table 7.1. The overburden, Wabiskaw sand (Unit A) and the limestone underburden (Unit H) were assumed linear elastic. The remaining units were assumed to be linear elastic perfectly plastic with a Mohr Coulomb yield criterion.

The dependence of Young's modulus on the minor principal effective stress, as defined by Equation 4.30, was assumed applicable for Units D, E and G. For Units B and C, which were classed as upper McMurray shale, the following linear relationship based on a linear regression curve fit to the Young's modulus data presented in Figure 4.45 was used to define the dependence of E on σ_3':

$$E = 120\sigma_3' \qquad [7.1]$$

For lower McMurray shale (Unit F), a linear regression curve fit to the Young's modulus data presented in Figure 4.49 was assumed to define the variation in Young's modulus with σ_3' and is defined as follows:

$$E = 555\sigma_3' \qquad [7.2]$$

Equations 7.1 and 7.2 include both 20°C and 220°C test results.

7.3 Geotechnical Cross Section Analysis

History matching the field instrumentation results was not the objective of the geotechnical cross section analysis. Consequently, the following presents the results from a single analysis of the geotechnical cross section for the material properties provided in Table 7.1. As presented and discussed in Chapter 5, variations in several key material properties will influence the predicted formation response to SAGD processes.

7.3.1 Mobilized Strength

The distribution of the failure index, as defined in §5.5.1, is used as an indicator of mobilized strength. Figures 7.3, 7.4, 7.5 and 7.6 provide the failure index distribution for times 3.9, 5.4, 7.9 and 9.3, respectively.

The magnitude of the failure index provides an excellent measure of the shear yield potential within the geotechnical cross section. In general, the predicted mobilized strength was relatively low; the failure index never decreased below approximately 3.0. The location of peak mobilized strength is occurring between wellpair A1 and A2 at time 5.4. As a trend, this correlates well with the ideal analysis results presented in Chapter 5 and the measured formation response described in Chapter 6. The volumetric strain distribution shown in Figure 6.55 was also concentrated between wellpair A1 and A2 at time 5.5 It was shown that the volumetric response in this region was due to bulk volume changes as a result of rising pore pressures, not shear induced volume changes. The failure index distribution shown in Figure 7.4 supports this conclusion as negligible shear induced volume changes occur for failure indices of 4 to 5.

For later times of 7.9 and 9.3, the failure index distributions illustrate a deformation mechanism which to this point has not been addressed, namely the development of shear induced volume changes in front of an advancing steam chamber. At these later times, the lateral growth of the steam chamber within the geotechnical cross section closely resembles the general nature of steam chamber advancement. Specifically, the lateral pore pressure growth occurs in advance of the steam chamber and the thermal induced stresses. As an analogue to general slope drainage growth within the reservoir, the failure index distributions in Figure 7.5 and 7.6 highlight a major geomechanical influence on the SAGD process. The zones exhibiting the greatest propensity for shear yield (i.e., the lowest failure indices) are shown to be to the left and right of wellpair A3 and A2, respectively. The major reason for the development of lower failure indices within these regions is the concurrent reduction in vertical effective stress or as illustrated in Figure 7.7, σ'_3, the minor principal effective stress. Results from the ideal analyses presented in Chapter 5 showed this to be the mechanism for shear yield *between* wellpairs; the present analyses indicate that this may also be a mechanism for volume changes *in front of* a growing steam chamber either from changes in effective confining stress or shear dilation. This phenomena is schematically illustrated in Figure 7.8.

7.3.3 Maximum Shear Strain

The distortional strains within the geotechnical cross section are presented in the maximum shear strain contours shown in Figure 7.9, 7.10, 7.11 and 7.12 for times 3.9, 5.4 7.9 and 9.3, respectively. The evolution of γ_{max} follows the same trends as the failure index. The zones of largest γ_{max} occur between wellpairs. At time 9.3, zones of high γ_{max} occur to the left and right of wellpair A3 and A2, respectively.

In comparison to the shear strain distributions obtained in Chapter 6 (§6.6.2.3), the distribution within the geotechnical cross section compares well over the analysis periods; however, the magnitude of γ_{max} does not. The underprediction of γ_{max} relative to the constitutive model chosen for the analyses was discussed in §5.6.4.

7.4 Comparison of Field Instrumentation and Numerical Results

The following briefly presents a comparison between the predicted response and measured response for the inclinometer and extensometer wells.

7.4.1 Inclinometer

Figures 7.13 to 7.17 offer a comparison of the surveyed horizontal displacements and the horizontal displacement predicted from the thermal-effective stress analysis of the geotechnical cross section for AGI1, AGI2, AGI3, AT1 and AT7. The following observations are possible from these comparisons:

- the predicted horizontal displacement profile for inclinometers which were within the steam chamber over most of the life of the project matched reasonably well the observed displacements, even the reversals in horizontal displacement measured at AT7 for time 9.7 (Figure 7.17); and
- the horizontal displacements at "far field" inclinometers, namely AGI1, AT1 and AGI3, are overpredicted and do not match the trend in measured horizontal displacements.

The overprediction of displacements would suggest that the stiffness properties chosen in the material models was low and would need to be increased to improve the match between predicted and observed displacements. However, a match for not only the magnitude but the distribution of horizontal displacements must be improved for "far-field" inclinometer well locations. Figure 7.18 illustrates the results of preliminary constant stiffness elastic analyses conducted prior to the elastic-plastic analysis. It is clear that while an increase in E reduces the maximum horizontal displacement, it also affects the pattern of horizontal displacements; quite dramatically in the case of AGI1.

The issue of three dimensional behavior can not be overlooked. The observed horizontal displacements illustrated in Figures 7.13 to 7.17 are only the west-east displacement component of the displacement vector. North-south displacements (out-of-plane) up to 25 mm have been measured; a clear indication that the plane strain conditions assumed in the geotechnical cross section analysis will limit the ability to accurately predict formation deformations.

7.4.2 Extensometer

Figure 7.19 illustrates the vertical strain predicted for AGE2, AGE3 and AGE4. Firstly, the predicted response is essentially the same for all extensometers; a maximum extensional vertical strain of 0.65% between elevation 275 m and 285 m. This is significantly less than the vertical strain observed from field observations which reached a maximum value of approximately 2.5% (Figure 6.48).

The similarity between the predicted response of AGE2 (which is situated above wellpair A1) and AGE3 and AGE4 (which are situated between wellpairs A1 and A2) based on the measured pore pressure and temperature illustrates the three dimensional growth of the steam chamber. Since the growth pattern of the steam chambers was primarily longitudinal along wellpairs A1 and A2, the steam chambers would "pierce" the geotechnical cross section from the north and induce similar deformations at AGE2, AGE3 and AGE4. This is reflected in Figure 7.19. In contrast, if the growth was dominated by lateral growth within the geotechnical cross section, dissimilar vertical straining would occur at AGE2 then at AGE3 or AGE4. This was demonstrated in the ideal analysis presented in Chapter 5. Figure 5.38 illustrates the possible differences in vertical strain distribution.

7.5 Summary

A thermal-effective stress analysis of the geotechnical cross section was performed using field measured pore pressures and temperatures. In general, the predicted mobilized strength was relatively low; the failure index never decreased below approximately 3.0. The distribution of γ_{max} compared well with the location of maximum mobilized strength and agrees reasonably well with the parameteric analysis results presented in Chapter 5. The magnitude of γ_{max} however, is substantially lower than the predicted response from the parametric analyses.

Horizontal displacements were overpredicted and vertical strains were underpredicted by the thermal-effective stress analysis of the geotechnical cross-section. General conclusions from the analysis indicate that the deformation response within the geotechnical cross section are not due exclusively to the pore pressure and temprature changes measured within the geotechnical cross section. Consequently, an analysis of deformations within the geotechnical cross section will require the consideration of deformations along the wellpairs and the three dimensional growth of the steam chambers.

Present analyses has revealed that formation yield *in front of* a growing steam chamber as opposed to *between* wellpairs may contribute to the propogation of permeability enhanced zone in front of growing steam chambers.

Parameter	Overburden	Unit A	Unit B&C	Units D.E & G	Unit F	Underburden (limestone)
Bulk Density, γ_t	2.153	2.153	2.153	2.153	2.153	2.153
Porosity, n_o			.32	.32	.32	
Friction Angle, ϕ'			45	60	50	
Cohesion,c' (kPa)			500	0	0	
Dilation Angle, ψ			10	15	0	
Initial Stress Ratio, K_o	1.5	1.5	1.5	1.5	1.5	1.5
Young's' Modulus Number, E_o			150	343	555	
Young's Modulus Exponent, α			1.0	.875	1.0	
Bulk Modulus, K (MPa)	208	500				4167
Shear Modulus, G (MPa)	96.2	204				1923
Poisson's ratio, ν	0.3	0.3	0.3	0.3	0.3	0.3
Volumetric Coefficient of Bulk Thermal Expansion °C^{-1}	6.0×10^{-5}					

- initial temperatures and pore pressures were set to zero since only the "change" in temperature and pore pressure were used in the analysis.

- the following table summarizes the initial compressive effective stress state within the model:

Elevation (m)	σ_x'	σ_y'	σ_z'
430	0	0	0
310	3798	2616	3798
306	3926	2617	3926
304	3989	2659	3989
140	9179	6119	9179

Table 7.1 Material Properties for Geotechnical Cross Section Analyses

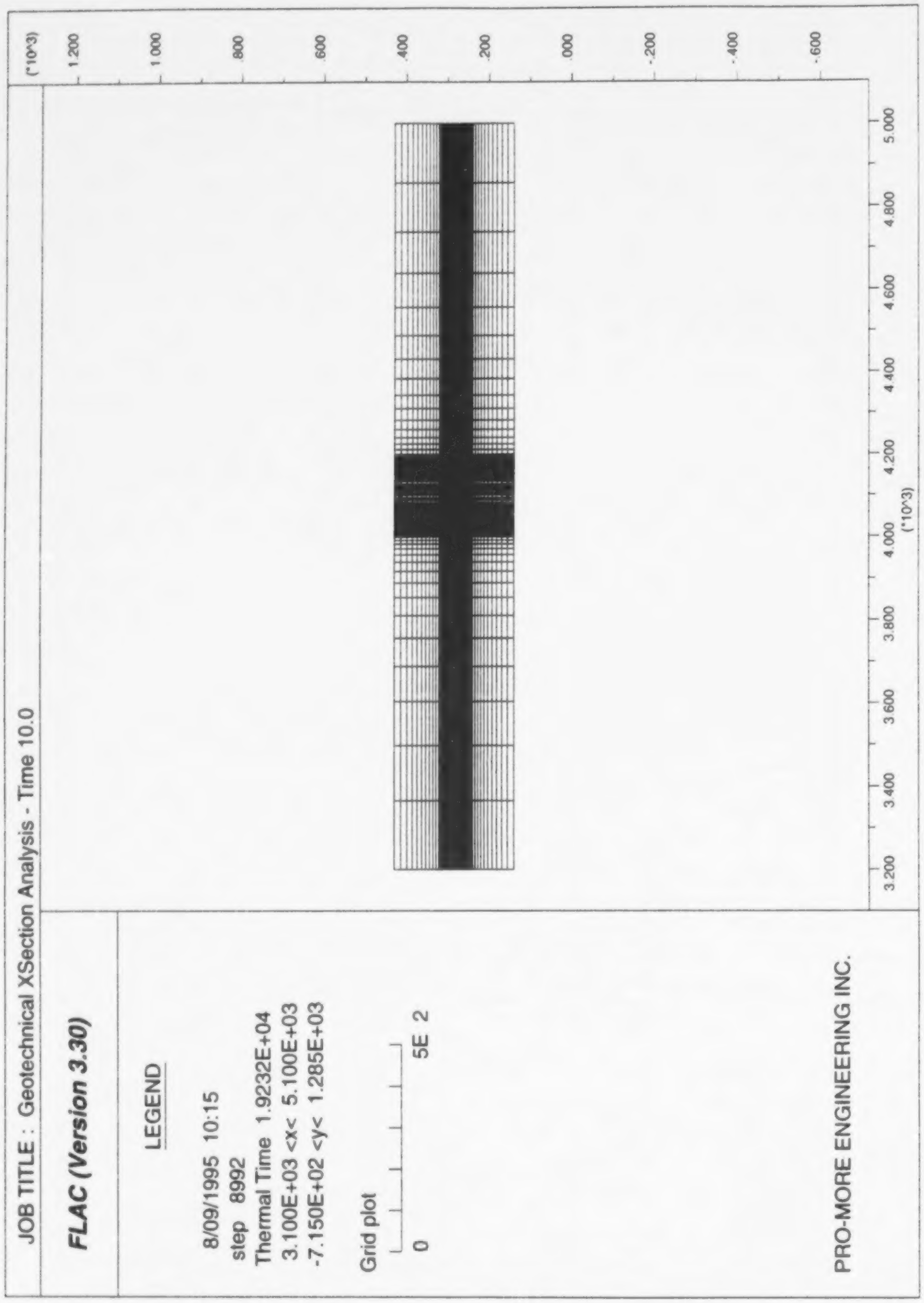
JOB TITLE : Geotechnical XSection Analysis - Time 10.0
FLAC (Version 3.30)
LEGEND
8/09/1995 10:15
step 8992
Thermal Time 1.9232E+04
3.100E+03 <x< 5.100E+03
-7.150E+02 <y< 1.285E+03
Grid plot
0
5E 2
PRO-MORE ENGINEERING INC.
(*10^3)
1.200
1.000
.800
.600
.400
.200
.000
-.200
-.400
-.600
3.200
3.400
3.600
3.800
4.000
4.200
4.400
4.600
4.800
5.000
(*10^3)

Figure 7.1 Complete Finite Difference Grid used for Geotechnical Cross Section Analysis

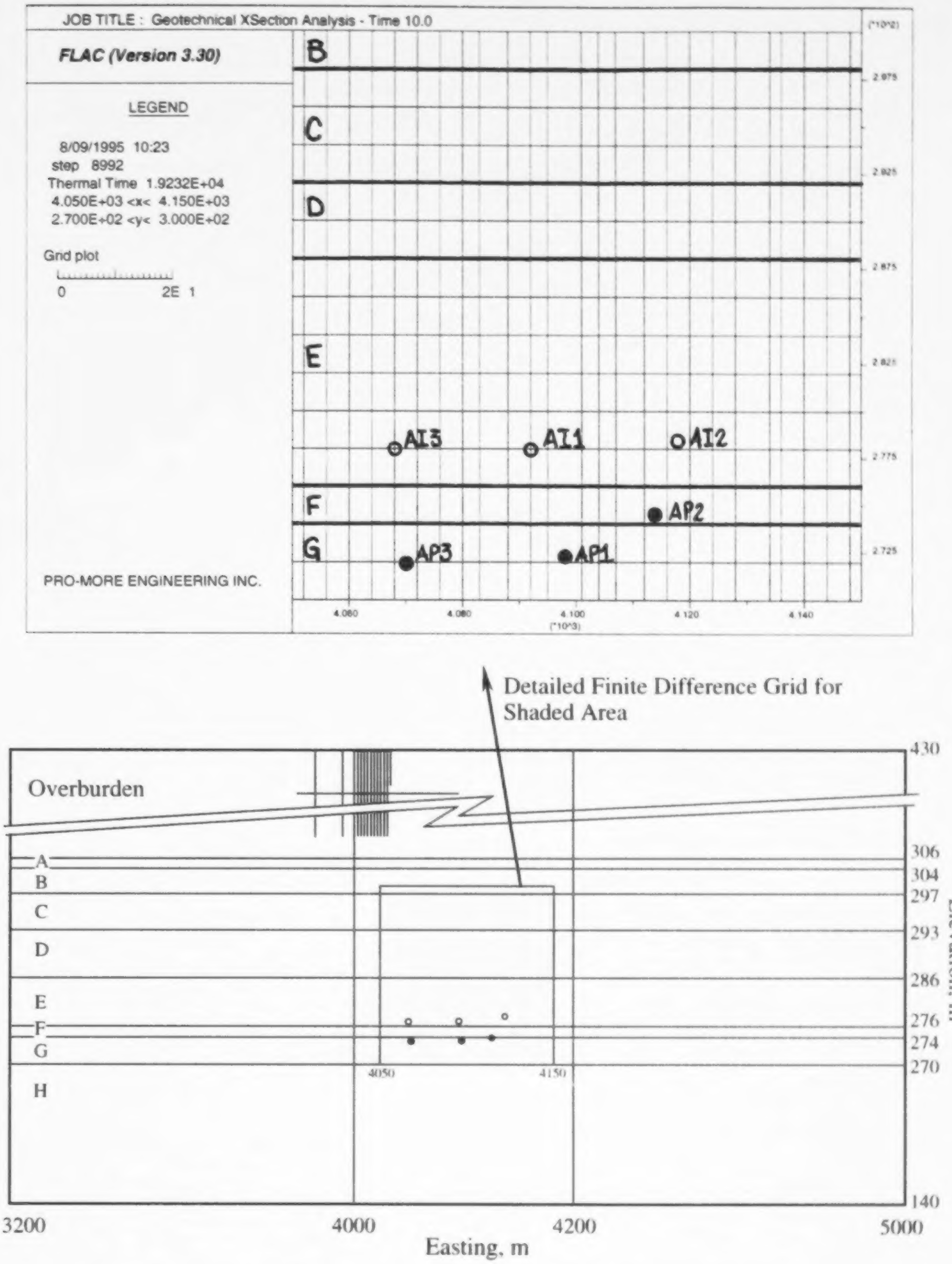
JOB TITLE : Geotechnical XSection Analysis - Time 10.0
FLAC (Version 3.30)
LEGEND
8/09/1995 10:23
step 8992
Thermal Time 1.9232E+04
4.050E+03 <x< 4.150E+03
2.700E+02 <y< 3.000E+02
Grid plot
0
2E 1
PRO-MORE ENGINEERING INC.
(*10^2)
2.975
2.925
2.875
2.825
2.775
2.725
4.060
4.080
4.100
4.120
4.140
(*10^3)
B
C
D
E
F
G
AI3
AI1
AI2
AP2
AP3
AP1
Detailed Finite Difference Grid for Shaded Area
Overburden
A
B
C
D
E
F
G
H
4050
4150
430
306
304
297
293
286
276
274
270
140
Elevation, m
3200
4000
4200
5000
Easting, m

☐ Area represented by pore pressure and temperature histories provided in Figures 6.5 to 6.21

Figure 7.2 Schematic Illustration of Finite Difference Grid Showing Dimensions and Assumed Geology

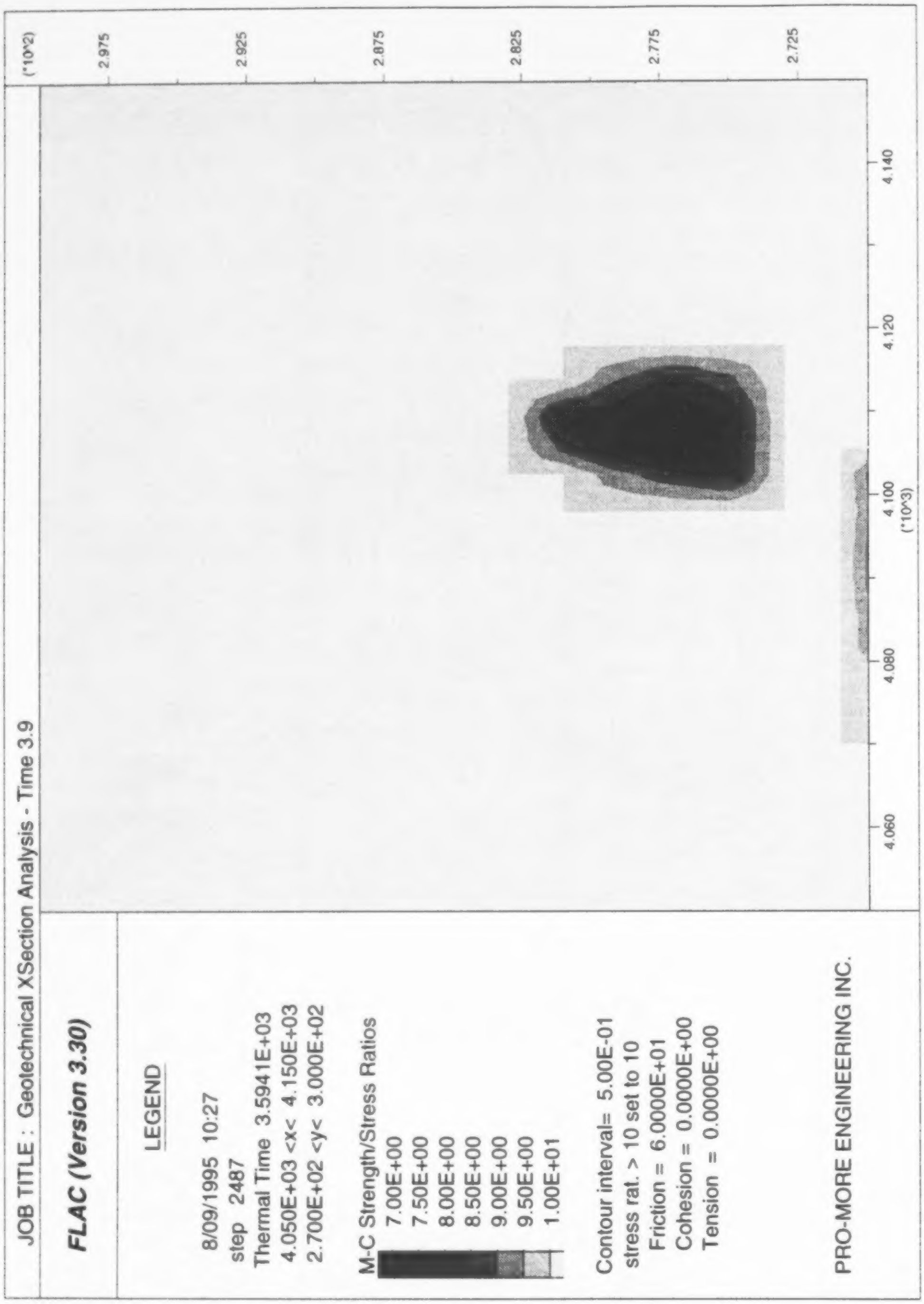

Figure 7.3 Failure Index at Time 3.9

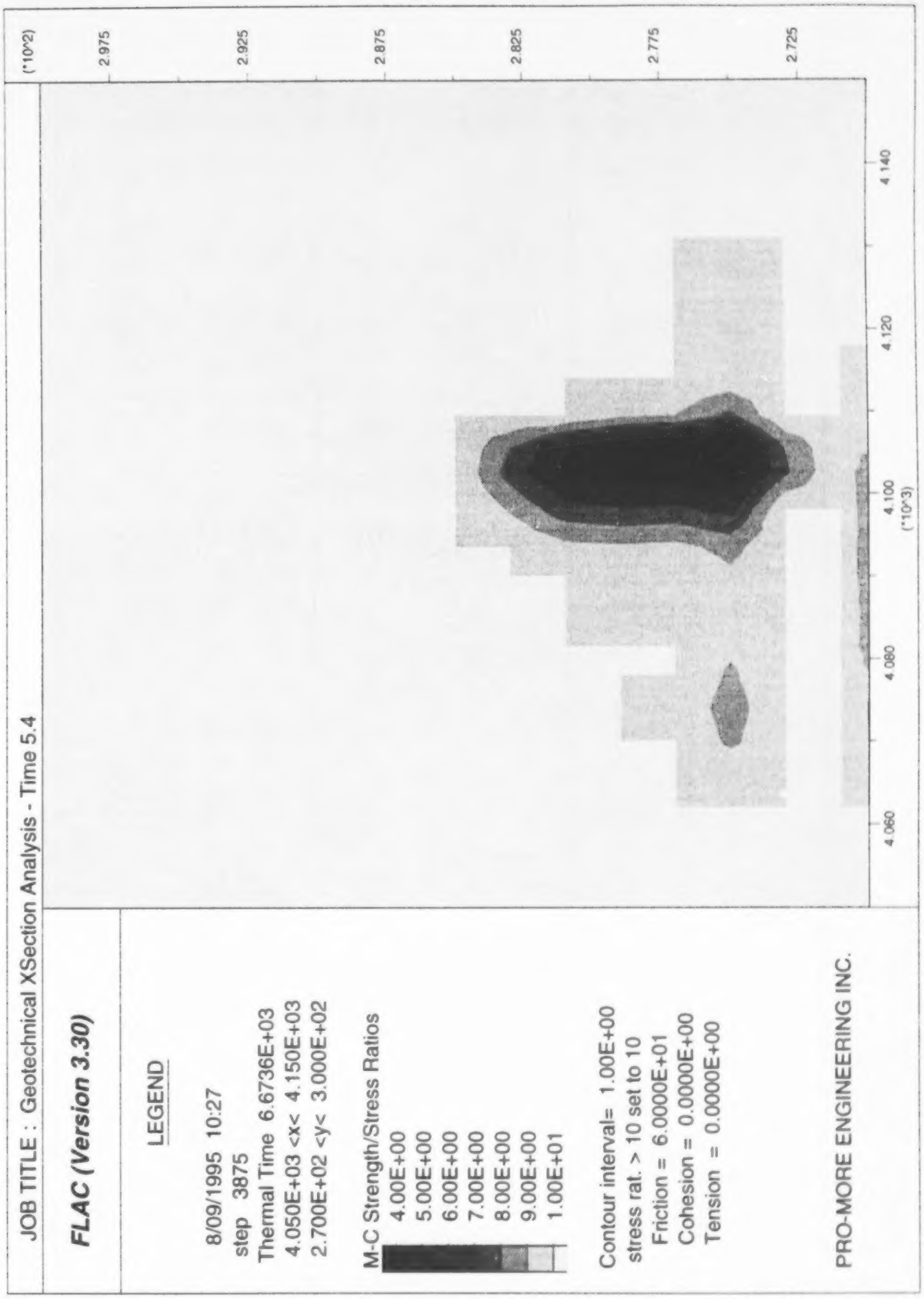

Figure 7.4 Failure Index at Time 5.4

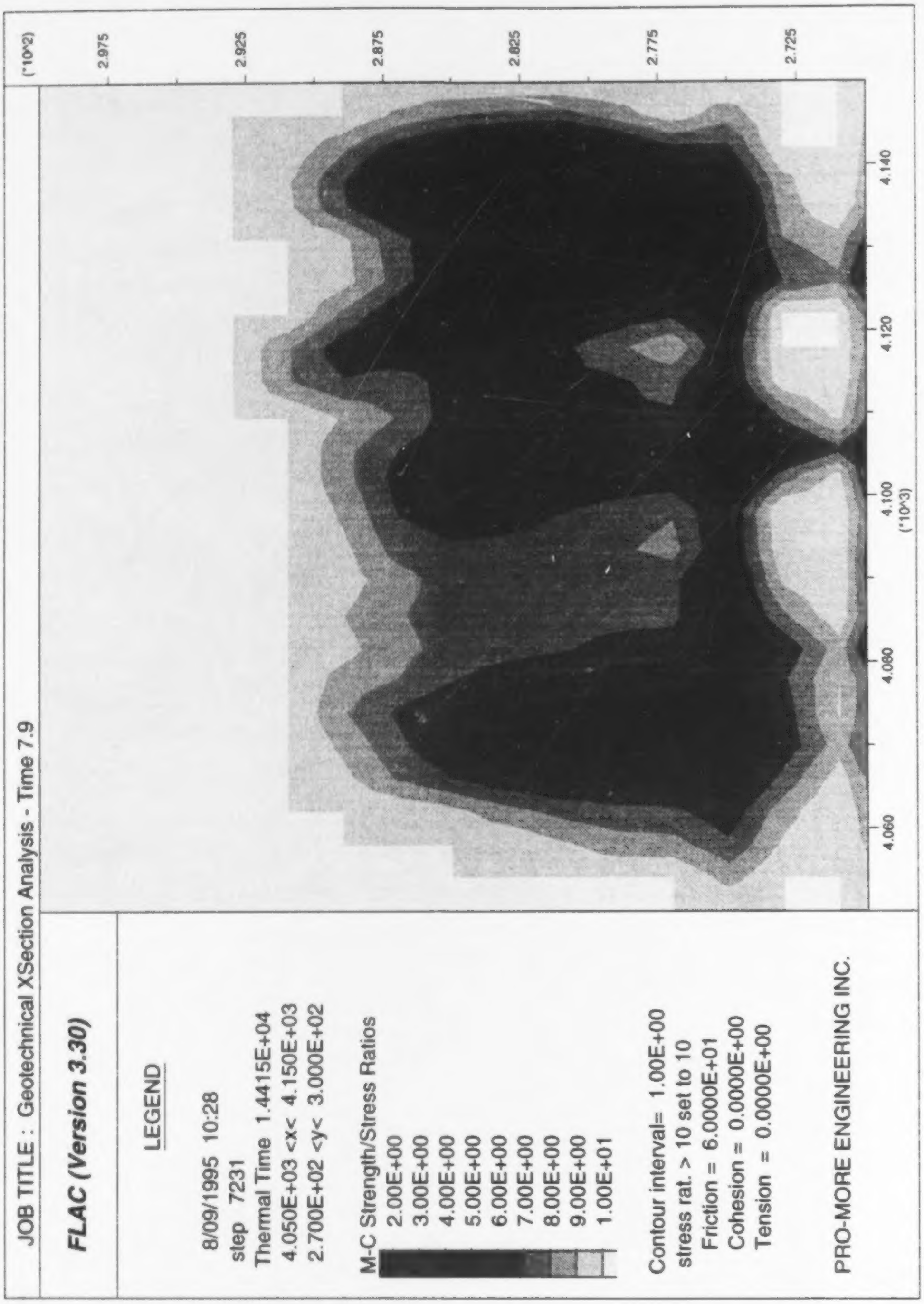

Figure 7.5 Failure Index at Time 7.9

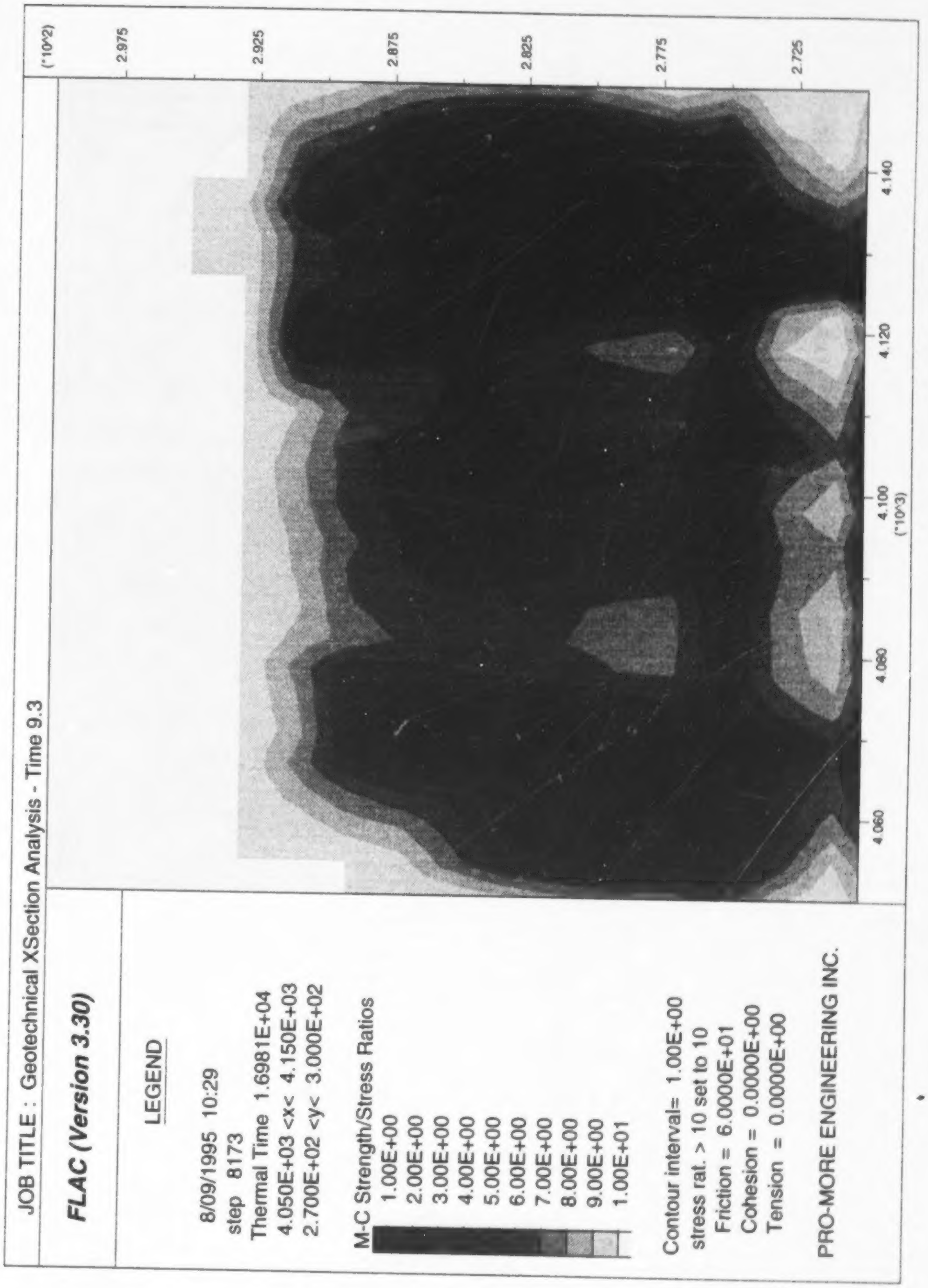

Figure 7.6 Failure Index at Time 9.3

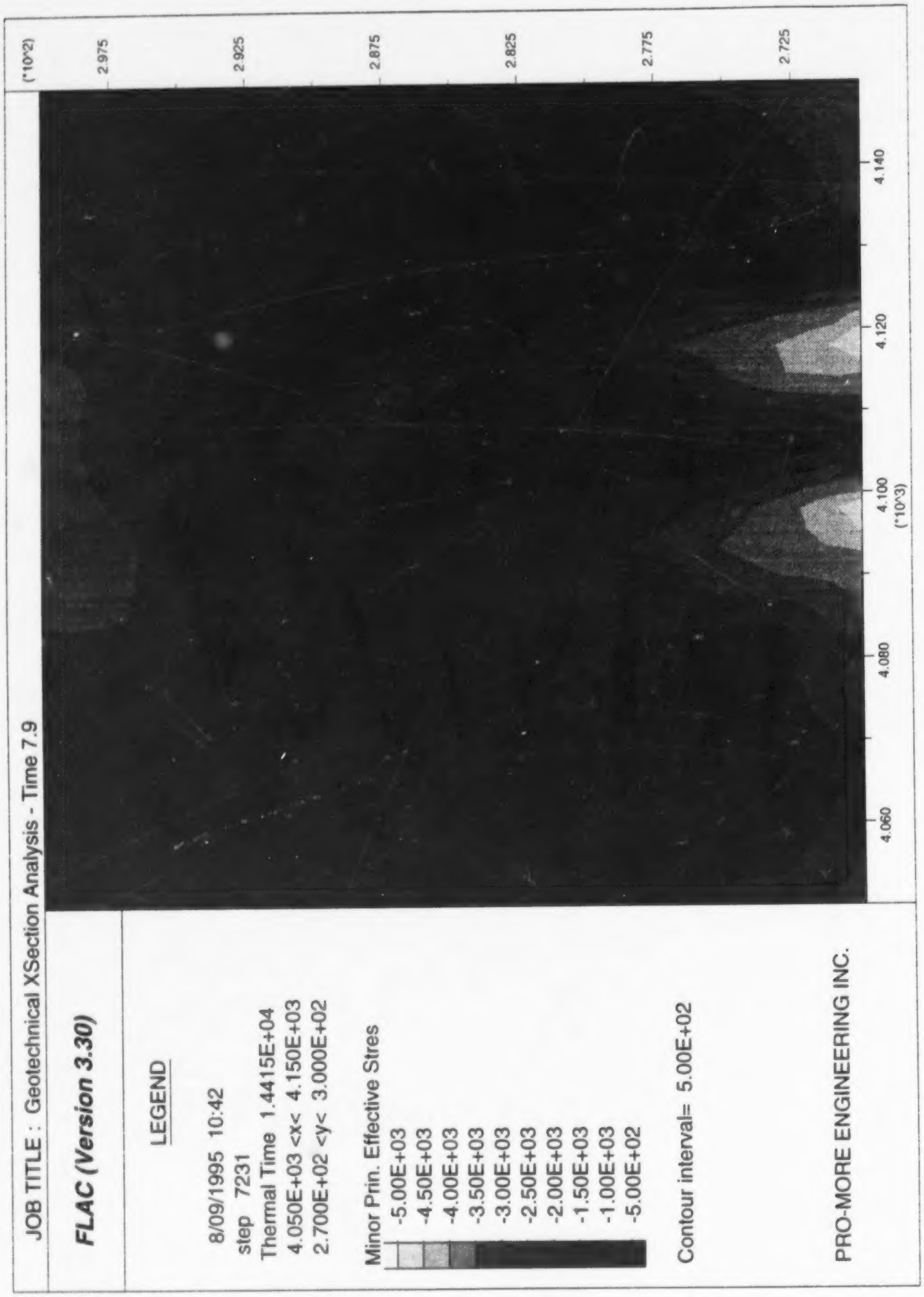

Figure 7.7 Minor Principal Effective Stress at Time 7.9

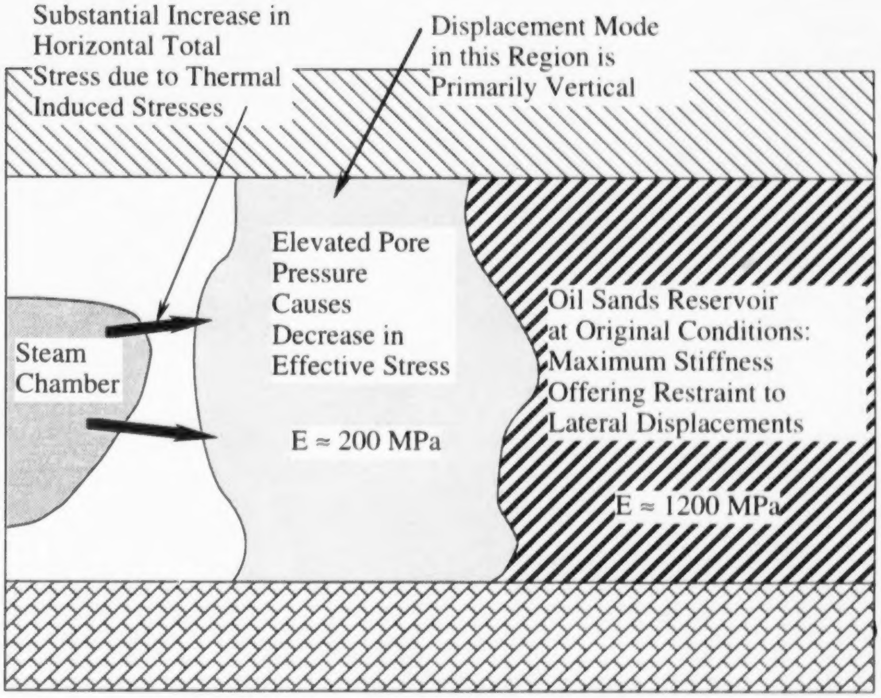
Substantial Increase in Horizontal Total Stress due to Thermal Induced Stresses
Displacement Mode in this Region is Primarily Vertical
Elevated Pore Pressure Causes Decrease in Effective Stress
E ≈ 200 MPa
Steam Chamber
Oil Sands Reservoir at Original Conditions: Maximum Stiffness Offering Restraint to Lateral Displacements
E ≈ 1200 MPa

Figure 7.8 Schematic Illustration of Mechanism for Shear Strain in Advance of Growing Steam Chamber

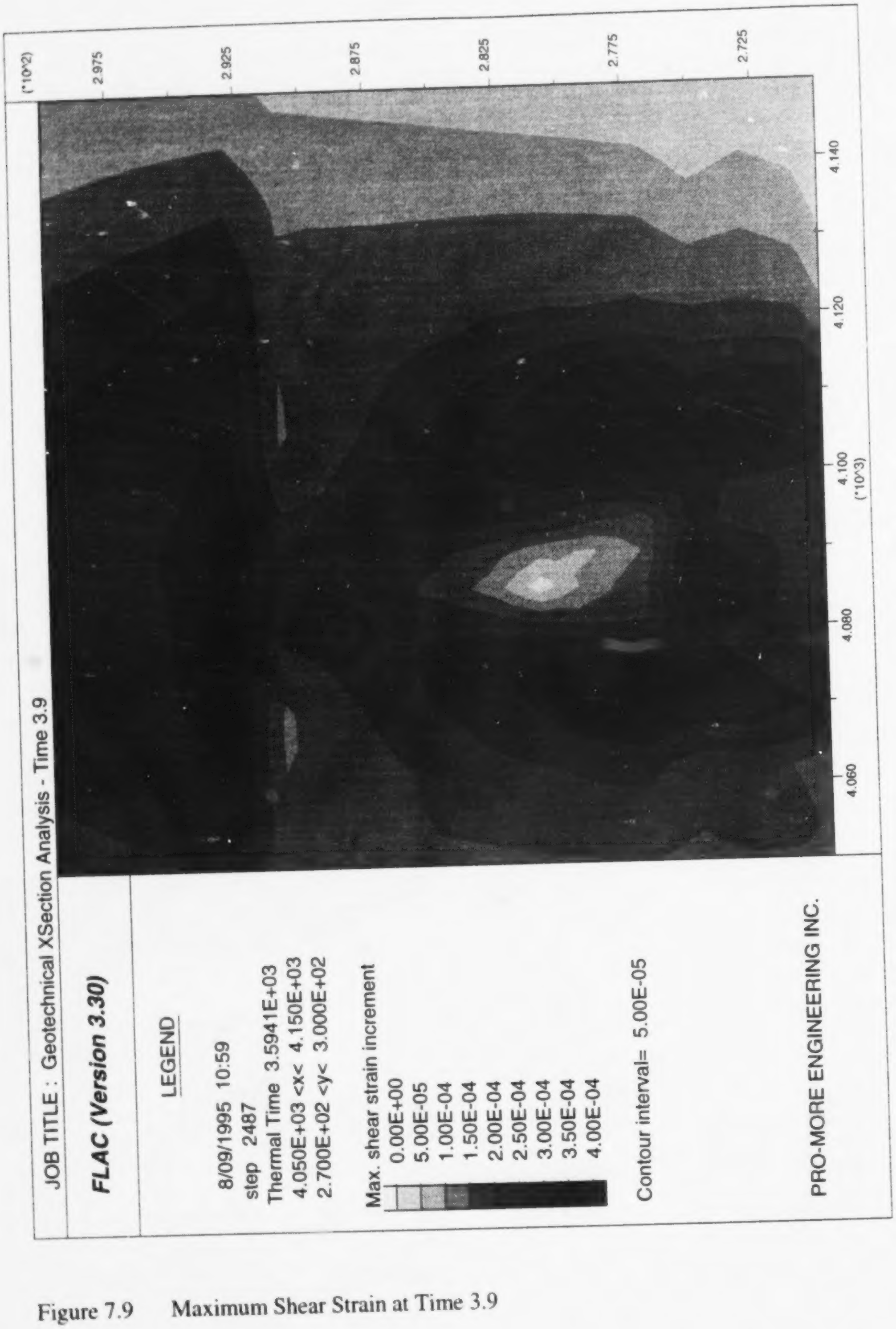

Figure 7.9 Maximum Shear Strain at Time 3.9

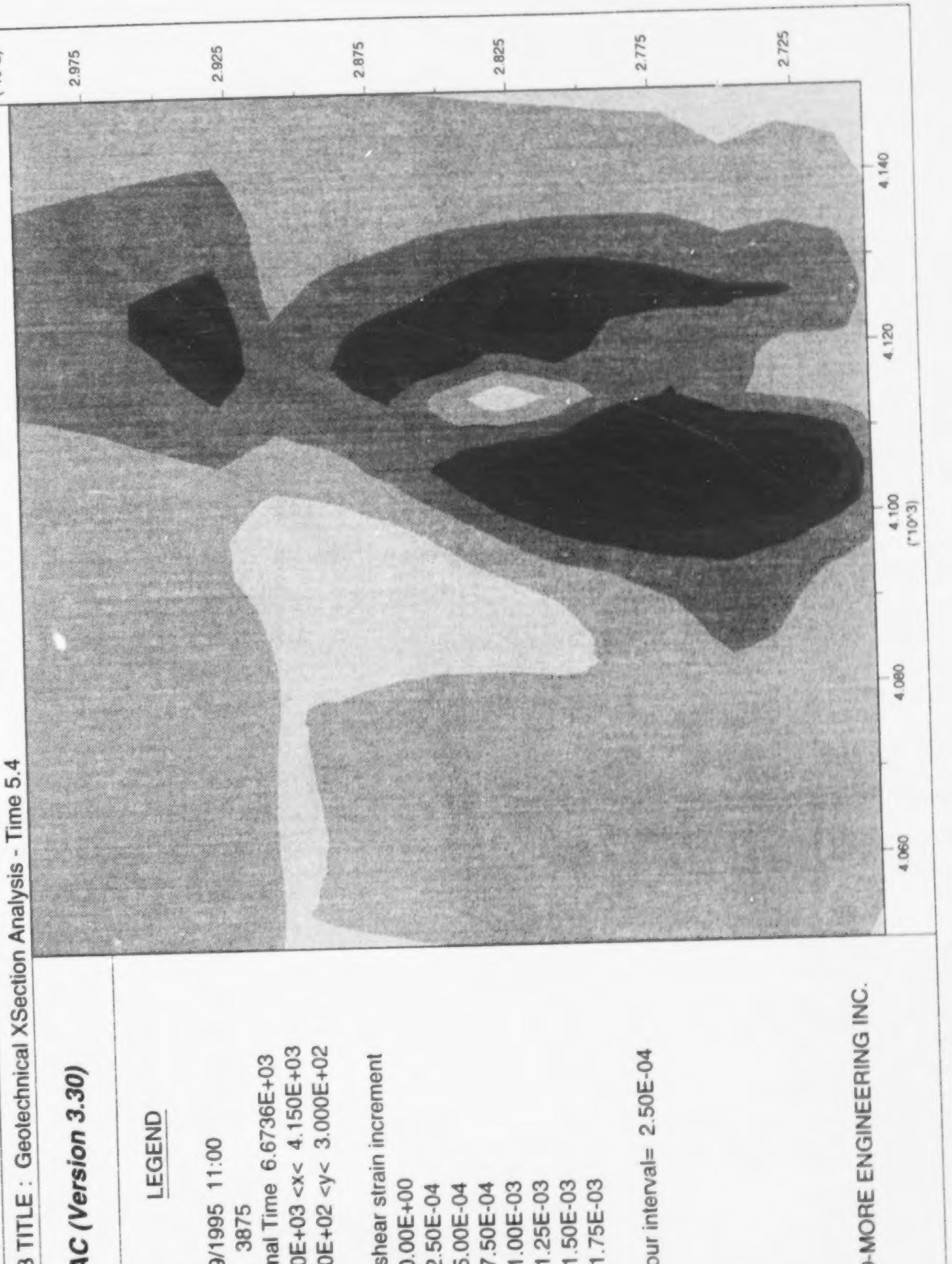

Figure 7.10 Maximum Shear Strain at Time 5.4

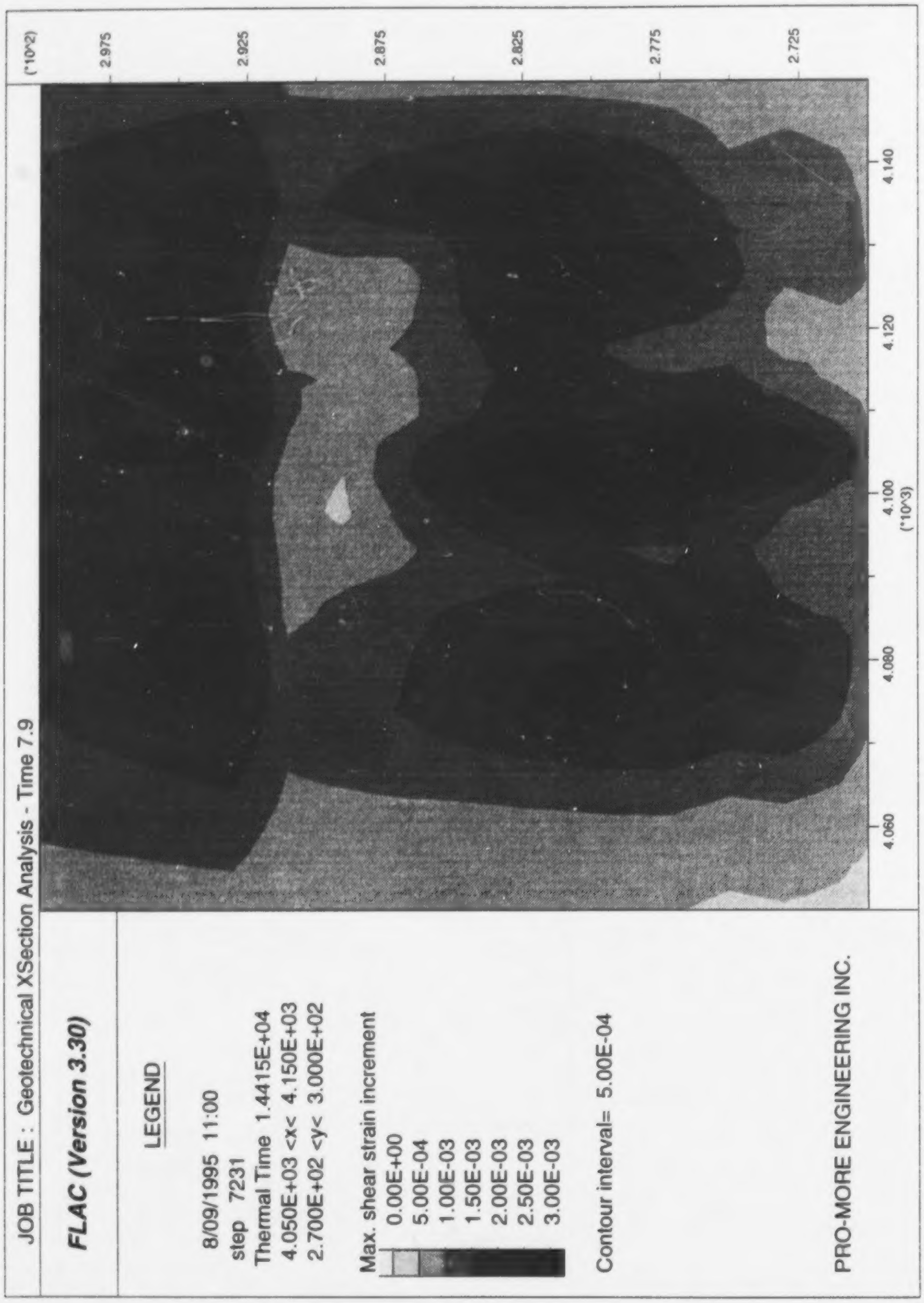

Figure 7.11 Maximum Shear Strain at Time 7.9

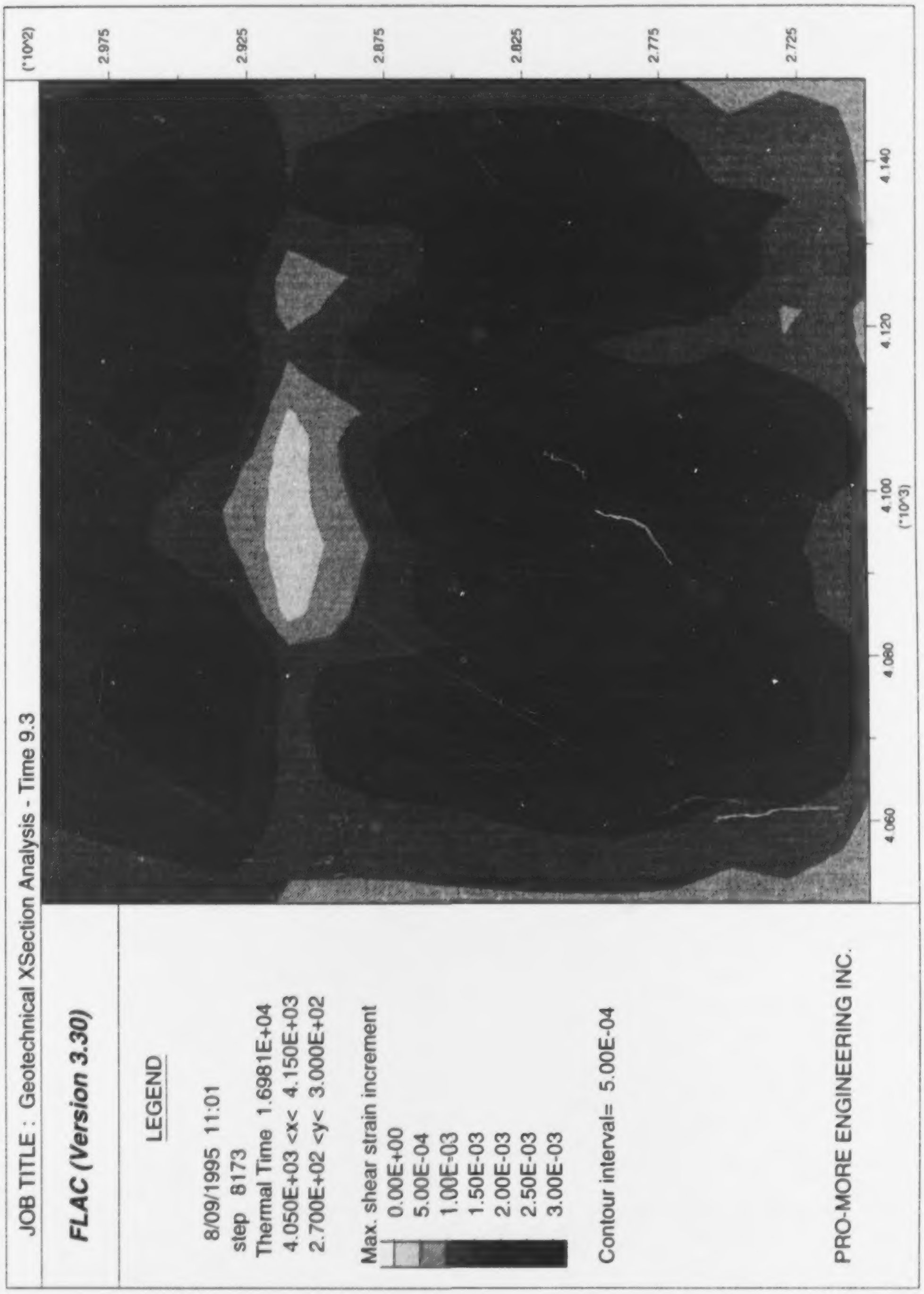

Figure 7.12 Maximum Shear Strain at Time 9.3

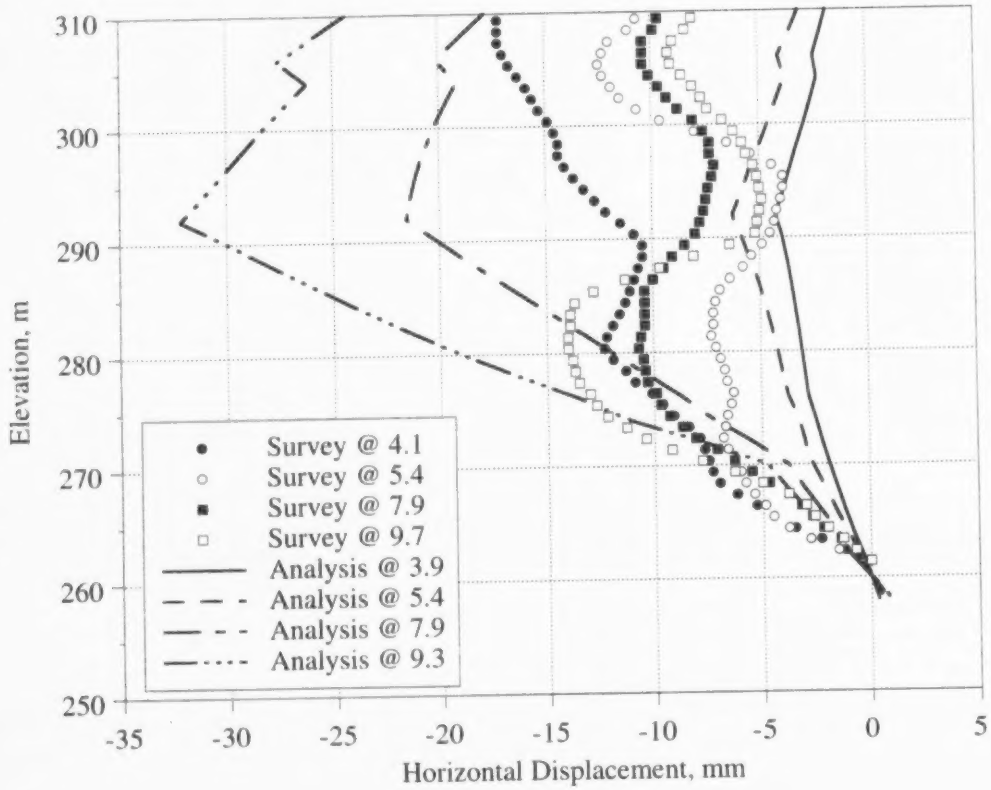

Figure 7.13 Comparison of Predicted versus Observed Horizontal Displacements at AGI1

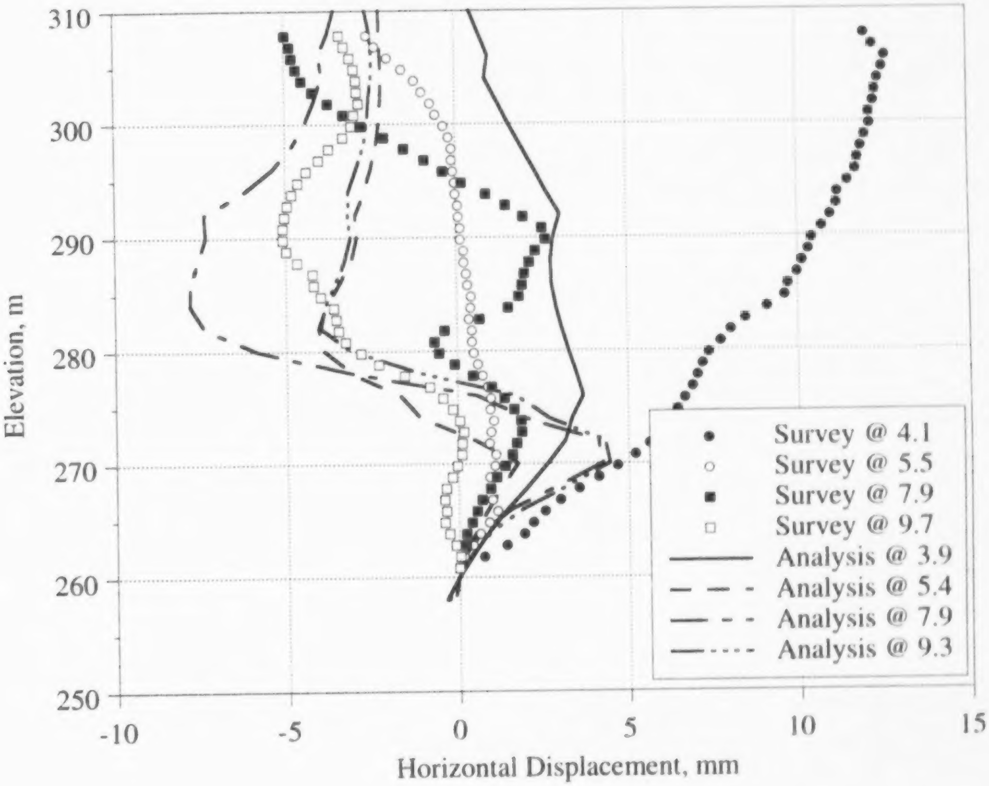

Figure 7.14 Comparison of Predicted versus Observed Horizontal Displacements at AGI2

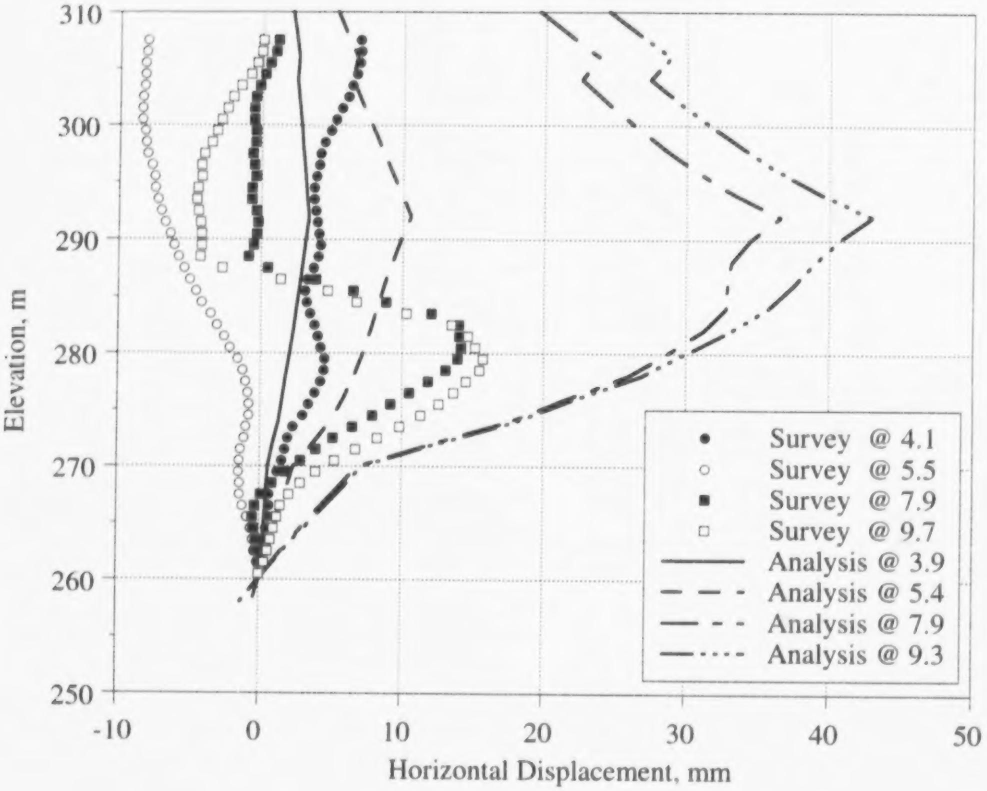

Figure 7.15 Comparison of Predicted versus Observed Horizontal Displacements at AGI3

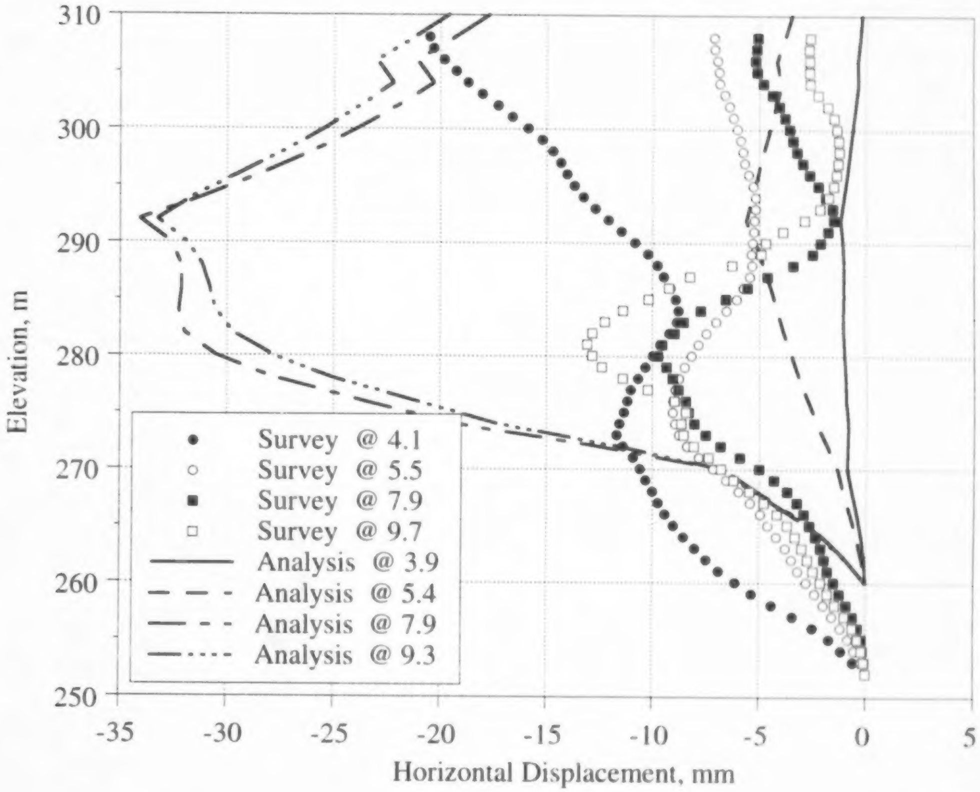

Figure 7.16 Comparison of Predicted versus Observed Horizontal Displacements at AT1

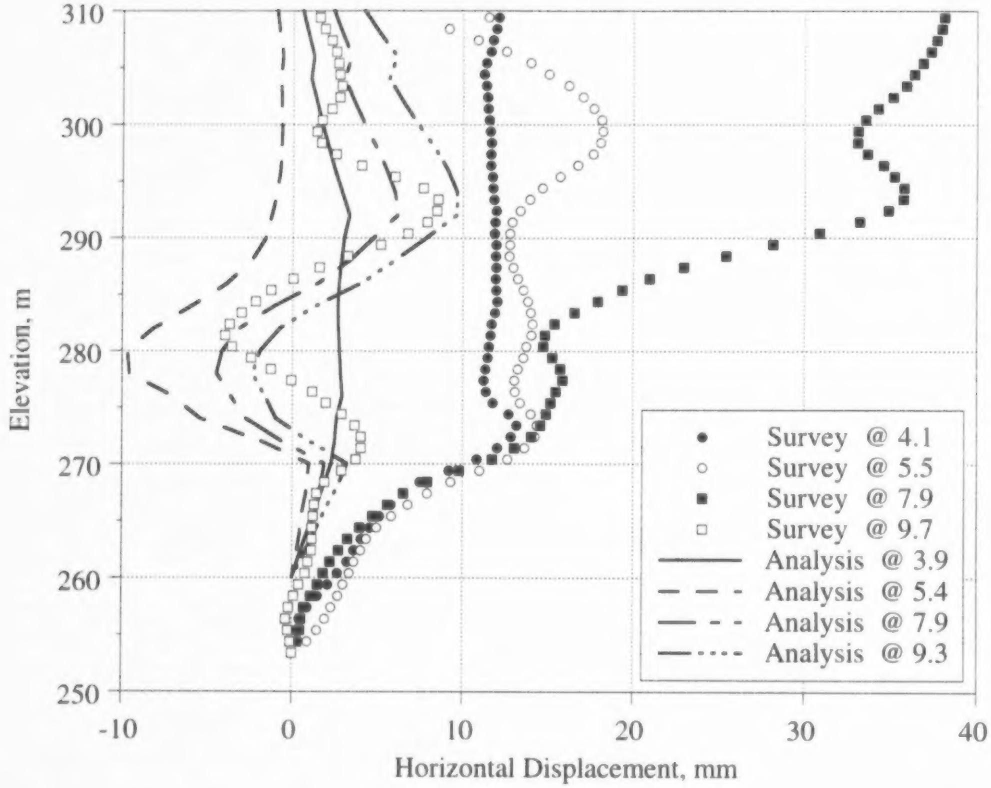

Figure 7.17 Comparison of Predicted versus Observed Horizontal Displacements at AT7

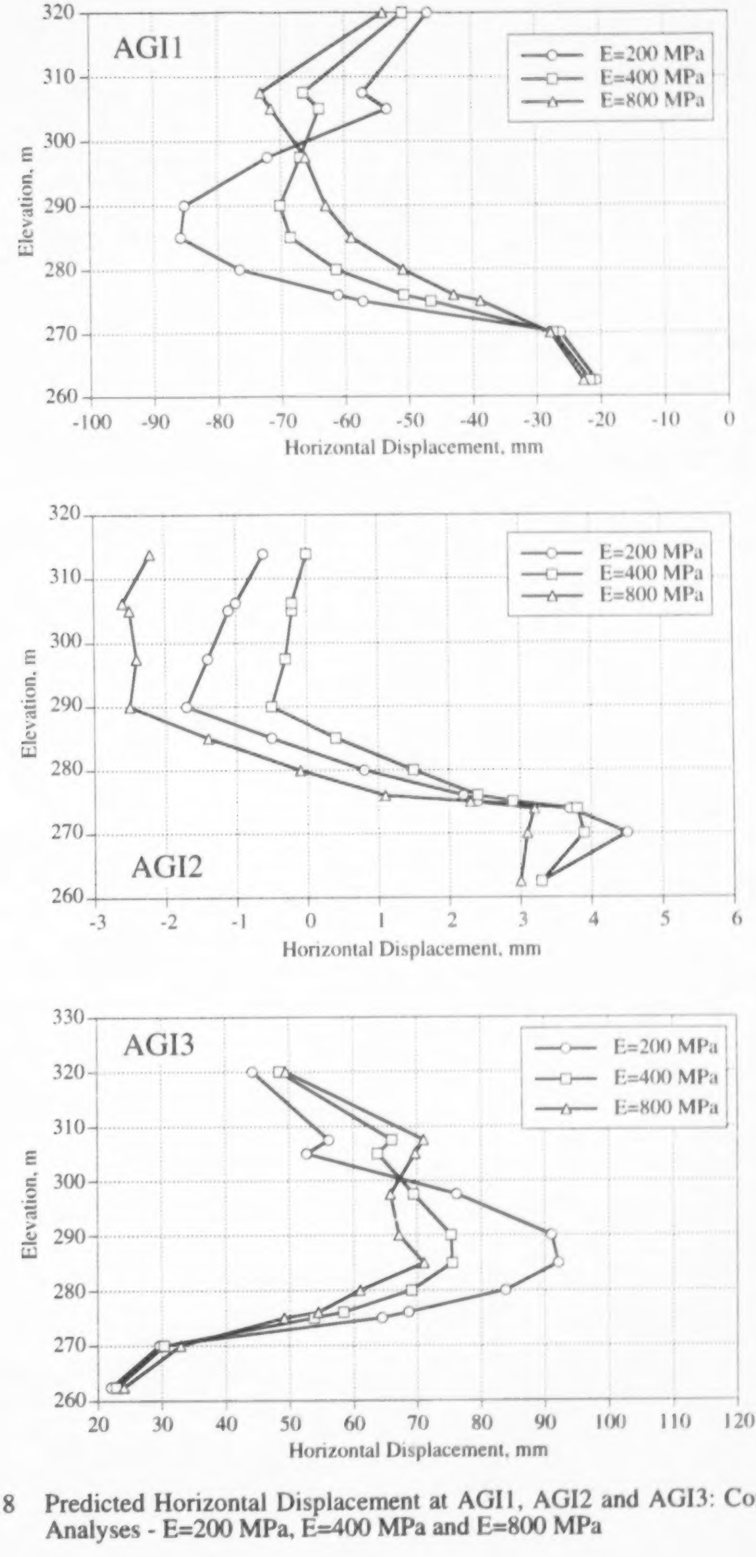

Figure 7.18 Predicted Horizontal Displacement at AGI1, AGI2 and AGI3: Constant Stiffness Analyses - E=200 MPa, E=400 MPa and E=800 MPa

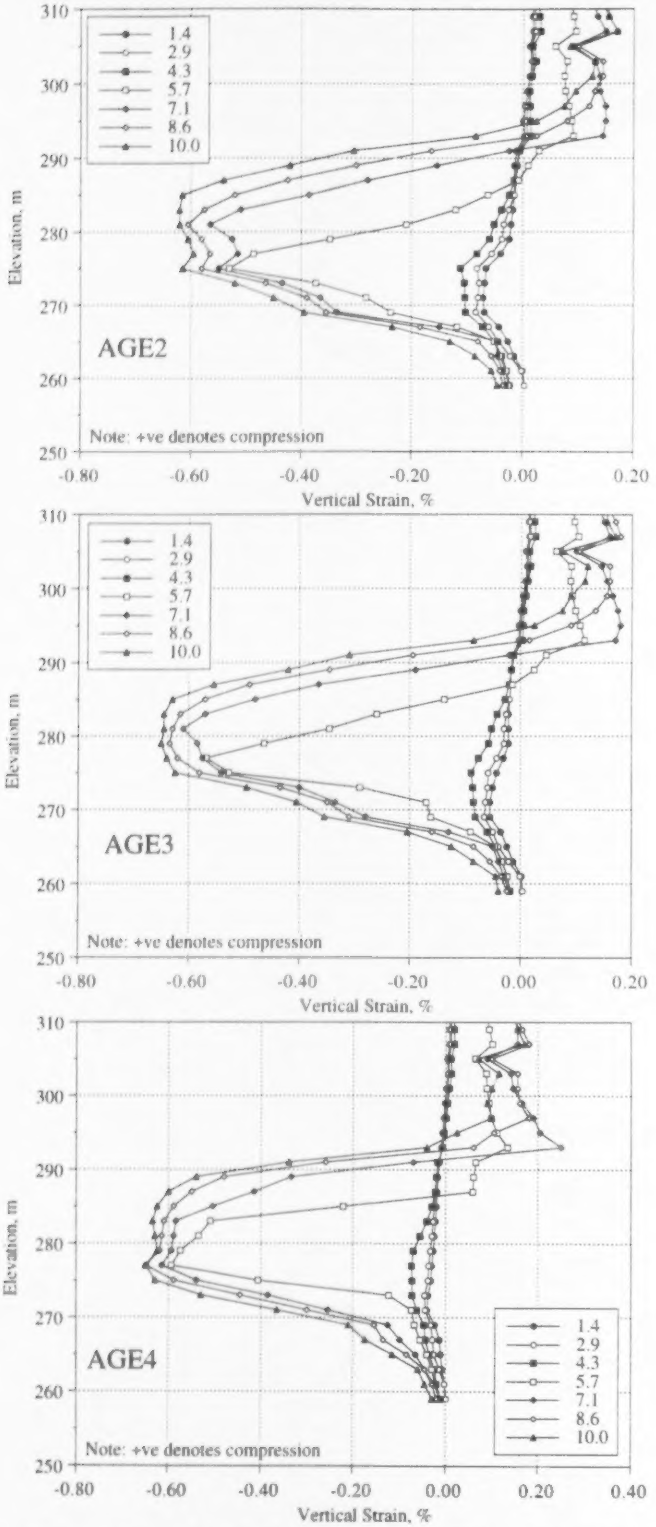

Figure 7.19 Predicted Vertical Strain Response at AGE2, AGE3 and AGE4

CHAPTER 8 CONCLUSIONS AND RECOMMENDATIONS

"Writing is easy; all you do is sit staring at a blank sheet of paper until drops of blood form on your forehead"
Gene Fowler

8.1 General

Joint Industry/AOSTRA economic studies in 1992 indicated that the SAGD process, when applied to larger scale operations (i.e. above 30,000 bbl/day), has the potential to produce bitumen from the Athabasca oil sands at a cost in the region of \$6/bbl to \$8/bbl; competitive with the best existing in situ oil sands development processes. Geological studies also showed that as much as half the Athabasca deposit may be accessible to the SAGD process (Rottenfusser and Hunt, 1991). In their review of the numerical simulation of the steam assisted gravity drainage process, Gittins et al., (1992) suggest that if economic performance combined with a high degree of predictability using numerical simulation can be demonstrated for commercial scale SAGD operations, then large scale commercial development using the SAGD process should rapidly follow. In a review of the Phase A SAGD test, Edmunds et al. (1991) state that very good numerical history matches were obtained by adjusting only the permeability distribution in the reservoir. Although not provided in the paper, it was stated that the range of permeability values required for the match correspond closely to the range of values measured in core samples. Siu et al. (1991) also state that vertical permeability within the reservoir was increased to improve history match results of the UTF SAGD results. So why geomechanics?

The answer to that question is embodied in the statements of Breitenbach (1991) in his state-of-the-art review of reservoir simulation. In reference to the history matching process of reservoir simulation, Breitenbach (1991) states that "after an acceptable history match is obtained, the model can be used to predict the future performance of a reservoir. The accuracy of these performance predictions will depend on how well the reservoir simulator matches the physics and fluid flow in the reservoir". The simulators used for history matching the UTF Phase A SAGD test do not include "geomechanical" physics. If the process of shear yield leading to shear induced volume changes and concomitant permeability enhancements was an integral component of the UTF Phase A SAGD process, then the implications of not including it in numerical simulations for process design in different reservoirs may have negative consequences.

The objective of this thesis has been to analyze experimental, numerical and field observations to determine the occurrence of geomechanical processes within the reservoir during the UTF Phase A SAGD test. It has been shown that formation displacements within the reservoir capable of significantly influencing reservoir properties, specifically absolute permeability, have occurred during the Phase A SAGD test. Vertical extensional strains of 2.5%, horizontal extensional strains of 0.3%, volumetric strains of 2.5% and a 30% increase in absolute permeability developed within the geotechnical cross section as a result of the steam assisted gravity drainage process.

The following sections provide specific conclusions regarding each component of the research; thermomechanical properties, numerical modeling and field observations of formation behavior.

8.2 Geomechanical Properties for SAGD Process

The thermomechanical properties of the UTF McMurray Formation oil sands, lower and upper McMurray Formation shale and the Waterways limestone have been characterized in an extensive laboratory testing program involving thermal expansion, thermal conductivity, compressibility, strength-deformation and gas evolution tests. The significance of each material property within the context of the SAGD process was discussed. The following summarizes the influence of these properties:

Thermal Volume Change:

- a relationship between the coefficient of pore volume thermal expansion, a value typically employed in reservoir simulators, and the coefficient of bulk thermal expansion, β_b , a value typically measured in geomechanical tests, was developed. Dramatic differences in the coefficient of pore volume thermal expansion can occur if careful attention is not given to the type of geomechanical test used in determining β_ϕ and the stress path followed within the reservoir;

- higher fines, low bitumen saturated oil sands will experience less cumulative volume change than low fines, high bitumen saturated oil sands. An average value of β_{cb}, the coefficient of constrained bulk thermal expansion, for low fines, rich oil sands was determined to be 6.0×10^{-5} °C^{-1}. For high fines oil sands, β_{cb} reduces to 3.0×10^{-5} °C^{-1}.

Thermal Conductivity:

- thermal conductivity of oil sands directly affects the steam front advance rate. It also affects the producing temperature of bitumen and condensate which is used as a process control variable (steam-trap control).

- for UTF McMurray Formation low fines, rich oil sands, k decreases from 1.7 W/m°C at 25°C to 1.5W.m°C at 225°C.

Compressibility:

- formation compressibility has a greater influence during the initial startup phase of the SAGD process than on long term production.

- the importance of recognizing the type of test from which compressibility was determined was discussed. In a constrained compression test a specimen experiences both shear strain and volume change, whereas during isotropic compression, a specimen does not undergo shear straining. As a result, the stress path followed by a specimen in each test is different and a distinction must be made between constrained compressibility and isotropic compressibility.

- a relationship between reservoir engineering "compressibility" and geotechnical engineering "compressibility was defined. Three coefficients of compressibility, namely rock (C_R), pore (C_ϕ) and bulk (C_b), were identified and an equation developed which described their interrelationship.

$$\phi_o C_R = (1-\phi_o)C_b - C_s = C_\phi$$

- isotropic bulk compressibility is a strong function of effective confining stress. As defined above, this creates a strong dependence of C_ϕ and C_R on effective confining stress. Consequently, reservoir simulations of SAGD must include the influence of effective confining stress in order to correctly simulate the compressibility behavior of oil sands. The following equation was developed for UTF McMurray Formation oil sands:

$$C_b = 0.6\text{x}10^{-6} + 2.5(\sigma'_m)^{-2} \quad [\text{kPa}^{-1}]$$

where σ'_m = mean effective stress [kPa].

Strength and Stress-Strain Behavior:

- For SAGD processes, it is the ***deformation*** response along a particular stress path that is of primary importance. If, under the actions of shear stress or changes in mean effective stress, reservoir deformations result in volumetric dilation or contraction, the porosity and hence k_a will be altered. Absolute permeability, k_a, which is inherently linked to porosity, imparts a substantial influence on the drainage of fluids from the reservoir. If SAGD processes create shear-induced volume changes within the ambient temperature zones of the reservoir, the effective permeability to water in this zone will increase dramatically. An increase in k_{ew} will increase the hydraulic conductivity and will permit injection pore pressures to migrate further into the reservoir. This leads to a reduction in effective confining stress, a reduction in strength and an increased propensity for volumetric deformations. These concurrent phenomena act to alter the reservoir conditions in advance of the steam chamber. Correctly identifying the magnitude of the strength-deformation behavior and its resulting impact on reservoir processes is important for understanding the effectiveness of the SAGD process.

Gas Evolution and Composition:

- the impact of non-condensable gases is greatest on the ceiling drainage rate and was found to be a complex function of the amount and composition of the gas, the permeability of the formation and time. In a high permeability sand ($k_v > 1$ d) , small amounts of gas greatly impede the rise rate of the steam chamber by preventing transport of steam to the advancing front. In a low permeability sand ($k_v < 1$ d), the presence of gas can actually improve drainage rates. Because steam transport is already restricted by the low permeability, a relatively thick zone of reservoir ahead of the front is heated by conduction to intermediate temperatures. This allows for the drainage of reasonably mobile oil (with respect to gas) before steam temperatures are achieved;

- two gas evolution tests and three gas composition tests were conducted on low fines, rich UTF McMurray Formation oil sands. A combined solubility coefficient of 0.16 cm^3/cm^3 @ 101 kPa was determined from the gas evolution tests. In reservoir engineering terms, the initial gas-oil ratio (GOR) of approximately 0.83 m^3/m^3 of pore liquid was also computed from these tests.

8.3 Geomechanical Modeling of SAGD Process

8.3.1 Parametric Analysis

To aid in determining fundamental geomechanical principles affecting the SAGD process and to gain insight into the reservoir response to thermal and pore pressure loading, a parametric analysis of the SAGD process was conducted. An ideal cross-section, with geologic simplicity and reasonable boundary conditions provided a problem of tractable size for analyses to identify the important and relevant geomechanical processes which are occurring during SAGD.

The parametric analyses revealed that for a series of horizontal wellpairs, zones of shear failure within the reservoir occur between wellpairs, *in advance of the steam chamber*. The primary geomechanical phenomena contributing to shear failure are:

- the shallow depth of the reservoir results in small increases in vertical total stress;

- opposing zones of thermal expansion from adjacent steam chambers cause large increases in the horizontal total stress; and

- the rapid advance of pore pressure ahead of the thermal front reduces the effective confining stress. For the UTF reservoir conditions, steam injection pressures were chosen very close to the total overburden stress creating low effective stress conditions within the reservoir.

Detailed examination of the results of a base case analysis and of a series of parametric analyses conducted to evaluate material property selection allowed the following observations:

- zones within the reservoir which undergo shear yield follow primarily an active compression stress path to failure. Following an extremely small volumetric contraction, dense oil sands dilate very quickly along the active compression stress path. The resulting shear induced volume changes lead to a 45% increase in the reservoir absolute permeability in advance of the steam chamber;
- early in the SAGD process, formation displacements are primarily horizontal or laterally outward from the wellpairs. At later times, in response to shear yield and an expanding steam chamber, the formation displacements are primarily vertical;
- at the wellpairs, the top of the steam chamber directly correlates with the elevation where vertical strains change from extension to compression; extension within the steam chamber, compression above the steam chamber;
- the development of extensional vertical strains midway between wellpairs occurs rapidly and exhibits high gradients of vertical strain;
- the zones of largest maximum shear strain correspond directly with zones undergoing shear yield;
- the selection of Young's modulus for oil sands has a significant effect on the stress-deformation response of the formation to SAGD;
- a high friction angle for oil sands combined with an active compression stress path results in relative insensitivity to the selection of K_0. The final extent of shear yield within the reservoir is not greatly affected for $1.0 \leq K_0 \leq 2.0$; and
- the selection of the coefficient of bulk thermal expansion significantly influences the predicted deformation response of the reservoir, the larger the coefficient, the larger the thermal induced stress increment and consequently, the larger the zone of shear yield.

8.3.2 Geotechnical Cross Section Analysis

A thermal-effective stress analysis of the geotechnical cross section was performed using field measured pore pressures and temperatures. In general, the mobilized strength was relatively low; the failure index never decreased below approximately 3.0. The distribution of γ_{max} compared well with the location of maximum mobilized strength and agrees reasonably well with the parametric analysis results presented in Chapter 5. The magnitude of γ_{max} however, is substantially lower than the predicted response from the parametric analyses.

Horizontal displacements were overpredicted and vertical strains were underpredicted by the thermal-effective stress analysis of the geotechnical cross-section. General conclusions from the analysis indicate that the deformation response within the geotechnical cross section are not due exclusively to the pore pressure and temperature changes measured within the geotechnical cross section. Consequently, an analysis of deformations within the geotechnical cross section will require the consideration of deformations along the wellpairs and the three dimensional growth of the steam chambers.

Analyses has revealed that formation yield *in front of* a growing steam chamber as opposed to *between* wellpairs contributes to the propagation of permeability enhanced zone in front of growing steam chambers.

8.4 Geomechanical Response of Reservoir to SAGD Process

The density of instrumentation wells within the UTF Phase A reservoir has permitted a detailed study of the evolution of pore pressure and temperature within the geotechnical cross section. The three dimensional growth of the steam chamber and the operational history of the wellpairs have been linked to the pore pressure and temperature within the geotechnical cross section to assist in the interpretation of geotechnical instrumentation results. The pore pressures increased in advance of the steam chamber boundaries and the resulting thermal front. In general, the distance between the pore pressure isobar equivalent to steam injection pressure and the temperature isotherm equivalent to steam temperature was approximately 20 m.

Pore pressure development during the startup phase for wellpair A1 clearly illustrated the large influence temperature has on bitumen viscosity and its concomitant impact on hydraulic conductivity. A temperature increase of 30°C is sufficient to reduce the bitumen viscosity such that the fluid mobility is increased and pore pressures can develop rapidly. A 30 °C temperature rise from 8 °C to 38°C will reduce the bitumen viscosity two orders of magnitude from 7,000,000 centipoise to approximately 70,000 centipoise.

Pore pressure reductions were measured within the geotechnical cross section as a result of a reduction in total mean stress caused by the expanding heated zone at the north end of wellpair A1. As vertical total stress is increased slightly near the newly growing steam chamber, minor reductions in vertical total stress occur beyond the steam chambers, which under undrained conditions, lead to small reductions in pore pressure.

A method was developed for interpreting the full strain field within the geotechnical cross section based on inclinometer and extensometer measurements. Uniqueness in the solution of vertical displacements from vertical strains was achieved by utilizing the results from a roof extensometer in an observation tunnel below the Phase A reservoir.

The behavior of the extensometers was complex, reacting to both temperature and pore pressure. A detailed review of the displacement history of each extensometer module revealed the complexity of their response to SAGD processes and highlighted their importance in understanding formation behavior, especially within the geotechnical cross section. A maximum vertical extensional strain of 2.5% was measured in the reservoir between wellpair A1 and A2.

A review of the design and construction of the extensometer modules discovered that elements within the extensometer design permitted displacement degrees of freedom which impacted the operation of the extensometer modules. For extension displacements, the rod of the LVDT can displace completely out of the LVDT body - there are no structural limitations to extension displacements. Beyond approximately 40 mm of extension, the calibration curve for the extensometer LVDT is nonlinear. A full displacement calibration curve was developed for the extensometers. For compression, the Invar rod separating module anchors will "shoulder" against the anchor after approximately 45 mm of compression effectively eliminating the possibility of monitoring compression behavior beyond this level.

Horizontal displacements within the geotechnical cross section were sensitive to both pore pressure and temperature changes. Early horizontal formation displacements were controlled primarily by pore pressure development within the reservoir. At later stages, the three dimensional steam chamber growth and the resulting thermal strains created a more complex horizontal displacement pattern. In general, thermal expansion controlled the direction of horizontal displacements in the latter stages of the Phase A test. Full strain field analyses showed a maximum horizontal extensional strain of -0.3% occurred within the reservoir.

Based on the full strain field analyses, a maximum shear strain of 3.0% and a volumetric strain of 2.6% occurred between wellpairs A1 and A2. Based on empirical correlation's linking absolute permeability change to volumetric strains, the absolute permeability within this region of the reservoir increased approximately 30%; increasing from 7.5 darcies to 9.8 darcies.

8.5 Recommendations for Further Research

The following recommendations may be useful for future studies of reservoir geomechanics related to SAGD or other processes:

- utilize a more complete constitutive model for the behavior of oil sands (e.g. Wan et al., 1989), with special emphasis on the volumetric behavior under isotropic and shear stress changes. This model could be used to conduct a three dimensional geomechanical history match analysis of the geotechnical instrumentation results.

- recent advances in the characterization of dense sands based on a state parameter and critical state soil mechanics and even more recently, a companion parameter to the state parameter, the reference stress ratio (RSR), may provide a better tool for understanding and representing the behavior of dense oil sands.

- The knowledge of the initial stress state in the reservoir and of the material properties is of fundamental importance both for understanding the formation behavior and modeling the process of SAGD. Utilizing a method of back analysis similar to that developed by Sakurai and Takeuchi (1983), the field measurements should be reanalyzed to derive the complete initial state of stress and material properties (i.e. Young's modulus).

REFERENCES

Aboustit, B.L., S.H. Advani, J.K. Lee and R.S. Sandhu, 1982. Finite Element Evaluations of Thermo-Elastic Consolidation. . Proc. 23rd US Symp. on Rock Mechanics: Issues in Rock Mechanics, Eds.Goodman and Heuze, Berkeley, pp. 587-595.

Agar, J.G., N.R. Morgenstern and J.D. Scott, 1986. Thermal Expansion and Pore Pressure Generation in Oil Sands. Can. Geot. J., Vol. 23, No. 3, pp. 327-333.

Agar, J.R., 1984. Geotechnical Behavior of Oil Sands at Elevated Temperatures and Pressures. Ph.D. dissertation, Department of Civil Engineering, University of Alberta, 906 p.

Aktan, T. and S.M. Farouq Ali, 1978. Finite Element Analysis of Temperature and Thermal Stresses Induced by Hot Water Injection., SPEJ, SPE 5765, Vol. 18, No. 6, pp. 457-469.

Amyx, J.W., D.M. Bass and R.L. Whiting, 1960. **Petroleum Reservoir Engineering**. McGraw-Hill, 99 p.

AOSTRA, 1990a. AOSTRA UTF Phase A Geotechnical Program, Volume 1: Main Report, Report Submitted to AOSTRA by Thurber Engineering, 120 p.

AOSTRA, 1990b. AOSTRA UTF Phase A Geotechnical Program, Volume 2: Instrumentation As-Built Report, Report Submitted to AOSTRA by Thurber Engineering, 120 p.

AOSTRA, 1990c. AOSTRA UTF Phase A Geotechnical Program, Volume 3: Instrumentation Data Report, Report Submitted to AOSTRA by Thurber Engineering, 120 p.

AOSTRA, 1990d. UTF Reservoir and Production Seminar, Confidential Report by N. Edmunds, N. Mukherjee, S. Gittins and B. Nzekwu, 161 p.

Aruna, M. N. Arihara and H.J. Ramey, Jr., 1977. The Effect of Temperature and Stress on the Absolute Permeability of Sandstones and Limestones. American Nuclear Society's Topical Meeting "Energy and Mineral Resource Recovery", CONF-770440, Colorado School of Mines, Golden, pp. 541-550.

Au, K.-S., 1983. The Strength-Deformation Properties of Alberta Oil Sands. M.Eng. Report, Department of Mineral Engineering, University of Alberta, 135 p.

Baldi, G., M. Borsetto, T. Hueckel and A. Peano, 1985. Coupling of Thermo-Plastic and Hydraulic Effects in a Clay Repository: Near Field Analysis. Proc. Int. Symp. on Coupled Processes Affecting the Performance of a Nuclear Waste Repository, 15 p.

Barnes, D.J., 1980. Micro-fabric and Strength Studies of Oil Sands. M.Sc. Thesis, University of Alberta, 244 p.

Beattie, C.I., T.C. Boberg and G.S. McNab, 1991. Reservoir Simulation of Cyclic Steam Stimulation in the Cold Lake Oil Sands. SPERE,SPE 18752, Vol. 6, No.2, pp. 200-206.

Blacic, J.D, P.H. Halleck, P. D'Onfro and R.E. Riecker, 1981. Thermomechanical Properties of Galesville Sandstone. Mechanical Behavior of Crustal Rocks, The Handin Volume, Geophysical Monograph 24, ed. Carter et al., Washington, pp. 153-159.

Branco, P., 1988. Isothermal Behavior of Gassy Soils. Ph.D. dissertation, Department of Civil Engineering, University of Alberta, 723 p.

Breitenbach, E.A., 1991. Reservoir Simulation: State of the Art. JPT, SPE 23472, September, pp. 1033-1036.

Butler, R.M. and C.T. Yee, 1986. A Theoretical Study of Steam Condensation in the Presence of Non-Condensible Gases in Porous Solids. AOSTRA Journal of Research, Vol. 3, No. 1.

Butler, R.M. and D.J. Stephens, 1981. The Gravity Drainage of Steam-Heated Heavy Oil to Parallel Horizontal Wells. JCPT, pp. 90-96.

Butler, R.M., 1981. New Interpretation of the Meaning of the Exponent "m" in the Gravity Drainage Theory for Continuously Steamed Wells. Proc. 2nd World Congress on Chemical Engineering, Vol. 2, Montreal, pp. 430-433.

Butler, R.M., 1986. The Expansion of Tar Sands During Thermal Recovery. JCPT, Vol. 25, No. 5, pp. 51-56.

Butler, R.M., 1992. "Steam-Assisted Gravity Drainage- Concept, Development, Performance and Future". Proc. 9th Annual Heavy Oil and Oil Sands Technical Symposium, Calgary, 24 p.

Butler, R.M., G.S. McNab and H.Y. Lo, 1981. Theoretical Studies on the Gravity Drainage of Heavy Oil During Steam Heating. Can. J. Chem. Eng., Vol. 59, pp. 455-460.

Byrne, P.M. and T.L. Eldridge, 1982. A Three Parameter Dilatant Elastic Stress-Strain Model for Sand. Int. Symp. Num. Models in Geomechanics, Zurich, pp. 73-80.

Byrne, P.M., H. Cheung and L. Yan, 1986. Soil Parameters for Deformation Analysis of Sands: Version 2. Soil Mechanics Series No. 104, Department of Civil Engineering, University of British Columbia, 41 p.

Byrne, P.M., H. Cheung and L. Yan, 1987. Soil Parameters for Deformation Analysis of Sand Masses. Can. Geot. Journal, Vol. 24, No. 3, pp. 366-376.

Campanella, R.G. and J.K. Mitchell, 1968. Influence of Temperature Variations on Soil Behavior. J. Soil Mech. and Found. Eng., ASCE, Vol. 94, No. SM3, pp. 709-734.

Carter, J.P. and J.R. Booker, 1987. Finite Element Analysis of Fully Coupled Transient Thermoelasticity. Proc. Int. Conf. Num. Methods in Engng: Theory and Applications, Swansea, Eds. Pande and Middleton, Vol. II, Paper T25, 8 p.

Chalaturnyk, R.J. and J.D. Scott, 1991. Evaluation of Reservoir Properties from Geomechanical Tests. Journal of Canadian Petroleum Technology, Vol. 31, No. 5, pp. 31-41.

Chalaturnyk, R.J. and J.D. Scott, 1995. Geomechanics Issues of Steam Assisted Gravity Drainage. Proc. SPE Int. Heavy Oil Symposium, SPE 30280, Calgary, pp. 319-333.

Charlwood, R.G., Byrne, P.M., D.W. McKinlay and E. Varoglu, 1980. Thermal-Geomechanical Analyses and Criteria for the Design of a Mine Assisted Heavy Oil Recovery Facility. Proc. Applied Oilsands Geoscience Conf., Edmonton, 56 p.

Chen, W.F., 1984. Constitutive Modelling in Soil Mechanics. Mechanics of Engng Materials, Chapter 5, eds. C.S Desai and R.H. Gallagher, pp. 91-120.

Chinna, H.S. and D.K. Bassi, 1987. UTF Project: Well AGP4 Mini Frac Tests - October 20-21, 187, Report to AOSTRA, 192 p.

Cividini, A., L. Jurina and G. Gioda, 1981. Some Aspects of Characterization Problems in Geomechanics. Int. J. Rock Mech. Min. Sci. & Geomech. Abstr., Vol. 18, pp. 487-503.

Cundall, P. and M. Board, 1988. A Microcomputer Program for Modeling Large Strain Plasticity Problems. Proc. 6th Int. Conf. Num. Methods in Geom., Vol. 3, pp. 2101-2108.

de Alencar, J.A., Jr., 1988. Deformation of Dams on Sheared Foundations. Ph.D. dissertation, Department of Civil Engineering, University of Alberta, 295 p.

Denbina, E.S., T.C. Boberg and M.B. Rotter, 1991. Evaluation of Key Reservoir Drive Mchanisms in the Early Cycles of Steam Stimulation at Cold Lake. SPERE, SPE ????, Vol 6, No. 2, pp. 207-211.

Dusseault, M.B, 1977. The Geotechnical Characteristics of the Athabasca Oil Sands, Ph.D. dissertation, Department of Civil Engineering, Unversity of Alberta, 653 p.

Dusseault, M.B. and L. Rothenburg, 1988. Shear Dilatancy and Permeability Enhancment in Oil Sands. Proc. 4th UNITAR/UNDP Conference on Heavy Crude and Tar Sands, Vol. I, Paper No. 32, 14 p.

Dusseault, M.B. and N.R. Morgenstern, 1978. Shear Strength of Athabasca Oil Sands. Can. Geot. J., Vol. 15, pp. 216-238.

Dusseault, M.B. and N.R. Morgenstern, 1979. Locked Sands. Q. Jl. Engng Geol., Vol. 12, pp. 117-131.

Edmunds, N.R, J.A. Kovalsky, S.D. Gittins and E.D. Pennachioli, 1992. Review of the Phase A Gravity Drainage Test: AOSTRA UTF. Proc. SPE Thermal Operations Symposium, SPE 21529, 16 p.

Edmunds, N.R. and P.M. Collins, 1989. Mechanics of the Steam Assisted Gravity Drainage Process at the AOSTRA UTF. Internal Report, AOSTRA, 103 p.

Edmunds, N.R. and S.D. Gittins, 1991. Effective Steam Assisted Gravity Drainage to Long Horizontal Well Pairs. Proc. CIM/AOSTRA 1991 Technical Conference, Banff, Vol. II, Paper 91-65, 13 p.

Edmunds, N.R., J.A. Haston and D.A. Best, 1988. Analysis and Implementation of the Steam Assisted Gravity Drainage Process at the AOSTRA UTF. Proc. 4th UNITAR/UNDP Conference on Heavy Crude and Tar Sands, Vol. 2, Paper No. 125, 17 p.

Finol, A. and S.M. Farouq Ali, 1975. Numerical Simulation of Oil Production with Simultaneous Ground Subsidence. SPEJ, Vol. 15, pp. 411-424.

Fung, L. S.-K., 1992. A Coupled Geomechanic-Multiphase Flow Model for Analysis of In Situ Recover in Cohesionless Oil Sands. JCPT, Vol. 31, No. 6, pp. 56-67.

Geraminegad, M. and S.K. Saxena, 1986. A Coupled Thermoelastic Model for Saturated-Unsaturated Porous Media. Geotechnique, Vo. 36, No. 4, pp. 539-550.

Gittins, S.D., N.R. Edmunds and N.J. Mukherjee, 1992. Numerical Simulation of the Steam Assisted Gravity Drainage Process at the Underground Test Facility. IEA Collaborative Project on Enhanced Oil Recovery Workshop and Symposium, Banff, September, Goldsmith, A.S., 1989. Permeability Decline and Compressibility in Sandstone Reservoir Rocks. Proc. ISRM-SPE Int. Symposium Rock at Great Depth,Vol. 2 Balkema, pp. 923-928.

Green, G.E. and D.W. Reades, 1975. Boundary Conditions, Anisotropy and Sample Shape Effects on the Stress-Strain Behavior of Sand in Triaxial Compression and Plane Strain. Geotechnique, Vol. 25, No. 2, pp. 333-356.

Green, S.L., 1984. The Behaviour of Deep Ocean Sediments in Response to Thermo-Mechanical Loading. Ph.D. dissertation, University of California, Berkley.

Gretener, P.E., 1981. Reflections on the Value of Laboratory Tests on Rocks. Mechanical Behavior of Crustal Rocks, The Handin Volume, Geophysical Monograph 24, ed. Carter et al., Washington, pp. 323-326.

Gronseth, J.M., 1989. Geomechanics Monitoring of Cyclic Steam Stimulation Operations in the Clearwater Formation. CIM District 4 Meeting, Calgary, October, Paper No. 34, 9 p.

Hardin, B.O., 1989. Low Stress Dilation Test. ASCE J. of Geot. Engng., Vol. 115, No. 6, pp. 769-787.

Hardy Associates (1978) Ltd., 1984. AOSTRA Underground Testing Facility Data Report No. 4: Hydrogeologic Studies. Report Submitted to AOSTRA, 168 p.

Hart, R.D. and C.M. St. John, 1981. A Fully Coupled Thermal-Hydraulic-Mechanical Model for Non-Linear Geologic Systems. Proc. 22nd US Symposium on Rock Mechanics, Cambridge, pp. 90-96.

Houston, S.L. and N.D. Williams, 1985. Thermo-Mechanical Behavior of Seafloor Sediments. Journal of Geotechnical Engineering, Vol. 111, No. 11, pp. 1249-1262.

Hyne, J.B., J.W. Gredidanus, J.D. Tykrer, D. Verona, C. Rizek, P.D. Clark, R.A. Clarke and J. Koo, 1982. Aquathermolysis of Heavy Oils. Proc. 2nd Int. Conf. on Heavy Crude and Tar Sands Proceedings, UNITAR, Caracas, February, pp. 404-411.

Itasca, 1995. FLAC: Fast Lagrangian Analysis of Continua. Volume I User's Manual.

Ito, Y., 1984. The Introduction of the Microchanneling Phenomenon to Cyclic Steam Stimulation and Its Application to the Numerical Simulator (Sand Deformation Concept), SPEJ, August, pp. 417-429.

Jing, X.D., J.S. Archer and T.S. Daltaban, 1992. Laboratory Study of the Electrical and Hydraulic Properties of Rocks Under Simulated Reservoir Conditions. Marine and Petroleum Geology, Vol. 9, April, pp. 115-127.

Khatrush, S.A., 1987. The Yielding of a Fine Sand in Triaxial Stress Space. Ph.D. dissertation, Department of Civil Engineering, University of Surrey, 300 p.

Kosar, K.M., 1989. Geotechnical Properties of Oil Sands and Related Strata. Ph.D. dissertation, Department of Civil Engineering, University of Alberta, 795 p.

Kovari, K., 1977. The Elasto-Plastic Analysis in the Design Practice of Underground Openings. Chapter 12 in Finite Elements in Geomechanics, ed. G. Gudehus, Wiley, pp. 377-412.

Kumar, P. and B. Singh, 1989. Thermal Stress Analysis of Underground Openings. Int. J. Num. Analy. Meth. Geom., Vol. 13, No. 4, pp. 411-425.

Lade, P.V. and R.B. Nelson, 1987. Modelling the Elastic Behavoiur of Granular Materials. Int. J. Num. Analytical Methods in Geom., Vol. 11, pp. 521-542.

Lade, P.V., R.B. Nelson and Y.M. Ito, 1987. Nonassociated Flow and Stability of Granular Materials. ASCE Jour. of Engng. Mech., Vol. 113, No. 9, pp. 1302-1318.

Laing, J.M., J.D. Scott, A.W. Stokes, J.C. Suggett and D.F. Wood, 1988. Geotechnical Instrumentation of the AOSTRA Mine-Assisted Underground Steaming Trial. Proc. 4th UNITAR/UNDP Conference on Heavy Crude and Tar Sands, Vol. 2, Paper No. 112, 18 p.

Larsson, H., R. Glamheden and G. Ahrling, 1989. Storage of Natural Gas at High Pressue in Lined Rock Caverns - Rock Mechanics Analysis. Proc. Storage of Gases in Rock Caverns, Balkema, pp. 177-184.

Lewis, R.W., C.E. Majorana and B.A. Schrefler, 1986. A Coupled Finite Element Model for the Consolidation of Nonisothermal Elastoplastic Porous Media. Transport in Porous Media, Vol. 1, No. 2, pp. 155-178.

Lo, K.Y., R.S.C. Wai, R.K. Rowe and L. Tham, 1982. Nonlinear Thermo-Mechanical Behavior and Stress Analysis in Rocks. Proc. 23rd US Symp. on Rock Mechanics, Berkeley, pp. 620-627.

Matsuoka, H. and T. Nakai, 1982. A New Failure Criterion for Soils in Three-Dimensional Stress Space. Proc. IUTAM Conf. on Deformation and Failure of Granular Materials, Delft, Balkema, pp. 253-263.

McKay, J.G., 1989. Undistrubed Oil Sand Sampling and Sample Quality Evaluation. M.Sc. dissertation, Department of Civil Engineering, University of Alberta, 227 p.

Morgenstern, N.R. and J.D. Scott, 1985. Numerical Analysis of Fully Coupled Heat Consolidation. Progress Report on Geotechnical Properties of Oil Sands at High Pressure and Temperature, AOSTRA, 86 p.

Mori, A. and T. Masahito, 1986. Effect of Dilatancy on Permeability in Sands Stabilized by Chemical Grout. Soils and Foundations, Vol. 26, No. 1, pp. 96-104.

Noorishad, J., C.F. Tsang and P.A. Witherspoon, 1984. Coupled Thermal-Hydraulic-Mechanical Phenomena in Saturated Fractured Porous Rocks: Numerical Approach. J. Geophy. Res., Vol. 89, No. B12, pp. 10,365-10,373.

Peacock, D., 1986. Gas Evolution in Athabasca Oil Sands. M.Sc. Thesis, University of Alberta, 341 p.

Plewes, H.D., 1987. Undrained Strength of Athabasca Oil Sands. M.Sc. Thesis, University of Alberta, 428 p.

Rhett, D.W. and L.W. Teufel, 1992. Effect of Reservoir Stress Path on Compressibility and Permeability of Sandstones. Proc. 67th SPE ATCE, SPE 24756, Washington, pp. 965-972.

Robinson, D.B and Associates, 1985. The Volume and Composition of Gases Dissolved In-Situ in Athabasca Tar Sand. Report written to Syncrude Canada Ltd., 87 p.

Rottenfusser, B.A., D.K. Cotterill and C.R. Kidston, 1990. Geology of AOSTRA Underground Test Facility: Facies and Depositional Environments. Alberta Research Council Report submitted to AOSTRA, 91 p. + Maps.

Rottenfusser, B.A., J.E. Palfreyman and N.K. Alwast, 1988. Geology of the AOSTRA Undergound Test Facility Site. Proc. 4th UNITAR/UNDP Conference on Heavy Crude and Tar Sands, Vol. II, Paper No. 115, 21 p.

Rottenfusser, B.A., N.K. Alwast, C.R. Kidston and D.K. Cotterill, 1989. Geology of UTF Phase A. Alberta Research Council Report submitted to AOSTRA, 36p. + Maps.

Rottenfusser, B.A., N.K. Alwast, C.R. Kidston and D.K. Cotterill, 1989. Appendices A to E: Geology of UTF Phase A. Alberta Research Council Report submitted to AOSTRA.

Rottenfusser, B.A., N.K. Alwast, C.R. Kidston and D.K. Cotterill, 1989. Appendix F: Geology of UTF Phase A. Alberta Research Council Report submitted to AOSTRA.

Rubin, B. and W.L. Buchanan, 1985. A General Purpose Thermal Model. SPEJ, SPE 11713, Vol. 25, No. 2, pp. 202-214.

Sakurai, S. and K. Takeuchi, 1983. Back Analysis of Measured Displacements of Tunnels. Rock Mechanics and Rock Engineering, Vol. 16, pp. 173-180.

Scott, J.D. and A.C. Seto, 1986. Thermal Property Measurements on Oil Sands. JCPT, Vol. 25, No. 6, pp. 70-77.

Scott, J.D., D. Adhikary and S.A. Proskin, 1991. Volume and Permeability Changes Associated with Steam Stimulation in an Oil Sands Reservoir. Proc. CIM/AOSTRA 1991 Technical Conference, Paper No. 91-63,

Scott, R.F., 1985. Plasticity and Constitutive Relations in Soil Mechanics. ASCE J. Geot. Engng., Vol. 111, No. 5, pp. 563-605.

Settari, A., 1988. Modeling of Fracture and Deformation Processes in Oil Sands. Proc. 4th UNITAR/UNDP Conference on Heavy Crude and Tar Sands, Vol. I, Paper No. 43, 14 p.

Settari, A., 1989. Physics and Modeling of Thermal Flow and Soil Mechanics in Unconsolidated Porous Media. Proc. Symposium on Reservoir Simulation, SPE 18420, Houston, pp. 155-168.

Settari, A., P.R. Kry and C.-T. Yee, 1988. Coupling of Fluid Flow and Soil Behavior to Model Injection into Unconsolidated Oil Sands. JCPT, Vol. 28, No. 1, pp. 81-92.

Siu, A.L., L.X. Nghiem, S.D. Gittins, B.I. Nzekwu and D.A. Redford, 1991. Modelling Steam-Assisted Gravity Drainage Process in the UTF Pilot Project. Proc. 66th Annual SPE Tech. Conf. and Exhibition, SPE 22895, Dallas, pp. 129-138.

Sobkowicz, J.C. , 1982. The Mechanicsl of Gassy Sediments. Ph.D. dissertation, Department of Civil Engineering, Unversity of Alberta, 531 p.

Sterne, K.B., 1981. Hollow Cylinder Testing of Oil Sands. M.Sc. Thesis, University of Alberta, 228 p.

Terzaghi, K. and R.B. Peck, 1967. **Soil Mechanics in Engineering Practice**. Wiley & Sons, New York, 729 p.

Thurber, 1989. Mini-Frac Testing: Well AO-83, UTF Site, January, 1989. Report Submitted to AOSTRA, 19 p.

Tortike, W.S. and S.M. Farouq Ali, 1991. Prediction of Oil Sand Failure Due to Steam-Induced Stresses. JCPT, Vol. 30, Jan-Feb, pp. 87-96.

Tortike, W.S., 1991. Numerical Simulation of Thermal, Multiphase Fluid Flow in an Elastoplastic Deforming Oil Reservoir. Ph.D. dissertation, Department of Mining, Metallurgical and Petroleum Engineering, University of Alberta, 429 p.

Towson, D.E. and T.C. Boberg, 1967. Gravity Drainage in Thermally Stimulated Wells. Proc. 18th Annual Tech. Mtg., Petroleum Soc. of CIM, Banff, 6 p.

Vaziri-Zanjani, H.H., 1986. Nonlinear Temperature and Consolidation Analysis of Gassy Soils. Ph.D. dissertation, Department of Civil Engineering, University of British Columbia, 357 p.

Vermeer, P.A. and R. de Borst, 1984. Non-Associated Plasticity for Soils, Concrete and Rock. HERON, Vol. 29, No. 3, 63 p.

Wan, R., D.H. Chan and K.M. Kosar, 1989. A Constitutive Model for the Effective Stress-Strain Behaviour of Oil Sands. Proc. 4th Annual CIM Tech. Mtg., Banff, Vol. II, Paper No. 89-40-66.

Williams, N., 1982. The Effects of Elevated Temperature on the Engineering Properties of Seafloor Sediments. Ph.D. dissertation, University of California, Berkley.

Wong, R.C.K., W.E. Barr and P.R. Kry, 1993. Stress-Strain Response of Cold Lake Oil Sands. Can. Geot. J., Vol. 30, No. 2, pp. 220-235.

Wood, D.M., 1984. Choice of Models for Geotechnical Predictions. Mechanics of Engng Materials, Chapter 32, eds. C.S Desai and R.H. Gallagher, pp. 633-654.

Zimmerman, R.W., 1982. Compressibilities and Effective Stress Coefficients for Linear Elastic Porous Solids: Lower Bounds and Results for the Case of Randomly Distributed Spheroidal Pores. Proc. 23rd US Symp. on Rock Mechanics, Berkeley, pp. 712-718.

Zimmerman, R.W., 1989. Thermal Conductivity of Fluid-Saturated Rocks. J. of Petroleum Science and Eng., Vol. 3, pp. 219-227.

Zoback, M.D. and J.D. Byerlee, 1975. Permeability and Effective Stress. The American Association of Petroleum Geologiest, Geologic Notes, pp. 154-158.

APPENDIX A

Field Thermocouple Results

One hundred and twenty seven thermocouple measurement points, divided into 14 strings of up to 12 sensors each, were installed in 14 wells. Each thermocouple string was sealed inside 1/8" diameter inconel-sheathed magnesium oxide-insulated cable up to an elevation where negligible temperature increases would occur. The type J thermocouples were created by joining the tips of a copper wire and a constantan wire. All thermocouple strings were suspended inside open casings except for wells AT9, AT4, AT12 and AT14, where the thermocouples were cemented in the hole along with piezometers. Occasional problems were encountered with fluid in the open casing flashing to steam and masking any temperature profile within the well. These problems were generally overcome by blowing the well dry. A traversing thermocouple string was also available for monitoring temperatures in any open cased wells. The general accuracy of thermocouples can be considered as ± 2°C.

The following plots provide the raw data records of the temperature history measured for each thermocouple well.

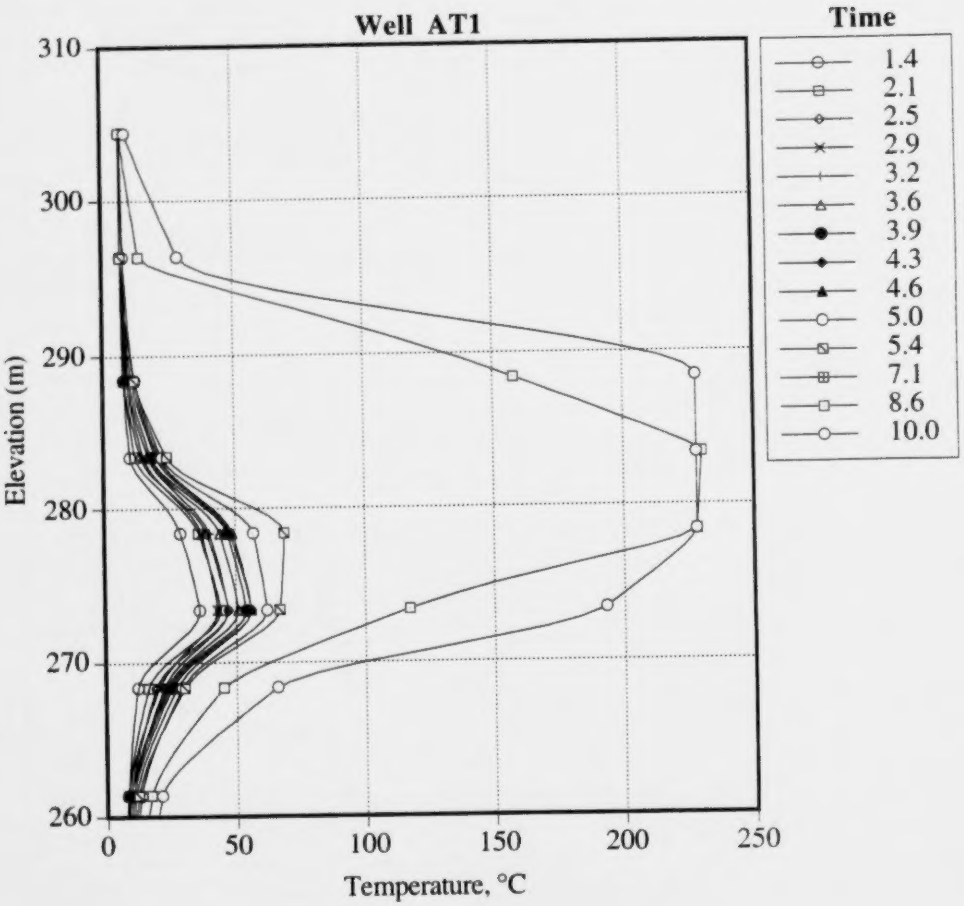

Figure A1 Temperature Profile in Well AT1

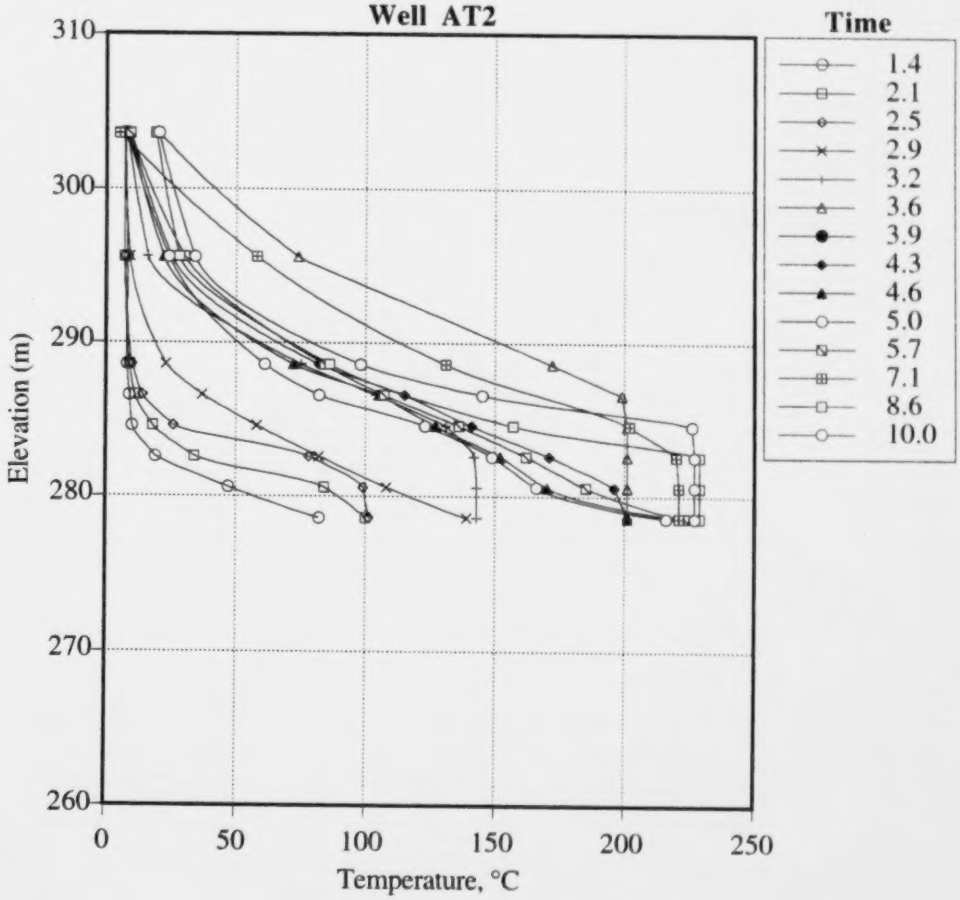

Figure A2 Temperature Profile in Well AT2

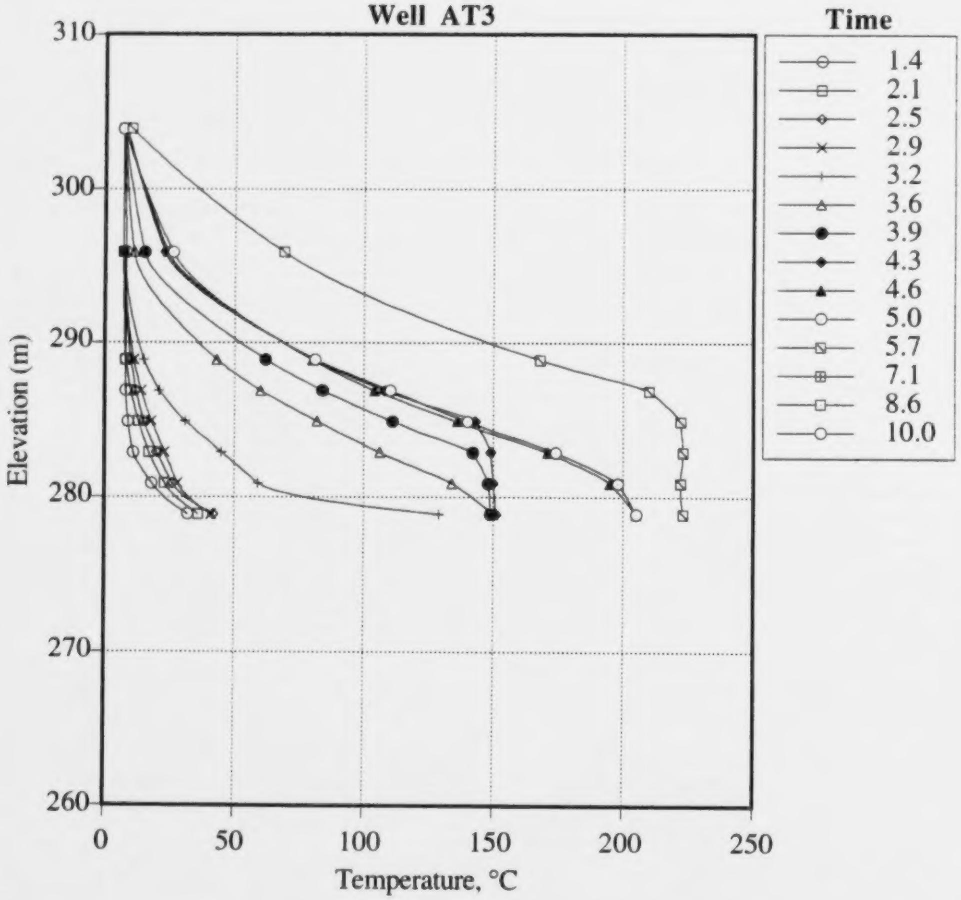

Figure A3 Temperature Profile in Well AT3

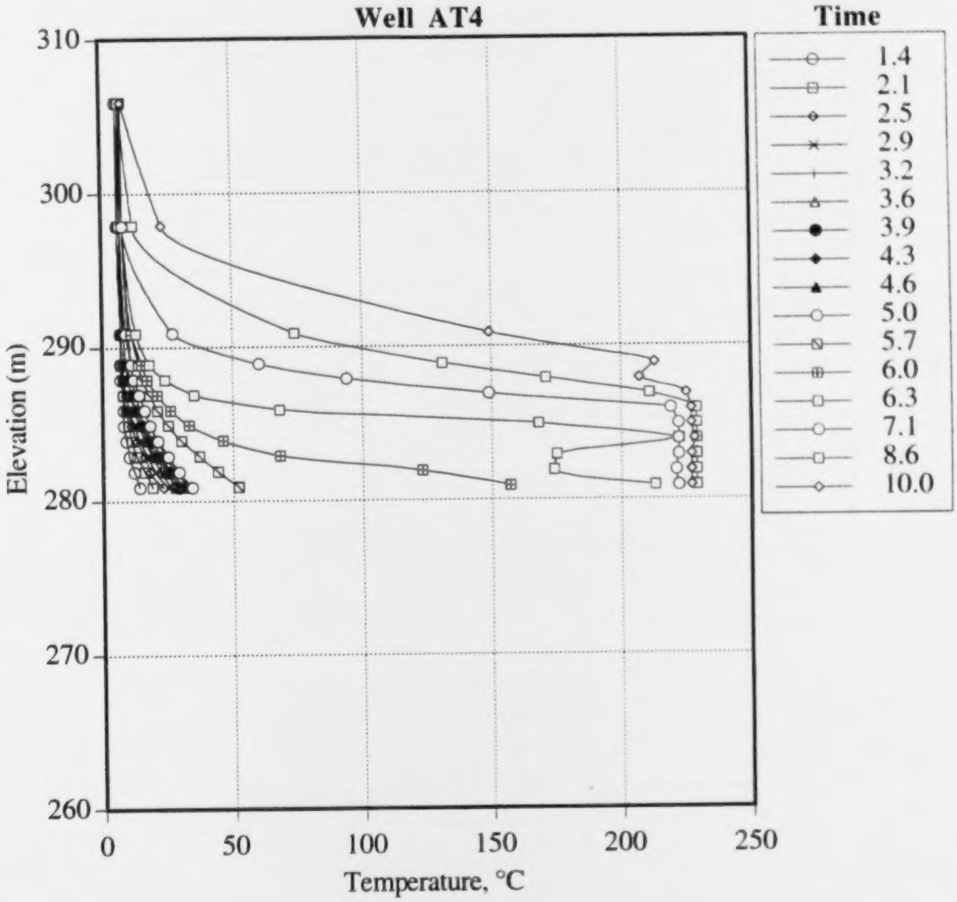

Figure A4 Temperature Profile in Well AT4

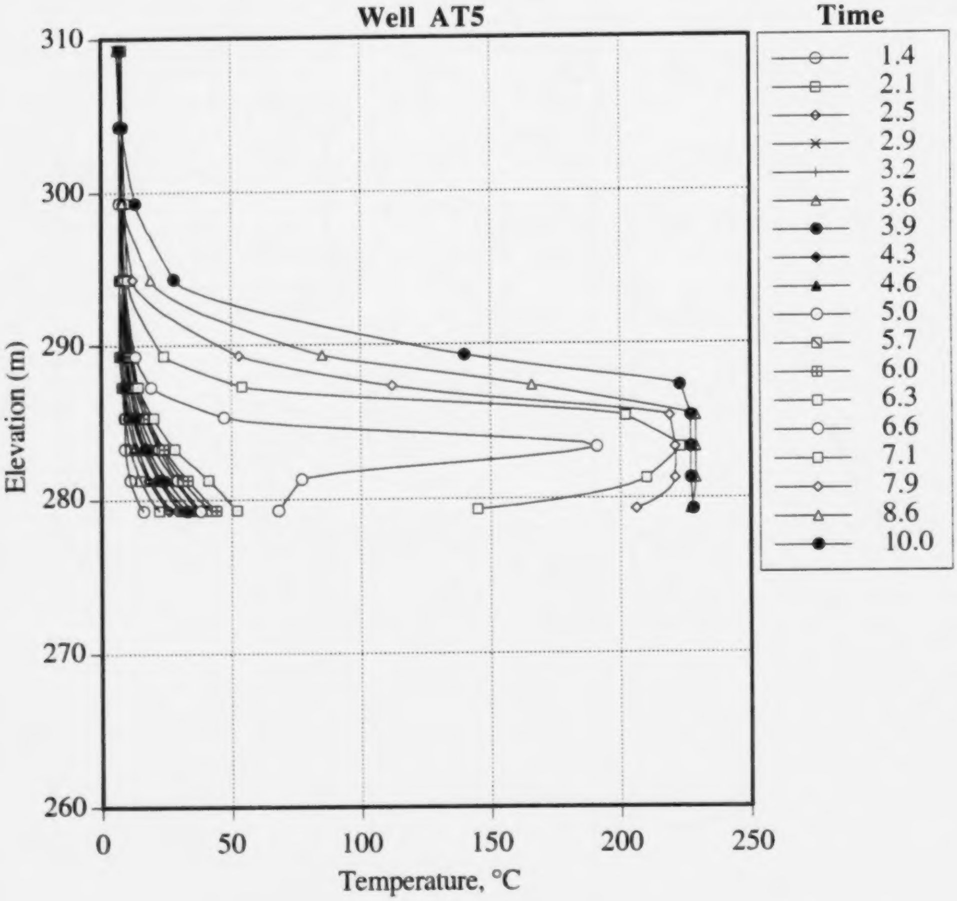

Figure A5 Temperature Profile in Well AT5

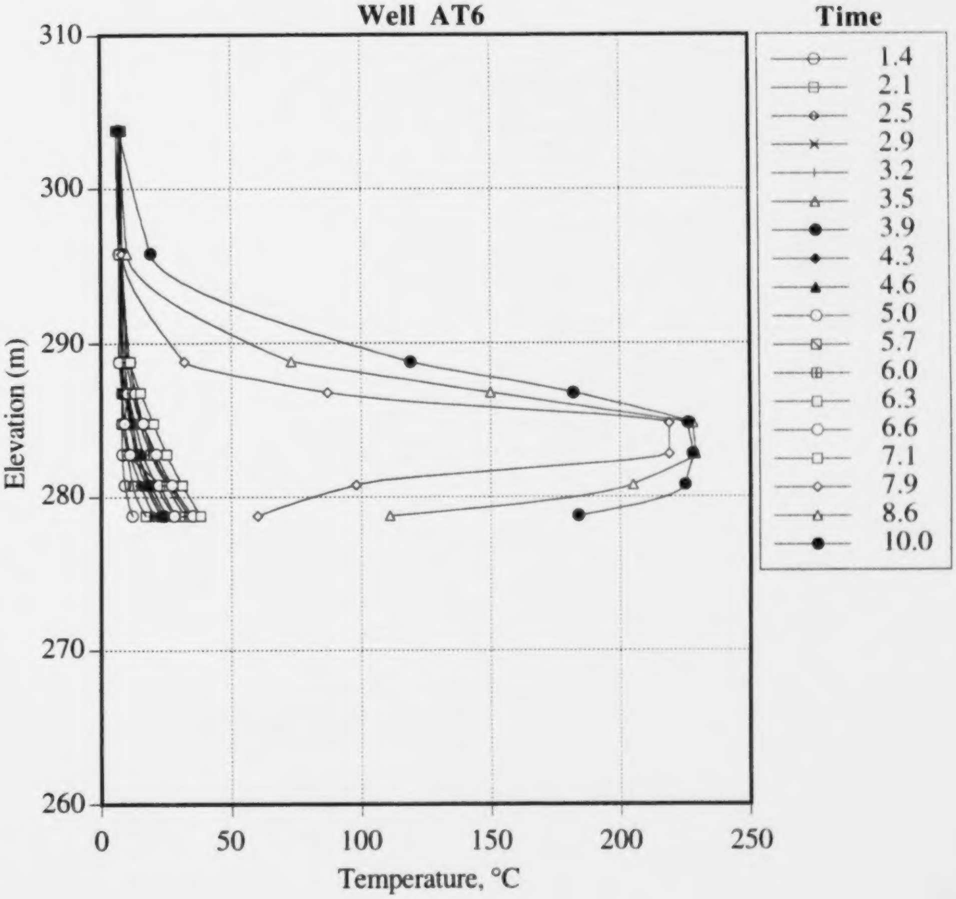

Figure A6 Temperature Profile in Well AT6

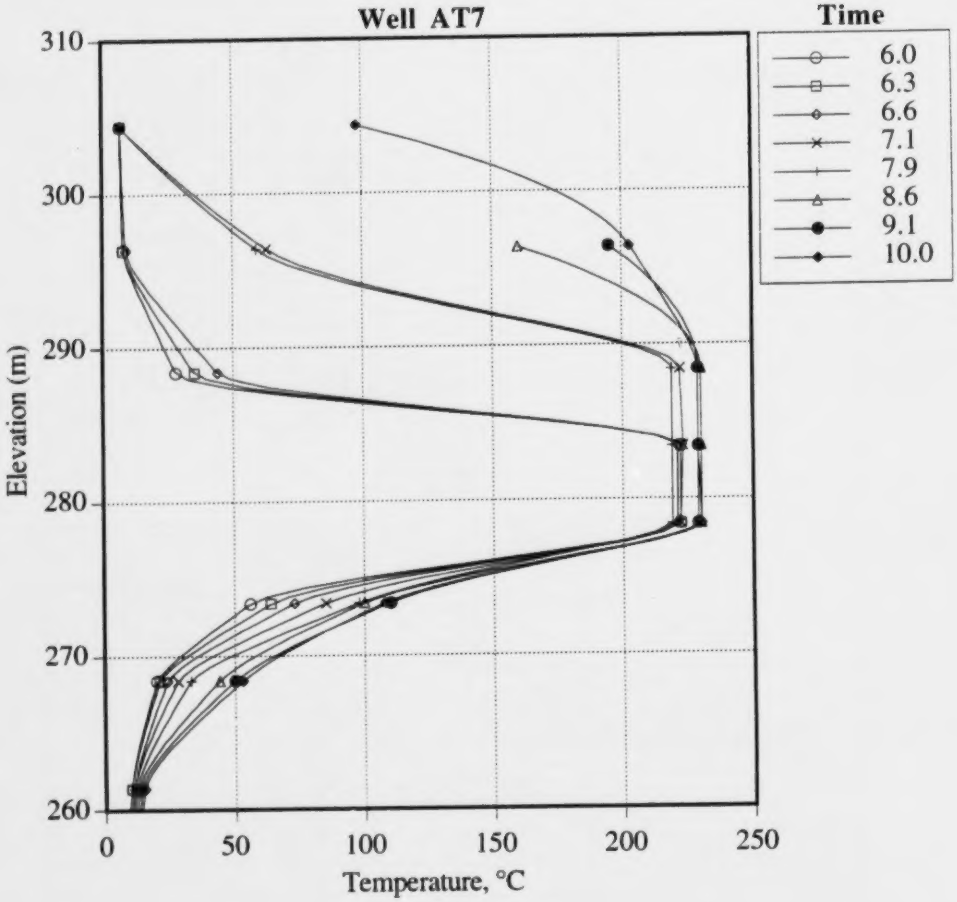

Figure A7 Temperature Profile in Well AT7

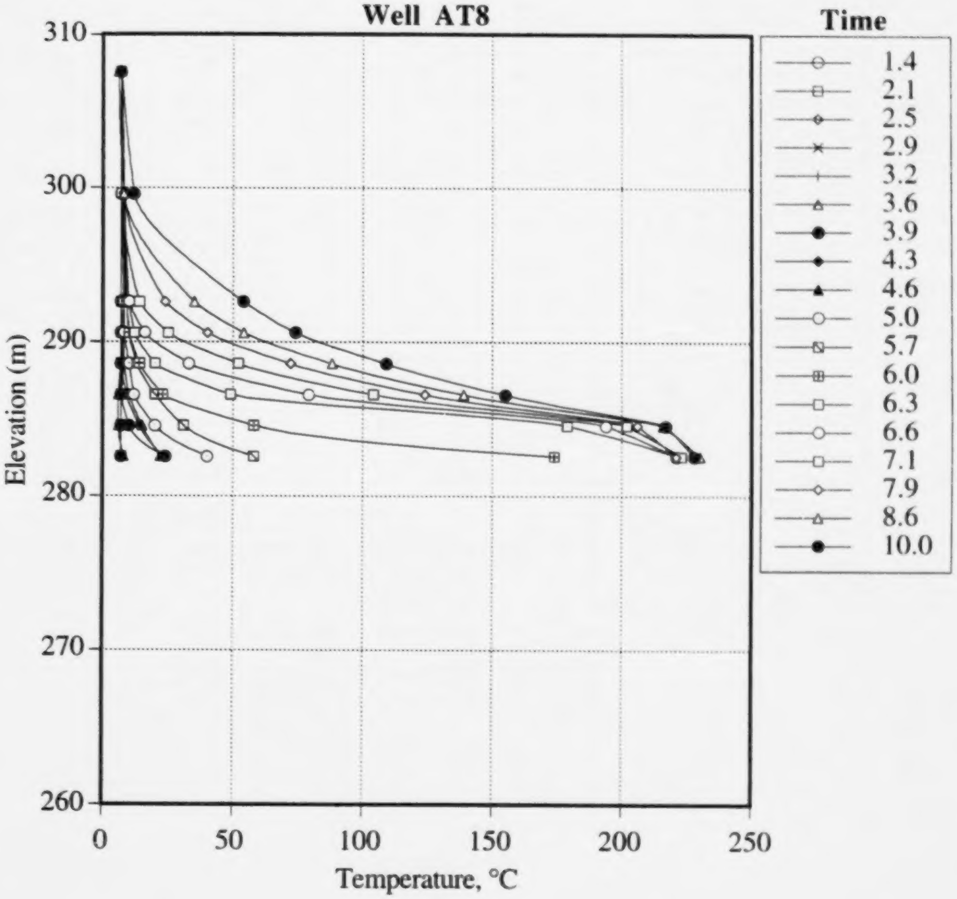

Figure A8 Temperature Profile in Well AT8

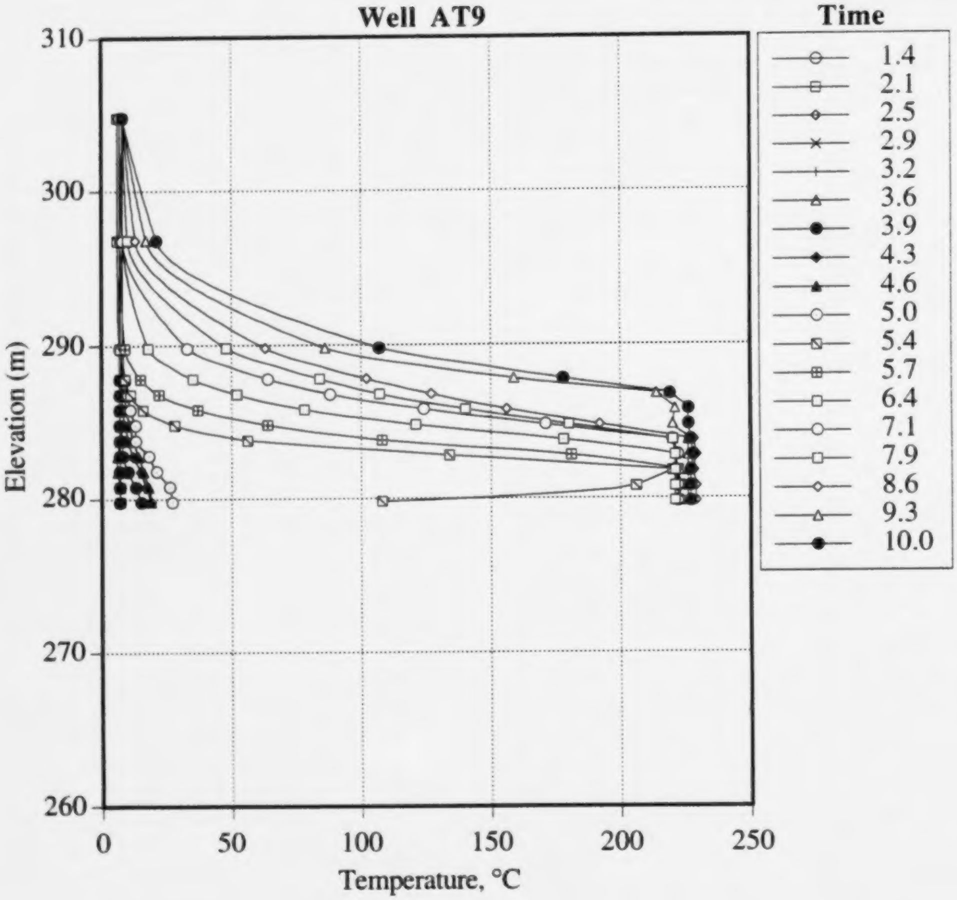

Figure A9 Temperature Profile in Well AT9

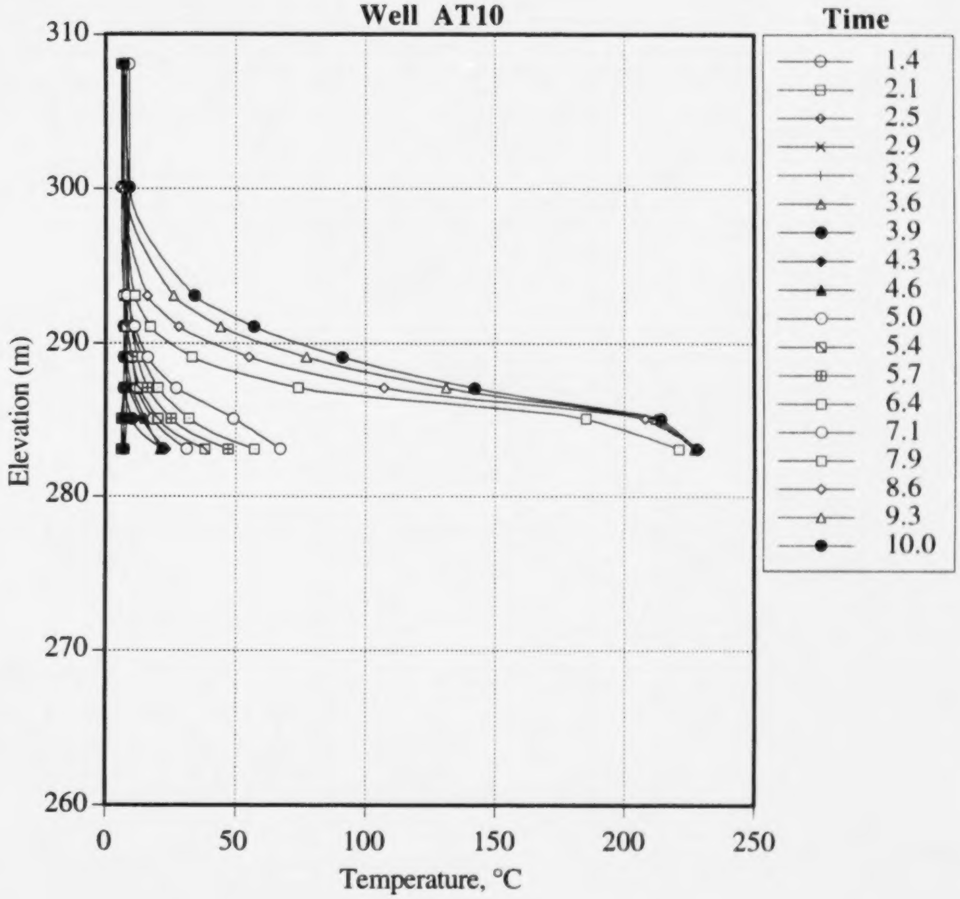

Figure A10 Temperature Profile in Well AT10

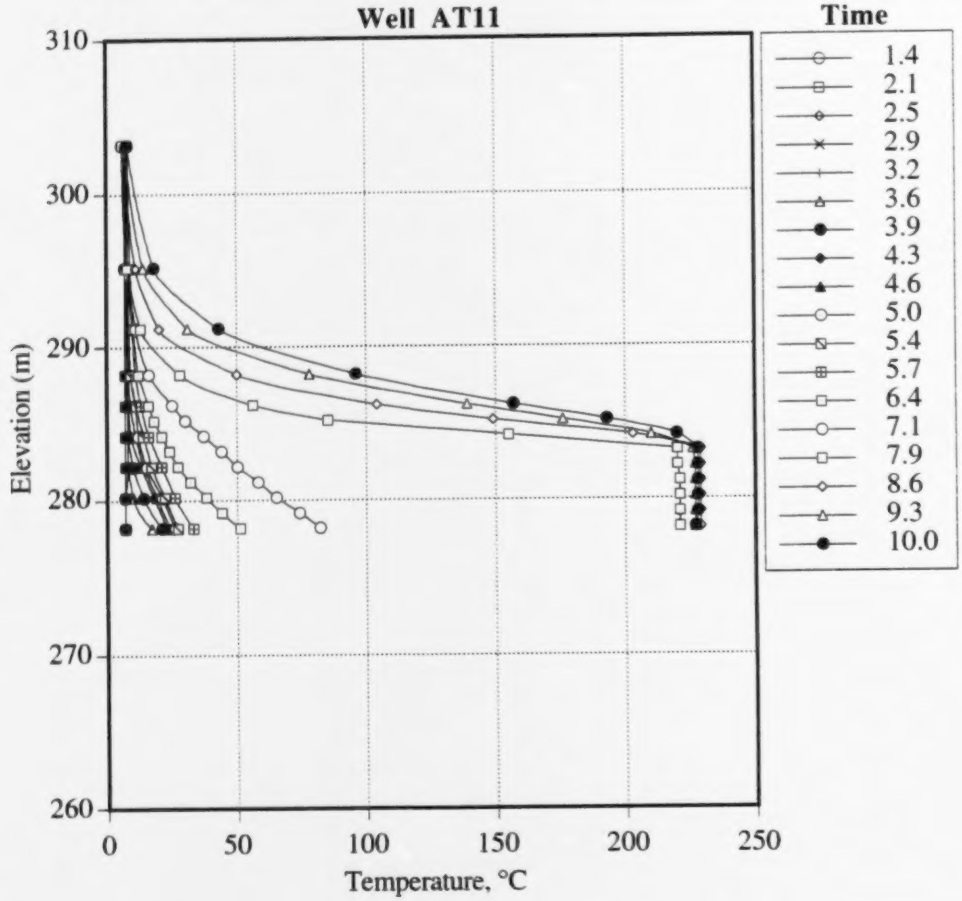

Figure A11 Temperature Profile in Well AT11

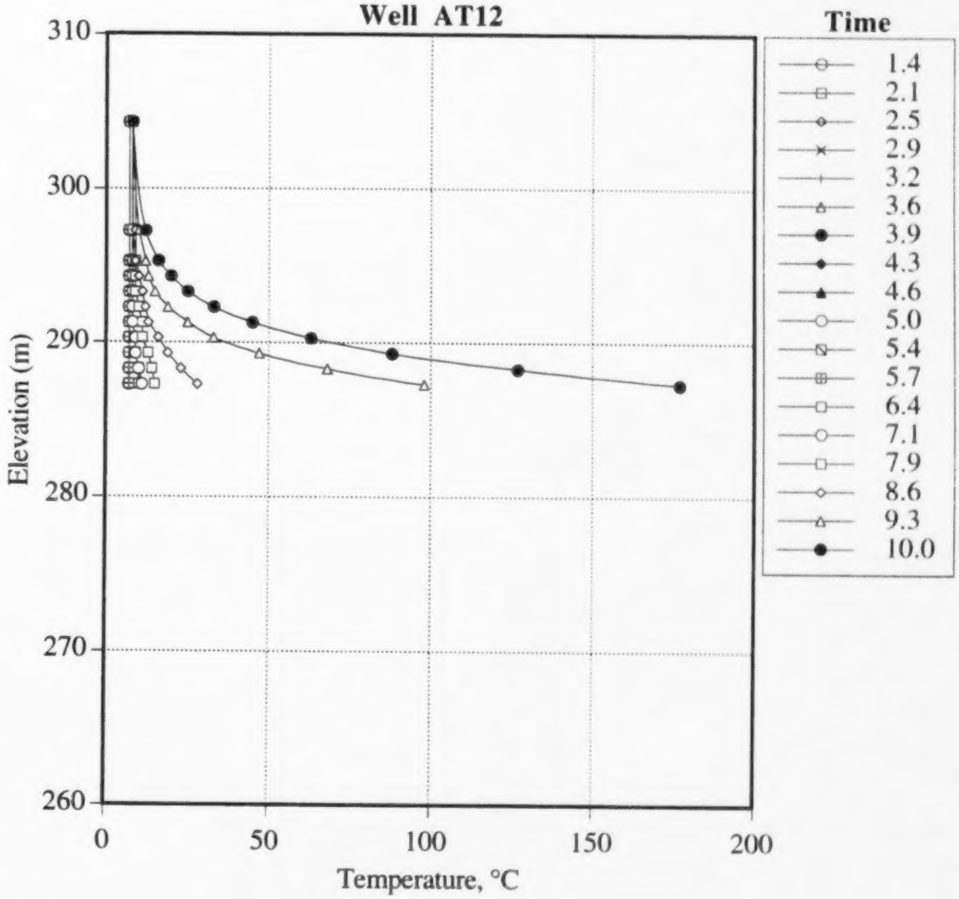

Figure A12 Temperature Profile in Well AT12

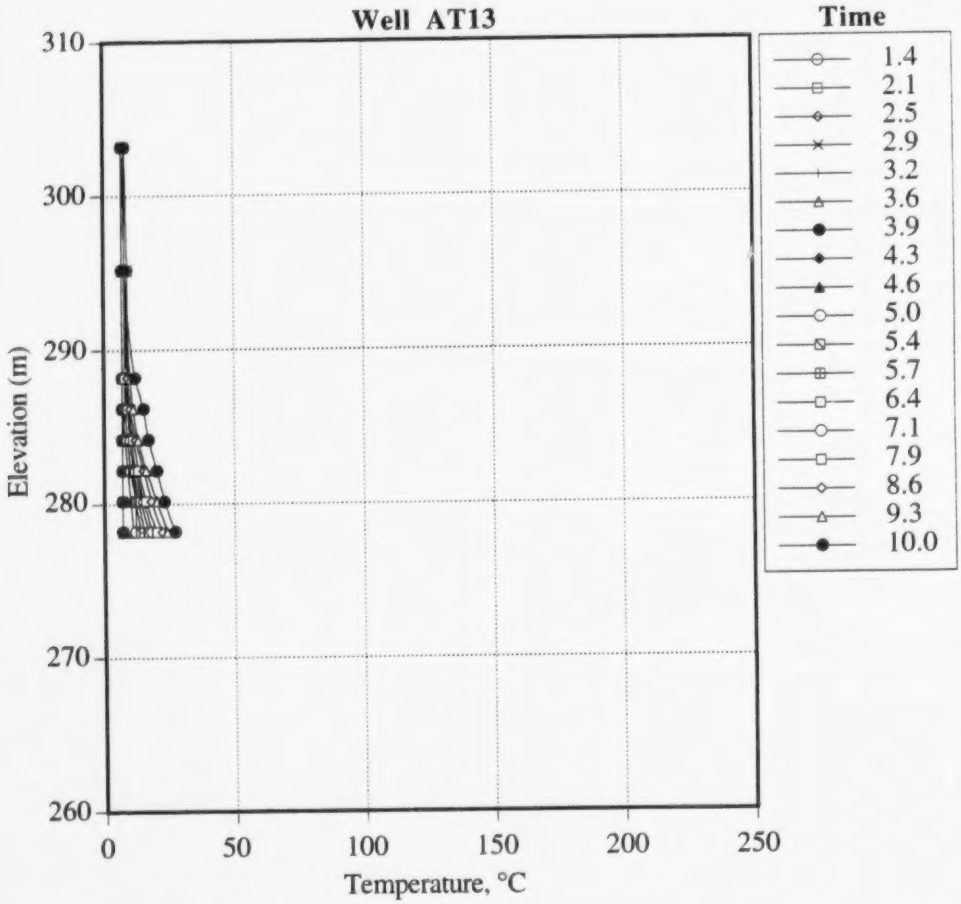

Figure A13 Temperature Profile in Well AT13

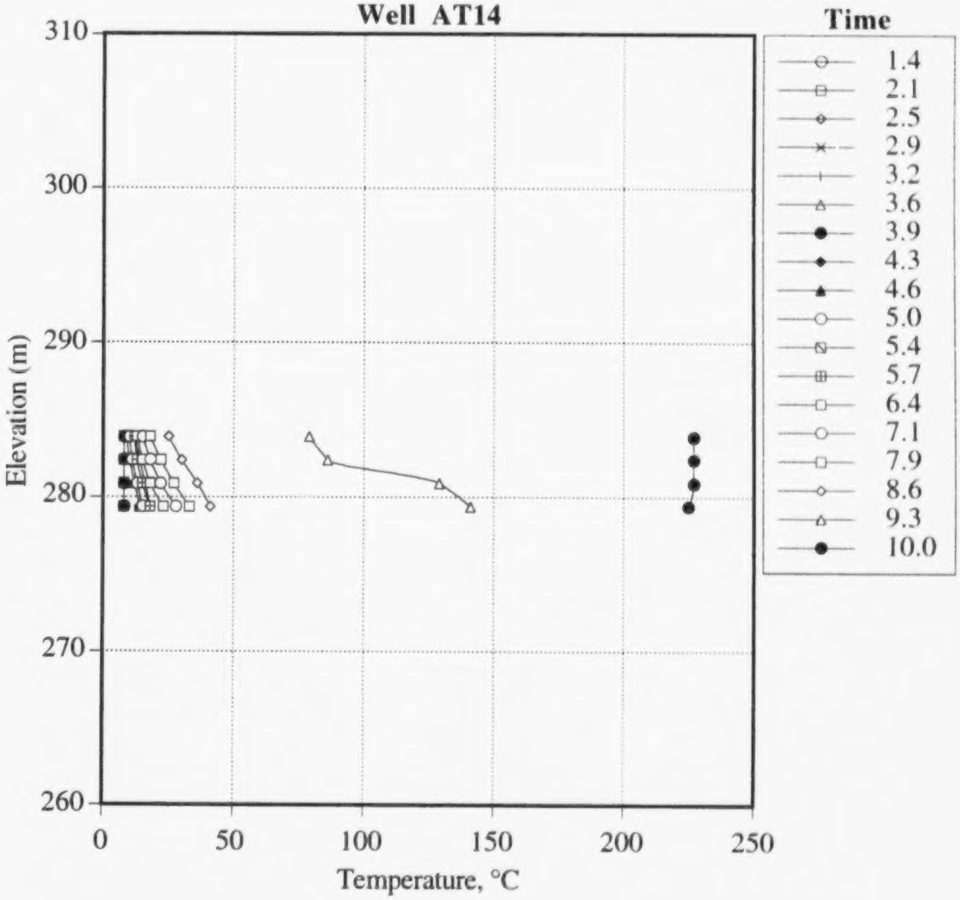

Figure A14 Temperature Profile in Well AT14

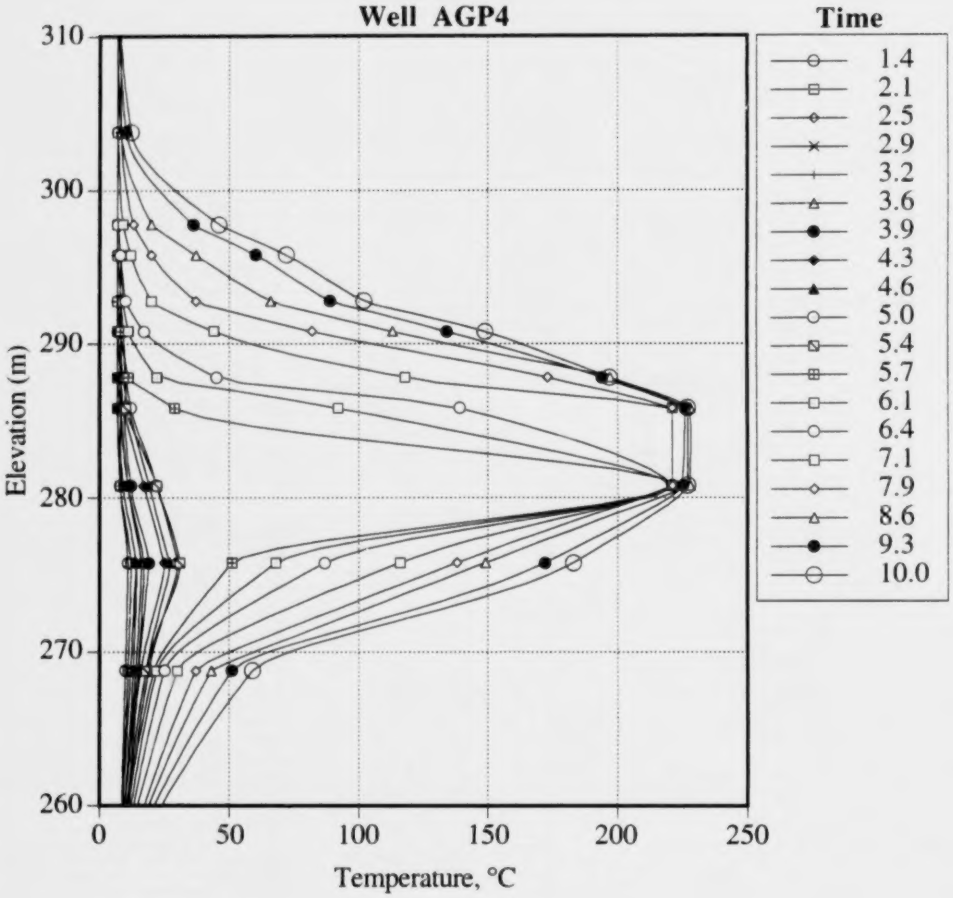

Figure A15 Temperature Profile in Well AGP4

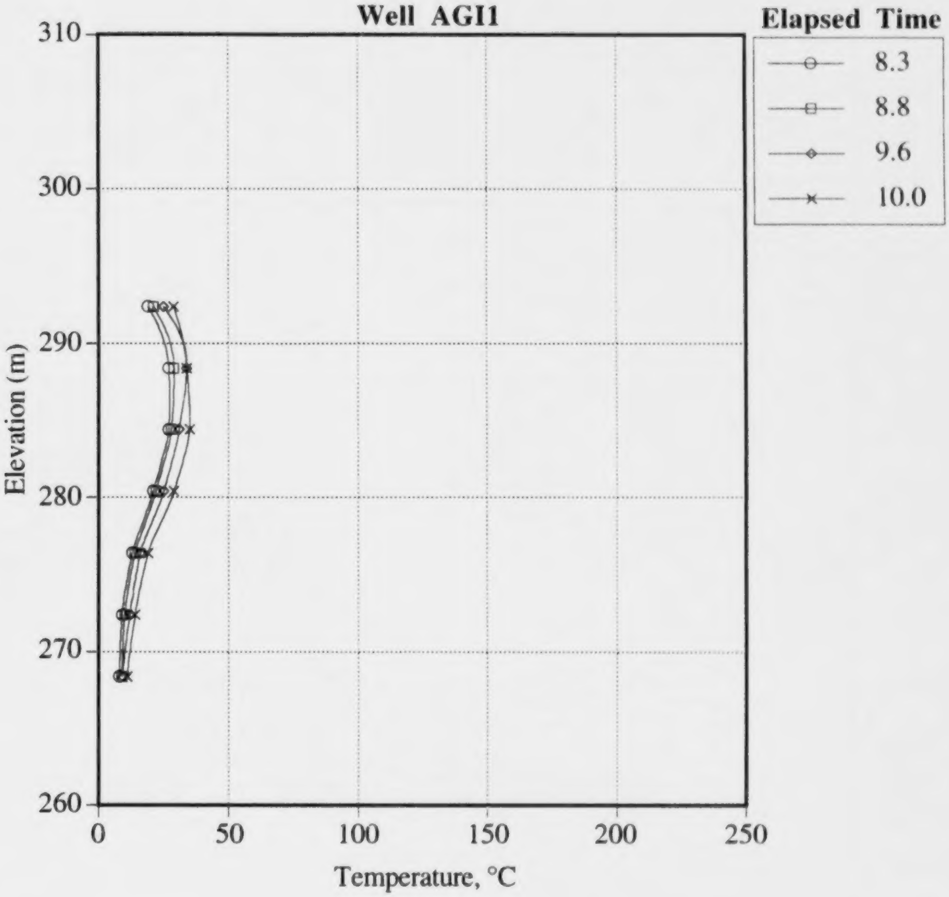

Figure A16 Temperature Profile in Well AGI1

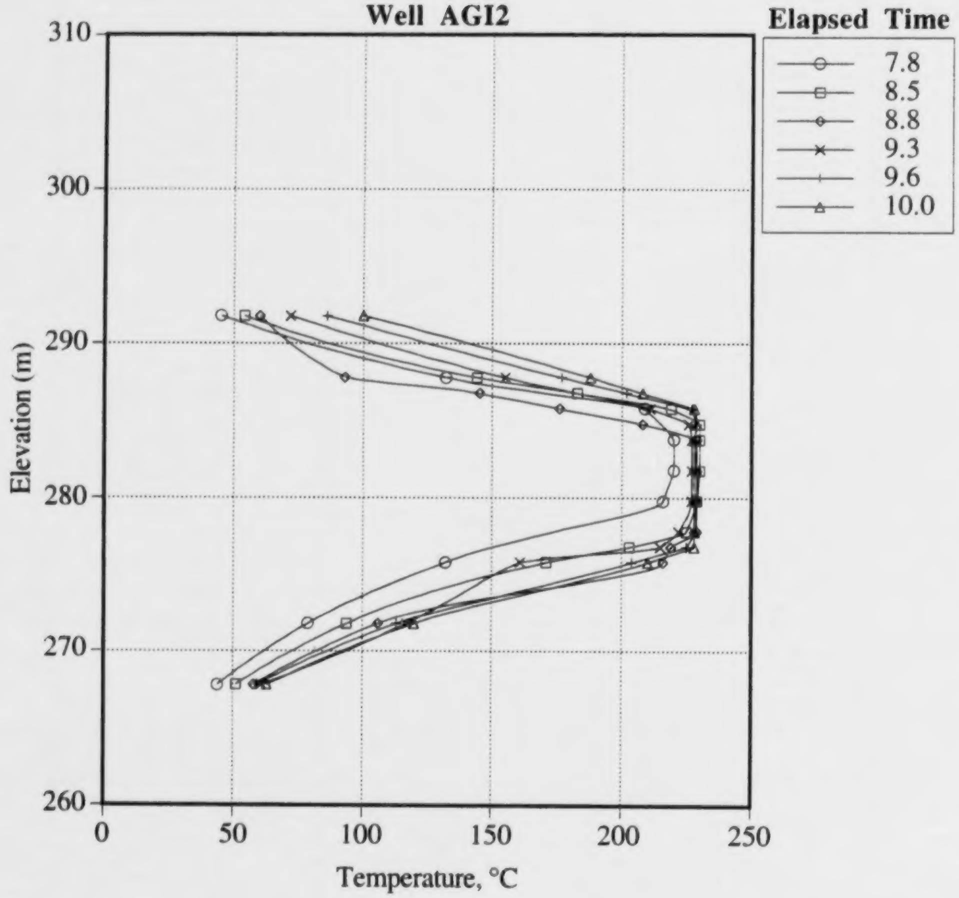

Figure A17 Temperature Profile in Well AGI2

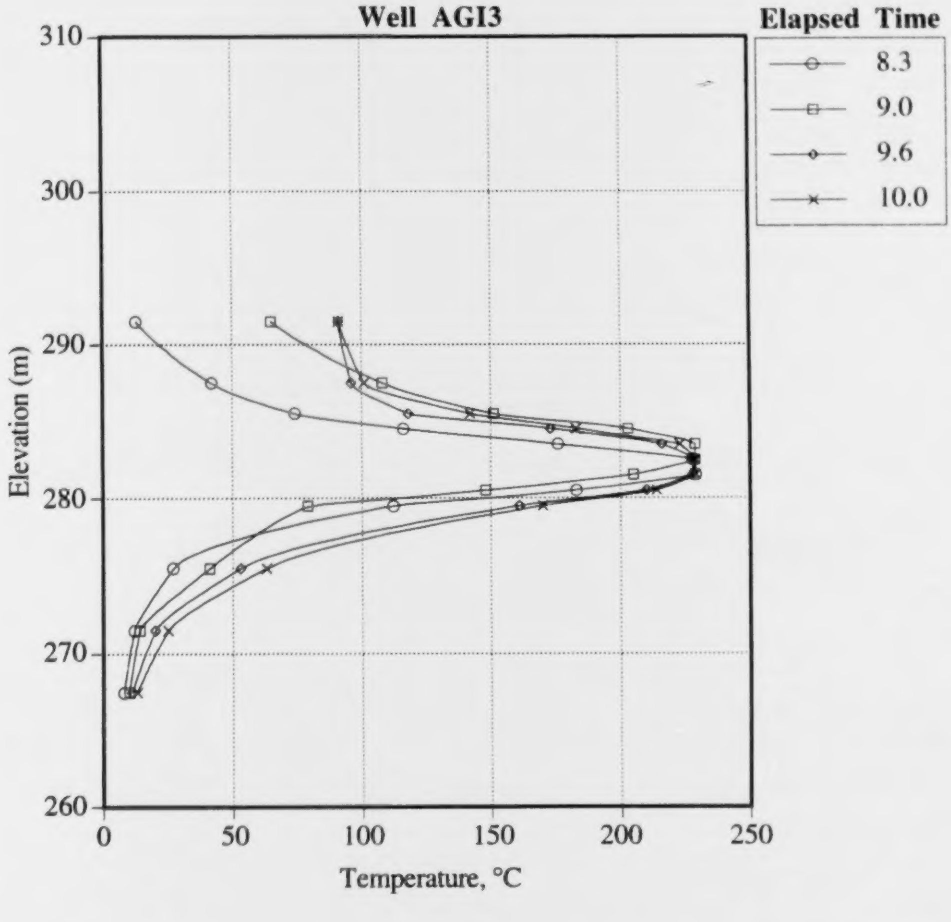

Figure A18 Temperature Profile in Well AGI3

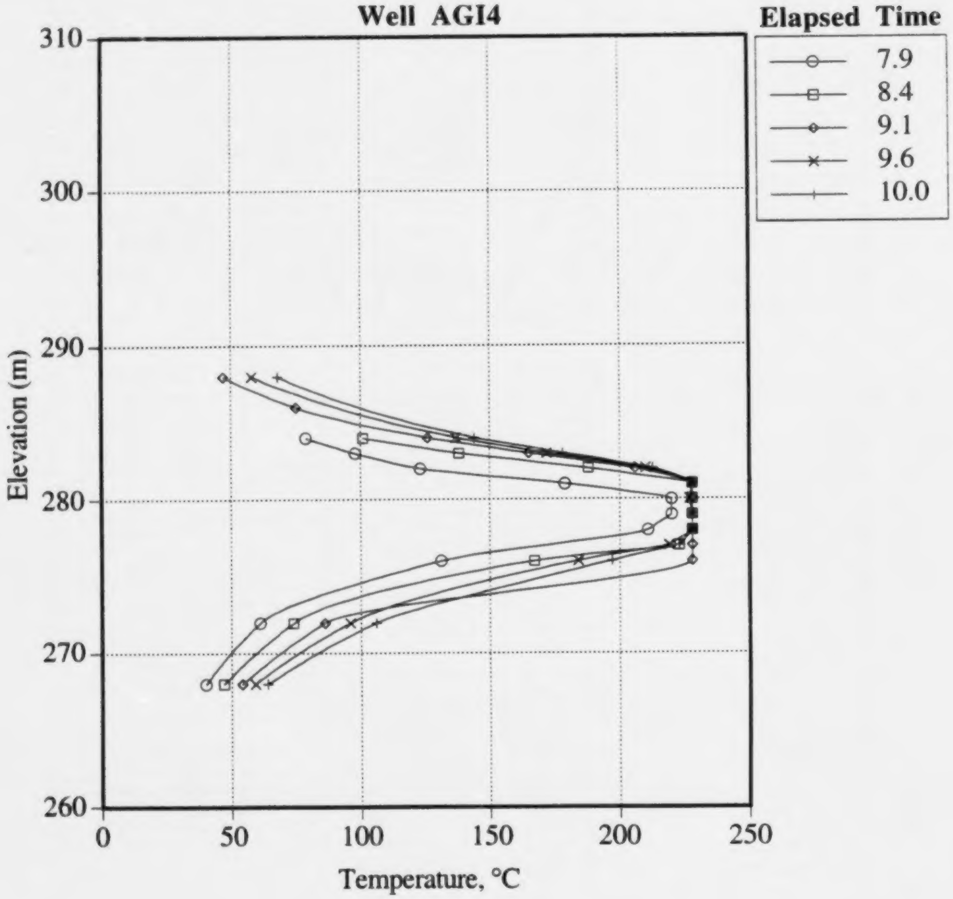

Figure A19 Temperature Profile in Well AGI4

APPENDIX B

Field Piezometer Results

A total of 18 high temperature vibrating wire piezometers were installed within the Phase A reservoir. One ambient temperature piezometer was installed within the Wabiskaw Member, a zone not expected to experience any significant temperature increase. These piezometers were constructed from stainless steel due to the extremely aggressive environment within the reservoir. Each vibrating wire piezometer had a pressure rating of 2800 kPa and a temperature rating of 200 °C. Each piezometer was attached to teflon insulated cable, rated to 200 °C, up to the Wabiskaw Member, and spliced to ambient temperature cable above this level. The manufacturers stated accuracy of these piezometers is ±0.1% of full scale (2800 kPa) or approximately ±3.0 kPa. Vibrating wire piezometers were also installed in two baseline piezometer wells offset from the Phase A area. These piezometers were intended to provide baseline data concerning zero drift or creep within the sensors.

A total of 18 pneumatic piezometers, installed adjacent to each vibrating wire piezometer, were utilized within the Phase A reservoir. A pneumatic piezometer consists of a twin-tube assembly connected across a flexible diaphragm attached to the piezometer transducer. As gas pressure is increased on the inlet tube under a constant but very low flow, the surface inlet pressure reading will rise. When the gas pressure exceeds the pore pressure P, the diaphragm moves outward, allowing gas to circulate through the outlet tube, such that the maximum indicated pressure gage reading is P.

Dual installations, vibrating wire and pneumatic piezometers, provided the redundancy in pressure measurement required at each location. The high temperature rating of 230°C for the pneumatic piezometers was achieved through stainless steel construction and attachment to stainless steel tubing up to a level where negligible temperature increases were expected to occur. The pneumatic piezometers were rated to 3000 kPa with an estimated accuracy of ±10 kPa.

The following piezometer results illustrate the field readings obtained for the piezometer wells within the Phase A pilot. The pressures provided on each plot are the best interpretation of pore pressures measured by both vibrating wire and pneumatic piezometers. A comparison of each piezometer response with the injection and production pressures is also provided.

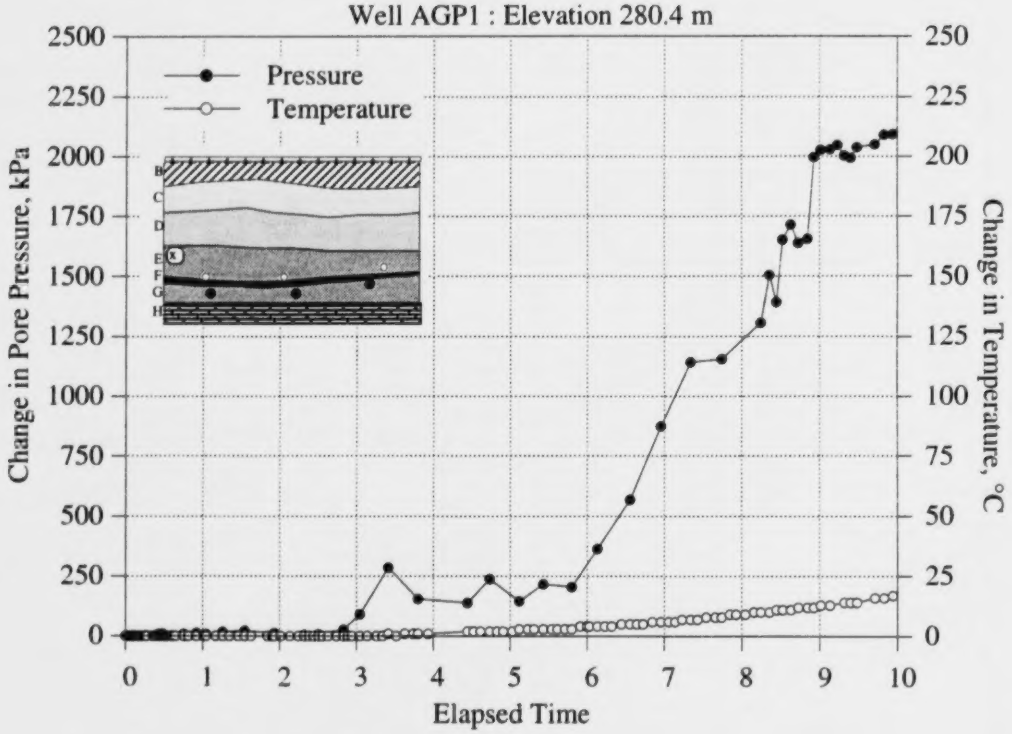

Figure B1 Change in Pressure for Piezometer at Elevation 280.4 m in Well AGP1

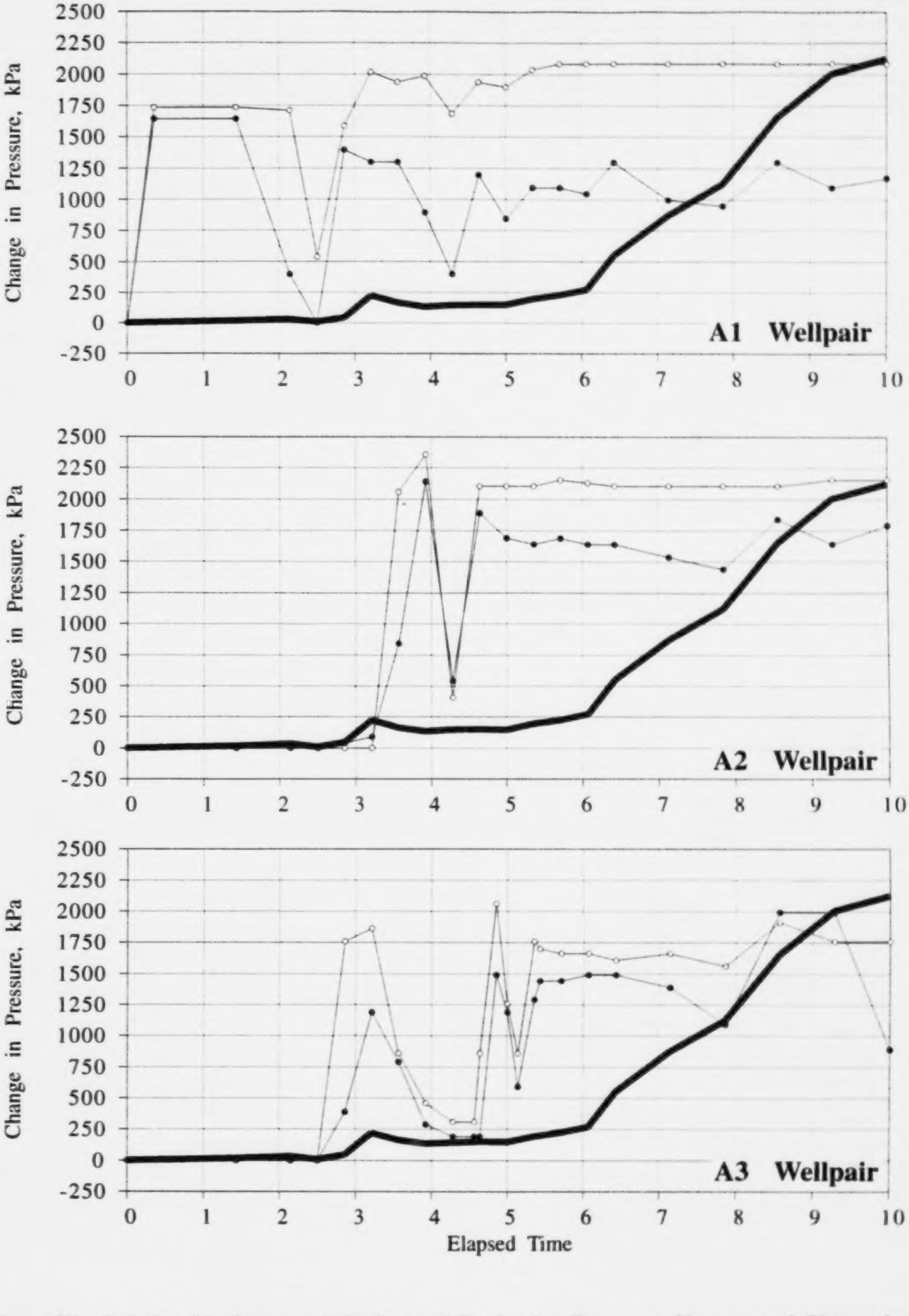

Figure B2 Relationship Between Injection and Production Pressures Changes and Change in Pressure for Piezometer at Elevation 280.4 m in Well AGP1

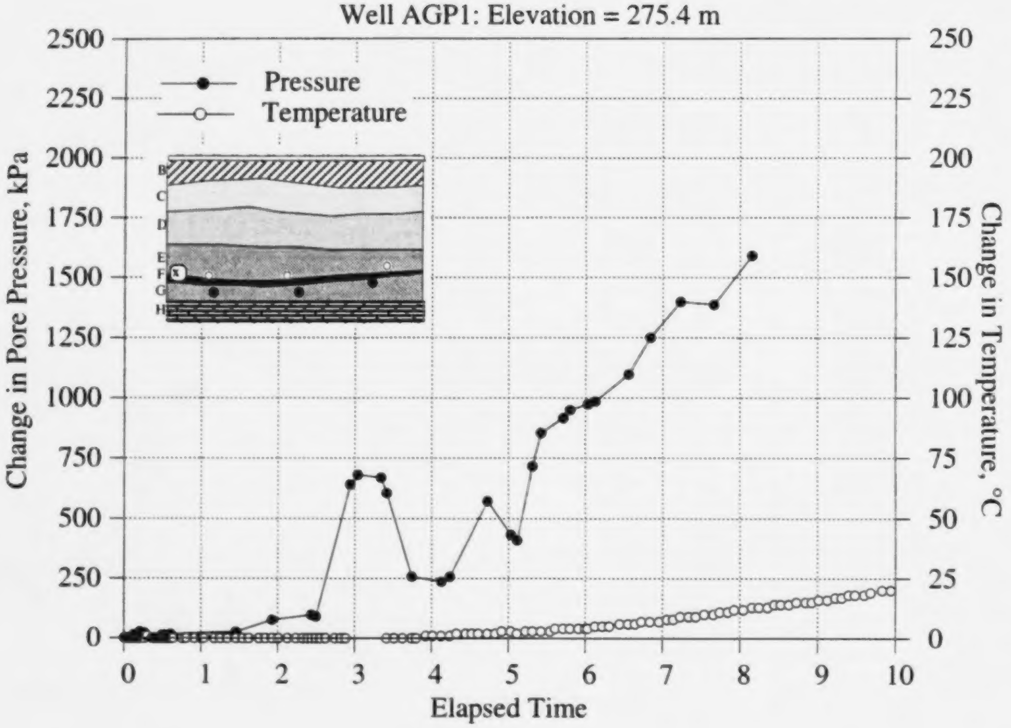

Figure B3 Change in Pressure for Piezometer at Elevation 275.4 m in Well AGP1

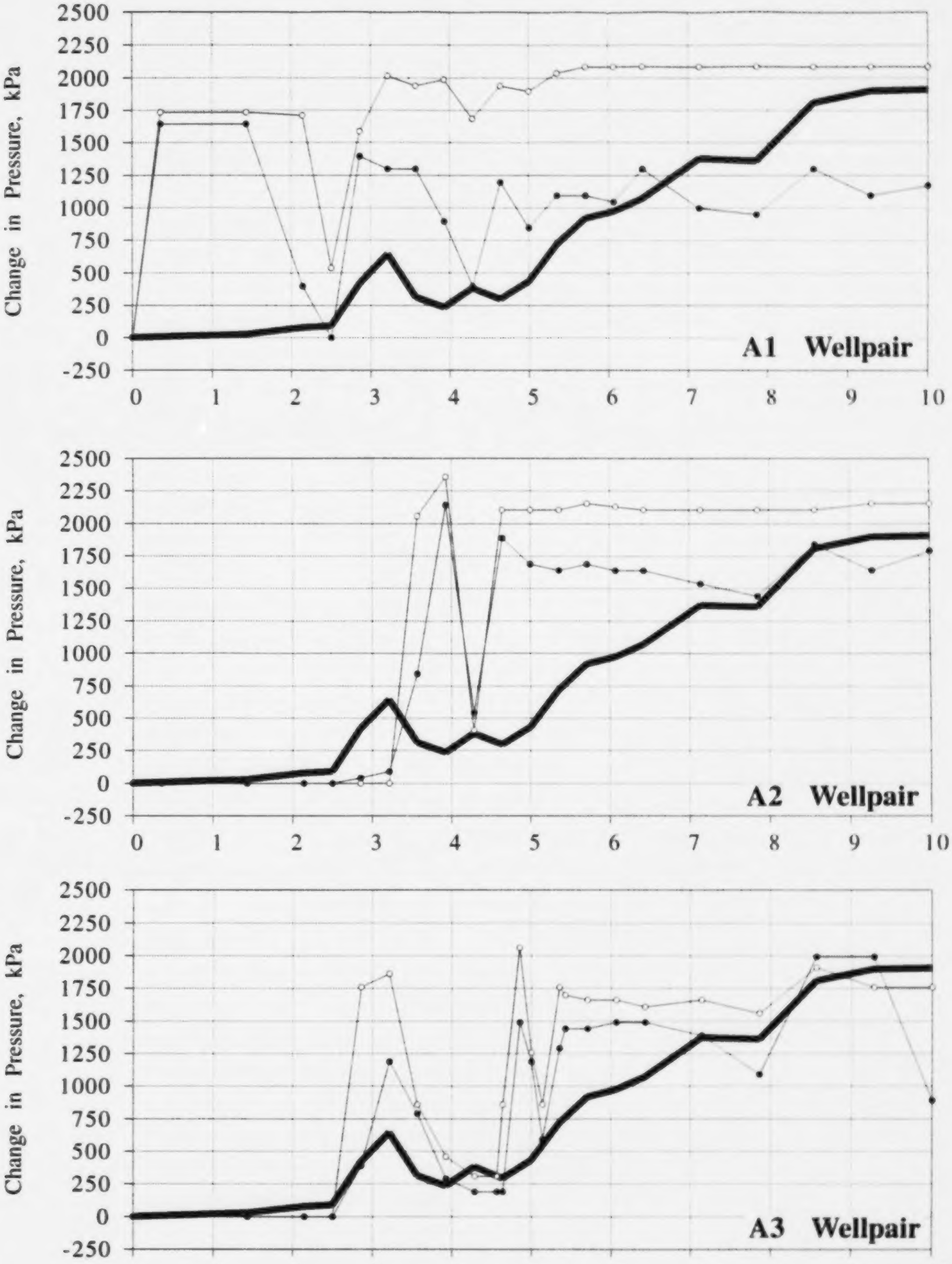

Figure B4 Relationship Between Injection and Production Pressures Changes and Change in Pressure for Piezometer at Elevation 275.4 m in Well AGP1

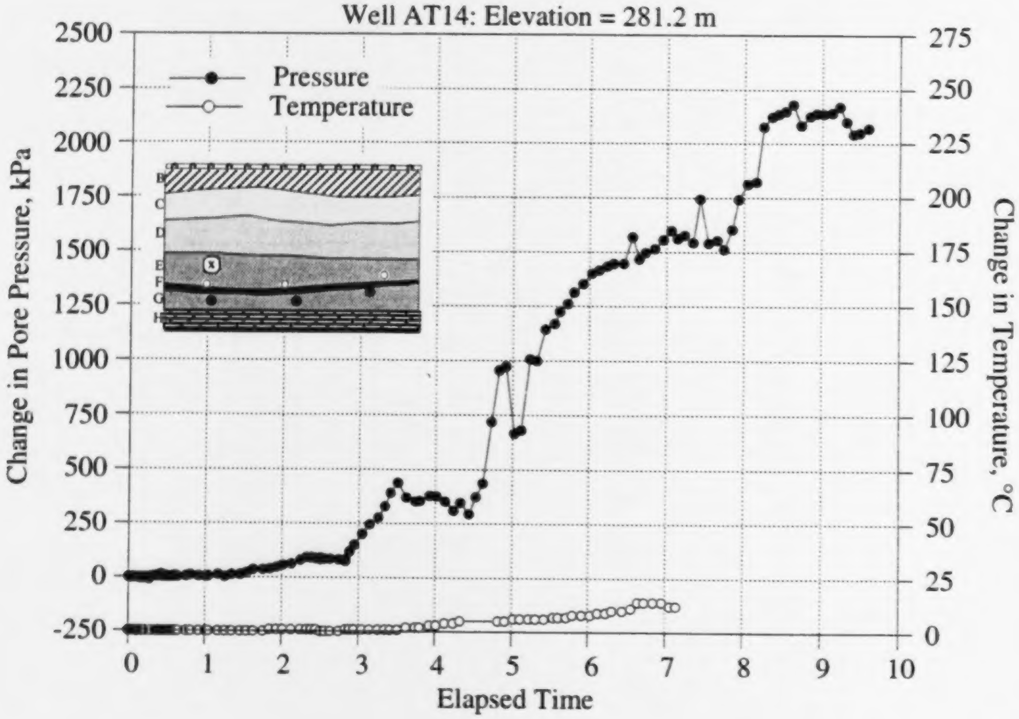

Figure B5 Change in Pressure for Piezometer at Elevation 281.2 m in Well AT14

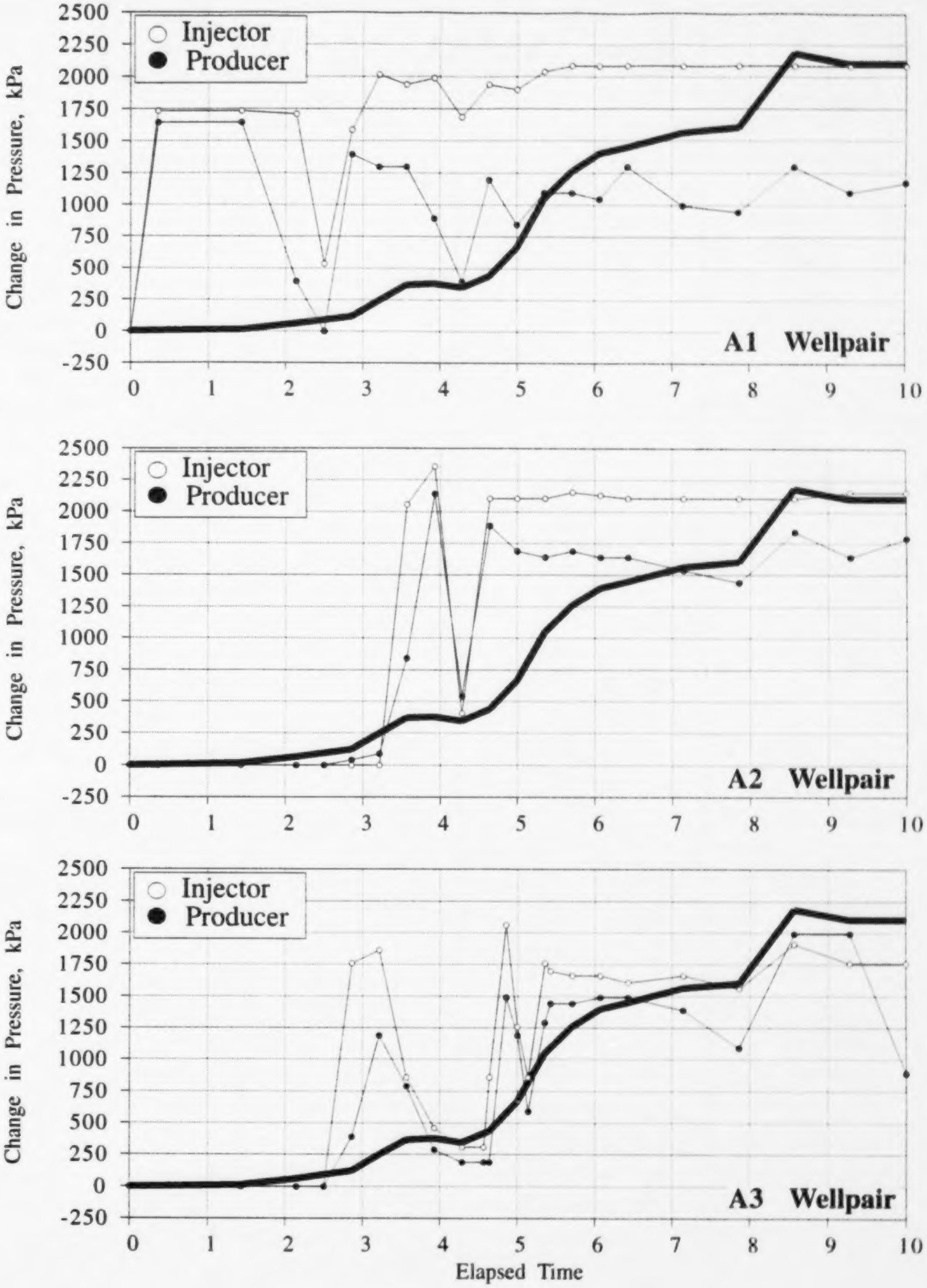

Figure B6 Relationship Between Injection and Production Pressures Changes and Change in Pressure for Piezometer at Elevation 281.2 m in Well AT14

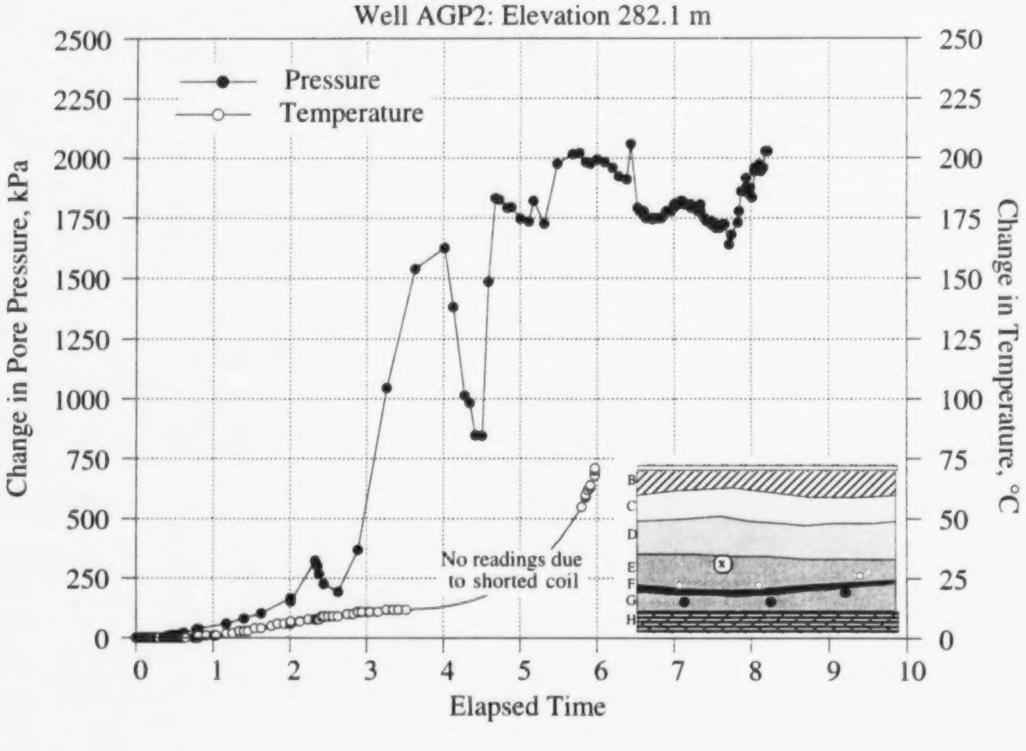

Figure B7 Change in Pressure for Piezometer at Elevation 282.1 m in Well AGP2

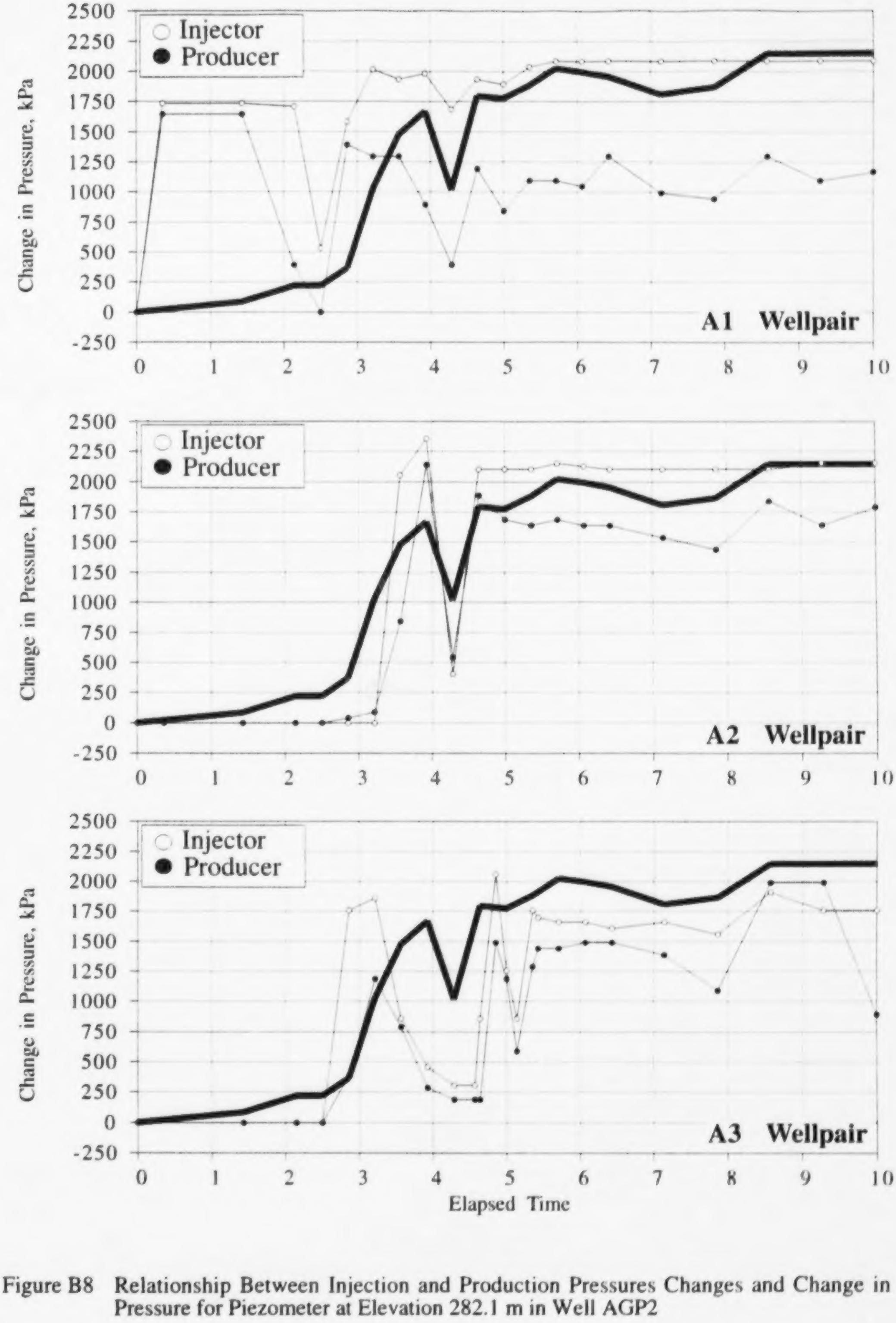

Figure B8 Relationship Between Injection and Production Pressures Changes and Change in Pressure for Piezometer at Elevation 282.1 m in Well AGP2

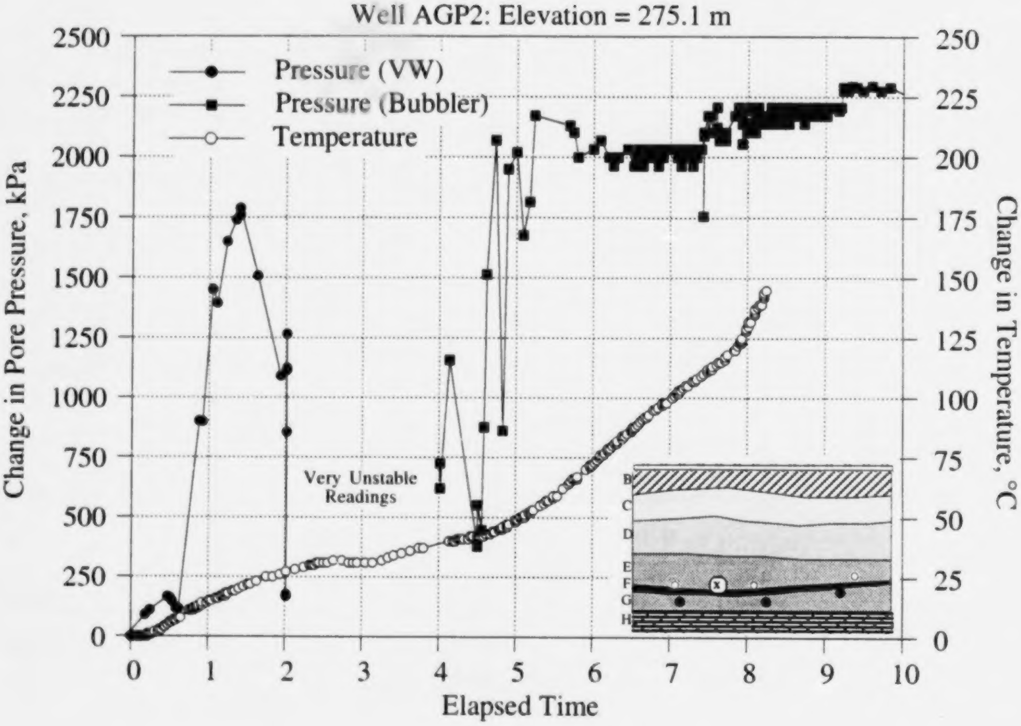

Figure B9 Change in Pressure for Piezometer at Elevation 275.1 m in Well AGP2

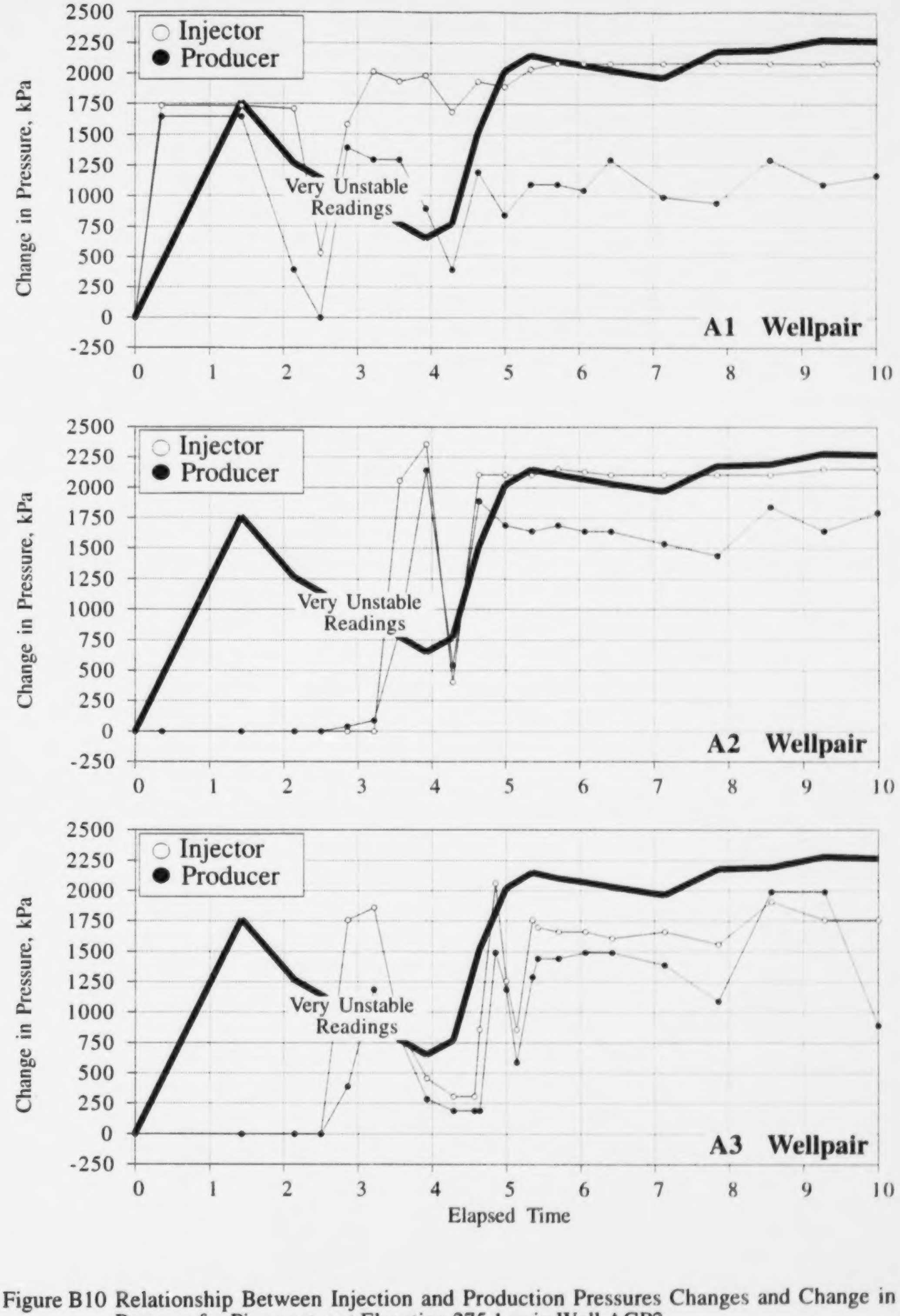

Figure B10 Relationship Between Injection and Production Pressures Changes and Change in Pressure for Piezometer at Elevation 275.1 m in Well AGP2

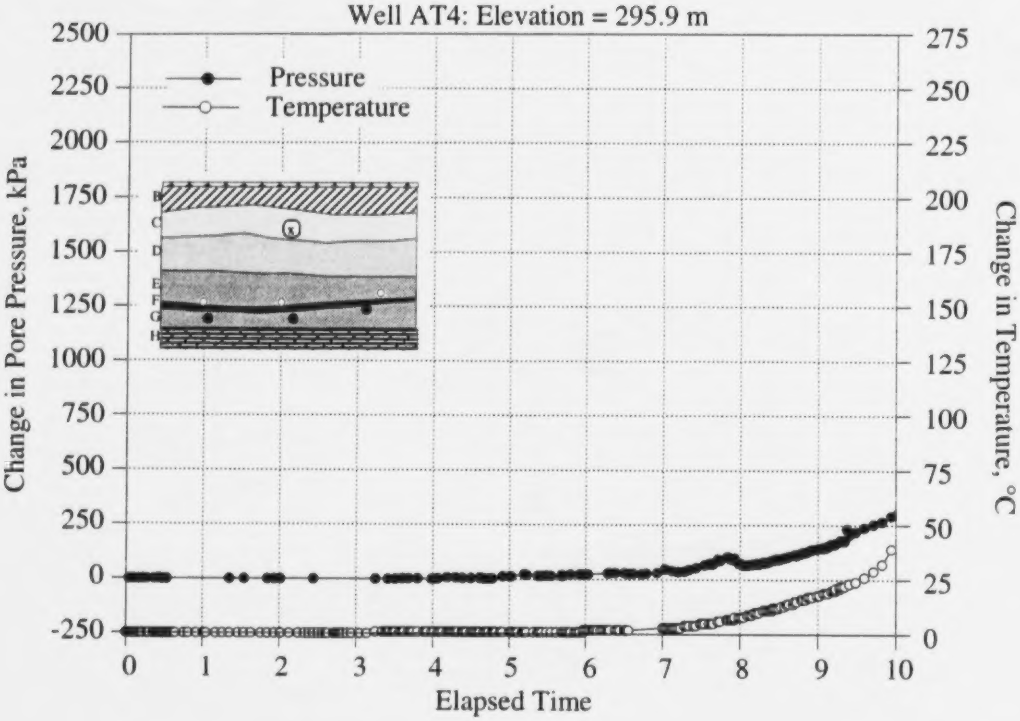

Figure B11 Change in Pressure for Piezometer at Elevation 295.9 m in Well AT4

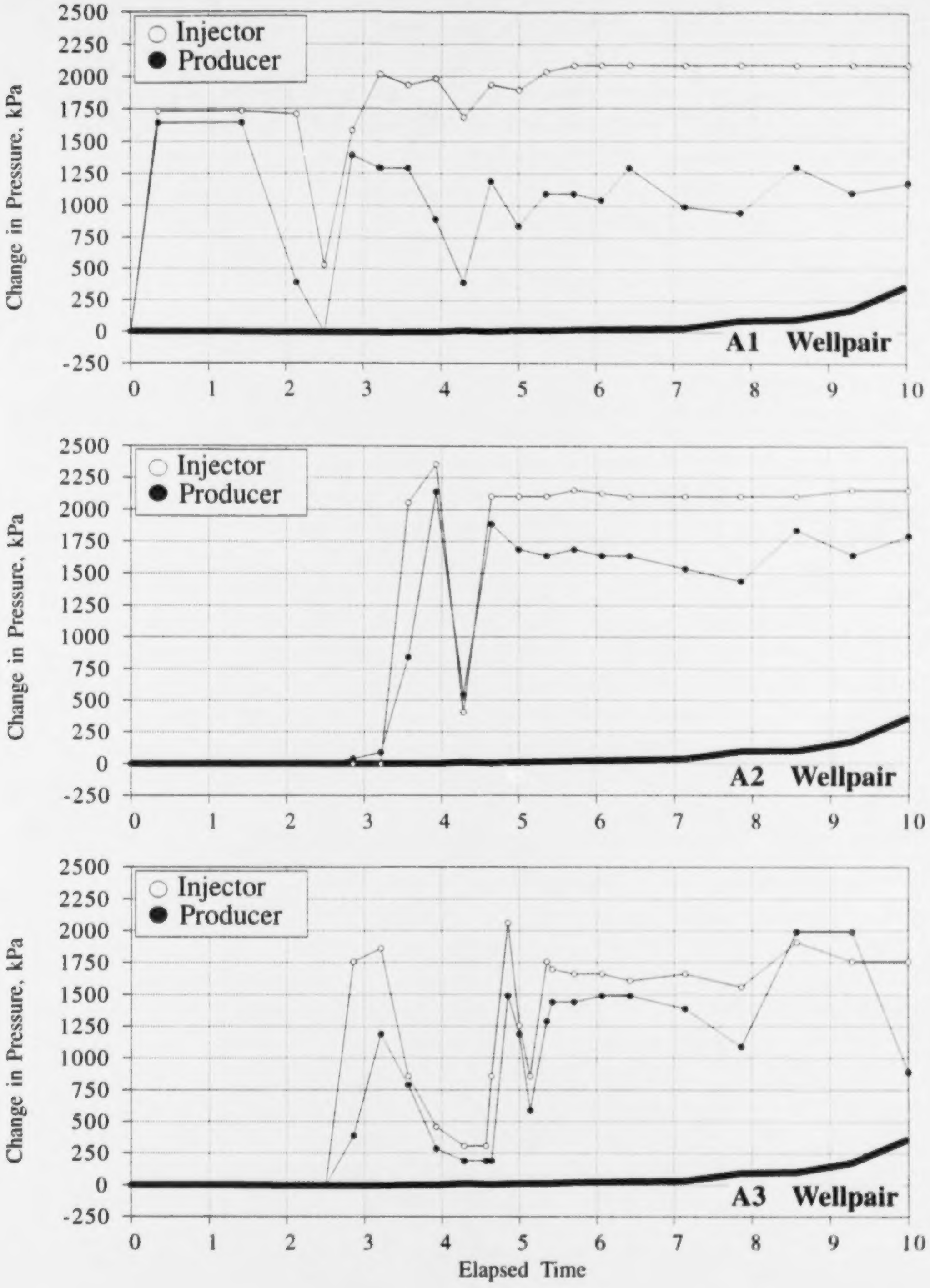

Figure B12 Relationship Between Injection and Production Pressures Changes and Change in Pressure for Piezometer at Elevation 295.9 m in Well AT4

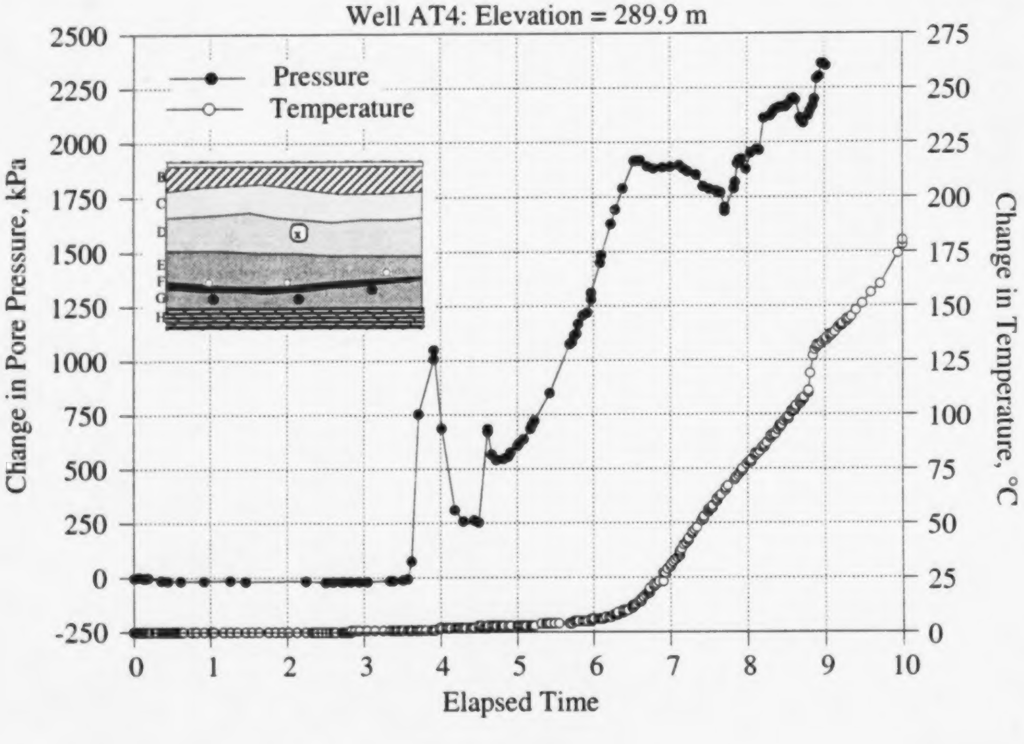

Figure B13 Change in Pressure for Piezometer at Elevation 289.9 m in Well AT4

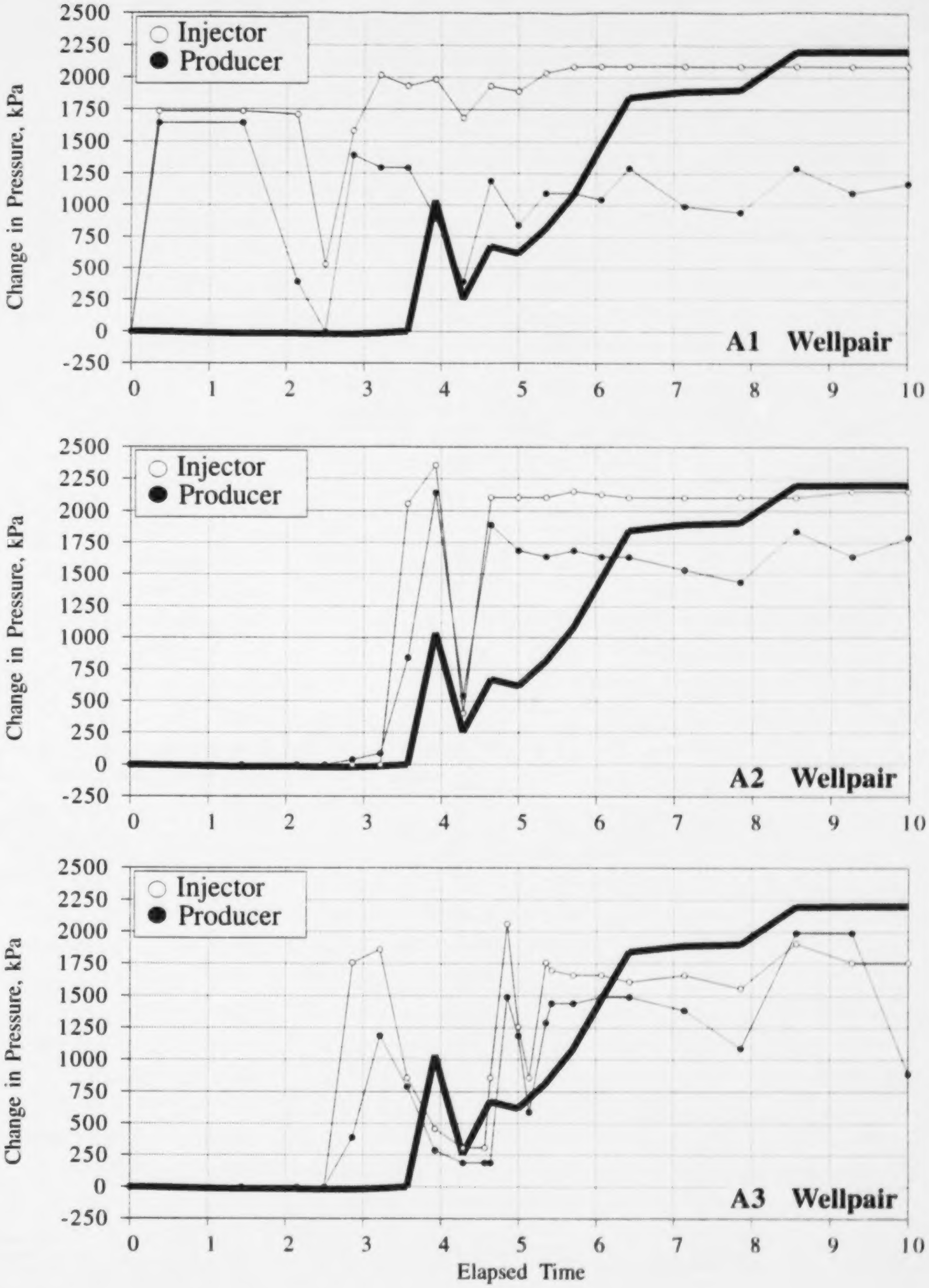

Figure B14 Relationship Between Injection and Production Pressures Changes and Change in Pressure for Piezometer at Elevation 289.9 m in Well AT4

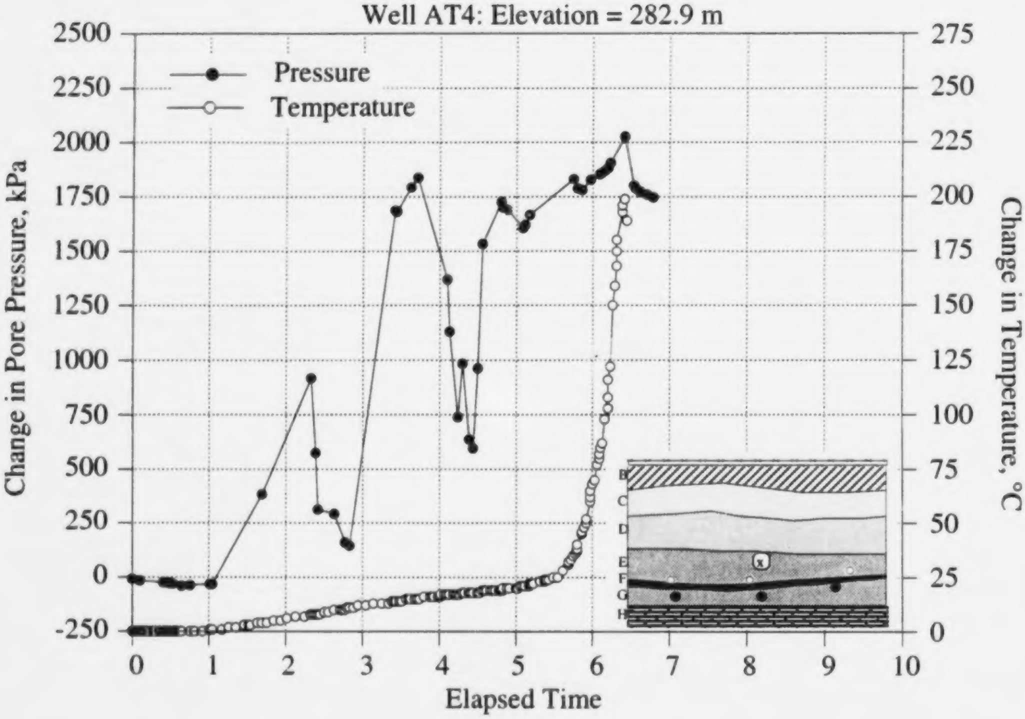

Figure B15 Change in Pressure for Piezometer at Elevation 282,9 m in Well AT4

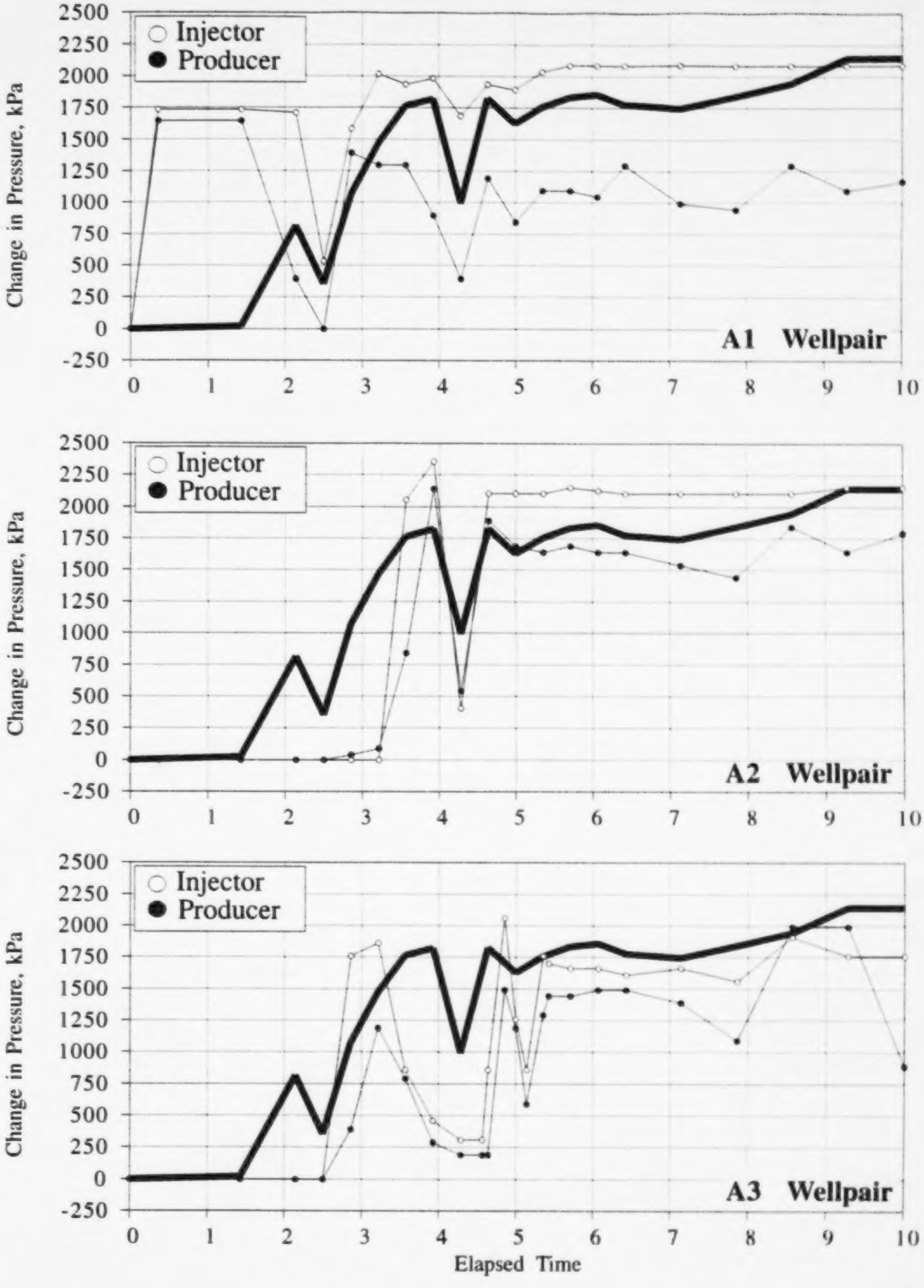

Figure B16 Relationship Between Injection and Production Pressures Changes and Change in Pressure for Piezometer at Elevation 282.9 m in Well AT4

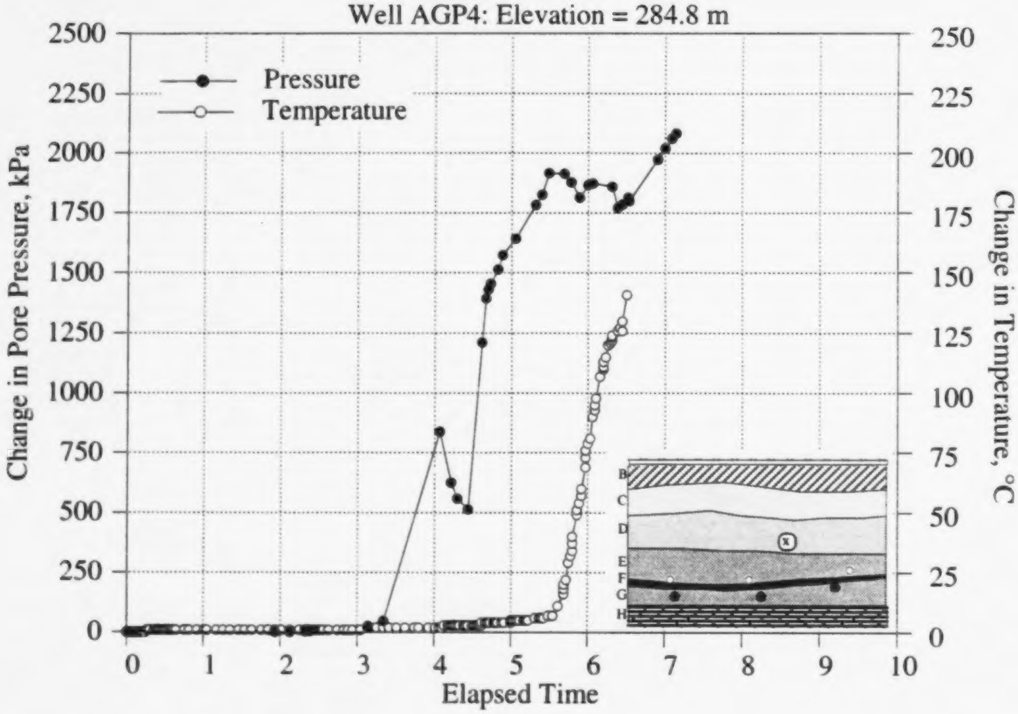

Figure B17 Change in Pressure for Piezometer at Elevation 284.8 m in Well AGP4

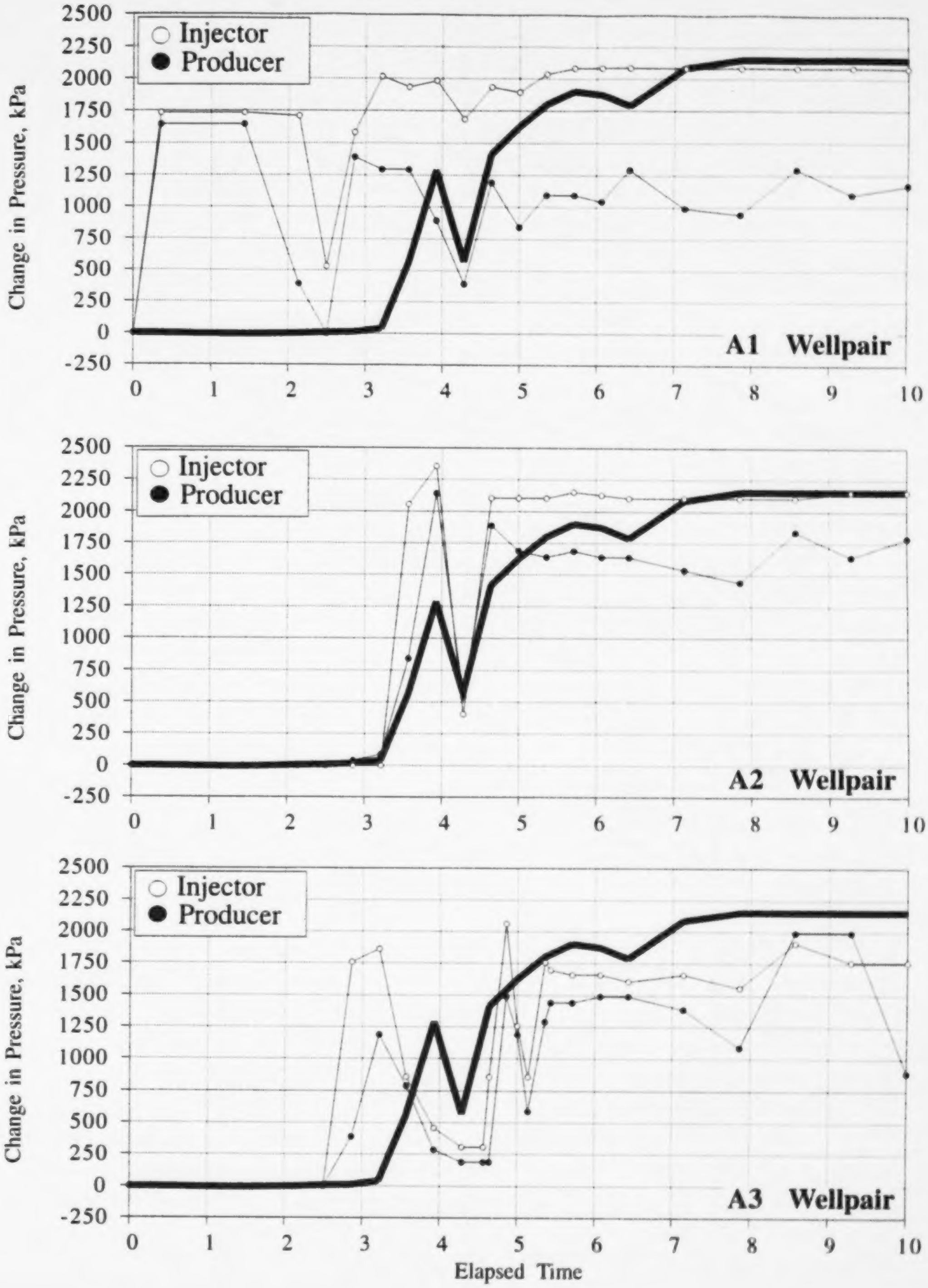

Figure B18 Relationship Between Injection and Production Pressures Changes and Change in Pressure for Piezometer at Elevation 284.8 m in Well AGP4

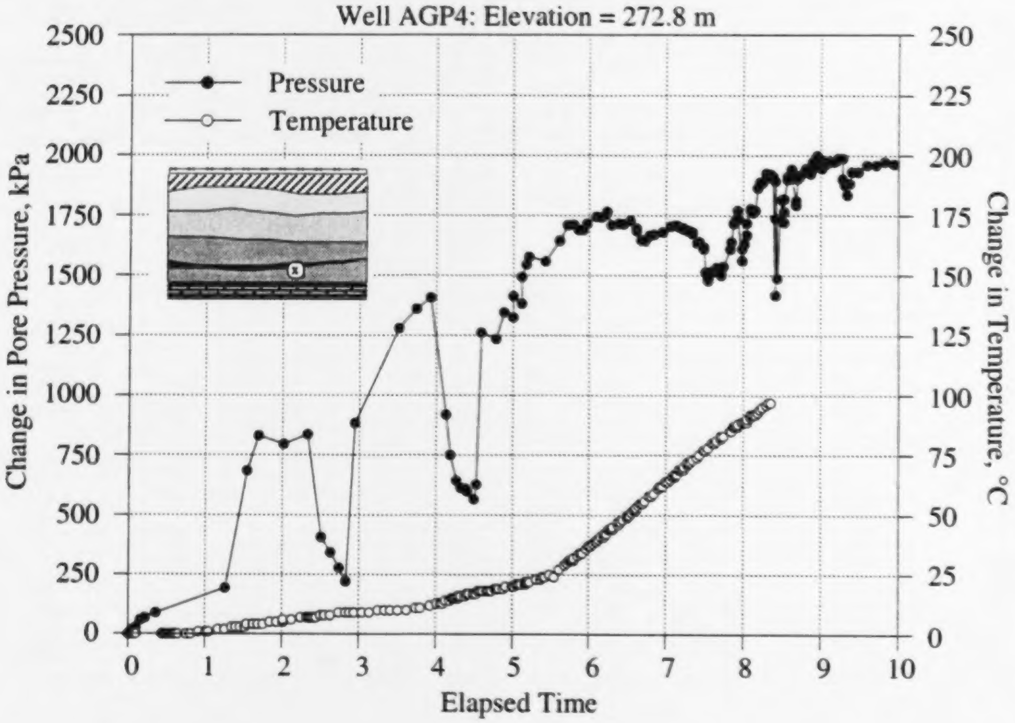

Figure B19 Change in Pressure for Piezometer at Elevation 272.8 m in Well AGP4

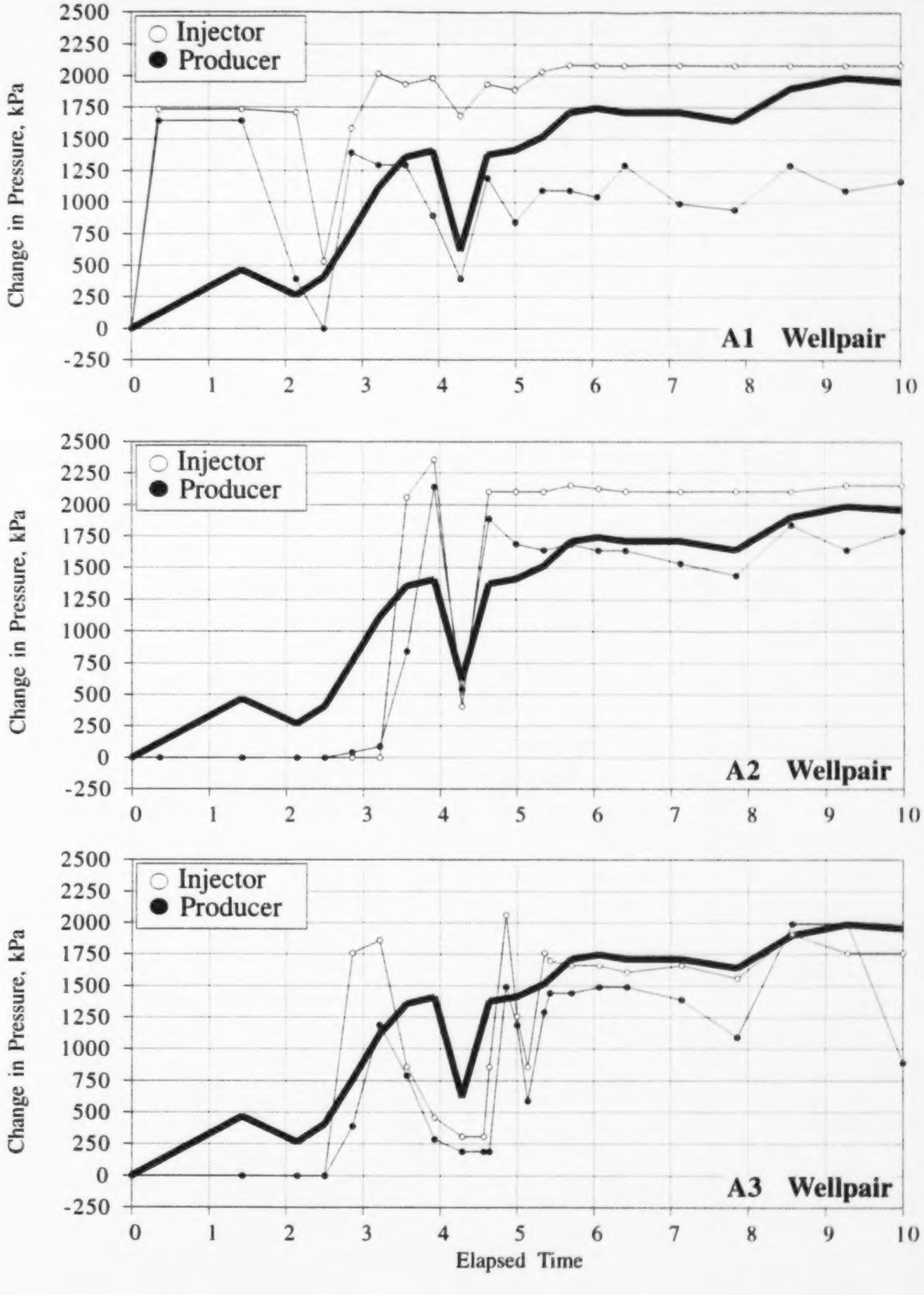

Figure B20 Relationship Between Injection and Production Pressures Changes and Change in Pressure for Piezometer at Elevation 272.8 m in Well AGP4

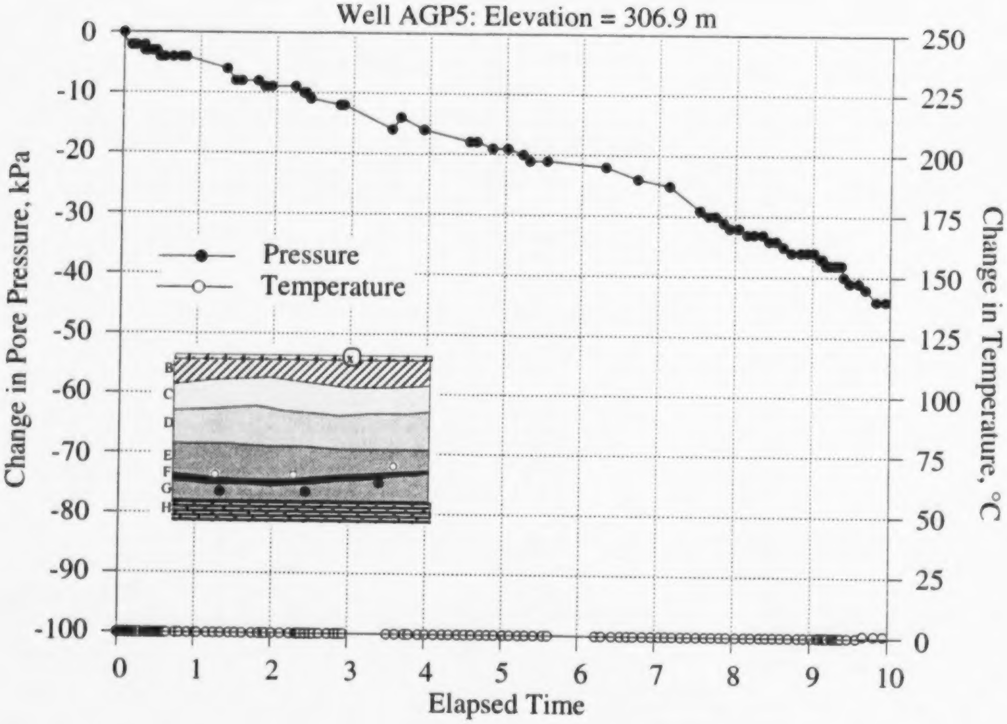

Figure B21 Change in Pressure for Piezometer at Elevation 306.9 m in Well AGP5

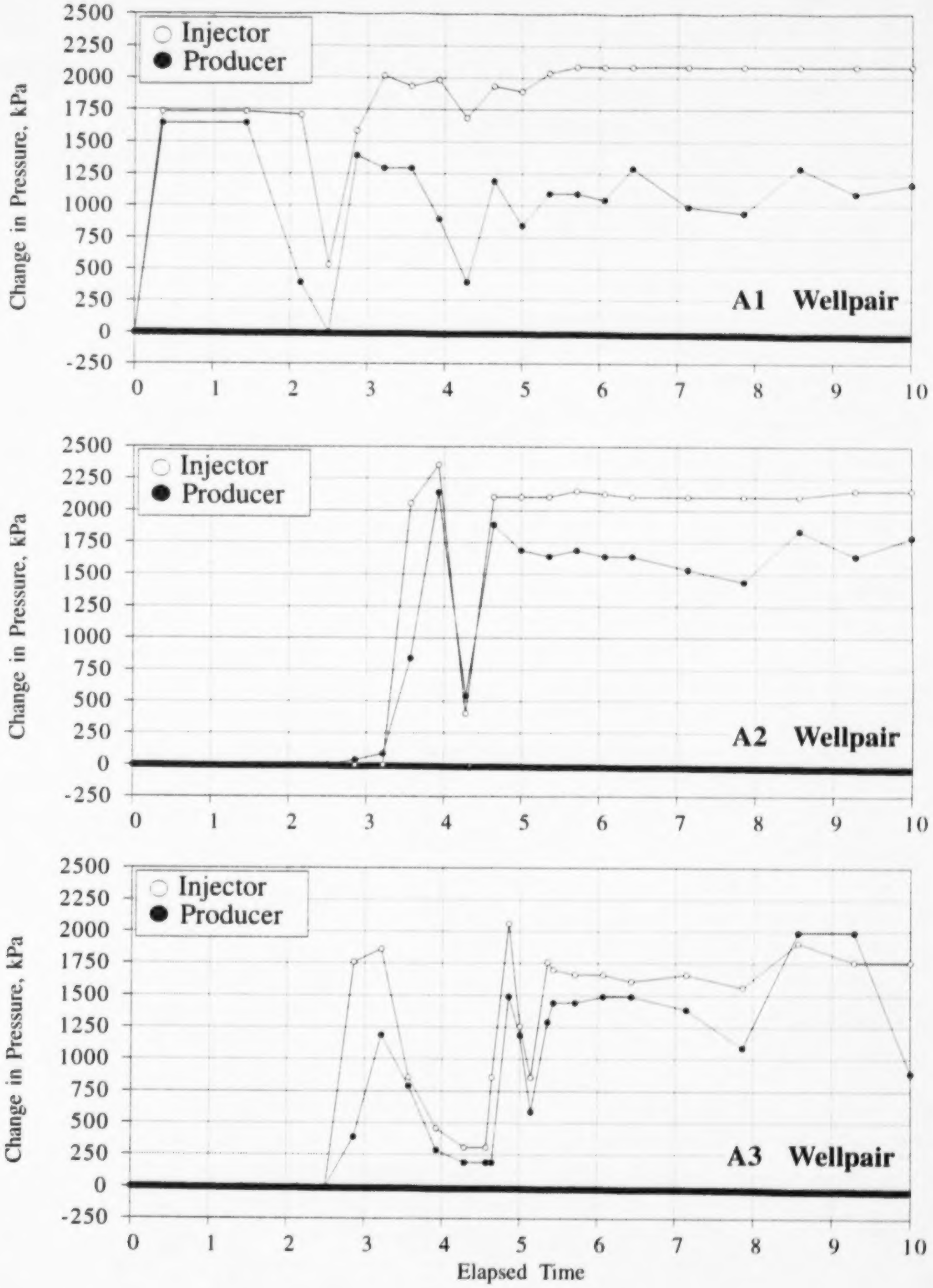

Figure B22 Relationship Between Injection and Production Pressures Changes and Change in Pressure for Piezometer at Elevation 306.9 m in Well AGP5

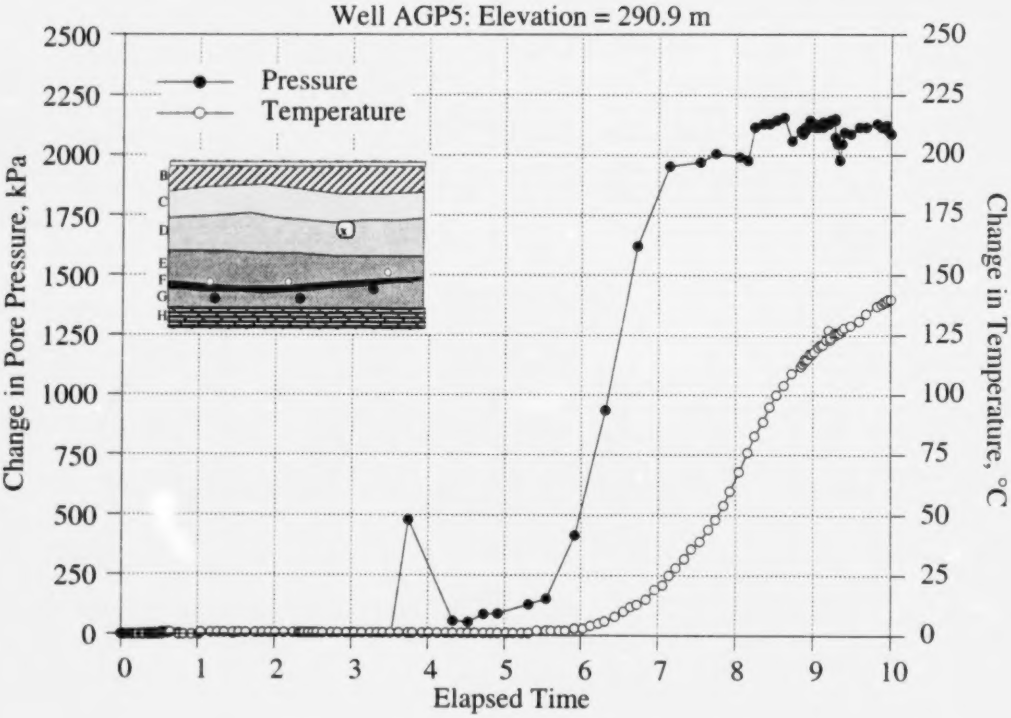

Figure B23 Change in Pressure for Piezometer at Elevation 290.9 m in Well AGP5

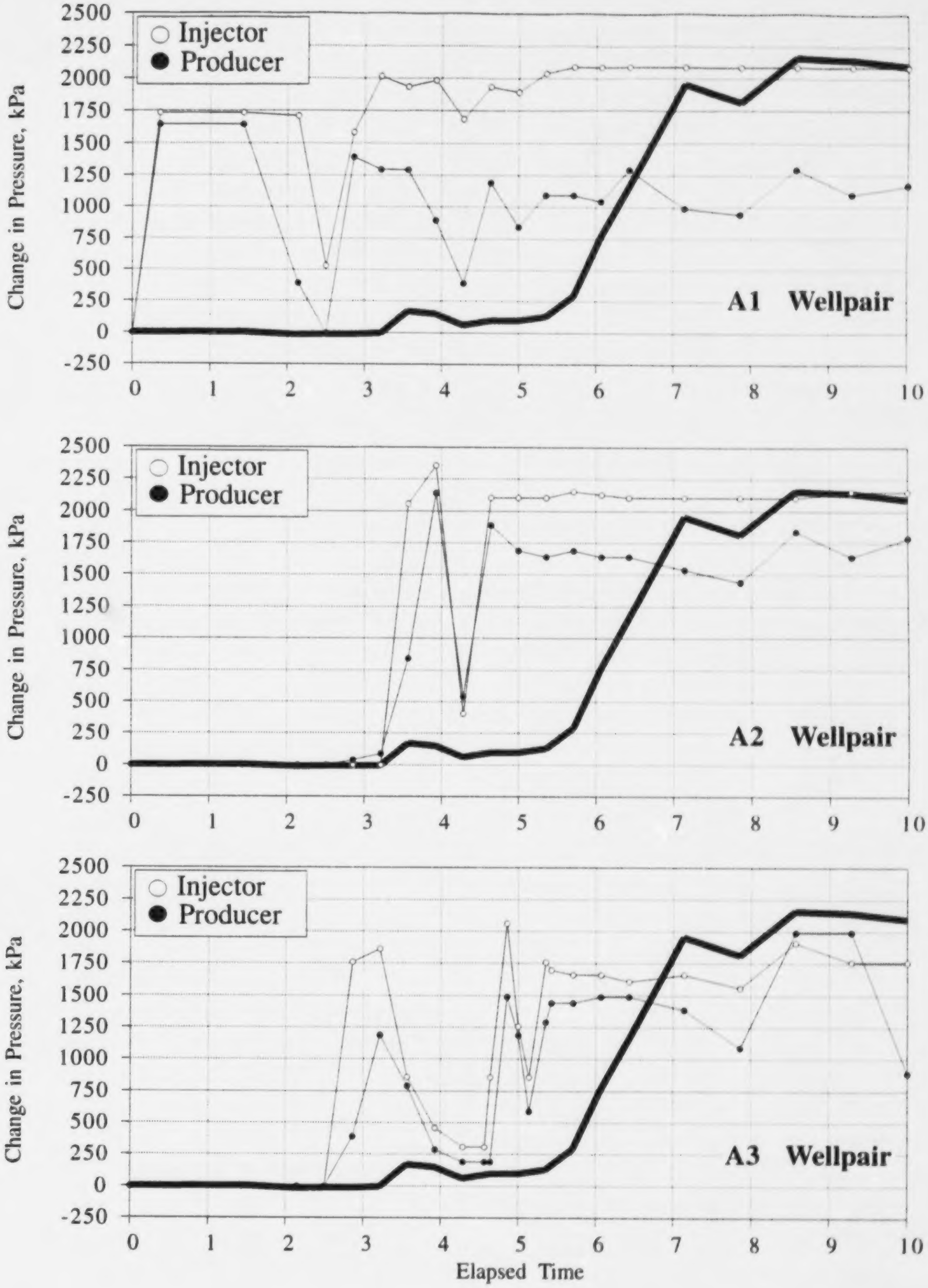

Figure B24 Relationship Between Injection and Production Pressures Changes and Change in Pressure for Piezometer at Elevation 290.9 m in Well AGP5

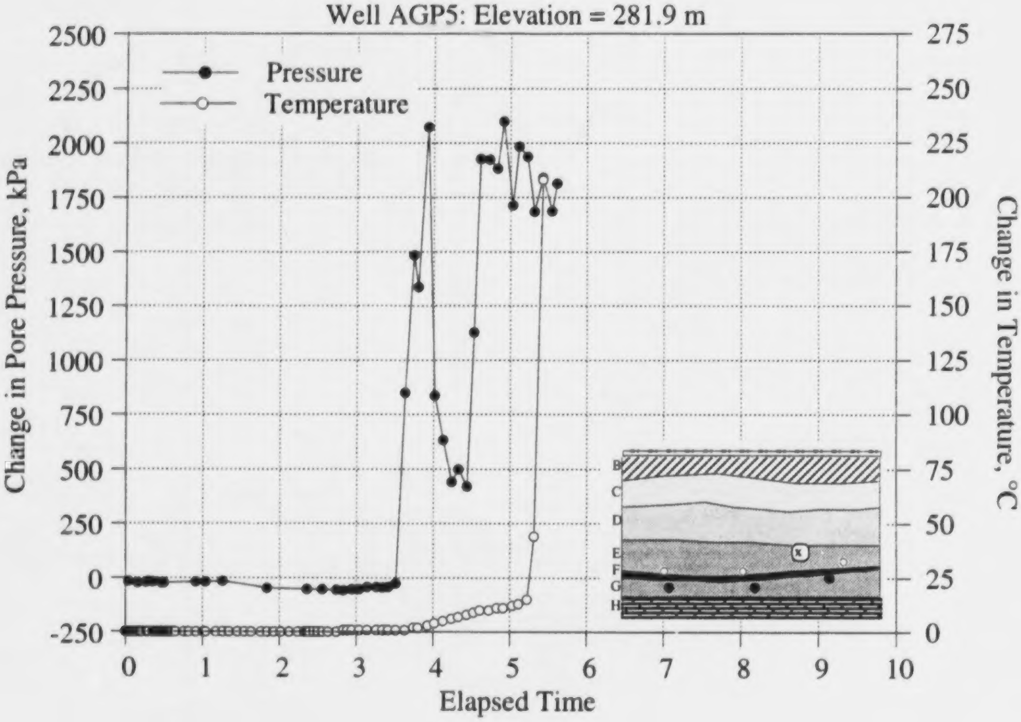

Figure B25 Change in Pressure for Piezometer at Elevation 281.9 m in Well AGP5

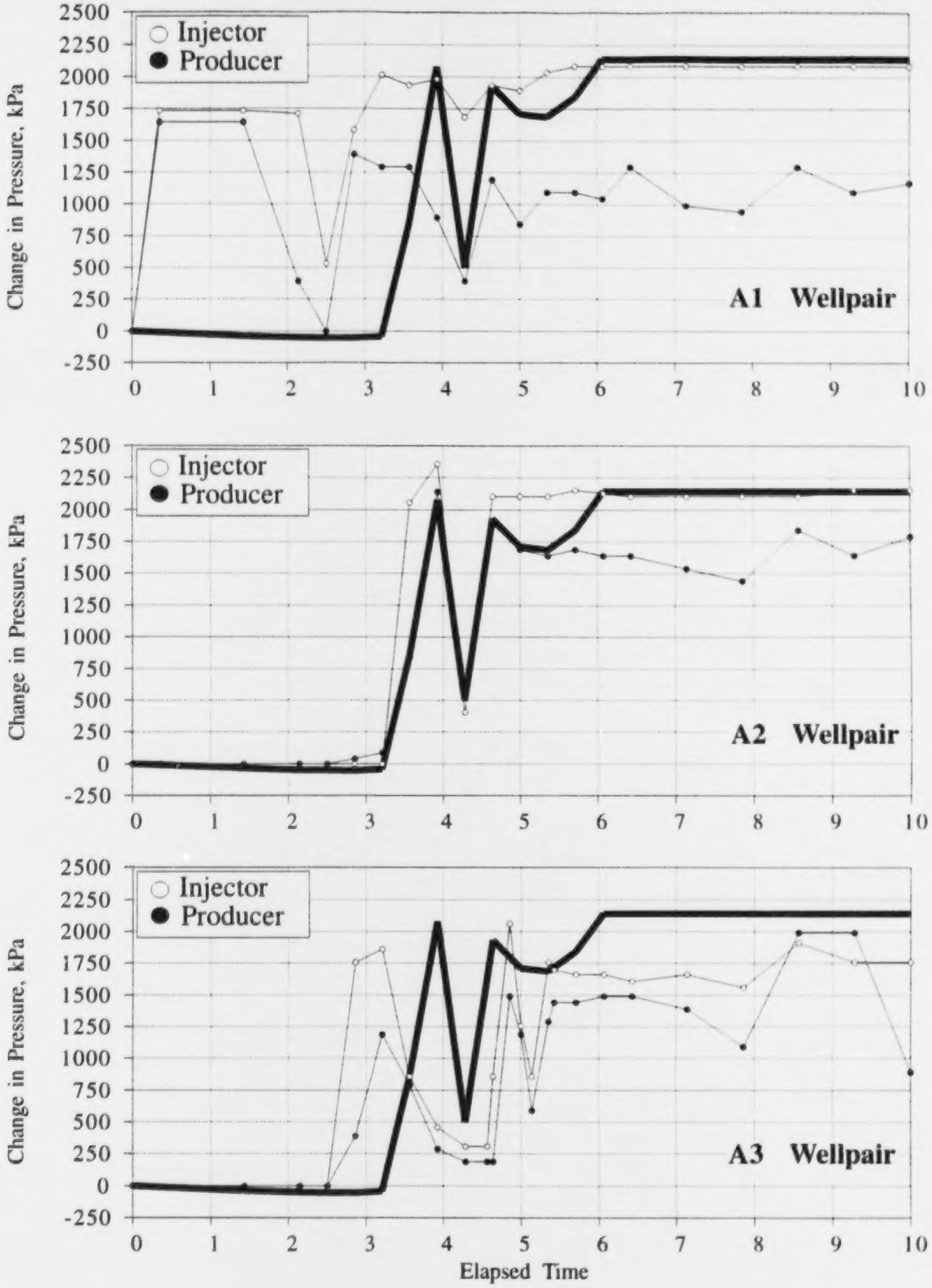

Figure B26 Relationship Between Injection and Production Pressures Changes and Change in Pressure for Piezometer at Elevation 281.9 m in Well AGP5

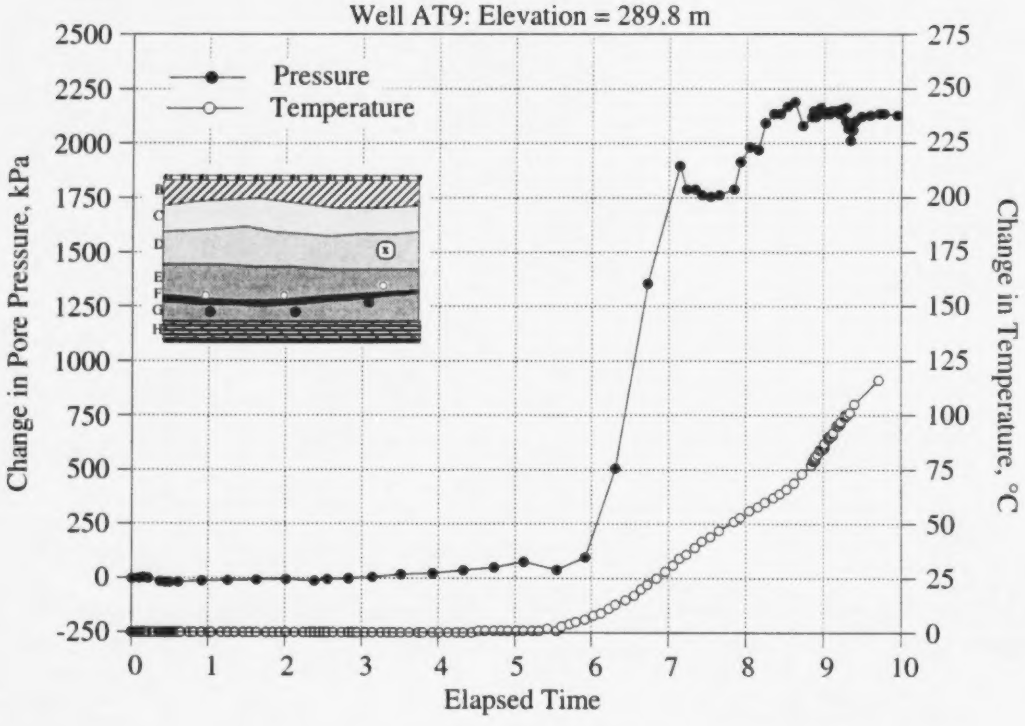

Figure B27 Change in Pressure for Piezometer at Elevation 289.8 in Well AT9

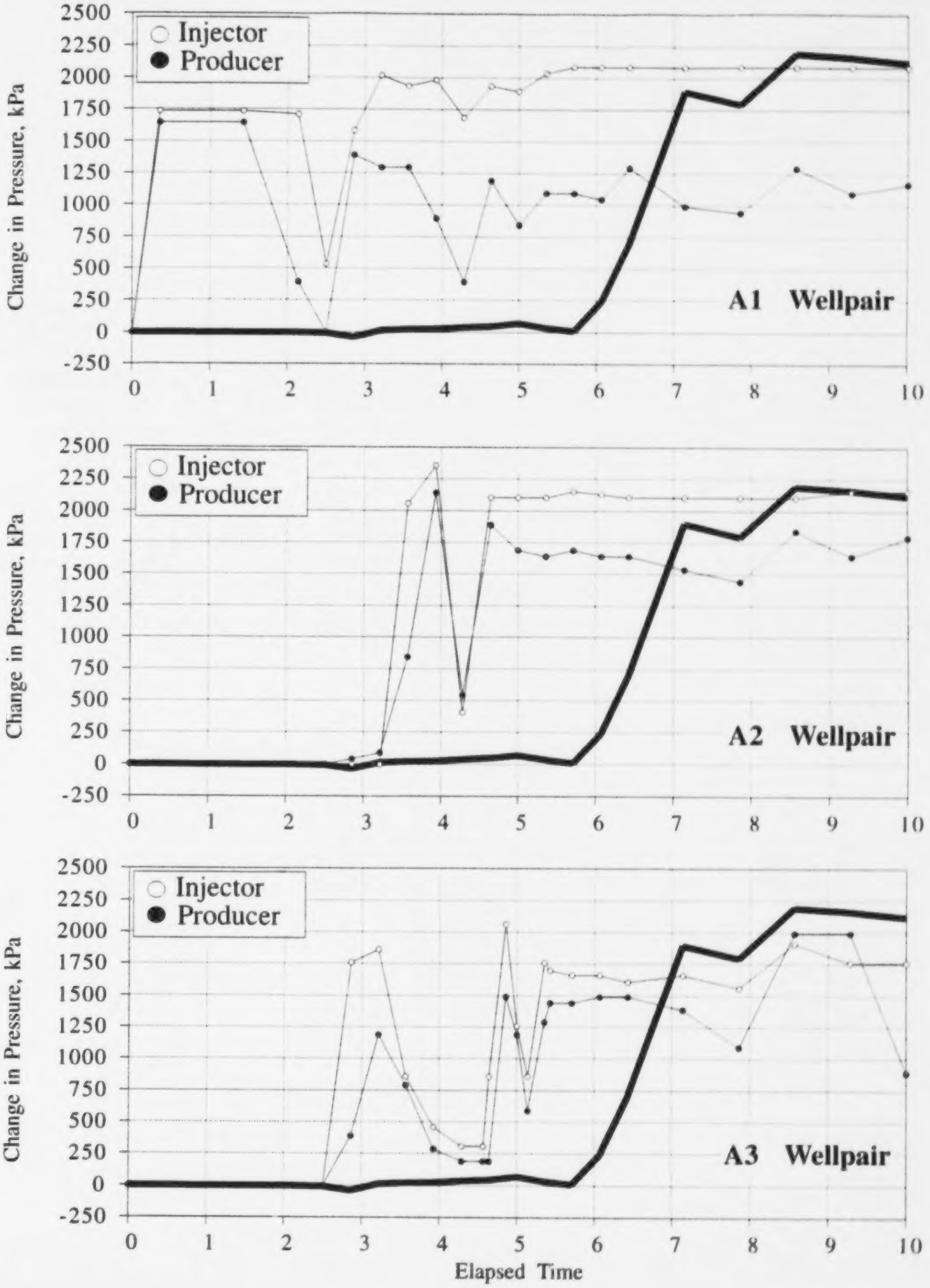

Figure B28 Relationship Between Injection and Production Pressures Changes and Change in Pressure for Piezometer at Elevation 289.8 in Well AT9

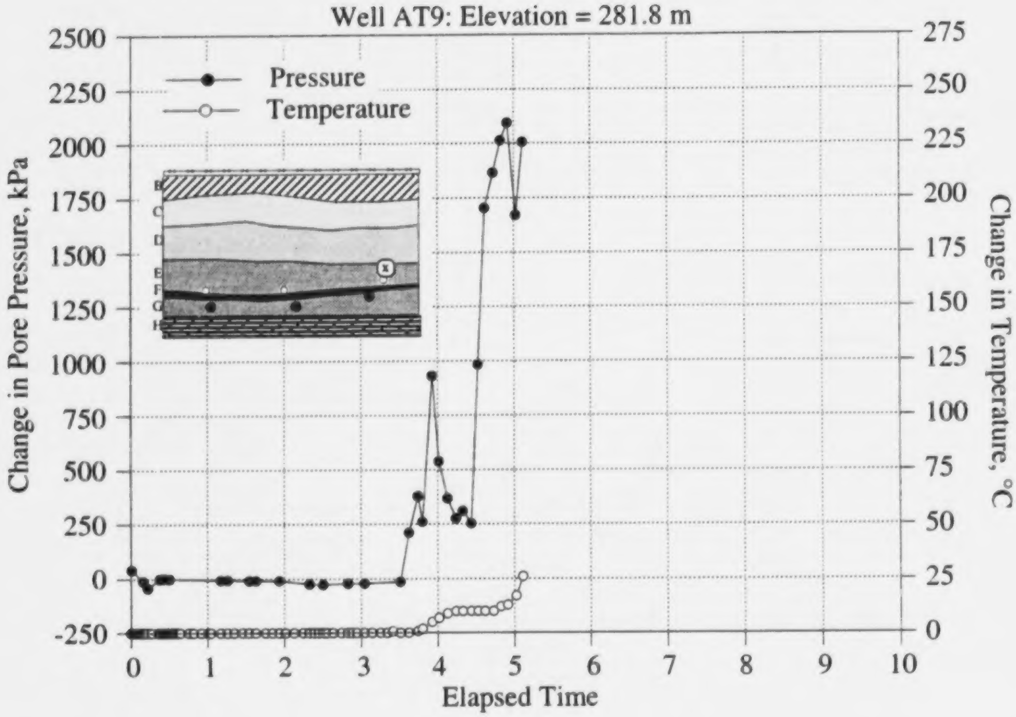

Figure B29 Change in Pressure for Piezometer at Elevation 281.8 m in Well AT9

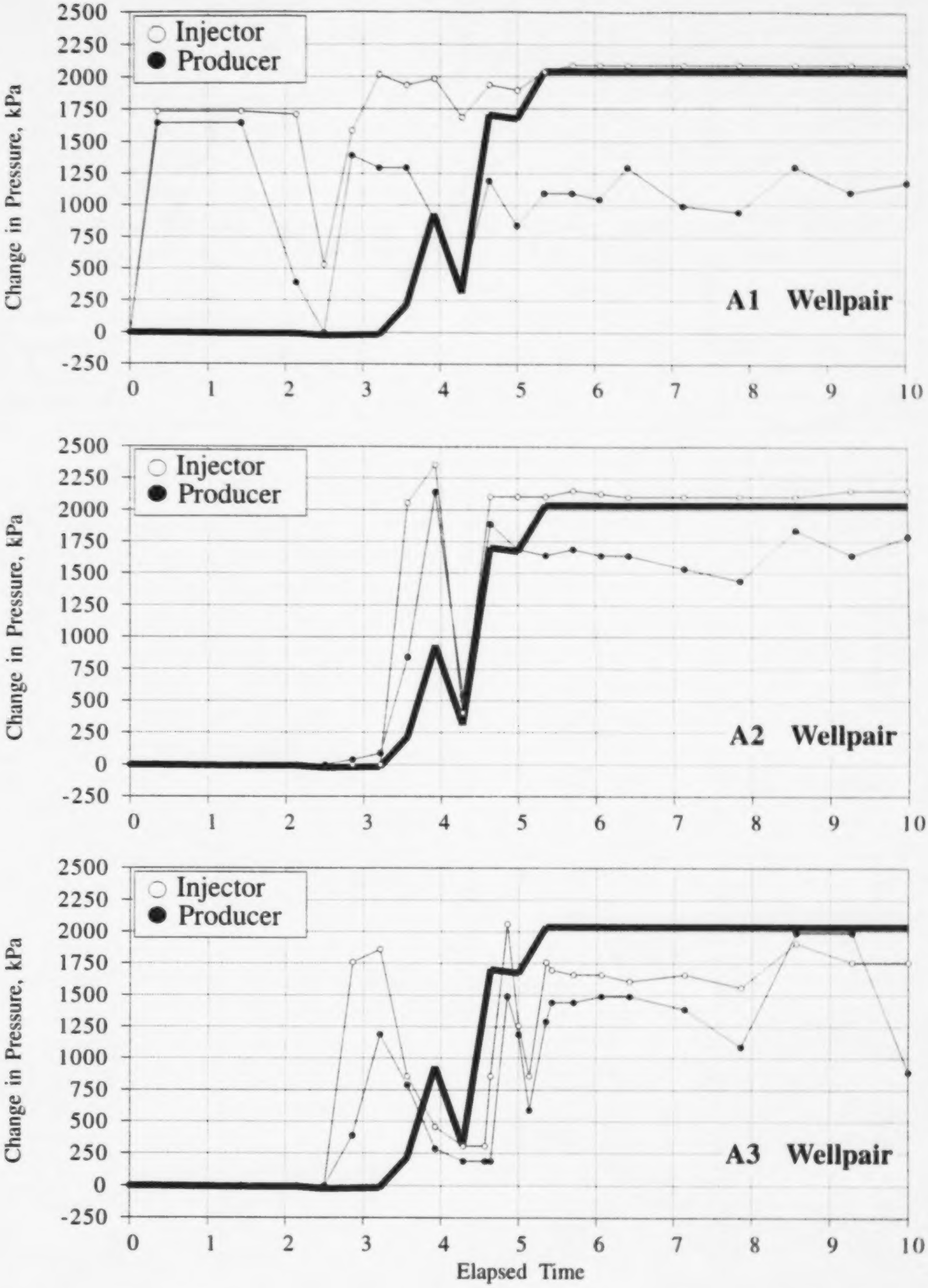

Figure B30 Relationship Between Injection and Production Pressures Changes and Change in Pressure for Piezometer at Elevation 281.8 m in Well AT9

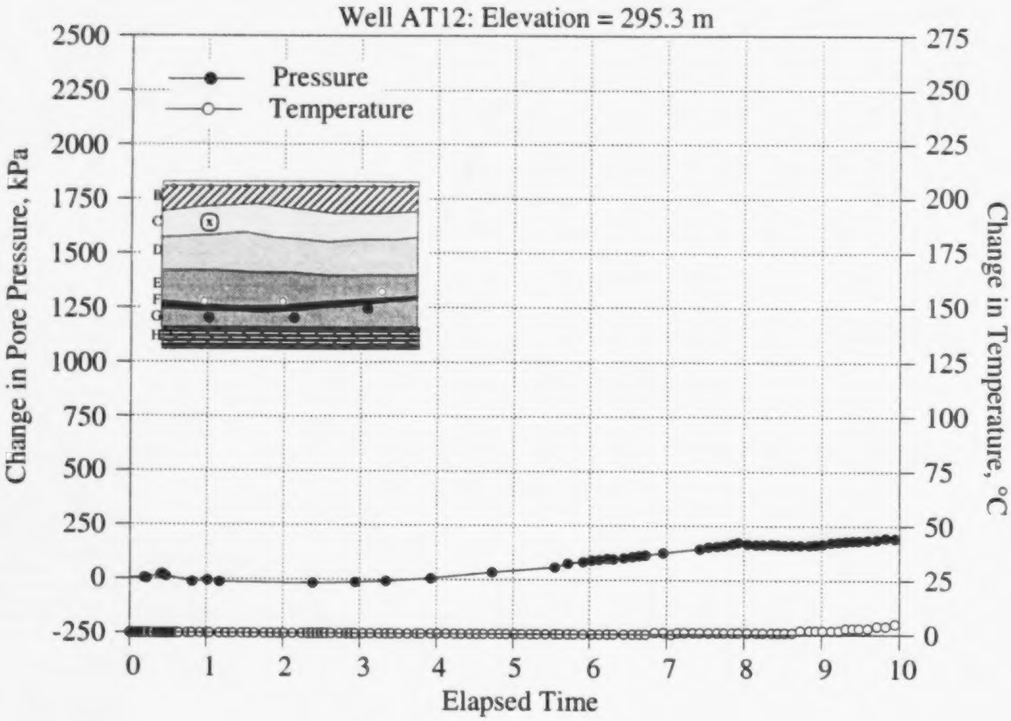

Figure B31 Change in Pressure for Piezometer at Elevation 295.3 m in Well AT12

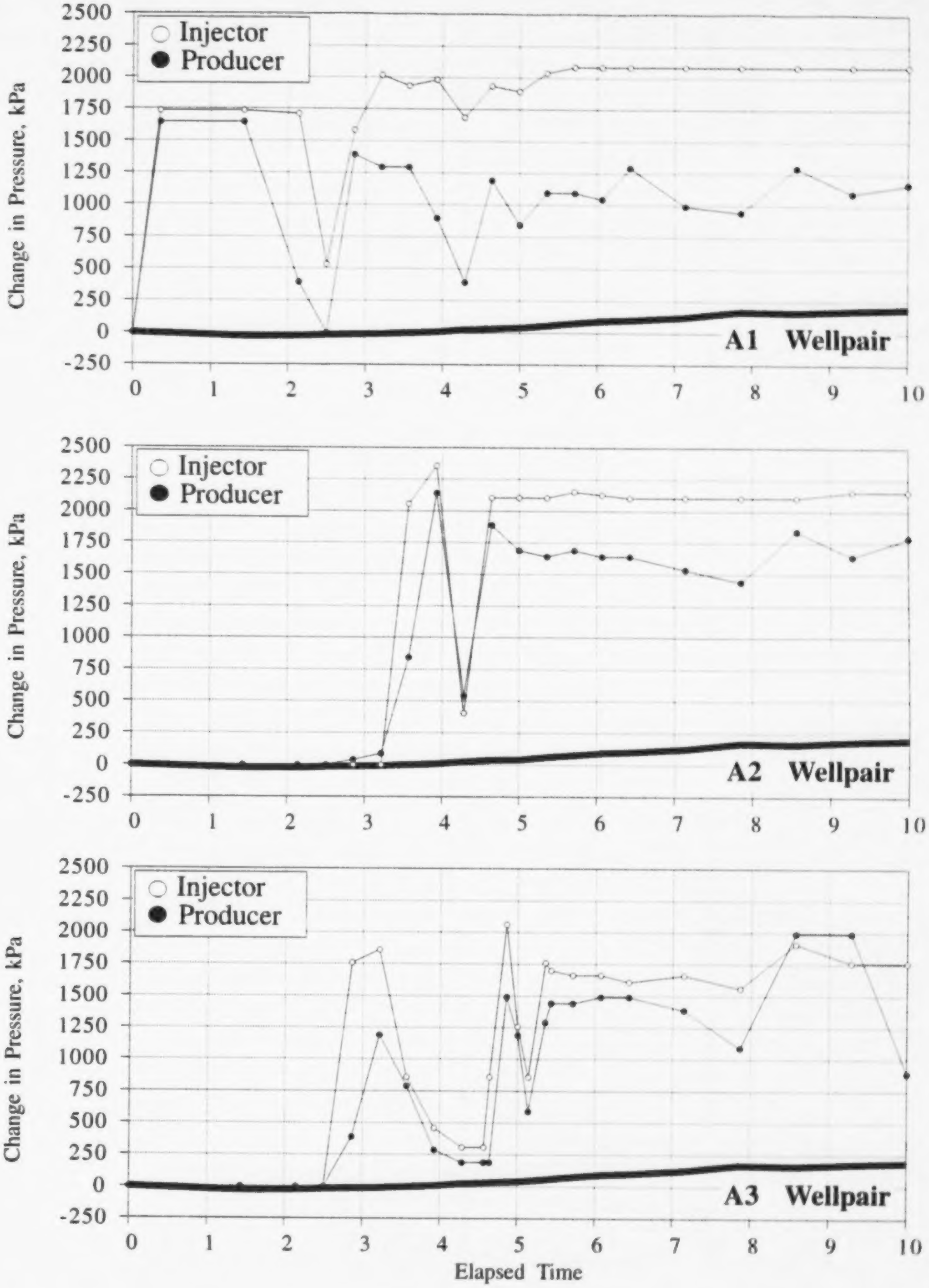

Figure B32 Relationship Between Injection and Production Pressures Changes and Change in Pressure for Piezometer at Elevation 295.3 m in Well AT12

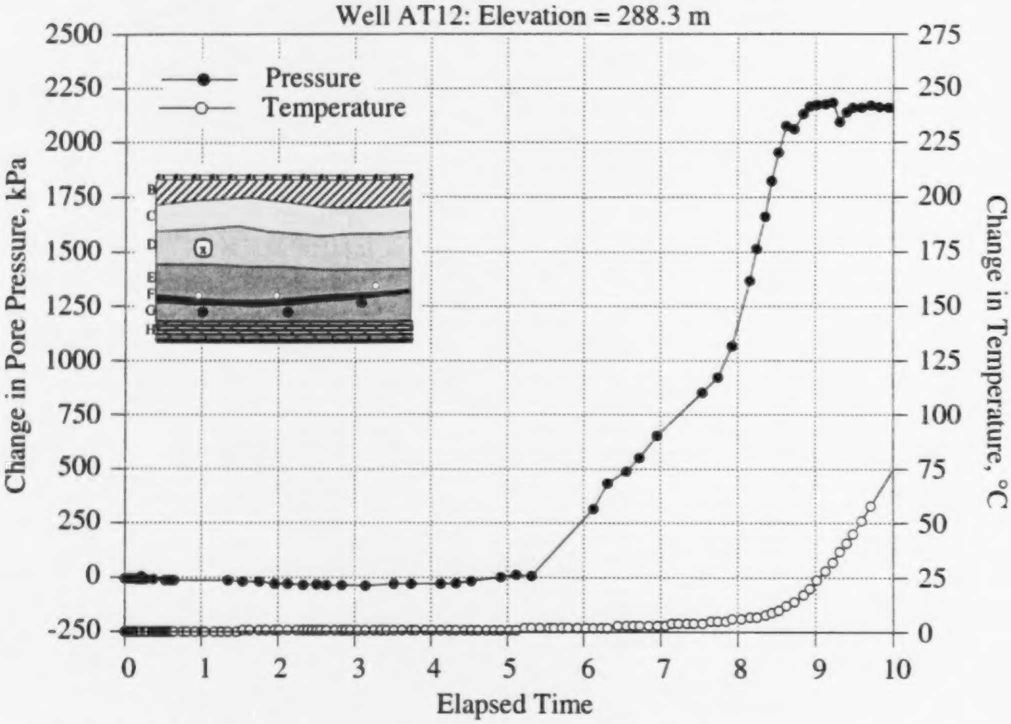

Figure B33 Change in Pressure for Piezometer at Elevation 288.3 m in Well AT12

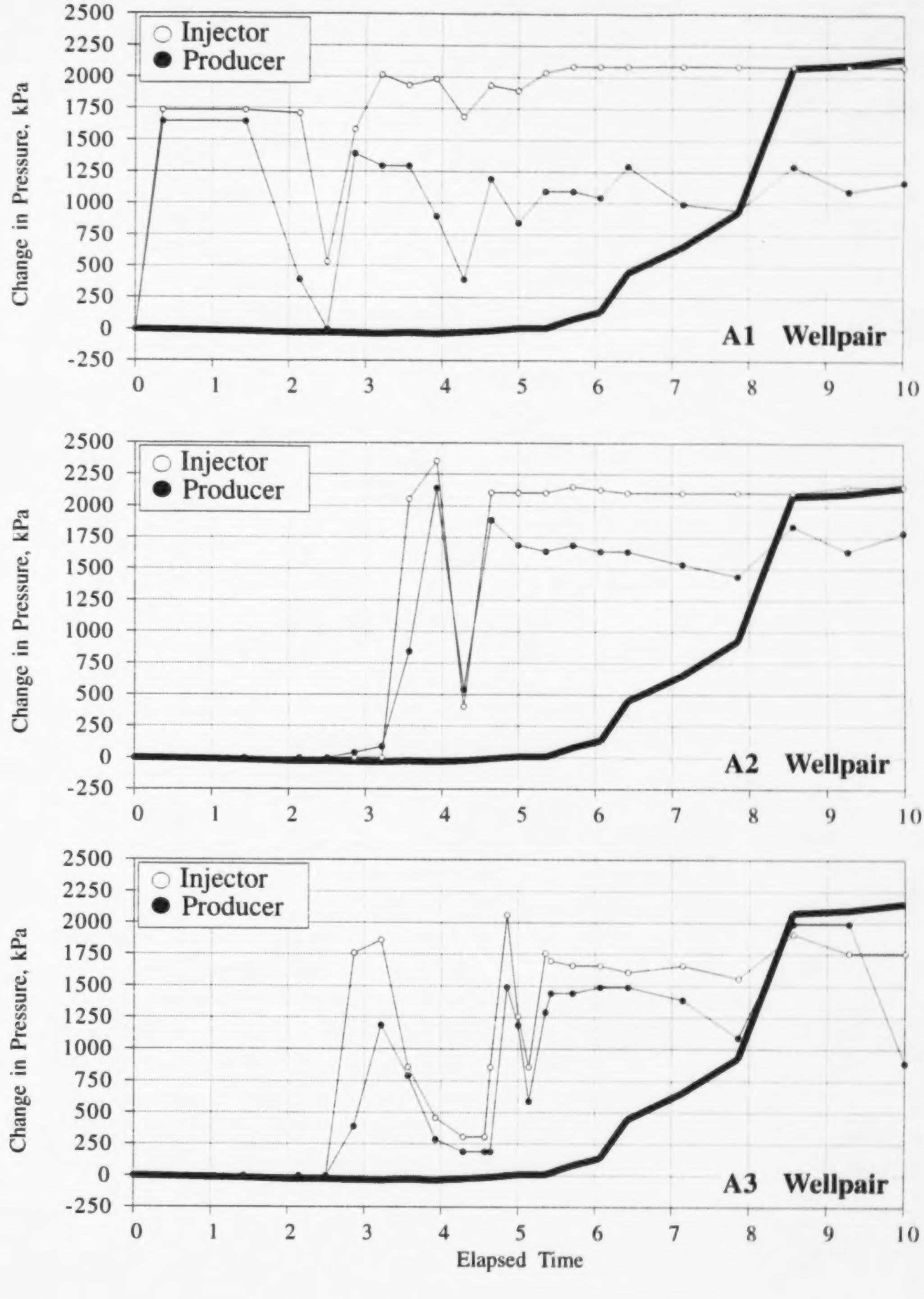

Figure B34 Relationship Between Injection and Production Pressures Changes and Change in Pressure for Piezometer at Elevation 288.3 m in Well AT12

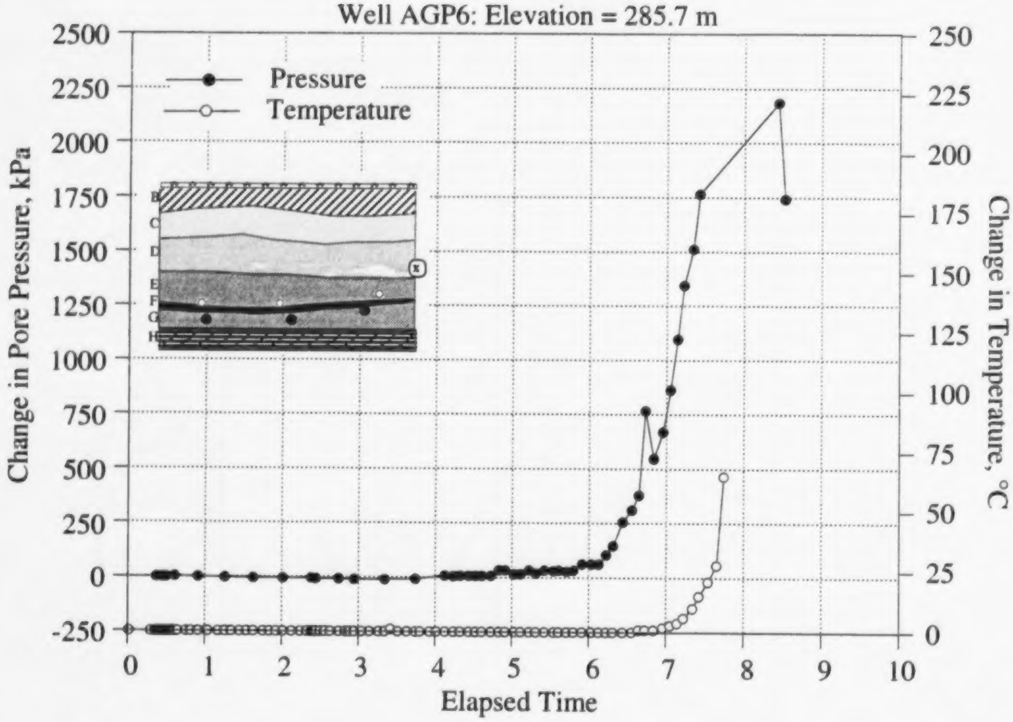

Figure B35 Change in Pressure for Piezometer at Elevation 285.7 m in Well AGP6

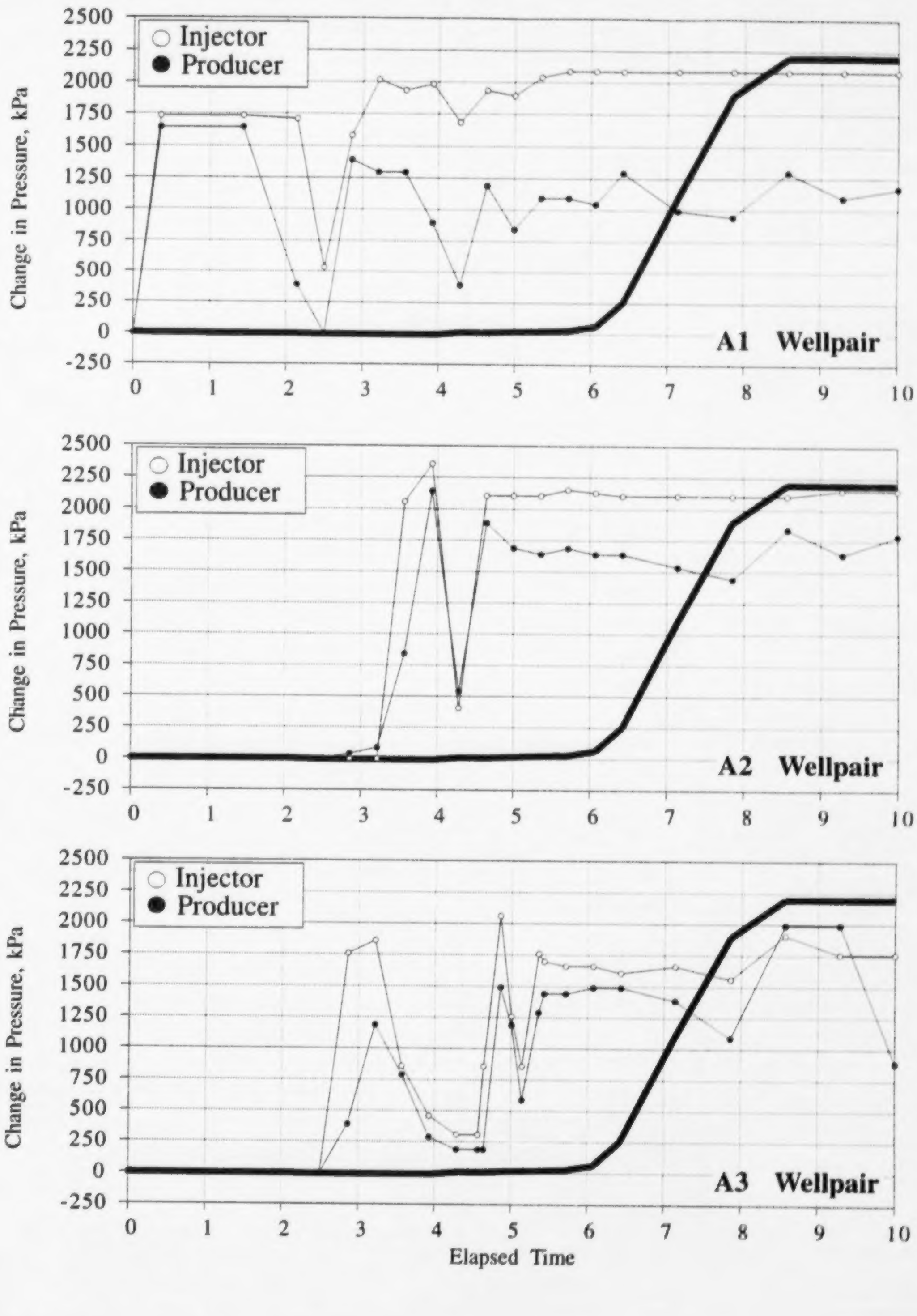

Figure B36 Relationship Between Injection and Production Pressures Changes and Change in Pressure for Piezometer at Elevation 285.7 m in Well AGP6

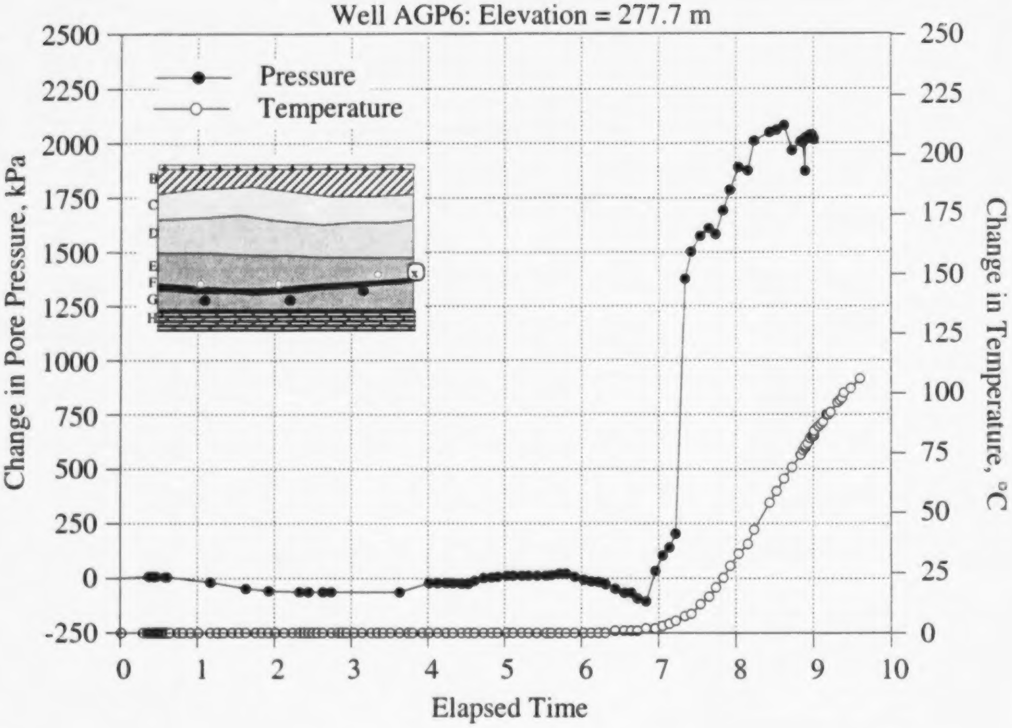

Figure B37 Change in Pressure for Piezometer at Elevation 277.7 m in Well AGP6

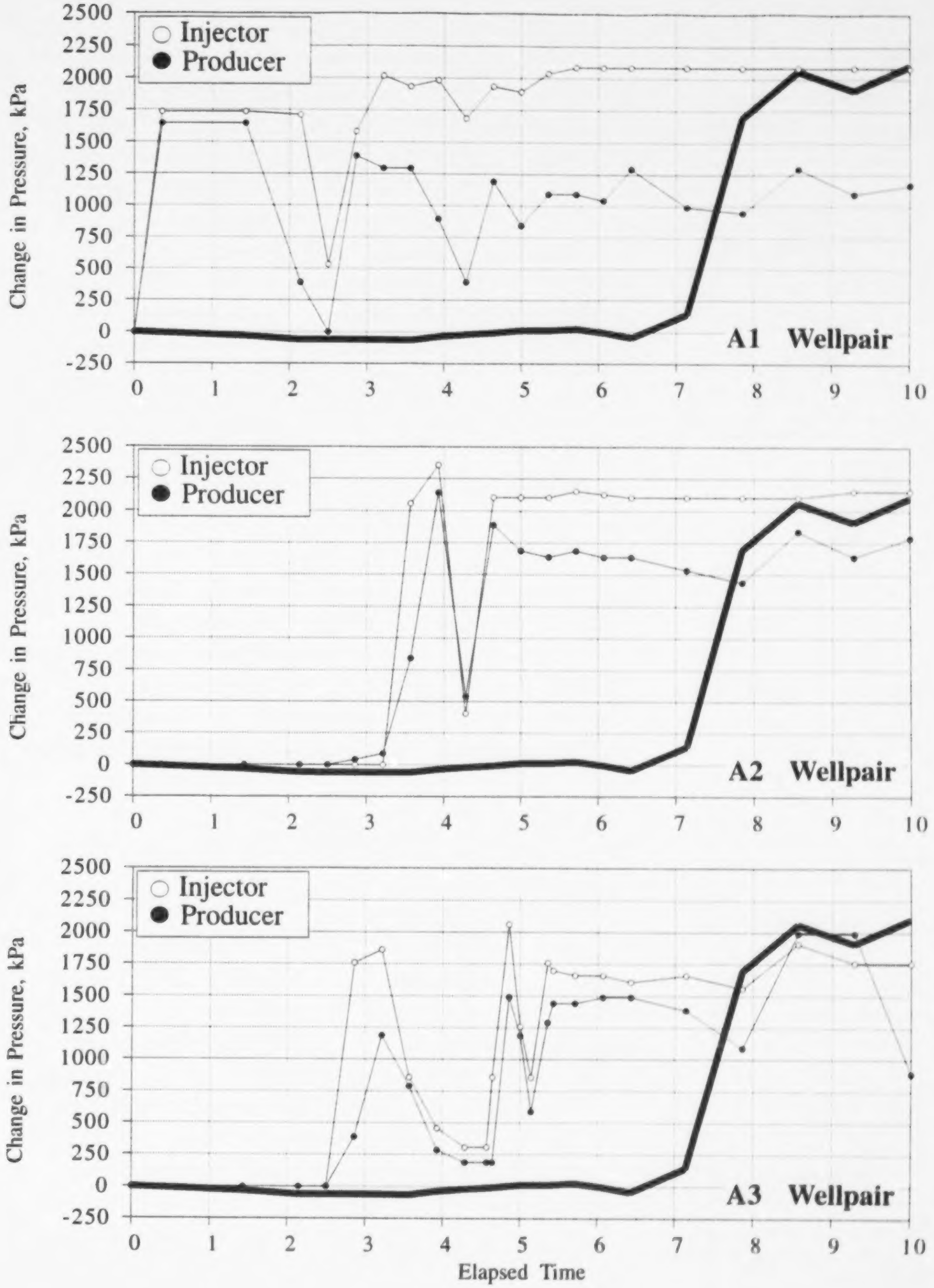

Figure B38 Relationship Between Injection and Production Pressures Changes and Change in Pressure for Piezometer at Elevation 277.7 m in Well AGP6

APPENDIX C

Field Extensometer Results

Vertical strains within the Phase A reservoir were measured using LVDT-based extensometer modules grouted in three vertical boreholes. These modules were based on a high temperature LVDT, rated to 225 °C, mounted inside an invar tube which connected the extensometer modules. The LVDT was accurate to ±0.2 mm and had a linear range of ±25 mm. The core of the LVDT straddled a telescoping joint in the invar rod adjacent to the lower anchor.

The telescoping joint was fixed during installation by rivets. The rivets were designed to shear under a small load, approximately 200 kg, allowing relative movement of the anchors. The telescoping joint was fixed with rivets such that the LVDT showed an initial compression of approximately 6.0 mm. This effectively left a linear range of 30 mm for extension and 20 mm for compression. The extensometer modules were separated by grouted anchors at 3 m spacing in well AGE2 and 5 m spacing in wells AGE3 and AGE4. With this spacing, the extensometers were accurate to 0.007% strain in AGE2 and 0.004% strain in AGE3 and AGE4. The modules were connected to high temperature resistant cable within the reservoir and spliced to ambient temperature cable above that level.

During installation, each anchor was retracted using a cable. The entire extensometer string, along with a grout pipe, were lowered into the borehole. When in place, the retracting cables were released, setting the anchors into the borehole wall. The well was cemented while removing the grout pipe.

This appendix provides the raw field data for each extensometer module as well as the field records during the installation of each module.

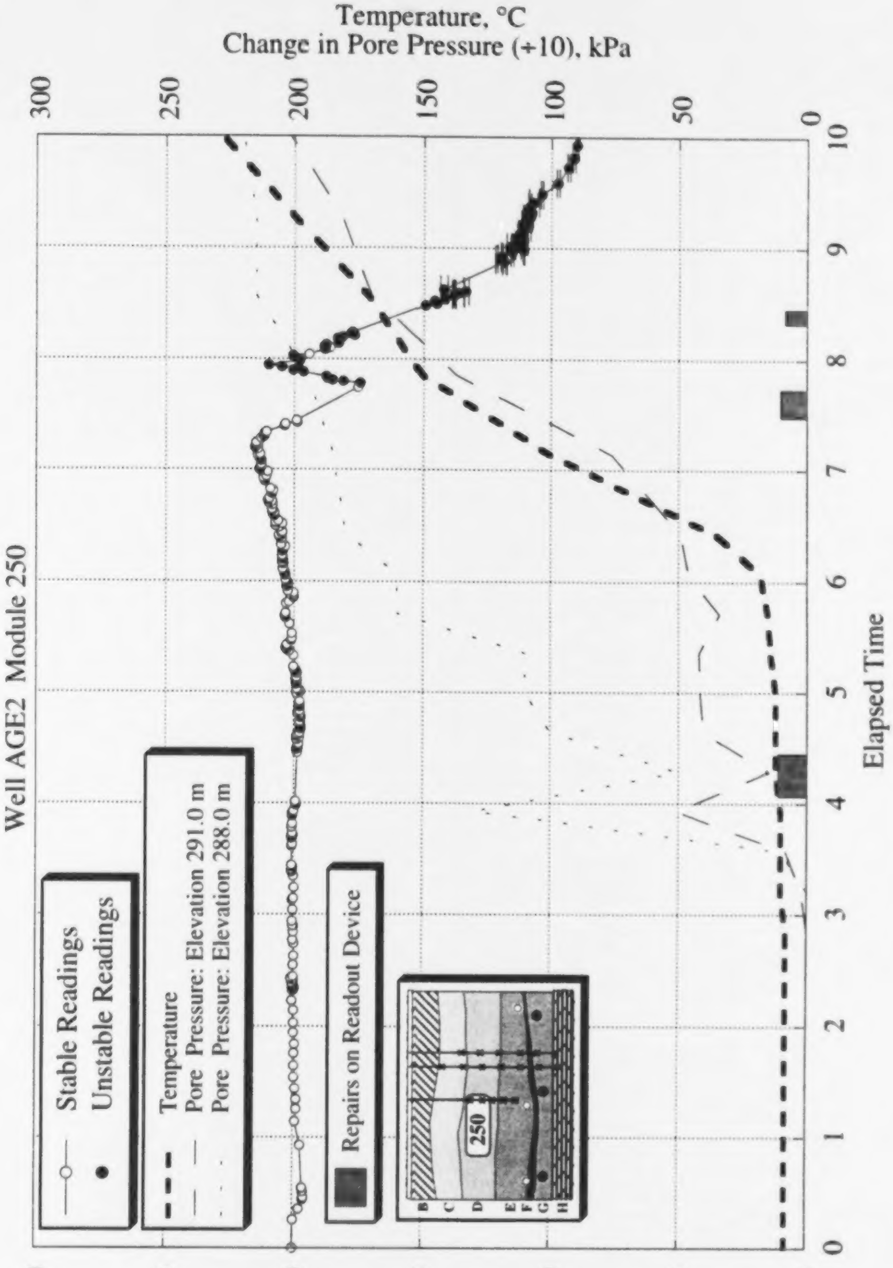

Figure C1 Extensometer History for Module 250 in Well AGE2: Elevation 291.0 to 288.0

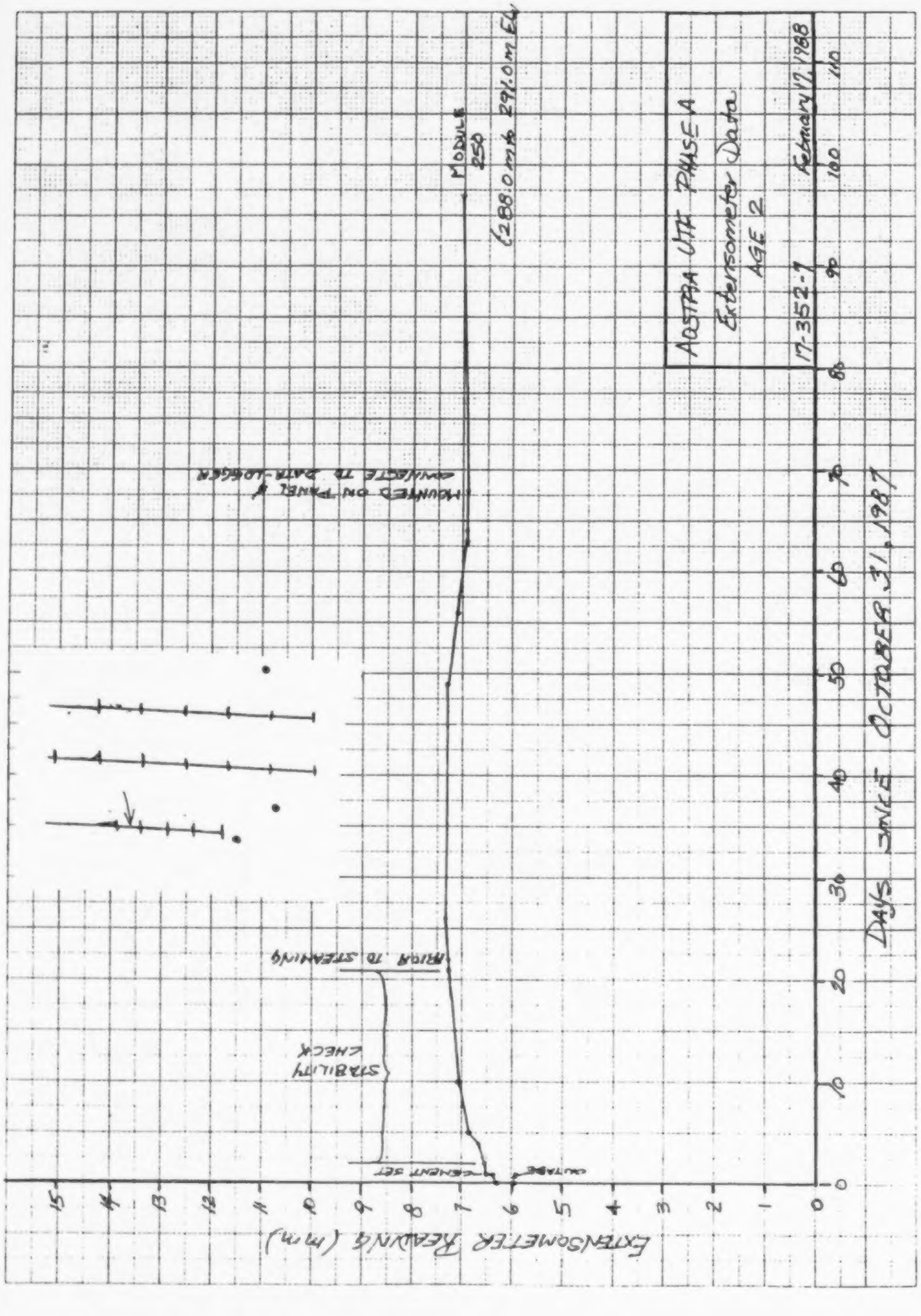

Figure C2 Well AGE2 - Module 250 History during Extensometer Installation

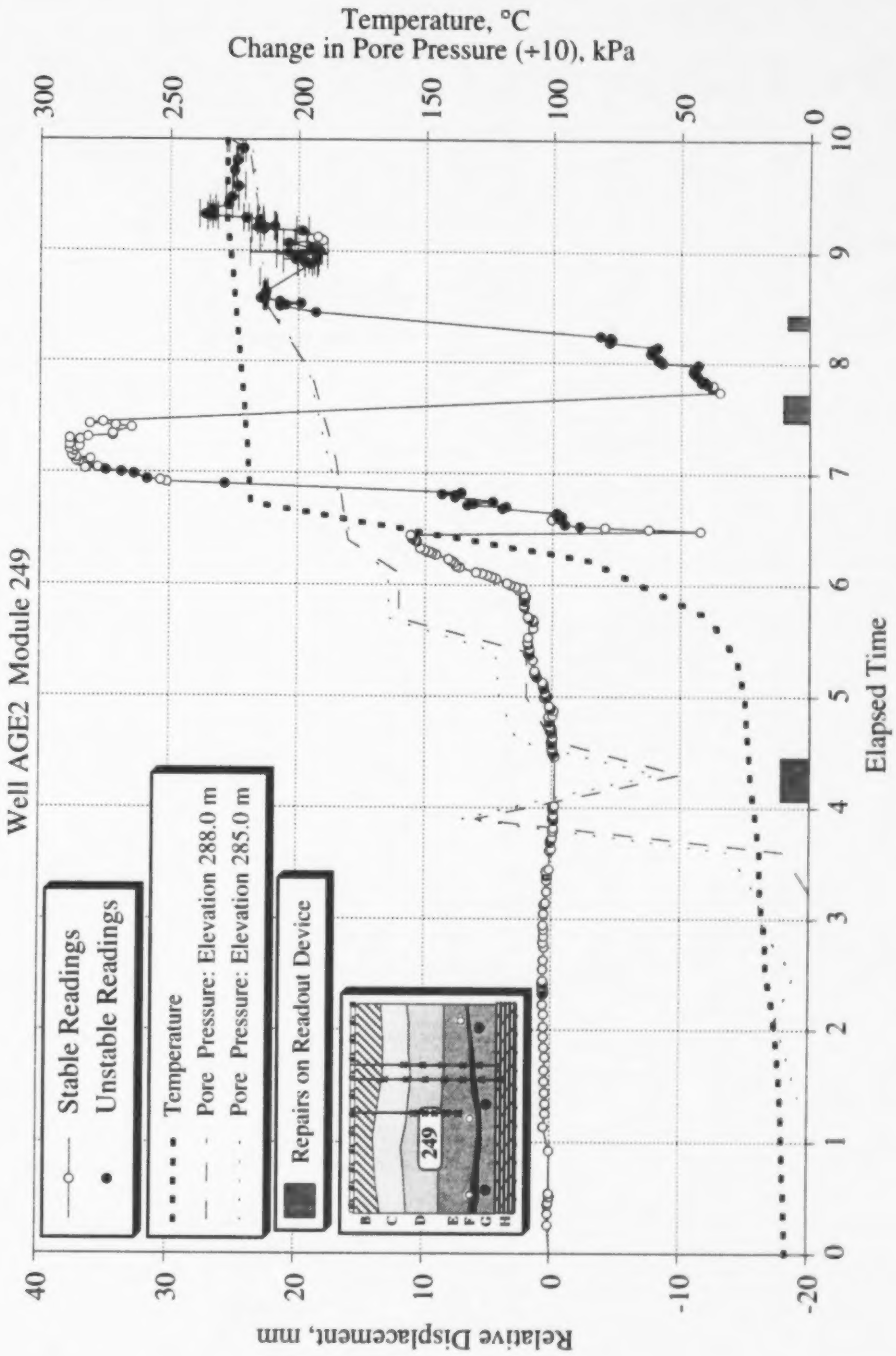

Figure C3 Extensometer History for Module 249 in Well AGE2: Elevation 288.0 to 285.0

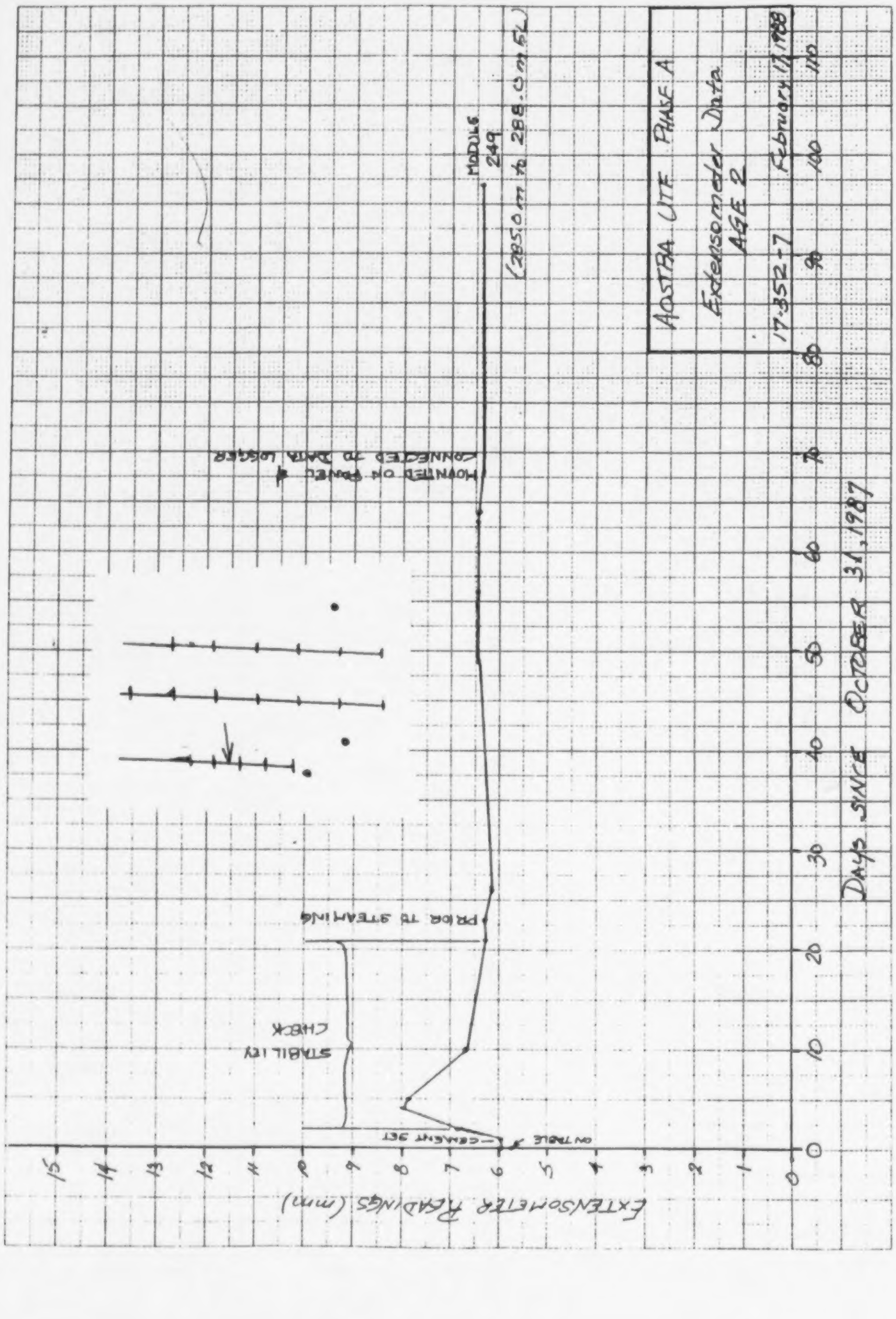

Figure C4 Well AGE2 - Module 249 History during Extensometer Installation

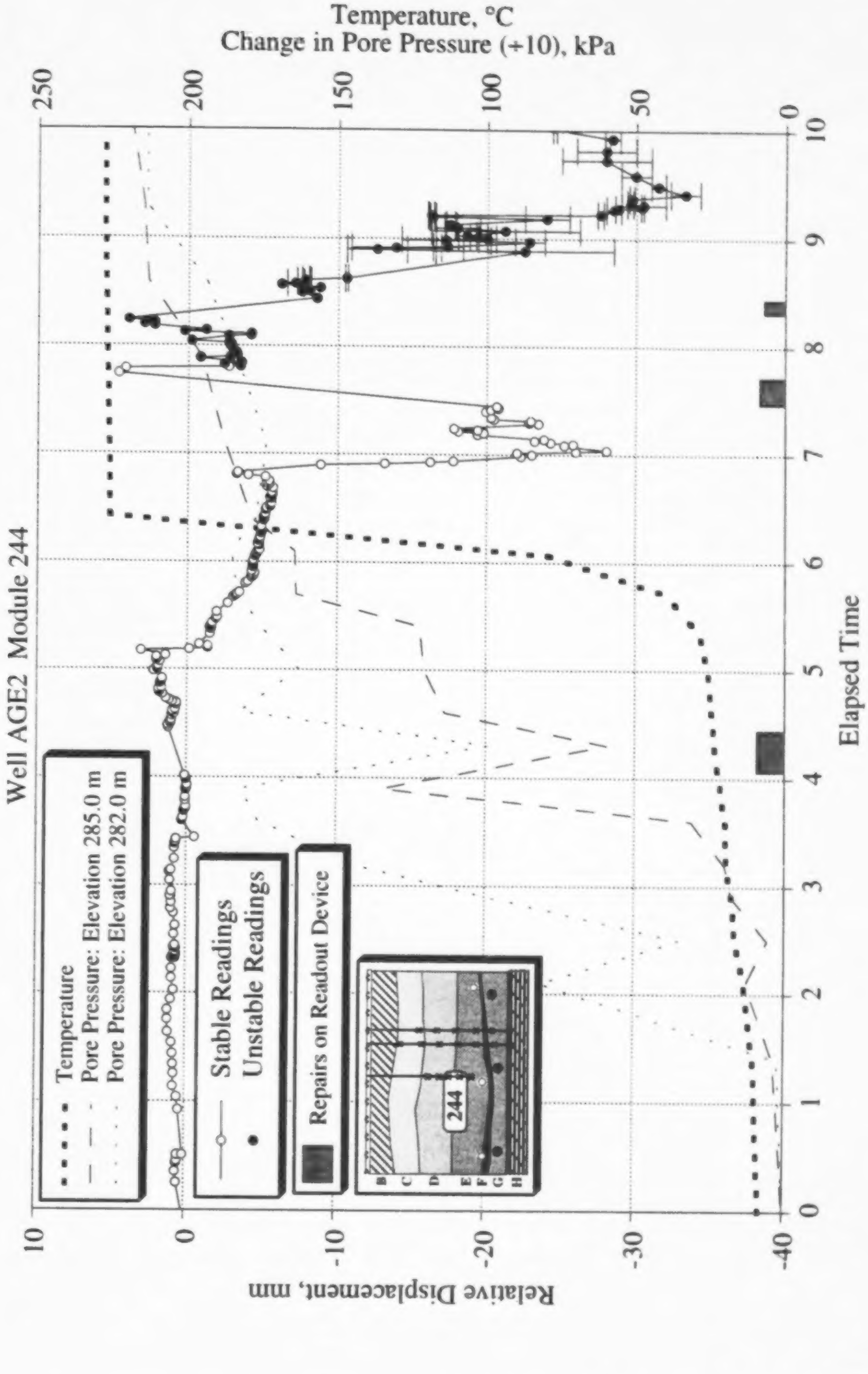

Figure C5 Extensometer History for Module 244 in Well AGE2: Elevation 285.0 to 282.0

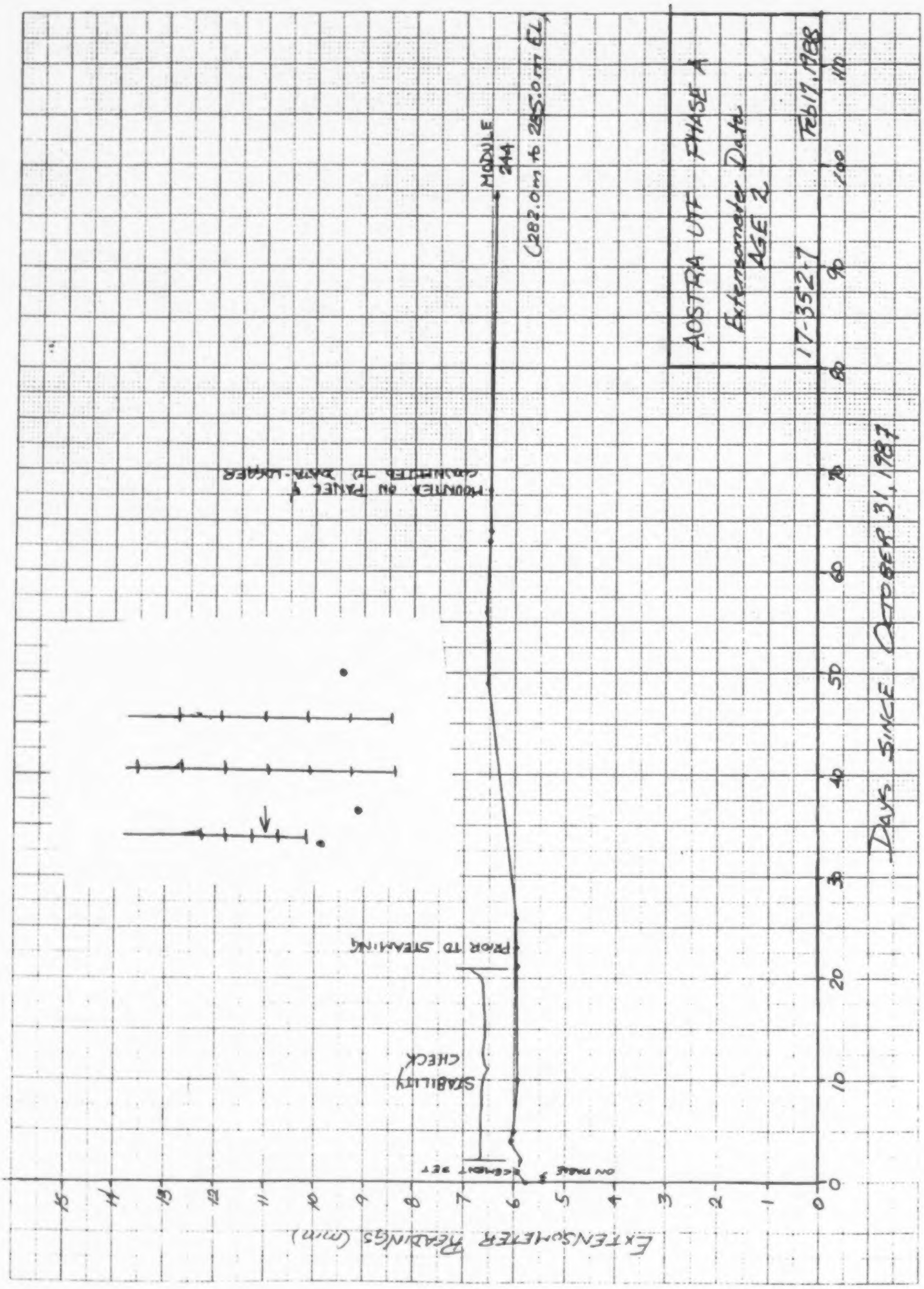

Figure C6 Well AGE2 - Module 244 History during Extensometer Installation

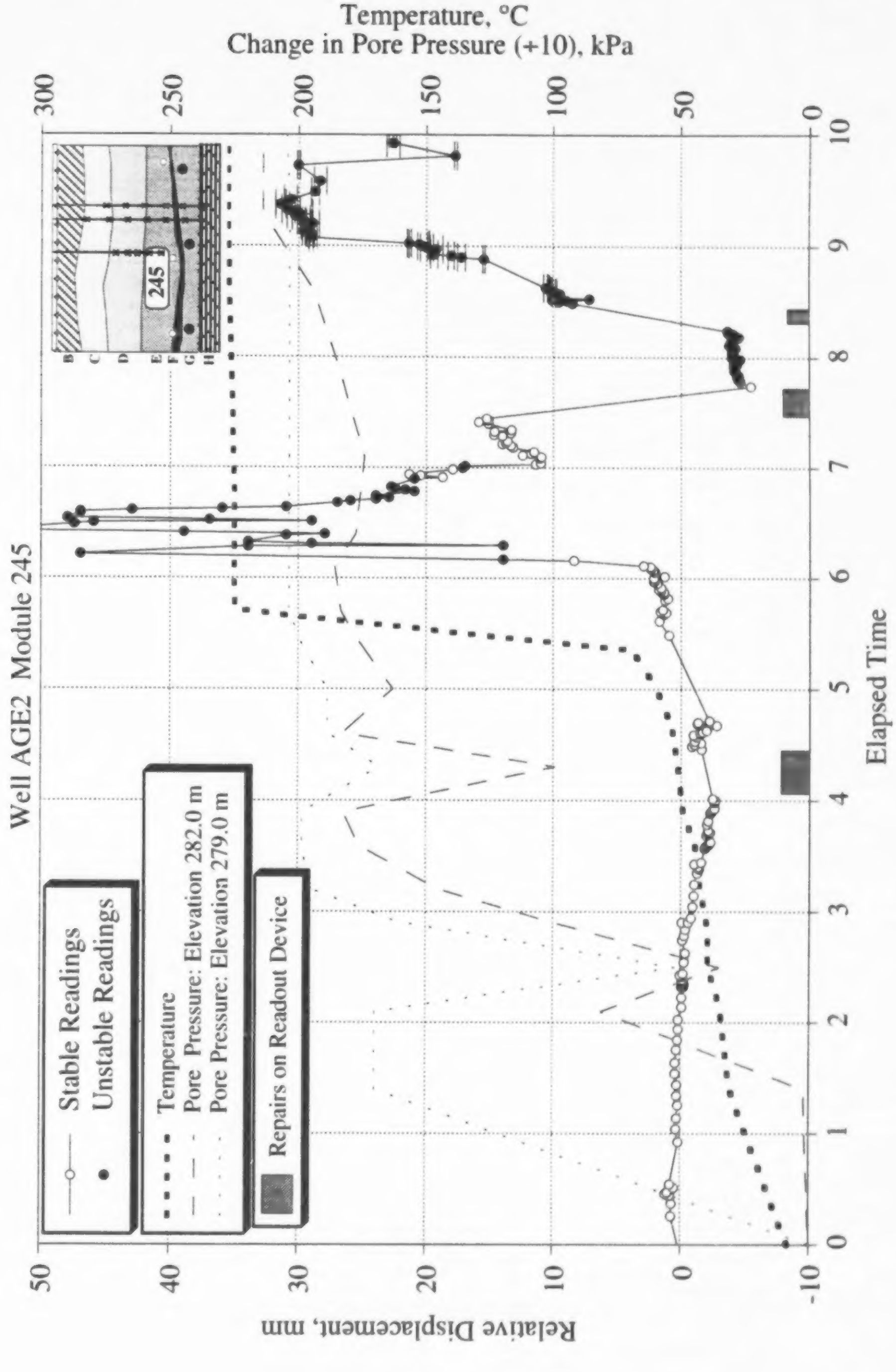

Figure C7 Extensometer History for Module 245 in Well AGE2: Elevation 282.0 to 279.0

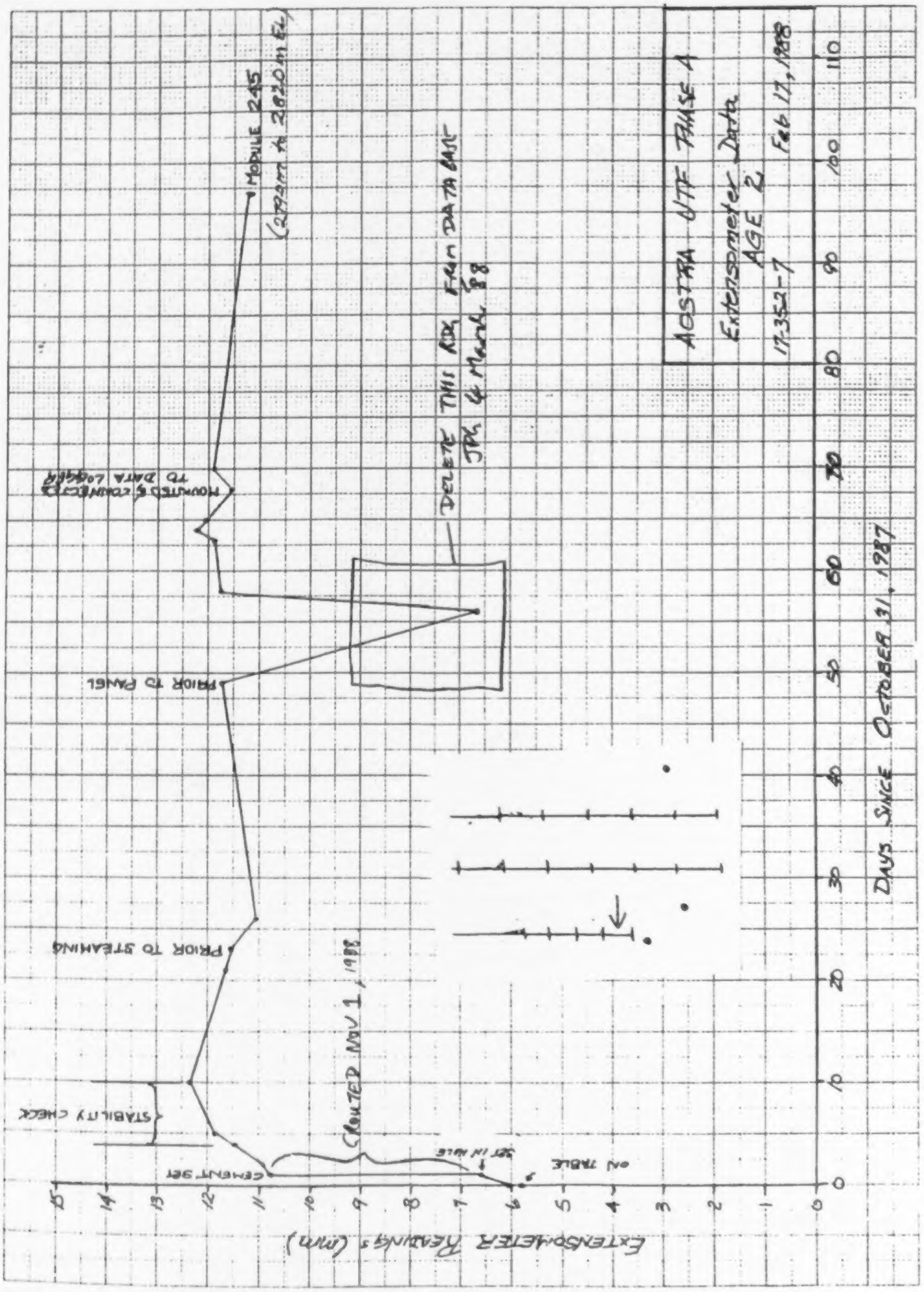

Figure C8 Well AGE2 - Module 245 History during Extensometer Installation

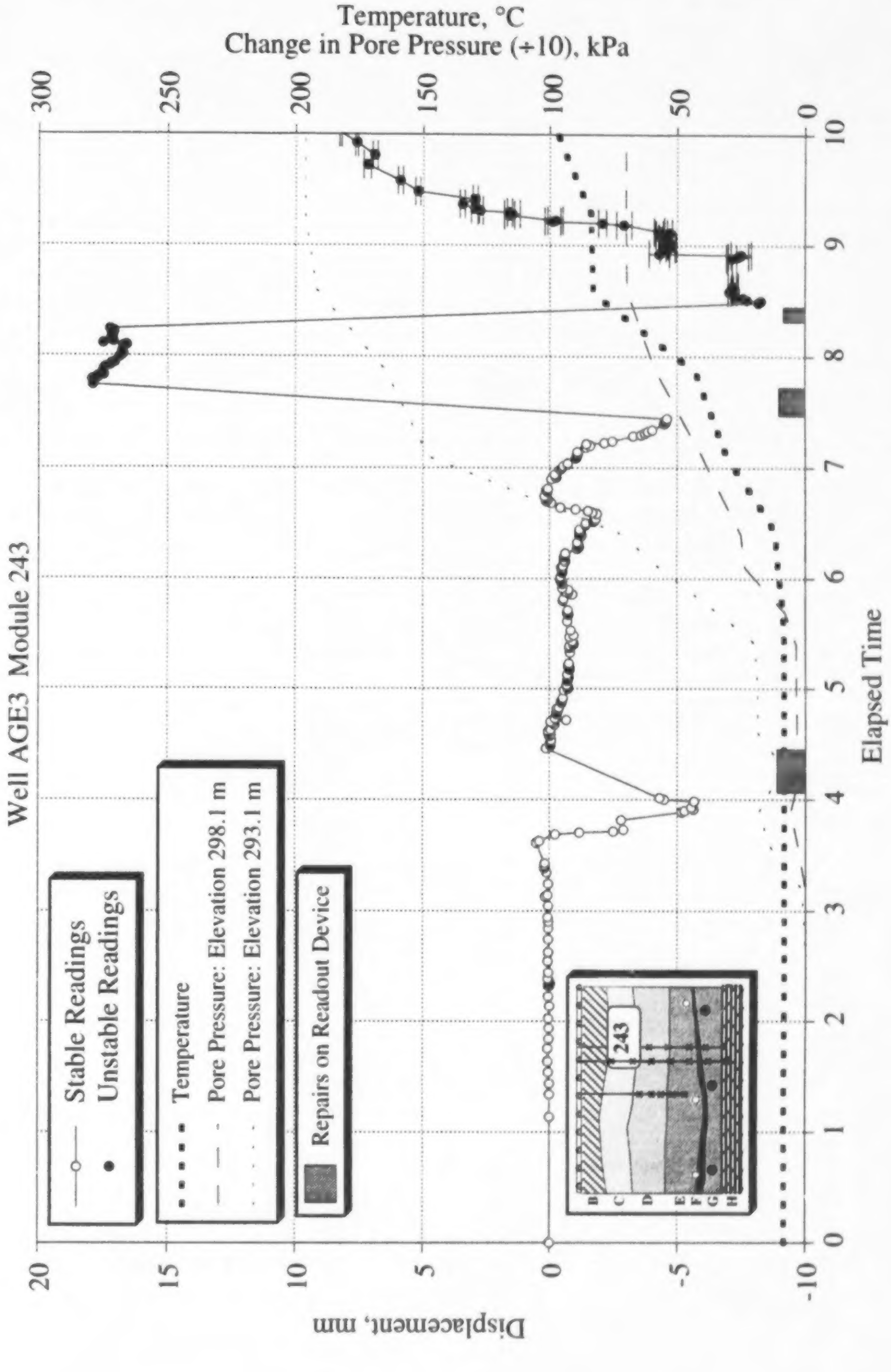

Figure C9 Extensometer History for Module 243 in Well AGE3: Elevation 298.1 to 293.1

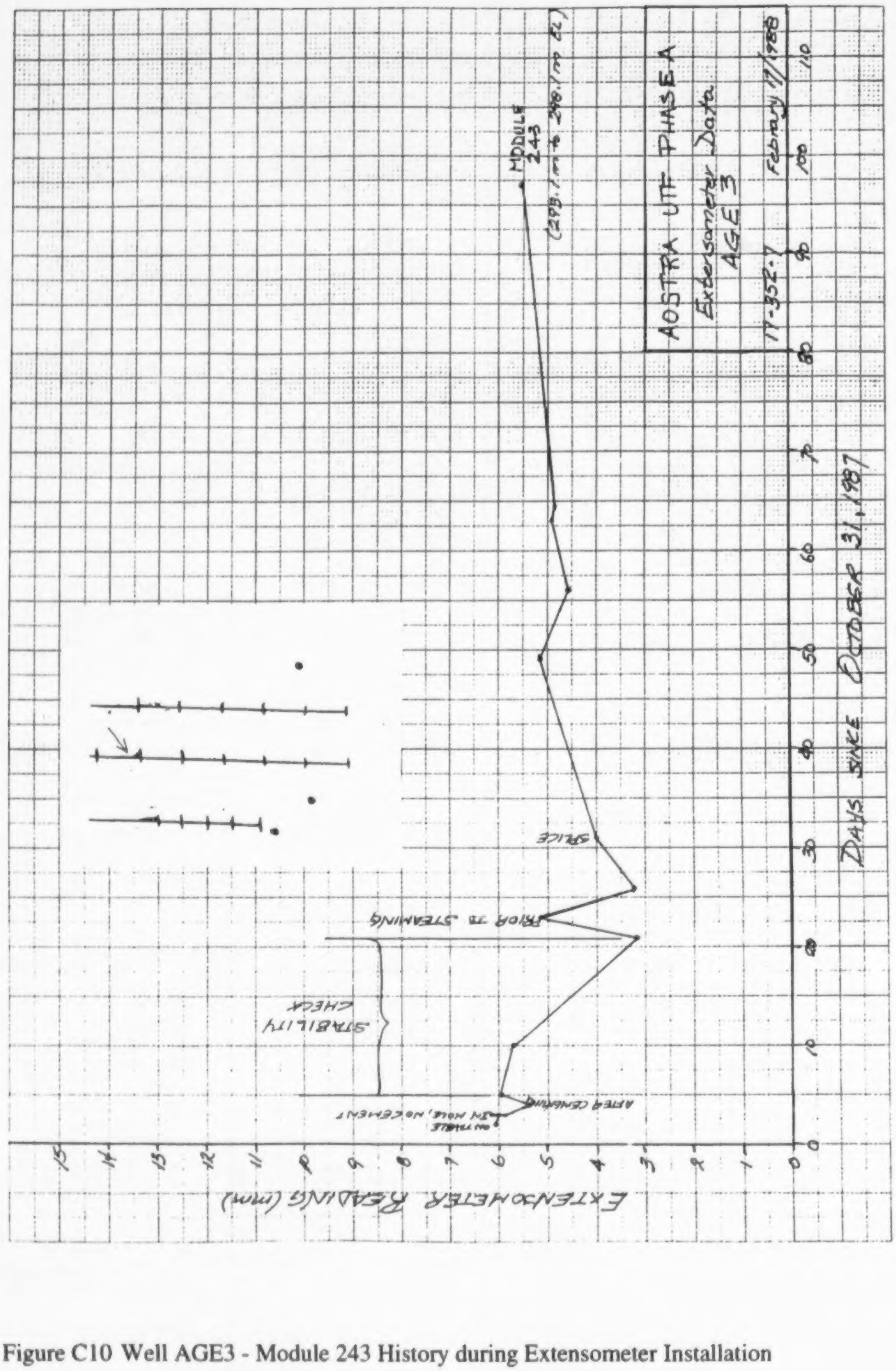

Figure C10 Well AGE3 - Module 243 History during Extensometer Installation

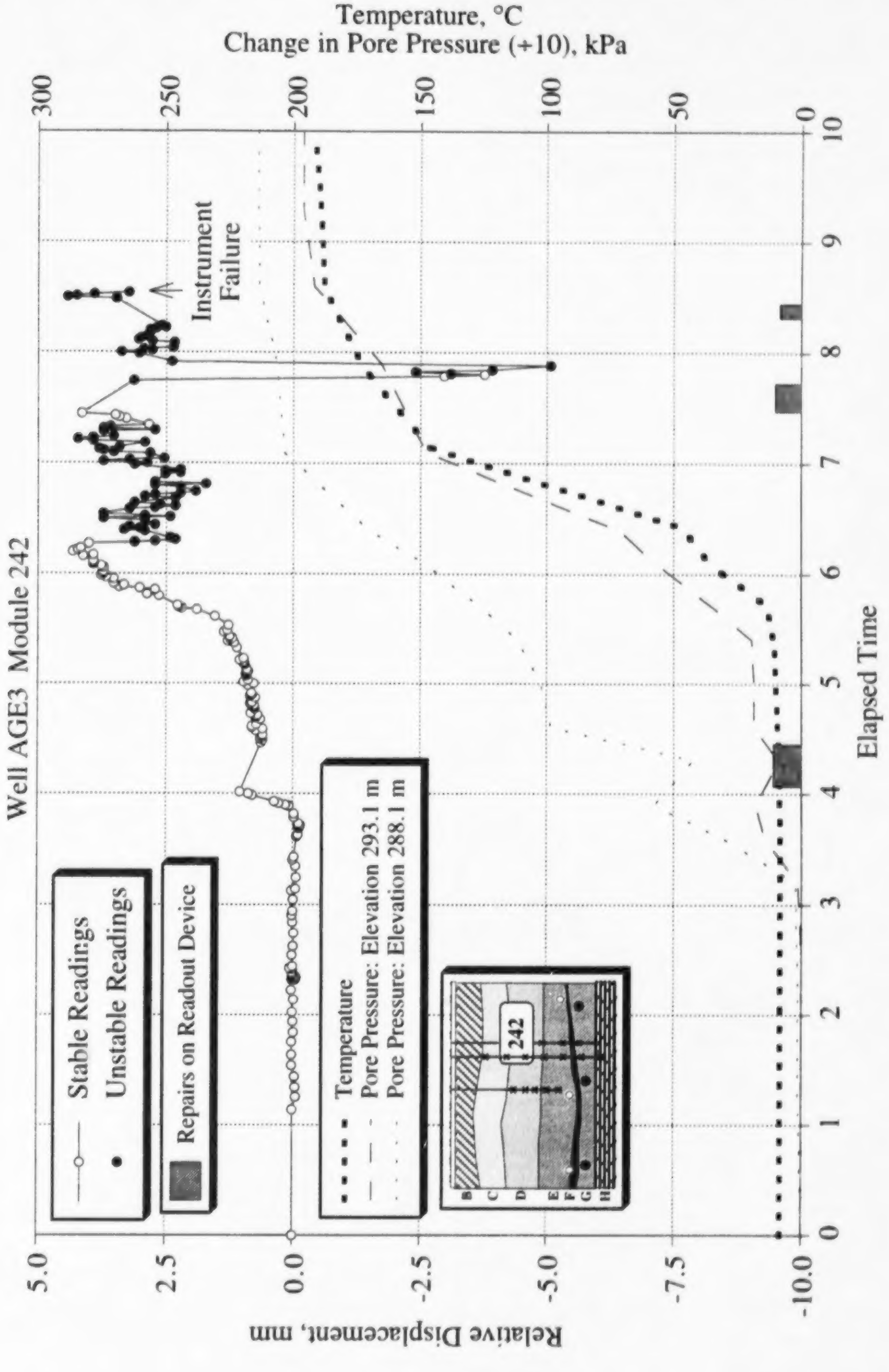

Figure C11 Extensometer History for Module 242 in Well AGE3: Elevation 293.1 to 288.1

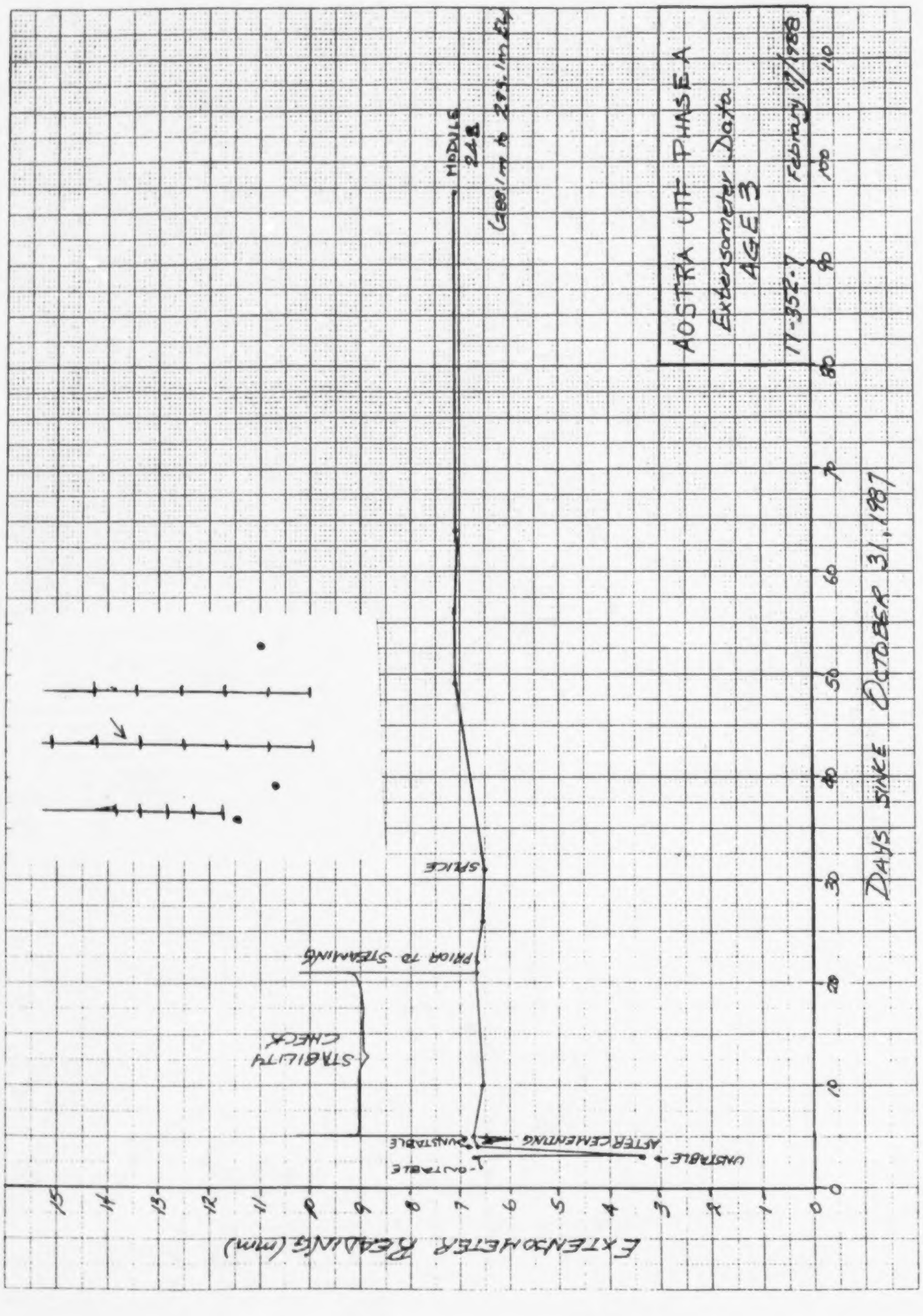

Figure C12 Well AGE3 - Module 242 History during Extensometer Installation

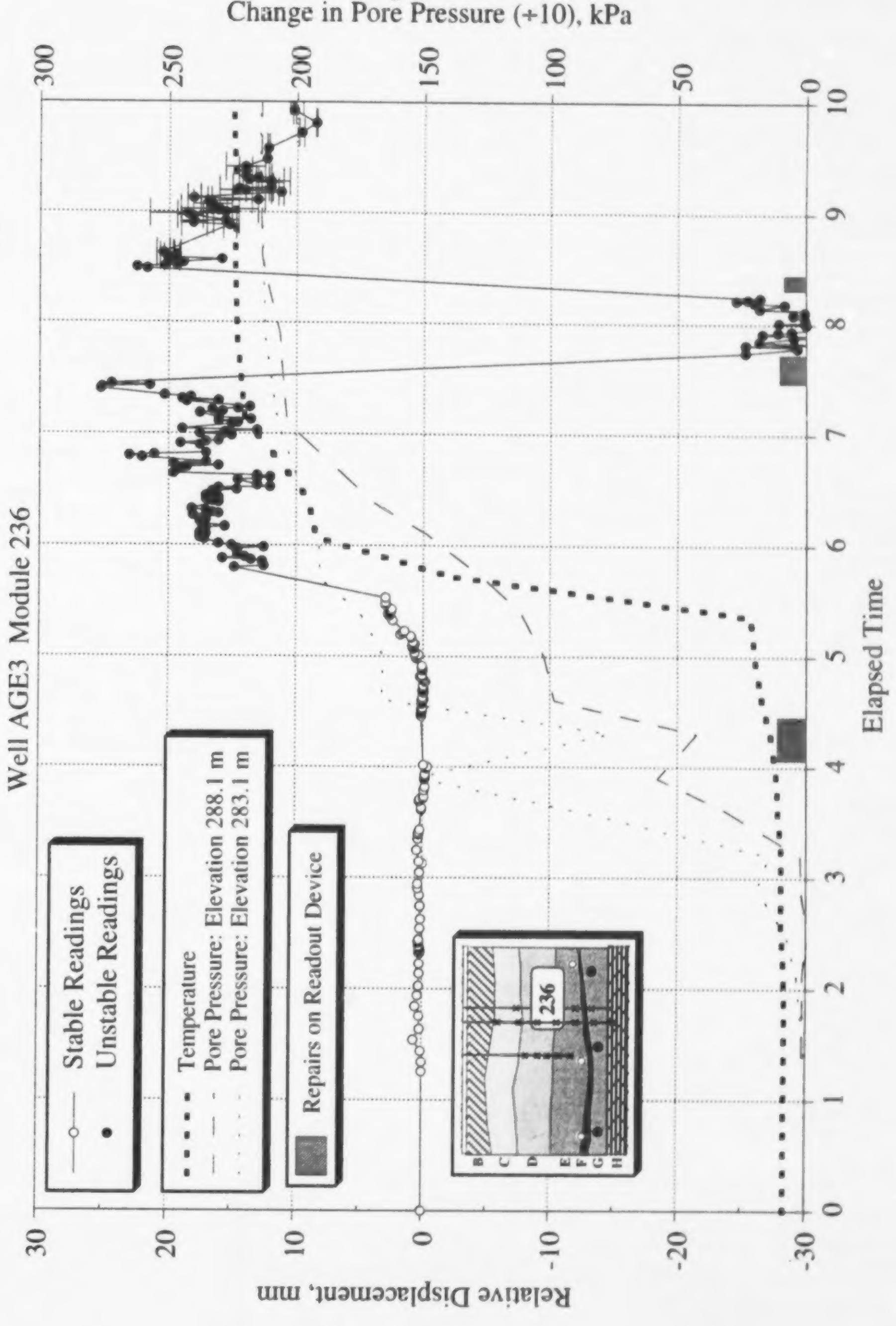

Figure C13 Extensometer History for Module 236 in Well AGE3: Elevation 288.1 to 283.1

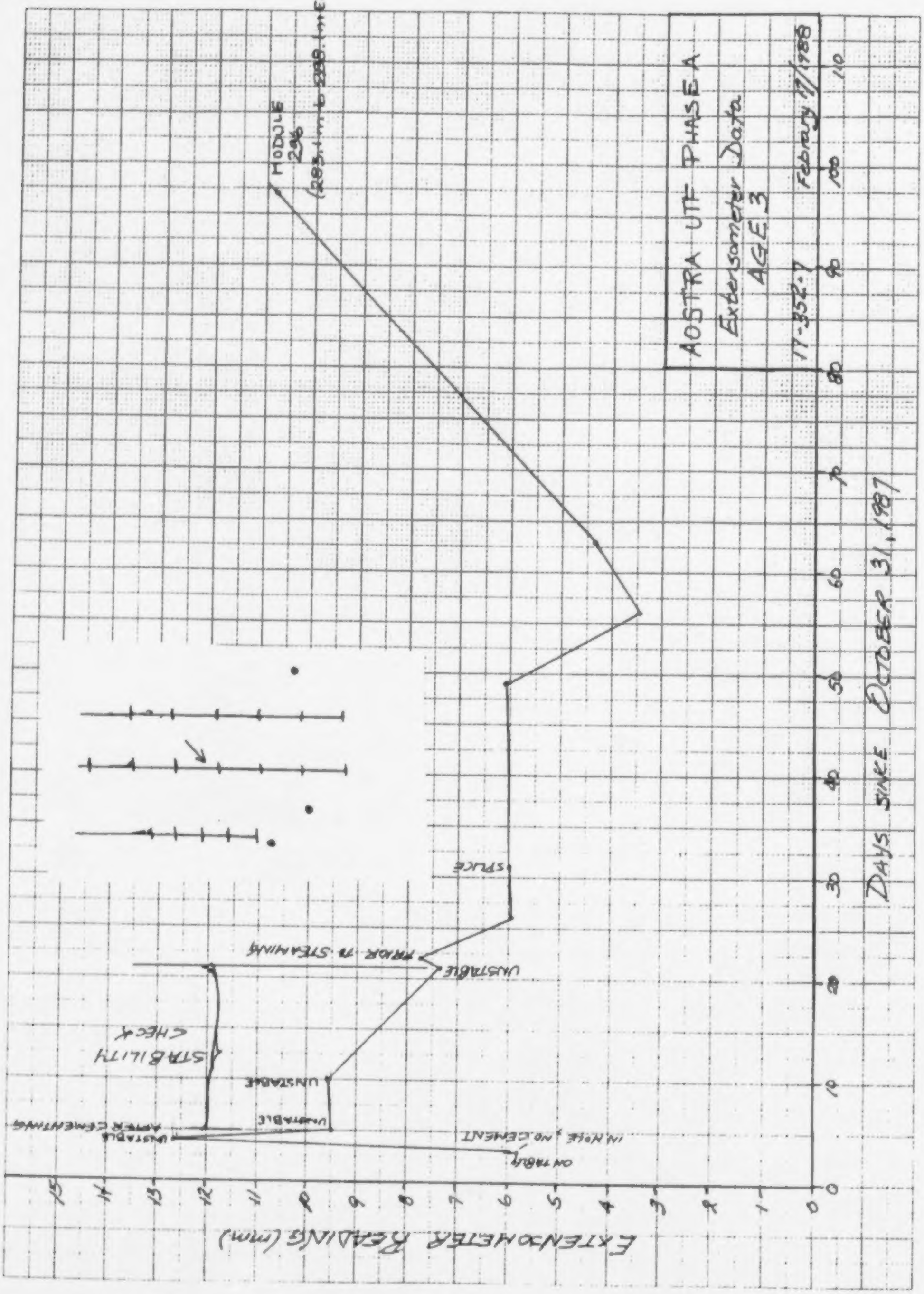

Figure C14 Well AGE3 - Module 236 History during Extensometer Installation

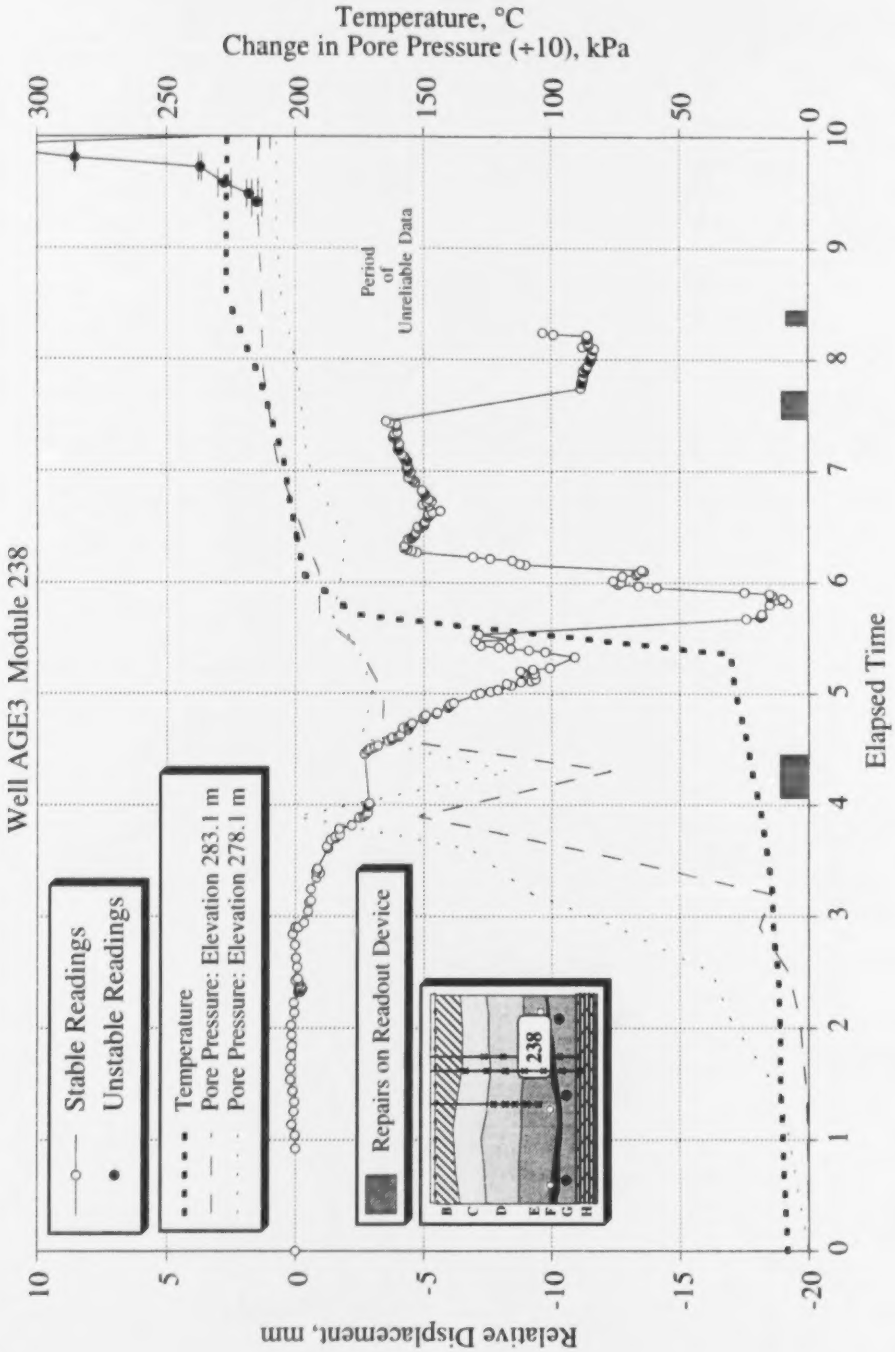

Figure C15 Extensometer History for Module 238 in Well AGE3: Elevation 283.1 to 278.1

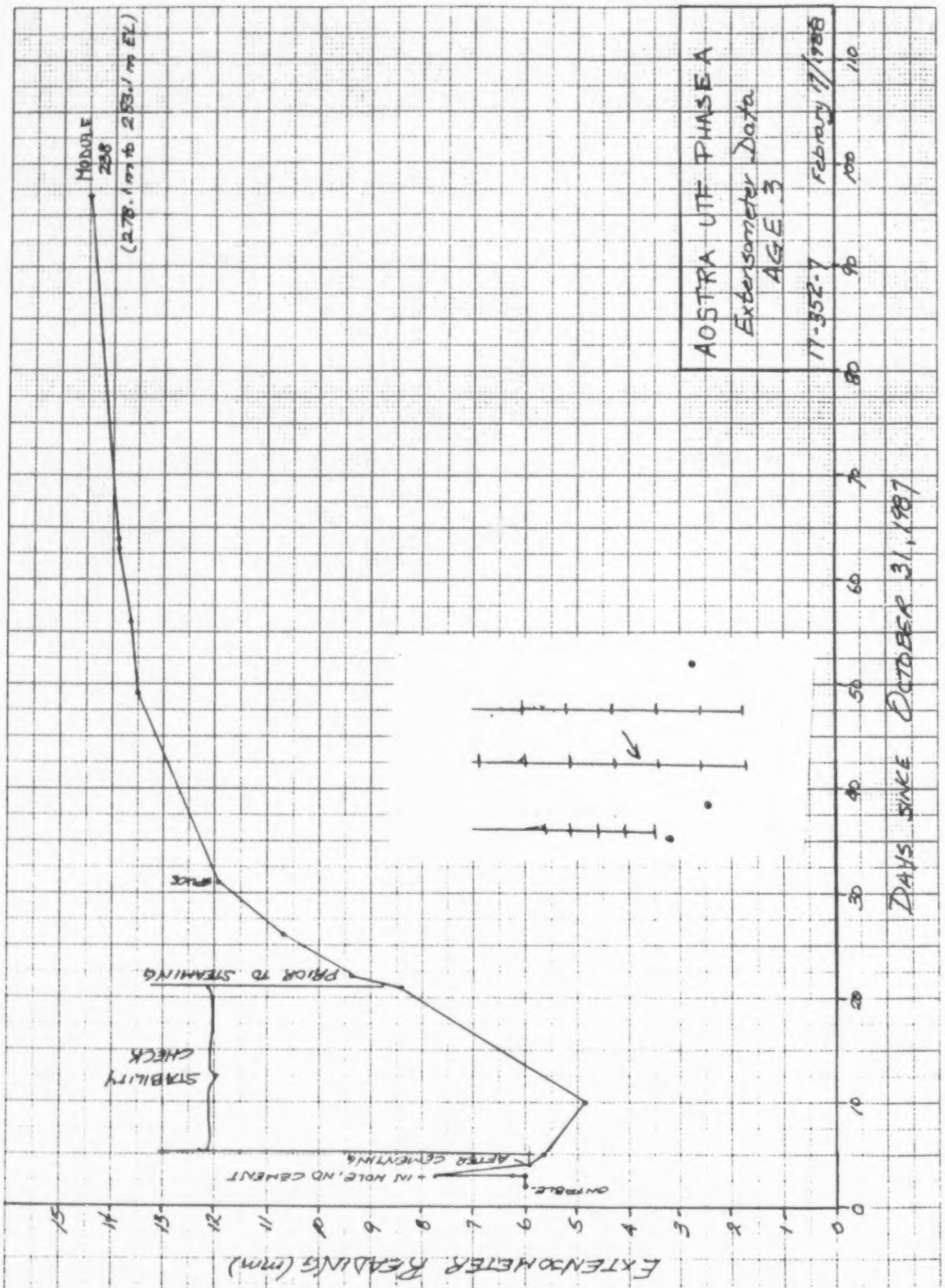

Figure C16 Well AGE3 - Module 238 History during Extensometer Installation

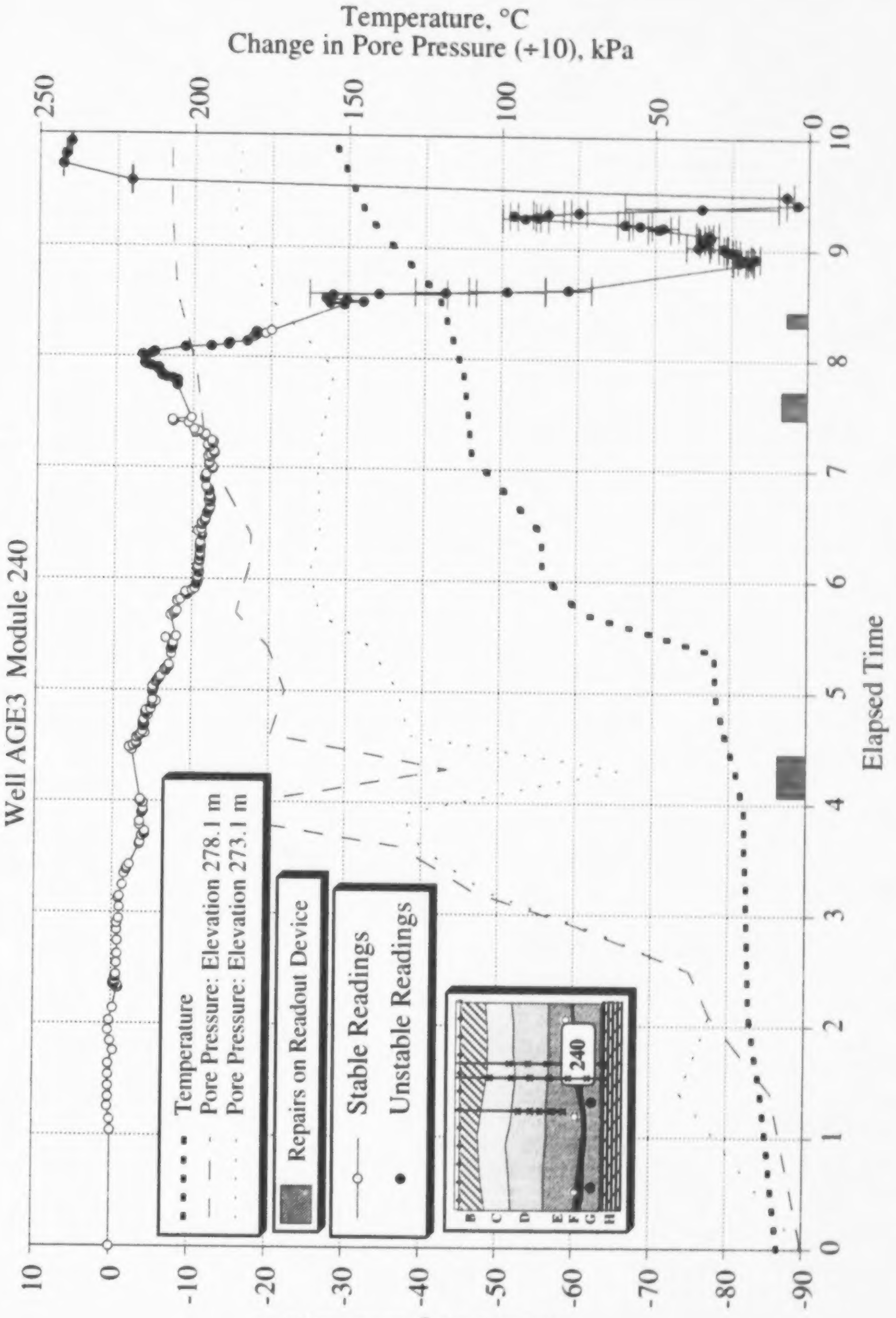

Figure C17 Extensometer History for Module 240 in Well AGE3: Elevation 278.1 to 273.1

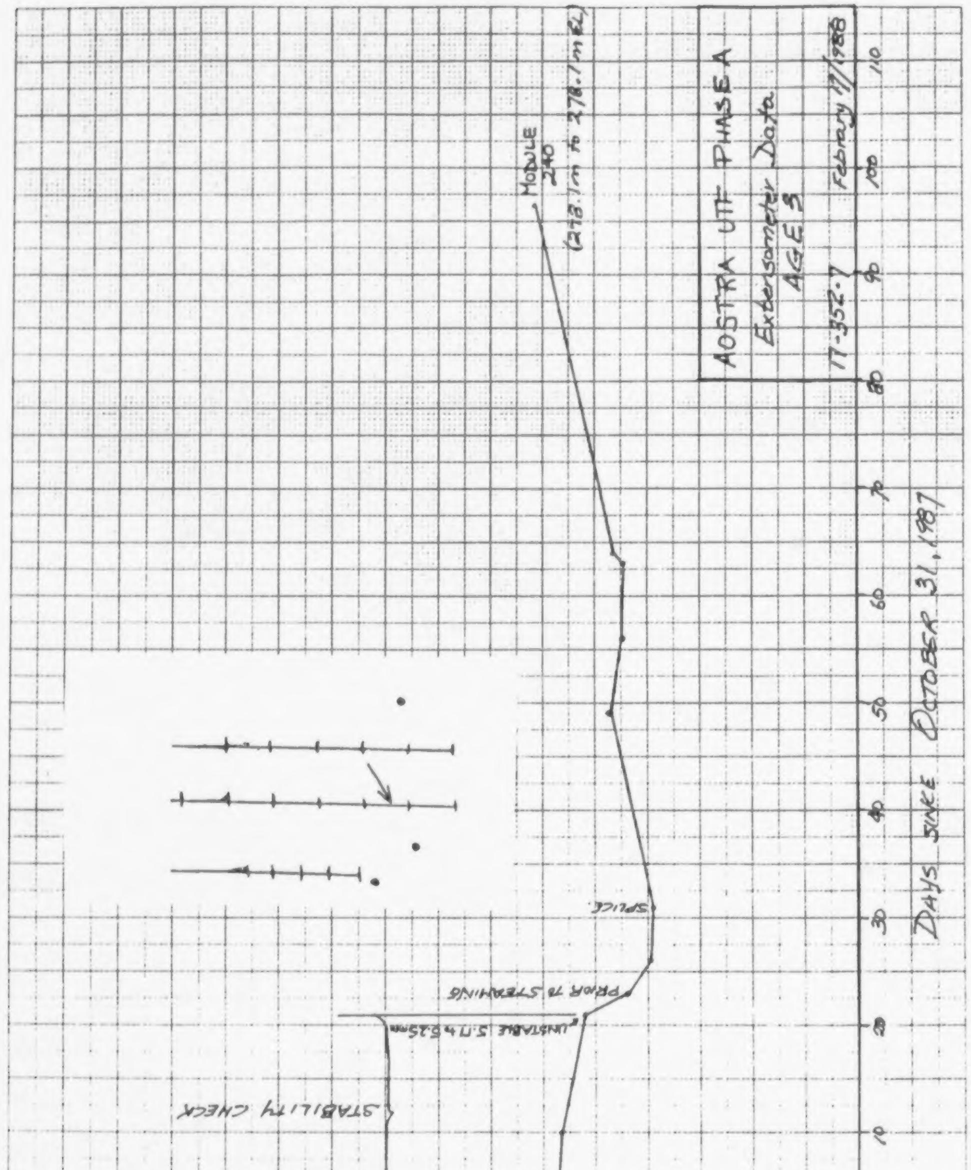

Figure C18 Well AGE3 - Module 240 History during Extensometer Installation

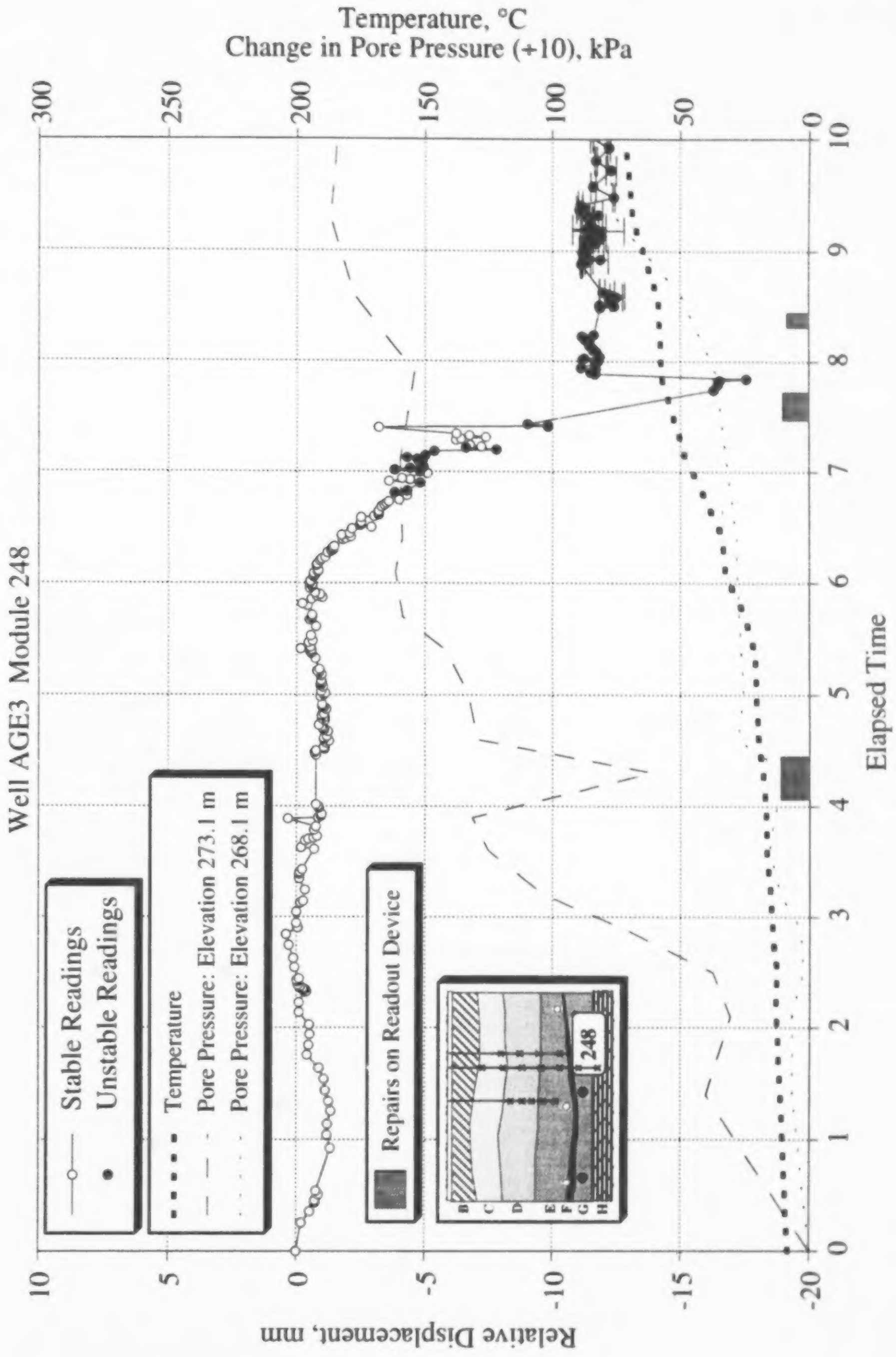

Figure C19 Extensometer History for Module 248 in Well AGE3: Elevation 273.1.0 to 268.1

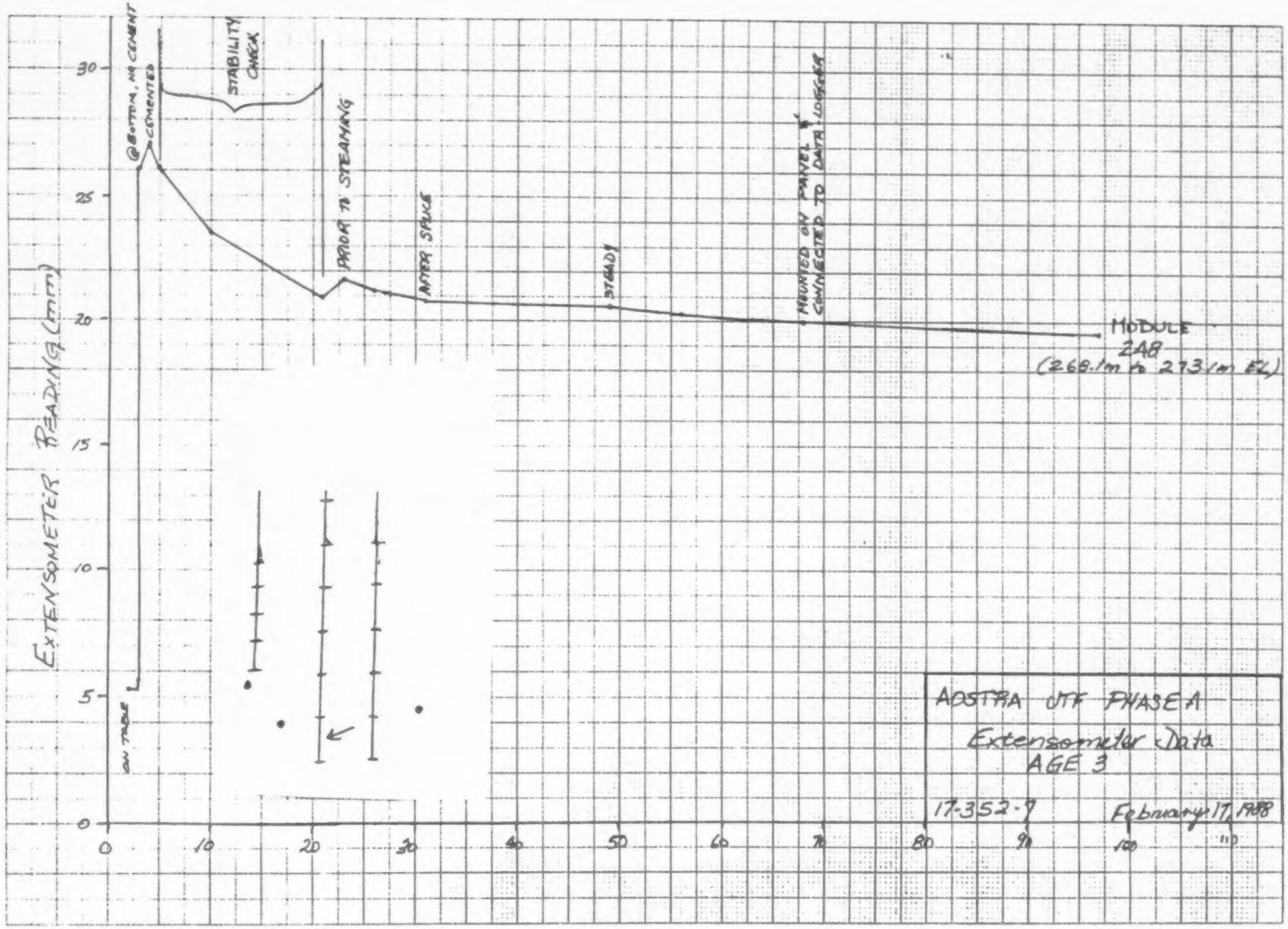

Figure C20 Well AGE3 - Module 248 History during Extensometer Installation

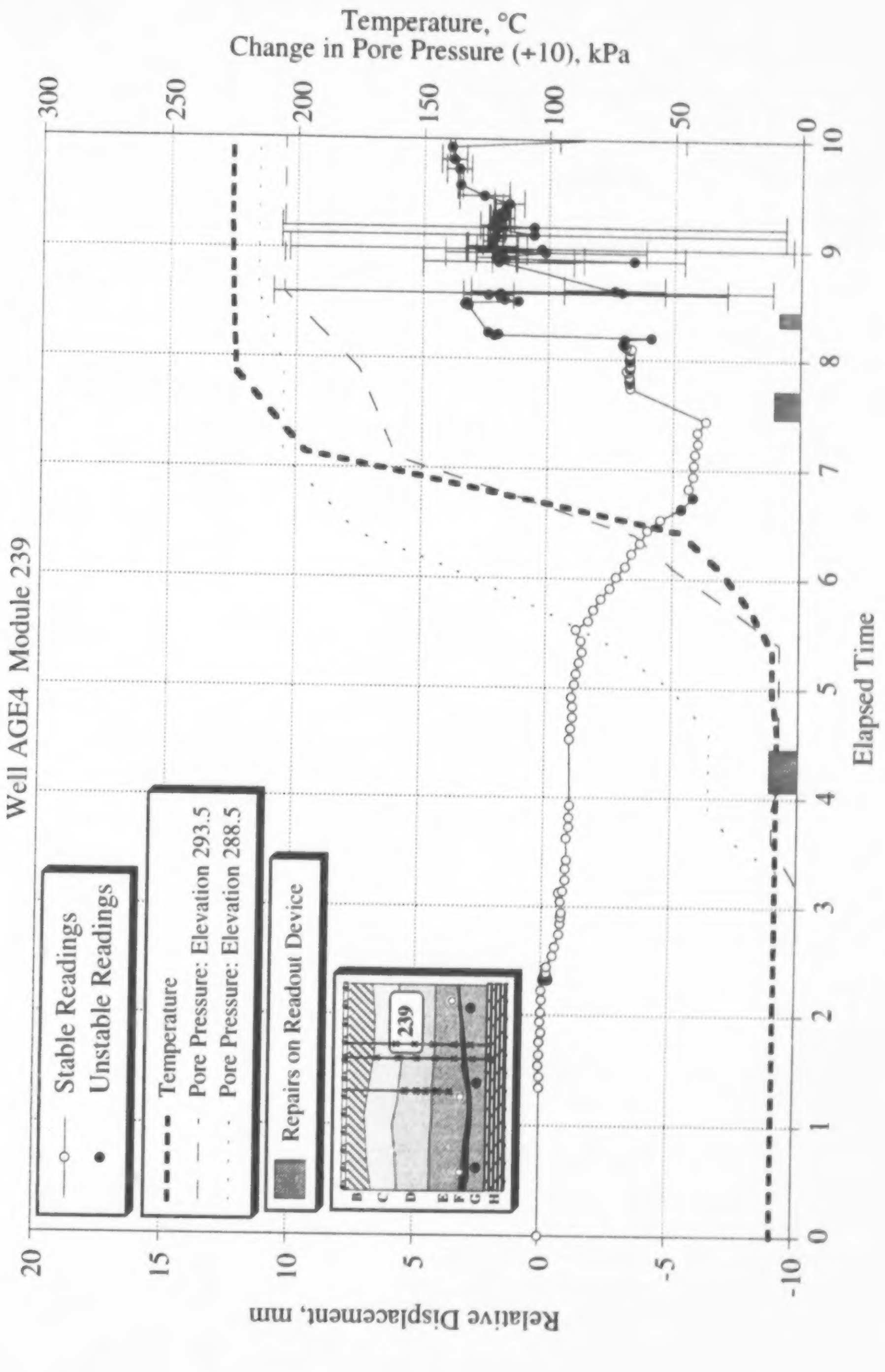

Figure C21 Extensometer History for Module 239 in Well AGE3: Elevation 293.5 to 288.5

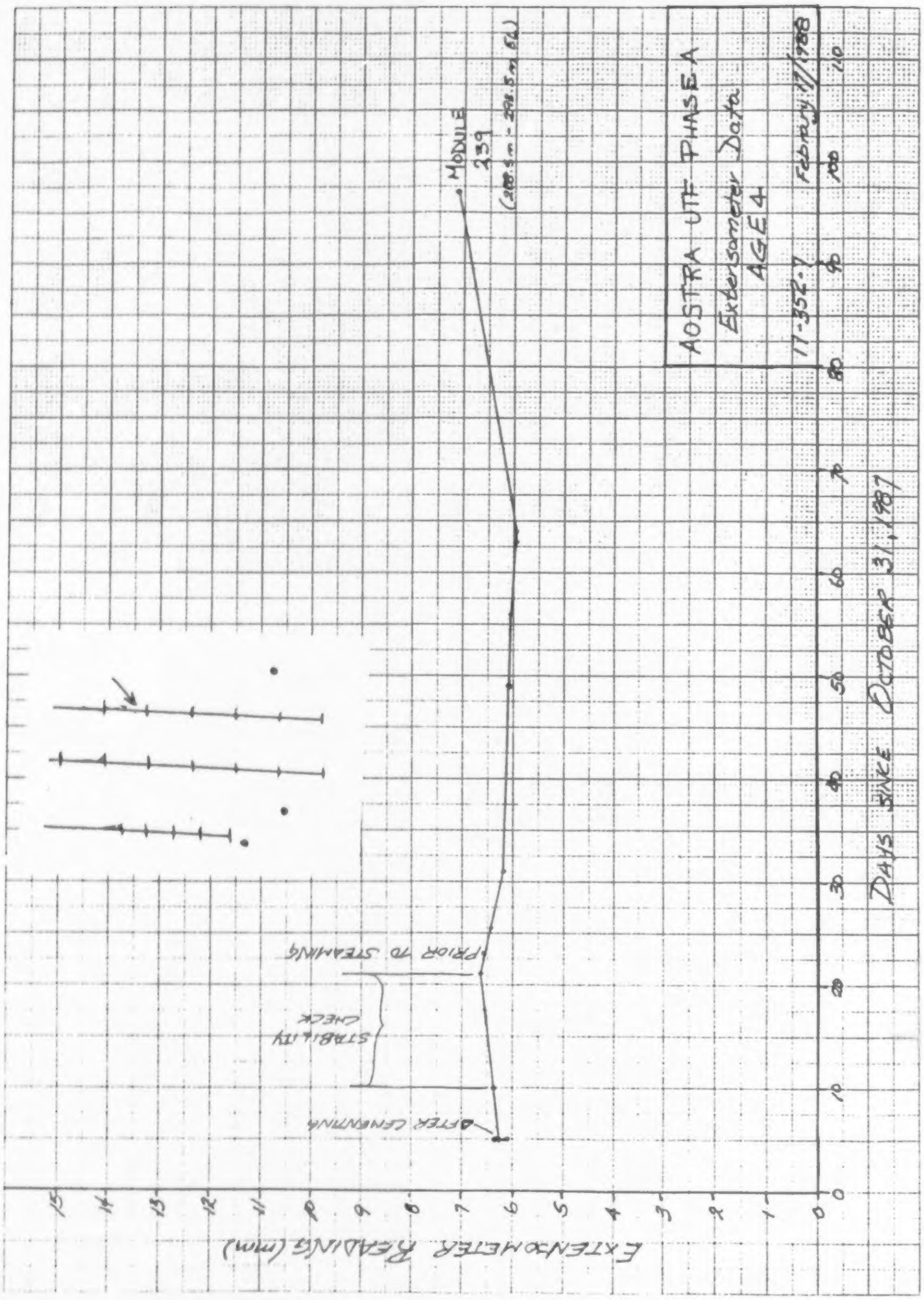

Figure C22 Well AGE3 - Module 239 History during Extensometer Installation

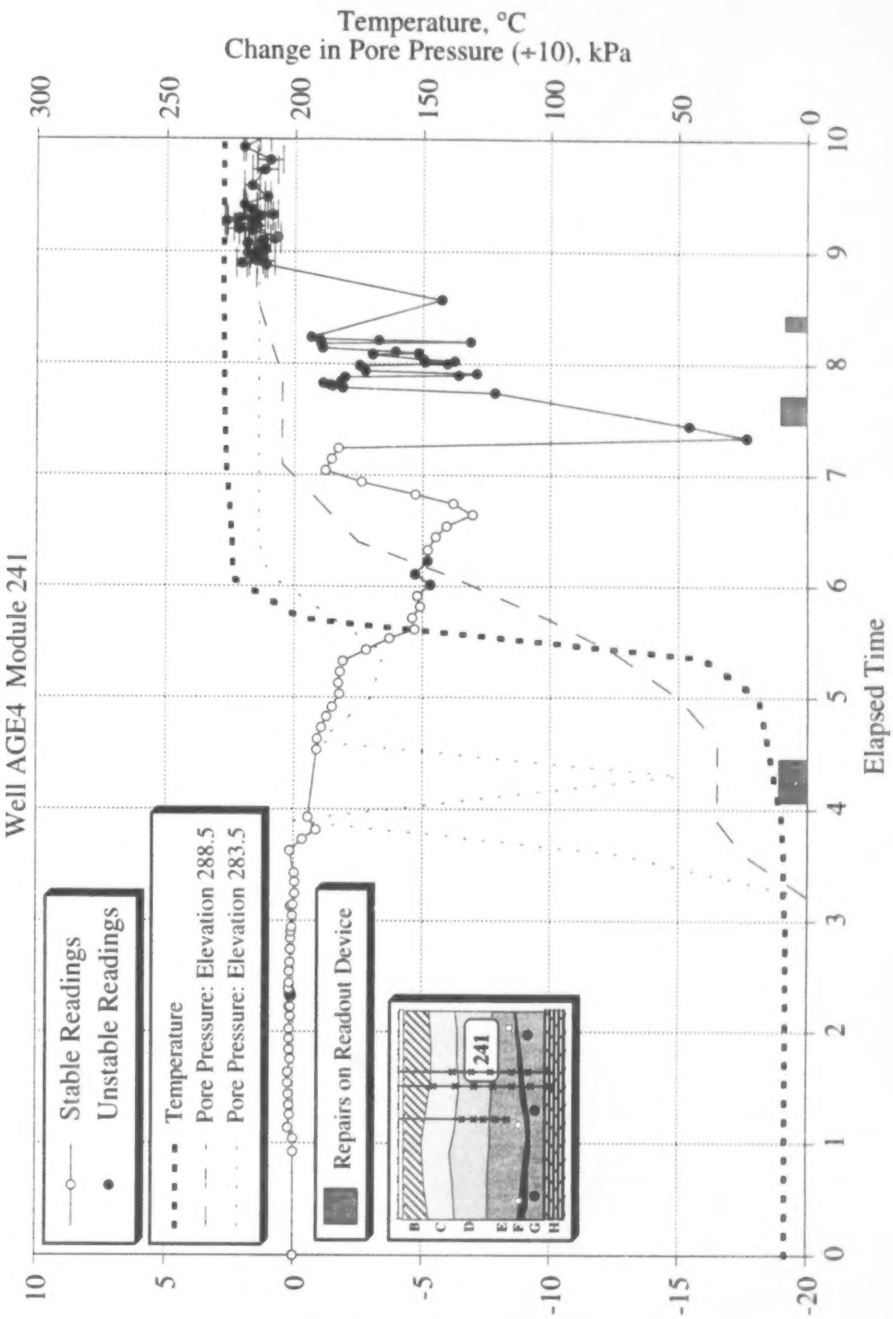

Figure C23 Extensometer History for Module 241 in Well AGE3: Elevation 288.5 to 283.5

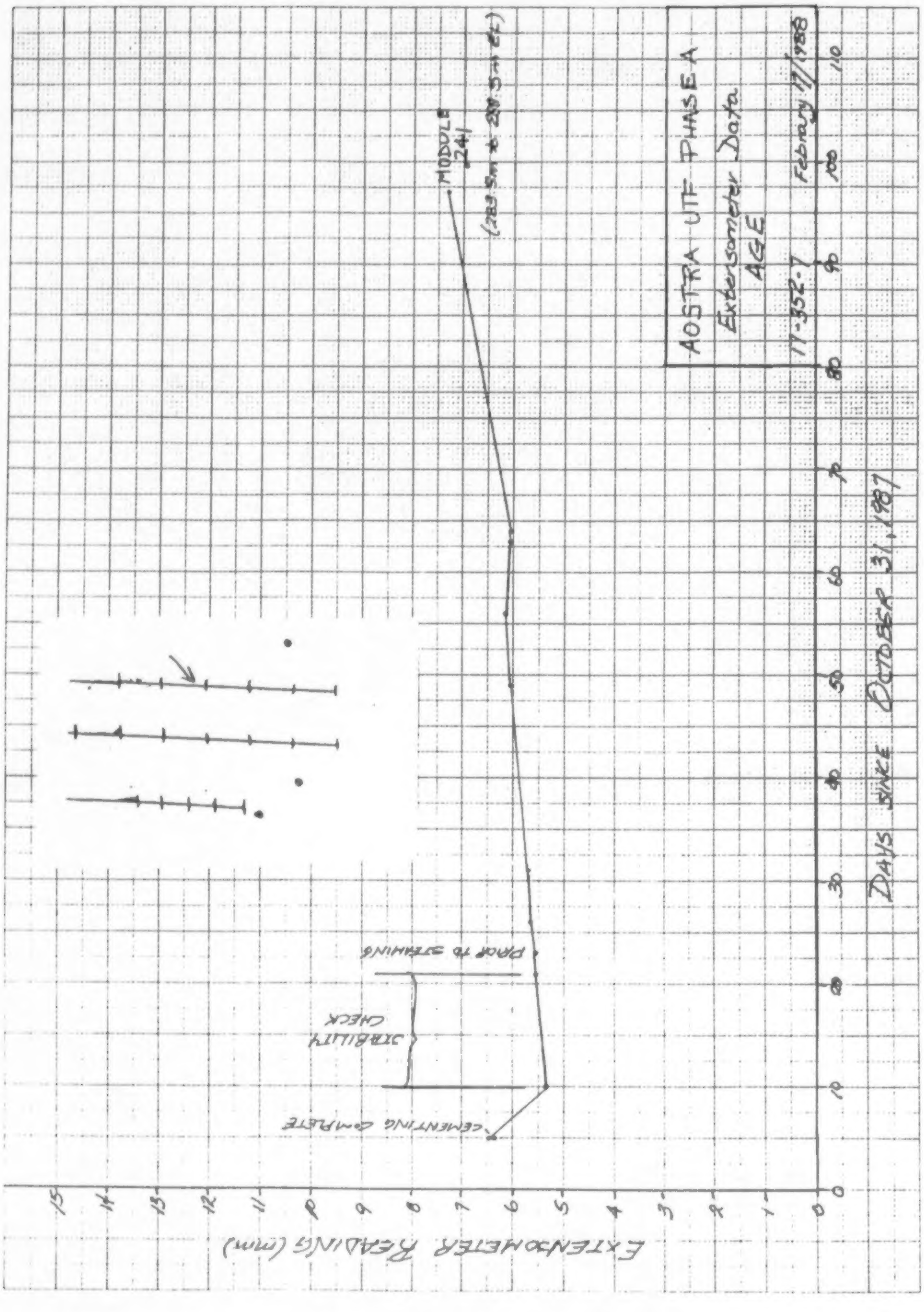

Figure C24 Well AGE3 - Module 241 History during Extensometer Installation

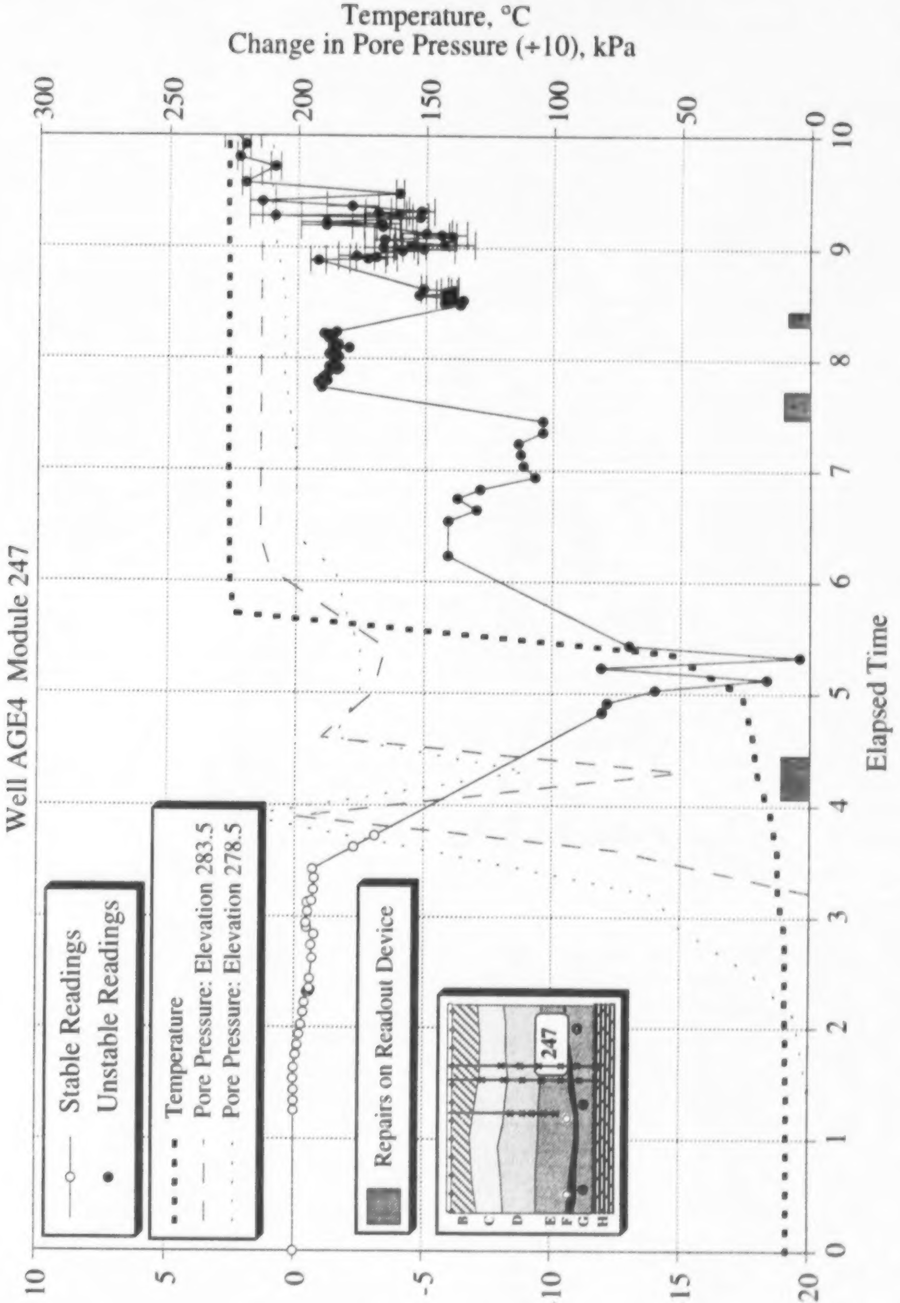

Figure C25 Extensometer History for Module 247 in Well AGE3: Elevation 283.5 to 278.5

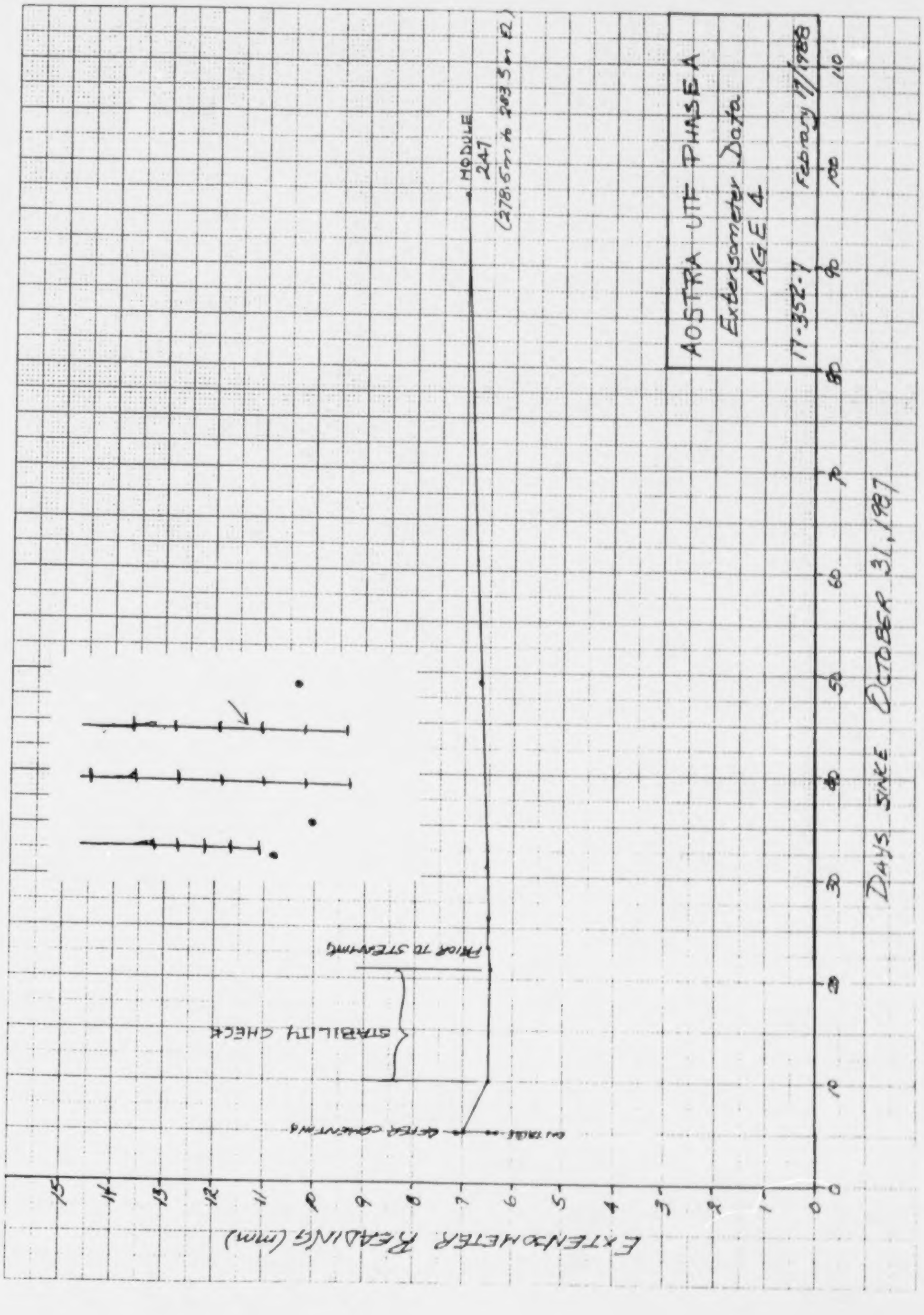

Figure C26 Well AGE3 - Module 247 History during Extensometer Installation

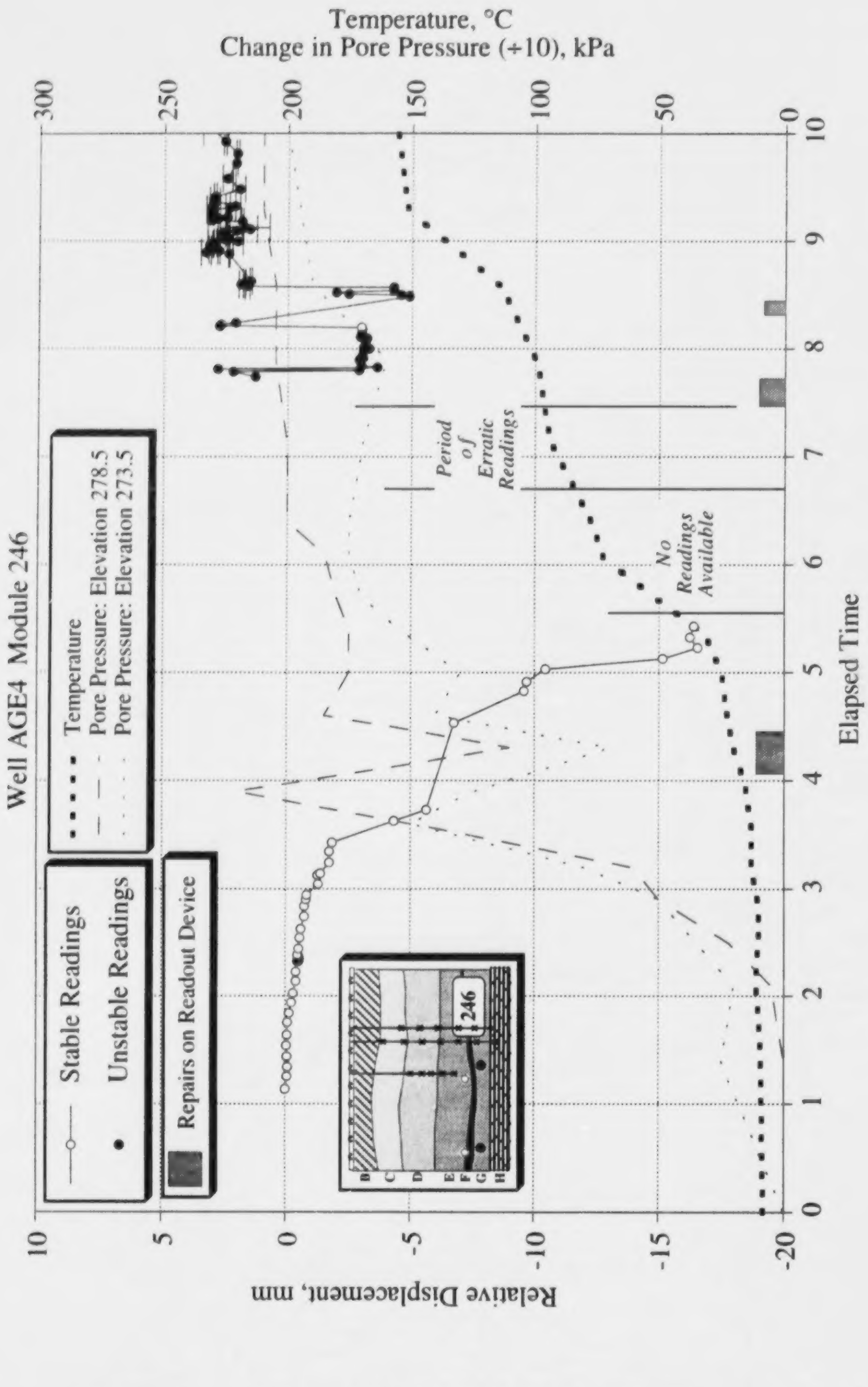

Figure C27 Extensometer History for Module 246 in Well AGE3: Elevation 278.5 to 273.5

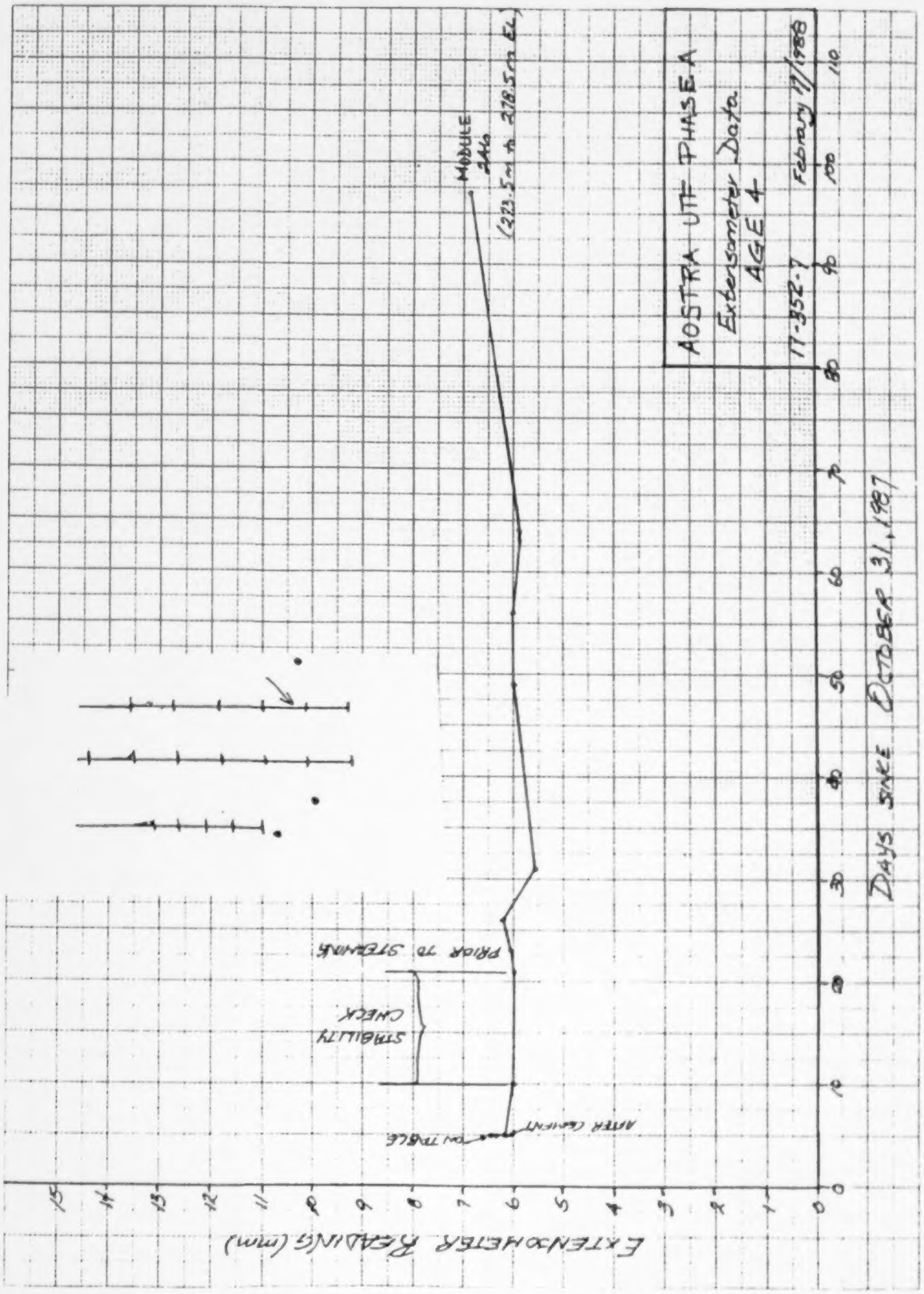

Figure C28 Well AGE3 - Module 246 History during Extensometer Installation

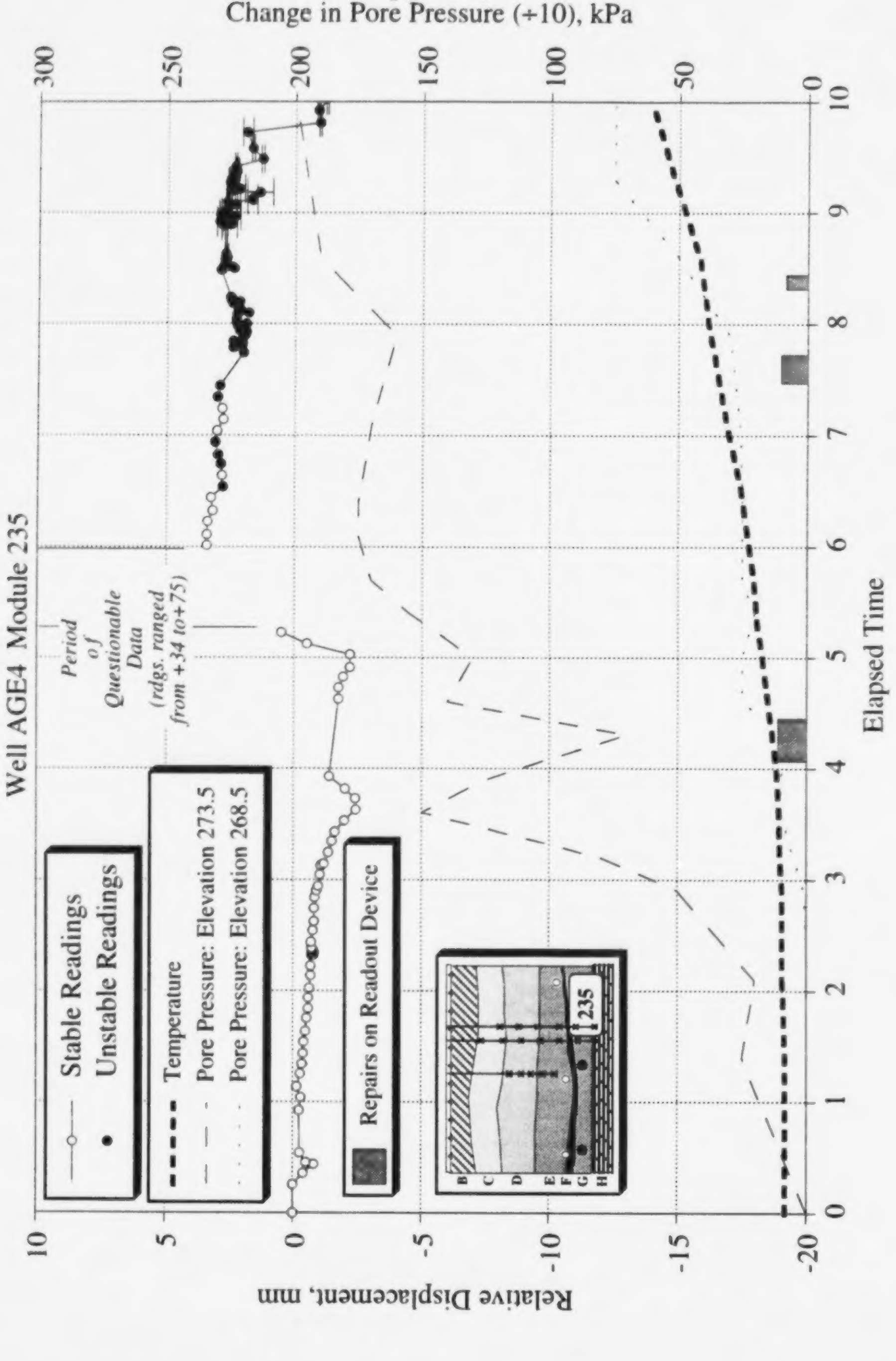

Figure C29 Extensometer History for Module 235 in Well AGE3: Elevation 273.5 to 268.5

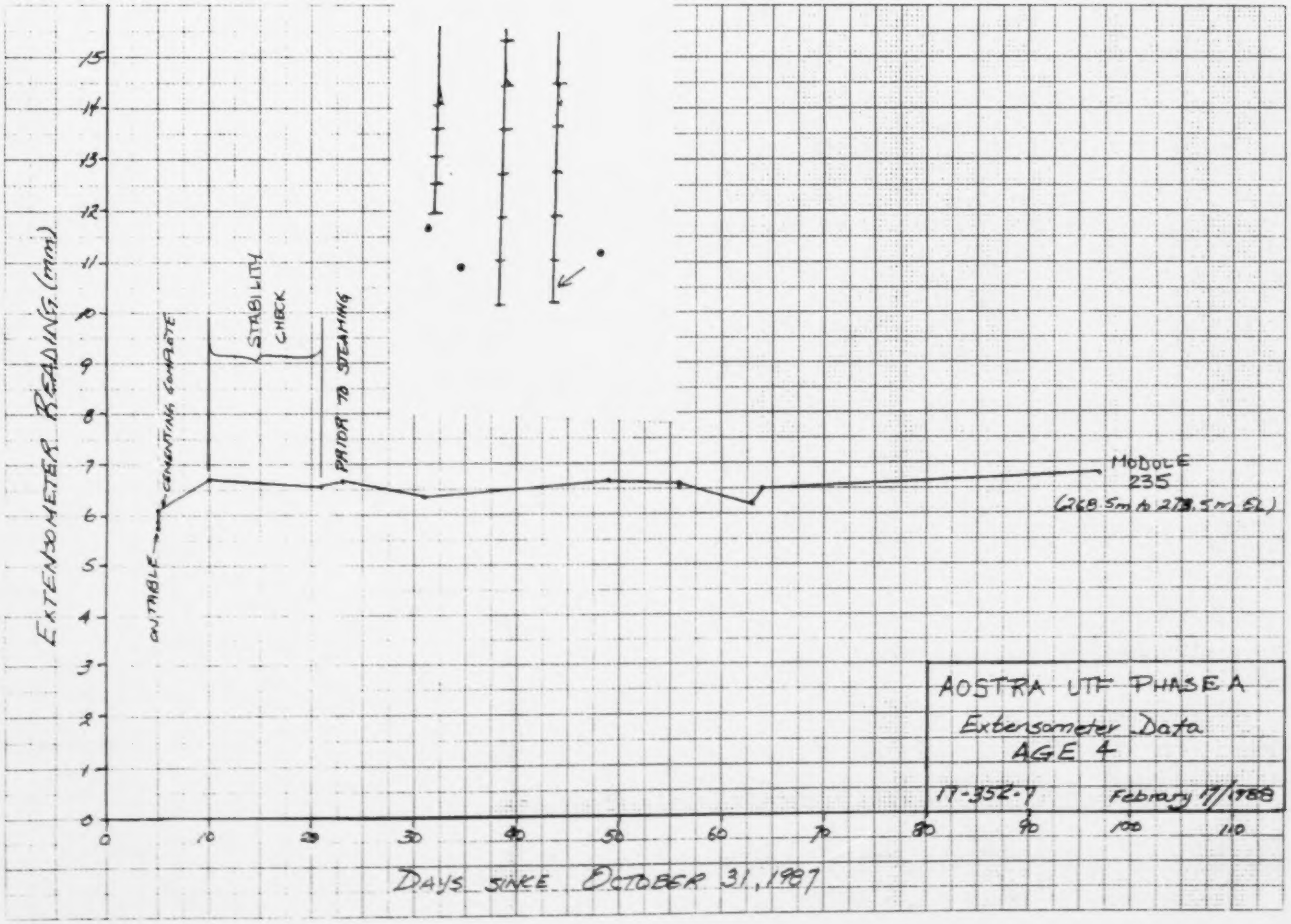

Figure C30 Well AGE3 - Module 235 History during Extensometer Installation

APPENDIX D

Field Inclinometer Results

Horizontal deformations within the reservoir were measured using a Gyrodata Wellbore Surveyor (GWS), an advanced directional surveying system used in the oil industry for wellbore positioning. The GWS operates in open cased wells without the need for special grooved casing as required with conventional slope indicator equipment. The GWS contains a biaxial inclinometer as well as a rate gyro which provides azimuth information. Manufacturer stated accuracy for the GWS was 0.1° in azimuth and 0.05° in inclination.

Since the GWS had not been used previously for these types of measurements, an examination of the accuracy or more precisely, repeatibility of the instrument was undertaken. The statistical approach used in examing instrument accuracy follows the model presented by Wolff and deWardt(1981), herein referred to as the WdW model. The GWS measures azimuth and inclination and through wireline measurements, measured depth at each survey station. Uncertainty in borehole position is associated with errors in each measurement. Azimuth error is composed of two physical errors: (1) compass error; and (2) tool misalignment error. Compass error is attributed only to the quality of the sensors, system electronics and software and the procedure for taking and processing measurements. For these elements, Uttecht and de Wardt (1983) found azimuth errors of 0.015° to 0.03° during early testing of the GWS: product literature states azimuth accuracy of 0.1°. Tool misalignment errors result from poor centralization of the tool within the casing. This can lead to inaccuracies in azimuth, inclination and measured depth. Non-axial wireline pull and sensitivity of the inclinometer within the GWS can also lead to inclination errors. Warren (1981) and Wolff and de Wardt (1983) report inclination errors of 0.2° while the manufacturer's literature reports an inclination accuracy to 0.05°.

The minimum curvature method was used in interpreting the GWS survey data. The uncertainty for each survey can been computed using a statistical model first presented by Wolff and de Wardt (1983). Utilizing this uncertainty model, this appendix provides both the raw field inclinometer results and a detailed uncertainty analysis for each inclinometer.

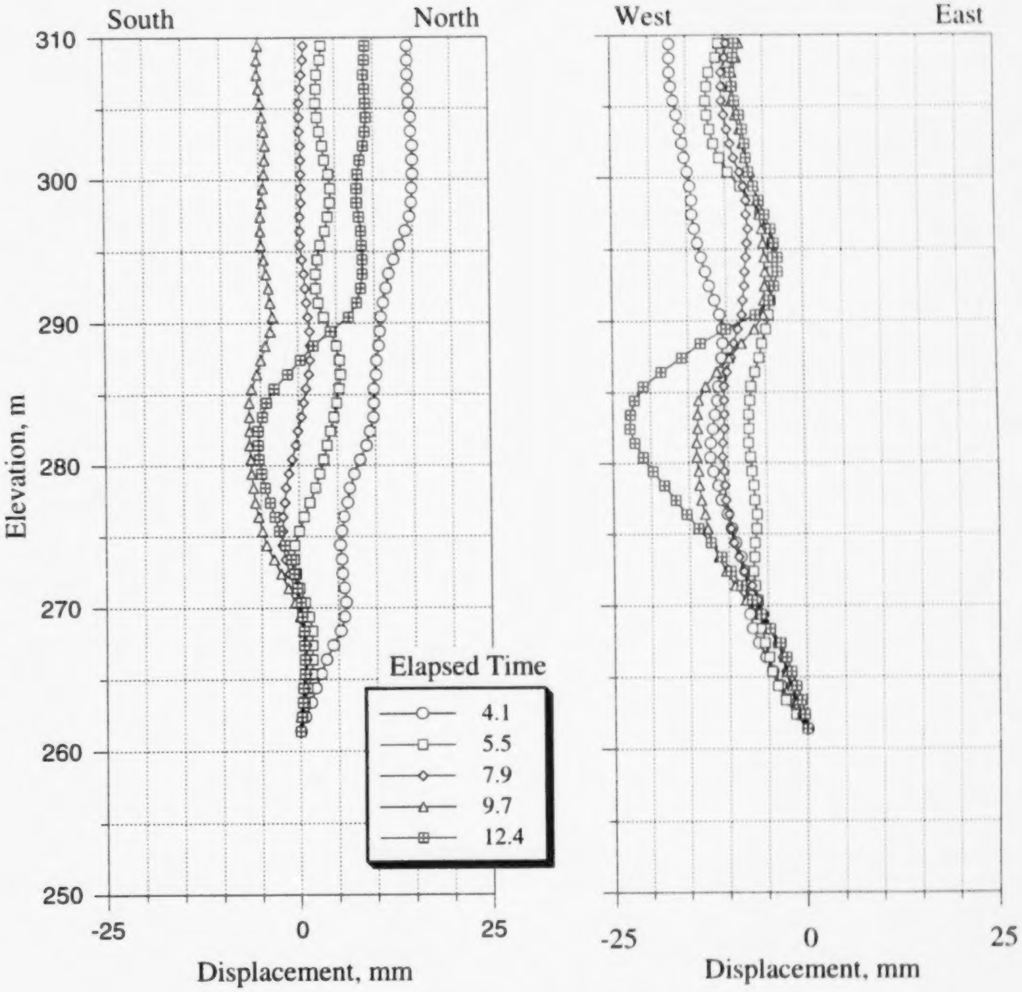

Figure D1 Horizontal Displacement Profile at Well AGI1

AOSTRA Underground Test Facility

(Borehole Position Uncertainty according to Wolff and de Wardt, 1981 with modifications by Dubrule and Nelson, 1986)

Well: AGI1
Date: Sept. 10/88
Elapsed Time = 0.0

Relative Depth Error: 5 mm
Inclination Error: 0.05 degrees
Azimuth Error: 0.10 degrees
Tool Misalignment Error: 0.01 degrees

DAH (m)	Inclination (degrees)	Azimuth (degrees)	Dogleg (degrees)	Dogleg Factor	North (m)	East (m)	Vertical (m)	ΔN (mm)	ΔE (mm)	Phi (°)
0	0.00	0.00			0.0000	0.0000	0.00	0.00	0.00	0.00
1	1.87	124.04	1.87	1.00	-0.0091	0.0135	1.00	0.14	0.15	-27.58
2	1.88	123.93	0.01	1.00	-0.0274	0.0407	2.00	0.30	0.33	-12.88
3	1.88	124.10	0.01	1.00	-0.0458	0.0678	3.00	0.46	0.52	-10.32
4	1.87	124.91	0.03	1.00	-0.0643	0.0948	4.00	0.62	0.70	-9.42
5	1.85	125.72	0.03	1.00	-0.0831	0.1213	5.00	0.78	0.89	-9.08
6	1.84	126.42	0.02	1.00	-0.1020	0.1473	6.00	0.95	1.07	-9.00
7	1.81	127.18	0.04	1.00	-0.1211	0.1728	7.00	1.11	1.25	-9.03
8	1.76	128.23	0.06	1.00	-0.1401	0.1975	8.00	1.27	1.43	-9.14
9	1.69	129.14	0.08	1.00	-0.1590	0.2210	9.00	1.43	1.61	-9.33
10	1.64	130.00	0.06	1.00	-0.1775	0.2434	10.00	1.59	1.78	-9.59
11	1.59	129.67	0.05	1.00	-0.1955	0.2650	10.99	1.75	1.94	-9.84
12	1.55	129.27	0.04	1.00	-0.2129	0.2862	11.99	1.91	2.11	-10.02
13	1.52	128.45	0.04	1.00	-0.2297	0.3070	12.99	2.06	2.28	-10.14
14	1.54	127.84	0.03	1.00	-0.2462	0.3280	13.99	2.21	2.44	-10.21
15	1.54	127.16	0.02	1.00	-0.2626	0.3493	14.99	2.37	2.61	-10.22
16	1.55	127.16	0.01	1.00	-0.2789	0.3708	15.99	2.52	2.77	-10.20
17	1.56	127.74	0.02	1.00	-0.2954	0.3924	16.99	2.67	2.94	-10.21
18	1.58	128.76	0.03	1.00	-0.3123	0.4139	17.99	2.83	3.11	-10.27
19	1.60	129.87	0.04	1.00	-0.3299	0.4353	18.99	2.99	3.28	-10.39
20	1.63	130.88	0.04	1.00	-0.3482	0.4568	19.99	3.14	3.44	-10.58
21	1.64	131.52	0.02	1.00	-0.3670	0.4783	20.99	3.30	3.61	-10.80
22	1.67	131.54	0.03	1.00	-0.3861	0.4999	21.99	3.47	3.78	-11.04
23	1.68	131.31	0.01	1.00	-0.4055	0.5218	22.99	3.63	3.95	-11.26
24	1.68	131.17	0.00	1.00	-0.4248	0.5439	23.99	3.79	4.12	-11.46
25	1.68	130.96	0.01	1.00	-0.4441	0.5660	24.99	3.95	4.29	-11.63
26	1.67	130.67	0.01	1.00	-0.4632	0.5881	25.99	4.11	4.46	-11.78
27	1.66	130.24	0.02	1.00	-0.4820	0.6102	26.99	4.27	4.63	-11.90
28	1.66	129.95	0.01	1.00	-0.5007	0.6324	27.99	4.43	4.80	-11.99
29	1.63	129.54	0.03	1.00	-0.5190	0.6544	28.99	4.59	4.97	-12.05
30	1.62	129.24	0.01	1.00	-0.5370	0.6763	29.99	4.75	5.14	-12.09
31	1.60	128.44	0.03	1.00	-0.5546	0.6982	30.99	4.91	5.31	-12.09
32	1.59	127.59	0.03	1.00	-0.5718	0.7202	31.99	5.06	5.48	-12.06
33	1.59	126.95	0.02	1.00	-0.5886	0.7422	32.99	5.22	5.65	-11.99
34	1.61	126.05	0.03	1.00	-0.6052	0.7647	33.99	5.37	5.82	-11.89
35	1.63	125.65	0.02	1.00	-0.6217	0.7876	34.99	5.53	5.99	-11.77
36	1.65	125.90	0.02	1.00	-0.6385	0.8108	35.98	5.68	6.16	-11.66
37	1.67	126.37	0.02	1.00	-0.6556	0.8342	36.98	5.84	6.33	-11.56
38	1.68	127.66	0.04	1.00	-0.6732	0.8575	37.98	6.00	6.51	-11.50
39	1.69	128.50	0.03	1.00	-0.6913	0.8807	38.98	6.16	6.68	-11.50
40	1.70	128.68	0.01	1.00	-0.7097	0.9038	39.98	6.32	6.86	-11.51
41	1.70	129.20	0.02	1.00	-0.7284	0.9269	40.98	6.48	7.03	-11.53
42	1.69	129.53	0.01	1.00	-0.7471	0.9498	41.98	6.64	7.20	-11.57
43	1.69	129.10	0.01	1.00	-0.7658	0.9726	42.98	6.80	7.37	-11.61
44	1.67	128.80	0.02	1.00	-0.7843	0.9954	43.98	6.96	7.55	-11.62
45	1.63	128.49	0.04	1.00	-0.8022	1.0179	44.98	7.12	7.72	-11.63
46	1.59	128.77	0.04	1.00	-0.8198	1.0398	45.98	7.27	7.89	-11.63
47	1.54	128.76	0.05	1.00	-0.8369	1.0611	46.98	7.43	8.05	-11.63
48	1.48	129.81	0.07	1.00	-0.8536	1.0815	47.98	7.58	8.21	-11.65

Table D1 Well AGI1 Borehole Uncertainty Analysis

AOSTRA Underground Test Facility

(Borehole Position Uncertainty according to Wolff and de Wardt, 1981 with modifications by Dubrule and Nelson, 1986)

Well: AGI1
Date: Sept. 10/88
Elapsed Time = 4.1

Relative Depth Error:	5	mm
Inclination Error:	0.05	degrees
Azimuth Error:	0.10	degrees
Tool Misalignment Error:	0.01	degrees

DAH (m)	Inclination (degrees)	Azimuth (degrees)	Dogleg (degrees)	Dogleg Factor	North (m)	East (m)	Vertical (m)	ΔN (mm)	ΔE (mm)	Phi (°)
0	0.00	0.00			0.0000	0.0000	0.00	0.00	0.00	0.00
1	1.87	124.02	1.87	1.00	-0.0091	0.0135	1.00	0.14	0.15	-27.55
2	1.88	123.87	0.01	1.00	-0.0274	0.0407	2.00	0.30	0.33	-12.84
3	1.89	123.79	0.01	1.00	-0.0457	0.0680	3.00	0.46	0.52	-10.25
4	1.88	124.28	0.02	1.00	-0.0641	0.0953	4.00	0.62	0.70	-9.25
5	1.87	125.12	0.03	1.00	-0.0827	0.1222	5.00	0.78	0.89	-8.85
6	1.85	125.91	0.03	1.00	-0.1016	0.1486	6.00	0.95	1.08	-8.71
7	1.82	126.59	0.04	1.00	-0.1205	0.1744	7.00	1.11	1.26	-8.70
8	1.78	127.70	0.05	1.00	-0.1395	0.1994	8.00	1.27	1.44	-8.79
9	1.71	129.02	0.08	1.00	-0.1584	0.2233	9.00	1.43	1.61	-8.97
10	1.65	129.71	0.06	1.00	-0.1770	0.2460	10.00	1.59	1.79	-9.22
11	1.60	129.86	0.05	1.00	-0.1951	0.2678	10.99	1.75	1.95	-9.47
12	1.56	129.44	0.04	1.00	-0.2127	0.2890	11.99	1.91	2.12	-9.69
13	1.57	129.41	0.01	1.00	-0.2301	0.3101	12.99	2.06	2.29	-9.88
14	1.59	128.61	0.03	1.00	-0.2474	0.3315	13.99	2.22	2.45	-10.03
15	1.59	127.85	0.02	1.00	-0.2646	0.3533	14.99	2.37	2.62	-10.10
16	1.59	127.25	0.02	1.00	-0.2815	0.3753	15.99	2.53	2.79	-10.12
17	1.60	127.59	0.01	1.00	-0.2984	0.3974	16.99	2.68	2.96	-10.13
18	1.62	128.41	0.03	1.00	-0.3157	0.4196	17.99	2.84	3.13	-10.17
19	1.63	129.72	0.04	1.00	-0.3336	0.4416	18.99	3.00	3.30	-10.28
20	1.65	130.55	0.03	1.00	-0.3520	0.4635	19.99	3.16	3.47	-10.45
21	1.64	132.12	0.05	1.00	-0.3710	0.4850	20.99	3.32	3.64	-10.68
22	1.67	132.20	0.03	1.00	-0.3904	0.5064	21.99	3.48	3.80	-10.96
23	1.68	131.87	0.01	1.00	-0.4099	0.5281	22.99	3.64	3.97	-11.22
24	1.68	131.65	0.01	1.00	-0.4295	0.5500	23.99	3.81	4.14	-11.44
25	1.67	131.30	0.01	1.00	-0.4488	0.5719	24.99	3.97	4.31	-11.64
26	1.66	131.23	0.01	1.00	-0.4680	0.5937	25.99	4.13	4.48	-11.81
27	1.67	131.48	0.01	1.00	-0.4872	0.6155	26.99	4.29	4.65	-11.99
28	1.67	131.15	0.01	1.00	-0.5064	0.6374	27.99	4.45	4.82	-12.15
29	1.66	131.00	0.01	1.00	-0.5255	0.6593	28.99	4.61	4.99	-12.29
30	1.68	129.45	0.05	1.00	-0.5443	0.6816	29.99	4.78	5.16	-12.38
31	1.63	128.37	0.06	1.00	-0.5625	0.7041	30.99	4.93	5.33	-12.37
32	1.64	127.64	0.02	1.00	-0.5800	0.7265	31.99	5.09	5.50	-12.33
33	1.63	126.65	0.03	1.00	-0.5973	0.7493	32.99	5.25	5.67	-12.24
34	1.64	125.89	0.02	1.00	-0.6142	0.7723	33.99	5.40	5.84	-12.12
35	1.66	125.05	0.03	1.00	-0.6309	0.7957	34.99	5.56	6.02	-11.97
36	1.68	124.75	0.02	1.00	-0.6475	0.8196	35.98	5.71	6.19	-11.81
37	1.67	126.01	0.04	1.00	-0.6645	0.8435	36.98	5.87	6.37	-11.67
38	1.69	126.94	0.03	1.00	-0.6819	0.8670	37.98	6.03	6.54	-11.59
39	1.69	128.06	0.03	1.00	-0.6998	0.8904	38.98	6.19	6.72	-11.55
40	1.72	129.17	0.04	1.00	-0.7184	0.9137	39.98	6.35	6.89	-11.56
41	1.75	129.52	0.03	1.00	-0.7376	0.9371	40.98	6.51	7.07	-11.61
42	1.78	129.84	0.03	1.00	-0.7573	0.9608	41.98	6.67	7.24	-11.66
43	1.75	129.47	0.03	1.00	-0.7769	0.9845	42.98	6.84	7.42	-11.71
44	1.73	128.61	0.03	1.00	-0.7961	1.0081	43.98	7.00	7.59	-11.73
45	1.71	128.13	0.02	1.00	-0.8147	1.0316	44.98	7.16	7.77	-11.72
46	1.66	128.53	0.05	1.00	-0.8329	1.0547	45.98	7.32	7.94	-11.71
47	1.62	128.62	0.04	1.00	-0.8508	1.0771	46.98	7.48	8.11	-11.71
48	1.56	128.71	0.06	1.00	-0.8681	1.0987	47.98	7.63	8.28	-11.71

Table D1 continued

AOSTRA Underground Test Facility

(Borehole Position Uncertainty according to Wolff and de Wardt, 1981 with modifications by Dubrule and Nelson, 1986)

Relative Depth Error: 5 mm
Well: AGI1
Inclination Error: 0.05 degrees
Date: Dec. 21/88
Azimuth Error: 0.10 degrees
Elapsed Time = 5.5
Tool Misalignment Error: 0.01 degrees

DAH (m)	Inclination (degrees)	Azimuth (degrees)	Dogleg (degrees)	Dogleg Factor	North (m)	East (m)	Vertical (m)	ΔN (mm)	ΔE (mm)	Phi (°)
0	0.00	0.00			0.0000	0.0000	0.00	0.00	0.00	0.00
1	1.84	125.57	1.84	1.00	-0.0093	0.0131	1.00	0.14	0.15	-29.71
2	1.86	124.90	0.03	1.00	-0.0280	0.0394	2.00	0.30	0.33	-14.58
3	1.87	124.65	0.01	1.00	-0.0465	0.0662	3.00	0.46	0.51	-11.49
4	1.87	124.76	0.00	1.00	-0.0651	0.0930	4.00	0.62	0.70	-10.25
5	1.86	125.00	0.01	1.00	-0.0837	0.1197	5.00	0.79	0.88	-9.63
6	1.84	125.46	0.02	1.00	-0.1023	0.1461	6.00	0.95	1.07	-9.29
7	1.83	126.03	0.02	1.00	-0.1210	0.1720	7.00	1.11	1.25	-9.14
8	1.79	126.70	0.05	1.00	-0.1398	0.1975	8.00	1.27	1.43	-9.09
9	1.74	126.87	0.05	1.00	-0.1582	0.2221	9.00	1.43	1.61	-9.10
10	1.71	127.66	0.04	1.00	-0.1764	0.2461	10.00	1.59	1.79	-9.15
11	1.65	128.37	0.06	1.00	-0.1945	0.2692	10.99	1.75	1.96	-9.25
12	1.61	128.39	0.04	1.00	-0.2122	0.2915	11.99	1.91	2.13	-9.38
13	1.58	128.45	0.03	1.00	-0.2294	0.3133	12.99	2.06	2.30	-9.49
14	1.56	128.42	0.02	1.00	-0.2465	0.3348	13.99	2.22	2.46	-9.60
15	1.55	128.05	0.01	1.00	-0.2633	0.3561	14.99	2.37	2.63	-9.68
16	1.55	127.53	0.01	1.00	-0.2798	0.3775	15.99	2.53	2.80	-9.73
17	1.55	127.62	0.00	1.00	-0.2963	0.3989	16.99	2.68	2.96	-9.76
18	1.55	127.88	0.01	1.00	-0.3129	0.4203	17.99	2.83	3.13	-9.80
19	1.56	129.06	0.03	1.00	-0.3298	0.4415	18.99	2.99	3.30	-9.88
20	1.57	130.09	0.03	1.00	-0.3472	0.4626	19.99	3.14	3.46	-10.02
21	1.61	131.31	0.05	1.00	-0.3653	0.4836	20.99	3.30	3.63	-10.22
22	1.63	131.83	0.02	1.00	-0.3840	0.5048	21.99	3.46	3.80	-10.46
23	1.66	132.28	0.03	1.00	-0.4033	0.5261	22.99	3.62	3.96	-10.72
24	1.68	132.04	0.02	1.00	-0.4228	0.5477	23.99	3.79	4.13	-10.98
25	1.69	131.56	0.02	1.00	-0.4424	0.5696	24.99	3.95	4.30	-11.21
26	1.68	131.29	0.01	1.00	-0.4619	0.5916	25.99	4.11	4.47	-11.40
27	1.68	131.02	0.01	1.00	-0.4812	0.6137	26.99	4.27	4.64	-11.57
28	1.67	130.60	0.02	1.00	-0.5003	0.6358	27.99	4.43	4.81	-11.71
29	1.66	130.13	0.02	1.00	-0.5191	0.6580	28.99	4.60	4.98	-11.81
30	1.65	129.76	0.01	1.00	-0.5376	0.6801	29.99	4.76	5.15	-11.89
31	1.63	129.23	0.03	1.00	-0.5558	0.7022	30.99	4.91	5.32	-11.93
32	1.63	128.72	0.01	1.00	-0.5737	0.7243	31.99	5.07	5.49	-11.95
33	1.62	127.82	0.03	1.00	-0.5913	0.7466	32.99	5.23	5.66	-11.94
34	1.62	127.30	0.01	1.00	-0.6085	0.7690	33.99	5.39	5.83	-11.89
35	1.63	126.53	0.02	1.00	-0.6256	0.7917	34.99	5.54	6.00	-11.81
36	1.65	125.95	0.03	1.00	-0.6425	0.8148	35.98	5.70	6.18	-11.72
37	1.66	125.90	0.01	1.00	-0.6594	0.8381	36.98	5.85	6.35	-11.61
38	1.67	126.09	0.01	1.00	-0.6765	0.8616	37.98	6.01	6.52	-11.51
39	1.68	126.93	0.03	1.00	-0.6939	0.8851	38.98	6.17	6.70	-11.44
40	1.69	127.87	0.03	1.00	-0.7118	0.9085	39.98	6.32	6.87	-11.40
41	1.71	128.55	0.03	1.00	-0.7301	0.9318	40.98	6.48	7.05	-11.41
42	1.71	128.89	0.01	1.00	-0.7488	0.9551	41.98	6.65	7.22	-11.42
43	1.71	128.65	0.01	1.00	-0.7675	0.9784	42.98	6.81	7.39	-11.44
44	1.71	128.76	0.00	1.00	-0.7861	1.0016	43.98	6.97	7.57	-11.46
45	1.69	128.41	0.02	1.00	-0.8046	1.0248	44.98	7.13	7.74	-11.46
46	1.65	127.94	0.04	1.00	-0.8226	1.0477	45.98	7.29	7.91	-11.45
47	1.61	127.42	0.04	1.00	-0.8400	1.0703	46.98	7.44	8.08	-11.43
48	1.56	127.60	0.05	1.00	-0.8569	1.0922	47.98	7.60	8.25	-11.40

Table D1 continued

AOSTRA Underground Test Facility

(Borehole Position Uncertainty according to Wolff and de Wardt, 1981 with modifications by Dubrule and Nelson, 1986)

Well: AGI1
Date: June 5/89
Elapsed Time = 7.9

Relative Depth Error: 5 mm
Inclination Error: 0.05 degrees
Azimuth Error: 0.10 degrees
Tool Misalignment Error: 0.01 degrees

DAH (m)	Inclination (degrees)	Azimuth (degrees)	Dogleg (degrees)	Dogleg Factor	North (m)	East (m)	Vertical (m)	ΔN (mm)	ΔE (mm)	Phi (°)
0	0.00	0.00			0.0000	0.0000	0.00	0.00	0.00	0.00
1	1.85	124.78	1.85	1.00	-0.0092	0.0133	1.00	0.14	0.15	-28.60
2	1.88	124.53	0.03	1.00	-0.0277	0.0400	2.00	0.30	0.33	-13.75
3	1.88	124.36	0.01	1.00	-0.0463	0.0671	3.00	0.46	0.51	-10.92
4	1.88	124.75	0.01	1.00	-0.0649	0.0941	4.00	0.62	0.70	-9.84
5	1.87	125.35	0.02	1.00	-0.0837	0.1209	5.00	0.79	0.89	-9.36
6	1.86	125.96	0.02	1.00	-0.1026	0.1473	6.00	0.95	1.07	-9.15
7	1.82	126.41	0.04	1.00	-0.1216	0.1732	7.00	1.11	1.25	-9.07
8	1.79	127.68	0.05	1.00	-0.1406	0.1984	8.00	1.27	1.44	-9.12
9	1.73	128.50	0.07	1.00	-0.1595	0.2226	9.00	1.43	1.61	-9.25
10	1.65	129.24	0.08	1.00	-0.1780	0.2455	10.00	1.59	1.78	-9.43
11	1.60	129.71	0.05	1.00	-0.1960	0.2674	10.99	1.75	1.95	-9.64
12	1.55	129.16	0.05	1.00	-0.2135	0.2886	11.99	1.91	2.12	-9.83
13	1.53	128.43	0.03	1.00	-0.2303	0.3096	12.99	2.06	2.28	-9.96
14	1.52	127.92	0.02	1.00	-0.2468	0.3305	13.99	2.22	2.45	-10.02
15	1.53	127.01	0.03	1.00	-0.2630	0.3516	14.99	2.37	2.62	-10.04
16	1.54	126.93	0.01	1.00	-0.2791	0.3730	15.99	2.52	2.78	-10.02
17	1.55	127.62	0.02	1.00	-0.2954	0.3945	16.99	2.67	2.95	-10.02
18	1.56	128.80	0.03	1.00	-0.3122	0.4158	17.99	2.83	3.12	-10.08
19	1.58	129.98	0.04	1.00	-0.3296	0.4370	18.99	2.98	3.28	-10.22
20	1.60	131.54	0.05	1.00	-0.3477	0.4580	19.99	3.14	3.45	-10.42
21	1.62	132.16	0.03	1.00	-0.3664	0.4789	20.99	3.30	3.61	-10.69
22	1.65	132.29	0.03	1.00	-0.3856	0.5001	21.99	3.46	3.78	-10.97
23	1.67	132.37	0.02	1.00	-0.4051	0.5215	22.99	3.63	3.95	-11.25
24	1.69	131.83	0.03	1.00	-0.4248	0.5432	23.99	3.79	4.12	-11.51
25	1.69	131.44	0.01	1.00	-0.4444	0.5653	24.99	3.95	4.29	-11.72
26	1.69	131.13	0.01	1.00	-0.4638	0.5874	25.99	4.12	4.46	-11.90
27	1.67	131.02	0.02	1.00	-0.4831	0.6095	26.99	4.28	4.63	-12.06
28	1.66	130.84	0.01	1.00	-0.5021	0.6315	27.99	4.44	4.80	-12.19
29	1.65	130.11	0.02	1.00	-0.5209	0.6534	28.99	4.60	4.97	-12.30
30	1.64	129.56	0.02	1.00	-0.5393	0.6755	29.99	4.76	5.14	-12.35
31	1.62	128.98	0.03	1.00	-0.5573	0.6975	30.99	4.92	5.31	-12.38
32	1.61	127.48	0.04	1.00	-0.5747	0.7196	31.99	5.07	5.48	-12.34
33	1.61	126.87	0.02	1.00	-0.5917	0.7420	32.99	5.23	5.65	-12.26
34	1.62	125.79	0.03	1.00	-0.6084	0.7647	33.99	5.38	5.82	-12.14
35	1.65	124.83	0.04	1.00	-0.6249	0.7880	34.99	5.54	5.99	-11.98
36	1.66	124.48	0.01	1.00	-0.6413	0.8118	35.98	5.69	6.16	-11.80
37	1.69	124.67	0.03	1.00	-0.6579	0.8358	36.98	5.85	6.34	-11.63
38	1.70	125.28	0.02	1.00	-0.6748	0.8601	37.98	6.00	6.52	-11.49
39	1.71	126.73	0.04	1.00	-0.6923	0.8841	38.98	6.16	6.69	-11.40
40	1.72	127.29	0.02	1.00	-0.7103	0.9080	39.98	6.32	6.87	-11.35
41	1.73	127.72	0.02	1.00	-0.7287	0.9319	40.98	6.48	7.05	-11.32
42	1.73	128.57	0.03	1.00	-0.7473	0.9557	41.98	6.64	7.22	-11.32
43	1.71	128.55	0.02	1.00	-0.7660	0.9791	42.98	6.80	7.40	-11.33
44	1.69	128.26	0.02	1.00	-0.7845	1.0024	43.98	6.96	7.57	-11.33
45	1.67	128.02	0.02	1.00	-0.8026	1.0254	44.98	7.12	7.74	-11.33
46	1.63	128.38	0.04	1.00	-0.8204	1.0481	45.98	7.28	7.91	-11.32
47	1.58	128.18	0.05	1.00	-0.8377	1.0701	46.98	7.44	8.08	-11.32
48	1.52	128.97	0.06	1.00	-0.8546	1.0912	47.98	7.59	8.25	-11.32

Table D1 continued

AOSTRA Underground Test Facility

(Borehole Position Uncertainty according to Wolff and de Wardt, 1981 with modifications by Dubrule and Nelson, 1986)

Relative Depth Error: 5 mm
Inclination Error: 0.05 degrees
Azimuth Error: 0.10 degrees
Tool Misalignment Error: 0.01 degrees

Well: AGI1
Date: Oct. 10/89
Elapsed Time = 9.7

DAH (m)	Inclination (degrees)	Azimuth (degrees)	Dogleg (degrees)	Dogleg Factor	North (m)	East (m)	Vertical (m)	ΔN (mm)	ΔE (mm)	Phi (°)
0	0.00	0.00			0.0000	0.0000	0.00	0.00	0.00	0.00
1	1.84	124.76	1.84	1.00	-0.0092	0.0132	1.00	0.14	0.15	-28.57
2	1.86	124.34	0.02	1.00	-0.0275	0.0398	2.00	0.30	0.33	-13.63
3	1.87	123.89	0.02	1.00	-0.0457	0.0667	3.00	0.46	0.51	-10.74
4	1.88	124.14	0.01	1.00	-0.0640	0.0938	4.00	0.62	0.70	-9.59
5	1.87	124.88	0.03	1.00	-0.0826	0.1208	5.00	0.78	0.89	-9.06
6	1.85	125.62	0.03	1.00	-0.1013	0.1473	6.00	0.94	1.07	-8.84
7	1.82	126.74	0.05	1.00	-0.1202	0.1732	7.00	1.11	1.25	-8.80
8	1.79	127.78	0.04	1.00	-0.1393	0.1982	8.00	1.27	1.43	-8.90
9	1.73	128.70	0.07	1.00	-0.1583	0.2224	9.00	1.43	1.61	-9.07
10	1.66	129.51	0.07	1.00	-0.1769	0.2453	10.00	1.59	1.78	-9.29
11	1.61	129.77	0.05	1.00	-0.1951	0.2673	10.99	1.75	1.95	-9.53
12	1.56	128.99	0.05	1.00	-0.2127	0.2887	11.99	1.91	2.12	-9.71
13	1.54	128.14	0.03	1.00	-0.2295	0.3098	12.99	2.06	2.29	-9.83
14	1.53	127.36	0.02	1.00	-0.2459	0.3310	13.99	2.21	2.45	-9.87
15	1.54	126.43	0.03	1.00	-0.2620	0.3524	14.99	2.37	2.62	-9.86
16	1.54	126.61	0.00	1.00	-0.2780	0.3740	15.99	2.52	2.78	-9.81
17	1.55	127.33	0.02	1.00	-0.2942	0.3955	16.99	2.67	2.95	-9.81
18	1.56	128.65	0.04	1.00	-0.3109	0.4169	17.99	2.83	3.12	-9.86
19	1.58	129.76	0.04	1.00	-0.3282	0.4382	18.99	2.98	3.29	-9.99
20	1.58	134.84	0.14	1.00	-0.3468	0.4585	19.99	3.14	3.45	-10.28
21	1.60	134.48	0.02	1.00	-0.3663	0.4783	20.99	3.30	3.61	-10.71
22	1.62	134.51	0.02	1.00	-0.3860	0.4983	21.99	3.46	3.77	-11.13
23	1.64	134.46	0.02	1.00	-0.4059	0.5186	22.99	3.63	3.94	-11.55
24	1.65	134.03	0.02	1.00	-0.4259	0.5392	23.99	3.79	4.10	-11.95
25	1.66	131.25	0.08	1.00	-0.4455	0.5604	24.99	3.95	4.27	-12.23
26	1.67	130.78	0.02	1.00	-0.4646	0.5823	25.99	4.11	4.44	-12.39
27	1.66	130.28	0.02	1.00	-0.4834	0.6044	26.99	4.28	4.61	-12.50
28	1.65	130.14	0.01	1.00	-0.5021	0.6265	27.99	4.44	4.78	-12.58
29	1.63	129.17	0.03	1.00	-0.5203	0.6485	28.99	4.59	4.95	-12.62
30	1.62	128.76	0.02	1.00	-0.5382	0.6706	29.99	4.75	5.12	-12.62
31	1.60	127.74	0.03	1.00	-0.5556	0.6926	30.99	4.91	5.29	-12.57
32	1.60	126.86	0.02	1.00	-0.5725	0.7148	31.99	5.06	5.46	-12.48
33	1.59	125.58	0.04	1.00	-0.5889	0.7373	32.99	5.22	5.63	-12.34
34	1.61	124.81	0.03	1.00	-0.6050	0.7601	33.99	5.37	5.80	-12.17
35	1.64	123.63	0.04	1.00	-0.6210	0.7835	34.99	5.52	5.97	-11.96
36	1.66	123.10	0.03	1.00	-0.6368	0.8076	35.99	5.68	6.15	-11.72
37	1.69	124.13	0.04	1.00	-0.6530	0.8319	36.98	5.83	6.33	-11.51
38	1.71	124.50	0.02	1.00	-0.6697	0.8564	37.98	5.99	6.50	-11.35
39	1.73	125.47	0.04	1.00	-0.6869	0.8810	38.98	6.14	6.68	-11.22
40	1.75	126.37	0.03	1.00	-0.7047	0.9056	39.98	6.30	6.86	-11.14
41	1.74	127.08	0.02	1.00	-0.7230	0.9300	40.98	6.46	7.04	-11.08
42	1.75	128.16	0.03	1.00	-0.7415	0.9541	41.98	6.62	7.21	-11.07
43	1.70	128.64	0.05	1.00	-0.7602	0.9777	42.98	6.79	7.39	-11.07
44	1.69	128.22	0.02	1.00	-0.7786	1.0009	43.98	6.94	7.56	-11.08
45	1.67	127.86	0.02	1.00	-0.7967	1.0240	44.98	7.10	7.74	-11.08
46	1.63	128.59	0.05	1.00	-0.8145	1.0466	45.98	7.26	7.91	-11.08
47	1.58	128.36	0.05	1.00	-0.8319	1.0685	46.98	7.42	8.08	-11.09
48	1.50	128.20	0.08	1.00	-0.8486	1.0896	47.98	7.57	8.24	-11.08

Table D1 continued

AOSTRA Underground Test Facility

(Borehole Position Uncertainty according to Wolff and de Wardt, 1981 with modifications by Dubrule and Nelson, 1986)

Relative Depth Error: 5 mm
Inclination Error: 0.05 degrees
Azimuth Error: 0.10 degrees
Tool Misalignment Error: 0.01 degrees

Well: AGI1
Date: April 20/90
Elapsed Time = 12.4

DAH (m)	Inclination (degrees)	Azimuth (degrees)	Dogleg (degrees)	Dogleg Factor	North (m)	East (m)	Vertical (m)	ΔN (mm)	ΔE (mm)	Phi (°)
0	0.00	0.00			0.0000	0.0000	0.00	0.00	0.00	0.00
1	1.86	124.59	1.86	1.00	-0.0092	0.0134	1.00	0.14	0.15	-28.33
2	1.87	124.01	0.02	1.00	-0.0276	0.0402	2.00	0.30	0.33	-13.34
3	1.89	123.95	0.02	1.00	-0.0459	0.0675	3.00	0.46	0.51	-10.57
4	1.89	124.08	0.00	1.00	-0.0643	0.0948	4.00	0.62	0.70	-9.46
5	1.88	125.18	0.04	1.00	-0.0830	0.1219	5.00	0.78	0.89	-8.99
6	1.86	126.31	0.04	1.00	-0.1021	0.1483	6.00	0.95	1.08	-8.86
7	1.83	127.46	0.05	1.00	-0.1214	0.1741	7.00	1.11	1.26	-8.92
8	1.79	128.67	0.06	1.00	-0.1409	0.1990	8.00	1.27	1.44	-9.10
9	1.72	128.99	0.07	1.00	-0.1601	0.2228	9.00	1.44	1.61	-9.31
10	1.67	128.90	0.05	1.00	-0.1787	0.2458	10.00	1.60	1.79	-9.51
11	1.61	128.95	0.06	1.00	-0.1967	0.2681	10.99	1.75	1.96	-9.67
12	1.58	126.89	0.06	1.00	-0.2138	0.2900	11.99	1.91	2.12	-9.73
13	1.54	128.24	0.05	1.00	-0.2304	0.3116	12.99	2.06	2.29	-9.76
14	1.55	127.04	0.03	1.00	-0.2468	0.3330	13.99	2.22	2.46	-9.80
15	1.56	126.59	0.02	1.00	-0.2631	0.3547	14.99	2.37	2.63	-9.79
16	1.54	127.86	0.04	1.00	-0.2794	0.3762	15.99	2.52	2.79	-9.79
17	1.55	128.92	0.03	1.00	-0.2962	0.3974	16.99	2.68	2.96	-9.87
18	1.56	130.67	0.05	1.00	-0.3136	0.4182	17.99	2.83	3.12	-10.03
19	1.55	136.77	0.17	1.00	-0.3323	0.4378	18.99	2.99	3.29	-10.41
20	1.57	142.26	0.15	1.00	-0.3530	0.4554	19.99	3.16	3.44	-11.16
21	1.62	136.31	0.17	1.00	-0.3740	0.4736	20.99	3.32	3.60	-11.98
22	1.62	138.52	0.06	1.00	-0.3948	0.4927	21.99	3.49	3.76	-12.65
23	1.65	136.97	0.05	1.00	-0.4159	0.5119	22.99	3.65	3.92	-13.39
24	1.66	136.69	0.01	1.00	-0.4370	0.5317	23.99	3.82	4.08	-14.05
25	1.68	131.49	0.15	1.00	-0.4573	0.5526	24.99	3.98	4.25	-14.47
26	1.67	132.92	0.04	1.00	-0.4769	0.5742	25.99	4.15	4.42	-14.68
27	1.69	129.95	0.09	1.00	-0.4963	0.5962	26.99	4.31	4.59	-14.83
28	1.69	128.68	0.04	1.00	-0.5150	0.6190	27.99	4.47	4.76	-14.78
29	1.68	127.78	0.03	1.00	-0.5332	0.6421	28.99	4.63	4.93	-14.63
30	1.66	127.28	0.02	1.00	-0.5509	0.6652	29.99	4.79	5.11	-14.44
31	1.66	125.02	0.07	1.00	-0.5680	0.6886	30.99	4.94	5.28	-14.17
32	1.63	125.46	0.03	1.00	-0.5846	0.7121	31.99	5.10	5.45	-13.86
33	1.64	123.96	0.04	1.00	-0.6008	0.7355	32.99	5.25	5.63	-13.55
34	1.66	123.31	0.03	1.00	-0.6168	0.7595	33.99	5.41	5.80	-13.21
35	1.68	122.42	0.03	1.00	-0.6326	0.7840	34.99	5.56	5.98	-12.86
36	1.69	123.87	0.04	1.00	-0.6486	0.8086	35.98	5.71	6.16	-12.55
37	1.71	124.45	0.03	1.00	-0.6653	0.8331	36.98	5.87	6.33	-12.31
38	1.73	125.27	0.03	1.00	-0.6825	0.8578	37.98	6.03	6.51	-12.13
39	1.74	126.49	0.04	1.00	-0.7002	0.8823	38.98	6.18	6.69	-12.00
40	1.74	127.00	0.02	1.00	-0.7184	0.9066	39.98	6.34	6.87	-11.92
41	1.76	127.57	0.03	1.00	-0.7369	0.9309	40.98	6.50	7.04	-11.87
42	1.74	127.95	0.02	1.00	-0.7556	0.9551	41.98	6.67	7.22	-11.83
43	1.71	128.52	0.03	1.00	-0.7742	0.9787	42.98	6.83	7.40	-11.81
44	1.70	128.12	0.02	1.00	-0.7927	1.0021	43.98	6.99	7.57	-11.80
45	1.67	127.88	0.03	1.00	-0.8108	1.0252	44.98	7.15	7.74	-11.78
46	1.62	128.52	0.05	1.00	-0.8285	1.0478	45.98	7.30	7.92	-11.76
47	1.56	128.61	0.06	1.00	-0.8458	1.0695	46.98	7.46	8.08	-11.76
48	1.50	129.58	0.07	1.00	-0.8626	1.0902	47.98	7.61	8.25	-11.77

Table D1 continued

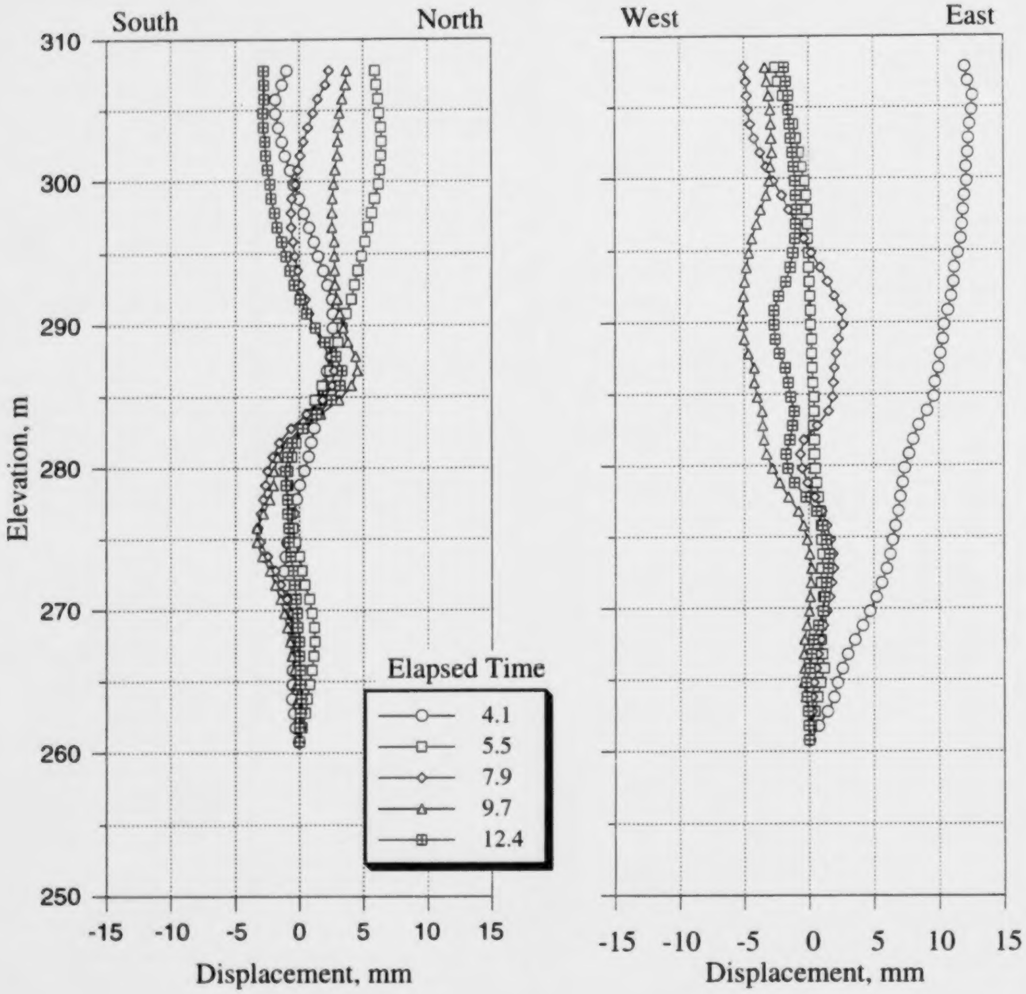

Figure D2 Horizontal Displacement Profile at Well AGI2

AOSTRA Underground Test Facility

(Borehole Position Uncertainty according to Wolff and de Wardt, 1981 with modifications by Dubrule and Nelson, 1986)

Relative Depth Error: 5 mm
Inclination Error: 0.05 degrees
Azimuth Error: 0.10 degrees
Tool Misalignment Error: 0.01 degrees

Well: AGI2 Survey #1
Date: Sept. 10/88
Elapsed Time = 0.0

DAH (m)	Inclination (degrees)	Azimuth (degrees)	Dogleg (degrees)	Dogleg Factor	North (m)	East (m)	Vertical (m)	ΔN (mm)	ΔE (mm)	Phi (°)
0	0.00	0.00			0.0000	0.0000	0.00	0.00	0.00	0.00
1	0.49	247.69	0.49	1.00	-0.0016	-0.0040	1.00	0.12	0.13	14.82
2	0.51	247.01	0.02	1.00	-0.0050	-0.0120	2.00	0.25	0.25	5.61
3	0.55	247.10	0.04	1.00	-0.0086	-0.0205	3.00	0.38	0.39	4.51
4	0.60	246.70	0.05	1.00	-0.0125	-0.0298	4.00	0.50	0.52	4.11
5	0.64	246.54	0.04	1.00	-0.0168	-0.0397	5.00	0.63	0.65	3.89
6	0.67	246.88	0.03	1.00	-0.0213	-0.0502	6.00	0.75	0.78	3.74
7	0.69	247.34	0.02	1.00	-0.0260	-0.0611	7.00	0.88	0.92	3.60
8	0.67	247.15	0.02	1.00	-0.0305	-0.0721	8.00	1.01	1.05	3.48
9	0.65	246.74	0.02	1.00	-0.0351	-0.0827	9.00	1.14	1.19	3.40
10	0.61	245.58	0.04	1.00	-0.0395	-0.0927	10.00	1.26	1.32	3.35
11	0.58	244.41	0.03	1.00	-0.0439	-0.1021	11.00	1.39	1.46	3.35
12	0.55	243.43	0.03	1.00	-0.0482	-0.1110	12.00	1.51	1.59	3.36
13	0.52	245.21	0.03	1.00	-0.0523	-0.1194	13.00	1.64	1.72	3.36
14	0.50	246.73	0.02	1.00	-0.0559	-0.1275	14.00	1.77	1.85	3.33
15	0.49	250.16	0.03	1.00	-0.0591	-0.1356	15.00	1.89	1.98	3.28
16	0.47	252.98	0.03	1.00	-0.0617	-0.1435	16.00	2.02	2.11	3.19
17	0.48	255.68	0.02	1.00	-0.0640	-0.1515	17.00	2.14	2.24	3.10
18	0.49	256.88	0.01	1.00	-0.0660	-0.1597	18.00	2.26	2.37	3.00
19	0.51	256.36	0.02	1.00	-0.0680	-0.1682	19.00	2.39	2.50	2.91
20	0.55	253.21	0.05	1.00	-0.0704	-0.1771	20.00	2.51	2.63	2.86
21	0.57	251.72	0.02	1.00	-0.0734	-0.1864	21.00	2.64	2.76	2.82
22	0.59	249.70	0.03	1.00	-0.0767	-0.1960	22.00	2.77	2.89	2.80
23	0.62	247.18	0.04	1.00	-0.0806	-0.2058	23.00	2.89	3.03	2.81
24	0.63	247.31	0.01	1.00	-0.0848	-0.2159	24.00	3.02	3.16	2.82
25	0.62	248.65	0.02	1.00	-0.0889	-0.2260	25.00	3.14	3.30	2.81
26	0.61	250.61	0.02	1.00	-0.0926	-0.2360	26.00	3.27	3.43	2.79
27	0.61	252.79	0.02	1.00	-0.0960	-0.2461	27.00	3.40	3.56	2.76
28	0.62	253.57	0.01	1.00	-0.0991	-0.2564	28.00	3.52	3.70	2.72
29	0.63	253.60	0.01	1.00	-0.1022	-0.2669	29.00	3.65	3.83	2.68
30	0.65	252.11	0.03	1.00	-0.1055	-0.2776	30.00	3.77	3.97	2.66
31	0.65	252.05	0.00	1.00	-0.1090	-0.2883	31.00	3.90	4.10	2.63
32	0.64	253.08	0.02	1.00	-0.1123	-0.2991	32.00	4.03	4.24	2.61
33	0.62	255.42	0.03	1.00	-0.1153	-0.3097	33.00	4.15	4.37	2.57
34	0.58	258.38	0.05	1.00	-0.1177	-0.3199	34.00	4.28	4.50	2.52
35	0.54	262.14	0.05	1.00	-0.1194	-0.3295	35.00	4.40	4.64	2.45
36	0.50	264.78	0.05	1.00	-0.1204	-0.3385	36.00	4.52	4.77	2.39
37	0.46	265.76	0.04	1.00	-0.1211	-0.3468	37.00	4.65	4.90	2.33
38	0.42	267.37	0.04	1.00	-0.1216	-0.3545	38.00	4.77	5.03	2.27
39	0.38	267.51	0.04	1.00	-0.1219	-0.3615	39.00	4.89	5.16	2.22
40	0.36	269.25	0.02	1.00	-0.1221	-0.3679	40.00	5.02	5.28	2.17
41	0.35	270.54	0.01	1.00	-0.1221	-0.3741	41.00	5.14	5.41	2.12
42	0.35	268.35	0.01	1.00	-0.1221	-0.3802	42.00	5.26	5.54	2.08
43	0.37	266.27	0.02	1.00	-0.1224	-0.3865	43.00	5.39	5.66	2.05
44	0.40	261.96	0.04	1.00	-0.1231	-0.3932	44.00	5.51	5.79	2.03
45	0.42	260.49	0.02	1.00	-0.1242	-0.4003	45.00	5.63	5.92	2.01
46	0.45	257.55	0.04	1.00	-0.1257	-0.4077	46.00	5.76	6.05	2.00
47	0.48	258.37	0.03	1.00	-0.1274	-0.4157	47.00	5.88	6.18	1.98

Table D2 Well AGI2 Borehole Uncertainty Analysis

AOSTRA Underground Test Facility

(Borehole Position Uncertainty according to Wolff and de Wardt, 1981 with modifications by Dubrule and Nelson, 1986)

Relative Depth Error: 5 mm
Inclination Error: 0.05 degrees
Azimuth Error: 0.10 degrees
Tool Misalignment Error: 0.01 degrees

Well: AGI2 Survey #2
Date: Nov. 11/87
Elapsed Time = 0.0

DAH (m)	Inclination (degrees)	Azimuth (degrees)	Dogleg (degrees)	Dogleg Factor	North (m)	East (m)	Vertical (m)	ΔN (mm)	ΔE (mm)	Phi (°)
0	0.00	0.00			0.0000	0.0000	0.00	0.00	0.00	0.00
1	0.48	247.83	0.48	1.00	-0.0016	-0.0039	1.00	0.12	0.13	14.70
2	0.50	246.87	0.02	1.00	-0.0049	-0.0118	2.00	0.25	0.25	5.61
3	0.54	246.61	0.04	1.00	-0.0085	-0.0201	3.00	0.38	0.38	4.55
4	0.59	246.72	0.05	1.00	-0.0124	-0.0292	4.00	0.50	0.52	4.15
5	0.63	246.54	0.04	1.00	-0.0166	-0.0389	5.00	0.63	0.65	3.92
6	0.66	246.85	0.03	1.00	-0.0210	-0.0493	6.00	0.75	0.78	3.76
7	0.69	247.69	0.03	1.00	-0.0256	-0.0601	7.00	0.88	0.92	3.62
8	0.68	247.21	0.01	1.00	-0.0302	-0.0712	8.00	1.01	1.05	3.49
9	0.65	246.63	0.03	1.00	-0.0347	-0.0819	9.00	1.13	1.19	3.41
10	0.62	245.78	0.03	1.00	-0.0392	-0.0920	10.00	1.26	1.32	3.36
11	0.59	244.77	0.03	1.00	-0.0436	-0.1016	11.00	1.39	1.45	3.35
12	0.56	243.05	0.03	1.00	-0.0480	-0.1106	12.00	1.51	1.59	3.37
13	0.53	244.69	0.03	1.00	-0.0522	-0.1191	13.00	1.64	1.72	3.37
14	0.51	246.11	0.02	1.00	-0.0560	-0.1274	14.00	1.77	1.85	3.35
15	0.49	249.20	0.03	1.00	-0.0593	-0.1355	15.00	1.89	1.98	3.30
16	0.48	251.42	0.02	1.00	-0.0622	-0.1434	16.00	2.02	2.11	3.24
17	0.48	255.91	0.04	1.00	-0.0645	-0.1515	17.00	2.14	2.24	3.14
18	0.49	256.76	0.01	1.00	-0.0665	-0.1597	18.00	2.27	2.37	3.03
19	0.51	256.28	0.02	1.00	-0.0686	-0.1682	19.00	2.39	2.50	2.94
20	0.55	254.85	0.04	1.00	-0.0709	-0.1771	20.00	2.51	2.63	2.88
21	0.57	251.82	0.04	1.00	-0.0737	-0.1865	21.00	2.64	2.76	2.83
22	0.59	249.55	0.03	1.00	-0.0770	-0.1960	22.00	2.77	2.90	2.81
23	0.61	247.78	0.03	1.00	-0.0808	-0.2058	23.00	2.89	3.03	2.82
24	0.62	247.44	0.01	1.00	-0.0849	-0.2157	24.00	3.02	3.16	2.82
25	0.62	248.22	0.01	1.00	-0.0890	-0.2257	25.00	3.14	3.30	2.82
26	0.61	250.46	0.03	1.00	-0.0928	-0.2358	26.00	3.27	3.43	2.80
27	0.61	252.20	0.02	1.00	-0.0962	-0.2459	27.00	3.40	3.56	2.77
28	0.62	254.00	0.02	1.00	-0.0993	-0.2561	28.00	3.52	3.70	2.73
29	0.62	253.88	0.00	1.00	-0.1023	-0.2665	29.00	3.65	3.83	2.69
30	0.65	252.33	0.03	1.00	-0.1055	-0.2771	30.00	3.77	3.97	2.66
31	0.66	251.99	0.01	1.00	-0.1090	-0.2880	31.00	3.90	4.10	2.64
32	0.64	253.04	0.02	1.00	-0.1124	-0.2988	32.00	4.03	4.24	2.61
33	0.62	255.42	0.03	1.00	-0.1154	-0.3094	33.00	4.15	4.37	2.57
34	0.60	257.61	0.03	1.00	-0.1179	-0.3198	34.00	4.28	4.50	2.53
35	0.55	261.22	0.06	1.00	-0.1198	-0.3296	35.00	4.40	4.64	2.47
36	0.50	264.22	0.06	1.00	-0.1210	-0.3387	36.00	4.52	4.77	2.40
37	0.47	265.77	0.03	1.00	-0.1217	-0.3471	37.00	4.65	4.90	2.34
38	0.43	266.76	0.04	1.00	-0.1222	-0.3550	38.00	4.77	5.03	2.28
39	0.39	266.63	0.04	1.00	-0.1226	-0.3621	39.00	4.89	5.16	2.23
40	0.36	268.84	0.03	1.00	-0.1229	-0.3687	40.00	5.02	5.28	2.18
41	0.35	270.19	0.01	1.00	-0.1229	-0.3748	41.00	5.14	5.41	2.14
42	0.35	268.51	0.01	1.00	-0.1230	-0.3810	42.00	5.26	5.54	2.10
43	0.37	266.62	0.02	1.00	-0.1233	-0.3872	43.00	5.39	5.66	2.06
44	0.39	263.08	0.03	1.00	-0.1239	-0.3938	44.00	5.51	5.79	2.04
45	0.43	260.60	0.04	1.00	-0.1249	-0.4009	45.00	5.63	5.92	2.02
46	0.45	257.76	0.03	1.00	-0.1263	-0.4085	46.00	5.76	6.05	2.01
47	0.47	258.46	0.02	1.00	-0.1280	-0.4163	47.00	5.88	6.18	1.99

Table D2 continued

AOSTRA Underground Test Facility

(Borehole Position Uncertainty according to Wolff and de Wardt, 1981 with modifications by Dubrule and Nelson, 1986)

Relative Depth Error: 5 mm
Inclination Error: 0.05 degrees
Azimuth Error: 0.10 degrees
Tool Misalignment Error: 0.01 degrees

Well: AGI2
Date: Sept. 10/88
Elapsed Time = 4.1

DAH (m)	Inclination (degrees)	Azimuth (degrees)	Dogleg (degrees)	Dogleg Factor	North (m)	East (m)	Vertical (m)	ΔN (mm)	ΔE (mm)	Phi (°)
0	0.00	0.00			0.0000	0.0000	0.00	0.00	0.00	0.00
1	0.48	241.02	0.48	1.00	-0.0020	-0.0037	1.00	0.12	0.13	21.33
2	0.50	246.16	0.05	1.00	-0.0058	-0.0113	2.00	0.25	0.25	7.61
3	0.55	248.17	0.05	1.00	-0.0094	-0.0198	3.00	0.38	0.38	5.37
4	0.60	247.86	0.05	1.00	-0.0131	-0.0291	4.00	0.50	0.52	4.52
5	0.63	248.45	0.03	1.00	-0.0171	-0.0390	5.00	0.63	0.65	4.05
6	0.66	248.49	0.03	1.00	-0.0213	-0.0495	6.00	0.75	0.78	3.76
7	0.69	248.94	0.03	1.00	-0.0255	-0.0605	7.00	0.88	0.92	3.56
8	0.67	248.52	0.02	1.00	-0.0298	-0.0715	8.00	1.01	1.05	3.40
9	0.65	249.76	0.02	1.00	-0.0339	-0.0823	9.00	1.13	1.19	3.26
10	0.61	247.28	0.05	1.00	-0.0380	-0.0925	10.00	1.26	1.32	3.18
11	0.58	246.63	0.03	1.00	-0.0420	-0.1021	11.00	1.39	1.46	3.15
12	0.55	245.60	0.03	1.00	-0.0460	-0.1111	12.00	1.51	1.59	3.14
13	0.54	247.64	0.02	1.00	-0.0498	-0.1198	13.00	1.64	1.72	3.12
14	0.50	249.22	0.04	1.00	-0.0531	-0.1283	14.00	1.76	1.85	3.07
15	0.49	252.16	0.03	1.00	-0.0560	-0.1364	15.00	1.89	1.98	3.01
16	0.48	254.09	0.02	1.00	-0.0584	-0.1445	16.00	2.01	2.11	2.93
17	0.50	256.55	0.03	1.00	-0.0606	-0.1528	17.00	2.14	2.24	2.84
18	0.50	256.92	0.00	1.00	-0.0626	-0.1613	18.00	2.26	2.37	2.76
19	0.52	255.96	0.02	1.00	-0.0647	-0.1699	19.00	2.39	2.50	2.69
20	0.56	252.70	0.05	1.00	-0.0672	-0.1790	20.00	2.51	2.63	2.65
21	0.59	251.06	0.03	1.00	-0.0704	-0.1885	21.00	2.64	2.77	2.63
22	0.60	249.01	0.02	1.00	-0.0739	-0.1983	22.00	2.76	2.90	2.63
23	0.63	246.85	0.04	1.00	-0.0780	-0.2082	23.00	2.89	3.03	2.65
24	0.67	247.21	0.04	1.00	-0.0824	-0.2187	24.00	3.02	3.17	2.67
25	0.66	247.92	0.01	1.00	-0.0868	-0.2294	25.00	3.14	3.30	2.68
26	0.63	250.16	0.04	1.00	-0.0908	-0.2399	26.00	3.27	3.44	2.66
27	0.63	251.67	0.02	1.00	-0.0944	-0.2503	27.00	3.40	3.57	2.64
28	0.64	252.59	0.01	1.00	-0.0978	-0.2609	28.00	3.52	3.70	2.62
29	0.64	252.48	0.00	1.00	-0.1012	-0.2715	29.00	3.65	3.84	2.59
30	0.66	251.14	0.03	1.00	-0.1047	-0.2823	30.00	3.77	3.97	2.58
31	0.67	251.37	0.01	1.00	-0.1085	-0.2933	31.00	3.90	4.11	2.56
32	0.66	252.12	0.01	1.00	-0.1121	-0.3043	32.00	4.03	4.25	2.54
33	0.63	254.73	0.04	1.00	-0.1153	-0.3151	33.00	4.15	4.38	2.51
34	0.61	257.77	0.04	1.00	-0.1179	-0.3256	34.00	4.28	4.51	2.47
35	0.56	261.12	0.06	1.00	-0.1198	-0.3356	35.00	4.40	4.65	2.41
36	0.52	266.16	0.06	1.00	-0.1208	-0.3450	36.00	4.53	4.78	2.34
37	0.49	267.96	0.03	1.00	-0.1213	-0.3538	37.00	4.65	4.91	2.27
38	0.46	267.87	0.03	1.00	-0.1216	-0.3621	38.00	4.77	5.04	2.21
39	0.42	268.07	0.04	1.00	-0.1219	-0.3697	39.00	4.90	5.17	2.16
40	0.39	270.03	0.03	1.00	-0.1220	-0.3768	40.00	5.02	5.30	2.10
41	0.38	270.63	0.01	1.00	-0.1219	-0.3835	41.00	5.14	5.43	2.06
42	0.37	267.32	0.02	1.00	-0.1221	-0.3901	42.00	5.27	5.55	2.02
43	0.39	266.26	0.02	1.00	-0.1224	-0.3967	43.00	5.39	5.68	1.99
44	0.41	263.55	0.03	1.00	-0.1231	-0.4036	44.00	5.51	5.81	1.96
45	0.46	262.13	0.05	1.00	-0.1240	-0.4112	45.00	5.64	5.94	1.94
46	0.49	260.16	0.03	1.00	-0.1253	-0.4194	46.00	5.76	6.07	1.92
47	0.51	260.73	0.02	1.00	-0.1267	-0.4280	47.00	5.88	6.20	1.90

Table D2 continued

AOSTRA Underground Test Facility

(Borehole Position Uncertainty according to Wolff and de Wardt, 1981 with modifications by Dubrule and Nelson, 1986)

Relative Depth Error: 5 mm
Inclination Error: 0.05 degrees
Azimuth Error: 0.10 degrees
Tool Misalignment Error: 0.01 degrees

Well: AGI2
Date: Dec. 21/88
Elapsed Time = 5.5

DAH (m)	Inclination (degrees)	Azimuth (degrees)	Dogleg (degrees)	Dogleg Factor	North (m)	East (m)	Vertical (m)	ΔN (mm)	ΔE (mm)	Phi (°)
0	0.00	0.00			0.0000	0.0000	0.00	0.00	0.00	0.00
1	0.46	247.32	0.46	1.00	-0.0015	-0.0037	1.00	0.12	0.13	15.14
2	0.48	246.83	0.02	1.00	-0.0047	-0.0113	2.00	0.25	0.25	5.73
3	0.52	246.77	0.04	1.00	-0.0082	-0.0193	3.00	0.37	0.38	4.61
4	0.58	246.51	0.06	1.00	-0.0120	-0.0281	4.00	0.50	0.51	4.22
5	0.62	246.25	0.04	1.00	-0.0162	-0.0377	5.00	0.63	0.65	3.99
6	0.66	246.06	0.04	1.00	-0.0207	-0.0479	6.00	0.75	0.78	3.85
7	0.68	246.70	0.02	1.00	-0.0254	-0.0586	7.00	0.88	0.92	3.72
8	0.67	245.78	0.01	1.00	-0.0301	-0.0694	8.00	1.01	1.05	3.63
9	0.65	245.16	0.02	1.00	-0.0349	-0.0799	9.00	1.13	1.18	3.57
10	0.62	244.26	0.03	1.00	-0.0396	-0.0899	10.00	1.26	1.32	3.55
11	0.59	243.34	0.03	1.00	-0.0443	-0.0994	11.00	1.39	1.45	3.55
12	0.56	241.96	0.03	1.00	-0.0489	-0.1083	12.00	1.51	1.58	3.57
13	0.53	243.26	0.03	1.00	-0.0533	-0.1167	13.00	1.64	1.71	3.59
14	0.51	244.89	0.02	1.00	-0.0573	-0.1249	14.00	1.77	1.84	3.58
15	0.49	247.95	0.03	1.00	-0.0608	-0.1329	15.00	1.89	1.97	3.53
16	0.48	250.04	0.02	1.00	-0.0638	-0.1408	16.00	2.02	2.10	3.46
17	0.49	253.27	0.03	1.00	-0.0665	-0.1488	17.00	2.14	2.23	3.37
18	0.49	254.55	0.01	1.00	-0.0688	-0.1570	18.00	2.27	2.36	3.27
19	0.51	253.87	0.02	1.00	-0.0712	-0.1654	19.00	2.39	2.49	3.18
20	0.55	252.36	0.04	1.00	-0.0739	-0.1743	20.00	2.52	2.63	3.12
21	0.58	249.39	0.04	1.00	-0.0771	-0.1836	21.00	2.64	2.76	3.09
22	0.60	246.37	0.04	1.00	-0.0810	-0.1931	22.00	2.77	2.89	3.09
23	0.62	244.66	0.03	1.00	-0.0854	-0.2028	23.00	2.89	3.02	3.11
24	0.64	245.73	0.02	1.00	-0.0900	-0.2128	24.00	3.02	3.16	3.12
25	0.63	245.50	0.01	1.00	-0.0946	-0.2229	25.00	3.15	3.29	3.13
26	0.62	248.36	0.03	1.00	-0.0989	-0.2329	26.00	3.27	3.42	3.11
27	0.61	250.85	0.03	1.00	-0.1026	-0.2430	27.00	3.40	3.56	3.08
28	0.62	252.65	0.02	1.00	-0.1060	-0.2532	28.00	3.53	3.69	3.03
29	0.62	253.55	0.01	1.00	-0.1091	-0.2635	29.00	3.65	3.83	2.98
30	0.64	252.87	0.02	1.00	-0.1123	-0.2740	30.00	3.78	3.96	2.94
31	0.64	252.62	0.00	1.00	-0.1156	-0.2847	31.00	3.90	4.09	2.90
32	0.64	253.98	0.02	1.00	-0.1188	-0.2954	32.00	4.03	4.23	2.86
33	0.61	257.04	0.04	1.00	-0.1216	-0.3060	33.00	4.15	4.36	2.80
34	0.59	259.03	0.03	1.00	-0.1237	-0.3162	34.00	4.28	4.50	2.73
35	0.55	262.78	0.05	1.00	-0.1253	-0.3260	35.00	4.40	4.63	2.65
36	0.49	266.60	0.07	1.00	-0.1262	-0.3351	36.00	4.53	4.76	2.57
37	0.46	268.28	0.03	1.00	-0.1265	-0.3433	37.00	4.65	4.89	2.49
38	0.43	268.35	0.03	1.00	-0.1268	-0.3511	38.00	4.77	5.02	2.42
39	0.39	267.68	0.04	1.00	-0.1270	-0.3583	39.00	4.90	5.15	2.36
40	0.36	268.63	0.03	1.00	-0.1272	-0.3648	40.00	5.02	5.28	2.31
41	0.34	269.52	0.02	1.00	-0.1273	-0.3709	41.00	5.14	5.40	2.26
42	0.35	267.28	0.02	1.00	-0.1275	-0.3769	42.00	5.27	5.53	2.22
43	0.39	264.22	0.04	1.00	-0.1280	-0.3834	43.00	5.39	5.66	2.19
44	0.41	262.09	0.02	1.00	-0.1288	-0.3903	44.00	5.51	5.78	2.16
45	0.44	259.73	0.03	1.00	-0.1300	-0.3976	45.00	5.64	5.91	2.14
46	0.47	256.09	0.04	1.00	-0.1317	-0.4054	46.00	5.76	6.04	2.13
47	0.48	256.50	0.01	1.00	-0.1336	-0.4134	47.00	5.89	6.17	2.12

Table D2 continued

AOSTRA Underground Test Facility

(Borehole Position Uncertainty according to Wolff and de Wardt, 1981 with modifications by Dubrule and Nelson, 1986)

	Relative Depth Error:	5	mm
Well: AGI2	Inclination Error:	0.05	degrees
Date: June 5/89	Azimuth Error:	0.10	degrees
Elapsed Time = 7.9	Tool Misalignment Error:	0.01	degrees

DAH (m)	Inclination (degrees)	Azimuth (degrees)	Dogleg (degrees)	Dogleg Factor	North (m)	East (m)	Vertical (m)	ΔN (mm)	ΔE (mm)	Phi (°)
0	0.00	0.00			0.0000	0.0000	0.00	0.00	0.00	0.00
1	0.49	243.89	0.49	1.00	-0.0019	-0.0038	1.00	0.12	0.13	18.33
2	0.51	243.41	0.02	1.00	-0.0058	-0.0117	2.00	0.25	0.25	7.23
3	0.55	244.56	0.04	1.00	-0.0098	-0.0200	3.00	0.38	0.38	5.70
4	0.59	244.46	0.04	1.00	-0.0141	-0.0290	4.00	0.50	0.52	5.07
5	0.62	244.05	0.03	1.00	-0.0187	-0.0385	5.00	0.63	0.65	4.74
6	0.65	245.14	0.03	1.00	-0.0234	-0.0485	6.00	0.76	0.78	4.50
7	0.67	245.69	0.02	1.00	-0.0282	-0.0589	7.00	0.88	0.92	4.29
8	0.65	244.88	0.02	1.00	-0.0330	-0.0694	8.00	1.01	1.05	4.13
9	0.62	244.78	0.03	1.00	-0.0378	-0.0794	9.00	1.14	1.18	4.01
10	0.58	244.22	0.04	1.00	-0.0423	-0.0889	10.00	1.26	1.32	3.93
11	0.56	243.30	0.02	1.00	-0.0467	-0.0978	11.00	1.39	1.45	3.91
12	0.52	242.59	0.04	1.00	-0.0509	-0.1062	12.00	1.52	1.58	3.89
13	0.49	244.10	0.03	1.00	-0.0549	-0.1141	13.00	1.64	1.71	3.86
14	0.46	246.32	0.04	1.00	-0.0584	-0.1216	14.00	1.77	1.84	3.81
15	0.46	249.98	0.03	1.00	-0.0614	-0.1291	15.00	1.89	1.97	3.73
16	0.44	253.20	0.03	1.00	-0.0638	-0.1365	16.00	2.02	2.10	3.61
17	0.45	257.08	0.03	1.00	-0.0658	-0.1440	17.00	2.14	2.22	3.47
18	0.50	260.89	0.06	1.00	-0.0674	-0.1521	18.00	2.26	2.35	3.31
19	0.52	260.42	0.02	1.00	-0.0688	-0.1609	19.00	2.39	2.49	3.15
20	0.54	258.22	0.03	1.00	-0.0706	-0.1700	20.00	2.51	2.62	3.02
21	0.58	252.39	0.07	1.00	-0.0731	-0.1795	21.00	2.64	2.75	2.96
22	0.60	247.15	0.06	1.00	-0.0766	-0.1891	22.00	2.76	2.88	2.95
23	0.65	243.30	0.07	1.00	-0.0812	-0.1990	23.00	2.89	3.02	2.99
24	0.68	241.78	0.03	1.00	-0.0866	-0.2093	24.00	3.02	3.15	3.05
25	0.71	246.26	0.06	1.00	-0.0919	-0.2202	25.00	3.15	3.29	3.07
26	0.67	247.78	0.04	1.00	-0.0966	-0.2313	26.00	3.27	3.42	3.06
27	0.61	250.83	0.07	1.00	-0.1005	-0.2417	27.00	3.40	3.56	3.01
28	0.61	251.46	0.01	1.00	-0.1040	-0.2518	28.00	3.52	3.69	2.98
29	0.60	252.84	0.02	1.00	-0.1072	-0.2618	29.00	3.65	3.82	2.93
30	0.62	250.08	0.04	1.00	-0.1106	-0.2719	30.00	3.78	3.96	2.91
31	0.63	249.63	0.01	1.00	-0.1143	-0.2822	31.00	3.90	4.09	2.90
32	0.63	252.32	0.03	1.00	-0.1179	-0.2926	32.00	4.03	4.22	2.87
33	0.60	257.92	0.07	1.00	-0.1207	-0.3029	33.00	4.15	4.36	2.80
34	0.58	261.21	0.04	1.00	-0.1226	-0.3130	34.00	4.28	4.49	2.73
35	0.54	264.08	0.05	1.00	-0.1238	-0.3227	35.00	4.40	4.62	2.64
36	0.51	267.44	0.04	1.00	-0.1245	-0.3319	36.00	4.53	4.76	2.56
37	0.47	269.76	0.04	1.00	-0.1247	-0.3404	37.00	4.65	4.89	2.47
38	0.44	268.73	0.03	1.00	-0.1248	-0.3484	38.00	4.77	5.02	2.40
39	0.40	269.10	0.04	1.00	-0.1250	-0.3557	39.00	4.90	5.15	2.34
40	0.37	270.44	0.03	1.00	-0.1250	-0.3624	40.00	5.02	5.27	2.28
41	0.36	271.71	0.01	1.00	-0.1249	-0.3688	41.00	5.14	5.40	2.22
42	0.36	269.76	0.01	1.00	-0.1248	-0.3751	42.00	5.26	5.53	2.18
43	0.38	266.38	0.03	1.00	-0.1250	-0.3815	43.00	5.39	5.65	2.14
44	0.40	263.18	0.03	1.00	-0.1256	-0.3883	44.00	5.51	5.78	2.11
45	0.43	260.40	0.04	1.00	-0.1267	-0.3954	45.00	5.63	5.91	2.09
46	0.46	256.96	0.04	1.00	-0.1282	-0.4031	46.00	5.76	6.04	2.08
47	0.47	257.85	0.01	1.00	-0.1300	-0.4110	47.00	5.88	6.17	2.06

Table D2 continued

AOSTRA Underground Test Facility

(Borehole Position Uncertainty according to Wolff and de Wardt, 1981 with modifications by Dubrule and Nelson, 1986)

Well: AGI2
Date: Oct. 10/89
Elapsed Time = 9.7

Relative Depth Error: 5 mm
Inclination Error: 0.05 degrees
Azimuth Error: 0.10 degrees
Tool Misalignment Error: 0.01 degrees

DAH (m)	Inclination (degrees)	Azimuth (degrees)	Dogleg (degrees)	Dogleg Factor	North (m)	East (m)	Vertical (m)	ΔN (mm)	ΔE (mm)	Phi (°)
0	0.00	0.00			0.0000	0.0000	0.00	0.00	0.00	0.00
1	0.48	245.73	0.48	1.00	-0.0017	-0.0038	1.00	0.12	0.13	16.57
2	0.50	244.79	0.02	1.00	-0.0053	-0.0116	2.00	0.25	0.25	6.46
3	0.55	245.82	0.05	1.00	-0.0091	-0.0199	3.00	0.38	0.38	5.16
4	0.59	246.81	0.04	1.00	-0.0131	-0.0290	4.00	0.50	0.52	4.53
5	0.63	246.33	0.04	1.00	-0.0174	-0.0388	5.00	0.63	0.65	4.20
6	0.67	246.18	0.04	1.00	-0.0219	-0.0492	6.00	0.75	0.78	4.01
7	0.70	247.14	0.03	1.00	-0.0267	-0.0602	7.00	0.88	0.92	3.84
8	0.69	247.09	0.01	1.00	-0.0314	-0.0713	8.00	1.01	1.05	3.68
9	0.67	246.84	0.02	1.00	-0.0360	-0.0822	9.00	1.14	1.19	3.57
10	0.63	246.19	0.04	1.00	-0.0405	-0.0927	10.00	1.26	1.32	3.49
11	0.60	246.34	0.03	1.00	-0.0449	-0.1025	11.00	1.39	1.46	3.44
12	0.57	244.31	0.04	1.00	-0.0491	-0.1118	12.00	1.52	1.59	3.42
13	0.54	245.80	0.03	1.00	-0.0532	-0.1205	13.00	1.64	1.72	3.40
14	0.51	247.10	0.03	1.00	-0.0569	-0.1289	14.00	1.77	1.85	3.36
15	0.49	249.95	0.03	1.00	-0.0601	-0.1371	15.00	1.89	1.98	3.30
16	0.48	253.99	0.04	1.00	-0.0627	-0.1451	16.00	2.02	2.11	3.21
17	0.48	257.39	0.03	1.00	-0.0648	-0.1532	17.00	2.14	2.24	3.10
18	0.48	258.90	0.01	1.00	-0.0665	-0.1614	18.00	2.27	2.37	2.98
19	0.50	258.49	0.02	1.00	-0.0682	-0.1698	19.00	2.39	2.50	2.87
20	0.51	257.10	0.02	1.00	-0.0700	-0.1784	20.00	2.51	2.63	2.79
21	0.56	249.89	0.08	1.00	-0.0727	-0.1873	21.00	2.64	2.76	2.77
22	0.61	246.46	0.06	1.00	-0.0765	-0.1968	22.00	2.77	2.90	2.79
23	0.62	240.10	0.07	1.00	-0.0813	-0.2064	23.00	2.89	3.03	2.85
24	0.66	239.68	0.04	1.00	-0.0869	-0.2160	24.00	3.02	3.16	2.93
25	0.65	241.78	0.03	1.00	-0.0925	-0.2260	25.00	3.15	3.30	2.98
26	0.63	246.04	0.05	1.00	-0.0974	-0.2360	26.00	3.27	3.43	3.00
27	0.59	249.49	0.05	1.00	-0.1015	-0.2459	27.00	3.40	3.56	2.98
28	0.60	252.09	0.03	1.00	-0.1049	-0.2557	28.00	3.53	3.70	2.95
29	0.59	252.68	0.01	1.00	-0.1080	-0.2656	29.00	3.65	3.83	2.91
30	0.61	248.86	0.04	1.00	-0.1115	-0.2755	30.00	3.78	3.96	2.89
31	0.64	247.45	0.03	1.00	-0.1155	-0.2856	31.00	3.90	4.10	2.89
32	0.63	251.69	0.05	1.00	-0.1194	-0.2960	32.00	4.03	4.23	2.87
33	0.60	256.21	0.06	1.00	-0.1224	-0.3063	33.00	4.16	4.36	2.82
34	0.58	261.78	0.06	1.00	-0.1244	-0.3164	34.00	4.28	4.50	2.74
35	0.54	263.82	0.04	1.00	-0.1256	-0.3260	35.00	4.40	4.63	2.66
36	0.50	267.16	0.05	1.00	-0.1263	-0.3351	36.00	4.53	4.76	2.57
37	0.47	268.26	0.03	1.00	-0.1266	-0.3435	37.00	4.65	4.89	2.49
38	0.43	269.50	0.04	1.00	-0.1268	-0.3514	38.00	4.77	5.02	2.42
39	0.40	269.20	0.03	1.00	-0.1269	-0.3586	39.00	4.90	5.15	2.36
40	0.36	270.53	0.04	1.00	-0.1269	-0.3653	40.00	5.02	5.28	2.30
41	0.35	271.63	0.01	1.00	-0.1268	-0.3715	41.00	5.14	5.40	2.24
42	0.35	270.71	0.01	1.00	-0.1267	-0.3776	42.00	5.27	5.53	2.20
43	0.37	267.45	0.03	1.00	-0.1268	-0.3839	43.00	5.39	5.66	2.16
44	0.38	263.65	0.03	1.00	-0.1273	-0.3904	44.00	5.51	5.78	2.13
45	0.42	260.71	0.04	1.00	-0.1282	-0.3973	45.00	5.64	5.91	2.11
46	0.45	257.33	0.04	1.00	-0.1297	-0.4047	46.00	5.76	6.04	2.09
47	0.47	257.49	0.02	1.00	-0.1314	-0.4126	47.00	5.88	6.17	2.08

Table D2 continued

AOSTRA Underground Test Facility

(Borehole Position Uncertainty according to Wolff and de Wardt, 1981 with modifications by Dubrule and Nelson, 1986)

Well: AGI2
Date: April 20/90
Elapsed Time = 12.4

Relative Depth Error: 5 mm
Inclination Error: 0.05 degrees
Azimuth Error: 0.10 degrees
Tool Misalignment Error: 0.01 degrees

DAH (m)	Inclination (degrees)	Azimuth (degrees)	Dogleg (degrees)	Dogleg Factor	North (m)	East (m)	Vertical (m)	ΔN (mm)	ΔE (mm)	Phi (°)
0	0.00	0.00			0.0000	0.0000	0.00	0.00	0.00	0.00
1	0.47	246.92	0.47	1.00	-0.0016	-0.0038	1.00	0.12	0.13	15.50
2	0.50	246.66	0.03	1.00	-0.0049	-0.0116	2.00	0.25	0.25	5.90
3	0.55	246.48	0.05	1.00	-0.0086	-0.0200	3.00	0.38	0.38	4.74
4	0.59	247.24	0.04	1.00	-0.0125	-0.0291	4.00	0.50	0.52	4.21
5	0.62	246.86	0.03	1.00	-0.0166	-0.0388	5.00	0.63	0.65	3.93
6	0.66	247.03	0.04	1.00	-0.0210	-0.0491	6.00	0.75	0.78	3.76
7	0.68	247.92	0.02	1.00	-0.0255	-0.0599	7.00	0.88	0.92	3.60
8	0.67	247.37	0.01	1.00	-0.0299	-0.0708	8.00	1.01	1.05	3.48
9	0.64	247.52	0.03	1.00	-0.0343	-0.0814	9.00	1.13	1.19	3.37
10	0.61	246.99	0.03	1.00	-0.0385	-0.0914	10.00	1.26	1.32	3.31
11	0.58	246.19	0.03	1.00	-0.0427	-0.1010	11.00	1.39	1.45	3.27
12	0.55	245.60	0.03	1.00	-0.0467	-0.1100	12.00	1.51	1.59	3.25
13	0.53	247.15	0.02	1.00	-0.0505	-0.1186	13.00	1.64	1.72	3.23
14	0.51	248.48	0.02	1.00	-0.0539	-0.1270	14.00	1.76	1.85	3.19
15	0.51	253.19	0.04	1.00	-0.0568	-0.1354	15.00	1.89	1.98	3.11
16	0.50	257.01	0.04	1.00	-0.0591	-0.1439	16.00	2.01	2.11	2.99
17	0.48	259.08	0.03	1.00	-0.0609	-0.1523	17.00	2.14	2.24	2.86
18	0.48	262.25	0.03	1.00	-0.0622	-0.1605	18.00	2.26	2.37	2.73
19	0.49	260.96	0.01	1.00	-0.0635	-0.1689	19.00	2.39	2.50	2.62
20	0.51	258.17	0.03	1.00	-0.0650	-0.1775	20.00	2.51	2.63	2.54
21	0.55	252.13	0.07	1.00	-0.0674	-0.1864	21.00	2.64	2.76	2.52
22	0.59	247.36	0.06	1.00	-0.0709	-0.1957	22.00	2.76	2.89	2.54
23	0.62	241.88	0.07	1.00	-0.0754	-0.2053	23.00	2.89	3.03	2.60
24	0.65	241.61	0.03	1.00	-0.0807	-0.2150	24.00	3.01	3.16	2.67
25	0.66	244.00	0.03	1.00	-0.0859	-0.2252	25.00	3.14	3.29	2.71
26	0.64	248.29	0.05	1.00	-0.0905	-0.2355	26.00	3.27	3.43	2.72
27	0.62	251.62	0.04	1.00	-0.0942	-0.2459	27.00	3.39	3.56	2.70
28	0.60	252.42	0.02	1.00	-0.0975	-0.2560	28.00	3.52	3.70	2.67
29	0.58	254.19	0.03	1.00	-0.1005	-0.2659	29.00	3.65	3.83	2.63
30	0.60	250.90	0.04	1.00	-0.1036	-0.2757	30.00	3.77	3.96	2.61
31	0.62	251.11	0.02	1.00	-0.1071	-0.2857	31.00	3.90	4.10	2.60
32	0.62	252.76	0.02	1.00	-0.1104	-0.2960	32.00	4.02	4.23	2.58
33	0.60	255.16	0.03	1.00	-0.1134	-0.3063	33.00	4.15	4.36	2.55
34	0.59	259.06	0.04	1.00	-0.1157	-0.3164	34.00	4.27	4.50	2.50
35	0.55	262.50	0.05	1.00	-0.1173	-0.3262	35.00	4.40	4.63	2.43
36	0.51	265.06	0.05	1.00	-0.1183	-0.3354	36.00	4.52	4.76	2.36
37	0.47	266.72	0.04	1.00	-0.1189	-0.3439	37.00	4.65	4.89	2.30
38	0.44	267.42	0.03	1.00	-0.1193	-0.3518	38.00	4.77	5.02	2.24
39	0.41	268.39	0.03	1.00	-0.1196	-0.3592	39.00	4.89	5.15	2.18
40	0.37	269.14	0.04	1.00	-0.1197	-0.3661	40.00	5.02	5.28	2.13
41	0.36	270.61	0.01	1.00	-0.1197	-0.3724	41.00	5.14	5.41	2.09
42	0.36	269.46	0.01	1.00	-0.1197	-0.3787	42.00	5.26	5.53	2.04
43	0.38	266.58	0.03	1.00	-0.1200	-0.3852	43.00	5.38	5.66	2.01
44	0.39	262.28	0.03	1.00	-0.1206	-0.3918	44.00	5.51	5.79	1.99
45	0.42	260.09	0.03	1.00	-0.1217	-0.3988	45.00	5.63	5.91	1.97
46	0.45	257.62	0.04	1.00	-0.1232	-0.4063	46.00	5.76	6.04	1.96
47	0.47	258.34	0.02	1.00	-0.1249	-0.4141	47.00	5.88	6.17	1.95

Table D2 continued

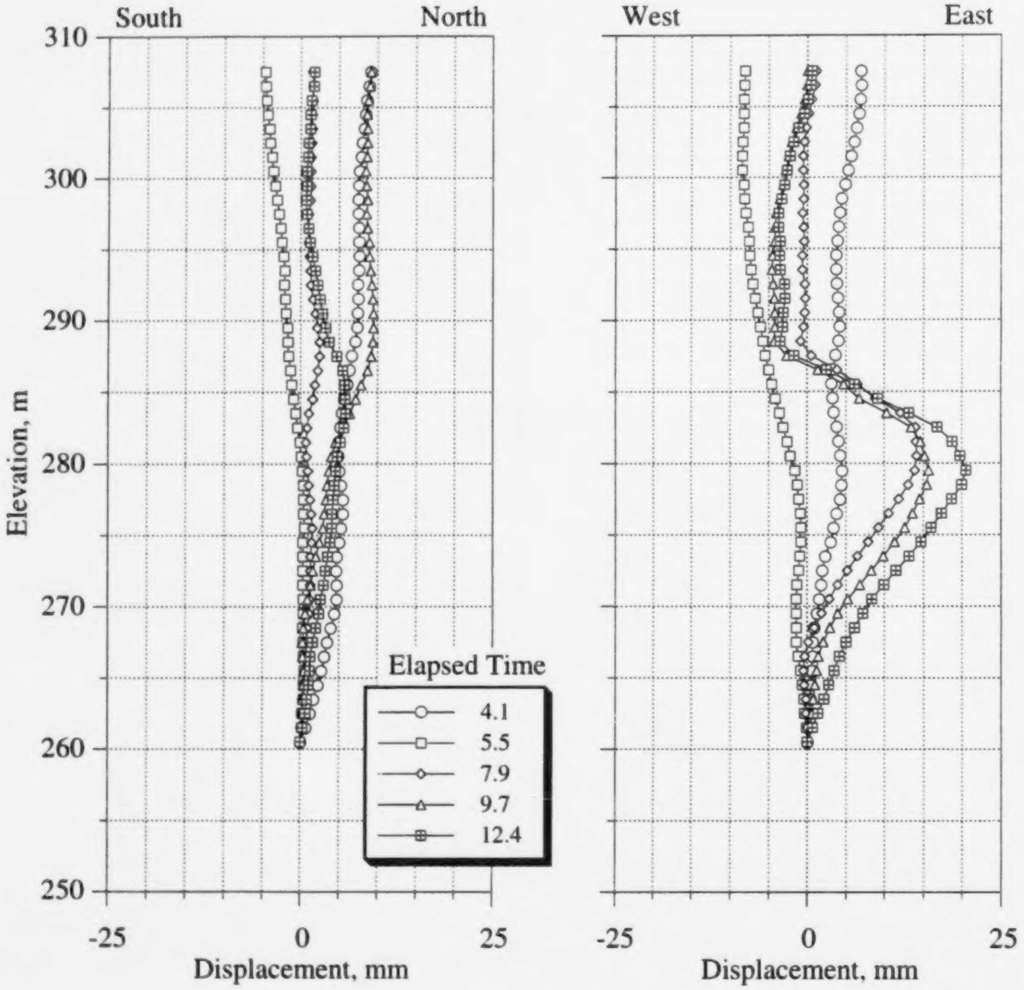

Figure D3 Horizontal Displacement Profile at Well AGI3

AOSTRA Underground Test Facility

(Borehole Position Uncertainty according to Wolff and de Wardt, 1981 with modifications by Dubrule and Nelson, 1986)

Well: AGI3
Date: Sept. 10/88
Elapsed Time = 0.0

Relative Depth Error: 5 mm
Inclination Error: 0.05 degrees
Azimuth Error: 0.10 degrees
Tool Misalignment Error: 0.01 degrees

DAH (m)	Inclination (degrees)	Azimuth (degrees)	Dogleg (degrees)	Dogleg Factor	North (m)	East (m)	Vertical (m)	ΔN (mm)	ΔE (mm)	Phi (°)
0	0.00	0.00			0.0000	0.0000	0.00	0.00	0.00	0.00
1	0.63	227.01	0.63	1.00	-0.0037	-0.0040	1.00	0.13	0.13	41.53
2	0.62	229.04	0.02	1.00	-0.0110	-0.0121	2.00	0.25	0.26	32.30
3	0.62	229.77	0.01	1.00	-0.0181	-0.0203	3.00	0.38	0.39	26.15
4	0.60	230.32	0.02	1.00	-0.0249	-0.0285	4.00	0.51	0.52	22.55
5	0.59	229.46	0.01	1.00	-0.0316	-0.0364	5.00	0.64	0.65	20.74
6	0.57	227.36	0.03	1.00	-0.0383	-0.0440	6.00	0.77	0.78	20.45
7	0.55	226.03	0.02	1.00	-0.0450	-0.0511	7.00	0.90	0.91	21.22
8	0.51	221.33	0.06	1.00	-0.0517	-0.0575	8.00	1.03	1.03	23.23
9	0.48	216.08	0.05	1.00	-0.0584	-0.0629	9.00	1.16	1.16	27.85
10	0.46	210.58	0.05	1.00	-0.0653	-0.0674	10.00	1.28	1.29	36.17
11	0.47	205.40	0.04	1.00	-0.0724	-0.0712	11.00	1.41	1.41	-41.40
12	0.47	200.84	0.04	1.00	-0.0800	-0.0745	12.00	1.54	1.54	-28.85
13	0.49	197.46	0.03	1.00	-0.0879	-0.0772	13.00	1.67	1.66	-20.18
14	0.51	197.21	0.02	1.00	-0.0962	-0.0798	14.00	1.80	1.78	-15.07
15	0.52	197.88	0.01	1.00	-0.1048	-0.0825	15.00	1.93	1.91	-12.10
16	0.54	199.96	0.03	1.00	-0.1135	-0.0855	16.00	2.06	2.03	-10.31
17	0.53	203.50	0.03	1.00	-0.1222	-0.0890	17.00	2.19	2.16	-9.20
18	0.53	209.05	0.05	1.00	-0.1305	-0.0931	18.00	2.32	2.28	-8.64
19	0.53	214.01	0.05	1.00	-0.1384	-0.0979	19.00	2.45	2.41	-8.42
20	0.54	217.92	0.04	1.00	-0.1459	-0.1034	20.00	2.58	2.54	-8.44
21	0.57	218.41	0.03	1.00	-0.1535	-0.1094	21.00	2.71	2.66	-8.57
22	0.58	218.32	0.01	1.00	-0.1614	-0.1156	22.00	2.84	2.79	-8.69
23	0.60	216.20	0.03	1.00	-0.1696	-0.1218	23.00	2.97	2.92	-8.76
24	0.61	214.56	0.02	1.00	-0.1782	-0.1279	24.00	3.11	3.05	-8.73
25	0.62	212.69	0.02	1.00	-0.1871	-0.1339	25.00	3.24	3.18	-8.62
26	0.61	211.76	0.01	1.00	-0.1962	-0.1396	26.00	3.37	3.30	-8.46
27	0.62	212.50	0.01	1.00	-0.2053	-0.1453	27.00	3.50	3.43	-8.33
28	0.63	216.41	0.04	1.00	-0.2143	-0.1515	28.00	3.63	3.56	-8.29
29	0.64	220.16	0.04	1.00	-0.2230	-0.1583	29.00	3.76	3.69	-8.39
30	0.66	224.89	0.06	1.00	-0.2313	-0.1660	30.00	3.90	3.82	-8.64
31	0.66	228.75	0.04	1.00	-0.2392	-0.1744	31.00	4.03	3.95	-9.04
32	0.66	232.26	0.04	1.00	-0.2465	-0.1833	32.00	4.16	4.08	-9.59
33	0.63	235.47	0.05	1.00	-0.2532	-0.1924	33.00	4.28	4.21	-10.27
34	0.60	236.92	0.03	1.00	-0.2592	-0.2013	34.00	4.41	4.34	-11.07
35	0.55	237.61	0.05	1.00	-0.2646	-0.2097	35.00	4.54	4.47	-11.91
36	0.53	238.62	0.02	1.00	-0.2696	-0.2177	36.00	4.66	4.60	-12.81
37	0.51	237.76	0.02	1.00	-0.2743	-0.2254	37.00	4.79	4.73	-13.77
38	0.51	236.34	0.01	1.00	-0.2792	-0.2329	38.00	4.92	4.86	-14.74
39	0.51	234.74	0.01	1.00	-0.2842	-0.2402	39.00	5.04	4.99	-15.69
40	0.54	233.23	0.03	1.00	-0.2896	-0.2477	40.00	5.17	5.12	-16.63
41	0.56	231.60	0.03	1.00	-0.2955	-0.2553	41.00	5.30	5.25	-17.55
42	0.56	229.41	0.02	1.00	-0.3017	-0.2628	42.00	5.42	5.38	-18.35
43	0.56	228.31	0.01	1.00	-0.3081	-0.2702	43.00	5.55	5.51	-19.02
44	0.57	226.95	0.02	1.00	-0.3148	-0.2774	44.00	5.68	5.64	-19.59
45	0.56	225.55	0.02	1.00	-0.3216	-0.2846	45.00	5.81	5.77	-20.03
46	0.52	226.55	0.04	1.00	-0.3281	-0.2914	46.00	5.94	5.89	-20.40
47	0.48	227.89	0.04	1.00	-0.3341	-0.2978	47.00	6.07	6.02	-20.83

Table D3 Well AGI3 Borehole Uncertainty Analysis

AOSTRA Underground Test Facility

(Borehole Position Uncertainty according to Wolff and de Wardt, 1981 with modifications by Dubrule and Nelson, 1986)

Well: AGI3
Date: Sept. 10/88
Elapsed Time = 4.1

Relative Depth Error: 5 mm
Inclination Error: 0.05 degrees
Azimuth Error: 0.10 degrees
Tool Misalignment Error: 0.01 degrees

DAH (m)	Inclination (degrees)	Azimuth (degrees)	Dogleg (degrees)	Dogleg Factor	North (m)	East (m)	Vertical (m)	ΔN (mm)	ΔE (mm)	Phi (°)
0	0.00	0.00			0.0000	0.0000	0.00	0.00	0.00	0.00
1	0.65	225.14	0.65	1.00	-0.0040	-0.0040	1.00	0.13	0.13	44.76
2	0.63	228.70	0.04	1.00	-0.0116	-0.0122	2.00	0.26	0.26	38.88
3	0.64	230.19	0.02	1.00	-0.0188	-0.0206	3.00	0.38	0.39	30.06
4	0.62	231.06	0.02	1.00	-0.0258	-0.0291	4.00	0.51	0.52	24.32
5	0.61	229.44	0.02	1.00	-0.0327	-0.0373	5.00	0.64	0.65	21.68
6	0.60	228.51	0.01	1.00	-0.0396	-0.0453	6.00	0.77	0.78	20.94
7	0.57	226.68	0.04	1.00	-0.0465	-0.0528	7.00	0.90	0.91	21.10
8	0.53	223.10	0.05	1.00	-0.0533	-0.0596	8.00	1.03	1.04	22.50
9	0.49	217.34	0.06	1.00	-0.0601	-0.0654	9.00	1.16	1.16	26.04
10	0.47	212.17	0.05	1.00	-0.0669	-0.0702	10.00	1.29	1.29	32.91
11	0.46	206.15	0.05	1.00	-0.0740	-0.0741	11.00	1.41	1.42	43.90
12	0.48	202.44	0.04	1.00	-0.0815	-0.0775	12.00	1.54	1.54	-33.18
13	0.49	197.77	0.04	1.00	-0.0894	-0.0804	13.00	1.67	1.66	-23.05
14	0.52	196.54	0.03	1.00	-0.0978	-0.0830	14.00	1.80	1.79	-16.74
15	0.52	197.29	0.01	1.00	-0.1065	-0.0856	15.00	1.93	1.91	-13.10
16	0.53	199.41	0.02	1.00	-0.1152	-0.0885	16.00	2.07	2.04	-11.00
17	0.53	201.84	0.02	1.00	-0.1239	-0.0918	17.00	2.20	2.16	-9.70
18	0.54	209.00	0.07	1.00	-0.1323	-0.0958	18.00	2.33	2.29	-9.03
19	0.56	214.34	0.05	1.00	-0.1404	-0.1008	19.00	2.46	2.41	-8.80
20	0.57	218.01	0.04	1.00	-0.1484	-0.1066	20.00	2.59	2.54	-8.80
21	0.59	219.61	0.03	1.00	-0.1563	-0.1130	21.00	2.72	2.67	-8.95
22	0.60	216.48	0.03	1.00	-0.1645	-0.1194	22.00	2.85	2.80	-9.05
23	0.61	214.59	0.02	1.00	-0.1731	-0.1255	23.00	2.98	2.93	-9.01
24	0.61	212.15	0.03	1.00	-0.1819	-0.1314	24.00	3.11	3.05	-8.87
25	0.62	211.14	0.01	1.00	-0.1911	-0.1370	25.00	3.24	3.18	-8.67
26	0.62	209.51	0.02	1.00	-0.2004	-0.1425	26.00	3.38	3.31	-8.44
27	0.61	212.46	0.03	1.00	-0.2096	-0.1480	27.00	3.51	3.44	-8.25
28	0.61	215.60	0.03	1.00	-0.2184	-0.1539	28.00	3.64	3.56	-8.20
29	0.64	222.42	0.08	1.00	-0.2269	-0.1608	29.00	3.77	3.69	-8.34
30	0.66	226.21	0.05	1.00	-0.2350	-0.1687	30.00	3.90	3.82	-8.65
31	0.69	229.38	0.05	1.00	-0.2429	-0.1775	31.00	4.03	3.95	-9.11
32	0.68	233.16	0.05	1.00	-0.2504	-0.1868	32.00	4.16	4.09	-9.70
33	0.67	235.43	0.03	1.00	-0.2573	-0.1963	33.00	4.29	4.22	-10.44
34	0.64	237.48	0.04	1.00	-0.2636	-0.2059	34.00	4.42	4.35	-11.31
35	0.56	238.83	0.08	1.00	-0.2691	-0.2147	35.00	4.55	4.48	-12.22
36	0.53	239.00	0.03	1.00	-0.2740	-0.2229	36.00	4.67	4.61	-13.19
37	0.53	238.28	0.01	1.00	-0.2788	-0.2308	37.00	4.80	4.74	-14.23
38	0.54	235.36	0.03	1.00	-0.2839	-0.2386	38.00	4.92	4.87	-15.27
39	0.54	233.34	0.02	1.00	-0.2894	-0.2463	39.00	5.05	5.00	-16.22
40	0.56	231.85	0.02	1.00	-0.2953	-0.2539	40.00	5.18	5.13	-17.12
41	0.57	230.14	0.02	1.00	-0.3015	-0.2615	41.00	5.31	5.26	-17.95
42	0.58	227.75	0.03	1.00	-0.3081	-0.2691	42.00	5.43	5.39	-18.64
43	0.59	226.26	0.02	1.00	-0.3150	-0.2766	43.00	5.56	5.52	-19.17
44	0.59	225.29	0.01	1.00	-0.3222	-0.2840	44.00	5.69	5.65	-19.58
45	0.59	224.51	0.01	1.00	-0.3295	-0.2912	45.00	5.82	5.78	-19.91
46	0.55	224.35	0.04	1.00	-0.3366	-0.2982	46.00	5.95	5.91	-20.14
47	0.51	224.96	0.04	1.00	-0.3432	-0.3047	47.00	6.08	6.03	-20.37

Table D3 continued

AOSTRA Underground Test Facility

(Borehole Position Uncertainty according to Wolff and de Wardt, 1981 with modifications by Dubrule and Nelson, 1986)

Relative Depth Error: 5 mm
Inclination Error: 0.05 degrees
Azimuth Error: 0.10 degrees
Tool Misalignment Error: 0.01 degrees

Well: AGI3
Date: Dec. 21/88
Elapsed Time = 5.5

DAH (m)	Inclination (degrees)	Azimuth (degrees)	Dogleg (degrees)	Dogleg Factor	North (m)	East (m)	Vertical (m)	ΔN (mm)	ΔE (mm)	Phi (°)
0	0.00	0.00			0.0000	0.0000	0.00	0.00	0.00	0.00
1	0.63	227.96	0.63	1.00	-0.0037	-0.0041	1.00	0.13	0.13	39.90
2	0.62	229.33	0.02	1.00	-0.0109	-0.0123	2.00	0.25	0.26	29.25
3	0.61	231.04	0.02	1.00	-0.0178	-0.0205	3.00	0.38	0.39	23.23
4	0.60	231.13	0.01	1.00	-0.0244	-0.0287	4.00	0.51	0.52	19.72
5	0.59	230.30	0.01	1.00	-0.0310	-0.0368	5.00	0.64	0.65	18.12
6	0.56	228.27	0.04	1.00	-0.0375	-0.0444	6.00	0.77	0.78	17.72
7	0.54	226.77	0.02	1.00	-0.0440	-0.0515	7.00	0.90	0.91	18.25
8	0.49	221.64	0.07	1.00	-0.0504	-0.0577	8.00	1.03	1.03	19.79
9	0.47	216.45	0.05	1.00	-0.0569	-0.0630	9.00	1.15	1.16	23.52
10	0.44	210.21	0.06	1.00	-0.0635	-0.0674	10.00	1.28	1.29	30.41
11	0.45	203.96	0.05	1.00	-0.0704	-0.0709	11.00	1.41	1.41	42.47
12	0.46	200.87	0.03	1.00	-0.0778	-0.0739	12.00	1.54	1.53	-33.12
13	0.48	196.69	0.04	1.00	-0.0855	-0.0766	13.00	1.67	1.66	-22.49
14	0.50	196.30	0.02	1.00	-0.0937	-0.0790	14.00	1.80	1.78	-16.23
15	0.52	196.14	0.02	1.00	-0.1023	-0.0815	15.00	1.93	1.91	-12.66
16	0.52	198.36	0.02	1.00	-0.1109	-0.0842	16.00	2.06	2.03	-10.54
17	0.52	202.03	0.03	1.00	-0.1195	-0.0873	17.00	2.19	2.16	-9.31
18	0.51	207.86	0.05	1.00	-0.1276	-0.0911	18.00	2.32	2.28	-8.65
19	0.52	212.45	0.04	1.00	-0.1354	-0.0956	19.00	2.45	2.41	-8.37
20	0.52	216.47	0.04	1.00	-0.1428	-0.1007	20.00	2.58	2.53	-8.32
21	0.54	217.55	0.02	1.00	-0.1502	-0.1063	21.00	2.71	2.66	-8.39
22	0.56	217.24	0.02	1.00	-0.1579	-0.1121	22.00	2.84	2.79	-8.48
23	0.57	214.32	0.03	1.00	-0.1659	-0.1179	23.00	2.97	2.92	-8.48
24	0.58	212.99	0.02	1.00	-0.1742	-0.1234	24.00	3.10	3.04	-8.39
25	0.59	211.13	0.02	1.00	-0.1829	-0.1289	25.00	3.23	3.17	-8.25
26	0.59	210.11	0.01	1.00	-0.1917	-0.1341	26.00	3.36	3.30	-8.06
27	0.59	211.12	0.01	1.00	-0.2006	-0.1394	27.00	3.49	3.43	-7.90
28	0.61	214.43	0.04	1.00	-0.2094	-0.1450	28.00	3.62	3.55	-7.83
29	0.63	219.40	0.06	1.00	-0.2180	-0.1515	29.00	3.76	3.68	-7.91
30	0.65	224.21	0.06	1.00	-0.2263	-0.1590	30.00	3.89	3.81	-8.13
31	0.65	228.38	0.05	1.00	-0.2342	-0.1672	31.00	4.02	3.94	-8.50
32	0.66	232.45	0.05	1.00	-0.2414	-0.1760	32.00	4.15	4.07	-9.02
33	0.64	234.94	0.03	1.00	-0.2482	-0.1851	33.00	4.28	4.20	-9.68
34	0.61	237.60	0.04	1.00	-0.2542	-0.1942	34.00	4.40	4.33	-10.44
35	0.56	238.53	0.05	1.00	-0.2596	-0.2028	35.00	4.53	4.46	-11.28
36	0.53	238.94	0.03	1.00	-0.2646	-0.2110	36.00	4.66	4.59	-12.17
37	0.52	238.40	0.01	1.00	-0.2693	-0.2188	37.00	4.78	4.72	-13.12
38	0.51	235.79	0.03	1.00	-0.2742	-0.2263	38.00	4.91	4.85	-14.05
39	0.51	234.69	0.01	1.00	-0.2793	-0.2336	39.00	5.03	4.98	-14.94
40	0.53	233.20	0.02	1.00	-0.2846	-0.2410	40.00	5.16	5.11	-15.83
41	0.54	231.08	0.02	1.00	-0.2904	-0.2484	41.00	5.29	5.24	-16.66
42	0.55	228.24	0.03	1.00	-0.2965	-0.2556	42.00	5.42	5.37	-17.35
43	0.55	226.98	0.01	1.00	-0.3030	-0.2627	43.00	5.54	5.50	-17.89
44	0.57	225.74	0.02	1.00	-0.3097	-0.2698	44.00	5.67	5.63	-18.34
45	0.56	225.01	0.01	1.00	-0.3167	-0.2768	45.00	5.80	5.76	-18.69
46	0.52	225.01	0.04	1.00	-0.3233	-0.2834	46.00	5.93	5.88	-18.97
47	0.48	226.26	0.04	1.00	-0.3294	-0.2897	47.00	6.06	6.01	-19.27

Table D3 continued

AOSTRA Underground Test Facility

(Borehole Position Uncertainty according to Wolff and de Wardt, 1981 with modifications by Dubrule and Nelson, 1986)

	Relative Depth Error:	5	mm
Well: AGI3	Inclination Error:	0.05	degrees
Date: June 5/89	Azimuth Error:	0.10	degrees
Elapsed Time = 7.9	Tool Misalignment Error:	0.01	degrees

DAH (m)	Inclination (degrees)	Azimuth (degrees)	Dogleg (degrees)	Dogleg Factor	North (m)	East (m)	Vertical (m)	ΔN (mm)	ΔE (mm)	Phi (°)
0	0.00	0.00			0.0000	0.0000	0.00	0.00	0.00	0.00
1	0.64	228.18	0.64	1.00	-0.0037	-0.0042	1.00	0.13	0.13	39.53
2	0.65	229.97	0.02	1.00	-0.0111	-0.0127	2.00	0.26	0.26	28.08
3	0.63	231.52	0.03	1.00	-0.0182	-0.0213	3.00	0.38	0.39	21.71
4	0.62	230.89	0.01	1.00	-0.0250	-0.0298	4.00	0.51	0.52	18.65
5	0.60	229.91	0.02	1.00	-0.0318	-0.0380	5.00	0.64	0.65	17.47
6	0.58	227.26	0.03	1.00	-0.0386	-0.0457	6.00	0.77	0.78	17.55
7	0.54	225.22	0.04	1.00	-0.0453	-0.0528	7.00	0.90	0.91	18.56
8	0.51	220.83	0.05	1.00	-0.0520	-0.0591	8.00	1.03	1.04	20.74
9	0.49	216.61	0.04	1.00	-0.0588	-0.0645	9.00	1.16	1.16	24.92
10	0.47	211.20	0.05	1.00	-0.0658	-0.0692	10.00	1.28	1.29	32.13
11	0.46	203.88	0.06	1.00	-0.0730	-0.0729	11.00	1.41	1.41	44.25
12	0.47	200.93	0.03	1.00	-0.0805	-0.0760	12.00	1.54	1.54	-31.84
13	0.49	199.86	0.02	1.00	-0.0883	-0.0790	13.00	1.67	1.66	-22.31
14	0.50	195.39	0.04	1.00	-0.0965	-0.0816	14.00	1.80	1.79	-16.41
15	0.51	196.09	0.01	1.00	-0.1050	-0.0840	15.00	1.93	1.91	-12.81
16	0.52	201.50	0.05	1.00	-0.1135	-0.0869	16.00	2.06	2.03	-10.85
17	0.52	205.03	0.03	1.00	-0.1218	-0.0904	17.00	2.19	2.16	-9.77
18	0.52	210.72	0.05	1.00	-0.1299	-0.0947	18.00	2.32	2.28	-9.21
19	0.54	217.37	0.06	1.00	-0.1375	-0.0999	19.00	2.45	2.41	-9.09
20	0.46	199.06	0.18	1.00	-0.1450	-0.1040	20.00	2.58	2.54	-8.65
21	0.49	196.69	0.04	1.00	-0.1529	-0.1066	21.00	2.71	2.66	-7.97
22	0.54	210.41	0.13	1.00	-0.1611	-0.1102	22.00	2.84	2.79	-7.62
23	0.54	199.62	0.10	1.00	-0.1696	-0.1141	23.00	2.97	2.91	-7.28
24	0.55	195.35	0.04	1.00	-0.1787	-0.1170	24.00	3.10	3.04	-6.78
25	0.62	210.78	0.17	1.00	-0.1879	-0.1210	25.00	3.24	3.16	-6.57
26	0.61	212.35	0.02	1.00	-0.1971	-0.1267	26.00	3.37	3.29	-6.52
27	0.61	212.36	0.00	1.00	-0.2061	-0.1323	27.00	3.50	3.42	-6.50
28	0.64	218.67	0.08	1.00	-0.2149	-0.1387	28.00	3.63	3.55	-6.57
29	0.68	225.15	0.08	1.00	-0.2235	-0.1464	29.00	3.76	3.68	-6.82
30	0.71	229.49	0.06	1.00	-0.2317	-0.1553	30.00	3.89	3.81	-7.21
31	0.71	233.43	0.05	1.00	-0.2394	-0.1650	31.00	4.03	3.94	-7.73
32	0.72	236.22	0.04	1.00	-0.2466	-0.1752	32.00	4.15	4.07	-8.39
33	0.70	238.54	0.04	1.00	-0.2533	-0.1856	33.00	4.28	4.20	-9.17
34	0.67	240.19	0.04	1.00	-0.2594	-0.1959	34.00	4.41	4.34	-10.07
35	0.61	241.50	0.06	1.00	-0.2648	-0.2057	35.00	4.54	4.47	-11.05
36	0.59	241.78	0.02	1.00	-0.2698	-0.2149	36.00	4.66	4.60	-12.13
37	0.57	240.74	0.02	1.00	-0.2747	-0.2237	37.00	4.79	4.73	-13.29
38	0.56	238.47	0.02	1.00	-0.2796	-0.2322	38.00	4.92	4.86	-14.46
39	0.56	236.62	0.02	1.00	-0.2849	-0.2405	39.00	5.04	4.99	-15.61
40	0.57	235.00	0.02	1.00	-0.2904	-0.2487	40.00	5.17	5.12	-16.74
41	0.57	232.37	0.03	1.00	-0.2963	-0.2567	41.00	5.30	5.25	-17.79
42	0.57	229.03	0.03	1.00	-0.3026	-0.2644	42.00	5.43	5.38	-18.64
43	0.56	227.18	0.02	1.00	-0.3092	-0.2717	43.00	5.55	5.51	-19.25
44	0.57	225.78	0.02	1.00	-0.3160	-0.2788	44.00	5.68	5.64	-19.72
45	0.56	224.81	0.01	1.00	-0.3229	-0.2859	45.00	5.81	5.77	-20.07
46	0.52	225.41	0.04	1.00	-0.3296	-0.2925	46.00	5.94	5.90	-20.36
47	0.49	228.05	0.04	1.00	-0.3356	-0.2989	47.00	6.07	6.02	-20.75

Table D3 continued

AOSTRA Underground Test Facility

(Borehole Position Uncertainty according to Wolff and de Wardt, 1981 with modifications by Dubrule and Nelson, 1986)

Well: AGI3
Date: Oct. 10/89
Elapsed Time = 9.7

Relative Depth Error: 5 mm
Inclination Error: 0.05 degrees
Azimuth Error: 0.10 degrees
Tool Misalignment Error: 0.01 degrees

DAH (m)	Inclination (degrees)	Azimuth (degrees)	Dogleg (degrees)	Dogleg Factor	North (m)	East (m)	Vertical (m)	ΔN (mm)	ΔE (mm)	Phi (°)
0	0.00	0.00			0.0000	0.0000	0.00	0.00	0.00	0.00
1	0.65	226.69	0.65	1.00	-0.0039	-0.0041	1.00	0.13	0.13	42.08
2	0.64	229.55	0.03	1.00	-0.0114	-0.0125	2.00	0.26	0.26	32.60
3	0.65	231.61	0.03	1.00	-0.0186	-0.0212	3.00	0.38	0.39	24.54
4	0.63	232.59	0.02	1.00	-0.0254	-0.0300	4.00	0.51	0.52	19.55
5	0.61	230.54	0.03	1.00	-0.0321	-0.0385	5.00	0.64	0.65	17.40
6	0.59	228.63	0.03	1.00	-0.0389	-0.0465	6.00	0.77	0.78	17.04
7	0.57	227.03	0.03	1.00	-0.0457	-0.0540	7.00	0.90	0.91	17.49
8	0.51	224.01	0.07	1.00	-0.0523	-0.0607	8.00	1.03	1.04	18.52
9	0.50	217.92	0.05	1.00	-0.0589	-0.0665	9.00	1.16	1.17	21.24
10	0.48	214.14	0.04	1.00	-0.0659	-0.0715	10.00	1.29	1.29	26.30
11	0.45	204.90	0.08	1.00	-0.0729	-0.0755	11.00	1.41	1.42	35.32
12	0.47	202.13	0.03	1.00	-0.0802	-0.0787	12.00	1.54	1.54	-40.67
13	0.49	199.41	0.03	1.00	-0.0881	-0.0817	13.00	1.67	1.66	-28.02
14	0.50	197.87	0.02	1.00	-0.0963	-0.0844	14.00	1.80	1.79	-19.92
15	0.51	195.45	0.02	1.00	-0.1047	-0.0870	15.00	1.93	1.91	-15.07
16	0.53	200.40	0.05	1.00	-0.1133	-0.0898	16.00	2.06	2.04	-12.32
17	0.53	203.80	0.03	1.00	-0.1219	-0.0932	17.00	2.19	2.16	-10.80
18	0.53	209.08	0.05	1.00	-0.1302	-0.0973	18.00	2.32	2.29	-9.99
19	0.54	213.46	0.04	1.00	-0.1381	-0.1022	19.00	2.45	2.41	-9.62
20	0.46	198.33	0.15	1.00	-0.1459	-0.1061	20.00	2.58	2.54	-9.00
21	0.50	188.87	0.09	1.00	-0.1540	-0.1080	21.00	2.71	2.66	-8.09
22	0.56	207.40	0.18	1.00	-0.1627	-0.1109	22.00	2.84	2.79	-7.57
23	0.57	202.83	0.05	1.00	-0.1716	-0.1151	23.00	2.98	2.91	-7.24
24	0.56	187.62	0.15	1.00	-0.1810	-0.1177	24.00	3.11	3.04	-6.64
25	0.62	203.01	0.17	1.00	-0.1908	-0.1204	25.00	3.24	3.16	-6.26
26	0.64	206.41	0.04	1.00	-0.2008	-0.1250	26.00	3.37	3.29	-6.07
27	0.62	209.25	0.04	1.00	-0.2105	-0.1302	27.00	3.51	3.42	-5.96
28	0.63	213.48	0.05	1.00	-0.2198	-0.1358	28.00	3.64	3.55	-5.95
29	0.68	223.35	0.12	1.00	-0.2287	-0.1429	29.00	3.77	3.67	-6.12
30	0.70	226.83	0.05	1.00	-0.2372	-0.1515	30.00	3.90	3.80	-6.41
31	0.71	231.31	0.06	1.00	-0.2453	-0.1608	31.00	4.03	3.94	-6.81
32	0.72	234.50	0.04	1.00	-0.2528	-0.1707	32.00	4.16	4.07	-7.32
33	0.72	236.99	0.03	1.00	-0.2599	-0.1811	33.00	4.29	4.20	-7.93
34	0.68	239.77	0.05	1.00	-0.2663	-0.1915	34.00	4.42	4.33	-8.64
35	0.64	240.10	0.04	1.00	-0.2721	-0.2015	35.00	4.55	4.46	-9.41
36	0.61	240.94	0.03	1.00	-0.2774	-0.2110	36.00	4.68	4.60	-10.25
37	0.60	240.63	0.01	1.00	-0.2826	-0.2202	37.00	4.80	4.73	-11.16
38	0.57	238.89	0.03	1.00	-0.2877	-0.2290	38.00	4.93	4.86	-12.08
39	0.56	237.13	0.02	1.00	-0.2930	-0.2374	39.00	5.06	4.99	-12.98
40	0.58	235.56	0.03	1.00	-0.2985	-0.2456	40.00	5.18	5.12	-13.88
41	0.57	233.53	0.02	1.00	-0.3043	-0.2538	41.00	5.31	5.25	-14.75
42	0.57	230.09	0.03	1.00	-0.3104	-0.2616	42.00	5.44	5.38	-15.49
43	0.57	228.92	0.01	1.00	-0.3169	-0.2692	43.00	5.57	5.51	-16.09
44	0.58	227.25	0.02	1.00	-0.3236	-0.2767	44.00	5.69	5.64	-16.62
45	0.57	226.63	0.01	1.00	-0.3304	-0.2840	45.00	5.82	5.77	-17.06
46	0.54	226.43	0.03	1.00	-0.3371	-0.2910	46.00	5.95	5.90	-17.44
47	0.51	229.53	0.04	1.00	-0.3432	-0.2978	47.00	6.08	6.02	-17.89

Table D3 continued

AOSTRA Underground Test Facility

(Borehole Position Uncertainty according to Wolff and de Wardt, 1981 with modifications by Dubrule and Nelson, 1986)

Relative Depth Error: 5 mm
Well: AGI3
Inclination Error: 0.05 degrees
Date: April 20/90
Azimuth Error: 0.10 degrees
Elapsed Time = 12.4
Tool Misalignment Error: 0.01 degrees

DAH (m)	Inclination (degrees)	Azimuth (degrees)	Dogleg (degrees)	Dogleg Factor	North (m)	East (m)	Vertical (m)	ΔN (mm)	ΔE (mm)	Phi (°)
0	0.00	0.00			0.0000	0.0000	0.00	0.00	0.00	0.00
1	0.65	227.47	0.65	1.00	-0.0038	-0.0042	1.00	0.13	0.13	40.74
2	0.65	229.31	0.02	1.00	-0.0114	-0.0127	2.00	0.26	0.26	30.67
3	0.65	231.82	0.03	1.00	-0.0186	-0.0214	3.00	0.38	0.39	23.53
4	0.64	231.78	0.01	1.00	-0.0255	-0.0303	4.00	0.51	0.52	19.24
5	0.62	230.99	0.02	1.00	-0.0324	-0.0389	5.00	0.64	0.65	17.32
6	0.59	228.03	0.04	1.00	-0.0392	-0.0469	6.00	0.77	0.78	16.93
7	0.57	227.48	0.02	1.00	-0.0460	-0.0544	7.00	0.90	0.91	17.44
8	0.52	222.89	0.07	1.00	-0.0527	-0.0611	8.00	1.03	1.04	18.60
9	0.50	218.22	0.05	1.00	-0.0595	-0.0669	9.00	1.16	1.17	21.50
10	0.46	213.35	0.06	1.00	-0.0663	-0.0718	10.00	1.29	1.29	26.50
11	0.45	203.68	0.08	1.00	-0.0732	-0.0756	11.00	1.41	1.42	36.01
12	0.45	201.25	0.02	1.00	-0.0805	-0.0786	12.00	1.54	1.54	-39.63
13	0.48	198.54	0.04	1.00	-0.0881	-0.0814	13.00	1.67	1.66	-27.29
14	0.48	195.92	0.02	1.00	-0.0961	-0.0839	14.00	1.80	1.79	-19.31
15	0.50	195.12	0.02	1.00	-0.1043	-0.0861	15.00	1.93	1.91	-14.66
16	0.52	202.21	0.07	1.00	-0.1128	-0.0890	16.00	2.06	2.04	-12.16
17	0.52	205.47	0.03	1.00	-0.1211	-0.0927	17.00	2.19	2.16	-10.83
18	0.51	211.24	0.05	1.00	-0.1290	-0.0969	18.00	2.32	2.29	-10.13
19	0.52	216.88	0.05	1.00	-0.1364	-0.1020	19.00	2.45	2.41	-9.94
20	0.36	198.59	0.21	1.00	-0.1430	-0.1057	20.00	2.58	2.54	-9.39
21	0.45	192.47	0.10	1.00	-0.1498	-0.1075	21.00	2.71	2.66	-8.64
22	0.49	204.41	0.11	1.00	-0.1575	-0.1101	22.00	2.84	2.79	-8.05
23	0.50	199.13	0.05	1.00	-0.1656	-0.1133	23.00	2.97	2.91	-7.59
24	0.51	188.15	0.10	1.00	-0.1741	-0.1154	24.00	3.10	3.04	-6.95
25	0.58	199.00	0.12	1.00	-0.1833	-0.1177	25.00	3.23	3.16	-6.49
26	0.60	204.45	0.06	1.00	-0.1928	-0.1215	26.00	3.36	3.29	-6.22
27	0.61	207.89	0.04	1.00	-0.2023	-0.1262	27.00	3.49	3.41	-6.08
28	0.62	213.55	0.06	1.00	-0.2115	-0.1316	28.00	3.63	3.54	-6.05
29	0.71	224.89	0.16	1.00	-0.2204	-0.1390	29.00	3.76	3.67	-6.27
30	0.71	228.40	0.04	1.00	-0.2289	-0.1480	30.00	3.89	3.80	-6.62
31	0.73	232.96	0.06	1.00	-0.2369	-0.1577	31.00	4.02	3.93	-7.09
32	0.71	235.27	0.04	1.00	-0.2442	-0.1679	32.00	4.15	4.06	-7.67
33	0.72	237.89	0.03	1.00	-0.2511	-0.1783	33.00	4.28	4.20	-8.37
34	0.69	240.05	0.04	1.00	-0.2574	-0.1888	34.00	4.41	4.33	-9.18
35	0.63	241.47	0.06	1.00	-0.2631	-0.1989	35.00	4.54	4.46	-10.07
36	0.62	241.26	0.01	1.00	-0.2683	-0.2085	36.00	4.66	4.59	-11.07
37	0.59	240.33	0.03	1.00	-0.2735	-0.2177	37.00	4.79	4.72	-12.11
38	0.57	238.22	0.03	1.00	-0.2786	-0.2264	38.00	4.91	4.85	-13.15
39	0.58	236.52	0.02	1.00	-0.2840	-0.2348	39.00	5.04	4.98	-14.18
40	0.59	234.98	0.02	1.00	-0.2898	-0.2433	40.00	5.17	5.11	-15.22
41	0.60	233.36	0.02	1.00	-0.2959	-0.2517	41.00	5.30	5.24	-16.23
42	0.60	231.48	0.02	1.00	-0.3022	-0.2600	42.00	5.43	5.38	-17.17
43	0.59	229.68	0.02	1.00	-0.3088	-0.2680	43.00	5.55	5.51	-17.98
44	0.61	228.71	0.02	1.00	-0.3157	-0.2759	44.00	5.68	5.64	-18.71
45	0.60	227.41	0.02	1.00	-0.3227	-0.2838	45.00	5.81	5.77	-19.33
46	0.56	227.59	0.04	1.00	-0.3296	-0.2913	46.00	5.94	5.90	-19.86
47	0.53	230.37	0.04	1.00	-0.3358	-0.2984	47.00	6.07	6.02	-20.48

Table D3 continued

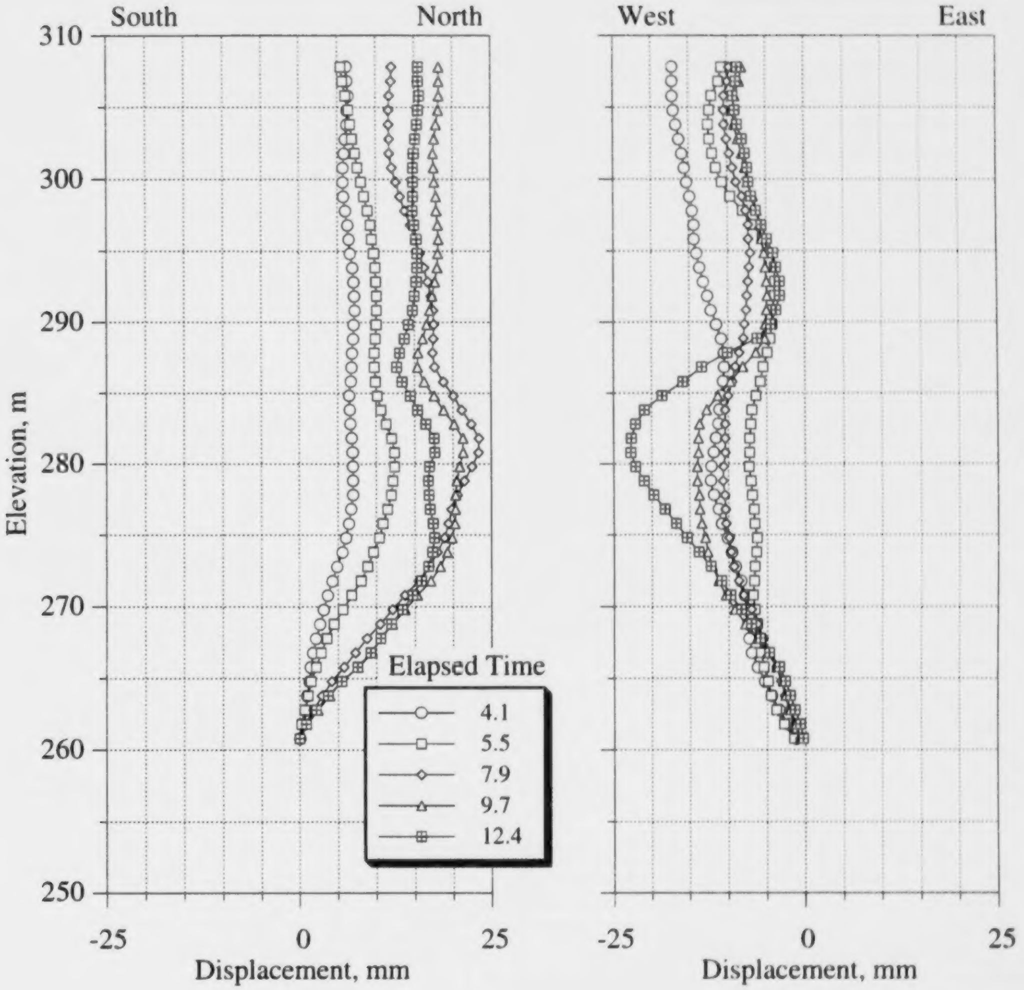

Figure D4 Horizontal Displacement Profile at Well AGI4

AOSTRA Underground Test Facility

(Borehole Position Uncertainty according to Wolff and de Wardt, 1981 with modifications by Dubrule and Nelson, 1986)

Well: AGI4
Date: Sept. 10/88
Elapsed Time = 0.0

Relative Depth Error: 5 mm
Inclination Error: 0.05 degrees
Azimuth Error: 0.10 degrees
Tool Misalignment Error: 0.01 degrees

DAH (m)	Inclination (degrees)	Azimuth (degrees)	Dogleg (degrees)	Dogleg Factor	North (m)	East (m)	Vertical (m)	ΔN (mm)	ΔE (mm)	Phi (°)
0	0.00	0.00			0.0000	0.0000	0.00	0.00	0.00	0.00
1	0.40	73.57	0.40	1.00	0.0010	0.0033	1.00	0.12	0.12	10.22
2	0.41	75.54	0.02	1.00	0.0029	0.0102	2.00	0.25	0.25	3.37
3	0.44	78.40	0.04	1.00	0.0045	0.0174	3.00	0.37	0.38	2.41
4	0.46	81.64	0.03	1.00	0.0059	0.0251	4.00	0.50	0.51	1.88
5	0.47	83.79	0.02	1.00	0.0069	0.0332	5.00	0.62	0.64	1.54
6	0.48	88.09	0.04	1.00	0.0075	0.0414	6.00	0.75	0.77	1.24
7	0.46	90.02	0.03	1.00	0.0076	0.0496	7.00	0.87	0.90	1.00
8	0.46	91.50	0.01	1.00	0.0075	0.0577	8.00	0.99	1.03	0.82
9	0.44	90.50	0.02	1.00	0.0074	0.0655	9.00	1.12	1.16	0.70
10	0.41	90.19	0.03	1.00	0.0073	0.0729	10.00	1.24	1.29	0.62
11	0.42	85.06	0.04	1.00	0.0077	0.0802	11.00	1.37	1.42	0.61
12	0.43	82.08	0.02	1.00	0.0085	0.0875	12.00	1.49	1.55	0.63
13	0.39	79.25	0.04	1.00	0.0096	0.0946	13.00	1.61	1.67	0.66
14	0.37	75.63	0.03	1.00	0.0111	0.1011	14.00	1.74	1.80	0.71
15	0.39	72.86	0.03	1.00	0.0129	0.1074	15.00	1.86	1.93	0.78
16	0.39	74.21	0.01	1.00	0.0148	0.1140	16.00	1.99	2.06	0.84
17	0.41	75.85	0.02	1.00	0.0166	0.1207	17.00	2.11	2.19	0.88
18	0.43	76.85	0.02	1.00	0.0183	0.1278	18.00	2.24	2.31	0.91
19	0.45	80.16	0.03	1.00	0.0199	0.1354	19.00	2.36	2.44	0.92
20	0.46	82.22	0.02	1.00	0.0211	0.1432	20.00	2.48	2.57	0.92
21	0.46	83.30	0.01	1.00	0.0221	0.1512	21.00	2.61	2.70	0.91
22	0.46	84.06	0.01	1.00	0.0230	0.1591	22.00	2.73	2.83	0.89
23	0.46	85.91	0.01	1.00	0.0237	0.1671	23.00	2.86	2.96	0.87
24	0.46	86.89	0.01	1.00	0.0242	0.1752	24.00	2.98	3.09	0.84
25	0.46	87.22	0.00	1.00	0.0246	0.1832	25.00	3.11	3.22	0.82
26	0.45	88.94	0.02	1.00	0.0249	0.1911	26.00	3.23	3.35	0.78
27	0.42	86.58	0.03	1.00	0.0251	0.1987	27.00	3.35	3.48	0.76
28	0.40	82.97	0.03	1.00	0.0258	0.2058	28.00	3.48	3.61	0.76
29	0.41	79.46	0.03	1.00	0.0269	0.2128	29.00	3.60	3.74	0.77
30	0.43	76.23	0.03	1.00	0.0284	0.2200	30.00	3.73	3.87	0.80
31	0.46	74.00	0.03	1.00	0.0304	0.2275	31.00	3.85	4.00	0.83
32	0.49	77.09	0.04	1.00	0.0325	0.2355	32.00	3.97	4.13	0.85
33	0.51	78.78	0.02	1.00	0.0343	0.2440	33.00	4.10	4.26	0.87
34	0.53	80.68	0.03	1.00	0.0359	0.2530	34.00	4.22	4.39	0.87
35	0.50	80.35	0.03	1.00	0.0374	0.2618	35.00	4.35	4.52	0.87
36	0.47	79.17	0.03	1.00	0.0389	0.2701	36.00	4.47	4.65	0.88
37	0.43	75.16	0.05	1.00	0.0406	0.2778	37.00	4.60	4.78	0.90
38	0.42	70.17	0.04	1.00	0.0428	0.2849	38.00	4.72	4.91	0.93
39	0.40	65.88	0.04	1.00	0.0455	0.2915	39.00	4.85	5.04	0.96
40	0.40	62.64	0.02	1.00	0.0485	0.2978	40.00	4.97	5.16	1.01
41	0.39	62.66	0.01	1.00	0.0517	0.3039	41.00	5.10	5.29	1.05
42	0.39	62.89	0.00	1.00	0.0548	0.3100	42.00	5.22	5.42	1.09
43	0.38	64.22	0.01	1.00	0.0578	0.3160	43.00	5.34	5.54	1.13
44	0.41	67.94	0.04	1.00	0.0606	0.3223	44.00	5.47	5.67	1.16
45	0.45	71.16	0.05	1.00	0.0632	0.3293	45.00	5.59	5.80	1.19
46	0.48	73.76	0.04	1.00	0.0657	0.3371	46.00	5.72	5.93	1.20
47	0.52	76.63	0.05	1.00	0.0679	0.3455	47.00	5.84	6.06	1.21

Table D4 Well AGI4 Borehole Uncertainty Analysis

AOSTRA Underground Test Facility

(Borehole Position Uncertainty according to Wolff and de Wardt, 1981 with modifications by Dubrule and Nelson, 1986)

Well: AGI4
Date: Sept. 10/88
Elapsed Time = 4.1

Relative Depth Error: 5 mm
Inclination Error: 0.05 degrees
Azimuth Error: 0.10 degrees
Tool Misalignment Error: 0.01 degrees

DAH (m)	Inclination (degrees)	Azimuth (degrees)	Dogleg (degrees)	Dogleg Factor	North (m)	East (m)	Vertical (m)	ΔN (mm)	ΔE (mm)	Phi (°)
0	0.00	0.00			0.0000	0.0000	0.00	0.00	0.00	0.00
1	0.42	72.79	0.42	1.00	0.0011	0.0035	1.00	0.12	0.12	10.78
2	0.43	75.48	0.02	1.00	0.0031	0.0106	2.00	0.25	0.25	3.49
3	0.46	79.98	0.05	1.00	0.0047	0.0182	3.00	0.37	0.38	2.36
4	0.48	82.82	0.03	1.00	0.0060	0.0263	4.00	0.50	0.51	1.80
5	0.49	85.66	0.03	1.00	0.0068	0.0347	5.00	0.62	0.64	1.42
6	0.49	89.19	0.03	1.00	0.0072	0.0433	6.00	0.75	0.77	1.12
7	0.48	90.60	0.02	1.00	0.0072	0.0518	7.00	0.87	0.90	0.90
8	0.47	90.65	0.01	1.00	0.0071	0.0600	8.00	0.99	1.03	0.75
9	0.45	90.70	0.02	1.00	0.0070	0.0681	9.00	1.12	1.16	0.64
10	0.42	87.12	0.04	1.00	0.0072	0.0757	10.00	1.24	1.29	0.60
11	0.43	83.87	0.03	1.00	0.0078	0.0830	11.00	1.37	1.42	0.60
12	0.41	80.38	0.03	1.00	0.0088	0.0903	12.00	1.49	1.55	0.63
13	0.38	76.51	0.04	1.00	0.0101	0.0971	13.00	1.61	1.68	0.68
14	0.38	72.95	0.02	1.00	0.0119	0.1035	14.00	1.74	1.81	0.75
15	0.39	72.92	0.01	1.00	0.0138	0.1099	15.00	1.86	1.93	0.82
16	0.39	73.61	0.00	1.00	0.0158	0.1164	16.00	1.99	2.06	0.87
17	0.42	75.74	0.03	1.00	0.0177	0.1232	17.00	2.11	2.19	0.92
18	0.46	79.44	0.05	1.00	0.0193	0.1307	18.00	2.24	2.32	0.94
19	0.48	81.50	0.03	1.00	0.0207	0.1388	19.00	2.36	2.45	0.94
20	0.49	83.66	0.02	1.00	0.0218	0.1472	20.00	2.48	2.58	0.92
21	0.50	83.52	0.01	1.00	0.0227	0.1558	21.00	2.61	2.71	0.91
22	0.50	86.27	0.02	1.00	0.0235	0.1645	22.00	2.73	2.84	0.88
23	0.50	86.40	0.00	1.00	0.0240	0.1732	23.00	2.86	2.97	0.85
24	0.51	86.29	0.01	1.00	0.0246	0.1820	24.00	2.98	3.10	0.83
25	0.52	86.92	0.01	1.00	0.0251	0.1909	25.00	3.11	3.23	0.80
26	0.50	87.94	0.02	1.00	0.0255	0.1998	26.00	3.23	3.37	0.77
27	0.48	87.17	0.02	1.00	0.0259	0.2084	27.00	3.36	3.50	0.75
28	0.46	83.38	0.04	1.00	0.0266	0.2166	28.00	3.48	3.63	0.75
29	0.45	80.69	0.02	1.00	0.0277	0.2244	29.00	3.60	3.76	0.75
30	0.47	77.32	0.03	1.00	0.0292	0.2323	30.00	3.73	3.89	0.78
31	0.50	77.69	0.03	1.00	0.0310	0.2406	31.00	3.85	4.02	0.80
32	0.52	80.12	0.03	1.00	0.0327	0.2493	32.00	3.98	4.15	0.81
33	0.54	82.23	0.03	1.00	0.0342	0.2584	33.00	4.10	4.28	0.81
34	0.52	84.28	0.03	1.00	0.0353	0.2676	34.00	4.23	4.41	0.80
35	0.49	84.51	0.03	1.00	0.0361	0.2764	35.00	4.35	4.54	0.79
36	0.42	83.08	0.07	1.00	0.0370	0.2843	36.00	4.48	4.67	0.78
37	0.37	77.66	0.06	1.00	0.0381	0.2911	37.00	4.60	4.80	0.79
38	0.37	72.43	0.03	1.00	0.0398	0.2973	38.00	4.72	4.93	0.81
39	0.36	67.04	0.04	1.00	0.0420	0.3033	39.00	4.85	5.05	0.85
40	0.36	64.80	0.01	1.00	0.0445	0.3090	40.00	4.97	5.18	0.88
41	0.36	63.12	0.01	1.00	0.0473	0.3147	41.00	5.10	5.31	0.92
42	0.37	63.85	0.01	1.00	0.0501	0.3204	42.00	5.22	5.43	0.96
43	0.37	66.22	0.02	1.00	0.0529	0.3262	43.00	5.34	5.56	0.99
44	0.40	68.59	0.03	1.00	0.0554	0.3324	44.00	5.47	5.69	1.02
45	0.47	74.46	0.08	1.00	0.0578	0.3396	45.00	5.59	5.82	1.04
46	0.51	77.14	0.05	1.00	0.0599	0.3479	46.00	5.72	5.95	1.06
47	0.53	79.67	0.03	1.00	0.0617	0.3568	47.00	5.84	6.08	1.06

Table D4 continued

AOSTRA Underground Test Facility

(Borehole Position Uncertainty according to Wolff and de Wardt, 1981 with modifications by Dubrule and Nelson, 1986)

Relative Depth Error: 5 mm

Well: AGI4

Inclination Error: 0.05 degrees

Date: Dec. 21/88

Azimuth Error: 0.10 degrees

Elapsed Time = 5.5

Tool Misalignment Error: 0.01 degrees

DAH (m)	Inclination (degrees)	Azimuth (degrees)	Dogleg (degrees)	Dogleg Factor	North (m)	East (m)	Vertical (m)	ΔN (mm)	ΔE (mm)	Phi (°)
0	0.00	0.00			0.0000	0.0000	0.00	0.00	0.00	0.00
1	0.42	70.47	0.42	1.00	0.0012	0.0035	1.00	0.12	0.12	12.54
2	0.42	72.90	0.02	1.00	0.0035	0.0104	2.00	0.25	0.25	4.16
3	0.44	76.40	0.03	1.00	0.0055	0.0176	3.00	0.37	0.38	2.94
4	0.46	79.65	0.03	1.00	0.0071	0.0253	4.00	0.50	0.51	2.32
5	0.48	82.36	0.03	1.00	0.0084	0.0334	5.00	0.62	0.64	1.91
6	0.48	85.85	0.03	1.00	0.0093	0.0418	6.00	0.75	0.77	1.56
7	0.47	87.44	0.02	1.00	0.0098	0.0500	7.00	0.87	0.90	1.31
8	0.46	87.85	0.01	1.00	0.0101	0.0581	8.00	0.99	1.03	1.14
9	0.44	87.97	0.02	1.00	0.0104	0.0660	9.00	1.12	1.16	1.01
10	0.42	86.15	0.02	1.00	0.0108	0.0735	10.00	1.24	1.29	0.94
11	0.42	83.00	0.02	1.00	0.0115	0.0808	11.00	1.37	1.42	0.91
12	0.41	80.15	0.02	1.00	0.0125	0.0879	12.00	1.49	1.55	0.92
13	0.39	77.27	0.03	1.00	0.0139	0.0948	13.00	1.62	1.68	0.95
14	0.38	74.24	0.02	1.00	0.0155	0.1013	14.00	1.74	1.80	0.99
15	0.40	73.39	0.02	1.00	0.0174	0.1078	15.00	1.86	1.93	1.05
16	0.40	74.12	0.01	1.00	0.0194	0.1145	16.00	1.99	2.06	1.09
17	0.42	76.16	0.02	1.00	0.0212	0.1215	17.00	2.11	2.19	1.12
18	0.44	77.90	0.02	1.00	0.0229	0.1288	18.00	2.24	2.32	1.13
19	0.46	80.75	0.03	1.00	0.0243	0.1365	19.00	2.36	2.45	1.13
20	0.47	83.64	0.03	1.00	0.0254	0.1445	20.00	2.49	2.58	1.10
21	0.48	83.70	0.01	1.00	0.0264	0.1528	21.00	2.61	2.71	1.08
22	0.50	82.59	0.02	1.00	0.0274	0.1613	22.00	2.73	2.84	1.06
23	0.50	84.37	0.02	1.00	0.0284	0.1699	23.00	2.86	2.97	1.04
24	0.52	83.54	0.02	1.00	0.0293	0.1788	24.00	2.98	3.10	1.02
25	0.53	82.92	0.01	1.00	0.0304	0.1879	25.00	3.11	3.23	1.00
26	0.51	84.04	0.02	1.00	0.0314	0.1969	26.00	3.23	3.36	0.98
27	0.44	87.14	0.07	1.00	0.0321	0.2051	27.00	3.36	3.49	0.95
28	0.42	83.65	0.03	1.00	0.0327	0.2126	28.00	3.48	3.62	0.94
29	0.40	81.20	0.03	1.00	0.0336	0.2197	29.00	3.60	3.75	0.93
30	0.41	78.12	0.02	1.00	0.0349	0.2267	30.00	3.73	3.88	0.95
31	0.43	77.42	0.02	1.00	0.0364	0.2338	31.00	3.85	4.01	0.96
32	0.46	80.07	0.04	1.00	0.0379	0.2414	32.00	3.98	4.14	0.96
33	0.48	82.33	0.03	1.00	0.0392	0.2496	33.00	4.10	4.27	0.96
34	0.46	84.45	0.03	1.00	0.0401	0.2577	34.00	4.23	4.40	0.95
35	0.44	85.40	0.02	1.00	0.0408	0.2655	35.00	4.35	4.53	0.93
36	0.38	86.38	0.06	1.00	0.0414	0.2727	36.00	4.47	4.65	0.91
37	0.34	82.69	0.05	1.00	0.0419	0.2789	37.00	4.60	4.78	0.91
38	0.32	76.58	0.04	1.00	0.0430	0.2846	38.00	4.72	4.91	0.91
39	0.31	70.09	0.04	1.00	0.0445	0.2898	39.00	4.85	5.03	0.94
40	0.31	65.77	0.02	1.00	0.0466	0.2948	40.00	4.97	5.16	0.97
41	0.33	63.30	0.02	1.00	0.0490	0.2999	41.00	5.09	5.28	1.00
42	0.32	64.74	0.01	1.00	0.0515	0.3050	42.00	5.22	5.41	1.03
43	0.33	65.34	0.01	1.00	0.0538	0.3101	43.00	5.34	5.54	1.07
44	0.36	69.05	0.04	1.00	0.0562	0.3157	44.00	5.47	5.66	1.09
45	0.40	71.95	0.04	1.00	0.0584	0.3219	45.00	5.59	5.79	1.11
46	0.45	75.52	0.06	1.00	0.0604	0.3290	46.00	5.71	5.92	1.13
47	0.49	76.82	0.04	1.00	0.0624	0.3370	47.00	5.84	6.05	1.14

Table D4 continued

AOSTRA Underground Test Facility

(Borehole Position Uncertainty according to Wolff and de Wardt, 1981 with modifications by Dubrule and Nelson, 1986)

Relative Depth Error: 5 mm
Inclination Error: 0.05 degrees
Azimuth Error: 0.10 degrees
Tool Misalignment Error: 0.01 degrees

Well: AGI4
Date: June 5/89
Elapsed Time = 7.9

DAH (m)	Inclination (degrees)	Azimuth (degrees)	Dogleg (degrees)	Dogleg Factor	North (m)	East (m)	Vertical (m)	ΔN (mm)	ΔE (mm)	Phi (°)
0	0.00	0.00			0.0000	0.0000	0.00	0.00	0.00	0.00
1	0.41	75.35	0.41	1.00	0.0009	0.0035	1.00	0.12	0.12	8.97
2	0.42	77.21	0.02	1.00	0.0026	0.0105	2.00	0.25	0.25	2.93
3	0.44	78.95	0.02	1.00	0.0042	0.0179	3.00	0.37	0.38	2.13
4	0.47	81.41	0.03	1.00	0.0055	0.0258	4.00	0.50	0.51	1.73
5	0.48	84.17	0.02	1.00	0.0066	0.0340	5.00	0.62	0.64	1.42
6	0.48	86.85	0.02	1.00	0.0072	0.0423	6.00	0.75	0.77	1.18
7	0.46	87.20	0.02	1.00	0.0077	0.0504	7.00	0.87	0.90	1.01
8	0.46	86.78	0.00	1.00	0.0081	0.0585	8.00	0.99	1.03	0.91
9	0.44	86.70	0.02	1.00	0.0085	0.0663	9.00	1.12	1.16	0.83
10	0.42	84.19	0.03	1.00	0.0091	0.0737	10.00	1.24	1.29	0.80
11	0.42	80.10	0.03	1.00	0.0101	0.0810	11.00	1.37	1.42	0.82
12	0.41	76.49	0.03	1.00	0.0116	0.0882	12.00	1.49	1.55	0.87
13	0.36	73.37	0.06	1.00	0.0133	0.0947	13.00	1.61	1.68	0.92
14	0.35	69.58	0.02	1.00	0.0153	0.1007	14.00	1.74	1.80	1.00
15	0.38	68.99	0.02	1.00	0.0176	0.1066	15.00	1.86	1.93	1.08
16	0.38	69.94	0.01	1.00	0.0199	0.1128	16.00	1.99	2.06	1.15
17	0.38	72.98	0.02	1.00	0.0220	0.1190	17.00	2.11	2.18	1.19
18	0.40	76.21	0.03	1.00	0.0238	0.1255	18.00	2.24	2.31	1.21
19	0.41	79.47	0.03	1.00	0.0253	0.1324	19.00	2.36	2.44	1.21
20	0.40	81.43	0.02	1.00	0.0264	0.1394	20.00	2.48	2.57	1.19
21	0.49	79.74	0.10	1.00	0.0277	0.1471	21.00	2.61	2.70	1.20
22	0.52	74.31	0.06	1.00	0.0297	0.1557	22.00	2.73	2.83	1.23
23	0.48	79.80	0.06	1.00	0.0317	0.1642	23.00	2.86	2.96	1.22
24	0.50	78.89	0.02	1.00	0.0333	0.1726	24.00	2.98	3.09	1.22
25	0.51	79.83	0.01	1.00	0.0349	0.1813	25.00	3.11	3.22	1.21
26	0.44	82.94	0.07	1.00	0.0362	0.1895	26.00	3.23	3.35	1.18
27	0.33	93.83	0.14	1.00	0.0364	0.1962	27.00	3.36	3.48	1.12
28	0.35	90.94	0.03	1.00	0.0362	0.2021	28.00	3.48	3.61	1.08
29	0.36	87.29	0.02	1.00	0.0363	0.2084	29.00	3.60	3.73	1.06
30	0.41	82.18	0.06	1.00	0.0369	0.2151	30.00	3.73	3.86	1.05
31	0.45	78.31	0.06	1.00	0.0382	0.2225	31.00	3.85	3.99	1.06
32	0.49	79.83	0.04	1.00	0.0398	0.2305	32.00	3.98	4.12	1.07
33	0.51	83.12	0.04	1.00	0.0411	0.2392	33.00	4.10	4.25	1.06
34	0.49	86.65	0.04	1.00	0.0418	0.2479	34.00	4.22	4.38	1.03
35	0.45	88.25	0.04	1.00	0.0422	0.2561	35.00	4.35	4.51	1.00
36	0.39	91.04	0.07	1.00	0.0423	0.2635	36.00	4.47	4.64	0.96
37	0.35	87.88	0.04	1.00	0.0423	0.2700	37.00	4.60	4.77	0.94
38	0.35	81.78	0.04	1.00	0.0429	0.2760	38.00	4.72	4.90	0.94
39	0.32	77.94	0.04	1.00	0.0439	0.2818	39.00	4.84	5.02	0.94
40	0.32	75.19	0.02	1.00	0.0452	0.2872	40.00	4.97	5.15	0.96
41	0.34	71.23	0.03	1.00	0.0468	0.2926	41.00	5.09	5.27	0.98
42	0.33	75.69	0.03	1.00	0.0485	0.2982	42.00	5.22	5.40	0.99
43	0.33	76.27	0.01	1.00	0.0499	0.3038	43.00	5.34	5.53	1.00
44	0.39	76.42	0.06	1.00	0.0514	0.3098	44.00	5.46	5.65	1.01
45	0.43	78.71	0.05	1.00	0.0529	0.3169	45.00	5.59	5.78	1.02
46	0.47	80.61	0.04	1.00	0.0543	0.3246	46.00	5.71	5.91	1.02
47	0.52	79.38	0.05	1.00	0.0558	0.3331	47.00	5.84	6.04	1.02

Table D4 continued

AOSTRA Underground Test Facility

(Borehole Position Uncertainty according to Wolff and de Wardt, 1981 with modifications by Dubrule and Nelson, 1986)

Well: AGI4
Date: Oct. 10/89
Elapsed Time = 9.7

Relative Depth Error: 5 mm
Inclination Error: 0.05 degrees
Azimuth Error: 0.10 degrees
Tool Misalignment Error: 0.01 degrees

DAH (m)	Inclination (degrees)	Azimuth (degrees)	Dogleg (degrees)	Dogleg Factor	North (m)	East (m)	Vertical (m)	ΔN (mm)	ΔE (mm)	Phi (°)
0	0.00	0.00			0.0000	0.0000	0.00	0.00	0.00	0.00
1	0.41	73.62	0.41	1.00	0.0010	0.0034	1.00	0.12	0.12	10.18
2	0.42	76.25	0.02	1.00	0.0029	0.0104	2.00	0.25	0.25	3.28
3	0.44	80.33	0.04	1.00	0.0044	0.0178	3.00	0.37	0.38	2.22
4	0.46	83.33	0.03	1.00	0.0055	0.0255	4.00	0.50	0.51	1.69
5	0.47	85.66	0.02	1.00	0.0063	0.0336	5.00	0.62	0.64	1.35
6	0.48	88.15	0.02	1.00	0.0067	0.0419	6.00	0.75	0.77	1.09
7	0.47	89.81	0.02	1.00	0.0069	0.0502	7.00	0.87	0.90	0.89
8	0.46	89.39	0.01	1.00	0.0069	0.0583	8.00	0.99	1.03	0.76
9	0.44	90.21	0.02	1.00	0.0070	0.0662	9.00	1.12	1.16	0.66
10	0.42	89.19	0.02	1.00	0.0070	0.0737	10.00	1.24	1.29	0.59
11	0.43	83.96	0.04	1.00	0.0075	0.0811	11.00	1.37	1.42	0.59
12	0.42	81.39	0.02	1.00	0.0084	0.0884	12.00	1.49	1.55	0.62
13	0.39	80.85	0.03	1.00	0.0095	0.0954	13.00	1.61	1.68	0.64
14	0.38	77.34	0.03	1.00	0.0108	0.1020	14.00	1.74	1.80	0.68
15	0.40	76.17	0.02	1.00	0.0123	0.1086	15.00	1.86	1.93	0.73
16	0.40	77.31	0.01	1.00	0.0139	0.1154	16.00	1.99	2.06	0.77
17	0.42	79.09	0.02	1.00	0.0154	0.1224	17.00	2.11	2.19	0.80
18	0.44	80.95	0.02	1.00	0.0167	0.1298	18.00	2.24	2.32	0.81
19	0.46	84.57	0.03	1.00	0.0177	0.1376	19.00	2.36	2.45	0.80
20	0.47	86.48	0.02	1.00	0.0183	0.1457	20.00	2.48	2.58	0.77
21	0.52	82.01	0.06	1.00	0.0192	0.1543	21.00	2.61	2.71	0.78
22	0.60	76.63	0.10	1.00	0.0210	0.1639	22.00	2.73	2.84	0.83
23	0.54	81.11	0.07	1.00	0.0230	0.1736	23.00	2.86	2.97	0.83
24	0.56	78.27	0.03	1.00	0.0247	0.1830	24.00	2.98	3.10	0.85
25	0.55	79.79	0.02	1.00	0.0265	0.1926	25.00	3.11	3.24	0.86
26	0.49	83.42	0.07	1.00	0.0279	0.2015	26.00	3.23	3.37	0.85
27	0.39	91.84	0.12	1.00	0.0282	0.2092	27.00	3.36	3.50	0.81
28	0.35	85.33	0.06	1.00	0.0284	0.2156	28.00	3.48	3.63	0.79
29	0.37	81.37	0.03	1.00	0.0291	0.2219	29.00	3.60	3.75	0.80
30	0.41	75.08	0.06	1.00	0.0305	0.2285	30.00	3.73	3.88	0.82
31	0.48	75.61	0.07	1.00	0.0325	0.2360	31.00	3.85	4.01	0.85
32	0.53	78.13	0.05	1.00	0.0345	0.2446	32.00	3.98	4.14	0.87
33	0.56	83.91	0.06	1.00	0.0359	0.2540	33.00	4.10	4.27	0.86
34	0.50	84.53	0.06	1.00	0.0369	0.2632	34.00	4.23	4.40	0.85
35	0.45	87.29	0.05	1.00	0.0375	0.2715	35.00	4.35	4.53	0.83
36	0.39	90.31	0.06	1.00	0.0377	0.2788	36.00	4.47	4.66	0.80
37	0.33	88.16	0.06	1.00	0.0377	0.2851	37.00	4.60	4.79	0.79
38	0.33	81.28	0.04	1.00	0.0383	0.2908	38.00	4.72	4.92	0.79
39	0.29	75.76	0.05	1.00	0.0393	0.2961	39.00	4.85	5.04	0.80
40	0.29	70.34	0.03	1.00	0.0408	0.3009	40.00	4.97	5.17	0.82
41	0.32	65.92	0.04	1.00	0.0428	0.3059	41.00	5.09	5.29	0.85
42	0.26	82.65	0.10	1.00	0.0442	0.3107	42.00	5.22	5.42	0.85
43	0.28	77.17	0.03	1.00	0.0450	0.3153	43.00	5.34	5.54	0.86
44	0.34	78.80	0.06	1.00	0.0462	0.3206	44.00	5.46	5.67	0.87
45	0.39	80.69	0.05	1.00	0.0473	0.3269	45.00	5.59	5.80	0.87
46	0.43	82.90	0.04	1.00	0.0483	0.3339	46.00	5.71	5.93	0.87
47	0.49	79.33	0.07	1.00	0.0496	0.3419	47.00	5.84	6.06	0.88

Table D4 continued

AOSTRA Underground Test Facility

(Borehole Position Uncertainty according to Wolff and de Wardt, 1981 with modifications by Dubrule and Nelson, 1986)

Well: AGI4
Date: April 20/90
Elapsed Time = 12.4

Relative Depth Error: 5 mm
Inclination Error: 0.05 degrees
Azimuth Error: 0.10 degrees
Tool Misalignment Error: 0.01 degrees

DAH (m)	Inclination (degrees)	Azimuth (degrees)	Dogleg (degrees)	Dogleg Factor	North (m)	East (m)	Vertical (m)	ΔN (mm)	ΔE (mm)	Phi (°)
0	0.00	0.00			0.0000	0.0000	0.00	0.00	0.00	0.00
1	0.41	73.03	0.41	1.00	0.0010	0.0034	1.00	0.12	0.12	10.61
2	0.41	75.69	0.02	1.00	0.0030	0.0103	2.00	0.25	0.25	3.40
3	0.43	79.60	0.03	1.00	0.0045	0.0175	3.00	0.37	0.38	2.34
4	0.45	82.98	0.03	1.00	0.0057	0.0251	4.00	0.50	0.51	1.79
5	0.46	85.64	0.02	1.00	0.0065	0.0330	5.00	0.62	0.64	1.42
6	0.47	88.91	0.03	1.00	0.0069	0.0411	6.00	0.75	0.77	1.13
7	0.46	90.61	0.02	1.00	0.0069	0.0492	7.00	0.87	0.90	0.90
8	0.45	90.69	0.01	1.00	0.0068	0.0571	8.00	0.99	1.03	0.75
9	0.43	91.01	0.02	1.00	0.0067	0.0648	9.00	1.12	1.16	0.64
10	0.41	90.45	0.02	1.00	0.0066	0.0721	10.00	1.24	1.29	0.56
11	0.43	82.03	0.06	1.00	0.0071	0.0794	11.00	1.37	1.42	0.59
12	0.42	80.04	0.02	1.00	0.0082	0.0867	12.00	1.49	1.55	0.63
13	0.39	79.99	0.03	1.00	0.0095	0.0937	13.00	1.61	1.67	0.65
14	0.38	76.21	0.03	1.00	0.0109	0.1003	14.00	1.74	1.80	0.70
15	0.41	74.70	0.03	1.00	0.0126	0.1069	15.00	1.86	1.93	0.77
16	0.39	76.57	0.02	1.00	0.0143	0.1137	16.00	1.99	2.06	0.81
17	0.41	79.26	0.03	1.00	0.0158	0.1205	17.00	2.11	2.19	0.83
18	0.43	81.45	0.03	1.00	0.0170	0.1278	18.00	2.23	2.31	0.84
19	0.45	83.79	0.03	1.00	0.0180	0.1354	19.00	2.36	2.44	0.83
20	0.46	86.91	0.03	1.00	0.0186	0.1433	20.00	2.48	2.57	0.80
21	0.50	85.68	0.04	1.00	0.0192	0.1516	21.00	2.61	2.70	0.78
22	0.62	76.32	0.15	1.00	0.0208	0.1613	22.00	2.73	2.84	0.83
23	0.56	83.20	0.09	1.00	0.0226	0.1714	23.00	2.86	2.97	0.82
24	0.56	81.34	0.02	1.00	0.0240	0.1810	24.00	2.98	3.10	0.83
25	0.55	80.69	0.01	1.00	0.0255	0.1906	25.00	3.11	3.23	0.83
26	0.49	82.96	0.06	1.00	0.0268	0.1996	26.00	3.23	3.37	0.82
27	0.38	92.36	0.13	1.00	0.0272	0.2072	27.00	3.36	3.49	0.78
28	0.37	86.27	0.04	1.00	0.0272	0.2137	28.00	3.48	3.62	0.77
29	0.40	78.96	0.06	1.00	0.0281	0.2203	29.00	3.60	3.75	0.78
30	0.44	75.79	0.05	1.00	0.0297	0.2275	30.00	3.73	3.88	0.81
31	0.51	74.42	0.07	1.00	0.0319	0.2355	31.00	3.85	4.01	0.84
32	0.55	75.32	0.04	1.00	0.0343	0.2444	32.00	3.98	4.14	0.87
33	0.57	80.04	0.05	1.00	0.0363	0.2540	33.00	4.10	4.27	0.88
34	0.54	83.59	0.05	1.00	0.0377	0.2635	34.00	4.23	4.40	0.87
35	0.49	85.03	0.05	1.00	0.0386	0.2725	35.00	4.35	4.54	0.86
36	0.41	86.14	0.08	1.00	0.0392	0.2803	36.00	4.47	4.67	0.84
37	0.38	83.86	0.03	1.00	0.0398	0.2872	37.00	4.60	4.79	0.83
38	0.36	80.53	0.03	1.00	0.0407	0.2936	38.00	4.72	4.92	0.84
39	0.32	75.22	0.05	1.00	0.0419	0.2994	39.00	4.85	5.05	0.85
40	0.31	71.71	0.02	1.00	0.0435	0.3047	40.00	4.97	5.17	0.87
41	0.33	68.56	0.03	1.00	0.0454	0.3099	41.00	5.09	5.30	0.89
42	0.27	81.23	0.09	1.00	0.0468	0.3149	42.00	5.22	5.42	0.89
43	0.29	78.50	0.02	1.00	0.0477	0.3197	43.00	5.34	5.55	0.90
44	0.35	80.02	0.06	1.00	0.0487	0.3252	44.00	5.47	5.68	0.90
45	0.41	80.92	0.06	1.00	0.0498	0.3317	45.00	5.59	5.80	0.91
46	0.44	82.42	0.03	1.00	0.0509	0.3391	46.00	5.71	5.93	0.91
47	0.50	78.41	0.07	1.00	0.0523	0.3472	47.00	5.84	6.06	0.92

Table D4 continued

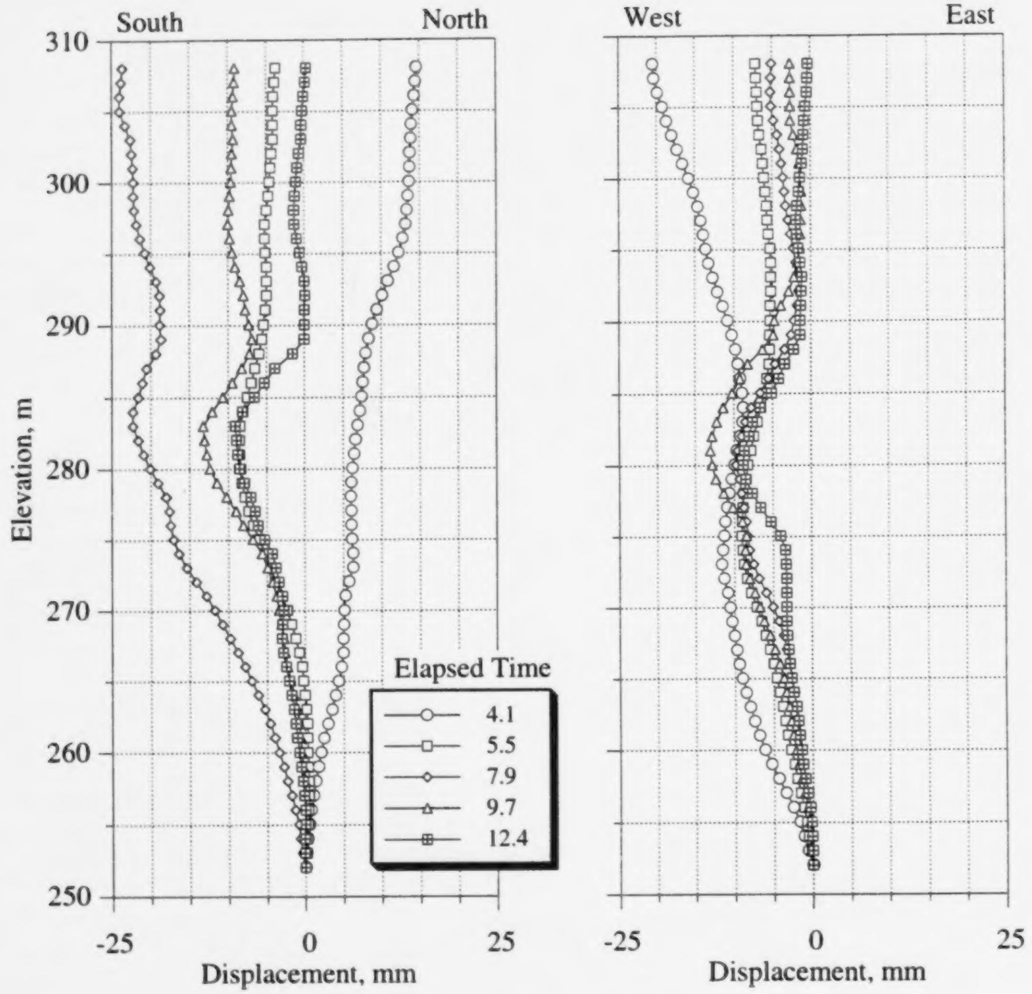

Figure D5 Horizontal Displacement Profile at Well AT1

AOSTRA Underground Test Facility

(Borehole Position Uncertainty according to Wolff and de Wardt, 1981 with modifications by Dubrule and Nelson, 1986)

Well: AT1
Date: Sept. 10/88
Elapsed Time = 0.0

Relative Depth Error:	5	mm
Inclination Error:	0.05	degrees
Azimuth Error:	0.10	degrees
Tool Misalignment Error:	0.01	degrees

DAH (m)	Inclination (degrees)	Azimuth (degrees)	Dogleg (degrees)	Dogleg Factor	North (m)	East (m)	Vertical (m)	ΔN (mm)	ΔE (mm)	Phi (°)
0	0.00	0.00			0.0000	0.0000	0.00	0.00	0.00	0.00
1	1.13	125.42	1.13	1.00	-0.0057	0.0081	1.00	0.13	0.13	-29.47
2	1.17	126.38	0.04	1.00	-0.0175	0.0243	2.00	0.27	0.28	-15.20
3	1.18	127.01	0.02	1.00	-0.0298	0.0408	3.00	0.41	0.43	-12.78
4	1.18	128.24	0.03	1.00	-0.0424	0.0572	4.00	0.55	0.58	-12.09
5	1.18	128.37	0.01	1.00	-0.0551	0.0733	5.00	0.69	0.73	-11.92
6	1.18	128.95	0.01	1.00	-0.0680	0.0894	6.00	0.83	0.88	-11.93
7	1.18	129.82	0.02	1.00	-0.0811	0.1054	7.00	0.98	1.03	-12.09
8	1.17	130.16	0.01	1.00	-0.0943	0.1211	8.00	1.12	1.18	-12.34
9	1.17	129.98	0.00	1.00	-0.1074	0.1367	9.00	1.26	1.33	-12.58
10	1.16	130.23	0.01	1.00	-0.1206	0.1523	10.00	1.41	1.47	-12.78
11	1.16	130.46	0.01	1.00	-0.1337	0.1677	11.00	1.55	1.62	-12.98
12	1.14	130.32	0.01	1.00	-0.1467	0.1830	12.00	1.69	1.77	-13.17
13	1.14	128.94	0.03	1.00	-0.1594	0.1983	13.00	1.83	1.92	-13.22
14	1.11	127.74	0.04	1.00	-0.1715	0.2136	14.00	1.97	2.06	-13.07
15	1.08	126.94	0.03	1.00	-0.1831	0.2288	15.00	2.11	2.21	-12.83
16	1.06	125.66	0.03	1.00	-0.1941	0.2439	16.00	2.25	2.36	-12.52
17	1.05	125.91	0.01	1.00	-0.2049	0.2589	17.00	2.39	2.50	-12.21
18	1.06	126.38	0.01	1.00	-0.2158	0.2738	18.00	2.53	2.65	-11.99
19	1.08	126.76	0.03	1.00	-0.2269	0.2888	19.00	2.66	2.80	-11.83
20	1.09	126.55	0.01	1.00	-0.2383	0.3040	20.00	2.80	2.94	-11.69
21	1.14	127.30	0.05	1.00	-0.2500	0.3196	21.00	2.94	3.09	-11.60
22	1.17	128.53	0.04	1.00	-0.2624	0.3355	22.00	3.08	3.24	-11.57
23	1.17	129.27	0.02	1.00	-0.2752	0.3514	23.00	3.23	3.39	-11.61
24	1.18	130.95	0.04	1.00	-0.2885	0.3671	24.00	3.37	3.54	-11.73
25	1.21	133.40	0.06	1.00	-0.3025	0.3826	25.00	3.51	3.69	-11.99
26	1.20	134.37	0.02	1.00	-0.3170	0.3977	25.99	3.66	3.83	-12.35
27	1.20	134.33	0.00	1.00	-0.3316	0.4126	26.99	3.80	3.98	-12.75
28	1.20	133.52	0.02	1.00	-0.3461	0.4277	27.99	3.95	4.13	-13.10
29	1.20	132.64	0.02	1.00	-0.3604	0.4430	28.99	4.10	4.28	-13.38
30	1.20	130.81	0.04	1.00	-0.3743	0.4586	29.99	4.24	4.42	-13.56
31	1.17	129.42	0.04	1.00	-0.3876	0.4743	30.99	4.38	4.57	-13.60
32	1.14	128.68	0.03	1.00	-0.4003	0.4900	31.99	4.53	4.72	-13.56
33	1.09	128.83	0.05	1.00	-0.4125	0.5051	32.99	4.67	4.87	-13.51
34	1.05	129.42	0.05	1.00	-0.4243	0.5197	33.99	4.81	5.01	-13.47
35	0.99	130.47	0.06	1.00	-0.4357	0.5333	34.99	4.94	5.16	-13.48
36	0.96	133.16	0.05	1.00	-0.4471	0.5460	35.99	5.08	5.30	-13.59
37	0.93	134.53	0.04	1.00	-0.4585	0.5579	36.99	5.22	5.43	-13.79
38	0.92	135.30	0.02	1.00	-0.4699	0.5693	37.99	5.36	5.57	-14.04
39	0.91	135.69	0.01	1.00	-0.4812	0.5804	38.99	5.49	5.71	-14.31
40	0.91	134.66	0.02	1.00	-0.4925	0.5916	39.99	5.63	5.84	-14.58
41	0.93	133.43	0.02	1.00	-0.5036	0.6032	40.99	5.77	5.98	-14.79
42	0.95	132.98	0.02	1.00	-0.5148	0.6151	41.99	5.91	6.12	-14.96
43	0.98	132.39	0.03	1.00	-0.5262	0.6275	42.99	6.04	6.26	-15.11
44	1.01	133.48	0.04	1.00	-0.5381	0.6402	43.99	6.18	6.40	-15.27
45	1.04	133.89	0.02	1.00	-0.5504	0.6531	44.99	6.32	6.54	-15.46
46	1.05	133.88	0.02	1.00	-0.5631	0.6663	45.99	6.46	6.68	-15.67
47	1.05	134.26	0.01	1.00	-0.5758	0.6795	46.99	6.60	6.82	-15.88
48	1.07	135.27	0.03	1.00	-0.5889	0.6926	47.99	6.75	6.97	-16.14
49	1.07	135.27	0.00	1.00	-0.6021	0.7057	48.99	6.89	7.11	-16.41
50	1.07	135.84	0.01	1.00	-0.6154	0.7188	49.99	7.03	7.25	-16.70
51	1.06	136.46	0.01	1.00	-0.6289	0.7317	50.99	7.17	7.39	-17.03
52	1.07	137.61	0.02	1.00	-0.6425	0.7444	51.99	7.32	7.53	-17.40
53	1.08	137.84	0.01	1.00	-0.6564	0.7570	52.99	7.46	7.67	-17.83
54	1.09	137.89	0.01	1.00	-0.6704	0.7697	53.99	7.60	7.81	-18.26
55	1.08	138.26	0.01	1.00	-0.6845	0.7823	54.99	7.75	7.96	-18.71
56	1.10	137.61	0.02	1.00	-0.6986	0.7951	55.99	7.89	8.10	-19.17

Table D5 Well AT1 Borehole Uncertainty Analysis

AOSTRA Underground Test Facility

(Borehole Position Uncertainty according to Wolff and de Wardt, 1981 with modifications by Dubrule and Nelson, 1986)

Relative Depth Error: 5 mm
Inclination Error: 0.05 degrees
Azimuth Error: 0.10 degrees
Tool Misalignment Error: 0.01 degrees

Well: AT1
Date: Sept. 10/88
Elapsed Time = 4.1

DAH (m)	Inclination (degrees)	Azimuth (degrees)	Dogleg (degrees)	Dogleg Factor	North (m)	East (m)	Vertical (m)	ΔN (mm)	ΔE (mm)	Phi (°)
0	0.000	0.000			0.0000	0.0000	0.00	0.00	0.00	0.00
1	1.159	125.305	1.16	1.00	-0.0058	0.0083	1.00	0.13	0.13	-29.31
2	1.202	125.749	0.04	1.00	-0.0178	0.0250	2.00	0.27	0.28	-14.82
3	1.215	126.648	0.02	1.00	-0.0303	0.0420	3.00	0.41	0.43	-12.30
4	1.215	127.409	0.02	1.00	-0.0430	0.0590	4.00	0.55	0.58	-11.54
5	1.213	127.356	0.00	1.00	-0.0559	0.0758	5.00	0.70	0.74	-11.22
6	1.222	128.015	0.02	1.00	-0.0689	0.0926	6.00	0.84	0.89	-11.10
7	1.213	128.720	0.02	1.00	-0.0821	0.1093	7.00	0.98	1.04	-11.13
8	1.206	128.976	0.01	1.00	-0.0953	0.1257	8.00	1.12	1.19	-11.26
9	1.200	129.206	0.01	1.00	-0.1086	0.1420	9.00	1.27	1.34	-11.39
10	1.190	129.966	0.02	1.00	-0.1219	0.1581	10.00	1.41	1.49	-11.58
11	1.176	130.283	0.02	1.00	-0.1352	0.1739	11.00	1.55	1.64	-11.81
12	1.178	130.753	0.01	1.00	-0.1485	0.1895	12.00	1.70	1.79	-12.08
13	1.166	129.614	0.03	1.00	-0.1617	0.2051	13.00	1.84	1.94	-12.27
14	1.160	128.461	0.02	1.00	-0.1745	0.2209	14.00	1.98	2.08	-12.30
15	1.137	127.924	0.03	1.00	-0.1869	0.2366	15.00	2.12	2.23	-12.21
16	1.118	126.220	0.04	1.00	-0.1987	0.2523	16.00	2.26	2.38	-12.03
17	1.104	126.449	0.01	1.00	-0.2102	0.2679	17.00	2.40	2.53	-11.81
18	1.106	126.635	0.00	1.00	-0.2217	0.2834	18.00	2.54	2.68	-11.65
19	1.123	126.594	0.02	1.00	-0.2333	0.2990	19.00	2.68	2.82	-11.51
20	1.120	126.701	0.00	1.00	-0.2450	0.3147	20.00	2.82	2.97	-11.38
21	1.162	127.319	0.04	1.00	-0.2570	0.3306	21.00	2.96	3.12	-11.31
22	1.184	128.066	0.03	1.00	-0.2695	0.3468	22.00	3.10	3.27	-11.29
23	1.191	129.576	0.03	1.00	-0.2825	0.3630	23.00	3.25	3.42	-11.33
24	1.196	131.251	0.04	1.00	-0.2960	0.3788	24.00	3.39	3.57	-11.47
25	1.205	134.354	0.07	1.00	-0.3102	0.3942	24.99	3.53	3.72	-11.76
26	1.194	135.904	0.03	1.00	-0.3250	0.4090	25.99	3.68	3.87	-12.19
27	1.186	135.260	0.02	1.00	-0.3399	0.4235	26.99	3.83	4.01	-12.65
28	1.195	134.699	0.01	1.00	-0.3546	0.4382	27.99	3.97	4.16	-13.07
29	1.191	133.468	0.03	1.00	-0.3691	0.4532	28.99	4.12	4.30	-13.42
30	1.181	131.642	0.04	1.00	-0.3830	0.4684	29.99	4.26	4.45	-13.65
31	1.150	129.483	0.05	1.00	-0.3963	0.4838	30.99	4.41	4.60	-13.72
32	1.136	129.189	0.01	1.00	-0.4089	0.4993	31.99	4.55	4.75	-13.70
33	1.080	128.681	0.06	1.00	-0.4211	0.5143	32.99	4.69	4.89	-13.65
34	1.029	129.367	0.05	1.00	-0.4327	0.5286	33.99	4.83	5.04	-13.60
35	1.001	131.289	0.04	1.00	-0.4441	0.5421	34.99	4.97	5.18	-13.64
36	1.019	133.613	0.04	1.00	-0.4560	0.5551	35.99	5.10	5.32	-13.79
37	0.948	134.175	0.07	1.00	-0.4679	0.5675	36.99	5.24	5.46	-13.99
38	0.932	134.824	0.02	1.00	-0.4794	0.5792	37.99	5.38	5.60	-14.22
39	0.920	135.160	0.01	1.00	-0.4908	0.5906	38.99	5.52	5.74	-14.48
40	0.927	133.822	0.02	1.00	-0.5021	0.6021	39.99	5.66	5.87	-14.71
41	0.940	133.111	0.02	1.00	-0.5134	0.6140	40.99	5.79	6.01	-14.89
42	0.976	132.743	0.04	1.00	-0.5247	0.6262	41.99	5.93	6.15	-15.05
43	1.015	132.733	0.04	1.00	-0.5365	0.6390	42.99	6.07	6.29	-15.20
44	1.053	133.201	0.04	1.00	-0.5488	0.6522	43.99	6.21	6.43	-15.37
45	1.079	133.891	0.03	1.00	-0.5616	0.6656	44.99	6.35	6.58	-15.56
46	1.092	133.858	0.01	1.00	-0.5748	0.6793	45.99	6.49	6.72	-15.77
47	1.106	134.001	0.01	1.00	-0.5881	0.6931	46.99	6.64	6.86	-15.98
48	1.111	134.267	0.01	1.00	-0.6015	0.7070	47.99	6.78	7.01	-16.20
49	1.118	134.224	0.01	1.00	-0.6151	0.7209	48.99	6.92	7.15	-16.43
50	1.122	134.497	0.01	1.00	-0.6288	0.7349	49.99	7.07	7.30	-16.66
51	1.116	135.049	0.01	1.00	-0.6425	0.7488	50.99	7.21	7.44	-16.90
52	1.121	135.999	0.02	1.00	-0.6565	0.7624	51.99	7.35	7.58	-17.19
53	1.109	137.007	0.02	1.00	-0.6706	0.7758	52.99	7.50	7.73	-17.53
54	1.115	137.219	0.01	1.00	-0.6848	0.7890	53.99	7.64	7.87	-17.92
55	1.114	137.194	0.00	1.00	-0.6991	0.8023	54.99	7.79	8.01	-18.31
56	1.121	136.361	0.02	1.00	-0.7133	0.8156	55.99	7.93	8.15	-18.67

Table D5 continued

AOSTRA Underground Test Facility

(Borehole Position Uncertainty according to Wolff and de Wardt, 1981 with modifications by Dubrule and Nelson, 1986)

Well: AT1
Date: Dec. 21/88
Elapsed Time = 5.5

Relative Depth Error:	5	mm
Inclination Error:	0.05	degrees
Azimuth Error:	0.10	degrees
Tool Misalignment Error:	0.01	degrees

DAH (m)	Inclination (degrees)	Azimuth (degrees)	Dogleg (degrees)	Dogleg Factor	North (m)	East (m)	Vertical (m)	ΔN (mm)	ΔE (mm)	Phi (°)
0	0.000	0.000			0.0000	0.0000	0.00	0.00	0.00	0.00
1	1.144	125.698	1.14	1.00	-0.0058	0.0081	1.00	0.13	0.13	-29.88
2	1.181	126.435	0.04	1.00	-0.0178	0.0245	2.00	0.27	0.28	-15.51
3	1.185	127.279	0.02	1.00	-0.0302	0.0410	3.00	0.41	0.43	-13.00
4	1.187	127.720	0.01	1.00	-0.0428	0.0574	4.00	0.55	0.58	-12.21
5	1.192	128.239	0.01	1.00	-0.0555	0.0738	5.00	0.69	0.73	-11.94
6	1.201	129.020	0.02	1.00	-0.0686	0.0901	6.00	0.84	0.88	-11.94
7	1.191	129.665	0.02	1.00	-0.0818	0.1063	7.00	0.98	1.03	-12.08
8	1.184	130.179	0.01	1.00	-0.0951	0.1222	8.00	1.12	1.18	-12.32
9	1.184	130.164	0.00	1.00	-0.1084	0.1379	9.00	1.27	1.33	-12.58
10	1.176	130.629	0.01	1.00	-0.1218	0.1536	10.00	1.41	1.48	-12.83
11	1.165	130.531	0.01	1.00	-0.1351	0.1691	11.00	1.55	1.63	-13.07
12	1.154	129.678	0.02	1.00	-0.1481	0.1846	12.00	1.69	1.77	-13.21
13	1.135	128.377	0.03	1.00	-0.1607	0.2001	13.00	1.84	1.92	-13.16
14	1.108	127.511	0.03	1.00	-0.1727	0.2156	14.00	1.98	2.07	-12.97
15	1.079	126.964	0.03	1.00	-0.1842	0.2307	15.00	2.12	2.22	-12.72
16	1.065	125.997	0.02	1.00	-0.1954	0.2458	16.00	2.25	2.36	-12.45
17	1.057	126.470	0.01	1.00	-0.2063	0.2607	17.00	2.39	2.51	-12.19
18	1.066	127.041	0.01	1.00	-0.2174	0.2756	18.00	2.53	2.65	-12.02
19	1.085	127.283	0.02	1.00	-0.2287	0.2905	19.00	2.67	2.80	-11.91
20	1.120	127.816	0.04	1.00	-0.2405	0.3058	20.00	2.81	2.95	-11.84
21	1.148	129.109	0.04	1.00	-0.2528	0.3213	21.00	2.95	3.10	-11.85
22	1.171	129.786	0.03	1.00	-0.2656	0.3369	22.00	3.09	3.24	-11.93
23	1.174	131.308	0.03	1.00	-0.2789	0.3524	23.00	3.23	3.39	-12.07
24	1.184	132.959	0.04	1.00	-0.2927	0.3677	24.00	3.38	3.54	-12.33
25	1.194	134.723	0.04	1.00	-0.3071	0.3827	25.00	3.52	3.69	-12.71
26	1.181	135.205	0.02	1.00	-0.3217	0.3973	25.99	3.67	3.83	-13.16
27	1.183	134.778	0.01	1.00	-0.3363	0.4119	26.99	3.82	3.98	-13.61
28	1.177	134.008	0.02	1.00	-0.3507	0.4266	27.99	3.96	4.13	-14.00
29	1.181	132.489	0.03	1.00	-0.3648	0.4416	28.99	4.11	4.27	-14.29
30	1.168	130.442	0.04	1.00	-0.3784	0.4570	29.99	4.25	4.42	-14.43
31	1.144	128.348	0.05	1.00	-0.3912	0.4725	30.99	4.39	4.57	-14.39
32	1.109	127.363	0.04	1.00	-0.4033	0.4881	31.99	4.53	4.72	-14.24
33	1.069	126.766	0.04	1.00	-0.4147	0.5032	32.99	4.67	4.86	-14.06
34	1.026	127.214	0.04	1.00	-0.4257	0.5178	33.99	4.81	5.01	-13.88
35	0.982	128.286	0.05	1.00	-0.4365	0.5317	34.99	4.94	5.15	-13.76
36	0.953	130.422	0.05	1.00	-0.4471	0.5447	35.99	5.08	5.29	-13.74
37	0.926	130.667	0.03	1.00	-0.4578	0.5572	36.99	5.22	5.43	-13.78
38	0.919	132.061	0.02	1.00	-0.4684	0.5693	37.99	5.35	5.57	-13.86
39	0.908	132.977	0.02	1.00	-0.4792	0.5810	38.99	5.49	5.71	-13.99
40	0.919	131.807	0.02	1.00	-0.4900	0.5928	39.99	5.63	5.85	-14.13
41	0.932	131.234	0.02	1.00	-0.5007	0.6049	40.99	5.76	5.98	-14.22
42	0.957	131.135	0.02	1.00	-0.5115	0.6173	41.99	5.90	6.12	-14.29
43	0.986	131.474	0.03	1.00	-0.5227	0.6300	42.99	6.04	6.26	-14.37
44	1.024	131.866	0.04	1.00	-0.5344	0.6431	43.99	6.17	6.41	-14.48
45	1.046	132.805	0.03	1.00	-0.5465	0.6565	44.99	6.31	6.55	-14.60
46	1.060	133.110	0.01	1.00	-0.5591	0.6699	45.99	6.46	6.69	-14.76
47	1.071	133.719	0.02	1.00	-0.5718	0.6834	46.99	6.60	6.83	-14.94
48	1.079	134.024	0.01	1.00	-0.5848	0.6970	47.99	6.74	6.98	-15.14
49	1.082	134.265	0.01	1.00	-0.5980	0.7105	48.99	6.88	7.12	-15.35
50	1.082	135.011	0.01	1.00	-0.6112	0.7239	49.99	7.02	7.26	-15.59
51	1.084	135.642	0.01	1.00	-0.6247	0.7372	50.99	7.17	7.40	-15.85
52	1.089	136.710	0.02	1.00	-0.6384	0.7503	51.99	7.31	7.55	-16.17
53	1.094	137.336	0.01	1.00	-0.6523	0.7633	52.99	7.45	7.69	-16.53
54	1.101	137.604	0.01	1.00	-0.6664	0.7763	53.99	7.60	7.83	-16.91
55	1.103	137.514	0.00	1.00	-0.6806	0.7893	54.99	7.74	7.97	-17.31
56	1.105	137.883	0.01	1.00	-0.6948	0.8022	55.99	7.89	8.11	-17.72

Table D5 continued

AOSTRA Underground Test Facility

(Borehole Position Uncertainty according to Wolff and de Wardt, 1981 with modifications by Dubrule and Nelson, 1986)

Well: AT1
Date: June 5/89
Elapsed Time = 7.9

Relative Depth Error: 5 mm
Inclination Error: 0.05 degrees
Azimuth Error: 0.10 degrees
Tool Misalignment Error: 0.01 degrees

DAH (m)	Inclination (degrees)	Azimuth (degrees)	Dogleg (degrees)	Dogleg Factor	North (m)	East (m)	Vertical (m)	ΔN (mm)	ΔE (mm)	Phi (°)
0	0.00	0.00			0.0000	0.0000	0.00	0.00	0.00	0.00
1	1.14	126.38	1.14	1.00	-0.0059	0.0080	1.00	0.13	0.13	-30.87
2	1.18	126.53	0.04	1.00	-0.0179	0.0242	2.00	0.27	0.28	-16.28
3	1.18	126.69	0.01	1.00	-0.0302	0.0408	3.00	0.41	0.43	-13.29
4	1.17	124.64	0.05	1.00	-0.0421	0.0574	4.00	0.55	0.58	-11.67
5	1.18	127.23	0.06	1.00	-0.0541	0.0740	5.00	0.69	0.73	-10.96
6	1.19	128.26	0.02	1.00	-0.0669	0.0904	6.00	0.83	0.88	-10.90
7	1.19	129.16	0.02	1.00	-0.0798	0.1066	7.00	0.98	1.03	-11.03
8	1.18	129.75	0.01	1.00	-0.0930	0.1226	8.00	1.12	1.18	-11.27
9	1.18	129.82	0.00	1.00	-0.1061	0.1383	9.00	1.26	1.33	-11.53
10	1.17	129.20	0.02	1.00	-0.1191	0.1541	10.00	1.40	1.48	-11.70
11	1.15	129.19	0.02	1.00	-0.1319	0.1698	11.00	1.55	1.63	-11.79
12	1.14	128.31	0.02	1.00	-0.1444	0.1854	12.00	1.69	1.77	-11.81
13	1.13	126.84	0.03	1.00	-0.1565	0.2011	13.00	1.83	1.92	-11.69
14	1.09	125.27	0.05	1.00	-0.1679	0.2168	14.00	1.97	2.07	-11.42
15	1.07	124.36	0.03	1.00	-0.1787	0.2323	15.00	2.10	2.22	-11.08
16	1.05	125.77	0.03	1.00	-0.1893	0.2474	16.00	2.24	2.37	-10.82
17	1.04	126.58	0.02	1.00	-0.2001	0.2621	17.00	2.38	2.51	-10.68
18	1.04	127.19	0.01	1.00	-0.2110	0.2767	18.00	2.52	2.66	-10.62
19	1.06	126.66	0.02	1.00	-0.2220	0.2913	19.00	2.65	2.80	-10.57
20	1.09	133.17	0.13	1.00	-0.2340	0.3056	20.00	2.79	2.95	-10.73
21	1.13	130.57	0.06	1.00	-0.2469	0.3200	21.00	2.94	3.09	-11.01
22	1.14	131.15	0.02	1.00	-0.2599	0.3350	22.00	3.08	3.24	-11.21
23	1.15	132.68	0.03	1.00	-0.2732	0.3499	23.00	3.22	3.38	-11.46
24	1.16	134.86	0.05	1.00	-0.2872	0.3644	24.00	3.36	3.53	-11.84
25	1.16	132.50	0.05	1.00	-0.3011	0.3791	25.00	3.51	3.68	-12.20
26	1.15	134.20	0.03	1.00	-0.3150	0.3938	26.00	3.65	3.82	-12.51
27	1.14	133.83	0.02	1.00	-0.3289	0.4081	26.99	3.80	3.97	-12.87
28	1.18	131.43	0.07	1.00	-0.3426	0.4230	27.99	3.94	4.11	-13.14
29	1.18	129.12	0.05	1.00	-0.3559	0.4387	28.99	4.08	4.26	-13.22
30	1.17	128.94	0.01	1.00	-0.3687	0.4546	29.99	4.23	4.41	-13.20
31	1.19	128.38	0.02	1.00	-0.3816	0.4706	30.99	4.37	4.56	-13.16
32	1.14	128.05	0.05	1.00	-0.3941	0.4866	31.99	4.51	4.71	-13.08
33	1.08	127.32	0.06	1.00	-0.4060	0.5019	32.99	4.65	4.86	-12.98
34	1.03	126.12	0.05	1.00	-0.4170	0.5167	33.99	4.79	5.00	-12.83
35	0.98	126.64	0.05	1.00	-0.4274	0.5309	34.99	4.92	5.15	-12.69
36	0.95	127.81	0.04	1.00	-0.4376	0.5443	35.99	5.06	5.29	-12.59
37	0.92	128.74	0.03	1.00	-0.4477	0.5571	36.99	5.19	5.43	-12.56
38	0.91	130.80	0.04	1.00	-0.4580	0.5694	37.99	5.33	5.57	-12.58
39	0.90	131.49	0.02	1.00	-0.4683	0.5812	38.99	5.47	5.71	-12.66
40	0.90	130.41	0.02	1.00	-0.4786	0.5930	39.99	5.60	5.84	-12.74
41	0.91	130.23	0.01	1.00	-0.4887	0.6050	40.99	5.74	5.98	-12.79
42	0.92	129.82	0.02	1.00	-0.4990	0.6173	41.99	5.87	6.12	-12.84
43	0.96	129.82	0.04	1.00	-0.5096	0.6299	42.99	6.01	6.26	-12.87
44	0.99	130.62	0.03	1.00	-0.5206	0.6429	43.99	6.14	6.40	-12.92
45	1.01	131.58	0.03	1.00	-0.5321	0.6561	44.99	6.28	6.54	-13.01
46	1.03	132.24	0.02	1.00	-0.5440	0.6694	45.99	6.42	6.69	-13.12
47	1.05	132.57	0.01	1.00	-0.5562	0.6828	46.99	6.56	6.83	-13.26
48	1.05	133.19	0.01	1.00	-0.5687	0.6962	47.99	6.70	6.97	-13.41
49	1.06	133.41	0.01	1.00	-0.5813	0.7096	48.99	6.84	7.11	-13.57
50	1.06	134.14	0.01	1.00	-0.5941	0.7229	49.99	6.99	7.26	-13.75
51	1.06	134.87	0.01	1.00	-0.6071	0.7361	50.99	7.13	7.40	-13.96
52	1.06	135.92	0.02	1.00	-0.6202	0.7491	51.99	7.27	7.54	-14.21
53	1.07	136.91	0.02	1.00	-0.6337	0.7619	52.99	7.41	7.68	-14.50
54	1.08	137.39	0.01	1.00	-0.6474	0.7746	53.99	7.55	7.82	-14.82
55	1.08	137.40	0.00	1.00	-0.6612	0.7873	54.99	7.70	7.96	-15.16
56	1.08	136.70	0.01	1.00	-0.6750	0.8002	55.99	7.84	8.10	-15.49

Table D5 continued

AOSTRA Underground Test Facility

(Borehole Position Uncertainty according to Wolff and de Wardt, 1981 with modifications by Dubrule and Nelson, 1986)

Well: AT1
Date: Oct. 10/89
Elapsed Time = 9.7

Relative Depth Error: 5 mm
Inclination Error: 0.05 degrees
Azimuth Error: 0.10 degrees
Tool Misalignment Error: 0.01 degrees

DAH (m)	Inclination (degrees)	Azimuth (degrees)	Dogleg (degrees)	Dogleg Factor	North (m)	East (m)	Vertical (m)	ΔN (mm)	ΔE (mm)	Phi (°)
0	0.00	0.00			0.0000	0.0000	0.00	0.00	0.00	0.00
1	1.14	125.92	1.14	1.00	-0.0058	0.0080	1.00	0.13	0.13	-30.19
2	1.18	126.41	0.04	1.00	-0.0177	0.0243	2.00	0.27	0.28	-15.74
3	1.19	127.70	0.03	1.00	-0.0301	0.0408	3.00	0.41	0.43	-13.24
4	1.18	127.29	0.01	1.00	-0.0427	0.0572	4.00	0.55	0.58	-12.38
5	1.20	127.60	0.02	1.00	-0.0554	0.0737	5.00	0.69	0.73	-11.92
6	1.21	128.59	0.02	1.00	-0.0684	0.0902	6.00	0.84	0.88	-11.79
7	1.19	129.65	0.04	1.00	-0.0816	0.1065	7.00	0.98	1.03	-11.87
8	1.18	130.22	0.01	1.00	-0.0948	0.1223	8.00	1.12	1.18	-12.13
9	1.18	130.29	0.00	1.00	-0.1081	0.1380	9.00	1.27	1.33	-12.42
10	1.17	130.49	0.01	1.00	-0.1214	0.1536	10.00	1.41	1.48	-12.67
11	1.15	130.59	0.02	1.00	-0.1345	0.1690	11.00	1.55	1.63	-12.90
12	1.13	129.66	0.03	1.00	-0.1474	0.1842	12.00	1.69	1.77	-13.04
13	1.11	128.47	0.03	1.00	-0.1597	0.1994	13.00	1.83	1.92	-13.02
14	1.08	127.21	0.05	1.00	-0.1714	0.2145	14.00	1.97	2.07	-12.82
15	1.03	126.13	0.05	1.00	-0.1824	0.2293	15.00	2.11	2.21	-12.53
16	1.01	126.83	0.02	1.00	-0.1930	0.2436	16.00	2.25	2.36	-12.27
17	0.99	127.22	0.02	1.00	-0.2036	0.2576	17.00	2.38	2.50	-12.09
18	1.02	125.88	0.03	1.00	-0.2140	0.2717	18.00	2.52	2.64	-11.93
19	1.08	125.96	0.06	1.00	-0.2247	0.2865	19.00	2.66	2.79	-11.75
20	1.01	134.70	0.18	1.00	-0.2364	0.3004	20.00	2.80	2.93	-11.82
21	1.13	131.39	0.14	1.00	-0.2491	0.3140	21.00	2.94	3.08	-12.23
22	1.18	133.42	0.07	1.00	-0.2628	0.3289	22.00	3.08	3.22	-12.56
23	1.16	133.02	0.02	1.00	-0.2768	0.3438	23.00	3.23	3.37	-12.91
24	1.21	137.40	0.10	1.00	-0.2914	0.3583	24.00	3.37	3.52	-13.45
25	1.20	134.69	0.06	1.00	-0.3066	0.3729	25.00	3.52	3.66	-14.07
26	1.14	134.85	0.06	1.00	-0.3210	0.3875	26.00	3.66	3.81	-14.51
27	1.21	133.60	0.07	1.00	-0.3353	0.4022	26.99	3.81	3.95	-14.95
28	1.17	131.65	0.05	1.00	-0.3494	0.4175	27.99	3.95	4.10	-15.19
29	1.20	129.24	0.05	1.00	-0.3628	0.4332	28.99	4.10	4.25	-15.23
30	1.20	125.53	0.08	1.00	-0.3755	0.4498	29.99	4.24	4.40	-15.00
31	1.18	125.37	0.02	1.00	-0.3875	0.4667	30.99	4.38	4.55	-14.61
32	1.18	124.32	0.02	1.00	-0.3993	0.4836	31.99	4.52	4.70	-14.23
33	1.02	125.59	0.16	1.00	-0.4102	0.4993	32.99	4.66	4.85	-13.85
34	1.02	127.37	0.03	1.00	-0.4208	0.5136	33.99	4.80	5.00	-13.67
35	0.98	128.44	0.04	1.00	-0.4315	0.5274	34.99	4.93	5.14	-13.57
36	0.97	129.78	0.03	1.00	-0.4422	0.5406	35.99	5.07	5.28	-13.55
37	0.94	131.96	0.04	1.00	-0.4531	0.5532	36.99	5.21	5.42	-13.61
38	0.93	133.47	0.03	1.00	-0.4642	0.5651	37.99	5.34	5.56	-13.75
39	0.92	132.95	0.01	1.00	-0.4752	0.5769	38.99	5.48	5.70	-13.92
40	0.94	132.10	0.03	1.00	-0.4862	0.5888	39.99	5.62	5.83	-14.07
41	0.94	131.88	0.01	1.00	-0.4972	0.6010	40.99	5.75	5.97	-14.18
42	0.96	130.19	0.03	1.00	-0.5081	0.6136	41.99	5.89	6.11	-14.25
43	0.98	131.03	0.03	1.00	-0.5191	0.6264	42.99	6.03	6.25	-14.30
44	1.01	131.15	0.02	1.00	-0.5305	0.6395	43.99	6.17	6.40	-14.37
45	1.04	132.58	0.04	1.00	-0.5424	0.6528	44.99	6.30	6.54	-14.47
46	1.05	132.90	0.02	1.00	-0.5548	0.6662	45.99	6.44	6.68	-14.62
47	1.06	133.51	0.02	1.00	-0.5674	0.6796	46.99	6.59	6.82	-14.79
48	1.08	134.02	0.01	1.00	-0.5803	0.6931	47.99	6.73	6.97	-14.99
49	1.07	134.09	0.00	1.00	-0.5934	0.7066	48.99	6.87	7.11	-15.19
50	1.07	134.67	0.01	1.00	-0.6065	0.7200	49.99	7.01	7.25	-15.41
51	1.08	135.20	0.01	1.00	-0.6198	0.7333	50.99	7.15	7.39	-15.66
52	1.08	136.92	0.03	1.00	-0.6334	0.7464	51.99	7.30	7.54	-15.96
53	1.09	137.34	0.01	1.00	-0.6473	0.7593	52.99	7.44	7.68	-16.32
54	1.09	137.92	0.01	1.00	-0.6613	0.7721	53.99	7.58	7.82	-16.71
55	1.09	137.95	0.00	1.00	-0.6754	0.7849	54.99	7.73	7.96	-17.13
56	1.10	137.33	0.01	1.00	-0.6895	0.7977	55.99	7.87	8.10	-17.53

Table D5 continued

AOSTRA Underground Test Facility

(Borehole Position Uncertainty according to Wolff and de Wardt, 1981 with modifications by Dubrule and Nelson, 1986)

Well: AT1
Date: April 20/90
Elapsed Time = 12.4

Relative Depth Error:	5	mm
Inclination Error:	0.05	degrees
Azimuth Error:	0.10	degrees
Tool Misalignment Error:	0.01	degrees

DAH (m)	Inclination (degrees)	Azimuth (degrees)	Dogleg (degrees)	Dogleg Factor	North (m)	East (m)	Vertical (m)	ΔN (mm)	ΔE (mm)	Phi (°)
0	0.00	0.00			0.0000	0.0000	0.00	0.00	0.00	0.00
1	1.14	126.42	1.14	1.00	-0.0059	0.0080	1.00	0.13	0.13	-30.93
2	1.17	126.74	0.03	1.00	-0.0179	0.0242	2.00	0.27	0.28	-16.41
3	1.18	128.07	0.03	1.00	-0.0303	0.0404	3.00	0.41	0.43	-13.83
4	1.18	128.15	0.00	1.00	-0.0430	0.0566	4.00	0.55	0.58	-13.05
5	1.18	128.87	0.02	1.00	-0.0559	0.0727	5.00	0.69	0.73	-12.77
6	1.19	129.78	0.02	1.00	-0.0690	0.0887	6.00	0.84	0.88	-12.84
7	1.18	130.77	0.02	1.00	-0.0824	0.1045	7.00	0.98	1.03	-13.12
8	1.16	130.83	0.02	1.00	-0.0957	0.1200	8.00	1.12	1.17	-13.47
9	1.17	130.68	0.01	1.00	-0.1090	0.1354	9.00	1.27	1.32	-13.78
10	1.15	130.68	0.02	1.00	-0.1222	0.1508	10.00	1.41	1.47	-14.00
11	1.15	130.11	0.01	1.00	-0.1352	0.1661	11.00	1.55	1.62	-14.14
12	1.14	129.21	0.02	1.00	-0.1480	0.1815	12.00	1.69	1.77	-14.13
13	1.13	127.54	0.03	1.00	-0.1603	0.1970	13.00	1.83	1.91	-13.91
14	1.11	126.69	0.03	1.00	-0.1721	0.2126	14.00	1.97	2.06	-13.54
15	1.08	125.99	0.04	1.00	-0.1834	0.2279	15.00	2.11	2.21	-13.12
16	1.06	126.18	0.02	1.00	-0.1944	0.2430	16.00	2.25	2.35	-12.76
17	1.05	126.28	0.01	1.00	-0.2052	0.2579	17.00	2.39	2.50	-12.47
18	1.06	126.24	0.01	1.00	-0.2161	0.2727	18.00	2.53	2.65	-12.23
19	1.09	127.08	0.04	1.00	-0.2273	0.2877	19.00	2.66	2.79	-12.07
20	1.13	136.35	0.18	1.00	-0.2402	0.3021	20.00	2.81	2.94	-12.33
21	1.17	131.98	0.10	1.00	-0.2541	0.3165	21.00	2.95	3.08	-12.83
22	1.17	132.79	0.02	1.00	-0.2680	0.3317	22.00	3.09	3.23	-13.13
23	1.18	133.69	0.02	1.00	-0.2821	0.3467	23.00	3.24	3.38	-13.50
24	1.18	138.72	0.10	1.00	-0.2969	0.3609	24.00	3.38	3.52	-14.10
25	1.20	133.31	0.11	1.00	-0.3118	0.3753	25.00	3.53	3.67	-14.75
26	1.16	135.59	0.06	1.00	-0.3262	0.3899	25.99	3.68	3.81	-15.16
27	1.17	135.01	0.02	1.00	-0.3406	0.4043	26.99	3.82	3.96	-15.69
28	1.19	132.43	0.05	1.00	-0.3549	0.4191	27.99	3.97	4.11	-16.05
29	1.20	130.11	0.05	1.00	-0.3686	0.4348	28.99	4.11	4.26	-16.15
30	1.21	126.92	0.07	1.00	-0.3817	0.4512	29.99	4.26	4.41	-15.97
31	1.22	127.13	0.01	1.00	-0.3944	0.4681	30.99	4.40	4.56	-15.65
32	1.18	124.84	0.06	1.00	-0.4067	0.4850	31.99	4.54	4.71	-15.27
33	1.11	124.11	0.07	1.00	-0.4180	0.5015	32.99	4.68	4.86	-14.82
34	1.02	127.39	0.11	1.00	-0.4289	0.5166	33.99	4.81	5.01	-14.50
35	0.98	129.73	0.06	1.00	-0.4398	0.5303	34.99	4.95	5.15	-14.40
36	0.95	131.76	0.05	1.00	-0.4508	0.5430	35.99	5.09	5.29	-14.44
37	0.92	133.51	0.04	1.00	-0.4618	0.5550	36.99	5.23	5.43	-14.57
38	0.91	135.79	0.04	1.00	-0.4730	0.5664	37.99	5.36	5.56	-14.81
39	0.92	135.91	0.01	1.00	-0.4844	0.5775	38.99	5.50	5.70	-15.13
40	0.92	134.21	0.03	1.00	-0.4958	0.5888	39.99	5.64	5.84	-15.40
41	0.92	132.47	0.03	1.00	-0.5068	0.6005	40.99	5.77	5.97	-15.57
42	0.94	131.03	0.04	1.00	-0.5176	0.6126	41.99	5.91	6.11	-15.66
43	0.97	131.48	0.03	1.00	-0.5286	0.6252	42.99	6.05	6.25	-15.72
44	1.02	131.72	0.04	1.00	-0.5402	0.6382	43.99	6.19	6.39	-15.80
45	1.04	132.62	0.03	1.00	-0.5522	0.6515	44.99	6.33	6.54	-15.91
46	1.05	133.04	0.01	1.00	-0.5646	0.6648	45.99	6.47	6.68	-16.06
47	1.06	133.60	0.01	1.00	-0.5772	0.6782	46.99	6.61	6.82	-16.23
48	1.06	134.07	0.01	1.00	-0.5900	0.6915	47.99	6.75	6.96	-16.42
49	1.07	134.20	0.00	1.00	-0.6030	0.7049	48.99	6.89	7.11	-16.64
50	1.07	134.90	0.01	1.00	-0.6161	0.7182	49.99	7.03	7.25	-16.87
51	1.07	135.40	0.01	1.00	-0.6293	0.7314	50.99	7.17	7.39	-17.14
52	1.08	136.63	0.02	1.00	-0.6428	0.7444	51.99	7.32	7.53	-17.45
53	1.09	137.94	0.03	1.00	-0.6567	0.7572	52.99	7.46	7.67	-17.85
54	1.09	137.97	0.00	1.00	-0.6708	0.7699	53.99	7.61	7.82	-18.30
55	1.08	137.76	0.01	1.00	-0.6849	0.7826	54.99	7.75	7.96	-18.73
56	1.09	137.57	0.01	1.00	-0.6989	0.7954	55.99	7.89	8.10	-19.17

Table D5 continued

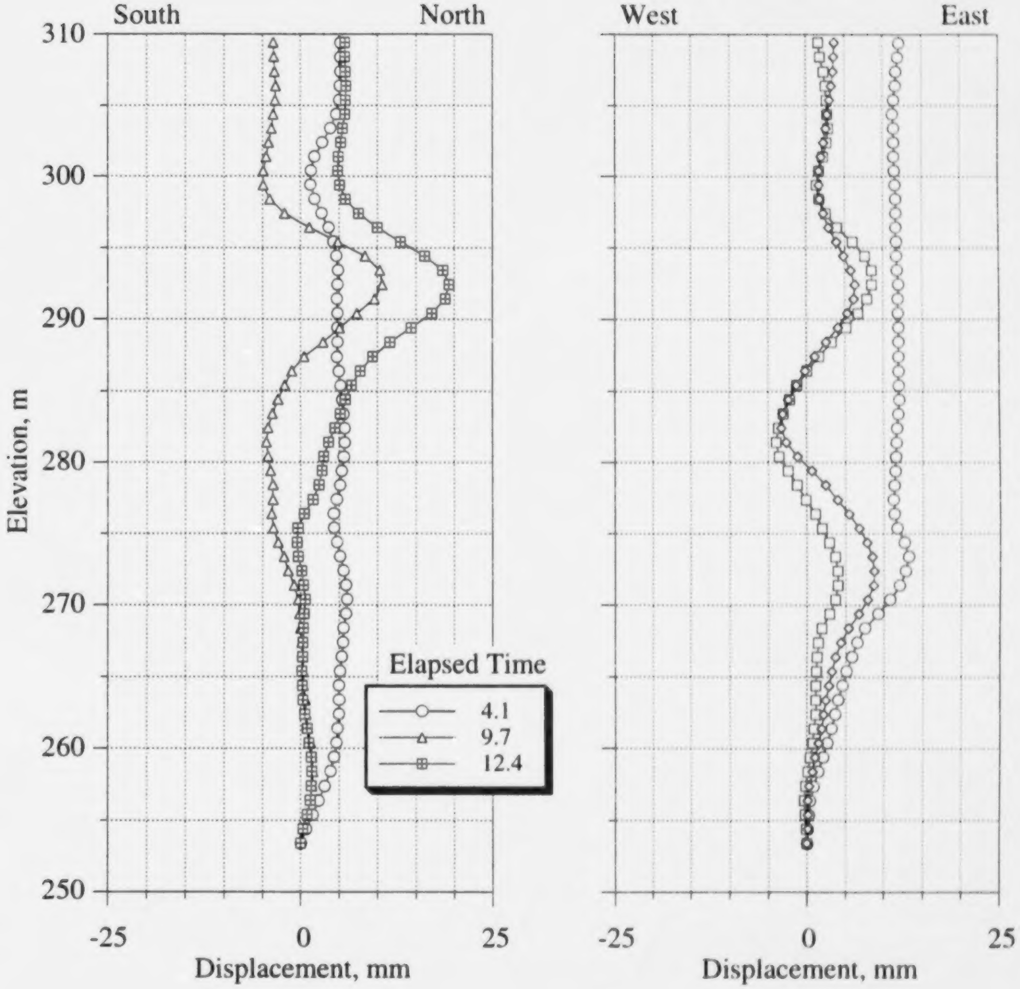

Figure D6 Horizontal Displacement Profile at Well AT7

AOSTRA Underground Test Facility

(Borehole Position Uncertainty according to Wolff and de Wardt, 1981 with modifications by Dubrule and Nelson, 1986)

Well: AT7
Date: Sept. 10/88
Elapsed Time = 0.0

Relative Depth Error:	5	mm
Inclination Error:	0.05	degrees
Azimuth Error:	0.10	degrees
Tool Misalignment Error:	0.01	degrees

DAH (m)	Inclination (degrees)	Azimuth (degrees)	Dogleg (degrees)	Dogleg Factor	North (m)	East (m)	Vertical (m)	ΔN (mm)	ΔE (mm)	Phi (°)
0	0.00	0.00			0.0000	0.0000	0.00	0.00	0.00	0.00
1	-0.51	249.99	0.51	1.00	-0.0015	-0.0042	1.00	0.12	0.13	12.92
2	0.51	247.57	0.02	1.00	-0.0047	-0.0125	2.00	0.25	0.26	4.96
3	0.51	245.84	0.02	1.00	-0.0083	-0.0207	3.00	0.38	0.39	4.16
4	0.49	244.92	0.02	1.00	-0.0119	-0.0286	4.00	0.50	0.52	3.89
5	0.48	245.11	0.01	1.00	-0.0155	-0.0363	5.00	0.63	0.64	3.76
6	0.48	246.45	0.01	1.00	-0.0189	-0.0439	6.00	0.75	0.77	3.66
7	0.45	246.50	0.03	1.00	-0.0221	-0.0513	7.00	0.88	0.90	3.54
8	0.44	246.84	0.01	1.00	-0.0252	-0.0585	8.00	1.00	1.03	3.46
9	0.43	245.95	0.01	1.00	-0.0283	-0.0654	9.00	1.13	1.16	3.42
10	0.41	245.35	0.02	1.00	-0.0313	-0.0721	10.00	1.25	1.29	3.39
11	0.40	243.03	0.02	1.00	-0.0344	-0.0785	11.00	1.38	1.42	3.41
12	0.38	243.25	0.02	1.00	-0.0374	-0.0845	12.00	1.50	1.54	3.43
13	0.35	244.68	0.03	1.00	-0.0402	-0.0903	13.00	1.63	1.67	3.42
14	0.34	245.94	0.01	1.00	-0.0428	-0.0957	14.00	1.75	1.80	3.41
15	0.35	248.35	0.02	1.00	-0.0451	-0.1013	15.00	1.87	1.92	3.38
16	0.36	248.50	0.01	1.00	-0.0474	-0.1070	16.00	2.00	2.05	3.34
17	0.37	249.51	0.01	1.00	-0.0496	-0.1130	17.00	2.12	2.18	3.30
18	0.38	248.79	0.01	1.00	-0.0520	-0.1191	18.00	2.25	2.30	3.27
19	0.40	249.44	0.02	1.00	-0.0544	-0.1255	19.00	2.37	2.43	3.24
20	0.40	248.50	0.01	1.00	-0.0569	-0.1320	20.00	2.50	2.56	3.20
21	0.41	248.23	0.01	1.00	-0.0595	-0.1386	21.00	2.62	2.69	3.18
22	0.42	248.47	0.01	1.00	-0.0622	-0.1453	22.00	2.75	2.82	3.16
23	0.43	247.30	0.01	1.00	-0.0650	-0.1522	23.00	2.87	2.94	3.15
24	0.42	246.21	0.01	1.00	-0.0679	-0.1590	24.00	3.00	3.07	3.14
25	0.43	245.66	0.01	1.00	-0.0709	-0.1657	25.00	3.12	3.20	3.15
26	0.42	245.68	0.01	1.00	-0.0740	-0.1725	26.00	3.25	3.33	3.15
27	0.42	243.32	0.02	1.00	-0.0771	-0.1791	27.00	3.37	3.46	3.17
28	0.41	241.92	0.01	1.00	-0.0805	-0.1855	28.00	3.50	3.58	3.20
29	0.41	241.98	0.00	1.00	-0.0838	-0.1919	29.00	3.62	3.71	3.23
30	0.41	241.97	0.00	1.00	-0.0872	-0.1982	30.00	3.75	3.84	3.25
31	0.41	240.83	0.01	1.00	-0.0906	-0.2045	31.00	3.87	3.97	3.29
32	0.42	239.94	0.01	1.00	-0.0942	-0.2108	32.00	4.00	4.10	3.33
33	0.44	240.39	0.02	1.00	-0.0979	-0.2173	33.00	4.12	4.22	3.37
34	0.45	239.03	0.01	1.00	-0.1019	-0.2240	34.00	4.25	4.35	3.42
35	0.47	237.61	0.02	1.00	-0.1061	-0.2308	35.00	4.37	4.48	3.47
36	0.48	237.13	0.01	1.00	-0.1105	-0.2378	36.00	4.50	4.61	3.53
37	0.50	236.42	0.02	1.00	-0.1152	-0.2449	37.00	4.62	4.74	3.60
38	0.50	235.28	0.01	1.00	-0.1201	-0.2522	38.00	4.75	4.87	3.67
39	0.49	234.64	0.01	1.00	-0.1251	-0.2592	39.00	4.88	4.99	3.74
40	0.49	234.59	0.00	1.00	-0.1300	-0.2662	40.00	5.00	5.12	3.81
41	0.48	235.13	0.01	1.00	-0.1349	-0.2731	41.00	5.13	5.25	3.87
42	0.47	235.22	0.01	1.00	-0.1396	-0.2799	42.00	5.25	5.38	3.92
43	0.47	236.24	0.01	1.00	-0.1443	-0.2867	43.00	5.38	5.51	3.98
44	0.49	235.81	0.02	1.00	-0.1489	-0.2937	44.00	5.51	5.64	4.03
45	0.52	234.09	0.03	1.00	-0.1540	-0.3009	45.00	5.63	5.77	4.10
46	0.57	232.22	0.05	1.00	-0.1597	-0.3085	46.00	5.76	5.90	4.19
47	0.62	231.47	0.05	1.00	-0.1661	-0.3166	47.00	5.89	6.03	4.29
48	0.66	230.96	0.04	1.00	-0.1731	-0.3254	48.00	6.02	6.16	4.41
49	0.68	229.95	0.02	1.00	-0.1806	-0.3344	49.00	6.14	6.29	4.52
50	0.69	229.98	0.01	1.00	-0.1883	-0.3435	50.00	6.27	6.42	4.64
51	0.67	231.53	0.03	1.00	-0.1958	-0.3527	51.00	6.40	6.55	4.74
52	0.64	234.42	0.04	1.00	-0.2027	-0.3618	52.00	6.53	6.68	4.81
53	0.61	237.57	0.05	1.00	-0.2088	-0.3709	53.00	6.66	6.82	4.84
54	0.61	242.80	0.06	1.00	-0.2141	-0.3801	54.00	6.79	6.95	4.84
55	0.59	248.73	0.07	1.00	-0.2184	-0.3896	55.00	6.91	7.08	4.78
56	0.59	251.88	0.03	1.00	-0.2218	-0.3993	56.00	7.04	7.21	4.70

Table D6 Well AT7 Borehole Uncertainty Analysis

AOSTRA Underground Test Facility

(Borehole Position Uncertainty according to Wolff and de Wardt, 1981 with modifications by Dubrule and Nelson, 1986)

Well: AT7
Date: Sept. 10/88
Elapsed Time = 4.1

Relative Depth Error:	5	mm
Inclination Error:	0.05	degrees
Azimuth Error:	0.10	degrees
Tool Misalignment Error:	0.01	degrees

DAH (m)	Inclination (degrees)	Azimuth (degrees)	Dogleg (degrees)	Dogleg Factor	North (m)	East (m)	Vertical (m)	ΔN (mm)	ΔE (mm)	Phi (°)
0	0.00	0.00			0.0000	0.0000	0.00	0.00	0.00	0.00
1	0.52	250.55	0.52	1.00	-0.0015	-0.0043	1.00	0.12	0.13	12.48
2	0.52	248.06	0.02	1.00	-0.0047	-0.0128	2.00	0.25	0.26	4.78
3	0.52	245.69	0.02	1.00	-0.0083	-0.0211	3.00	0.38	0.39	4.06
4	0.51	244.87	0.01	1.00	-0.0120	-0.0293	4.00	0.50	0.52	3.84
5	0.49	241.28	0.04	1.00	-0.0160	-0.0371	5.00	0.63	0.65	3.85
6	0.50	240.03	0.01	1.00	-0.0202	-0.0446	6.00	0.75	0.78	4.00
7	0.48	239.74	0.02	1.00	-0.0245	-0.0520	7.00	0.88	0.90	4.09
8	0.46	241.25	0.02	1.00	-0.0286	-0.0591	8.00	1.00	1.03	4.13
9	0.43	243.64	0.04	1.00	-0.0321	-0.0660	9.00	1.13	1.16	4.09
10	0.40	246.50	0.04	1.00	-0.0352	-0.0726	10.00	1.25	1.29	3.98
11	0.38	249.86	0.03	1.00	-0.0377	-0.0789	11.00	1.38	1.42	3.84
12	0.36	251.80	0.02	1.00	-0.0399	-0.0850	12.00	1.50	1.54	3.69
13	0.33	251.24	0.03	1.00	-0.0418	-0.0907	13.00	1.63	1.67	3.55
14	0.33	250.40	0.00	1.00	-0.0437	-0.0961	14.00	1.75	1.80	3.47
15	0.34	249.85	0.01	1.00	-0.0456	-0.1016	15.00	1.87	1.92	3.41
16	0.35	249.74	0.01	1.00	-0.0477	-0.1073	16.00	2.00	2.05	3.36
17	0.37	248.53	0.02	1.00	-0.0500	-0.1131	17.00	2.12	2.18	3.33
18	0.39	249.32	0.02	1.00	-0.0524	-0.1193	18.00	2.25	2.30	3.29
19	0.39	248.66	0.00	1.00	-0.0548	-0.1257	19.00	2.37	2.43	3.26
20	0.40	248.93	0.01	1.00	-0.0573	-0.1321	20.00	2.50	2.56	3.23
21	0.41	247.70	0.01	1.00	-0.0599	-0.1387	21.00	2.62	2.69	3.21
22	0.42	249.32	0.02	1.00	-0.0626	-0.1454	22.00	2.75	2.82	3.18
23	0.42	248.76	0.00	1.00	-0.0652	-0.1523	23.00	2.87	2.94	3.15
24	0.42	247.67	0.01	1.00	-0.0679	-0.1591	24.00	3.00	3.07	3.14
25	0.42	247.35	0.00	1.00	-0.0707	-0.1658	25.00	3.12	3.20	3.13
26	0.43	247.14	0.01	1.00	-0.0736	-0.1727	26.00	3.25	3.33	3.12
27	0.42	244.55	0.02	1.00	-0.0766	-0.1795	27.00	3.37	3.46	3.13
28	0.42	241.78	0.02	1.00	-0.0799	-0.1860	28.00	3.49	3.59	3.16
29	0.42	241.17	0.00	1.00	-0.0834	-0.1924	29.00	3.62	3.71	3.19
30	0.42	240.63	0.00	1.00	-0.0870	-0.1988	30.00	3.75	3.84	3.23
31	0.43	238.49	0.02	1.00	-0.0907	-0.2052	31.00	3.87	3.97	3.28
32	0.43	237.27	0.01	1.00	-0.0947	-0.2116	32.00	4.00	4.10	3.34
33	0.44	238.35	0.01	1.00	-0.0988	-0.2180	33.00	4.12	4.22	3.40
34	0.41	237.93	0.03	1.00	-0.1027	-0.2243	34.00	4.25	4.35	3.44
35	0.40	235.84	0.02	1.00	-0.1065	-0.2302	35.00	4.37	4.48	3.49
36	0.47	239.89	0.08	1.00	-0.1106	-0.2367	36.00	4.50	4.61	3.55
37	0.52	240.88	0.05	1.00	-0.1148	-0.2442	37.00	4.62	4.74	3.60
38	0.54	240.06	0.02	1.00	-0.1194	-0.2522	38.00	4.75	4.87	3.64
39	0.56	239.34	0.02	1.00	-0.1242	-0.2605	39.00	4.88	5.00	3.68
40	0.59	239.29	0.03	1.00	-0.1293	-0.2691	40.00	5.00	5.13	3.73
41	0.55	238.90	0.04	1.00	-0.1345	-0.2777	41.00	5.13	5.26	3.76
42	0.51	237.18	0.04	1.00	-0.1393	-0.2855	42.00	5.26	5.39	3.79
43	0.51	237.60	0.00	1.00	-0.1441	-0.2930	43.00	5.38	5.52	3.84
44	0.52	237.01	0.01	1.00	-0.1490	-0.3006	44.00	5.51	5.65	3.89
45	0.55	235.70	0.03	1.00	-0.1542	-0.3084	45.00	5.63	5.78	3.95
46	0.59	233.86	0.04	1.00	-0.1599	-0.3165	46.00	5.76	5.91	4.02
47	0.64	232.22	0.05	1.00	-0.1664	-0.3251	47.00	5.89	6.04	4.12
48	0.69	231.76	0.05	1.00	-0.1735	-0.3342	48.00	6.02	6.17	4.23
49	0.71	231.42	0.02	1.00	-0.1811	-0.3438	49.00	6.15	6.30	4.33
50	0.73	230.02	0.03	1.00	-0.1891	-0.3535	50.00	6.28	6.44	4.45
51	0.72	231.11	0.02	1.00	-0.1971	-0.3633	51.00	6.41	6.57	4.56
52	0.69	232.77	0.04	1.00	-0.2047	-0.3730	52.00	6.53	6.70	4.64
53	0.66	235.22	0.04	1.00	-0.2116	-0.3825	53.00	6.66	6.83	4.70
54	0.63	238.98	0.05	1.00	-0.2177	-0.3919	54.00	6.79	6.97	4.72
55	0.62	245.23	0.07	1.00	-0.2228	-0.4016	55.00	6.92	7.10	4.70
56	0.60	249.33	0.05	1.00	-0.2270	-0.4114	56.00	7.04	7.23	4.64

Table D6 continued

AOSTRA Underground Test Facility

(Borehole Position Uncertainty according to Wolff and de Wardt, 1981 with modifications by Dubrule and Nelson, 1986)

Well: AT7
Date: Dec. 21/88
Elapsed Time = 5.5

Relative Depth Error: 5 mm
Inclination Error: 0.05 degrees
Azimuth Error: 0.10 degrees
Tool Misalignment Error: 0.01 degrees

DAH (m)	Inclination (degrees)	Azimuth (degrees)	Dogleg (degrees)	Dogleg Factor	North (m)	East (m)	Vertical (m)	ΔN (mm)	ΔE (mm)	Phi (°)
0	0.44	238.35			0.0000	0.0000	0.00	0.00	0.00	0.00
1	0.44	238.35	0.00	1.00	-0.0040	-0.0065	1.00	0.13	0.13	5.66
2	0.44	238.35	0.00	1.00	-0.0081	-0.0131	2.00	0.25	0.26	5.66
3	0.44	238.35	0.00	1.00	-0.0121	-0.0196	3.00	0.38	0.38	5.66
4	0.44	238.35	0.00	1.00	-0.0161	-0.0261	4.00	0.50	0.51	5.66
5	0.44	238.35	0.00	1.00	-0.0201	-0.0327	5.00	0.63	0.64	5.66
6	0.44	238.35	0.00	1.00	-0.0242	-0.0392	6.00	0.75	0.77	5.66
7	0.44	238.35	0.00	1.00	-0.0282	-0.0458	7.00	0.88	0.90	5.66
8	0.44	238.35	0.00	1.00	-0.0322	-0.0523	8.00	1.00	1.02	5.66
9	0.44	238.35	0.00	1.00	-0.0363	-0.0588	9.00	1.13	1.15	5.66
10	0.44	238.35	0.00	1.00	-0.0403	-0.0654	10.00	1.26	1.28	5.66
11	0.44	238.35	0.00	1.00	-0.0443	-0.0719	11.00	1.38	1.41	5.66
12	0.44	238.35	0.00	1.00	-0.0484	-0.0784	12.00	1.51	1.54	5.66
13	0.44	238.35	0.00	1.00	-0.0524	-0.0850	13.00	1.63	1.66	5.66
14	0.44	238.35	0.00	1.00	-0.0564	-0.0915	14.00	1.76	1.79	5.66
15	0.44	238.35	0.00	1.00	-0.0604	-0.0981	15.00	1.88	1.92	5.66
16	0.44	238.35	0.00	1.00	-0.0645	-0.1046	16.00	2.01	2.05	5.66
17	0.44	238.35	0.00	1.00	-0.0685	-0.1111	17.00	2.14	2.18	5.66
18	0.44	238.35	0.00	1.00	-0.0725	-0.1177	18.00	2.26	2.30	5.66
19	0.44	238.35	0.00	1.00	-0.0766	-0.1242	19.00	2.39	2.43	5.66
20	0.44	238.35	0.00	1.00	-0.0806	-0.1307	20.00	2.51	2.56	5.66
21	0.44	238.35	0.00	1.00	-0.0846	-0.1373	21.00	2.64	2.69	5.66
22	0.44	238.35	0.00	1.00	-0.0887	-0.1438	22.00	2.76	2.82	5.66
23	0.44	238.35	0.00	1.00	-0.0927	-0.1504	23.00	2.89	2.94	5.66
24	0.44	238.35	0.00	1.00	-0.0967	-0.1569	24.00	3.01	3.07	5.66
25	0.44	238.35	0.00	1.00	-0.1007	-0.1634	25.00	3.14	3.20	5.66
26	0.44	238.35	0.00	1.00	-0.1048	-0.1700	26.00	3.27	3.33	5.66
27	0.44	238.35	0.00	1.00	-0.1088	-0.1765	27.00	3.39	3.46	5.66
28	0.44	238.35	0.00	1.00	-0.1128	-0.1830	28.00	3.52	3.58	5.66
29	0.44	238.35	0.00	1.00	-0.1169	-0.1896	29.00	3.64	3.71	5.66
30	0.44	238.35	0.00	1.00	-0.1209	-0.1961	30.00	3.77	3.84	5.66
31	0.44	238.35	0.00	1.00	-0.1249	-0.2027	31.00	3.89	3.97	5.66
32	0.44	238.35	0.00	1.00	-0.1289	-0.2092	32.00	4.02	4.10	5.66
33	0.44	238.35	0.00	1.00	-0.1330	-0.2157	33.00	4.15	4.22	5.66
34	0.41	239.78	0.03	1.00	-0.1368	-0.2221	34.00	4.27	4.35	5.64
35	0.42	239.65	0.01	1.00	-0.1404	-0.2283	35.00	4.40	4.48	5.62
36	0.46	238.72	0.04	1.00	-0.1444	-0.2349	36.00	4.52	4.61	5.63
37	0.51	239.01	0.05	1.00	-0.1488	-0.2422	37.00	4.65	4.74	5.64
38	0.54	237.45	0.03	1.00	-0.1536	-0.2500	38.00	4.77	4.87	5.66
39	0.58	235.92	0.04	1.00	-0.1590	-0.2581	39.00	4.90	5.00	5.70
40	0.61	235.72	0.03	1.00	-0.1648	-0.2667	40.00	5.03	5.13	5.75
41	0.58	235.7	0.03	1.00	-0.1706	-0.2753	41.00	5.16	5.26	5.78
42	0.56	234.73	0.02	1.00	-0.1763	-0.2835	42.00	5.28	5.39	5.81
43	0.55	234.53	0.01	1.00	-0.1819	-0.2914	43.00	5.41	5.52	5.86
44	0.57	233.64	0.02	1.00	-0.1877	-0.2993	44.00	5.54	5.65	5.92
45	0.59	232.12	0.03	1.00	-0.1938	-0.3074	45.00	5.67	5.78	6.00
46	0.63	229.04	0.05	1.00	-0.2005	-0.3156	46.00	5.79	5.91	6.12
47	0.68	228.05	0.05	1.00	-0.2081	-0.3241	47.00	5.92	6.04	6.28
48	0.72	227.46	0.04	1.00	-0.2163	-0.3332	48.00	6.05	6.17	6.45
49	0.74	226.52	0.02	1.00	-0.2250	-0.3425	49.00	6.18	6.30	6.64
50	0.76	226.08	0.02	1.00	-0.2341	-0.3520	50.00	6.31	6.44	6.85
51	0.74	227.39	0.03	1.00	-0.2430	-0.3615	51.00	6.45	6.57	7.03
52	0.71	229.73	0.04	1.00	-0.2514	-0.3710	52.00	6.58	6.70	7.16
53	0.68	232.69	0.05	1.00	-0.2590	-0.3804	53.00	6.70	6.83	7.24
54	0.68	236.65	0.05	1.00	-0.2659	-0.3901	54.00	6.83	6.97	7.25
55	0.67	242.69	0.07	1.00	-0.2718	-0.4002	55.00	6.96	7.10	7.18
56	0.67	246.16	0.04	1.00	-0.2769	-0.4108	56.00	7.09	7.23	7.03

Table D6 continued

AOSTRA Underground Test Facility

(Borehole Position Uncertainty according to Wolff and de Wardt, 1981 with modifications by Dubrule and Nelson, 1986)

Well: AT7
Date: June 5/89
Elapsed Time = 7.9

Relative Depth Error: 5 mm
Inclination Error: 0.05 degrees
Azimuth Error: 0.10 degrees
Tool Misalignment Error: 0.01 degrees

DAH (m)	Inclination (degrees)	Azimuth (degrees)	Dogleg (degrees)	Dogleg Factor	North (m)	East (m)	Vertical (m)	ΔN (mm)	ΔE (mm)	Phi (°)
0	0.00	0.00			0.0000	0.0000	0.00	0.00	0.00	0.00
1	0.49	266.30	0.49	1.00	-0.0003	-0.0043	1.00	0.12	0.13	2.14
2	0.50	263.73	0.02	1.00	-0.0010	-0.0129	2.00	0.25	0.26	0.98
3	0.49	262.01	0.02	1.00	-0.0021	-0.0214	3.00	0.37	0.39	0.92
4	0.48	260.82	0.01	1.00	-0.0034	-0.0298	4.00	0.50	0.52	0.93
5	0.47	259.81	0.01	1.00	-0.0048	-0.0380	5.00	0.62	0.65	0.96
6	0.48	260.22	0.01	1.00	-0.0062	-0.0461	6.00	0.75	0.78	0.98
7	0.47	260.79	0.01	1.00	-0.0076	-0.0543	7.00	0.87	0.91	0.97
8	0.46	261.46	0.01	1.00	-0.0088	-0.0623	8.00	1.00	1.04	0.96
9	0.43	263.28	0.03	1.00	-0.0098	-0.0700	9.00	1.12	1.17	0.92
10	0.38	266.89	0.06	1.00	-0.0105	-0.0771	10.00	1.24	1.29	0.85
11	0.36	268.94	0.02	1.00	-0.0107	-0.0835	11.00	1.37	1.42	0.79
12	0.28	284.47	0.12	1.00	-0.0102	-0.0890	12.00	1.49	1.55	0.65
13	0.29	286.02	0.01	1.00	-0.0088	-0.0938	13.00	1.61	1.67	0.52
14	0.29	291.55	0.03	1.00	-0.0072	-0.0986	14.00	1.74	1.80	0.38
15	0.32	286.87	0.04	1.00	-0.0055	-0.1036	15.00	1.86	1.92	0.27
16	0.36	276.16	0.07	1.00	-0.0043	-0.1094	16.00	1.98	2.05	0.22
17	0.42	263.81	0.10	1.00	-0.0044	-0.1162	17.00	2.11	2.18	0.25
18	0.49	257.38	0.09	1.00	-0.0057	-0.1240	18.00	2.23	2.31	0.32
19	0.55	250.48	0.09	1.00	-0.0083	-0.1327	19.00	2.36	2.44	0.45
20	0.58	247.48	0.04	1.00	-0.0118	-0.1419	20.00	2.48	2.57	0.58
21	0.57	248.78	0.02	1.00	-0.0155	-0.1512	21.00	2.61	2.70	0.69
22	0.55	251.41	0.03	1.00	-0.0189	-0.1604	22.00	2.73	2.83	0.77
23	0.52	252.72	0.03	1.00	-0.0217	-0.1693	23.00	2.86	2.97	0.82
24	0.49	253.96	0.03	1.00	-0.0243	-0.1777	24.00	2.98	3.10	0.86
25	0.48	255.16	0.01	1.00	-0.0265	-0.1859	25.00	3.11	3.23	0.90
26	0.48	253.90	0.01	1.00	-0.0288	-0.1940	26.00	3.23	3.36	0.93
27	0.45	253.00	0.03	1.00	-0.0311	-0.2018	27.00	3.36	3.49	0.96
28	0.40	251.77	0.05	1.00	-0.0333	-0.2088	28.00	3.48	3.62	0.99
29	0.37	249.06	0.04	1.00	-0.0356	-0.2152	29.00	3.60	3.74	1.03
30	0.35	249.35	0.02	1.00	-0.0378	-0.2210	30.00	3.73	3.87	1.06
31	0.36	248.23	0.01	1.00	-0.0400	-0.2268	31.00	3.85	4.00	1.10
32	0.43	241.76	0.08	1.00	-0.0430	-0.2330	32.00	3.98	4.12	1.17
33	0.45	244.29	0.03	1.00	-0.0465	-0.2399	33.00	4.10	4.25	1.22
34	0.44	246.57	0.02	1.00	-0.0497	-0.2469	34.00	4.23	4.38	1.27
35	0.44	247.65	0.01	1.00	-0.0527	-0.2540	35.00	4.35	4.51	1.30
36	0.46	246.83	0.02	1.00	-0.0557	-0.2613	36.00	4.48	4.64	1.35
37	0.50	248.03	0.04	1.00	-0.0589	-0.2690	37.00	4.60	4.77	1.39
38	0.51	247.95	0.01	1.00	-0.0622	-0.2772	38.00	4.73	4.90	1.42
39	0.54	247.44	0.03	1.00	-0.0657	-0.2856	39.00	4.85	5.03	1.46
40	0.56	247.97	0.02	1.00	-0.0693	-0.2945	40.00	4.98	5.16	1.50
41	0.52	248.63	0.04	1.00	-0.0728	-0.3033	41.00	5.10	5.29	1.53
42	0.49	248.00	0.03	1.00	-0.0761	-0.3115	42.00	5.23	5.42	1.55
43	0.47	248.12	0.02	1.00	-0.0792	-0.3192	43.00	5.35	5.55	1.57
44	0.49	247.40	0.02	1.00	-0.0824	-0.3270	44.00	5.48	5.68	1.60
45	0.51	245.92	0.02	1.00	-0.0858	-0.3350	45.00	5.60	5.81	1.64
46	0.55	242.18	0.05	1.00	-0.0899	-0.3433	46.00	5.73	5.94	1.68
47	0.58	242.16	0.03	1.00	-0.0945	-0.3520	47.00	5.85	6.07	1.73
48	0.61	241.28	0.03	1.00	-0.0994	-0.3612	48.00	5.98	6.20	1.79
49	0.62	240.60	0.01	1.00	-0.1046	-0.3706	49.00	6.11	6.34	1.84
50	0.64	240.27	0.02	1.00	-0.1101	-0.3801	50.00	6.23	6.47	1.89
51	0.62	242.04	0.03	1.00	-0.1154	-0.3897	51.00	6.36	6.60	1.94
52	0.59	245.12	0.04	1.00	-0.1201	-0.3992	52.00	6.48	6.73	1.97
53	0.56	248.38	0.04	1.00	-0.1240	-0.4084	53.00	6.61	6.87	1.98
54	0.57	252.31	0.04	1.00	-0.1274	-0.4177	54.00	6.74	7.00	1.99
55	0.58	258.30	0.06	1.00	-0.1299	-0.4274	55.00	6.86	7.13	1.97
56	0.58	261.89	0.04	1.00	-0.1316	-0.4374	56.00	6.99	7.26	1.94

Table D6 continued

AOSTRA Underground Test Facility

(Borehole Position Uncertainty according to Wolff and de Wardt, 1981 with modifications by Dubrule and Nelson, 1986)

Relative Depth Error: 5 mm
Inclination Error: 0.05 degrees
Azimuth Error: 0.10 degrees
Tool Misalignment Error: 0.01 degrees

Well: AT7
Date: Oct. 10/89
Elapsed Time = 9.7

DAH (m)	Inclination (degrees)	Azimuth (degrees)	Dogleg (degrees)	Dogleg Factor	North (m)	East (m)	Vertical (m)	ΔN (mm)	ΔE (mm)	Phi (°)
0	0.00	0.00			0.0000	0.0000	0.00	0.00	0.00	0.00
1	0.48	249.49	0.48	1.00	-0.0015	-0.0039	1.00	0.12	0.13	13.32
2	0.49	247.53	0.02	1.00	-0.0046	-0.0118	2.00	0.25	0.25	5.11
3	0.50	245.00	0.02	1.00	-0.0080	-0.0197	3.00	0.37	0.38	4.33
4	0.49	244.43	0.01	1.00	-0.0117	-0.0275	4.00	0.50	0.51	4.06
5	0.48	243.09	0.02	1.00	-0.0155	-0.0351	5.00	0.63	0.64	3.98
6	0.48	243.73	0.01	1.00	-0.0192	-0.0426	6.00	0.75	0.77	3.95
7	0.48	245.79	0.02	1.00	-0.0228	-0.0502	7.00	0.88	0.90	3.86
8	0.48	246.50	0.01	1.00	-0.0262	-0.0578	8.00	1.00	1.03	3.76
9	0.46	244.93	0.02	1.00	-0.0296	-0.0653	9.00	1.13	1.16	3.69
10	0.41	247.28	0.05	1.00	-0.0326	-0.0723	10.00	1.25	1.29	3.58
11	0.34	252.12	0.08	1.00	-0.0349	-0.0784	11.00	1.38	1.42	3.42
12	0.27	267.21	0.11	1.00	-0.0360	-0.0836	12.00	1.50	1.54	3.15
13	0.22	283.09	0.08	1.00	-0.0356	-0.0878	13.00	1.62	1.67	2.84
14	0.21	296.50	0.05	1.00	-0.0344	-0.0913	14.00	1.74	1.79	2.52
15	0.26	279.04	0.09	1.00	-0.0332	-0.0952	15.00	1.87	1.91	2.33
16	0.32	257.15	0.12	1.00	-0.0335	-0.1001	16.00	1.99	2.04	2.28
17	0.40	246.79	0.10	1.00	-0.0355	-0.1061	17.00	2.11	2.17	2.33
18	0.47	239.45	0.09	1.00	-0.0389	-0.1128	18.00	2.24	2.30	2.46
19	0.54	236.44	0.07	1.00	-0.0436	-0.1203	19.00	2.37	2.42	2.64
20	0.54	244.24	0.07	1.00	-0.0483	-0.1284	20.00	2.49	2.55	2.73
21	0.58	237.39	0.08	1.00	-0.0531	-0.1369	21.00	2.62	2.69	2.86
22	0.55	239.80	0.04	1.00	-0.0582	-0.1453	22.00	2.74	2.82	2.95
23	0.53	244.44	0.05	1.00	-0.0626	-0.1537	23.00	2.87	2.95	2.99
24	0.50	243.84	0.03	1.00	-0.0665	-0.1618	24.00	3.00	3.08	3.01
25	0.49	243.37	0.01	1.00	-0.0704	-0.1695	25.00	3.12	3.21	3.04
26	0.48	243.37	0.01	1.00	-0.0742	-0.1771	26.00	3.25	3.33	3.07
27	0.46	242.71	0.02	1.00	-0.0779	-0.1844	27.00	3.37	3.46	3.09
28	0.41	241.93	0.05	1.00	-0.0814	-0.1911	28.00	3.50	3.59	3.11
29	0.36	240.87	0.05	1.00	-0.0846	-0.1970	29.00	3.62	3.72	3.13
30	0.33	239.16	0.03	1.00	-0.0876	-0.2022	30.00	3.75	3.85	3.16
31	0.35	238.02	0.02	1.00	-0.0907	-0.2073	31.00	3.87	3.97	3.21
32	0.36	232.10	0.04	1.00	-0.0943	-0.2124	32.00	4.00	4.10	3.28
33	0.40	235.48	0.05	1.00	-0.0982	-0.2177	33.00	4.12	4.22	3.37
34	0.40	238.97	0.02	1.00	-0.1019	-0.2236	34.00	4.25	4.35	3.42
35	0.39	239.39	0.01	1.00	-0.1055	-0.2295	35.00	4.37	4.48	3.45
36	0.44	239.19	0.05	1.00	-0.1092	-0.2357	36.00	4.50	4.61	3.50
37	0.47	239.07	0.03	1.00	-0.1133	-0.2425	37.00	4.62	4.73	3.55
38	0.48	239.34	0.01	1.00	-0.1175	-0.2497	38.00	4.75	4.86	3.59
39	0.51	238.81	0.03	1.00	-0.1219	-0.2571	39.00	4.87	4.99	3.64
40	0.54	239.04	0.03	1.00	-0.1267	-0.2649	40.00	5.00	5.12	3.69
41	0.51	238.44	0.03	1.00	-0.1314	-0.2728	41.00	5.13	5.25	3.72
42	0.48	237.53	0.03	1.00	-0.1360	-0.2801	42.00	5.25	5.38	3.76
43	0.47	236.88	0.01	1.00	-0.1405	-0.2870	43.00	5.38	5.51	3.80
44	0.49	236.38	0.02	1.00	-0.1451	-0.2940	44.00	5.50	5.64	3.85
45	0.52	234.96	0.03	1.00	-0.1501	-0.3013	45.00	5.63	5.77	3.92
46	0.56	232.86	0.04	1.00	-0.1556	-0.3089	46.00	5.76	5.90	4.00
47	0.62	232.50	0.06	1.00	-0.1619	-0.3171	47.00	5.89	6.03	4.10
48	0.66	232.49	0.04	1.00	-0.1687	-0.3260	48.00	6.01	6.16	4.20
49	0.68	231.78	0.02	1.00	-0.1758	-0.3352	49.00	6.14	6.29	4.30
50	0.70	231.71	0.02	1.00	-0.1833	-0.3447	50.00	6.27	6.42	4.40
51	0.69	232.61	0.01	1.00	-0.1907	-0.3542	51.00	6.40	6.55	4.49
52	0.65	234.45	0.05	1.00	-0.1977	-0.3636	52.00	6.53	6.69	4.55
53	0.62	236.27	0.04	1.00	-0.2040	-0.3728	53.00	6.66	6.82	4.60
54	0.61	239.91	0.04	1.00	-0.2097	-0.3819	54.00	6.78	6.95	4.62
55	0.60	246.13	0.07	1.00	-0.2145	-0.3913	55.00	6.91	7.08	4.59
56	0.59	250.34	0.04	1.00	-0.2183	-0.4009	56.00	7.04	7.21	4.53

Table D6 continued

AOSTRA Underground Test Facility

(Borehole Position Uncertainty according to Wolff and de Wardt, 1981 with modifications by Dubrule and Nelson, 1986)

Well: AT7
Date: April 20/90
Elapsed Time = 12.4

Relative Depth Error: 5 mm
Inclination Error: 0.05 degrees
Azimuth Error: 0.10 degrees
Tool Misalignment Error: 0.01 degrees

DAH (m)	Inclination (degrees)	Azimuth (degrees)	Dogleg (degrees)	Dogleg Factor	North (m)	East (m)	Vertical (m)	ΔN (mm)	ΔE (mm)	Phi (°)
0	0.00	0.00			0.0000	0.0000	0.00	0.00	0.00	0.00
1	0.51	250.41	0.51	1.00	-0.0015	-0.0042	1.00	0.12	0.13	12.59
2	0.52	248.33	0.02	1.00	-0.0047	-0.0126	2.00	0.25	0.26	4.81
3	0.52	246.44	0.02	1.00	-0.0081	-0.0210	3.00	0.38	0.39	4.01
4	0.51	245.80	0.01	1.00	-0.0118	-0.0292	4.00	0.50	0.52	3.75
5	0.50	244.57	0.01	1.00	-0.0155	-0.0372	5.00	0.63	0.65	3.66
6	0.49	244.93	0.01	1.00	-0.0192	-0.0450	6.00	0.75	0.78	3.61
7	0.48	245.55	0.01	1.00	-0.0227	-0.0527	7.00	0.88	0.91	3.56
8	0.46	246.02	0.02	1.00	-0.0261	-0.0602	8.00	1.00	1.03	3.50
9	0.44	246.46	0.02	1.00	-0.0292	-0.0674	9.00	1.13	1.16	3.44
10	0.40	248.96	0.04	1.00	-0.0320	-0.0741	10.00	1.25	1.29	3.34
11	0.36	251.60	0.04	1.00	-0.0343	-0.0804	11.00	1.38	1.42	3.22
12	0.31	261.61	0.08	1.00	-0.0357	-0.0860	12.00	1.50	1.55	3.02
13	0.26	272.56	0.07	1.00	-0.0360	-0.0910	13.00	1.62	1.67	2.77
14	0.26	278.83	0.03	1.00	-0.0355	-0.0955	14.00	1.75	1.80	2.53
15	0.27	280.68	0.01	1.00	-0.0347	-0.1001	15.00	1.87	1.92	2.31
16	0.29	262.24	0.09	1.00	-0.0346	-0.1049	16.00	1.99	2.05	2.22
17	0.36	249.01	0.10	1.00	-0.0361	-0.1103	17.00	2.12	2.17	2.24
18	0.43	242.66	0.08	1.00	-0.0389	-0.1166	18.00	2.24	2.30	2.34
19	0.52	237.83	0.10	1.00	-0.0431	-0.1238	19.00	2.37	2.43	2.50
20	0.56	235.19	0.05	1.00	-0.0483	-0.1316	20.00	2.49	2.56	2.67
21	0.56	237.33	0.02	1.00	-0.0537	-0.1397	21.00	2.62	2.69	2.82
22	0.53	240.69	0.04	1.00	-0.0586	-0.1479	22.00	2.74	2.82	2.90
23	0.53	242.49	0.02	1.00	-0.0630	-0.1560	23.00	2.87	2.95	2.96
24	0.50	243.79	0.03	1.00	-0.0671	-0.1640	24.00	3.00	3.08	2.99
25	0.49	243.79	0.01	1.00	-0.0709	-0.1718	25.00	3.12	3.21	3.01
26	0.47	243.06	0.02	1.00	-0.0746	-0.1793	26.00	3.25	3.34	3.04
27	0.43	237.75	0.06	1.00	-0.0785	-0.1861	27.00	3.37	3.47	3.08
28	0.38	231.32	0.07	1.00	-0.0826	-0.1919	28.00	3.50	3.59	3.16
29	0.34	230.05	0.04	1.00	-0.0866	-0.1967	29.00	3.62	3.72	3.25
30	0.32	231.09	0.02	1.00	-0.0902	-0.2012	30.00	3.75	3.84	3.33
31	0.35	229.15	0.03	1.00	-0.0940	-0.2057	31.00	3.87	3.97	3.43
32	0.39	225.06	0.05	1.00	-0.0984	-0.2104	32.00	4.00	4.09	3.56
33	0.42	226.70	0.03	1.00	-0.1033	-0.2155	33.00	4.12	4.22	3.71
34	0.41	232.04	0.04	1.00	-0.1080	-0.2209	34.00	4.25	4.35	3.81
35	0.42	234.40	0.02	1.00	-0.1123	-0.2267	35.00	4.38	4.47	3.89
36	0.45	237.48	0.04	1.00	-0.1166	-0.2330	36.00	4.50	4.60	3.96
37	0.48	237.81	0.03	1.00	-0.1209	-0.2399	37.00	4.63	4.73	4.01
38	0.51	238.12	0.03	1.00	-0.1255	-0.2472	38.00	4.75	4.86	4.06
39	0.54	238.16	0.03	1.00	-0.1303	-0.2550	39.00	4.88	4.99	4.11
40	0.56	238.84	0.02	1.00	-0.1354	-0.2632	40.00	5.01	5.12	4.16
41	0.54	238.90	0.02	1.00	-0.1403	-0.2714	41.00	5.13	5.25	4.18
42	0.51	238.07	0.03	1.00	-0.1451	-0.2792	42.00	5.26	5.38	4.21
43	0.50	237.48	0.01	1.00	-0.1498	-0.2867	43.00	5.38	5.51	4.24
44	0.51	237.24	0.01	1.00	-0.1546	-0.2941	44.00	5.51	5.64	4.28
45	0.54	235.65	0.03	1.00	-0.1596	-0.3017	45.00	5.64	5.77	4.34
46	0.58	234.23	0.04	1.00	-0.1652	-0.3097	46.00	5.76	5.90	4.41
47	0.62	233.70	0.04	1.00	-0.1714	-0.3182	47.00	5.89	6.03	4.49
48	0.66	232.79	0.04	1.00	-0.1781	-0.3271	48.00	6.02	6.16	4.58
49	0.69	232.31	0.03	1.00	-0.1853	-0.3365	49.00	6.15	6.29	4.68
50	0.70	231.82	0.01	1.00	-0.1927	-0.3461	50.00	6.28	6.42	4.78
51	0.69	232.70	0.01	1.00	-0.2001	-0.3556	51.00	6.41	6.56	4.87
52	0.66	234.98	0.04	1.00	-0.2071	-0.3652	52.00	6.54	6.69	4.92
53	0.62	237.10	0.05	1.00	-0.2133	-0.3744	53.00	6.66	6.82	4.95
54	0.62	240.08	0.03	1.00	-0.2190	-0.3836	54.00	6.79	6.95	4.97
55	0.61	246.73	0.07	1.00	-0.2238	-0.3932	55.00	6.92	7.09	4.93
56	0.59	250.53	0.04	1.00	-0.2276	-0.4030	56.00	7.04	7.22	4.84

Table D6 continued

APPENDIX E

Temperature Distribution within Geotechnical Cross Section

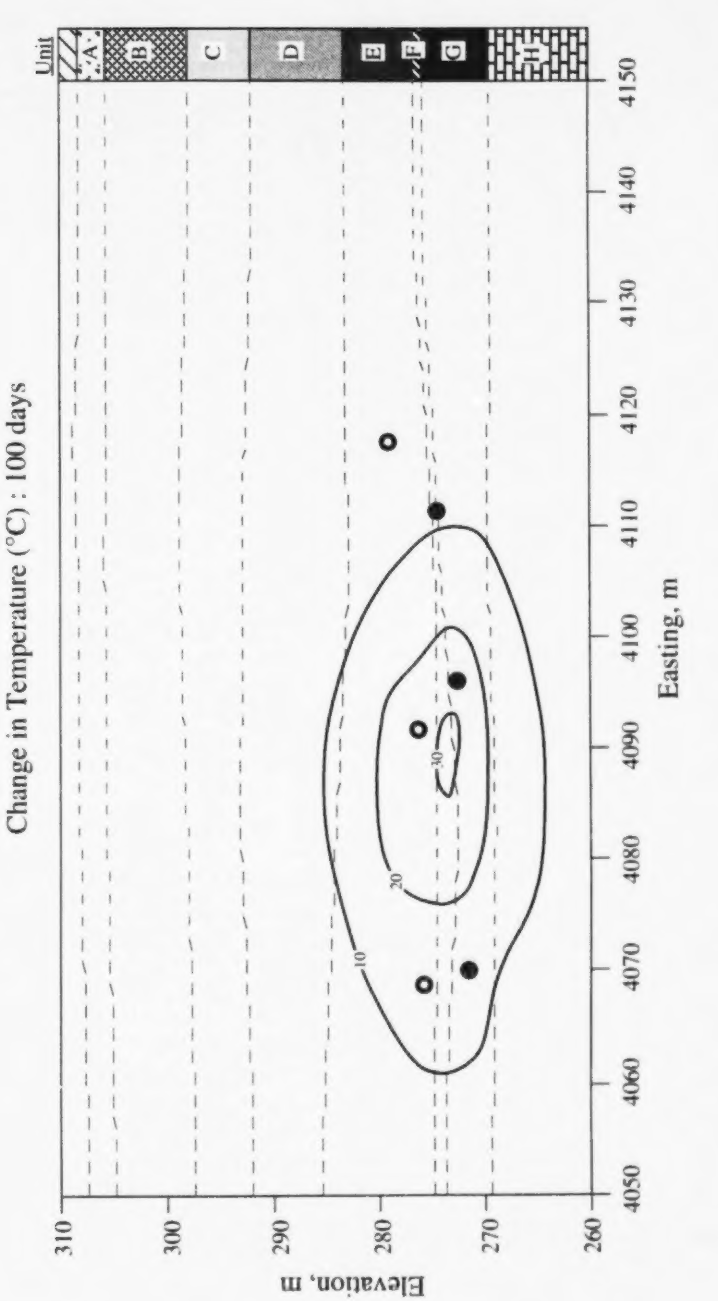

Figure E1 Temperature Distribution within Geotechnical Cross Section at Time 1.4

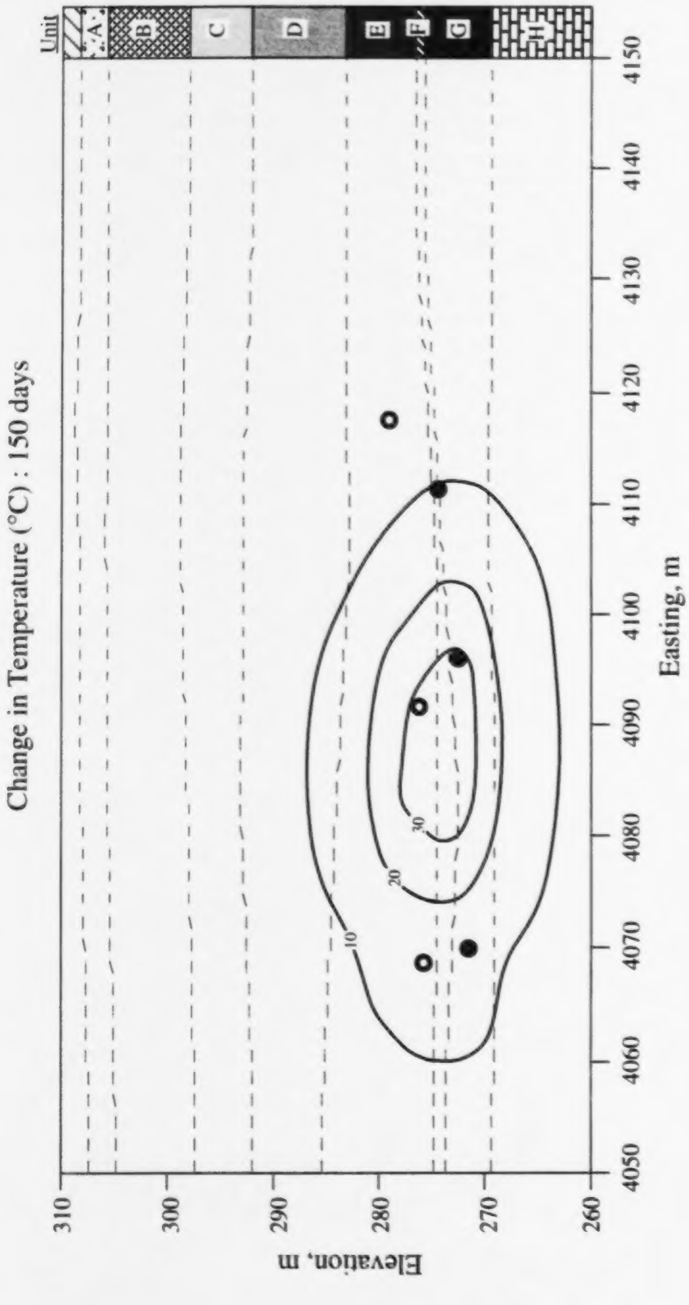

Figure E2 Temperature Distribution within Geotechnical Cross Section at Time 2.1

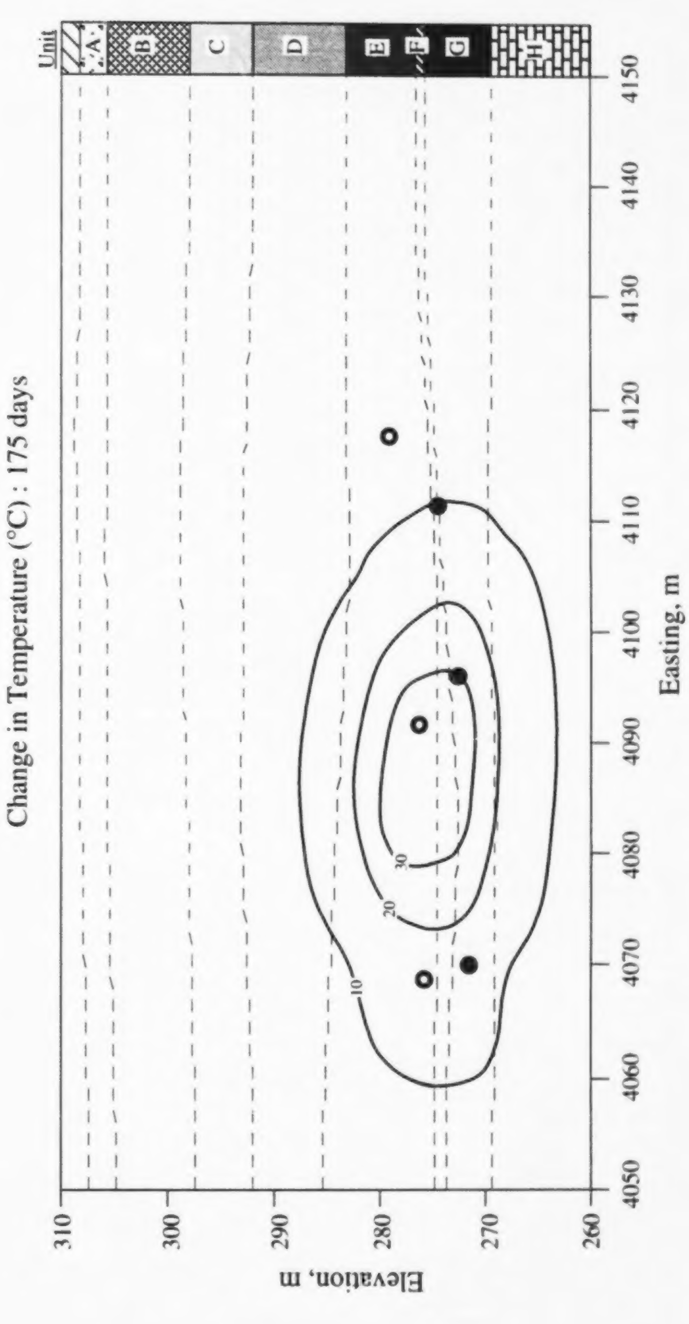

Figure E3 Temperature Distribution within Geotechnical Cross Section at Time 2.5

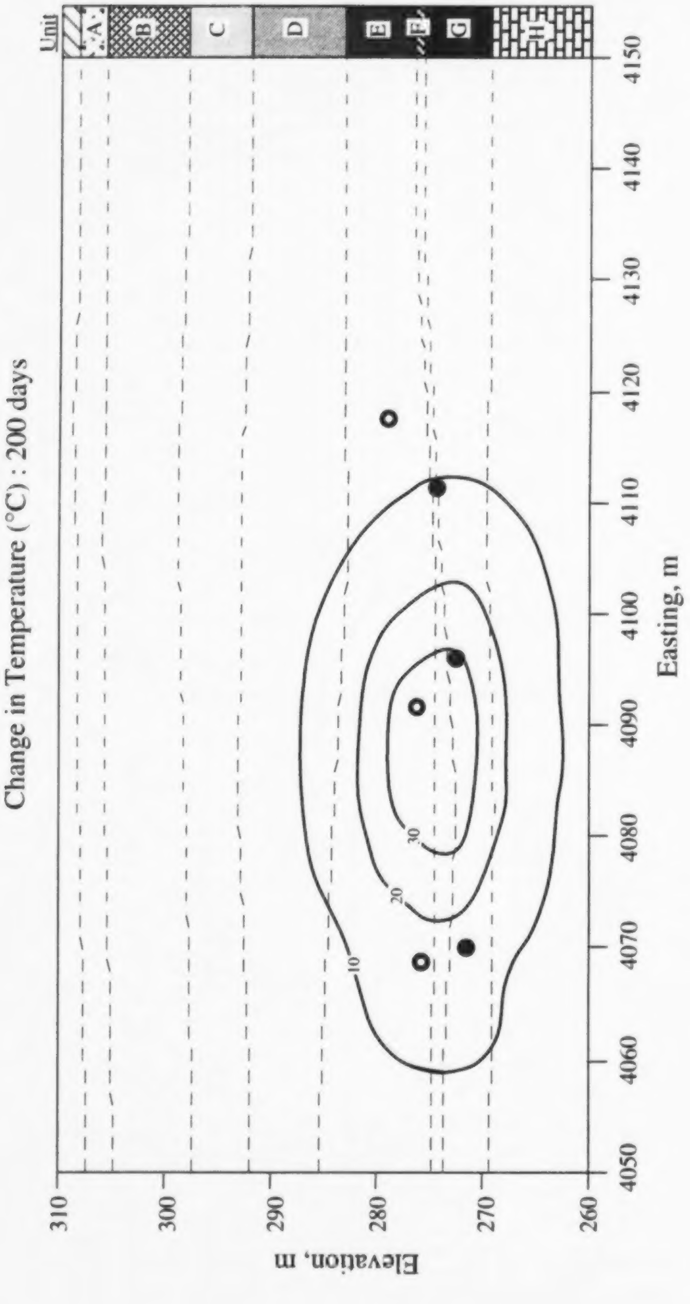

Figure E4 Temperature Distribution within Geotechnical Cross Section at Time 2.9

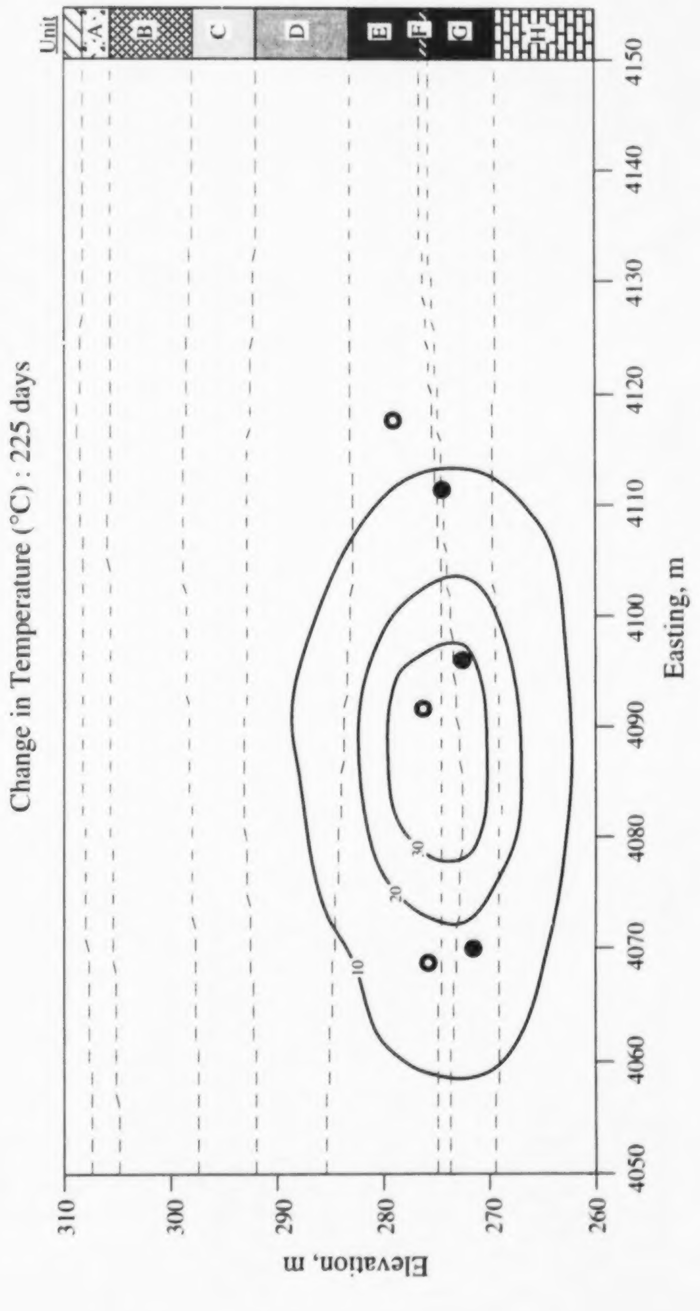

Figure E5 Temperature Distribution within Geotechnical Cross Section at Time 3.2

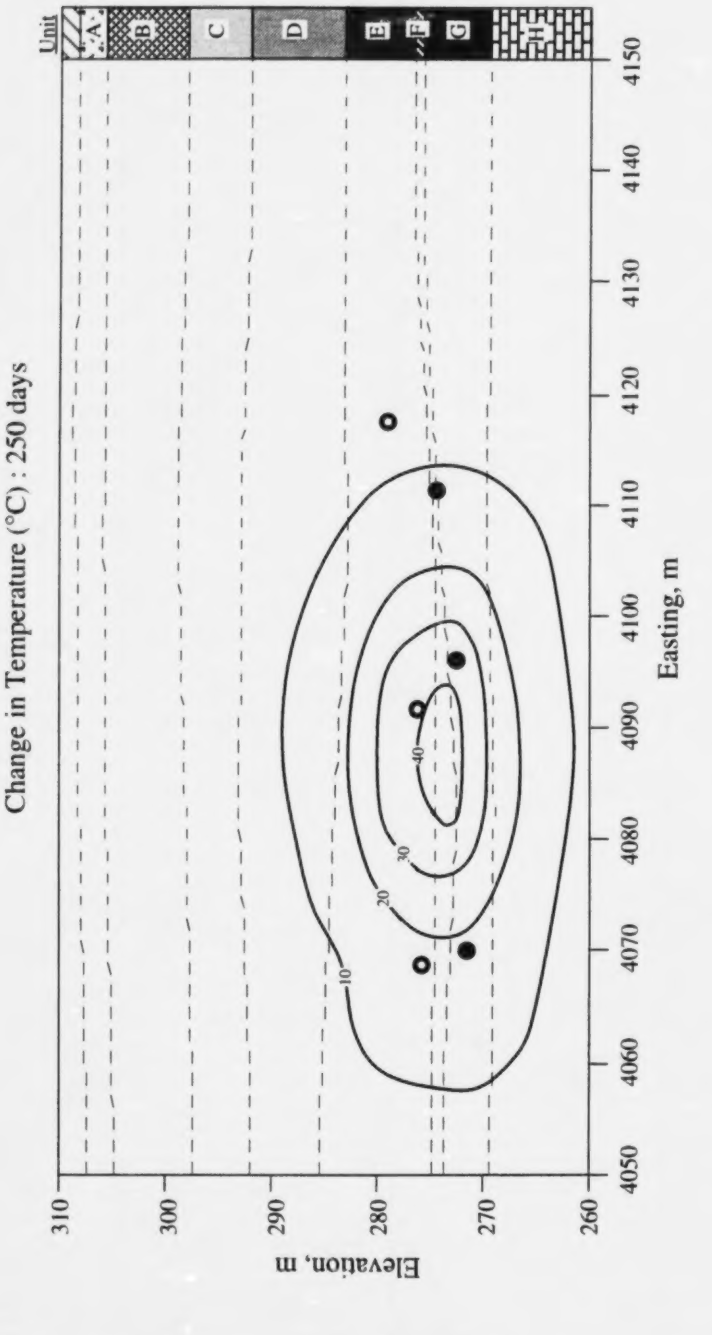

Figure E6 Temperature Distribution within Geotechnical Cross Section at Time 3.6

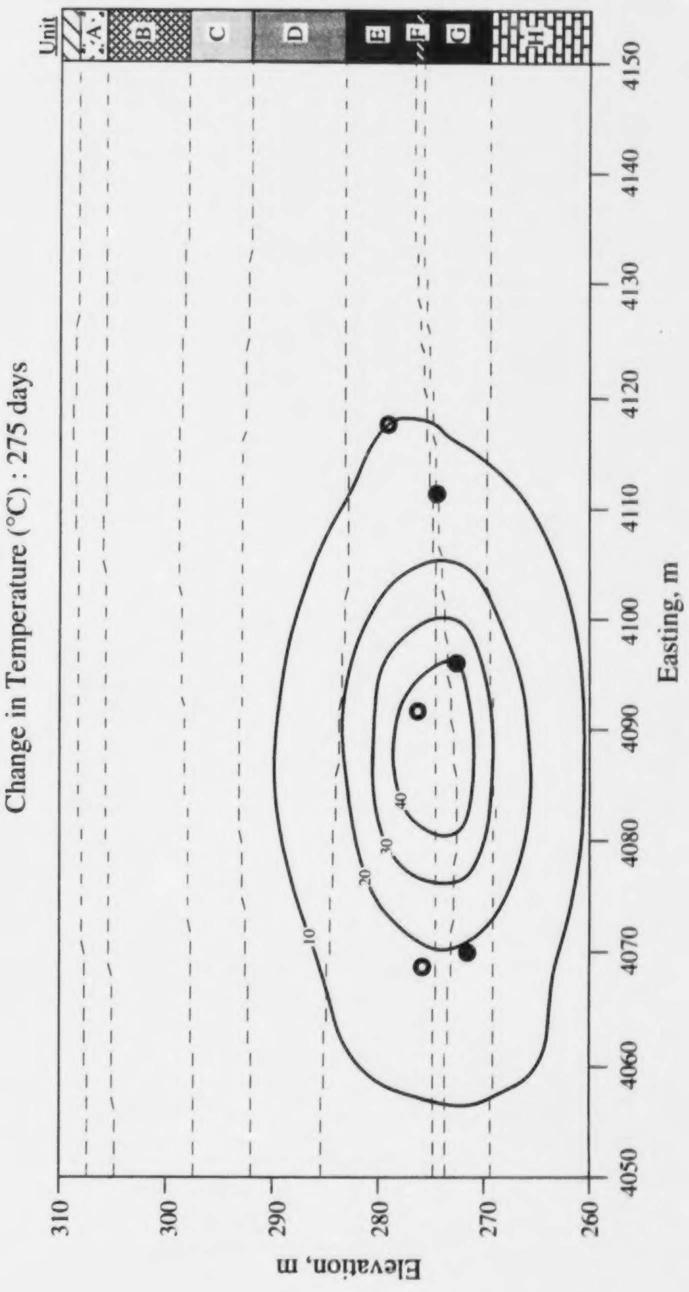

Figure E7 Temperature Distribution within Geotechnical Cross Section at Time 3.9

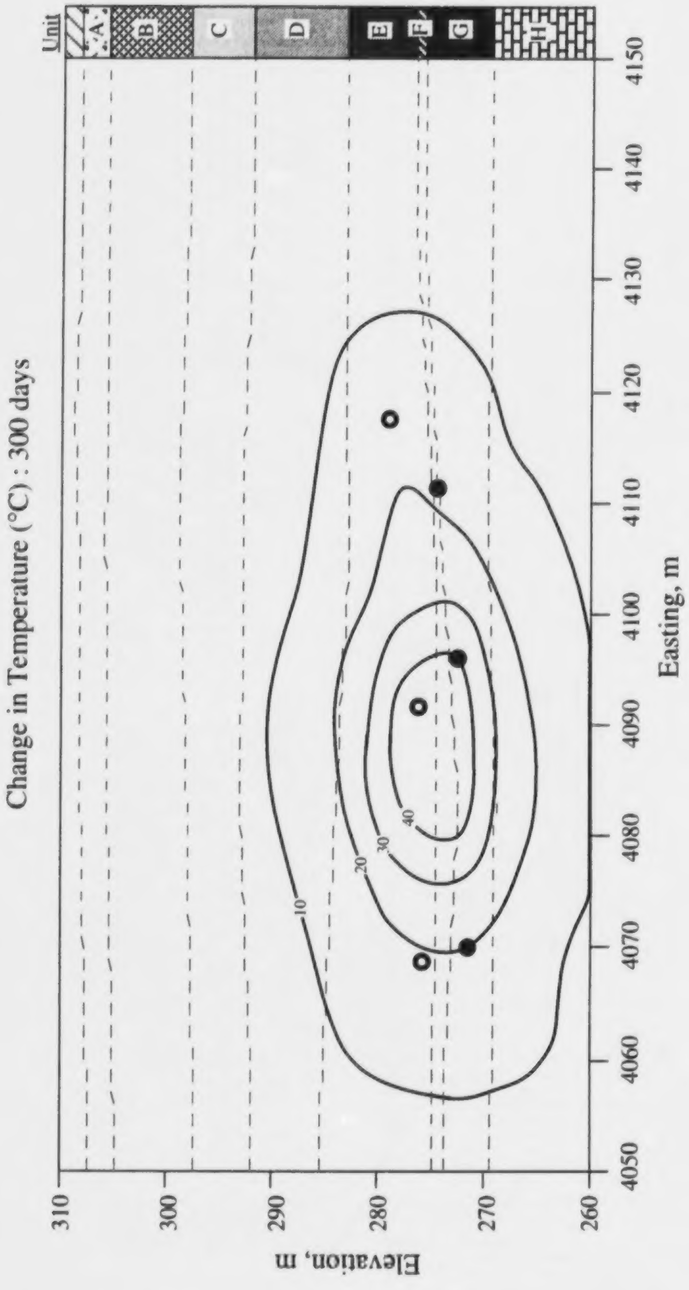

Figure E8 Temperature Distribution within Geotechnical Cross Section at Time 4.3

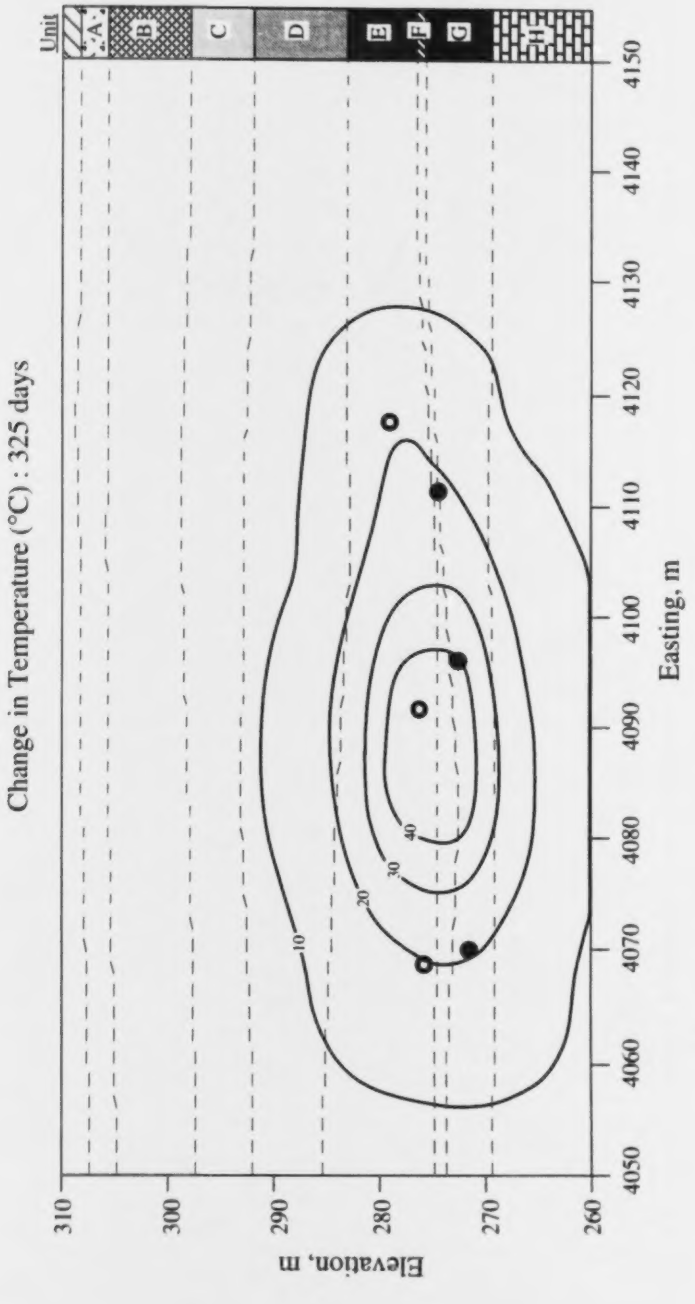

Figure E9 Temperature Distribution within Geotechnical Cross Section at Time 4.6

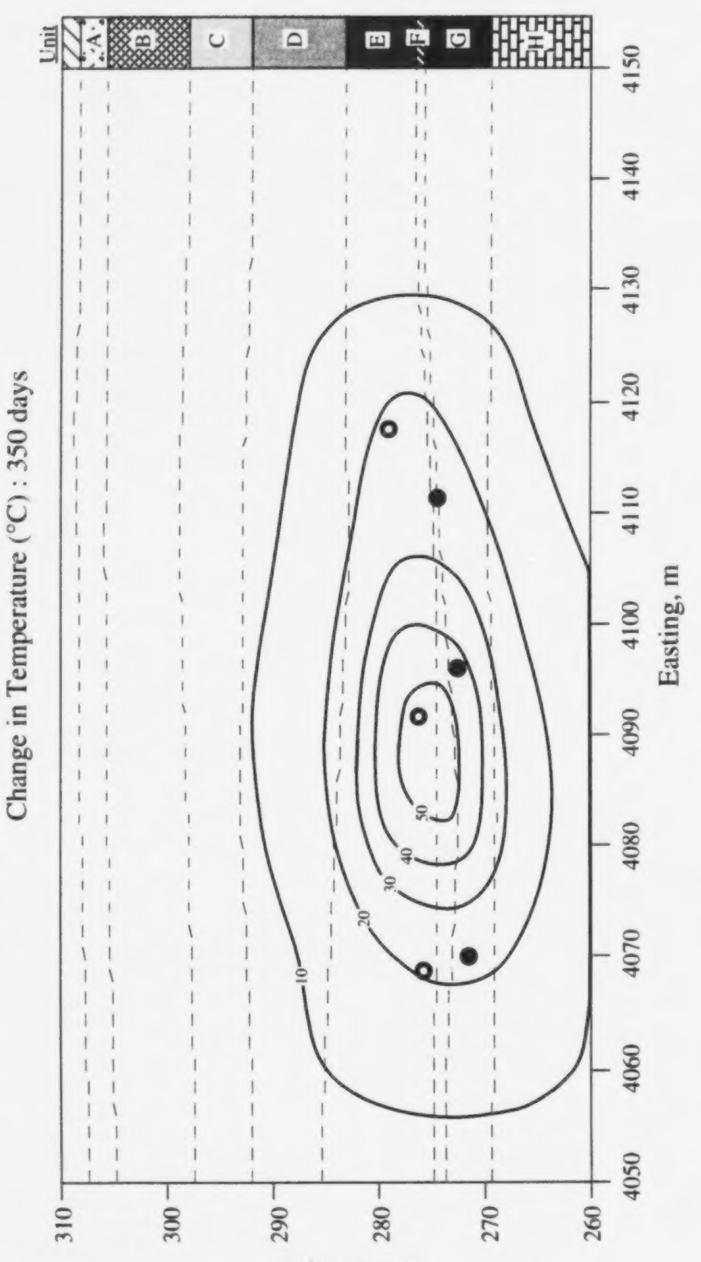

Figure E10 Temperature Distribution within Geotechnical Cross Section at Time 5.0

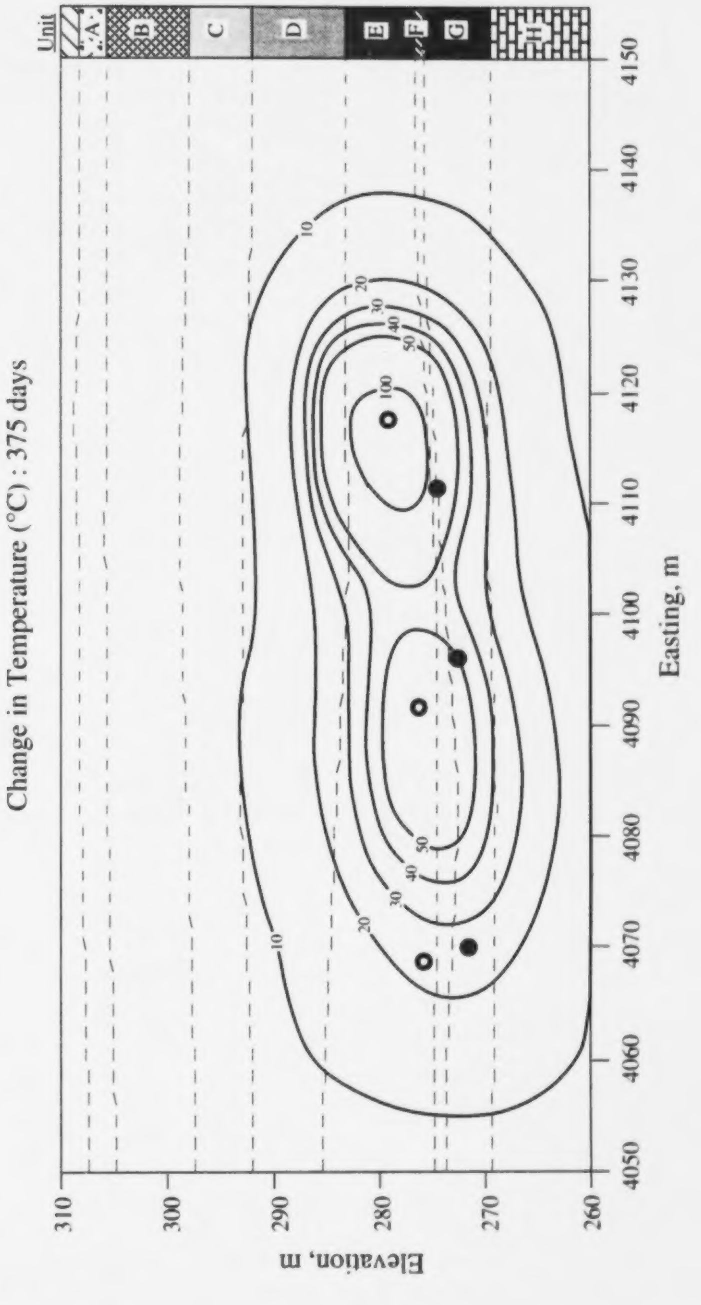

Figure E11 Temperature Distribution within Geotechnical Cross Section at Time 5.4

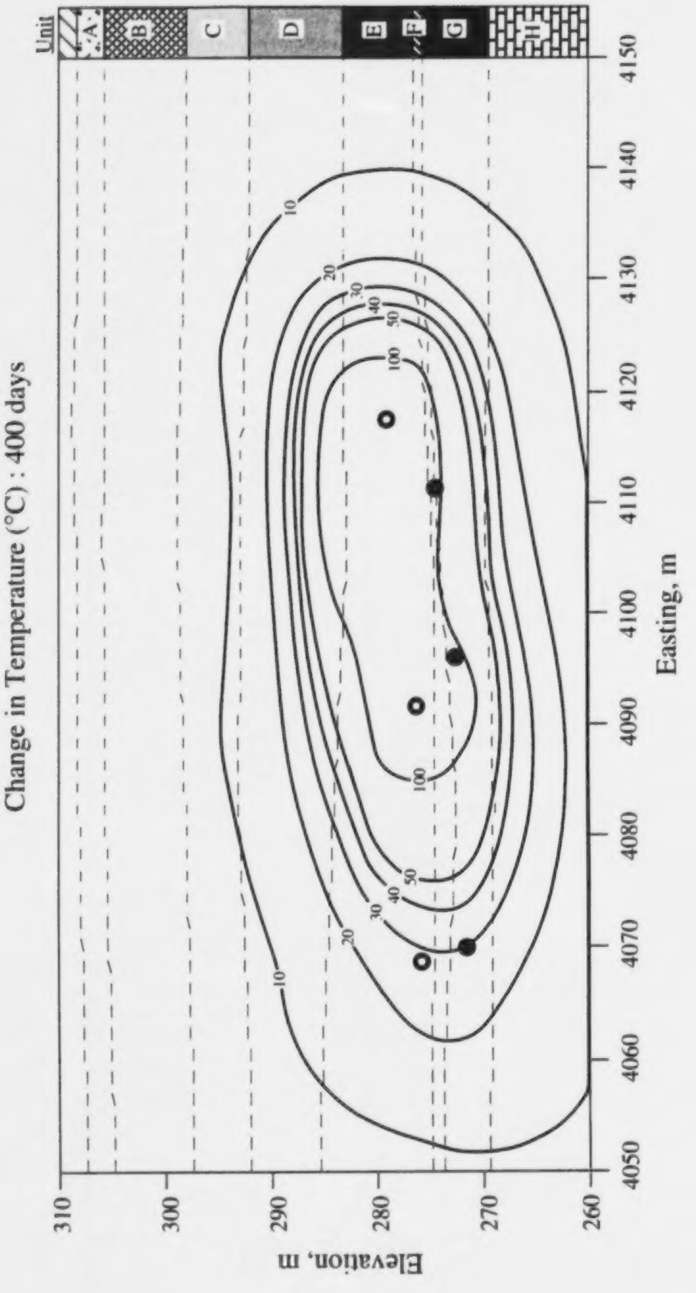

Figure E12 Temperature Distribution within Geotechnical Cross Section at Time 5.7

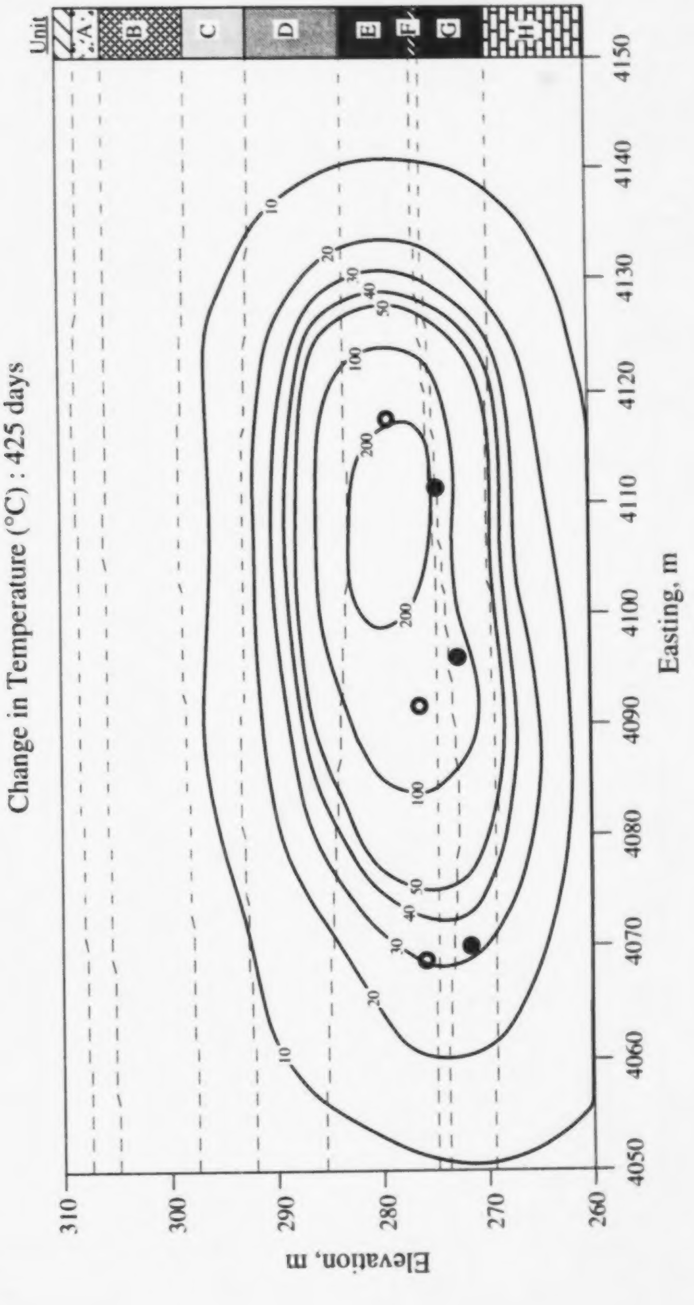

Figure E13 Temperature Distribution within Geotechnical Cross Section at Time 6.1

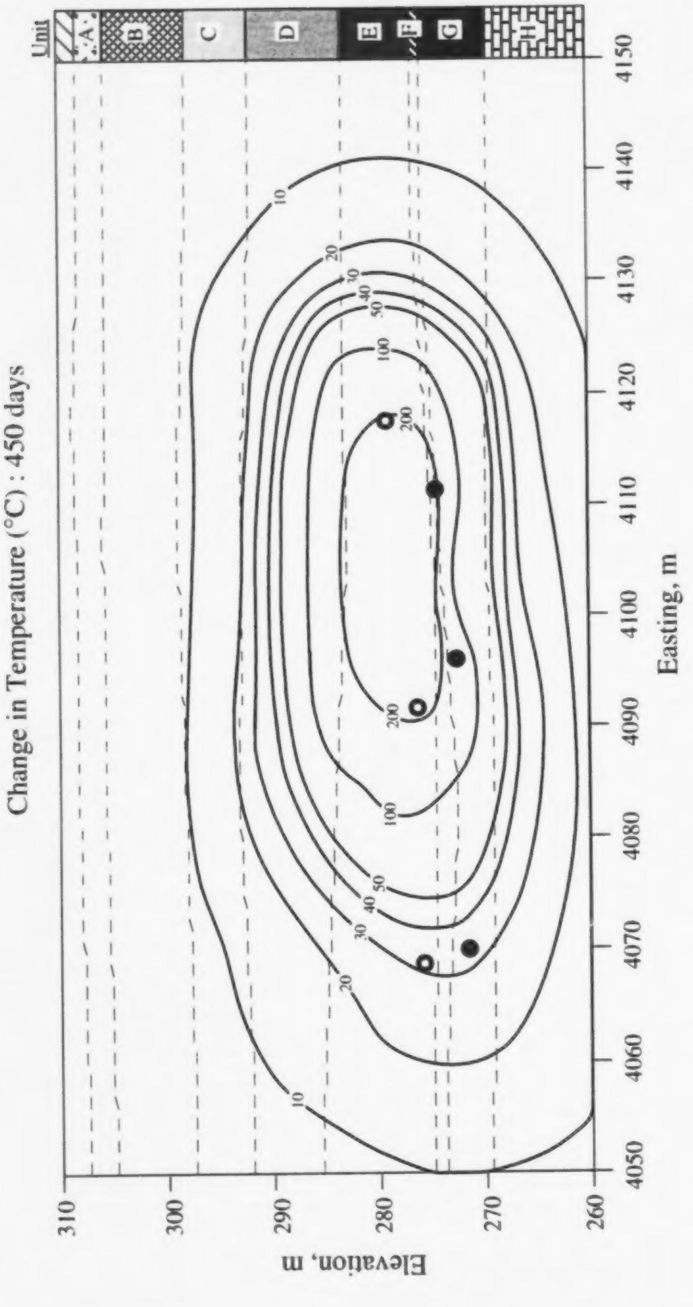

Figure E14 Temperature Distribution within Geotechnical Cross Section at Time 6.4

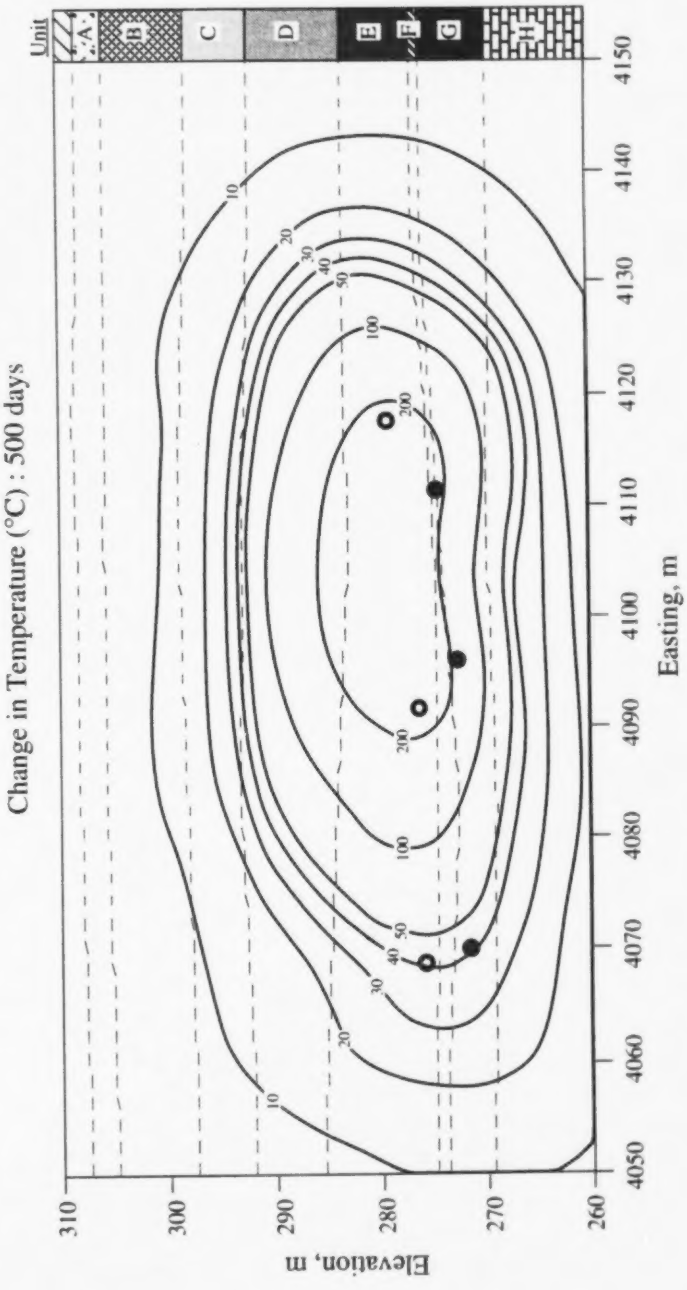

Figure E15 Temperature Distribution within Geotechnical Cross Section at Time 7.1

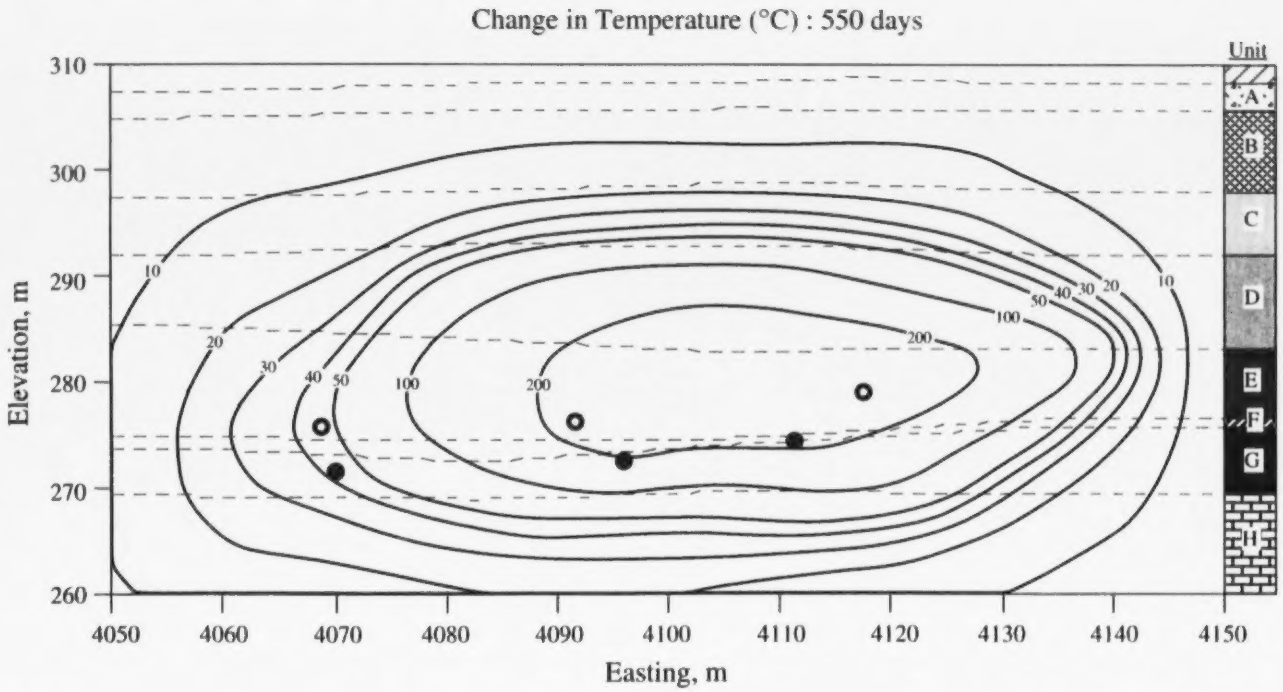

Change in Temperature (°C) : 550 days

Figure E16 Temperature Distribution within Geotechnical Cross Section at Time 7.9

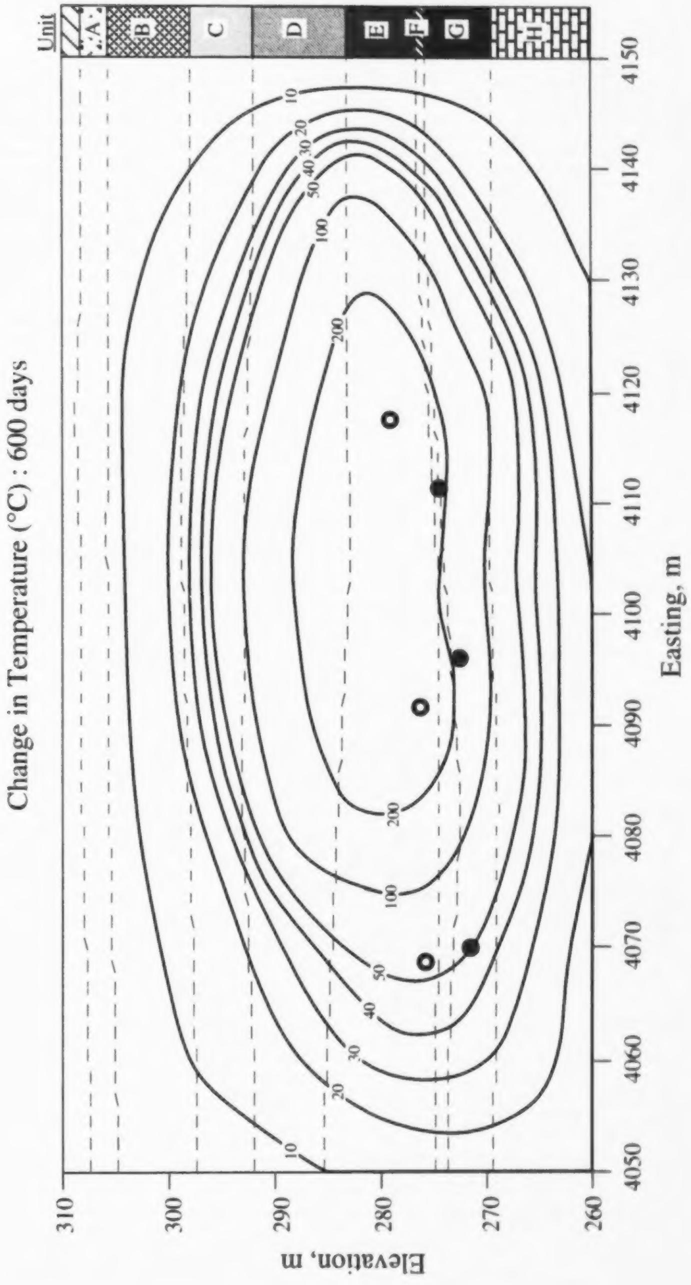

Figure E17 Temperature Distribution within Geotechnical Cross Section at Time 8.6

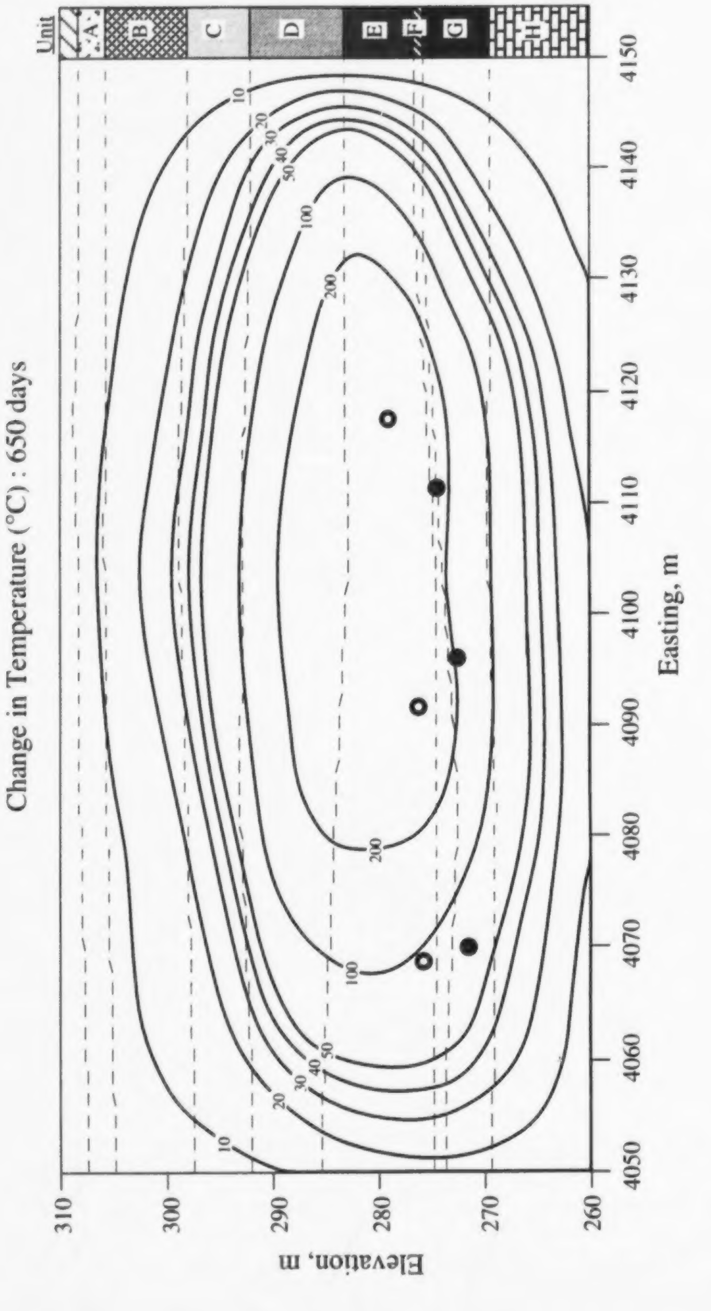

Figure E18 Temperature Distribution within Geotechnical Cross Section at Time 9.3

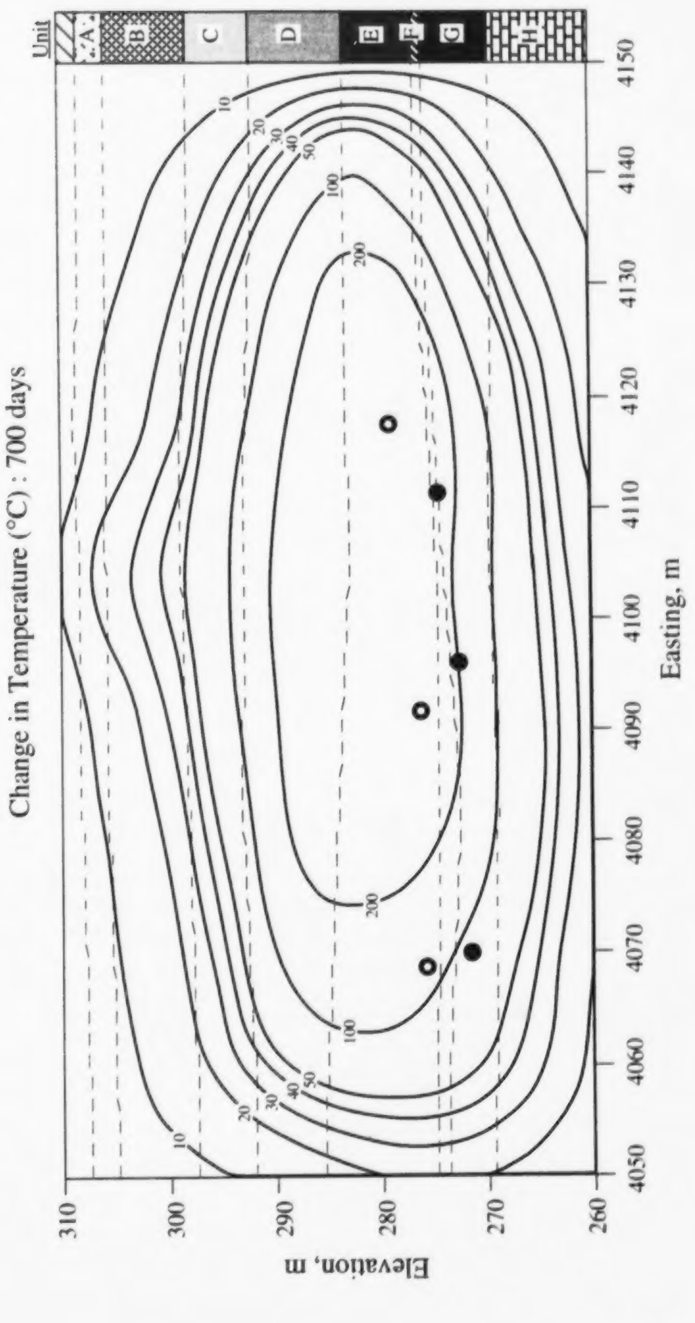

Figure E19 Temperature Distribution within Geotechnical Cross Section at Time 10.0

APPENDIX F

Pore Pressure Distribution within Geotechnical Cross Section

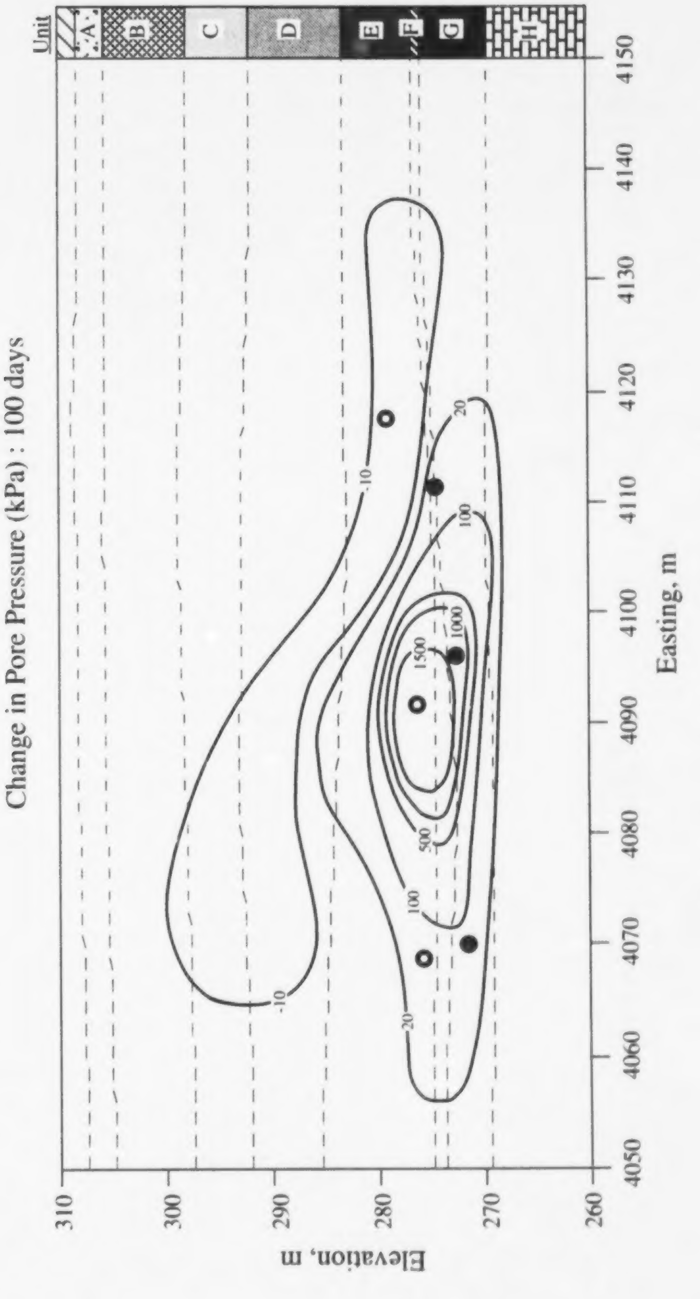

Figure F1 Pore Pressure Distribution within Geotechnical Cross Section at Time 1.4

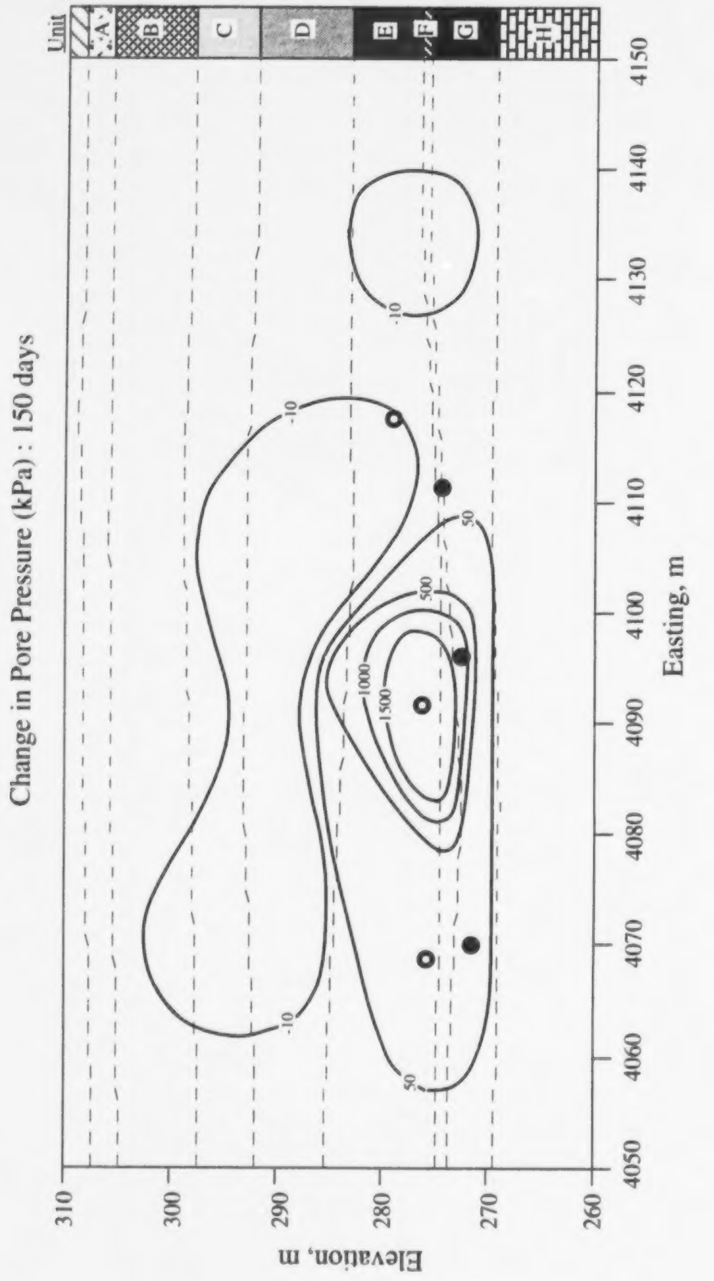

Figure F2 Pore Pressure Distribution within Geotechnical Cross Section at Time 2.1

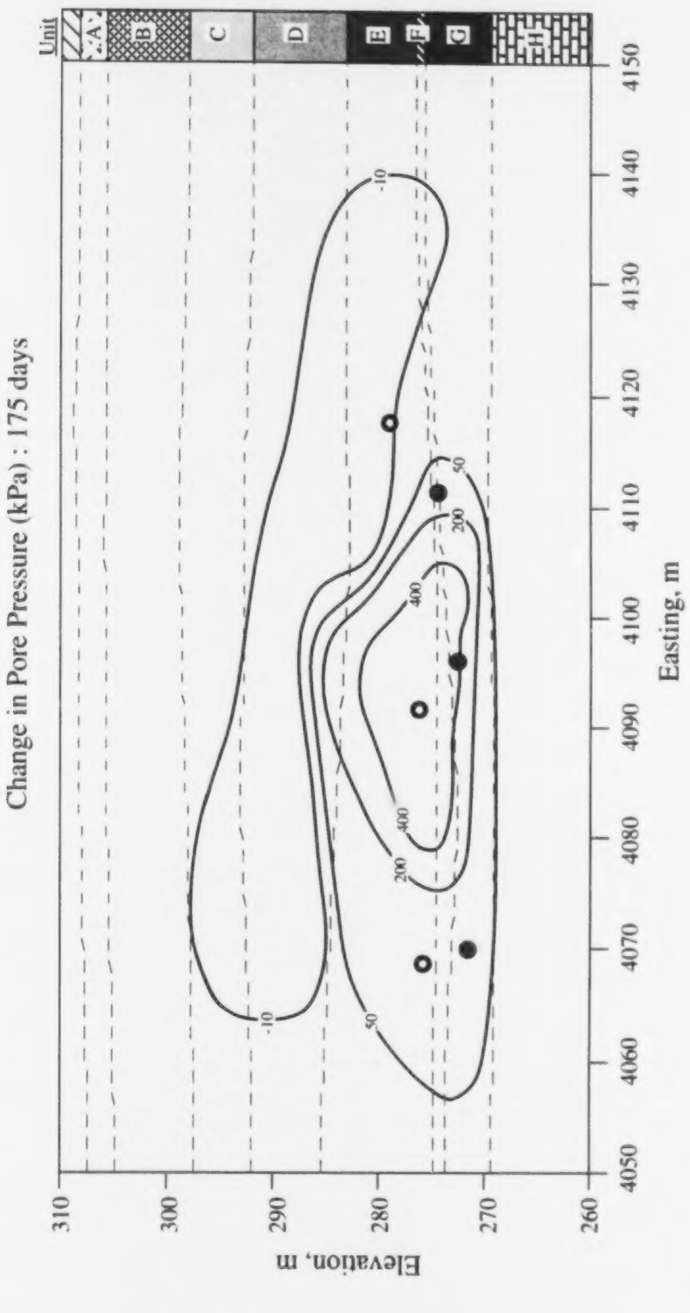

Figure F3 Pore Pressure Distribution within Geotechnical Cross Section at Time 2.5

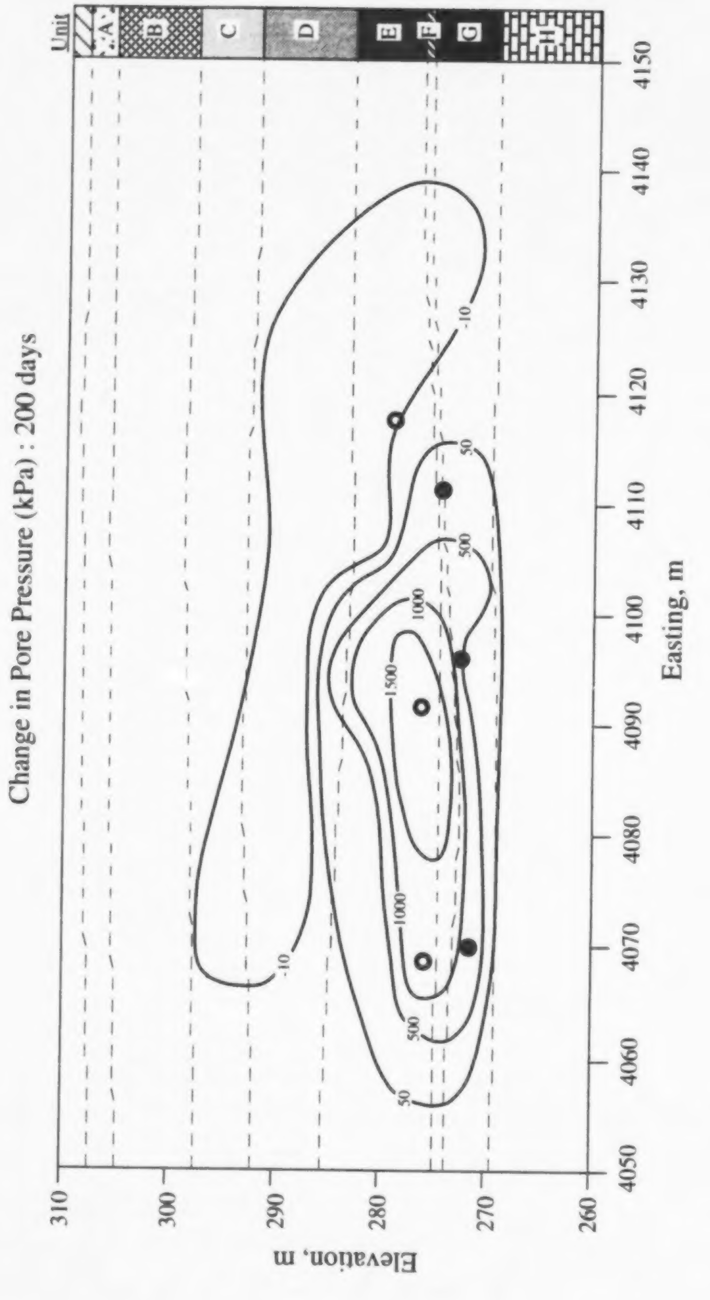

Figure F4 Pore Pressure Distribution within Geotechnical Cross Section at Time 2.9

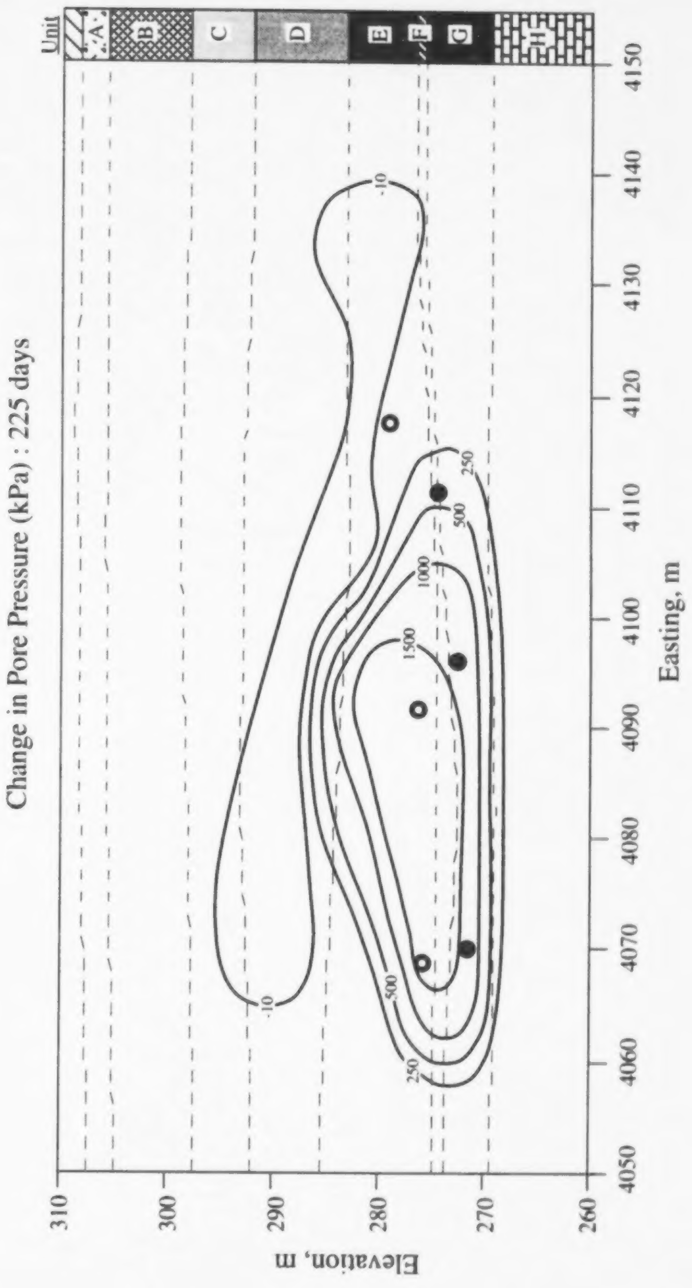

Figure F5 Pore Pressure Distribution within Geotechnical Cross Section at Time 3.2

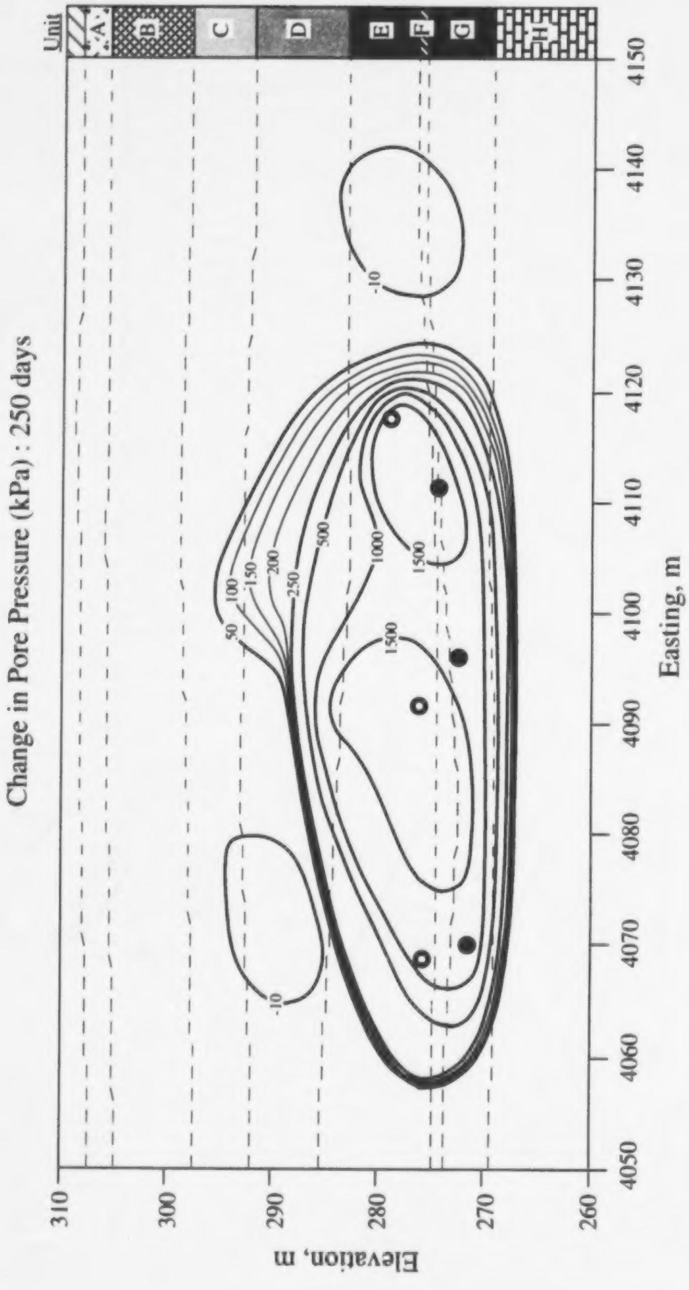

Figure F6 Pore Pressure Distribution within Geotechnical Cross Section at Time 3.6

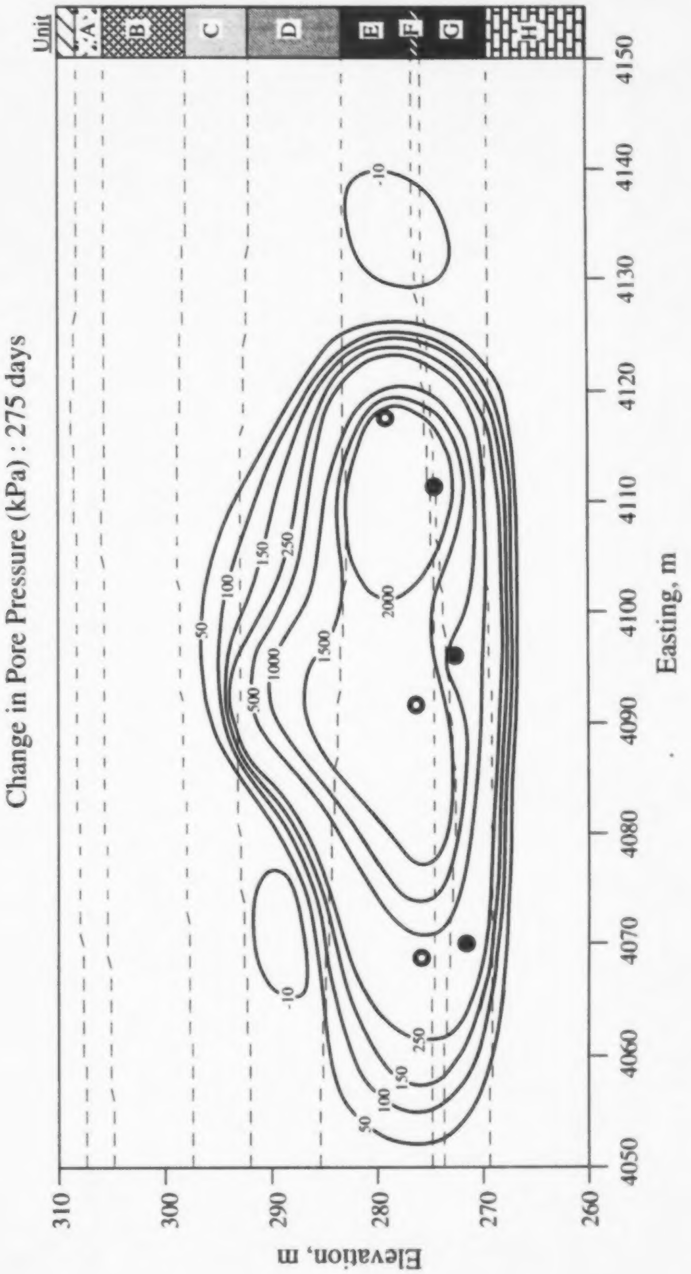

Figure F7 Pore Pressure Distribution within Geotechnical Cross Section at Time 3.9

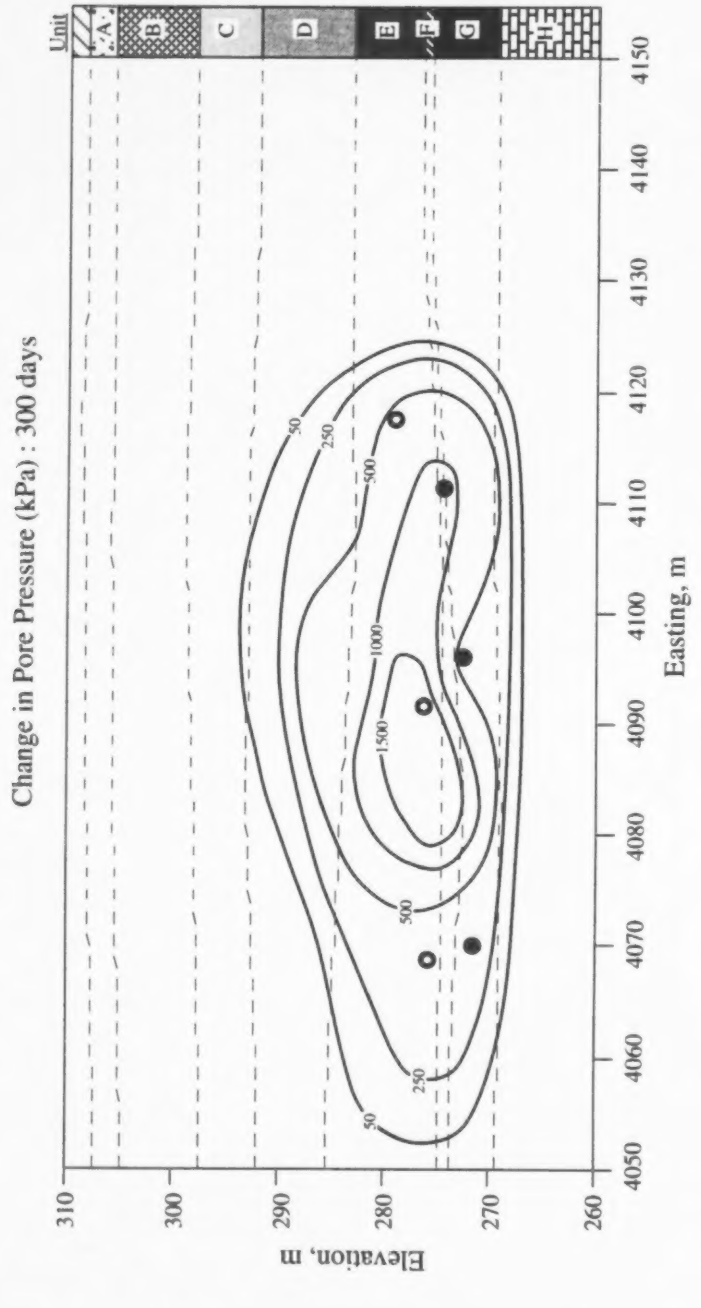

Figure F8 Pore Pressure Distribution within Geotechnical Cross Section at Time 4.3

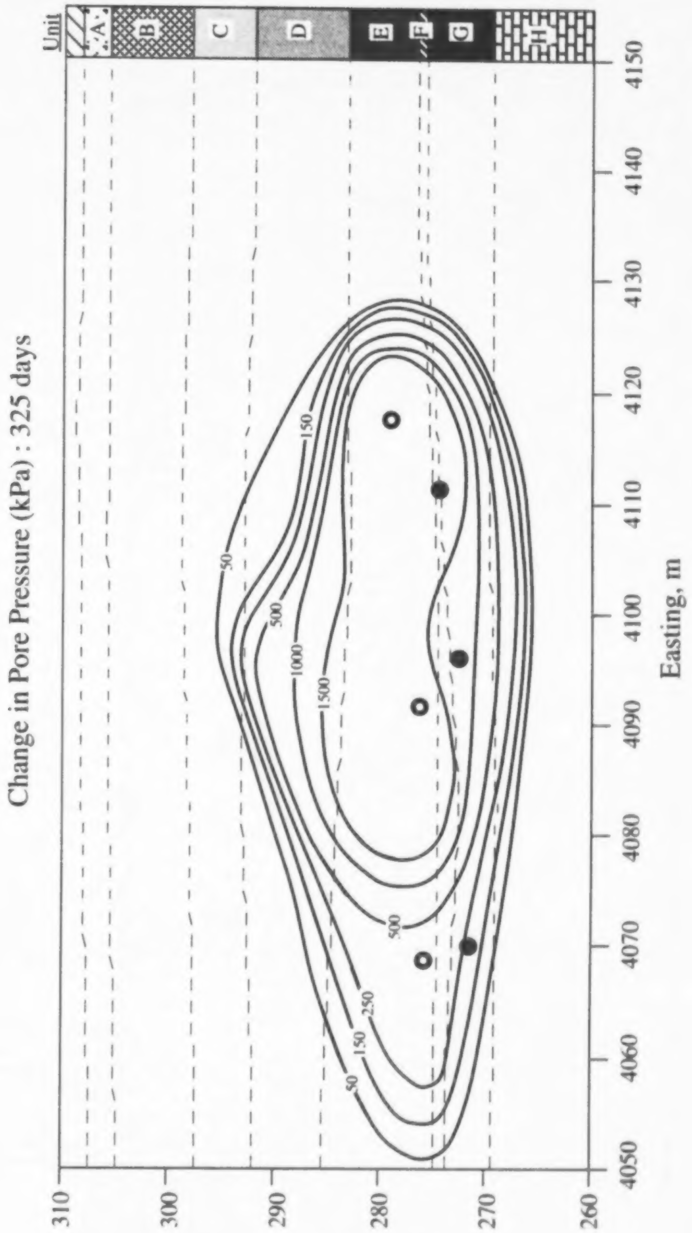

Figure F9 Pore Pressure Distribution within Geotechnical Cross Section at Time 4.6

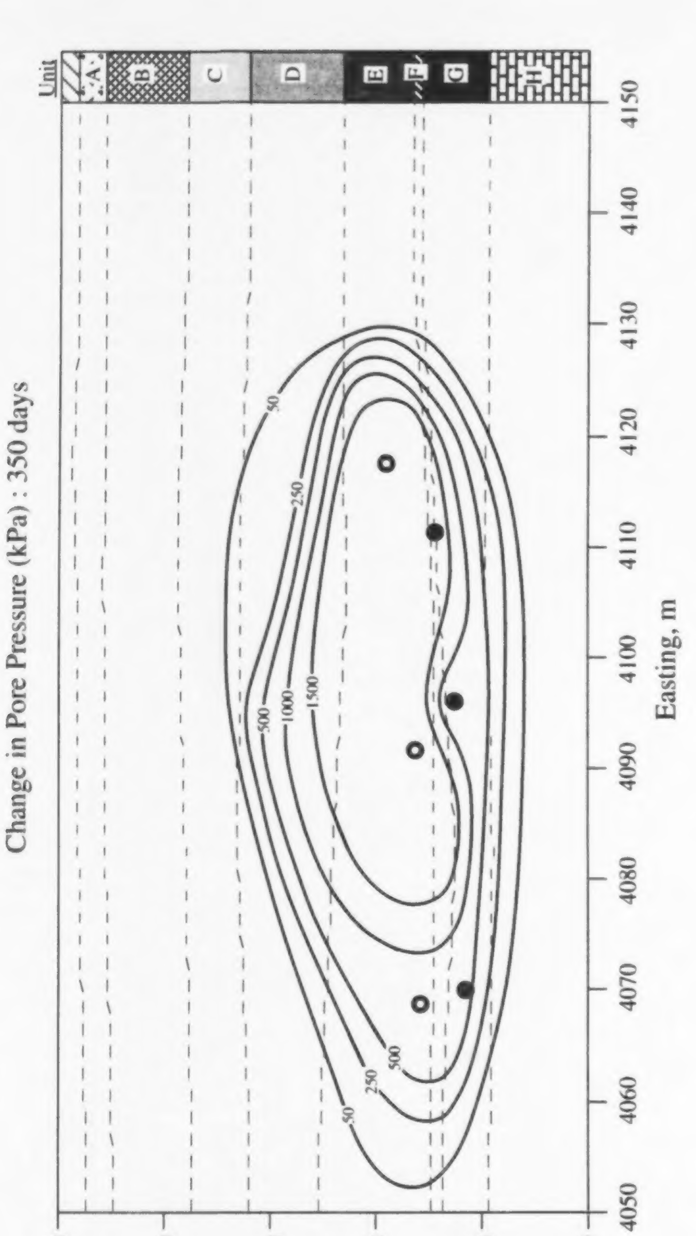

Figure F10 Pore Pressure Distribution within Geotechnical Cross Section at Time 5.0

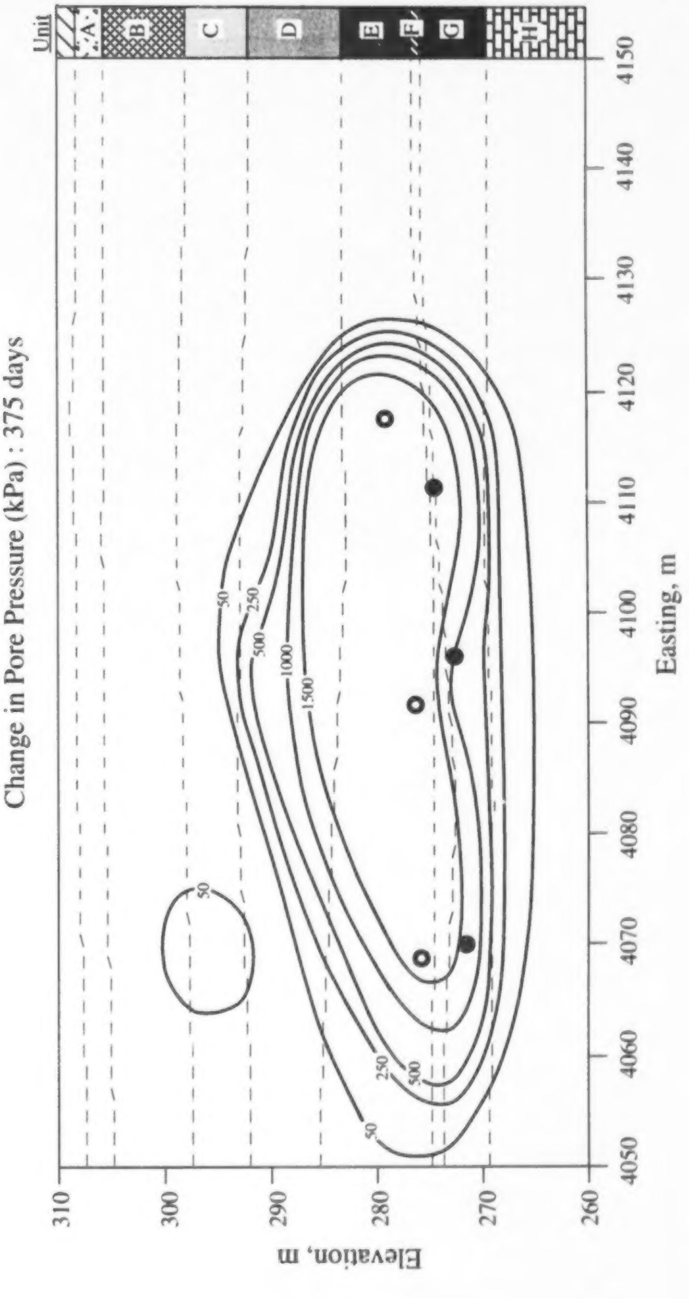

Figure F11 Pore Pressure Distribution within Geotechnical Cross Section at Time 5.4

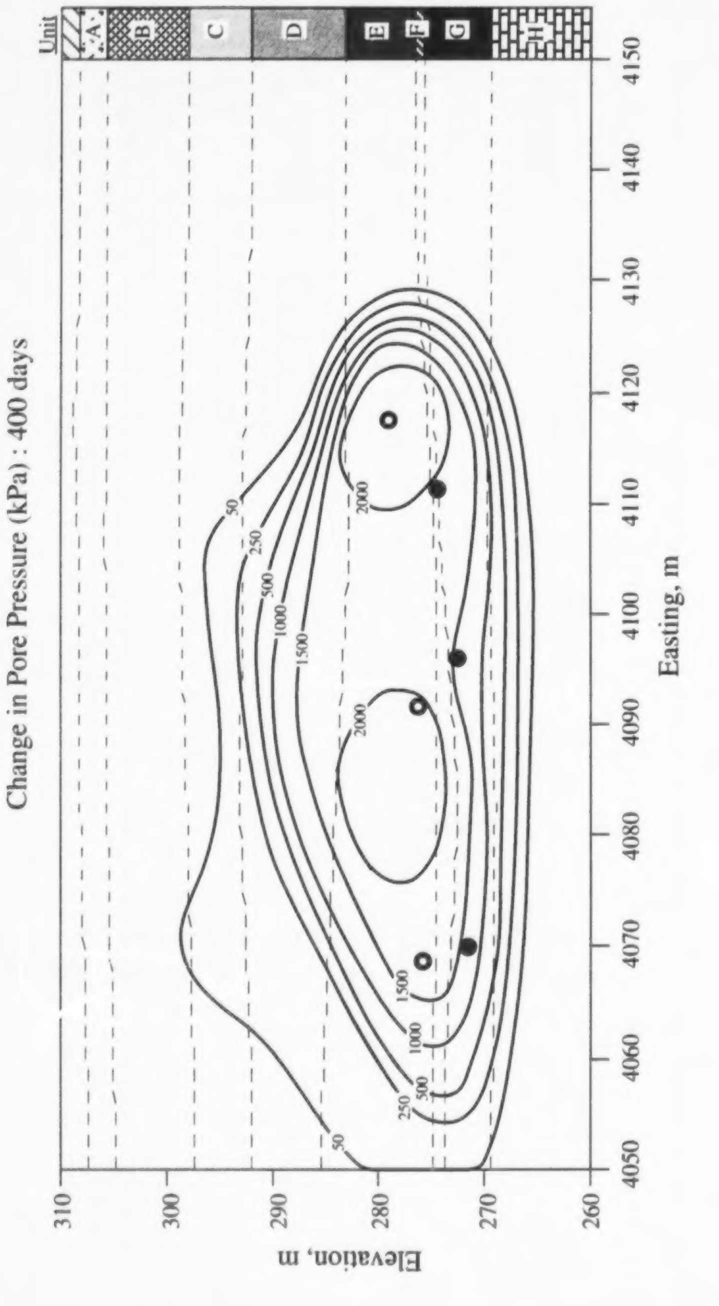

Figure F12 Pore Pressure Distributiŏn within Geotechnical Cross Section at Time 5.7

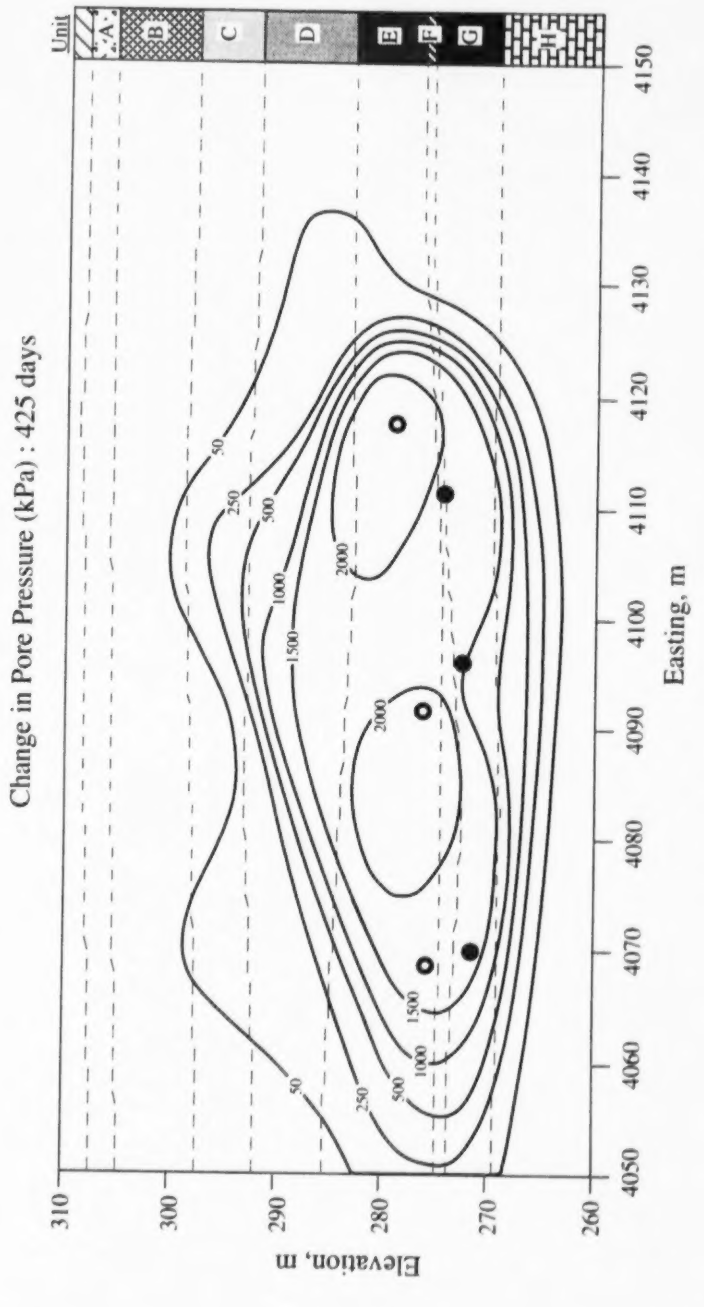

Figure F13 Pore Pressure Distribution within Geotechnical Cross Section at Time 6.1

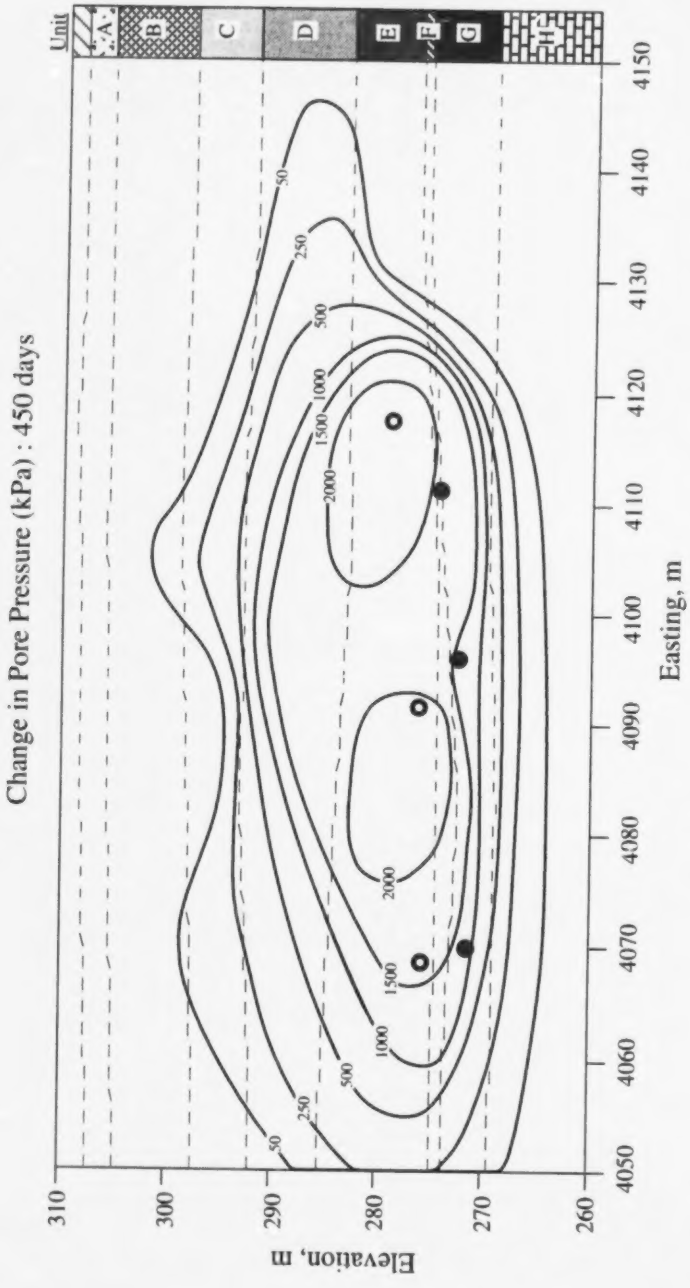
Change in Pore Pressure (kPa) : 450 days

Figure F14 Pore Pressure Distribution within Geotechnical Cross Section at Time 6.4

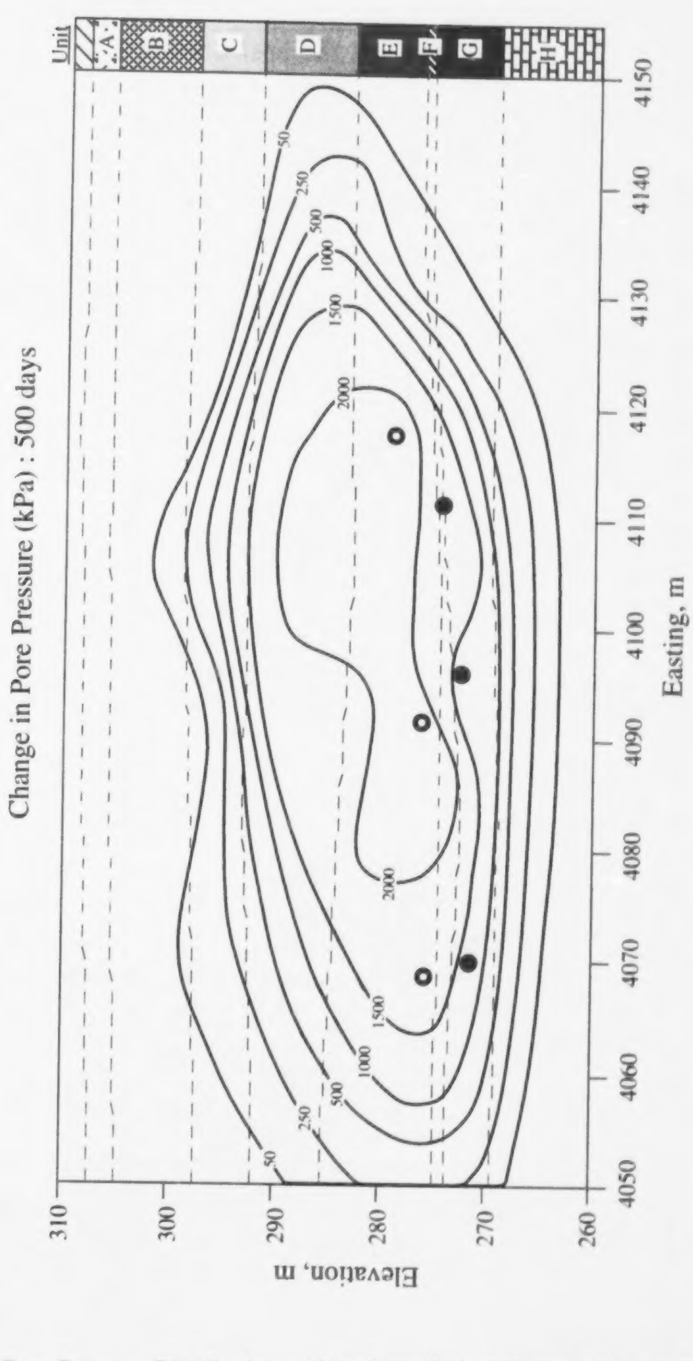

Figure F15 Pore Pressure Distribution within Geotechnical Cross Section at Time 7.1

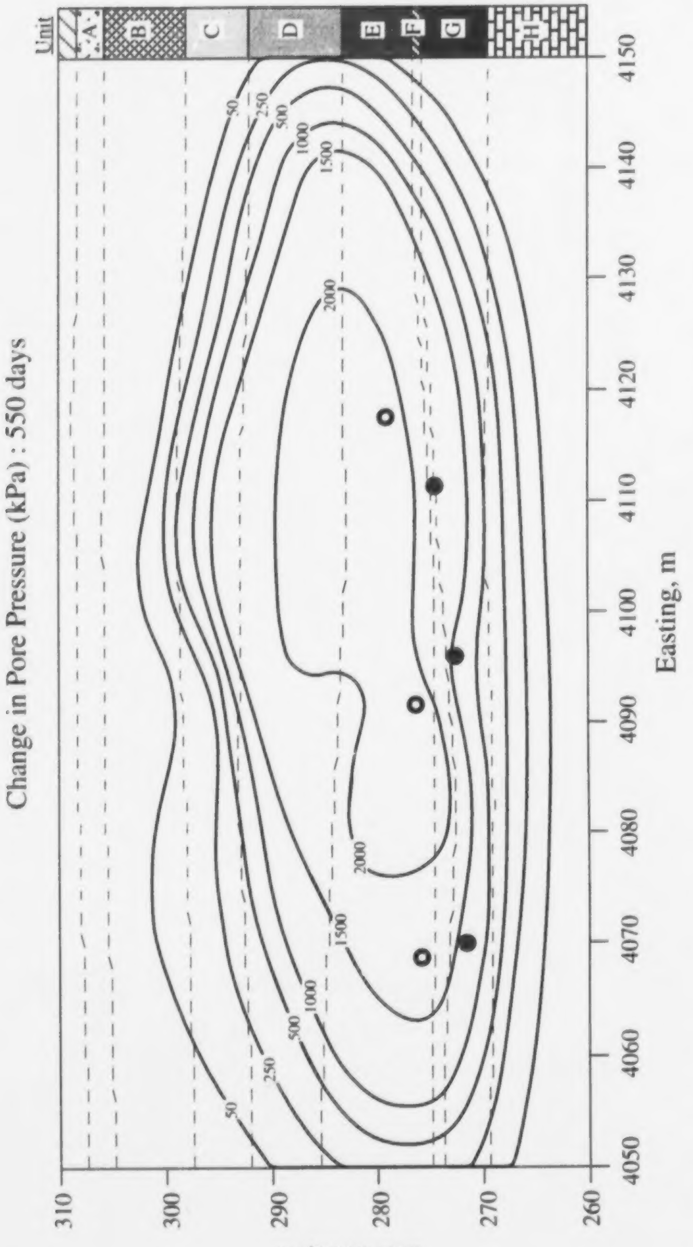

Figure F16 Pore Pressure Distribution within Geotechnical Cross Section at Time 7.9

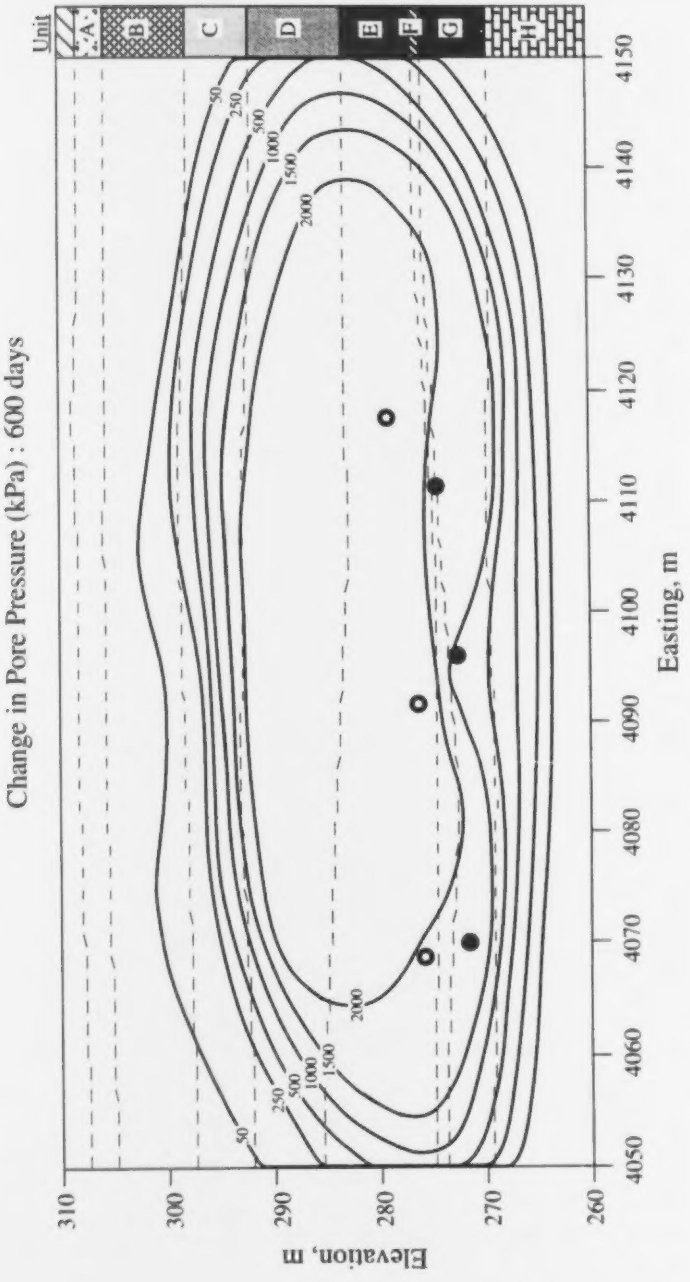

Figure F17 Pore Pressure Distribution within Geotechnical Cross Section at Time 8.6

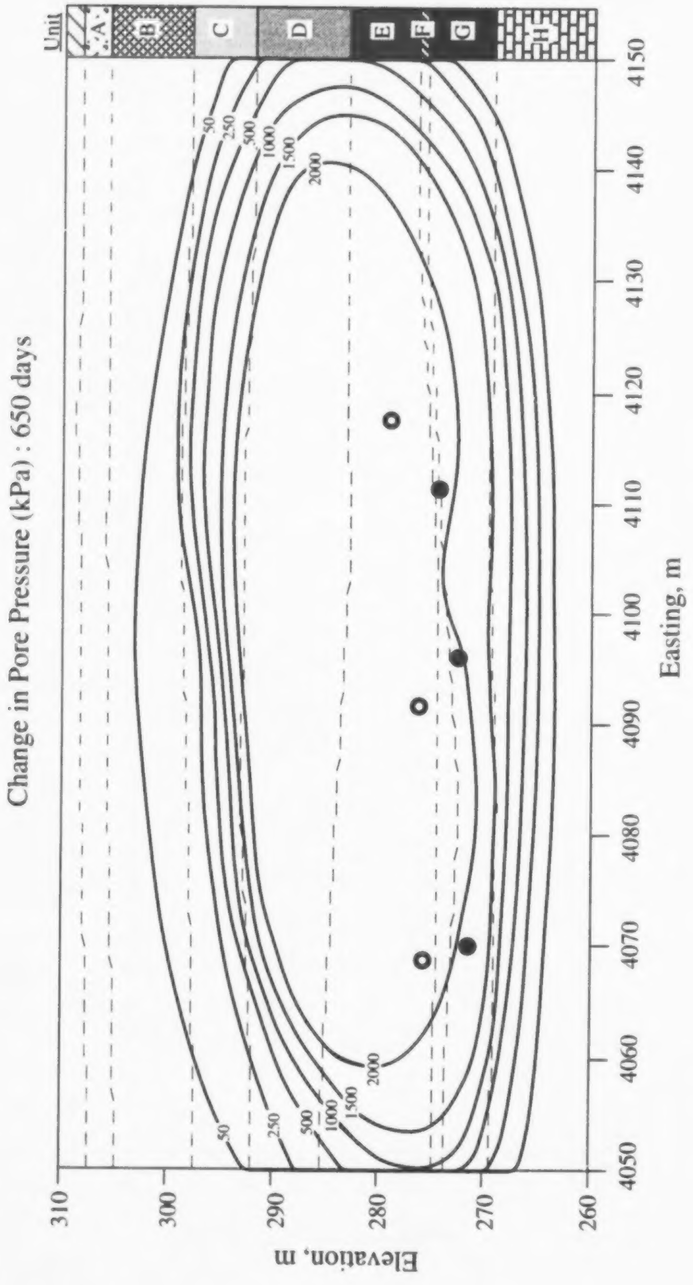

Figure F18 Pore Pressure Distribution within Geotechnical Cross Section at Time 9.3

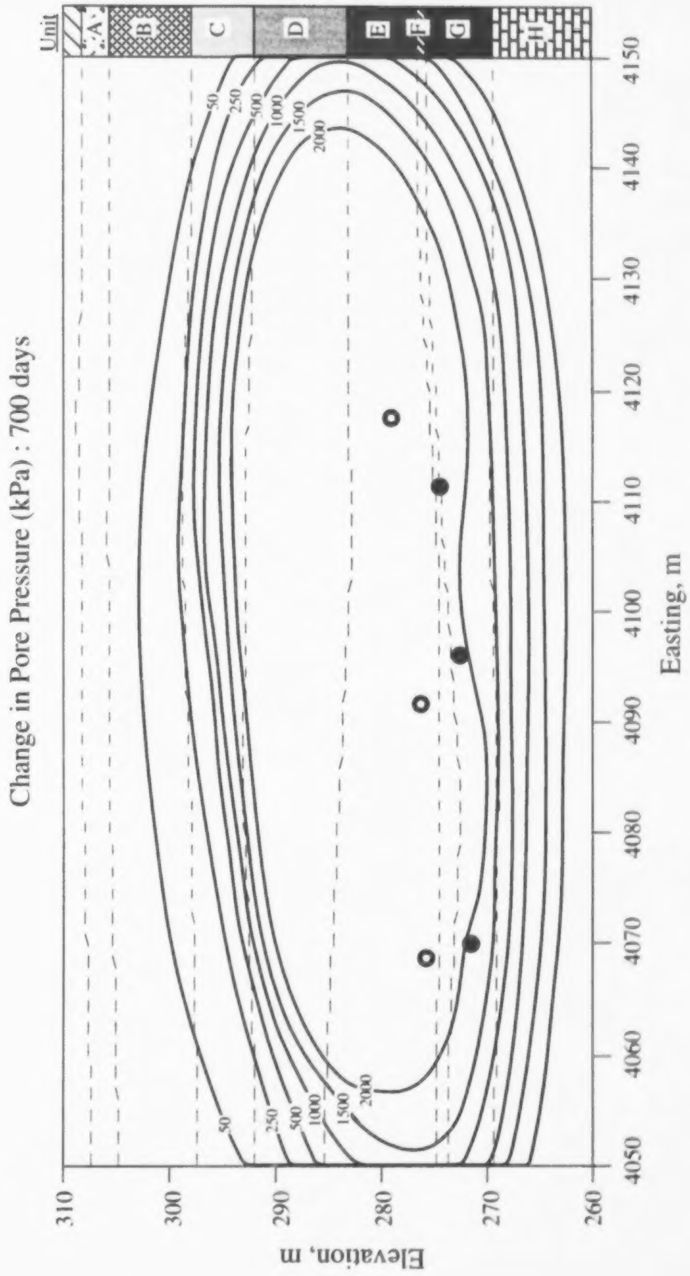

Figure F19 Pore Pressure Distribution within Geotechnical Cross Section at Time 10.0

APPENDIX G

Specimen Data

Test Name: OSDTE1
Apparatus: Consolidometer
Sample Elev.: 284.15 m
UTF Well: AGI4
Geologic Unit: D

Specimen Data

Diameter	5.33	cm
Height	3.22	cm
Volume	71.78	cm^3
Mass	133.30	grams
Density	1.86	gm/cm^3
V_s	41.09	cm^3
V_v	30.69	cm^3
I_D	16.3	%

Soxhlet Extraction:

	Before			After	
Water	4.2	%	Water	1.3	%
Bitumen	14.1	%	Bitumen	14.9	%
Solids	81.7	%	Solids	83.8	%

Fluid Saturation	77.7	%
Porosity	42.7	%
Specific Gravity	2.66	
Fines Content (< 74 μm)	4.2	%

Grain Size Analysis

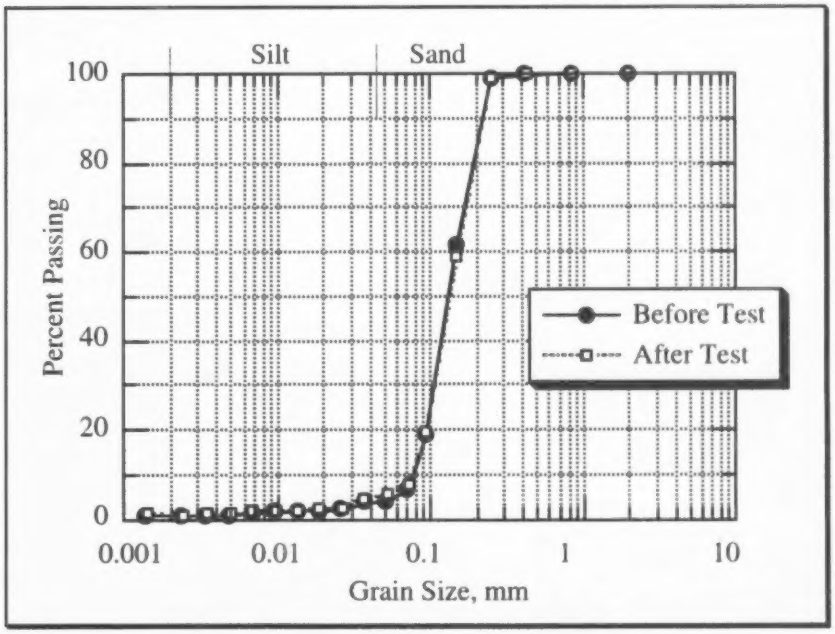

Test Name: OSDTE2
Apparatus: Consolidometer
Sample Elev.: 284.55 m
UTF Well: AGI4
Geologic Unit: D

Specimen Data

Diameter	5.33	cm
Height	2.88	cm
Volume	64.33	cm^3
Mass	128.6	grams
Density	2.00	gm/cm^3
V_s	40.72	cm^3
V_v	23.62	cm^3
I_D	10.5	%

Soxhlet Extraction:

	Before			After	
Water	3.0	%	Water	10.8	%
Bitumen	13.1	%	Bitumen	6.2	%
Solids	83.9	%	Solids	83.0	%

Fluid Saturation	85.6	%
Porosity	36.7	%
Specific Gravity	2.65	
Fines Content (< 74 μm)	13.3	%

Grain Size Analysis

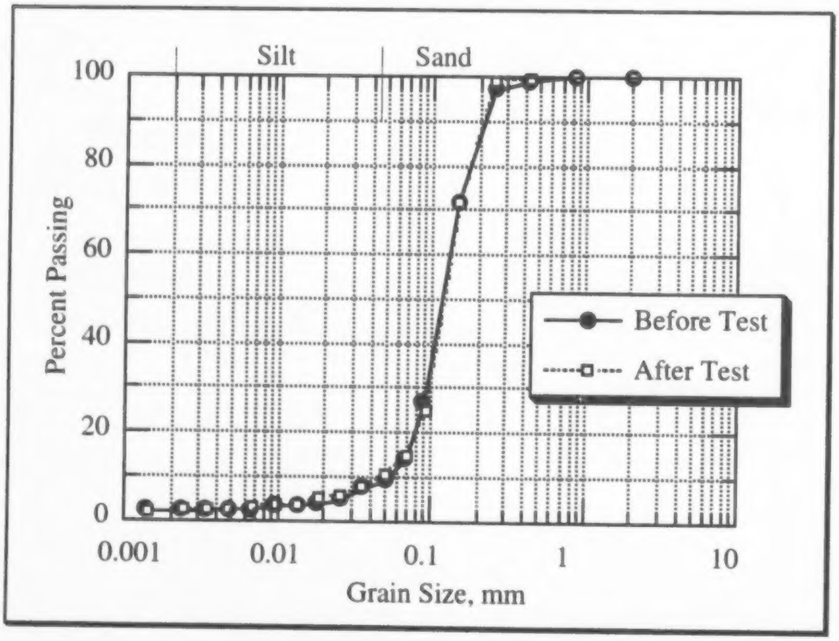

Test Name:	OSUTE1
Apparatus:	Consolidometer
Sample Elev.:	284.45 m
UTF Well:	AGI4
Geologic Unit:	D

Specimen Data

Diameter	5.31	cm
Height	2.66	cm
Volume	58.91	cm^3
Mass	117.9	grams
Density	2.00	gm/cm^3
V_s	37.33	cm^3
V_v	21.58	cm^3
I_D	10.5	%

Soxhlet Extraction:

	Before			After	
Water	3.0	%	Water	9.1	%
Bitumen	13.1	%	Bitumen	8.8	%
Solids	83.9	%	Solids	82.1	%

Fluid Saturation	88.0	%
Porosity	36.6	%
Specific Gravity	2.65	
Fines Content (< 74 μm)	8.0	%

Grain Size Analysis

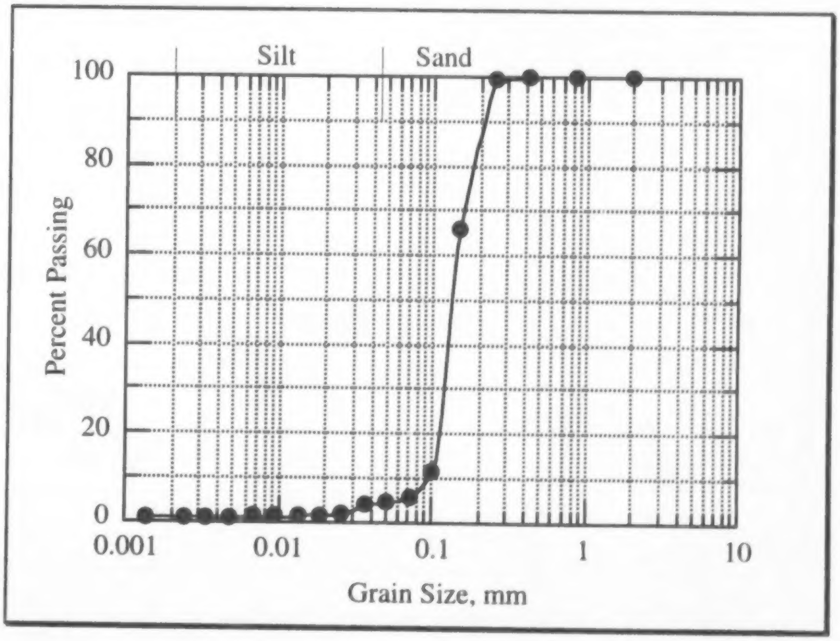

Test Name: OSUTE2
Apparatus: Consolidometer
Sample Elev.: 284.35 m
UTF Well: AGI4
Geologic Unit: D

Specimen Data

Diameter	5.31	cm
Height	2.76	cm
Volume	61.12	cm^3
Mass	122.5	grams
Density	2.00	gm/cm^3
V_s	38.78	cm^3
V_v	22.34	cm^3
I_D	10.6	%

Soxhlet Extraction:

	Before			After	
Water	3.0	%	Water	5.2	%
Bitumen	13.1	%	Bitumen	11.4	%
Solids	83.9	%	Solids	83.4	%

Fluid Saturation	86.2	%
Porosity	36.6	%
Specific Gravity	2.68	
Fines Content (< 74 μm)	3.3	%

Grain Size Analysis

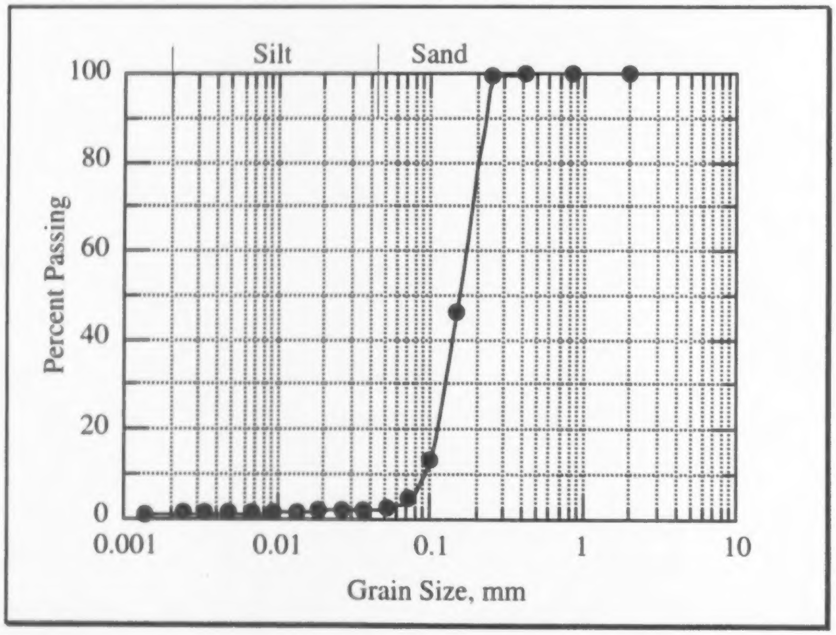

Test Name: OSTHC1
Apparatus: Thermal Conductivity Cell
Sample Elev.: 280.3 m
UTF Well: AGI1
Geologic Unit: E

Specimen Data

Outer Diam.	7.61	cm
Inner Diam.	.635	cm
Height	16.50	cm
Volume	745.26	cm^3
Mass	1426.9	grams
Density	1.92	gm/cm^3
V_s	451.22	cm^3
V_v	294.10	cm^3
I_D	18.6	%

Soxhlet Extraction:

	Before			After	
Water	1.9	%	Water	n/a	%
Bitumen	14.3	%	Bitumen	n/a	%
Solids	83.8	%	Solids	n/a	%

Fluid Saturation	76.6	%
Porosity	39.5	%
Specific Gravity	2.67	
Fines Content (< 74 μm)	1.8	%

Grain Size Analysis

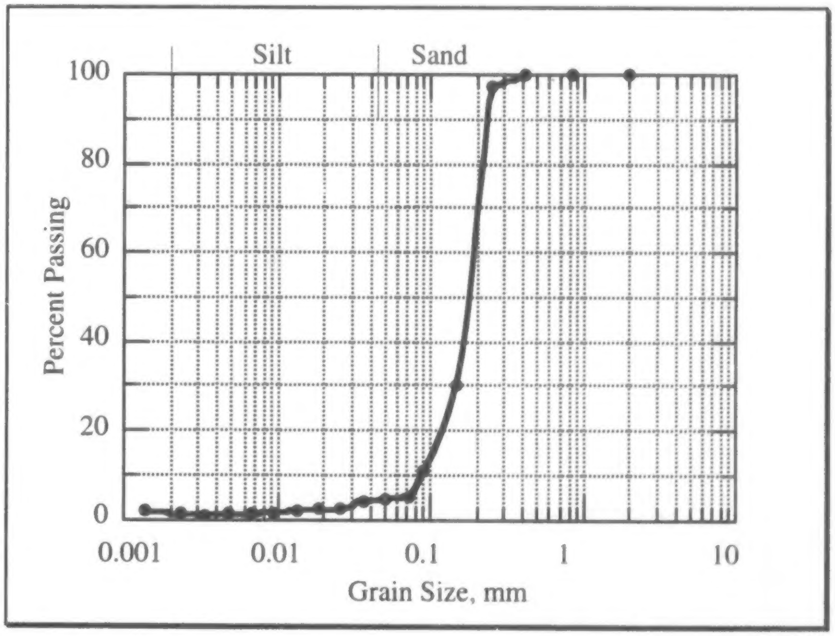

Test Name: OSTHC2
Apparatus: Thermal Conductivity Cell
Sample Elev.: 280.05 m
UTF Well: AGI1
Geologic Unit: E

Specimen Data

Outer Diam.	7.53	cm
Inner Diam.	.635	cm
Height	16.0	cm
Volume	707.3	cm^3
Mass	1365.1	grams
Density	1.93	gm/cm^3
V_s	430.1	cm^3
V_v	277.2	cm^3
I_D	16.0	%

Soxhlet Extraction:

Before			After		
Water	1.9	%	Water	2.8	%
Bitumen	14.6	%	Bitumen	14.8	%
Solids	83.5	%	Solids	82.4	%

Fluid Saturation	79.2	%
Porosity	39.2	%
Specific Gravity	2.64	
Fines Content (< 74 μm)	5.7	%

Grain Size Analysis

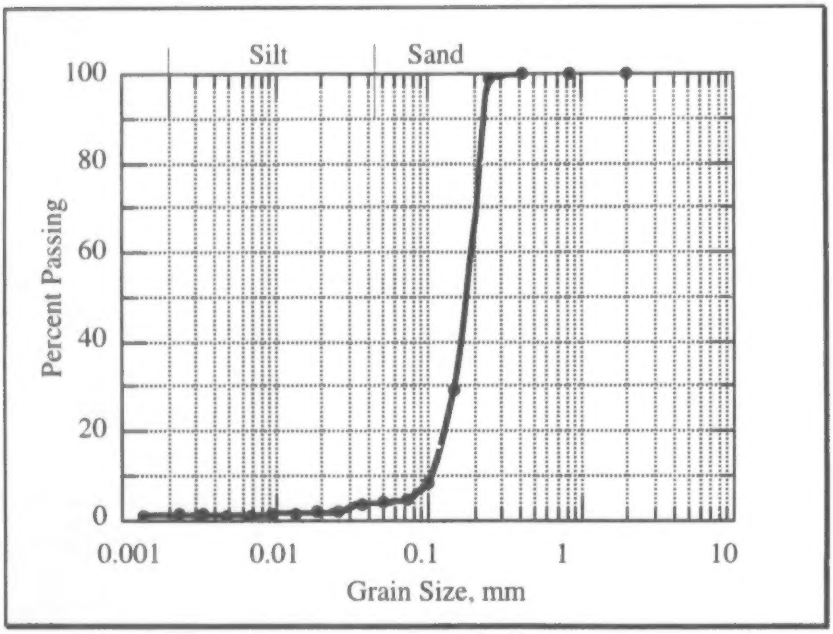

Test Name: OSRTR1
Apparatus: High Temperature Triaxial Cell
Sample Elev.: 274.8 m
UTF Well: AGI1
Geologic Unit: E

Specimen Data

Diameter	5.33	cm
Height	10.59	cm
Volume	236.18	cm^3
Mass	441.85	grams
Density	1.87	gm/cm^3
V_s	137.1	cm^3
V_v	99.1	cm^3
I_D	17.0	%

Soxhlet Extraction:

	Before			After	
Water	2.1	%	Water	n/a	%
Bitumen	15.7	%	Bitumen	n/a	%
Solids	82.2	%	Solids	n/a	%

Fluid Saturation	77.3	%
Porosity	42.0	%
Specific Gravity	2.65	
Fines Content (< 74 µm)	n/a	%

Test Name: OSRTR2
Apparatus: High Temperature Triaxial Cell
Sample Elev.: 275.7 m
UTF Well: AGI1
Geologic Unit: E

Specimen Data

Diameter	5.35	cm
Height	10.78	cm
Volume	242.40	cm^3
Mass	465.02	grams
Density	1.92	gm/cm^3
V_s	143.0	cm^3
V_v	99.4	cm^3
I_D	11.0	%

Soxhlet Extraction:

	Before			After	
Water	1.8	%	Water	n/a	%
Bitumen	16.7	%	Bitumen	n/a	%
Solids	81.5	%	Solids	n/a	%

Fluid Saturation	84.3	%
Porosity	41.0	%
Specific Gravity	2.65	
Fines Content (< 74 µm)	n/a	%

Test Name: OSRTR3
Apparatus: High Temperature Triaxial Cell
Sample Elev.: 280.4 m
UTF Well: AGI4
Geologic Unit: E

Specimen Data

Diameter	5.35	cm
Height	10.79	cm
Volume	242.37	cm^3
Mass	444.74	grams
Density	1.84	gm/cm^3
V_s	138.8	cm^3
V_v	103.6	cm^3
I_D	21.8	%

Soxhlet Extraction:

	Before			After	
Water	1.8	%	Water	n/a	%
Bitumen	15.5	%	Bitumen	n/a	%
Solids	82.7	%	Solids	n/a	%

Fluid Saturation	72.4	%
Porosity	42.7	%
Specific Gravity	2.65	
Fines Content (< 74 μm)	n/a	%

Test Name: OSGAS1
Apparatus: Gas Evolution Cell
Sample Elev.: 279.85 m
UTF Well: AGI1
Geologic Unit: E

Specimen Data

Diameter	4.91	cm
Height	10.12	cm
Volume	191.42	cm^3
Mass	376.11	grams
Density	1.97	gm/cm^3
V_s	119.3	cm^3
V_v	72.1	cm^3
V_{water}	5.0	cm^3
$V_{bitumen}$	53.4	cm^3
I_D	14.6	%

Soxhlet Extraction:

	Before			After	
Water	1.3	%	Water	n/a	%
Bitumen	14.6	%	Bitumen	n/a	%
Solids	84.1	%	Solids	n/a	%

Fluid Saturation	81.0	%
Porosity	37.7	%
Specific Gravity	2.65	
Fines Content (< 74 μm)	n/a	%

Test Name: OSGAS2
Apparatus: Gas Evolution Cell
Sample Elev.: 272.05 m
UTF Well: AGI4
Geologic Unit: G

Specimen Data

Diameter	5.06	cm
Height	10.19	cm
Volume	205.07	cm^3
Mass	393.60	grams
Density	1.92	gm/cm^3
V_s	120.7	cm^3
V_v	84.4	cm^3
V_{water}	11.1	cm^3
$V_{bitumen}$	60.9	cm^3
I_D	10.2	%

Soxhlet Extraction:

Before			After		
Water	2.8	%	Water	n/a	%
Bitumen	15.9	%	Bitumen	n/a	%
Solids	81.3	%	Solids	n/a	%

Fluid Saturation	85.3	%
Porosity	41.2	%
Specific Gravity	2.65	
Fines Content (< 74 μm)	n/a	%

Test Name: OSGSS1 & OSGSS2
Apparatus: Gas Evolution Cell
Sample Elev.: 279.8 m
UTF Well: AGI1
Geologic Unit: E

Specimen Data

Diameter	5.04	cm
Height	10.16	cm
Volume	202.23	cm^3
Mass	396.32	grams
Density	1.96	gm/cm^3
V_s	124.9	cm^3
V_v	77.4	cm^3
V_{water}	5.19	cm^3
$V_{bitumen}$	58.5	cm^3
I_D	13.3	%

Soxhlet Extraction:

Before			After		
Water	1.3	%	Water	n/a	%
Bitumen	15.2	%	Bitumen	n/a	%
Solids	83.5	%	Solids	n/a	%

Fluid Saturation	82.3	%
Porosity	38.3	%
Specific Gravity	2.65	
Fines Content (< 74 μm)	n/a	%

Test Name: OSGSS3
Apparatus: Gas Evolution Cell
Sample Elev.: 272.05 m
UTF Well: AGI4
Geologic Unit: G

Specimen Data

Diameter	5.04	cm
Height	10.16	cm
Volume	202.29	cm^3
Mass	386.9	grams
Density	1.91	gm/cm^3
V_s	120.0	cm^3
V_v	82.3	cm^3
V_{water}	7.51	cm^3
$V_{bitumen}$	59.7	cm^3
I_D	13.1	%

Soxhlet Extraction:

Before			After		
Water	1.9	%	Water	n/a	%
Bitumen	15.9	%	Bitumen	n/a	%
Solids	82.2	%	Solids	n/a	%

Fluid Saturation	81.6	%
Porosity	40.6	%
Specific Gravity	2.65	
Fines Content (< 74 µm)	n/a	%

Test Name: LSUTE1
Apparatus: Consolidometer
Sample Elev.: 275.85 m
UTF Sample #: GT92
UTF Well: AGI3
Geologic Unit: F

Specimen Data

Diameter	5.27	cm
Height	2.93	cm
Volume	63.75	cm^3
Mass	143.99	grams
Density	2.29	gm/cm^3
V_{solids}	49.4	cm^3
V_{voids}	14.4	cm^3

Soxhlet Extraction:

Water	6.7	%
Bitumen	2.0	%
Solids	91.3	%

Fluid Saturation	88.3	%
Porosity	22.6	%
Specific Gravity	2.7	
W (Before)	6.7	%
W (After)	9.0	%

Test Name: LSTHC1
Apparatus: Thermal Conductivity Cell
Sample Elev.: 275.7 m
UTF Sample #: GT93
UTF Well: AGI3
Geologic Unit: F

Specimen Data

Diameter	7.42	cm
Height	16.22	cm
Volume	700.32	cm^3
Mass	1641.1	grams
Density	2.34	gm/cm^3
V_{solids}	550.7	cm^3
V_{voids}	144.4	cm^3

Soxhlet Extraction: (same as GT92)

Water	6.7	%
Bitumen	2.0	%
Solids	91.3	%
Fluid Saturation	97.4	%
Porosity	20.8	%
Specific Gravity	2.7	
W (Before)	5.1	%
W (After)	n/a	%

Supplementary Data:

Compression Wave Velocity .... $V_P = 775$ m/s
Shear Wave Velocity .... $V_S = 478$ m/s

Test Name: LSRTR1
Apparatus: Room Temperature Triaxial Cell
Sample Elev.: 275.0 m
UTF Sample #: GT98
UTF Well: AGI2
Geologic Unit: F

Specimen Data

Diameter	5.10	cm
Height	9.76	cm
Volume	198.98	cm^3
Mass	412.12	grams
Density	2.07	gm/cm^3
V_{solids}	136.2	cm^3
V_{voids}	62.8	cm^3

Soxhlet Extraction:

Water	4.8	%
Bitumen	6.0	%
Solids	89.2	%
Fluid Saturation	69.7	%
Porosity	31.6	%
Specific Gravity	2.7	
W (Before)	5.7	%
W (After)	n/a	%

Test Name: LSRTR2
Apparatus: Room Temperature Triaxial Cell
Sample Elev.: 271.45 m
UTF Sample #: GT22
UTF Well: AGI1
Geologic Unit: F

Specimen Data

Diameter	5.09	cm
Height	9.73	cm
Volume	197.89	cm^3
Mass	458.08	grams
Density	2.32	gm/cm^3
V_{solids}	159.8	cm^3
V_{voids}	38.1	cm^3

Soxhlet Extraction:

Water	5.8	%
Bitumen	0.1	%
Solids	94.2	%

Fluid Saturation	69.8	%
Porosity	19.3	%
Specific Gravity	2.7	
W (Before)	5.0	%
W (After)	n/a	%

Test Name: LSRTR3
Apparatus: Room Temperature Triaxial Cell
Sample Elev.: 270.6 m
UTF Sample #: GT23
UTF Well: AGI1
Geologic Unit: F

Specimen Data

Diameter	5.05	cm
Height	10.11	cm
Volume	202.45	cm^3
Mass	459.32	grams
Density	2.27	gm/cm^3
V_{solids}	158.0	cm^3
V_{voids}	44.4	cm^3

Soxhlet Extraction:

Water	6.4	%
Bitumen	0.7	%
Solids	92.9	%

Fluid Saturation	73.2	%
Porosity	21.9	%
Specific Gravity	2.7	
W (Before)	10.0	%
W (After)	n/a	%

Test Name: LSHTR1
Apparatus: High Temperature Triaxial Cell
Sample Elev.: 273.65 m
UTF Sample #: GT100
UTF Well: AGI2
Geologic Unit: F

Specimen Data

Diameter	5.34	cm
Height	10.80	cm
Volume	241.88	cm^3
Mass	535.61	grams
Density	2.21	gm/cm^3
V_{solids}	181.9	cm^3
V_{voids}	59.9	cm^3

Soxhlet Extraction:

Water	7.2	%
Bitumen	2.1	%
Solids	90.7	%

Fluid Saturation	82.5	%
Porosity	24.8	%
Specific Gravity	2.67	
W (Before)	8.4	%
W (After)	n/a	%

Test Name: LSHTR2
Apparatus: High Temperature Triaxial Cell
Sample Elev.: 273.75 m
UTF Sample #: GT99
UTF Well: AGI2
Geologic Unit: F

Specimen Data

Diameter	5.38	cm
Height	10.77	cm
Volume	244.92	cm^3
Mass	541.33	grams
Density	2.21	gm/cm^3
V_{solids}	179.4	cm^3
V_{voids}	65.6	cm^3

Soxhlet Extraction:

Water	7.4	%
Bitumen	3.8	%
Solids	88.8	%

Fluid Saturation	91.6	%
Porosity	26.8	%
Specific Gravity	2.68	
W (Before)	2.7	%
W (After)	n/a	%

Test Name: LSHTR3
Apparatus: High Temperature Triaxial Cell
Sample Elev.: 276.0 m
UTF Sample #: GT91
UTF Well: AGI3
Geologic Unit: F

Specimen Data

Diameter	5.34	cm
Height	10.74	cm
Volume	240.53	cm^3
Mass	540.51	grams
Density	2.25	gm/cm^3
V_{solids}	180.2	cm^3
V_{voids}	60.4	cm^3

Soxhlet Extraction:

Water	9.2	%
Bitumen	0.8	%
Solids	90.0	%

Fluid Saturation	89.3	%
Porosity	25.1	%
Specific Gravity	2.70	
W (Before)	7.8	%
W (After)	n/a	%

Test Name: USDTE1
Apparatus: Consolidometer
Sample Elev.: 291.75 m
UTF Sample #: GT54
UTF Well: AGI1
Geologic Unit: C

Specimen Data

Diameter	5.28	cm
Height	2.38	cm
Volume	52.06	cm^3
Mass	116.57	grams
Density	2.24	gm/cm^3
V_{solids}	38.7	cm^3
V_{voids}	13.3	cm^3

Soxhlet Extraction:

Water	8.3	%
Bitumen	2.0	%
Solids	89.7	%

Fluid Saturation	89.5	%
Porosity	25.6	%
Specific Gravity	2.70	
W (Before)	3.8	%
W (After)	12.3	%

Test Name: USUTE1
Apparatus: Consolidometer
Sample Elev.: 293.8 m
UTF Sample #: GT81
UTF Well: AT7
Geologic Unit: C

Specimen Data

Diameter	5.29	cm
Height	2.42	cm
Volume	52.98	cm^3
Mass	120.95	grams
Density	2.28	gm/cm^3
V_{solids}	40.3	cm^3
V_{voids}	12.7	cm^3

Soxhlet Extraction:

Water	4.6	%
Bitumen	5.4	%
Solids	90.0	%
Fluid Saturation	94.0	%
Porosity	23.9	%
Specific Gravity	2.70	
W (Before)	6.8	%
W (After)	12.7	%

Supplementary Data:
Hard, grey shale with no visible lenses of oil sands
General Composition: ≈ 0% oil sands and ≈ 100% shale

Test Name: USUTE2
Apparatus: Consolidometer
Sample Elev.: 304.75 m
UTF Sample #: GT41
UTF Well: AGI1
Geologic Unit: B

Specimen Data

Diameter	5.30	cm
Height	3.03	cm
Volume	66.81	cm^3
Mass	140.50	grams
Density	2.10	gm/cm^3
V_{solids}	46.0	cm^3
V_{voids}	20.8	cm^3

Soxhlet Extraction:

Water	11.0	%
Bitumen	0.6	%
Solids	88.4	%
Fluid Saturation	78.2	%
Porosity	31.1	%
Specific Gravity	2.70	
W (Before)	9.0	%
W (After)	n/a	%

Supplementary Data:

Primarily shale with ≈ 3mm thick lenses of oil sands
General Composition: ≈ 15% oil sands and ≈ 85% shale

Test Name: USTHC1
Apparatus: Thermal Conductivity Cell
Sample Elev.: 295.0 m
UTF Sample #: GT80
UTF Well: AT7
Geologic Unit: C

Specimen Data

Diameter	7.57	cm
Height	14.43	cm
Volume	643.65	cm^3
Mass	1428.9	grams
Density	2.22	gm/cm^3
V_{solids}	476.3	cm^3
V_{voids}	167.4	cm^3

Soxhlet Extraction:

Water	4.6	%
Bitumen	5.4	%
Solids	90.0	%

Fluid Saturation	84.0	%
Porosity	26.0	%
Specific Gravity	2.70	
W (Before)	8.0	%
W (After)	n/a	%

Supplementary Data:

Dark grey shale with thin lenses of oil sands
General Composition: ≈ 10% oil sands and ≈ 90% shale

Compression Wave Velocity .... $V_P = 743$ m/s
Shear Wave Velocity .... $V_S = 449$ m/s

Test Name: USRTR1
Apparatus: High Temperature Triaxial Cell
Sample Elev.: 302.3 m
UTF Sample #: GT44
UTF Well: AGI1
Geologic Unit: B

Specimen Data

Diameter	5.38	cm
Height	10.57	cm
Volume	239.80	cm^3
Mass	515.58	grams
Density	2.15	gm/cm^3
V_{solids}	176.3	cm^3
V_{voids}	63.5	cm^3

Soxhlet Extraction:

Water	7.5	%
Bitumen	1.2	%
Solids	91.3	%

Fluid Saturation	70.3	%
Porosity	26.5	%
Specific Gravity	2.67	
W (Before)	6.3	%
W (After)	n/a	%

Test Name: USRTR2
Apparatus: High Temperature Triaxial Cell
Sample Elev.: 287.45 m
UTF Sample #: GT89
UTF Well: AGI3
Geologic Unit: D

Specimen Data

Diameter	5.34	cm
Height	10.30	cm
Volume	230.50	cm^3
Mass	479.60	grams
Density	2.08	gm/cm^3
V_{solids}	156.6	cm^3
V_{voids}	73.9	cm^3

Soxhlet Extraction:

Water	5.7	%
Bitumen	7.1	%
Solids	87.2	%

Fluid Saturation	81.7	%
Porosity	32.1	%
Specific Gravity	2.67	
W (Before)	6.9	%
W (After)	n/a	%

Test Name: USRTR3
Apparatus: High Temperature Triaxial Cell
Sample Elev.: 304.4 m
UTF Sample #: GT137
UTF Well: AT4
Geologic Unit: B

Specimen Data

Diameter	5.35	cm
Height	10.78	cm
Volume	242.09	cm^3
Mass	504.80	grams
Density	2.09	gm/cm^3
V_{solids}	166.7	cm^3
V_{voids}	75.4	cm^3

Soxhlet Extraction:

Water	11.2	%
Bitumen	0.3	%
Solids	88.5	%

Fluid Saturation	76.9	%
Porosity	31.1	%
Specific Gravity	2.68	
W (Before)	12.7	%
W (After)	n/a	%

Test Name: USRTR4
Apparatus: High Temperature Triaxial Cell
Sample Elev.: 301.45 m
UTF Sample #: GT45
UTF Well: AGI1
Geologic Unit: B

Specimen Data

Diameter	5.37	cm
Height	10.79	cm
Volume	244.67	cm^3
Mass	500.95	grams
Density	2.05	gm/cm^3
V_{solids}	168.9	cm^3
V_{voids}	75.8	cm^3

Soxhlet Extraction:

Water	7.1	%
Bitumen	2.9	%
Solids	90.0	%

Fluid Saturation	65.5	%
Porosity	31.0	%
Specific Gravity	2.67	
W (Before)	9.1	%
W (After)	n/a	%

Test Name: USHTR1
Apparatus: High Temperature Triaxial Cell
Sample Elev.: 300.0 m
UTF Sample #: GT47
UTF Well: AGI1
Geologic Unit: B

Specimen Data

Diameter	5.37	cm
Height	10.78	cm
Volume	244.15	cm^3
Mass	511.75	grams
Density	2.10	gm/cm^3
V_{solids}	170.1	cm^3
V_{voids}	74.0	cm^3

Soxhlet Extraction:

Before			After		
Water	2.6	%	Water	9.5	%
Bitumen	16.5	%	Bitumen	2.9	%
Solids	80.9	%	Solids	87.6	%

Fluid Saturation	74.4	%
Porosity	30.3	%
Specific Gravity	2.68	
W (Before)	8.5	%
W (After)	n/a	%

Test Name: USHTR2
Apparatus: High Temperature Triaxial Cell
Sample Elev.: 283.95 m
UTF Sample #: GT97
UTF Well: AGI2
Geologic Unit: D

Specimen Data

Diameter	5.35	cm
Height	10.78	cm
Volume	242.23	cm^3
Mass	523.71	grams
Density	2.16	gm/cm^3
V_{solids}	177.1	cm^3
V_{voids}	65.2	cm^3

Soxhlet Extraction:

Before			After		
Water	6.4	%	Water	5.4	%
Bitumen	3.0	%	Bitumen	5.4	%
Solids	90.6	%	Solids	89.2	%

Fluid Saturation	74.8	%
Porosity	26.9	%
Specific Gravity	2.68	
W (Before)	4.9	%
W (After)	n/a	%

Test Name: USHTR3
Apparatus: High Temperature Triaxial Cell
Sample Elev.: 302.65 m
UTF Sample #: GT43
UTF Well: AGI1
Geologic Unit: B

Specimen Data

Diameter	5.32	cm
Height	10.77	cm
Volume	239.31	cm^3
Mass	485.24	grams
Density	2.03	gm/cm^3
V_{solids}	167.0	cm^3
V_{voids}	72.3	cm^3

Soxhlet Extraction:

Before			After		
Water	6.9	%	Water	10.0	%
Bitumen	1.3	%	Bitumen	2.4	%
Solids	91.8	%	Solids	87.6	%

Fluid Saturation	54.1	%
Porosity	30.2	%
Specific Gravity	2.67	
W (Before)	10.8	%
W (After)	n/a	%

Test Name: USHTR4
Apparatus: High Temperature Triaxial Cell
Sample Elev.: 298.3 m
UTF Sample #: GT49
UTF Well: AGI1
Geologic Unit: B

Specimen Data

Diameter	5.33	cm
Height	10.88	cm
Volume	242.76	cm^3
Mass	493.64	grams
Density	2.03	gm/cm^3
V_{solids}	166.1	cm^3
V_{voids}	76.6	cm^3

Soxhlet Extraction:

Before			After		
Water	7.4	%	Water	5.6	%
Bitumen	2.5	%	Bitumen	5.2	%
Solids	90.1	%	Solids	89.2	%

Fluid Saturation	62.7	%
Porosity	31.6	%
Specific Gravity	2.68	
W (Before)	6.3	%
W (After)	n/a	%

Test Name: LTDTE1
Apparatus: Consolidometer
Sample Elev.: 265.15 m
UTF Sample #: GT6 (1)
UTF Well: AT1
Geologic Unit: H

Specimen Data

Diameter	5.21	cm
Height	2.78	cm
Volume	59.27	cm^3
Mass	157.87	grams
Density	2.66	gm/cm^3

Moisture Content	2.0	%
Saturation	100.0	%
Porosity	5.1	%
Specific Gravity	2.75	
V_{solids}	56.3	cm^3
V_{voids}	3.0	cm^3

Test Name: LTDTE2
Apparatus: Consolidometer
Sample Elev.: 265.05 m
UTF Sample #: GT6 (2)
UTF Well: AT1
Geologic Unit: H

Specimen Data

Diameter	5.28	cm	Moisture Content	2.0	%
Height	2.42	cm	Saturation	76.3	%
Volume	52.88	cm^3	Porosity	6.7	%
Mass	138.37	grams	Specific Gravity	2.75	
Density	2.62	gm/cm^3	V_{solids}	49.3	cm^3
			V_{voids}	3.6	cm^3

Test Name: LTUTE1
Apparatus: Consolidometer
Sample Elev.: 269.15 m
UTF Sample #: GT101
UTF Well: AGI2
Geologic Unit: H

Specimen Data

Diameter	5.33	cm	Moisture Content	8.2	%
Height	2.56	cm	Saturation	100.0	%
Volume	56.97	cm^3	Porosity	18.1	%
Mass	136.36	grams	Specific Gravity	2.7	
Density	2.39	gm/cm^3	V_{solids}	46.7	cm^3
			V_{voids}	10.3	cm^3

Test Name: LTTHC1
Apparatus: Thermal Conductivity Cell
Sample Elev.: 263.25 m
UTF Sample #: GT29
UTF Well: AGI1
Geologic Unit: H

Specimen Data

Diameter	7.46	cm	Moisture Content	1.2	%
Height	15.8	cm	Saturation	50.0	%
Volume	685.37	cm^3	Porosity	6.1	%
Mass	1758.5	grams	Specific Gravity	2.70	
Density	2.57	gm/cm^3	V_{solids}	643.6	cm^3
			V_{voids}	41.8	cm^3

Supplementary Data:

Compression Wave Velocity.............. V_P = 3080 m/s
Shear Wave Velocity .... V_S = 1261 m/s

Test Name: LTTHC2
Apparatus: Thermal Conductivity Cell
Sample Elev.: 265.7 m
UTF Sample #: GT5
UTF Well: AT1
Geologic Unit: H

Specimen Data

Diameter	7.25	cm	Moisture Content	1.9	%
Height	15.6	cm	Saturation	100.0	%
Volume	638.80	cm^3	Porosity	4.6	%
Mass	1707.1	grams	Specific Gravity	2.70	
Density	2.67	gm/cm^3	V_{solids}	609.2	cm^3
			V_{voids}	29.6	cm^3

Supplementary Data:

Compression Wave Velocity.............. V_P = 3298 m/s
Shear Wave Velocity .... V_S = 1829 m/s

Test Name: LTTHC3
Apparatus: Thermal Conductivity Cell
Sample Elev.: 260.9 m
UTF Sample #: GT11
UTF Well: AT1
Geologic Unit: H

Specimen Data

Diameter	7.52	cm	Moisture Content	1.5	%
Height	15.47	cm	Saturation	100.0	%
Volume	682.55	cm^3	Porosity	3.7	%
Mass	1801.61	grams	Specific Gravity	2.70	
Density	2.64	gm/cm^3	V_{solids}	657.5	cm^3
			V_{voids}	26.3	cm^3

Supplementary Data:

Compression Wave Velocity .... $V_P = 2609$ m/s
Shear Wave Velocity .... $V_S = 2444$ m/s

Test Name: LTRUC1
Apparatus: Uniaxial Load Frame
Sample Elev.: 268.4 m
UTF Sample #: GT94 (1)
UTF Well: AGI3
Geologic Unit: H

Specimen Data

Diameter	7.39	cm	Moisture Content	n/a	%
Height	14.97	cm	Saturation		%
Volume	642.10	cm^3	Porosity		%
Mass	1712.3	grams	Specific Gravity	2.70	
Density	2.67	gm/cm^3	V_{solids}		cm^3
			V_{voids}		cm^3

Supplementary Data:

Argillaceous, nodular, olive green, soft calcareous claystone matrix

Test Name: LTRUC2
Apparatus: Uniaxial Load Frame
Sample Elev.: 260.5 m
UTF Sample #: GT32
UTF Well: AGI1
Geologic Unit: H

Specimen Data

Diameter	7.41	cm	Moisture Content	0.7	%
Height	14.94	cm	Saturation	56.7	%
Volume	644.21	cm^3	Porosity	3.2	%
Mass	1695.0	grams	Specific Gravity	2.70	
Density	2.63	gm/cm^3	V_{solids}	623.4	cm^3
			V_{voids}	20.8	cm^3

Supplementary Data:
Biogenic limestone with intraclastic, light grey, very hard microcrystalline clasts

Compression Wave Velocity.............. $V_P = 3159$ m/s
Shear Wave Velocity .... $V_S = 2220$ m/s

Test Name: LTRUC3
Apparatus: Uniaxial Load Frame
Sample Elev.: 260.85 m
UTF Sample #: GT31
UTF Well: AGI1
Geologic Unit: H

Specimen Data

Diameter	7.49	cm	Moisture Content	0.7	%
Height	14.38	cm	Saturation	76.0	%
Volume	633.60	cm^3	Porosity	2.4	%
Mass	1680.8	grams	Specific Gravity	2.70	
Density	2.65	gm/cm^3	V_{solids}	618.2	cm^3
			V_{voids}	15.4	cm^3

Supplementary Data:

Biogenic limestone
Compression Wave Velocity.............. $V_P = 5574$ m/s
Shear Wave Velocity .... $V_S = 2917$ m/s

Test Name: LTRTR1
Apparatus: High Temperature Triaxial Cell
Sample Elev.: 262.7 m
UTF Sample #: GT8
UTF Well: AT1
Geologic Unit: H

Specimen Data

Diameter	5.11	cm	Moisture Content	1.6	%
Height	9.25	cm	Saturation	60.0	%
Volume	189.83	cm^3	Porosity	6.7	%
Mass	485.60	grams	Specific Gravity	2.70	
Density	2.56	gm/cm^3	V_{solids}	177.0	cm^3
			V_{voids}	12.8	cm^3

Supplementary Data:

Argillaceous nodular limestone with mainly sub-horizontal and elongated micritic, moderately hard nodules set in a olive to light grey, calcareous claystone matix

Test Name: LTRTR2
Apparatus: High Temperature Triaxial Cell
Sample Elev.: 258.05 m
UTF Sample #: GT13
UTF Well: AT1
Geologic Unit: H

Specimen Data

Diameter	5.09	cm	Moisture Content	1.9	%
Height	9.94	cm	Saturation	100.0	%
Volume	202.53	cm^3	Porosity	4.7	%
Mass	531.05	grams	Specific Gravity	2.70	
Density	2.62	gm/cm^3	V_{solids}	193.0	cm^3
			V_{voids}	9.5	cm^3

Supplementary Data:

Alternating layers of very weak intraclastic limestone and very stong biogenic limestone

Compression Wave Velocity .... $V_P = 4457$ m/s
Shear Wave Velocity .... $V_S = 2313$ m/s

Test Name: LTRTR3
Apparatus: High Temperature Triaxial Cell
Sample Elev.: 255.9 m
UTF Sample #: GT15
UTF Well: AT1
Geologic Unit: H

Specimen Data

Diameter	5.06	cm	Moisture Content	2.4	%
Height	10.14	cm	Saturation	100.0	%
Volume	203.91	cm^3	Porosity	5.7	%
Mass	541.58	grams	Specific Gravity	2.75	
Density	2.66	gm/cm^3	V_{solids}	192.3	cm^3
			V_{voids}	11.6	cm^3

Supplementary Data:

Biohermal, intraclastic massive zones of very hard, light grey aphanitic limestone interbedded with dark brown, moderately soft calcareous carbonate mud

Test Name: LTRTR4
Apparatus: High Temperature Triaxial Cell
Sample Elev.: 268.4 m
UTF Sample #: GT25 (1)
UTF Well: AGI1
Geologic Unit: H

Specimen Data

Diameter	5.10	cm	Moisture Content	1.3	%
Height	10.16	cm	Saturation	90.0	%
Volume	207.14	cm^3	Porosity	3.7	%
Mass	545.38	grams	Specific Gravity	2.70	
Density	2.63	gm/cm^3	V_{solids}	199.4	cm^3
			V_{voids}	7.7	cm^3

Supplementary Data:

Argillaceous, nodular olive green, soft calcareous claystone matrix

Compression Wave Velocity .... $V_P = 3353$ m/s
Shear Wave Velocity .... $V_S = 2460$ m/s

Test Name: LTRTR5
Apparatus: High Temperature Triaxial Cell
Sample Elev.: 256.06 m
UTF Sample #: GT68
UTF Well: AT7
Geologic Unit: H

Specimen Data

Diameter	5.36	cm	Moisture Content	n/a	%
Height	10.39	cm	Saturation	n/a	%
Volume	234.62	cm^3	Porosity	n/a	%
Mass	630.30	grams	Specific Gravity	2.70	
Density	2.69	gm/cm^3	V_{solids}	n/a	cm^3
			V_{voids}	n/a	cm^3

Supplementary Data:

Massive zones of very hard light grey aphanitic limestone interbedded with dark brown, moderately soft carbonate mud with clasts, heavily bioturbated

Test Name: LTHTR1
Apparatus: High Temperature Triaxial Cell
Sample Elev.: 262.0 m
UTF Sample #: GT9
UTF Well: AT1
Geologic Unit: H

Specimen Data

Diameter	5.40	cm	Moisture Content	1.5	%
Height	10.78	cm	Saturation	71.7	%
Volume	246.75	cm^3	Porosity	5.4	%
Mass	640.01	grams	Specific Gravity	2.70	
Density	2.59	gm/cm^3	V_{solids}	233.5	cm^3
			V_{voids}	13.3	cm^3

Supplementary Data:

Argillaceous limestone, modular, mainly sub-horizontal and elongated micrite, moderately hard light grey within an olive to light grey argillaceous calcareous claystone

Test Name: LTHTR2
Apparatus: High Temperature Triaxial Cell
Sample Elev.: 268.9 m
UTF Sample #: GT1
UTF Well: AT1
Geologic Unit: H

Specimen Data

Diameter	5.39	cm	Moisture Content	2.0	%
Height	10.77	cm	Saturation	77.9	%
Volume	246.02	cm^3	Porosity	6.5	%
Mass	645.07	grams	Specific Gravity	2.75	
Density	2.62	gm/cm^3	V_{solids}	230.1	cm^3
			V_{voids}	15.9	cm^3

Supplementary Data:

Argillaceous, nodular, olive green, soft calcareous claystone matrix

Test Name: LTHTR3
Apparatus: High Temperature Triaxial Cell
Sample Elev.: 268.55 m
UTF Sample #: GT25 (2)
UTF Well: AGI1
Geologic Unit: H

Specimen Data

Diameter	5.40	cm	Moisture Content	1.3	%
Height	10.81	cm	Saturation	79.0	%
Volume	246.99	cm^3	Porosity	4.3	%
Mass	646.75	grams	Specific Gravity	2.70	
Density	2.62	gm/cm^3	V_{solids}	236.5	cm^3
			V_{voids}	10.5	cm^3

Supplementary Data:

Argillaceous, nodular, olive green in a soft calcareous claystone matrix

Compression Wave Velocity............. $V_P = 3353$ m/s (from GT25 (1))
Shear Wave Velocity .... $V_S = 2460$ m/s (from GT25 (1))

Test Name: LTHTR4
Apparatus: High Temperature Triaxial Cell
Sample Elev.: 251.3 m
UTF Sample #: GT19 (1)
UTF Well: AT1
Geologic Unit: H

Specimen Data

Diameter	5.41	cm	Moisture Content	0.3	%
Height	10.76	cm	Saturation	27.7	%
Volume	247.02	cm^3	Porosity	2.8	%
Mass	649.93	grams	Specific Gravity	2.70	
Density	2.63	gm/cm^3	V_{solids}	240.0	cm^3
			V_{voids}	7.0	cm^3

Test Name: LTHTR5
Apparatus: High Temperature Triaxial Cell
Sample Elev.: 251.3 m
UTF Sample #: GT19 (2)
UTF Well: AT1
Geologic Unit: H

Specimen Data

Diameter	5.35	cm	Moisture Content	0.3	%
Height	10.03	cm	Saturation	29.7	%
Volume	225.48	cm^3	Porosity	2.7	%
Mass	594.22	grams	Specific Gravity	2.70	
Density	2.64	gm/cm^3	V_{solids}	219.4	cm^3
			V_{voids}	6.1	cm^3

Supplementary Data:

Biohermal, light grey, very hard, massive

Compression Wave Velocity.............. $V_P = 14464$ m/s
Shear Wave Velocity .... $V_S = 6230$ m/s

Test Name: LTHTR6
Apparatus: High Temperature Triaxial Cell
Sample Elev.: 261.8 m
UTF Sample #: GT65
UTF Well: AT7
Geologic Unit: H

Specimen Data

Diameter	5.33	cm	Moisture Content	0.39	%
Height	10.59	cm	Saturation	19.8	%
Volume	236.38	cm^3	Porosity	5.0	%
Mass	608.42	grams	Specific Gravity	2.70	
Density	2.57	gm/cm^3	V_{solids}	224.5	cm^3
			V_{voids}	11.9	cm^3

Supplementary Data:

Argillaceous, nodular subrounded to angular nodules, micrite, moderately hard nodules within an olive green to light grey argillaceous claystone matrix

Compression Wave Velocity .... $V_P = 6919$ m/s
Shear Wave Velocity .... $V_S = 3808$ m/s